

# Sandwich Structures 7: Advancing with Sandwich Structures and Materials

*Edited by*

O.T. Thomsen, E. Bozhevolnaya and A. Lyckegaard



SANDWICH STRUCTURES 7: ADVANCING WITH SANDWICH  
STRUCTURES AND MATERIALS

# Sandwich Structures 7: Advancing with Sandwich Structures and Materials

Proceedings of the 7th International Conference  
on Sandwich Structures, Aalborg University,  
Aalborg, Denmark, 29–31 August 2005

*Edited by*

O.T. THOMSEN

*Aalborg University, Aalborg, Denmark*

E. BOZHEVOLNAYA

*Aalborg University, Aalborg, Denmark*

and

A. LYCKEGAARD

*Aalborg University, Aalborg, Denmark*

A C.I.P. Catalogue record for this book is available from the Library of Congress.

ISBN-10 1-4020-3444-X (HB)  
ISBN-13 978-1-4020-3444-2 (HB)  
ISBN-10 1-4020-3848-8 (e-book)  
ISBN-13 978-1-4020-3848-8 (e-book)

---

Published by Springer,  
P.O. Box 17, 3300 AA Dordrecht, The Netherlands.

*www.springeronline.com*

*Printed on acid-free paper*

The cover depicts the ICSS-7 logo, by Kjeld Moseholm and Anders Lyckegaard.  
© Institute of Mechanical Engineering, Aalborg University, Denmark. Used by permission.

All Rights Reserved

© 2005 Springer

No part of this work may be reproduced, stored in a retrieval system, or transmitted in any form or by any means, electronic, mechanical, photocopying, microfilming, recording or otherwise, without written permission from the Publisher, with the exception of any material supplied specifically for the purpose of being entered and executed on a computer system, for exclusive use by the purchaser of the work.

Printed in the Netherlands.

# TABLE OF CONTENTS

Preface	xvii
---------	------

## KEYNOTE LECTURES

Sandwich structures: Past, present, and future <i>J.R. Vinson</i>	3
Sandwich structures technology in commercial aviation <i>A.S. Herrmann, P.C. Zahlen and I. Zuardy</i>	13
Damage assessment and damage tolerance of FRP sandwich structures <i>B. Hayman</i>	27

## SESSIONS ORGANISED BY THE ONR (Office of Naval Research, U.S. Navy, Program Manager Dr. Y. Rajapakse)

### MECHANICS & ANALYSIS

Geometrical non-linear response of modern sandwich panels – Localized effects <i>Y. Frostig</i>	47
Global buckling of wide sandwich panels with orthotropic phases: An elasticity solution <i>G.A. Kardomateas</i>	57
Parametric study of structurally graded core junctions <i>A. Lyckegaard, E. Bozhevolnaya and O.T. Thomsen</i>	67
Local effects induced by core junctions in sandwich beams under general loading conditions <i>E. Bozhevolnaya, A. Lyckegaard and O.T. Thomsen</i>	77

Material characterization of PVC foam under static and dynamic loading <i>D.C. Loup, R.C. Matteson and A.W.J. Gielen</i>	87
DYNAMICS	
Dynamic response of anisotropic sandwich panels to underwater and in-air explosions <i>L. Librescu, S.-Y. Oh and J. Hohe</i>	97
Enhancement of blast resistance of sandwich plates <i>G.J. Dvorak and Y.A. Bahei-El-Din</i>	107
FAILURE, FRACTURE, DAMAGE AND FATIGUE	
A two-property yield, failure (fracture) criterion for isotropic matrix materials <i>R.M. Christensen</i>	117
On crack extension in foam cored sandwich fracture specimens <i>R.C. Matteson, L.A. Carlsson, F. Aviles and D.C. Loup</i>	121
Effect of geometric constraint on fracture toughness of PVC foam core sandwich beams <i>K. Shivakumar, H. Chen and A. Bhargava</i>	131
Damage evaluation of sandwich structures using vibration and thermal signatures <i>A. Cecchini, F. Just-Agosto, D. Serrano and B. Shafiq</i>	143
Fatigue performance and size effects in sandwich composites <i>B. Shafiq, A. Quispitupa, F. Just and M. Banos</i>	153
Study of fatigue endurance of conventional and modified core junctions in sandwich beams <i>E. Bozhevolnaya, A. Lyckegaard and O.T. Thomsen</i>	161
Fatigue of closed cell foams <i>D. Zenkert, A. Shipsha and M. Burman</i>	171

<i>Table of Contents</i>	vii
Fatigue of pure and nanophased sandwich composites under shear loading <i>H. Mahfuz, S. Zainuddin, M.F. Uddin, V.K. Rangari and S. Jeelani</i>	183
ENVIRONMENTAL DEGRADATION	
Sea water effects on polymeric foams and their sandwich lay-ups <i>Y.J. Weitsman, X. Li and A. Ionita</i>	193
<b>MODELLING, ANALYSIS AND DESIGN</b>	
Sandwich plates: Stresses, deflection, buckling and wrinkling loads <i>H.-R. Meyer-Piening</i>	201
Modelling of viscoelastically damped sandwich beams: A comparative study <i>H. Hu, S. Belouettar, E. Daya and M. Potier-Ferry</i>	211
A homogenization based theory for laminated and sandwich beams <i>J.S. Hansen, G. Kennedy and S.F.M. de Almeida</i>	221
Modelling of composite and sandwich plates by a trigonometric layerwise theory and multiquadrics <i>C.M.C. Roque, A.J.M. Ferreira and R.M.N. Jorge</i>	231
Stability behaviour of cylindrical and conical sandwich shells with flexible core <i>C. Zhong and H.-G. Reimerdes</i>	241
High order nonlinear contact effects in the dynamic behavior of delaminated sandwich panels with a flexible core <i>H. Schwarts-Givli, O. Rabinovitch and Y. Frostig</i>	251
Bending behavior of sandwich panels with a “soft” core and embedded rigid inserts <i>O. Rabinovitch and E. Hamed</i>	261
Elastic behaviour of Z reinforced sandwich beams <i>M. Leite, A. Silva and M. Freitas</i>	271

Wrinkling of shallow sandwich shells for the general case of multi-axial orthotropy, curvature and loading <i>V. Skvortsov and O.T. Thomsen</i>	281
Transverse stresses of a filler under multipoint loading of a sandwich panel <i>V.A. Polyakov, R.P. Shlitsa, V.V. Khitrov and V.I. Zhigun</i>	291
A triangular finite element for sandwich plates accounting for transverse core compressibility <i>S. Demiray, W. Becker and J. Hohe</i>	301
Finite element for the static and stability analysis of sandwich plates <i>M. Linke, W. Wohlers and H.-G. Reimerdes</i>	311
Two FE formulations for a rapid 3D stress analysis of composite sandwich structures <i>A. Wetzel and L. Kärger</i>	321
Sandwich materials selection charts <i>J. Pflug and I. Verpoest</i>	331
Optimal design of laminated extended & honeycomb cores sandwich panels under out-of-plane load with simply supported boundary conditions using genetic algorithm <i>M.J. Jamali, I. Rajabi and M.H. Kadivar</i>	341
Designing sandwich inserts and core junctions for maximum structural stiffness using discrete material optimization <i>J. Stegmann and E. Lund</i>	351
<b>FRACTURE AND DAMAGE TOLERANCE</b>	
On residual compressive strength prediction of composite sandwich panels after low-velocity impact damage <i>Z. Xie, A.J. Vizzini and M. Yang</i>	363
Investigation of parameters dictating damage and energy adsorption characteristics in sandwich panels <i>G. Zhou, M. Hill and N. Hookham</i>	373

<i>Table of Contents</i>	ix
Real-time damage detection of honeycomb sandwich structures using small-diameter fiber Bragg grating sensors <i>S. Minakuchi, Y. Okabe and N. Takeda</i>	383
The influence of face sheet wrinkle defects on the performance of FRP sandwich structures <i>B. Hayman, C. Berggreen and R. Pettersson</i>	393
Residual strength of debonded sandwich panels loaded with lateral pressure <i>P. Jolma, S. Segercrantz and C. Berggreen</i>	403
Measurement of interface fracture toughness of sandwich structures <i>R.C. Østergaard and B.F. Sørensen</i>	413
Numerical study of fractured sandwich composites under flexural loading <i>E.E. Theotokoglou, L.A. Carlsson, C.D. Vrettos and H. Mahfuz</i>	423
Dependence of sandwich damage initiation and crack propagation on core material fracture properties <i>L. Berger, M. Morgenthaler, W. Cantwell, K. Feichtinger and R. Elkin</i>	433
Dependence of inplane sandwich shear deformation on core material type and thickness <i>M. Morgenthaler, L. Berger, K. Feichtinger and R. Elkin</i>	441
Residual strength of in-plane loaded debonded sandwich panels. Experimental investigation <i>C. Lundsgaard-Larsen, C. Berggreen and A. Nøkkentved</i>	451
Residual strength of in-plane loaded debonded sandwich panels. Fracture mechanical modelling <i>C. Berggreen and B.C. Simonsen</i>	461
Resistance of fastenings of sandwich panels <i>P. Hassinen</i>	471

Experimental failure mode determination of GRP/PVC-foam sandwich T-joints <i>A.W.J. Gielen, W. Trouwborst and D.C. Loup</i>	477
Flexural behaviour of aluminium foam/composite structures <i>M. Styles, P. Compston and S. Kalyanasundaram</i>	487
Repair classification for sandwich panels with hail damage <i>M. Das, E. Madenci and H. Razi</i>	497
Damage tolerance assessment of repaired composite sandwich structures <i>R. Trask, B. Cripps and A. Sheno</i>	507
<b>DYNAMICS, VIBRATION AND SOUND</b>	
Dynamical transient response of shallow sandwich panel subjected to pressure field <i>S. Kadyrov and V. Skvortsov</i>	519
Effect of transverse core compressibility on dynamic buckling of sandwich structures <i>J. Hohe, L. Librescu and S.Y. Oh</i>	527
Dynamic characterisation of marine sandwich structures <i>M. Battley, I. Stenius, J. Breder and S. Edinger</i>	537
Local free vibration analysis of initially stressed curved sandwich beam <i>W. Wang and R.A. Sheno</i>	547
Vibration analysis of composite sandwich plates and layup optimization <i>H. Sekine, H. Shirahata and M. Matsuda</i>	557
Flexural vibrations of a three-layer sandwich beam <i>D. Backström and A. Nilsson</i>	567
An effective 2D linear elasticity vibrational model for layered and sandwich clamped-clamped unidirectional strips <i>S. Karczmarzyk</i>	577

<i>Table of Contents</i>	xi
Minimization of acoustic radiation from composite sandwich structures <i>H. Denli and J.Q. Sun</i>	587
On wave propagation in sandwich plates under heavy fluid loading <i>S. Sorokin and N. Peake</i>	597
Wave propagation in a sandwich plate loaded by a viscous compressible fluid <i>A.V. Chubinskiy and S.V. Sorokin</i>	605
<b>IMPACT</b>	
Impact damage on lightweight sandwich panels <i>D. Zhou and W.J. Stronge</i>	615
Ballistic resistance of 2D & 3D woven sandwich composites <i>A. Shukla, J. Grogan, S.A. Tekalur, A. Bogdanovich and R.A. Coffelt</i>	625
Impact and indentation behavior of sandwich panels <i>C.-J. Lindholm</i>	635
A comparison of low energy impact behaviour in aluminium foam and polymer foam sandwich structures <i>P. Compston, M. Styles and S. Kalyanasundaram</i>	643
Numerical modeling of sandwich panel response to ballistic loading <i>J. Kepler and M.R. Hansen</i>	653
Low velocity impact investigations of sandwich panels with different cores <i>W. Göttner and H.-G. Reimerdes</i>	661
Mechanical behavior of rubber-filled multifunctional honeycomb sandwich composite <i>H. Hao, C.-R. Joe and D.-U. Kim</i>	671
Stitching effect on static and dynamic behaviour of sandwich structures <i>B. Lascoup, Z. Aboura, K. Khellil and M. Benzeggagh</i>	681

**PROCESSING AND FABRICATION**

Continuous manufacturing and performance of 3D reinforced sandwich structures <i>G. Le Roy, C. Binetruy and P. Krawczak</i>	693
A novel extrusion-welded sandwich structure for thermoplastic composite storage tanks <i>E. Lagardere, M.-F. Lacrampe, O. Skawinski, P. Krawczak, C. Ducret and M. Giletti</i>	703
The opportunities of flexible foam processing for rigid foam sandwich cores <i>H. Mispreuve and L. den Haan</i>	713
Formability of lightweight, vibration damping and medium perfused sandwich sheets <i>R. Kopp, M. Nutzmann and J. van Santen</i>	723
Fabrication and mechanical properties of functionally graded micro porous metals by MIM-base powder space holder method <i>K. Nishiyabu, S. Matsuzaki and S. Tanaka</i>	733
Sandwich injection moulding and physical properties of cup-stacked carbon nanotube/polypropylene and polypropylene <i>K. Okubu, S. Tanaka, N. Oya, K. Nishiyabu, T. Yanagisawa and M. Tomita</i>	743
New ROHACELL <sup>®</sup> development for resin infusion processes <i>J. Scherble and T. Jahn</i>	753
Development and validation of a continuous production concept for thermoplastic honeycomb <i>J.P. Bratfisch, D. Vandepitte, J. Pflug and I. Verpoest</i>	763
Sandwich panel with a periodical and graded core <i>J. Nygaard, A. Lyckegaard and J. Christiansen</i>	773
Investigation of the cure process for thick composite sandwich panels <i>D.K. Jensen</i>	783

**NDE AND ENVIRONMENTAL DEGRADATION**

Automated ultrasonic inspection of large-scale sandwich structures 795  
*T.M. Wulf*

Evaluation of sandwich materials using ultrasonic air-coupled scanning technique 805  
*K.K. Borum*

Structural NDE of CFRP composite materials using Fiber Bragg Grating sensors 815  
*J. Leng, Y. Liu, X. Xu and S. Du*

Study of the hygro-mechanical behavior of corrugated cardboard 823  
*S. Allaoui, Z. Aboura and M. Benzeggagh*

**NEW MATERIALS AND MATERIALS CHARACTERISATION**

New concepts for sandwich structures 835  
*J.L. Grenestedt*

Magnesium integral foam – A new metallic sandwich structure 845  
*M. Hirschmann, C. Körner and R.F. Singer*

New improved foam core materials for advanced processing 855  
*S. Reuterlöv*

Characterisation of novel K-cor sandwich structures 865  
*P. Casari, D. Cartié and P. Davies*

Finite element analysis on out-of-plane compression properties of thermoplastic honeycomb 875  
*X. Fan, I. Verpoest and D. Vandepitte*

Deformation of foam cores in uniaxial compression-tension cycle 885  
*V. Koissin and A. Shipsha*

Loading rate effects on foam cores for marine sandwich structures 895  
*E. Lolive, P. Casari and P. Davies*

Characterization of the thermal expansion behaviour of a PVC foam core: Non-linearities and gradients across the width <i>P. Casari, C. Ferreira and F. Jacquemin</i>	905
Determination of in-plane and out-of-plane elastic constants for medium-thickness sandwich composite skins <i>H. Toftegaard and S. Goutianos</i>	915
Stochastic homogenization of polymeric foams <i>J. Hohe</i>	925
Stochastic finite element models of foam materials <i>S. Hallström and S. Ribeiro-Ayeh</i>	935
<b>APPLICATIONS AND DESIGN SOLUTIONS</b>	
Application of load carrying sandwich elements in large wind turbine blades <i>J.F. Jensen, J.P. Schultz, C. Berggreen and K. Branner</i>	947
Thermoplastic composite sandwich structure for sportive applications <i>M.M. Sommer, M. Päßler, R. Schledjewski and M. Stack</i>	957
Study of snowboard sandwich structures <i>C. Borsellino, L. Calabrese, R. Passari and A. Valenza</i>	967
Development and evaluation of an RTM bicycle frame <i>N.G. Pantelidis</i>	977
Development of new reinforced load introductions for sandwich structures <i>M.A. Roth</i>	987
Sandwich structures with composite inserts: Experimental studies <i>G. Nageswara Rao, U. Agrawal and N.K. Naik</i>	997
Development and evaluation of FRP sandwich beams containing glass fibers into phenolic foam core <i>G. Ben, A. Shoji and M. Souma</i>	1007

<i>Table of Contents</i>	xv
Experimental and numerical analysis of hollow and foam-filled A-stringer/A-former under axial compression load and bending moment <i>R. Krämer and M.A. Roth</i>	1017
Author Index	1027
Subject Index	1031

## **PREFACE**

This publication contains the printed version of the scientific articles presented at the 7th International Conference on Sandwich Structures (ICSS-7). The conference was organised by the Institute of Mechanical Engineering of Aalborg University, Aalborg, Denmark, to take place at Aalborg University on 29–31 August 2005.

Previous conferences in this series were held at the Royal Institute of Technology (KTH), Stockholm, Sweden, in 1989; the University of Florida, Gainesville, Florida, in 1992; Southampton University, Southampton, U.K., in 1995; the Royal Institute of Technology (KTH), Stockholm, Sweden, in 1998; the Federal Institute of Technology (ETH), Zurich, Switzerland, in 2001; and in Ft. Lauderdale, Florida, in 2003.

Over the last years the science and technology of sandwich structures and materials has gained an impressive momentum, and the use of sandwich structures and materials in a large variety of products covering the range from sporting goods to satellites is on the increase.

The overall objective of this conference (ICSS-7) is to provide a forum for the presentation and discussion of the latest research and technology on all aspects of sandwich structures and materials, spanning the entire spectrum of research to applications in many fields including aircraft, spacecraft, train and automotive applications, wind turbine blades, boat/ship hulls and superstructures and many others.

Looking towards the future, all forecasts show that the use of sandwich structures technology will increase even further, as this will provide many options for the effective design of affordable, reliable, and durable structures with multifunctional capabilities. The ICSS-7 and future conferences in this series will play an important role in this, and provide a forum for discussion and exchange of the latest research, as well as to act as an incubator and source of inspiration for further developments.

### **Technical Programme**

The presentations and the papers at the ICSS-7 are grouped into several broad areas, including: Modelling, analysis and design; Fracture and damage tol-

erance; Dynamics, vibration and sound; Impact and energy absorption; Processing and fabrication; NDE and environmental degradation; New materials and materials characterisation, Applications and design solutions.

The technical program of the conference consists of the presentation of 102 scientific papers in 3 parallel sessions. The truly international nature of the ICSS-7 is highlighted by the fact, that the authors of the presentations represent 30 countries from the 5 continents Asia, Europe, North America, South America and Oceania.

The ICSS-7 technical program includes 3 keynote lectures, one each morning of the days of the conference. The first, presented by Professor, Ph.D. Jack Vinson, University of Delaware, Delaware, USA, is entitled “Sandwich structures – Past, present and future”, and addresses the technical aspects of sandwich materials and structures technology in a historical perspective. The second keynote lecture, presented by Professor, Dr. Axel Herrmann, Airbus, Composite Technology Center, Stade, Germany, is entitled “Sandwich structures technology in commercial aviation – Present applications and future trends”, and addresses the state of the arts and future directions of sandwich structures technology in civil aviation. Finally, the third keynote lecture, given by Dr. Brian Hayman, of “Det Norske Veritas” (DNV), Norway, is entitled “Damage assessment and damage tolerance of FRP sandwich structures”, and addresses the very important topics of damage assessment and damage tolerance in sandwich structures.

Included in the conference are also 4 special sessions with a total of 16 presentations organised by the U.S. Navy, Office of Naval Research (ONR, Program Manager Dr. Y. Rajapakse). These special sessions present research of special interest to navy applications of sandwich structures, and sponsored entirely or in part by the ONR.

## **Acknowledgements**

The organisers of this conference wish to acknowledge the contributions of the members of the international scientific and organising committee (listed on the following page) towards the success of the ICSS-7. Their significant help in reviewing and selecting the contributions for the conference has made it possible to ensure a very high scientific standard.

The sponsors of the conference (listed on the following page) are also thanked duly for their belief in the necessity of this professional gathering and their generous financial and moral support. The support received for the general cost associated with the ICSS-7, as well as to social events throughout the conference days, has made it possible to keep the conference registration fee at a reasonable level. In addition, the support of the sponsors has made it possible to invite the keynote lecturers, and to support the attendance of

researchers from countries where the financial situation would otherwise not have allowed this.

The organisers of the ICSS-7 would like also to acknowledge and thank Springer, the publisher of the conference proceedings (in particular Nathalie Jacobs and Anneke Pot), and Jolanda Karada (Karada Publishing Services) for their patience and professionalism in preparing the printed proceedings.

Ole Thybo Thomsen  
Elena Bozhevolnaya  
Anders Lyckegaard  
Aalborg University, 10 May 2005

## **International Organising and Scientific Committee**

Dr. Mark Battley, Industrial Research Limited, New Zealand  
Professor Christophe Binetruy, Ecole des Mines de Douai, France  
Dr. Antonio Ferreira, University of Porto, Portugal  
Professor Yeoshua Frostig, Technion, Israel  
Dr. Brian Hayman, DNV, Norway  
Professor Axel Herrmann, Airbus, CTC GmbH, Germany  
Mr. Gunnar Holm, VTT, Finland  
Professor George Kardomateas, Georgia Institute of Technology, U.S.A.  
Professor Hans-Reinhard Meyer-Piening, ETH, Switzerland  
Dr. Yapa Rajapakse, Office of Naval Research, U.S.A.  
Professor Bhavani Sankar, University of Florida, U.S.A.  
Professor R. Ajit Sheno, University of Southampton, U.K.  
Professor Vitaly Skvortsov, St. Petersburg State Marine University, Russia  
Dr. Alois Starlinger, Stadler Altenrhein AG, Switzerland  
Professor C. T. Sun, Purdue University, U.S.A.  
Professor Roberto Teti, University of Naples, Italy  
Professor Jack R. Vinson, University of Delaware, U.S.A.  
Professor Dan Zenkert, Royal Institute of Technology (KTH), Sweden

## **Sponsors**

### *Primary Sponsors:*

The Obel Family Foundation, Aalborg, Denmark ([www.obel.com](http://www.obel.com))  
The Office of Naval Research, Materials S & T Division (ONR 332),  
Arlington, Virginia, U.S.A.  
([http://www.onr.navy.mil/sci\\_tech/engineering/332\\_materials](http://www.onr.navy.mil/sci_tech/engineering/332_materials))  
*Dr. Yapa D.S. Rajapakse, Program Manager, Solid Mechanics*

Degussa, Röhm GmbH & Co. KG, Germany ([www.rohacell.com](http://www.rohacell.com))  
Alcan Airex AG, Switzerland ([www.alcanairex.com](http://www.alcanairex.com) &  
[www.alcancomposites.com](http://www.alcancomposites.com))

*Sponsors:*

LM Glasfiber A/S, Denmark ([www.lmglassfiber.com](http://www.lmglassfiber.com))  
The Danish Plastics Federation, Division of Composite Materials  
([www.plastics.dk](http://www.plastics.dk))  
Institute of Mechanical Engineering, Aalborg University ([www.ime.aau.dk](http://www.ime.aau.dk))  
Faculty of Engineering and Science, Aalborg University ([www.aau.dk](http://www.aau.dk))

*Main Event Sponsor:*

DIAB Group International ([www.diabgroup.com](http://www.diabgroup.com))

*Professional Society Sponsorship and Endorsers:*

The European Society for Composite Materials (ESCM)  
The Danish Society of Mechanical Engineers under the Danish Society of  
Engineers ([www.ida.dk](http://www.ida.dk))  
Springer ([www.springeronline.com](http://www.springeronline.com))

# **KEYNOTE LECTURES**

# SANDWICH STRUCTURES: PAST, PRESENT, AND FUTURE

Jack R. Vinson

*Department of Mechanical Engineering, University of Delaware, Newark, DE 19716, USA*

**Abstract** The use of sandwich structures continues to increase rapidly for applications ranging from satellites, aircraft, ships, automobiles, rail cars, wind energy systems, and bridge construction to mention only a few. The many advantages of sandwich constructions, the development of new materials, and the need for high performance, low-weight structures insure that sandwich construction will continue to be in demand. The equations describing the behavior of sandwich structures are usually compatible with the equations developed for composite material thin-walled structures, simply by employing the appropriate in-plane, flexural, and transverse shear stiffness quantities. Only if a very flexible core is used, is a higher order theory needed.

**Keywords:** sandwich structures, sandwich history, sandwich uses, sandwich future.

## 1. INTRODUCTION

The use of sandwich structures continues to increase rapidly for applications ranging from satellites, aircraft, ships, automobiles, rail cars, wind energy systems, and bridge construction to mention only a few. The many advantages of sandwich constructions, the development of new materials, and the need for high performance, low-weight structures insure that sandwich construction will continue to be in demand. The equations describing the behavior of sandwich structures are usually compatible with the equations developed for composite material thin-walled structures, simply by employing the appropriate in-plane, flexural, and transverse shear stiffness quantities. Only if a very flexible core is used, is a higher order theory needed.

Most often there are two faces, identical in material, fiber orientation and thickness, which primarily resist the in-plane and lateral (bending) loads.

However, in special cases the faces may differ in thickness, materials, or fiber orientation, or any combination of these three. This may be due to the fact that in use one face is an external face while the other is an internal face the former sandwich is regarded as a mid-plane symmetric sandwich, the latter a mid-plane asymmetric sandwich.

A comparison between an isotropic sandwich construction and a monocoque (thin walled) construction is worthwhile. If the sandwich construction employs two identical faces of thickness  $t_f$  and a core depth of  $h_c$ , and the monocoque construction is a flat plate construction of thickness  $2t_f$ , then the monocoque plate has the same weight as the faces of the sandwich construction using the same materials. If the ratio of face thickness to core depth is  $1/20$ , the flexural stiffness of the sandwich construction has 300 times the flexural stiffness of the monocoque construction. As a result, for a given lateral load the sandwich construction results in a much lower lateral deflection, much higher overall buckling load, and much higher flexural natural vibration frequencies than does the monocoque construction of nearly the same weight. In sandwich constructions subjected to in-plane compressive or shear loads, however, in addition to overall buckling, core shear instability, face wrinkling and monocell buckling (in honeycomb cores) must also be considered.

For a comparison in face stresses, consider the same sandwich and monocoque constructions discussed above subjected to a bending moment per unit width,  $M$ . To continue the example used previously, the maximum bending stress in the sandwich face is  $1/30$  the maximum stress at the surfaces of the monocoque construction subjected to the same bending moment.

Thus for many applications, even if the weight of the core causes the weight of the sandwich to be as much as twice the weight of the monocoque construction the fact that the bending stiffness is 300 times while the maximum stresses are  $1/30$  that of the monocoque construction makes the sandwich construction very desirable.

In the following, because of page limitations, references will not be given, but the interested reader can easily obtain them by finding the publication list of the authors cited.

## 2. PAST

Noor, Burton and Bert state that the concept of sandwich construction dates back to Fairbairn in England in 1849. Also in England, sandwich construction was first used in the Mosquito night bomber of World War II which employed plywood sandwich construction. Feichtinger states also that

during World War II, the concept of sandwich construction in the United States originated with the faces made of reinforced plastic and a low density core. In 1943, Wright Patterson Air Force Base designed and fabricated the Vultee BT-15 fuselage using fiberglass-reinforced polyester as the face material using both a glass-fabric honeycomb and a balsa core.

The first research paper concerning sandwich construction was written by Marguerre in Germany in 1944 dealing with sandwich panels subjected to in-plane compressive loads. In 1948, Nicholas J. Hoff derived the differential equations and boundary conditions for the bending and buckling of sandwich plates using the Principle of Virtual Displacements, but pursued only the buckling problem. In the same year, Libove and Batdorf published a small deflection theory for sandwich plates. In 1949, Flugge published on the structural optimization of sandwich panels in which he presented nomograms for the solution of several problems. In all the above the materials were isotropic.

Also in the late 1940s, two young World War II veterans formed Hexcel Corporation, which over the decades has played the most important role of any firm in the growth of sandwich structures. Starting with honeycomb cores, even today they make well over 50% of the world's honeycomb core materials.

In 1951, Bijlaard studied sandwich optimization for the case of a given ratio between core depth and face thickness, as well as for a given thickness.

At about that time, sandwich publications began to emanate from the U.S. Forest Products Laboratory (USFPL), which was attached to the University of Wisconsin. As the name implies they were associated with the use of wood products which are in general especially orthotropic. However, their numerous publications of methods of analysis of wood sandwich structures were applicable to the same structures made of composite materials. Their publications dominated the analysis methods for sandwich structures for well over a decade, and are still valuable. Names such as March, Kuenzi and Ericksen were prolific authors with the USFPL. Also, Military Handbook 23 was published which largely involved the results of the many publication issued by the USFPL. This became the definitive document for use by industry.

In 1956, Gerard discusses sandwich plate optimization in one chapter of his landmark book, "Minimum Weight Analysis of Compression Structures." In 1957, Kaechele published a USFPL Report on the minimum weight design of sandwich panels. In 1960, Heath published a paper on the correlation among and an extension of the existing theories for flat sandwich panels subjected to lengthwise compression, including optimum design.

In 1966, Plantema, in the Netherlands, published the first book on sandwich structures, followed by another book on sandwich structures by

H.G. Allen in England in 1969. These books remained the “bibles” for sandwich structures until the mid 1990s.

Also in the mid 1960s, the U.S. Naval Air Engineering Center sponsored research with Dyna/Structures, Inc. to develop fiberglass composite sandwich constructions to compete in weight with conventional aluminum aircraft construction for aircraft. This effort was directed toward achieving a “stealth” aircraft, although that word had not yet been coined. Much of this research effort was in the development of minimum weight optimization methods. Many of these methods were later published by Vinson.

In the seventies tremendous activity began in Sweden regarding the use of composite sandwich construction for naval ship hulls. This was due largely to the leadership of Karl-Axel Olsson of the Royal Institute of Technology (KTH) in Stockholm. He led the effort among the KTH, the Swedish Royal Navy, the Swedish shipbuilders, and the Swedish banks to change the navy from continuing to use steel hulls, and switch to fiberglass composite sandwich constructions. This effort involved analysis, optimization, small scale tests, full scale tests for both underwater explosions and air explosions, etc. They were able to show that a properly designed composite sandwich hull could be as structurally sound as a steel hull. As a result, from some date in the eighties, all Royal Navy ship hulls were made of sandwich construction—a new world first. Olsson then turned his attentions to the rest of the Scandinavian countries and led them to many of the same results. Today many Scandinavian naval ship hulls are composite sandwich, as well as hundreds of the ferry boats that traverse the waters in and among the Scandinavian countries. There is no single person that has done more to contribute to the use of sandwich structures as Dr. Karl-Axel Olsson

In 1989, Ha published an overview of finite element analysis applied to sandwich construction, that was referenced even in a 2005 paper. In 1991, Bert provided a review of sandwich plate analysis, while in 1996, a review of sandwich structures by Noor, Burton and Bert provided over 800 references, all discussed in the review, and another 559 references as a supplemental bibliography.

In 1995, a monograph by Zenkert supplemented much of the material contained earlier in the Plantema and Allen texts (which by that time were out of print). Zenkert followed this by a sandwich textbook in 1996. In 1999, another sandwich textbook was published by Vinson. Hence today there are only four texts dealing primarily with sandwich Structures: Plantema, Allen, Zenkert and Vinson.

To date there have been seven International Conferences on Sandwich Constructions. They are as follows: the first in Stockholm, hosted by Karl-Axel Olsson in 1989; the second in Gainesville in 1992; the third in Southampton, hosted by H.G.Allen in 1995; the fourth in Stockholm in

1998, again hosted by Olsson; the fifth in Zurich, hosted by Hans-Reinhard Meyer-Piening in 2000; the sixth in Ft. Lauderdale, hosted by Jack R. Vinson in 2003; and now the seventh Conference is being held in Aalborg, Denmark in 2005, hosted by Ole T. Thomsen.

In 1999, the Journal of Sandwich Structures and Materials was initiated and it is the only Journal fully devoted to sandwich structures and Materials. Over 180 research papers have been published in the journal to date.

### **3. SANDWICH STRUCTURES TODAY**

In 1992 Bitzer of Hexcel gave an excellent overview of honeycomb core materials and their applications. Bitzer states that every two (or more) engine aircraft in the western world utilizes some honeycomb core sandwich, and that while only 8% of the wetted surface of the Boeing 707 is sandwich, 46% of the wetted surface of the newer Boeing 757/767 is honeycomb sandwich. In the Boeing 747, the fuselage cylindrical shell is primarily Nomex honeycomb sandwich, and the floors, side-panels, overhead bins and ceiling are also of sandwich construction.

The Beech Starship uses Nomex honeycomb with graphite and Kevlar faces for the entire structure-the first all sandwich aircraft. Also, a major portion of the space shuttle is a composite-faced honeycomb-core sandwich. Almost all satellite structures employ sandwich construction.

The U. S. Navy uses honeycomb sandwich construction for bulkheads, deck houses, and helicopter hangars to reduce weight above the waterline. Also recently, they have incorporated a complete hexagonally shaped mast on the USS Radford that is ninety three feet tall and weighs 90 tons. Not only is this a foam core sandwich but the use of exterior materials for stealth purposes make this an asymmetric sandwich. Pleasure boat hulls today are made primarily of fiberglass sandwich.

As stated earlier, the Royal Swedish navy has been using fiberglass and graphite composite sandwich construction for more than twenty years. The newest ship, the YP2000 Visby, is a stealth-optimized graphite/epoxy composite vessel using sandwich construction primarily. Similarly, the Royal Australian Navy uses high performance foam composite sandwich for its inshore mine hunters.

Since 1980, composite front cabs of locomotives have been built for the XPT locomotives in Australia, the ETR 500 locomotives in Italy, the French TGV and the Swiss locomotive 2000. Interestingly, the major design criteria are the pressure waves occurring during the crossing of two high speed trains in a tunnel. In Japan, the new Nozomi 500 bullet trains use honeycomb sandwich for the primary structure.

Also in 1995, Starlinger and Reif reported that sandwich construction is now being used in double-decker buses.

In the U.S., approximately 40% of bridges are structurally deficient or not capable of handling present demands. There are not enough tax dollars to replace all of the bridges in the conventional way. The American Society of Civil Engineers 2005 Report Card gives a “D” for the crumbling infrastructure and states that billions are needed over the next five year period. Half of the cost of bridge replacement is in rerouting traffic during construction. Using composite sandwich construction, pre-made sandwich deck panels can be put in place in days, rather than weeks by conventional construction. Add to this the advantage of no corrosion, and the light weight afforded by the composite sandwich construction. The state of Ohio instituted a plan to replace one bridge in each county with a composite sandwich bridge deck.

In Europe, COBRAE was founded (Composite Bridge Alliance Europe) which is leading the way in promoting composite bridges throughout the European Union.

Another major use for sandwich composite structures during the last decade is wind energy systems. GE Energy states they have 6900 installations worldwide, and that their growth rate is 20% per annum. The Global Wind Energy Council ranks the leaders in wind energy installations as: Germany, Spain, U.S., and Denmark.

The core of a sandwich structure can be of almost any material or architecture, but in general, cores fall into four types:

- a) Foam or solid core
- b) Honeycomb core
- c) Truss core
- d) Web core

The two most common honeycomb types are the hexagonally-shaped cell structure (hexcell) and the square cell (egg-crate). Web core construction is analogous to a group of I-beams with their flanges welded together. The U.S. Navy refers to this web core construction as “double hull” construction. Truss or triangulated core construction is being widely used for the bridge constructions discussed above. In most foam core and honeycomb core sandwich constructions, one can assume for all practical purposes that the in-plane and lateral bending loads are carried by the faces only. However in truss core and web core constructions, a portion of these loads are carried by the core.

Hexcel’s latest honeycomb core is Hex Web HRH-36 Flexcore involving a phenolic resin for high strength retention at 350F/175C. Foam or solid cores are relatively inexpensive and can consist of balsa wood or an almost

infinite selection of foam/plastic materials with a continuous variety of densities and shear moduli, many of which are polyvinylchloride (PVC).

As in all composite constructions, thermal and hygrothermal considerations must be taken into account. Concerning the thermal effects, with increased temperature, there are three effects: thermal expansion, degradation of elastic properties; and an increase in nonlinear creep/viscoelastic effects.

For the “hygro” part of the effects, there is moisture expansion in all polymer materials, which is mathematically analogous to the thermal expansion. The good news is that if one has the thermal effect solution then one also has the “hygro” solution and they can be superimposed. Moisture also affects the glass transition temperature. One major difference between the thermal and the moisture effects on a polymer matrix structure difference is in the time scales. It takes weeks or months to have a saturated specimen or structure. Weitsman points out that the deleterious effects of moisture continue even after the ten or more years after composites have been soaking in salt water, according to his experiments.

Most materials have significantly different mechanical properties when subjected to dynamic loads that cause high strain rates. However, most structural designs today are made using static properties. See publications of Lindholm, Daniel, La Bedz and Liber, Nicholas, Zukas, Sierakowski, and Feichtinger for discussions of high strain rate effects and test methods.

A research program was conducted at the University of Delaware under ONR sponsorship of the high strain rate effects on many materials that are used in sandwich faces up to strain rates of 1600/sec. It is clear that dynamic properties should be used rather than static properties for structures primarily subjected to dynamic and shock loads. However, there are no means by which dynamic properties can be predicted from known static material properties. Testing at high strain rates is necessary.

Most sandwich structures can be analyzed by using the laminate analysis methods of composite material structures by employing the appropriate A, B and D stiffness matrices. Only in the case of sandwich constructions with a very flexible core must a higher order sandwich theory be used. For an easy example, consider that the lower face is lamina 1, the core is lamina 2, and the upper face is lamina 3. In this way one can also easily handle sandwich constructions of mid-plane asymmetry as well as symmetric sandwich constructions. Also by involving the 44, 45 and 55 terms in the analysis, one can include the effects of transverse shear deformation. Likewise you can include thermal, hygrothermal and piezoelectric effects.

Localized loads are one of the major causes of failure in sandwich constructions, because the faces are significantly thinner than the same

material used in a monocoque construction to resist the same loads. These localized loads can cause the loaded face to deform significantly different from that of the unloaded face. The loaded face acts as a beam, plate or shell on an elastic foundation, i.e., the core. This causes the core to be subjected to significant deformations locally, which can cause high shear and normal stresses that can exceed the allowable stress for the flexible, weak core material. In addition because of the significant deformation of one face the stiffness matrix quantities shown above in equations and, can be locally reduced significantly. This can cause a weak spot in the overall structure which can precipitate a premature failure

To account for these conditions in design and analysis, a higher order sandwich theory must be employed. Since the 1990s this problem has been investigated, accounting for the soft core, differing boundary conditions and behavior for the upper and lower faces. Frostig (along with his collaborators, Baruch, Thomsen, Shenhar and Rabinovitch) has developed a consistent rigorous closed-form, higher order theory for sandwich plates, curved panels and shells. The theory is valid for any loadings (localized or distributed), accounts for discontinuities in load and geometry (ply drops) and includes transverse flexibility of the core. This theory has been used for buckling, vibrations, delaminations, tapered beam and stress concentration problems. It has also been used in comparisons with photoelasticity experiments by Thomsen and Frostig, and found to be very accurate. Most recently this higher order theory has been used by Thomsen to determine the behavior of non-circular boxy shells typical of a fuselage or truck tank, under internal pressure.

Composite sandwich construction also provides a unique opportunity to incorporate piezoelectric, optical and other materials for sensing, monitoring and advising regarding the “health” of the structure during manufacture and use. Piezoelectric effects on a structure are analogous to thermal and hygrothermal effects, analytically, and therefore can be treated analogously. Recently, J-Q Sun has studied the effects of piezoelectric (PZT) patch actuators on curved sandwich trim panels for improved acoustic control in vehicle interiors.

Most recently, a team involving Thomsen, Rabinovitch, Bogetti, Drysdale Arters, Weinacht, and Vinson has investigated the use of piezoelectric materials in flight projectile fins to transform a ballistic projectile into a maneuvering vehicle. Several designs evolved, analysis and structural optimization was performed, and models were constructed. Within the last year these models have been tested in wind tunnels at the University of Maryland and Texas A&M at wind speeds up to 200mph, and the piezoactuators worked as predicted.

One very important dynamic loading unique to ship hulls is wave slamming. Allen and Shenoï have performed extensive experimental research on sandwich beams involving two million cycles each lasting for one second, realistic of the loads on ship hull structures.

Ramachandra and Meyer-Piening report a significant reduction in natural frequencies when a sandwich (or any other) panel is in contact with water on one surface. Their equations should be used when designing or analyzing ship hulls.

Dobyns has provided the methods by which to calculate the natural flexural frequencies for orthotropic and isotropic sandwich plates, including the effects of transverse shear deformation. He has provided forced vibration response solutions for these panels subjected to dynamic sine loads, step function loads, triangular loads, exponential decay (blast) loads, and stepped triangular loads (nuclear blasts). The solutions are given in easy to use Duhamel Integral formulations. Solutions for many static load problems are given as well. Concerning vibration damping, the texts by Nashif, Jones and Henderson, and another by Inman are highly recommended.

For buckling, there are five major textbooks dealing primarily with elastic instability or buckling. These are authored by Bleich, Timoshenko and Gere, Brush and Almroth, Simites, and Jones. Although these texts deal primarily with structures other than sandwich, the solutions can be applied to sandwich structures to investigate overall buckling of sandwich structures by using the appropriate flexural stiffnesses.

For the overall instability of honeycomb and solid core sandwich panels subjected to in-plane compressive loads or in-plane shear loads, for all boundary conditions, the solutions first appeared in USFPL reports and in Military Handbook 23. Also, the equations to predict core shear instability are given as well. Another local buckling that can occur is face wrinkling. There are two equations that have been given to express this type of buckling. One is by Heath and the other by Hoff and Mautner. There is still disagreement on which of these equations to use. For honeycomb sandwich structures, both hexagonally shaped cells or the rectangular (egg-crate) type, monocell buckling or face dimpling can also occur. For truss core sandwich panels, the elastic and geometric constants were first derived and presented by Libove and Hubka and by Anderson. Overall buckling was treated by Seide and given in Mil HDBK 23.

For a truss core sandwich, care must be taken to insure that the faces do not buckle locally, and that the core plates do not buckle as well, for both in-plane compressive loads and in-plane shear loads. For web core sandwich panels, the equation for overall buckling is given by Seide. Again care must be taken to insure that the face plates do not buckle locally, and that the core plates do not buckle as well.

Minimum weight optimization studies have been performed for the honeycomb core, the foam or solid core, the truss core and the web core sandwich panels subjected to in-plane compressive loads, and in-plane shear loads as well. In the process figures of merit were determined that are most helpful in material selection and comparison. In addition, these methods also provide the optimum stacking sequence for the face plates if a laminated construction is used. This research has appeared in many papers.

Shell structures behave significantly different than plate and beam structures, in that under laterally distributed loads for example there exists a “bending boundary layer” in which bending stresses are superimposed upon the membrane type stresses over a small region close to any structural, load or material discontinuity. Further away from these discontinuities, the stresses are membrane only. The bending boundary layer length in shells is on the order of four times the square root of the product of the local radius of curvature times the structural wall thickness.

Regarding the buckling of shells, sandwich or not, shells buckle usually at a fraction of the load predicted by standard methods of analysis, because shells are very imperfection sensitive. This requires the use of empirical factors with the equations.

#### **4. FUTURE**

The future for sandwich construction looks bright indeed. Sandwich construction will continue to be the primary structure for satellites. In aircraft, sandwich construction will be increasingly used particularly for large aircraft. Several countries are now using composite sandwich constructions for their navy’s ship hulls. However one of the largest uses will be for bridge constructions. Not only will it be used in those states whose Departments of Transportation (DOT) are or become knowledgeable, but there is a large international market in developing countries who may welcome the advantages, thus leapfrogging their bridge constructions into the 21<sup>st</sup> century without all of the conventional constructions used in the major countries today. Finally, with the growing need for alternative sources of energy, wind energy mill systems are being developed all of which rely heavily on composite sandwich constructions.

Thus the “big ticket items”, the major uses of sandwich construction in the future will be ship hulls, bridge structures and wind energy systems. These will drive the industry throughout the world.

# SANDWICH STRUCTURES TECHNOLOGY IN COMMERCIAL AVIATION

## *Present Applications and Future Trends*

Axel S. Herrmann<sup>1</sup>, Pierre C. Zahlen<sup>2</sup> and Ichwan Zuardy<sup>3</sup>

<sup>1</sup>*Airbus Deutschland GmbH, Ottenbecker Damm, 21684 Stade, Germany*

<sup>2</sup>*Composite Technology Center GmbH, Airbus-Strasse 1, 21684 Stade, Germany*

<sup>3</sup>*Faserinstitut Bremen e.V., IW3, Am Biologischen Garten 2, 28359 Bremen, Germany*

**Abstract** This paper gives a brief overview of sandwich application history in general and present composite sandwich structures at Airbus. Current R&D developments for sandwich in primary structures are being outlined followed by a discussion of potentials and challenges for composite sandwich structures.

**Keywords:** cost/weight effectiveness, continuous stiffening, sandwich primary structure, composite adapted architecture.

## 1. INTRODUCTION

The challenge of making a structure as light as possible without sacrificing strength is fundamental in aircraft design. Inevitably, the requirement leads to the need to stabilize thin surfaces to withstand tensile and compressive loads and the combination of the two, in tension, torsion and bending. Traditional airframe structural design has in the past, and still does to some extent, overcome this difficulty by use of longitudinal stiffeners and stabilizing rings with stringers and ribs or frames. But this is not a very elegant solution in composite design and, in fact, the stabilization of a surface – creating a resistance to deforming forces – can in many cases be more efficiently effected by the use of twin skins with a stabilizing medium between them [1].

## 2. BRIEF HISTORY OF SANDWICH APPLICATIONS

Sandwich is a common principle in nature and hence the concept is older than mankind itself. The branches of the elder tree are a good example for a foam core sandwich structure. The bones in the skeletons of animals and humans are sandwich structures with foam-like core materials as well. Natural sandwich structures are subjected to complex load cases. The bones in legs have to withstand repetitive, super positioned bending and compression loads. Moreover nature imposes a strict demand for lightweight primary structures (e.g. skeletons of birds). All the mentioned examples show the principle of structural optimisation: minimum use of material for maximum performance.

W. Fairbairn was reported to be the first person to describe the sandwich construction principle in 1849 for the Britannia Tubular Bridge in North Wales. The sandwich comprised iron compression sheets riveted to both sides of a wood core. In 1924 T. von Karman and P. Stock patented a glider plane applying sandwich for fuselage structure. Following his predecessor von Karman, Mautner designed a plane having sandwich elements in the wing structure. The chief designer of De Havilland, E. Bishop, was the first person to use the sandwich principle in a powered aircraft. He used the sandwich concept in the fuselage of the Comet Racer, the Albatross and in the wing and fuselage of their successor, the famous Mosquito (figure 1).

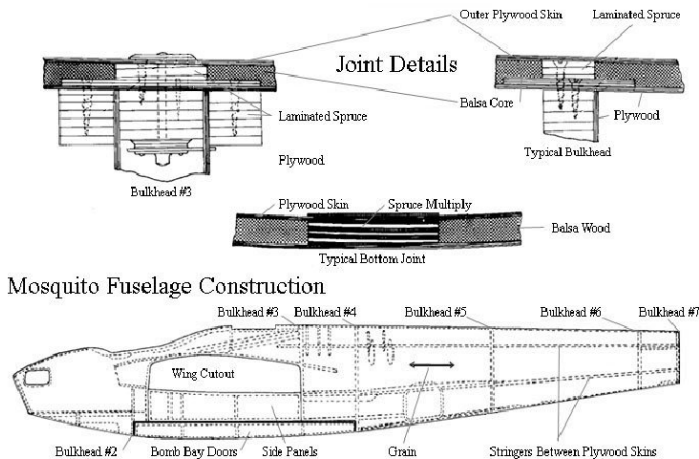


Figure 1. Fuselage of the De Havilland Mosquito, source: Toronto Aerospace Museum.

For these aircraft the sandwich core was balsawood while the facings consisted of birch plywood and were joined to the cores by bonding. The adhesive used for the bonding was based on phenolic resins (Bakelites). However the use of bio-degradable materials like wood is problematic due to their susceptibility to biota like fungi. Metal-wood sandwich was applied in the floor panels of the older Fokker F27. In this case the elements had a core of balsa and facings of aluminium.

The invention of modern honeycomb sandwich structures goes back into 1940's and was the idea of the circus proprietor George May, who showed at Farnborough his invention, that looked like a cross between a book and a concertina. Improvements made through impregnating the paper with phenolic resin led to the honeycomb semi finished products known nowadays [1, 2].

The use of sandwich structure in the Apollo project, that successfully landed on the moon in 1969, showed the high potential of sandwich structure in the field of aerospace. With the help of this unique technology, it was possible to construct the Apollo capsule and its heat shield, which was light and yet strong enough to sustain the stresses of acceleration during the start and re-entry phase [4].

Application of composites for large structures at AIRBUS started in 1983 when the A310 was the first aircraft in the AIRBUS fleet to be equipped with a composite honeycomb sandwich rudder. The composite Vertical Tail Plane for the A310 was soon to follow in 1985. Ever since, the experience with large composite structures was extended. Current developments are being outlined later in this paper.

Today a large variety of sandwich cores are being applied in structural engineering (see figure 2) [7, 8].

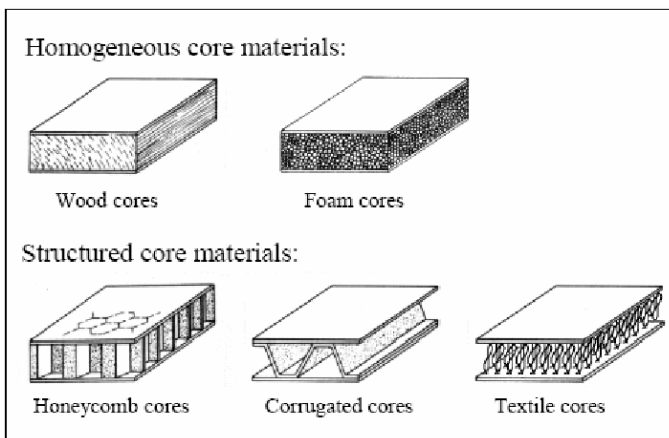


Figure 2. Different sandwich core types.

This short review of the implementation of sandwich structures in nature and in the past of aviation summarizes the concept of sandwich structures. They are very efficient with respect to their integral structural behaviour, weight and manufacturing costs. Validation of new calculation methods and tools, better understanding of effects of defects, improved and more economic Non Destructive Testing (NDT) capabilities (also for large area inspection), advanced core materials, novel manufacturing methods and integration of structural and non-structural functions are some areas of current research work being conducted in the composite sandwich R&D community. The development of sandwich structures and their application does advance and has great potential in the near and mid-term future of commercial aviation [5, 12, 13, 14, 16, 17, 18].

### **3. STATE OF THE ART COMPOSITE SANDWICH STRUCTURES AT AIRBUS**

There is a broad range of composite sandwich structures application in Airbus aircraft. Typical external structures are aerodynamic fairings, covers and doors. Examples are radomes, belly fairings, leading and trailing edge fairings, engine cowlings and landing gear doors. Moreover there is a variety of composite sandwich control surfaces throughout the Airbus fleet (e.g. rudder, aileron, spoiler). Examples for the application of composite sandwiches inside the aircraft are fairings and floor panels in the passenger compartment. Figure 3 gives an overview of composite sandwich applications in the A380 aircraft.

The requirements for composite sandwich structures in commercial aviation aircraft are very diverse. External structures face a wide range of operational temperatures and high aerodynamic loads. Radomes and leading edge fairings are exposed to impacts due to bird strike and hail, lightning strikes and abrasion caused by rain and dust. Moreover electromagnetic transmissibility for radar and avionics is required. Foreign object damage (FOD) caused by runway debris is a characteristic threat for all surfaces on the lower side of the aircraft. Floor panels in the passenger compartment must withstand transverse, discrete loads caused by passengers (e.g. high heel shoes). These examples underline the diversity of operational and environmental requirements for the different sandwich applications. It is crucial to be aware of the different requirements early in the design process in order to develop an appropriate structure accordingly.

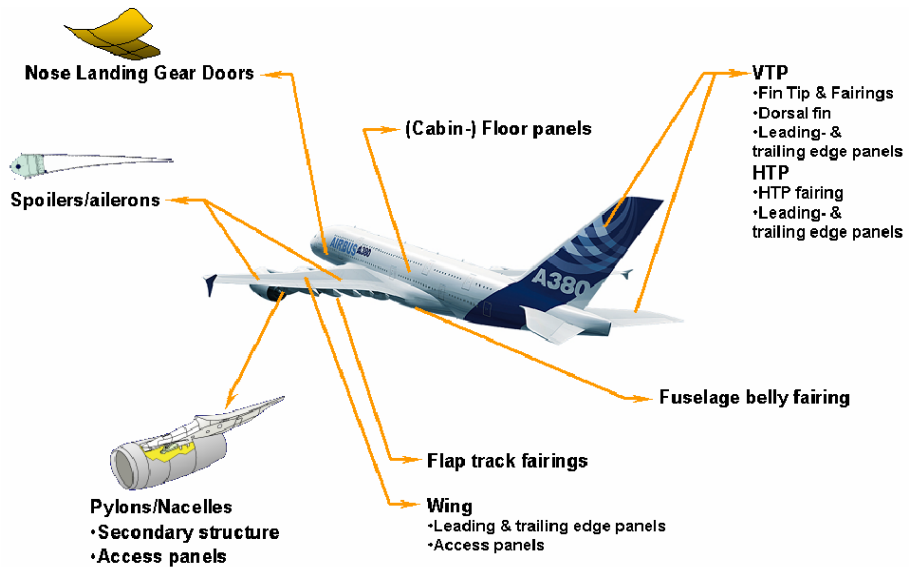


Figure 3. Examples for sandwich applications A380.

To fulfill the different requirements a variety of material combinations can be found in the current composite sandwich structures. Predominate skin materials are glass fiber and carbon fiber reinforced prepreps with epoxy resin matrices. The predominate core material for sandwiches is NOMEX<sup>®</sup> honeycomb. Due to fire, smoke and toxicity requirements (FST) less hazardous phenolic resins are being applied in the manufacture of surface layers of cabin interiors. ROHACELL<sup>®</sup> PMI hard foam is being applied as a manufacturing aid (lost tool; e.g. hat profiles for A340 and A380 rear pressure bulkhead).

#### 4. VERTICAL TAIL PLANE (VTP)

Vertical tail planes of Airbus aircraft consist of 5 major structural assemblies (see figure 4):

1. Leading edge fairings (including tip and dorsal fin)
2. Center box structure (including the interface to the fuselage)
3. Trailing edge fairings
4. Rudder
5. Fin – fuselage fairing

For the A340 VTP the leading edge, trailing edge, dorsal fin, tip, the fin-fuselage fairing and the rudder are produced with composite sandwiches.



Figure 4. VTP major structural assemblies (example A380).

The leading edge fairings (including tip and dorsal fin) have to withstand aerodynamic loads, abrasion and hail-, bird- and lightning strike. Antennas are mounted behind the leading edge and the tip, therefore they have to allow for electromagnetic transmission. The Material combination for these areas is glass fibre reinforced prepreg and NOMEX<sup>®</sup> honeycomb.

The largest sandwich structure in the A340 VTP is the rudder. It consists of the following major components:

- Left and right hand skin panel (NOMEX<sup>®</sup> honeycomb and carbon fibre prepreg; layers of glass fibre prepreg in specific areas for corrosion protection)
- Front spar (monolithic carbon fibre prepreg)
- Root rib (monolithic carbon fibre prepreg)
- Diverse fittings (aluminium parts)
- Diverse small parts

The dimensions of the rudder are:

- Length at front spar: ~9,9m
- Length at trailing edge: ~9,3m
- Width at tip: ~0,9m
- Width at root rib: ~2,6m
- Overall surface: ~15,3m<sup>2</sup>

Sandwich is the ideal structure for this large component as stiffness to weight ratio is a critical requirement for control surfaces.

## **5. FUSELAGE**

A full composite fuselage is one focus of current R&D and development activities ongoing in commercial aviation. Boeing intends to build its new airplane, the 787, with a full composite fuselage [21]. Although it seems that the first generation full composite fuselage for commercial airliners will be monolithic, several sandwich concepts were investigated by different companies within the last years.

The “Deutsches Zentrum für Luft und Raumfahrt” (DLR) proposed a sandwich fuselage concept in which the outer skin is only intended to be an aerodynamic fairing. Frames can be attached to the uninterrupted (no stringers) surface of the inner skin [3, 13].

An evaluation of a composite sandwich fuselage concept done by NASA/Boeing suggests that the tested structure with twice the original frame spacing is capable of sustaining design ultimate load conditions without damage and of sustaining design limit load conditions with a 1-inch-long notch [22].

Airbus initiated a CFRP fuselage project in 1999 supported by the German government. In the first four years of the project, a wide screening of technologies was carried out and several design concepts for a CFRP fuselage were evaluated. In this context the whole fuselage was taken into account, implementing also neighbourhood engineering areas such as cabin, interior, equipment, system installation and insulation. This investigation leads to the integrated double shell design (IDS), which enables the implementation of more functions into fewer parts. Two different double shell concepts, SoFi (Stringers outside, Frames inside) and VeSCo (Ventable Shear Core), are now under investigation and are being optimised through tol 2007.

SoFi aims to provide maximum thermal and noise insulation and impact-protection accompanied by attractive weight savings. The SoFi core material consists of a carbon pin reinforced foam where the reinforcement can be tailored accordingly with the outer skin providing the aerodynamic surface.

The VeSCo concept is shown schematically in figure 5. VeSCo is designed to provide a maximum of weight saving while still offering attractive protection against impact and noise. Again with the outer skin providing the aerodynamic surface. In between the two skins there is a core material that is ventable in order to avoid moisture accumulation.

Compared to an aluminium reference fuselage, SoFi and VeSCo may achieve weight savings of about 24-29% [12, 15].

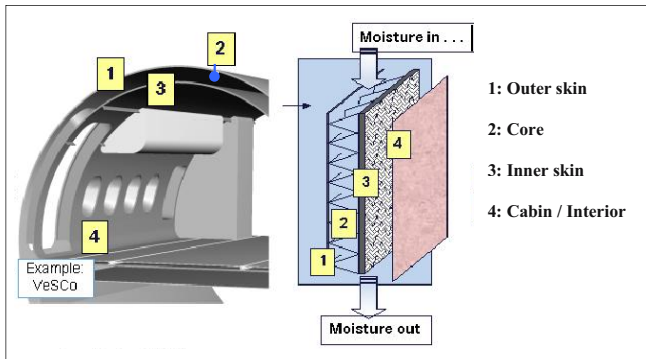


Figure 5. VeSCo concept (schematically shown).

Current R&D shows that there is a high potential for CFRP sandwich applications to save weight and cost in fuselage structures. Metal fuselage structures have been optimised for more than 80 years now and further optimisation becomes more and more difficult. Introduction of a new technology, like composite monolithic or sandwich structures, will lead to a step improvement and a new, steep learning curve.

## 6. SANDWICH POTENTIALS

Composite sandwich structures offer a wide range of advantages and potentials considering aircraft structural design.

Sandwich structures are very weight effective when it comes to stiffening of skins. The stiffeners are not discrete as in classical stiffened skins resulting in a continuous stiffness distribution in the skin panel. Hence the resulting, non interrupted surface of sandwich skins leads to further advantages, as it is possible to avoid complex cross-overs of stiffening elements (e.g. frames and stringers) which will finally lead to the reduction of analysis-, manufacturing- and maintenance complexity in these areas. Moreover the integral, continuous stiffening permits a reduced parts count for assemblies and therefore less logistics, parts manufacturing- and assembly work. In addition simple skin topography without protruding elements simplifies the vacuum build up (bagging) of the component and reduces manufacturing risk caused by bagging errors (e.g. bridging of vacuum foil, pin holes, strong wrinkling and deformation of foil – see figure 6). The less complex surface geometry allows simple introduction of

technologies for automated vacuum build up can be more easily introduced in order to increase reproducibility and quality.



*Figure 6.* Complex vacuum build up because of protruding elements.

Advanced manufacturing methods like resin infusion technologies combined with homogeneous cores (e.g. foam) and dry fibre preforming open up further possibilities. The level of structural integrity may be significantly improved by integration of textile preformed lugs and attachment fittings which leads to further parts count reduction. Some infusion processes do not require autoclave technology – an oven and vacuum for curing delivers parts with an acceptable fibre volume content (around 60%) for aircraft components. During part build up there are less health and safety hazards within the infusion technology working environment since there is no direct contact with the resin. Furthermore foam cores can be more easily machined and handled than honeycombs of comparable geometry (less distortion and deformation).

In the area of load introduction a foam core sandwich structure features various possibilities for reinforcements. State of the art reinforcing technologies (e.g. pin reinforcement, stitching, etc.) offer a large variety of tailoring for optimum material behaviour. In addition this tailoring improves key sandwich properties like the compression after impact behaviour.

Besides the mentioned examples other promising concepts exist for load introduction in foam core sandwich. Reinforcements in the foam will also serve as crack stoppers [9, 10].

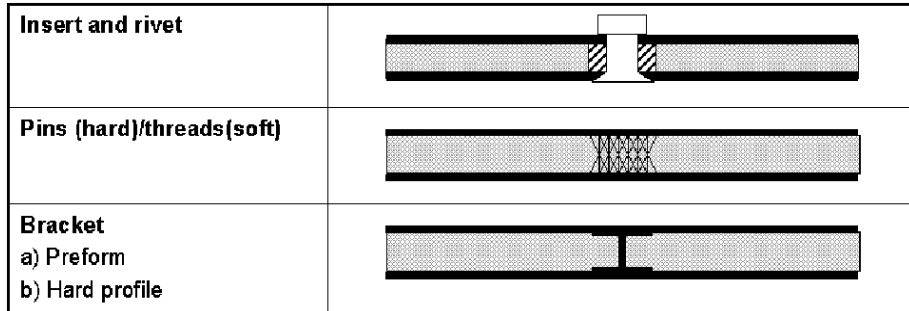


Figure 7. Examples for different sandwich reinforcement concepts.

Sandwich Structures have an excellent damping behaviour and good energy absorption can be achieved by appropriate design [11]. Introduction of sandwich structures in fuselage shells reduces the noise level inside the cabin and thus increases passenger comfort. In this application an integration (at least partial) of thermal isolation of the passenger compartment is also possible.

However, the outlined potentials can not be transferred in to every possible application. For each target application it is the task of engineering in a proper development process to assess the necessary requirements, do trade-off studies for possible concept solutions and validate chosen approaches in simulations and tests to finally show compliance with airworthiness-, customer and company requirements.

This overview is not exhaustive but underlines the large amount of present and future potentials and the multiple possibilities for functional integration in sandwich structures. Because of their inherent properties and qualities advanced sandwich structures represent a composite adapted architecture challenging the quasi metal-derived design and manufacturing of conventional, monolithic composite skins with differentially joined stiffening elements.

At present the potentials of sandwich structures are not fully opened up and applied in commercial aviation. Moreover there are still no primary structure applications of sandwich. For a more widespread application of composite sandwich structures in commercial aviation and to further exploit the benefits of sandwich structures several challenges will have to be mastered in the near and mid-term future.

## **7. MAJOR CHALLENGES**

The application of sandwich structures in commercial aviation is currently restricted to secondary structures. For a more widespread application and in order to introduce sandwich in primary structures several challenges must be met.

For primary structures the possibility of a failure that leads to a catastrophic failure of the aircraft must be prevented. Therefore the structure needs to be evaluated in order to prove that damage occurring during the service life of the aircraft will not lead to failure or excessive structural deformation until the damage is detected. Full compliance to this requirement needs to be shown by simulation and test.

One challenge is to understand in detail how different damages influence the structure and what their behavior in-service is. On one hand the combination of tests and simulation will provide the allowed material values for proper sizing of the structure and will prove new design principles. On the other hand the methods and tools for simulation (e.g. impact behavior, crack growth) will need to be developed/adjusted and finally verified according to the new requirements of a primary sandwich structure and the outcome of the tests. Obviously this is an iterative process that usually starts at a generic hardware level (coupons and elements) and proceeds to more and more complex structural components. One result of this process is the definition of maximum allowable damages and their visibility.

With the information of maximum allowable damages at hand one has to understand the detectability of these damages in the service life. It is a disadvantage for sandwich structure that structural failures (especially in the core) cannot always be detected by common methods (e.g. visual inspection, ultrasonic pulse-echo). One sided access only and large area inspection poses further challenges. A number of NDT technologies are available and under development that better fit the needs to inspect sandwich panels [16, 17, 18, 19]. Novel structural health monitoring technologies are another option to facilitate NDT in service [20]. Once a specific sandwich structure is understood with respect to maximum allowable damages an appropriate detection method has to be chosen and a NDT concept needs to be developed taking into account requirements for economic in service behaviour.

Another important issue is the ability to perform fast and effective repairs. Advanced in-service repair methods (e.g. temporary, infield repairs) have to be developed according to the detailed concept of sandwich primary structures. Important factors for repair methods are the required time and complexity, required infrastructure and tools, achievable material strength after repair and other economical advantages and disadvantages compared to state of the art methods [23].

Naturally any approach to introduce sandwich as a primary structure depends heavily on the design, architecture and material selection of the sandwich structure itself. Innovative, crack stopper and load introduction concepts will be one key issue. The ability of the overall structure to behave fail-safe – means the ability of load redistribution after partial, obvious damage/single failure without loss of overall structural load bearing function – is another key issue. Toughness of the chosen material combinations and the ability to withstand impact damages is also a key driver. The aim must be to produce a design that has optimum robustness within the strict weight requirements of commercial aviation.

## 8. CONCLUSIONS

This paper gives a brief overview of past and present sandwich applications. Several R&D activities in the area of sandwich for commercial aviation primary structures are described followed by a discussion of potentials and challenges for advanced sandwich structures.

Major commercial aviation sandwich potentials outlined in this paper:

- Weight effectiveness
- Continuous stiffness distribution
- Reduced complexity of surfaces – no protruding elements (e.g. stringers)
- Highly integrated structures possible → reduced parts count
- Reduced production effort and logistics
- Tailoring of reinforcements and load introduction areas
- Advanced manufacturing methods will open up further potentials
- Excellent damping properties
- Possibility of functional integration (e.g. thermal insulation)

Major commercial aviation sandwich challenges outlined in this paper:

- Sandwich as primary structure
- Verified simulation methods and tools for simulating the damage behaviour of complex sandwich structures
- Cost effective, in service non-destructive testing (NDT) methods for complex sandwich structures
- Introduction of structural health monitoring (SHM)
- Advanced in-service repair methods for existing and new sandwich concepts
- Novel load introduction and reinforcement concepts
- New material systems with improved toughness and impact behaviour

The ultimate aim of all activities must be a robust design that can be operated economically.

The overview given in this paper is not exhaustive but underlines the large amount of present and future potentials and the multiple possibilities for functional integration in sandwich structures as well as the challenges that need to be overcome to further promote the application of sandwich in commercial aviation. Advanced sandwich structures represent a composite adapted architecture challenging the quasi metal-derived design and manufacturing of conventional, monolithic composite skins with differentially joined stiffening elements.

## REFERENCES

1. Widjaja D., Herrmann A. S., Entwurf und Berechnung von Leichtbaustrukturen mit hybriden, räumlichen Netzwerken, DLR Interner Bericht, Braunschweig, Germany, 1993.
2. van Tooren, M. J. L., Sandwich Fuselage Design, Delft University Press, Delft, the Netherlands, 1998.
3. Wilmes H., Kolesnikov B., Fink A., "New Design Concepts for a CFRP Fuselage", Workshop at German Aerospace Centre (DLR) on Final Project of Black Fuselage, Braunschweig, Germany, 2002.
4. Tan J. C., A Brief History of Sandwich Technology, URL: <http://www.msm.cam.ac.uk/mmc/research/steelsheet/sandwichbase/briefhistory.htm>, 2005.
5. Herrmann A. S., "Design and Manufacture of Monolithic Sandwich Structures with Cellular Cores", Sandwich Construction 4, Vol. 2, pp 719-728, 1998.
6. Military Handbook, Structural Sandwich Composite, Washington, USA, 1968.
7. Pflug J., Xinyu F., Vangrimde B., Verpoest I., "Development of a Sandwich Material with Polypropylene/natural Fibre Skins and Paper Honeycomb Core", Proc. of 10<sup>th</sup> European Conference on Composite Materials (ECCM-10), pp 331, 2002.
8. Pflug J., Vangrimde B., "New Sandwich Material Concepts – Continuously Produced Honeycomb Cores" COMPOSIT Workshop on New Material Concepts for Composite Transportation Structures, Leuven, Belgium, 2003.
9. Lascoup B., Khellil K., Benzeggagh M., Aboura Z., Maquet J., "Stitched Sandwich Panel Materials for Resin Infusion Structures", SAMPE Journal, Vol. 41, No. 1, pp 42-48, 2005.
10. Cartié D. D., Fleck N. A., "The Effect of Pin Reinforcement upon the Through-Thickness Compressive Strength of Foam-cored Sandwich Panels", Composites Science and Technology 63, pp 2401-2409, 2003.
11. Majamäki J., "Impact Simulations of a Composite Helicopter Structure with MSC.Dytran" (URL: <http://www.mssoftware.com/events/aero2002/abstracts/pdf/p00701a.pdf>) MSC - Worldwide Aerospace Conference & Technology Showcase, Toulouse, France, 2002.
12. Kolax M., "Advanced Composite Fuselage Structures", JEC Composites, No. 10, pp 31-33, 2004.

13. Kleineberg M., Wenner U., Hanke M., "Cost Effective CFRP-Fuselage Manufacturing with Liquid Resin Infusion (LRI) – Technologies", Workshop at German Aerospace Centre (DLR) on Final Project of Black Fuselage, Braunschweig, Germany, 2002.
14. Ley R. P., Lin W., Mbanefo U., Facesheet Wrinkling in Sandwich Structures, NASA/CR-1999-208994, Virginia, USA, 1999.
15. Kupke M., Kolax M., "CFRP-Fuselage – Ensuring Future Competitiveness", SAMPE Conference, Paris, 2004.
16. Hilger W., Meier R. Henrich R., "Inspection of CFRP Components by Ultrasonic Imaging with Air-coupling", InSight Vol. 46 No. 3 pp 147-150, 2004.
17. Andersson J., van den Bos B., "NDI on Bonded Sandwich Structures with Foam Cores and Stiff Skins – Shearography the Answer?", Application Report No. 02. 01 of Attemeyer AG, [http://www.dantec-ettmeyer.com/pdf/shearography\\_ndt\\_2\\_01.pdf](http://www.dantec-ettmeyer.com/pdf/shearography_ndt_2_01.pdf).
18. Gustafsson J., "Nondestructive Large Area Testing Using Shearography", Application Report No. 01. 02 of Attemeyer AG, [http://www.dantec-ettmeyer.com/pdf/shearography\\_ndt\\_01\\_02.pdf](http://www.dantec-ettmeyer.com/pdf/shearography_ndt_01_02.pdf)
19. Anastasi R. F., Zalameda J. N., Madaras E. I., "Damage Detection in Rotorcraft Composite Structures Using Thermography and Laser-Based Ultrasound", SEM X International Congress and Exposition on Experimental and Applied Mechanics, Costa Mesa, CA, 2004.
20. Bois C., Hochard C., "Monitoring of Laminated Composites Delamination Based on Electro-Mechanical Impedance Measurement", Journal of Intelligent Material Systems and Structures Vol. 15 pp 59-67, 2004.
21. Boeing, "Boeing Completes First 7E7 Composite Fuselage Section", [http://www.boeing.com/news/releases/2005/q1/nr\\_050111g.html](http://www.boeing.com/news/releases/2005/q1/nr_050111g.html), 2005.
22. Rouse M., Ambur D. R., Bodine J., Dopker B., "Evaluation of a Composite Sandwich Fuselage Side Panel with Damage and Subjected to Internal Pressure", NASA Technical Memorandum 110309, Virginia, USA, 1997.
23. Armstrong K. B., Barrett R. T., Care and repair of Advanced Composites, Society of Automotive Engineers (SAE), PA, USA, 1997.

# DAMAGE ASSESSMENT AND DAMAGE TOLERANCE OF FRP SANDWICH STRUCTURES

Brian Hayman

*Section for Structural Integrity and Laboratories, Det Norske Veritas AS, N-1322 Høvik, Norway*

**Abstract** A review is made of production defects and in-service damage types that arise in sandwich structures having fibre reinforced polymer (FRP) face sheets. A brief overview is given of relevant defect and damage models and how these models can be used in an assessment of criticality with regard to local and global structure, as a basis for deciding on corrective measures, for the case of a naval ship. Challenges resulting from limitations in inspection techniques are discussed. The concept of damage tolerance is discussed in the light of the above. It is argued that the most suitable and economical approach to achieving damage tolerance is dependent on the application.

**Keywords:** FRP sandwich structures, defects, damage, damage assessment, damage tolerance.

## 1. INTRODUCTION

Composite structures consisting of fibre reinforced plastics (FRP) contain imperfections resulting from either the production processes or subsequent handling and use. This applies also to sandwich structures in which the face sheets are made of FRP. Many FRP structures, such as those used in marine applications, have traditionally been designed without explicitly addressing such defects and damage; production defects have been allowed for implicitly by applying sufficiently high factors of safety, and a certain robustness in relation to accidental events has been built-in by such means as the minimum thickness or minimum reinforcement requirements in classification society rules.

In contrast, the aircraft industry has focused more explicitly on defects and damage by requiring fail-safe or damage tolerant design. As more optimised, lightweight composite designs are finding their way into marine applications, particularly for naval and high-speed vessels, the need for introducing damage tolerance principles in these applications is increasing. However, because the in-service inspection regimes and safety considerations are different from those for aircraft, there must be differences in the way a damage tolerance approach is implemented.

A start has been made in the recently completed international project THALES JP3.23: Inspection and Repair of Sandwich Structures in Naval Ships (SaNDI) [1]. In this project attention has been focused on the types of defects and damage that need to be taken into account when naval ships built in FRP sandwich are designed, built, maintained and operated, on the methods available to detect such defects and damage, on the ways in which their influence on structural performance may be assessed, and on the methods available for their repair. The project has developed an integrated methodology [2,3] for the inspection, assessment and repair of defects and damage, with attention to the important questions of whether, when, where and how defects and damage should be repaired and, in the case of in-service damage, whether measures should be taken to impose operational restrictions in the interim period while a repair is pending. An overview of some of the main results is presented here, with discussion of the implications for introducing more damage tolerant design in FRP structures in ships and other applications.

## **2. DEFECTS AND DAMAGE IN FRP SANDWICH STRUCTURES**

The terms “defect” and “damage” are not uniquely defined, and are sometimes used synonymously. The author prefers the terms “production defect” and “in-service damage” to make the major distinction that is relevant in practice. In all FRP composite structures it is important to be able to detect and rectify both production defects and in-service damage.

For single-skin laminates and face laminates of sandwich structures, production defects include dry zones, voids, delaminations, wrinkles, misalignment of fibres, and poor curing (giving reduced physical properties). For sandwich structures, core/skin debonds must be considered in addition, and also voids and inclusions in the core, and lack of bond (edge-to-edge and face-to-face) between core sheets.

In aircraft structures the main type of in-service damage is impact damage, typically from bird strikes, hail and objects thrown up from the

runway during landing and takeoff. Ship structures, however, may encounter a wide range of contact damage (quasi-static contact, e.g. during berthing, as well as impact), incidences of heat damage and numerous types of damage resulting from overloading. This last category includes core fracture or crushing, skin/core debonds, laminate rupture, delamination either within a laminate or at a secondary lamination, and failure at equipment fastenings. Impact damage may be confined to the impacted face laminate (with or without penetration of the laminate), or may involve crushing and/or cracking of the core. In extreme cases, penetration of the entire sandwich may occur. More substantial damage cases include the removal of whole panels or assemblies by fire or collision. For naval vessels some types of damage may be caused by weapon effects such as air blast, underwater explosions, and fragment or missile hits.

### **3. INSPECTION AND DETECTION**

#### **3.1 Non-destructive inspection**

Numerous non-destructive inspection (NDI) methods are available for FRP sandwich structures. Selection of an NDI method for a particular application depends on many parameters, including the following:

- The environment in which the inspection has to be carried out
- The purpose of inspection – whether it is an initial scan or a detailed inspection, or an inspection of a repair
- The extent of the area to be inspected
- The accessibility of the region to be inspected (including whether access is possible to both sides of the sandwich or only one side)
- The type of defect or damage that is suspected
- The sandwich lay-up in the area to be inspected
- The size of the damage that must be detected (e.g. the size that is considered critical)
- The nature of the sandwich surface to be inspected, e.g. whether it is flat or curved, even or uneven, and what surface preparation is feasible
- The available supporting facilities like electrical power, compressed air, water, etc.
- Whether equipment of a given type, and the necessary personnel, are available, and what cost.

Two of the most important parameters are the type and thickness of material to be inspected. Techniques developed for lightweight aerospace structures can rarely be applied directly on ship structures without modification. Rigorous benchmarking of a limited number of NDI methods

for application to FRP structures in naval ships was carried out in the EUCLID RTP3.8 Project [4-6]. In the SaNDI Project attention was confined to sandwich structures, but a wider range of techniques was considered:

- Ultrasound (pulse-echo and through-transmission modes, water- and air-coupled, hand-held and automated scanning)
- Mechanical impedance
- Microwave
- Laser shearography with vacuum, heat and vibration loadings
- Thermography (static and pulsed)
- X-ray real-time imaging and backscatter scanning
- An acoustic transmission technique.

Some evaluation was also made of visual inspection techniques and of manual coin-tapping. Tables and charts were compiled to assist in the selection of appropriate methods for a given application. Some of the results on specific methods are presented in [7-9]. The following section gives some selected conclusions from this and the earlier work, but a comprehensive overview of the techniques and their capabilities has yet to be published.

### **3.2 Some conclusions regarding NDI techniques**

Some challenges remain if a fully integrated system for defect/damage inspection, assessment and repair is to be implemented in practice:

- The potential for detecting deep defects/damage in thick sandwich structures remains limited, especially for methods that can readily be used on board or around a ship.
- Sandwich structures with cores of end-grain balsa are especially difficult to inspect because the defects are masked by natural features in the core.
- It is generally not possible to detect far-side defects with one-sided inspection methods, though this has now been achieved in isolated cases.
- Thick coatings may have to be removed when ships are inspected in service.
- Although there have been considerable improvements recently in automated scanning techniques [9], there is still a need for more rapid scanning methods for large areas.
- At present there is insufficient knowledge about the sensitivity and reliability of many NDI systems when applied to composites to enable detectability limits and probabilities of detection to be quantified. These are essential for implementation of a comprehensive damage tolerance approach to design, inspection and maintenance.

### **3.3 Structural health monitoring**

Improved sensor techniques using, for example, fibre optic technology, combined with specially developed data recording and processing systems, now permit continuous monitoring of ship structural responses. Such systems have been used to monitor the global responses of merchant ships and of naval vessels built in sandwich composite materials [10]. Response monitoring systems can be used to indicate when the loads on the structure have exceeded a level that is likely to have caused damage.

It is more difficult to devise systems that can effectively monitor structural health directly by indicating that damage has actually occurred, though the availability of such a structural health monitoring system could have a major influence on future inspection and repair strategies. To detect reliably the appearance of small cases of damage requires an extremely high density of sensors since the changes in response are usually confined to an area close to the damage. The damage has to involve a significant volume of material in order to change the response characteristics significantly at a more global level. Methods of excitation and signal processing have recently been developed that show some potential for reducing the density of sensors, such as the broadband gapped smoothing method (BGSM) described by Ratcliffe and Crane [11], but as far as the author is aware such systems for damage detection are not yet implemented on ships in service.

## **4. THE INFLUENCE OF DAMAGE ON STRUCTURAL PERFORMANCE**

### **4.1 Damage assessment scheme**

In the SaNDI Project a comprehensive damage assessment scheme has been developed for naval ships that has the potential for including all possible threats and evaluating the influence of the damage on the structural performance and functionality of the separate parts and of the ship as a whole. The damage assessment procedure for cases where strength is the main consideration is basically as follows [2, 3]:

- Estimate the strength reduction caused by the damage or defect.
- Determine the allowable strength reduction based on the original design assumptions, operational envelope, etc.
- Compare these. If the residual strength is smaller than the allowable value, consider the possibilities for restricting the operational envelope and/or accepting a lower safety factor until repair can be effected.

- If this is not sufficient, carry out an emergency repair or take other emergency measures as necessary.

To do this, one may need to consider the damage in the local, panel and global (ship) contexts, as illustrated in Figure 1. The scheme as a whole is shown in Figure 2.

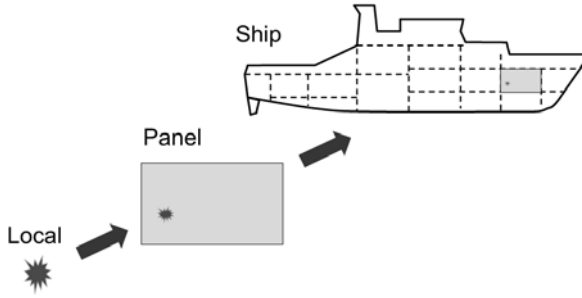


Figure 1. Damage illustrated in local, panel and global (ship) contexts.

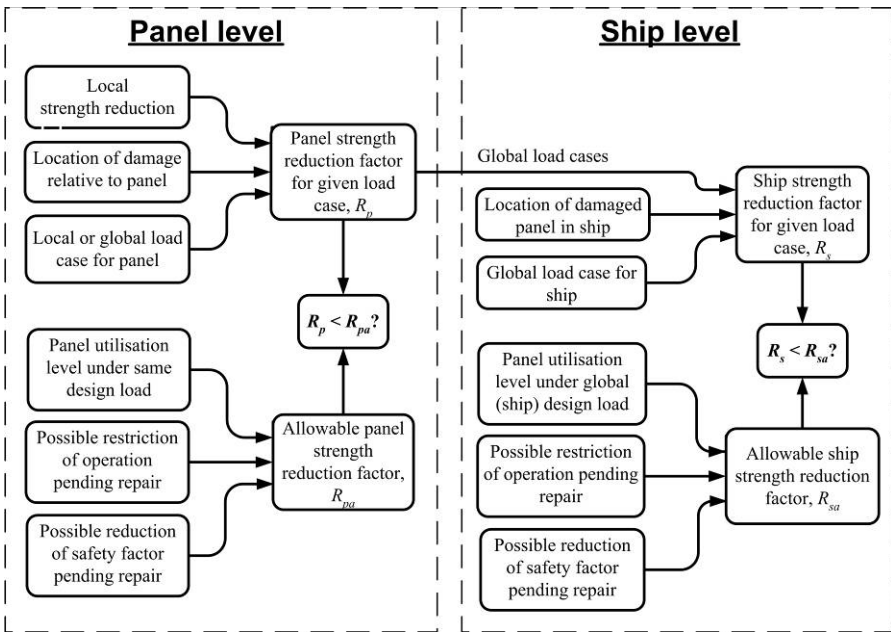


Figure 2. Scheme for damage assessment for a naval ship built in FRP sandwich.

For damage confined to a single panel, the influence of the damage on the affected panel or component is first considered by estimating a strength reduction factor for the panel,  $R_p$ , where  $R_p \leq 1$ , for each load case. This is

compared with an allowable strength reduction for the panel,  $R_{pa}$ . If the panel suffers from a reduced load bearing capacity, it is necessary to consider the implications of this at the global (ship) level. For this purpose it is possible to calculate a ship strength reduction factor  $R_s$ , which again must be compared with an allowable global strength reduction factor,  $R_{sa}$ .

## 4.2 Damage levels

It is convenient to divide damage into the following classes or levels, which determine the procedure to be followed for damage assessment.

### 4.2.1 Level 1 damage

Level 1 damage (small local damage) covers a small part of a panel so that its influence on the panel stiffness and on stresses at points on the panel some way from the damage can be neglected. When considering uniform in-plane loading (e.g. in-plane compression) it is possible to find a value of the far-field stress or strain at which failure occurs. Its value depends on the damage size but not on the width or length of the panel. Examples are small impact damages. Small core/skin debonds may also lie in this category. The influence of Level 1 damage on panel strength can be assessed in three steps:

1. Determine a local strength reduction factor  $R_l$  in terms of the reduction in the far-field stress or strain at failure (for a given in-plane loading).
2. Determine a sensitivity factor  $S_p$  that accounts for the location of the damage in relation to the stress field in the panel for the real loading case.
3. Combine these to give the panel strength reduction factor  $R_p = R_l S_p$ .

The factor  $S_p$  is referred to as the local location and load case factor. It is defined as the ratio of the load that causes the critical stress or strain component at the damage location to reach its maximum allowable value ignoring the damage to the maximum allowable value of load on the intact panel. For face sheet damage, the critical stress or strain component is usually taken to be the in-plane compressive stress or strain at the point in question.  $S_p$  can never be smaller than unity. Note that it is calculated from the properties of the intact panel. Maps of  $S_p$  values can readily be drawn for panels with given dimensions and lay-ups for simple load configurations like uniform lateral pressure. Such maps show the extent to which a given panel is sensitive to Level 1 damage at each potential damage location.

For Level 1 damage, it is possible to neglect redistribution of stresses between panels (and other elements) in the structure when estimating the influence of the damage on global strength.

#### 4.2.2 Level 2 damage

Level 2 damage (medium local damage) is confined to one panel but does not meet the requirements for Level 1 damage so that the influence of the damage on the panel strength has to be considered for the particular damage size, damage location and load case. However, the damage is not so severe that it influences the stiffness of the panel significantly, so that redistribution of stresses in the global structure can be neglected in assessing the reduction of global ship strength. Examples include moderately large impact damage, moderately large debonds, and moderate core shear cracking.

#### 4.2.3 Level 3 damage

Level 3 damage (large local damage) is confined to one panel but is so severe that it significantly influences the stiffness of the panel. Redistribution of stresses cannot be neglected in assessing the reduction of global ship strength. Examples include large impact damage, large debonds, and developed core shear cracking with debonding. The influence of the damage on the panel strength has to be considered for the particular damage size, damage location and load case. In extreme cases it may be appropriate to assume that the panel's contributions to the global strength and stiffness have been completely destroyed. In this case the panel is removed from the global analysis model of the ship and the loads adjusted accordingly.

#### 4.2.4 Level 4 damage

Level 4 damage (extensive damage) affects two or more panels and/or supporting structure. Each case must be considered individually. Generally this type of damage leads to redistribution of stresses in the remaining structure. It may or may not be relevant to consider the damaged panels as fully removed for the purpose of the analysis.

### 4.3 Checks on strength reduction

There is normally no need to consider an allowable strength reduction if  $R_p = 1$ . If  $R_p < 1$  the possibility of accepting a reduction of panel strength must be considered unless the damage can be fully repaired immediately. If  $R_p < 1$ , the global strength reduction  $R_s$  must also be evaluated. For Level 1 and Level 2 damage, it is possible to neglect redistribution of stresses between panels (and other elements) in the structure when estimating the influence of the damage on the global strength. This enables  $R_s$  to be found from  $R_p$  by a procedure analogous to that for deriving  $R_p$  from  $R_l$ . This uses a

global (ship) location and load case factor  $S_s$  analogous to  $S_p$ . Maps of  $S_s$  can be drawn for the ship; these show to what extent different parts of the ship are sensitive to damage. For larger damage cases (Level 3 or 4), alternative procedures must be used as discussed in [2, 3].

In some cases it is not possible to accept any reduction in the global or local strength of the structure. However, not all parts of the structure of a ship are highly stressed. In many cases a given panel may be exposed to a maximum loading that is lower than the allowable value because the design gave more than the minimum required reserve of strength, i.e. there is a lower utilisation of the panel than the maximum that is allowed. This is often due to the fact that a limited number of standard sandwich lay-ups are used in a given vessel. In such cases it will normally be acceptable to reduce the panel strength by an amount that reflects this extra reserve of strength in the intact structure. The same may apply at the global ship level if the ship has been generally over-designed against the global loads (e.g. because the local load requirements were more severe). These aspects are dealt with here by using utilisation factors  $U_p$  and  $U_s$  at the panel and ship levels. Normally the allowable strength reductions  $R_{pa}$  and  $R_{sa}$  for panel and global strength will be set equal to the respective utilisation factors.

There are two main additional considerations that may make a strength reduction acceptable:

- Reducing the loads (relative to original design) by restricting the operation in some way.
- Accepting a reduced factor of safety in the interim period until a repair is effected.

The first of these leads in effect to a lowering of the utilisation level in that the extreme design loads are now decreased. The second leads to a lowering of the utilisation level in that the allowable loads are increased.

#### **4.4 Aspects other than strength: functionality**

The procedure described so far deals only with strength considerations. Considerations of functionality (which may include that of stiffness as embodied in deflection criteria) must be made separately. Functionality requirements may override repair decisions based on load carrying capacity and include aspects such as

- watertightness
- weathertightness
- smoke-tightness
- fire division effectiveness
- equipment functioning (machinery, instrumentation)
- signatures and shielding

## 5. SPECIFIC DAMAGE MODELS

### 5.1 Introduction

Models have been developed with which it is possible to estimate the influence of individual defects and damage on structural performance. In the SaNDI Project attention was focused mainly on the estimation of residual strength under single, quasi-static loading, rather than on damage growth and fatigue under repeated loading. The following models are now available, though their accuracy in some cases is not fully established.

### 5.2 Face/core debonds

A face-core debond reduces the strength of a sandwich panel subjected to in-plane compression. A debond may also reduce the capacity of a panel with lateral loading if the face laminate at the debond is in compression, though the behaviour may also be influenced by out-of-plane shear stresses.

The reduction in in-plane compressive strength caused by face/core debonds below a certain size is found to be insensitive to the panel size and their influence on panel stiffness is very small. Thus small face/core debonds can be treated as Level 1 defects, at least for the case of in-plane compressive loading.

The local strength reduction  $R_l$  may be established using a number of alternative approaches using fracture mechanics techniques, including those of Berggreen [12-14] and Lord and Greenhalgh [15]. The latter method uses the DEBUGS software [16, 17], which was originally developed for modelling delaminations in laminates.

In fact Berggreen [12] developed a 2-dimensional crack propagation model and a 3-dimensional residual strength model that both take full account of mode mixity, which is often significant in sandwich interface problems because of the large difference in properties between the faces and the core. The models are both based on the crack surface displacement extrapolation (CSDE) approach and have been implemented using the commercial FE software ANSYS.

Figure 3 shows a plot of local strength reduction factor  $R_l$  as a function of debond diameter, based on the results reported by Berggreen [12, 14] using the 3-D residual strength model. This applies to sandwich lay-ups with GRP face laminates and H80 and H200 PVC foam cores. The GRP laminates each have quasi-isotropic, quadriaxial reinforcement and also a layer of CSM at the interface with the core and on the outer surface. Also shown is a corresponding plot based on experimental results [12, 13] for panels with the same sandwich lay-up. The test results for small debonds are affected by

wrinkling and other premature failures that are not properly taken account of in the model, but the agreement for larger debonds is acceptable.

Berggreen's model has also been applied to cases with non-uniform compression [18,19] and out-of-plane pressure loading [20].

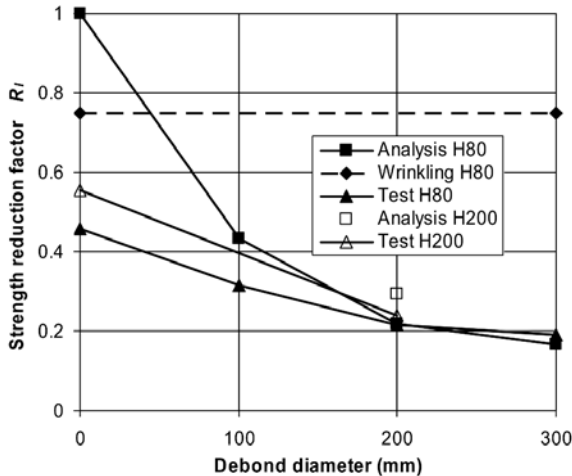


Figure 3. Local strength reduction factor for circular face/core debonds.

### 5.3 Contact damage

As argued by Hayman and Zenkert [2, 3], small cases of impact damage can usually be treated as Level 1 damage. For cases of in-plane compressive loading, local impact damage involving only the face sheet can be analysed using equivalent hole and equivalent crack models as described by Bull, Edgren and co-workers [21-25]. For damage involving fibre fracture it may be appropriate to use either model; Bull and Edgren [24] provide guidance on how to determine the equivalent hole diameter or equivalent crack length.

For less severe cases where the damage does not involve fracture of the fibres, it may still be possible to apply the equivalent hole model, but if there is permanent damage to the underlying core it may be necessary to consider an alternative residual dent model [21, 26, 27], and also to check for delamination buckling.

For impact damage represented by the equivalent hole model, the local strength reduction for quasi-isotropic CFRP laminates is shown in Figure 4. This applies for all face laminates of this lay-up provided the hole diameter is less than about 25% of the panel width. The corresponding curve for the equivalent crack model is also shown in Figure 4.

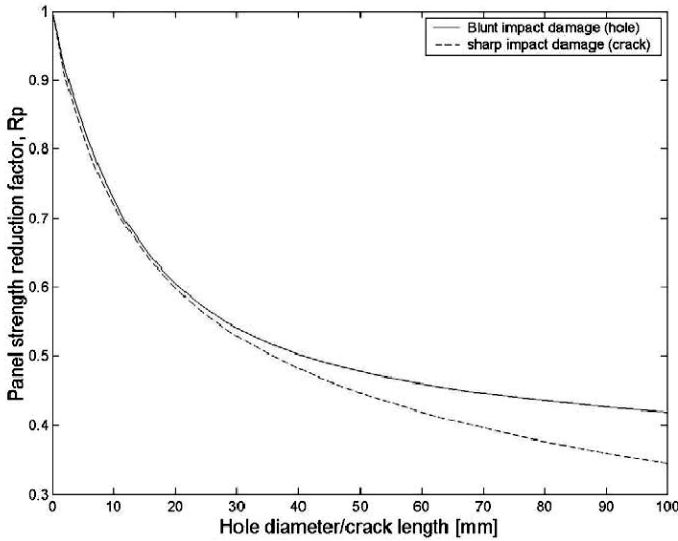


Figure 4. Local strength reduction factor for face laminate impact damage, equivalent crack and hole models.

## 5.4 Other defect and damage models

In the SaNDI Project and related activity, residual strength models have also been investigated for face sheet wrinkle defects [28] and for dry zones in laminates [29]. These may be treated as respectively Level 2 and Level 1 damage cases. Although no detailed model has yet been established, some information has been gathered concerning the influence of core shear cracks and associated debonding on the in-plane compressive strength of sandwich panels, and a way of treating such damage in a damage assessment context has been proposed. A model for deck face sheet pull-off at a deck-house corner in a ship undergoing global hull girder bending has also been developed using Berggreen's 2D delamination model [12, 30]. A series of more severe Level 3 and Level 4 damage cases has also been investigated.

## 6. DAMAGE TOLERANCE

### 6.1 Basic concept

In its simplest form, damage tolerance may be defined as the ability of a structure to accommodate damage without an unacceptable deterioration in its performance. Here the term "damage" is usually considered as including manufacturing defects as well as in-service damage. In practice, this implies that the residual strength and/or the residual life following the incidence of

damage are sufficient to meet a prescribed set of structural performance criteria.

## **6.2 Damage tolerance in aircraft structures**

Certification of metal aircraft structures has generally been based on one or more of the following three principles [31]:

**Safe-life:** It is shown by means of a fatigue strength investigation that the structure is able to withstand the repeated loads expected in service.

**Fail-safe:** It is shown that catastrophic failure of the structure is not probable after fatigue failure, or obvious partial failure, of a principal structural element, and that the remaining structure is able to withstand the maximum design loads (with a specified reduced factor of safety).

**Damage tolerant:** The probable locations and modes of damage due to fatigue, corrosion, or accidental damage are determined and a damage extent consistent with the initial detectability and subsequent growth under repeated loads is established. The evaluation consists of repeated load and static analyses. The residual strength evaluation must show that the remaining structure is able to withstand the design loads.

The damage tolerant design philosophy leads to two damage limits:

- Allowable damage limit (ADL), which is the maximum extent of defect or damage that the aircraft must survive while maintaining the original design factor of safety.
- Critical damage threshold (CDT), which is the maximum extent of damage that the aircraft must survive when subjected to the maximum load expected during its lifetime.

For composite aircraft structures only the damage tolerant option is allowed by the FAA. The threshold level and growth rate for growth of damage that may occur from fatigue, corrosion, manufacturing flaws or impact damage, under repeated loads expected in service, are established. The damage growth, between initial detectability and the value selected for residual strength demonstrations, factored to obtain inspection intervals, must allow development of an inspection programme suitable for application by operation and maintenance personnel.

Structural components for which the damage tolerance method is shown to be impractical must be shown to be able to withstand the repeated loads of variable magnitude expected in service. Damage up to the threshold of detectability must be considered.

The essential element of the damage tolerance approach is thus that any defect or damage that cannot be detected by the anticipated inspection procedures must be able to exist at a given inspection without causing failure by the time of the next scheduled inspection.

In the aircraft industry, damage tolerance considerations for FRP components have been mainly focused on delaminations as production defects and impact damage as in-service damage.

### **6.3 Damage tolerance approach to ship design and maintenance**

The damage tolerance philosophy described in Section 6.2 is made possible by the strict inspection and maintenance regimes that exist in the aircraft industry. Other decisive features are the mass production of most aircraft types in combination with stringent safety requirements, which make high development and qualification costs acceptable. The difficulty of access to large parts of a ship's structure at all times except for periodic dockings (which are typically at intervals from one year upwards) make it more difficult to apply such a philosophy in its entirety to ships, so some modification seems necessary. Furthermore, ships are generally produced in shorter series and they are less safety-critical (owing to the existence of effective life-saving systems) so that lower development and qualification costs for a series are essential.

In the case of ships, the set of defect and damage models described earlier can be used at the design stage to ensure damage tolerance at an appropriate level. These models and associated methodologies can also compensate for less rigorous built-in damage tolerance by ensuring that, if damage does occur, it can be assessed rapidly and appropriate corrective actions taken so that overall safety is not compromised.

A present limitation is that focus has been on residual strength of the structure with defect or damage (though often based on fracture mechanics methods) rather than damage growth under repeated loadings. This and the need for further development of NDI techniques are the main challenges remaining for the application of a more comprehensive damage tolerant design to FRP sandwich structures (and for FRP generally) in ships.

### **6.4 Damage tolerance approach to wind turbine blade design and maintenance**

Wind turbine blades present a special challenge in that they are produced in large numbers, similar to aircraft, but the possibilities for regular in-service inspection are much more limited or simply non-existent. For these structures the only viable approach at present appears to be safe-life design in which one takes account of the worst combination of production defects that is likely to go undetected during production, and the worst in-service damage that is likely to occur without being noticed. If this approach is to be

implemented in a systematic way, the manufacturer must obtain a reliable overview of the defects that may occur in practical production (described in statistical terms) and of possible in-service damage events. The former presents a major challenge for the industry since competition between manufacturers limits the amount of information they are able to share while differences in production techniques make the production defects more manufacturer-dependent than in many other industries.

A development that may improve this situation for wind turbines is structural health monitoring of blades using, for example, fibre optic sensors. These may be used both to detect abnormal events and to detect changes in dynamic response associated with the incidence of damage or major growth of a defect. This is already done to some extent by detecting out-of-balance conditions in the machinery. In contrast to an aircraft or a ship, a wind turbine can be taken out of service relatively quickly without having to land or seek refuge in a harbour. Furthermore, wind turbines are not generally as safety-critical as aircraft or ships. In the circumstances, the approach suggested here may well be the most cost-effective to apply in practice.

## **7. CONCLUSIONS**

A methodology for assessing the influence of production defects and in-service damage on the performance of FRP sandwich structures in naval ships has been presented as a basis for deciding on corrective measures. This incorporates models for a range of specific types of defects and damage. For a given ship, most of the required data for defect/damage assessment can be readily assembled during the design calculation stage, making it possible to provide decision support tools for both production control and in-service damage assessment.

Limitations in inspection techniques, combined with less rigorous and less frequent inspection and maintenance regimes associated with the lower safety risk, make a full damage tolerance philosophy similar to that in the aircraft industry both impractical and uneconomic for FRP sandwich structures in ships, as for many other large FRP structures such as wind turbine blades. The most suitable and economical approach to achieving damage tolerance is thus dependent on the application.

## **ACKNOWLEDGEMENT**

The paper is based largely on experience from the recently completed SaNDI (THALES JP3.23) Project “Inspection and Repair of Sandwich

Structures in Naval Ships”, with participants from Norway, Denmark, Sweden, Finland and the United Kingdom. The support of the Ministries of Defence of the five participating nations is gratefully acknowledged.

## REFERENCES

1. Hayman, B. Inspection and Repair of Sandwich Structures Based on Damage Tolerance Principles, 6th Int. Conf. on Sandwich Structures, Fort Lauderdale, Florida, USA, 2003.
2. Hayman, B. and Zenkert, D. The Influence of Defects and Damage on the Strength of FRP Sandwich Panels for Naval Ships, PRADS 2004, Travemünde, Germany, 2004.
3. Hayman, B. Defect and Damage Assessment for Ships Built in FRP Sandwich, RINA Conference on High Speed Craft, London, England, November 2004.
4. Weitzenböck, J.R., Echtermeyer, A.T., Artiga-Dubois, F. and Parmar, M. Nondestructive Inspection and Evaluation Methods for Sandwich Panels, 4th Int. Conf. on Sandwich Construction, Stockholm, Sweden, 1998.
5. Weitzenböck, J.R., Echtermeyer, A.T., Grönlund, P.K., Artiga-Dubois, F. and Parmar, M. Nondestructive Inspection and Evaluation Methods for Composites Used in the Marine Industry, 12th Int. Conf. on Composite Materials (ICCM-12), Paris, France, 1999.
6. Artiga-Dubois, F., Parmar, M., Echtermeyer, A.T. and Weitzenböck, J.R. Nondestructive Testing of Composites for Naval Applications. 20th Int. SAMPE Europe Conf., Paris, France, 1999.
7. Borum, K.K., Berggreen, C. Examination of Sandwich Materials Using Air-Coupled Ultrasonics, Proc. 16th World Conf. on Non Destructive Testing, 2004, Montréal, Canada.
8. Borum, K. Evaluation of Sandwich Materials Using Ultrasonic Air-Coupled Scanning Technique, 7th Int. Conf. on Sandwich Structures, Aalborg, Denmark, 2005.
9. Wulf, T.M. Automated Ultrasonic Inspection of Large-Scale Sandwich Structures, 7th Int. Conf. on Sandwich Structures, Aalborg, Denmark, 2005.
10. Jensen, A.E., Taby, J., Pran, K., Sagvolden, G. and Wang, G. Global load measurement on a surface effect ship using a network of fibre optic strain sensors and detailed FE analysis. Proc. 7th Int. Conf. on Composites Engineering (ICCE/7), Denver, Col., USA, 2000.
11. Ratcliffe, C. and Crane, R.M. Locating Manufacturing and Structural Irregularities in Large Composite Sandwich Structures, 6th Int. Conf. on Sandwich Structures, Fort Lauderdale, Florida, USA, 2003.
12. Berggreen, C. Damage tolerance of debonded sandwich structures, Ph.D. Thesis, Department of Mechanical Engineering, Technical University of Denmark, 2004.
13. Lundsgaard-Larsen, C., Berggreen, C. and Nøkkentved, A. Residual Strength of In-plane Loaded Debonded Sandwich Panels - Experimental Investigation, 7th Int. Conf. on Sandwich Structures, Aalborg, Denmark, 2005.
14. Berggreen, C. and Simonsen, B. C. Residual Strength of In-plane Loaded Debonded Sandwich Panels - Fracture Mechanical Modelling, 7th Int. Conf. on Sandwich Structures, Aalborg, Denmark, 2005.
15. Lord, S.J. and Greenhalgh, E.S. Modelling of Delamination and Debonding in Laminated Composites using a Moving Mesh Approach. 11th European Conference on Composite Materials, Rhodes (Greece), 2004.

16. Nilsson, K-F., Asp, L. and Alpman, J. Delamination buckling and growth at global buckling, First Int. Conf. on Damage and Failure of Interfaces, Ed. H.-P. Rossmanith, Vienna, pp193-202, 1997.
17. Nilsson, K-F., Asp, L.E., Alpman, J.E. and Nystedt, L.. Delamination buckling and growth for delaminations at different depths in a slender composite panel, FFA TN-1999-09, Aeronautical Research Institute of Sweden, 1999.
18. Nøkkentved, A., Lundsgaard-Larsen, C. and Berggreen, C. Non-Uniform Compressive Strength of Debonded Sandwich Panels - I. Experimental Investigation, *Jnl. of Sandwich Structures and Materials*, in press, 2005
19. Berggreen, C., Simonsen, B. C. Non-Uniform Compressive Strength of Debonded Sandwich Panels - II. Fracture Mechanics Investigation, *Jnl. of Sandwich Structures and Materials*, in press, 2005
20. Jolma, P., Segercrantz, S. and Berggreen, C. Residual Strength of Debonded Sandwich Panels Loaded with Lateral Pressure - Experimental Investigation and Fracture Mechanical Modelling, 7th Int. Conf. on Sandwich Structures, Aalborg, Denmark, 2005.
21. Zenkert, D., Shipsha, A., Bull, P. and Hayman, B. Damage Tolerance Assessment of Composite Sandwich Panels with Localised Damage, submitted for publication in *Composites Science and Technology*, 2005.
22. Bull, P.H., *Damage Tolerance and Residual Strength of Composite Sandwich Structures*, Ph.D. thesis, Department of Aeronautical and Vehicle Engineering, Kungliga Tekniska Högskolan, TRITA-AVE.2004:16, 2004.
23. Bull, P.H. and Edgren, F. Residual strength of impact damaged CFRP-foam core sandwich panels, Proc. 6th Int. Conf. on Sandwich Construction, Fort Lauderdale, USA, 2003.
24. Bull P.H. and Edgren F., Compressive Strength after Impact of CFRP-Foam Core Sandwich Panels, *Composites Part B: Engineering*, 2004:35(6-8), pp 535-541.
25. Edgren F., Asp L.E. and Bull P.H., Compressive Failure of Impacted NCF Composite Sandwich Panels - Characterisation of the Failure Process, *Journal of Composite Materials*, 38(6), pp 495-514, 2004.
26. Zenkert D., Shipsha A. and Persson K. Static Indentation and Unloading Response of Sandwich Beams, *Composites Part B*, 35(6-8), pp 511-522, 2004.
27. Shipsha, A., Hallström, S. and Zenkert, D. Failure Mechanisms and Modelling of Impact Damage in Sandwich Beams - A 2D approach: Part I - Experimental Investigation, *Journal of Sandwich Structures and Materials*, 5(1), pp 7-32, 2004.
28. Hayman, B., Berggreen, C. and Petterson, R. The Influence of Face Sheet Wrinkle Defects on the Performance of FRP Sandwich Structures, 7th Int. Conf. on Sandwich Structures, Aalborg, Denmark, 2005.
29. Johansson, A. Dry-zones in sandwich panels, MSc Thesis, Royal Institute of Technology, Stockholm, Sweden, 2005.
30. Berggreen, C., Simonsen, B. C., Törnqvist, R. Modelling of Debond and Crack Propagation in Sandwich Structures Using Fracture and Damage Mechanics. 6th Int. Conf. on Sandwich Structures, Ft. Lauderdale, Florida, USA, 2003, CRC Press, Boca Raton.
31. Tomblin, J. Lacy, T., Smith, B., Hooper, S, Vizzini, A. and Lee, S. Review of Damage Tolerance for Composite Sandwich Airframe Structures, Office of Aviation Research Report DOT/FAA/AR-99/49, 1999.

# **SESSIONS ORGANISED BY THE ONR**

**(Office of Naval Research, U.S. Navy, Program Manager Dr. Y. Rajapakse)**

# GEOMETRICAL NON-LINEAR RESPONSE OF MODERN SANDWICH PANELS – LOCALIZED EFFECTS

Y. Frostig

*Faculty of Civil and Environmental Engineering, Technion-Israel Institute of Technology, Haifa, 32000, Israel*

**Abstract** The paper presents the results of an investigation on the role of localized effects in the geometrically non-linear response of modern sandwich panels made of a “soft” core. The adopted non-linear analysis approach incorporates the effects of the vertical flexibility of the core, and it is based on the approach of the High-Order Sandwich Panel Theory (HSAPT). The non-linear governing equations are solved using the multi-point shooting method along with parametric and arc-length continuation procedures. And the non-linear response is described in terms of deflections and stress resultants in the face sheets, as well as in terms of the interfacial stress components at the upper and lower face-core interfaces and equilibrium path curves of the load versus the extreme absolute values of some structural quantities. The numerical study investigates the localized effects and how do they attenuate with the deformations in the case of a panel with a reinforced core at its mid region and subjected to a uniform distributed load. The results are compared with a panel that has a core with uniform properties. One of the findings of this research is that a typical modern panel exhibits a limit point response as a result of a load that causes bending, with and without localized effects, even when subjected to uniformly distributed loads and the material discontinuity of the core leads to localized effects that significantly affects the non-linear response.

**Keywords:** non-linear, limit point, localized effects.

## 1. INTRODUCTION

Modern sandwich panels are widespread within the aerospace, naval/marine, automotive and general transportation industries. They are considered as efficient extremely lightweight structural components with

very high bending stiffness, high strength and high buckling resistance. Such panels consist of metallic or composite face sheets that are interconnected through a thick, lightweight and compliant core material usually made of foam or light weight and low strength non-metallic honeycomb. The general structural response of a sandwich panel consists mainly of a couple, i.e. compression and tension forces in the face sheets, and shear stresses in the core. The composite action is defined as the ratio between the bending moment of the couple and the overall bending moment. In general, the bending resistance of the panel, when no localized loads are involved, is totally resisted by the couple. However, when localized effects exist additional local bending moments in the face sheets and high interfacial stresses at the face-core interfaces and the core occur which reduces, to some extent, the contribution of the couple to the over bending moment resistance or the composite action.

The existence of a compliant core in modern sandwich panels lead to a structure that is notoriously sensitive to localized effects. These effects exist in the vicinity of concentrated loads or partially distributed loads, at points or lines of support, at geometric and material discontinuities and also when the panel undergoes large deformations. Although sandwich structures are well suited for the transfer of overall bending and shear stress especially when distributed loads are involved, the localized shear and bending effects, as a result of even uniformly distributed loads, induce severe vertical normal and interfacial shear stresses which may endanger the safety of the panel. Hence, the general design approach of a sandwich panel to withstand overall as well as localized effects is through a strength approach with allowable stress criteria.

In addition, the compressive in-plane stress resultant in the face sheets may initiate buckling of this face that may propagate into an unstable behavior, such as a limit point response, and thereby seriously affect the structural integrity. The vast majority of failures in sandwich structures, due to either static overloading or fatigue loading conditions, are caused by localized effects. In addition, geometrically non-linear behavior strongly influence and attenuate the described localized effects. As such it is important to develop a physically consistent model that enables accurate assessment of the role of the localized effects in the geometrically non-linear response of sandwich structures.

The classical analysis approaches, see Allen [1], Plantema [2], Zankert [3] and Vinson [4], for traditional sandwich panels of anti-plane cores, such as metallic honeycomb core, ignore the presence of localized effects, and are in fact unable to detect and quantify them. In general, the approaches used for bending, overall buckling and vibration analyses, in most cases, replace the layered structure with a solid homogeneous panel of a single layer and

with equivalent properties, see Reddy's high-order theories [6]. Notice that the use of the equivalent single layer approach is strictly valid only for sandwich panels with incompressible core, and may yield erroneous results when applied for the analysis of modern sandwich panels with a "soft" core material.

Localized effects in sandwich panels, especially in the vicinity of localized and concentrated loads and supports have been investigated by several authors. See for example Thomsen, see [7, 8], using an elastic foundation approach and Frostig *et al.*, see [9], uses an enhanced model with the High-Order Sandwich Panel Theory (HSAPT) approach. The advantages of the high-order approach are its ability to detect localized effects within a global analysis of the sandwich panel. It has been successfully applied to linear and nonlinear applications by the author as well as by others, such as: buckling of a unidirectional panel, see Frostig and Baruch [10], buckling of a sandwich plate, see Frostig [11], non-linear response of a panel with rigid and non-rigid interfaces including branching behavior due to in-plane compressive loads, see Sokolinsky and Frostig [12] and Sokolinsky *et al.* [13] and an experimental and analytical study of four points bending case, see Sokolinsky *et al.* [14], where the non-linear response is experimentally defined. Recently, Frostig and Thomsen, see [15-16], have investigated the attenuation of the localized effects when large deformations occur in the present of concentrated loads and debonded regions and the results have been compared with FE results in a Frostig *et al.*, see [17].

The literature survey reveals that most of the research works on localized effects have been limited to linear mathematical models such the linear theory of elasticity, linear elastic foundation model approaches or the linear high-order sandwich theory approach. Only a few research works have studied the role of these effects with large deformations and how do they attenuate in the presence of in-plane compressive load or concentrated ones. Hence, the main objective of the present study is to clarify and explain how the localized effects change, in the present of reinforced core zones, when large deformations are involved and uniform distributed loads are considered.

The paper presents a numerical study of the non-linear response of a unidirectional sandwich panel subjected to a uniform distributed load that yields localized effects as a result of the discontinuity in the core material. The analysis presented is based on the non-linear high-order sandwich panel theory, see Frostig and Thomsen [15].

## 2. NUMERICAL STUDY

In general, sandwich panels are best suited for distributed loads and the linear response is not associated with localized effects. However, the following numerical study reveals that this postulate is correct, to some extent, as long as the panel undergoes small deformations and incorrect when large deformations are involved and the non-linear response governs.

The numerical study investigates the role of the localized effects in the non-linear regime when subjected to a uniform distributed load for a panel with a reinforced core at its mid region. The results are compared with a panel made of a core with uniform properties throughout the length of the panel. The simply-supported panel, at its upper and lower face sheets and the core, consists of two face sheets made of Kevlar with an equivalent modulus of elasticity of 27.4 GPa and a core made of Rohacell WF type of foams. The mid-region, of the panel,  $120 \leq x \leq 180$ , has been reinforced with a heavier foam, 200 WF foam, while the other parts use a lighter foam of 51 WF. See Fig 1a for geometry and mechanical properties.

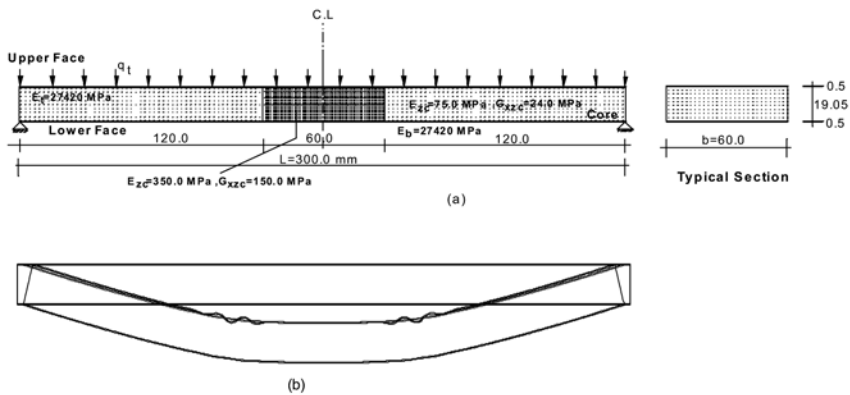


Figure 1. A reinforced panel: (a) geometry, external loads and mechanical properties, (b) deformed shape deep in the non-linear regime.

The deformed shape of the panel deep in the no-linear region, beyond the limit point, that occurs at  $q_{lm} = 13.73 \text{ N/mm}$ , appears in Fig. 1b. The localized effects occur in the vicinity of discontinuity of the core where its properties changes from a light one into an heavier one. They are associated with non-uniform buckling waves of the compressed core that propagate into the region with the lighter core.

The vertical displacements of the face sheets, see Fig. 2a, exhibit a linear response as long as the non-linear regime has not been reached. Within the non-linear regime, the buckling waves in the compressed face occur left of

the discontinuity location of the core. The maximum mid-span displacement in the non-linear case is more than doubled as compared with the linear cases.

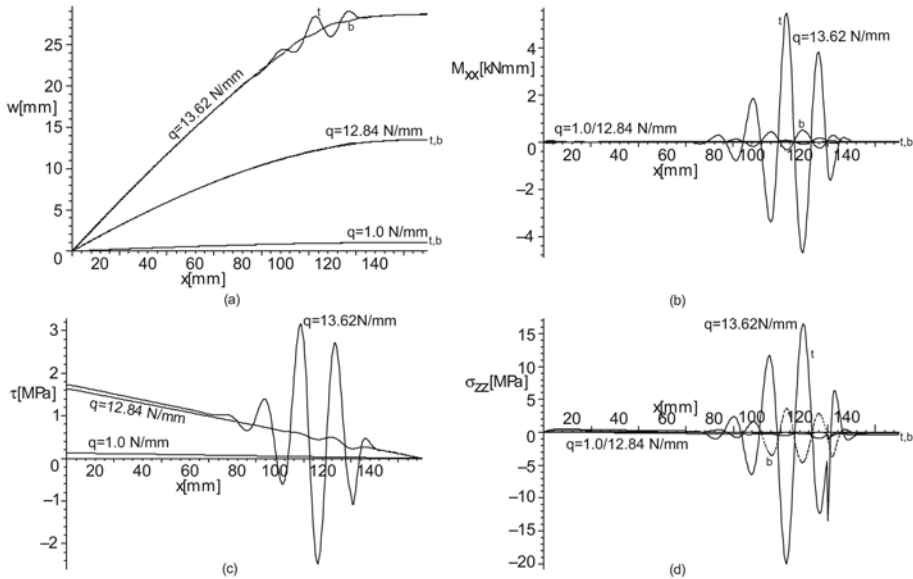


Figure 2. Non-linear response at various load levels: at face sheets: (a) vertical displacements, (b) bending moments; and at the core and its interfaces: (c) shear stresses, (d) interfacial vertical normal.

In addition, a pronounced tendency of displacement localization occurs in the wavy buckled zone for the non-linear case, where the large displacements and buckling waves are associated with extremely large bending moments, see Fig. 2b. The magnitude of the bending moments, within the non-linear regime, in the upper face sheet is extremely high and is about 4 to 6 times larger than that of the lower face sheet and much higher than the linear results. Again, the wavy bending moments concentrate left of the discontinuity location into the lighter core. The wavy tendency in the vicinity of the discontinuity location is also observed in the shear stresses of the core, see Fig. 2c. Finally, the interfacial vertical normal stresses reach extremely large values deep in the non-linear response and are associated with a wavy type of stress patterns, see Fig. 2d and also here the waves extend from the discontinuity location into the lighter core.

The results in the vicinity of the location of the material discontinuity of the core, at  $x=120.0$  mm, appear in Fig. 3.

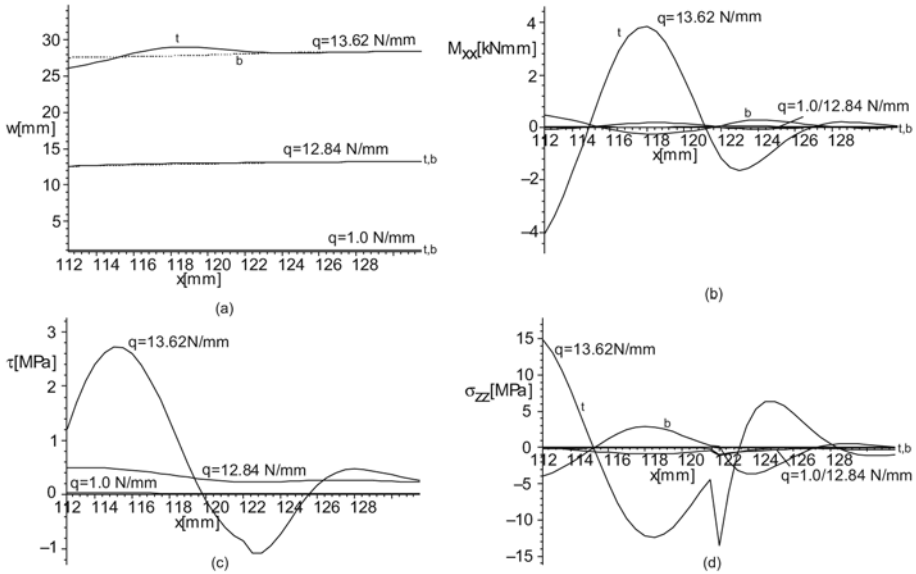


Figure 3. Non-linear response at various load levels in the vicinity of core discontinuity: at face sheets: (a) vertical displacements, (b) bending moments; and at the core and its interfaces: (c) shear stresses, (d) interfacial vertical normal stresses. Legend: \_\_\_\_\_ t upper face/interface, - - - - b Lower face/interface.

The vertical displacements, see Fig. 3a, reveal that the buckling waves, deep in the non-linear regime, penetrate also into the heavy core. The wavy type of the bending moments appears in Fig. 3b and of large magnitude. The same wavy type of response is observed in the case of the shear stresses in the core, see Fig. 3c. The vertical interfacial stresses appear in Fig. 3d and it exhibits an abrupt change in the stresses in the close vicinity of location of the core discontinuity due to differences in cores rigidities.

The equilibrium path curves of load versus the extreme values described above for the panel with a reinforced core, denoted by RC, of a discontinuity at  $x=120.0$  mm, and the light core, 51WF that is uniform throughout the length of the panel, denoted by UC, appears in Fig. 4. In both cases, a limit point is observed and it is at a load level of 13.64 N/mm for the panel with a uniform core and 13.73 N/mm for the reinforced one. Notice that the difference between the two limit points load is very small although a fifth of the length of the panel has been reinforced by a core that is about five times heavier than the other parts. In addition, the load level of the limit point for a panel using a uniform heavier core, made of 200 WF, is almost 2.5 times that of the lighter one. Hence, the contribution of the reinforced core to the overall response in terms of the limit point load level is insignificant.

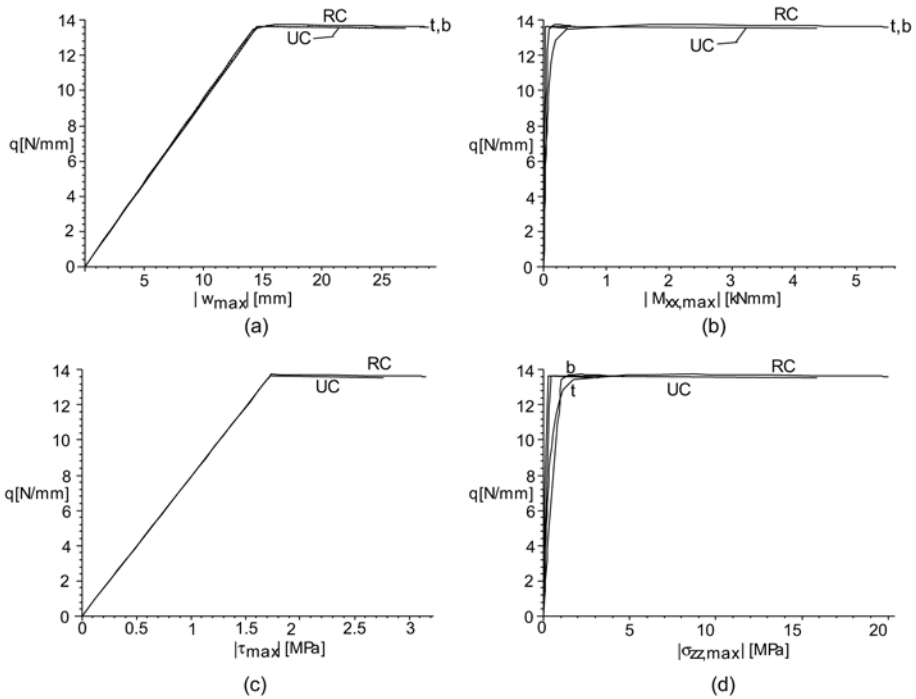


Figure 4. Equilibrium path curves of a panel with a reinforced core (RC) and with a uniform one (UC): at face sheet: (a) vertical displacements, (b) bending moments; and in core and its interfaces: (c) shear stresses, (d) interfacial vertical normal stresses. Legend:  $t$  upper face/interface,  $b$  Lower face/interface.

The equilibrium path curves reveal that in both cases the behavior is almost linear up to the limit point. In the case of a panel with a uniform core the limit point develops suddenly while in the case of the reinforced one an intermediate region between the linear and the non-linear regimes occurs, see Fig. 4a. The difference between the two types of panels is more pronounced when the bending moments and the vertical interfacial stresses are considered, see Figs. 4b and 4d. The response of the shear stresses in the core is almost identical with a linear response up to the limit point, see Fig. 4c. The similarity in the results between the two types of panels is a due to the attenuation of the localized effects in the vicinity of the discontinuity of the core materials which severely affects also the overall non-linear response of the panel and reduces its capacity.

### 3. SUMMARY AND CONCLUSIONS

The role of localized effects upon the non-linear response of sandwich panels subjected to uniformly distributed loads and a panel with a reinforced core has been presented. The analysis is based on the non-linear high-order sandwich panel theory approach along with the multiple points shooting method of solution and the parametric and arc-length continuation methods.

The role of the localized effects in the non-linear response has been demonstrated through the study of sandwich panels loaded by a uniformly distributed load. The results of the panel with the reinforced core have been compared with those of an identical panel with the same load but with a light core that is uniform through the length of the panel.

The localized effects, due to the core discontinuity change the strength problem that is associated with high stresses only in the linear regime into a stability problem with buckling of the upper face sheet and with very high stresses in the non-linear regime. The non-linear response, in many cases, is associated with an unstable limit-point behavior that is characterized by a couple, whose magnitude nearly doesn't change, along with large bending moments induced in the compressed face sheet as the load increases. These large bending moments are also associated with large shear stresses and interfacial ones at the compressed face sheet and the core. Or in other words, at this load level the composite action of the sandwich panel, in the vicinity of the core discontinuity, reduces significantly and any additional loads are being carried only through bending moments in the loaded face sheet and high interfacial stresses without any increase in the magnitude of the couple.

In the vicinity of the location of the core discontinuity the linear response usually consists of stress accumulation in the face sheets as well as in the core and at its interfaces. They are expressed by significant bending moments and compressive vertical normal stresses at the upper core interface, and with peak shear and tensile interfacial vertical normal stresses at the lower face-core interface. In the non-linear range all these effects are magnified in a disproportionate manner as a result of the stability problem that emerges. Thus, the bending stresses and the compressive stresses in the upper face increase significantly, and buckling waves are developed in the compressed face sheet from the edges of the reinforced core into the light one. These buckling waves significantly magnify the bending moments in the face sheets and the interfacial tensile vertical normal stresses along with peaks in the shear stresses. The existence of a discontinuity in the properties of the core, in the non linear regime, reduces the capacity of the reinforced panels almost to that of a panel with a light core. Hence, the localized effects induced by the mismatch of the core material properties plays a role of some kind of an imperfection that reduces the load of the limit point. The

existence of a limit point response, even in the case of a uniformly distributed load, redefines the way the failure load should be determined, even for very strong sandwich panels. It actually states that the failure load should be controlled by stability criteria rather than stress constraints.

The non-linear effects, especially at the compressed face, are associated with significant stresses induced near the discontinuity of the core material. Hence, prediction of the localized effects described in terms of displacements and stresses using the linear response formulation are erroneous especially when large displacement and material discontinuity are involved.

The results presented herein, based on the non-linear HSAPT formulation, suggests that the non-linear response of a sandwich panel in some cases should be the basis for a reliable safe design, especially in zones with localized/concentrated loads or material discontinuity and especially when transversely flexible core materials are of concern.

## REFERENCES

1. Allen, H.G., *Analysis and Design of Structural Sandwich Panels*, London, Pergamon Press, 1969.
2. Plantema, F.J., *Sandwich Construction*, New York, John Wiley and Sons, 1966.
3. Zenkert, D., *An Introduction to Sandwich Construction*, Chameleon Press Ltd., London, 1995.
4. Vinson J.R. *The behavior of Sandwich Structures of Isotropic and Composite Materials*, Lancaster, Technomic Publishing Co. Inc, 1999.
5. Mindlin, R. D. "Influence of Transverse Shear Deformation on the Bending of Classical Plates", *Transaction of ASME, Journal of Applied Mechanic*, 8, 1951, pp. 18-31.
6. Reddy, J. N., *Energy and variational Methods in Applied Mechanics*, John Wiley and Sons, Inc., New York, 1984.
7. Thomsen, O.T., "Analysis of Local Bending Effects in Sandwich Plates with Orthotropic Face Layers Subjected to Localised Loads". *Composite Structures*, 25, 1993, pp. 511-520.
8. Thomsen, O.T., "Theoretical and Experimental Investigation of Local Bending Effects in Sandwich Plates". *Composite Structures*, 30(1), 1995, pp. 85-101.
9. Frostig, Y., Baruch, M., Vilnay, O. and Sheinman, I., "A High Order Theory for the Bending of Sandwich Beams with a Flexible Core", *Journal off ASCE, EM Division*, 118(5), May 1992, pp. 1026-1043.
10. Frostig, Y., Baruch, M., "Buckling of Simply-Supported Sandwich Beams with Transversely Flexible Core - A High Order Theory", *Journal of ASCE, EM Division*, 119(3), March 1993, pp. 476-495.
11. Frostig, Y. "Buckling of Sandwich Panels with a Transversely Flexible Core - High-Order Theory", *International Journal of SOLIDS and STRUCTURES*, 35(3-4), 1998, pp. 183-204.
12. Sokolinsky V., Frostig, Y. "Branching Behavior in the Non-Linear Response of Sandwich panels with a transversely Flexible Core", *International Journal of SOLIDS and STRUCTURES*, 37, November 2000, pp. 5745-5772.

13. Sokolinsky V. S., Frostig Y., and Nutt S. R., "Special Behavior of Sandwich Panels with Transversely Flexible Core under Statical Loading", *International Journal of Non-Linear Mechanics*, special issue in honor of Prof. Johann Arbocz at his retirement from the Delft University of Technology, 37(4-5), June 2002, pp. 869-895.
14. Sokolinsky V.S., Shen, H. Vaikhanski L., Nutt, S.R. "Experimental and Analytical Study of Nonlinear Bending Response of Sandwich Beams", *Composite Structures*, 60 (2), May 2003, pp. 219-229.
15. Frostig Y. and Thomsen, O. T., "Localized Effects in the Non-Linear Behavior of Sandwich Panels with a Transversely Flexible Core", *Journal of SANDWICH STRUCTURES and MATERIALS* 7 (1), January 2005, pp. 53-75.
16. Frostig Y. and Thomsen, O. T., "Non-Linear Behavior of Delaminated Sandwich Panels with Partial Contact and a Transversely Flexible Core", *Int. J. of Non-Linear Mechanics* (In press) September 2004.
17. Frostig Y. and Thomsen, O. T., Sheinman I., "On the Non-Linear High-Order Theory of Unidirectional Sandwich Panels with a Transversely Flexible Core", *Int. J. of Solid and Structures* 42 (5-6), March 2005, pp. 1443-1463.

# GLOBAL BUCKLING OF WIDE SANDWICH PANELS WITH ORTHOTROPIC PHASES: AN ELASTICITY SOLUTION

George A. Kardomateas

*School of Aerospace Engineering, Georgia Institute of Technology,  
Atlanta, GA 30332-0150, USA*

george.kardomateas@aerospace.gatech.edu

**Abstract** There exist several formulas for the global buckling of sandwich plates, each based on a specific set of assumptions and a specific plate or beam model. It is not easy to determine the accuracy and range of validity of these rather simple formulas unless an elasticity solution exists. In this paper, we present an elasticity solution to the problem of global buckling of wide sandwich panels (equivalent to sandwich columns) subjected to axially compressive loading (along the short side). The emphasis on this study is on the global (single-wave) rather than the wrinkling (multi-wave) mode. The sandwich section is symmetric and all constituent phases, i.e., the facings and the core, are assumed to be orthotropic. The buckling problem is formulated as an eigen-boundary-value problem for differential equations, with the axial load being the eigenvalue. The complication in the sandwich construction arises due to the existence of additional “internal” conditions at the face sheet/core interfaces. Results are produced for a range of geometric configurations and these are compared with the different global buckling formulas in the literature.

**Keywords:** buckling, sandwich, elasticity, column.

## 1. INTRODUCTION

The compressive strength of thin sheets can be realized only if they are stabilized against buckling. In sandwich construction, two such sheets (face-sheets) are bonded to a core slab of different (light) material. Both the core and the face-sheets can be isotropic or anisotropic.

Panels of this construction give rise to a set of problems of strength, stiffness, and stability analogous to, but by no means identical with, the well-known problems of ordinary homogeneous elastic beam/plates. One of these is “cylindrical buckling”. Referring to Figure 1, the panel is so wide that lines

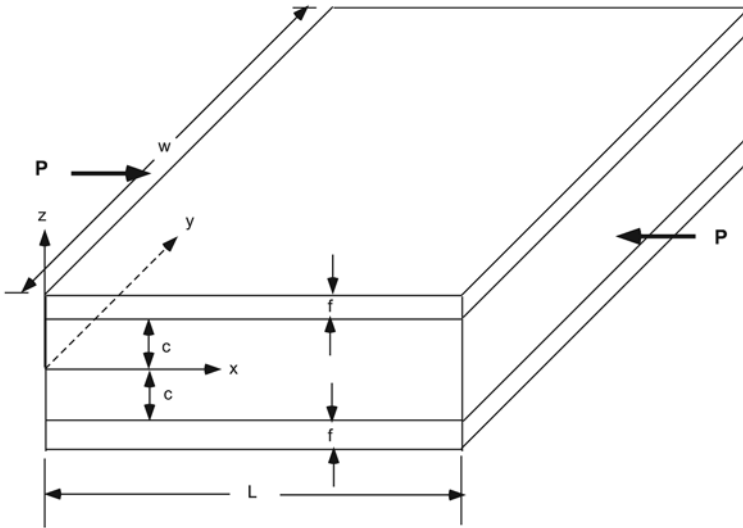


Figure 1. Definition of the geometry for a sandwich wide panel/beam under axial compression.

along the  $y$  axis can be taken as uncarved. Therefore, a unit width can be treated as an Euler column. Buckling is either like column buckling (Euler or global buckling) or a short wave “wrinkling” of the face sheets. In the former, the core may exhibit a substantial shearing deformation; in the latter, it acts like an elastic foundation and the buckling deformation is mainly confined to the layers adjacent to the face sheets.

A few global buckling formulas for sandwich construction can be found in the literature. In particular, a whole chapter is devoted to buckling in Allen’s book [1]. Two formulas are presented, one for thin faces and one for thick faces. Another formula is in Bazant and Cedolin’s book [2]. As far as wrinkling, several investigations have led to simple formulas, with the most known the one by Hoff and Mautner [3].

The existence of different buckling formulas based on various beam or plate models underscores the need for an elasticity solution, in order to compare the accuracy of the predictions from the simple beam/plate formulas. Elasticity solutions for buckling have become available mainly for the axisymmetric cylindrical shell geometry, due to the availability of three-dimensional elasticity solutions for the pre-buckling state and the ease of formulation afforded by the axisymmetry [4-6]. As far as sandwich structures, a three dimensional elasticity solution for the buckling of a sandwich long shell under external pressure was recently done by Kardomateas and Simites [7]. In all these studies, a pre-requisite to obtaining elasticity solutions for shell buckling is the existence

of three-dimensional elasticity solutions to the pre-buckling problem. For the monolithic homogeneous cylindrical shells, the elasticity solutions for orthotropy provided by Lekhnitskii [8] were used, whereas for the sandwich shells, the elasticity solution of Kardomateas [9] was used.

In this paper we make again the simplifying assumption of a two-dimensional problem by considering a wide plate. Because the plate is wide, lines along the long dimension can be taken as uncurved during buckling and the problem reduces to two-dimensional (equivalent to a beam rather than a plate assumption). The elasticity solution for the pre-buckling state derived for the case of a sandwich plate with generally orthotropic phases under axial loading is used [10]. Subsequently, the governing buckling equations along with the corresponding boundary conditions are derived. These reduce to a eigen-boundary value problem for differential equations with the axial load being the eigenvalue. The complication in the sandwich construction arises due to the existence of additional “internal” conditions at the face sheet/core interfaces. The shooting method is used to solve the problem thus formulated.

## 2. FORMULATION

By considering the equations of equilibrium in terms of the second Piola-Kirchhoff stress tensor, subtracting these at the perturbed and initial conditions, and making order of magnitude assumptions on the products of stresses and strains/rotations, based on the fact that a characteristic feature of stability problems is the shift from positions with small rotations to positions with rotations substantially exceeding the strains, the buckling equations for a cartesian coordinate system can be obtained [11].

The associated boundary conditions can be obtained from the traction (stress resultant) relationships in terms of the second Piola-Kirchhoff stress tensor, and in the general case of an external hydrostatic pressure loading (in which case the magnitude of the surface load remains invariant under deformation, but its direction changes). By writing these equations for the initial and the perturbed equilibrium position and then subtracting them and using the previous arguments on the relative magnitudes of the rotations, the boundary conditions on a surface which has outward unit normal  $(\hat{l}, \hat{m}, \hat{n})$  and is under the action of a hydrostatic pressure,  $p$ , are obtained [11]. For the bounding surfaces,  $\hat{l} = \hat{m} = 0$  and  $\hat{n} = \pm 1$ . These conditions will also be used when we impose traction continuity at the core/face sheet interfaces.

### 2.1 Pre-buckling state

Let us assume general orthotropy for the face sheet,  $i = f$ , or the core,  $i = c$ :

$$\begin{bmatrix} \sigma_{xx}^{(i)} \\ \sigma_{yy}^{(i)} \\ \sigma_{zz}^{(i)} \\ \tau_{yz}^{(i)} \\ \tau_{xz}^{(i)} \\ \tau_{xy}^{(i)} \end{bmatrix} = \begin{bmatrix} c_{11}^i & c_{12}^i & c_{13}^i & 0 & 0 & 0 \\ c_{12}^i & c_{22}^i & c_{23}^i & 0 & 0 & 0 \\ c_{13}^i & c_{23}^i & c_{33}^i & 0 & 0 & 0 \\ 0 & 0 & 0 & c_{44}^i & 0 & 0 \\ 0 & 0 & 0 & 0 & c_{55}^i & 0 \\ 0 & 0 & 0 & 0 & 0 & c_{66}^i \end{bmatrix} \begin{bmatrix} \epsilon_{xx}^{(i)} \\ \epsilon_{yy}^{(i)} \\ \epsilon_{zz}^{(i)} \\ \gamma_{yz}^{(i)} \\ \gamma_{xz}^{(i)} \\ \gamma_{xy}^{(i)} \end{bmatrix}, \quad (i = f, c) \quad (1)$$

where  $c_{kl}^i$  are the stiffness constants (we have used the notation  $1 \equiv x$ ,  $2 \equiv y$ ,  $3 \equiv z$ , see Fig. 1).

The pre-buckling solution was derived in Kardomateas [10] and the normal pre-buckling stresses are in the form (for  $i = f, c$ ):

$$\sigma_{xx}^{0(i)} = P [c_{11}^i d_1 + c_{12}^i d_2 + c_{13}^i (d_3 z^2 + d_4)], \quad (2a)$$

$$\sigma_{yy}^{0(i)} = P [c_{12}^i d_1 + c_{22}^i d_2 + c_{23}^i (d_3 z^2 + d_4)], \quad (2b)$$

$$\sigma_{zz}^{0(i)} = P [c_{13}^i d_1 + c_{23}^i d_2 + c_{33}^i (d_3 z^2 + d_4)], \quad (2c)$$

whereas the shear strains and stresses are zero:

$$\tau_{xy}^0 = \tau_{xz}^0 = \tau_{yz}^0 = 0. \quad (2d)$$

The constants  $d_1, d_2, d_3$  and  $d_4$  are found from the condition of zero tractions at the bounding surfaces,  $\sigma_{zz} = 0$ , i.e. at  $z = \pm(c + f)$ ; the condition of zero resultant force on the bounding sides normal to the  $y$  axis,  $\int \sigma_{yy} w dz = 0$ , at  $y = 0, w$ ; the condition of the resultant applied compressive load,  $P$ , on the bounding sides normal to the  $x$  axis,  $\int \sigma_{xx} w dz = -P$ , i.e. at  $x = 0, L$ ; and, finally, the traction continuity at the face-sheet/core interface, i.e. at  $z = \pm c$ ,  $\sigma_{zz}^c = \sigma_{zz}^f$ .

## 2.2 Perturbed state

The buckling equations can be written in terms of the buckling displacements  $u, v$  and  $w$  by using the strain vs displacement relations and then using the stress-strain relations. The first of these equations is:

$$\begin{aligned} c_{11} u_{,xx} + \left( c_{66} - \frac{\sigma_{yy}^0}{2} \right) u_{,yy} + \left( c_{55} + \frac{\sigma_{zz}^0}{2} \right) u_{,zz} + \left( c_{12} + c_{66} - \frac{\sigma_{yy}^0}{2} \right) v_{,xy} + \\ + \left( c_{13} + c_{55} - \frac{\sigma_{zz}^0}{2} \right) w_{,xz} + \frac{\sigma_{zz,z}^0}{2} (u_{,z} - w_{,x}) = 0. \end{aligned} \quad (3a)$$

Two other equations are obtained; these equations apply at every point through the thickness, but for convenience we have dropped the superscript  $i$ .

Three corresponding traction boundary conditions at the bounding surfaces for  $\hat{l} = \hat{m} = 0$  and  $\hat{n} = 1$  are also obtained; for illustration, the first of these is:

$$\left(c_{55} + \frac{\sigma_{zz}^0}{2}\right) u_{,z} + \left(c_{55} - \frac{\sigma_{zz}^0}{2}\right) w_{,x} = 0. \quad (3b)$$

In the perturbed position we seek two-dimensional equilibrium modes as follows:

$$u_i = U_i(z) \cos \lambda x; \quad v_i = 0; \quad w_i = W_i(z) \sin \lambda x, \quad \lambda = \frac{\pi}{L} \quad i = f, c \quad (4)$$

Substituting results in the following two linear homogeneous ordinary differential equations of the second order for  $U_i(z)$ ,  $W_i(z)$ , where  $i = c$  for  $0 \leq z \leq c$  and  $i = f$  for  $c \leq z \leq (c + f)$ :

$$\begin{aligned} & \left(c_{55}^{(i)} + \frac{\sigma_{zz}^{0(i)}}{2}\right) U_i'' + \frac{\sigma_{zz,z}^{0(i)}}{2} U_i' - c_{11}^{(i)} \lambda^2 U_i + \\ & + \left(c_{13}^{(i)} + c_{55}^{(i)} - \frac{\sigma_{zz}^{0(i)}}{2}\right) \lambda W_i' - \frac{\sigma_{zz,z}^{0(i)}}{2} \lambda W_i = 0, \end{aligned} \quad (5a)$$

and

$$c_{33}^{(i)} W_i'' - \left(c_{55}^{(i)} + \frac{\sigma_{xx}^{0(i)}}{2}\right) \lambda^2 W_i - \left(c_{13}^{(i)} + c_{55}^{(i)} - \frac{\sigma_{xx}^{0(i)}}{2}\right) \lambda U_i' = 0. \quad (5b)$$

The associated boundary conditions are as follows:

(a) At the bounding surfaces,  $z = c + f$ , we have the following two traction-free conditions:

$$c_{55}^{(f)} U_f' + c_{55}^{(f)} \lambda W_f = 0, \quad (6a)$$

$$c_{33}^{(f)} W_f' - c_{13}^{(f)} \lambda U_f = 0. \quad (6b)$$

(b) At the face-sheet/core interface,  $z = c$ , we have the following four conditions at each of the interfaces:

Displacement Continuity:

$$U_f = U_c; \quad W_f = W_c, \quad (6c)$$

Traction Continuity:

$$\begin{aligned} & \left(c_{55}^{(f)} + \frac{\sigma_{zz}^0}{2}\right) U_f' + \left(c_{55}^{(f)} - \frac{\sigma_{zz}^0}{2}\right) \lambda W_f = \\ & = \left(c_{55}^{(c)} + \frac{\sigma_{zz}^0}{2}\right) U_c' + \left(c_{55}^{(c)} - \frac{\sigma_{zz}^0}{2}\right) \lambda W_c, \end{aligned} \quad (6d)$$

$$c_{33}^{(f)} W_f' - c_{13}^{(f)} \lambda U_f = c_{33}^{(c)} W_c' - c_{13}^{(c)} \lambda U_c . \quad (6e)$$

(c) At the axis of symmetry,  $z = 0$ , we have the following anti-symmetry conditions:

$$U_c = W_c' = 0 . \quad (6h)$$

Notice that since the construction is assumed to be symmetric, only half of the sandwich needs to be considered.

### 2.3 Solution of the eigen-boundary-value problem for differential equations

Equations (5)-(6) constitute an eigenvalue problem for differential equations, with the axial load,  $P$ , the parameter (two point boundary value problem). An important point is that the pre-buckling stresses  $\sigma_{jj}^{0(i)}(z)$ , depend *linearly* on the applied axial load,  $P$  (the parameter) through expressions in the form of Equations (2) and this makes possible the direct application of standard solution techniques.

With respect to the method used there is a difference between the present problem and the homogeneous orthotropic body (apart from being shell geometry) solved by Kardomateas [4]. The complication in the present problem is due to the fact that the displacement field is continuous but has a slope discontinuity at the face-sheet/core interfaces. This is the reason that the displacement field was not defined as one function but as two distinct functions for  $i = f$ , and  $i = c$ , i.e. the face sheet and the core. Our formulation of the problem employs, hence, “internal” boundary conditions at the face-sheet/core interface, as outlined above. Due to this complication, the shooting method (Press *et al* [12]) was deemed to be the best way to solve this eigen-boundary-value problem for differential equations. A special version of the shooting method was formulated and programmed for this problem. In fact, for each of the two constituent phases of the sandwich structure, we have five variables:  $y_1 = U_i$ ,  $y_2 = U_i'$ ,  $y_3 = W_i$ ,  $y_4 = W_i'$ , and  $y_5 = P$ . The five differential equations are:  $y_1' = y_2$ , the first equilibrium Equation (5a),  $y_3' = y_4$ , the second equilibrium Equation (5b) and  $y_5' = 0$ .

The method starts from the middle of the core,  $z = 0$  and integrates the five first order differential equations from  $z = 0$  to the face-sheet/core interface  $z = c$  (i.e., through the core). At the start point,  $z = 0$ , we have three conditions as follows:  $U_c = y_1 = 0$ ,  $W_c' = y_4 = 0$  and a third condition of (arbitrarily) setting  $W_c = y_3 = 1.0$ , therefore we have two freely specifiable variables, the  $P = y_5$  and the  $U_c' = y_2$ .

The freely specifiable starting values at  $z = 0$  are taken as the values from the simple plate/beam theory solutions available in the literature (described later).

### 3. GLOBAL BUCKLING FORMULAS IN THE LITERATURE, RESULTS AND DISCUSSION

In the following, we list the formulas in the literature for global buckling of sandwich columns. First, the Euler load is simply:

$$P_{Eul} = \frac{\pi^2(EI)_{eq}}{L^2} \quad (EI)_{eq} = 2w \left[ E_f \frac{f^3}{12} + E_f f \left( \frac{f}{2} + c \right)^2 + E_c \frac{c^3}{3} \right]. \quad (7a)$$

A formula for thin faces, which accounts for transverse shear, is in Allen's book [1] as follows:

$$\frac{1}{P_{crA}^{thin}} = \frac{1}{P_{E1}} + \frac{1}{P_c} \quad (7b)$$

where

$$P_{E1} = E_f w f (2c + f)^2 \frac{\pi^2}{2L^2}; \quad P_c = G_c \frac{w(2c + f)^2}{2c}. \quad (7c)$$

i.e.,  $P_{E1}$  represents the Euler load of the sandwich column in the absence of core shear strains and the bending stiffness of the core ignored and with the local bending stiffness of the faces ignored as well (because they are thin), and  $P_c$  may be described as the shear buckling load.

Although not explicitly stated, the structure of the formula indicates that it is an adaptation for sandwich configurations of the Engesser's [13] column buckling formula.

For thick faces, Allen gives another formula,

$$P_{cr,A}^{thick} = P_{E2} \left\{ \frac{1 + \frac{P_{Ef}}{P_c} - \frac{P_{Ef} P_{E2}}{P_c P_{E2}}}{1 + \frac{P_{E2}}{P_c} - \frac{P_{Ef}}{P_c}} \right\}, \quad (8a)$$

where

$$P_{E2} = E_f \frac{\pi^2}{L^2} \left[ \frac{wf^3}{6} + \frac{wf(2c + f)^2}{2} \right]; \quad (8b)$$

$$P_{Ef} = E_f \frac{\pi^2}{L^2} \frac{wf^3}{6}; \quad P_c = G_c \frac{w(2c + f)^2}{2c}, \quad (8c)$$

i.e.,  $P_{E2}$  represents the Euler load of the sandwich column in the absence of core shear strains and with the bending stiffness of the core ignored, but with the local bending stiffness of the faces included;  $P_{Ef}$  represents the sum of the Euler loads of the two faces when they buckle as independent struts (i.e., when the core is absent) and  $P_c$  is the shear buckling load, same as in (7c).

Another formula is in Bazant and Cedolin's book [2], which was derived from adapting Engesser's [13] formula for the sandwich configuration:

$$P_{cr,BC} = \frac{P_{E2}}{1 + \frac{P_{E2}}{(GA)_0}}, \quad (9a)$$

where  $P_{E2}$  is given in (8b) and

$$(GA)_0 = G_c w (f + 2c) \left( 1 + \frac{f^2}{3(f + 2c)^2} \right). \quad (9b)$$

One important point: Since we deal with a wide panel, in the above formulas we shall use the  $E'_f = E_f / (1 - \nu_{13}^f \nu_{31}^f)$  and  $E'_c = E_c / (1 - \nu_{13}^c \nu_{31}^c)$  in place of  $E_f$  and  $E_c$ . Also, we use  $G_{31}^c$  in place of  $G_c$ , since the core material is in general orthotropic and therefore this can be an independent material property.

Results are produced for the following configuration: Two face sheet over total thickness ratios,  $f/h = 0.02$  and  $0.05$  (where  $h = 2(f + c)$  is the total plate thickness) and for a range of length over thickness ratios,  $L/h$ , from 20 to 60; we also assigned the width  $w/L = 3$ .

Illustrative results are presented in Table 1 for graphite/epoxy unidirectional facings and hexagonal glass/phenolic honeycomb core. The graphite/epoxy facings moduli are (in GPa):  $E_1^f = 181$ ,  $E_2^f = E_3^f = 10.3$ ,  $G_{23}^f = 5.96$ ,  $G_{12}^f = G_{31}^f = 7.17$ ; and the facings Poisson's ratios:  $\nu_{12}^f = 0.28$ ,  $\nu_{23}^f = 0.49$ , and  $\nu_{31}^f = 0.0159$ . The honeycomb core moduli are (in GPa):  $E_1^c = E_2^c = 0.032$ ,  $E_3^c = 0.390$ ,  $G_{23}^c = G_{31}^c = 0.048$ ,  $G_{12}^c = 0.013$ ; and the core Poisson's ratios:  $\nu_{31}^c = \nu_{32}^c = \nu_{21}^c = 0.25$ .

It should also be mentioned that in all cases we made sure that wrinkling would not occur (i.e. the wrinkling load, as provided by the Hoff and Mautner's formula [3], is above the elasticity value).

From these results we can make the following observations:

- (a) Allen's two formulas [1] and the Bazant and Cedolin [2] formula are always conservative and all three give similar values, with small differences.
- (b) The thicker face sheets lead in most cases to better agreement with the elasticity solution.
- (c) The Bazant and Cedolin [2] formula is slightly more conservative than the two Allen's [1] formulas.

Table 1. Critical loads for graphite-epoxy faces and hexagonal glass/phenolic honeycomb core; loads normalized with the Euler load (w/o shear), Eqn (7a).

$L/h$	$\tilde{P}_{cr, Elast}$	$\tilde{P}_{cr, A}^{thin}$ (% difference from elasticity)	$\tilde{P}_{cr, A}^{thick}$	$\tilde{P}_{cr, BC}$
$f/h = 0.02$				
20	0.5318	0.5263 (-1.04%)	0.5264 (-1.01%)	0.5212 (-2.00%)
30	0.7242	0.7139 (-1.43%)	0.7140 (-1.41%)	0.7097 (-2.00%)
40	0.8299	0.8156 (-1.73%)	0.8157 (-1.71%)	0.8126 (-2.09%)
50	0.8910	0.8732 (-2.00%)	0.8733 (-1.98%)	0.8710 (-2.24%)
60	0.9287	0.9080 (-2.23%)	0.9081 (-2.21%)	0.9064 (-2.40%)
$f/h = 0.05$				
20	0.3238	0.3218 (-0.61%)	0.3228 (-0.32%)	0.3104 (-4.13%)
30	0.5193	0.5162 (-0.60%)	0.5171 (-0.42%)	0.5032 (-3.11%)
40	0.6590	0.6545 (-0.67%)	0.6554 (-0.53%)	0.6428 (-2.45%)
50	0.7529	0.7472 (-0.75%)	0.7481 (-0.63%)	0.7376 (-2.03%)
60	0.8163	0.8095 (-0.84%)	0.8104 (-0.73%)	0.8018 (-1.78%)

- (d) Given the very strong orthotropy and the large effect of transverse shear expected in the material, all formulas perform very well, with the Allen's thick faces formula [1] being the most accurate and, indeed, performing remarkably well. In fact, if there is one conclusion to be made, this would be that all three formulas provide an impressively close (and slightly conservative) estimate of the critical load.

## ACKNOWLEDGEMENTS

The financial support of the Office of Naval Research, Ship Structures and Systems, S&T Division, Grants N00014-90-J-1995 and N00014-0010323, and the interest and encouragement of the Grant Monitor, Dr. Y.D.S. Rajapakse, are both gratefully acknowledged.

## REFERENCES

- [1] Allen, H.G., *Analysis and Design of Structural Sandwich Panels*, Chapter 8, Pergamon Press, Oxford, 1969.

- [2] Bazant, Z.P. and Cedolin, L., *Stability of Structures*, Oxford University Press, New York, 1991, pp. 30–35.
- [3] Hoff, N.J. and Mautner, S.F. “The Buckling of Sandwich-Type Panels”, *Journal of the Aeronautical Sciences*, Vol. 12, No. 3, 1945, pp. 285–297.
- [4] Kardomateas, G.A., “Buckling of Thick Orthotropic Cylindrical Shells Under External Pressure”, *Journal of Applied Mechanics (ASME)*, Vol. 60, 1993, pp. 195–202, .
- [5] Kardomateas, G.A., “Stability Loss in Thick Transversely Isotropic Cylindrical Shells Under Axial Compression”, *Journal of Applied Mechanics (ASME)*, Vol. 60, 1993, pp. 506–513.
- [6] Kardomateas, G.A., “Bifurcation of Equilibrium in Thick Orthotropic Cylindrical Shells Under Axial Compression”, *Journal of Applied Mechanics (ASME)*, Vol. 62, 1995, pp. 43–52.
- [7] Kardomateas, G.A. and Simitse, G.J., “Elasticity Solution for the Bucking of Long Sandwich Cylindrical Shells Under External Pressure”, *Journal of Applied Mechanics (ASME)*, 2005, in press.
- [8] Lekhnitskii, S.G., *Theory of Elasticity of an Anisotropic Elastic Body*, Holden Day, San Francisco, 1963, also Mir Publishers, Moscow, 1981.
- [9] Kardomateas, G.A., “Elasticity Solutions for a Sandwich Orthotropic Cylindrical Shell Under External Pressure, Internal Pressure and Axial Force”, *AIAA Journal*, Vol. 39, No. 4, 2001, pp. 713–719.
- [10] Kardomateas, G.A., “Wrinkling of Wide Sandwich Panels/Beams with Orthotropic Phases by an Elasticity Approach”, *Journal of Applied Mechanics (ASME)*, 2005, in press.
- [11] Novozhilov, V.V., *Foundations of the Nonlinear Theory of Elasticity*, Graylock Press, Rochester, NY, 1953.
- [12] Press, W.H., Flannery, B.P., Teukolsky, S.A. and Vetterling, W.T., *Numerical Recipes*, Cambridge University Press, Cambridge, 1989.
- [13] Engesser, F., Die Knickfestigkeit gerader Stäbe, *Zentralblatt der Bauverwaltung*, Vol. 11, 1891, pp. 483–486.

# PARAMETRIC STUDY OF STRUCTURALLY GRADED CORE JUNCTIONS

Anders Lyckegaard, Elena Bozhevolnaya and Ole Thybo Thomsen  
*Institute of Mechanical Engineering, Aalborg University, Pontoppidanstræde 105,  
DK-9220 Aalborg Øst, Denmark*  
al@ime.aau.dk

**tract** In practical sandwich constructions it is often necessary to reinforce the core with high strength inserts to facilitate concentrated loads. The junction between the main core and the core insert is a potential weak spot of the sandwich structure. This section of the sandwich structure is investigated using finite element analysis and the results are compared with experimental data. Furthermore, parameters concerning the shape of the core junction are investigated using finite element analysis.

**Keywords:** core inserts, graded core material, local bending effects, parametric study.

## 1. INTRODUCTION

A sandwich structure is typically a three layered structure comprised of two thin, stiff and strong face sheets separated by a thick, compliant and lightweight core material. This construction has gained widespread acceptance as an excellent way to obtain extremely lightweight components and structures with very high bending stiffness, high strength and high buckling resistance, see e.g. Zenkert [1] or Allen [2]. Sandwich structures are often used in lightweight applications such as aircraft, marine applications and wind turbine blades.

Introducing concentrated loads into a sandwich structure should be done with much care to avoid core indentation and local bending of the face sheets, which limits strength of the sandwich structure. The preferred design solution is to introduce stiff core inserts made from wood, metal or dense polymeric foams under the concentrated load.

This design introduces new difficulties near the junction between the core insert and the main core, where stress concentrations in the cores and local bending of the faces sheets will occur due to the different elastic properties of

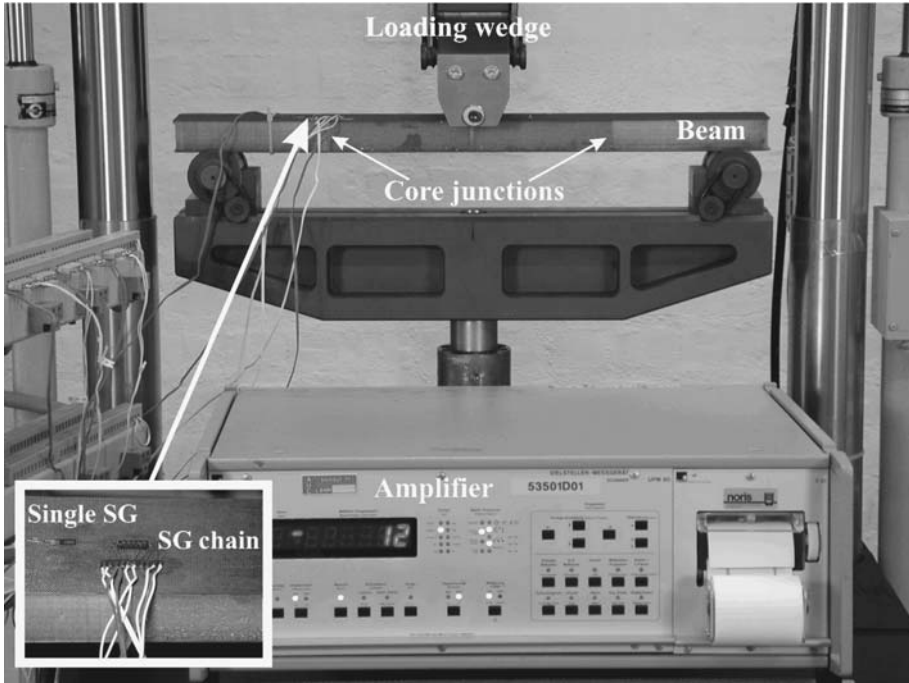


Figure 1. Experimental set-up for three point bending of sandwich beams.

the two adjoining core materials. This was analysed analytically by Skvortsov and Thomsen [3].

In the present investigation a sandwich beam in three point bending will be the object of the experimental and numerical studies. Experiments with a sandwich beam comprised of carbon fibre (CFRP) face sheets and two types of PVC foams have been conducted, see Figure 1.

Numerical simulation based on Finite Element Analysis (FEA) models will be used for detailed analyses of the sandwich beams tested experimentally.

Furthermore, a parametric study will be conducted to investigate the influence of the various model parameters upon the structural response and the characteristic failure behaviour. Parameters such as face thickness, core stiffnesses and termination angle will be considered.

## 2. TEST SPECIMEN AND EXPERIMENTAL SETUP

The geometry, layout and general loading scheme of the test specimen are shown in Figures 1 and 2, and the elastic properties of the beam constituents are shown in Table 1. The sandwich beam specimen is assembled from two

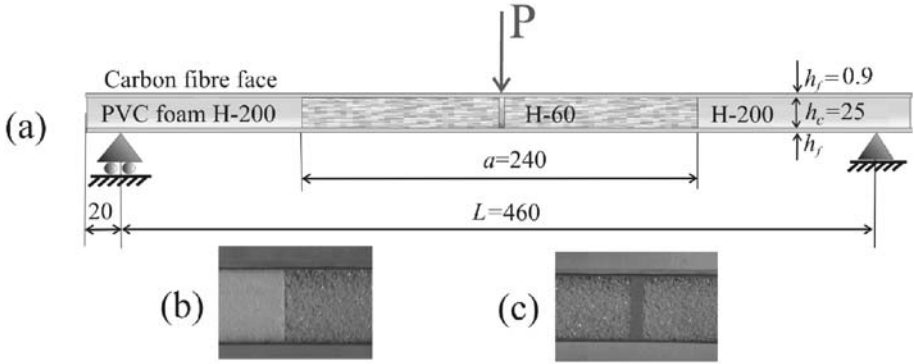


Figure 2. (a) Geometry of the test specimen. (b) the core junction. (c) a centre diaphragm is used to support the concentrated load.

Table 1. Material data used in the Finite element model.

Material	Young's modulus	Poisson's ratio	Tensile strength
Centre core (H60)	$E = 60 \text{ MPa}$	$\nu = 0.32$	1.6 MPa
Outer core (H200)	$E = 310 \text{ MPa}$	$\nu = 0.32$	7.0 MPa
Faces (CFRP)	$E = 83,300 \text{ MPa}$	$\nu = 0.33$	

composite laminated faces with a symmetrical lay-up of  $[0^\circ/90^\circ/0^\circ]$ , and two types of PVC foam cores. All components of the panel are joined using an epoxy resin, Araldite® 2022 (Huntsman Adv. Materials).

The face laminates were made of UD carbon fibre prepreps (SP Systems [4]), and were manufactured by means of a manual lay-up with subsequent vacuum bagging at the prescribed temperature and pressure [5]. The tensile stiffness of the composite laminates was measured experimentally by means of modal analysis [6, p. 269] and standard tensile tests [7]. Both methods yielded the same equivalent modulus of elasticity for the laminate face equal to 83.3 GPa with an error of measurement that did not exceed 4%.

Two types of core materials were used in the investigated beams: a compliant core, H60, and a stiff core H200 (Divinycell from DIAB Group [8]) with densities  $60 \text{ kg/m}^3$  and  $200 \text{ kg/m}^3$ , respectively. The compliant core was used in the central part of the beam, and the stiff core was used at the beam ends. The latter prevented indentation of the sandwich structure at the edge supports.

The material data for the core materials is supplied by the manufacturer, see [8].

The test specimen is fitted with strain gauges on the top and bottom face sheets, see Figure 1. One strain gauge is mounted away from the junction on

either face sheet, and a strain gauge chain is mounted across the core junction on either face sheet.

The width of the panel was 58 mm and the load on the panel was 1500 N.

### 3. FINITE ELEMENT MODEL

The finite element modelling was performed using ANSYS® 9.0 [9]. The modelling was done in 2D using plane strain assumptions, and only half of the beam was modelled by introducing symmetry boundary conditions in the middle of the beam. The model was constructed using 8-node isoparametric elements (plane183), see [9].

It should be mentioned here, that the numerical results concerning the local effects at the tri-material wedges/corners are strongly mesh-size dependent, since the problem is that of a stress singularity within the framework of linear elasticity, see e.g. [10].

Thus, at the point, where the three materials meet, the stresses become infinitely large, which implies that the FE-model cannot provide accurate results. Therefore, a point stress approach was adopted as a core failure criterion. In this criterion, which has previously been applied to brittle cross-linked PVC foams, see e.g. [11], the stresses are evaluated at a characteristic distance from the stress singularity. Here the characteristic distance was taken as the average cell size of the foam material [8]: a cell 0.6 mm for Divinycell H60.

Furthermore, the first principal stress is the stress component used for comparison stress instead of the tangential stress as in [11, 12]. This choice is justified by the assumption that crack growth is independent of coordinate system. Finally, it is assumed that tensile stresses are the primary contributors to crack growth, whereas compressive stresses may introduce local damage to the foam micro structure, but do not lead to crack growth.

Accordingly, the sandwich core stresses appearing in the following were read at a characteristic distance of 0.6 mm from the core junctions. The meshing of the FEA-models were refined in such a way, that convergence of the stresses was obtained at the distance 0.6 mm away from the tri-material wedges. The final mesh size adjacent to the junctions was such that the element edge length was no larger than 0.5 mm.

### 4. DESIGN PARAMETERS

For the parametric study the combination of materials remains the same as outlined in Section 2. The objective of this investigation is to determine whether changing the shape of the core junction can be used as a means of decreasing the stress levels in the core materials.

Two different design modifications of the core junction are considered, which are based on the patent application by Bozhevolnaya et al. [13]. Firstly, vari-

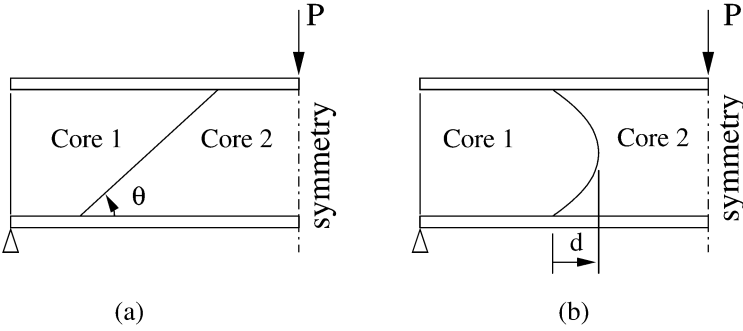


Figure 3. The modified design of the core junction. (a) definition of the termination angle  $\theta$ . (b) B-spline geometry where the middle point is offset the distance  $d$  horizontally ( $d$  is shown in the positive direction).

ation of the termination angle  $\theta$  is allowed, see Figure 3(a). In this case the following angles were considered:

$$\theta = \{45^\circ, 60^\circ, 90^\circ, 120^\circ, 130^\circ\} \quad (1)$$

Secondly, the core junctions shaped as a B-spline curve are considered, which is defined by three points, see [9]. The two end points are placed at the upper and lower face-core interface, respectively, and the lengths of the tangent vectors at the end points are set to zero. The middle point is placed in the middle of the core and off-set a distance  $d$  horizontally, see Figure 3(b). The following values of the distance  $d$  are considered:

$$d = \{-2.5, 0.0, 2.5, 7.5\} \quad (2)$$

The value corresponding to  $d = 0.0$  represents the ordinary butt junction, which is equivalent to the design featuring a termination angle equal to  $\theta = 90^\circ$ .

## 5. RESULTS AND DISCUSSION

The strains measured using strain gauges on the butt core junction configuration shown in Figures 1 and 2 are shown in Figure 4 along with the results of the FE model. There is a good correlation between the FEA results and the strain gauge measurements. Note the variation of strain across the junction, which is due to the local bending of the face sheets. The (numerical) decrease of the strain level on the outer side of the face sheets is followed by a corresponding increase at the face-core interface. Hence, there will be a significant increase of strain level compared with the nominal strain level at the junction. This increase of strain, and in turn stress level, may be fatal to the whole structure if it is not considered in the design process.

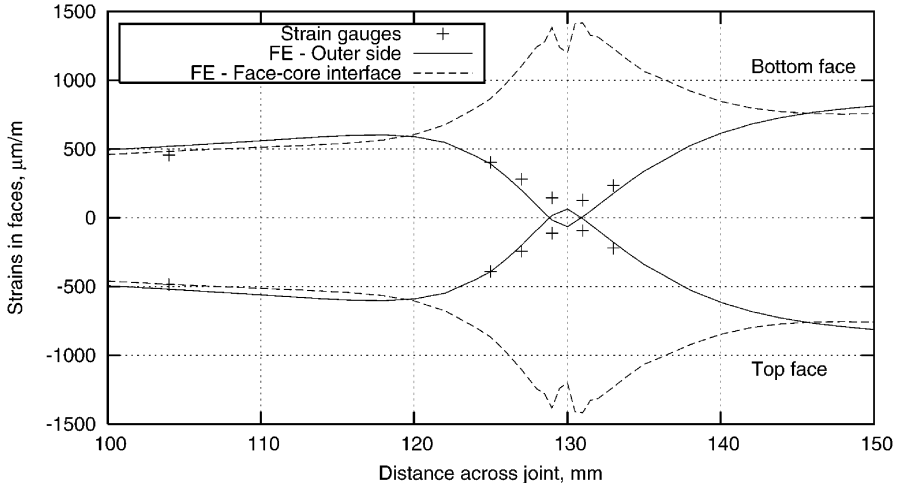


Figure 4. Comparison of measured strain and FE results on the top and bottom face sheets.

## 5.1 Variation of termination angle

The strains in the faces at the face-core interface for different termination angles are shown in Figure 5 (left). It is clear that the strain level is decreased near the junction whenever the termination angle is either increased or decreased relative to  $90^\circ$  (i.e. the butt junction).

The core stresses found using FEA are shown in Figure 6. Here the first principal stress is plotted along the sandwich face  $0.6\text{ mm}$  above the bottom face-core interface. The data corresponding to the termination angle  $\theta = 90^\circ$  (butt junction) show a dramatic increase of stresses in the outer (stiff) core material. The stress at the junction is increased by almost four times compared with the nominal stress level, i.e. the stress in the core away from the junction. In the centre core the stresses increase about 50% at the junction compared with the nominal stresses. When the termination angle is increased to  $\theta = 120^\circ$  the stresses in the outer core increases even more, while the stresses in the centre core is decreased slightly compared with the butt junction. When the termination angle is  $\theta = 135^\circ$  the stresses in the stiff core are still very high. The stresses in the centre core are lower than the nominal stresses.

Decreasing the termination angle to  $\theta = 60^\circ$  cause a decrease of the stresses in both outer and centre core compared with the stress levels in the butt junction ( $\theta = 90^\circ$ ). The stresses are decreased even further when the termination angle is decreased to  $\theta = 45^\circ$ , where only a slight variation in the core stresses is observed compared with the nominal stresses.

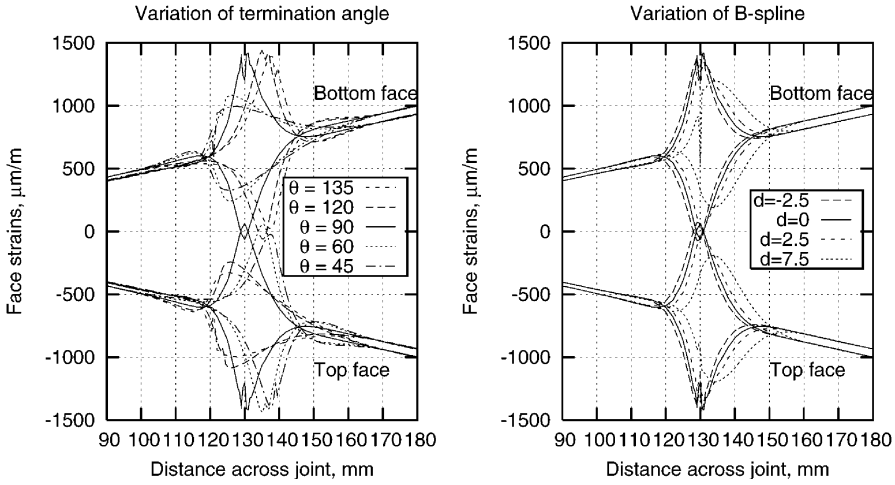


Figure 5. The strain distribution in the faces subject to variation of termination angle (left) and B-spline variation (right).

A physical interpretation of these phenomena is that the shear stresses tend to be transferred through the stiffer material. With angles larger than  $\theta = 90^\circ$  the stiff outer core extends into the domain of the soft centre core at the bottom. Hence, the shear stress prefer to transfer through the three-lateral corner at the bottom face-core interface. When the angle  $\theta$  is smaller than  $90^\circ$  degrees the shear stress tend to transfer through the upper three-lateral corner. Hence, there is a decrease of the stress level at the lower corner.

The upper corner is not as vulnerable as the lower, because the in-plane normal stresses in the upper half of the beam are compressive, contrary to the lower half of the beam, where they are tensile. Hence, the first principal stress,  $\sigma_1$ , which contain contributions from both shear and in-plane normal stresses, is in all cases lower at the upper corner than at the lower corner under these loading conditions.

These investigations show, that the variation of the termination angle  $\theta$  can be used to decrease the stress levels at the core junction. If the load has alternating directions or if the direction of the load is not known, then this method is not useful.

### 5.2 B-spline variation

The strains in the faces at the face-core interface for different B-spline geometries are shown in Figure 5 (right). In this case there is a minor increase of the face strains when the distance  $d$  is  $-2.5$  mm compared with the standard

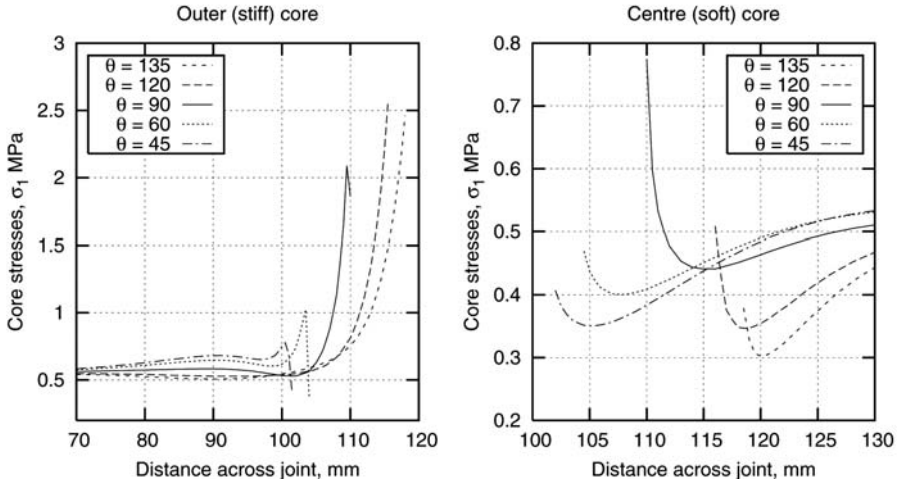


Figure 6. First principal stresses in outer stiff core (left) and in the centre soft core (right). The angle  $\theta$  is the termination angle, see Figure 3(a). The stresses are plotted along the bottom face-core interface 0.6 mm above this interface.

butt junction ( $d = 0$ ). If the distance  $d$  is positive then there is a decrease of face strains. The local bending of the face are, however, still present in all cases.

The first principal stresses in the core materials are shown in Figure 7. As before the “ $d = 0$ ” shows a significant increase of stresses at the junction in both outer and centre core. When  $d = -2.5$  mm the stresses are even higher, however, in both core materials. Increasing  $d$  to first  $d = 2.5$  mm, and then  $d = 7.5$  mm, decreases the stress level in the core significantly. When  $d = 2.5$  mm the growth of stresses is significantly smaller than for the butt junction in both core materials. When  $d = 7.5$  mm the stress level is reduced almost to the level of the nominal core stress, i.e. to the stress in the core away from the junction.

These phenomena may be explained by the same physical interpretation as previously. When  $d$  is negative the stiff core extend into the soft core by its corners at the upper and lower face-core interfaces. Hence, the shear stresses tend to pass through this part of the core, yielding very high stresses at the corners. When  $d$  is positive the middle rounded nose of the stiff core extends into the soft core, such that the shear passes through this part of the core, while the corners are avoided. Thus, the stress level at the junction is reduced significantly.

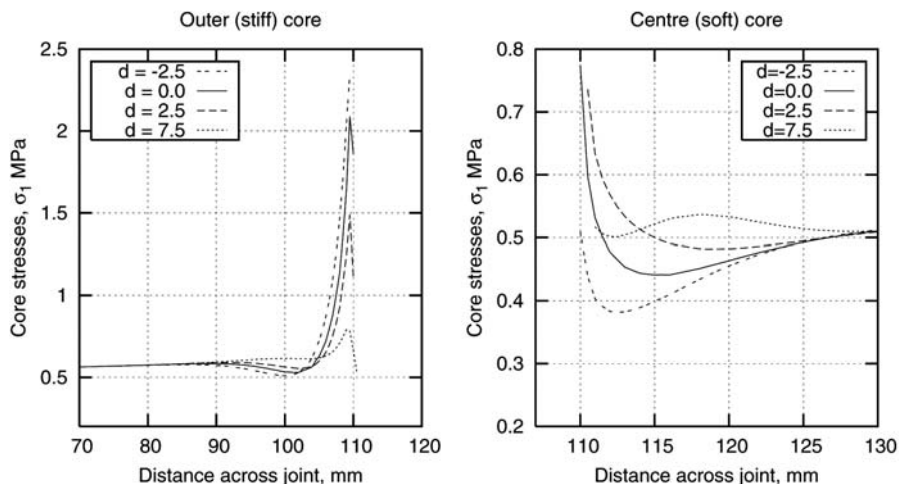


Figure 7. First principal stresses in outer stiff core (left) and in the centre soft core (right). The distance  $d$  is the off-set of the middle node, see Figure 3. The stresses are plotted along the bottom face-core interface 0.6 mm above this interface.

The B-spline shape is efficient for decreasing the stress levels in the core. It is more difficult to manufacture compared to a scarf core junction, but it is the best solution if the load is alternating, or if the direction of the load is unknown.

## 6. CONCLUSION

Three point bending of a sandwich beam with a core insert is investigated. Experiments show that local bending of the face sheets occur at the junction of the main core material and the core insert. These results are confirmed by finite element analyses. The analyses also show a significant increase of stresses in the core near the junction.

A parametric study demonstrates that it is possible to decrease the local bending in the face sheets and the localised stresses in the core by changing the termination angle of the core junction or by choosing an appropriate B-spline shape for the junction. The B-spline shape is particularly efficient for decreasing the core stress concentrations at the core junction.

## REFERENCES

- [1] D. Zenkert. *An Introduction to Sandwich Construction*. Chameleon Press, London, 1995.
- [2] H.G. Allen. *Analysis and design of structural sandwich panel*. Pergamon Press, 1969.
- [3] V.S. Skvortsov and O.T. Thomsen. Analytical estimates for the stresses in face sheets of sandwich panels at junctions between different core materials. In J.R. Vinson, Y.D.S.

- Rajapakse and L.A. Carlson (eds), *6th International Conference on Sandwich Structures*, pp. 551–559. CRC Press, 2003.
- [4] SP Product Catalogue, 2004.
  - [5] SP Systems, Newport, Isle of Wright, UK. *SE 84 Low Temperature Cure Epoxy Prepreg System*.
  - [6] D.J. Ewins. *Modal Testing: Theory and Practice*. Research Studies Press Ltd., 1985.
  - [7] Annual Book of ASTM Standards. *Standard Test Method for Young's Modulus, Tangent Modulus, and Chord Modulus*, E111-82 edition, August 1982. reapproved 1988.
  - [8] DIAB Group. *Technical Manual H-grade: Divinycell®*, 2003.
  - [9] *ANSYS Release 9.0 Documentation*.
  - [10] S.S. Pageau, P.F. Joseph and S.B. Biggers, Jr. The order of stress singularities for bonded and disbanded three-material junctions. *International Journal of Solids and Structures*, 31(21):2979–2997, 1994.
  - [11] S. Ribeiro-Ayeh and S. Hallström. Strength prediction of beams with bimaterial butt-joints. *Engineering Fracture Mechanics*, 70:1491–1507, 2003.
  - [12] Hallström S. and J.L. Grenestedt. Mixed mode fracture of cracks and wedge shaped notches in expanded PVC foam. *International Journal of Fracture*, 88:343–358, 1997.
  - [13] E. Bozhevolnaya, A. Lyckegaard, L. Jakobsen, and O.T. Thomsen. Sandwich panel and a method of producing a sandwich panel. application, 2003. Application No./Patent No. 03027020.1.

# LOCAL EFFECTS INDUCED BY CORE JUNCTIONS IN SANDWICH BEAMS UNDER GENERAL LOADING CONDITIONS

Elena Bozhevolnaya, Anders Lyckegaard and Ole Thybo Thomsen  
*Institute of Mechanical Engineering, Aalborg University, Pontoppidanstræde 101,  
DK-9220 Aalborg East, Denmark*

**Abstract** Local effects occurring near junctions between different cores in sandwich structures subjected to axial and transverse forces and bending moments are considered. These local effects are associated with large stress concentrations in the faces and the core near the core junctions. The local effects are studied for two typical cases representing industrial applications. Finite element analyses show that significant stress concentrations are induced near core junctions subjected to transverse, tension/compression as well as bending loads. Finally, improved designs of core junctions are discussed.

**Keywords:** core junctions, local effects, stress concentrations, design.

## 1. INTRODUCTION

Structural sandwich panels can be considered as a special type of composite laminate where two thin, stiff, strong and dense faces are separated by a thick, lightweight and compliant core material. Such sandwich structures have gained widespread acceptance within the aerospace, naval/marine, automotive and general transportation industries as an excellent way to obtain extremely lightweight components and structures with very high bending stiffness, high strength and high buckling resistance.

Despite the many advantages of sandwich structures, a number of unsolved problems still exist. Thus, sandwich panels are notoriously sensitive to failure by the application of concentrated transverse (through-the-thickness) loads. Moreover, the practical application and use of sandwich panels implies the necessity to assemble (join) them with adjoining structures/components as well as also to introduce various rigging/furnishing

appliances. This involves the use of a variety of “sub-structures” in the form of cores of higher stiffness, edge and corner stiffeners, backing plates, through-the-thickness and partially potted inserts, etc. [1, 2]. Examples of typical generic “sub-structures” in sandwich panels are shown in Figure 1.

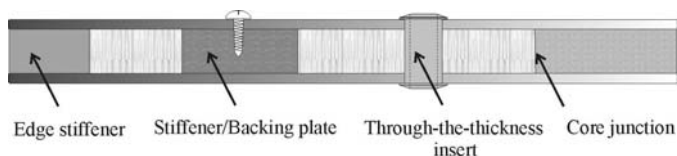


Figure 1. Typical “sub-structures” in sandwich panels.

A “sub-structure” is often designed to transfer direct localized transverse loading (force or couple), and this inevitably leads to local stress concentrations in and around the “sub-structure”. In some cases, the existence of a material discontinuity, e.g. the presence of a core joint or a manufacturing defect [3], leads to local stress concentrations caused by the global loads applied far away from the discontinuity.

It should be pointed out that in spite of the large variety of possible “sub-structures”, the active physical mechanisms in the local phenomena developing in different sandwich “sub-structures” are the same. These are displayed by the inducement of local stress concentrations due to the presence of material discontinuities in the adjoined materials. Thus, although only junctions between different core materials will be considered in the following, the overall results and conclusions may be applied to any “sub-structure” shown in Figure 1.

The local stress concentrations appearing near core junctions subjected to transverse shear loading were characterized quantitatively using closed-form analytical solutions in [4], which revealed that significant stress concentrations occur in all sandwich constituents. Experimental validation of these results was subsequently performed in [5], and a generalization of the model for the case of round inserts in sandwich plates, and its verification by means of Finite Element Analysis, followed in [6]. These studies were exclusively devoted to the case of transverse shear loading of core junctions.

## 2. CORE JUNCTIONS UNDER DIFFERENT LOADS

Figure 2 illustrates the physics of the local effects induced near junctions between two sandwich cores of different stiffness. In case (a), the in-plane axial tensile load  $F$  causes the inducement of larger in-plane strains, and, consequently, larger transverse strains in the left part of the beam. The transverse strains are due to the Poisson's effect, hence the local effects

depend not only on the in-plane strains, but also on the Poisson's ratios of the two core materials. The mismatch of the transverse dimensions on either side of the junction leads to face bending and to the subsequent development of local bending stresses in the faces adjacent to the junction. If the structure is to preserve its integrity, the curvature of the face should be concave down over the softer core, and concave up over the stiffer core, as illustrated in Figure 2a. The core parts beneath the bent face will follow its deformation, and core transverse normal stresses are induced: tensile in the softer core, and compressive in the stiffer core, for the chosen direction of  $F$  in Figure 2a.

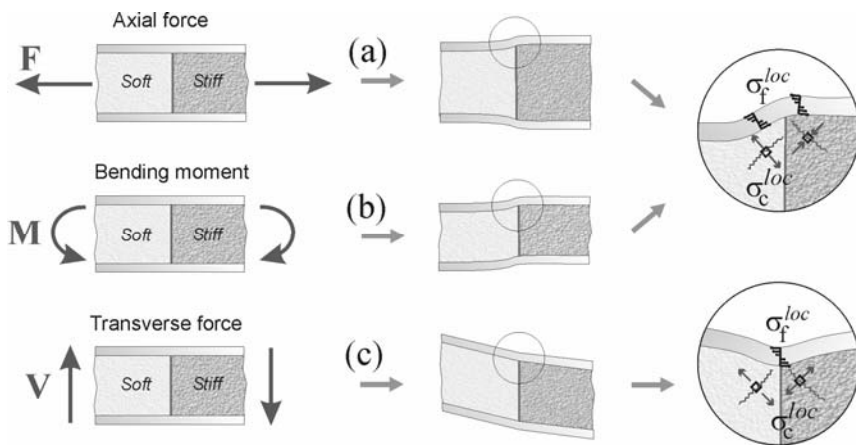


Figure 2. Junctions of the soft and stiff cores in sandwich beams/panels subjected to (a) axial loading, (b) pure bending and (c) transverse load.

The case of pure bending with a constant moment  $M$  shown in Figure 2b is similar to the in-plane case, since the upper and lower parts of the sandwich are loaded in tension and compression, respectively. Thus, a mismatch of transverse strain occurs locally at the upper and lower parts of the core near the junction. Consequently, the same conclusions as given above for axial tension (Figure 2a) can be drawn, i.e. core transverse normal stresses and local bending stresses in the faces are induced as shown in Figures 2a–2b. All the stresses will be of opposite sign at the lower face, which is loaded in compression.

The case of a transverse shear force  $V$  acting at the junction is shown in Figure 2c). The stiffer core, which is situated to the right from the junction, undergoes smaller shear strains than the more compliant core. This leads to a disagreement between the angles of relative rotations of the left and right segments of the sandwich beam, and, consequently, to local bending of the faces at the tri-material wedges/corners. The presence of local face bending

near the junction is accompanied by the inducement of core transverse normal stresses. At the upper interface, the core transverse normal stresses are tensile (“peeling” mode), while the local transverse normal stresses in the core at the lower tri-material wedges/corners are compressive.

The scale and intensity of the described local effects will be clarified in the following.

### 3. CASE STUDIES AND FINITE ELEMENT MODEL

The two case studies presented in Table 1 have been considered, where each case represents different realistic combinations of material and geometrical properties. The sandwich beam with symmetric faces and two different cores used for the numerical simulations is shown in Figure 3.

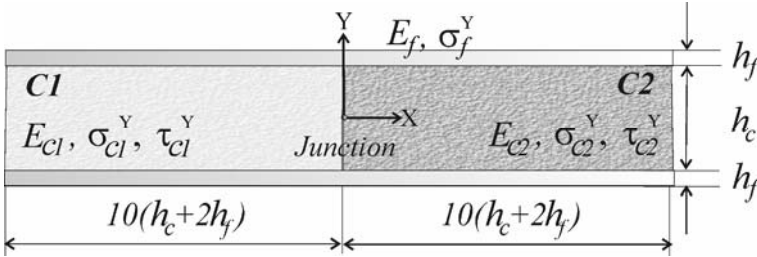


Figure 3. Geometry of a sandwich beam with core junction:

c1 – a soft core and c2 – a stiff core:  $E_{c1} < E_{c2}$ .

Table 1. Cases studied.

	Composition and material properties	Thicknesses
Case 1	Faces: <i>Glassfibre/polyester</i>	$h_f=3$ mm
	$E_f=10.5$ GPa; $\sigma_f^Y=270$ Mpa (yield stress/proportional limit)	
	Cores: <i>PVC foams (Divinycell) H-60 &amp; H-200:</i>	$h_c=10$ mm
	$E_{c1}=60$ MPa; $\sigma_{c1}^Y=1.4/-0.8$ MPa; $\tau_{c1}^Y=0.7$ MPa $E_{c2}=310$ MPa; $\sigma_{c2}^Y=7.0/-4.5$ MPa; $\tau_{c2}^Y=3.7$ MPa	
Case 2	Faces: <i>Glassfibre/polyester</i>	$h_f=5$ mm
	$E_f=10.5$ GPa; $\sigma_f^Y=270$ MPa	
	Cores: <i>Balsa D-57 (Baltek) &amp; Steel insert</i>	$h_c=50$ mm
	$E_{c1}=2.2$ GPa; $G_{c1}=108$ MPa; $\sigma_{c1}^Y=6.9/-6.5$ MPa <sup>along fibres</sup> ; $\tau_{c1}^Y=1.8$ MPa; $E_{c2}=200$ GPa; $\sigma_{c2}^Y=340$ MPa	

The finite element analysis (FEA) software package ANSYS<sup>®</sup>, version 8.1, was employed for the numerical modelling. The FEA meshing of the sandwich beams (with a zoom on the junction) is shown in Figure 4, where

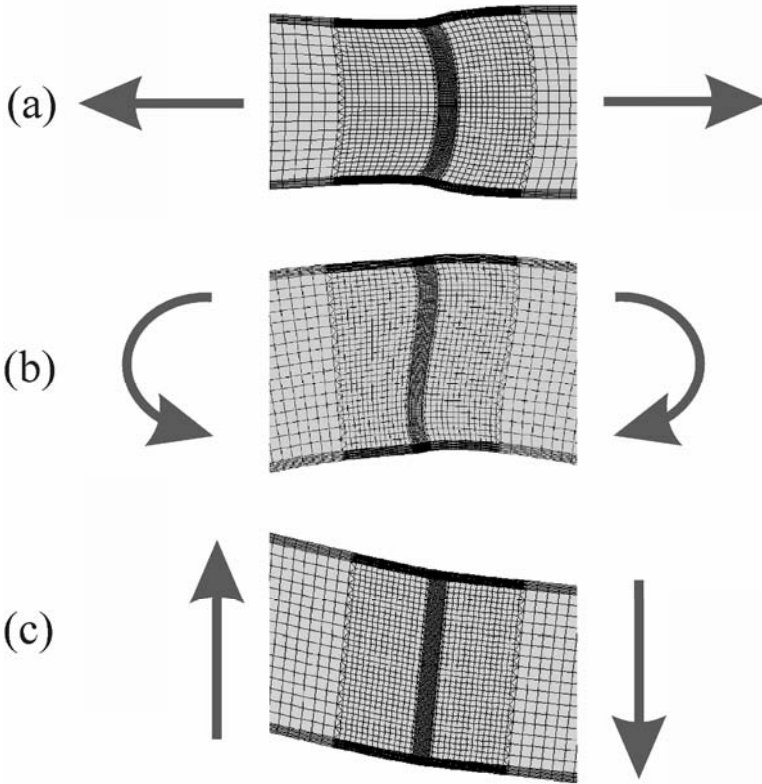


Figure 4. FE modelling of study case 1: Deformed shapes of core junctions subject to (a) axial, (b) pure bending and (c) and transverse shear loading.

the deformed shapes of the junctions are shown for the tensile, bending and transverse loadings.

Isoparametric 2-D elements with 8-nodes (plane183) were used to model all the sandwich constituents under plane strain assumptions, and 16 layers of elements were used in the faces in order to capture the local bending effects near the core junctions.

It should be mentioned here that the numerical results concerning the local effects at the tri-material wedges/corners are strongly mesh-size dependent, since the problem is that of a stress singularity within the framework of linear elasticity, see e.g. Pageau et al. [7]. Thus, at the point, where the three materials meet, the stresses become infinitely large, which implies that the FE-model cannot provide accurate results. Therefore, a point stress approach was adopted as a core failure criterion. In this criterion, which has previously been applied to brittle cross-linked PVC foams [8], the stresses are evaluated at a characteristic distance from the stress singularity.

Here the characteristic distance was taken as the average cell size of the foam material [9]:  $a_{cell} \sim 0.6$  mm for Divinycell H-60. Accordingly, the sandwich core stresses appearing in Tables 2 and 3 were read at a characteristic distance of 0.6 mm from the core junctions. The meshing of the FEA-models was refined in such a way, that convergence of the stresses was obtained at the distance 0.6 mm away from the tri-material wedges. The final mesh size adjacent to the junctions was such that the element edge length was not larger than 0.1 mm.

#### 4. NUMERICAL RESULTS

Each of the two study cases presented in Table 1 and Figure 3 was subjected to all three types of loads shown in Figure 2. In the case of an in-plane force  $F$  and a bending moment  $M$ , the numerical value of the load was chosen such that the face nominal stress (in the left part of the beam) was equal to half of the proportional limit stress of the face material. In the case of an out-of-plane shear force  $V$ , the nominal shear stress in the soft core equals half of the core shear yield stress.

For case 1, subjected to all three types of loading, the stress distributions in the sandwich faces and the core are shown in Figure 5, and the most important quantitative stress characteristics are given in Table 2.

Table 2. Study case 1 – local effects at core junction.

Applied load	Faces:	Core 1:	Core 2:
	Nominal stress / Max. stress, MPa	Nominal stress / Max principal stress, MPa	Nominal stress / Max principal stress, MPa
Tension 1.39 kN/mm	135 / 144	0.78 / <b>2.2</b>	3.6 / <b>4.4</b>
Bending 34.3 kN·mm/mm	135 / 136	0.65 / <b>1.4</b>	3.1 / 3.1
Shear 19.25 N/mm	0 / ±13.5	0.35 / <b>0.65</b>	0.35 / 1.9

The face stresses are shown in Figure 5 along the outer free surfaces and the face-core interfaces. For the beam loaded in tension, the stresses are constant along the beam span far from the junction, and the stresses do not vary through the face thickness (Figure 5a). The nominal stress  $\sigma_f^{nom} = 135$  MPa in the face mentioned in Table 2 is the stress in the face adjacent to the soft core. Near the junction a sudden variation of the face stresses occurs. The face stress reaches a maximum value  $\sigma_f^{max} \approx 144$  MPa at the face-core

interface, and this value is included in Table 2 as a measure of the intensity of the local effects. The results shown in Figure 5a demonstrate that the stresses in the face change significantly through the thickness near the junction, even though, the face stresses do not exceed the proportional limit. The distribution of stresses in the core along the upper face-core interface is illustrated in Figure 5b. Far from the junction,  $\sigma_x$  is constant, and, as expected, the transverse normal and shear stresses  $\sigma_y$  and  $\tau_{xy}$  are zero. However, near the junction,  $\sigma_y$  and  $\tau_{xy}$  become non-zero and attain substantial magnitudes. Due to this, the core principal stresses near the tri-material wedge may attain values beyond the core yield limit. The peak principal stresses are tensile (“crack opening”) in the soft core, and compressive (“crack closing”) in the stiff core for this particular type of loading. The maximum values of the principle stresses in the cores (a distance 0.6 mm from the interface) are given in Table 2.

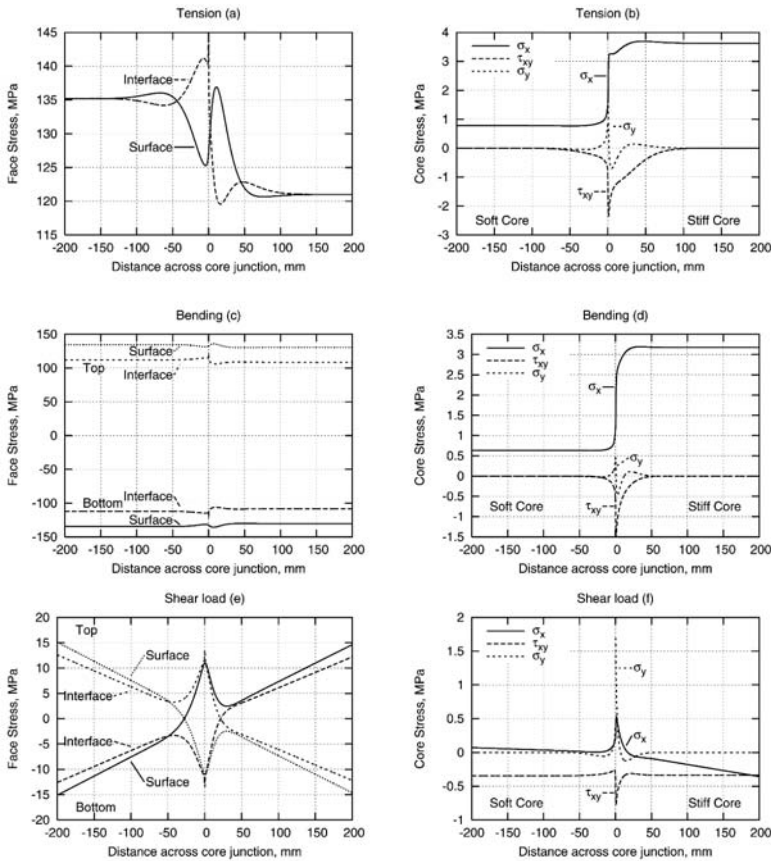


Figure 5. FEA results for case 1. Upper and lower face stresses and core stresses at upper core-face interface for the cases of (a)-(b) axial loading, (c)-(d) pure bending and (e)-(f) transverse shear loading.

In Tables 2 and 3, the nominal stress in each core is the main stress far from the junction, while the maximum principal stress is located near the junction. If the stresses exceed the yield/proportional limits of the material (given in Table 1), this is indicated in bold types in Tables 2 and 3. From Tables 1–3 it is seen that the principal stresses in both cores exceed the yield limits for the uniaxial tension load case.

The stress distributions in the top and bottom faces are shown in Figure 5c for the bending load case. Although the behaviour is similar to tension loading, the level of the local effects is smaller even though the same load criterion was applied for both tension and bending loads. For bending loading, the maximum face stress is  $\sigma_f^{max} = 136$  MPa. The core stresses are given in Figure 5d. From Table 2, it is observed that a maximum principal stress of 1.4 MPa in the soft core is reached, and this exceeds the strength of the H-60 core by a factor of two.

The face stresses due to transverse shear loading are shown in Figure 5e. Here, the soft core is the limiting factor, and a load criterion associated with the core stresses was used,  $\tau_f^{nom} = 0.5 \tau_f^Y = 0.35$  MPa. An additional bending moment  $M = 10V(h_c + 2h_f)$  was added to ensure global equilibrium. Thus, the “global” face stress is zero at the junction as indicated in Figure 5e, while the maximum local stress achieves a modest value of  $\pm 13.5$  MPa. These bending stresses will not cause face failure for this particular sandwich configuration (case 1), but their presence induces substantial local stresses in the adjacent cores. The peak principal stress in the soft core is equal to 0.65 MPa, which may cause failure. It can be seen that the peak of  $\sigma_y$  shown in Figure 5f is much higher than the maximum principal stress of 0.65 MPa specified in Table 2. The reason being, that the FEA-results included in Tables 2 and 3 were read at the characteristic distance of 0.6 mm from the tri-material wedge, since convergence of the numerical results was accomplished at this distance. It should be noticed also that the principal core stresses at the upper interface are compressive, while they are tensile at the lower interface.

Table 3. Study case 2 – local effects at core junction.

Applied load	Faces: Nominal stress/ Maximum stress, MPa	Core 1: Nominal stress / Max principal stress, MPa	Core 2: Nominal stress / Max principal stress, MPa
Tension 875 N/mm	135 / <b>292</b>	5.9 / <b>11.8</b>	55 / 68
Bending 4.4 kN·mm/mm	135 / 135	3.1 / <b>7.4</b>	57 / 57
Shear 4.7 N/mm	0 / $\pm 10.9$	0.35 / 0.64	0.44 / 2.8

## 5. DISCUSSION AND CONCLUSIONS

The qualitative behaviour of the stresses in the sandwich constituents corresponding to case 2 (Table 3) is similar to the results displayed in Figure 5. From this it is clear that the intensity of the local effects may be partly characterized by the maximum face stress  $\sigma_f^{max}$ , which will always be found at the face-core interface close to the junction for all three loading types. The maximum principal core stresses,  $\sigma_{c1}^{max}$  and  $\sigma_{c2}^{max}$ , help to access the stress state in the adjoined cores. Again, it is emphasized that the core stresses are traced inside the core at a characteristic distance of  $0.6\text{ mm}$  (equal to the maximum core cell size) away from the tri-material wedge, which makes the stress estimates mesh independent. Thus, the stresses  $\sigma_f^{max}$ ,  $\sigma_{c1}^{max}$  and  $\sigma_{c2}^{max}$  are proposed to be objective characteristics of the intensity of the local effects, and these stresses are included in Tables 2 and 3 accordingly.

Analysis of Tables 2 and 3 shows that the maximum principal stresses in the soft core generally exceed the yield strength. This happens for all three loads for case 1 (Table 2), and for the tension and bending loads in case 2 (Table 3). This indicates that the weakest point in sandwich structures with core junctions is usually the soft core. However, the face stresses may also exceed the strength limit, as case 2 (see Tables 1 and 3) demonstrates.

The local stress concentrations are especially dangerous for sandwich cores, but it is important to realize that these local failures may also trigger a global collapse of the whole sandwich panel due to the presence of the long interfaces, which immediately reroute failure further into the layered sandwich structure due to delamination.

A recent patent application [10] suggests a novel design concept of structural grading of sandwich “sub-structures”. The main idea of the concept is the following. Wherever a material discontinuity occurs due to the introduction of a sub-structural component, redesign of the sub-structure is performed through change of its geometry. Substitution of a butt core junction by a scarf core junction, and modification of stiffeners and through-the-thickness inserts are examples of this approach as presented in Figure 6. Thus, the proposed structural grading (redesign) of typical “sub-structures” suppresses the local effects, and thereby increases the global performance of the entire sandwich assembly. The realization of this concept with respect to core junctions subjected to transverse shear loads was verified in [19, 20].

It should be noticed that the sketches shown in Figure 6 do not represent the “optimal” solutions for each particular type of “sub-structure”, but merely suggests some general trends.

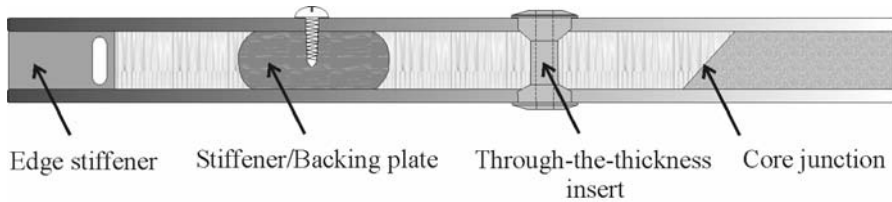


Figure 6. Design modifications of typical “sub-structures” in sandwich panels.

## REFERENCES

1. Zenkert D. (ed.), *The Handbook of Sandwich Construction*, EMAS Publishing, London, 1997.
2. Shenoj R.A. and Wellicome J.F. (eds), *Composite Materials in Maritime Structures*, Cambridge University Press, 1993.
3. Zenkert, D., “Effect of manufacture-induced flaws on the strength of foam core sandwich beams”, in *Proceedings of International Symposium on Damage Detection and Quality Assurance in Composite Materials*, ASTM Special Technical Publication 1128, 1992, pp. 137–151.
4. Skvortsov, V. and Thomsen, O.T., “Analytical estimates for the stresses in face sheets of sandwich panels at the junctions between different core materials”, *Proceedings of the 6-th International Conference on Sandwich Structures (ICSS-6)*, Ft. Lauderdale, Florida, 2003, CRC Press, New York, 2003, pp. 501–509.
5. Bozhevolnaya, E., Thomsen, O.T., Kildegaard, A. and Skvortsov, V., “Local effects across core junctions in sandwich panels”, *Composites. Part B: Engineering*, Vol. 34, 2003, pp. 509–517.
6. Bozhevolnaya, E., Lyckegaard, L., Thomsen, O.T. and Skvortsov, V., “Local effects in the vicinity of inserts in sandwich panels”, *Composites. Part B: Engineering*, Vol. 35, 2004, pp. 619–627.
7. Pageau, S.S., Joseph, P.F. and Biggers, S.B., Jr., “The order of stress singularities for bonded and disbanded three-material junctions”, *International Journal of Solids and Structures*, Vol. 31, No. 21, 1994, pp. 2979–2997.
8. Ribeiro-Ayeh, S. and Hallström, S., “Strength prediction of beams with bimaterial butt joints”, *Engineering Fracture Mechanics*, Vol. 70, 2003, pp. 1491–1507.
9. *Technical Manual H-grade: Divinycell®*, DIAB Group, 2003.
10. Bozhevolnaya, E., Lyckegaard, A., Jakobsen, L. and Thomsen, O.T., *Sandwich Panel and a Method of Producing a Sandwich Panel*, Application No./Patent No. 03027020.1, 2003.
11. Bozhevolnaya, E. and Thomsen, O.T., “Structurally graded core junctions in sandwich beams: Quasi static loading conditions”, *Composite Structures*, in press.
12. Bozhevolnaya, E. and Thomsen, O.T., “Structurally graded core junctions in sandwich beams: Fatigue loading conditions”, *Composite Structures*, in press.

# MATERIAL CHARACTERIZATION OF PVC FOAM UNDER STATIC AND DYNAMIC LOADING

D.C. Loup<sup>1</sup>, R.C. Matteson<sup>1</sup> and A.W.J. Gielen<sup>2</sup>

<sup>1</sup>Naval Surface Warfare Center, Carderock Division, 9500 MacArthur Blvd, West Bethesda, MD 20817, USA

<sup>2</sup>TNO Built Environment and Geosciences – Centre for Maritime and Mechanical Structures, P.O. Box 49, 2600 AA Delft, The Netherlands

**Abstract** To support the development of sandwich composite failure models, a series of material coupon tests were performed to characterize foam core material response under quasi-static and dynamic tension loading. Material stress-strain response was found to be highly nonlinear and dependent on the loading orientation relative to the axis of the foam sheet. At low to moderate strain rates, less than  $150 \text{ sec}^{-1}$ , tension strength and modulus were both increased and ultimate strain at failure decreased.

**Keywords:** PVC foam, nonlinear response, high strain rate response.

## 1. INTRODUCTION

The understanding and analytical estimation of failure of joints in composite marine constructions under dynamic loading presents a complex problem requiring characterization and modeling of both the overall structural response as well as the material response in detail. Investigators have developed failure models for composite single skin and stiffened skin joints utilizing the finite element method and data from selected substructure joint detail and material tests [1, 2]. An effort is ongoing to extend these models to sandwich composite constructions and specifically the details that are typically represented in foam core sandwich composite joints.

An accurate understanding and representation of the material stress-strain response through failure is an essential aspect in the development of a material model. The nonlinear aspect of the stress-strain response of these types of foam cores is well known. In particular, Viana and Carlsson [3], have described the nonlinear tensile stress-strain response of cross-linked PVC foams at quasi-static loading rates. In order to support the development of detailed material response models, a more detailed representation of the nonlinear material response is required.

Under dynamic loading, typical of indirect shock or impact of sandwich composite marine constructions, the primary material response is typically characterized by strain rates below  $100 \text{ sec}^{-1}$ . A limited amount of data from tension testing at rates in the range of interest has been reported for ductile and cross-linked PVC foams [4, 5]. However, most dynamic testing has been performed in compression at much higher rates [6, 7]. Consequently little data is available which characterizes foam core materials at loading rates in the range of interest for these structural models.

The work reported herein addresses each of these loading effects. The results of these characterizations will be utilized in the development of dynamic response and failure models under development.

## **2. EXPERIMENT**

### **2.1 Materials**

The specific material tested in this investigation was a cross-linked, closed cell, PVC foam with a nominal density of  $100 \text{ kg/m}^3$  manufactured by DIAB, and designated as H100.

A single 38 mm thick sheet of the material was obtained for this effort. The majority of the sheet was used to fabricate components of t-joint test articles. The remainder of the sheet was used for material coupons to develop a detailed characterization of the specific material used in the t-joint tests.

The average density of the material tested was  $91 \text{ kg/m}^3$ . This is slightly lower than the nominal density, but within the expected range for this designation. It was expected that the mechanical properties would match or be somewhat lower than the nominal values reported by DIAB [8]. To generalize the observations for cross-linked PVC foam cores of this type, the results reported in this paper are normalized by the nominal strengths and modulus values reported by DIAB.

A cylindrical spool shaped specimen similar to that used by Olsson and Lönnö [9] was used for this investigation. The overall length of the

specimen was 38 mm. The diameter at the ends of the specimen was 38mm, transitioning to a 25 mm diameter straight cylindrical section approximately 25 mm in length. The tapering transition region was a constant radius of approximately 12 mm. With this geometry, the same size and shape test specimen could be used for testing both through-thickness and in-plane directions. The specimens were fabricated by bonding square blocks of the foam material to cylindrical aluminum bars. The blocks were then machined to the spool shape on a lathe using an abrasive cutting tool.

## 2.2 Testing

The quasi-static tension testing was performed using a servo-hydraulic testing machine. As noted above, the spool specimens were bonded to aluminum bars. Pins were passed through the bars to attach the specimen to a clevis-type loading device that ensured loading alignment with the specimen axis. The quasi-static tension specimen in this configuration is shown in Figure 1. The specimen deformation was recorded by an extensometer attached to the center of the specimen, spanning the straight cylindrical section. Loading rate for the quasi-static testing was 2 mm/min.



*Figure 1.* Spool specimen in test configuration for quasi-static tension.

Dynamic testing was also performed using the same spool specimen geometry. However, the specimens were directly attached to the load frame through threaded studs in the ends of the aluminum bars. The fixed end of the specimen was attached using an instrumented load cell stud to allow a more direct reading of the load applied to the specimen and to provide the necessary dynamic response. The specimen strain was measured using a capacitance type displacement gage.

Two different loading arrangements were used for the dynamic testing. The preferred method was an MTS 810 high rate servohydraulic test system. This load frame utilized a closed-loop servohydraulic system with nitrogen-charged accumulators that enable actuator displacement rates of up to 5000 mm/sec. The machine was equipped with a slack-adaptor grip, which allowed up to 75 mm of cross-head travel before engaging the specimen. The load cell stud was attached to the lower end of the specimen and then threaded into the fixed base of the load frame. The upper end was threaded into an end of the slack-adaptor grip. The slack-adaptor allowed the loading grip to accelerate to the preselected rate before loading the specimen

In an attempt to resolve some ringing problems believed to be associated with the relatively small failure loads and the loading introduction associated with the servo-hydraulic machine and the slack-adaptor mechanism, an impact type loading apparatus was used. The loading apparatus with a specimen installed for testing is shown in Figure 2. The upper end of the specimen is attached to a fixed part of the load frame. The lower end is attached to a moveable frame that is free to slide vertically. The load is introduced by dropped weight impact to a soft aluminum cone at the upper end of the moveable frame. The loading rate is determined in part by the impact velocity, but also in large part by the acceleration of the loading frame during the crushing of the aluminum cone. As a consequence, the strain rates for this arrangement were limited to approximately 30 to 60 sec<sup>-1</sup>. Another concern with this testing arrangement was that the loading rate continually increased as the loading frame was accelerated downward by the impact. The strain rate of the specimen was found to increase approximately linearly through failure.

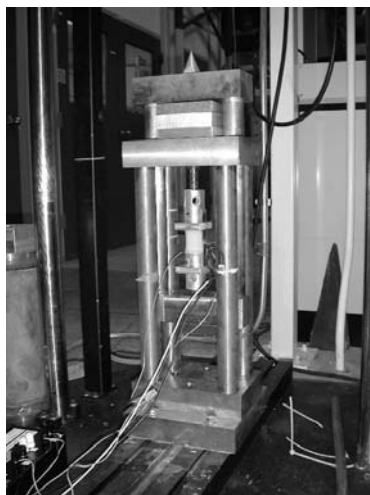


Figure 2. Test specimen mounted in impact tension test loading frame.

### 3. RESULTS

#### 3.1 Quasi-static tension

The stress-strain response measured in both in-plane and through-thickness orientations are shown in Figure 3. The stress has been normalized by the corresponding nominal strengths of the foam. The ultimate strengths for each orientation exceed the nominal strengths. However, the material exhibits a relatively strong nonlinear response at stresses below the nominal strength. The onset of the nonlinear response was evident at less than 2% strain for either orientation, and at stress levels approximately 60% of the nominal strengths. The average strain to failure observed in these quasi-static tension tests was approximately 6% and 10% in the through-thickness and in-plane orientations respectively.

To assess the extent of the nonlinearity, the tangent modulus was calculated from the stress-strain response over small strain increments over the full strain range to failure. The incremental tangent modulus normalized by the respective nominal tension modulus for each orientation is shown in Figure 4. As indicated in this figure, the material exhibits a relatively strong nonlinear softening response, experiencing an approximate 20% reduction in modulus from 0 to 2% strain, an additional 40% reduction from 2 to 4% strain, and reaches a relatively constant value of approximately 10% of initial modulus from 4% strain to failure.

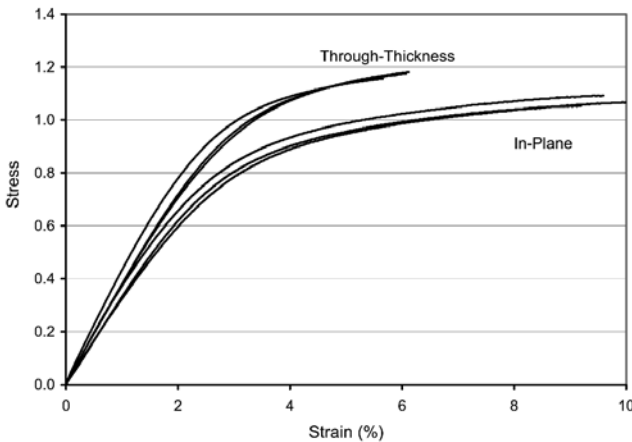


Figure 3. Quasi-static tension stress-strain response, stress normalized by nominal in-plane and through-thickness tension strengths.

### 3.2 Dynamic tension

Figure 5 shows representative tension stress-strain responses for material tested in the through-thickness orientation at three strain rates, with the strain rate near failure indicated for each result. The stresses have been normalized by the nominal through-thickness, quasi-static strength. Several material response trends noted in these high rate tests are evident in this Figure. As the strain rate increased over the range evaluated in this investigation, the ultimate strength and initial modulus also increased. The strain to failure decreased with increasing strain rate.

In addition, an effect of the loading rate variation experienced during the test can be seen in the  $36 \text{ sec}^{-1}$  rate stress-strain response measured in a dropped weight impact test. The initial slope for that curve is similar to the quasi-static response. For the impact loaded tests, due to the steady acceleration and related continual increase in loading rate during the test, the initial material response is representative of lower strain rates than the response near failure. How that loading rate variation may have affected the strengths or strain to failure was not determined. Results for all tests, including tension modulus, are reported at strain rates determined as averages over the final approximate 1% strain near specimen failure.

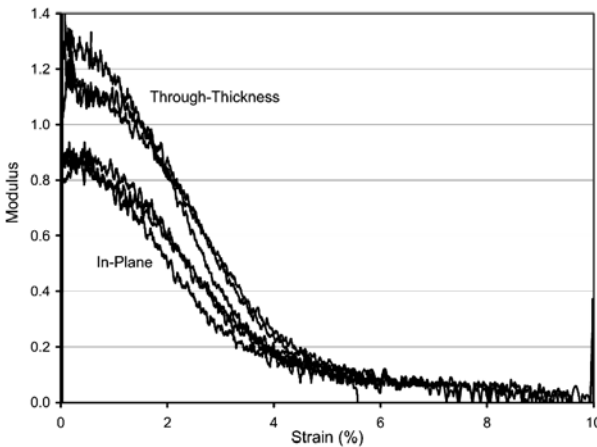


Figure 4. Incremental tangent modulus as a function of applied strain, for quasi-static tension loading. Modulus normalized by nominal in-plane and through-thickness tension modulus.

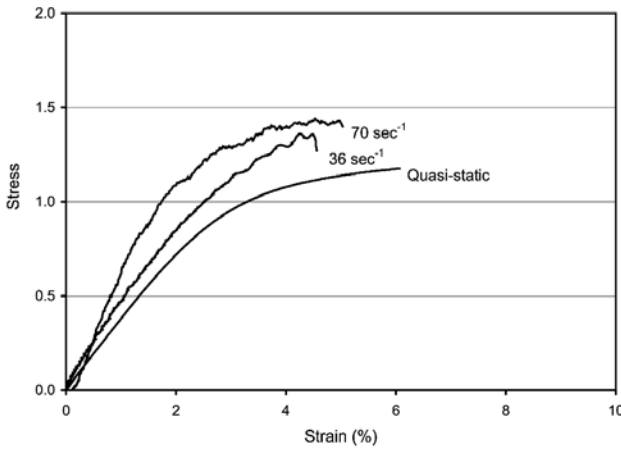


Figure 5. Through-thickness stress-strain response at three loading rates, stress normalized by nominal static through-thickness strength.

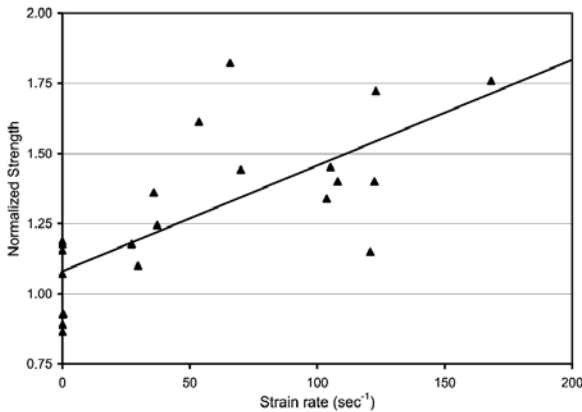
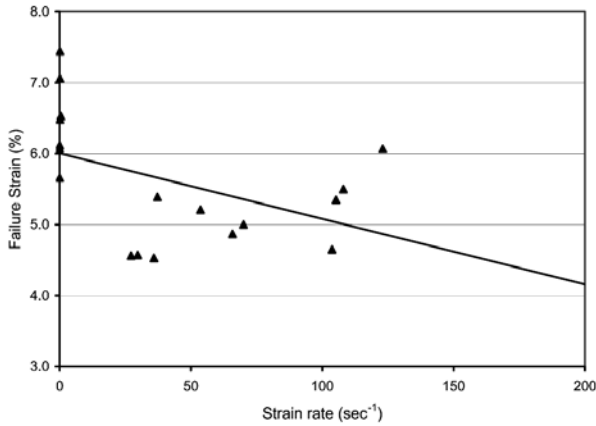


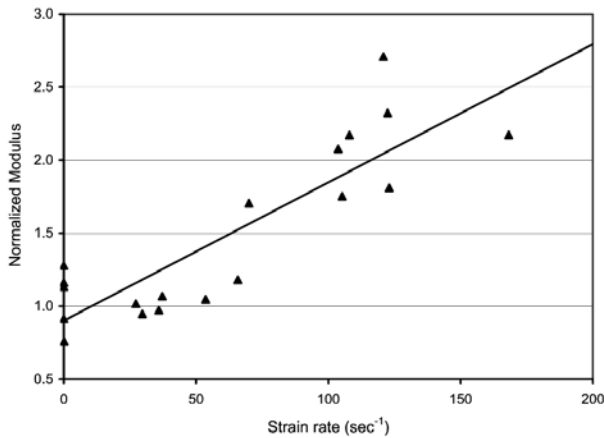
Figure 6. In-plane and through-thickness tension strengths as a function of strain rate near failure, strengths normalized by nominal static strengths. Linear least-squares best fit trendline shown.

Figure 6 shows the material strengths for specimens tested at elevated strain rates in both the in-plane and through-thickness orientations, normalized by the respective quasi-static strengths. A linear least-squares best-fit line is shown in the figure. As indicated by this trend line, the material exhibits a 50% increase in the material strength at a strain rate of  $100 \text{ sec}^{-1}$ .

Figure 7 shows the strain to failure of the material tested in the through-thickness orientation. Again a linear best fit of the data indicates that the strain to failure of the material was reduced from approximately 6% at quasi-static rates to 5% at 100 sec<sup>-1</sup>.



*Figure 7.* Through-thickness tension strain to failure as a function of strain rate near failure. Linear least-squares best fit trendline shown.



*Figure 8.* Through-thickness tension modulus as a function of strain rate near failure, modulus normalized by nominal static through-thickness tension modulus. Linear least-squares best fit trendline shown.

Figure 8 shows the initial tangent modulus for material tested in both orientations, normalized by the nominal modulus. As mentioned above, the

impact test results may have been representative of somewhat lower rates than depicted. The linear best fit of all of the data indicates an increase in modulus by a factor of 2 at strain rates of approximately  $125 \text{ sec}^{-1}$ .

#### **4. SUMMARY**

Several aspects of the response of cross-linked PVC foams were demonstrated and evaluated in this effort. The material demonstrated a material orientation dependence, comparable to the nominal values reported by the manufacturer. For the particular sheet of material tested in this study, the through-thickness properties were under-estimated by the nominal values and the in-plane properties were over-estimated. The material exhibited a highly nonlinear response, evident at strains as low as one-third of the ultimate failure strains and approximately 60% of the nominal strengths. The nominal tension modulus for the through-thickness and in-plane orientations was found to be representative for the initial, 0 to 2% strain, response.

The dynamic tension response of the material showed a relatively strong effect at low to intermediate strain rates in the range of 50 to  $150 \text{ sec}^{-1}$ . Material strength and initial modulus were both increased and strain at failure was decreased.

#### **ACKNOWLEDGEMENTS**

The results of this research were obtained in the “Dycoss-2” project, a joint research project executed by NSWCCD and TNO. The project is sponsored by the Office of Naval Research and the Royal Netherlands Navy.

#### **REFERENCES**

1. Meijer, G.J., Rasmussen, E.A., Lemmen, P.P.M., Lemmen, R.L.C., and Palmer, D., “Dynamic Behavior of Composite Ship Structures (DYCOSS); Tests and Analyses Efforts”, 70th Shock and Vibration Symposium, Albuquerque NM USA, 15-19 November 1999.
2. Lemmen, P.P.M., Meijer, G.J., and Rasmussen, E.A., “Dynamic Behavior of Composite Ship Structures (DYCOSS) Failure Prediction Tool”, 70th Shock and Vibration Symposium, Albuquerque NM USA, 15-19 November 1999.
3. Viana, G. and Carlsson, L.A., “Mechanical Properties and Fracture Characterization of Cross-Linked PVC Foams, *Journal of Sandwich Structures and Materials*, Vol 4, pp 99-113, April 2002.

4. Wennhage, P. and Olsson, K.A., “High Strain Rate Testing Techniques of Ductile Core Materials”, Composite and Sandwich Structures, Proceedings of the Second North European Engineering and Science Conference (NESCO II), pp 49–67, 1997.
5. Stibe, M. and Danielsson, M., “A New Toughened Foam Core Material – Evaluation of Material Properties”, Composites and Sandwich Structures, Proceedings of the Second North European Engineering and Science Conference (NESCO II), 1997.
6. Mahfuz, H., Mamun, W.A., Haque, A., Turner, S., Mohamed, H., and Jeelani, S., “An Innovative Technique for Measuring the High Strain Rate Response of Sandwich Composites”, Composites and Structures, 50, pp 279-285, 2000.
7. Thomas, T., Mahfuz, H., Carlsson, L.A., Kanny, K., and Jeelani, S., “Dynamic Compression of Cellular Cores: Temperature and Strain Rate Effects”, Composites and Structures, 58, pp 505-512, 2002.
8. Divinycell, Technical Manual, H-Grade, 1991.
9. Olsson, K.A. and Lönnö, A., “Test Procedures for Foam Core Materials”, Sandwich Constructions 1, Proceedings of the First Intl Conference on Sandwich Constructions, EMAS, pp 293-318, 1989.

# DYNAMIC RESPONSE OF ANISOTROPIC SANDWICH PANELS TO UNDERWATER AND IN-AIR EXPLOSIONS

Liviu Librescu and Sang-Yong Oh

*Department of Engineering Science and Mechanics, Virginia Polytechnic Institute and State University, Blacksburg, VA 24061, USA*

librescu@vt.edu, sangyong@vt.edu

Jörg Hohe

*Fraunhofer-Institut für Werkstoffmechanik, Wöhlerstr. 11-13, 79108 Freiburg/Brsg., Germany*

joerg.hohe@iwf.fraunhofer.de

**Abstract** A study devoted to the dynamic response of sandwich panels to underwater and in-air explosions is presented. The study is carried out in the context of a geometrically nonlinear model of sandwich structures featuring anisotropic laminated face sheets and a transversally compressible orthotropic core. The unsteady pressure generated by the explosion and acting on the face of the sandwich panel includes the effect of the pressure wave transmission through the core. Its implications on the structural time-histories as corresponding to the underwater and in-air explosions are put into evidence. The effects of the transverse core compressibility on dynamic response are highlighted. In this sense, one of its major implications is the possibility to capture interactively the global and local (wrinkling) dynamic response of the panel. It is shown that implementation of the structural tailoring technique in the face sheets can constitute an important mechanism toward enhancing the dynamic load carrying capacity of sandwich panels when exposed to blast pulses. Effects of the core, as well as the ones due to the ply-thickness, combined with that of ply-angle and stacking sequence of face sheets, orthotropy of the material of the core, geometrical nonlinearities, initial geometric imperfections and of the damping ratio are investigated, and their implications upon the dynamic response are highlighted and pertinent conclusions are outlined.

**Keywords:** underwater/in-air explosion, sandwich panel, dynamic response, core effects, face sheet ply-angle.

## 1. INTRODUCTION

Sandwich constructions have emerged as a most promising type of structure for Navy applications. Its many advantages resulting, among others, from their improved fatigue performance, superior energy absorption that yields an increased resistance to impact, reduced susceptibility to corrosion, superior thermal and acoustic insulation, have generated an increased interest for the extensive incorporation of sandwich composites in the construction of naval constructions. A similar interest is present also in the context of aeronautical/aerospace constructions.

In modern warfare, naval ships can be exposed to blasts generated by underwater and in-air explosions that can inflict significant damage to their structure. The same is valid when these are exposed during their missions to sonic-boom and shock-waves.

In order to achieve a reliable design, advanced analytical models of sandwich structures and proper expressions for the blast pulses generated either by underwater explosions or in-air explosions (identified in the sequel by the acronyms, UNDEX and INEX, respectively), are needed.

The same is valid for the pressure pulses induced by the sonic-boom and shock waves. In this context, the study of the dynamic response of flat sandwich panels impacted by such explosive pressure pulses can play an important role in their rational design.

In contrast of the case of the homogeneous or standard laminated composite structures where the effects of transverse normal compressibility can be ignored, for sandwich type constructions this effect can be essential. Indeed, as it was shown quite recently (see Frostig [1] and Hohe and Librescu [2–4]), by including the effect of the core compressibility in the modeling of sandwich structures one can capture both the global and the local (wrinkling) dynamic responses. Moreover, as it was shown in the previously indicated works, the global and local responses are not independent phenomena, but interacting ones.

The problems of the global and wrinkling response in the context of the dynamic response of flat sandwich panels to UNDEX and INEX are analyzed in this work.

In the former case, one supposes that we deal with a submerged panel, while in the latter one, with a topside sandwich panel of ship superstructures, or with a panel of an aeronautical/aerospace sandwich construction. In this context, in order to put into evidence the implications of various non-classical effects, such as those of geometrical non-linearities, initial geometric imperfections, anisotropy of face sheets and their ply-sequence, transverse shear orthotropy properties of the core layer, etc., an advanced model of sandwich constructions

will be used. The basic equations of this structural model have been derived in a number of previous papers [2–4].

In this context one should remark that, to the best of the authors knowledge, with the exception of the works by Hayman [5], Mäkinen [6], and Librescu et al. [7] where special issues on the dynamic response of sandwich panels to underwater explosions have been explored, no other studies on this topic are available in the specialized literature.

## 2. THE STRUCTURAL MODEL

The global mid-plane of the sandwich structure is selected to coincide with that of the core layer. Its points are referred to a curvilinear and orthogonal coordinate system  $x_\alpha$  ( $\alpha = 1, 2$ ). The through-the-thickness coordinate  $x_3$  is considered positive when measured in the direction of the downward normal. For the sake of convenience, the quantities affiliated with the core layer are identified by the superscript  $c$ , while the ones associated with the bottom or top face sheets are identified by superscript  $f$ .

The sandwich structural model considered in this paper is based on the following assumptions: (i) the face-sheets are composed of a number of orthotropic material laminae, the axes of orthotropy of the individual plies being rotated with respect to the geometrical axes  $x_\alpha$  of the structure, (ii) the material of the core features transverse orthotropic properties, the axes of orthotropy being parallel to the geometrical axes  $x_\alpha$ , (iii) the core layer is capable of carrying transverse shear stresses only, and as result we deal with a *weak core*. Moreover, one assumes that it is extensible in the transverse normal direction, (iv) a perfect bonding between the face sheets and the core, and between the constituent laminae of the face sheets is assumed to be valid, (v) the layers constituting the faces are assumed to be thin; as a result, transverse shear effects are neglected in the face sheets, (vi) the structure as a whole, as well as both the top and bottom laminated face sheets are assumed to exhibit mechanical and geometrical symmetry properties with respect to both the mid-plane of the core layer and about their own mid-planes, as well, and finally, (vii) a Lagrangian description of the non-linear model of sandwich structures is adopted in conjunction with the implementation of the von-Kármán non-linear kinematic model and of initial geometric imperfections.

In conjunction with the previously formulated assumptions, the basic kinematic relationships have been derived by Hohe and Librescu [2–4]. As a result, these are not supplied here.

In conjunction with the postulated displacement representations for the face sheets and the core, consistent equations of motion and boundary conditions are derived from Hamilton's principle. These equations can be found in the papers by the present authors [2–4].

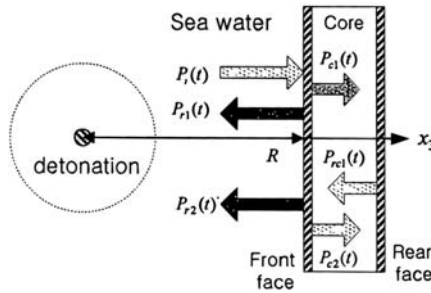


Figure 1. Sandwich panel exposed to an underwater explosion.

### 3. BLAST LOADS INDUCED BY UNDERWATER AND IN-AIR EXPLOSIONS

Due to the presence of the core layer, the transmission of pressure waves through the sandwich panel renders the problem of determination of the resultant unsteady pressure more intricate than in the case of the monolithic/laminated panel counterparts. While in the latter case, the theory on which the determination of the pressure time-history on the front face of the panel follows the line established by Kirkwood–Bethe–Cole, in the former case, the ideas developed specifically for the case of a sandwich panels by Hayman [5], and used subsequently by Mäkinen [6] will be adopted here.

As it will be seen later, the pressure time-histories based on the previously mentioned structural models feature significant quantitative and qualitative differences that affect the dynamic response of the panel in question. Basically, the unsteady pressure model by Hayman [5] represents an extension of that devised for a monolithic/laminated panel, in the sense of the inclusion also of the pressure transmitted through the core, reflected at the rear face of the sandwich panel, and then transmitted out into the water (see Figure 1).

Having in view the large front of the explosion, the resulting pressure is considered uniformly distributed over the plate surface.

As a result, the total pressure in front of the sandwich panel can be represented in the form

$$p_3(t) (\equiv P(t)) = P_i(t) + P_{r1}(t) + P_{r2}(t), \quad (1)$$

where  $P_i(t)$  denotes the free-field pressure due to the incident shock wave;  $P_{r1}(t)$  is the pressure reflected on the front face, while  $P_{r2}(t)$  is the pressure transmitted into the core, reflected at the rear face and transmitted out into the water. Their expressions are not supplied here.

It should be remarked that the equations that define the expression of the unsteady pressure apply to both underwater and in-air explosions. However, in the former case the speed of sound and mass density of the sea water at 20°C

are:  $c = 1476$  m/sec,  $\rho = 1009$  kg/m<sup>3</sup>, while their in-air counterparts are  $c = 330$  m/sec and  $\rho = 1.20$  kg/m<sup>3</sup>. The large differences in the values of  $c$  and  $\rho$  in sea water and air turn out to have significant implications on dynamic response.

As it will be revealed later, inclusion of the core effects will bring considerable differences on the pressure and structural time-histories in the two investigated cases of UNDEX and INEX.

In the simulations related to the dynamic response to INEX we are also considering the cases of the sandwich panel impacted by a sonic-boom and a triangular blast. In a compact form, their expressions are

$$P(t) = q_m(1 - t/t_p)[H(t) - \delta_b H(t - rt_p)]. \tag{2}$$

In (2),  $H(t)$  denotes the Heaviside step function,  $\delta_b$  is a tracer that takes the values 1 or 0 depending on whether the sonic-boom or the triangular blast is considered, respectively,  $t_p$  denotes the positive phase duration of the pulse measured from the time of impact of the structure,  $r$  denotes the shock pulse length factor. For  $r = 1$ , the sonic-boom reduces to a triangular explosive pulse, while for  $r = 2$  it corresponds to a symmetric sonic-boom pulse.

Within the INEX problem we will consider also the tangential blast to the panel surface in the direction of the coordinate  $x_1$  in the form of a traveling-wave

$$P(t) = q_m H(ct - x_1) \exp(-\eta(ct - x_1)), \tag{3}$$

where  $c$  is the wave speed in the medium surrounding the structure, while  $\eta$  is an exponent characterizing the blast decay.

## 4. RESULTS

Selected results on the dynamic response of sandwich panels to UNDEX and INDEX are presented next: In the simulations the elastic characteristics for the face sheets and the core as used in [7] are adopted also here.

The results supplied in Figures 2a and 2b correspond to the pressure time-history on the face of a sandwich panel, induced by an UNDEX. While in Figure 2a the effects of the transmission of pressure waves through the core have been included, in Figure 2b, the results correspond to the discard of these effects.

From these figures, qualitative and quantitative differences are emerging. First of all, one can observe that in the case of the inclusion of the core effects, the time at which the cavitations occurs (i.e. the time corresponding to the instant when the resultant pressure becomes a zero-valued quantity), is much larger than that corresponding to the discard of core effects. In addition, in the former case, almost two simultaneous cavitation events occur, one on the front face of sandwich panel and the second one at a small distance in front of

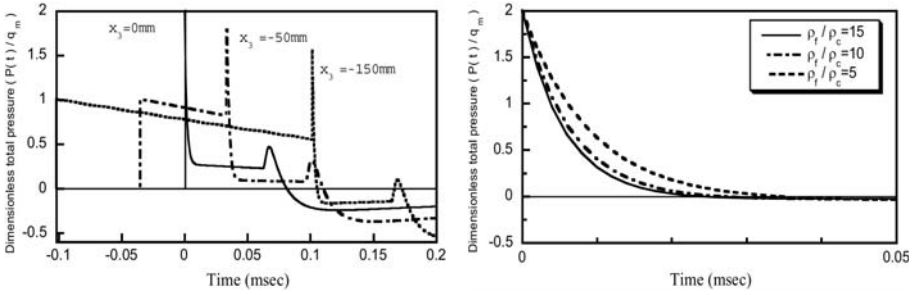


Figure 2. (a) Dimensionless pressure time-history for various distance from panel front surfaces in UNDEX. Effect of the pressure transmission through the core included ( $Q = 30$  kg,  $R = 10$  m,  $\rho_f/\rho_c = 5$ ). (b) Dimensionless pressure time-history in UNDEX. Effect of pressure transmission through the core discarded ( $Q = 30$  kg,  $R = 10$  m,  $x_3 = 0$ ,  $\rho_f = 15.28$  kg/m<sup>3</sup>).

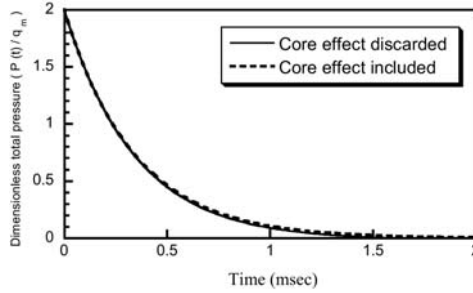


Figure 3. Dimensionless pressure time-histories at the panel surface in INEX ( $Q = 30$  kg,  $R = 10$  m,  $\rho_f/\rho_c = 5$ ).

it, while in the latter one, a single cavitation takes place. These results are in excellent agreement with those reported by Hayman [8] and Mäkinen [9]. It is also interesting to see the pressure time-history due to an INEX when the core effects are included or discarded.

In this sense, Figure 3 reveals that, on one hand, the in-air explosion is much more severe than in the water, and on the other hand, that the transmission of the pressure wave through the core and its reflection on the rear face does not bring any change as compared to the case of the discard of this effect.

In Figure 4a the global deflection time-history of the sandwich panel as influenced by the structural damping and by incorporation/discard of the face wrinkling is depicted. As it clearly appears, the effect of the wrinkling effect on the global response is immaterial.

On the other hand, in Figure 4b, the dimensionless wrinkling displacement time-history for the case of two values of the damping parameter is presented. The results reveal that the face wrinkling whose occurrence should be con-

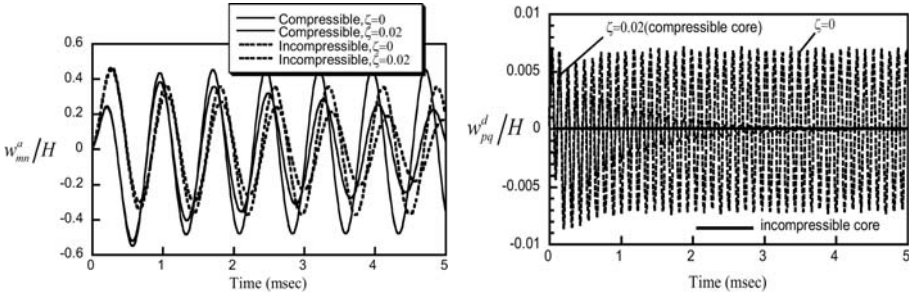


Figure 4. (a) The global dimensionless transverse deflection time-history ( $Q = 30$  kg,  $R = 10$  m,  $w_{mn}^0 = 0.1H$ ,  $w_{pqd}^0 = 0.01H$ ). (b) Dimensionless face wrinkling deflection time-history of the panel subjected to UNDEX ( $Q = 30$  kg,  $R = 10$  m,  $w_{mn}^0 = 0.1H$ ,  $w_{pqd}^0 = 0.01H$ ).

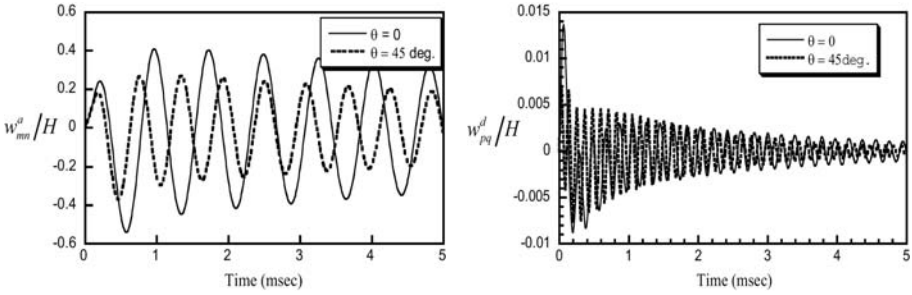


Figure 5. (a) Effect of the ply angles of faces on the global transverse deflection time-history ( $Q = 30$  kg,  $R = 5$  m,  $w_{mn}^0 = 0.1H$ ,  $w_{pqd}^0 = 0.01H$ ,  $G_{13} = 11 \times 10^6$  Pa,  $G_{23} = 2G_{13}$ ,  $\zeta = 0.01$ ). (b) Effect of the ply angle of face sheet on the face wrinkling deflection time-history ( $Q = 30$  kg,  $R = 5$  m,  $w_{mn}^0 = 0.1H$ ,  $w_{pqd}^0 = 0.01H$ ),  $G_{13} = 11 \times 10^6$  Pa,  $G_{23} = 2G_{13}$ ) UNDEX.

tained at any price, is very sensitive to the damping, in the sense that even for  $\zeta = 0.02$ , the face wrinkling oscillations will damp out after a very short time.

In Figure 5a, the implications of the implementation of the tailoring technique in the face sheets on the global deflection time-history are presented. The results reveal that a notable reduction of the oscillation amplitude is obtained by a proper selection of the ply-angle in the face sheets.

However, for the wrinkling deflection time-history (Figure 5b), the implementation of the tailoring technique appears to be less efficient than in the case of the global response. As concerns the effect of the increase of the transverse Young's modulus on the global and wrinkling response, Figures 6a and 6b reveal that the increase is strongly beneficial in the case of the wrinkling

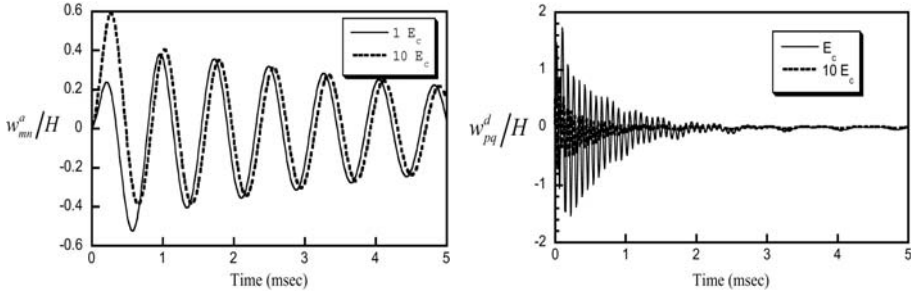


Figure 6. (a) The effect of the transverse Young’s modulus of the core on the overall transverse deflection time-history of the panel subjected to UNDEX. ( $Q = 30$  kg,  $R = 5$  m,  $L_1/H = L_2/H = 15$ ,  $w_{mn}^0 = 0.1H$ ,  $w_{pqd}^0 = 0.01H$ ,  $E_c = 30 \times 10^6$  Pa,  $\zeta = 0.02$ ). (b) Effect of the transverse Young’s modulus of the core on the face wrinkling deflection time-history. ( $Q = 30$  kg,  $R = 5$  m,  $w_{mn}^0 = 0.1H$ ,  $w_{pqd}^0 = 0.01H$ ,  $E_c = 30 \times 10^6$  Pa,  $\zeta = 0.02$ ).

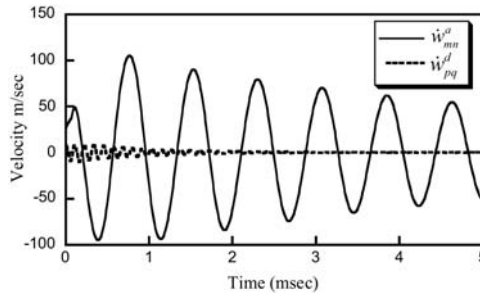


Figure 7. Velocity time-history on global and face wrinkling of the panel subjected to underwater explosion ( $Q = 30$  kg,  $R = 5$  m,  $w_{mn}^0 = 0.1H$ ,  $w_{pqd}^0 = 0.01H$ ,  $\zeta = 0.02$ ).

displacement, and it appears to be rather marginal in the case of the global response.

In Figure 7, there are supplied the effects of the stand-off and weight charge, respectively, on the velocity time-history of the center of the panel subjected to an underwater explosion. The values of the velocity response in UNDEX as presented here are in agreement with those reported by Jiang and Olsen (1994).

The considerable increase of the severity of the in-air explosion (these results are not supplied here) as compared to those in the INEX should be noticed. The dynamic response, global and local to a sonic-boom pulse, and in this sense, the effects of the symmetry of the pulse in terms of the parameter  $r$  are presented in Figures 8a and 8b, respectively.

The results reveal that the asymmetric sonic-boom ( $r = 1.2$ ) is more severe than the symmetric one ( $r = 1$ ).

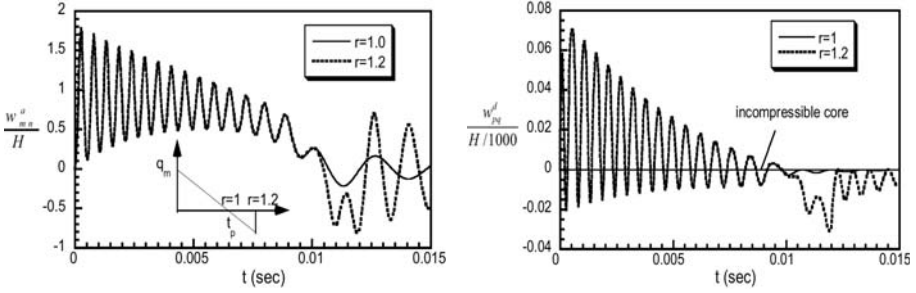


Figure 8. (a) Effect of sonic-boom pulse on the global dynamic response of a flat sandwich panel ( $\xi = 0.1, w_{mn}^0 = 0.01H, w_{pqd}^0 = 0.0001H, L/H = 15, t_p = 0.01$  sec,  $q_m = 10$  MPa. (b) Counterpart of Figure 8a for the wrinkling dynamic response.

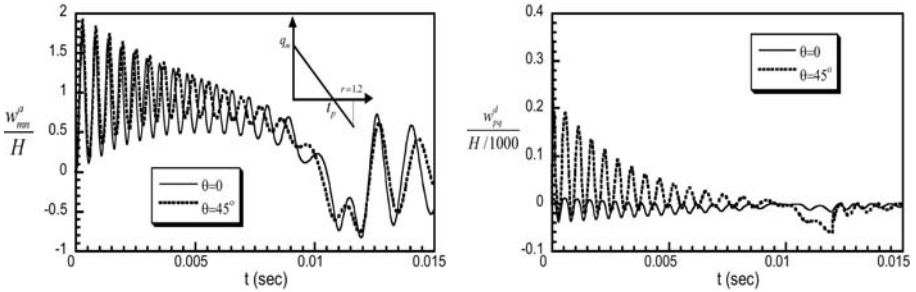


Figure 9. (a) Effect of ply-angle of face sheets on the global instability of the sandwich panel ( $\xi = 0.1, w_{mn}^0 = 0.01H, w_{pqd}^0 = 0.0001H, q_m = 10$  MPa,  $G_{23c} = 5G_{13c} = 11$  MPa,  $t_p = 0.01, r = 1.2$ ). (b) Counterpart of Figure 9a for the wrinkling instability of the sandwich panel.

In Figures 9a and 9b the effects on both the global and wrinkling response to a sonic boom are presented, respectively. The results show that the tailoring of face-sheets has a strong effect especially, on the wrinkling response and less on the global response.

### 5. CONCLUSIONS

Problem of the dynamic response of sandwich flat panels subjected to explosive blast loadings produced by both underwater and in-air explosions have been addressed. The implications of a number of structural and geometrical characteristics of the sandwich panel, as well as of the ones related to the respective blasts have been highlighted and related conclusions have been drawn. Incorporation of the core effects in UNDEX and INEX, has been shown to

result in qualitative and quantitative different results, both from the pressure time-history and of the structural response points of view.

The obtained results can be extended without too much difficulty as to determine the time-histories of strain and stress components at various points of the structure. These items are essential toward determining the failure of the structure.

It should be stressed that in some previous work [7], the dynamic response problem to UNDEX and INEX was addressed in the context of a less refined structural model [8, 9], in the sense of considering a non-extensible core in transverse normal direction.

As a result of this feature, the possibility of capturing the global and wrinkling dynamic responses was precluded.

## ACKNOWLEDGEMENTS

The financial support of the Office of Naval Research Program on Composites for Marine Structures, Grant N000014-02-1-0594, and the interest, advice and encouragement of the Program Manager, Dr. Y. D. S. Rajapakse, are gratefully acknowledged.

## REFERENCES

- [1] Y. Frostig. Buckling of sandwich panels with a flexible core-high-order theory, *International Journal of Solids and Structures*, 35:183-204, 1998.
- [2] J. Hohe and Librescu. A nonlinear theory for doubly curved anisotropic sandwich shells with transversely compressible core, *International Journal of Solids and Structures*, 40:1059-1088, 2003.
- [3] J. Hohe and L. Librescu. Core and face sheet anisotropy in deformation and buckling of sandwich panels, *AIAA Journal*, 42:149-158, 2004.
- [4] J. Hohe and L. Librescu. Advances in the structural modeling and behavior of sandwich panels, *Mechanics of Advanced Materials and Structures*.
- [5] B. Hayman. Underwater explosion loading on foam-cored sandwich panels, *Sandwich Construction*, 3, EMAS, Proceedings for the Third International Conference on Sandwich Construction, May 11–15, Southampton, England, 1995.
- [6] K. Mäkinen. Underwater shock loaded sandwich structures, Department of Aeronautics, Royal Inst. of Technology, Report 99-01, Stockholm, Sweden, 1999.
- [7] L. Librescu, S-Y Song and J. Hohe. Linear and nonlinear dynamic response of sandwich panels to blast loading, *Composites B, Special Issues on Marine Composites*, Y.D.S. Rajapakse and D. Hui (eds), 35(6-8):795-803, 2004.
- [8] L. Librescu, T. Hause and C. J. Camarda. Geometrically nonlinear theory of initially imperfect sandwich plates and shells incorporating non-classical effects, *AIAA Journal*, 35(8):1392-1403, 1997.
- [9] L. Librescu and T. Hause. Recent development in the modeling and behavior of advanced sandwich constructions: A survey, *Journal of Composite Structures*, 48(1-3):1-17, 2000.

# ENHANCEMENT OF BLAST RESISTANCE OF SANDWICH PLATES

George J. Dvorak and Yehia A. Bahei-El-Din

*Department of Mechanical, Aerospace and Nuclear Engineering,  
Rensselaer Polytechnic Institute, Troy, NY 12180-3590, U.S.A.*

**Abstract** This research examines the effect of design modifications on response of sandwich plates to impulse pressure loads. The objective is to limit damage by delamination of the laminated face sheets and by crushing of the structural foam core that dominates response of conventionally designed sandwich plates. This is achieved by introducing structural elements that store the incident energy and thus reduce damage-related energy dissipation. In particular, ductile interlayers inserted between the outer face sheet and the foam core, can absorb a significant part of the incident energy, and protect the foam core from excessive deformation. These design concepts have been developed in our earlier work on the effect of low and medium velocity impact on sandwich plates, where they enhanced resistance to local deflections of the face sheet, foam crushing and interface delaminations.

**Keywords:** sandwich plates, blast, dynamic finite element analysis.

## 1. INTRODUCTION

One standard Design (1) and three modified sandwich plate Designs (2)-(4) have been analyzed and evaluated under blast load. The modified designs included thin, ductile interlayers, which separate the outer face sheet and the foam core. The interlayers were selected as the relatively stiff Isoplast 101 polyurethane manufactured by Dow Plastics, and a fairly compliant elastomeric foam. Two of the new Designs (2) & (3) had a single interlayer inserted between the outer face sheets and the foam core. Most successful was Design (4), where the polyurethane interlayer was combined with another interlayer made of the elastomeric foam. In this combination, the

stiff polyurethane layer offers good support to the outer face sheet, while the easily compressible elastomeric foam layer protects the inner foam core from damaging contact with the outer face sheet or the polyurethane interlayer. In comparison with the conventional design, Design (4) shows significant reduction in the peak kinetic energy, face sheet deflection and core crushing.

Explicit dynamic finite element solutions were developed with the LS-Dyna software. Contact algorithms were invoked to model intermittent separation and rejoining of the face sheets and the inner core following delamination. Both impulse and explosive pressure loads were applied to the outer facesheet of a section of a continuously supported plate.

The results show almost instant facesheet delamination and permanent crushing of the foam core in all designs. However, the pair of polyurethane and elastomeric foam interlayers reduced the peak kinetic energy and core compression by approximately 50%. The longitudinal strain in the outer facesheet was also reduced in the new sandwich design to magnitudes which fall below the ultimate tensile limit. The deformation mechanisms leading to this enhanced performance under blast loads are mainly the hyperelastic behavior of the polyurethane rubber and the collapse of the low density elastomeric polyethylene foam. Both these effects reduced the amplitude and velocity of the incident compression wave and protected the foam core. As a result, the core compression was both delayed and reduced, and this led to a significant reduction in the plate deflection at mid-span and in curvature at the supports.

## 2. GEOMETRY, MATERIAL PROPERTIES, LOADS

A sandwich panel, continuously supported by equally spaced rigid stiffeners is considered, with the dimensions indicated in Figs. 1 & 2. The total width, measured in the  $X_2$ -direction of Figure 1 is assumed to be sufficiently large, so that the plate can be analyzed in plane strain, with displacements  $u_2 = 0$  everywhere. The four structural arrangements of the plate examined in this study are shown in Figure 2. In the standard Design (1), the laminated composite facesheets are bonded to a structural foam core, to form a symmetric sandwich cross-section. Modifications of the standard design were motivated by results of our past studies, of the effect of low and medium velocity impact on stress distribution and damage evolution in such laminates (Dvorak and Suvorov 2005, Suvorov and Dvorak 2005a,b). These studies examined Designs (2) and (3), modified by replacing a part of the foam core by a ductile interlayer, inserted between the loaded or outer face sheet and the remaining part of the foam core. In particular, a relatively stiff polyurethane (PUR) interlayer was used in Design (2); this interlayer

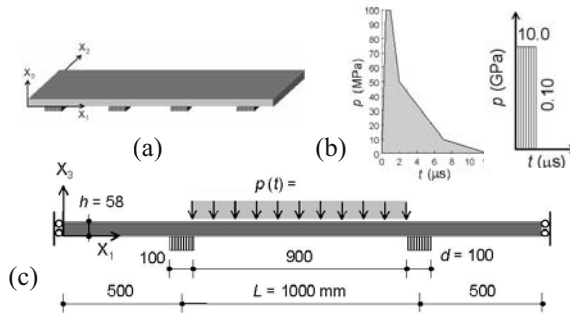


Figure 1. Geometry and loading of a continuous sandwich plate.

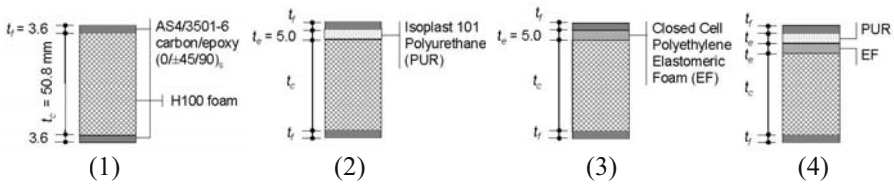


Figure 2. Cross sections of standard and modified designs of sandwich plates.

improves the support of the outer facesheet and does not elevate overall deflection under applied uniform pressure. Design (3) employs a fairly compliant elastomeric foam (EF) interlayer, which offers better protection of the foam core, albeit at the expense of higher local and overall deflections. Design (4) utilizes both PUR and EF interlayers, each 5.0 mm thick, in an effort to combine the described benefits.

The facesheets are made of a AS4/3501-6 carbon/epoxy fibrous composite laminate, and each consists of eight plies arranged in a quasi-isotropic  $(0/\pm 45/90)_s$  symmetric layup. They are assumed to remain linearly elastic during the loading cycle and are modeled as homogeneous orthotropic material layers, using *LS-Dyna Material Type 2*.

The polyurethane (PUR) interlayer was selected as Isoplast 101 manufactured by Dow Plastics. It was modeled as an isotropic, nearly incompressible, hyperelastic rubber material, using the formulation of Blatz and Ko (1962). The stress-strain response of polyurethane under uniaxial tension is shown in Figure 3. In the finite element analysis, the PUR interlayer was represented by *LS-Dyna Material Type 7*.

The elastomeric (EF) foam is a low density, closed-cell polyethylene. The stress-strain response under uniaxial compression is shown in Figure 3. *LS-Dyna Material Type 63* represented the elastomeric foam interlayer.

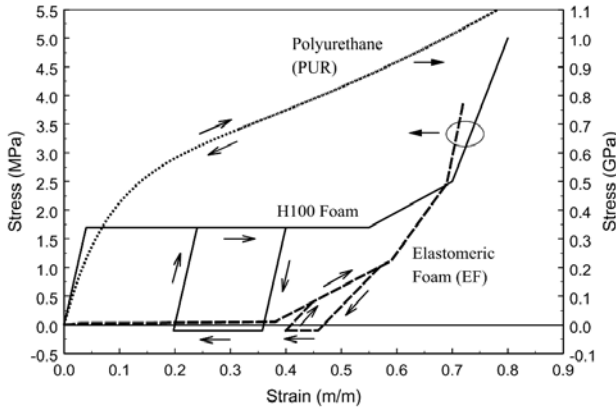


Figure 3. Comparison of stress-strain behavior of elastomeric foam and H100 closed cell foam under compression, and of polyurethane under uniaxial load.

The structural foam core material is H100 Divinycell, an isotropic, closed cell foam. Under uniaxial compression, it deforms as shown Figure 3 (Fleck 2004). In the finite element calculations, the foam was also modeled by LS-Dyna Material Type 63.

Specific material properties of the face sheet laminates, interlayers and foam core are listed in Table 1.

Selection of adhesives and their properties are beyond the present scope, hence the interfaces are assumed to be well bonded. Delamination cracks are expected to occur in the Divinycell structural foam, along a path adjacent to its interface with either one of the face sheets or interlayers. To this end, the foam core was subdivided such that a thin layer of elements was present at such interfaces. The delamination of the foam core from either the laminated face sheets or PUR or EF interlayers is modeled by removing from the mesh the thin foam interface elements, using the material erosion capability of LS-Dyna. Maximum strain failure criteria are utilized to initiate failure of the foam interface elements and their elimination from the mesh when ultimate strains of the H100 foam (Table 1) are exceeded.

Blast loads were idealized by a uniform pressure impulse  $p(t) = p_0 \delta(t)$  as shown in Figure 1b.

### 3. FINITE ELEMENT MODELS

Response of the four sandwich plate designs to blast loading was examined using the LS-Dyna software (LSTC 2003). It performs a Lagrangian dynamic analysis using an explicit, central difference integration scheme. The solution domain is selected as a 'unit cell' consisting of a single span that extends over the support on either side, to the middle of the next

span, as shown in Figure 1c. Under a uniform load applied as shown in Figure 1c, the plate deformations are symmetric with respect to the  $X_2X_3$ -plane located at the center of the middle span. In this case, the solution domain was reduced from that shown in Figure 1c to one which contains half of the loaded span, and half of the adjacent span, Figure 4. The pressure impulse of Figure 1b was applied as a uniform stress, perpendicular to the exterior surfaces of the outer laminated facesheet elements.

The inserts in Figure 4 show details of the mesh for the four Designs (1-4).

Table 1. Elastic properties and dimensions of sandwich plate constituents.

Property (units)	(0/±45/90) <sub>s</sub> AS4/3501-6 Carbon/epoxy	H100 Divinycell foam	Isoplast 101 Polyurethane Foam (PUR)	Elastomeric Foam (EF)	
Material type	Orthotropic, elastic	Isotropic, crushable	Isotropic, hyperelastic	Isotropic, crushable	
LS-Dyna material #	2	63	7	63	
$E_1 = E_2$ (MPa)	55022.0	111.0	1500.0	10.0	
$E_3$ (MPa)	10792.0				
$G_{12}$ (MPa)	21319.0	50.45	513.0	5.0	
$G_{13} = G_{23}$ (MPa)	4953.0				
$\nu_{12}$	0.29	0.1	0.463	0.0	
$\nu_{13} = \nu_{23}$	0.248				
$\rho$ (kg/m <sup>3</sup> )	1580	100	1200	148	
Compressive yield strength (MPa)	-	1.7	-	0.0264	
Tensile strength (MPa)	-	0.3	-	0.1	
Maximum tensile strain (%)	-	0.28	-	-	
Maximum shear strain (%)	-	3.5	-	-	
Thickness (mm)	Design (1)	3.6	50.8	-	-
	Design (2)		45.8	5.0	-
	Design (3)		45.8	-	5.0
	Design (4)		40.8	5.0	5.0

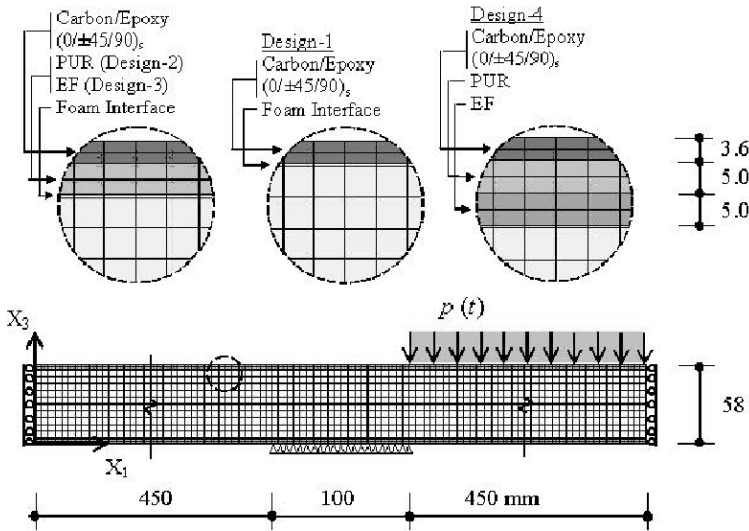


Figure 4. Finite element solution domain and mesh.

Surface to surface contact conditions were introduced to prevent the face sheet and core parts from interpenetrating each other upon erosion of the thin foam surface layers. Finally, to prevent element deformations into negative volumes, particularly in the crushable H100 foam elements, LS-Dyna's interior contact capability was activated.

#### 4. RESPONSE TO A FULL-SPAN PRESSURE IMPULSE

When the pressure impulse of Figure 1b is applied to the entire middle span of the sandwich plate, Figure 1c, each of the four designs of Figure 2 undergoes a particular deformation history, which determines the distribution of the kinetic and strain energy absorbed by the different layers of the sandwich structure.

The extent of delamination and compression of the foam core, and the overall deformation of the standard sandwich plate Design (1) and the enhanced Design (4) is illustrated in Figure 5 at  $t = 0.1, 0.2$  ms, which are well beyond the transient response loading period. The foam core undergoes large compressive or crushing deformation in the top half of the core layer, resulting in substantial reduction of the core thickness. Under the uniformly applied pressure, the foam compression is largest in center of the span, and then decreases in sections that are located closer to supports. During loading,

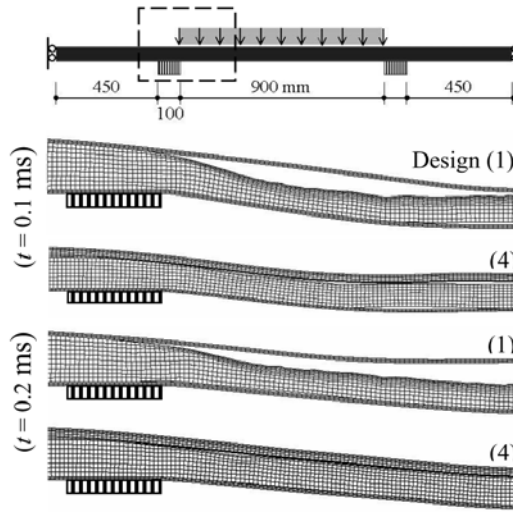


Figure 5. Deformed geometry of a sandwich plate with a standard Design (1) and modified Design (4).

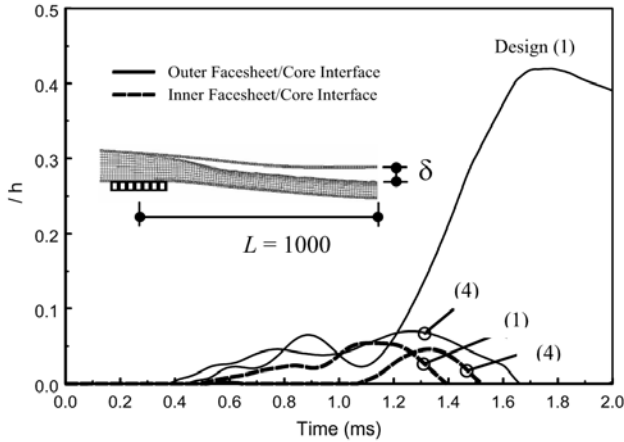


Figure 6. Comparison of facesheet/core interface opening displacement of a sandwich plate with a standard Design (1) and modified Design (4).

large displacement gradients are present in both the outer and inner facesheets. In the outer facesheet, these are associated with the significant deflections of its surface under the applied pressure. On the other hand, the displacement gradient in the inner facesheet is caused by the deflection constraints imposed by the supports.

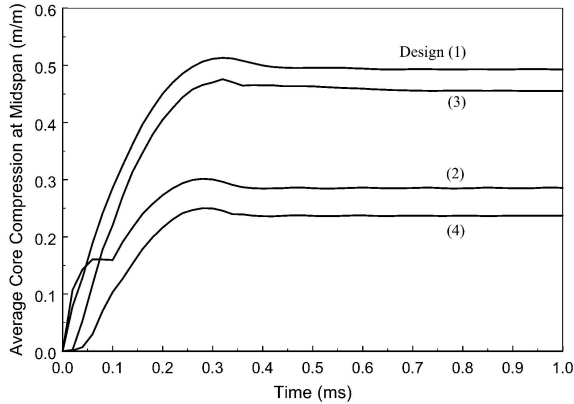


Figure 7. Comparison of average core compression of a sandwich plate with a standard Design (1) and modified Designs (2-4).

Delamination of both outer and inner facesheets from the core was detected, in the form of displacement jumps in both normal and tangential directions to the initially bonded interface. The latter, sliding separation mode is marked by the misalignment of the finite element mesh at certain closed parts of the facesheet/core interface, as seen in Figure 5. Both normal and sliding modes may materialize and interact at a particular interface point during the response time period. An illustration of the evolution of facesheet delamination in the standard Design (1), and the modified Design (4) of Figure 2, is shown in Figure 6 where the normal displacement jump across the facesheet/core interface is plotted as a function of time for the mid-span plate section. The results show a rapid growth of the opening displacement at the debonded outer interface for the standard Design (1). The peak displacement was reduced by a factor of 5.0 in the modified Design (4). Facesheet delamination also occurs at the inner interface with similar opening displacement histories for Designs (1,4).

Averaged core compression at midspan, computed as the ratio  $\Delta t_c / t_c$ , where  $t_c$  is thickness of the foam core and  $\Delta t_c$  is the change in its magnitude, is plotted in Figure 7 as a function of time. Both fully bonded and gradually debonding face sheets are considered. A steady state is reached within about 0.2 ms, after a rapid rise to average strains of 0.3-0.5. However, much larger local compressive or crushing strains are present in the foam core. The stiff PUR interlayer found in Design (2) appears to absorb the induced shockwave, and thus better protect the inner foam core from crushing, which is reduced to about 60% of that in Design (1). On the other hand, the compressible elastomeric foam (EF) interlayer found in Design (3) does not offer a significant improvement in protecting core crushing over the standard sandwich design. However, utilizing a pair of

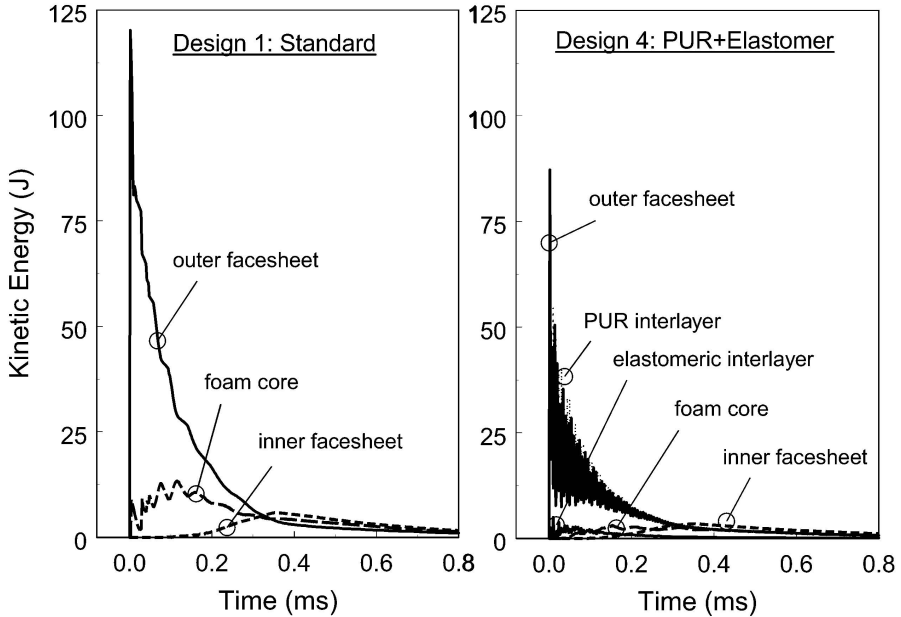


Figure 8. Comparison of kinetic energy distribution in standard Design (1) and Design (4) with polyurethane and elastomeric foam interlayers.

PUR and EF interlayers in Design (4) provides the best protection for the foam core. In this case, the average compressive strain in the core thickness is reduced to about 50% of that in Design (1), Figure 7.

The total energy imparted by the applied pressure impulse is converted, in part, in the strain energy stored in the elastic materials parts of the structure, the energy dissipated by structural and EF foam crushing and face sheet delamination, and the kinetic energy of the moving parts of the sandwich structure. The elastic strain energy is stored primarily in the outer face sheet, and its amount is not much affected by the underlying materials. It is also stored in the PUR and EF interlayers. The inner face sheet stores a relatively small amount. Distribution of the kinetic energy among the structural components of each of the four designs is presented in Figure 8. A comparison of Designs (1) and (4) shows that the kinetic energy of the latter is reduced by about 40%.

## 5. DISCUSSION AND CONCLUSIONS

The work presented has demonstrated the role of the interlayers in enhancing structural performance of sandwich plates under blast loads.

Compared to conventional sandwich plate designs, the benefits gained from the modified designs can be enumerated as follows:

1. The imparted kinetic energy is reduced by almost a factor of two.
2. Energy absorption is increased due to protection of the foam core.
3. Compression of the crushable core is reduced by more than 50%.
4. Opening displacement at debonded facesheet/core interfaces is reduced by a factor of five.
5. Longitudinal strain in the facesheets is reduced by more than 50%.
6. Plate deflection is reduced by 15%.
7. Curvature of the inner facesheet at the supports is substantially lowered.

The results suggest that even better enhancement of blast and impact resistance of sandwich plates could be achieved by more extensive or total replacement of the crushable foam core. A polyurethane core, or one made of a similar material capable of large elastic deformations at high strain rates appear to be suitable candidates. Delaminations could be reduced if the new core would serve as a matrix in the facesheets. For example, Kevlar fiber layers could be inserted in the surface layers of both inner and outer faces of the core, and even inside the core to support high tensile stresses, using advanced fiber architectures and available tire making technology.

## **ACKNOWLEDGEMENT**

The authors gratefully acknowledge the support provided by the Office of Naval Research. Dr. Yapa D.S. Rajapakse served as program monitor.

## **REFERENCES**

- Blatz, P.J. and Ko W.L., 1962, "Application of finite element theory to the deformation of rubbery materials," *Transactions of the Society of Rheology*, Vol. 6, 1962, pp. 223-251.
- Dvorak, G.J. and Suvorov, A.P., 2005, "Protection of sandwich plates from low-velocity impact," *Journal of Composite Materials*, to appear.
- Fleck N.A., 2004, "Collapse mechanisms of sandwich beams with composite faces and foam core, loaded in three-point bending. Part II: experimental investigation and numerical modeling," *International Journal of Mechanical Sciences*, Vol. 46, pp. 585-608.
- LSTC, 2003, LS-Dyna 970, Livermore Software Technology Corporation, Livermore, CA 94550.
- Suvorov, A.P. and Dvorak, G.J., 2005a, "Enhancement of low-velocity impact resistance of sandwich plates," *International Journal of Solids and Structures*, Vol. 42, pp. 2323-2344.
- Suvorov, A.P. and Dvorak, G.J., 2005b, "Dynamic response of sandwich plates to medium-velocity impact," *Journal of Sandwich Structures and Materials*, to appear.

# A TWO-PROPERTY YIELD, FAILURE (FRACTURE) CRITERION FOR ISOTROPIC MATRIX MATERIALS

Richard M. Christensen

*Lawrence Livermore National Laboratory, Livermore, CA 94550; and  
Stanford University, Stanford, CA 94305, USA*

**Abstract** A yield/failure criterion is coordinated with a separate fracture criterion to provide a comprehensive three dimensional description of failure for isotropic materials. Two properties provide the entire calibration for the two criteria.

**Keywords:** yield, fracture, failure criterion.

For three dimensionally isotropic materials, take a polynomial expansion for any scalar, physical quantity of interest in terms of stress,  $\sigma_{ij}$ , one specific form, given most compactly in tensor notation, is

$$L = \Delta\sigma_{ii} + \zeta\sigma_{ii}^2 + \eta s_{ij}s_{ij}, \quad (1)$$

where  $\Delta$ ,  $\zeta$ , and  $\eta$  are the specifiable parameters,  $\sigma_{ii}$  is the dilatational stress and the deviatoric (shear) stress is given by

$$s_{ij} = \sigma_{ij} - \frac{\delta_{ij}}{3}\sigma_{kk}. \quad (2)$$

The expansion (1) is one of several different but equivalent forms of the most general polynomial expansion of second degree for an isotropic representation in terms of stress. Form (1) with  $\Delta = 0$  is widely used as a representation for the elastic energy.

It is now hypothesized that the fundamental stress state descriptors used for characterizing the elastic energy are also likely to be the best stress state descriptors that could be used for characterizing the limit of the elastic energy range, beyond which irreversible deformation and damage occurs. In fact, it would appear that the method to be followed here is one of the few internally consistent approaches for a general treatment of both the elastic energy representation and the limiting range of the elastic energy representation (failure).

This method should not be confused with simply using the elastic energy itself as the failure criterion, rather, the same source for each is being used.

Following the procedure just specified, take the polynomial expansion (1) as also controlling the failure form in terms of stress. Impose the physical assumption that the homogeneous material does not fail under a state of hydrostatic pressure, although it could fail under hydrostatic tension. The plausibility of this condition goes back at least as far as to Kelvin. This assumption or condition requires that the  $\zeta$  parameter in (1) be taken as vanishing. The resulting failure criterion directly from (1) is shown by Christensen [1] to take the form

$$\alpha \left( \frac{\sigma_{ij}}{\kappa} \right) + \frac{3}{2}(1 + \alpha) \left( \frac{s_{ij}}{\kappa} \right) \left( \frac{s_{ij}}{\kappa} \right) \leq 1, \quad (3)$$

where the two failure parameters  $\alpha$  and  $\kappa$  are given by

$$\kappa = |\sigma_{11}^C| \quad \text{and} \quad \alpha = \frac{|\sigma_{11}^C|}{\sigma_{11}^T} - 1 \quad (4)$$

for the class of homogeneous materials for which  $\alpha \geq 0$ . In (3) and (4)  $\sigma_{11}^T$  and  $\sigma_{11}^C$  are the uniaxial stress state yield or failure values in tension and compression. Parameter  $\alpha$  is of nondimensional form and it is shown to cover the range from very ductile behavior at  $\alpha = 0$  to very brittle behavior as  $\alpha \rightarrow \infty$ .

A basic premise of fracture behavior would be that no component of normal stress could be larger than  $\sigma_{11}^T$ , for the range of brittle materials. This premise will now be implemented as the fracture restriction that must be included as part of the overall failure criterion. The brittle range of behavior is shown to be  $\alpha > 1$ . The fracture restriction is accordingly given by

$$\sigma_1 \leq \sigma_{11}^T \quad \text{if} \quad \alpha > 1, \quad (5)$$

where  $\sigma_1$  is the largest principal stress.

It is important to recognize that this fracture restriction, along with (3) does not impose any new failure parameters. It is simply a statement of the basic nature of fracture intervention from the competing fracture mode under certain stress states for brittle materials. The fracture restriction is considered to be basic to the present failure theory, which still remains at the two-parameter level. The effect of the fracture restriction (5) is to provide a ‘‘fracture cutoff’’ for the forms from (3) in certain subspaces of stress for materials in the brittle range of behavior (but not in the ductile range).

Pae [2] has produced general yield properties data for the polypropylene type of material (polymer). In addition to standard testing at atmospheric pressure, tests were conducted at states of elevated pressure. Yield properties  $\sigma_{11}^T$  and  $\sigma_{11}^C$  were used to calibrate the present yield/failure theory form. The calibrated theories were used to predict the yield behavior of the material at a level

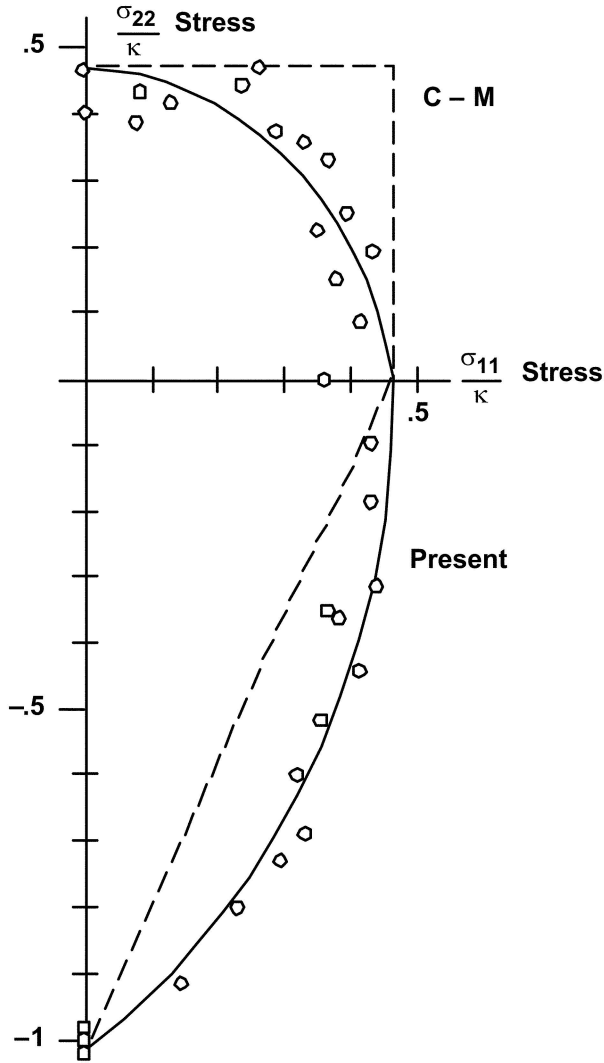


Figure 1. “Innoculated” iron yield/failure, Cornet and Grassi [3].

of 1 kbar superimposed pressure. The present theory predicted the measured values with a 7% error while the Coulomb–Mohr method had a 24% error. An example of a fairly brittle material is shown in Figure 1 for a type of cast iron. Again, the Coulomb–Mohr form is seen not to fit the data as well as the present approach.

## **ACKNOWLEDGMENT**

This work was performed under the auspices of the U.S. Department of Energy by the University of California, Lawrence Livermore National Laboratory under Contract No. W-7405-Eng-48. The author would like to acknowledge ONR contract support, Dr. Y.D.S. Rajapakse, Program Director.

## **REFERENCES**

- [1] Christensen, R.M., 2004, "A Two-Property Yield, Failure (Fracture) Criterion for Homogeneous, Isotropic Materials", *J. Engr. Mats. and Technology*, **126**:45–52.
- [2] Pae, K.D., 1977, "The Macroscopic Yielding Behavior of Polymers in Multiaxial Stress Fields", *J. Mater. Sci.*, **12**:1209–1214.
- [3] Cornet, I., and Grassi, R.C., 1955, "Fracture of Inoculated Iron Under Biaxial Stress", *ASME J. Appl. Mech.* **22**:172–174.

# ON CRACK EXTENSION IN FOAM CORED SANDWICH FRACTURE SPECIMENS

R.C. Matteson<sup>1</sup>, L.A. Carlsson<sup>2</sup>, F. Aviles<sup>2</sup> and D.C. Loup<sup>1</sup>

<sup>1</sup>*Marine Composites Branch, NSWC, Carderock Division, West Bethesda, MD 20817, USA*

<sup>2</sup>*Department of Mechanical Engineering, Florida Atlantic University, Boca Raton, FL 33431, USA*

**Abstract** The crack propagation path in foam cored sandwich DCB specimen is analyzed using laminated beam analysis. The analysis determines whether the crack would propagate self-similarly or kink upwards or downwards, and the steady state position of the crack. Kink direction and crack propagation path predictions are in agreement with experimental observations. Fracture toughness data related to the various propagation paths is presented. The resistance curves recorded for various initial crack positions indicate some mixed mode influence on the toughness, with a minimum toughness in the range of 500–600 J/m<sup>2</sup> corresponding to pure mode I.

**Keywords:** crack extension, DCB, sandwich.

## 1. INTRODUCTION

Understanding crack propagation in sandwich structures is crucial to the safe design of Naval structures. The double cantilever beam (DCB) and tilted sandwich debond (TSD) specimens have been used to determine face/core debond fracture toughness of sandwich specimens [1–6]. Shivakumar and Smith [4] recognized that the DCB sandwich specimen may be used also for in-situ fracture toughness determination of the foam core. Self-similar crack growth is desirable in fracture testing. A face/core crack should propagate at the interface, and a core crack should remain so in order to justify application of fracture mechanics principles for evaluation of the fracture toughness. Commonly, however, “crack kinking” is observed in DCB fracture testing of foam cored sandwich specimens [2], where the crack deflects in a direction different from the initial plane of the crack.

In this study we will present a simple laminated beam model for analysis of the crack propagation path in foam cored DCB sandwich specimens. The results will be compared to experiments on symmetric and unsymmetric DCB

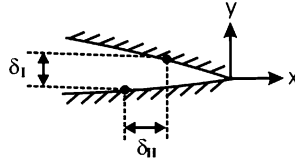


Figure 1. Opening and tangential displacements of the crack faces corresponding to mode I and mode II crack tip loading.

sandwich specimens with PVC foam core. Fracture toughness data will be presented in the form of R-curves for the various propagation paths.

## 2. CONDITIONS FOR CRACK KINKING

Cracks in homogeneous isotropic materials tend to propagate in planes free from shear stresses, i.e., in pure mode I, regardless of the initial orientation of the crack [7, 8]. Figure 1 illustrates the opening ( $\delta_I$ ) and tangential displacement ( $\delta_{II}$ ) discontinuities of a point located on the crack flanks before the geometry was loaded. The displacements shown in Figure 1 are consistent with positive values of the stress intensity factors  $K_I$  and  $K_{II}$ , i.e., tension and positive shear on stress elements at the crack tip.

The direction of kinking,  $\Omega$ , is governed by the sign of the shear stress ahead of the crack tip. If the shear stress is positive, the kink angle,  $\Omega$ , will be positive as defined for a DCB sandwich specimen in Figure 2a. This is a consequence of the orientation of the major principal stress plane in a core element ahead of the crack tip. Conversely, a negative shear stress would cause the crack to kink upwards,  $\Omega < 0$  in Figure 2b.

## 3. CRACK KINKING ANALYSIS

Analysis of crack kinking is based on the stress intensity factors “near the crack tip”. Near crack tip indicates that the distance to the tip,  $r$ , is within the singular zone of dominance where the first-order expressions for displacements, strains and stresses scale with the classical square-root singularity [9]. If the influence of the singular strain field in the small domain near the crack tip is neglected, it is possible to calculate the relative sliding displacement,  $\delta_{II}$  (Figure 1), of two initially coincident points on the crack flanks of the DCB specimen at a distance,  $r$ , from the crack tip as

$$\delta_{II} = r(\varepsilon_x^L - \varepsilon_x^U), \quad (1)$$

where  $\varepsilon_x^L$  and  $\varepsilon_x^U$  are the bending strains in the crack flanks in the lower (L) and upper (U) legs near the tip of the crack. According to this analysis, kinking would be promoted by a strain mismatch between the lower and upper legs of

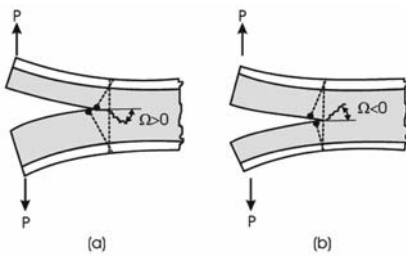


Figure 2. Illustration of crack displacements in a symmetric DCB sandwich specimen for two unsymmetric crack locations. (a) Kinking down, (b) kinking up.

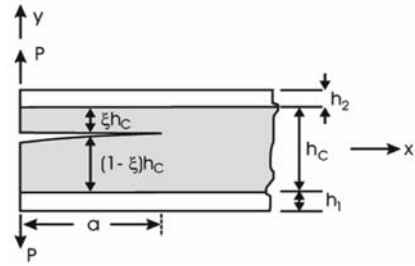


Figure 3. Generic sandwich DCB configuration. The parameter  $\xi$  ( $0 < \xi < 1$ ) represents the location of the initial core crack.

the DCB sandwich specimen. A positive difference would promote kinking downwards, and negative difference kinking upwards as shown in Figure 2. Zero difference would promote self-similar growth.

To quantify the strain mismatch, the generic DCB sandwich configuration shown in Figure 3 is considered.

The crack is located at a distance  $(1 - \xi)h_c$  from the lower face/core (F/C) interface, and a distance  $\xi h_c$  from the upper F/C interface, where  $h_c$  is the core thickness and the parameter  $\xi$  is bounded by  $0 \leq \xi \leq 1$ . Consequently,  $\xi = 0$  corresponds to a crack at the upper F/C interface, and  $\xi = 1$  represents a crack at the lower F/C interface. The face sheets may be of different materials and thicknesses ( $h_1$  and  $h_2$ ). We will here assume that each sub-beam (leg) consists of a homogeneous orthotropic face sheet bonded to an isotropic core. A detailed beam analysis for determining the near tip strains in the lower (L) and upper (U) legs of the DCB specimen, Figure 3, is presented in a previous related publication by the authors [10].

We will demonstrate the crack kinking analysis on some typical DCB sandwich specimens consisting of glass/vinylester (G/VE) and carbon/vinylester (C/VE) face sheets over a H100 PVC foam core. The G/VE and C/VE face sheets had a Young’s moduli ( $E$ ) of 27.6 and 82.7 GPa, respectively [10], while the H100 foam core had  $E = 105$  MPa [11]. Symmetric and unsymmetric DCB sandwich specimens were considered as specified in Table 1.

Figure 4 shows crack tip strains in the upper and lower legs of I45, I41, I43 and T1 DCB specimens (Table 1) plotted against the crack location parameter,  $\xi$ , defined in Figure 3.

Consider first the strain results in Figure 4a for the symmetric I45 specimen with quite thick and stiff C/VE face sheets (Table 1). For a crack at the top interface,  $\xi = 0$ , there is a very large strain mismatch. The strain in the lower leg is much larger than in the upper leg, which would indicate kinking down-

Table 1. DCB specimens examined.

Spec. ID	Faces					Crack location d, mm	$\xi$
	Bottom		Top		Core		
	Mater.	$h_1$ , mm	Mater.	$h_2$ , mm			
I30	G/VE	4.04	G/VE	4.04	14.2	7.6	0.54
I40	G/VE	2.43	G/VE	2.43	15.6	0.7	0.04
I41	G/VE	2.41	G/VE	2.41	17.6	8.12	0.46
I43	C/VE	3.89	G/VE	2.37	17.2	8.9	0.52
I45	C/VE	3.95	C/VE	3.95	17.6	1.2	0.07
I50	C/VE	3.98	G/VE	2.41	17.3	16.9	0.98
T1	G/VE	2.41	G/VE	2.41	37.9	0.8	0.02

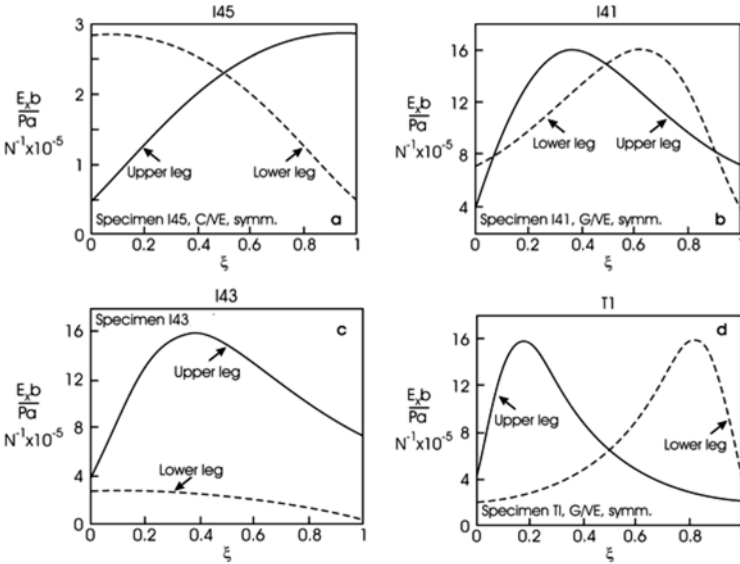


Figure 4. Crack tip strains in the upper and lower legs of DCB sandwich specimens. (a) I45, (b) I41, (c) I43, (d) T1 (Table 1).

wards, Figure 2a, until the crack reaches a stable position at the center of the core ( $\xi = 0.5$ ) where the strains match. With the same reasoning, a crack at the lower F/C interface ( $\xi = 1$ ) would kink up and propagate towards the center of the core. An initial crack placed at the center of the core ( $\xi = 0.5$ ), however, would not kink, and continue to propagate along the center of the core.

Figure 4b shows the strains for the specimen with thin G/VE faces, I41. Because the faces are thin and made from glass fibers they are less stiff in flexure

and the core will influence the flexural rigidity of the legs of the specimen. It is noted that the strains are equal at three locations,  $\xi = 0.08, 0.5$  and  $0.92$ . The location,  $\xi = 0.5$ , is obvious since the specimen is symmetric, while the near interface locations ( $\xi = 0.08$  and  $0.92$ ) are less obvious. According to this analysis, a crack located at the top interface ( $\xi = 0$ ), would kink down until it reaches an equilibrium location where the strains are equal ( $\xi = 0.08$ ). This is a stable location since for any small perturbation the crack would tend to return to this location. Similarly, a crack at the lower F/C interface would kink up until a stable position is reached at  $\xi = 0.92$ . The actual distance from the interface is only 1.4 mm for this specimen, and the crack propagating at this location would be considered as “near interface”. A crack positioned in the upper half region of the core between  $\xi = 0.08$  and  $0.5$  would kink up (Figure 2b) towards the  $\xi = 0.08$  location, and a center crack ( $\xi = 0.5$ ) would potentially remain at the center, but would not be stable, since any small disturbance would promote kinking up or down towards the  $\xi = 0.08$  or  $0.92$  locations.

For the highly unsymmetric specimen (I43 in Table 1) with a thick C/VE face on the bottom and a thin G/VE face on the top the results shown in Figure 4c indicate that a crack at the top F/C interface ( $\xi = 0$ ) would remain there, and that a crack at any other location would kink up towards the top F/C interface.

The results for the symmetric specimen with thin G/VE faces and a thick core, T1, shown in Figure 4d, indicate that a F/C crack at the upper (or lower) interface,  $\xi = 0$  (or  $1$ ) would remain interfacial, and that a center crack would be unstable, and any disturbance would cause the crack to veer away from the center towards one of the interfaces. Notice in Table 1, that the only difference between specimens I41 and T1 is the core thickness.

#### 4. EXPERIMENTAL

Sandwich panels consisting of E-glass/vinylester (G/VE) and carbon/vinylester (C/VE) face sheets over a H100 PVC foam core were manufactured at the NAVSEA Carderock Division using the vacuum assisted resin transfer molding (VARTM) process with a single infusion. The panels were injected and cured at room temperature, which should minimize residual stresses. DCB specimens of nominal planar dimensions 25.4 mm (width) by 152 mm (length) were machined from the cured panels, and hinges for load application were attached using epoxy adhesive and mechanical fasteners (4 mm screws) drilled and tapped into the face sheets. The specimens were precracked using a table saw with a 1 mm wide blade, followed by a razor blade for the final  $\sim 2$  mm crack length.

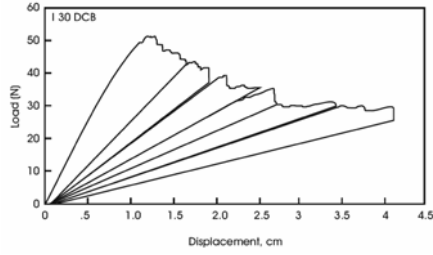


Figure 5. Load-displacement record for I30 DCB sandwich specimen.

The specimens (Table 1) were mounted in wedge grips in an Instron test frame and loaded using a crosshead speed of 2.5 mm/min while the crack tip region was monitored using an  $8\times$  magnification traveling microscope. The specimens were loaded until the crack propagated in a stable or unstable manner. After the crack propagated a certain distance (about 5 mm), the specimen was unloaded and loaded again to obtain multiple compliance and critical load data. A typical load-displacement record for the symmetric I30 specimen is shown in Figure 5.

Debond fracture toughness expressed as critical strain energy release rate,  $G_c$ , may be reduced from the experimental load-displacement records using several method, see the investigation by Shivakumar et al. [5]. These authors applied several methods developed for composite DCB specimens in the ASTM Standard D5528-01 [13]. Since the basis for these methods is the experimental compliance calibration method [9], they may also apply for the sandwich DCB specimen. The compliance,  $C$ , is defined as the displacement of the loading point,  $\delta$ , divided by the applied load,  $P$ ,  $C = \delta/P$ . The most accurate method to determine compliance from an experimental test is to evaluate the inverse of the slope of the load-displacement record. Shivakumar et al. [5] advocate the “modified beam theory” (MBT) method for evaluation of the fracture toughness. In this method, which we will adopt in this paper, the  $C^{1/3}$  data collected at several discrete crack lengths is plotted vs. crack length,  $a$ , and a straight line is fitted to the data using the least squares method. Generally, the line intercepts the  $a$ -axis at a negative value  $\Delta$ ,  $\Delta < 0$ , see [5,13]. Once  $\Delta$  has been established for a particular test specimen, the toughness is calculated at each crack length from

$$G_c = \frac{3P_c\delta_c}{2b(a + |\Delta|)}, \quad (2)$$

where  $b$  is the specimen width,  $|\Delta|$  is the magnitude of  $\Delta$ ,  $P_c$  is the critical load and  $\delta_c$  is the critical crack displacement ( $\delta_c = CP_c$ ). Such a procedure yields a toughness value for each crack length.

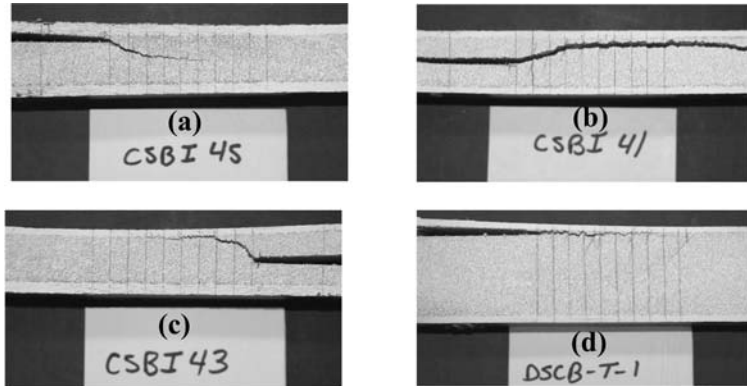


Figure 6. Experimentally observed crack propagation paths in foam cored sandwich DCB specimens. (a) I45, (b) I41, (c) I43, (d) T1.

## 5. OBSERVED CRACK PROPAGATION PATHS AND FRACTURE TOUGHNESS

The crack kinking results are summarized in Table 2. Photos for some of the tested specimens are shown in Figure 6. For a more complete display of the crack propagation paths, see [10].

Figure 6a shows the propagation path for the symmetric specimen, I45, with an initial crack near the F/C interface, kinking downwards followed by propagation in the center of the specimen. This is consistent with the results in Figure 4a. Figure 6b shows the propagation path for the symmetric flexible G/VE face sheet specimen I41. The original crack is located just above the center of the core ( $\xi = 0.46$ ). It is observed that the crack kinks upwards and then meanders at a steady-state location at a distance of about 1–3 mm from the upper F/C interface, which is consistent with the strain results for specimen I41 shown in Figure 4b. As discussed, the center crack path is not stable, and the near center initial crack in this specimen ( $\xi = 0.46$ ) should, according to Figure 4b, kink upwards and reach a position  $\xi = 0.08$ , which corresponds to a distance of 1.4 mm for this specimen. The crack path for the thin-thick unsymmetric face sheet specimen, I43, is shown in Figure 6c. The near center initial crack can be seen to kink steeply upwards to propagate near the upper F/C interface. This is consistent with the results shown in Figure 4c, where the large strain mismatch for a center crack in the unsymmetric specimen would drive the crack upwards. For the thick core specimen, T1, shown in Figure 6d, the near interface crack remains so, as expected by the results shown in Figure 4d.

Table 2. Kink direction and angles.

Specimen ID	Kink Direction		Kink Angle, $\Omega$ (deg.)
	Exp.	Beam Analysis	Exp.
I30	none	none	0
I40	down	down	9
I41	up	up	-14
I43	up	up	-60
I45	down	down	22
I50	up	up	-78
T1	none	none	0

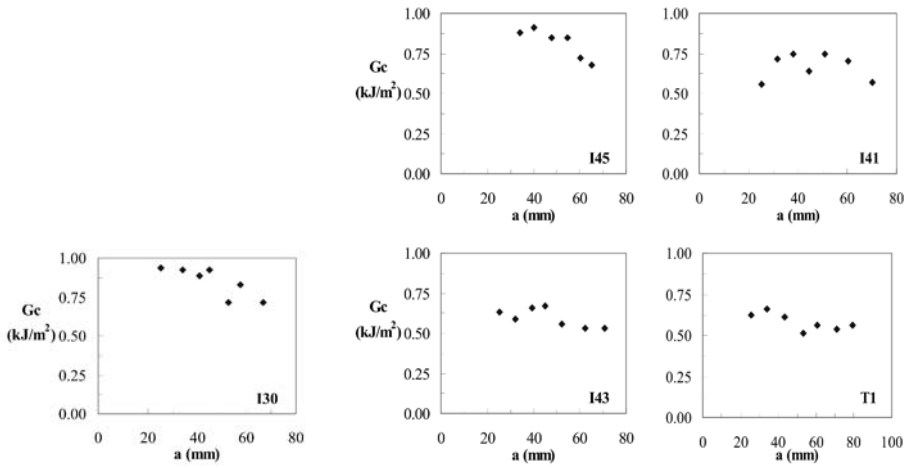


Figure 7. Resistance curve for I30 DCB sandwich specimen.

Figure 8. Resistance curves for DCB sandwich specimens. (a) I45, (b) I41, (c) I43, (d) T1.

The summary of all results in this investigation is shown in Table 2. The kinking predictions from the beam analysis (up or down) agree with experiments without exceptions.

Figure 7 shows fracture toughness data for the I30 specimen determined at various crack lengths (R-curve).

It was observed that the near center initial crack in this specimen propagated in the center of the core, consistent with beam analysis predictions. As discussed above, thick and stiff faces promote stable growth in the center of the core. The toughness is about 900 J/m<sup>2</sup> for the first 20 mm of crack propagation and decreases to values of about 750 J/m<sup>2</sup> at longer crack lengths. It should be pointed out that the initial crack is off-centered ( $\xi = 0.54$ ) (Table 1) and is

subject to some amount of mixed mode loading as indicated by the strain mismatch. It is known from several other studies, see the review in [12], that shear loading tends to increase the toughness over that in pure mode I, which should prevail at longer crack lengths when the crack has reached the core center. The toughness values observed here are larger than those measured for sandwich specimens with H100 core by Shivakumar and Smith [4] ( $560 \text{ J/m}^2$ ) and Viana and Carlsson [14] ( $370 \text{ J/m}^2$ ), but those studies considered cracks growing near the interface. Moreover, it is speculated that the effect of partial, fractured foam cells and effects of resin intrusion into the open cells near the interface may contribute the reduction in fracture toughness.

Figure 8 shows R-curves for the test specimens I45, I41, I43 and T1 (Table 1), with crack propagation paths shown in Figure 6. For specimen I45, the R-curve shown in Figure 8a is very similar to that shown for specimen I30 in Figure 7. The crack starts near the interface and reaches the center of the core in this symmetric specimen after about 20 mm of crack growth, see Figure 6a. As discussed for the I30 specimen, it may be argued that the crack starts to grow in a mixed mode field that should elevate the toughness and that the toughness approaches the minimum ( $G_{Ic}$ ) at steady state.

For specimen I41 with thinner face sheets, the crack initiates from a near center position and approaches a distance of 1.4 mm from the interface as evident in Figure 6b. The toughness values scatter about a mean of about  $670 \text{ J/m}^2$ , which is quite consistent with the steady state values for specimen I45 discussed above. For the unsymmetric I43 specimen with an initial near-center crack, the crack rapidly kinked towards the upper face/core interface, see Figure 6c, and continued to propagate in the interface region. Although Figure 4c indicates some strain mismatch at  $\xi = 0$ , which is a sign of mixed mode crack loading, the difference is quite small suggesting mode I dominated growth. The corresponding average toughness is about  $530 \text{ J/m}^2$ . For the T1 specimen with a near (top) interface initial crack (Table 1), the crack continues to propagate near the face/core interface (Figure 6d) at an average  $G_c$  value of  $580 \text{ J/m}^2$ . Figure 4d indicates a small strain mismatch at  $\xi = 0$  and mode I dominated growth.

## 6. CONCLUSIONS

A laminated beam analysis has been presented for analysis of the crack path in symmetric and unsymmetric double cantilever beam (DCB) sandwich fracture specimens with crosslinked PVC foam core. The analysis is able to predict if the crack would propagate self-similarly, or if it would kink upwards or downwards, although it cannot predict the magnitude of kink angle. The beam analysis can also project the stability of crack path and equilibrium position of the crack after kinking. The beam analysis predictions agree favorably

with experimental observations on the crack propagation path. Also the equilibrium location of the crack agreed favorably with the beam analysis predictions. The resistance curves recorded for various initial crack positions indicate some mixed mode influence on the toughness, with a minimum toughness in the range of 500–600 J/m<sup>2</sup> corresponding to pure mode I.

## ACKNOWLEDGEMENTS

The participation in this project by LAC and FA was sponsored by the Office of Naval Research (ONR) (Grant # N00014-03-1-0600) with Dr. Yapa D.S. Rajapakse as the program manager. Additional support from Mr. Patrick Potter of ONR made the stay at Carderock by LAC over part of the summer of 2004 possible. We are grateful for typing assistance from Ms. Riti Waghray and graphics production by Ms. Shawn Pennell.

## REFERENCES

- [1] S. Prasad and L.A. Carlsson, "Debonding and Crack Kinking in Foam Core Sandwich Beam – I. Analysis of Fracture Specimens", *Eng. Fracture Mech.*, Vol. 47, 1994, pp. 813–824.
- [2] S. Prasad and L.A. Carlsson, "Debonding and Crack Kinking in Foam Core Sandwich Beam – II. Experimental Investigation", *Eng. Fracture Mech.*, Vol. 47, 1994, pp. 825–841.
- [3] X. Li and L.A. Carlsson, "The Tilted Sandwich Debond (TSD) Specimen for Face/Core Interface Fracture Characterization", *J. Sandwich Struct. Mater.*, Vol. 1, 1999, pp. 60–75.
- [4] K.N. Shivakumar and S.A. Smith, "In-Situ Fracture Toughness Testing of Core Materials in Sandwich Panels", *J. Compos. Mater.*, Vol. 38, 2004, pp. 655–668.
- [5] K. Shivakumar, H. Chen and S.A. Smith, "An Evaluation of Data Reduction Methods for Opening Mode Fracture Toughness of Sandwich Panels", *J. Sandwich Struct. Mater.*, Vol. 7, 2005, pp. 77–90.
- [6] X. Li and L.A. Carlsson, "Fracture Mechanics Analysis of Tilted Sandwich Debond (TSD) Specimen", *J. Compos. Mater.*, Vol. 35, 2001, pp. 2145–2168.
- [7] F. Erdogan and G.C. Sih, "On the Crack Extension in Plates under Plane Loading and Transverse Shear", *J. Basic Eng.*, Vol. 85, 1963, pp. 519–527.
- [8] M.Y. He and J.W. Hutchinson, "Kinking of a Crack out of an Interface", *J. Appl. Mech.*, Vol. 56, 1989, pp. 270–278.
- [9] H.L. Ewalds and R.J.H. Wanhill, *Fracture Mechanics*, Edward Arnold, London, 1989.
- [10] L.A. Carlsson, R.C. Matteson, F. Aviles and D.C. Loup, "Crack Path in Foam Cored DCB Sandwich Fracture Specimens", submitted to *Compos. Sci. Tech.*, 2005.
- [11] DIAB, Divinycell, "Technical Specification", Divinycell International, Laholm.
- [12] J.W. Hutchinson and Z. Suo, "Mixed Mode Cracking in Layered Materials", *Adv. Appl. Mech.*, Vol. 29, 1992, pp. 63–191.
- [13] ASTM Standard D5528-01, Standard Test Method for Mode I Interlaminar Fracture Toughness of Unidirectional Fiber-Reinforced Polymer Matrix Composites, American Society for Testing and Materials, West Conshohocken, PA, 2001.
- [14] G.M. Viana and L.A. Carlsson, "Mechanical Properties and Fracture Characteristics of Cross-Linked PVC Foams", *J. Sandwich Struct. Mater.*, Vol. 4, 2002, pp. 99–113.

# EFFECT OF GEOMETRIC CONSTRAINT ON FRACTURE TOUGHNESS OF PVC FOAM CORE SANDWICH BEAMS

Kunigal Shivakumar, Huanchun Chen and Anil Bhargava

*Center for Composite Materials Research, Department of Mechanical Engineering, North Carolina A&T State University, 1601 E. Market St., Greensboro, NC 27411, USA*

**Abstract** Purpose of this study was to understand the effect of core material thickness ( $t_c$ ) on the core deformation constraint and the associated mode I fracture toughness in Double Cantilever Sandwich Beam (DCSB) specimens. Specimens were made from woven roving glass fiber/vinyl ester composite face sheet with PVC core, whose thickness ranged from 3.18 mm to 40.6 mm. The specimens were tested in mode I loading and measured fracture initiation ( $G_{IC}$ ) and resistance ( $G_{IR}$ ) toughnesses. The  $G_{IC}$  was found to be practically same for core thicknesses from 3.18 to 40.6 mm. The  $G_{IR}$  was found to be 1.02, 0.88 and 0.91 kJ/m<sup>2</sup> for  $t_c$ 's 3.18, 6.25, and 12.7 mm. For  $t_c \geq 25.4$  mm, the crack grew by only few mm's before it deflected to face sheet. Larger  $G_{IR}$  for  $t_c = 3.18$  mm is probably due to resin densification of foam cells in the co-cure processing of panels. Three dimensional, material nonlinear finite element (FE) analysis very well simulated the test data. The  $J_{IC}$  integrals from FE analysis agreed well with  $G_{IC}$  from the test. The analysis revealed that the deformation constraint was nearly the same for all core thicknesses considered and thus resulting in nearly identical fracture toughness.

**Keywords:** sandwich beam, composite material, fracture toughness, geometric constraint, double cantilever sandwich beam.

## 1. INTRODUCTION

Foam core sandwich composite structures have been used for many years in aerospace, marine, and mass transport industries because of their extremely high specific flexural and transverse shear stiffnesses as well as acoustic damping properties. Disbond between the face sheet and the core is one of the common problems in sandwich structures. A number of studies [1–13] have been made to understand and characterize the interfacial fracture mechanics of sandwich beams. Carlsson et al. [5, 13] and Shivakumar et al. [9–12] showed through experiments that the fracture toughness of PVC core sandwich

panel increased with the core density and this toughness is much higher than the PVC core toughness [13]. Viana and Carlsson's explanation [13] through plastic zone size concept of Shivakumar and Crews [14] did not provide a clarification of why the interfacial toughness of two different core thicknesses of cracked sandwich beams were different. The present study is to explain how the core thickness could influence the material constraint and hence the measured toughness of the material.

As explained in metallic fracture, the fracture toughness of a material depends on specimen geometry and the material ductility. For a given material, the plane-strain condition offers the maximum constraint thus we get the lowest toughness. ASTM E-399 test method provides the guidelines for selection of specimen geometry and testing. In sandwich beams the stiff face sheets constrain the deformation of the flexible core in the thickness as well as in the lateral directions of the specimen. Therefore the core thickness is one of the parameters that can influence the core material toughness. This paper presents the experimental and analytical results of mode-I fracture toughness of a PVC foam core cracked sandwich beam for various core thicknesses (thick to thin). Results are used to explain the differences in toughness through a geometric constraint parameter.

## 2. PROBLEM DEFINITION

Figure 1 describes the specimen configuration, and all the geometric parameters used in this paper. Crack length is  $a$ , measured from the load point and located at the mid plane. The specimen width is  $b$ , length is  $L$ , face sheet thickness is  $t_{fs}$ , and the core thickness  $t_c$ . The loading is transverse to the crack plane causing mode-I stress state with crack front. The core material is constrained by the facesheet and this constraint could vary with core thickness. Therefore five different core thicknesses were chosen, namely, 3.18, 6.35, 12.7, 25.4, and 40.5 mm. Fracture data for  $t_c = 0$  were taken from [16]. Fracture tests were conducted and measured fracture initiation toughness ( $G_{IC}$ ) and resistance  $G_{IR}$ . Three dimensional, material nonlinear finite element analysis was conducted to simulate the fracture initiation and the associated J-integral along the crack front was calculated and compared with the measurement.

## 3. MATERIALS AND SANDWICH PANELS

The fabric material chosen for the face sheet is 6-ply Fiber Glass Industries's Rovcloth 1854 woven roving E-glass fabric with FGI's Super 317 sizing for ease of handling and fast wet out and compatibility with a number of resins including vinyl ester. The matrix system for face sheet is Dow Chemical's Derakane 510A-40 vinyl ester brominated for fire resistance property. The face sheet thickness was about 30.5 mm. Properties of face sheet [15] are

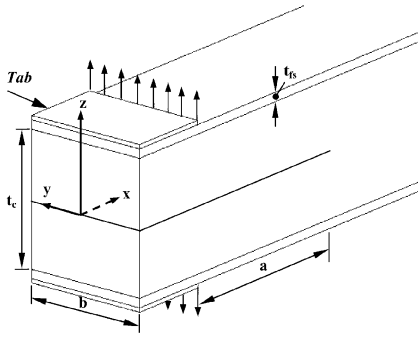


Figure 1. Specimen configuration and the coordinate system for experiment and analysis.

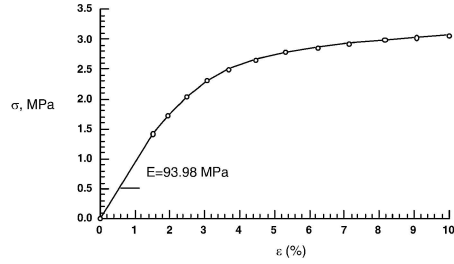


Figure 2. Multilinear stress-strain response of Divinycell H100 PVC foam.

Table 1. Mechanical properties of face sheet and core material.

Property	FGI1854/Dow 510A-40 face sheet	Divinycell H100 PVC foam
Tensile modulus $E_x$ , GPa	29.2	0.094 (measurement)
Tensile modulus $E_y$ , GPa	23.9	0.094
Poisson's ratio $\nu_{xy}$	0.16	0.32
Properties used in 3-D FE analysis		
Flexural modulus $E_x$ , GPa	24.7	
$E_y$ , GPa	23.9	
$E_z$ , GPa	5.0	
$\nu_{xy}$	0.16	
$\nu_{yz}=\nu_{zx}$	0.3	
$G_{xy}=G_{yz}=G_{zx}$ , GPa	4.50	

summarized in Table 2. The core material used was Diab Divinycell H100 PVC foam. This is a semi-rigid foam which has a closed-cell structure with a density of  $100 \text{ kg/m}^3$ . Tensile properties of H100 were measured using a dog bone test specimen used in metallic materials. The stress-strain response is shown in Figure 2. Measured tensile modulus and Poisson's ratio are listed in Table 1 and the multi linear stress-strain data is used in finite element (FE) analysis. All other data for H100 listed are taken from the manufacturer's data sheet.

Five panels of  $0.23 \text{ m}$  (9 in)  $\times$   $0.3 \text{ m}$  (12 in) were fabricated with different core thicknesses of 3.18 mm (1/8 in), 6.35 mm (1/4 in), 12.7 mm (1/2 in), 25.4 mm (1 in) and 40.6 mm (1.6 in), respectively. Vacuum Assisted Resin Transfer Molding (VARTM) [17] was used to manufacture panels. In this one-step manufacturing process, the bonding of the face sheet to the core material is performed while the face sheet being fabricated. Thus the potential for manufacturing defects like disbonds is reduced to the scale of small air bubbles.

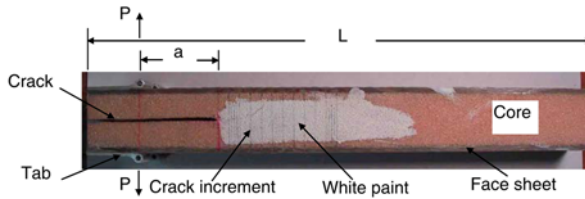


Figure 3. Configuration of DCSB specimen.

#### 4. SPECIMEN PREPARATION

Double Cantilever Sandwich Beam (DCSB) specimens were used in the fracture tests. The specimens were cut from the panels using a water-cooled tile saw with a diamond-coated blade. The nominal length and width of the specimens were 0.25 m (10 in) and 38 mm (1.5 in), respectively. After machining the specimens to their final dimensions, aluminum piano hinges were adhesively bonded to the face sheets from the end of the specimen. A delamination was cut in the middle of the core thickness using a table saw to approach the initial crack length. A surgical knife was used to reach the desired initial crack length of 38 mm (1.5 in). White paint was applied along edges of the core and marked increments were spaced at certain intervals to facilitate the tracking of the crack-tip. Figure 3 shows the configuration of the DCSB specimen.

#### 5. FRACTURE TEST

To determine the mode-I fracture toughness of the sandwich material, the fracture test as specified in ASTM standard D5528-94a [18] was used. The test was carried out in a MTS test machine using a 890N (200-lb) load cell. The piano hinge tabs of the specimen were mounted in the hydraulic grips of the load frame. The tests were conducted by displacement control loading with a cross-head rate of 0.5 mm (0.02 in)/min. Load and cross-head displacement were recorded throughout the test. A magnifying camera was mounted on a traversing stand (both vertical and horizontal) with vernier scale. The camera was connected to a TV monitor to locate and track the crack tip. Figure 4 shows the fracture test setup.

At the start of each test the crack-tip location was noted. The cross-head displacement was started and the crack -tip propagation was monitored through the camera. The specimen was loaded at a constant cross-head rate and the load and displacement values were recorded continuously. The load-displacement data was recorded when the visual onset of crack movement was observed on the edge of the specimen. The initial loading was stopped after an increment of crack growth of about 5 mm (0.2 in). The specimen was unloaded at a constant cross-head rate of up to 25 mm (1 in)/min. After unloading, the position of the



Figure 4. Test setup.

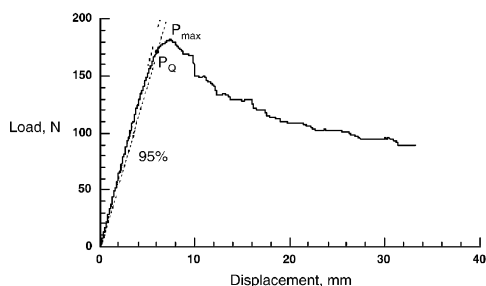


Figure 5. Load-displacement response and  $P_Q$  determination.

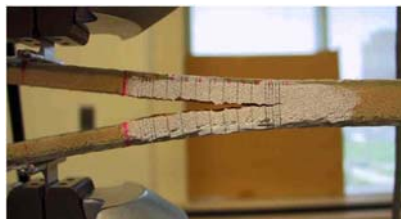


Figure 6. Crack propagation of 12.7 mm thick core specimen.

crack tip was marked on both edges of the specimen. If the crack length on the two edges differs by more than 2 mm (0.1 in), the test is invalid. The specimen was reloaded at the same constant cross-head speed of 0.5 m (0.02 in)/min without stopping or unloading until the final delamination length increment is reached. The load and displacement values were recorded at every 1 mm (0.04 in) increment in the first 5 mm (0.2 in) crack growth increment. Subsequently, load and displacement data were recorded at every 5 mm (0.2 in) crack growth, until the crack had propagated for 45 mm (1.8 in) and again at every 1 mm (0.04 in) increment for the last 5 mm (0.2 in) of crack propagation.

## 6. TEST RESULTS

### 6.1 $P_Q$ Determination

The load-displacement response of a specimen is shown in Figure 5. Several initiation  $G_{IC}$  values may be determined from the load-displacement plots [18]. They are deviation from linearity (NL), visual observation (VIS) and 5% offset/maximum load (5%/Max). In this paper, the 5%/maximum load

method was used to determine  $G_{IC}$  values. A line was drawn from the origin and offset by a 5% increase in compliance from the original linear region of load-displacement curve. The intersection of this offset line with the load-displacement curve determines the  $P_Q$  and corresponding displacement  $\delta_Q$  which should be used to calculate  $G_{IC}$ . If the intersection occurs after the maximum load point, the maximum load should be used for calculation. Figure 5 shows the determination of  $P_Q$ .

## 6.2 $G_I$ Calculation

It was found that the modified beam theory (MBT) is valid for fracture toughness data reduction of sandwich beam [12]. Therefore, in this paper MBT method was used to calculate the energy release rate  $G_I$ .

The modified beam theory equation is expressed by:

$$G_I = \frac{3P\delta}{2b(a + |\Delta|)}, \quad (1)$$

where  $P$  = load,  $\delta$  = load point displacement,  $b$  = specimen width, and  $a$  = crack length. The parameter  $\Delta$  is a crack length correction parameter for not perfectly built-in condition of the DCB. The  $\Delta$  was determined [12] by generating a least square plot of the cube root of compliance,  $C^{1/3}$ , as a function of crack length. The compliance,  $C$ , is the ratio of the load point displacement to the applied load,  $\delta/P$ .

The crack propagation remained in the mid-plane of the specimen for 3.18 mm (1/8 in), 6.35 mm (1/4 in) and 12.7 mm (1/2 in) thick core specimens. Figure 6 shows this typical crack propagation of a 12.7 mm (1/2 in) thick core specimen. Energy release rate  $G_I$  was calculated using Equation (1) for different crack lengths. Figures 7 to 9 describe the  $G_I$  versus crack extension  $da$  for 3.18 mm (1/8 in), 6.35 mm (1/4 in) and 12.7 mm (1/2 in) thick cores, respectively. The  $G_{IC}$  values for all three thicknesses and each of the five specimens are listed in Table 2.

For 25.4 mm (1 in) and 40.6 mm (1.6 in) thick core specimens, the crack deviated from the mid-plane and moved to face sheet-core interface after 5 mm (0.2in) to 10 mm (0.4 in) propagation. The crack was then propagated along the interface. Any small unsymmetry in the specimen or the loading can result in this crack propagation deviation. It happens in thick core specimens because of less constraint in the core compared to thin core specimens. In this case, the crack length correction parameter  $\Delta$  cannot be determined by the compliance and crack length data from the fracture test because the crack length cannot be precisely measured. Furthermore, for the same reason, only the initial energy release rate  $G_{IC}$  can be determined validly. In order to get valid  $\Delta_C$ , two new DCSB specimens of 25.4 mm (1 in) and 40.6 mm (1.6 in) core thickness were tested to measure compliance as a function of  $a$ . The specimen was cut to a cer-

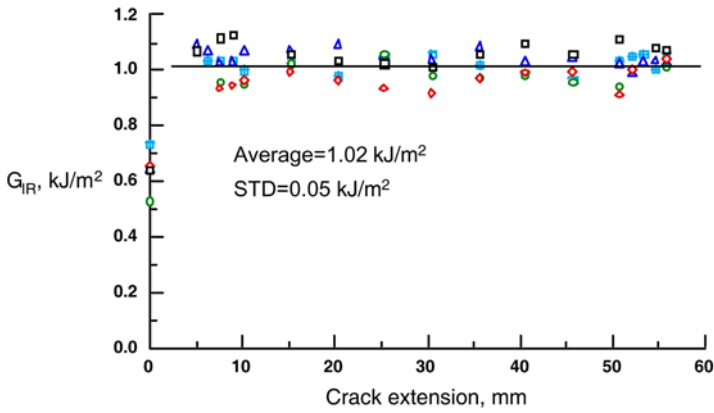


Figure 7. Energy release rate versus crack extension for 3.18 mm thick core specimens.

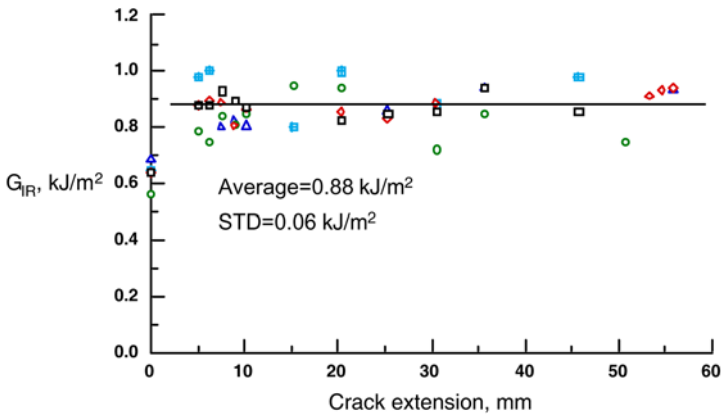


Figure 8. Energy release rate versus crack extension for 6.35 mm thick core specimens.

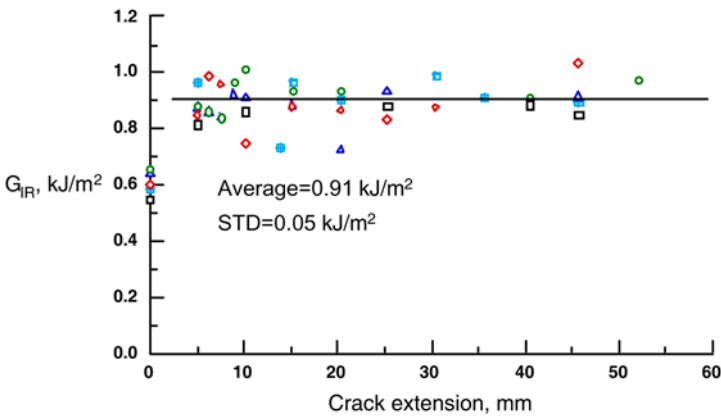


Figure 9. Energy release rate versus crack extension for 12.7 mm thick core specimens.

tain crack length and applied a load not to initiate the crack propagation. The crack length, load and the corresponding displacement were recorded. This procedure was repeated for other crack lengths from short to long. From the compliances and crack lengths data  $\Delta$  was determined and then it was used to calculate  $G_{IC}$  in the fracture test. Table 2 summarizes the initiation fracture toughness  $G_{IC}$  and the  $\Delta$  values for all five different core thickness specimens.

Table 2.  $G_{IC}$  and crack length correction parameter  $\Delta$  for various core thicknesses.

Specimen#	$G_{IC}$ (kJ/m <sup>2</sup> )					
	Specimen thickness, mm					
	0	3.18	6.35	12.7	25.4	40.6
$\Delta$	0.22	0.44	0.42	0.59	0.57	0.97
1	3.02	0.64	0.64	0.55	0.65	0.75
2	0.91	0.65	0.64	0.60	0.67	0.65
3	1.68	0.53	0.56	0.66	0.70	0.78
4	1.37	0.65	0.69	0.65	0.73	0.68
5	2.87	0.74	0.65	0.59	0.63	0.69
Average	1.97	0.64	0.64	0.61	0.68	0.71
STD	0.93	0.07	0.05	0.04	0.04	0.05
Analytical	-	0.71	0.70	0.66	0.62	0.70

### 6.3 Discussions

$G_{IC}$  values of all five core thicknesses and DCB ( $t_c = 0$ ) data are summarized in Table 2. The average  $G_{IC}$  values of all five  $t_c$ 's are within the margin of data scatter although a small variation in  $G_{IC}$  is noticed.  $G_{IC}$  decreased with increased  $t_c$  from 3.18 mm to 12.7 mm and then increased with further increase with  $t_c$ . It is hard to generalize or explain the differences from the experimental data alone. This indicates that the deformation constraint in all five specimens is nearly the same.

Fracture resistance ( $G_{IR}$ ) of specimens 3.18 to 12.7 mm  $t_c$ 's are constant with crack extension (see Figures 7–9). This indicates that material property is constant over the domain of crack singular field and over the length of crack growth.  $G_{IR}$  for  $t_c = 3.18$  mm is 1.02 kJ/m<sup>2</sup> while for  $t_c = 6.25$  and 1.27 mm are 0.88 and 0.91 respectively. Figure 11 shows the plot of  $G_{IC}$  and  $G_{IR}$  against the thickness. Possible reasons for higher  $G_{IR}$  for  $t_c = 3.18$  mm are properties of core material might have influenced by densification of core cells by the resin during the VARTM process, small thickness core might have altered the constraint by the stiff adherents, or crack would have deflected towards one of the interface thus creating the mixed mode stress state. The second reason may not be right because the higher constraint should have reduced the resistance. The third reason is unlikely, because none of the specimen tested showed the evidence of crack deflection. To understand the mech-

anics of fracture a three dimensional nonlinear finite element analysis was conducted to simulate same conditions.

### 7. FINITE ELEMENT ANALYSIS

Because of page limitations only a summary of the analysis is presented. A quarter symmetric model of the test specimen was idealized by 8-noded hexahedron elements (Element type solid 45) in ANSYS. The model was refined and graded such that stress gradients were accurately captured in both elastic and inelastic analysis. The core was treated as isotropic with multi-linear stress strain response shown in Figure 2. The face sheet was treated as orthotropic (flexural modulus in  $x$  direction) elastic material and tab as linear elastic isotropic aluminum with  $E = 69$  GPa and  $\nu = 0.3$ . Material properties used in the FE analysis are given in Table 1. The 3-D analysis was conducted to match the load and load-point displacement of the test specimen at the time of crack initiation. Then the J-integral along the crack front (mid-plane to free surface) was calculated. Then the average value over the whole crack length of the specimen was calculated and compared with the test data.

Table 3. Comparison of experimental load and load-point displacement and finite element predicted displacement.

Core thickness, mm	Experiment		FE Analysis (Predicted)
	Load, kN	Displacement, mm	Displacement, mm
3.18	0.15	5.41	5.40
6.35	0.15	5.31	5.42
12.7	0.16	5.36	5.01
25.4	0.21	4.50	3.97
40.6	0.31	3.63	3.41

Table 3 lists the load and the load-point displacement at the fracture initiation condition (5% change in compliance) based five specimen data for all five core thicknesses. Finite element predicted displacements are listed in Table 3 for the total load same as the experimental values. The agreement between the analysis and experiment is excellent to reasonably good. Calculated average J-integral are plotted in Figure 10 by square symbols. Predicted  $J_{IC}$  agreed with the experimental  $G_{IC}$ . The difference is within the experimental scatter. Thus the analysis accurately simulated the experimental results for all five core thicknesses.

Variation of  $J$  along the crack front for all five core thicknesses are shown in Figure 11. Interestingly all five curves are closed to each other all along the crack front, which indicates that deformation constraints for all five core thicknesses were the same and remained same all along the crack front. An

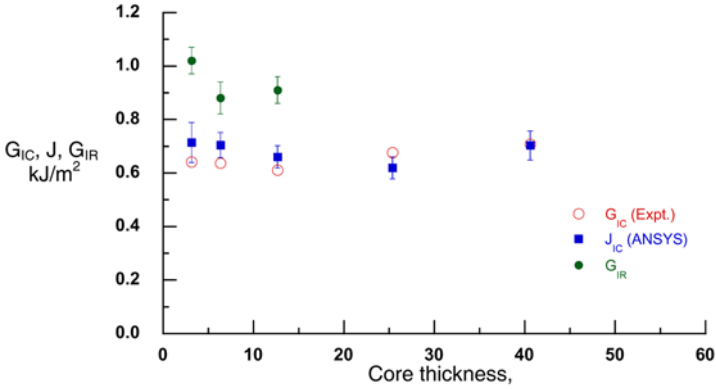


Figure 10. Comparison of  $G_{IC}$  and  $G_{IR}$  from experiment and  $J_{IC}$  from finite element analysis.

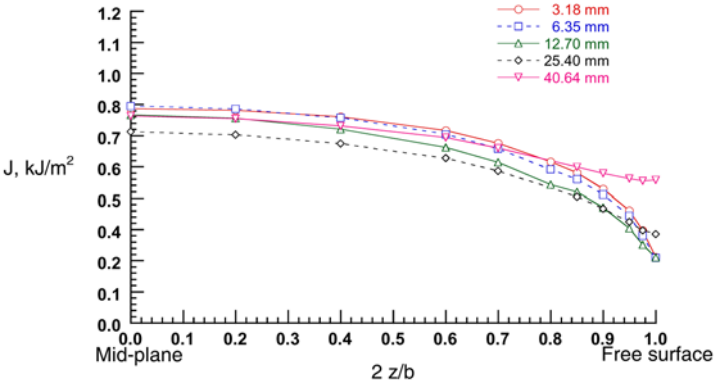


Figure 11. Variation of  $J$  along the specimen width at critical load.

examination of plastic zones was found to be small indicating that the plastic deformation is not large to require material nonlinear analysis. A more detailed study of plastic zones at fracture initiation and crack growth is underway.

## 8. CONCLUSIONS

Purpose of this study was to understand the effect of core material thickness ( $t_c$ ) on the core deformation constraint and the associated mode I fracture toughness in Double Cantilever

Sandwich Beam (DCSB) specimens. Specimens were made from woven roving glass fiber/vinyl ester composite face sheet with PVC core, whose thickness ranged from 3.18 mm to 40.6 mm. The specimens were tested in mode I loading and measured fracture initiation ( $G_{IC}$ ) and resistance ( $G_{IR}$ ) toughnesses. The  $G_{IC}$  was found to be practically same for core thicknesses from 3.18 to 40.6 mm. The  $G_{IR}$  was found to be 1.02, 0.88 and 0.91 kJ/m<sup>2</sup> for  $t_c$ 's

3.18, 6.25, and 12.7 mm. For  $t_c \geq 25.4$  mm, the crack grew by only few mm's before it deflected to face sheet. Larger  $G_{IR}$  for  $t_c = 3.18$  mm is probably due to resin densification of foam cells in the co-cure processing of panels. Three dimensional, material nonlinear finite element (FE) analysis very well simulated the test data. The  $J_{IC}$  integrals from FE analysis agreed well with  $G_{IC}$  from the test. The analysis revealed that the deformation constraint was nearly the same for all core thicknesses considered and thus resulting in nearly identical fracture toughness.

## ACKNOWLEDGEMENTS

The authors acknowledge the support of Offices of Naval Research through a grant N 00014-01-1-1033, Dr. Yapa Rajapakse, program manager. The authors also thank Fiber Glass Industries (FGI) for supplying the glass fabrics.

## REFERENCES

- [1] K.A. Olsson, "Sandwich Structures Design and Experience", 6th International Conference on Sandwich Structures, CRC Press, 2003, pp. 3–11.
- [2] L.A. Carlsson, L.S. Sendlein and S.L. Merry, "Characterization of Face Sheet/Core Shear Fracture of Composite Sandwich Beams", *Journal of Composite Materials*, Vol. 25, 1991, pp. 101–116.
- [3] L.A. Carlsson and S. Prasad, "Interfacial Fracture of Sandwich Beams", *Engineering Fracture Mechanics*, Vol. 44, No. 4, 1993, pp. 581–590.
- [4] S. Prasad and L.A. Carlson, "Debonding and Crack Kinking in Foam Core Sandwich Beams – I. Analysis of Fracture Specimens", *Engineering Fracture Mechanics*, Vol. 47, Nov. 6, 1994, pp. 813–824.
- [5] S. Prasad and L.A. Carlsson, "Debonding and Crack Kinking in Foam Core Sandwich Beams – II. Experimental Investigation", *Engineering Fracture Mechanics*, Vol. 47, No. 6, 1994, pp. 825–841.
- [6] W.J. Cantwell and P. Davies, "A Test Technique for Assessing Core-Skin Adhesion in Composite Sandwich Structures", *Journal of Material Science Letters*, Vol. 13, 1994, pp. 203–205.
- [7] W.J. Cantwell, R. Scudamore, J. Ratcliffe and P. Davies, "Interfacial Fracture in Sandwich Laminates", *Composites Science and Technology*, Vol. 59, 1999, pp. 2079–2085.
- [8] D. Loop, Private Communication, 2004.
- [9] S.A. Smith and K. Shivakumar, "Evaluation of Interfacial Fracture Toughness of VARTM Sandwich Panels Using the Mode-I Cracked Beam Specimen", *AIAA Paper 2000-1493*, 2000.
- [10] S.A. Smith and K.N. Shivakumar, "Modified Mode-I Cracked Sandwich Beam (CSB) Fracture Test", *AIAA Paper 2001-1221*, 2001.
- [11] K.N. Shivakumar and S.A. Smith, "Insitu Fracture Toughness Testing of Core materials in Sandwich Panels", *J. Composite Materials*, Vol. 38, No. 8, 2004, pp. 655–668.
- [12] K.N. Shivakumar, H. Chen and S.A. Smith, "An Evaluation of Data Reduction Methods for Opening Mode Fracture Toughness of Sandwich Panels", *Journal of Sandwich Structures and Materials*, Vol. 7, No. 1, 2005, pp. 77–90.

- [13] G.M. Viana and L.A. Carlsson, "Mode Mixity and Crack Tip Yield Zones in TSD Sandwich Specimens with PVC Foam Core", *Journal of Sandwich Structures and Materials*, Vol. 4, 2002, pp. 141–155.
- [14] K.N. Shivakumar and J.H. Crews, Jr., "Energy Dissipation Associated with Crack Extension in an Elastic-Plastic Material", *Engineering Fracture Mechanics Journal*, Vol. 28, 1987, pp. 319–330.
- [15] G. Swaminathan and K.N. Shivakumar, "Mechanical Performance for Glass and Carbon/Vinyl Ester Composites for Marine Structures", AIAA Paper No. AIAA 2005-, 2005.
- [16] K.N. Shivakumar and H. Chen, "A total Fatigue Life Model for Composite Structures", ICCES'04 Conference, Proceedings, Maderia, Portugal, July 2004.
- [17] R.L. Sadler, K.N. Shivakumar and M. Sharpe, "Interlaminar Fracture Properties of Split Angle-Ply Composites", 47th International SAMPE Symposium, 2002, pp. 428–435.
- [18] "Standard Test Method for Mode I Interlaminar Fracture Toughness of Unidirectional Fiber-Reinforced Polymer Matrix Composites", ASTM Standard D5528-94a, ASTM Annual Book of ASTM Standard, Vol. 15.03, American Society for Testing and Materials, 1999, pp. 283–292.

# DAMAGE EVALUATION OF SANDWICH STRUCTURES USING VIBRATION AND THERMAL SIGNATURES

Andres Cecchini<sup>1</sup>, Frederick Just-Agosto<sup>1</sup>, David Serrano<sup>1</sup> and Basir Shafiq<sup>2</sup>

<sup>1</sup>*Department of Mechanical Engineering, University of Puerto Rico, Mayagüez, PR 00681, USA*

<sup>2</sup>*Department of General Engineering, University of Puerto Rico, Mayagüez, PR 00681, USA*

**Abstract** Combining NDE techniques can prove to be beneficial in assessing the physical state of health of composite sandwich structures. Several NDE techniques were examined from which vibration and thermal responses were selected. A Neural Network (NN) was chosen as a means to interpret and classify the information such that the type of damage, severity and location could be identified. Numerical simulations were used to train the NN and experimental measurements were used to test and validate the approach.

**Keywords:** damage detection, sandwich structures, vibrations, thermographics.

## 1. INTRODUCTION

Marine, aerospace, ground and civil structures can receive unexpected loading that may compromise integrity during their life span. Therefore, improvement in detecting damage can save revenue and lives depending upon the application. The prognostic capability is usually a function of the examiner's experience, background and data collection during the evaluation. Methods are varied and specific to a given type of system (material, damage type, loading and environmental scenarios). As a result, one method of damage detection alone cannot examine all possible conditions and may even give false readings. In other words, by using more than one test for a damage of unknown origin, the probability of ensuring a more accurate detection increases.

This research examined various existing non-destructive techniques to assess damage in sandwich composites including: matrix updating, modal curvature response, transient thermal response, and fatigue behavior. Vinyl ester sandwich composites consisting of two carbon fiber face sheets laminated onto a urethane foam core with an epoxy matrix were experimentally and analytically characterized using vibration, and thermal response to detect the presence of various types of damage. Numerical simulations were used to produce data used to train a probabilistic neural network to evaluate the health of the sandwich composite material. This paper examines a neural network that uses vibration and thermal signatures to determine the condition of a composite sandwich structure.

Literature offers substantial evidence of the validity of each of the chosen damage detection schemes separately, however, this paper shows that these methods can work jointly to complement each other in detecting the state of a composite sandwich structure.

## 2. RELATED WORK

Ratcliffe and Bagaria [1] presented an experimental nondestructive vibration based technique for locating damage on a composite beam. The study was limited to de-laminations and could operate only with data obtained from the damaged structure. Byon and Nishi [2] presented the application of hierarchical NNs for damage identification in a carbon fiber reinforced plastic laminated beam using the first three natural frequencies and/or the third mode shape as inputs to a NN that estimated the location and amount of damage.

Toro, Shafiq, Serrano and Just [3] applied a curvature-based technique to detect localized damage in geometrically complex sandwich composite structures using 3D orthotropic FEA. Probabilistic NNs were used to identify damage in 3D geometries based on training performed with the finite element simulations.

Sahin and Shenoj [4,5] investigated global and local vibration based analysis data as input for a feedforward back propagation NN for location and severity prediction of damage in fiber reinforced plastic laminates and steel beams. In both cases studied, the selection of features used as input data was considered crucial in the accuracy of damage prediction.

Kessler, Spearing, Atalla, Cesnik and Soutis [6] presented an experimental and analytical method for the in situ detection of damage in composite materials using modal analysis techniques (frequency response and impedance) for representative damage such as holes, and deformation by impact and delaminations.

Plotnikov and Winfree [7] presented comparisons of results from thermal contrast, time derivative and phase analysis methods for defect visualization. These comparisons were based on 3D simulations (finite difference) of a test case representing a plate with multiple delaminations. Comparisons were also based on experimental data obtained from a specimen with flat bottom holes and a composite panel with delaminations. The authors concluded that both thermal contrast and phase thermography are effective methods for defect edge extraction while time derivative is suitable to measure the defect depth.

### 3. VIBRATIONS APPROACH

The use of fundamental displacement mode shape curvatures was investigated as a means to identify damage sites. By examining the absolute difference between curvature changes in the mode shapes, damage can show up as spikes as shown in Figure 1. The method successfully identified tool drop impact damage and face sheet de-lamination. However, the experimental method was not successful in determining small face sheet damage such as a perforation less than 1/8 inch.

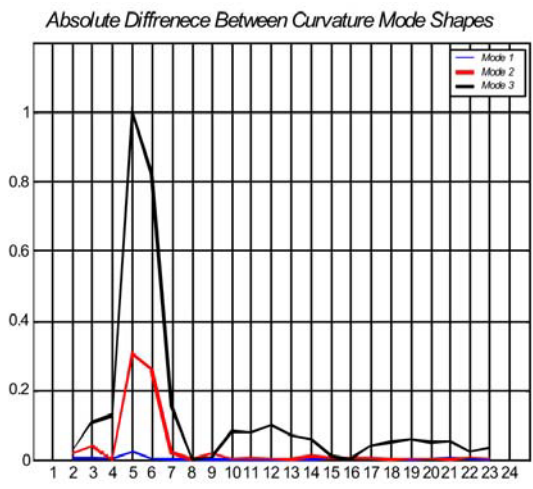


Figure. 1. Curvature based analysis for a composite beam.

The fundamental displacement mode shapes (1<sup>st</sup>, 2<sup>nd</sup>, and 3<sup>rd</sup>) could be used to identify the damage sites corresponding to structural changes that were represented as stiffness reduction. A 3D orthotropic finite element

analysis was used to simulate damage scenarios. Nominal values of material properties found in literature would not produce accurate results with FEA modeling when compared to experimental results. Therefore, a sensitivity analysis was performed to determine which parameters had the most influence on the measured mechanical behavior (natural frequency, and mode shape). These turned out to be the longitudinal modulus of elasticity and the density of both the laminate and core material. In order to obtain the best material property values, an optimization technique was performed yielding a model that would produce less than a three percent error and was therefore suitable for neural network training.

Table 1. Elastic properties of the FEM.

Property	Face Sheet	Ref. Values	Foam Core	Ref. Values
Mass density (lb/in <sup>3</sup> )	1.97x10 <sup>-4</sup>	1.5x10 <sup>-4</sup>	1.56x10 <sup>-5</sup>	3x10 <sup>-6</sup> - 1.8x10 <sup>-5</sup>
Longitudinal modulus of elasticity (lbf/in <sup>2</sup> )	8.13x10 <sup>6</sup>	8-20 x10 <sup>6</sup>	1x10 <sup>2</sup>	1-2x10 <sup>2</sup>
Transversal modulus of elasticity (lbf/in <sup>2</sup> )	8.13x10 <sup>6</sup>	8-20 x10 <sup>6</sup>	—	—
Major Poisson's ratio	0.3	—	0.3	—
Minor Poisson's ratio	0.3	—	—	—
Shear modulus of elasticity (lbf/in <sup>2</sup> )	9x10 <sup>4</sup>	5x10 <sup>5</sup>	5.6x10 <sup>3</sup>	—

#### 4. THERMO-GRAPHIC APPROACH

Nondestructive thermographic methods using transient temperature response were also investigated. The surface temperature distribution along the face sheet was studied and modeled for transient temperature responses. Thermal experimentation was performed using direct surface heating and convection heating (using a blower) on the structure. The thermo-graphic transient temperature signature was found to be limited to detecting damages on the face sheet of the composite, due to a significant mismatch in properties of each constituent in the composite. Thermal conduction could not be detected in the foam core. Various defects consisting of cracks, holes, slots and de-limitations representing mechanical damage of various extents

were tested to determine the feasibility of the approach. Transient data was obtained to identify the same three types of damage tested with the curvature based modal experimentation. The method successfully identified small face sheet damage (of the order of 1/16 inch dia. and cracks of 0.4 inch in length) but could not identify tool drop impact damage that did not physically fracture the face sheet. In addition, the method was not successful in identifying face sheet de-lamination. Yet the technique is suitable for complementing the Curvature Based Modal method because of its ability to detect small face sheet fractures and holes invisible to the vibration technique.

A virtual model was developed using Finite Elements initially and results were transformed into the appropriate format for use in neural network training. During the validation of the thermal model it was discovered that the convection effects were picked by the experimental setup (IR camera) while the FE model software used was not capable of modeling such behavior. A transient temperature simulation using finite differences was developed to model the convective effects. In order to optimize physical properties, such as diffusivity, convection heat coefficient, conductivity, density and specific heat, the numerical model was validated with experimental results. This enabled the development of a suitable library of thermal signatures under various damage conditions in order ensure appropriate neural network training data.

## **5. NEURAL NETWORKS**

The diagnosis of a structure based on its response is an inverse process; the causes must be discerned from the effects. Interpretation of the changes in the structural response or properties due to damage is a critical task that can be viewed as a classification problem. A unique solution often does not exist for an inverse problem, especially when insufficient data may exist. Thus, it is very difficult to evaluate an existing structure that has suffered some unknown type of damage using traditional damage detection methods based on a priori knowledge of damage scenarios. Algorithms are necessary to decipher, interpret the collected experimental data. Examples of algorithms that have been used include spectral analysis [8] and codes that perform wavelet decomposition [9]. The merits of wavelet analysis lie in its ability to examine local data to provide multiple levels of details and approximations of the original signal. However, other algorithms are more appropriate for implementation in fault diagnosis and detection such as rule based systems [10], fuzzy logic systems [11] and Neural Networks (NN).

Neural Networks have the advantage of using unsupervised learning [10]. An unsupervised system learns from training data that are clustered

into patterns to form classes. The classification and the generalization properties of neural networks allow the identification of both damage scenarios and in addition, can estimated extent of damage. In the approaches using NNs, the data required to model an inverse relation are obtained as the solution of the direct problem. For example, the changes in a structure parameter can be identified from the known structure response when the network has been trained properly. These structural responses may be collected through computer damage simulation from an adequate numerical model such as Finite Elements or through experimental measurements. The advantages of using NNs are their capacity to diagnose correctly, even when trained with partially inaccurate data, and their ability to continue learning and improve their performance when presented with new training data.

The current work deals with the recognition of features extracted from different NDE techniques and used concurrently in the NN. The information is represented in diverse formats (vectors and bitmaps) and may be contaminated by noise (experimental data). In addition, discrepancies may occur when matching these features with known patterns. To solve these issues a statistical based approach is implemented using Bayesian classifier that stores a single probabilistic summary for each class. Probabilistic neural networks (PNNs) belong to Bayesian classifiers and are implemented for pattern recognition.

The NN training data was obtained from numerical simulations as explained in sections 3 and 4 rather than from experimental data therefore allowing a large number of scenarios to be simulated for training. In order to prepare the data from the different NDE techniques suitable preprocessing algorithms were required. Algorithms from digital signal processing were incorporated to filter, homogenize and perform feature extraction in order to improve the NN performance.

Consider the bitmaps used for the Thermo-Graphic approach, the original thermal images, were first converted to grayscale by eliminating the hue and saturation information while retaining the luminance. Then, 2D adaptive noise removal filtering was performed. Later a defect edge extraction procedure based on image gradient computation was applied to the images resulting in a set of binary images. This method allowed the extraction of relevant features from the images for damage characterization purposes. The processing method for the thermal images is shown in Figure 2.

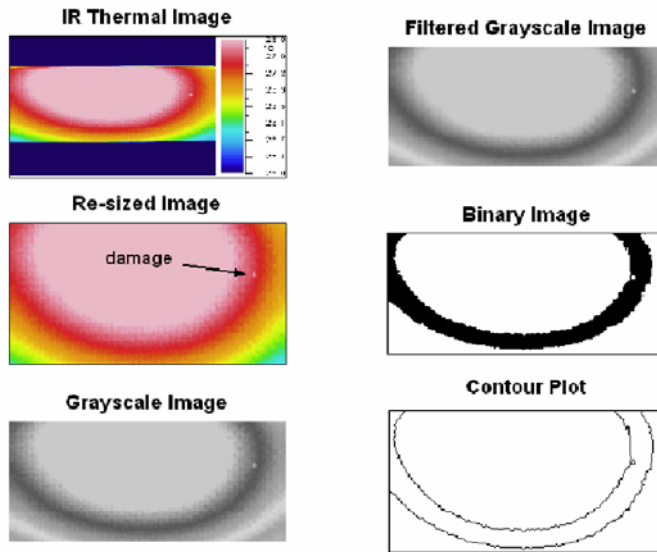


Figure 2. Preprocessing of thermal images.

A set of images resulting from the numerical simulation was used to train the PNN for damage scenarios including an indentation damage of 1/16 inch at different locations. The NN was then tested with a thermal image obtained experimentally. Figure 3 shows the simulated damages as red spots in the training images (top four images).

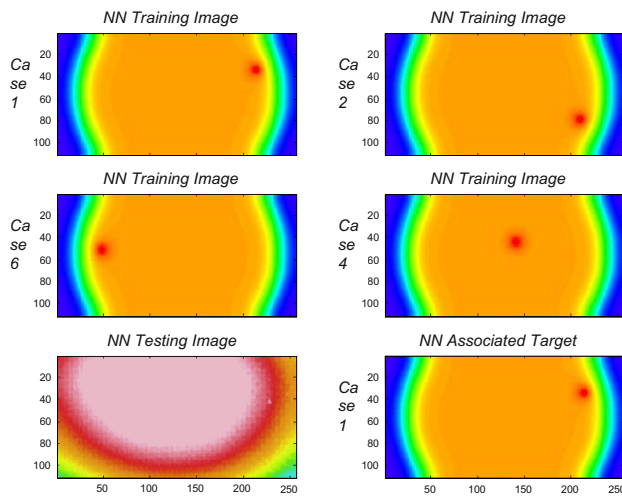


Figure 3. Training images and test image (last row).

Each single feature of a thermal image is analyzed separately by the NN and classified according to the training data. The bottom row in Figure 3 contains the test image from the IR Camera and the case determined to be the closest match to the scenario presented.

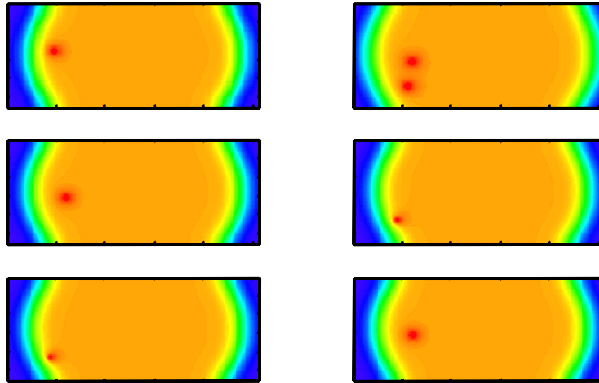


Figure 4. Training images (first column) Test Case Multiple damage.

The technique has been successfully tested with single damage cases using both curvature based analysis and thermo-graphic analysis, as in the previous example, Figure 3. In addition, testing as occurred with multiple damage scenarios using both curvature based analysis and thermo-graphic analysis. Figure 4 shows multiple damage scenarios. Training sets are shown in the first column and the test case is shown in the top second column. Notice no multiple damage scenarios are used in the training, yet the result corresponds to two cases that together produce the closest match to the test case (last two images in second column).

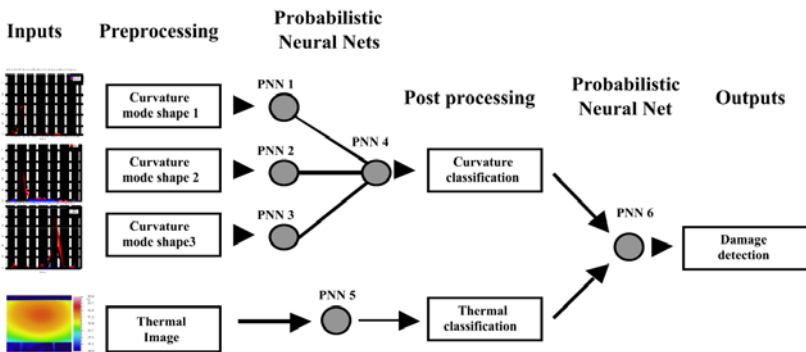


Figure 5. Overall Neural Network system implementation.

Figure 5 shows the approach taken for the overall Neural Network system implementation. A total of 6 PNN subsystems are used along with the pre and post processing algorithms mentioned above.

It was found that neural networks successfully identified damage under novel conditions not included in the training data in addition to handling multiple damage scenarios without the need of additional training. The NN approach was capable of identifying damage scenarios from both of the NDE techniques, therefore minimizing false diagnostics as they complement each other to confirm a diagnostic.

## **6. CONCLUSIONS**

Various NDE methods were evaluated and two were selected for use in the Neural Network damage detection system. A vibration based technique and a Thermographic technique were chosen. In the vibrations based technique modal curvature response and FE modeling were used to locate and determine damage that successfully identified impact damage and face sheet de-lamination. However, the experimental method was not successful in determining small face sheet damage, such as, a small perforation (less than 1/8 inch dia.). In addition to the vibration method, location and severity of the damage was also obtained using changes in thermal properties of the composites. Transient temperature data was obtained to identify the same three types of damage as was tested with the curvature based modal experimentation. The thermal analysis could not identify tool drop impact scenarios that did not physically fracture the face sheet nor face sheet de-lamination. Transient thermal behavior was found to successfully detect damage in face sheet surface cracks, small punctures and other anomalies while the curvature based analysis detected de-laminations and surface damage (greater than 1/8 inch dia.). When both methods were used together with a Bayesian probabilistic neural network, curvature and thermal base analysis complement each other to augment the damage detection capabilities for sandwich composite materials identifying the type, location and extent of the damage.

## **ACKNOWLEDGEMENTS**

The authors wish to acknowledge the financial support of the ONR-Composites for Marine Structures Division. Special thanks are due to Dr. Yapa Rajapakse, the ONR program manager for his guidance.

## REFERENCES

1. F. Just, B. Shafiq, J. Jairo and D. Serrano: "Damage Detection Using Transient Temperature Response", *International Journal of Natural Disasters, Accidents and Civil Structures*, Vol.3, No. 3, pp. 129-141, June 2004.
2. Colin P. Ratcliffe, "Damage Detection using a modified Laplacian Operator on Mode Shape Data" *Journal of Sound and Vibrations*, 1997.
3. C. P. Ratcliffe and W. J. Bagaria, "A Vibration Technique for Locating Delamination in a Composite Beam", *AIAA Journal* **36(6)**, 1074-1077, 1998.
4. O. Byon (G. Ben) and Y. Nishi, "Damage Identification of CFRP Laminated Cantilever Beam by Using Neural Network", *Key Engineering Materials* **141-143**, 55-64, 1988.
5. C. Toro, B. Shafiq, D. Serrano, F. Just: "Eigen-Parameter Based Damage Detection in Sandwich Composite Ship Hull Structures", *Journal of Mechanical Behavior*, to appear in the next issue.
6. M. Sahin and R. A. Shenoi, "Vibration Based Damage Identification in Beam like Composite Laminates by Using Artificial Neural Networks", *Journal of Mechanical Engineering Science* **217** Part C, 2003.
7. M. Sahin and R. A. Shenoi, "Quantification and Localization of Damage in Beam like Structures by Using Artificial Neural Networks with Experimental Validation", *Engineering Structures* **25**, 1785-1802, 2003.
8. S. S. Kessler, S. M. Spearing, M. J. Atalla and C. E. Cesnik, "Damage Detection in Composite Materials Using Frequency Response Methods", *Department of Aeronautics and Aeronautics, Massachusetts Institute of Technology*, Cambridge, MA, USA. Constantinos Soutis, *Department of Aeronautics, Imperial College of Science Technology and Medicine*, London, UK.
9. Y. A. Plotnikov and W. P. Winfree, "Advanced Image Processing for Defect Visualization in Infrared Thermography", *NASA Langley Research Center*, M.S. 231, Hampton, VA 23681-0001.
10. S. Wu, J. Ghaboussi and J. H. Garret Jr., "Use of Neural Networks in Detection of Structural Damage", *Comp. and Struct.*, **42(4)**, 649-659, 1992
11. Z. Hou, M. Noori and R. St. Amand, "Wavelet Based Approach for Structural Damage Detection", *Journal of Engineering Mechanics* **126(7)**, 677-683, 2000
12. S. H. Liao, "Expert Systems Methodologies and Applications, a decade review from 1995 to 2004", *Expert Systems with Applications* **28**, 93-103, 2004.
13. J. P. Sawyer and S. S. Rao, "Structural Damage Detection and Identification Using Fuzzy Logic", *AIAA Journal* **38(12)**, 2328-2335, 2000.

# FATIGUE PERFORMANCE AND SIZE EFFECT IN SANDWICH COMPOSITES

Basir Shafiq, Amilcar Quispitupa, Frederick Just and Miguel Banos  
*College of Engineering, University of Puerto Rico, Mayaguez, PR 00681, USA*

**tract** Results of sandwich composite static and fatigue loading are presented. To discern cracking in various constituents of the sandwich composite, AE technique is used. Core damage has been found to be the predominant failure activity. Fiber rupture triggered the onset of catastrophic failure. Mode I cracking was observed in the core while fiber rupture took place in mode I.

**Keywords:** sandwich composites, fatigue.

## 1. INTRODUCTION

Damage detection in sandwich composites is a difficult but crucial task [1]. In contrast to many conventional non-destructive evaluation (NDE) techniques, acoustic emission (AE) technique permits continuous damage inspection, classification and identification of modes of failure in various constituents of the composite in real time, which is critical for taking preventive measures [2,3]. In spite of widespread use of AE technique in various engineering application, literature on AE application in fatigue crack growth (FCG) in sandwich composites is scarce [1].

Failure characterization is rendered quite complex in sandwich composites due to the presence of various constituents of differing elastic properties [1,4,5]. Presence of multiple cracks is an important feature of sandwich composites which hampers the development and/or use of conventional lifetime or FCG models [1,4,5]. Furthermore, large variation in the lifetime data as a consequence of heterogeneity of sandwich composite constituents necessitates stochastic analysis [6].

## 2. EXPERIMENTAL SETUP AND PRELIMINARY RESULTS

Sandwich composite beams made of two face sheets and a core material were used in this study. Each face sheet was composed of one layer of 0.5 mm

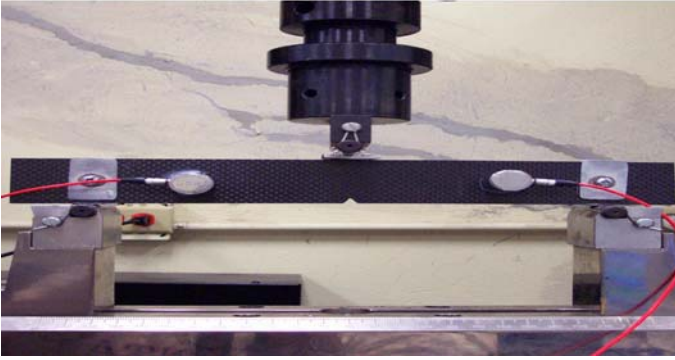


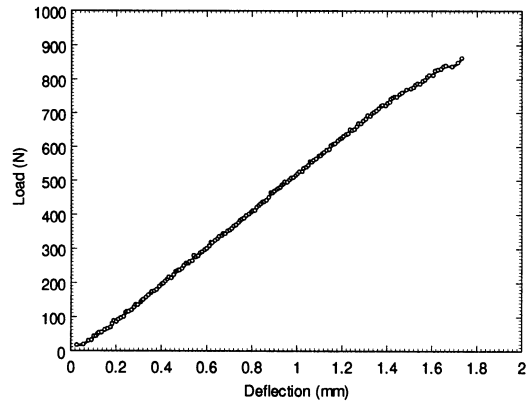
Figure 1. Test setup and a failed specimen.

thickness 161 g plain weave epoxy matrix carbon fiber, whereas, the core material was 6.0 mm thick urethane foam filled kraft paper honeycomb bonded to the facesheets with 1.5 oz vinyl ester resin. Testing was performed on SEN specimens of dimensions 250 mm  $\times$  38 mm  $\times$  12.7 mm (60° notch depth) under three point bending. Over ten specimens were tested for each set of loading parameters.

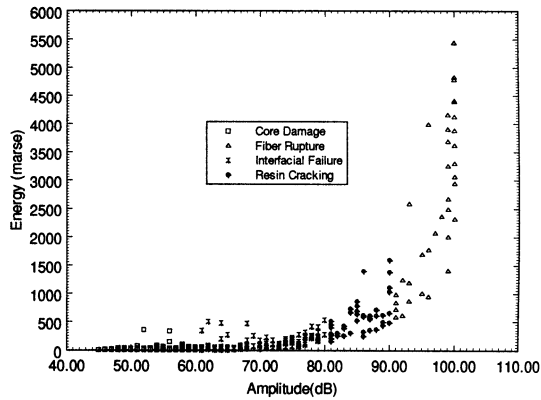
Under load control and at a rate of loading of 222 N/mim, an average of about 1200 N for ultimate static strength was obtained that was used as a basis to design fatigue tests. Flexural fatigue tests were performed between stress levels of 70 and 95% of the ultimate static load at a load ratio of 0.1 and a frequency of 2 Hz. Fatigue life was observed to be unlimited below 75% of the ultimate static strength. All tests were performed on a servo-hydraulic testing machine attached to a data acquisition system, an eight channel AE setup, and a digital microscope. The test setup and a typical failure of the specimen are shown in Figure 1.

With the analysis of AE events, energy and position, damage was classified in various constituents of the sandwich composite, such as, core, interface between core and the facesheets, resin and facesheets. Figure 2a shows the load-deflection curve, while Figure 2b shows corresponding amplitude vs energy plot. Figure 2b shows irreversible evolution of AE activity from low (core damage and inherent specimen defects accommodation) to high AE activity corresponding to fiber rupture leading to catastrophic failure.

AE analysis was used to classify damage in various constituents of the sandwich composite as a function of AE amplitude and energy levels as presented in Table 1. Amplitude and energy level were found to be independent of the type of test, specimen geometry, damage induced or loading type for the sandwich composite used. This classification qualitatively matched well with the damage sequence reported in the literature [1, 3].



(a)



(b)

Figure 2. (a) Typical load vs displacement curve. (b) Amplitude vs energy plot and damage classification.

Table 1. Sequence of failure and corresponding amplitude and energy ranges.

Failure Mode	AE Amplitude (dB)	AE Energy (marse)
Core Damage	45–59	0–25
Interface Failure	60–79	3–219
Resin Cracking	80–89	88–374
Fiber Rapture	Above 90	347–13568

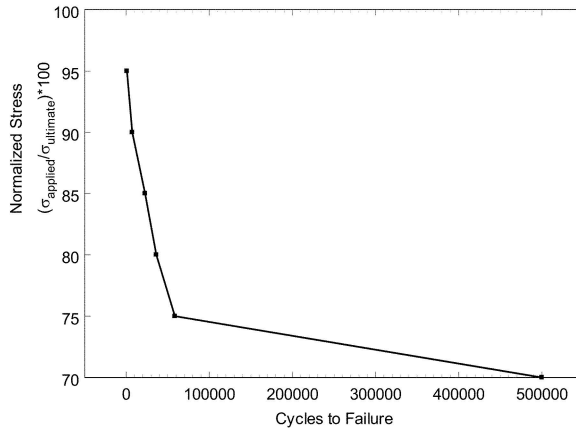


Figure 3. Normalized S–N curve.

### 3. EXPERIMENTAL FATIGUE CHARACTERISTICS

Both mode I (opening) and mode II (shearing) were observed, however catastrophic failure consistently occurred under mode I. Substantial crack growth activity was observed in mode II that propagated near the interface between the facesheets and the core and lead to weakening of the two phase action and subsequent cracking of the facesheets. Somewhat similar failure sequence has been reported in the literature [1, 3–5] for flexural fatigue tests on sandwich composites, however, unlike the reported results significant fiber rupture never took place until catastrophic failure in the current study. Test results indicate presence of multiple crack fronts and periodic FCG with long intermittent dormant intervals as evidenced by AE analysis.

AE activity tended to be high as the stress levels were enhanced. Multiple crack propagation fronts were also observed in the facesheets near the notch tip. However, insignificant crack propagation was observed in the facesheets parallel to the applied load (mode I) until catastrophic failure. Whereas, various small scale facesheet crack propagations were observed near the notch tip in a direction perpendicular to the applied load (along the fiber layered out in  $0^\circ$  direction). The literature does not list a clear endurance limit for sandwich composites, however, flexural fatigue life has been reported for as low as 60% of the ultimate static load [4]. In the current study, life was found to be unlimited below 75%. The high endurance limit may be attributed to multiple mode I and II crack fronts observed as they serve to dissipate energy, thus effectively reducing crack tip stress intensity and, therefore, stagnating crack tip(s) advancement. The results of endurance limit given by the S–N curve are shown in Figure 3.

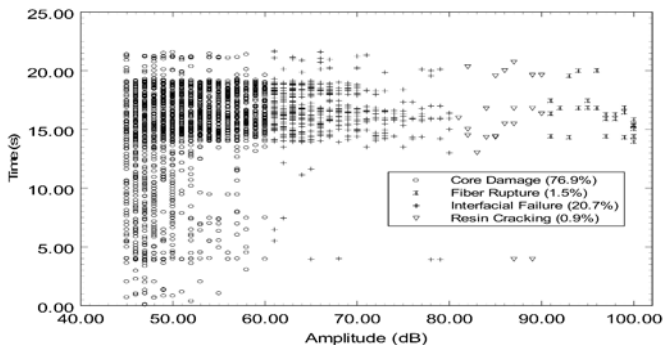


Figure 4. Amplitude vs time data and corresponding number of events in each constituent of the sandwich composite during a typical interval in the fatigue test.

Table 2. An example of stiffness reduction model applied to actual AE fatigue data.

$X_{core} = 2.01\%$	$X_{interface} = 23.65\%$	$X_{facesheet} = 73.34\%$	
$D_1$	$D_2$	$D_3$	$\Delta\varepsilon$
76.9	21.6	1.5	7.77
85.9	13.9	0.2	5.16
73.1	24.4	2.4	9.03

Catastrophic failure was preceded by almost sudden and significant fiber rupture that lead to severe facesheet stiffness reduction. This stage was arrived at after substantial weakening of the multi-phase action that exists among various constituents of the sandwich composite, mainly as a result of damage to the core and the interface. Lifetime results obtained in the current study qualitatively compared well with the reported sandwich composite fatigue characteristics, however, adequate quantitative differences were observed as expected, as the different material systems and loading parameters were used in the current study [1, 4, 5].

#### 4. STIFFNESS REDUCTION MODEL

To account for the extent of damage in various constituents of the sandwich composite, an AE based stiffness reduction model was developed. The stiffness reduction parameters were based on the overall AE activity during the fatigue test. The underlying assumption was that the extent of the damage (or cracking) in each constituent of the sandwich composite is directly proportional to the AE activity in that constituent [7]. Stiffness reduction parameter ‘ $\Delta\varepsilon(t)$ ’ under static or fatigue testing can then be represented as,

$$\Delta\varepsilon(t) = [D_1(t)] * X_1 + [D_2(t)] * X_2 + [D_3(t)] * X_3, \tag{1}$$

Table 3. Weibull parameters and probability density function and examples of survival probabilities at various number of cycles.

Stress Level	Shape Parameter $\alpha_s$	Scale Parameter $\nu_s$	Example $N$	Corresponding $SF(N)$
95 %	1.3	1047	500	68.21%
90%	1.81	8592	3000	86.20%
85%	1.3153	26176	10000	75.40%
80%	0.955	39180	10000	76.20%
75%	1.51	69265	20000	85.80%

where  $D_i(t)$  reflects cumulative percent damage in the core, interface and the facesheet for a given time (or #cycles) interval, respectively; and  $X_1$ ,  $X_2$  and  $X_3$  are the corresponding weight factors. This model is quite robust as it can be implemented in real time as the AE data can generally be collected continuously for a component in service. Thus this model becomes an important tool for calculating remaining lifetime or loss of lifetime at a given instant in the fatigue life. An example shown in Table 2 with data taken from actual fatigue test during a 25 sec interval (as shown in Figure 4) clearly indicate significant jump in stiffness reduction corresponding to slight increase in the percentage of facesheet damage.

## 5. STOCHASTIC ANALYSIS

Stochastic analysis was performed to make sense out of the large scatter observed in sandwich composite lifetime data tested between 75% and 95% stress levels. To analyze current data, three parameter Weibull distribution was used that can be expressed as [6],

$$SF(N) = \exp \left[ - \left( \frac{N - n_{0,s}}{\nu_s - n_{0,s}} \right)^{\alpha_s} \right], \quad (2)$$

where the survival probability  $SF(N)$  is the probability that life will be longer than  $N$ ,  $N$  is a random variable denoting fatigue life,  $\alpha_s$  is the shape parameter designating the spread in the data and  $\nu_s$  is the scale parameter.  $n_{0,s}$ , the location parameter denoting minimum life was set equal to zero in the current analysis. Taking the logarithm twice on both sides of Eq. 2 yielded the linear form of the survival probability as,

$$\ln \left[ \ln \left( \frac{1}{SF(N)} \right) \right] = \alpha_s \ln(N) - \alpha_s \ln(\nu_s). \quad (3)$$

Eq. 3 can be applied at any number of cycles to ascertain the survival probability. In order to apply Eq. 3, lifetime data was arranged in an ascending order and regression analysis plots of  $\ln(\ln(1/SF))$  vs.  $\ln(N)$  were generated

as shown in Figure 5 at various stress levels. Figure 5 shows an apparent linear trend, however, the accuracy of this linear system generally increases as the number of lifetime data is increased. In the final step, the corresponding shape ( $\alpha_s$ ) and scale ( $\nu_s$ ) parameters are calculated, as shown in Table 3 at each stress level. Table 3 indicates substantial scatter in the lifetime data ( $\alpha_s > 1$  indicates large scatter), independent of the stress level. However, the scale parameter ( $\nu_s$ ) indicates a clear ascending trend as a function of stress level as seen in Table 3. Some examples of assumed life ( $N$ ) and corresponding probability of survival are also presented in Table 3. The main advantage of using this survival probability method is its simplicity in ascertaining remaining lifetime information.

To check the accuracy of the proposed Weibull distribution, Kolmogorov Smirnov (K-S) Goodness-of-Fit tests were performed. To perform this test,  $F^*(N^i)$ , the observed cumulative distribution histogram and  $F(N_i)$ , the hypothesized cumulative distribution function (given by Eq. 3) were evaluated at 5% confidence level. The maximum vertical distance between the hypothesized and observed distribution was obtained from Eq. 4 as,

$$M = \max_{i=1}^n |F^*(N^i) - F(N^i)|. \quad (4)$$

The results show  $M$  to be well within the 5% confidence level. Therefore, K-S test assures the proposed stochastic model to yield the results within 5% accuracy.

## 6. CONCLUSIONS

AE analysis yielded very accurate information about the extent and location of damage in various constituents of sandwich composites. AE and post-test analysis indicated core failure to be the predominant damage mechanism followed by interfacial failure, whereas, fiber rupture triggered the onset of catastrophic failure. Multiple crack fronts in various constituents of the sandwich composite prohibited calculation of conventional FCG and lifetime parameters. AE based stiffness reduction model seemed to capture the essence of material degradation in sandwich composites under static or fatigue loading conditions. Weibull distribution accounted for large scatter in lifetime within 5% accuracy.

## ACKNOWLEDGMENTS

The authors wish to acknowledge the authorities at ONR-Composites' for Marine Structures division for their financial support for this work. Special thanks are due to Dr. Yapa Rajapakse, the ONR program manager for his unrelenting support and guidance.

## REFERENCES

- [1] Burman, M., Fatigue Behavior Initiation and Propagation in Sandwich Structures, Royal Institute of Technology, Report No. 98–29, ISSN 0280-4646, 2000, Sweden.
- [2] Daniel, I., Experimentation and Modeling of Composite Materials, *Experimental Mechanics*, 1999, 39(1):1–19.
- [3] Huang, M., Using Acoustic Emission in Fatigue and Fracture Materials Research, *JOM*, 1998, 50(11):1–14.
- [4] Mahi, A., Farooq, M. and Sahraoui, D., Mechanical behavior of Sandwich Composite Material under Cyclic Fatigue, *New Trends in Fracture and Fatigue-Metz*, April 2002, France.
- [5] Kulkarni, N., Mahfuz, H., Jeelani, S. and Carlsson, L., Fatigue Crack Growth and Life Prediction of Foam Core Sandwich Composite under Flexural Loading, *Composite Structures*, 2003, 59: 499–505.
- [6] Sobczyk, K. and Spencer, B., *Random Fatigue: From Data to Theory*, 1992, Academic Press, New York.
- [7] Quispitupa, A., Shafiq, B., Just, F. and Serrano, D., Acoustic Emission Based Tensile Characteristics of Sandwich Composites, *Composites Part B: Engineering*, 2004, 35(6–8):563–571.

# STUDY OF FATIGUE ENDURANCE OF CONVENTIONAL AND MODIFIED CORE JUNCTIONS IN SANDWICH BEAMS

Elena Bozhevolnaya, Anders Lyckegaard and Ole Thybo Thomsen  
*Institute of Mechanical Engineering, Aalborg University, Pontoppidanstræde 101,  
DK-9220 Aalborg East, Denmark*

**Abstract** Local effects occurring near junctions between different cores in sandwich structures are considered. Two groups of sandwich beams with conventional butt and reinforced butt core junctions, respectively, were examined experimentally in three-point bending under static and fatigue loadings. A rigorous statistical treatment of the obtained data has shown unambiguously that sandwich beams with modified, that is reinforced, butt junctions display superior structural performance compared with sandwich beams with the traditional core junctions.

**Keywords:** core junctions, local effects, stress concentrations, design.

## 1. INTRODUCTION

Structural sandwich elements have gained widespread acceptance within the aerospace, marine, automotive, building and sustainable energy industries as an excellent way to obtain extremely lightweight components and structures with very high bending stiffness, high strength and high buckling resistance. Despite the many advantages of sandwich structures, a number of unsolved problems still exist since their practical design often involves the use of cores of different densities in the form of backing plates, inserts, edge stiffeners, etc. [1–3] within the same structural sandwich element. An abrupt change of the geometry and difference of the elastic properties of the joined core materials causes the inducement of local stresses in the core as well as in the faces, and this may jeopardize the structural integrity of the whole sandwich assembly, especially under fatigue loading conditions.

A conventional core “butt” junction [4] presents a straight interface between two adjoining cores, see Figure 1, where the interface plane terminates with an angle of  $90^\circ$  relative to the sandwich faces. A closed-form analytical model [5] has shown that severe stress concentrations are induced in all constituents of sandwich plates in the near vicinity of core junctions subjected to transverse loading. Experimental and numerical investigations [6, 7] confirmed that these stress concentrations display themselves as an increase of the core principal stresses and a local increase of the bending stresses in the faces near the three-material corners (see Figure 1).

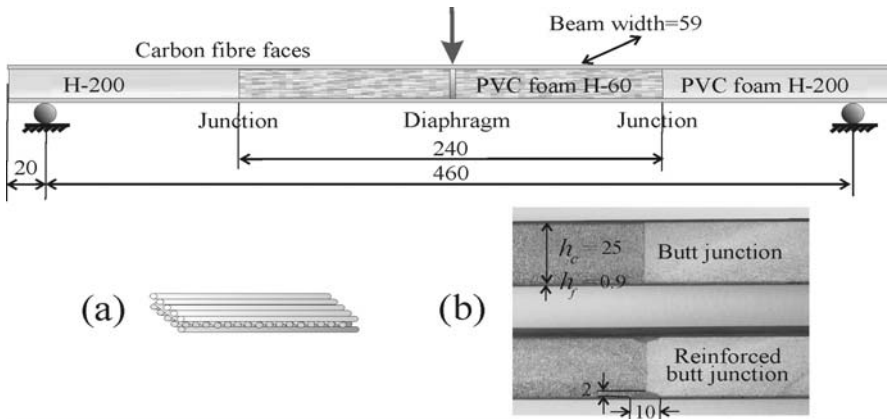


Figure 1. Constitution of the experimentally investigated sandwich beams with (a) the face laminate layout (stacking sequence) and (b) a zoom on the two junction types.

Sandwich beams subjected to static and fatigue bending loading conditions were experimentally studied in [8, 9], with special emphasis on the influence of the shape of the core junction on the fatigue performance. The idea of adopting a structurally graded core junction concept, introduced in [10], implies a structural/design optimisation of a conventional junction (i.e. the interface/boundary between two cores) with the purpose of reducing/diminishing the local stress concentrations near the junction. The conceptual idea of using structurally graded core junctions was substantiated in [8, 9], in which geometrically modified core junctions were shown to be structurally superior to conventional core butt junctions.

An alternative method of suppressing local effects is to use local reinforcements of the faces in the near vicinity of core junctions [10], see Figure 1. The introduction of reinforcing patches (see Figure 1) appears to be a fast, inexpensive and technologically friendly method of improving the structural performance and quality of core junctions. Accordingly, the purpose of the work presented here is to demonstrate the benefit of such a design modification through an experimental investigation of sandwich

beams with conventional and modified core junctions subjected to the static and fatigue bending loads.

## 2. SPECIMENS AND EXPERIMENTAL SET-UP

The geometry, layout and general loading scheme of the test specimens are shown in Figure 1, and the elastic properties of the beam constituents are indicated in Table 1. The sandwich beam specimens are assembled from two composite laminated faces with a symmetrical lay-up of  $[0^\circ/90^\circ/0^\circ]$ , and two types of PVC foam cores. All the components of the panel are joined using an epoxy resin, Araldite® 2022 (Huntsman Adv. Materials), with the help of a vacuum bagging technique.

The face laminates (Figure 1a) were made of carbon fibre prepreps (SP Systems [11]), and were manufactured by means of a manual lay-up with subsequent vacuum bagging at the prescribed temperature and pressure [12]. The tensile stiffness of the composite laminates was measured experimentally by means of modal analysis [13] and standard tensile tests [14]. Both methods yielded the same equivalent modulus of elasticity for the laminate face equal to 83.3 GPa with an error of measurement that did not exceed 4%. The mechanical properties of a single lamina appear in Table 1 according to [11].

	Faces: Carbon fibre/ epoxy laminate	Compliant core: PVC foam H60	Stiff core: PVC foam H200
Modulus of elasticity, MPa	83300	60	310
Shear modulus, MPa	-	22	90
Strength/yield stress, MPa	1190 compression-along fibres 2840 tension-along fibres 12 across fibre	0.8 compression 1.4 tension	4.5 compression 4.8 tension
Shear yield strength, MPa	-	0.7	3.3

*Table 1.* Properties of the sandwich beam constituents.

Two types of core materials were used in the investigated beams: a compliant core, H-60, and a stiff core, H-200 (Divinycell from DIAB Group [15]) with densities  $60 \text{ kg/m}^3$  and  $200 \text{ kg/m}^3$ , respectively. The compliant core was used in the central part ends of the specimens, and the stiff core was used at the beam ends. The latter prevented indentation of the sandwich structure at the edge supports.

Two groups of sandwich beams, each containing 7 specimens, were manufactured. The first group included beams with conventional butt junctions, and the second group included beams with reinforced butt junctions as shown in Figure 1b. The reinforcing patches were achieved by the machining of circular segment grooves across the junctions, and subsequently filling these grooves with adhesive (Araldite<sup>®</sup> 2022), while attaching the faces to the core. Clearly, this is a simple technological operation, which can be routinely used in the production of sandwich panels in order to enhance the distribution of the bonding agent. It should be noted that the geometry of the segment-like reinforcing patch shown in Figure 1b has been substantiated with the help of Finite Element Analysis with the purpose of effectively suppressing the local bending of the faces at core junctions [8, 9].

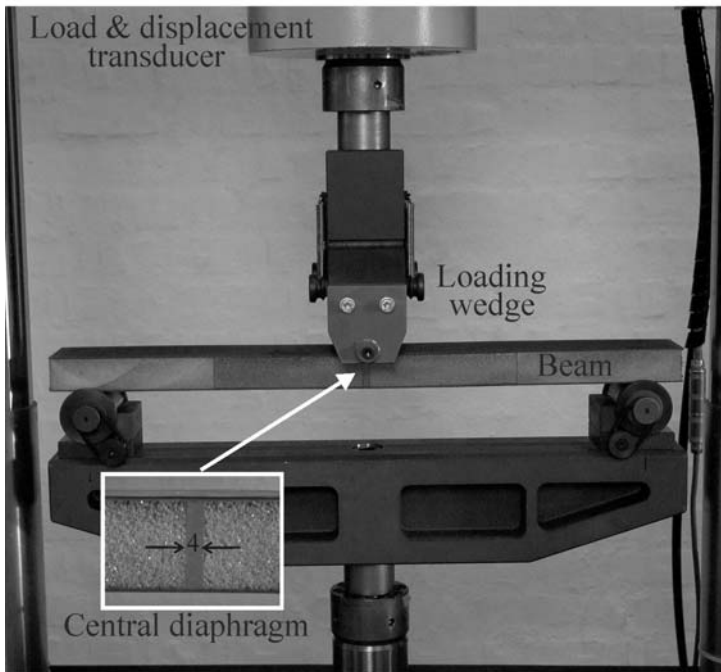


Figure 2. Experimental setup for three-point bending of sandwich beams with a zoom on the central diaphragm.

A three-point bending scheme, as shown in Figure 2, was chosen for the experimental investigation of the sandwich beams [16]. The test-rig was mounted in a servo hydraulic test machine, SCHENK Hydropuls<sup>®</sup> PSB [17], and provided with a computerized data acquisition system. The test-rig was operated in displacement control mode, with an accuracy of the load

measurements better than 0.2%. Video recording of the experiments with a resolution of 25 frames per second was also enabled.

It is important to mention here that sandwich structures are generally prone to various failure modes depending on the geometric and elastic properties of the constituents as well as on the imposed loading and boundary conditions [18, 19]. Accordingly, it was extremely important to eliminate undesired failure modes and conduct the experiment in such a way that the smallest critical load, which would trigger the failure of the sandwich beam, would correspond to a yield of the compliant core at the core junction. Reference is made to [8] for details of the critical load estimates for various types of failures, as well as for design considerations concerning the sandwich specimens used for the three-point bending tests.

However, it should be explained here that the issue of the central loading point and prevention of indentation of the compliant core in the centre of the specimen was addressed with the help of a rigid central diaphragm as shown in Figure 2. The diaphragms with a thickness of 4 mm, was manufactured in a separate mould step from the same adhesive (epoxy), which was used for bonding the sandwich components, and subsequently it was bonded into a rectangular groove machined in the centre of the core material prior to attaching the second face.

### 3. RESULTS AND DISCUSSION

From each group of specimens, two sandwich beams were subjected to quasi-static loading and five were subjected to cyclic loading until failure occurred.

The quasi-static loading was applied at a loading rate of 0.05 mm/s. The obtained load vs. central displacement diagrams for the sandwich specimens with conventional and reinforced butt junctions are presented in Figure 3. These load-displacement curves are linear up to approximately 1.5 kN, which corresponds to a central deflection of about 5 mm (cf. with the total thickness of the sandwich beams being 27 mm). The static failure loads are considered as the maximal loads achieved in the testing, and for the specimens with both types of junctions they lie in the narrow interval of 2.36-2.42 kN. These strength values are very close (though slightly larger) to a simple estimate of the critical load based on the shear strength of the compliant core from the Table 1:  $\tau^y \cdot area = 2 \cdot 0.7 \cdot 59 \cdot 25 = 2.1$  kN. It is worth to notice in Figure 3 that the sandwich beams with modified junctions allow at least 10% larger final deflection than the beams with conventional junctions.

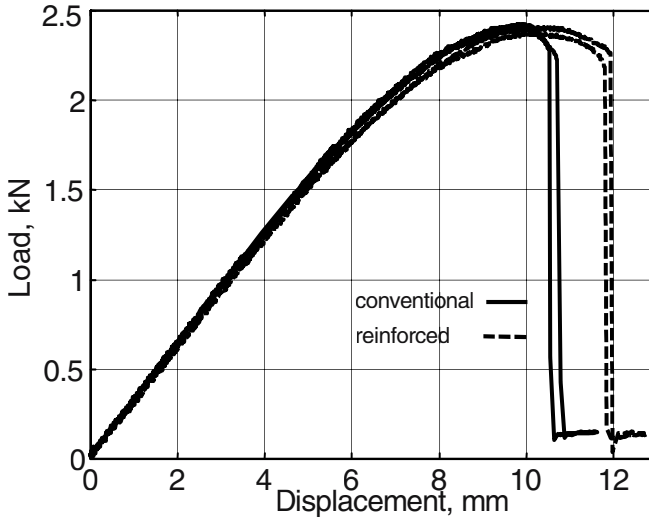


Figure 3. Load vs. central displacement curves for sandwich beams with conventional and reinforced butt junctions subjected to the quasi-static three-point bending loading.

Video recordings of the specimens subjected to quasi-static loading allowed the acquisition of some information about the initiation of fracture, see Figure 4. The consecutive video frames shown in Fig. 4 are separated by a time interval of 1/25 sec. A 45°-shadow in frame 2 appearing in the soft core, suggests that it is the compliant core, which failed first in the sandwich beams with both conventional and modified/reinforced junctions. The visual evidence of Figure 4 is not enough to draw an unambiguous conclusion about where exactly in the compliant core that fracture started before it propagated, either along directions perpendicular to the principle tensile core stresses and/or into a delamination mode of the face-core interfaces. However, the fact that the majority of the sandwich beams subjected to quasi-static or fatigue loadings neither suffered delamination of the face-core interfaces at the beam edges nor in the central loading point area, effectively ruled out all other possibilities than a shear yield of the compliant core. Fracture or crack propagation might as well have started at the three-material corners, and it should be noticed how the shadows in frames 2 are tied to the three-material corners.

It was chosen to subject both sandwich specimens groups to cyclic fatigue loading of the same level, which was selected to be approximately 70% of the static critical load, i.e. 1.75 kN. A loading ratio of  $R = 0.1$  provided a fixture of the specimens during testing, and a loading frequency of 3 Hz was used (see Table 2). The testing was conducted using load-amplitude control. The application of displacement shut-limit control

guaranteed that the fracture propagation in the ruptured specimen was stopped before the occurrence of total collapse of the specimens.

*Table 2.* Fatigue test loading parameters.

Static failure load, kN	Fatigue load amplitude, kN	R-ratio	Frequency, Hz
2.36-2.42	1.75	0.1	3

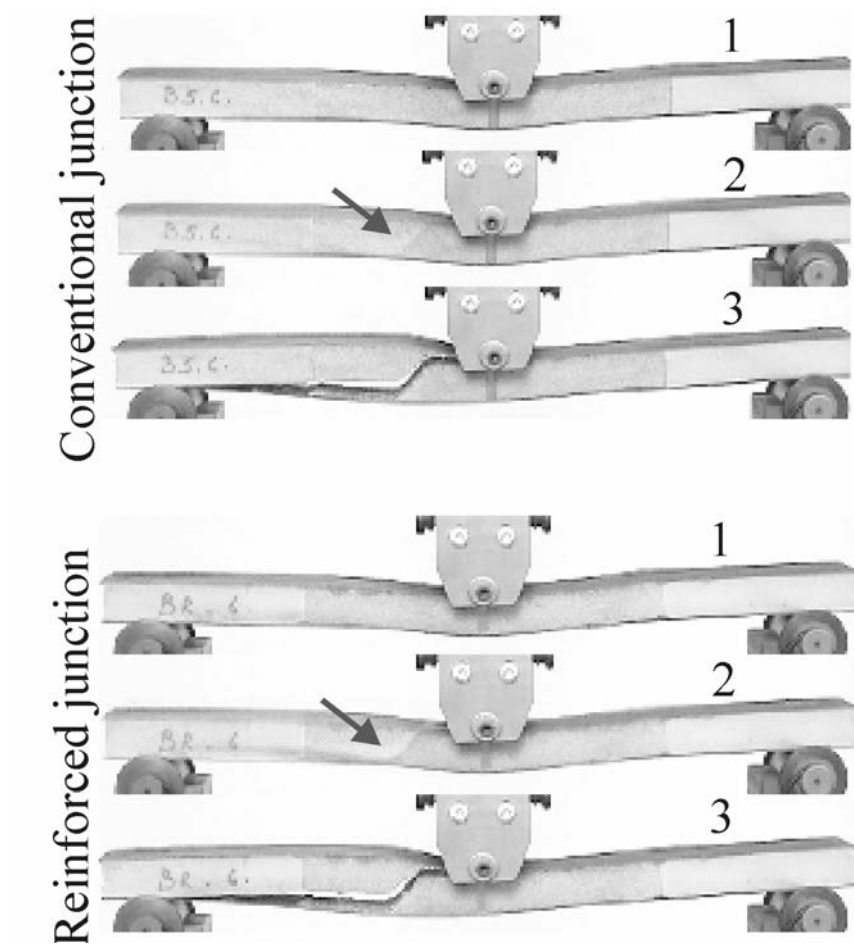


*Figure 4.* Crack initiation and final rupture in sandwich beams with conventional and reinforced butt junctions subjected to quasi-static loading. The time interval between the consecutive video frames 1, 2 and 3 equals 1/25 sec.

The typical crack patterns are shown in Figure 5, from which it is observed that they are identical for quasi-static and fatigue loadings.

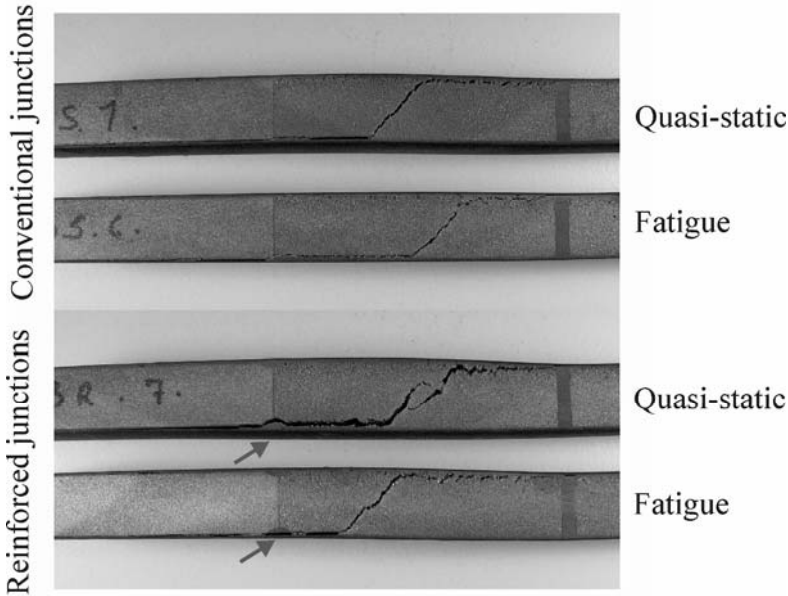


Figure 5. Characteristic crack patterns in sandwich beams with conventional and reinforced butt junctions subjected to quasi-static and fatigue loading conditions.

The number of cycles to failure was measured for the 5 sandwich beams with conventional butt junctions and for the 5 sandwich beams with reinforced butt junctions. The results are shown schematically in Figure 6. Fatigue life times in the interval [19671–57675 cycles] were obtained for the sandwich beams with conventional junctions, whereas fatigue life times obtained for the sandwich beams with reinforced butt junctions were in the interval [78535–146023 cycles]. It should be noticed, that in spite of the scatter of the experimental data observed for both specimen groups, the minimal life time of sandwich beams with reinforced junctions was substantially longer than the maximum life time of sandwich beams with conventional junctions. A rigorous statistical treatment of the obtained data was performed to obtain the average value of the fatigue life of each group of sandwich specimens. From the analysis of the test data it was established that the sandwich beams with conventional core junctions displayed a significantly lower mean number of cycles (by factor 3) to failure than the sandwich beams with modified core junctions: 36,422 cycles to failure for conventional joints, and 105,458 cycles to failure for reinforced core joints.

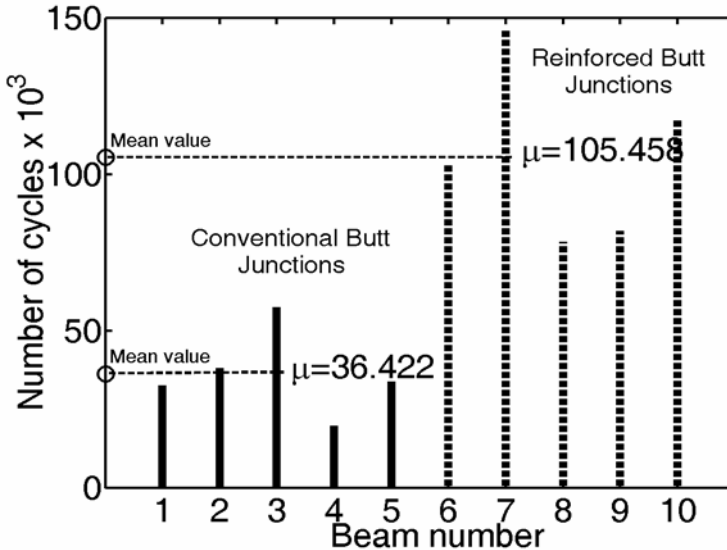


Figure 6. Fatigue life of sandwich beams with conventional and reinforced butt junctions. The loading parameters are specified in Table 2.

#### 4. CONCLUSIONS

It has been demonstrated that the use of sandwich panel core joints modified with reinforcing patches improves the fatigue life expectancy significantly, compared with sandwich panels with conventional “butt” core joints. For the particular sandwich panel configuration studied herein, the fatigue life was increase by a factor of almost 3.

It should be stressed that the manufacturing of the inner reinforcing patches is a low-cost operation, which is already routinely used in production of sandwich panels (though with the purpose to increase the resin flow and achieve a faster redistribution of resin). Thus, the placement of such “resin redistribution” grooves along junctions between different core materials would improve the fatigue strength of the sandwich structures.

#### REFERENCES

1. Smith, C.S., Design of Marine Structures in Composite Materials, Elsevier, London, 1990.
2. Zenkert, D. (ed.), The Handbook of Sandwich Construction, EMAS Publishing, London, 1997.
3. Gay, D., Hoa, S.V. and Tsai, S.N., Composite Materials: Design and Application, CRC Press, New York, 2003.

4. Adams, R.D. and Wake, W.C., *Structural Adhesive Junctions in Engineering*, Elsevier, London, 1984.
5. Skvortsov, V. and Thomsen, O.T., “Analytical estimates for the stresses in face sheets of sandwich panels at the junctions between different core materials”, in *Proceedings of the 6<sup>th</sup> International Conference on Sandwich Structures (ICSS-6)*, Ft. Lauderdale, Florida, March 31–April 2, 2003, CRC Press, New York, 2003, pp. 501–509.
6. Bozhevolnaya, E., Thomsen, O.T., Kildegaard, A. and Skvortsov, V., “Local effects across core junctions in sandwich panels”, *Composites. Part B: Engineering*, Vol. 34, 2003, pp. 509–517.
7. Bozhevolnaya, E., Lyckegaard, L., Thomsen, O.T. and Skvortsov, V., “Local effects in the vicinity of inserts in sandwich panels”, *Composites. Part B: Engineering*, Vol. 35, 2004, pp. 619–627.
8. Bozhevolnaya, E. and Thomsen, O.T., “Structurally graded core junctions in sandwich beams: quasi static loading conditions”, *Composite Structures*, in press.
9. Bozhevolnaya, E. and Thomsen, O.T., “Structurally graded core junctions in sandwich beams: fatigue loading conditions”, *Composite Structures*, in press.
10. Bozhevolnaya, E., Lyckegaard, A., Jakobsen, L. and Thomsen, O.T., *Sandwich Panel and a Method of Producing a Sandwich Panel*. Application No./Patent No. 03027020.1, 2003.
11. Product Catalog, *SP Systems Product Catalog* [online database], URL: [http://www.spsystems.com/solutions/general\\_pdfs/UK\\_2004\\_PC\\_v1.pdf](http://www.spsystems.com/solutions/general_pdfs/UK_2004_PC_v1.pdf) [cited November 2004].
12. Prepregs and Adhesive Films, *SP Systems Product Selector Guide* [online database], URL: [http://www.spsystems.com/solutions/solutions\\_pdfs/pdfs\\_productdatasheets/prepreg/SE\\_84.pdf](http://www.spsystems.com/solutions/solutions_pdfs/pdfs_productdatasheets/prepreg/SE_84.pdf) [cited November 2004].
13. Ewins, D.J., *Modal Testing: Theory and Practice*, Research Studies Press, 1985, p.269.
14. Standard Test Method for Young’s Modulus, Tangent Modulus, and Chord Modulus, E111-82, *Annual Book of ASTM Standards*, published August 1982 (reapproved 1988).
15. Structural Foam Cores, *DIAB Products* [online database], URL: [http://www.diabgroup.com/europe/products/e\\_prods\\_2.html](http://www.diabgroup.com/europe/products/e_prods_2.html) [cited November 2004].
16. Standard Test Method for Flexural Properties of Sandwich Constructions, C393-00, *Annual Book of ASTM Standards*, published April 2000.
17. SCHENK Hydropuls® System, *Instruction Manual*, Carl Schenk AG, Darmstadt, 1986. Updated 2001.
18. Triantafillou, T.C. and Gibson, L.J., “Failure mode maps for foam core sandwich beams”, *Material Science and Engineering*, Vol. 95, 1987, pp. 37–53.
19. Daniel, J.J., Gdoutos E.E., Wank K.-A. and Abot, J.L., “Failure modes of composite sandwich beams”, *International Journal of Damage Mechanics*, Vol. 11, 2002, pp. 309–334.

# FATIGUE OF CLOSED CELL FOAMS

Dan Zenkert, Andrey Shipsha and Magnus Burman

*Department of Aeronautical and Vehicle Engineering, Kungliga Tekniska Högskolan (KTH), SE-100 44 Stockholm, Sweden*

**Abstract** This paper deals with fatigue of closed cell foams. The main idea is to use a few simple tests to predict the tension-tension fatigue properties of foams. The required testing consists of crack propagation rate measurements and one tension-tension fatigue test performed at yield stress for the foam. This data can then be combined to construct a synthetic S-N curve for the foam. Tests on three densities of Divinycell H-grade foam are performed and the results support this approach. Some preliminary results from two densities of Rohacell WF-grade are given as well. Static properties of foams scale with relative density and once this scaling can be obtained through various static tests and the same scaling appears to be valid for both crack propagation rates and fatigue properties of foams. The implication of this is that once the fatigue behaviour of one relative density foam is established, one can predict the fatigue behaviour of all other relative density foams within the same class of materials.

**Key words:** cellular materials, fatigue, crack propagation, scaling.

## 1. INTRODUCTION

Rigid cellular foams are used extensively as a structural core in load carrying sandwich structures. The usage stretches over applications in aerospace, automotive, marine, transportation and infra structure. There are numerous examples of applications and a few worth noticing here are for example the new Swedish Navy Corvette Visby, wind-mill blades, and novel train car structures. In all of these and most other foam core sandwich applications, the core is typically a closed cell polymer foam, designed to carry a substantial part of the load. The core in a sandwich structure has a

multitude of functions; carry transverse loads (through shear) and distribute load between the face sheets, stabilise the face sheets to avoid instability, transfer local loads acting on the face sheets or via fasteners, etc. The core usually also provides a number of other functions, such as thermal insulation, acoustic insulation, etc. More and more has been focused on the core material recently due to increased demands for material properties and models to use in the design of sandwich structures. Fracture and fatigue of load carrying foam cores still remains to a large extent unknown. The reason for this is the inherent structure of foams, constituted of a complicated 3-dimensional network of thin membranes (cell walls), enclosing each cell. At the intersection of cell walls, edges with concentrated mass build up rods or beams. A foam is thus not really a material, but a micro-structure. The macroscopic properties of this structure (material) depend on many parameters and not only the properties of the material building up these walls and edges. One important property is of course the relative density,  $\bar{\rho}$ , defined as the ratio of the density of the foam  $\rho$  divided by the density of the solid material  $\rho_s$ . The cell structure itself will also strongly affect the macroscopic properties of the foam. Yet another important parameter is the amount of solid material that builds up the cell walls and edges, respectively. It is well known that open cell foams (with all the solid material is in edges) behave differently than closed cell foams.

In the well-known textbook by Gibson and Ashby [1] cellular foams (3D cellular structure materials) are modelled using the relative density as the primary variable. A variety of properties are modelled using the relative density, the properties of the solid cell edge/face material and the cell structure. Rather straight forward kinematic relations are used and very useful, simple formulae for design are derived. In essence, most properties of foams can be written as

$$\bar{x} = \alpha \bar{\rho}^n \quad (1)$$

where  $x$  is some mechanical property of the foam normalised with its value for the fully dense material (bulk property) of which the cell edges and faces are made of, in the case of polymer foam thus the solid polymer material property. Herein, we shall assume that the properties of the foam can be described by means of eq. (1), where the exponent  $n$  will be found from fitting experimental data. However, this exponent must have a value  $1 \leq n \leq 2$  [1].

## 2. MATERIALS

Two closed cell foams were used in this study; Divinycell H-grade and Rohacell WF-grade. Both have a closed cell structure and belong to the category of high-performance rigid polymer foams used as load carrying core materials in various applications

Divinycell is a cross-linked rigid cellular PVC foam and it is produced in a variety of densities where mechanical properties (higher strength and moduli) increase with density. Even a small variation in density will cause differences in the mechanical properties. The fracture behaviour of this material is in the regime between ductile and brittle. Divinycell qualities used in this survey were H60, H100 and H200, where H stands for the grade and the number corresponds to the nominal density in  $\text{kg/m}^3$ . Any details on this material can be found in [2].

The other material used in this study is Rohacell, a PMI foam with predominantly closed cells and which is more brittle than the PVC foam. The qualities used herein were WF51 and WF200, where WF is the particular grade of Rohacell and the number corresponds to the nominal density in  $\text{kg/m}^3$ . Details on this material can be found [3].

Both foams have similar micro-structure with most of the solid material in the faces or cell walls. There is a portion of material concentration at the edges, the junctions where the cell walls meet. One could assume that these materials then should behave close to that of a perfect closed cell structure exhibiting a cell wall stretching deformation mechanism. However, the concentration of mass in the junction has some effect. By fitting data from tests performed in-house on various densities and also using data supplied by the manufacturers the relations between properties and relative density was adapted to an equation of the type in eq.(1). The values for  $\rho_s$  and  $E_s$  are simply estimates using handbook data for similar polymeric materials. It was found to be difficult to obtain bulk properties for these polymer blends. Changing these bulk data will imply changes in the curve fitting parameters, though the slope  $n$  will not change presumably. Different testing methods give slightly different results, but in short it was found that the slope according to eq.(1) varied between 1.1 and 1.2 for all static mechanical properties of Divinycell H (elastic modulus, ultimate tensile and compressive strength, shear strength, and fracture toughness). A value of  $n = 1.1$  gives quite decent curve fits to all tensile properties. The exponent number for Rohacell WF appear also to be around  $n = 1.1$ . These are the values used in subsequent scaling of test results.

### 3. STATIC FOAM PROPERTIES

A number of static tests were performed on the materials. They were performed using the same test up as in the tension-tension fatigue testing, which is described below. Figure 1a shows tensile stress-strain curves for H60, H100 and H200. The same curves are plotted again in Figure 1b, where the stress is normalised with the relative ratio so that  $\bar{\sigma} = \sigma / \bar{\rho}^n$ . As seen in Figure 1b, the three stress-strain responses for three different relative densities collapse into a single curve. A similar normalisation with results from Rohacell WF materials gives similar results.

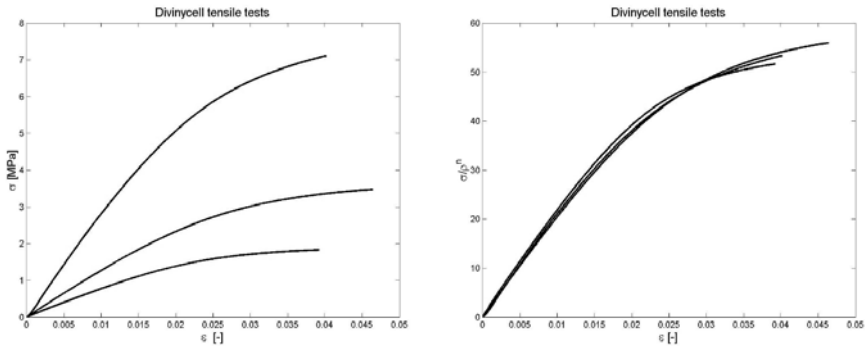


Figure 1. (a) Typical stress-strain relations for H60, H100 and H200 (from bottom to top) and (b) normalised stress-strain relations.

From this testing, all the necessary material characteristics used in this investigation can be extracted, including the Young's modulus,  $E$ , and the yield strength  $\sigma_y$ , here defined as the stress at 0.2% offset strain, as commonly defined for other engineering materials which does not exhibit a distinct yield point. The material data for the materials used herein are given in Table 1.

Table 1. Material data for Divinycell H and Rohacell WF materials (\* dimension obtained using  $da/dN$  in m/cycle in eq. (1)).

	H60	H100	H200	WF51	WF200
$E$ [MPa]	78	126	304	89	n.a.
$\sigma_{0.2}$ [MPa]	1.31	2.37	4.61	1.46	n.a.
$\sigma_{ult}$ [MPa]	1.83	3.34	7.14	1.60	n.a.
$K_{Ic}$ [MPa $\sqrt{m}$ ]	0.13	0.21	0.41	0.10	0.34
$C$ [*]	2.44	0.139	1.87E-3	2.01E+11	2.69E+3
$m$	5.68	5.91	5.48	13.1	13.5

### 4. CRACK PROPAGATION RATE TESTING

Before moving on to fatigue testing, a short review of some earlier tests results is necessary. In [4] crack propagation tests of Divinycell H and Rohacell WF were performed using a modified version of the compact tension (CT) specimen. The crack propagation measurements were fitted using Paris' law, which reads

$$\frac{da}{dN} = C\Delta K_I^m \text{ where } da/dN \text{ is given in m/cycles} \tag{1}$$

There are few important findings from this investigation; the crack growth rates yield very high Paris' law exponents  $m = 5.5-6$  for Divinycell H and as a large as  $m = 13$  for Rohacell WF. The numbers for  $C$  and  $m$  for the material used herein are given in Table 1. It was previously shown by Huang and Lin [5] that fatigue data for open cell foams can normalized with relative density.

The Paris' law curves for Divinycell H60, H100 and H200 are shown in Figure 2a. The same type of normalisation can again be done by normalising  $\Delta K$  with the relative density using  $\Delta K/\rho^n$  and if this is done the curves will collide into one single relation, as shown in Figure 2b.

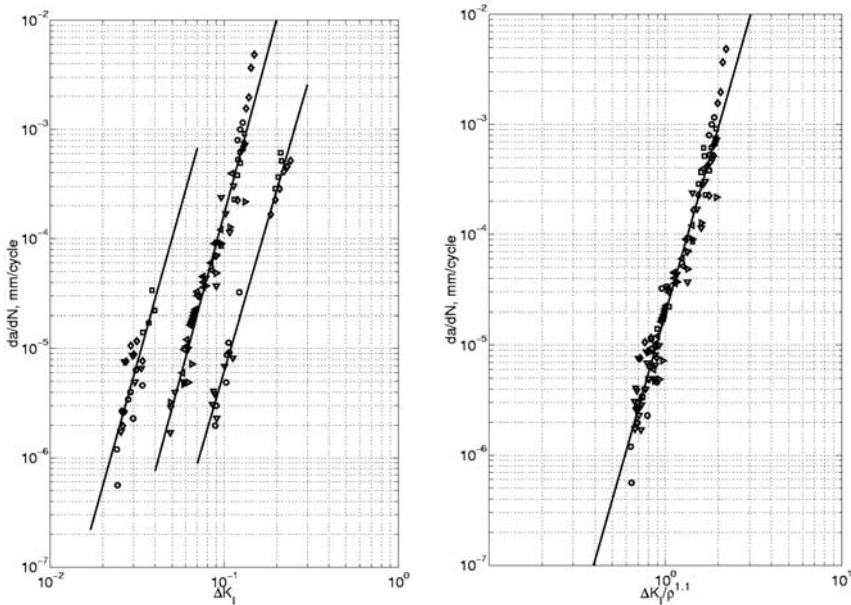


Figure 2. (a)  $da/dN$  vs.  $\Delta K$  curves for Divinycell H60, H100 and H200 (left to right) and (b) the same curves but for a density normalised  $\Delta K$ .

As seen in Figure 2b, the Paris' law relation also appears to be generic for a class of foams. In short, this implies that once the property – relative density relation is known, one test should be ample to know the properties for all densities of the same material. In this case, the property – relative density relation can be found by performing static Mode I fracture toughness tests of various foam densities. To create one master curve for all  $da/dN$  data we can find the slope in Figure 2b, which is around  $m = 6$  and the corresponding number for  $C$  in the normalized graph. This can then be extracted for all relative densities and used for predictions.

## 5. TENSION-TENSION FATIGUE TESTING

The fatigue test procedure used an axi-symmetric dog bone specimen, described in ASTM D1623-78 “Tensile and tensile adhesion properties of rigid cellular plastics“ [6]. The test fixture consists of two similar aluminium cylinders with one flat end to which the test specimen was bonded and one threaded end that was fixed in a hydraulic test machine. The specimens were cut from blocks of foam core, bonded between the two cylinders and a waist was milled to the correct shape and size in a lathe. The two cylinders were threaded in opposite directions in order to simplify the fastening into the test machine. The test rig with a specimen is shown in Figure 3.

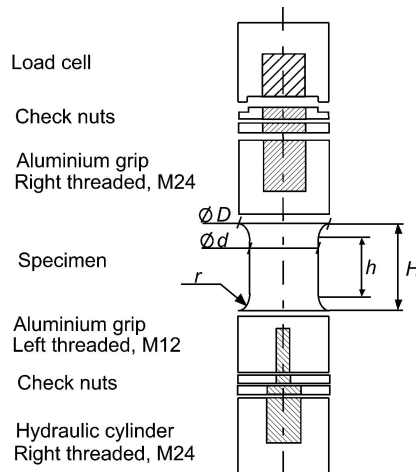


Figure 3. Schematic drawing of the test set-up with a temperature sensor mounted on the specimen. Dimension used  $D = 50$  mm,  $d = 30$  mm,  $H = 50$  mm, and  $h = 32$  mm.

Static tests were performed in tension under a constant deformation rate of 2 mm/min at room temperature using the same specimen type. The fatigue

tests were performed under a load controlled sinusoidal cycle using a servo hydraulic testing machine, MTS 50kN. The load ratio used was in all cases  $R = 0.1$ ,  $R = \sigma_{min}/\sigma_{max}$  and a testing frequency of 5 Hz. The fatigue life of the specimens is characterised as the number of cycles to ultimate failure.

## 6. STRESS-LIFE AND PARIS' LAW CORRELATION

The analytical background is based on converting the classical Paris' law to a Basquin's type expression by calculating an inherent initial flaw size. This initial flaw size appears to be the same for all densities of a particular class of foams. The flaw size can be obtained from one fatigue test performed at the yield stress, and is thus not very time consuming.

By assuming crack growth in closed cell polymer foam to be continuous, as in a continuum, we can use the measured crack growth data in a similar way to what commonly is done for metals. Assuming the foam to behave like a continuum implies that there is no evident length scale present for cracked bodies. The approach to find a link between the S-N curve and the crack growth measurements is then similar to that of homogeneous materials. We take the S-N curve to be a crack growth test from some *initial flaw size*  $a_0$  to a final crack size  $a_f$ . The initial flaw size is then considered to be some typical defect present in the volume of the material and the final crack size is simply some defect size in the test specimen which causes fracture at the maximum stress in the load cycle. Starting from Paris' law we have

$$\frac{da}{dN} = C\Delta K_I^m = C(\Delta\sigma_0\sqrt{\pi a})^m = C\Delta\sigma_0^m(\pi a)^{m/2} \quad (2)$$

with experimentally known coefficients. We can integrate this to find the number of cycles required to propagate a crack of some initial length  $a_0$ , usually denoted the *initial flaw size*, to a critical length  $a_f$ . The critical length is simply given by some length that leads to static failure at peak load during a fatigue cycle. This is given by

$$a_f = \frac{1}{\pi} \left( \frac{K_{Ic}}{\Delta\sigma_{0,max}} \right)^2 = \frac{1}{\pi} \left( \frac{K_{Ic}}{\Delta\sigma_0/(1-R)} \right)^2 \quad (3)$$

The number of cycles to failure is then

$$\int_0^{N_f} dN = \int_{a_0}^{a_f} \frac{da}{C\Delta\sigma_0^m (\pi a)^{m/2}} \quad (4)$$

The number of load cycles to failure,  $N_f$ , is then given by

$$N_f = \frac{1}{C\Delta\sigma_0^m (\pi)^{m/2}} \left( \frac{(a_f)^{1-m/2} - (a_0)^{1-m/2}}{1 - m/2} \right) \quad (5)$$

This is obviously simplified to the point that the stress intensity factor has no finite width correction factor and only depends on the square root of the actual crack length. For simplicity, let us also first assume that the final crack size is much larger than the initial one, so that the fatigue life of a small specimen is the same as for a large one. The first reason being that the exponent in Paris' law is quite high, for example  $m = 6$  for Divinycell and approximately 13 for Rohacell. The second reason is that the critical flaw size comes out as a rather small number, using the fracture toughness of the materials used. If so, the number of cycles to failure will be

$$N_f \approx \frac{1}{C\Delta\sigma_0^m (\pi)^{m/2}} \left( \frac{(a_0)^{1-m/2}}{m/2 - 1} \right) \quad (6)$$

For example, if we consider a sheet of H100 with a central crack. The critical crack length can be evaluated by means of the following; If  $\sigma_{0,\max}$  equals the yield strength (2.37 MPa) and the fracture toughness is approximately  $0.21 \text{ MPa}\sqrt{\text{m}}$ , the critical flaw size  $a_f$  becomes only 2.5 mm. This is commonly much smaller than typical test specimen dimensions. Eq.(6) can now be rewritten to a Basquin's law type equation

$$\Delta\sigma_0 \approx \frac{(a_0)^{1/m-1/2}}{C^{1/m} \sqrt{\pi}} (m/2 - 1)^{-1/m} N_f^{-1/m} \quad (7)$$

or

$$\sigma_{0,\max} \approx \frac{(1-R)(a_0)^{1/m-1/2}}{C^{1/m} \sqrt{\pi}} (m/2 - 1)^{-1/m} N_f^{-1/m} \quad (8)$$

where  $\sigma_{0,max}$  is the maximum stress. The slope of this curve is  $-1/m$  and is thus linked to the slope of the Paris' law curve. This equation has limited validity, i.e., we go from high-cycle fatigue described by Basquin's law, to low-cycle fatigue when the maximum applied stress exceeds the yield strength  $\sigma_y$ , here defined as  $\sigma_{0,2}$ . This occurs when

$$N_{f,limit} \approx \frac{(1-R)^m}{C\sigma_{0,2}^m (\pi)^{m/2}} \left( \frac{(a_0)^{1-m/2}}{m/2-1} \right) \tag{9}$$

Now we run into some problems since both  $N_{f,limit}$  and  $a_0$  are unknown. The way to proceed proposed in here is to perform at least one tension-tension fatigue test at which  $\Delta\sigma_{0,max} = \sigma_{0,2}$  to get an estimate for  $N_{f,limit}$ . Once this number is established, the initial flaw size can be calculated. This is done by converting eq.(9) to

$$a_0 \approx N_f^{\frac{1}{1-m/2}} (m/2-1)^{\frac{1}{1-m/2}} C^{\frac{1}{1-m/2}} \Delta\sigma_0^{\frac{m}{1-m/2}} (\pi)^{\frac{m}{2(1-m/2)}} \tag{10}$$

We can get the initial flaw size by means of knowing the Paris' law constant  $C$ , the Paris' law exponent  $m$  and one point on the S-N curve. This point is chosen as the number of cycles to failure when the maximum stress equals the yield strength of the foam and thus requires testing only up to a finite number of cycles. This S-N curve is then valid for cycle numbers in the high-cycle fatigue regime, i.e., down to  $N_{f,limit}$ .

## 7. RESULTS AND DISCUSSION

The results from the tension-tension fatigue testing Divinycell H60, H100 and H200 are presented in Figure 4a as a log stress vs. log number of cycles to failure. The horizontal line corresponds to the yield stress ( $\sigma_{0,2}$ ) of the material. In order to get the synthetic S-N curve for the material the following data has been used; firstly, the number of cycles to failure for the specimens tested at a maximum stress  $\sigma_{max} = \sigma_{0,2}$  has been used find the initial flaw size,  $a_0$ , through eq.(10). For Divinycell, the number of cycles to failure at yield stress is approximately 10000, as seen from Figure 4a, but this is a lower limit. This gives an initial flaw size in order of 0.2 mm. For Rohacell the corresponding transition from low-cycle to high-cycle fatigue is around 100 cycles as a conservative estimate and this gives an initial flaw size of approximately 0.3 mm.

Figure 4b shows the results re-plotted by normalising the stress with the relative density. The relative density normalised S-N curves appear to collapse into one single master curve. The slightly different slopes on the predicted S-N curve (straight lines in Figure 4) are due to that the Paris' law exponents are slightly different for the different densities.

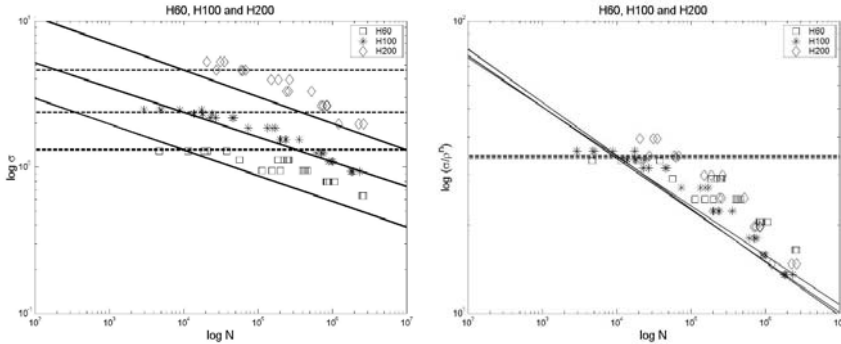


Figure 4. S-N curves for (a) H60, H100 and H200. (b) Stress normalised S-N curves for all materials.

## 8. CONCLUSIONS AND FUTURE WORK

The main aim with this investigation was to use Paris' law data to predict the fatigue life of foams under tension loading. Paris law data for the foams were used together with one tension-tension fatigue test to predict the S-N curve for the foam. The correlation between this prediction and the experimental obtained fatigue data is quite satisfactory. It is further seen that static properties of a certain class of foams can be normalised with the relative density and a unique, density independent property can be obtained. The same normalisation can also be performed on Paris law relations and fatigue data. The conclusion of this is that the fatigue life in tension for one class of foams appears to be possible using one (or perhaps a few) tension-tension fatigue tests at e.g. yield stress and the crack propagation data for one foam quality. These tests are both fairly fast and cheap to perform. Fatigue data can then be predicted for other densities using relative density normalisation. Although only test results for Divinycell H-grade foams are presented herein, the same approach appears feasible for Rohacell WF-grade foams.

The long-term aim of this project is to be able to predict the fatigue life of foams, under general loading conditions, without the need for extensive testing. This could be particularly important in the design process of

structures. Secondly, gaining certainty into issues like fatigue, safety factors could potentially be decreased thus saving structural weight.

The next problem treated is fatigue under compression loading. Fatigue tests will be performed at reversed loading with reference to the compressive strength of the foam. The reason for this is the correlation with shear loading [7], being a combination of tension and compression. From this, comparisons can be made with fatigue test results from beams in which the core is mainly subjected to shear fatigue loading.

## ACKNOWLEDGEMENTS

The financial support for this investigation has been provided by The Office of Naval Research (ONR) through programme officer Dr. Yapa D.S. Rajapakse (Grant No. N00014-99-1-0316). DIAB Sweden and Röhm GmbH are also acknowledged for supplying the materials. Special thanks to Anders Bäckman for performing the tension-tension fatigue testing.

## REFERENCES

1. Gibson L.J. and Ashby M.F., *Cellular Solids – Structure and Properties*, 2nd edition, Cambridge University Press, Cambridge, UK, 1997.
2. *Divinycell H-grade, Technical Manual*, DIAB AB, Laholm, Sweden, [www.diabgroup.com](http://www.diabgroup.com).
3. *Rohacell WF*, Röhm Degussa-Hüls group, [www.roehm.com](http://www.roehm.com)
4. Shipsha A., Burman M. and Zenkert D., “On Mode I Fatigue Crack Growth in Foam Core Materials for Sandwich Structures”, *Journal of Sandwich Structures*, Vol 2, 2000, pp. 103-116.
5. Huang, J.S. and Lin, J.Y. “Fatigue of cellular materials”, *Acta Materialia*, Vol 44, no 1, pp. 289-296, 1996.
6. *Annual Book of the ASTM Standards*, American Society for Testing and Materials, Philadelphia, PA.
7. Burman, M., *Fatigue Crack Initiation and Propagation in Sandwich Structures*, Ph.D. Dissertation, Dept. of Aeronautics, Kungliga Tekniska Högskolan, Chapter 8, Report 98-29, 1998.

# FATIGUE OF PURE AND NANOPHASED SANDWICH COMPOSITES UNDER SHEAR LOADING

Hassan Mahfuz<sup>1</sup>, Shaik Zainuddin<sup>2</sup>, Mohammed F. Uddin<sup>2</sup>, Vijaya K. Rangari<sup>2</sup> and Shaik Jeelani<sup>2</sup>

<sup>1</sup>*Department of Ocean Engineering, Florida Atlantic University, Boca Raton, FL 33431, USA, E-mail: hmahfuz@oe.fau.edu*

<sup>2</sup>*Center for Advanced Materials (T-CAM), Tuskegee University, Tuskegee, AL 36088, USA*

## Abstract

Sandwich structures are widely used in marine, automotive, and aerospace structures because of their high stiffness and strength to weight ratio. In all of these applications, core plays an important role in controlling the extent of damage in sandwich structures especially when subjected to repetitive dynamic loading. When a sandwich structure is subjected to transverse loads, the face sheets carry bending moments as tensile and compressive stresses and the core carries transverse forces as shear stresses. The core is typically the weakest part of the structure and is first to fail in shear. Hence strengthening of core materials will essentially enhance the overall performance of sandwich structures. In this study foam core materials have been strengthened with the infusion of acicular nanoparticles such as carbon nanotubes and carbon nanofibers in the polymer precursor. This infusion has been carried through a sonic cavitation process. Once the core was modified, sandwich composites were fabricated through a traditional resin transfer molding (RTM) process. Shear fatigue behavior of sandwich composites having both pure and nanophased polyurethane foams as core materials have been investigated. The density of the core materials was identical in both cases. Static shear tests reveal that nanophased foams are more ductile, have higher strength and stiffness, and better crack propagation resistance when compared to pure foams. Shear fatigue tests were conducted at room temperature, at a frequency of 3 Hz and at a stress ratio,  $R = 0.1$ . S-N curves were generated and shear fatigue characteristics were determined. The number of cycles to failure for the nanophased sandwich was substantially higher than that of the neat ones. SEM micrographs show that the cell structures of nanophased polyurethane foams are stronger and larger in size with thicker walls and edges. These stronger cell structures subsequently strengthen the sub interfaces when the sandwich composite is fabricated. The high intrinsic toughness of the sub interface delays the initiation of fatigue cracks and thereby increases the fatigue life of the nanophased sandwich composites. There was no volume change for either the neat or the nanophased foam during shear deformation, and the material failed by shearing in the vicinity of the centerline of the specimen along

the longitudinal axis. In both cases numerous  $45^\circ$  shear cracks formed across the width and the cracks traversed through the entire thickness of the specimen signaling the final failure event during fatigue.

**Keywords:** nanoparticles, polyurethane foam, sandwich, fatigue, shear.

## 1. INTRODUCTION

In most of the applications, sandwich beams are subjected to repetitive transverse loading. Because of this, sandwich beams constituents are subjected to various kinds of loading. The face sheets exhibit membrane tension/compression behavior and the core exhibit the most critical stress i.e. pure shear [1]. The most common failure of sandwich construction is the core shear failure that occurs when the shear stress reaches its critical value [2]. Many researchers have extensively studied sandwich structures emphasizing face sheets and it is generally agreed that behavior of face sheets is well known. On the other hand, comparatively very less has been done to study the core behavior of sandwich structures. It has been demonstrated over time [3, 4] that either flexural or shear loading, of core basically controls the failure of the sandwich. Studies [5, 6] on the flexural behavior of foam core sandwiches showed that numerous cracks initiated in the core sub-interface area. These cracks grew together and propagated on the compression side of the beam, immediately below the sub-interface. Cracks then propagated in the core, parallel to the beam. Shipsha et al. [7] performed tests on H100 foams and found that crack continuously propagated along the interface in the core material below the resin rich cells with diagonal secondary fracture cracks. In all these cases, the core shear stresses produced global deformation. Therefore it is understood that if the core shear properties can be enhanced, the overall performance of the sandwich structure will be improved.

Also in recent years, infusion of nanoparticles into polymer foam cores showed considerable enhancement in mechanical properties [8–11]. It has been shown that by infusing a small percentage of nanoparticles in the foam core, materials, the static properties of sandwich structures can be improved significantly [5]. Similar trend has been shown when nanophased foam core sandwich structure tested under compression and high strain loadings.

In this study, polyurethane foam core properties have been modified by dispersing nanoparticles. Modified core materials were then used to fabricate sandwich composites using the VARTM process. In parallel, control sandwich panels were also fabricated using core materials without any particle infusion. Quasi-static and fatigue behavior of these sandwich composites have been studied under shear loading.

## 2. MANUFACTURING OF SANDWICH COMPOSITES

The following materials systems, as shown in Table 1, were used for making various sandwich panels:

Table 1. Materials used in the sandwich composites.

Face sheet (skin)		Core materials		
Fiber		Resin	Foam	Nanoparticles (1%w)
No. of layers	Type	Epoxy SC 15	Polyisocyanurate with density 80 kg/m <sup>3</sup>	CNF
3	S-2 Glass 240 F			Dia: 200 nm, aspect ratio: 500

The manufacturing of sandwich composites was carried out in three steps; the first was the dispersion of nanoparticles into liquid polyurethane, the second, casting of the foam (core materials) and the final, fabrication of sandwich panels. In addition, a number of sandwich panels were also made with pure polyurethane foam without having any nanoparticle infusion.

### 2.1 Dispersion of nanoparticles into liquid polyurethane

The liquid foam used in this investigation is Polyisocyanurate. It has two parts, part A (Diphenylmethane Diisocyanate) and part B (Flurocarbon blown Polyol). Part-A was selected for infusion of nanoparticles since it is less reactive than part-B. Carbon nanofibers (CNF) nanoparticles were first carefully measured along with Part-A to have a 1% loading by weight. The mixing was carried out in a Sonic Vibra Cell ultrasonic liquid processor (Ti-horn, 20 kHz, 100W/cm<sup>2</sup>) as shown in Figure 1 for about 30 minutes at 5°C temperature. At this time it was found that nanoparticles were uniformly dispersed in Part-A. In order to avoid temperature rise during sonication, external cooling system was used. After infusion of nanoparticles, the modified Part-A was mixed with Part-B at a ratio of 48:52 by using a high speed mechanical stirrer. The mixture was then cast in a steel rectangular mold as shown in Figure 2. The mold was heated to about 65°C prior to pouring the mixture. After about 8–9 hours the cast foam was demolded and post cured for about 20 minutes at 80°F.

### 2.2 Sandwich fabrication

The resin transfer molding (RTM) process was employed to fabricate the sandwich panels. Since both the top and bottom face sheets had to be infused simultaneously, a co-injection resin infusion process was used to process the sandwich composites. A schematic of the co-injection process is shown in Figure 3. Dry fabric preforms with required orientations were first laid out on the top of a flat aluminum tool. The fabric used in this investigation was plane



Figure 1. Ultrasound mixing.

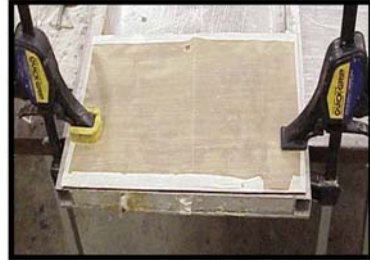


Figure 2. Casting of foam in a rectangular mould.

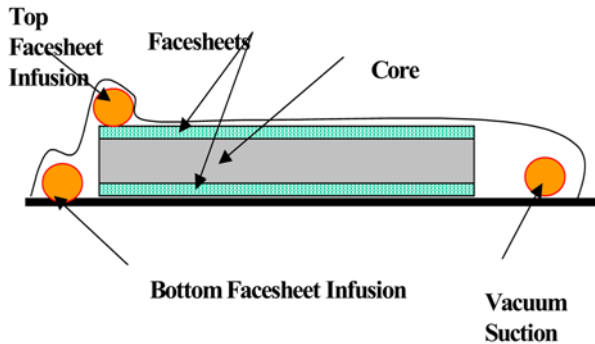


Figure 3. CIRT process for sandwich manufacturing.

weave S2-Glass fibers. Three layers of fabrics were used for each face sheet. The core was then placed on the top of the bottom face sheet fabrics, and upon which the preforms for the top face sheets were stacked. Two types of core materials were used during the fabrication; one was pure polyurethane, and the other was doped with CNF. After stacking, infusion lines were installed and the assembly was vacuum bagged. Before infusion the system was debulked for several hours. SC-15 epoxy resin (Part-A: epoxy, Part-B: Hardener, Alkyl Polyamine) manufactured by Applied Poleramic, Inc. was used in this study. After the resin infusion, the vacuum was kept on until the complete cure took place. No additional adhesives were used for the skin-core bonding, since it developed during the cure process. It is to be noted that the surfaces of the nanophased foams had to be sanded prior to setting them up in the RTM mold. This allowed better adhesion between the core and the skin. Several panels were fabricated in this manner, and were machined for shear characterization.

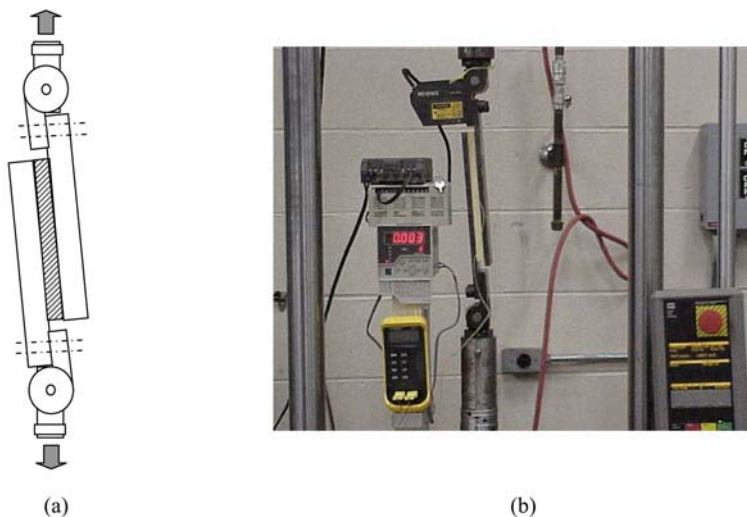


Figure 4. (a) Schematic of shear test fixture. (b) Photograph showing experimental setup.

### 3. EXPERIMENTAL

#### 3.1 Quasi-static shear tests

Five replicate of pure and nanophased polyurethane foam sandwich specimen of dimension 40 mm × 160 mm were cut from 12.5 mm thick panels, using a diamond coated steel blade, as per ASTM C273-61 [12] standard test method. The specimen was bonded between the two parallel loading steel plates as shown in the test set up in Figure 4a which shows a schematic of the shear fatigue test fixture. The arrows indicate the direction of loading. The steel plates were truly parallel since a small deviation in parallelism of the loading plates can cause considerable errors in the calculation of the shear strength and shear modulus. A two-part epoxy, Hysol EA 9309.3 NA was used as the adhesive to bond the foam to the steel plates. The epoxy was allowed to cure at room temperature for a minimum of 48 hours prior to testing. The fixture was fitted into a servo hydraulic testing machine (MTS) equipped with a 100kN load cell as shown in Figure 4b. The tests were conducted at room temperature in displacement control at a crosshead speed of 1.27 mm/min. A Keyence laser displacement unit coupled to a RD-50R controller was installed to measure the sliding movement of the loading plates relative to each other in the direction parallel to the loading plates.

#### 3.2 Fatigue test

Shear fatigue tests were performed at room temperature under load control on the foam specimens at a load ratio of  $R = |P_{\min}|/|P_{\max}| = 0.1$ , using the

MTS machine at a frequency of 3 Hz. The run out cycle number was set at  $10^6$  cycles. Fatigue data for each specimen were generated at stress levels of: 90%, 80%, 70%, 60%, and 50% of the static shear strength.

#### 4. SCANNING ELECTRON MICROSCOPY ANALYSIS

Virgin surfaces were examined in a JEOL JSM 5800 scanning electron microscope. The specimens were glued to an aluminum base and coated with gold to prevent charge build-up by the electrons absorbed by the specimen. Micro-structural analysis were performed on both pure and nanophased polyurethane foams.

### 5. RESULTS AND DISCUSSION

#### 5.1 Static tests

These tests were conducted primarily to obtain strength values for the fatigue tests. The load was applied to the pure and nanophased sandwich specimen via the steel plates as shown in Figure 4a. The laser displacement unit recorded displacement of the moving steel plate relative to the fixed plate. This displacement was used to calculate the shearing strain,  $\gamma$ . Figure 5 shows representative stress-strain ( $\tau$ - $\gamma$ ) curves for pure and nanophased sandwiches. The failure loads of nanophased specimens were higher than the pure foam sandwich specimens. Small cracks were noticed immediately in the core but upon reaching the critical load, the specimen elongated up to a threshold value whereupon these cracks intensified. Rapid shearing of the core occurred at this stage causing failure from the sub-interface section. Similar trend was also noticed with sandwiches made from pure foam.

The stress strain behavior of both nanophased and pure sandwich composites as seen in Figure 5 is more or less identical except that the nanophased sandwich has higher strength and stiffness. Data from static shear tests are shown in tabular form in Table 2.

The shear strength and shear modulus of the nanophased foam sandwiches were approximately 33% and 19% higher than that of the pure foam sandwiches, respectively. An approximation of the area under the stress-strain curves indicates that the energy absorption capability of the nanophased foam sandwich is almost 30% higher than the pure foam sandwich.

Figure 6 shows a schematic of a foam specimen subjected to static shear load. The foam specimen deformed as shown in Figure 6. The first crack initiated at the free edge in the uppermost section of the specimen adjacent to the epoxy interface. The crack then propagated parallel to the plate for approximately 15 mm after which, it kinked into the core moving diagonally toward the opposite end. In a few specimens free edge effects occurred, i.e. the

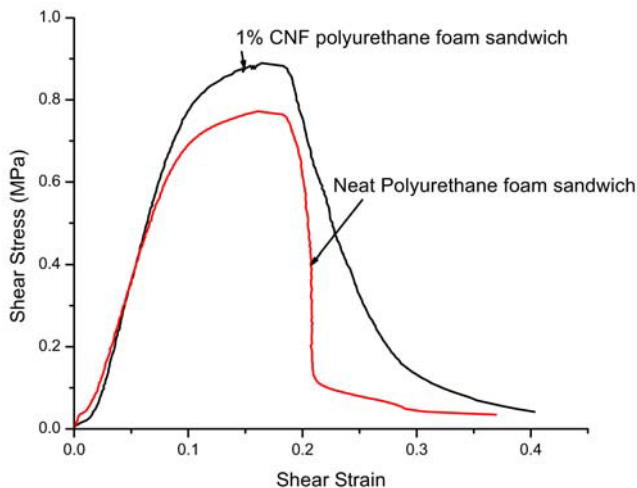


Figure 5. Stress-strain curves for pure and nanophased foam sandwich.

Table 2. Static shear test data.

Property	Neat polyurethane foam sandwich	1% CNF polyurethane foam sandwich	% Improvement
Shear strength (MPa)	0.55	0.83	+33
	0.64	0.81	
	0.66	0.78	
	<b>Ave.: 0.61</b>	<b>Ave.: 0.81</b>	
	<b>Std. Dev. -0.014</b>	<b>Std. Dev -0.02</b>	
Shear modulus (Mpa)	11.7	13.7	+19
	11.9	14.9	
	12.4	14.4	
	<b>Ave.: 12.0</b>	<b>Ave.: 14.3</b>	
	<b>Std. Dev. -0.35</b>	<b>Std. Dev -0.32</b>	

foam specimen tore away from the plate at either of the free ends in the upper corners.

## 5.2 Fatigue Tests

S–N diagram with normalized shear stress is presented in Figure 7.

Under constant amplitude loading many engineering materials exhibit a plateau in the stress life plot typically beyond about  $10^6$  cycles, which was also true in this case. Accordingly, the run out cycle number was taken as  $10^6$  cycles. The fatigue limit was found to be about 55% of the ultimate strength for nanophased specimen and 50% for pure specimen. It is seen in Fig 7 that at each of the stress levels, the number of cycles to failure for nano-

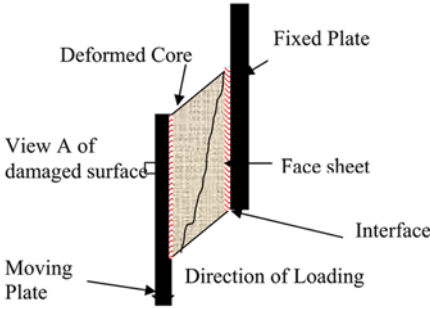


Figure 6. Schematic of deformed specimen showing crack propagation.

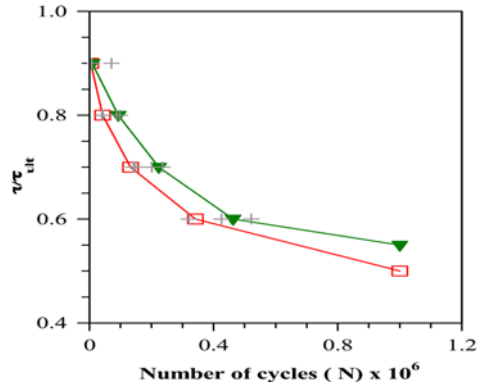
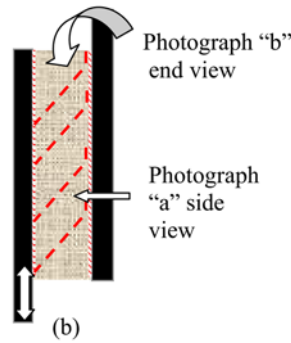


Figure 7. S-N curves for neat and nanophased specimens. Stress ratio,  $R = 0.1$  and frequency = 3 Hz.



(a)



(b)

Figure 8. Side views of a failed nanophased foam sandwich and its schematic.

phased foam was higher than that of pure foam specimen. The damage formation process in both the nanophased foams and pure foams were similar.

Shortly prior to failure, numerous small cracks formed in the foam just below the interface area on the side of the fixed plate (side b). The cracks then coalesce into a more dominant crack, which propagate parallel to the steel plate. In the next stage, the crack kinks at an angle of approximately 45° into the core, advancing towards the moving plate (side a). The crack arrests at the interface area (side a), apparently having insufficient energy at the crack tip to penetrate the cured epoxy. Upon the onset of the first crack, similar cracks appear in the core on side b at fairly equidistant locations along the length of the specimen. Each of these cracks propagates in the same way as the first one until final tearing and separation from the face sheet. Figure 8 shows the damaged surface of nanophased foam specimen.

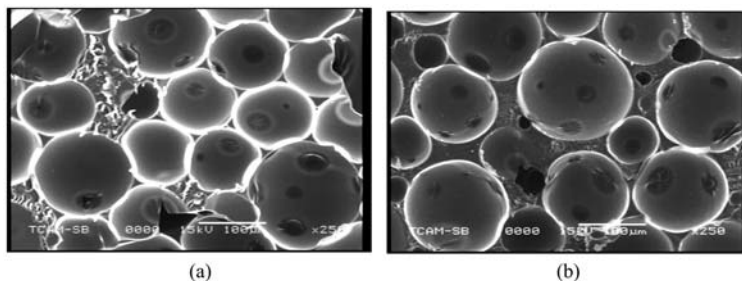


Figure 9. Micrographs of cell structures: (a) neat foam and (b) nanophased foam.

It is believed that as the resin gets filled into the partially opened cells, it soaks around and down the cell walls and edges. When the resin is cured, these soaked cell materials become stronger than the regular dry foam cells just underneath. A sub-interface is therefore created between these so-called soaked and dry foam cells, which are apparently weaker than the actual core-skin interface mentioned earlier. It is also known that infusion of nanoparticles acts as catalyst and increases the cell size and edge thickness which is shown in SEM micrographs of Figure 9. This might be the reason that formation of cracks in nanophased foams during fatigue is somewhat delayed as a result of more resin absorption in thicker cell walls and edges when compared with pure polyurethane foams.

### 5.3 SEM analysis

To investigate the microstructural effect of nanoparticles infusion in polyurethane foam, SEM analyses were carried out on both the pure and nanophased foam as shown in Figures 9a and b. The micrographs show that both foams have a fairly uniform distribution of regular cells. The cell sizes are found to be larger for the nanophased polyurethane foam by about 30%.

The cell walls and cell edges of the nanophased foams appear thicker than the pure foam. This was estimated from enlarged photographs (same scale) using a caliper. It was found that on an average of five specimens that the cell wall thickness of the pure and nanophased foams was  $3\ \mu\text{m}$  and  $5.3\ \mu\text{m}$  while the cross sectional area of the cell edges were approximately  $217\ \mu\text{m}^2$  and  $345\ \mu\text{m}^2$ , respectively. Stronger cell walls and edges eventually make the nanophased foam tougher and less prone to premature failure.

## 6. SUMMARY

In summary, this study reveals that

1. Nanoparticle infusion improves the static shear strength and stiffness of the sandwich composites by 20–30% over the over their neat counter-

parts.

2. This improvement is carried also to the cyclic loading when the sandwich composites are subjected to shear fatigue.
3. The improvement in the performances both at static and cyclic loading comes from the fact that nanoparticle infusion causes significant changes to the cell dimension, thereby strengthening the cell walls and cell edges.
4. Changes in the cell geometry and dimension are due to the presence of nanoparticles which apparently work as catalysts and control the rate of formation of CO<sub>2</sub> during the blowing reaction.
5. There is no significant difference in the failure mechanisms of sandwich composites due to nanoparticle loading, but because of the relatively stronger core materials, the initiation of failure is significantly delayed in nanophased sandwich composites.

## REFERENCES

- [1] Zenkert, D., "The Handbook of Sandwich Construction", EMAS Ltd. Solihull, UK, 1995.
- [2] Gdoutos, E.E., Daniel, I.M. and Wang, K.A., "Failure of Cellular Foams under Multiaxial Loading" *J. of Comp. Part A*, Vol. 33, 2002, pp. 163–176.
- [3] Kulkarni, N., Mahfuz, H., Jeelani, S. and Carlsson, L.A., "Fatigue Crack Growth and Life Prediction of Foam Core Sandwich Composites under Flexural Loading", *Composite Structures*, Vol. 59, No. 4, March 2003, pp. 499–505.
- [4] Krishnan Kanny, Hassan Mahfuz, Tonnia Thomas and Shaik Jeelani, "Static and Dynamic Characterization of Polymer Foams Under Shear Loads" *J. of Composite Materials*, Vol. 38, No. 8, 2004.
- [5] Mahfuz, H., Islam, M.S., Rangari, V.K., Saha, M.C. and Jeelani, S., "Response of Sandwich Composites with Nanophased Cores under Flexural Loading", *Composites Part B: Engineering*, Vol. 35, Nos 6–8, September–December 2004, pp. 543–550.
- [6] Kanny, K., Mahfuz, H., Carlsson, L.A., Thomas T. and Jeelani, S., "Dynamic Mechanical Analyses and Flexural Fatigue of PVC Foams", *Composite Structures*, Vol. 58, No. 2, November 2002, pp. 175–183.
- [7] Shinsa, A., Burman, M. and Zenkert, D., "Interfacial Fatigue Crack Growth in Foam Core Sandwich Structures", *International Journal of Fatigue & Fracture of Engineering Materials & Structures*, Vol. 22, 1999, pp. 123–131.
- [8] Reynaud, E., Gautier, C. and Perez, J., "Nanophases in Polymers", *Review Metallurgie*, Vol. 96, 1999, pp. 169–176.
- [9] Chun, L.W., Ming, Q.Z., Min, Z.R. and Klaus, F., "Tensile Performance Improvement of Low Nanoparticle-Filled Polypropylene Composites", *Composites Science and Technology*, Vol. 62, 2002, pp. 1327–1340.
- [10] Mahfuz, H., Chisholm, N. and Jeelani, S., "Mechanical Characterization of Nanophased Carbon Composites", 2002 ASME winter Annual Meeting, New Orleans, Louisiana.
- [11] Mahfuz, H., Rangari, V., Islam, M., and Jeelani, S., "Fabrication, Synthesis and Mechanical Characterization of Nanoparticles Infused Polyurethane Foams", *Composites Part A: Applied Science and Manufacturing*, Vol. 35, 2004, pp. 453–460.
- [12] ASTM Standard: C 273-61 Standard Test Methods for the Shear Properties in Flatwise Plane or Flat Sandwich Constructions or Sandwich Cores.

# SEA WATER EFFECTS ON POLYMERIC FOAMS AND THEIR SANDWICH LAYUPS

Y.J. Weitsman, X. Li and A. Ionita

*Mechanical, Aerospace and Biomedical Engineering Department, The University of Tennessee, Knoxville, TN 37996-2030, USA*

**Abstract** The ingress of sea water and its damaging effects on polymeric foams was investigated experimentally and explained by a mechanics model. Similarly, the reduction in delamination toughness at the core/facing interface was recorded and explained by means of fracture mechanics.

**Keywords:** foams, sandwich layups, effects of sea water.

## 1. INTRODUCTION

Sandwich layups, consisting of closed cell polymeric foams and fiber reinforced polymeric facings are utilized in naval craft. This article presents an investigation regarding some effects of sea water on such layups.

## 2. SEA WATER INGRESS AND INDUCED DAMAGE IN POLYMERIC FOAMS

It was noted by means of several experimental methods [1] that sea water remains concentrated in the outer layers of exposed foams. In addition to earlier data [1], this conclusion was confirmed by weight-loss measurements, recorded during the re-drying of several slices cut from a pre-immersed cubic foam sample plotted in Figure 1. It can be seen that the most significant weight loss occurred in the outmost layer.

Typical observations of sea water induced damage are shown in Figures 2a, b, with a comparative view of a dry and undamaged foam given in Figure 2c. Note the swelling of the walls and pitting at the bottom of exposed cells.

It was also recorded that sea water induced expansional strains of  $\varepsilon_H = 2.8\%$  in H100 and  $0.4\%$  in H100 and H200 PVC foams, respectively. The comparable value for composite facings is  $0.15\text{--}0.2\%$ .

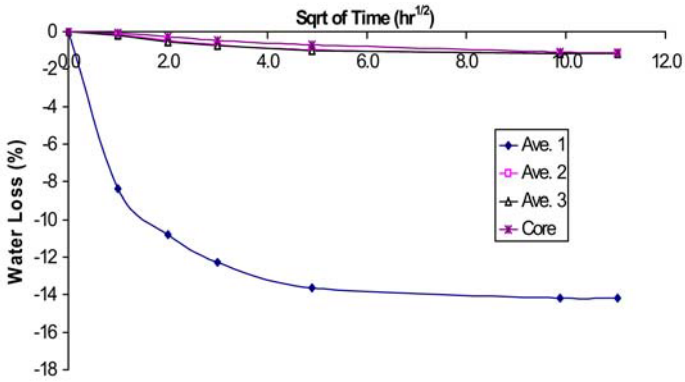


Figure 1. Weight loss during the re-drying of several layers at various distances from the exposed boundary. Significant loss was confined to the outer layer.

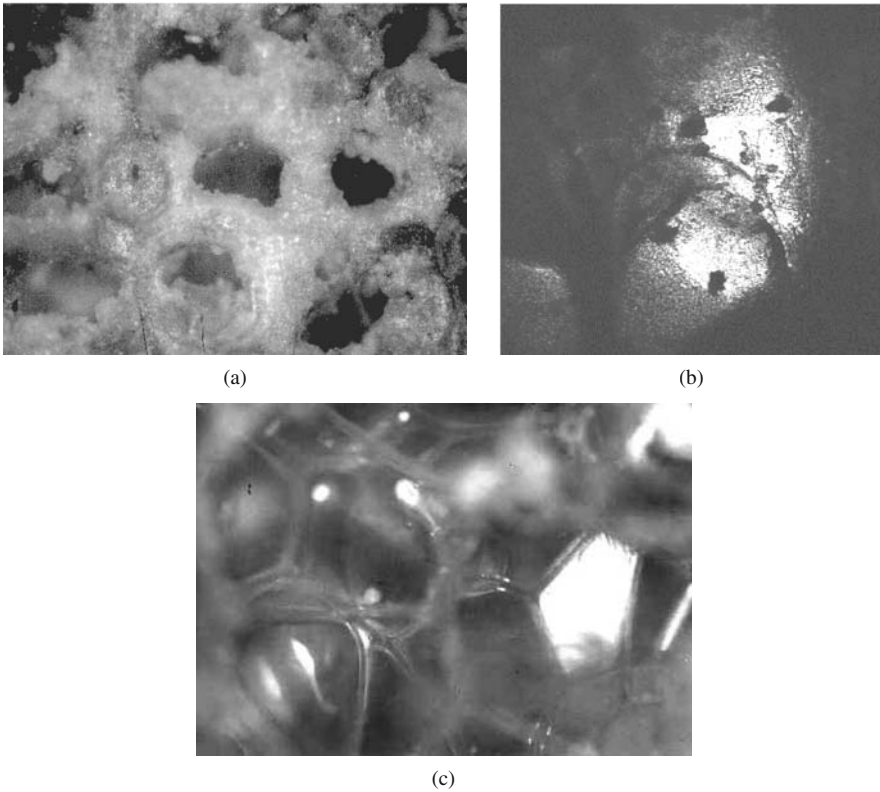


Figure 2. Undamaged PVC foams and sea-water induced damage in the same foam materials. (a) Sea-water causes swelling of foam cell walls. (b) A confocal microscope photograph shows pits forming at the bottom of a cavity (2.8 mm below the surface). (c) Undamaged dry PVC foams.

### 3. A MODEL OF SEA WATER INDUCED DAMAGE IN POLYMERIC FOAMS [2]

The modeling of damage utilizes a Voronoi cell configuration generated in a way to simulate observed foam structure. It is assumed that sea water instantly penetrates the outermost, exposed outer cells and then diffuses across those walls to their neighboring cells. In view of the exceedingly small wall thickness,  $\delta = 10^{-2}$  mm, saturation occurs within about one hour, which can be considered instantaneous relative to the overall duration of the water ingress process in the much thicker foam core. The aforementioned saturation is associated with wall swelling. However, since wall extension is constrained by the undeformed dry interior, it follows that the aforementioned neighboring walls are subjected to compression.

Akin to all polymers, water highly enhances the creep and relaxation of PVC, whereby it is possible to express its time dependent relaxation modulus  $E(t)$  by

$$E(t) = A/(1 + at^n), \quad t \geq 0, \quad (1)$$

where  $t$  denotes time.

Failure of exposed walls is assumed to occur by buckling, when the critical force  $P_{cr}$  attains the value of

$$P_{cr} = kE(t)/\ell^2. \quad (2)$$

The modeling of the failure process required the evaluation of all forces  $P_i$  within the network of Voronoi cellular walls of random lengths  $\ell_i$  and, employing Equations (1) and (2), determine their disparate failure times  $t_i$ . At each failure time, sea water is assumed to penetrate the cell adjacent to the broken wall and start diffusing across newly exposed walls, with  $t \rightarrow t - t_i$  in Equation (1) and with an updated force system  $P_i$  corresponding to the revised Voronoi configuration. In this manner it was possible to generate the sequel of damage progression within the foam. Weight-gain values vs. time can be predicted by adding up the weight of water in all broken cells.

Results, for several random geometries, are shown in Figures 3 and 4. These were based upon  $E_H = 2.8\%$ ,  $a = 0.12$ ,  $n = 0.15$  and  $C = kA = 0.3$ .

### 4. EFFECT OF SEA WATER ON CORE/FACING DEBOND

The debond energy was recorded for H100 and H200 PVC foams and glass/vynil ester composite facing by means of a custom made debonding mechanism [1]. Fracture toughness was evaluated from sequentially recorded load-displacement data at increasing crack lengths for both dry and immersed states. However, in order to ascertain the presence of "wet" crack fronts it was ne-

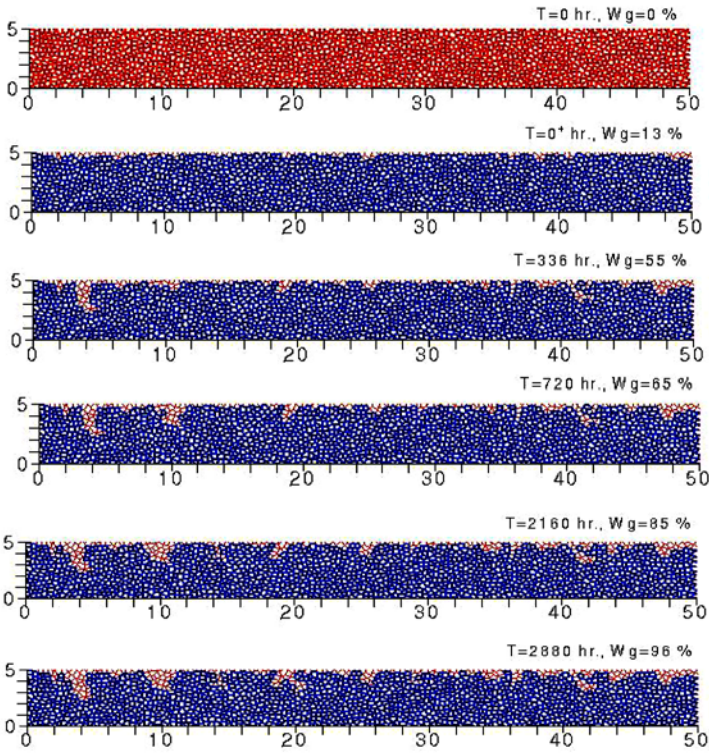


Figure 3. Predicted profiles of water ingress into cellular foam after several exposure times.

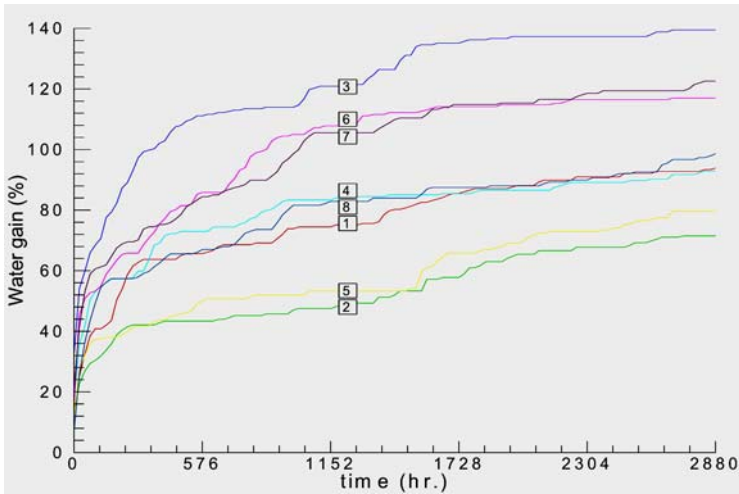


Figure 4. Predicted weight gains in cellular foams for several random selections of Voronoi cellular configurations.

Table 1. Debonding fracture toughness data.

Status	H100		H200	
	$G_{IC}$ (J/m <sup>2</sup> )	$\Omega$ (°)*	$G_{IC}$ (J/m <sup>2</sup> )	$\Omega$ (°)*
Dry	505	~10	1258	~-8
P-Wet**	338	~5	1077	~-15
F-Wet**	424	~5	1038	~-3

\*Negative values of the angle  $\Omega$  indicate crack inclination towards the face/core interface line.

\*\*P-Wet denotes partially wet and F-Wet fully wet.

cessary to re-immerses all exposed samples at each intermediate crack length. Results are summarized in Table 1 [1].

The aforementioned results were confirmed by finite element stress analysis, which enabled the further evaluation of modes I and II components as well as crack orientation angles. These computations explained the observed tendency of debonding cracks to remain closer to the interface in the “wet” case than in the dry circumstance.

A similar investigation is currently in progress for carbon reinforced composite facings.

## 5. CONCLUDING REMARKS

It has been shown that exposure to sea water damages the structure of cellular foams and degrades the delamination fracture toughness at the core/facing interfaces of sandwich layups. However, those detrimental effects are confined to the outer layers of the foams and the near vicinities of crack tips.

## ACKNOWLEDGEMENT

This research was supported by ONR Contract N00014-00-1-0586, under a program managed by Dr. Y. Rajapakse.

## REFERENCES

- [1] Li, X. and Weitsman, Y.J., “Sea Water effects on Foam-cored Composite Sandwich Layups”, *Composites, Part B*, 35, 2004 pp. 451–453.
- [2] Ionita, A. and Weitsman, Y.J., “A Mechanics Model for the Ingress of Sea Water into Cellular Polymeric Foams”, in preparation.

# **MODELLING, ANALYSIS AND DESIGN**

# SANDWICH PLATES: STRESSES, DEFLECTION, BUCKLING AND WRINKLING LOADS

## *A Case Study*

H.-R. Meyer-Piening  
*ETH Zurich, IMES, Switzerland*

**Abstract** This paper deals with the linear static and buckling analysis of an asymmetric and orthotropic stiffened 3-layered square sandwich plate. Three different analytical formulas (Model 1, 2 and 3) have been taken from Ref. [1], slightly modified to account for unequal faces and different Poisson's ratios and applied to a square sandwich plate of fixed dimensions but different face layer thickness. The obtained deflections and buckling loads are compared with the results of a 3D analysis [2] and of Finite Element calculations. Objectives are to evaluate the limits of validity of the formulas in view of thick face layers and orthotropic properties. The properties of the two considered specimen are listed in Tables 1 and 2. The obtained results might serve as benchmark for further studies.

**Keywords:** sandwich plates, plate deflections, plate buckling, wrinkling.

## 1. INTRODUCTION

Available closed form solutions to the linear analysis of sandwich plates are mainly limited to isotropic material properties and symmetric lay-up. On the basis of a three-dimensional analysis (elasticity solution) a case study is performed to provide insight into the limits of applicability of the published formulas. This study is based on the equations (10.13a), (10.13b), (10.14), (10.44) and (10.46) of Ref. [1]. Two specimens are investigated, the dimensions and properties of which are given in Tables 1 and 2. Both specimens are square plates of 1 by 1 m and 40 mm total thickness, being simply supported along all edges. Specimen 1 has isotropic material properties while Specimen 2 is heavily stiffened in x-direction. Considered load cases are: Case "q" (constant pressure), Case "P" (constant pressure over a centered small rectangular area). The deflections at the plate center will be evaluated for these cases, as well as instability loads. A crosscheck with results obtained from two different FE models is conducted.

Table 1. Data for specimen 1.

Layer	$E_x$	$E_y$	$E_z$	$G_{xz}$	$G_{yz}$	$G_{xy}$	$\nu_{xz}$	$\nu_{yz}$	$\nu_{xy}$
1	70'000	70'000	70'000	26'900	26'000	26'000	.28	.28	.28
2	27	27	27	10.5	11	11	.18	.18	.18
3	70'000	70'000	70'000	26'900	26'000	26'000	.28	.28	.28
$a$	$b$	$t_1$	$t_2$	$t_3$	$h_1$	$h_2$	$h_3$	$m, n$	$p$
1000	1001	var.	var.	var.	$= t_1$	$t_1 + t_2$	$H = 40$	$\leq 61$	$-0.025$

Table 2. Data for specimen 2.

Layer	$E_x$	$E_y$	$E_z$	$G_{xz}$	$G_{yz}$	$G_{xy}$	$\nu_{xz}$	$\nu_{yz}$	$\nu_{xy}$	$\nu_{yx}$
1	135'000	10'000	10'000	3'800	3'800	3'500	.27	.27	.27	.02
2	27	27	27	10.5	11	11	.18	.18	.18	.18
3	135'000	10'000	10'000	3'800	3'800	3'500	.27	.27	.27	.02

## 2. SPECIMENS

The specimens are defined in Tables 1 and 2, assuming a variation of the face layer thickness with a thickness ratio of typically 1:5 or 1:10; the load is applied on the thinner face ( $z = H$ , linear denting effect in the elastic core).

## 3. ANALYSIS AND RESULTS

### 3.1 Original equations

The deflection pattern due to a harmonic pressure distribution is taken from Ref.[1] and labeled as Model 1, ref. equ. (10.12)<sup>1</sup>, Model 2, ref. equ. (10.13b) and Model 3, ref. equ. (10.14):

$$w = \sum_{n=1}^{\infty} \sum_{m=1}^{\infty} \frac{q_{mn}(1 - \nu^2)}{D} \frac{1 + \frac{D}{S(1-\nu^2)}[\alpha_m^2 + \beta_n^2]}{[\alpha_m^2 + \beta_n^2]^2} \sin(\alpha_m x) \sin(\beta_n y) \quad (1)$$

with  $\alpha_m = m\pi/a$ ;  $\beta_n = n\pi/b$

$$w = \sum_{n=1}^{\infty} \sum_{m=1}^{\infty} \frac{q_{mn}b^4(1 - \nu^2)}{D} \frac{1 + \pi^2\Theta [(mb/a)^2 + n^2]}{\pi^4 [(mb/a)^2 + n^2]^2} \sin(\alpha_m x) \sin(\beta_n y) \quad (2)$$

with  $\Theta = D_0/b^2S$ ;  $D_0 = D - D_{f1} - D_{f2} - D_c$  (1, 2 = faces, c = core)

$$w = \sum_{n=1}^{\infty} \sum_{m=1}^{\infty} \frac{\hat{q}_{mn}}{K_{mn}} \left( 1 + \frac{D_0}{S(1 - \nu^2)} [\alpha_m^2 + \beta_n^2] \right) \sin(\alpha_m x) \sin(\beta_n y) \quad (3)$$

with

$$K_{mn} = \frac{2D_f D_0}{S(1 - \nu^2)^2} [\alpha_m^2 + \beta_n^2]^3 + \frac{2D_f + D_0}{1 - \nu^2} [\alpha_m^2 + \beta_n^2]^2 \quad (4)$$

and

$D_f/(1 - \nu^2)$  bending stiffness of a (wide) face layer per unit width  
 $= Et_f^3/(12(1 - \nu^2))$

$D/(1 - \nu^2)$  bending stiffness of the (wide) sandwich plate per unit width

$D_0/(1 - \nu^2)$  bending stiffness of the (wide) sandwich plate per unit width reduced by the bending stiffness of both faces i.e.,

$$D_0/(1 - \nu^2) = D/(1 - \nu^2) - D_{f1}/(1 - \nu^2) - D_{f2}/(1 - \nu^2)$$

$\hat{q}_{mn}$  amplitude of transverse harmonic load component

$S_x = G_{xz}d^2/t_c$  effective shear stiffness of the plate per unit width:

$d$  distance between the neutral axes of both face layers.

Buckling line loads ( $N_x c r$ ) are obtained from ref.(10.44) and ref.(10.46):

$$\frac{D}{(1 - \nu^2)} [\alpha_m^2 + \beta_n^2]^2 = [\bar{N}_x \alpha_m^2 + \bar{N}_y \beta_n^2] \left[ 1 + \frac{D}{S(1 - \nu^2)} (\alpha_m^2 + \beta_n^2) \right] \quad (5)$$

$$\begin{aligned} \frac{2D_f}{(1 - \nu^2)} [\alpha_m^2 + \beta_n^2]^3 + (D_0 + 2D_f) \frac{S}{D_0} [\alpha_m^2 + \beta_n^2]^2 = \\ [\bar{N}_x \alpha_m^2 + \bar{N}_y \beta_n^2] \left[ \frac{S(1 - \nu^2)}{D_0} + (\alpha_m^2 + \beta_n^2) \right] \end{aligned} \quad (6)$$

The involved bending stiffness constants are defined as follows

$$\frac{D_x}{(1 - \nu^2)} = \bar{D}_x = \sum_{k=1}^3 \frac{E_x^{(k)}}{3(1 - \nu_{xy}^{(k)} \nu_{yx}^{(k)})} [(h_k - z_{sx})^3 - (h_{k-1} - z_{sx})^3] \quad (7)$$

and in  $y$  direction accordingly.  $z_{sx}$  is the position of the elastic centre.

$$\begin{aligned} \frac{D_{xxy}}{(1 - \nu^2)} = \sum_{k=1}^3 \frac{1}{3} \left[ \frac{\nu_{xy}^{(k)} E_x^{(k)}}{(1 - \nu_{xy}^{(k)} \nu_{yx}^{(k)})} + 2G_{xy}^{(k)} \right] \times \\ [(h_k - z_{sx})^3 - (h_{k-1} - z_{sx})^3] = \bar{D}_{xxy} \end{aligned} \quad (8)$$

$\bar{D}_{xxy}$  accordingly:  $\nu_{yx}^{(k)} E_y^{(k)}$ ,  $G_{yx}^{(k)}$ ;  $2\bar{D}_{xy} = \bar{D}_{xxy} + \bar{D}_{xyy}$

Bending stiffness per unit width of a face layer and the core;

(for faces  $k = 1, 3$ , for core:  $k = 2$ . Dashes indicate that  $(1 - \nu^2)$  is accounted for).

$$\frac{D_{fx}^{(k)}}{(1 - \nu_{fxy}^{(k)} \nu_{fyx}^{(k)})} = \overline{D}_{fx}^{(k)} = \frac{E_x^{(k)} \cdot t_k^3}{12(1 - \nu_{fxy}^{(k)} \nu_{fyx}^{(k)})}; \quad k = 1, 3 \quad (9)$$

$$\frac{D_{fxy}^{(k)}}{(1 - \nu_{fxy}^{(k)} \nu_{fyx}^{(k)})} = \overline{D}_{fxy}^{(k)} = \frac{\nu_{fxy}^{(k)} E_x^{(k)} t_k^3}{12(1 - \nu_{fxy}^{(k)} \nu_{fyx}^{(k)})} + \frac{(G_{xz}^{(k)} + G_{yz}^{(k)}) t_k^3}{12} \quad (10)$$

$$\frac{D_{0x}}{(1 - \nu^2)} = \overline{D}_{0x} = \overline{D}_x - \overline{D}_{fx}^{(1)} - \overline{D}_{fx}^{(3)} \quad (11)$$

$$\frac{D_{0y}}{(1 - \nu^2)} = \overline{D}_{0y} = \overline{D}_y - \overline{D}_{fy}^{(1)} - \overline{D}_{fy}^{(3)} \quad (12)$$

$$\frac{D_{0xy}}{(1 - \nu^2)} = \overline{D}_{0xy} = \overline{D}_{xy} - \overline{D}_{fxy}^{(1)} - \overline{D}_{fxy}^{(3)} \quad (13)$$

### 3.2 Proposed equations

Some abbreviations

$$D_{mn} = \overline{D}_x \alpha_m^4 + (\overline{D}_{xy} + \overline{D}_{yx}) \alpha_m^2 \beta_n^2 + \overline{D}_y \beta_n^4 \quad (14)$$

$$D_{0mn} = \overline{D}_{0x} \alpha_m^4 + (\overline{D}_{0xy} + \overline{D}_{0yx}) \alpha_m^2 \beta_n^2 + \overline{D}_{0y} \beta_n^4 \quad (15)$$

$$D_{fmn} = (\overline{D}_{xf1} + \overline{D}_{xf2}) \alpha_m^4 + 2(\overline{D}_{xyf1} + \overline{D}_{xyf2}) \alpha_m^2 \beta_n^2 + (\overline{D}_{yf1} + \overline{D}_{yf2}) \beta_n^4 \quad (16)$$

$$S_{mn} = S_x \alpha_m^2 + S_y \beta_n^2 \quad (17)$$

$$K_{mn} = \frac{D_{fmn} D_{0mn}}{S_{mn}} + D_{mn} \quad (18)$$

$$w = \sum_{n=1}^{n_e} \sum_{m=1}^{m_e} \frac{\hat{q}_{mn} \sin(m\pi x/a) \sin(n\pi y/b)}{1/(1/D_{mn} + 1/S_{mn}) + \overline{N}_{x0} \alpha_m^2 + \overline{N}_{y0} \beta_n^2} \quad (\text{Model 1}) \quad (19)$$

$$w = \sum_{n=1}^{n_e} \sum_{m=1}^{m_e} \frac{\hat{q}_{mn} \sin(m\pi x/a) \sin(n\pi y/b)}{1/(1/D_{0mn} + 1/S_{mn}) + \overline{N}_{x0} \alpha_m^2 + \overline{N}_{y0} \beta_n^2} \quad (\text{Model 2}) \quad (20)$$

$$w = \sum_{n=1}^{n_e} \sum_{m=1}^{m_e} \frac{\hat{q}_{mn} \sin(m\pi x/a) \sin(n\pi y/b)}{K_{mn}/(1 + D_{0mn}/S_{mn}) + \overline{N}_{x0} \alpha_m^2 + \overline{N}_{y0} \beta_n^2} \quad (\text{Model 3}) \quad (21)$$

$$(\overline{N}_{0x} \alpha_m^2 + \overline{N}_{0y} \beta_n^2)_{cr} = \frac{-1}{1/D_{mn} + 1/S_{mn}} \quad (22)$$

$$(\overline{N}_{0x} \alpha_m^2 + \overline{N}_{0y} \beta_n^2)_{cr} = \frac{-K_{mn}}{1 + D_{0mn}/S_{mn}} \quad (23)$$

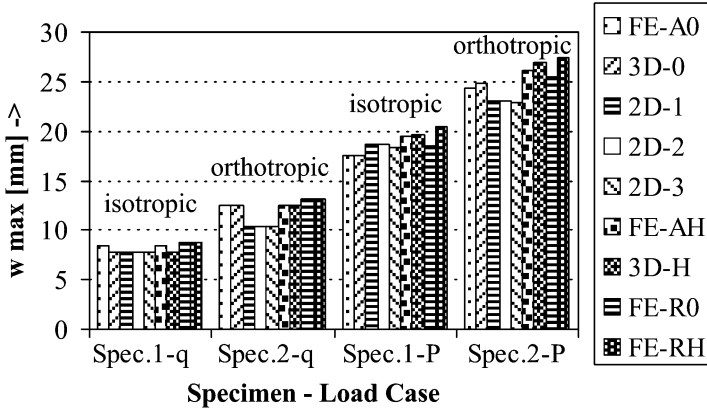


Figure 1. Maximum lateral deflection of the plate for both specimens and for load cases “*q*” and “*P*”.

### 3.3 Elasticity solution

The three dimensional analyses are performed as outlined in Ref [2] with the assumption that all displacements along all edges are zero (hinged boundary). Stiffness properties are defined via engineering constants with  $-\nu_{xy}E_y = -\nu_{yx}E_x$ . The equilibrium conditions in 3 directions are exact fulfilled by assuming harmonic displacement functions in plate directions ( $x, y$ ) and exponential functions through the thickness of each individual layer. No shear constants ( $S$ ) need to be defined and no bending stiffness constants need to be developed. However, so far only simply supported edges can be evaluated. The obtained results include linear denting, resulting from transverse core elasticity, and face wrinkling.

### 3.4 FE analyses

Two Finite Element quarter plate models have been evaluated: The RWTH model (FE-R) of the Institute of Lightweight Structures in Aachen, and the Aalborg model (FE-A) of the Inst. of Mech. Engg., Univ. Aalborg (DK). The first model uses 6391 plate elements MITC4 for modeling each face while in Aalborg core and faces are modeled with volume elements. Typical total number of elements is 36'346 in the former model and up to 77'000 in the latter.

### 3.5 Deflection results

The obtained deflections for cases “*q*” (constant pressure of  $-0.025$  MPa) and “*P*” (a pressure value of  $-2.5$  MPa acting on a centered rectangle of  $a_x, b_y = 60, 80$  mm) are compiled in Figure 1 for both specimens. The thickness

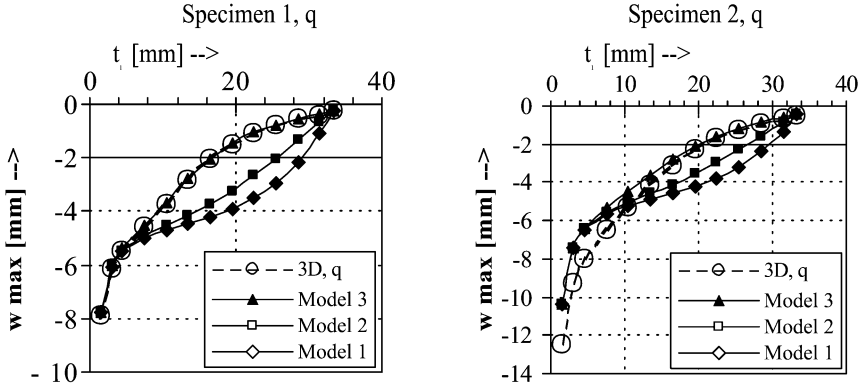


Figure 2. Max. deflection value for the complete range of face thickness,  $t_3 = t_1/5$ , Specimen 1 (left), Specimen 2 (right).

of the face layers is  $t_1 = 1.5$  mm,  $t_3 = 0.3$  mm (loaded face). Shown is the value of the maximum deflection at the center of the plate underneath the lateral load ( $z = H$ ) or at the opposite face ( $z = 0$ ) for the 3D analysis or the Finite Element calculations (FE-R, FE-A). The individual columns relate to FE-A,0 (FE-A analysis,  $z = 0$ ), 3D-0 (3D analysis for  $z = 0$ ). The 2D analysis results are labeled 2D:1 through 2D:3 for the 3 models (Eqs. 19, 20, 21) and, finally, the FE-R and FE-A and the 3D results at  $(a/2, b/2, z = H)$  are shown. The cases evaluated are: Specimen 1-case “q”, Specimen 2-case “q”, Specimen 1-case “P” and Specimen 2-case “P”. It can be seen that for the treated cases with thin faces all results agree quite well, however, heavy unidirectional stiffening (Specimen 2) leads to an overestimate of the stiffness of the structure in the order of 20% when applying Model 1 through Model 3.

When the face layers are thicker, as shown in Figure 2 for a maintained ratio  $t_3/t_1 = 0.2$ , then Model 3 of the 2D (plate) analyses only, developed by Yen et. al. [3], yields satisfying results beyond  $t_1 = 6$  mm. It may be of interest that the approaches 3D, FE and 2D-3 yield acceptable results up to a vanishing core thickness, i.e., the solid plate solution.

### 3.6 Buckling results

Buckling results are compared in Figure 3. The individual columns relate to 2D-3 (Model 3), 2D-1 (Model 1), 3D and FE for the isotropic Specimen 1 and the orthotropic Specimen 2. The latter yields buckling loads, which are somewhat higher than those of the 3D approach. The variation of the thickness of the faces is evaluated in Figure 3 up to vanishing core height. In order to include the “face-only” case where  $t_2 \rightarrow 0$ , the shear stiffness  $S$  has to be modified to account for the shear stiffness of the face material instead and no

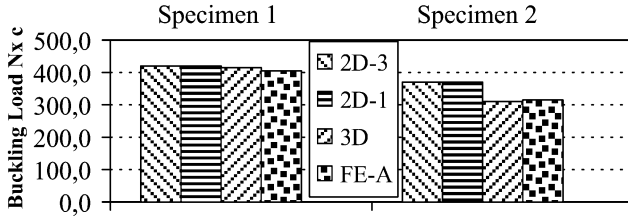


Figure 3. Buckling loads for  $t_1 = 1.5$  mm,  $t_3 = 0.3$  mm, Models 1, 3, 3D and FE, Specimen 1 (left) and 2 (right).

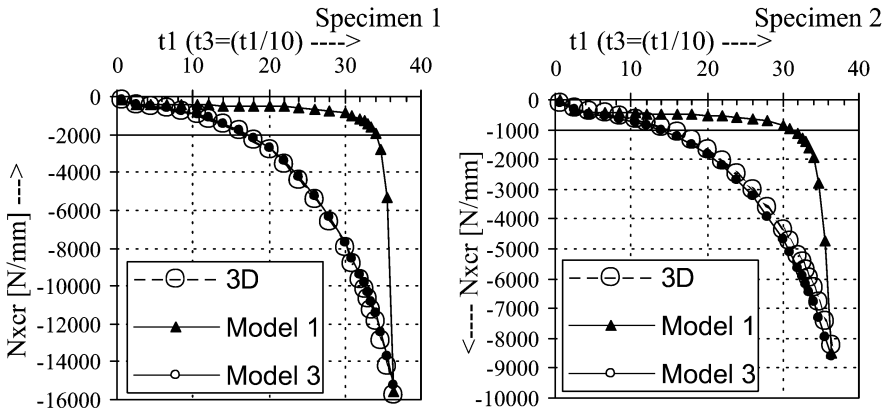


Figure 4. Global buckling load value for the complete range of face thickness, Specimen 1 (left) and 2 (right).

longer to that of the vanishing core. It can be stated that 3D and Model 3 results agree rather well, while Model 1 produces no useful results beyond a thickness of  $t_1 = 6$  mm. Model 1 also contains the phenomenon of shear buckling: With increasing values of  $m$  and  $n$  in Eq. 19 the term  $1/D_{mn}$  becomes negligible and the buckling load converges to the value of the shear constant  $S$ . This result is a consequence of the initial assumption that shear deformation and bending displacements are uncoupled.

### 3.7 Wrinkling results

A two-dimensional analysis cannot evaluate wrinkling modes, while the 3D analysis accounts for individual deflections of both faces. In Figure 5 the analytical buckling stress values for modes with  $m$  half waves in x-direction and  $n = 1$  half wave in y-direction are plotted versus  $m$ , while  $N_y = 0$ . Only the instability mode, which has the absolute smallest buckling stress, is expected to occur. This may be the case for Specimen 1 for which the lowest buckling stress is related to an  $m = 19$ ,  $n = 2$  mode at  $\sigma = -204$  MPa, at which the

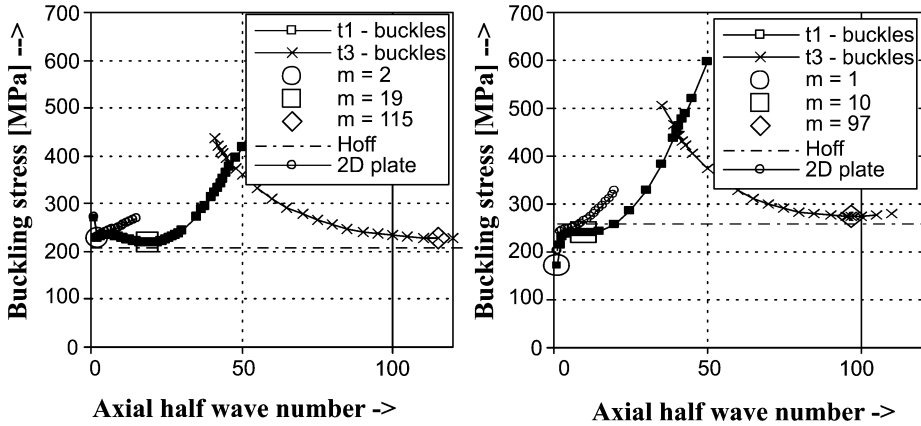


Figure 5. Buckling and wrinkling stresses for  $t_1 = 1.5$  mm,  $t_3 = 0.3$  mm, Specimen 1 (left) and 2 (right).

thick face wrinkles, while at almost the same stress level the thin face wrinkles with  $m = 115$  (Specimen 1) or  $m = 97$  (Specimen 2) half waves. Global buckling of the orthotropic Specimen 2 is predicted to occur at a face stress level of  $-170$  MPa with  $n = 1$ .

For comparison the recommendation of Hoff and Mautner [4],  $\sigma_{wr} = k\sqrt[3]{E_f E_c G_c}$ , is plotted as a straight line in both Figures, implementing a constant value of  $k = 0.76$  in both plots. It should be kept in mind, that no allowance is made for imperfect geometry, load introduction details, geometry or material related non-linearity, so that a further knock-down factor may be needed for design verification.

### 3.8 Stresses

Local stress values have been used to calibrate or crosscheck the validity of FE and 3D calculations. A typical result is plotted in Figure 6. The center of Specimen 1 is at  $x = 0$  and the pressure loaded zone of case “P” ends at  $x = 30$  mm. Layer 1 is positioned at the bottom and layer 3 (0.3 mm thick) is at the top. The interface to the core (layer 2) is labeled “inside” while the outer surfaces are “outside”. In the 3D analysis  $m, n \leq 131$  half waves (= 4356 terms in the series) have been used; the FE mesh size was 2.5 mm. It can be seen that the agreement is satisfying. Furthermore, it can be seen that the maximum local compressive stress level is for this loading close to  $-500$  MPa, thus exceeding the wrinkling stress (Figure 5) by a factor of 2.5.

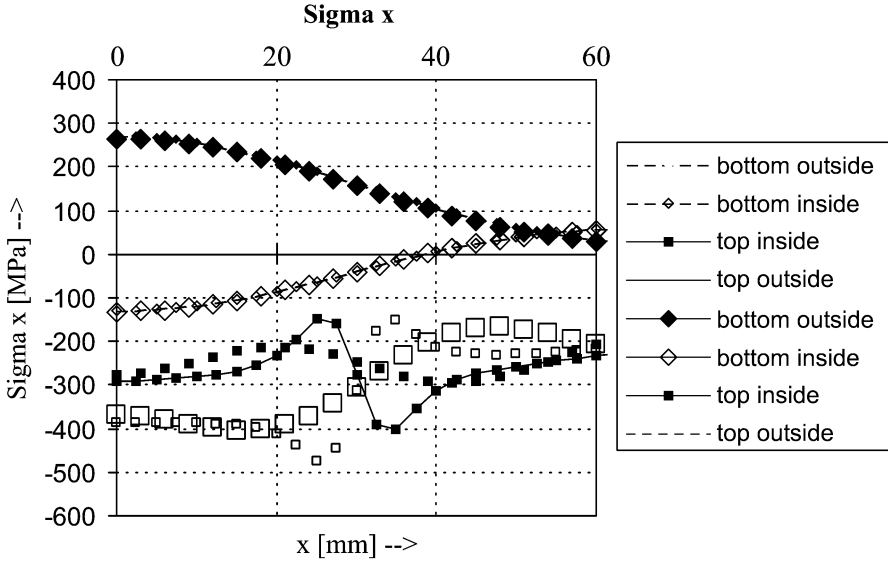


Figure 6. Stresses in x-direction along the center line  $y = 0$ , load case “P”, Specimen 1:  $t_1 = 1.5$  mm,  $t_3 = 0.3$  mm (top). Load zone  $0 \leq x \leq 30$  mm, first 4 symbols FE, others 3D.

#### 4. SUMMARY

The data provided can be considered as benchmark for a linear sandwich plate analysis. The proposed analytical formulas (19 and 21) result in similar deflection and buckling load results as FE and 3D calculations for any  $t_1$  and  $t_3$ . For heavy UD reinforcement the discrepancy can grow to about 20%, underestimating the deflection or overestimating the buckling load.

#### ACKNOWLEDGEMENTS

For conducting the FE analyses, the efforts of Dr. A. Lyckegaard, IME, University of Aalborg, and of Dipl.-Ing. M. Linke, RWTH Aachen, Inst. f. Leichtbau, are gratefully acknowledged.

#### NOTE

1. Equation number of the original reference

#### REFERENCES

[1] D. Zenkert. *An Introduction to Sandwich Construction*. Chameleon Press Ltd., London, UK, 1995.

- [2] H.-R. Meyer-Piening. Application of the Elasticity Solution to Linear Sandwich Beam, Plate and Shell Analysis. *Journal of Sandwich Structures and Materials*, 6(4):295–312, 2004.
- [3] K.T. Yen, S. Gunturkum and F.V. Pohle. Deflections of a Simply Supported Rectangular Sandwich Plate Subjected to Transverse Loads. Technical Report TN 2581, NACA, 1951.
- [4] N.J. Hoff and S.E. Mautner. The Buckling of Sandwich-Type Panels. *Journal of the Aeronautical Sciences*, 285–297, 1945.

# MODELLING OF VISCOELASTICALLY DAMPED SANDWICH BEAMS: A COMPARATIVE STUDY

H. Hu<sup>1,2</sup>, S. Belouettar<sup>1</sup>, E. Daya<sup>2</sup> and M. Potier-Ferry<sup>2</sup>

<sup>1</sup>*Laboratoire de Technologies Industrielles, Centre de Recherche Public Henri Tudor, 70, Rue de Luxembourg, L-4002 Esch sur Alzette, Luxembourg*

<sup>2</sup>*LPMM, Université Paul Verlaine, Ile du Saulcy, F-57040 Metz Cedex, France*

**Abstract** The aim of this paper is to evaluate classical models for sandwich beams. These models are compared in the static and the dynamic fields. In all cases the Finite-Element-based solution is considered as reference.

**Keywords:** sandwich beam, viscoelastic layer, damping, zig-zag models, finite element.

## 1. INTRODUCTION

Vibration and noise control in structures by means of viscoelastically damped sandwich panels has gained wide acceptance, particularly in the aerospace industry. Significant weight, cost, performance, and reliability pay-offs are possible in situations where resonant vibration cannot be avoided. However, the analysis of general structures to predict the damping due to an integral or add-on layered treatment or dumped viscoelastic elements is by no means a routine activity.

Typically viscoelastic damped structures are sandwich structures in which a viscoelastic layer is sandwiched between two identical elastic ones. In his situation, the damping is introduced by important transverse shear in the core. It is due to the difference between in-plane displacement of the elastic faces and also to the low stiffness of the core. Numerical simulation of these structures requires, first the use of an adequate model to obtain a reasonable computational cost, second a proper account of the shearing action of the core. Many investigations have been devoted to the static and dynamic analysis of these structures and various theories and models have been proposed for the two-dimensional modelling of multi-layered plates and shells. The discontinuity of physical-mechanical properties in the thickness direction makes inadequate those theories, which were originally developed for one-layered structures, e.g., the Cauchy–Poisson–Kirchhoff–Love thin plate/shell theory [1–4],

or the Reissner–Mindlin theory [5, 6], as well as higher order models such as the one by Reissner. These theories are, in fact, notable to reproduce piecewise continuous displacement and transverse stress fields in the thickness direction, which are experienced by multi-layered structures [7, 8]. The aim of this paper is firstly to compare these so called classical models (Kirchhoff–Love, see [10, 11]) to a finite element based solution and to assess their efficiency. For these purposes, two problems will be considered:

**Problem-1:** This problem concerns the deformation study of simply supported sandwich beam under a constant transverse loading (three-point bending test).

**Problem-2:** In this problem the free vibration analysis of simply supported viscoelastically damped sandwich beams is considered.

In second stage these models are used to establish the zig-zag models which describe a piecewise continuous displacement field. Indeed, this kind of models permit to get a good approximation of damping properties of viscoelastic damped sandwich structures [12–15]. These modal parameters are classically the natural frequency and the loss factor. These models are compared to the classical ones and the frequencies and the loss factors are the two evaluations element. A qualitative assessment of displacement and stress fields in a single-layered and a multi-layered structure is shown.

## 2. KINEMATICS OF THE MODELS

Consider a three-layer sandwich beam with a viscoelastic core as in Figure 1. Let  $x$  be the mid-surface co-ordinate of the beam and  $z$  is the one transverse to the thickness.  $H_f$  and  $E_f$  are the thickness and Young's modulus of the elastic faces.  $H_c$  is the thickness of the core of which the viscoelastic properties are introduced by a constant complex modulus  $E_c(1 + i\eta_c)$  [12–15].  $E_c$  is the delayed elasticity modulus which is always and is the core loss factor.

The length of the beam and the total thickness are respectively  $L$  and  $H_t$ .

In order to evaluate accurately the shear deformation in the sandwich structure, the classical hypothesis are used [12–15]:

- (1) All points on a normal to the beam axis have the same transverse displacement  $w(x, t)$ .
- (2) The displacement is continuous at the interfaces.
- (3) All points of the elastic layers on a normal have the same rotations.
- (4) The core material is homogeneous, isotropic and viscoelastic with a constant complex modulus.

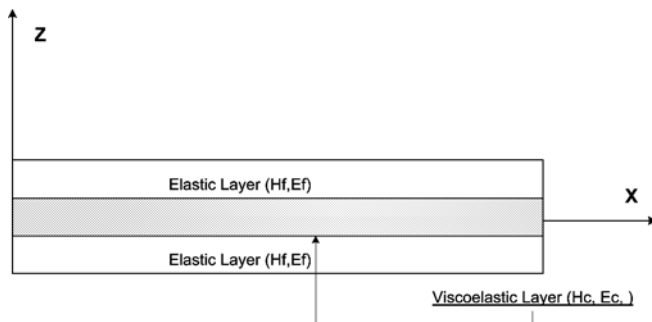


Figure 1. Sketch of a sandwich beam with a viscoelastic layer.

The kinematics of non zig-zag models can be written with a general expression:

$$U(x, z, t) = U_0(x, t) - z \frac{\partial w(x, t)}{\partial x} + f(z)\beta(x, t). \quad (1)$$

$U(x, z, t)$  is the longitudinal displacement and  $U_0(x, t)$  is the longitudinal displacement of the mid-plane of core.  $\beta(x, t)$  is the additional rotation of the normal to the mid-plane,  $f(z)$  can be considered as “shear functions” and can take the following expressions:

- Model-1:  $f(z) = 0$ , Kirchhoff–Love kinematical assumptions;
- Model-2:  $f(z) = z$ , Mindlin kinematical assumptions;
- Model-3:  $f(z) = z - 4z^3/(3H_t^2)$ , Reddy kinematical assumptions;
- Model-4:  $f(z) = H_t \sin(\pi z/H_t)/\pi$ , Touratier kinematical assumptions.

In the Kirchhoff–Love model (Model-1, the transverse displacement field is linear and the transverse strain is null everywhere in the sandwich. Considering the importance of the transverse stress in the modelling of sandwich structures, one can conclude that Model-1 is unsuited for the core modelling, however it can be appropriate for the modelling displacement field in the sandwich faces. In Model-2, proposed by Mindlin, the transverse shear stress is non-null everywhere in the sandwich. But it is well known that the transverse shear stress on the surfaces is equal to zero and therefore a shear correction factor must be introduced. In 1984, Reddy proposed a new model (model-3) where the transverse displacement is a parabolic one with zeros at the surfaces. Model-4, introduced by Touratier in 1989, that can describe all previous models. In zig-zag models, the displacement is divided in three parts to reproduce piecewise continuous displacement and transverse stress fields in the thickness

direction

$$\begin{cases} U_1(x, z, t) = U_1^0(x, t) - \left(z - \frac{H_c + H_f}{2}\right) \frac{\partial w(x, t)}{\partial x}, & \frac{H_c}{2} < z \leq \frac{H_1}{2} \\ U_2(x, z, t) = U_2^0(x, t) - z \frac{\partial w(x, t)}{\partial x} + \sum_{j=1}^n f_j(z) \beta_j(x, t), & -\frac{H_c}{2} \leq z \leq \frac{H_c}{2} \\ U_3(x, z, t) = U_3^0(x, t) - \left(z + \frac{H_c + H_f}{2}\right) \frac{\partial w(x, t)}{\partial x}, & -\frac{H_f}{2} \leq z < -\frac{H_c}{2} \end{cases} \quad (2)$$

$U_1^0(x, t)$ ,  $U_2^0(x, t)$ ,  $U_3^0(x, t)$  are the three axial longitudinal displacements of the mid-plane of the layers.

Here, we consider Kirchhoff–Love’s model for the faces and the following models for the core:

- Model-5:  $n = 1$ ,  $f_1(z) = z$ , Mindlin model;
- Model-6:  $n = 1$ ,  $f_1(z) = z$ , Mindlin with Kerwin assumption (Rao);
- Model-7:  $n = 1$ ,  $f_1(z) = z - 4z^3/(3H_c^2)$ , Reddy’s model;
- Model-8:  $n = 2$ ,  $f_1(z) = z$ ,  $f_2(z) = z^3$ , Mix model.

In Model-5, the transverse shear strain is constant in the core and zero at the faces. In Model-5, Mindlin’s model is used in the core and at the interfaces of the core. Rao [15] (Model-6) used the same kinematical assumptions as in Model-5. In addition, he supposed that the core layer deforms mainly through shear stress, and does not carry any axial force (Kerwin assumption).

### 3. BASIC EQUATIONS

The sandwich-beam equations can be obtained by using the virtual work principal:

$$\delta P_{\text{ext}} + \delta P_{\text{int}} = \delta P_{\text{acc}}. \quad (3)$$

As many authors [10, 11, 16, 17] have studied non zig-zag models, here we just derive the basic equations for zig-zag models. Considering the continuity of the displacements at the interfaces, we can express the fields  $U_1(x, z, t)$  and  $U_3(x, z, t)$  as follows:

$$\begin{aligned} U_1(x, z, t) &= U_2^0(x, t) - z \frac{\partial w(x, t)}{\partial x} + \sum_{j=1}^n f_j(z) \beta_j(x, t) \\ U_3(x, z, t) &= U_2^0(x, t) - z \frac{\partial w(x, t)}{\partial x} - \sum_{j=1}^n f_j(z) \beta_j(x, t). \end{aligned} \quad (4)$$

One can see from these expressions, that the independent generalized displacements are reduced to  $U_2^0(x, z, t)$ ,  $x(x, t)$  and  $\beta_i(x, t)$ . According to Hooke’s

law and by using (3), one can obtain (5), (6) and (7) respectively for problem-1 (simply supported sandwich beam study under three point flexure testing) and problem-2 (free vibration analysis of simply supported sandwich beam):

$$\int_0^L \left[ (M_1 + M_2 + M_3) - \frac{H_c + H_f}{2}(N_1 - N_3) \right] \frac{\partial^2 \delta w}{\partial x^2} dx - F \delta w(L/2) = 0, \tag{5}$$

$$\int_0^L \left[ (M_1 + M_2 + M_3) - \frac{H_c + H_f}{2}(N_1 - N_3) \right] \frac{\partial^2 \delta w}{\partial x^2} dx - \int_0^L (2\rho_f S_f + \rho_c S_c) \frac{\partial^2 w}{\partial t^2} \delta w dx = 0. \tag{6}$$

Eq (7) can be deduced for both our two problems:

$$\int_0^L (N_1 - N_3) \sum_{j=1}^n f_j \left( \frac{H_c}{2} \right) \frac{\partial \delta \beta_j}{\partial x} + \int_{S_c} \sigma_{xx} \sum_{j=1}^n f_j \frac{\partial \delta \beta_j}{\partial x} dS_c + \int_{S_c} \sigma_{xz} \sum_{j=1}^n \frac{\partial f_j}{\partial z} \delta \beta_j dS_c dx = 0 \tag{7}$$

where  $M_i$  and  $N_i$  are the bending moment and axial force for the  $i$ -th layer and

$$M_t = (M_1 + M_2 + M_3) - \frac{H_c + H_f}{2}(N_t - N_3)$$

is the total bending moment. By using partial integration of Equations (5) and (7) and by introducing the boundary conditions of simply supported beam as in Table 1, we can obtain:

$$\begin{aligned} & \frac{H_c + H_f}{2} E_f H_f f_f \left( \frac{H_c}{2} \right) \frac{\partial^3 w}{\partial x^3} - 2E_f H_f f_k \left( \frac{H_c}{2} \right) f_j \left( \frac{H_c}{2} \right) \frac{\partial^2 \beta_j}{\partial x^2} + \\ & + E_c \int_{-\frac{H_c}{2}}^{\frac{H_c}{2}} z f_k(z) dz \frac{\partial^3 w}{\partial x^3} - E_c \int_{-\frac{H_c}{2}}^{\frac{H_c}{2}} f_k(z) f_j(z) dz \frac{\partial^2 \beta_j}{\partial x^2} + \\ & + G_c \int_{-\frac{H_c}{2}}^{\frac{H_c}{2}} z \frac{\partial f_k(z)}{\partial z} \frac{\partial f_j(z)}{\partial z} dz \beta_j = 0 \quad (k, j = 1, 2, \dots, n). \end{aligned} \tag{8}$$

The total moment,  $M_t$ , is given in terms of  $\partial^2 w / \partial x^2$  and  $\partial \beta_j / \partial x$ . Using (8), and the boundary conditions (see Table 1), one can find that the differential equation of the beam deflection  $w$  depends on the index  $j$ . The analytical

Table 1. Boundary conditions.

End conditions ( $x = 0$ or $x = L$ )	$x = L/2$
$w = 0,$	$\partial w / \partial x = 0$
$\partial^2 w / \partial x^2 = 0,$	$\beta_j = 0$
$\partial^4 w / \partial x^4 = 0,$	$\partial M_t / \partial x = -F/2$
$\partial \beta_j / \partial x = 0,$	–
$\partial^2 \beta_j / \partial x^2 = 0.$	–

solution of the deflection of the simply supported sandwich beam under three point flexure testing is given as the sum of a polynomial and exponential functions. In order to solve problem-2, the deflection function form for harmonic vibrations is assumed as:

$$w = Ae^{j\Omega t} e^{kx}, \quad (9)$$

where  $\Omega$  and  $k$  denote the unknown complex natural frequency and characteristic values that have to be addressed. By using the same end conditions as in Table 1, a six-order characteristic determinant which has to be zero for non-trivial solution is then established and the deflection,  $w$ , is expressed as:

$$w = Ae^{j\Omega t} \sin(n\pi x/L). \quad (10)$$

Finally, substituting (10) to (6) yields the expression of the complex frequency  $\Omega$ . From this, one can define the loss factor  $\eta$  the natural frequency  $\omega_0$  of the damped sandwich beam using the following definition:

$$\Omega^2 = \omega_0^2(1 + j\eta), \quad \eta = \text{Im}(\Omega^2)/\text{Re}(\Omega^2). \quad (11)$$

#### 4. NUMERICAL RESULTS

In this section, we present and compare the results obtained from the numerical and analytical studies of the two above considered problems. For the numerical studies, two-dimensional finite elements analysis is also considered using the ANSYS commercial code. The PLANE82 from ANSYS library-plane element defined by eight nodes having two degrees of freedom at each node (translations in the nodal  $x$  and  $y$  directions have been used). Because this element does not imply any kinematical assumptions, the so obtained results can be considered as reference solutions of problem-1 and problem-2. Some materials data of the beam are presented in Table 2.

So, three principal parameters of the sandwich beams were retained for these comparative studies: the ratio of length to thickness ( $L/H_t$ ), the ratio of rigidities ( $E_c/E_f$ ) and the ratio of core and face thickness ( $H_c/H_f$ ). The results are shown for problem-1 and problem-2 respectively in Tables 3 and 4. From these tables the following analyses can be pointed out.

Table 2. Materials parameters and dimensions.

Young's modulus of face	$E_f = 6.9 e^{10}$ Pa
Poisson's ratio	$\nu_f = \nu_c = 0.3$
Loss factor of core	$\eta_c = 0.3$

Table 3. [Problem 1], P1:  $w(L/2, 0)$ ; P2:  $\tau_{xz}(L/4, 0)$ ; P3:  $\sigma_{xx}(L/4, H_t/2)$  (Pa).

$H_c/H_f = 1.1$ $E_c/E_f = 0.0001$		Reddy	Touratier	Reddy in core	Mindlin in the core	Mix in core	ANSYS
$L/H_t = 10$	P1	-4.02E-7	-4.04E-7	-2.56E-6	-2.76E-6	-2.76E-6	-2.79E-6
	P2	-1.77E1	-1.96E1	-4.27E3	-3.11E3	-3.11E3	-3.13E3
	P3	-7.79E4	-7.79E4	-1.86E5	-1.99E5	-1.99E5	-2.01E5
$L/H_t = 20$	P1	-3.06E-6	-3.07E-6	-1.00E-5	-1.11E-5	-1.11E-5	-1.12E-5
	P2	-1.77E+1	-1.96E+1	-6.92E+1	-5.30E+3	-5.30E+3	-5.33E+3
	P3	-1.56E+5	-1.56E+5	-2.15E+5	-2.29E+5	-2.29E+5	-2.30E+5
$L/H_t = 100$	P1	-3.77E-4	-3.77E-4	-4.23E-4	-4.32E-4	-4.32E-4	-4.33E-4
	P2	-1.77E+1	-1.96E+1	-8.65E+3	-6.92E+3	-6.92E+3	-6.92E+3
	P3	-7.79E+5	-7.79E+5	-7.79E+5	-7.79E+5	-7.79E5	-7.79E+5
$H_c/H_f = 1$ $L/H_t = 50$ $E_c/E_f = 1$		Reddy	Touratier	Reddy in core	Mindlin in the core	Mix in core	ANSYS
$\bar{E}_c/E_f = 0.01$	P1	-4.53E-05	-4.53E-05	-4.53E-05	-4.53E-05	-4.53E-05	-4.53E-05
	P2	-7.50E+3	-7.74E+03	-9.17E+03	-7.22E+03	-7.50E+03	-7.46E+03
	P3	-3.75E+05	-3.75E+05	-3.75E+05	-3.75E+05	-3.75E+05	-3.75E+05
$E_c/E_f = 0.0001$	P1	-4.71E-05	-4.72E-05	-4.94E-05	-4.99E-05	-4.99E-05	-4.99E-05
	P2	-1.75E+02	-1.93E+02	-8.66E+03	-6.93E+03	-6.93E+03	-6.93E+03
	P3	-3.89E+05	-3.89E+05	-3.89E+05	-3.89E+05	-3.89E+05	-3.89E+03
$H_c/H_f = 1.1$ $E_c/E_f = 0.0001$		Reddy	Touratier	Reddy in core	Mindlin in the core	Mix in core	ANSYS
P3	-3.89E+05	-3.89E+05	-6.40E+05	-6.90E+05	-6.90E+05	-6.92E+03	

Table 4. Problem-2.

$H_c/H_f = 1.1$ $E_c/E_f = 0.0001$	Reddy	Touratier	Reddy in core	Mindlin in the core	Mix in core	ANSYS
$L/H_t = 10$	2441.40	931.45	969.55	932.02	932.02	924.11
	0.00	0.410	0.443	0.410	0.410	
$L/H_t = 20$	623.23	333.33	351.39	333.50	333.50	330.23
	0.000	0.557	0.552	0.557	0.557	

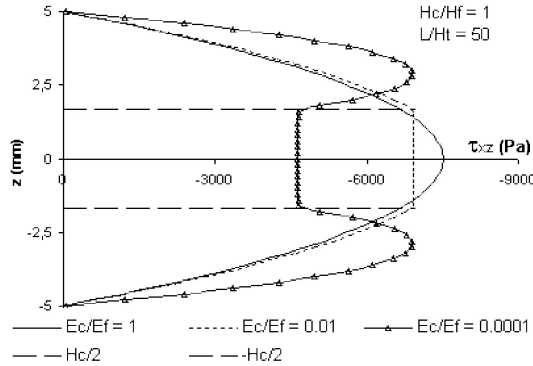


Figure 2. Transverse shear stress at the section  $x = L/4$ .

### 4.1 Influence of the ratio of length to thickness

For small,  $L/H$ , ratios, the analytical and numerical (FEA) solutions present big disparities. However if this ratio is large enough, all the presented models gave satisfactory results for the calculation of  $w(L/2, 0)$ ,  $\sigma_{xx}(L/4, H_t/2)$  and low frequencies  $\omega_0$ , but for the calculation of high frequencies, a zig-zag model should be used, because it is similar to decrease the ratio of  $L/H$ .

### 4.2 Influence of the ratio of rigidities

Non zig-zag models are not sensitive the stiffnesses ratio ( $E_c/E_f$ ). The relative error between the analytical and the finite element solutions increase with the decrease of the stiffnesses ratio. For ratio values close to 1, sandwich beam can be considered as an isotropic beam and all analytical models can give an accurate values of  $w(L/2, 0)$ , and  $\sigma_{xx}(L/4, H_t/2)$ . One can note that, for soft core, Rao’s model is more precise (“Mindlin in core” and the “Mix in core” models). On the contrary, for stiff cores, where Kerwin’s assumptions are not satisfied, this previous remark is not still valid and the relative error on loss factors is larger.

Figure 2 describes the finite element distribution of transverse shear stress for various stiffnesses ratios. One can see from such distribution is not a parabolic one for sandwich beams and that zig-zag models are more accurate than non zig-zag models. For stiffness ratios close to 1, one can consider that the sandwich beam could be modelled as a Timoshenko beam and the displacement curve is a parabolic one. For ratios less than 1, one can find that the shear stress is almost constant through the core. One can conclude that Rao’s and “Mindlin in core” are the most accurate models.

### 4.3 Influence of the ratio of core and face thickness

The disparities in results between models are the highest when the ratio,  $H_c/H_f$ , is close to 1. For smaller and larger ratios, the sandwich beam could be considered as isotropic one and all the presented models give similar results.

## 5. CONCLUSION

In the case of  $E_c/E_f > 0.01$ ,  $L/H_t > 100$ , all the proposed models can give, comparatively, the same results in terms of  $w(L/2, 0)$ ,  $\sigma_{xx}(L/4, H_t/2)$  and  $\omega_0$ . Zig-zag models are always more accurate than non zig-zag models and non zig-zag models are imprecise in the case of very weak cores. Between non zig-zag models, Touratier's model is more accurate than Reddy's model, and Reddy's model is more accurate than Kirchhoff's model. Between zig-zag models, Rao's model can be used for the modelling of weak cores. The model "Mindlin in core" and the model "Mix in core" are very stable and very approach with the results of ANSYS, in the other hand, they give always the same results, that's to say we do not need to enrich the "Mindlin in core" if we use zig-zag principal. In conclusion, the model "Mindlin in core" is the best model, which can be used for all configurations in the static field and in the dynamic field.

## REFERENCES

- [1] Cauchy, A.L. (1828), Sur l'équilibre et le mouvement d'une plaque solide, Exercices de Mathematique 3, 328–355.
- [2] Poisson, S.D. (1829), Memoire sur l'équilibre et le mouvement des corps élastique, Mem. Acad. Sci. 8, 357.
- [3] Kirchhoff, G. (1850), Uber das Gleichgewicht und die Bewegung eine elastischen Scheibe, J. Angew Math. 40, 51–88.
- [4] Love, A.E.H. (1927), The Mathematical Theory of Elasticity, 4th Edition, Cambridge UnivPress, Cambridge
- [5] Reissner, E. (1945), The effect of transverse shear deformation on the bending of elastic plates, ASME J. Appl. Mech. 12, 69–76.
- [6] Mindlin, R.D. (1951), Influence of rotatory inertia and shear in flexural motions of isotropic elastic plates, ASME J. Appl. Mech. 18, 1031–1036.
- [7] Hildebrand, F.B., Reissner, E. and Thomas, G.B. (1938), Notes on the foundations of the theory of small displacements of orthotropic shells, NACA TN-1833, Washington DC.
- [8] Pagano, N.J. (1969), Exact solutions for composite laminates in cylindrical bending, J. Compos. Mater. 3, 398–411.
- [9] Carrera, E. (1995), A class of two dimensional theories for multilayered plates analysis, Atti. Acc. Sci. Torino, Mem Sci Fis (19–20), 49–87.
- [10] Reddy, J.N., A simple higher-order theory of laminated composite plate. Journal of Applied Mechanics 51, 745–752.

- [11] Touratier, M., An efficient standard plate theory. *International Journal of Engineering Science*, 29, 901–916.
- [12] Daya, E.M. and Potier-Ferry, N. (2002), A shell element for viscoelastically damped sandwich structures, *Revue européenne des éléments finis*, Volume 11, No. 1, 39–56.
- [13] He, J.F. and Ma, B.A. (1992), Vibration analysis of viscoelastically damped sandwich plates, *Journal of Sound and Vibration* 152, 107–123.
- [14] Mead D.J. and Markus, S. (1974), The forced vibration of three-layer damped sandwich beam with arbitrary boundary conditions, *Journal of Sound and Vibration* 33, 335–352.
- [15] Rao, D.K., Frequency and loss factor of sandwich beams under various boundary conditions, *Journal of Mechanical Engineering Sciences* 20(5), 271–282.
- [16] Carrera, E. (2003), Historical review of zig-zag theories for multilayered plates and shells, *Appl. Mech. Rev.* 56(3), 287–308.

# A HOMOGENIZATION BASED THEORY FOR LAMINATED AND SANDWICH BEAMS

Jorn S. Hansen and Graeme Kennedy

*Institute for Aerospace Studies, University of Toronto, Toronto, Ontario, Canada*

hansen@utias.utoronto.ca, graeme.kennedy@utoronto.ca

Sergio F.M. de Almeida

*Instituto Tecnológico de Aeronautica, Department of Mechanical Engineering,  
Sao Jose dos Campos - SP, Brasil*

frascino@ita.br

**Abstract** A theory for laminated and sandwich beams is developed based on far-field stress and strain solutions called Fundamental State Solutions. Through-thickness stress and strain moments of the Fundamental Solutions are used to obtain homogenized axial, flexural and shear stiffness as well as a shear-strain moment correction. A sequence of beam models with similarity to the Timoshenko model are obtained. Excellent agreement is shown for all stress and strain components when compared to accurate two-dimensional finite element results.

**Keywords:** sandwich beams, homogenization, beam theory.

## 1. INTRODUCTION

Beam, plate and shell theories for laminated and sandwich structure have been the subject of an extensive literature both from a model development perspective and from the application of these models in design. There are essentially two requirements driving the theoretical development. First, it is desirable to obtain accurate displacement solutions; second, accurate and complete through-thickness stress/strain distributions are crucial in the prediction of failure/delamination. The challenge is to do both with minimal computational effort. The difficulty results from the fact that the through-thickness stress, strain and displacement fields are in general non-differentiable and may be discontinuous; thus accurately modelling the through-thickness response is complex and using through-thickness polynomials leads in general to poor approximations.

The literature on this subject is vast; reviews of laminated composite theory may be found in [1]- [4] . The appropriate beam theory is due to Timoshenko [5, 6] while the analogous plate results are due to Reissner [7] and Mindlin [8]. The de facto standard method of analyzing sandwich beams, plates or shells is to use a Timoshenko or Reissner-Mindlin formulation, the so called first-order shear deformation theory, with appropriate transverse shear stiffness and shear correction factors and then complete a post-processing calculation in which the in-plane stresses are used to determine approximations for the transverse shear stresses. The present work adopts a very different point of view and, as will be shown, leads to an extremely accurate modelling capability.

## 2. THE ESSENTIAL IDEA

Beam, plate and shell theories contain a number of internal modelling inconsistencies. In the present approach these are eliminated. That is: all approximations made are internally consistent; solutions obtained are equally accurate for both stress and strain; stress or strain obtained in a post-processing calculation are consistent with the stress and strain approximations used in developing the theory.

Solutions are sought in terms of through-thickness moments (averages) of stress, strain and displacement rather than being modelled as through-thickness polynomials; thus difficulties associated with lack of through-thickness differentiability and/or discontinuities are avoided.

The present theory assumes approximate solutions can be modelled as a superposition of a sequence of calculated far field solutions referred to as Fundamental State Solutions. This assumption has important consequences:

1. No through-thickness polynomial approximations are made.
2. The problem is completely and accurately represented in terms of stress, strain and displacement moments.
3. Accurate 'average' structural stiffnesses are calculated based on stress and strain moments obtained from the Fundamental State Solutions.
4. Accurate and internally consistent through-thickness stress and strain distributions are obtained from the Fundamental States and are used in a straight-forward post-processing step to determine an accurate approximation of the stress and strain fields.

## 3. STRESS, STRAIN AND DISPLACEMENT MOMENTS

Moments of a system variable are evaluated in terms of the through-thickness coordinate  $z$  and with respect to the beam middle-surface  $z = 0$ . The axial coordinate is represented as  $x$  while  $y$  is normal to the  $x - z$  plane.

The  $n^{th}$  through-thickness stress or strain moment is defined as

$$s^n(x) \triangleq \int_A \sigma(x, y, z) z^n dA \quad ; \quad e^n(x) \triangleq \int_A \epsilon(x, y, z) z^n dA \quad (1)$$

where  $dA = dz dy$  and  $A$  is the beam cross-sectional area. The  $n^{th}$  normalized displacement moments are defined as

$$u_n(x) \triangleq \frac{1}{A_{2n}} \int_A u(x, y, z) z^n dA \quad ; \quad w_n(x) \triangleq \frac{1}{A_{2n}} \int_A w(x, y, z) z^n dA \quad (2)$$

where  $A_{2n}$  is the  $(2n)^{th}$  moment of the beam cross-sectional area with respect to  $z$ . The displacement moments have been normalized in the manner indicated in order that the final displacement-moment equilibrium equations adopt a form similar to the classical Timoshenko equilibrium equations.

#### 4. FUNDAMENTAL STATES

The beam approximation is based on a sum of reference solutions referred to as Fundamental State Solutions. The essence of the Fundamental States is that  $(y,z)$  dependent but  $x$ -invariant stress/strain distributions exist for all load states corresponding to zero, constant, linear,  $\dots$  flexural states. Such invariant properties always occur for axially invariant beam cross-sections subjected to surface tractions expressed as a polynomial with respect to  $x$ . These invariant forms are defined as the Fundamental State Components. The sequence of problems used to generate the set of invariant states are defined in an hierarchical manner corresponding to a complete sequence of bending moments. The following is illustrative for the case of pressure loads being applied to the top and/or bottom of a beam.

State 0- Constant axial stress resultant: Zero bending

State 1- Pure bending: Constant bending moment

State 2- Pure shear: Linear bending moment

State 3- Constant pressure at top or bottom of beam: Quadratic bending.

State 4- Linearly varying pressure at top or bottom: Cubic bending.

⋮

State M-  $(M-3)^{rd}$  degree pressure :  $(M-1)^{st}$  degree bending.

The solution approximation includes two sets of variables. The first are the Fundamental State Components which are written as

$${}_m\sigma(y, z) \quad , \quad {}_m\epsilon(y, z) \quad : \quad m = 0, M \quad (3)$$

Note that these components are functions of  $y$  and  $z$  but are independent of  $x$ ; the preceding subscript  $m$  refers to the Fundamental State. The second set are called the Fundamental State Variables and are written as

$$\alpha_m(x) \quad : \quad m = 0, M \quad (4)$$

These are the ‘amplitudes’ associated with each Fundamental State. Also, the Fundamental State Components have been normalized such that  $\alpha_m(x)$  corresponds to the magnitude of the stress resultant, bending moment, shear resultant, constant pressure amplitude  $\dots$ . The total stress and strain fields are approximated as a sum of the Fundamental State Components multiplied by the appropriate Fundamental State Variable. That is

$$\begin{aligned}\sigma^T(x, y, z) &\approx \alpha_0(x) {}_0\sigma(y, z) + \alpha_1(x) {}_1\sigma(y, z) + \dots + \alpha_n(x) {}_n\sigma(y, z) \\ \epsilon^T(x, y, z) &\approx \alpha_0(x) {}_0\epsilon(y, z) + \alpha_1(x) {}_1\epsilon(y, z) + \dots + \alpha_n(x) {}_n\epsilon(y, z)\end{aligned}\quad (5)$$

where the superscript  $T$  means total. It is important to note that of all  $\alpha_m(x)$  it is only those of States 0, 1 and 2 (Stress Resultant, Pure Bending and Constant Shear) which are unknown. The remaining State Variables are uniquely specified by the surface tractions acting on the beam. Thus the beam problem will have at most three undetermined variables;  $\alpha_0(x)$ ,  $\alpha_1(x)$  and  $\alpha_2(x)$ . This means that a Timoshenko like model is all that is required in any situation. The procedure used to determine the fundamental state solutions is completely developed by Hansen and Almeida [9]. Finally, once the  $\alpha_m$ ;  $m = 0, M$  have been determined then the complete stress and strain fields may be obtained from Equations (5) in a straight-forward post-processing calculation.

## 5. HOMOGENIZED STIFFNESS

Each Fundamental State Solution defines unique inter-relationships between the stress and strain for that state; these inter-relationships are interpreted to define stiffness relations between those state components. It is these relationships which are used to obtain homogenized stiffness properties.

### 5.1 Homogenized membrane-bending stiffness

The beam cross-section is non-symmetric, which implies membrane-bending coupling. Therefore, the coupled axial, membrane-bending and bending homogenized stiffness are defined as a relation between the zeroth and first moments of  $\sigma_x(x, y, z)$  and  $\epsilon_x(x, y, z)$  corresponding to States 0 and 1. That is

$$\begin{bmatrix} a_{11} & a_{12} \\ a_{21} & a_{22} \end{bmatrix} \triangleq \begin{bmatrix} {}_0s_x^0 & {}_1s_x^0 \\ {}_0s_x^1 & {}_1s_x^1 \end{bmatrix} \begin{bmatrix} {}_0e_x^0 & {}_1e_x^0 \\ {}_0e_x^1 & {}_1e_x^1 \end{bmatrix}^{-1}\quad (6)$$

where  $a_{ij}$  are the homogenized stiffness properties. This definition is effectively a ‘ratio’ of stress moments divided by strain moments and is therefore an extension of the standard definition of material stiffness. The normalization of the Fundamental States (Hansen and Almeida [9] and Kennedy [10]) imposes  ${}_0s_x^0 = 1$ ,  ${}_0s_x^1 = 0$ ,  ${}_1s_x^0 = 0$ ,  ${}_1s_x^1 = 1$ , therefore Equation (6) becomes

$$\begin{bmatrix} a_{11} & a_{12} \\ a_{21} & a_{22} \end{bmatrix} \triangleq \frac{1}{{}_0e_x^0 {}_1e_x^1 - {}_0e_x^1 {}_1e_x^0} \begin{bmatrix} {}_1e_x^1 & -{}_1e_x^0 \\ -{}_0e_x^1 & {}_0e_x^0 \end{bmatrix}\quad (7)$$

Thus an homogenized stress moment - strain moment constitutive relation

$$\begin{bmatrix} s_x^0 \\ s_x^1 \end{bmatrix} = \begin{bmatrix} a_{11} & a_{12} \\ a_{21} & a_{22} \end{bmatrix} \begin{bmatrix} e_x^0 \\ e_x^1 \end{bmatrix} \tag{8}$$

is obtained. Furthermore, this relation is exact for loading states corresponding to any combination of Fundamental States 0 and 1.

### 5.2 Homogenized shear stiffness

The homogenized transverse shear stiffness is defined as the ratio of the zeroth moments of  $\sigma_{xz}$  and  $\gamma_{xz}$  evaluated for State 2

$$G_{xz} \triangleq \frac{2s_{xz}^0}{2e_{xz}^0} \tag{9}$$

In a manner similar to Equation (8), this result guarantees that

$$s_{xz}^0 = G_{xz}e_{xz}^0 \tag{10}$$

is exact for load states corresponding to a state of pure shear (State 2). No shear correction factor is required! Furthermore, for a single layer material,  $G_{xz}$  is identical to the exact transverse shear stiffness, independent of the stress and/or strain distribution or the beam cross-sectional geometry. Such a result is not true for conventional laminated or sandwich beam theory.

## 6. DISPLACEMENT REPRESENTATION

Only the  $x$  and  $z$  displacements enter the analysis. These displacements are decomposed into two components

$$u^T(x, y, z) = u(x, y, z) + \bar{u}(x, y, z); w^T(x, y, z) = w(x, y, z) + \bar{w}(x, y, z) \tag{11}$$

where  $u^T(x, y, z), w^T(x, y, z)$  are called the total displacements;  $u(x, y, z), w(x, y, z)$  are components corresponding to Fundamental States 0, 1, 2 and are ‘unknown’;  $\bar{u}(x, y, z), \bar{w}(x, y, z)$  are components corresponding to fundamental states other than 0, 1, 2. and are effectively ‘known’ being defined by the surface tractions. The displacements never enter the analysis explicitly and are not determined as it is the moments

$$u_0(x) = \frac{1}{A_0} \int_A u^T(x, y, z) dA \quad ; \quad u_1(x) = \frac{1}{A_2} \int_A u^T(x, y, z) z dA$$

$$w_0(x) = \frac{1}{A_0} \int_A w^T(x, y, z) dA \tag{12}$$

which are the problem unknowns. The variables  $A_0 = A$  and  $A_2 = I$  are the beam cross-sectional area and the second moment of the area respectively.

## 7. STRAIN MOMENT – DISPLACEMENT MOMENT RELATIONS

Using the classical linear strain-displacement relations, the strain moments of Equation (1) and the displacement moments of Equations (12) yields

$$\begin{aligned}
 T_{e_x^0}(x) &= A \frac{\partial u_0(x)}{\partial x} \\
 T_{e_x^1}(x) &= I \frac{\partial u_1(x)}{\partial x} \\
 T_{e_{xz}^0}(x) &= \left[ \int_A \frac{\partial u^T(x, y, z)}{\partial z} dA \right] + A \frac{\partial w_0(x)}{\partial x} \quad (13)
 \end{aligned}$$

The first two of the above relations are exact. However [.] in the third relation cannot be determined exactly in terms of  $u_0(x)$ ,  $u_1(x)$ ; therefore, an approximation is required. Noting that [.] depends only on the odd part of  $u^T(x, y, z)$  (with respect to  $z$ ), implies [.] can depend only on  $u_1(x)$  and cannot depend on  $u_0(x)$ . Thus the shear-strain moment correction is defined as

$$C_{xz} \triangleq \left\{ \frac{T_{e_{xz}^0}(x)}{A \left[ u_1(x) + \frac{\partial w_0(x)}{\partial x} \right]} \right\}_{\text{State 2}} \quad (14)$$

This correction is the ratio of the exact shear-strain moment to the approximation of the shear-strain moment expressed in terms of  $u_1(x)$ ,  $w_0(x)$  all evaluated for State 2 (constant shear). For a rectangular, isotropic beam this correction corresponds exactly to that obtained by Cowper [11] although the interpretation is different. For plates this definition yields a plane-strain correction [12]. This definition is at odds with the usual interpretation of a shear correction factor and also yields slightly different values; therefore, it is given a more accurate name – *shear-strain moment correction*.

## 8. MOMENT EQUILIBRIUM EQUATIONS

The moment equilibrium equations are consistent with the Timoshenko approximation. For a beam of rectangular cross-section with thickness  $2c$  and unit width they become

$$\begin{aligned}
 \frac{d T_{s_x^0}}{dx} &= - [T_{xz}^+(x) + T_{xz}^-(x)] \\
 \frac{d T_{s_x^1}}{dx} - T_{s_{xz}^0} &= -c [T_{xz}^+(x) - T_{xz}^-(x)]
 \end{aligned}$$

$$\frac{d T_{xz}^0}{dx} = - [T_z^+(x) + T_z^-(x)] \quad (15)$$

where  $T_{xz}^+(x)$ ,  $T_{xz}^-(x)$ ,  $T_z^+(x)$ ,  $T_z^-(x)$  are the tractions acting on the upper and lower surfaces of the beam. Substitution for stress moments in terms of displacement moments yields equations similar to those of Timoshenko beam theory with two important differences. First,  $u_0(x)$ ,  $u_1(x)$ ,  $w_0(x)$  are displacement moments rather than middle-surface displacements. Second, there are higher-order-state corrections  $\bar{e}_x^0(x)$ ,  $\bar{e}_x^1(x)$  and  $\bar{e}_{xz}^0(x)$  which provide a hierarchy of approximations. Hansen and Almeida [9, 13] and Kennedy [10] provide details.

## 9. NUMERICAL EXAMPLE: SANDWICH BEAM

The capabilities of this approach are illustrated for a cantilever sandwich beam in which the face sheets may have different stiffness. The beam is 100mm long, 10mm thick and 10mm wide. The face sheets are 2.5mm thick while the core is 5mm thick. The top layer has a Young's modulus  $E = 70$  GPa and a Poisson's ratio  $\nu = 0.3$ ; the core material has  $E = 0.01 \times 70$  GPa and  $\nu = 0.3$ ; the lower face sheet has  $E = \alpha \times 70$  GPa and  $\nu = 0.3$  with  $\alpha = 1.0, 0.1, 0.01$ . Thus the structure may have either a symmetric or a non-symmetric cross-section. Comparisons between the present approach and a two-dimensional ANSYS finite element calculation are presented. The finite element model used  $200 \times 40$  bi-quadratic elements along the length and through the thickness respectively. The sandwich-beam is subjected to a linearly varying surface pressure applied on top of the beam.

Typical results at beam mid-length ( $x/L = 0.5$ ) are presented in Figures 1 to 4 when the normal surface traction varies from 100 kPa at the root to 0 kPa at the free end. There is excellent agreement between the beam theory and the finite element calculations. The presented results, axial strain  $\epsilon_x$ , transverse shear strain  $\gamma_{xz}$ , transverse shear stress  $\sigma_{xz}$  and transverse normal stress  $\sigma_z$  have been chosen for presentation as they illustrate characteristics that cannot be captured using existing beam theories. Complete results show that at the beam mid-length the finite element and beam theory predictions are virtually numerically identical for all stress and strain components. At a distance of  $1/2$  a beam thickness from the cantilever root the maximum worst case error in the shear stress is approximately 11%; this error is attributed to three-dimensional boundary effects. The through-thickness displacement moments have a typical maximum worst case error of approximately 1% over the length of the beam. A complete development for symmetric beams presented in [9, 13] shows equally outstanding accuracy.

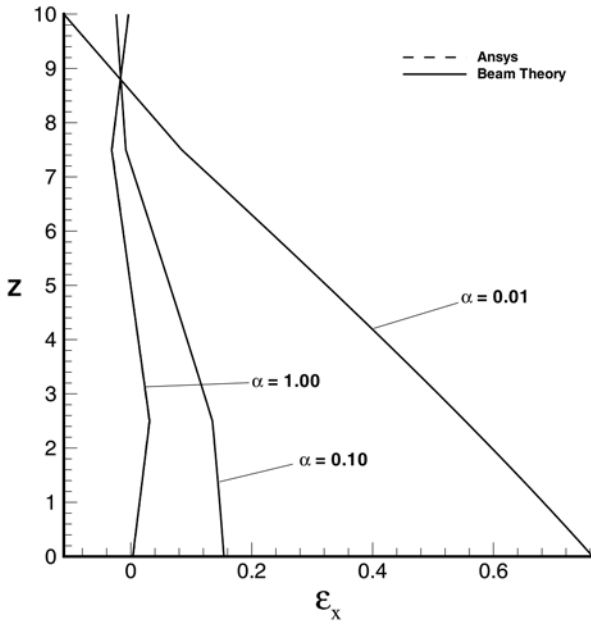


Figure 1. Axial strain  $\epsilon_x (\times 10^{-5})$  at  $x/L = 0.5$ .

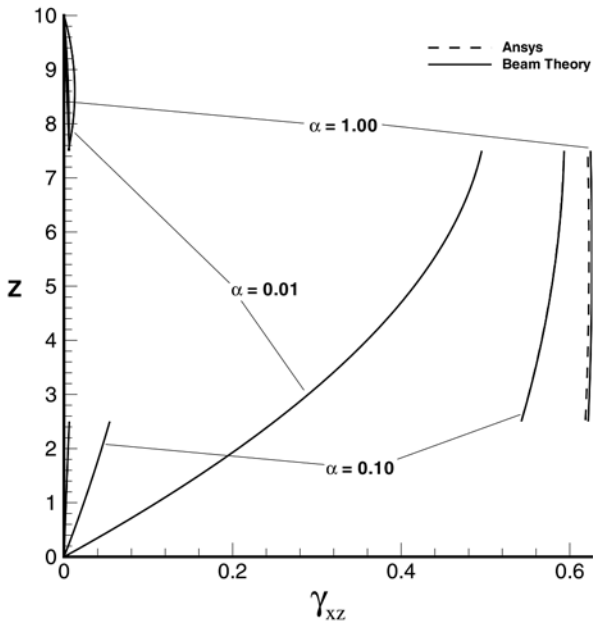


Figure 2. Transverse shear strain  $\gamma_{xz} (\times 10^{-5})$  at  $x/L = 0.5$ .

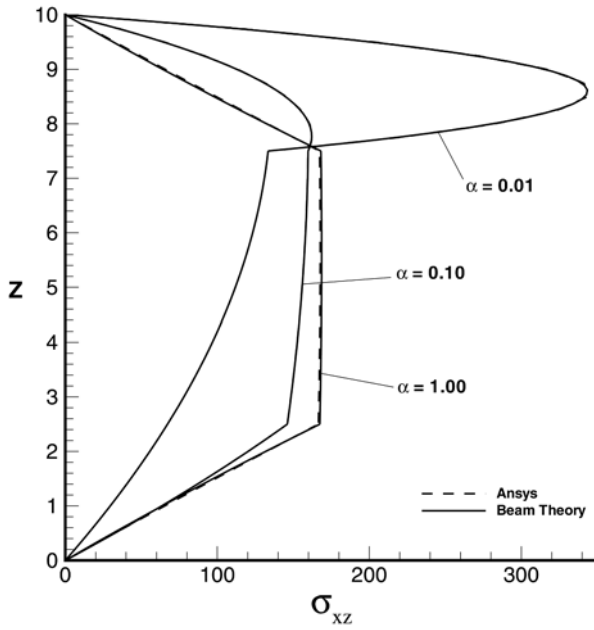


Figure 3. Transverse shear stress  $\sigma_{xz}$  (kPa). at  $x/L = 0.5$ .

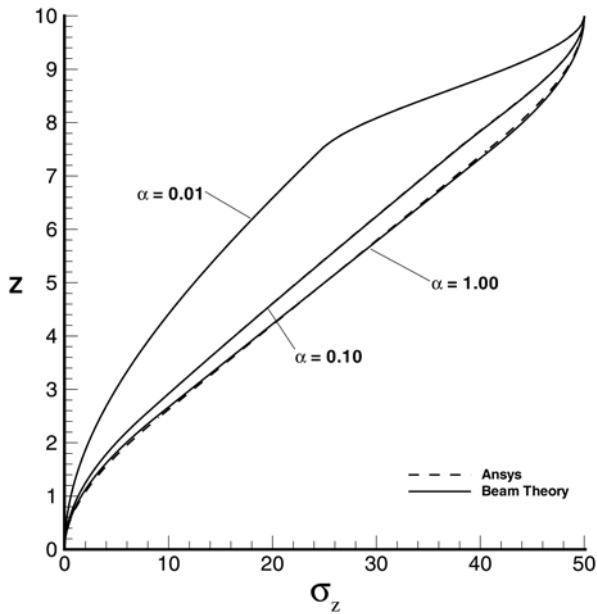


Figure 4. Transverse normal stress  $\sigma_z$  (kPa). at  $x/L = 0.5$ .

## 10. SUMMARIZING COMMENTS

This work presents a straight-forward beam theory which yields exceptionally accurate results for average displacements as well as complete two-dimensional stress and strain fields. The theory as presented is quite complete for laminated and sandwich beams. The application to sandwich plates [12] does not, in general, yield a typical Reissner/Mindlin plate theory. For the case of isotropic homogeneous layers a Reissner/Mindlin type model results; however, for sandwich structures with general laminated face sheets a new model is required. Space precludes the inclusion of plate results.

## REFERENCES

- [1] Noor, A.K. and Burton, W.S., "Assessment of Shear Deformation Theories for Multilayer Composite Plates", *Applied Mechanics Reviews*, Vol. 42, No. 1, 1989, pp. 1-13.
- [2] Kapania, R.K., "A Review on the Analysis of Laminated Shells", *ASME Journal of Pressure Vessel Technology*, Vol. 111, May 1989, pp. 88-96.
- [3] Noor, A.K. and Burton, W.S., "Assessment of Computational Models for Multilayer Composite Shells", *Applied Mechanics Reviews*, Vol. 43, No. 4, 1990, pp. 67-97.
- [4] Reddy, J.N., "A Review of Refined Theories of Laminated Composite Plates", *The Shock and Vibration Digest*, Vol. 22, No. 7, 1990, pp. 3-17.
- [5] Timoshenko, S.P., "On the Correction for Shear of the Differential Equation for Transverse Vibrations of Prismatic Bars", *Philosophical Magazine*, Vol. 21, 1921, pp. 744-746.
- [6] Timoshenko, S.P., "On the Transverse Vibrations of Bars of Uniform Cross-Section", *Philosophical Magazine*, Vol. 43, 1922, pp. 125-131.
- [7] Reissner, E., "The Effect of Transverse Shear Deformation on the Bending of Elastic Plates", *Journal of Applied Mechanics*, Vol. 12, No. 2, 1945, pp. 69-77.
- [8] Mindlin, R.D., "Influence of Rotary Inertia and Shear on The Effect of Transverse Shear Deformation on Flexural Motions of Isotropic, Elastic Plates", *Journal of Applied Mechanics*, Vol. 18, No. 1, 1951, pp. 31-38.
- [9] Hansen, J.S. and Almeida, S.F.M., "A Theory for Laminated Composite Beams", Final Report submitted April 2001, FAPES Grant No. 00/06183-0, São Paulo, Brasil, 157 pages.
- [10] Kennedy, G., "A Hierarchical Beam theory for Beams with Asymmetric Cross-Sections", B.A.Sc. Thesis, Division of Engineering Science, Faculty of Engineering, University of Toronto, Dec. 2004.
- [11] Cowper, G.R., "The Shear Coefficient in Timoshenko's Beam Theory", *Journal of Applied Mechanics*, Vol. 33, June 1966, pp. 335-340.
- [12] Guimatsia, I. and Hansen, J.S., "A Homogenization Based Laminated Plate Theory", 2004 ASME International Mechanical Engineering Congress and RD & D EXPO, Anaheim, California, Nov. 13-19, 2004.
- [13] Hansen, J.S. and Almeida, S.F.M., "A Homogenization Based Laminated Beam Theory", 21st International Congress of Theoretical and Applied Mechanics (ICTAM 2004), Warsaw, Poland, 16-20 August 2004.

# MODELLING OF COMPOSITE AND SANDWICH PLATES BY A TRIGONOMETRIC LAYERWISE THEORY AND MULTIQUADRICS

Carla M.C. Roque

*Instituto de Engenharia Mecânica e Gestão Industrial, Rua do Barroco, 174-215,  
4465-591 Leça do Balio, Portugal*

croque@fe.up.pt

António J.M. Ferreira and Renato M.N. Jorge

*Faculdade de Engenharia da Universidade do Porto, DEMEGI, Rua Dr. Roberto Frias,  
4200-465 Porto, Portugal*

ferreira@fe.up.pt, rnatal@fe.up.pt

**Abstract** In this paper we use a trigonometric layerwise deformation theory for modelling symmetric composite plates. We use a meshless discretization method based on global multiquadric radial basis functions. The results obtained are compared with solutions derived from other models and numerical techniques. The results show that the use of trigonometric layerwise deformation theory discretized with multiquadrics provides very good solutions for composite plates and excellent solutions for sandwich plates.

**Keywords:** trigonometric layerwise deformation theory, composite plates, radial basis functions, symmetric laminates.

## 1. INTRODUCTION

The use of shear deformation theories for composite and sandwich plates has been the subject of intense research. First-order shear deformation theories (FSDT) [1, 2, 3], higher-order shear deformation theories (HSDT) [4, 5, 6] were developed and discretized by various numerical schemes, such as the finite element method or more recent meshless methods. Both such theories consider laminate-wise rotations whereas layerwise theories consider layerwise rotations, being more adequate for sandwich plate analysis. Some layerwise or zig-zag theories have been presented by Di Sciuva [7], Murakami [8], Ren [9], Ferreira [10], Reddy [11] and Carrera [12].

Trigonometric layerwise deformation theories were recently applied to composite beams by Arya et al. [13] and Shimpi [14]. These theories provide continuity of displacements and zero transverse shear stresses at top and bottom surfaces of the laminate, without the burden of extra rotational degrees of freedom as in layerwise formulations. The use of trigonometric layerwise theory provides a combination of higher-order and layerwise concepts being specially adequate for sandwich structures. These theories do not increase the number of degrees of freedom as in [10]. Therefore are computationally economical without losing accuracy.

The present paper is an extension to composite plates of the work of Arya et al. [13] for composite beams. Furthermore, the discretization of the governing equations and boundary conditions is performed by multiquadrics.

The multiquadric radial basis function method was first used by Hardy [15, 16] for the interpolation of geographical scattered data and later used by Kansa [17, 18] for the solution of partial differential equations (PDEs).

The method was previously applied by the authors in the analysis of composite plates and beams [19, 20, 21, 10]. A specialized version of this theory without the layerwise concept was proposed by the authors [22].

## 2. THE TRIGONOMETRIC LAYERWISE MODEL

In the present trigonometric layerwise approach, the displacement field in the  $k^{th}$  layer can be defined, for a plate with global thickness  $h$ , as

$$\begin{aligned} u^k(x, y, z) &= u_0(x, y) - z \frac{\partial w_0(x, y)}{\partial x} + \left( A^k + zB^k + \sin \frac{\pi z}{h} \phi_x(x, y) \right) \\ v^k(x, y, z) &= v_0(x, y) - z \frac{\partial w_0(x, y)}{\partial y} + \left( C^k + zD^k + \sin \frac{\pi z}{h} \phi_y(x, y) \right) \\ w(x, y, z) &= w_0(x, y) \end{aligned} \quad (1)$$

where  $u^k$  and  $v^k$  are the inplane displacements at any point  $(x^k, y^k, z)$  in layer  $k$ ,  $u_0$  and  $v_0$  denote the inplane displacement of the point  $(x, y, 0)$  on the midplane,  $w$  is the deflection,  $\phi_x$  and  $\phi_y$  are the rotations of the normals to the midplane about the  $y$  and  $x$  axes, respectively. Parameters  $A^k$ ,  $B^k$ ,  $C^k$  and  $D^k$  are obtained by imposing transverse shear stress and in-plane displacement continuity at each layer interface as

$$\begin{aligned} B^k &= \frac{Q_{55}^{k-1}}{Q_{55}^k} B^{k-1} + \frac{\pi}{h} \cos \frac{\pi h_k}{h} \left( \frac{Q_{55}^{k-1}}{Q_{55}^k} - 1 \right) \\ A^k &= A^{k-1} + z^k (B^{k-1} - B^k); \end{aligned}$$

$$\begin{aligned}
 D^k &= \frac{Q_{44}^{k-1}}{Q_{44}^k} D^{k-1} + \frac{\pi}{h} \cos \frac{\pi h_k}{h} \left( \frac{Q_{44}^{k-1}}{Q_{44}^k} - 1 \right) \\
 C^k &= C^{k-1} + z^k (D^{k-1} - D^k)
 \end{aligned} \tag{2}$$

where first layer parameters for symmetric laminates are given by

$$B^1 = D^1 = 0, [A^1; C^1] = - \sum_{i=2}^{k_{\text{midplane}}} z(i) [(B^{i-1} - B^i); (D^{i-1} - D^i)] \tag{3}$$

Equations (1) and (3) represent an equivalent but perhaps simpler form than those proposed by Arya et al. [13]. The Euler-Lagrange equations can be written as:

$$\frac{\partial N_{xx}}{\partial x} + \frac{\partial N_{xy}}{\partial y} = 0; \quad \frac{\partial N_{xy}}{\partial x} + \frac{\partial N_{yy}}{\partial y} = 0 \tag{4}$$

$$\frac{\partial^2 M_{xx}}{\partial x^2} + \frac{\partial^2 M_{yy}}{\partial y^2} + 2 \frac{\partial^2 M_{xy}}{\partial x \partial y} + q = 0 \tag{5}$$

$$\frac{\partial N_{Axx}}{\partial x} + \frac{\partial M_{Bxx}}{\partial x} + \frac{\partial N_{sxx}}{\partial x} + \frac{\partial N_{Axy}}{\partial y} + \frac{\partial M_{Bxy}}{\partial y} + \frac{\partial N_{sxy}}{\partial y} - T_{Bxz} - \frac{\pi}{h} T_{cxz} = 0 \tag{6}$$

$$\frac{\partial N_{Cyy}}{\partial y} + \frac{\partial M_{Dyy}}{\partial y} + \frac{\partial N_{syy}}{\partial y} + \frac{\partial N_{Cxy}}{\partial x} + \frac{\partial M_{Dxy}}{\partial x} + \frac{\partial N_{sxy}}{\partial x} - T_{Dyz} - \frac{\pi}{h} T_{cyz} = 0 \tag{7}$$

where resultants are given by

$$\left\{ \begin{array}{l} N_{\alpha\beta} \\ N_{A\alpha\beta} \\ N_{C\alpha\beta} \\ N_{s\alpha\beta} \\ M_{\alpha\beta} \\ M_{B\alpha\beta} \\ M_{D\alpha\beta} \end{array} \right\}, \left\{ \begin{array}{l} T_{D\alpha z} \\ T_{B\alpha z} \\ T_{C\alpha z} \end{array} \right\}$$

$$= \sum_{z=1}^{nc} \int_{-h/2}^{h/2} \sigma_{\alpha\beta} \left\{ \begin{array}{l} 1 \\ A^k \\ C^k \\ \sin \frac{\pi z}{h} \\ z \\ z B^k \\ z D^k \end{array} \right\}, \tau_{\alpha z} \left\{ \begin{array}{l} D^k \\ B^k \\ \cos \frac{\pi z}{h} dz \end{array} \right\} dz \tag{8}$$

where  $\alpha, \beta$  take the symbols  $x, y$ .

### 3. A MULTIQUADRIC FORMULATION

The numerical methods for PDE problems should be high-order accurate, flexible with geometry, easy to implement and computationally efficient. The discretization methods used so far are typically finite differences and finite elements. Finite differences require a structured grid. Finite elements are flexible but higher-order accuracy is hard to achieve and both coding and meshing is time consuming, particularly when space dimension increases. Radial basis functions (RBFs) are a recent method that do not require a grid, depend only on the distance to a center point  $\mathbf{x}_j$  and is of the form  $g(\|\mathbf{x} - \mathbf{x}_j\|)$ . Consider a set of nodes  $x_1, x_2, \dots, x_N \in \Omega \subset \mathbb{R}^n$ . The multiquadric radial basis functions centered at  $\mathbf{x}_j$  are defined as  $g_j(\mathbf{x}) = (\|\mathbf{x} - \mathbf{x}_j\|^2 + c^2)^{\frac{1}{2}}$ , where  $c$  is a shape (user-defined) parameter. Consider a boundary-valued-problem with a domain  $\Omega \subset \mathbb{R}^n$  and a linear elliptic partial differential equation of the form

$$Lu(x) = s(x) \subset \mathbb{R}^n; Bu(x)|_{\partial\Omega} = f(x) \in \mathbb{R}^n \quad (9)$$

where  $L, B$  are differential operators in the domain  $\Omega$  and on the boundary  $\partial\Omega$ . We use points along the boundary  $(\mathbf{x}_j, j = 1, \dots, N_B)$  and in the interior  $(\mathbf{x}_j, j = N_B + 1, \dots, N)$ .

## 4. NUMERICAL EXAMPLES

### 4.1 Four layer $[0^\circ/90^\circ/90^\circ/0^\circ]$ square cross-ply laminated plate under sinusoidal load

A simply supported square laminated plate of side  $a$  and thickness  $h$  is composed of four equally layers oriented at  $[0^\circ/90^\circ/90^\circ/0^\circ]$ . The plate is subjected to a sinusoidal vertical pressure of the form  $p_z = P \sin\left(\frac{\pi x}{a}\right) \sin\left(\frac{\pi y}{a}\right)$ , with the origin of the coordinate system located at the lower left corner on the midplane. The orthotropic material properties are given by  $E_1 = 25.0E_2, G_{12} = G_{13} = 0.5E_2, G_{23} = 0.2E_2, \nu_{12} = 0.25$ .

In Table 1 the present method is compared with a finite strip formulation by Akhras [23, 24], an analytical solution by Reddy [25] using a higher-order formulation and an exact three dimensional solution by Pagano [26]. The present solution is also compared with another higher-order solution by the authors [21], a layerwise formulation by Ferreira [10] and a trigonometric shear deformation by the authors [22]. The in-plane displacements, the transverse displacements, the normal stresses and the in-plane and transverse shear stresses are presented in normalized form as  $\bar{w} = \frac{10^2 w_{max} h^3 E_2}{Pa^4}, \bar{\sigma}_{xx} = \frac{\sigma_{xx} h^2}{Pa^2}, \bar{\sigma}_{yy} = \frac{\sigma_{yy} h^2}{Pa^2}, \bar{\tau}_{zx} = \frac{\tau_{zx} h}{Pa}, \bar{\tau}_{xy} = \frac{\tau_{xy} h^2}{Pa^2}, \bar{u} = \frac{E_2 u_{max}}{hq}$ . The membrane stresses were evaluated at the following locations:  $\bar{\sigma}_{xx}(a/2, b/2, \frac{h}{2}), \bar{\sigma}_{yy}(a/2, b/2, \frac{h}{4})$ , and  $\bar{\tau}_{xy}(a, b, -\frac{h}{2})$ . The transverse shear stresses are calculated using the equilibrium equations at locations  $\bar{\tau}_{zx}(0, b/2, k = 1 \text{ and } 3)$ . We used three nodal

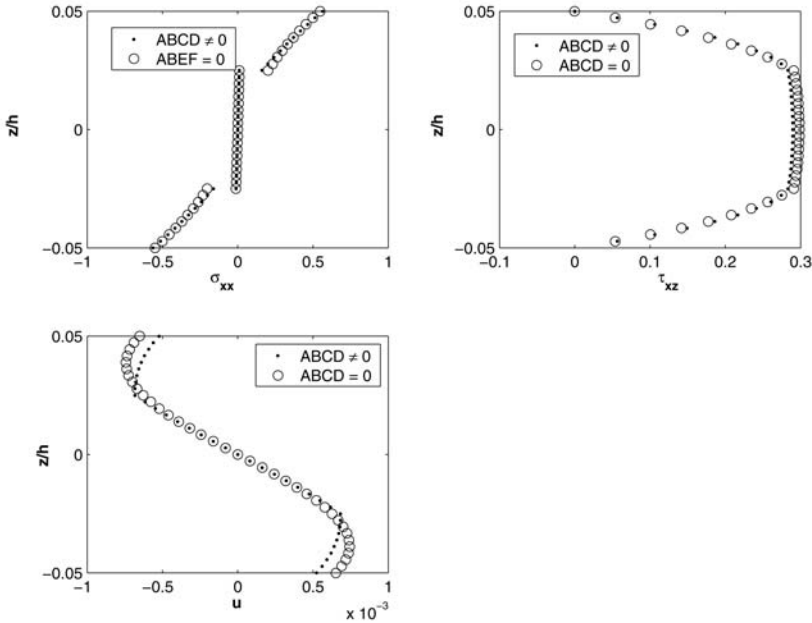


Figure 1. Normalized stresses,  $(\bar{\sigma}_x, \bar{\tau}_{xz})$  and in-plane displacement,  $\bar{u}$  for  $[0^\circ/90^\circ/90^\circ/0^\circ]$  square plate with  $N = 15, a/h = 10$

grids, with  $N = 11 \times 11, 15 \times 15$  and  $21 \times 21$  points. The present trigonometric layerwise deformation theory discretized with multiquadrics are a bit better results than previous results by Ferreira et al. [21]. Results are better than Akhras and Reddy when referred to the exact solutions. Results are worse than the layerwise theory of Ferreira [10], but better than the trigonometric higher order theory by Ferreira et al. [22]. The transverse shear stresses are calculated from equilibrium equations and are in good agreement with exact results. Normal and in-plane shear stresses are evaluated directly from the constitutive equations and are in very good agreement with exact solutions. Finally the profiles of the in-plane displacement,  $\bar{u}$ , the normal stress,  $\bar{\sigma}_{xx}$ , and the transverse shear stress,  $\bar{\tau}_{xz}$ , are illustrated in Figure 1. As can be seen there is a good and smooth evolution of all three fields.

### 4.2 Three layer square sandwich plate, under uniform load

The well-known sandwich example of Srinivas [27] is presented and discussed. It considers a simply supported square sandwich plate under uniform pressure. The ratio of side to thickness,  $a/h$  is taken as 10. The sandwich laminate considers two outside layers (skins) of thickness  $h_1 = h_3 = 0.1h$  and

Table 1.  $[0^\circ/90^\circ/90^\circ/0^\circ]$  square laminated plate under sinusoidal load.

$\frac{a}{h}$	Method	$\bar{w}$	$\bar{\sigma}_{xx}$	$\bar{\sigma}_{yy}$	$\bar{\tau}_{zx}$	$\bar{\tau}_{xy}$
4	Finite strip [23]	1.8939	0.6806	0.6463	0.2109	0.0450
	HSDT [25]	1.8937	0.6651	0.6322	0.2064	0.0440
	FSDT [24]	1.7100	0.4059	0.5765	0.1398	0.0308
	elasticity [26]	1.954	0.720	0.666	0.270	0.0467
	Ferreira et al. [21] (N=21)	1.8864	0.6659	0.6313	0.1352	0.0433
	Ferreira (layerwise) [10] (N=21)	1.9075	0.6432	0.6228	0.2166	0.0441
	Ferreira et al. [22] (N=21)	1.8987	0.6856	0.6316	0.2093	0.0438
	present (N=11)	1.8703	0.7580	0.6734	0.1975	0.0400
	present (N=15)	1.8800	0.7566	0.6764	0.1925	0.0414
	present (N=21)	1.8842	0.7560	0.6777	0.1885	0.0430
10	Finite strip [23]	0.7149	0.5589	0.3974	0.2697	0.0273
	HSDT [25]	0.7147	0.5456	0.3888	0.2640	0.0268
	FSDT [24]	0.6628	0.4989	0.3615	0.1667	0.0241
	elasticity [26]	0.743	0.559	0.403	0.301	0.0276
	Ferreira et al. [21] (N=21)	0.7153	0.5466	0.4383	0.3347	0.0267
	Ferreira (layerwise) [10] (N=21)	0.7309	0.5496	0.3956	0.2888	0.0273
	Ferreira et al. [22] (N=21)	0.7194	0.5491	0.6909	0.2999	0.0266
	present (N=11)	0.7320	0.5635	0.4046	0.2865	0.0264
	present (N=15)	0.7341	0.5638	0.4052	0.2897	0.0269
	present (N=21)	0.7350	0.5637	0.4055	0.2908	0.0272
100	Finite strip[23]	0.4343	0.5507	0.2769	0.2948	0.0217
	HSDT [25]	0.4343	0.5387	0.2708	0.2897	0.0213
	FSDT [24]	0.4337	0.5382	0.2705	0.1780	0.0213
	elasticity [26]	0.4347	0.539	0.271	0.339	0.0214
	Ferreira et al. [21] (N=21)	0.4365	0.5413	0.3359	0.4106	0.0215
	Ferreira (layerwise) [10] (N=21)	0.4374	0.5420	0.2697	0.3232	0.0216
	Ferreira et al. [22] (N=21)	0.4339	0.5384	0.2707	0.3360	0.0213
	present (N=11)	0.4329	0.5381	0.2706	0.3256	0.0208
	present (N=15)	0.4342	0.5387	0.2710	0.3319	0.0211
	present (N=21)	0.4345	0.5388	0.2710	0.3354	0.0213

one inner layer (core) of thickness  $h_2 = 0.8h$ . The skin orthotropic properties are obtained by multiplying an integer,  $R$ , by the core orthotropic properties, given by

$$\bar{Q}_{core} = \begin{bmatrix} 0.999781 & 0.231192 & 0 & 0 & 0 \\ 0.231192 & 0.524886 & 0 & 0 & 0 \\ 0 & 0 & 0.262931 & 0 & 0 \\ 0 & 0 & 0 & 0.266810 & 0 \\ 0 & 0 & 0 & 0 & 0.159914 \end{bmatrix}$$

The skin properties are obtained by  $\bar{Q}_{skin} = R\bar{Q}_{core}$ . In this example we considered three nodal grids, as in example 1. Results are compared with exact results of Srinivas [27] and finite element results of Pandya and Kant [28].

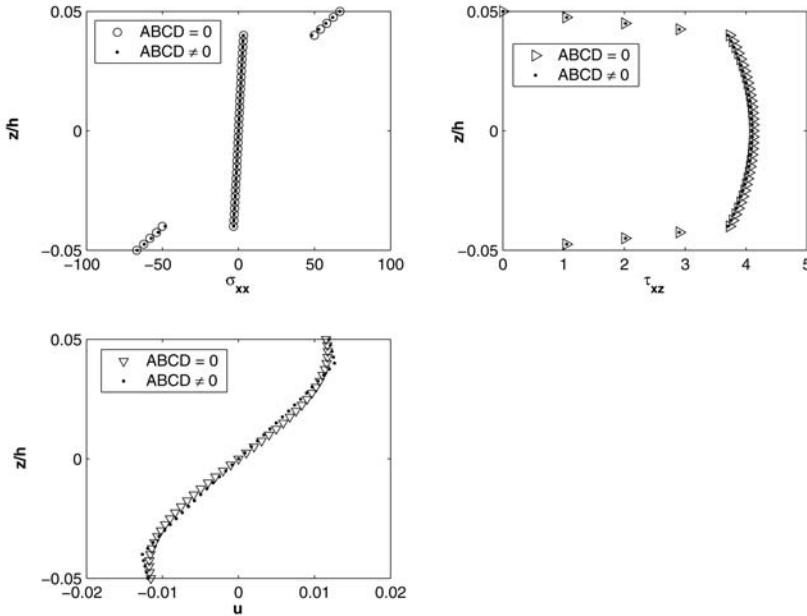


Figure 2. Normalized stresses,  $(\bar{\sigma}_{xx}, \bar{\tau}_{xz})$  and displacement,  $\bar{u}$  for a sandwich square plate with  $N = 15, a/h = 10, R = 15$ .

We also compare results with a shell finite formulation by Ferreira & Barbosa [29] and first order shear formulation with multiquadrics by Ferreira [19]. The present solution is also compared with another higher-order solution by the authors [21], a layerwise formulation by Ferreira [10] and a trigonometric shear deformation by the authors [22]. In-plane displacements, transverse displacement and stresses are normalized through factors  $\bar{w} = w \frac{0.999781}{hq}, \bar{\sigma}_{\alpha\alpha} = \frac{\sigma_{\alpha\alpha}}{q}, \bar{\tau}_{\alpha\beta} = \frac{\tau_{\alpha\beta}}{q}, \bar{u} = \frac{0.999781u}{hq}$ . The locations are given in Table 2, where  $R = 15$  is considered. The present formulation produces results that are in good agreement with all higher order formulations and in excellent agreement with exact results. The present formulation is specially adequate for sandwich-type structures, providing similar results to Ferreira et al. [10]. In Figure 2 the evolution of the normalized stresses,  $(\bar{\sigma}_{xx}, \bar{\tau}_{xz})$  and in-plane displacement,  $\bar{u}$  for  $R = 15$  is illustrated. The evolution of the transverse shear stresses  $\bar{\tau}_{xz}$  is quite interesting, showing that the trigonometric theory of Arya et al. [13] is excellent for this type of laminates.

## 5. CONCLUSIONS

In this paper we use a trigonometric layerwise deformation theory for modelling symmetric composite plates. The governing equations and the boundary

Table 2. Square laminated plate under uniform load,  $R = 15$ .

Method	$\bar{w}$	$\bar{\sigma}_{xx}^1$	$\bar{\sigma}_{xx}^2$	$\bar{\sigma}_{xx}^3$	$\bar{\tau}_{xz}^1$	$\bar{\tau}_{xz}^2$
	(a/2,a/2,0)	(a/2,a/2,h/2)	(a/2,a/2,2h/5)	(a/2,a/2,2h/5)	(0,a/2,0)	(0,a/2,-2h/5)
HSDT[28]	110.43	66.62	51.97	3.465	3.035	2.691
FSDT[28]	90.85	70.04	56.03	3.753	3.091	2.764
CLT	81.768	69.135	55.308	3.687	4.2825	3.8287
Ferreira & Barbosa [29]	121.821	65.650	47.090	3.140	3.466	3.466
Ferreira (N=15) [19]	121.184	63.214	50.571	3.371	3.466	3.099
exact [27]	121.720	66.787	48.299	3.238	3.964	3.577
Ferreira et al. [21] (HSDT) (N=21)	114.644	66.920	50.323	3.355	3.021	2.275
Ferreira (layerwise) [10] (N=21)	120.988	66.291	47.899	3.193	3.831	3.256
Ferreira et al. [22] (N=21)	115.460	66.870	50.041	3.336	4.177	3.771
present (N=11)	120.950	66.378	47.962	3.197	3.951	3.577
present (N=15)	121.680	66.659	48.148	3.210	4.105	3.705
present (N=21)	121.880	66.730	48.204	3.214	4.167	3.742

conditions are easily discretized via multiquadric radial basis function method. The results obtained are compared with solutions derived from other models and numerical technics. The results show that the use of trigonometric layerwise deformation theory discretized with multiquadrics provides very good solutions for composite plates and excellent results for sandwich plates. The trigonometric theory of Arya et al. [13] for beams was extended to composite plates and showed excellent behaviour particularly in transverse shear stresses. This layerwise approach is an evolution of a higher order trigonometric shear deformation technique presented by the authors. The multiquadric radial basis function method proved to yield convergent and accurate solutions.

## REFERENCES

- [1] J.M. Whitney and N.J. Pagano. Shear deformation in heterogeneous anisotropic plates. *ASME J. of Appl. Mech.*, 37:1031–1036, 1970.
- [2] E. Reissner. A consistent treatment of transverse shear deformations in laminated anisotropic plates. *AIAA J.*, 10(5):716–718, 1972.
- [3] J.N. Reddy. *Energy and Variational Methods in Applied Mechanics*. John Wiley, New York, 1984.
- [4] C.T. Sun. Theory of laminated plates. *J. of Applied Mechanics*, 38:231–238, 1971.
- [5] J.M. Whitney and C.T. Sun. A higher order theory for extensional motion of laminated anisotropic shells and plates. *J. of Sound and Vibration*, 30:85–97, 1973.
- [6] J.N. Reddy. A simple higher-order theory for laminated composite plates. *J. of Applied Mechanics*, 51:745–752, 1984.
- [7] M. Di Sciuva. An improved shear-deformation theory for moderately thick multilayered shells and plates. *J. of Applied Mechanics*, 54:589–597, 1987.
- [8] H. Murakami. Laminated composite plate theory with improved in-plane responses. *Journal of Applied Mechanics*, 53:661–666, 1986.

- [9] J.G. Ren. A new theory of laminated plate. *Composite Science and Technology*, 26:225–239, 1986.
- [10] A.J.M. Ferreira. Analysis of composite plates using a layerwise shear deformation theory and multiquadrics discretization. *Mechanics of Advanced Materials and Structures*, 2004, to appear.
- [11] D.H. Robbins and J.N. Reddy. Modelling of thick composites using a laminate layerwise theory. *Int. J. Num. Meth. Eng.*, 36:655–677, 1993.
- [12] E. Carrera.  $C^0$  reissner-mindlin multilayered plate elements including zig-zag and interlaminar stress continuity. *International Journal of Numerical Methods in Engineering*, 39:1797–1820, 1996.
- [13] H. Arya, R.P. Shimpi, and N.K. Naik. A zigzag model for laminated composite beams. *Composite structures*, 56:21–24, 2002.
- [14] R.P. Shimpi and A.V. Ainapure. A beam finite element based on layerwise trigonometric shear deformation theory. *Composite structures*, 53:153–162, 2001.
- [15] R.L. Hardy. Multiquadric equations of topography and other irregular surfaces. *Geophys. Res.*, 176:1905–1915, 1971.
- [16] R.L. Hardy. Theory and applications of the multiquadric-biharmonic method: 20 years of discovery. *Computers Math. Applic.*, 19(8/9):163–208, 1990.
- [17] E.J. Kansa. Multiquadrics- a scattered data approximation scheme with applications to computational fluid dynamics. i: Surface approximations and partial derivative estimates. *Comput. Math. Appl.*, 19(8/9):127–145, 1990.
- [18] E.J. Kansa. Multiquadrics- a scattered data approximation scheme with applications to computational fluid dynamics. ii: Solutions to parabolic, hyperbolic and elliptic partial differential equations. *Comput. Math. Appl.*, 19(8/9):147–161, 1990.
- [19] A.J.M. Ferreira. A formulation of the multiquadric radial basis function method for the analysis of laminated composite plates. *Composite Structures*, 59:385–392, 2003.
- [20] A.J.M. Ferreira. Thick composite beam analysis using a global meshless approximation based on radial basis functions. *Mechanics of Advanced Materials and Structures*, 10:271–284, 2003.
- [21] A.J.M. Ferreira, C.M.C. Roque, and P.A. L.S. Martins. Analysis of composite plates using higher-order shear deformation theory and a finite point formulation based on the multiquadric radial basis function method. *Composites: Part B*, 34:627–636, 2003.
- [22] A.J.M. Ferreira, C.M.C. Roque, and R.M.N. Jorge. Analysis of composite plates by trigonometric shear deformation theory and multiquadrics. *submitted*, 2004.
- [23] G. Akhras, M.S. Cheung, and W. Li. Finite strip analysis for anisotropic laminated composite plates using higher-order deformation theory. *Computers & Structures*, 52(3):471–477, 1994.
- [24] G. Akhras, M.S. Cheung, and W. Li. Static and vibrations analysis of anisotropic laminated plates by finite strip method. *Int. J.Solids Struct*, 30(22):3129–3137, 1993.
- [25] J.N. Reddy. A simple higher-order theory for laminated composite plates. *J. Appl. Mech.*, 51:745–752, 1984.
- [26] N.J. Pagano. Exact solutions for rectangular bidirectional composites and sandwich plates. *J. Compos. Mater*, 4:20–34, 1970.
- [27] S. Srinivas. A refined analysis of composite laminates. *J. Sound and Vibration*, 30:495–507, 1973.

- [28] B.N. Pandya and T. Kant. Higher-order shear deformable theories for flexure of sandwich plates-finite element evaluations. *Int. J. Solids and Structures*, 24:419–451, 1988.
- [29] A.J.M. Ferreira and J.T. Barbosa. Buckling behaviour of composite shells. *Composite Structures*, 50:93–98, 2000.

# STABILITY BEHAVIOUR OF CYLINDRICAL AND CONICAL SANDWICH SHELLS WITH FLEXIBLE CORE

Congying Zhong and Hans-G. Reimerdes

*Institut für Leichtbau, RWTH Aachen University, Wüllnerstraße 7, D-52062 Aachen, Germany*

zhong@ilb.rwth-aachen.de, hg\_reim@ilb.rwth-aachen.de

**Abstract** A higher-order theory for the analysis of cylindrical and conical sandwich shells with flexible core is presented. The governing differential equations are derived on the basis of a three-layer model and solved by numerical integration. The theory is verified by comparison of achieved results to those published in the literature and to finite element computations.

**Keywords:** three-layer theory, stability, sandwich shell.

## 1. INTRODUCTION

Static and stability of sandwich structures have been studied by many researchers in recent years [1], [2], [3] and [4]. In order to describe the behaviour of sandwich shells with a flexible core, a “three-layer sandwich model” has been developed by Bansemir [1] as well as by Frostig and Baruch [2]. Using this modeling approach the governing differential equations are established by treating the face sheets and the core as three individual layers. The equations for the layers are combined by using the conditions of continuity of the deformations and the stress distribution at the interface between face sheets and core. Karyadi [3] developed the theory to study the collapse behaviour of cylindrical sandwich shells. Karyadi solved the differential equations by use of the finite difference method. Zhong [4] derived differential equations for cylindrical and conical sandwich shells. For the face sheets Zhong used a consistent shell bending theory established by Rittweger [5], and achieved stiffness matrices for closed shell sections by numerical integration of the differential equations.

This paper continues the work presented in [4]. The structural model will be briefly repeated. For the load introduction at the edges global boundary conditions are used. Example calculations for cylindrical and conical sandwich

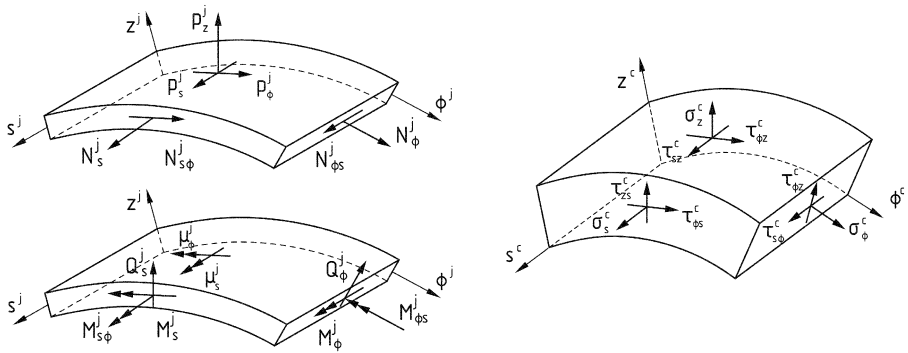


Figure 1. External loads and internal resultants in the face sheets, stresses in the core.

shells are conducted. The effects of parameters like core stiffness, as well as cone vertex half-angle are presented.

## 2. STRUCTURAL MODEL

Here, the structural model is repeated briefly. A detailed description is given in [4].

### 2.1 Assumptions

The theoretical model is based on the following assumptions:

- The face sheets are considered as thin shells satisfying the Kirchhoff–Love hypothesis. Rittweger’s formulation [5] is used.
- The in-plane extensional and shear stiffnesses of the core are neglected.
- The deformations and the stress distribution are continuous at the interface between core and face sheets.

In Figure 1 the resulting internal and external forces in the face sheets and the considered stresses in the core are shown.

### 2.2 Governing equations

The equilibrium equations and the consistent boundary conditions are derived according to the principle of minimum potential energy. The principle states:

$$\delta(U + V) = \delta(U_f + V_f) + \delta(U_c + V_c) = 0 \quad (1)$$

where the subscripts  $f$  and  $c$  represent the face sheets and the core, respectively. For the three-layer model a system of 18 partial differential equations of

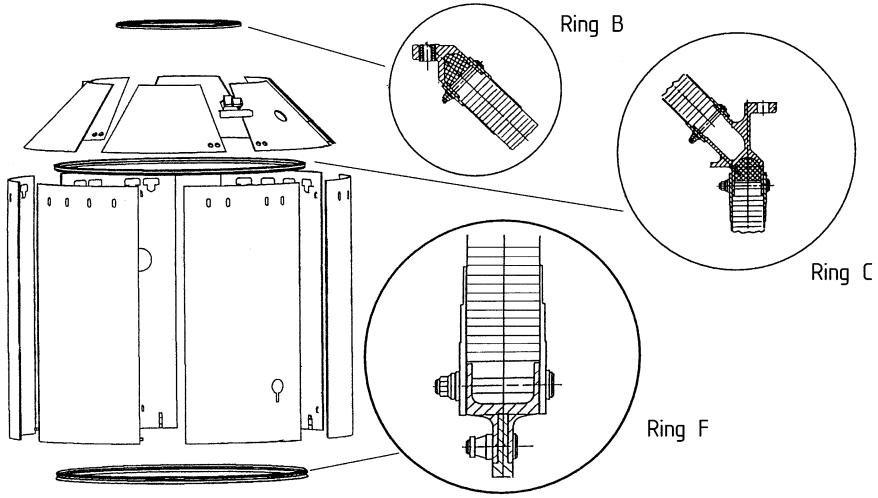


Figure 2. SPELTRA sandwich shell (Ariane 5).

first order as presented in [4] is achieved:

$$\{\mathbf{Y}(s, \phi)\}_s = [\mathbf{A}(s, \phi)]\{\mathbf{Y}(s, \phi)\} \tag{2}$$

with the state vector (t - top face; b - bottom face; c - core):

$$\{\mathbf{Y}(s, \phi)\} = \{u^t, v^t, w^t, \beta^t, W^c, u^b, v^b, w^b, \beta^b, \hat{N}_s^t, \hat{N}_{s\phi}^t, \hat{Q}_s^t, M_s^t, \tau_{sz}^c, \hat{N}_s^b, \hat{N}_{s\phi}^b, \hat{Q}_s^b, M_s^b\}^T$$

### 2.3 Boundary conditions at stiff edges

For the treatment of realistic sandwich structures with load introduction elements (e.g. stiff rings shown in Figure 2) the local deformations and stress resultants of the face sheets (local boundaries) are transformed to global boundaries acting at the centerline of a stiff ring with radius  $r^g$ . The assumption of rigid load introduction elements (Figure 3, [3]) results in the following relations for deformations and stress resultants:

$$\begin{aligned} u^g &= \frac{r^g - r^b}{r^t - r^b} u^t + \frac{r^t - r^g}{r^t - r^b} u^b & w^g &= w^t = w^b \\ v^g &= \frac{r^g - r^b}{r^t - r^b} v^t + \frac{r^t - r^g}{r^t - r^b} v^b & w_{r_s}^g &= \frac{u^t - u^b}{r^t - r^b} \\ \bar{N}_s^g r^g &= r^b \hat{N}_s^b + r^t \hat{N}_s^t & \bar{N}_{s\phi}^g r^{g2} &= r^{b2} \hat{N}_{s\phi}^b + r^{t2} \hat{N}_{s\phi}^t \end{aligned}$$

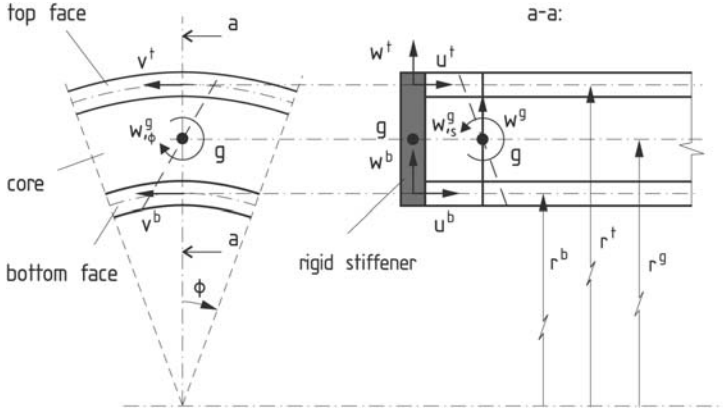


Figure 3. Local and global boundary conditions.

$$\begin{aligned} \bar{Q}_s^g r^g &= r^b \hat{Q}_s^b + r^t \hat{Q}_s^t - \frac{r^g - r^b}{r^g} \hat{N}_{s\phi}^b r^b + \frac{r^t - r^g}{r^g} \hat{N}_{s\phi}^t r^t \\ \bar{M}_s^g r^g &= r^b (r^g - r^b) \hat{N}_s^b + r^b M_s^b + r^t (r^g - r^t) \hat{N}_s^t + r^t M_s^t \end{aligned}$$

## 2.4 Consideration of prebuckling deformation and/or imperfections

In order to perform nonlinear stability investigations or to consider geometrical imperfections, prebuckling deformations are introduced in the differential equations. In a first step, only axis-symmetric radial deformations are considered.

## 3. SOLUTION STRATEGIES

The partial differential equations (2) are reduced to ordinary ones by expanding the variables into trigonometric Fourier series and applying Galerkin's method:

$$\{\mathbf{Y}(s)\}_{r_s} = [\mathbf{A}(s)]\{\mathbf{Y}(s)\} \tag{3}$$

Numerical integration of these differential equations leads to the transfer matrix:

$$\begin{Bmatrix} d_1 \\ p_1 \end{Bmatrix} = \begin{bmatrix} \mathbf{B}_{11} & \mathbf{B}_{12} \\ \mathbf{B}_{21} & \mathbf{B}_{22} \end{bmatrix} \begin{Bmatrix} d_0 \\ p_0 \end{Bmatrix} + \begin{Bmatrix} P_d \\ P_f \end{Bmatrix} \tag{4}$$

This is transformed into the stiffness matrix of the sandwich element:

$$\begin{Bmatrix} p_0 \\ p_1 \end{Bmatrix} = \begin{bmatrix} \mathbf{K}_{11} & \mathbf{K}_{12} \\ \mathbf{K}_{21} & \mathbf{K}_{22} \end{bmatrix} \begin{Bmatrix} d_0 \\ d_1 \end{Bmatrix} + \begin{Bmatrix} P_0 \\ P_1 \end{Bmatrix} \tag{5}$$

For the complete sandwich shell structure the general stiffness matrix  $[\mathbf{K}_g]$  is assembled.

### Linear Static

Applying the direct-stiffness-method gives:

$$\{\mathbf{P}\} = [\mathbf{K}_g]\{\mathbf{D}\} \quad (6)$$

For a given load vektor  $\{\mathbf{P}\}$  and defined boundary conditions the deformations  $\{\mathbf{D}\}$  are computed by solving equation (6). Using these and the element stiffness matrices, the stress distributions in the face sheets and the core are calculated.

### Nonlinear Static

With the membrane stresses of the linear static analysis used as pre-stresses the stiffness matrix is computed again:

$$\{\mathbf{P}\} = [\mathbf{K}_{g,pre}]\{\mathbf{D}\} \quad (7)$$

The solution of equation (7) gives improved results for the deformations.

### Linear Stability

The linear stability investigation is based on the principle of virtual work, which states for the pre-stressed structure in equilibrium:

$$[\mathbf{K}_{g,pre}]\{\delta\mathbf{D}\} = 0 \quad (8)$$

The stiffness matrix  $[\mathbf{K}_{g,pre}]$  is splitted into the linear part and the geometrical stiffness matrix:

$$[\mathbf{K}_{g,pre}(N_i)] = \left( [\mathbf{K}_g] - [\mathbf{K}_{\sigma_i}] \right) \quad (9)$$

Linearization results in:

$$[\mathbf{K}_{g,pre}(\lambda_i N_i)] = \left( [\mathbf{K}_g] - \lambda_i [\mathbf{K}_{\sigma_i}] \right) \quad (10)$$

which leads to the following general eigenvalue problem:

$$\left( [\mathbf{K}_g] - \lambda_i [\mathbf{K}_{\sigma_i}] \right) \{\delta\mathbf{D}\} = 0 \quad (11)$$

The solution of equation (11) may be improved by an iteration procedure.

### Nonlinear Stability/Imperfections

Presently, the nonlinear stability investigation is conducted based on the nonlinear stiffness matrix  $[\mathbf{K}_{g,pre/def}]$  which is achieved, if in addition to the pre-stresses the pre-deformations including the geometrical imperfections are considered in the nonlinear terms. An iteration procedure leads finally to the nonlinear bifurcation load of the structure.

Table 1. Shell geometry und material properties.

Geometry:			
$L = 762$ mm	(Length)	$t^f = 0.257$ mm	(Thickness of the face sheets)
$R^c = 457.2$ mm	(Radius)	$t^c = 10.29$ mm	(Thickness of the core)
Material properties:			
face sheets (isotropic):		$E_f = 6.895 \cdot 10^4$ N/mm <sup>2</sup>	$\nu = 0.3$
Honeycomb core:			
$E_c$ [N/mm <sup>2</sup> ]	=	$6.895 \cdot 10^4$ ,	$1.379 \cdot 10^3$ ,
		$1.379 \cdot 10^2$ ,	$6.895 \cdot 10^{-1}$
$G_s = G_\phi = G_c = E_c/5$			

Table 2. Axial compression – linear stability analysis, simply supported.

$E_c$ [N/mm <sup>2</sup> ]	$N_s^{cr}$ [N/mm]			Failure mode
	[Bartelds]	[MSC/MARC]	[ilb-SAND]	
$6.895 \cdot 10^4$	-858.22	-854.63	-843.63	global buckling
$1.379 \cdot 10^3$	-678.84	-676.72	-670.99	symmetrical wrinkling
$1.379 \cdot 10^2$	-214.98	-219.50	-212.16	symmetrical wrinkling
$6.895 \cdot 10^{-1}$	-13.49	-13.49	-13.49	asymmetrical wrinkling

## 4. NUMERICAL RESULTS

In order to verify the developed sandwich shell element, example computations are performed. First, the achieved results are compared to those published in the literature and obtained by Finite-Element computations. After that parametric studies are performed.

### 4.1 Verification computation

A cylindrical sandwich shell reported by Bartelds [6] is investigated. Geometry and material properties of the shell are presented in Table 1. The stiffness of the core is varied in order to trigger different failure modes.

In Table 2 results for the axisymmetric buckling state achieved with the sandwich shell element presented here are compared to Bartelds's results and to those achieved by using finite element program MSC/MARC. Here axisymmetric thin shell elements and solid elements are used to create the face sheets and the core respectively.

The results show a good agreement. The critical buckling mode for the case of the very stiff honeycomb core is according to ilb-SAND computation not axisymmetric. With a circumferential wavenumber of  $m = 4$  the critical buckling load is  $N_s^{cr} = -780.74$  N/mm.

Baker [7] presents test data for two axially compressed sandwich cone frusta having a vertex half-angle  $\alpha = 15^\circ$ . The details of the test specimen are shown in Table 3. A comparison of our computational results to Baker's test results

Table 3. Geometry and material properties of Baker’s cone frustum.

Geometry:	
Length of generator:	$L = 1309 \text{ mm}$
inside radius: small end, large end	$R_s^b = 500 \text{ mm}, R_l^b = 848.5 \text{ mm}$
Thickness: face sheets, core	$t^f = 0.366 \text{ mm}, t^c = 5.08 \text{ mm}$
Material properties:	
face sheets (7178-T6 aluminium isotropic):	$E_f = 7.240 \cdot 10^4 \text{ N/mm}^2 \quad \nu = 0.33$
Al 1/8 505215P Hexcel honeycomb core:	$E_c = 1.027 \cdot 10^3 \text{ N/mm}^2$
	$G_s = 5.295 \cdot 10^2 \text{ N/mm}^2, \quad G_\phi = 2.537 \cdot 10^2 \text{ N/mm}^2$

Table 4. Critical buckling loads.

$P_{cr}$ [Baker]	$P_{cr}$ [Seide/Wiedemann]	$P_{cr}$ [NASTRAN]	$P_{cr}$ [ilb-SAND]
$-0.903 \cdot 10^6 \text{ N}$	$-1.718 \cdot 10^6 \text{ N}$	$-1.734 \cdot 10^6 \text{ N} (m = 6)$	$-1.704 \cdot 10^6 \text{ N} (m = 6)$

is not useful as his shell buckles plastically. Therefore in Table 4 a classical approximation of the buckling load and a finite element result are given in addition.

According to Seide [8], the critical load of a cone frusta can be approximated by that of an equivalent cylinder multiplied by the square of the cosine of the vertex half-angle. Using the critical load formula for a sandwich cylinder given by Wiedemann [9], the following approximation for the critical load of a cone is achieved:

$$P_{cr_{cone}} = \frac{4\pi E_f t^f t^c}{\sqrt{1 - \nu^2}} \left( 1 - \frac{E_f t^f}{2G_c R_e \sqrt{1 - \nu^2}} \right) \cos^2 \alpha \quad (12)$$

The finite element result is computed using MSC/NASTRAN. Here a shear flexible shell element was used to idealize the sandwich shell.

The different theoretical analyses show a good agreement. At least for the vertex half-angle  $\alpha = 15^\circ$ , Seide’s approach gives a very good estimate.

## 4.2 Variation of the vertex half-angle

In the following the axial buckling load is computed for conical sandwich shells depending on the vertex half-angle. Two cases are investigated. The first represents configurations, leading to global buckling while the second set of results is achieved for shell dimensions, leading to symmetrical wrinkling.

**Global buckling.** The computations for this case are based on the shell structure given in Table 3. The vertex half-angle  $\alpha$  is varied from  $0^\circ$  to  $60^\circ$  in  $15^\circ$  increments. The radius at the top of the shell ( $R_s^b = 500 \text{ mm}$ ) is kept constant as well as the length in axial direction ( $L = 1264 \text{ mm}$ ). The achieved

Table 5. Critical loads depending on the vertex half-angle – global buckling.

$\alpha$	0°	15°	30°	45°	60°
$P_{cr}$ ( $10^6$ N)	-1.795	-1.686	-1.368	-0.924	-0.473
$P_{cr}/P_{cr,0^\circ}$	1.0	0.939	0.762	0.515	0.264
$\cos^2 \alpha$	1.0	0.933	0.750	0.500	0.250

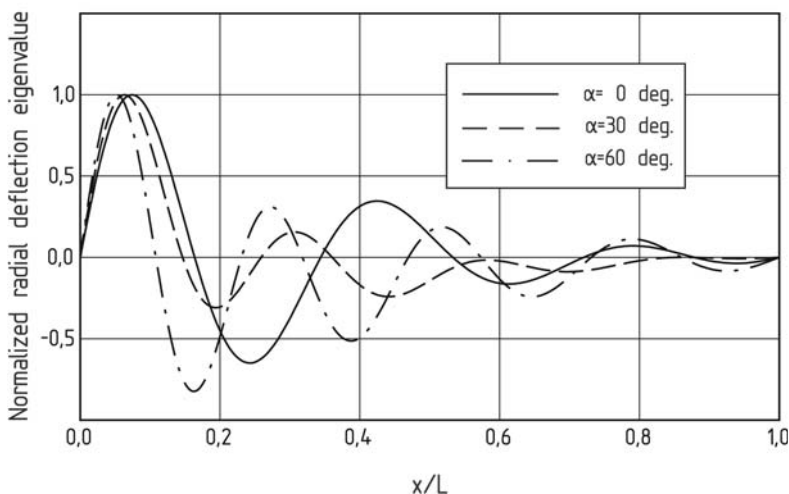


Figure 4. Global buckling modes of the cones.

results are presented in Table 5. One can see that Seide's approximation gives a very good estimate and that equation (12) is useful for design purposes. The buckling mode shapes in longitudinal direction are presented in Figure 4. They show for all investigated vertex half-angles global buckling.

**Local buckling – symmetrical wrinkling.** For this investigation the shell given in Table 1 with a core stiffness of  $E_c = 1.379 \cdot 10^2$  N/mm<sup>2</sup> is selected. The vertex half-angle  $\alpha$  is varied from 0° to 45° in 15° increments. The radius at the top of the shell ( $R_s^c = 457.2$  mm) is again kept constant. The length in axial direction is reduced to  $L = 381$  mm and kept constant, too. In Table 6 the achieved results are presented. They show that the critical axial load changes almost linearly with the cosine of the vertex half-angle. This is due to the fact that the local buckling strength is rarely dependent on the radius of curvature. The buckling mode shapes are shown in Figure 5. It can be seen that in case of the conical shell the failure is to be expected close to the small radius at the upper end of the shell. The half-wave length of the buckling pattern is independent of the vertex half-angle.

Table 6. Critical loads depending on the vertex half-angle – local buckling.

$\alpha$	0°	15°	30°	45°
$P_{cr}$ ( $10^6$ N)	0.609	0.603	0.550	0.456
$P_{cr}/P_{cr,0^\circ}$	1.0	0.989	0.903	0.748
$\cos \alpha$	1.0	0.966	0.866	0.707

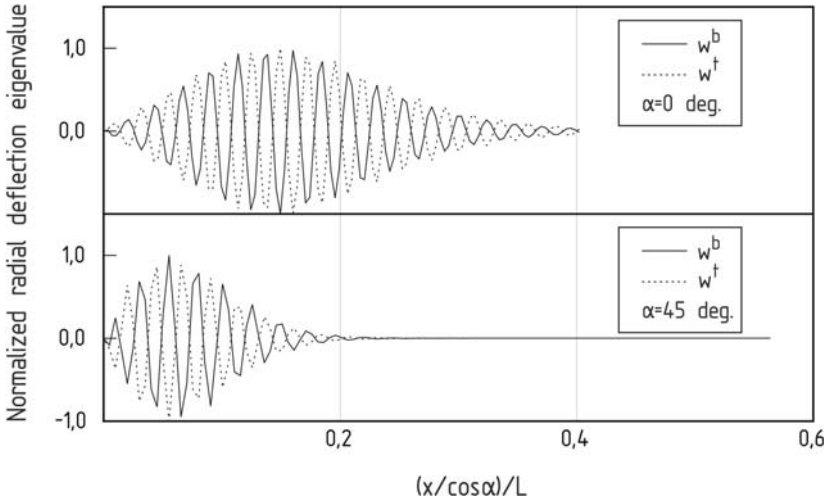


Figure 5. Local buckling modes of the cones.

## 5. CONCLUSION

A higher-order theory based on a three-layer model for the stability investigation of cylindrical and conical sandwich shells is introduced. The comparisons of example computation to results from literature or from FEM computation verify that the theory is suitable to find global and local instability modes. The effects of core stiffness, as well as of the cone’s vertex half-angle to the stability of cylindrical and conical sandwich shells are investigated. The achieved results give insight into the behaviour of such structures and allow to establish design recommendations.

## ACKNOWLEDGMENT

Part of the research work presented is sponsored by Deutsche Forschungsgemeinschaft (German Research Association) through Graduiertenkolleg “Transportvorgänge in Hyperschallströmungen” at RWTH Aachen University, Germany.

**REFERENCES**

- [1] H. Bansemir. *Ein Beitrag zur Biegetheorie von Sandwichplatten und Plattenstreifen sowie zur Krafteinleitung in versteifte orthotrope Scheiben*. PhD thesis, TU-München, Germany, 1973.
- [2] Y. Frostig and M. Baruch. High-order buckling analysis of sandwich beams with transversely flexible core. *Journal of ASCE, EM Division*, 119(3):476–495, 1993.
- [3] E. Karyadi. *Collapse Behavior of Imperfect Sandwich Cylindrical Shells*. PhD thesis, University Delft, The Netherlands, 1998.
- [4] C. Zhong and H.-G. Reimerdes. A higher-order theory for stability analysis of cylindrical and conical shells with flexible cores. *Proceedings of the Fifth international Conference on Sandwich Construction*, 1:117–127, 2000.
- [5] A. Rittweger. *Statik, Stabilität und Eigenschwingungen anisotroper Rotationsschalen beliebigen Meridians mit der Übertragungsmatrizen-Methode*. PhD thesis, RWTH Aachen, Germany, 1992.
- [6] G. Bartelds. *Unified theory for nonlinear bending and buckling of sandwich shells (application to buckling of circular cylinders in axial compression)*. PhD thesis, Stanford University, 1967.
- [7] E.H. Baker. Experimental investigation of sandwich cylinders and cones subjected to axial compression. *AIAA Journal*, 6(9):117–127, September 1968.
- [8] P. Seide. Axisymmetrical buckling of circular cones under axial compression. *Journal of Applied Mechanics*, 23:625–628, December 1956.
- [9] J. Wiedemann. *Leichtbau 1: Element*. Springer-Verlag, Berlin, 1996.

# HIGH ORDER NONLINEAR CONTACT EFFECTS IN THE DYNAMIC BEHAVIOR OF DELAMINATED SANDWICH PANELS WITH A FLEXIBLE CORE

H. Schwarts-Givli, O. Rabinovitch and Y. Frostig

*Faculty of Civil and Environmental Engineering, Technion, Israel Institute of Technology, Haifa 32000, Israel*

**Abstract** The dynamic behavior of sandwich panels with a flexible core and debonded region with and without contact is studied. The investigation uses the high-order theory of sandwich panels and considers geometrical nonlinear effects and the nonlinearity associated with the contact characteristics of the delaminated surfaces. The rotary inertia of the face-sheets and the core and the high order velocity and acceleration fields through the depth of the core are included. The dynamic governing equations, boundary conditions and continuity requirements are derived through the Hamilton principle. Numerical results that reveal the influence of the contact characteristics on the dynamic response of the sandwich panel are also presented and discussed.

**Keywords:** delamination, contact effects, nonlinear, flexible core, high-order.

## 1. INTRODUCTION

Modern sandwich panel are commonly made of cores made of plastic foam or lightweight honeycomb, denoted also as “soft” core. Such core materials posses a shear resistance, but they are very flexible in the longitudinal and vertical directions. These characteristics of the “soft” core introduce localized deformations and stresses, which may lead to a relative displacement between the upper and lower face-sheets, to a change in the core height, and to a non-linear pattern of a plane-section. In addition, the dynamic behavior of such soft core sandwich panels is characterized by global modes, localized modes, and vibrations through the depth of the core.

This effect is associated with wave like behavior thorough the depth of the core during motion. While these effects are critical, they can not be predicted by classical theories for sandwich panels [1].

The layered configuration of the sandwich panel, along with considerable difference between the elastic properties of the face-sheets and the core, and the manufacturing process make the sandwich structure susceptible to delamination between the face-sheets and core. The delamination affects the integrity of the structure, reduces the overall stiffness, and modifies the dynamic behavior of the panel.

The delaminated surfaces are characterized by a horizontal slip between the core and the adjacent face-sheet, and therefore they are free of shear stresses. However, they can accommodate vertical normal compressive stress if contact between the delaminated surfaces exists. The interaction between the delaminated surfaces depends on their relative position during motion. In certain circumstances, the delaminated surfaces separate from each other. As a result, contact does not exist and the surfaces are free of shear and vertical normal stresses. Under different conditions, the surfaces tend to close and vertical contact exists between the face-sheet and the core. Delaminated regions, denoted by "partial contact" regions, may include both types of contact characteristics due to the inertial forces, buckling of the face-sheets or stress concentration due to external loads. Moreover, the contact characteristics may change during the motion of the panel. The existence (or absence) of the interfacial vertical normal stresses within the delaminated zone affects the behavior of the structure and dominates the stress and deformation fields in the face sheets and the core. These effects are even more pronounced when dynamic loads and time dependent contact characteristics are involved. Neglecting the effects of the nonlinear constraints associated with the contact phenomenon may lead to inconsistent results such as overlapping of the core and the face-sheet or development of tensile stresses at the delaminated interface.

The dynamic behavior of delaminated sandwich panels has been examined only in a small number of studies [2, 3]. In these studies, the high order displacements of the core and the contact behavior of the delaminated surfaces were not considered. Other studies that focused on laminated composite panels did consider the contact phenomenon associated with the delaminated surfaces, see [4, 5], however, they assume that the existence (or absence) of contact at the delaminated interface does not change during the motion. A complete contact analysis, which results from the nonlinear geometric behavior, has been performed for the static behavior of delaminated panels, see [6, 7], and for the dynamic response of sandwich structures with an incompressible core [8]. The dynamic behavior of delaminated sandwich panels with a soft core, which considers the partial

and time-dependent contact between the debonded surfaces, has not been addressed yet.

The main goal of this research is to investigate the dynamic behavior of delaminated sandwich panels. The analysis considers the nonlinear effects associated with the time dependent contact characteristics between the delaminated surfaces, as well as the high order displacement, velocity and acceleration fields in the core. Also, since the response of the delaminated panel is usually associated with large displacements, nonlinear kinematic relations for the face-sheets are included. Another objective of the study is to examine the common assumption that the two limiting cases associated with fully constrained (the surfaces in the delaminated region are always in contact) and completely free delaminated surfaces yield upper and lower bounds for the time depended contact characteristics of the panel.

## 2. MATHEMATICAL FORMULATION

The field equations for the delaminated panel are derived through the Hamilton principle and following the procedure described in [9-12]. The face-sheets are considered as ordinary unidirectional panels with inplane and flexural rigidities, negligible shear strains, and within an intermediate class of deformations. The core, which is assumed to undergo small deformations, is linear elastic and can resist shear and vertical normal stresses, while its longitudinal stresses are neglected. The height of the core may change, and its plane section does not remain planer under loading.

For the core, it is assumed that the longitudinal and vertical displacements take a cubic and quadratic polynomial variation through the thickness, respectively. This displacement field enables a general and consistent variational formulation in terms of displacement unknowns, and avoids the mixed formulation used in [13]. Thus, the displacements fields of the core read:

$$\begin{aligned}
 w_c(x, z_c, t) &= w_0(x, t) + w_1(x, t)z_c + w_2(x, t)z_c^2 \\
 u_c(x, z_c, t) &= u_0(x, t) + u_1(x, t)z_c + u_2(x, t)z_c^2 + u_3(x, t)z_c^3
 \end{aligned}
 \tag{1}$$

where  $u_c(x, z_c, t)$ ,  $w_c(x, z_c, t)$  are the displacements in the longitudinal and vertical directions of the core, respectively;  $u_i(x, t)$  ( $i = 0,1,2,3$ ) and  $w_i(x, t)$  ( $i = 0,1,2$ ) are unknown.

A sandwich panel which is debonded at one of its face-core interfaces includes two types of regions: a fully bonded region and a delaminated region, in which the interfacial surfaces may longitudinally slip with respect to one another, but may be in contact vertically. Moreover, the delaminated

regions may consist of two types of sub-regions: The first one is a debonded "with contact" sub-region, in which the vertical normal stress develops at the interface. The second one is a debonded "without contact" sub-region, where the interfacial surfaces are stress-free. The stress and displacement fields in the core along with the interfacial continuity conditions, associated with each type of region/sub-region lead to a unique set of governing equations for each region/sub-region, as follows, see [12]:

$$\begin{aligned}
 & -M_{xxt,xx} + M_t \ddot{w}_t - \psi N_{xxt,x} w_{t,x} - \psi N_{xxt} w_{t,xx} + \\
 & + m_{t,x} - q_t - \left( I_{mt} + \alpha_3 \frac{3M_c c^2}{875} + \alpha_1 \frac{3M_c d_t^2}{140} \right) \ddot{w}_{t,xx} \\
 & \left( \frac{\alpha_3}{5c} + \frac{\alpha_1}{c} + \frac{2\alpha_1 d_t}{c^2} \right) M_{Q1c,x} + \left( \frac{2\alpha_3}{5c^2} - \frac{2\alpha_1}{c^2} - \frac{6\alpha_1 d_t}{c^3} \right) M_{Q2c,x} + \\
 & (\alpha_3 + \alpha_1) \left( \frac{4M_{zc}}{c^2} - \frac{R_{zc}}{c} \right) + \alpha_1 \frac{3M_c d_t}{70} \ddot{u}_{ot,x} + \\
 & \left( \frac{\alpha_1 d_t}{140} - \frac{11\alpha_3 c}{1750} \right) M_c \ddot{u}_{ob,x} + \left( \frac{\alpha_1 d_t d_b}{280} - \frac{11\alpha_3 c d_b}{3500} \right) M_c \ddot{w}_{b,xx} + \\
 & \left( \frac{\alpha_1 d_t}{30} - \frac{71\alpha_3 c}{2625} \right) M_c \ddot{u}_{0,x} + \left( \frac{17\alpha_3 c^2}{1750} - \frac{\alpha_1 c d_t}{140} \right) M_c \ddot{u}_{1,x} - \\
 & (\alpha_3 + \alpha_1) \frac{M_c}{15} \ddot{w}_0 + (\alpha_1 + \alpha_3) \frac{M_c \ddot{w}_b}{30} + (\alpha_1 + \alpha_3) \frac{2M_c \ddot{w}_t}{15} = 0
 \end{aligned} \tag{2}$$

$$\begin{aligned}
 & -M_{xxb,xx} - \psi N_{xxb,x} w_{b,x} - \psi N_{xxb} w_{b,xx} + M_b \ddot{w}_b + \\
 & \alpha_2 \left( \frac{4c^2}{2625} - \frac{11c d_b}{2625} \right) M_c \ddot{w}_0 - (\alpha_1 + \alpha_3) \frac{M_c}{30} \ddot{w}_t + \left( 1 - \frac{17\alpha_2}{9} \right) \frac{M_c}{15} \ddot{w}_0 \\
 & \left( \frac{2}{c^2} + \frac{2\alpha_2}{15c^2} + \frac{24d_b}{5c^3} + \frac{6\alpha_1 d_b}{5c^3} \right) M_{Q2c,x} + \left( \frac{2}{15} + \frac{5\alpha_2}{135} \right) M_c \ddot{w}_b \\
 & - \left( I_{mb} + \frac{83M_c d_b^2}{3500} - \alpha_1 \frac{2M_c d_b^2}{875} + \alpha_2 \frac{M_c c}{2625} \left( c + \frac{11d_b}{2} \right) \right) \ddot{w}_{b,xx} \\
 & - \left( \frac{12d_b}{5c^2} + \frac{1}{c} + \frac{2\alpha_1 d_b}{5c^2} + \frac{\alpha_2}{c} \right) M_{Q1c,x} - \left( \frac{101\alpha_1 d_b}{5250} - \frac{46d_b}{875} \right) M_c \ddot{u}_{0,x} \\
 & \left( \frac{\alpha_1 d_b d_t}{280} - \frac{11\alpha_3 c d_b}{3500} \right) M_c \ddot{w}_{t,xx} + \left( 4 - \frac{4\alpha_2}{3} \right) \frac{M_{zc}}{c^2} + \left( 1 + \frac{\alpha_2}{3} \right) \frac{R_{zc}}{c} \\
 & + \left( \frac{c d_b}{1750} - \frac{27\alpha_1 c d_b}{3500} - \frac{17\alpha_2 c^2}{5250} \right) M_c \ddot{u}_{1,x} - \alpha_1 \frac{M_c d_b}{140} \ddot{u}_{ot,x} + \\
 & \left( \frac{4\alpha_1 d_b}{875} + \frac{11\alpha_2 c}{5250} - \frac{83d_b}{1750} \right) M_c \ddot{u}_{ob,x} + m_{b,x} - q_b = 0
 \end{aligned} \tag{3}$$

$$-N_{xxt,x} - n_t + M_t \ddot{u}_{ot} + \alpha_1 \left( \frac{4M_{Q1c}}{c^2} - \frac{12M_{Q2c}}{c^3} + \frac{M_c d_b}{140} \ddot{w}_{b,x} - \frac{3M_c d_t}{70} \ddot{w}_{t,x} - \frac{M_c c}{70} \ddot{u}_1 + \frac{3M_c}{35} \ddot{u}_{ot} + \frac{M_c}{70} \ddot{u}_{ob} + \frac{M_c}{15} \ddot{u}_0 \right) = 0 \quad (4)$$

$$\begin{aligned} & -N_{xxb,x} + M_b \ddot{u}_{ob} + \frac{24M_{Q1c}}{5c^2} + \frac{48M_{Q2c}}{5c^3} + \left( \frac{92}{875} - \frac{101\alpha_1}{2625} \right) M_c \ddot{u}_0 \\ & + \left( \frac{83d_b}{1750} - \frac{8d_b\alpha_1}{1750} - \frac{11c\alpha_2}{5250} \right) M_c \ddot{w}_{b,x} + \alpha_1 \left( -\frac{4M_{Q1c}}{5c^2} + \frac{12M_{Q2c}}{5c^2} \right) \\ & + \left( \frac{11\alpha_3 c}{1750} - \frac{\alpha_1 d_t}{140} \right) M_c \ddot{w}_{t,x} + \frac{22\alpha_2 c}{2625} M_c \ddot{w}_{0,x} + \alpha_1 \frac{M_c}{70} \ddot{u}_{ot} \\ & - \left( \frac{1}{875} - \frac{27\alpha_1}{1750} \right) M_c c \ddot{u}_1 + \left( \frac{83}{875} - \frac{8\alpha_1}{875} \right) M_c \ddot{u}_{ob} - n_b = 0 \end{aligned} \quad (5)$$

$$\begin{aligned} & \alpha_1 \frac{M_c}{15} \ddot{u}_{ot} + \left( \frac{71\alpha_3 c}{2625} - \frac{\alpha_1 d_t}{30} \right) M_c \ddot{w}_{t,x} + \alpha_2 \frac{284M_c c}{7875} \ddot{w}_{0,x} \\ & \left( \frac{92}{875} - \frac{101\alpha_1}{2625} \right) M_c \ddot{u}_{ob} - (\alpha_2 + \alpha_3) \frac{48M_{Q2c}}{5c^3} \\ & \left( \frac{608}{875} - \frac{724\alpha_1}{2625} \right) M_c \ddot{u}_0 - (\alpha_3 + \alpha_2) \frac{172M_c c}{2625} \ddot{u}_1 + \\ & - (24 + 16\alpha_1) \frac{M_{Q1c}}{5c^2} + \left( \frac{46d_b}{875} - \frac{101\alpha_1 d_b}{5250} - \frac{71\alpha_2 c}{7875} \right) M_c \ddot{w}_{b,x} = 0 \end{aligned} \quad (6)$$

$$\begin{aligned} & Q_c + \left( \frac{\alpha_1 c d_t}{140} - \frac{17\alpha_2 c^2}{1750} \right) M_c \ddot{w}_{t,x} - (\alpha_3 + \alpha_2) \frac{172M_c c}{2625} \ddot{u}_0 \\ & + \left( \frac{116}{2625} - \frac{66\alpha_1}{2625} \right) M_c c^2 \ddot{u}_1 - (\alpha_3 + \alpha_2) \frac{8M_{Q1c}}{5c} - \\ & (36 + 24\alpha_1) \frac{M_{Q2c}}{5c^3} + \left( \frac{27\alpha_1}{1750} - \frac{1}{875} \right) M_c c \ddot{u}_{ob} - \alpha_1 \frac{M_c c}{70} \ddot{u}_{ot} \\ & + \left( -\frac{d_b c}{1750} + \frac{27\alpha_1 c d_b}{3500} + \frac{17\alpha_2 c^2}{5250} \right) M_c \ddot{w}_{b,x} - \alpha_2 \frac{34M_c c^2}{2625} \ddot{w}_{0,x} = 0 \end{aligned} \quad (7)$$

$$\begin{aligned}
 & -Q_{c,x} - \left(4 + \frac{8\alpha_2}{15}\right) \frac{M_{Q2c,x}}{c^2} + \alpha_2 \frac{4M_{Q1c,x}}{15c} + (\alpha_1 + \alpha_3) \frac{M_c \ddot{w}_t}{15} \\
 & + \left(1 - \frac{2}{3}\alpha_2\right) 8M_{zc} + \left(\frac{1}{15} - \frac{17\alpha_2}{135}\right) M_c \ddot{w}_b + \alpha_2 \left(\frac{34M_c c^2}{2625} \ddot{u}_{1,x} \right. \\
 & \left. - \frac{284M_c c}{7875} \ddot{u}_{0,x} - \frac{16M_c c^2 \ddot{w}_{0,x}}{2625} - \frac{4R_{zc}}{3c} - \frac{22M_c c \ddot{u}_{ob}}{2625}\right) \\
 & \left(4c^2 - 11cd_b\right) \frac{M_c}{2625} \ddot{w}_{b,xx} + \left(\frac{8}{15} + \frac{56\alpha_2}{135}\right) M_c \ddot{w}_0 = 0
 \end{aligned} \tag{8}$$

where  $\alpha_1, \alpha_2$  and  $\alpha_3$  are flags that define the type of region/sub-region as follows:  $\alpha_1 = 1$  and  $\alpha_2 = \alpha_3 = 0$  for fully bonded regions;  $\alpha_2 = 1$  and  $\alpha_1 = \alpha_3 = 0$  for debonded regions without contact;  $\alpha_3 = 1$  and  $\alpha_2 = \alpha_1 = 0$  for debonded regions with vertical contact (which can accommodate for either vertical compressive or vertical tensile stress).  $u_{oi}$  and  $w_i$  ( $i = t, b$ ) are the displacements of the face-sheets in the longitudinal and vertical directions, respectively;  $N_{xxi}(x, t)$  ( $i = t, b$ ) are the inplane stress resultants at the upper and lower face-sheets;  $M_{xxi}(x, t)$  ( $i = t, b$ ) are the bending moments resultants at the upper and lower face-sheets;  $Q_c(x, t)$ ,  $M_{Q1c}(x, t)$ ,  $M_{Q2c}(x, t)$ ,  $R_{zc}(x, t)$  and  $M_{zc}(x, t)$  are the high-order stress resultants in the core;  $M_i$  ( $i = t, b, c$ ) is the mass of the face-sheets and the core;  $I_{mi}$  ( $i = t, b$ ) is the rotary inertia of the face-sheets; and  $\psi$  is a special factor, and when  $\psi = 1.0$  the geometrically nonlinear conditions are included in the analysis, while with  $\psi = 0$  the analysis becomes geometrically linear.

Using the appropriate values for  $\alpha_1, \alpha_2$  and  $\alpha_3$  and the constitutive relations, the governing equations of each region and sub region are defined. For brevity, these sets of equations are presented in terms of differential operators.

For the fully bonded region, the set of the governing equations reads:

$$L_k^{fb}(w_t, w_b, u_{ot}, u_{ob}, w_0, u_0, u_1) = F_k(x, t) \quad k = 1..7 \tag{9}$$

where  $L_k^{fb}$  is a differential operator in time and space; and  $F_k(x, t)$  is the external force. These equations are non-linear due to the geometrical nonlinearity of the face-sheets.

The governing equations of the debonded region with contact are valid only for interfacial compressive stress. For a debonded region without contact, the set of governing equations is valid only if the delaminated surfaces do not overlap. In fact, the two conditions coincide and the contact characteristics of the debonded region only depend on a single

parameter  $\zeta = (-4w_0 + w_b + 3w_t)$ . Thus, if  $\zeta > 0$ , the delaminated surfaces are in contact, whereas if  $\zeta < 0$ , the delaminated surfaces are not in contact. Using a step function, a unified set of the non-linear differential equations for the debonded region is obtained. This set of equations is:

$$L_i^{db-woc}(w_t, w_b, u_{ot}, u_{ob}, w_0, u_0, u_1) + H(\zeta) \cdot L_i^{db-wc}(w_t, w_b, u_{ot}, u_{ob}, w_0, u_0, u_1) = F_i(x, t) \quad i = 1..7 \tag{10}$$

where  $L_k^{db-woc}$  is a differential operator in time and space which is associated with a debonded region without contact;  $L_k^{db-wc}$  is a complementary operator such that  $L_k^{db-woc} + L_k^{db-wc}$  refer to the equations of a debonded region with contact; and  $H(\xi)$  is the step function.

The delaminated sandwich panel consists of bonded and debonded regions, where each region is governed by its own set of partial nonlinear differential equations in space and in time. The regions are connected through continuity requirements, which for brevity are not presented here. The numerical solution of the governing equations is accomplished through discretization in time using the Newmark-Beta method [14]. The solution in space uses the Multiple Shooting method combined with the Newton-Raphson iterative scheme.

### 3. NUMERICAL RESULTS

The dynamic behavior of a delaminated sandwich panel that is simply supported at the lower face sheet is studied numerically. The mechanical properties of the face sheets correspond to an isotropic glass-ceramic of density  $4400 \text{ kg/m}^3$  with  $E_t = E_b = 36 \text{ GPa}$ . The core corresponds to an isotropic polymethacrylimide rigid foam of density  $52.0 \text{ kg/m}^3$  with  $E_c = 0.05 \text{ GPa}$  and  $G_c = 0.02 \text{ GPa}$ . The geometrical layout of the panel and the location of the delaminated region appear in Fig. 3a. The numerical study takes advantage of the symmetry conditions.

The numerical example studies the dynamic behavior of a panel subjected to a localized sinusoidal load with amplitude of  $0.025 \text{ KN}$  and a frequency of  $1.1 \text{ rad/ms}$ . The time domain response of the delaminated panel in terms of the midspan vertical displacement of the upper and lower face-sheets appears in Fig.1a. The response is studied for three cases which correspond to the following models: debonded region without contact, debonded region with contact, and a fully nonlinear analysis which involves partial and time-dependent contact characteristics. It is seen that at the first 6 ms, the results of the “partial contact” model follow either of the other two models.

However, later on, the “partial contact” model enables the formation of high-order modes, which do not exist in the other models. It is seen, see Fig. 1c, that at  $t=4.55\text{ms}$ , a vertical compressive stress develops almost through the entire debonded region, and therefore the behavior of the panel is similar to that of the “with contact” model. However, at  $t=9.45\text{ms}$ , Fig. 1d, a partial contact state exists at the delaminated region and the behavior significantly differs from the other models. Moreover, the stress levels when partial contact exists are much higher as compared to the levels observed using the simpler models.

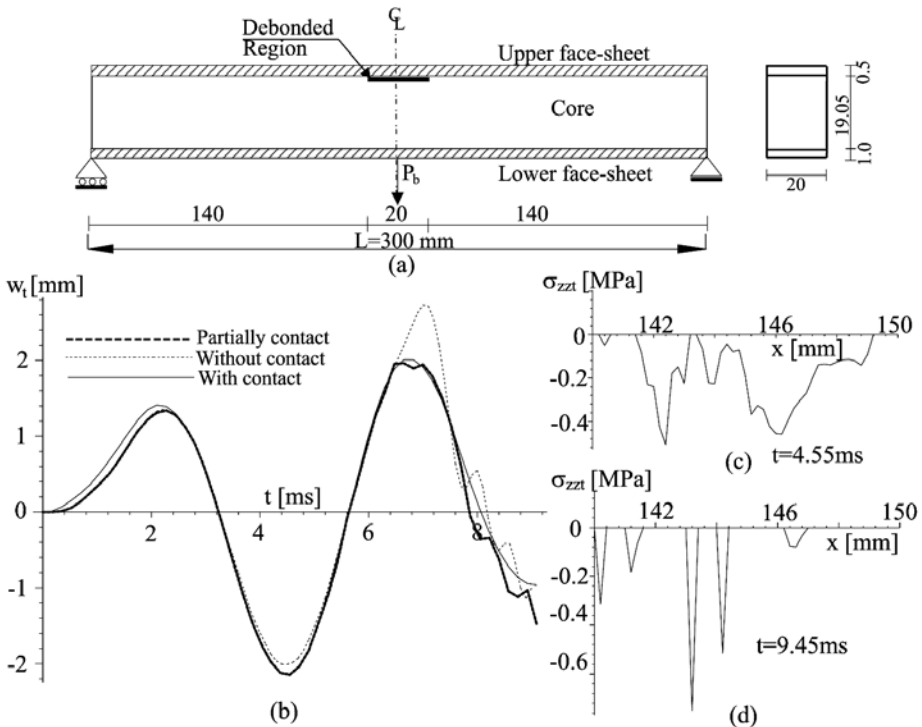


Figure 1. Dynamic response of a delaminated sandwich panel subjected to a localized sinusoidal load (a) Layout; (b) Vertical displacement of the upper face-sheet versus time; (c) Upper interfacial vertical normal stress along the delaminated region at  $t=4.55\text{ms}$ ; (d) Upper interfacial vertical normal stress along the delaminated region at  $t=9.45\text{ms}$ .

In order to demonstrate the inherent error in the linear models (i.e, in the models that a-priori assume with contact or without contact characteristics and do not account for the changes through the time domain) the value of  $\zeta$  are presented for the simplified models in Fig. 2. Since in both cases  $\zeta$  changes its sign during the motion, it is clear that the basic assumptions of the simplified models are not satisfied.

The interfacial vertical normal stresses in the fully bonded region at the delamination tip are described in Fig. 3. The stresses at this point are expected to govern the stability (tendency to propagate) of the delamination. It is seen that at the beginning of the motion ( $t < 6\text{ms}$ ), the behavior of the partial contact model follows either of the other two other models. However, at  $t > 6\text{ms}$ , when the high-order modes and the wave like behavior within the core start to develop, the stresses determined by the “partial contact” model significantly differ from the prediction of the two simplified linear models.

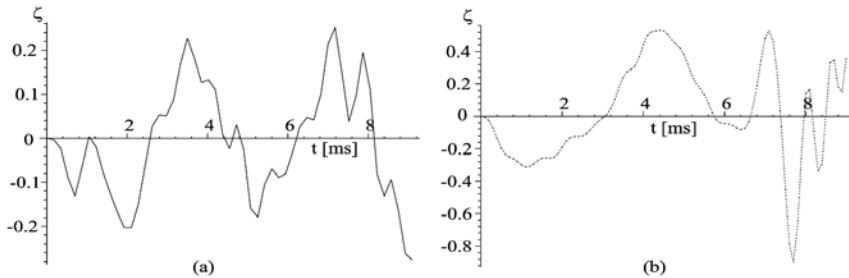


Figure 2. Time-domain response in terms of the midspan condition of contact: (a) with contact; (b) without contact.

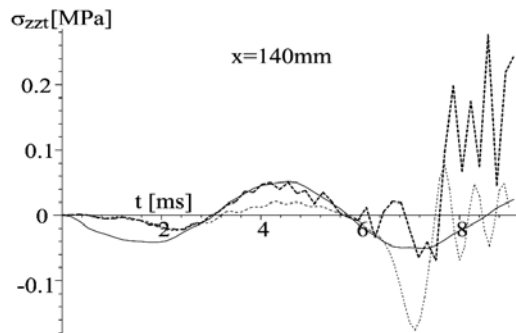


Figure 3. Time-domain response in terms of the vertical normal stress in the vicinity of the tip of the debonded region in the fully bonded zone.

#### 4. SUMMARY AND CONCLUSIONS

In this work, the dynamic behavior of a delaminated sandwich panel with a soft core has been studied, taking into account the contact effects at the delaminated surfaces, the nonlinear velocity fields in the core, and the geometric nonlinear behavior of the face-sheets. The rotary inertia of the face-sheets and the core has also been included. A numerical example that examined the effects of the contact behavior of the delaminated surfaces and its influence on the dynamic behavior of the panel has been presented. The

results have revealed that the contact effects are not negligible and introduce high order vibration modes which can not be explained by simpler models. Contrary to the model proposed in this work, current models encounter deformation modes that are inconsistent and allow overlapping between the two delaminated surfaces or development of tensional vertical normal stress at the delaminated faces. This observation demonstrates that the models that are based on “with contact” or “without contact” presumptions, which are commonly used and reported in the literature may turn to be incorrect. Thus, it highlights the necessity of a non linear model of the type described in this paper.

## REFERENCES

1. Allen, H.G., (1969). “*Analysis and Design of Structural Sandwich Panels*”. Pergamon Press, London, Oxford.
2. Hu, J.S. and Hwu, C., (1995). “Free vibration of delaminated composite sandwich beams”. *AIAA Journal*, **33**(10), 1911-1918.
3. Rossetto, J.N., (1998). “Effects of a delamination and initial curvature on the fundamental frequency of sandwich beams”. *Journal of Sound and Vibration*, **210**(1), 153-161.
4. Tracy, J.J. and Pardoan, G.C., (1989). “Effect of delamination on the natural frequencies of composite laminates”, *Journal of Composite Materials*, **23**(12), 1200-1215.
5. Lu, X., Lestari, W. and Hanagud, S., (2001). “Nonlinear vibration of a delaminated beam”, *International Journal of Vibration and control*, **7**(6), 803-831.
6. Giannakopoulos, A. E., Nilsson, K. F. and Tsamasphyros, G., (1995). “The contact problem at delamination”, *Journal of Applied Mechanics*, **62**(4), 989-996.
7. Tian, Z. and Swanson, S. R., (1992). “Effect of delamination face overlapping on strain energy release rate calculations”, *Composites Structures*, **21**(4), 195-204.
8. Kwon, Y.W. and Lannamann, D.L., (2002). “Dynamic numerical modeling and simulation of interfacial cracks in sandwich structures for damage detection”. *Journal of Sandwich Structures and Materials*, **4**(2), 175-199.
9. Frostig Y. and Baruch, M., (1994). “Free vibration of sandwich beams with a transversely flexible core: a high order approach”. *Journal of Sound and Vibration*, **176**(2), 195-208.
10. Frostig, Y., (1992). “Behavior of delaminated sandwich beam behavior with transversely flexible core – high order theory”, *Composite Structures*, **20**(1), 1-16.
11. Frostig, Y. and Thomsen, O.T., (2004). “High-order free vibration of sandwich panels with a flexible core”, *International Journal of Solids and Structures*, **41**(5-6), 1697-1724.
12. Schwarts-Givli, H., Rabinovitch, O., and Frostig, Y. (2005). “High Order Nonlinear Contact Effects in the Dynamic Behavior of Delaminated Sandwich Panels with flexible core”, *submitted*.
13. Sokolinsky, V.S., Nutt, S.R., Frostig, Y. and Lesko, J.J.J., (2003). “Free vibrations of debonded sandwich beams-Higher order theory approach”. 6<sup>th</sup> international conference on sandwich structures, 996-1005, CRC PRESS.
14. Newmark, N.M., (1959). “A method of computation for structural dynamics”. *Journal of the Engineering Mechanics Division*, **85**(EM3), 67-94.

# BENDING BEHAVIOR OF SANDWICH PANELS WITH A “SOFT” CORE AND EMBEDDED RIGID INSERTS

Oded Rabinovitch and Ehab Hamed

*Faculty of Civil and Environmental Engineering, Technion – Israel Institute of Technology, Haifa, 32000, Israel*

**Abstract** The bending behavior of sandwich panels with a “soft” core hosting embedded rigid inserts is analytically investigated. Three approaches for the mathematical modeling of the sandwich panel hosting the rigid insert are discussed. In addition, the continuity conditions between the regions hosting the rigid insert and the adjacent sandwich regions are derived. Numerical results that demonstrate the capabilities of the model and highlight some of the effects that characterize the response of the panel are also presented.

**Keywords:** sandwich structures, compressible core, rigid bodies, localized effects.

## 1. INTRODUCTION

Sandwich structures are employed today in a broad range of aeronautical, space, marine, automotive, and civil structural applications. The advantages of combining thin face sheets made of metallic or composite materials with a thick, compliant (“soft”), and lightweight core materials are utilized to provide a light, strong, and stiff element. This configuration further allows much versatility in the design, manufacturing, and use of the advanced panel. One aspect of the design flexibility is the ability to embed rigid inserts in the thick core layer, see [1-6]. Some examples in which rigid bodies are embedded in a soft-core sandwich panel appear in Figure 1 and include:

- Embedded structural or nonstructural components such as pipelines for water, fuel, oil, or hydraulic systems, ducts for electric or communication lines, air-conditioning systems, etc.

- Embedded sensors such as temperature gauges, hygrometers, accelerometers, motion detectors, piezoelectric transducers, etc.
- Reinforced openings. In some cases, openings that are not extended through the depth of the core are created. The edge of the opening is usually reinforced with a layer of stiffer material that forms a relatively stiff region within the core.
- Composite structural armor panels [6] in which rigid ceramic tiles are embedded in a compliant rubber and resin environment and sandwiched between two E-glass/Epoxy plates.

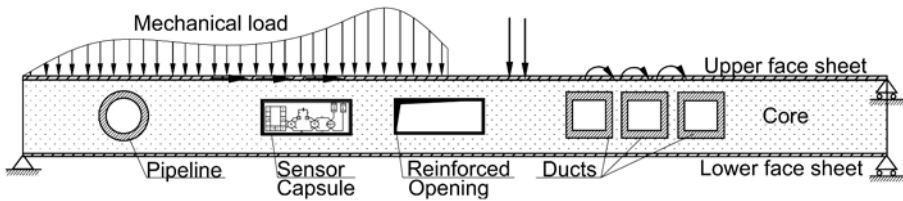


Figure 1. A sandwich panel with various rigid inserts.

Investigating this type of structural members, Found et al. [1] showed that the use of rigid inserts extended through the depth of the core increases the load carrying capacity and the deformability of the sandwich structure. Thomsen and Rits [2], and Thomsen [3] examined sandwich plates with through the thickness inserts and analytically revealed the stresses concentrations that develop near the edges of the rigid bodies. Mamalis et al. [4] experimentally examined the behavior of sandwich panels with inserts under longitudinal and transverse compressive loading and revealed that the use of the inserts improves the stiffness and crash energy absorption characteristics of the panel. Bozhevolnaya et al. [5] indicated that the introduction of the inserts leads to transition of the stress concentration developed under concentrated loads to the edges of the inserts. These studies show that the use of the rigid inset affects the behavior of the panel. However, it appears that an inclusive and quantitative explanation of the unique structural behavior of this type of panel, and especially the localized effects near the "floating" embedded rigid insert, is still needed.

In this study, the bending behavior of sandwich panels with a compressible "soft" core and embedded rigid inserts is analytically investigated. Motivated by the nature of the soft core, its interaction with the embedded bodies, and the stress transfer mechanism between the rigid insert, the core, and the face sheet, a high-order sandwich theory [7-8] is employed. Three different approaches are proposed for the mathematical modeling of the rigid insert and its implementation in the model for the entire panel. Emphasis is placed on the interaction of the rigid insert with the adjacent

components and on the conditions used for joining the various parts of the panel together. A numerical example that illustrates the capabilities of the model and highlights some aspects of the structural behavior of the panel is also presented.

## 2. MATHEMATICAL FORMULATION

The general layout of the panel that appears in Figure 1 shows that the sandwich panel includes 3 layers regions as well as regions with 5 layers that host the rigid insert. The mathematical formulation for the various regions adopts the High Order Sandwich Theory [7] which directly apply for the 3-layers regions. On the other hand, three different approaches are suggested for the mathematical modeling of the 5-layers region hosting the rigid insert. These approaches are outlined next and they are followed by a discussion of the continuity conditions between the two types of regions.

**The first approach** takes a practical point of view and assumes that the insert is indeed much stiffer than the other flexural components; however, it is not infinitely rigid. Hence, it can be mathematically modeled as a beam or as a panel with extensional and flexural rigidities that are several orders of magnitudes higher than the rigidities of the other components. As a result, the 5-layers region may be considered as a sandwich panel with three “face-sheets”, namely two outer face-sheets and one “inner” face sheet, and two layers of core material. The mathematical formulation for this type of region appears in [8], and, for brevity, it is not presented here.

**The second approach** for the modeling this unique region assumes that the stiffness of the rigid insert embedded in the core is infinitely large. Nevertheless, it claims that the issue of the stiffness of the insert is a matter of its constitutive behavior only. Hence, the variational principle of virtual work, which is independent of the constitutive behavior of the various materials [9], is used for the derivation of the equilibrium equations for the various components including the rigid insert. As a result, the field equations for the 5-layers panel derived in [8] and used in the first approach, hold for this case as well whereas the difference lies in the constitutive relations.

The constitutive relations for the upper and the lower face sheets adopt the classical lamination theory and read:

$$N_{xx}^i = bA_{11}^i u_{oi,x} - bB_{11}^i w_{i,xx} \quad ; \quad M_{xx}^i = bB_{11}^i u_{oi,x} - bD_{11}^i w_{i,xx} \quad (i=t,b) \quad (1)$$

where  $w_i$  and  $u_{oi}$  are the vertical and longitudinal displacements at the reference line at mid-height of the upper ( $i=t$ ) and the lower ( $i=b$ ) face-sheets and  $A_{11}^i$ ,  $B_{11}^i$  and  $D_{11}^i$  ( $i=t,b$ ) are the extensional, extensional-bending,

and flexural rigidities of the face sheets. On the other hand, the constitutive laws for the insert represent its infinite rigidity and take the following form:

$$u_{m,x}=0; \quad w_{m,xx}=0 \quad (2a,b)$$

Using the closed form solutions for the stress and displacement fields of the upper and lower core layers (see [8]), along with the equilibrium equations, the constitutive laws, and the compatibility conditions, the governing equations for the 5-layers region with the rigid insert are:

$$bA_{11}^t u_{ot,xx} - bB_{11}^t w_{t,xxx} + b\tau^{tc} = -n^t \quad (3)$$

$$bD_{11}^t w_{t,xxx} - bB_{11}^t u_{ot,xxx} - \frac{b(c_{tc} + d_t)\tau_{,x}^{tc}}{2} + \frac{bE_c}{c_{tc}}(w_t - w_m) = q^t \quad (4)$$

$$N_{xx,x}^m - b\tau_{xz}^{tc}(z_{ct} = c_t) + b\tau_{xz}^{bc}(z_{cb} = 0) = 0 \quad (5)$$

$$u_{m,x}=0; \quad (6)$$

$$M_{xx,xx}^m + (c_{bc} + d_m)\frac{b\tau_{,x}^{bc}}{2} + (c_{tc} + d_m)\frac{b\tau_{,x}^{tc}}{2} - \frac{bE_c}{c_{bc}}(w_m - w_b) + \frac{bE_c}{c_{tc}}(w_t - w_m) = 0 \quad (7)$$

$$w_{m,xx}=0 \quad (8)$$

$$bA_{11}^b u_{ob,xx} - bB_{11}^b w_{b,xxx} - b\tau_{bc} = -n^b \quad (9)$$

$$bD_{11}^b w_{b,xxx} - bB_{11}^b u_{ob,xxx} - \frac{b(c_{bc} + d_b)\tau_{,x}^{bc}}{2} - \frac{bE_c}{c_{bc}}(w_m - w_b) = q^b \quad (10)$$

$$u_{ot} - u_{om} - \frac{(c_{tc} + d_t)}{2} w_{t,x} - \frac{(c_{tc} + d_m)}{2} w_{m,x} + \frac{\tau_{,xx}^{tc} c_{tc}}{G_c} - \frac{\tau_{,xx}^{tc} c_{tc}^3}{12E_c} = 0 \quad (11)$$

$$u_{om} - u_{ob} - \frac{(c_{bc} + d_b)}{2} w_{b,x} - \frac{(c_{bc} + d_m)}{2} w_{m,x} + \frac{\tau_{,xx}^{bc} c_{bc}}{G_c} - \frac{\tau_{,xx}^{bc} c_{bc}^3}{12E_c} = 0 \quad (12)$$

where the superscripts  $t$ ,  $m$ ,  $b$ ,  $tc$ , and  $bc$  refer to the upper face-sheet, the insert, the lower face sheet, the upper core and the lower core, respectively;  $N_{xx}^i$  and  $M_{xx}^i$  ( $i=t,m,b$ ) are the stress resultants in the face sheets and the insert;  $b$  is the width of the panel;  $\tau_{xz}^{tc}$  and  $\tau_{xz}^{bc}$  are the shear stresses in the upper and lower core layers;  $\sigma_{zz}^{tc}$  and  $\sigma_{zz}^{bc}$  are the vertical normal stresses in

the upper and the lower core layer, respectively;  $d_m$ ,  $d_b$  and  $d_t$  are the heights of the rigid insert, and the upper and lower face sheets, respectively;  $c_{tc}$  and  $c_{bc}$  are the thicknesses of the upper and lower core layers;  $n^i$  and  $q^i$  ( $i=t,b$ ) are the external loads; and  $E_c$  and  $G_c$  are the elastic and shear moduli of the core.

The integration of equations (6) and (8) yields:

$$u_m=C_1; \quad w_m=C_2x+C_3 \tag{13a,b}$$

where  $C_1-C_3$  are constants of integration that are determined through the boundary and continuity conditions. In physical terms,  $C_1$  and  $C_3$  are the horizontal and vertical components of the rigid body translation of the insert and  $C_2$  is its rigid body rotation. Also, note that the constitutive laws in the form of equations (2a-b) necessitate stating the problem in terms of unknown displacement and unknown stress resultants. Yet, the order of the governing equation, which equals 22, is the same as the order of governing equations derived based on the first approach (see [8]).

**The third approach** claims that due to the rigid body displacement field and the null strains and curvatures of the insert, its strain energy is null and it is omitted from the variational expression. Alternatively, the interaction with the rigid body is achieved by adopting its displacement field in the form of equations (13) and introducing the compatibility constraints into the variational formulation using Lagrange multipliers. This approach yields a formulation that involves differential and integral equations; yet, it can be shown that it is equivalent to the one obtained through the second approach.

Along with the governing equations for the various regions, the **continuity conditions** at the connection point between the 5-layers region hosting the rigid insert and the ordinary 3-layers regions have also to be derived. In order to address this challenge, the variational formulation is used. The continuity conditions in the outer face sheets require continuity of the displacements and the slopes and equilibrium of the internal forces and the external loads (see [8]). On the other hand, the continuity conditions through the height of the core are more complicated. Assuming, for example, that the 5-layers region is right of the 3-layers one, the remaining variational terms that refer to the continuity conditions at the  $x=x_j$  are:

$$-M_{xx}^{m(-)} \delta w_{m,x}^{(-)} + N_{xx}^{m(-)} \delta u_{om}^{(-)} + b \int_0^{c_{tc}} \tau^{tc(-)} \delta w_{tc}^{(-)} dz_{tc} + V_{xx}^{m(-)} \delta w_m^{(-)} + b \int_0^{c_{bc}} \tau^{bc(-)} \delta w_{bc}^{(-)} dz_{bc} - b \int_0^c \tau^{c(+)} \delta w_c^{(+)} dz_c = 0 \tag{14}$$

where  $w_{tc}$  and  $w_{bc}$  are the vertical displacements of the upper and lower core layers, respectively,  $c=c_{tc}+d_m+c_{bc}$  is the depth of the core in the 3-layers region, and  $V_{xx}^m$  is the shear force in the rigid insert that is defined by:

$$V_{xx}^m = M_{xx,x}^m + bd_m \tau^{tc} / 2 + bd_m \tau^{bc} / 2 \tag{15}$$

Since the variational functions (the  $\delta$  terms) are arbitrary and the only unknowns multiplied by  $\delta w_{m,x}$  and  $\delta u_{om}$  are  $M_{xx}^m$ , and  $N_{xx}^m$ , respectively, both the inplane and the bending moment resultants in the rigid insert at the connection point are zero, thus,  $M_{xx}^{m(-)} = 0$  and  $N_{xx}^{m(-)} = 0$ .

The continuity conditions regarding the vertical deflections and the vertical equilibrium at the connection line result from the remaining terms in equation (14). Yet, in this case, the continuity conditions for the vertical deflections involve conditions along the vertical connection line. Alternatively, the condition of continuous vertical deflection can be imposed on the averaged deflection through the depth of the core as follows:

$$\frac{1}{c_{tc} + d_m + c_{bc}} \left[ \int_0^{ctc} w_{tc}^{(-)} dz_{tc} + \int_{-dm/2}^{dm/2} w_m^{(-)} dz_m + \int_0^{cbc} w_{bc}^{(-)} dz_{bc} \right] = \frac{1}{c} \left[ \int_0^c w_c^{(+)} dz_c \right] = 0 \tag{16}$$

Since the shear stresses  $\tau^{tc}$ ,  $\tau^{bc}$ , and  $\tau^c$ , which is the shear stress in the 3 layers region, are uniform through the depth of each core, Eq. (14) becomes:

$$b \tau^{tc(-)} \int_0^{ctc} \delta w_{tc}^{(-)} dz_{tc} + V_{xx}^{m(-)} \delta w_m^{(-)} + b \tau^{bc(-)} \int_0^{cbc} \delta w_{bc}^{(-)} dz_{bc} - b \tau^{c(+)} \int_0^c \delta w_c^{(+)} dz_c = 0 \tag{17}$$

Introducing equation (16) into (17) yields:

$$b \int_0^{ctc} (\tau^{tc(-)} - \tau^{c(+)} ) \delta w_{tc}^{(-)} dz_{tc} + (V_{xx}^{m(-)} - bd_m \tau^{c(+)} ) \delta w_m^{(-)} + b \int_0^{cbc} (\tau^{bc(-)} - \tau^{c(+)} ) \delta w_{bc}^{(-)} dz_{bc} = 0 \tag{18}$$

Thus, the kinematic (displacement) continuity requirement for the inner layers is the average deflection condition in the form of equation (14) and the corresponding three static (forces or stresses) conditions are:

$$\tau^{tc(-)} - \tau^{c(+)} = 0; \quad V_{xx}^{m(-)} - bd_m \tau^{c(+)}; \quad \tau^{bc(-)} - \tau^{c(+)} = 0 \tag{19}$$

### 3. NUMERICAL EXAMPLE

The geometry, boundary conditions, loading scheme, and mechanical properties of the investigated panel appear in Figure 2a. The deformed shape of the panel hosting the rigid inserts and the deformed shape of the ordinary panel appear in Figures 2b-c, respectively. These figures clearly reveal the modification in the bending pattern due to the presence of the rigid bodies. This modification results in a stiffening effect and a reduction in the overall

vertical deflection. The deformed shapes also reveal the interaction of the corners of the rigid insert with the adjacent face sheet. For example, on the inner face of the insert, the lower corner (D) pulls the lower face sheet upwards, whereas the upper corner (C) is compressed against the upper face sheet. At the other side, the upper corner (A) pulls the upper face sheet downwards, whereas corner B is compressed against the lower face sheet.

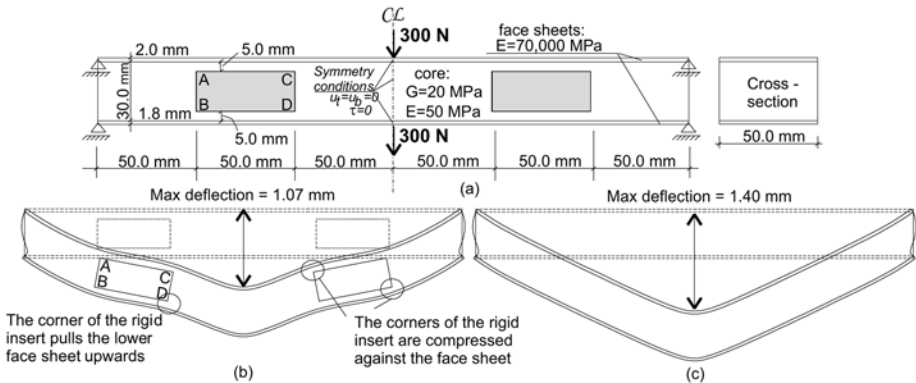


Figure 2. Geometry, mechanical properties, deformed shapes (a) geometry and mechanical properties, (b) deformed shape with rigid inserts; (c) deformed shape without rigid inserts.

The distributions of the inplane, bending, and shear resultant in the face sheets and in the rigid insert appear in Figure 3. Figures 3a shows that in this case, the magnitudes of the inplane stress resultants in the rigid insert are rather negligible. On the other hand, Figures 3b-c reveal that the bending moments and shear forces in the insert are of the same order of magnitude as the tractions developed in the outer face sheets. The results also reveal the localized effects in the form of localized bending moments and shear stresses in the face sheets near the rigid insert. However, it appears that in this case, the magnitudes of these effects are smaller than the localized tractions near the concentrated loads or near the supports.

The influence of the presence of the rigid insert on the development of the shear and vertical normal stresses in the core is investigated in Figure 4. The shear stresses that are plotted in Figure 4a and compared to the ordinary panel in Figure 4b reveal that the presence of the rigid insert modifies the shear stress distribution along the beam, however, it does not considerably increase its magnitudes. Figure 4a also shows that in this case, the shear stresses in the core layer above the rigid insert are very close to the ones observed in the core layer below the insert. This observation is attributed to the geometrical configuration examined here, whereas in other cases, the differences between the upper and the lower shear stresses may be more considerable. The vertical normal stresses at the core-face sheet interface

appear in Figures 4c and 4d and reveal the interaction of the corners of the rigid insert with the face sheets. The curves quantitatively reveal the vertical compressive stresses that evolve due to the interaction of points B and C with the lower and the upper interfaces, respectively, and the tensile stresses resulting from the interaction with points A and D.

Finally, the distributions of the shear and vertical normal stresses at the interfaces of the rigid insert and the hosting core are presented in the form of free body diagrams in Figure 5a-b. This type of representation demonstrates that the global moment resulting from shear stresses is balanced by the sign reversing distribution of the vertical normal stresses. This effect, which is a consequence of embedding the rigid insert in the shear carrying core material, results in the rotation of the rigid body, the interaction with the adjacent core layers, and the localized stress concentrations observed in Figures 3 and 4.

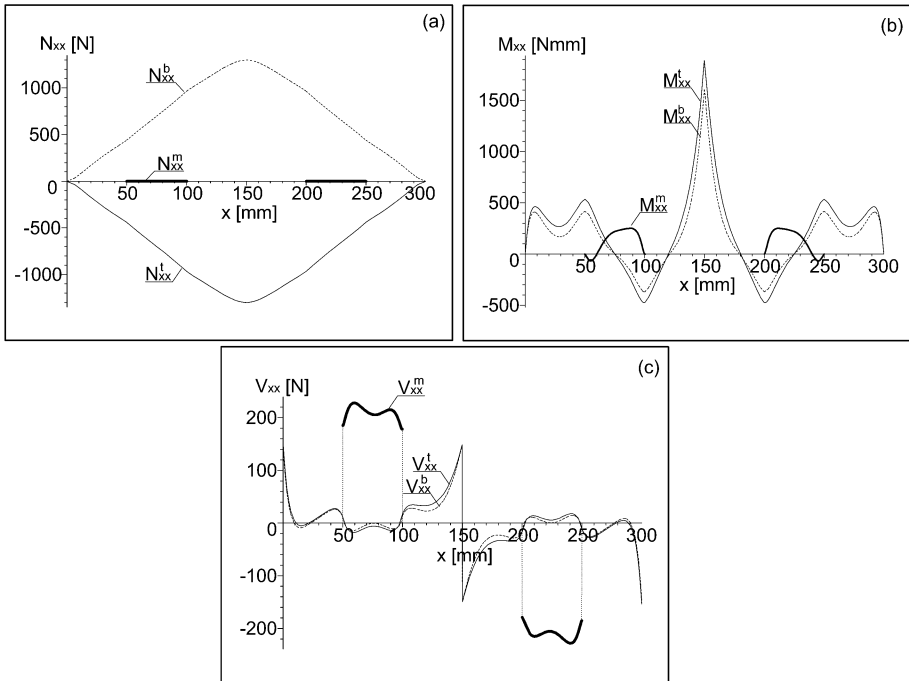


Figure 3. Stress resultants in the face sheets (a) inplane forces; (b) bending moments; (c) shear forces; (Legend: — upper face sheet --- lower face sheet, ——— rigid insert).

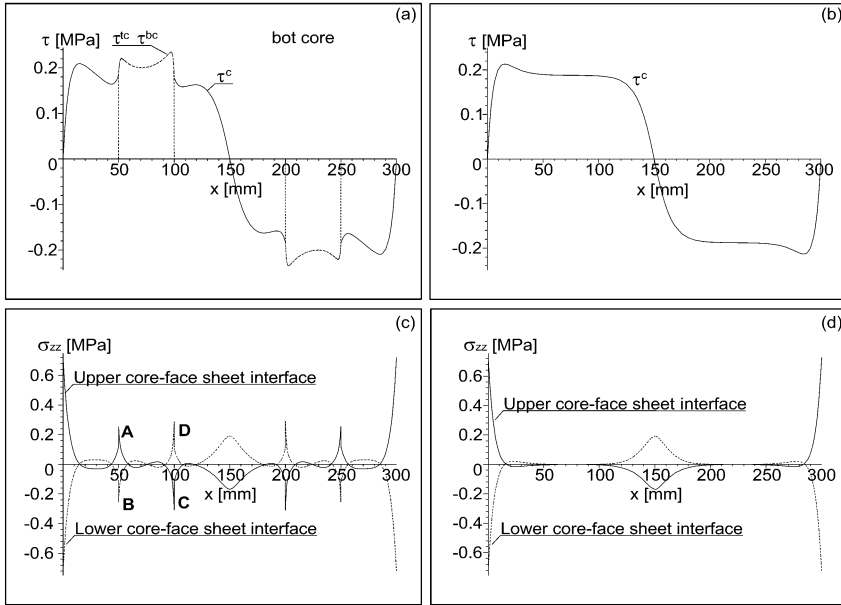


Figure 4. Stresses at the core – face sheet interfaces (a,b) shear stresses (c,d) vertical normal stresses (a,c) with inserts (b,d) without inserts (Legend: — upper interface; --- lower interface)

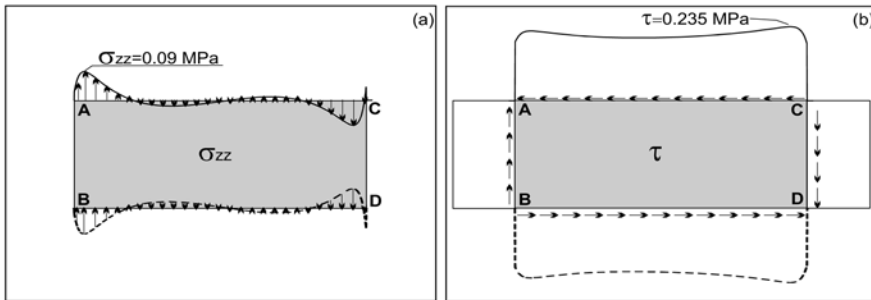


Figure 5. Free body diagrams for the left insert (a) vertical normal stresses (b) shear stresses.

#### 4. SUMMARY AND CONCLUSIONS

The bending behavior of sandwich panels with “soft” core hosting embedded rigid inserts has been analytically investigated. Three different approaches for the modeling of the sandwich panel with the rigid insert have been proposed. The first approach adopts a realistic standpoint and considers the rigid insert as an additional “face sheet” with equivalent inplane and bending rigidities. The second approach uses a variational principle and a

unique constitutive model for the rigid inserts. The third approach is also based on variational principles, whereas the interaction of the insert with the adjacent components is introduced using Lagrange multipliers. The continuity conditions that result from the variational principle and allow the assembly of the various regions into a whole panel have also been discussed.

The capabilities of the proposed model and some of the unique aspects of the bending behavior of such sandwich panels have been numerically examined. The numerical results have shown that the presence of the rigid insert modifies the deformed shape of the panel and reduces its vertical deflections. It is also associated with a modification of the distributions of the stress resultants in the face sheets. However, it appears that in the case studied here, the localized tractions resulting from the interaction with the rigid insert are not notably higher than the ones induced by the concentrated load or the reactions. In terms of the shear and vertical normal stresses in the core, the results have quantitatively revealed the localized stress concentrations due to the interaction of the corners of the rigid insert with the adjacent components. These effects may lead to premature failure of this unique structural member, and thus they should be carefully considered.

## REFERENCES

1. Found, MS, Robinson, AM, and Carruther, JJ (1997), "The influence of FRP inserts on the energy absorption of a foam-cored sandwich panel" *Composite Structures* **38**(1-4):373-381
2. Thomsen, O.T. and Rits, W. (1998) "Analysis and design of sandwich plates with inserts – a high order sandwich plate theory approach" *Composites part B* **29**(6):795-807
3. Thomsen, O.T. (1998) "Sandwich plates with 'through-the-thickness' and 'fully-potted' inserts: evaluation of differences in structural performance" *Composites Structures* **40**(2):159-174
4. Mamalis, A.G., Manolakos, D.E., Ioannidis, M.B., Papapostolou, D.P., Kostazos, P.K., and Konstantinidis, D.G. (2002) "On the compression of hybrid sandwich composite panels reinforced with internal tube inserts: experimental" *Composite Structures* **56**(2):191–199
5. Bozhevolnaya, E., Lyckegaarda, A. Thomsen, O.T. and Skvortsov, B. (2004) "Local effects in the vicinity of inserts in sandwich panels" *Composites part B* **35**(6-8):619-627
6. Mahdi, S. and Gillespie J.W. (2004) "Finite element analysis of tile-reinforced composite structural armor subjected to bending loads" *Composites Part B* **35**(1):57-71
7. Frostig, Y., Baruch, M., Vilmay, O., Sheinman, I. (1992) "High-Order Theory for Sandwich-Beam Bending with Transversely Flexible Core", *Journal of Engineering Mechanics*, **118**(5):1026-1043
8. Frostig, Y., and Rabinovitch O. (2000), "Behavior of Sandwich Panels with Multi-skin Construction or a Multi-layered Core – a High-Order Approach", *Journal of Sandwich Structures and Materials*, **2**(3):181-213
9. Washizu, K (1974) *Variational methods in elasticity and plasticity* Pergamon, Oxford, UK

# ELASTIC BEHAVIOUR OF Z REINFORCED SANDWICH BEAMS

Marco Leite, Arlindo Silva and Manuel de Freitas

*Department of Mechanical Engineering, ICEMS, Instituto Superior Técnico, Lisbon, Portugal*

**Abstract** Reinforced sandwich panels are frequently used in refrigerated trailer construction. There is a need to reinforce the sandwich panels because they can achieve some very large dimensions and consequently lose their ability to support the working loads. Work has been developed in the field of elastic and fracture behaviour of several sandwich beams with Z reinforcements. It was concluded that some reinforcements highly increase the beams rigidity. A few specialized analytical models were developed for linear elastic analysis, and some numerical models were built to analyze the different types of beams tested experimentally in three-point bending. The models contribute to a better understanding of the deformation phenomena involved and help in isolating and characterising the critical terms of divergence between theory and experiment. The present work contributes to the establishment of design and analysis parameters necessary to this type of construction.

**Keywords:** sandwich, 3 point bending, polymeric foams core, Z reinforced sandwich, ASTM C273.

## 1. INTRODUCTION

In refrigerated transportation of perishable goods, with temperature and humidity control, sandwich construction is suitable because of its flexural stiffness and low thermal conductivity contribution from foamed core. Polyurethane foams are used because of the low thermal conductivity but it is also possible to use polystyrene foam for lower cost and PVC foams for their higher resistance. The faces are usually built in composite fibre glass fabric in polyester resin [1]. Depending on the size of the trailer, it is common to reinforce the foam core to increase the sandwich structural performance [2]. These stiffeners must be polymeric so that the sandwich panels maintain their isothermal capacity. Work has been developed in the

field of elastic and fracture behaviour of several sandwich beams with Z reinforcements. It was concluded that some reinforcements contribute to a much higher flexural rigidity of the beams. A few specialized analytical models were developed for linear elastic analysis, and some numerical models were built to analyze the different types of beams tested experimentally in three-point bending.

## **2. EXPERIMENTAL PROCEDURE AND MATERIALS**

The sandwich beams were tested in a three-point bending test fixture, with 1000 mm span, on an electro-mechanical testing machine with maximum load capacity of 100 kN. The test was controlled in displacement, with a crosshead constant speed of 5 to 10 mm/min. The applied load and the actuator stroke were stored with an appropriate sampling rate [3].

Figure 1 shows the cross sections of the beams studied on this paper: sandwich beams and Z reinforced sandwich beams.

All the sandwich beams were fabricated in vacuum bag process and two specimens of each were cut with 1500 mm x 300 mm. The top and bottom faces, built by hand lay up, consist of two layers of random glass fibre fabrics with 450 g/m<sup>2</sup> cured in polyester resin and with a nominal thickness of 2.5 mm. A 40 kg/m<sup>3</sup> polyurethane foam (PUR) and a 40 kg/m<sup>3</sup> polystyrene (XPS) with 50 mm thickness were used for the core.

Previous uniaxial tension tests on the face materials yielded a modulus of elasticity of 6.1 GPa [2]. Polyurethane foam properties were obtained by uniaxial compression tests giving a modulus of elasticity in compression of 7.5 MPa and Polystyrene foam core has a modulus of elasticity in compression of 18 MPa [3].

Eight groups of different sandwich beams were built. Four groups had no reinforcement and the other four were Z reinforced. 10 sandwich beams with PUR were fabricated with three types of adhesive solution (Table 1). The first solution consists of two-component polyurethane adhesive. The second adhesive solution is polyester resin. The third solution consists on the reinforcement of the polyester resin with random fibre glass fabrics. Two types of glass fibre fabrics/mats were used, a 400 g/m<sup>2</sup> and 300 g/m<sup>2</sup>. The PUR Z reinforced sandwich beams were bonded with polyester resin.

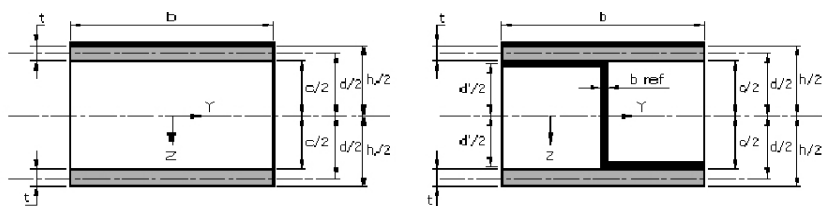


Figure 1. Three point bending fixture and geometries.

Table 1. Characteristics for sandwich beams.

Beam ref.	Adhesive
#1A; #2A; #F1; #F2	PU adhesive
#1B; #2B	Polyester resin
#3B; #4B	Polyester resin + T400 $g/m^2$
#5B; #6B	Polyester resin + T300 $g/m^2$

Table 2. Characteristics for Z reinforced sandwich beams.

Beam ref.	Reinforcement fabric [ $g/m^2$ ]	Reinforcement thickness [mm]
#A1-2; #A1-3	T300	0.8
#A1; #A2; #7; #8	T500	1.2
#3; #4	T300+300	1.5
#G1; #G2	T500+500	2

### 3. THREE-POINT BENDING RESULTS

From the three-point bending results of all beams its possible to study the influence of the adhesive solution and of the Z reinforcement in the flexural behaviour of sandwich beams. Experimental results for the adhesive influence in Table 3 show that there is no important difference between polyester resin and polyurethane adhesive. If one adds a glass fabric of  $400 g/m^2$  to the polyester resin, the flexural stiffness increases by 8%. For the Z stiffener influence (Table 4 and Figure 2) the results are more evident. The flexural stiffness of the Z reinforced sandwich are, for the Z made with a  $1000 g/m^2$ , more than 4 times the plain sandwich. As the Z reinforcements decrease its specific weight and thickness the flexural stiffness decreases to 166 N/m.

Table 3. Experimental results for the sandwich beams.

Beam ref	Adhesive	F [N]	Mid Span Deflection [mm]	Flexural Stiffness [N/mm]
#1A; #2A; #F-1; #F-2	PUR adhesive	2000	20.60	96.47
#1B; #2B	RP	2000	20.26	95.25
#3B; #4B	RP + T400	2000	18.955	103.75
#5B; #6B	RP + T300	2000	19.055	101.25

Table 4. Experimental results of the Z sandwich beams.

Beam ref	Glass Fibre Fabric [g/m <sup>2</sup> ]	F [N]	Mid Span Deflection [mm]	Flexural Stiffness [N/mm]
#G1; #G2	1000	2000	5.03	430.6
#3; #4	600	2000	7.34	269.4
#A1; #A2; #7; #8	500	9.22	215.4	
#A1-2; #A1-3	300	2000	10.935	166.6

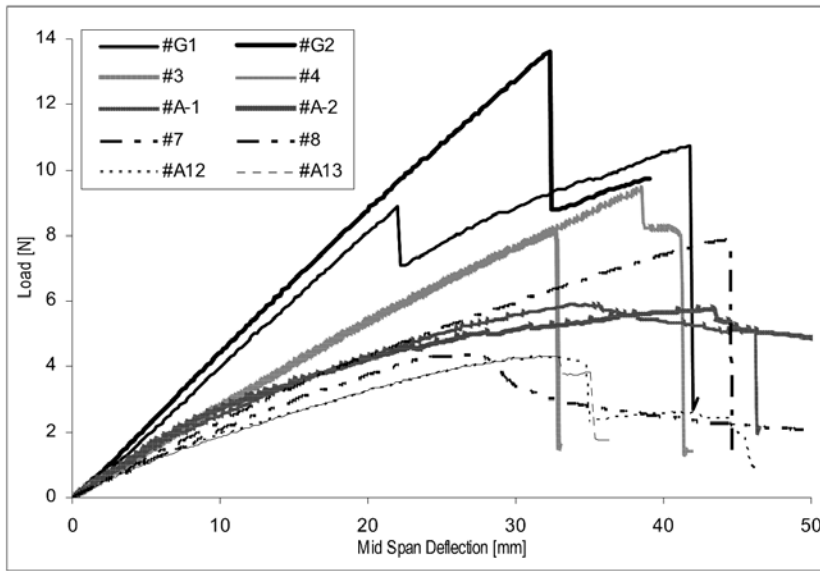


Figure 2. Load vs. mid span deflection results of the Z reinforced sandwich.

#### 4. ANALYTICAL MODELS

The theory for engineering stresses in beams is easily adapted to sandwich beams with some modifications. The effects of shear deflections in the core must be added and certain terms may be neglected when calculating flexural rigidity.

From [4] the mid span deflection of a sandwich beam is given by:

$$w = \frac{PL^3}{48D} + \frac{PL}{4U} \quad (1)$$

where  $D$  is the panel bending stiffness and  $U$  is the panel shear rigidity.  $P$  is the load and  $L$  is the span length.

To use ordinary beam theory we should first find the flexural stiffness, denoted by  $D$ , of the beam. In the ordinary beam theory  $D$  would be the product of the module of elasticity,  $E$ , and the second moment of area  $I$ . In sandwich beams,  $D$  is the sum of the flexural rigidities of the different parts, measured about the centroidal axis of the entire section (Figure 1):

$$D = 2E_f b \frac{t^3}{12} + E_f b t \frac{d^2}{2} + E_c \frac{bc^3}{12} \quad (2)$$

where indexes  $f$  and  $c$  are for faces and core, the first and second terms in Equation (2) represent the bending stiffness of the faces; the third term is the bending stiffness of the core. The term  $2t^3/12$  is less than 0.1% of  $td^2/2$ , so it's possible to neglect it. The core bending stiffness is neglected because it is 0.1% of the faces. So Equation (2), for sandwich with weak cores and thin faces, is approximately [5]:

$$D = E_f b \frac{td^2}{2} \quad (3)$$

Shear deflections are also the sum of shear rigidity of the face and core. Assuming the approximations for a sandwich with thin faces, weak core, and that shear modulus of the faces to be large, the shear rigidity is approximately, [5]:

$$U = G_c b \frac{d^2}{c} \quad (4)$$

where  $G$  is the beam core shear modulus.

Close review of Equations (1), (3) and (4) shows that for a given geometry there is two ways to increase shear rigidity: by introducing stiffeners or by increasing foam core shear modulus.

Figure 3 shows the influence of shear modulus increase in the mid span deflection due to bending and shear. It also shows experimental results for unreinforced sandwich beams.

The experimental results agree quite well with Equation (1), although that equation predicted more stiffness for the beams. Possibly this happens because of the material properties estimations. Since the faces are made of random mats, isotropic approximation of an anisotropic material is made, giving some data scattering. Foam properties were obtained by compression tests and the shear modulus obtained by the isotropic materials relation law. Although experimental results had good correlation, the difficulty was to obtain the Poisson coefficient.

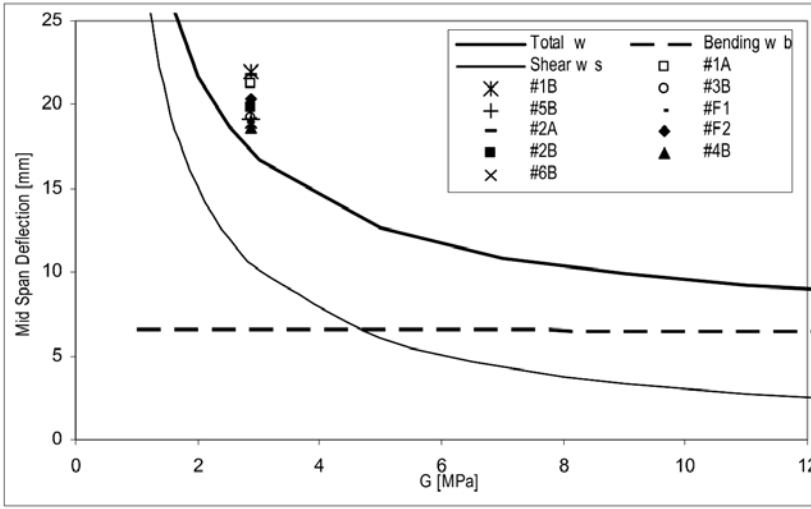


Figure 3. Influence of bending and shear deflections in the overall deflection with foam shear modulus.

To increase foam core shear rigidity, one must have an increase on its density, as [6]:

$$G_c \approx E_s \frac{3}{8} \left\{ \phi^2 \left( \frac{\rho^*}{\rho_s} \right)^2 + (1-\phi) \frac{\rho^*}{\rho_s} \right\} \tag{5}$$

where  $E_s$  and  $\rho_s$  are the properties from the original solid material and  $\rho^*$  is the density of the foam.  $\phi$  is the percentage of material in cell walls versus cell faces. Note that the thermal conductivity increases with foam density so one must consider it when increasing density.

The other way to increase panel shear rigidity is the introduction of a stiffener (Figure 1). For the sandwich beams with Z stiffeners it's necessary to adapt Equations (3) and (4). The stiffeners increase bending stiffness and shear rigidity. Equation (3) becomes:

$$D = E_f b t \frac{d^2}{2} + \frac{1}{12} E_{ref} b_{ref} c^3 + E_{ref} \frac{b}{2} b_{ref} \frac{d'^2}{2} \tag{6}$$

where index *ref* is for the stiffener. The total thickness  $h$  is increased by the thickness of the stiffener  $b_{ref}$  and  $d' = d - t - b_{ref}$ . Note that the second term represents less than 2%, and for this study can be neglected, and that the third term of the equation represents approximately 25% of the bending capacities of the reinforced sandwich.

For the Shear term, Equation (4) becomes:

$$U = G_c \left( b - b_{ref} \right) \frac{d^2}{c} + G_{ref} b_{ref} c \tag{7}$$

Also note that the second term of the equation represents approximately 80% of core shear capacities of the reinforced sandwich.

Figure 4 shows the influence of an increase of the Z stiffener thickness in the mid span deflection due to bending and shear. It also shows experimental results for Z reinforced sandwich beams. From [2,3]  $G_c = 2.88 \text{ MPa}$ ,  $E_{ref} = 6 \text{ GPa}$  and  $G_{ref} = 2.3 \text{ GPa}$ .

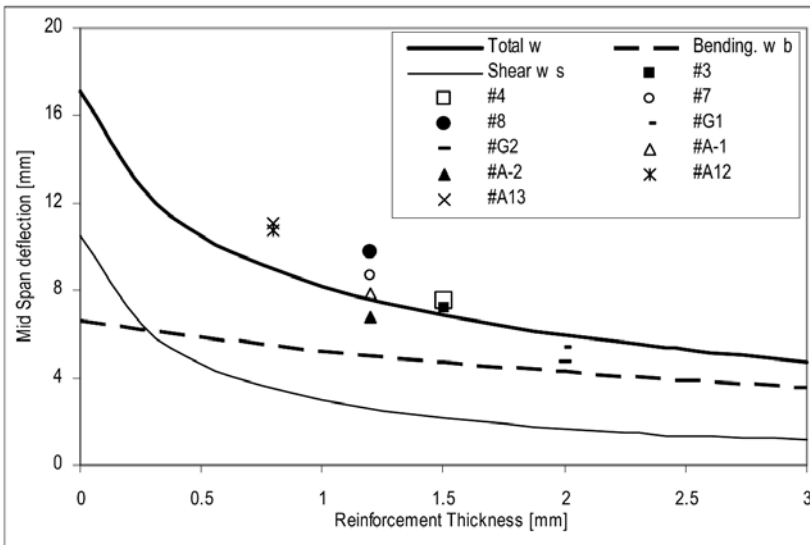


Figure 4. Influence of bending and shear deflections in the overall deflection with Z stiffener thickness (PUR core).

### 5. FEM MODELS

The commercial code ANSYS has the following element types available to model layered composite materials: SHELL99, SHELL91, SHELL181, SOLID46, and SOLID191. SOLID45 and SHELL63 may be used, with special considerations to model sandwich behaviour [6].

Five different approaches are studied to model sandwich beams behaviour. First approach is the full solid model. In this approach all materials in the sandwiches are modelled separately and the real constants

result from the 3D geometry. The second approach is a solid/shell model, where the core is a solid and the faces and reinforcements are modelled as shells. The third, fourth and fifth approach consists in using the layered elements available to model the sandwiches. Solid and two different shells were used. Both types of sandwich beams were studied, see Figure 1, five tests were created, resulting in ten different tests conducted. All models are thoroughly explained in [3, 8].

For the sandwich beams, the first approach, Test 1.1, consist of full solid modelling using SOLID45, an 8 node structural solid used for three-dimensional modelling of solid structures. The second approach, Test 1.2, consists in using solid/shell modelling. SOLID45 and SHELL63 are used to model core and faces. SHELL63 is a 4 node elastic shell and has both bending and membrane capacities, and is used to model thin to moderately thick plate and shell structures. The third approach, Test 1.3, consists in using element SOLID46. This element is a layered version of the 8-node structural solid, SOLID45, designed to model layered thick shells or solids. The fourth approach, Test 1.4, consists in using element SHELL99, an 8 node layered structural shell element. It is designed to model thin to moderately thick plate and shell structures. The fifth approach, Test 1.5, consists in using element SHELL91, an 8 node layered structural shell element that uses "sandwich logic." This logic is specifically designed for sandwich construction with thin faceplates and a thick, relatively weak, core. The core is assumed to carry the entire transverse shear; the faceplates carrying none. Conversely, the faceplates are intended to carry all, or almost all, of the bending load. Both faceplates are assumed to have the same number of layers, up to seven layers each [7].

For the Z reinforced sandwich beams the first approach, Test 2.1, consist of a full solid modelling with elements SOLID45. The second approach, Test 2.2, consists of a mixed solid/shell modelling with elements SOLID95 for core and SHELL99 for the Z stiffener and the faces. SOLID95 is a higher order version of the 3-D 8-node solid element SOLID45. SHELL99 has an option for nodes placement. Mid side nodes are the default but nodes on top or bottom are also possible. So, in this case, the core thickness is maintained and no correction to core shear modulus is required. Third approach, Test 2.3, consists of solid/shell modelling with elements SOLID46 for the sandwich and SHELL63 for the web of the Z stiffener. Fourth approach, Test 2.4, consists of shell/beam modelling with elements SHELL99 for a 5 layer sandwich and BEAM4 for the web of the Z stiffener. One of the layers is used to model a thin layer of core foam to get an accurate geometry. Fifth approach, Test 2.5, consists of shell/beam modelling with elements SHELL91 for a 5 layer sandwich and BEAM4 for the web of the Z stiffener.

BEAM4 is a 3D elastic beam with tension, compression, torsion, and bending capabilities.

## 5.1 FEM results

The results are analysed for the beam mid span deflection for all beams at the load of 2000 N. The numerical results are compared with the analytical and experimental results obtained.

Tables 5 and 6 show the results for mid span deflection, the experimental and the analytical results, for a load of 2000 N. They also show the ratio of the results to the analytical solution.

Numerical results for the unreinforced sandwich beams (Table 5), show a mid span deflection within 10% from target solution for all tests, except in Test 1.4 where the SHELL99 element is used. Results for all other approaches show good accuracy when compared to the analytical and experimental work. Test 1.4 has a ratio of 0.385, predicting a much stiffer beam when compared with experimental and analytical results. Element SHELL99 is designed to model thin to moderately thick structural plates and shells, which is inappropriate when modelling these sandwich panels.

Numerical results for the Z sandwich beams (Table 6), show also good results, within 10% from target solution, except Test 2.4 using SHELL99/BEAM4 element approach that has a ratio of 0.697. Results for the 3D models show a lower flexural stiffness when compared with the analytical solution, and 2D models show a stiffer result. All 3D approaches, Test 2.1, 2.2 and 2.3, are useful to model 3D structures. For 2D structural modelling, SHELL91 is the solution. Like in the sandwich beam Test 1.4, results for SHELL99 are inappropriate to model these sandwich Z reinforced beams.

Table 5. Numerical results for the sandwich beams (load = 2000 N).

	Test 1.1	Test 1.2	Test 1.3	Test 1.4	Test 1.5	Experimental Result	Analytical Solution
Mid Span Deflection	17.054	17.868	18.499	<b>6.58</b>	18.865	18.64 (#4B)	<b>17.077</b>
Ratio	0.998	1.046	1.083	<b>0.385</b>	1.104	1.091	<b>1</b>

Table 6. Numerical results for the sandwich beams (load = 2000 N).

	Test 2.1	Test 2.2	Test 2.3	Test 2.4	Test 2.5	Experimental Result	Analytical Solution
Mid Span Deflection	7.549	7.636	7.549	<b>4.81</b>	6.541	7.50 (#4)	<b>6.90</b>
Ratio	1.094	1.106	1.094	<b>0.697</b>	0.947	1.086	<b>1</b>

## 6. CONCLUSIONS

Conclusions are: (a) the Z reinforcement increases drastically the stiffness of sandwich beams in three point bending; (b) the analytical models proposed give accurate predictions of the reinforced sandwich behaviour; (c) some adjustments have to be made to model effectively their behaviour in FEM solvers like ANSYS; (d) the adhesive solution has a small effect on the flexural stiffness of the sandwich beams tested.

## REFERENCES

1. Robinson, "How to produce a modern, lightweight composite semi-trailer". Engineering Integrity, Vol. 12, July 2002, pp. 6-9.
2. Freitas, M., P.B. Rodrigues, and A. Silva, "Análise da flexão de vigas sanduíche com reforços em Z". In VI Congresso da Mecânica Aplicada e Computacional, Aveiro, 2000, pp. 367-375 (in Portuguese).
3. Leite, M., "Experimental, analytical and numerical study of reinforced sandwich beams applied to refrigerated transport of perishable goods", MsC Thesis, Instituto Superior Técnico, 2004, 154 pp. (in Portuguese).
4. ASTM, *C393-00 Standard Test Method for Flexural Properties of Sandwich Constructions*. 2000, Volume 15.03, Issued October 2003.
5. Zenkert, D., *The Handbook of Sandwich Construction*, Cradley Heath: EMAS Publishing, 1997.
6. Gibson Lorna, J. and F. Ashby Michael, *Cellular Solids: Structure & Properties*, Oxford: Pergamon, 1988.
7. *ANSYS Release 7.0 - Documentation*, Canonsburg, PA: ANSYS Inc., 2003.
8. Leite, M. A. Silva, and M. Freitas, "Elastic behaviour of sandwich beams – Part 1: experimental study". In 9th Portuguese Conference on Fracture, Setúbal, Portugal, 2004.
9. Leite, M., A. Silva, and M. Freitas, "Elastic behaviour of sandwich beams – Part 2: numerical study". In 9th Portuguese Conference on Fracture, Setúbal, Portugal, 2004.

# WRINKLING OF SHALLOW SANDWICH SHELLS FOR THE GENERAL CASE OF MULTI-AXIAL ORTHOTROPY, CURVATURE AND LOADING

Vitaly Skvortsov<sup>1</sup> and Ole Thybo Thomsen<sup>2</sup>

<sup>1</sup>*State Marine Technical University of St.-Petersburg, Leninski Prospect 101, 198262 St.-Petersburg, Russia*

<sup>2</sup>*Institute of Mechanical Engineering, Aalborg University, 9220 Aalborg, Denmark*

**Abstract** The paper considers wrinkling of orthotropic faces of a shallow sandwich shell with an isotropic core for a general case of in-plane multi-axial loading. The principal axes of loading do not necessarily coincide with the principal axes of orthotropy and curvature. The technique of the obtained closed-form solutions are based on minimization of critical forces with respect to wavelengths and angles of wrinkling.

**Keywords:** wrinkling, shallow sandwich shell, orthotropy, multi-axial loading.

## 1. INTRODUCTION

Local buckling (wrinkling) of one or two faces (thin and stiff external layers) separated by a core (thick and weak/compliant internal layer) is a mode of failure of sandwich beams, plates and shells that often occurs in practice. Consequently, wrinkling has been studied thoroughly almost since the beginning of the practical use of sandwich structures.

In most cases, analysis of wrinkling is reduced to the determination of the minimum critical compressive force that leads to the loss of local stability. Moreover, for the simplest situation, the direction of wrinkling is known a priori. This enabled several authors to obtain closed-form analytical or numerical solutions based on various models for the core (Winkler's foundation, elastic half-space, layer of finite thickness, polynomial

approximation of the response on interface stresses) and the faces (similar or dissimilar thickness, similar or dissimilar compression, inclusion of imperfections, inclusion of plastic deformations, etc.).

However, for the more complex case, analysis of wrinkling requires simultaneous consideration of the orthotropy of the faces, arbitrary thickness of the core, multi-axial loading and curvature of the structure. Many of these factors were earlier accounted for separately, see [1–4].

The authors of [2] remarked that for the general case of a finitely thick core and dissimilar principal axes requires minimization with respect to two parameters, and therefore needs a considerable amount of computing time. One more factor that complicates the analysis of wrinkling is the possible initial curvature of the sandwich structure considered. The influence of curvature on the global stability has been investigated within framework of shallow shell models in many investigations (e.g. [5]), but local stability has never been studied before.

The research aims to model wrinkling instability covering a wide range of a core thicknesses and arbitrary mutual orientation of the principal axes of orthotropy (i.e. general orthotropy), curvature and loading. Moreover, the research concentrates on the derivation of closed-form analytical solutions that are practically applicable for parametric studies of different sandwich structure/panel lay-ups.

## 2. MODELING OF SANDWICH FACES

### 2.1 General assumptions

Referring to Figure 1, the modeling is based on the following assumptions for the sandwich faces of a shallow sandwich shell:

- The faces are shallow thin shells according to Vlasov [6], and the model is valid for  $L^2 \ll R^2$ , where  $L$  is a typical length of deformation, and  $R$  is a typical radius of curvature of the shell mid-surfaces.
- The faces are orthotropic, and the in-plane elastic constants  $E_1$ ,  $E_2$ ,  $\nu_{12}$ ,  $\nu_{21}$ ,  $G_{12}$  (standard notation, [7]) of the faces are defined along the axes of the co-ordinate system  $x$ - $y$ . The amount of cross-ply laminae, that constitute the faces, is sufficiently large to provide an averaging of the elastic properties. In addition, it is assumed that the elastic moduli of the faces are much larger than the elastic core moduli, i.e.,  $E_f \gg E_c$ .
- The face thickness is small compared with the core thickness,  $h_f \ll h_c$ .

- The principal radii of curvature of a shell midsurface are determined in the co-ordinate system that is rotated relatively the principal material co-ordinates  $xy$  (1, 2), see Figure 1. Thus, in the principal material co-ordinates, three curvatures  $\kappa_1=1/R_1$ ,  $\kappa_2=1/R_2$ ,  $\kappa_{12}=1/R_{12}$  are non-zero. In the small area of wrinkling they can be considered as constants with respect to  $x, y$ .
- In accordance with the standard hypothesis of thin shell structures, it is assumed that the transverse normal stress is negligible compared with in-plane stresses, i.e.,  $\sigma_3 \equiv \sigma_z \approx 0$ .

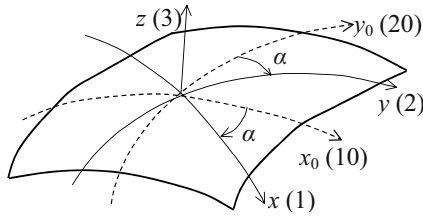


Figure 1. Shallow sandwich shell face: material co-ordinates  $x-y$  (1,2) and lines of principal curvature  $x_0-y_0$  (10,20).

The constitutive elastic relations for the orthotropic faces that express the 3-D strains in terms of stresses can be written in the form:

$$\sigma_1 = C_{11}\varepsilon_1^{3D} + C_{12}\varepsilon_2^{3D}, \quad \sigma_2 = C_{12}\varepsilon_1^{3D} + C_{22}\varepsilon_2^{3D}, \quad \tau_{12} = C_{66}\gamma_{12}^{3D} \quad (1)$$

The elastic moduli in Eq. (1) together with the initial moduli gives the integral 2-D moduli of the thin shell:

$$B_1 = E_1 h_f, \quad B_2 = E_2 h_f, \quad B_{66} = G_{12} h_f, \\ D_1 = C_{11} \frac{h_f^3}{12}, \quad D_2 = C_{22} \frac{h_f^3}{12}, \quad D_{12} = C_{12} \frac{h_f^3}{12}, \quad D_{66} = C_{66} \frac{h_f^3}{12} \quad (2)$$

## 2.2 Governing equations for the faces

The behavior of a differential shallow shell element loaded by initial compressive and shear forces  $P_1, P_2, P_{12} \approx P_{21}$  is described by the displacements  $u, v, w$ , the membrane stress resultants  $N_1, N_2, N_{12} \approx N_{21}$  and the bending and torsion moment resultants  $M_1, M_2, M_{12} \approx M_{21}$ . The transverse shear stress resultants and the rotations can be directly expressed in terms of these variables.

The assumptions adopted for the face geometry and lay-up enables a simplification of description of the face shell behavior compared with a general shell theory:

- Curvature is taken into account in the transverse equilibrium equations but neglected in the membrane equilibrium equations.
- Curvature is taken into account in the membrane kinematical relations but neglected in the transverse kinematical relations connecting rotations with displacements.
- The influence of interface shear stress on the equilibrium is ignored and membrane interface displacements are small, so that the only external load considered is the interface normal stress  $\sigma$ , which depends only on deflection  $w$ .

The reader is referred to [8] for the full details of the mathematical modeling. The resulting governing equation for the transverse deflection for the faces is [8]:

$$\left(H_D + H_B^{-1} H_R^2\right)w + H_P w + \sigma = 0 \quad (3)$$

where the differential operators  $H_D$ ,  $H_B$ ,  $H_R$  and  $H_P$  are defined by

$$\begin{aligned} H_B &= \frac{1}{B_1} \partial_{yyyy}^4 + \frac{2}{B_0} \partial_{xxyy}^4 + \frac{1}{B_2} \partial_{xxxx}^4, \\ H_D &= D_1 \partial_{xxxx}^4 + 2D_0 \partial_{xxyy}^4 + D_2 \partial_{yyyy}^4, \\ H_P &= P_1 \partial_{xx}^2 + 2P_{12} \partial_{xy}^2 + P_2 \partial_{yy}^2, \quad H_R = \kappa_1 \partial_{yy}^2 - 2\kappa_{12} \partial_{xy}^2 + \kappa_2 \partial_{xx}^2 \end{aligned} \quad (4)$$

and

$$\frac{2}{B_0} = \frac{1}{B_{66}} - \frac{\nu_{12}}{B_1} - \frac{\nu_{21}}{B_2}, \quad D_0 = D_{12} + 2D_{66}. \quad (5)$$

### 3. CORE RESPONSE AND MODES OF WRINKLING

The interface transverse normal stress  $\sigma$  appearing in the governing Eq. (3) is the response of the core material to the wrinkling of a face. The approach adopted is to describe the wrinkling as a periodic deflection  $w$ , which depends on the in-plane co-ordinates with a certain orientation of the periodicity:

$$w = w_0 \sin \lambda t, \quad \lambda = \pi/L, \quad t = x \cos \varphi + y \sin \varphi + \text{const} \quad (6)$$

where  $w_0$  is the amplitude of the wrinkles,  $L$  is the half-length of “wrinkle”,  $\lambda$  is a wave number,  $t$  is a co-ordinate along the line of the wrinkling and  $\varphi$  is the angle between  $t$  and  $x$ .

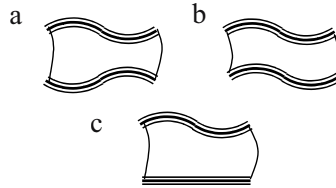


Figure 2. Wrinkling modes: (a) - symmetric, (b) - anti-symmetric, (c) - non-symmetric.

With reference to Figure 2, the following three wrinkling modes exist:

- Symmetric wrinkling of two similar faces. In the case of an isotropic core, this failure mode hardly occurs in practice, and is disregarded.
- Anti-symmetric wrinkling of two similar faces.
- Non-symmetric wrinkling where one face wrinkles, while the opposite face remains straight. This failure can arise in the case of strong tension of the opposite face or for the case where the bending stiffness non-wrinkled face is much larger than that of the wrinkled face.

The interface transverse normal stress is modeled by:

$$\sigma = K_c F_i(\xi) w, \quad K_c = \frac{4E_c(1-\nu_c)}{h_c(1+\nu_c)(3-4\nu_c)}, \quad \xi = \frac{\lambda h_c}{2} = \frac{\pi h_c}{2L}. \tag{7}$$

The parameter  $\xi$  is a dimensionless wave number, which is the argument of the non-dimensional core response functions  $F_i$ , where  $i = s, a$  or  $n$  corresponding to the three wrinkling modes (“s”=symmetric; “a”=asymmetric and “n”=nonsymmetric). These functions were obtained by Allen [5] for the plane stress state of the core using exact 2-D theory of elasticity. Generalization to the case of state of plane strain yields:

$$F_s = \frac{\xi \cosh^2 \xi}{\sinh \xi \cosh \xi - \xi / (3 - 4\nu_c)}, \tag{8}$$

$$F_a = \frac{\xi \sinh^2 \xi}{\sinh \xi \cosh \xi + \xi / (3 - 4\nu_c)}, \quad F_n = \frac{F_s + F_a}{2}$$

The extension of this solution to the case of a doubly curved core layer is justified by the assumption of shallowness, i.e.  $L^2 \ll R^2$ .

#### 4. DETERMINATION OF CRITICAL LOAD

The general solution to the governing equation for non- and anti-symmetric wrinkling Eq. (3) for an orthotropic shallow shell is to be obtained in the form Eq. (6), where neither the angle  $\varphi$  between the axis of wrinkling  $t$  and the material axis  $x$ , nor the wave number  $\lambda$  are known in advance. However, this is overcome by adopting a procedure, where the wrinkling analysis is reduced to the minimization of approximate expressions for the dimensionless critical forces  $\bar{P}_i$  ( $i = a, n$ ) with respect to the dimensionless wave number  $\xi$  and wrinkling angle  $\varphi$ . The first step of the minimization yields the critical forces as functions of  $\varphi$ :

$$\bar{P}_{a.cr.\varphi} \equiv \frac{3h_c^2 P_{a.cr.\varphi}}{C_f h_f^3} = \frac{1}{f_P} \left( \frac{2f_D f_R \mu^2 \rho^2 \sqrt{f_D - \rho^3 / 8n_0^2}}{\sqrt{f_B}} + \frac{3}{2} \rho^3 \right)$$

if  $\frac{2f_B n_0^2 \rho^3 + f_R^2 \mu^4 \rho^4}{16f_B f_D n_0^4} \leq 1,$

$$\bar{P}_{n.cr.\varphi} \equiv \frac{3h_c^2 P_{n.cr.\varphi}}{C_f h_f^3} = \frac{1}{f_P} \left( 2 \sqrt{\frac{f_D}{f_B} (2f_B n_0 n_1 \rho^3 + f_R^2 \mu^4 \rho^4)} + \frac{n_0 \rho^3}{2n_1} \right) \quad (9)$$

if  $\frac{2f_B n_0 n_1 \rho^3 + f_R^2 \mu^4 \rho^4}{16f_B f_D n_1^4} \leq 1,$

$$\bar{P}_{a.cr.\varphi} = \bar{P}_{n.cr.\varphi} = \frac{3}{f_P} f_D^{1/3} n_0^{2/3} \rho^2 \Phi \quad \text{otherwise,}$$

where  $f_D, f_B, f_R, f_P$  are functions that depend on the relations between the elastic moduli, curvatures, the initial forces and the wrinkling angle  $\varphi$ , while the coefficients  $n_0, n_1$  depend on the core Poisson's ratio.

In Eq. (9) an additional function  $\Phi$  is defined using the solution of a polynomial equation of the fourth order with the aid of Cardano's formula:

$$\Phi \equiv \frac{3\gamma^{3/4} (\gamma^{3/4} + \sqrt{2 - \gamma^{3/2}}) + 1 - \gamma^3}{3\gamma^{1/2} (1 + \gamma^{3/4} \sqrt{2 - \gamma^{3/2}})},$$

$$\gamma \equiv \left( \sqrt{\frac{f_D}{n_0^4} \left( \frac{4\mu^4 f_R^2}{3f_B} \right)^3 + \frac{1}{4} + \frac{1}{2}} \right)^{1/3} - \left( \sqrt{\frac{f_D}{n_0^4} \left( \frac{4\mu^4 f_R^2}{3f_B} \right)^3 + \frac{1}{4} - \frac{1}{2}} \right)^{1/3} \quad (10)$$

and the governing structural parameters of stiffness  $\rho$  and curvature  $\mu$  are introduced:

$$\rho \equiv \left( \frac{G_c h_c^3}{C_f h_f^3} \right)^{1/3}, \quad \mu \equiv \left( \frac{3E_f C_f^{1/3} h_f^2}{4G_c^{4/3} R^2} \right)^{1/4} \tag{11}$$

in which  $R$  is the maximum radius of curvature.

In the second step, the forces defined by Eq. (9) are to be minimized analytically or numerically with respect to  $\varphi$ .

## 5. EXAMPLE RESULTS

Two groups of solutions have been derived. The first group concerns analytical solutions that explicitly demonstrate the influence of curvature on the wrinkling behavior. The second group exhibits examples of solutions where the wrinkling directions do not coincide with the principal directions of loading and orthotropy.

### 5.1 Results – “group 1” (influence of stiffness and curvature)

The special case of an arbitrary core and sandwich faces as isotropic spherical shallow shells is considered. For an arbitrary relative core thickness, the dependency of the dimensionless critical loads of the governing structural parameters  $\rho$  and  $\mu$  are given by Eqs. (9), where  $f_D = f_B = f_R = f_P = 1$ . Graphs for the critical loads for non- and anti-symmetric modes of wrinkling versus  $\rho$  for several values of  $\mu$  for  $\nu_c = 1/3$  are shown in Fig. 3.

Table 1. Specific points in Fig. 3 and values of the constitutive parameters.

Points	$G_c = 20 \text{ MPa},$ $C_f = 60 \text{ GPa}$		$G_c = 20 \text{ MPa},$ $C_f = 20 \text{ GPa}$		$G_c = 60 \text{ MPa},$ $C_f = 20 \text{ GPa}$		$G_c = 120 \text{ MPa},$ $C_f = 15 \text{ GPa}$	
	$h_c/R$	$h_f/h_c$	$h_c/R$	$h_f/h_c$	$h_c/R$	$h_f/h_c$	$h_c/R$	$h_f/h_c$
A	0.28	0.07	0.4	0.1	0.56	0.14	0.8	0.2
B	0.2	0.05	0.28	0.07	0.4	0.1	0.56	0.14
C	0.14	0.07	0.2	0.1	0.28	0.14	0.4	0.2
D	0.1	0.1	0.14	0.14	0.2	0.2	0.28	0.28
E	0.07	0.07	0.1	0.1	0.14	0.14	0.2	0.2

Additionally, several specific points corresponding to typical values of moduli of materials and ratios of sizes are placed on the graphs. The description of the points is listed in Table 1. The points enable correlation between the face/core moduli ratio, the face/core thickness ratio, the

thickness/radius ratio and the corrective factor compared to the classical solutions ( $\mu = 0$ , i.e. zero curvature).

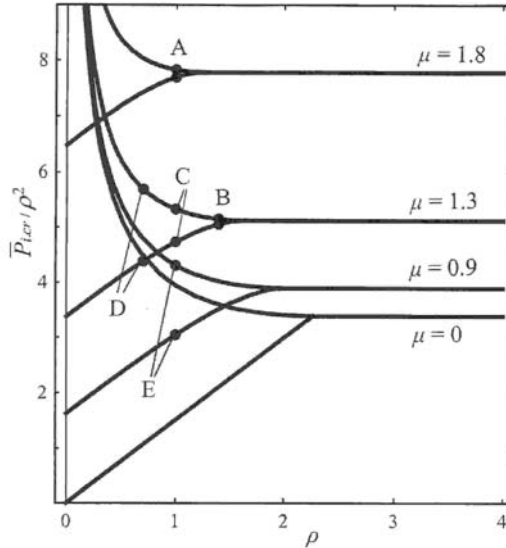


Figure 3. Dimensionless critical forces vs. the stiffness parameter for isotropic spherical shell.

**5.2 Results – “group 2” (wrinkling angle  $\varphi$  not coincident with principal directions of loading and orthotropy)**

The following shallow sandwich shell example is considered:

*Material properties:*  $C_{11} = 20$  GPa,  $C_{22} = 10$  GPa,  $C_{12} = 1$  GPa,  
 $G_{12} = 2$  GPa,  $G_c = 40$  MPa,  $\nu_c = 1/3$ .

*Thicknesses:*  $h_f = 5$  mm,  $h_c = 30$  mm.

*Curvature:*  $\kappa_1 = 0.002$  mm<sup>-1</sup> ( $R_1 = 500$  mm),  $\kappa_2 = 0,004$  mm<sup>-1</sup>  
( $R_1 = 250$  mm),  $\kappa_{12} = 0$ .

*Loading:*  $P_2 / P_1 = 0.4$ ,  $P_{12} / P_1 = 0.2$ .

The reinforcement of the faces dominates in the 0° ( $x$ ) and 90° ( $y$ ) directions. The face stiffness reaches a minimum value at an angle  $\varphi_D = 1.05$  rads (60°) relative to the  $x$ -axis. The loading is multi-axial with a compressive force in the 0° direction as the highest component, and the principal load direction is inclined an angle  $\varphi_P = 0.3$  rads (17°) relative to the  $x$ -axis. The dimensionless structural stiffness parameter is  $\rho = 0.95$

(corresponding to a fairly thin core). The dimensionless structural curvature parameter is  $\mu=0.74$  (corresponding to a moderate curvature).

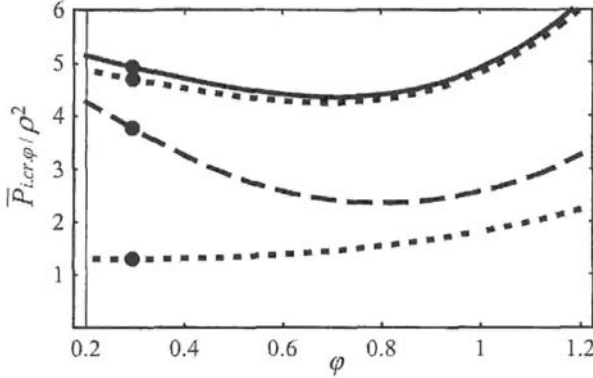


Figure 4. Dimensionless compressive forces versus angle (rads): non-symmetric mode (solid line), anti-symmetric mode (dashed line), the cases of absence of curvature (dotted line), points of direction of maximum compression loading (principal loading direction).

The results in Figure 4 show that non-symmetric wrinkling occurs at the angle  $\varphi_0 = 40^\circ$  between the angles of maximum compression and minimum stiffness. The critical load is slightly lower than the loads at  $\varphi_D$  and  $\varphi_P$ . Anti-symmetric wrinkling happens at  $\varphi_0 = 46^\circ$  and the critical load is about 15% lower than the load at  $\varphi_D$  and 50% lower than the load at  $\varphi_P$ , respectively. In the case of a plate (dotted line) the angle of anti-symmetric wrinkling shifts to  $\varphi_P$  and diminishes by a factor of 2.

## 6. CONCLUSIONS

A mathematical model for local instability of orthotropic shallow sandwich shells has been derived for the two main modes: anti-symmetric and non-symmetric “wrinkling”.

The main model features and the main results can be outlined as:

- The mathematical model describes wrinkling of shallow sandwich shells, where the principal axes of orthotropy, curvature and external loading do not coincide with each other.
- Closed-form solutions for critical forces are obtained for several particular cases by minimizations of the compressive loads of instability with respect to the angle of wrinkling. The results

demonstrate that wrinkling may occur in directions inclined from the principal axes of loading.

## ACKNOWLEDGMENT

The work presented was conducted during the period of a visiting professorship of the first author with the Institute of Mechanical Engineering at Aalborg University. The visiting professorship and the research presented herein were sponsored by the US Navy, Office of Naval Research (ONR), Grant/Award No. N00014-04-1-0112: "Failure and Fatigue Phenomena Associated with Discontinuities and Localized Impact Loading in Advanced Lightweight Sandwich Structures". The ONR program manager was Dr. Yapa Rajapakse. The financial support received is gratefully acknowledged.

## REFERENCES

1. Stiftinger, M.A., Rammersdorfer, F.G. and Starlinger, A., "Face layer wrinkling in anisotropic sandwiches", In: Sandwich Construction 3, Proceedings of the 3rd International Conference on Sandwich Construction, Southampton, September 1995, pp. 325-334.
2. Stiftinger, M.A. and Rammersdorfer, F.G., "Face layer wrinkling in sandwich shells – theoretical and experimental investigations", Thin-Walled Structures, Vol. 29, No. 1-4, pp. 113-127, 1998.
3. Vonach, W.K. and Rammersdorfer, F.G., "Wrinkling of thick orthotropic sandwich plates under general loading conditions", Archive of Applied Mechanics, 70, pp. 338-348, 2000.
4. Birman V. and Bert C.W., "Wrinkling in composite-facing sandwich panels under biaxial loading", Journal of Sandwich Structures and Materials, Vol. 6, No. 3, pp. 217-238, 2004.
5. Allen, H.G., Analysis and Design of Structural Sandwich Panels, Oxford, Pergamon Press, 1969.
6. Vlasov, V.Z., "General theory of shells and its application to engineering", Moscow-Leningrad, 1949. NASA Technical Translation NASA-TT-F-99, 1964.
7. Jones, R.M., Mechanics of Composite Materials, London, Taylor & Francis, 1999.
8. Skvortsov, V. and Thomsen, O.T., "Local instability of shallow sandwich shells for the general case of orthotropy, curvature and loading", accepted for publication in Composite Structures, 2004.

# TRANSVERSE STRESSES OF A FILLER UNDER MULTIPOINT LOADINGS OF A SANDWICH PANEL

V.A. Polyakov, R.P. Shlitsa, V.V. Khitrov and V.I. Zhigun  
*Latvian University, Institute of Polymer Mechanics, LV-1006 Riga, Latvia*

**Abstract** Finite solution for deformation of a sandwich panel by two systems of forces applied symmetrically and nonsymmetrically to the upper and lower faces were examined. The simple estimates of transverse normal stresses in the midlayer of a sandwich panel at squeezing from the infinite system of ribs located on either face surface have been deduced.

**Keywords:** sandwich panel, infinite strip, point forces, transverse normal stress.

## 1. INTRODUCTION

The methods of the technical theory of layered composite materials are continuously being replenished due to the affected set of physical hypotheses and kinematic models is adapting itself to the various problems in the proper way.

Since the formal rigor of the applied theory is achieved by satisfying all initial equations before introducing simplifying hypotheses, the discrete model of a layered structure appears to be most precise. However, due to the high order of the system of equations, which depends on the number of layers, their solution is found by applying a numerical method of FEM-type or a computing algorithm derived specially for this particular problem and using a preliminary approximation of the functions across the thickness of the structure. In paper [1], dedicated to the investigation of bending of a sandwich panel, approximations by high-degree power exponential functions were assumed for transverse stresses in the soft filler. Due to the small thickness and increased stiffness of the face layers, their bending was assumed to follow the Kirchhoff model. The calculation difficulties in solving the problem by this model were associated with the multisegment method of integration in the panel plan.

In the technical theory of bending, which refers to a monolithic construction (a plate or beam made from the nonlaminar solid), the edge effects are examined using boundary functions that damp together with their derivatives on

an infinite extent of the structure. For structures of finite sizes, commensurable with the length of the boundary zone, the solution and the analysis of its convergence in the case of discontinuous surface loads and point forces becomes complicated. This is associated with the use of all fundamental functions of the solution, including the boundary functions, to satisfy the boundary conditions. The calculation difficulties of the methods employing functional series are associated with the drop in the exponent of the numbers of a natural series, which stands in the denominator of the expansion coefficients, with concentration of the surface load [2]. Thus, the greatest deflection for a uniform load is found at a value of the counter equal to  $1/m^5$  with an odd number  $m$ , whereas for a point force, the value of the counter rises to  $1/m^3$ . The second derivative of the deflection, which defines the bending stresses, depends respectively on the values of the counter equal to  $1/m^3$  and  $1/m$ , in the latter case, the “quality” of convergence of functional series must be determined from its comparison with the harmonic series of numbers. Taking into account the fact that the calculation expressions for the coefficients of the series depend on the model parameters and loading conditions, the analysis of accuracy of the values of partial sums of the series in relation to these parameters is always urgent. It should be mentioned that, for time-dependent point forces, the terms of the infinite series of the solution include, as is known, harmonics in form of trigonometric time functions, and the estimation of the limit of the sum becomes complicated in this case. At best, restricting ourselves, with an admissible error, to one or two terms of the series, we obtain formulas convenient in practice. In other cases, general expressions for the series coefficients and tabulated values of corresponding partial sums, for different parameters of the model, are presented [2].

We should point here to the known analytical method for obtaining solutions to the bending problem for plates, which makes it possible to evaluate easily the “rate” of convergence of the series representing the bending stresses. The idea, as indicated in [2], is based on the Nadai *method of images*, which permits one to obtain deflections and bending moments for a plate of *finite length* from the corresponding quantities for an *infinitely long* plate, i.e., when they are determined by means of boundary functions. In essence, this method employs the summation of solutions of similar type for an infinite plate according to the method of superposition. The advantage of this method is that the analytical expression of each addend in the sum is simple and contains an exponential function with a negative index. Using this method, it is easy to obtain a solution to the problem of cylindrical bending of a simply supported plate of finite length  $2l_1$  within the framework of the Kirchhoff hypothesis. First of all one ought to notice that the item involved has a certain attitude toward the bending model of an infinite strip with one degree of deformation freedom, i.e., with unified deflection for the strip transverse section. The self-balanced reactions of the supports in the cross section BB' can be excluded from the

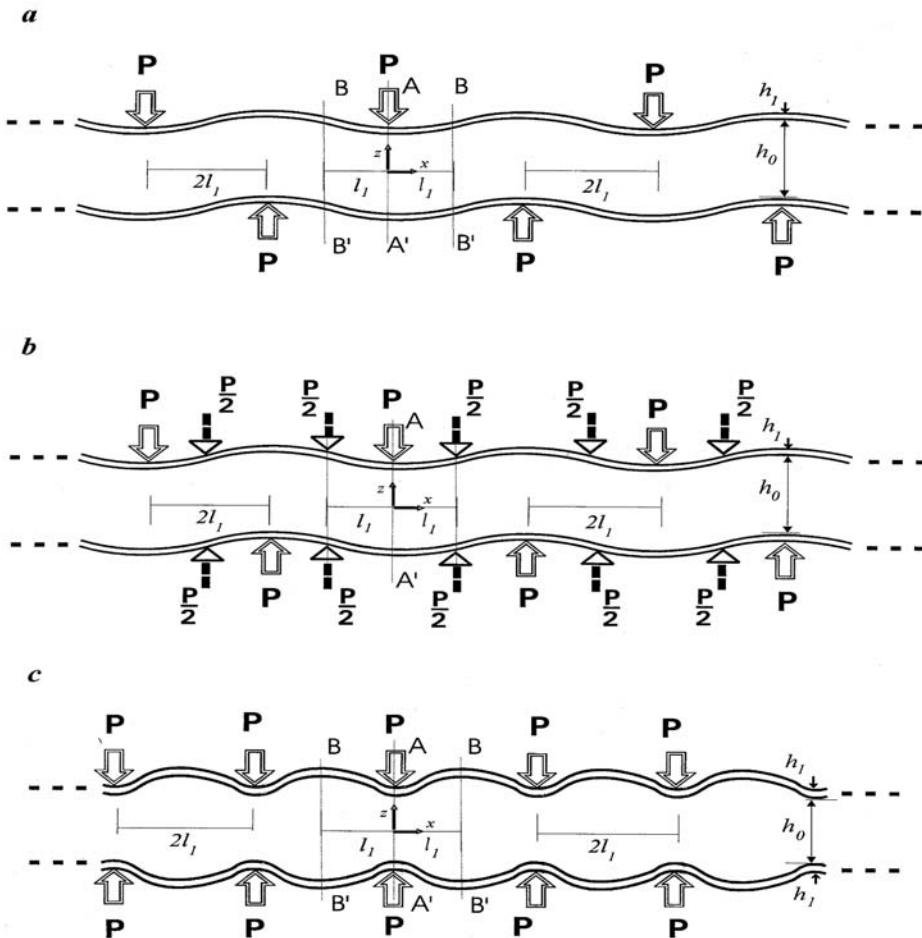


Figure 1. Multipoint distribution of point forces along an infinite sandwich strip: *a* – relative shift of the forces, *b* – combined loading, and *c* – symmetric forces.

general loading scheme of the strip, i.e., upon bending according to the simplified Kirchhoff model, the distinction between the loading schemes shown in Figures 1a, b disappears.

So the deflection and the bending moment in cross sections BB', see Figure 1a, in the case of an infinite number of periodically distributed forces  $P$ , are equal to zero if the deflection function is independent of the points of a transverse section. It should be noted a crucial issue in the problem when the model is characterized by more than one surface for deflections. In the latter case not all the calculation values of bending of an infinite strip within the in-

terval  $[-l_1, l_1]$  will be equal to the corresponding calculated values for a finite panel simply supported at edges. The discrete model of an infinite sandwich strip is characterized by two bending surfaces – for the upper and lower face layers. In the strip model, despite the coincidence of the cross sections of layers along the line BB' in the adjacent schemes of three-point loading, see Figure 1b, the support reactions are applied to the opposite side of the panel in all alternating schemes and are not excluded from consideration. The rotation of contacting cross sections BB' of the strip does not coincide with that of a *free cross section* of a separate layer on the support of a panel of finite length.

The solution for an infinite strip obtained by the discrete model of three-point bending is much simpler than that for a panel of finite length. Application of the Laplace operational method to the solution of equations allows one to obtain this solution in a closed form [3] and to avoid series expansions. Therefore the analytical solution to the bending problem of an infinite sandwich strip loaded according to the three-point scheme on the sampling interval of its length [4] has been taken as the analytical basis of the design for a multipoint scheme.

## 2. STRESSES IN THE FILLER OF A SANDWICH STRIP

The indicated feature of the discrete model must be kept in mind when calculating the transverse normal stress  $\sigma_z$  in an infinite strip loaded with a periodic set of point forces. Generally in this study the periodic system of ribs located on both face surfaces along the width of the panel, see Figure 1, was conceived of as point-load distribution when the distance between forces is arbitrarily given.

In the above-mentioned model of a panel [4], the transverse normal stress in the soft midlayer is determined in proportion to the difference between the deflections of face layers of the panel, i.e., it depends on the symmetric part of the solution  $w_s = (w_2 - w_1)/2$ . In the case of a load symmetric about the midplane of a panel of a symmetric structure, the deflection  $w_2$  is identified with the symmetric part of the solution  $w_s$ , while its antisymmetric part is  $w_{as} = (w_2 + w_1)/2 = 0$ . We should note that two forces equal in magnitude and opposite in direction, applied to the upper and the lower points of the panel cross section, see Figure 1c, determine two different bending surfaces:  $w_2(x) = -w_1(x)$ . In the case of incompressibility of the normal, we have  $w_1 = w_2 = w(x)$ ,  $w_s = 0$ , and the forces, which operate in the same cross section of the panel, cancel out. The general solution, obtained according to the discrete model in the case of symmetric point forces and expressed in terms of boundary functions [5], actually coincides with the solution to the problem of bending of a long sandwich panel from two diametrical forces applied at

the center [4]. In the case of a shift of the force system on the upper surface of the sandwich strip with respect to the force system on its lower surface, the antisymmetric component of deflections  $w_{as}$  is not zero, see Figures 1a, b.

The key parameters for determining the transverse normal stress in the mid-layer of a symmetric sandwich panel, according to the solution from [4], are

$$\begin{aligned} \mu &= \frac{h_1}{h_1 + h_0}, \quad \xi = \frac{x}{h_0 + h_1}, \quad \xi_1 = \frac{l_1}{h_1 + h_0}, \\ \kappa_\alpha &= \frac{1}{4\alpha} [1 + e^{-\alpha\xi_1} (\cos \alpha\xi_1 - \sin \alpha\xi_1)], \quad \alpha = \left[ \frac{6E_z(1 - \nu_1^2)}{E_x(1 - \mu)\mu^3} \right]^{1/4}, \\ \hat{w}_\Delta &= 2w_s(0)/q_0 = \frac{1}{4\alpha^3} [1 + e^{-\alpha\xi_1} (\cos \alpha\xi_1 + \sin \alpha\xi_1)], \\ q_0 &= \frac{6P(1 - \nu_1^2)}{b(h_0 + h_1)E_s\mu^3}, \quad w_1''(0) = -q_0(\hat{\xi}_1/2 + \kappa_\alpha), \\ w_2''(0) &= -q_0(\hat{\xi}_1/2 - \kappa_\alpha), \end{aligned} \tag{1}$$

where  $E_x$ , and  $E_z$ , are the elastic moduli in the longitudinal direction of the face layer and in the transverse direction of the midlayer, respectively, and  $\nu_1$  is the Poisson ratio of the face layer. Here the relative mean curvature  $\hat{\xi}_1/2 = -(h_0 + h_1)/(R_{mid}q_0)$ , the local additive for the curvature of a separate layer  $\kappa$ , and the transverse compression strain  $w_\Delta$  were introduced at the central cross section of a sandwich panel. Restricting ourselves to the consideration of a region  $0 \leq x \leq l_1$  of the infinite strip under loading by three forces, we obtain the following expression for the transverse normal stress in the midlayer [4]:

$$\begin{aligned} \hat{\sigma}_z(\xi) &= -\frac{q_0 E_z}{1 - \mu} \cdot \frac{1}{4\alpha^3} \left\{ e^{-\alpha\xi} (\cos \alpha\xi + \sin \alpha\xi) + \frac{e^{-\alpha(\xi_1 - \xi)}}{2} [\cos \alpha(\xi_1 - \xi) \right. \\ &\quad \left. + \sin \alpha(\xi_1 - \xi)] + \frac{e^{-\alpha(\xi_1 + \xi)}}{2} [\cos \alpha(\xi_1 + \xi) + \sin \alpha(\xi_1 + \xi)] \right\} \end{aligned} \tag{2}$$

To apply the superposition method, allowing us to consider the effect of systems of three-point forces, see Figure 1b, on the stress  $\sigma_z$ , in the finite interval  $0 \leq \xi \leq \xi_1$ , it is necessary to take into account the summands for  $\xi > (2m - 1)\xi_1$ ,  $m = 1, N$ , in the generalized formula from [4]. As a result, we obtain the following expression for the transverse stress  $\sigma_z$  in the central interval of the infinite strip:

$$\begin{aligned} \sigma_z(\xi) &= \hat{\sigma}_z(\xi) + \sum_{m=1}^N \{ -\hat{w}_\Delta c h \alpha (2m\xi_1 \mp \xi) \cos \alpha (2m\xi_1 \mp \xi) \\ &\quad + \frac{\kappa_\alpha}{\alpha^2} s h \alpha (2m\xi_1 \mp \xi) \sin \alpha (2m\xi_1 \mp \xi) \} \end{aligned}$$

$$\begin{aligned}
& + \frac{1}{4\alpha^3} [sh\alpha(2m\xi_1 \mp \xi) \cos \alpha(2m\xi_1 \mp \xi) \\
& - ch\alpha(2m\xi_1 \mp \xi) \sin \alpha(2m\xi_1 \mp \xi)] \\
& + \frac{1}{4\alpha^3} [sh\alpha((2m-1)\xi_1 \mp \xi) \cos \alpha((2m-1)\xi_1 \mp \xi) \\
& - ch\alpha((2m-1)\xi_1 \mp \xi) \sin \alpha((2m-1)\xi_1 \mp \xi)] \}. \quad (3)
\end{aligned}$$

The primed capital sigma means that the summation is performed over all terms: first for  $-\xi$ , and then for  $+\xi$ , from the interval  $0 \leq \xi \leq \xi_1$ .

Now, substituting the parameters  $\kappa_\alpha$  and  $\hat{w}_\Delta$  from Eq. (1) into Eq. (3) and taking into account Eq. (2), we obtain limiting expression at  $N \rightarrow \infty$ , for the transverse stress in the midlayer upon compression of the strip according to the scheme in Figure 1b:

$$\begin{aligned}
\sigma_z^{(b)}(\xi) = \hat{\sigma}_z(\xi) - \hat{\sigma}_z^0 \left\{ \left( 1 - \frac{sh2\alpha\xi_1 + \sin 2\alpha\xi_1}{ch2\alpha\xi_1 - \cos 2\alpha\xi_1} \right) \left[ ch\alpha\xi \cos \alpha\xi \right. \right. \\
\left. \left. + \frac{1}{2}(ch\alpha(\xi_1 - \xi) \cos \alpha(\xi_1 - \xi) + ch\alpha(\xi_1 + \xi) \cos \alpha(\xi_1 + \xi)) \right] \right. \\
\left. - \left( 1 - \frac{sh2\alpha\xi_1 - \sin 2\alpha\xi_1}{ch2\alpha\xi_1 - \cos 2\alpha\xi_1} \right) \left[ sh\alpha\xi \sin \alpha\xi \right. \right. \\
\left. \left. + \frac{1}{2}(sh\alpha(\xi_1 - \xi) \sin \alpha(\xi_1 - \xi) + sh\alpha(\xi_1 + \xi) \sin \alpha(\xi_1 + \xi)) \right] \right\}, \\
0 \leq \xi \leq \xi_1. \quad (4)
\end{aligned}$$

Here, we have introduced a designation for the transverse normal stress at the center of a sandwich panel in three-point loading with a large span, i.e., calculated from Eq. (2) at  $\xi_1 \gg 1$ :

$$\hat{\sigma}_z^0 = \hat{\sigma}_z(0) = -\frac{q_0 E_z}{1 - \mu} \cdot \frac{1}{4\alpha^3} = -\frac{P\alpha}{4b(h_1 + h_0)}. \quad (5)$$

This stress coincides with the transverse stress upon compression of an infinite panel by two opposite forces  $P/2$ . As a result, for the stress in a strip loaded with two opposite forces  $P$ , we get instead of Eq. (2)

$$\hat{\sigma}_z(\xi) = 2\hat{\sigma}_z^0 e^{-\alpha\xi} (\cos \alpha\xi + \sin \alpha\xi). \quad (6)$$

Applying the above-mentioned transformation to Eq. (3) for the loading scheme shown in Figure 1c, we obtain a limiting expression for the stress in the repeating interval:

$$\sigma_z^{(c)}(\xi) = 2\hat{\sigma}_z^0 \left[ e^{-\alpha\xi} (\cos \alpha\xi + \sin \alpha\xi) - \left( 1 - \frac{sh2\alpha\xi_1 + \sin 2\alpha\xi_1}{ch2\alpha\xi_1 - \cos 2\alpha\xi_1} \right) \right]$$

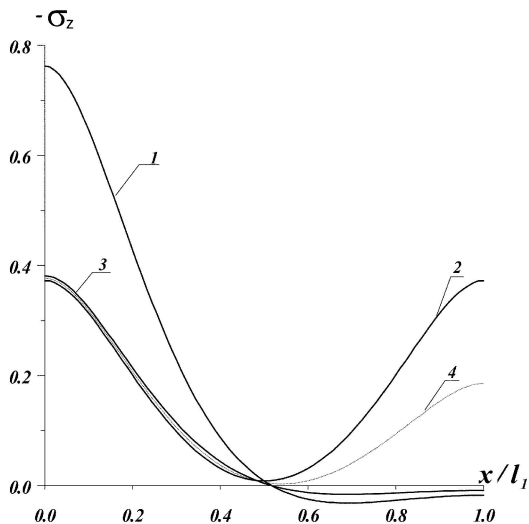


Figure 2. Transverse normal stresses in the filler along the strip length  $[0, l_1]$ : 1, 2, 3 – according to the  $c, b, a$  diagrams in Figure 1, and 4 – three-point bending of an infinite strip;  $E_x = 40$  GPa,  $E_x^0 = 0.310$  GPa,  $l_1/h = 3$ ,  $h_0 = 2h_1 = 0.006$  m.

$$\times ch\alpha\xi \cos \alpha\xi + \left( 1 - \frac{sh2\alpha\xi_1 - \sin 2\alpha\xi_1}{ch2\alpha\xi_1 - \cos 2\alpha\xi_1} \right) sh\alpha\xi \sin \alpha\xi \Big],$$

$$0 \leq \xi \leq \xi_1. \tag{7}$$

For a sandwich strip loaded according to the scheme presented in Figure 1a, we have

$$\sigma_z^{(a)}(\xi) = \sigma_z^{(b)}(\xi) - \frac{1}{2}\sigma_z^{(c)}(\xi_1 - \xi), \quad 0 \leq \xi \leq \xi_1, \tag{8}$$

where the second summand is found from Eq. (7) by replacing the variable  $\xi$  with the difference  $\xi_1 - \xi$ . Formally, when calculating  $\sigma_z^{(a)}(\xi)$  within the interval  $0 \leq \xi \leq \xi_1$ , we can use the expression  $\sigma_z^{(b)}(\xi)$  from Eq. (4), changing previously the sign of the addends containing the difference  $\xi_1 - \xi$  as an argument.

The curves and surface presented in Figures 2, 3 show the parametric variation in the transverse stress in the midlayer of the filler for the above cases of multipoint loading. As the rated value of the point force, constant on the line along the width the sandwich strip,  $b$ , is taken the force  $P$  for which  $P/bh = 1$  Mpa, ( $h = 2h_1 + h_0$ ).

It is noteworthy in Figure 2 that despite the different curvature of the deflection line for the two multipoint loading in accordance with the schemes  $a$  and  $c$  in Figure 1, the differences in the symmetric component of the deflections of face layers remain proportional over the whole interval  $0 \leq x \leq l_1$ .

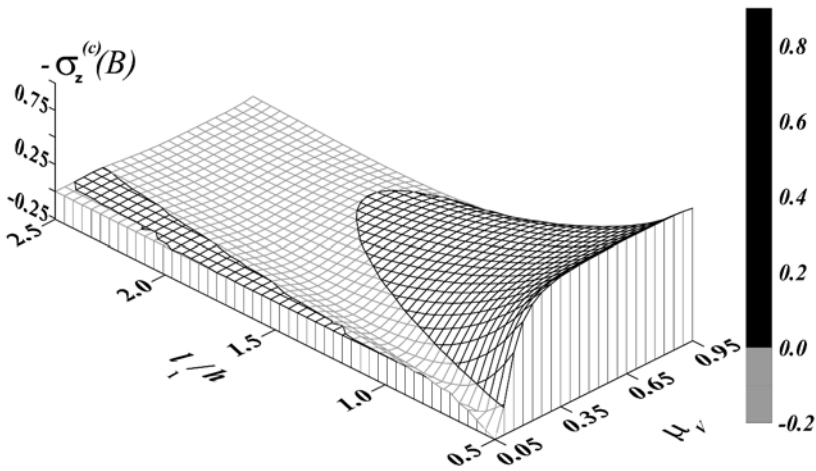


Figure 3. Transverse stresses in the intermediate cross section  $B(x = l_1)$  vs. the relative parameters, according to the diagram  $c$ , in Figure 1. Designations as in Figure 2.

This can be easily verified by comparing formulae (7) and (8), which gives  $\sigma_z^{(a)}(\xi) = 0.5\sigma_z^{(c)}(\xi)$ ,  $0 \leq \xi \leq \xi_1$ . We should note that, for the applicability of latter relation, the distance between the forces on each face surface of the sandwich strip in the case of a nonsymmetric system of forces (scheme  $a$ ) must be twice that in the case of a symmetric one (scheme  $c$ ).

The positive stresses  $\sigma_z$  arise owing to the oscillating functions of the solution. At a small tensile strength of the filler these stresses can be dangerous due to their ability to initiate fracture. Under the multipoint loading according to the schemes  $a$  and  $c$  shown in Figure 1, in a sandwich strip with equal volumes of the filler and load-carrying layers, see Figure 2, the tensile stresses  $\sigma_z$  are more than an order of magnitude smaller than the greatest compressive stresses. The tensile stresses  $\sigma_z$  usually arise in the central part of the interval between the forces. At small distances between the forces, the stresses  $\sigma_z(x) = const$  are compressive over the whole interval. The compressive stress of the filler in the cross section under the force ( $x = 0$ ) varies insignificantly at great values of  $l_1$ , but increases sharply at small  $l_1$ . For this stress, we have from Eq. (7)

$$\sigma_z^{(c)}(0) = -\frac{P\alpha}{2b(h_1 + h_0)} \cdot \frac{sh2\alpha\xi_1 + \sin 2\alpha\xi_1}{ch2\alpha\xi_1 - \cos 2\alpha\xi_1}. \tag{9}$$

The change in the transverse stress  $\sigma_z^{(c)}(\xi_1)$  in the middle of the interval between the forces,  $x = l_1$ , relative to the parameters describing the thickness of the face layer and the distance between the forces in the scheme in Figure 1c, differs qualitatively from the above-considered change in the stress in the cross

section  $x = 0$ . As seen from Figure 3, the change of the sign of  $\sigma_z^{(c)}(\xi_1)$  and the considerable increase in the positive value of this stress take place at small  $\mu_V < 0.1$  and  $2l_1 < 1.5h$ . At great values of  $\mu_V$  and  $l_1/h$ , the positive value of this stress is an order of magnitude lower.

### 3. CONCLUSIONS

An analysis of the solution obtained to the bending problem for a sandwich strip reveals the peculiarities of the effect of local loads on the bending characteristics in relation to the distribution frequency of point forces. As a result, we arrive at the following conclusions:

- The average values of transverse normal stresses over the thickness of the midlayer, from an infinite system of equally spaced nonsymmetric transverse point forces can be determined, using a coefficient  $1/2$ , from simpler formulae for a symmetric system of forces spaced at a twice as small distance as in the previous case.
- In the cross section halfway between the forces, the change of the sign of  $\sigma_z(\xi_1)$ , due to the oscillating components of the solution, occurs at sufficiently small thicknesses of face layers, stiffnesses of the filler, and distances between the forces. With increase in these parameters, the greatest positive values of  $\sigma_z(\xi_1)$  decrease by about an order of magnitude. The compressive stress  $\sigma_z(\xi_1)$  becomes stabilized and reaches its greatest value with increase in the thickness of the face layer, decrease in the distance between the forces, and drop in the stiffness of the filler material.

### REFERENCES

- [1] Thomsen, O.T. "General theory for the modeling of laminated multi-layer plates and its application for the analysis of sandwich panels with ply drops". Proc. of the 12th Int. Conf. on Composite Materials. Paris, July 5–9, 1999. Proceedings on a CD-ROM, Vol. Composite Structures, paper 133., Abstracts, ed. by T. Massard, 1999, p. 116.
- [2] Timoshenko, S.P. & Woinowsky – Krieger, *Theory of Plates and Shells*, McGraw-Hill Book Company: New York, Toronto & London, 1959.
- [3] Polyakov, V.A. "Analytical refinement of sandwich plate bending problem considering local effects. Part 1", *Journal of Sandwich Structures & Materials*, 1(3), 1999.
- [4] Polyakov, V.A., Zhigun, I.G., Shiitsa, R.P. and Khitrov, V.V., "A refined model for three-point bending of sandwich panels. 2. Transverse stresses", *Mech. Compos. Mater.*, 34, No. 1, p.p. 50–69, 1998.
- [5] 5. Bolotin V.V. and Novichkov Yu.N., *Mechanics of Multilayered Structures*, [in Russian], Mashinostroenie, Moscow, 1980.

# A TRIANGULAR FINITE ELEMENT FOR SANDWICH PLATES ACCOUNTING FOR TRANSVERSE CORE COMPRESSIBILITY

Serkan Demiray and Wilfried Becker

*Technische Universität Darmstadt, Institut für Mechanik, Hochschulstr. 1, 64289 Darmstadt, Germany*

demiray@mechanik.tu-darmstadt.de, becker@mechanik.tu-darmstadt.de

Jörg Hohe

*Fraunhofer Institut für Werkstoffmechanik, Wöhlerstr. 11, 79108 Freiburg, Germany*

joerg.hohe@iwm.fraunhofer.de

**Abstract** The present study is concerned with a triangular higher-order finite element for sandwich plates with transversely compressible core. The element formulation utilizes a v. Kármán type multilayer theory, adopting the discrete Kirchhoff approach for the contribution of the face sheets and a simplified three-dimensional formulation for the core. The discretized nonlinear problem is solved by the Newton-Raphson method.

**Keywords:** core compressibility, finite element, large deformation, face wrinkling.

## 1. INTRODUCTION

Standard structural sandwich panels are consisting of two stiff high-density face sheets which are adhesively bonded to a thick core layer made from a soft low-density material. Due to the low stiffness of the central layer, soft core sandwich structures are transversely compressible, resulting in the possible development of local face wrinkling instabilities.

It has been shown by Frostig et al. [5, 6], Hohe and Librescu [7, 8] that the development of the face wrinkling instability can have distinct effects even on the global response of sandwich plates and shells. Due to nonlinear coupling effects, the overall buckling mode and the local face wrinkling instability are coupled rather than independent effects. Hence, the transverse core compressibility is a non-negligible feature even in the analysis of the global response of sandwich structures. Other recent studies on combined global and local

buckling include the work of Bozhevolnaya and Frostig [2], Starlinger and Rammerstorfer [9], da Silva and Santos [3] or Wadee and Hunt [11].

To account for the effect of the transverse core compressibility, an appropriate higher-order sandwich shell model is required. A general model of this type for both plane and doubly curved sandwich shells has recently been provided by Hohe and Librescu [7]. The model utilizes an effective multilayer formulation, where the standard Kirchhoff–Love hypothesis is adopted for the face sheets, whereas a second order power series expansion is used for the core displacements, Geometrical nonlinearities are incorporated in the v. Kármán sense. In the original study, an extended Galerkin procedure is used to determine an analytical solution for some basic buckling and postbuckling problems concerning simply supported sandwich shells with rectangular projection.

The present study is concerned with a finite element implementation of this model. A triangular element with three nodes on each face sheet and six degrees of freedom per node is derived by modelling the three principal layers independently. For the face sheets, the discrete Kirchhoff approach presented by Batoz et al. [1] is utilized. For the core layer, a simplified three-dimensional approach is employed. According to the original approach by Hohe and Librescu [7], only the strain energy due to the transverse normal and shear deformation is considered whereas the strain energy due to the in-plane deformation is neglected. A reduced integration scheme is employed to avoid shear locking. The new finite element is applied to several numerical examples concerning the deformation and buckling response of different sandwich plates. It is observed that the transverse compressibility of the core might have significant effects even in the overall response of sandwich structures.

## 2. HIGHER-ORDER SANDWICH SHELL MODEL

Consider a sandwich plate according to Figure 1. The plate is assumed to be symmetric with respect to the global midplane forming the reference plane. The thicknesses of the face sheets and the core are denoted by  $t^f$  and  $t^c$ . Since in general the face sheets are thin, the three dimensional displacements  $v_i^t$  and  $v_i^b$  can be approximated by

$$v_\alpha^t = u_\alpha^t + \left( x_3 + \frac{1}{2}(t^c + t^f) \right) \varphi_\alpha^t \quad (1)$$

$$v_3^t = u_3^t \quad (2)$$

$$v_\alpha^b = u_\alpha^b + \left( x_3 - \frac{1}{2}(t^c + t^f) \right) \varphi_\alpha^b \quad (3)$$

$$v_3^b = u_3^b \quad (4)$$

in terms of the midplane displacements and rotations  $u_i^t(x_\alpha)$ ,  $\varphi_\alpha^t(x_\alpha)$ ,  $u_i^b(x_\alpha)$  and  $\varphi_\alpha^b(x_\alpha)$  of the top and bottom face sheets respectively ( $i = 1, 2, 3$  and

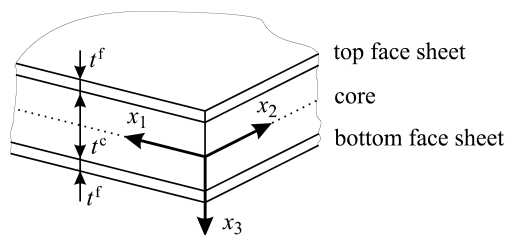


Figure 1. Structural sandwich plate.

$\alpha = 1, 2$ ). The Kirchhoff–Love hypothesis assumes that the rotations are interrelated with the midplane displacements by

$$\varphi_\alpha^t = -u_{3,\alpha}^t \tag{5}$$

$$\varphi_\alpha^b = -u_{3,\alpha}^b \tag{6}$$

discarding the shear deformation of the face sheets. For the core displacement field, a second order power series expansion

$$v_\alpha^c = \frac{1}{2} (u_\alpha^t + u_\alpha^b) - \frac{2x_3}{t^c} (u_{3,\alpha}^t - u_{3,\alpha}^b) + \frac{t^f}{4} (\varphi_\alpha^t - \varphi_\alpha^b) - \frac{x_3 t^f}{2t^c} (\varphi_\alpha^t + \varphi_\alpha^b) + \left( \left( \frac{2x_3}{t^c} \right)^2 - 1 \right) \Omega_\alpha^c \tag{7}$$

$$v_3^c = \frac{1}{2} (u_3^t + u_3^b) - \frac{x_3}{t^c} (u_3^t - u_3^b) \tag{8}$$

is adopted, satisfying the interface continuity requirements. The displacement functions  $\Omega_\alpha^c(x_\beta)$  describe the warping of the core.

From the power series expansion of the face sheet and core displacements, the deformation of the three individual layers are expressed in terms of the components

$$\gamma_{ij} = \frac{1}{2} (u_{i,j} + u_{j,i} + u_{i,k} u_{j,k}) \tag{9}$$

of the Green–Lagrange strain tensor. In the v. Kármán sense, only the nonlinear terms with respect to the transverse ( $x_3$ -) direction are kept whereas all other nonlinear terms are discarded.

In consistence with the previous assumptions, the tangential and bending stress resultants

$$\{N_{\alpha\beta}^b, M_{\alpha\beta}^b\} = \int_{\frac{1}{2}t^c}^{t^f + \frac{1}{2}t^c} \tau_{\alpha\beta}^t \left\{ 1, x_3 - \frac{1}{2}(t^c + t^f) \right\} dx_3 \tag{10}$$

$$\{N_{i3}^c, M_{i3}^c\} = \int_{-\frac{1}{2}t^c}^{\frac{1}{2}t^c} \tau_{i3}^t \{1, x_3\} dx_3 \tag{11}$$

$$\{N_{\alpha\beta}^t, M_{\alpha\beta}^t\} = \int_{-t^f - \frac{1}{2}t^c}^{-\frac{1}{2}t^c} \tau_{\alpha\beta}^t \left\{ 1, x_3 + \frac{1}{2}(t^c + t^f) \right\} dx_3 \quad (12)$$

are introduced for the three principal layers to replace the three-dimensional components  $\tau_{ij}$  of the second Piola-Kirchhoff stress tensor. Full details on the utilized nonlinear sandwich model are given in the original papers by Demiray et al. [4] as well as by Hohe and Librescu [7].

### 3. FINITE ELEMENT IMPLEMENTATION

The sandwich shell theory outlined in Section 2 is implemented into a finite element formulation. Hence, the domain  $\Omega$  of the entire sandwich structure is discretized into prismatic six node elements according to Figure 2. Nodes 1-3 are situated on the midplane of the top face sheet whereas nodes 4-6 are situated on the bottom face sheet. Each of the nodes has six degrees of freedom. The degrees of freedom for each node  $n$  ( $n = 1, \dots, 6$ ) are arranged in the nodal displacement vectors

$$\mathbf{a}^{(n)} = ( u_1^t \ u_2^t \ u_3^t \ \varphi_1^t \ \varphi_2^t \ \varphi_3^t ), \quad n = 1, 2, 3 \quad (13)$$

$$\mathbf{a}^{(n)} = ( u_1^b \ u_2^b \ u_3^b \ \varphi_1^b \ \varphi_2^b \ \varphi_3^b ), \quad n = 4, 5, 6 \quad (14)$$

so that the vector

$$\mathbf{a} = ( \mathbf{a}^{(1)} \ \mathbf{a}^{(2)} \ \mathbf{a}^{(3)} \ \mathbf{a}^{(4)} \ \mathbf{a}^{(5)} \ \mathbf{a}^{(6)} )^T \quad (15)$$

contains all 36 degrees of freedom of the element.

For the mathematical formulation, the prismatic element is decomposed into the core and the face sheets. Since it is assumed that the face sheets can be described by a standard Kirchhoff-Love plate model, the corresponding standard finite element formulations for this type of structural model can be adopted. Hence, the in-plane displacement and strain components of the face sheets are approximated by the shape functions  $N^{\text{CST}}$  and the strain displacement matrices  $\mathbf{B}^{\text{CST}}$  of the standard constant strain triangular (CST) element (Zienkiewicz and Taylor [12]) in conjunction with the v. Kármán assumption. Thus, the in-plane displacements  $u_1^t, u_2^t, u_1^b$  and  $u_2^b$  are interpolated linearly between the nodes on the respective face sheet. For the bending deformation, the discrete Kirchhoff triangular (DKT) element formulation presented by Batoz et al. [1] is employed. In this formulation, the transverse displacements  $u_3^t$  and  $u_3^b$  and the rotations  $\varphi_i^t$  and  $\varphi_i^b$  are interpolated linearly between the nodes on the respective face sheet, initially defining a shear flexible element. Subsequently, the Kirchhoff constraint (5) and (6) is applied on three discrete points. This formulation avoids inconsistencies in the interpolation of the displacement and rotation fields.

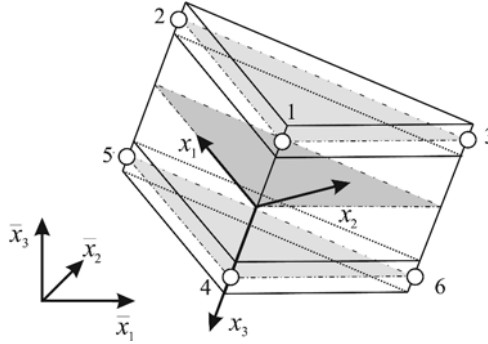


Figure 2. Prismatic six node sandwich plate element.

The membrane and bending strains of the top and bottom face sheets are given by

$$\begin{pmatrix} \gamma_{11}^k & \gamma_{22}^k & \gamma_{12}^k \end{pmatrix}^T = \mathbf{B}^{\text{CST}k} \mathbf{a} \tag{16}$$

$$\begin{pmatrix} \kappa_{11}^k & \kappa_{22}^k & \kappa_{12}^k \end{pmatrix}^T = \mathbf{B}^{\text{DKT}k} \mathbf{a} \tag{17}$$

where  $k = t, b$ . In addition to the CST and DKT formulations governing the displacements and the rotations with respect to the tangential ( $x_1$ - and  $x_2$ -) axes, the rotations with respect to the transverse ( $x_3$ -) axis are restrained by a fictitious rotational stiffness.

The discretized strain displacement relations of the core are obtained by substituting the continuous displacements  $u_i^t$  and  $u_i^b$  as well as the continuous rotations  $\varphi_\alpha^t$  and  $\varphi_\alpha^b$  in the power series expansion (7) and (8) of the core displacement field with the discretized expressions in terms of the shape functions  $\mathbf{N}^{\text{CST}}$  and  $\mathbf{N}^{\text{DKT}}$  of the face sheets. Similar as in the analytical approach by Hohe and Librescu [7], the warping functions are chosen such that the antisymmetric part of the transverse shear deformation vanishes. Assuming that the strain energy associated with the in-plane deformation of the core is negligible, the in-plane components  $\gamma_{\alpha\beta}^c$  do not enter the expression for the total strain energy. The transverse strains of the core are interrelated with the nodal displacements by

$$\begin{pmatrix} \gamma_{33}^c & \gamma_{23}^c & \gamma_{13}^c \end{pmatrix}^T = \left( \mathbf{B}^{\text{Cl}} + \frac{1}{2} \mathbf{B}^{\text{Cnl}} \right) \mathbf{a} \tag{18}$$

where explicit expressions for the linear and nonlinear strain displacement matrices  $\mathbf{B}^{\text{Cl}}$  and  $\mathbf{B}^{\text{Cnl}}$  are given by Demiray et al. [4].

The face sheet membrane and bending strains  $\gamma_{\alpha\beta}^t, \gamma_{\alpha\beta}^b, \kappa_{\alpha\beta}^t$  and  $\kappa_{\alpha\beta}^b$  for the top and bottom face sheets as well as the transverse strains  $\gamma_{i3}^c$  together with the corresponding discretized expressions for the virtual strains  $\delta\gamma_{\alpha\beta}^t, \delta\gamma_{\alpha\beta}^b, \delta\kappa_{\alpha\beta}^t$ ,

$\delta\kappa_{\alpha\beta}^b$  and  $\delta\gamma_{i3}^t$  are substituted into the principle of virtual work

$$\delta U - \delta W = 0 \quad (19)$$

where  $U$  and  $W$  are the total strain energy in the body  $\Omega$  and the work done by the external forces respectively. Within the resulting expression, the stress components together with the integrals with respect to the transverse direction are substituted with the in-plane and bending stress resultants according to Equations (10) to (12). The total area of the sandwich plate is decomposed into the individual elements. Adopting Hooke's law in its anisotropic form as the constitutive equation for the different principal layers, a nonlinear governing equation for the vector  $\mathbf{a}^{\text{tot}}$  containing the nodal degrees of freedom of all nodes in the discretized problem is obtained. The system has the form

$$\left( \sum_e \mathbf{K}^{\text{tan}}(\mathbf{a}^{\text{tot}}) \right) \mathbf{a}^{\text{tot}} - \mathbf{f} = \mathbf{0} \quad (20)$$

where  $\mathbf{K}^{\text{tan}}$  is the tangential stiffness matrix and  $\mathbf{f}$  is the nodal force vector. The integration of the strain energy for determination of the tangential stiffness matrix is performed numerically. For the core, a reduced one point Gaussian integration scheme is employed to avoid shear locking effects. In this context, no spurious modes of deformation can develop, since within the employed sandwich plate model, all bending loads are transmitted through the face sheets.

The nonlinear system is solved numerically by means of the Newton-Raphson method. Full details on the finite element formulation are given in a preceding paper by the present authors [4].

## 4. EXAMPLES

As a first example, the sandwich plate element derived in Sections 2 and 3 is applied to an analysis of the postbuckling response of a square sandwich plate under uniaxial in-plane compression. The plate has an edge length of 500 mm, aluminum face sheets with  $E^f = 70$  GPa,  $\nu^f = 0.3$  and  $t^f = 0.5$  mm whereas a weak low density material with  $E^c = 0.7$  GPa and  $\nu^c = 0.3$  is assumed for the core layer with  $t^c = 23$  mm thickness. The plate is assumed to be simply supported along all four edges which are movable with respect to the in-plane directions (Demiray et al. [4]).

In order to study the convergence of the present finite element formulation, the sandwich plate is discretized by a variable number of triangular elements arranged in union jack pattern. Due to the symmetries of the problem, only one quarter of the structure is discretized. In order to regularize the postbuckling behavior, a small initial geometric imperfection of the sinusoidal type with a modal amplitude of  $x_3^{\text{imp}} = 0.1$  mm is assumed.

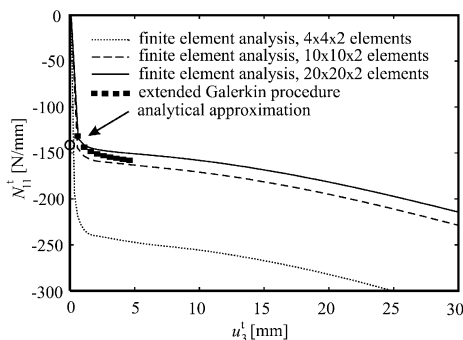


Figure 3. Postbuckling deformation of square simply supported plate.

The results are presented in Figure 3 for three different meshes consisting of  $4 \times 4$ ,  $10 \times 10$  and  $20 \times 20$  quadrilaterals consisting of two triangular elements. Obviously, the coarse mesh is insufficient since it overestimates the stiffness of the structure in the postbuckling range. The results based on the two finer meshes are rather close to each other. A further mesh refinement does not result in significant changes compared to the results based on the finest mesh consisting of  $20 \times 20 \times 2$  elements. Therefore, the results obtained for finer meshes are not presented in Figure 3.

The results based on the fine mesh with  $20 \times 20 \times 2$  elements are in good agreement with the estimation of the buckling load for the corresponding, geometrically perfect structure obtained by the approximate formula given by Vinson [10]. Since this formula is in good agreement with experimental data, the present finite element approach can be regarded as validated. A comparison with analytical results obtained by the extended Galerkin procedure presented by Hohe and Librescu [7] shows a good agreement in the initial stage of the postbuckling range. For higher load levels, the analytical scheme overestimates the stiffness of the deformed structure due to the type of displacement field assumed in the analytical procedure.

As a more sophisticated example, a four point bending test on a sandwich beam is considered. The sandwich specimen has an overall length of  $l = 200$  mm. It is simply supported at the bottom face sheets at the specimen ends. One support is assumed to be immovable whereas the other one is freely movable within the longitudinal direction. The specimen is loaded by a prescribed transverse displacement of two points on the upper face sheets situated on the top face sheet at a distance of  $a = 50$  mm from the specimen ends. Isotropic aluminum face sheets with  $E^f = 70$  GPa,  $\nu^f = 0.3$  and a thickness of  $t^f = 1.5$  mm are considered. The core is assumed to consist of an isotropic low density material with the elastic constants  $E^c = 0.7$  GPa and  $\nu^c = 0.25$ . The core thickness is  $t^c = 23$  mm.

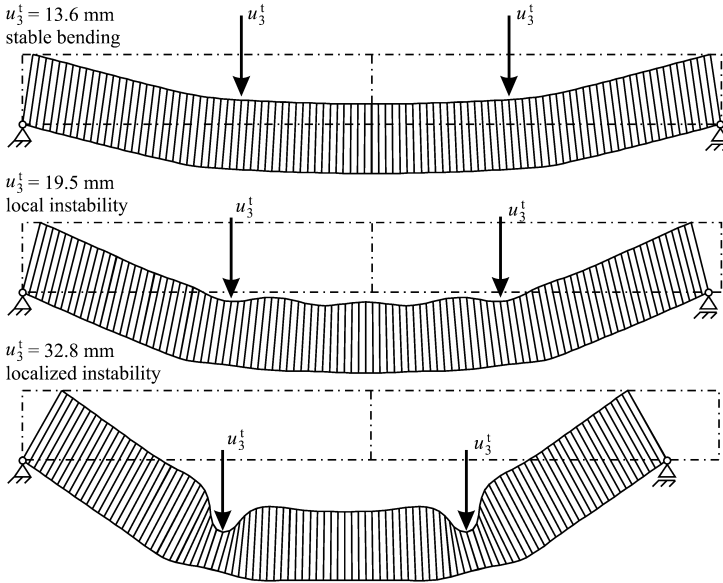


Figure 4. Deformation of four point bending specimen.

In Figure 4, the deformed configurations are presented at three different load levels. The load deflection response is presented in Figure 5. Four different stages are observed during the deformation history of the specimen. Initially, a pure bending mode of deformation develops. Due to the initially small in-plane stresses, both face sheets remain stable. If the level of the prescribed displacements is increased, the level of the compressive stresses in the top face sheet between the two load points is increased, resulting in the development of a face wrinkling mode in this area (see Figure 4, second load level with  $u_3^t = 19.5$  mm). The development of the face wrinkling mode causes a decrease in the resulting compressive load (see Figure 5). Notice that due to the local core compression in the vicinity of the supports and the loading device, no bifurcation and therefore no buckling in the Eulerian sense occurs, even if no initial geometric imperfection is considered. Therefore, no rigorous separation of the pre- and postbuckling ranges is possible in the present example. The classical sandwich plate model without consideration of the transverse compressibility of the core proves to be insufficient already during the early stage of deformation since it does not account for the local compression of the core in the vicinity of the supports and the loading device.

If the prescribed displacement is increased further, a localized instability mode develops, where the deformation is localized in the vicinity of the load points. Since this localization causes a decrease in the level of the compressive stresses in the top face sheet, the face wrinkling deformation vanishes. In the

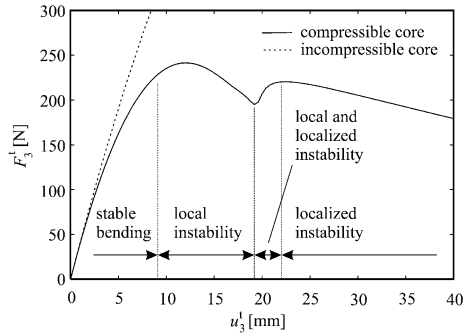


Figure 5. Reaction force in four point bending test.

load displacement characteristic presented in Figure 5, the change of the type of instability from the local (face wrinkling) mode to the localized mode results in a temporary increase in the overall compressive load level. Afterwards, the level of the resulting load decreases during the fourth stage of the deformation history when the instability is of the pure localized type.

## 5. CONCLUSION

The present study is concerned with the finite element implementation of an enhanced model for sandwich structures accounting for the transverse core compressibility. The model adopts the Kirchhoff–Love hypothesis for the face sheets whereas a higher-order power series expansion is employed for the core displacements. Geometrical nonlinearities are included in the v. Kármán sense. For the interpolation of the face sheet displacements, the shape functions for the constant strain and the discrete Kirchhoff triangular elements are adopted. No specific type of interpolation is necessary for the core since in the underlying theory, all core displacements are described in terms of the face sheet displacements.

The developed finite element is applied to the deformation and postbuckling analysis of sandwich plates. In the analysis of a four point bending test, it is observed that the transverse compressibility of the core has distinct effects even on the overall structural response of the specimen where both, the pre- and the postbuckling range are affected. In a comparison with previous studies, the present finite element proves to be both, accurate and numerically efficient. Thus the present finite element can be employed as an efficient tool for the enhanced analysis of sandwich structures accounting for local failure modes.

**REFERENCES**

- [1] J.L. Batoz, K.J. Bathe and L.W. Ho. A Study of Three-Node Triangular Plate Bending Elements. *International Journal for Numerical Methods in Engineering* 15:1771-1812, 1980.
- [2] E. Bozhevolnaya and Y. Frostig. Nonlinear Closed-Form High-Order Analysis of Curved Sandwich Panels. *Composite Structures* 38:383-394, 1997.
- [3] L.A.P.S. da Silva and J.M.C. Santos. Localised formulations for thick “sandwich” laminated and composite structures. *Computational Mechanics* 22:211-224, 1998.
- [4] S. Demiray, W. Becker and J. Hohe. A triangular v. Kármán type finite element for sandwich plates with transversely compressible core. *Computer Methods in Applied Mechanics and Engineering* 193:2239-2260, 2004.
- [5] Y. Frostig. Buckling of sandwich panels with a flexible core–high-order theory. *International Journal of Solids and Structures* 35:183-204, 1998.
- [6] Y. Frostig, M. Baruch, O. Vilnay and I. Sheiman. High-order buckling theory for sandwich-beam behavior with transversely flexible core. *Journal of Engineering Mechanics* 118:1026-1043, 1992.
- [7] J. Hohe and L. Librescu. A nonlinear theory for doubly curved anisotropic sandwich shells with transversely compressible core. *International Journal of Solids and Structures*, 40:1059–1088, 2003.
- [8] J. Hohe and L. Librescu. Core and face sheet anisotropy in deformation and buckling of sandwich panels. *AIAA Journal*, 42:149-158, 2004.
- [9] A. Starlinger and F.G. Rammerstorfer. A finite element formulation for sandwich shells accounting for local failure phenomena. In: D. Weissman-Berman and K.A. Olsson (eds.). *Sandwich Construction 2*. Proc. 2<sup>nd</sup> Int. Conf. Sandwich Constructions (Gainesville, FL, USA, March 09-12 1992). EMAS Publishing, London 1992, 161-179.
- [10] J.R. Vinson. *The Behavior of Sandwich Structures of Isotropic and Composite Materials*. Technomic Publishing, Lancaster, PA 1999.
- [11] M.A. Wadee and G.W. Hunt. Interactively induced localized buckling in sandwich structures with core orthotropy. *Journal of Applied Mechanics* 65:523-528, 1998.
- [12] O.C. Zienkiewicz and R.L- Taylor. *The Finite Element Method*. Butterworth-Heinemann, Oxford 2000.

# FINITE ELEMENT FOR THE STATIC AND STABILITY ANALYSIS OF SANDWICH PLATES

Markus Linke, Wolfgang Wohlers and Hans-Günther Reimerdes

*Department of Aerospace and Lightweight Structures, RWTH Aachen University, Wüllnerstr. 7, D-52062 Aachen, Germany*

linke@ilb.rwth-aachen.de, wohlers@ilb.rwth-aachen.de, hg\_reim@ilb.rwth-aachen.de

**Abstract** A finite element for the static and stability analysis of sandwich plates is formulated based on a three-layer sandwich model and its underlying differential equations. The Kirchhoff–Love hypothesis is assumed for the face sheets. The core is modelled by a three-dimensional material law neglecting the in-plane core stiffnesses. A stability analysis is performed on the basis of the geometric stiffness matrix considering the membrane prestresses of the face sheets.

**Keywords:** finite element, sandwich plate, static/stability analysis.

## 1. INTRODUCTION

In many industrial applications sandwich structures with low strength honeycomb or foam cores are being used due to their high bending stiffness to weight ratio. These core materials exhibit a nonlinear deformation pattern in the through-thickness direction which can affect significantly the global sandwich behaviour. In order to consider the deformation behaviour of these core materials, several authors (see e.g. [1] or [2]) introduced higher-order theories which account for the resulting nonlinear displacement field of the sandwich. These approaches are based on the assumption that the in-plane core stiffnesses are negligible and that the structural behaviour can be described with sufficient precision based on a three-layer sandwich model distinguishing between the face sheets and the core.

In this paper, the above mentioned modelling approach is used to develop a three-dimensional finite element for the static as well as the stability analysis of sandwich plates. The core behaviour is based on an orthotropic material law comparable to the one that is used in [3] to formulate a finite sandwich element. This approach leads to a three-dimensional displacement field in which the out-of-plane displacement is a quadratic function and the in-plane displacements

are cubic functions of the through-thickness coordinate of the sandwich. In contrast to [3], here, the stress field resulting from the differential equations of the three-layer sandwich model is used to reduce the number of necessary degrees of freedom of the finite element. The behaviour of the face sheets is described by classical finite plate elements using the Kirchhoff–Love hypothesis. In order to perform linear stability analyses the geometric stiffness matrix is used which contains the membrane prestresses of the face sheets.

A static and a stability analysis based on the proposed element formulation are performed with MSC/NASTRAN. The results are compared to those achieved by the finite element (FE-)program MSC/MARC. These computations are based on a detailed discretisation of the face sheets as well as of the core. The aim of this investigation is to identify the limits of the underlying theory and its simplifications.

## 2. INTERPOLATION FUNCTIONS

The formulation of the finite sandwich element is based on a three-layer model subdividing the sandwich into the face sheets and the core as individual components. The geometry of the finite element is shown in Figure 1. The values of the face sheets are denoted by the indices  $f1$  and  $f2$  for the bottom and top face sheet and the ones of the core are indicated by the index  $c$ .

### 2.1 Face sheets

The face sheets are modelled as plate elements based on the Kirchhoff–Love hypothesis. For the in-plane displacement field bi-linear interpolation functions are selected. The out-of-plane displacement field is idealised with a displacement assumption of twelve unknowns which is given in [4]. The introduced degrees of freedom per face sheet are illustrated in Figure 1 and comprise the displacements  $u_{fi}$ ,  $v_{fi}$  and  $w_{fi}$  in the  $x$ -,  $y$ - and  $z$ -direction as well as the rotations  $\Theta_{xfi}$  and  $\Theta_{yfi}$  about the  $x$ - and  $y$ -axis of the face sheet  $i$  with  $i = 1, 2$ . In the usual way, the coefficients of the assumed displacement functions are determined by the selected degrees of freedom resulting in the interpolation functions of the face sheets.

### 2.2 Sandwich core

For practical applications the in-plane stiffnesses of the core  $E_{x_c}$ ,  $E_{y_c}$  and  $G_{xy_c}$  are much smaller than the counterparts of the face sheets so that the resulting strain energies of the core are also much smaller than the ones of the face sheets. As a consequence, the in-plane core stiffnesses are often neglected ( $E_{x_c}, E_{y_c} \ll E_{x_{fi}}, E_{y_{fi}}; G_{xy_c} \ll G_{xy_{fi}}$ ) in setting up a mathematical model of a sandwich (see e.g. [3] for a more elaborate explanation). Here, this as-

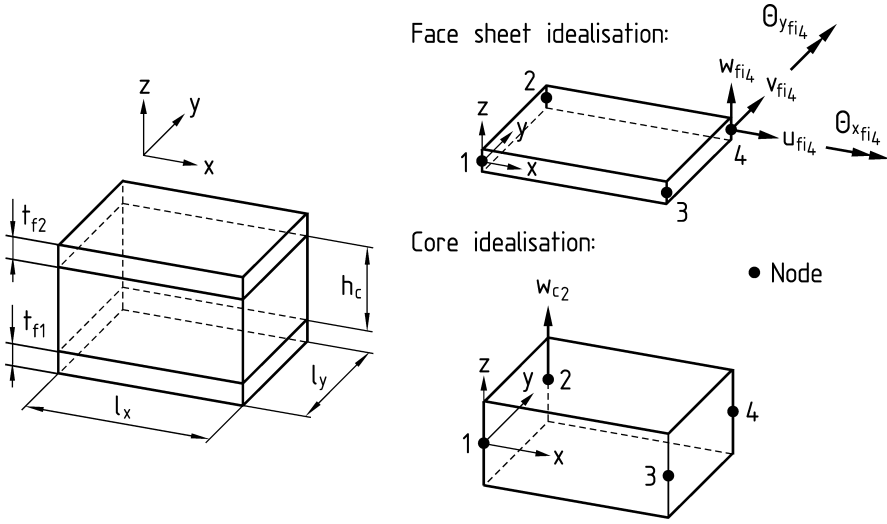


Figure 1. Geometry of the finite element and corresponding degrees of freedom.

sumption is also used to simplify the material law of the core resulting in an orthotropic behaviour ( $E_{x_c}, E_{y_c}, G_{xy_c} \approx 0$ ).

The differential equations of the core are set up based on the equilibrium of forces at an infinitesimal core element and by considering the displacement-strain relation. The resulting system of partial differential equations is analytically integrated in the through-thickness direction leading to polynomials of the state variables in the  $z$ -direction. The displacements of the core and the core stresses are expressed as

$$u_c(x, y, z) = a_0(x, y) + a_1(x, y) \cdot z + a_2(x, y) \cdot z^2 + a_3(x, y) \cdot z^3$$

$$v_c(x, y, z) = b_0(x, y) + b_1(x, y) \cdot z + b_2(x, y) \cdot z^2 + b_3(x, y) \cdot z^3$$

$$w_c(x, y, z) = c_0(x, y) + c_1(x, y) \cdot z + c_2(x, y) \cdot z^2$$

$$\sigma_z(x, y, z) = d_0(x, y) + d_1(x, y) \cdot z$$

$$\tau_{xz}(x, y, z) = e_0(x, y), \quad \tau_{yz}(x, y, z) = f_0(x, y)$$

where  $u_c$ ,  $v_c$  and  $w_c$  are the displacements in the  $x$ -,  $y$ - and  $z$ -direction of the core and where  $\sigma_z$  is the peeling stress and  $\tau_{xz}$  as well as  $\tau_{yz}$  are the shear stresses in the core.

The polynomials are used to derive the displacement functions of the finite sandwich element. The coefficients of the polynomials are determined by introducing the compatibility conditions between the face sheets and the core as well as by defining additional degrees of freedom for the core.

### 2.3 Interconnection of face sheets and core

The interpolation functions of the core are determined by using the displacements of the face sheets as boundary conditions and by introducing four displacements in the midplane of the core, each with one degree of freedom in the  $z$ -direction (see Figure 1).

The connection between the core and the face sheets is assumed to be perfect. The core is attached to the midplane of the face sheet elements. This is due to the fact that the computation results are compared to standard FE-computations where the core is connected to the face sheets in the same way.

If in agreement with the sketched formulae according to Section 2.2 the shear stresses  $\tau_{xz}$  and  $\tau_{yz}$  are set constant in the through-thickness direction and the peeling stress  $\sigma_z$  is assumed to be linearly dependent on  $z$ , the displacement field of the core is clearly defined. As a result, the interpolation functions of the face sheets as well as of the core are available enabling the determination of the stiffness matrix of the finite sandwich element.

## 3. LINEAR STIFFNESS MATRIX

In the following, the stiffness matrix of the finite sandwich element is derived for geometric linear and linear elastic behaviour. The principle of virtual work gives:

$$\delta U - \delta W = \int_V \delta \vec{\varepsilon}^T [Q] \vec{\varepsilon} dV - \delta \vec{u}^T \vec{F} = 0 \quad (1)$$

where  $\delta$  indicates variations,  $U$  and  $W$  are the strain energy and the work by the external forces respectively,  $\vec{\varepsilon}$  is the strain vector,  $[Q]$  is the global elasticity matrix,  $V$  is the element volume,  $\vec{u}$  is the displacement vector and  $\vec{F}$  is the corresponding force vector of the considered element.

The integral according to (1) is separated into the three subsystems of the face sheets and the core leading to:

$$\begin{aligned} \int_V \delta \vec{\varepsilon}^T [Q] \vec{\varepsilon} dV = & \int_0^{l_x} \int_0^{l_y} \left( \int_{\frac{-h_c-t_1}{2}}^{\frac{-h_c+t_1}{2}} \delta \vec{\varepsilon}^T [\tilde{Q}_{f1}] \vec{\varepsilon} dz \right. \\ & \left. + \int_{-\frac{h_c}{2}}^{\frac{h_c}{2}} \delta \vec{\varepsilon}^T [\tilde{Q}_c] \vec{\varepsilon} dz + \int_{\frac{h_c-t_2}{2}}^{\frac{h_c+t_2}{2}} \delta \vec{\varepsilon}^T [\tilde{Q}_{f2}] \vec{\varepsilon} dz \right) dy dx \quad (2) \end{aligned}$$

where  $[\tilde{Q}_{fi}]$  and  $[\tilde{Q}_c]$  are the elasticity matrices of the face sheet  $i$  with  $i = 1, 2$  and of the core respectively and where the geometry values  $h_c, l_x, l_y, t_{f1}$  as well as  $t_{f2}$  are defined according to Figure 1. The strain vector  $\vec{\varepsilon}$  takes the form

$$\vec{\varepsilon}^T = [\vec{\varepsilon}_{f1}, \vec{\varepsilon}_c, \vec{\varepsilon}_{f2}]^T$$

where

$$\tilde{\varepsilon}_{fi}^T = \left[ \frac{\partial u_{fi}}{\partial x}, \frac{\partial v_{fi}}{\partial y}, \frac{\partial u_{fi}}{\partial y} + \frac{\partial v_{fi}}{\partial x}, \frac{\partial^2 w_{fi}}{\partial x^2}, \frac{\partial^2 w_{fi}}{\partial y^2}, 2 \frac{\partial^2 w_{fi}}{\partial x \partial y} \right]$$

and where

$$\tilde{\varepsilon}_c^T = \left[ \frac{\partial w_c}{\partial z}, \frac{\partial u_c}{\partial z} + \frac{\partial w_c}{\partial x}, \frac{\partial v_c}{\partial z} + \frac{\partial w_c}{\partial y} \right]$$

The individual elasticity matrices take the forms:

$$[\tilde{Q}_{f1}] = \begin{bmatrix} [Q_{f1}] & 0 & 0 \\ 0 & 0 & 0 \\ 0 & 0 & 0 \end{bmatrix}, \quad [\tilde{Q}_{f2}] = \begin{bmatrix} 0 & 0 & 0 \\ 0 & 0 & 0 \\ 0 & 0 & [Q_{f2}] \end{bmatrix}$$

$$\text{and} \quad [\tilde{Q}_c] = \begin{bmatrix} 0 & 0 & 0 \\ 0 & [Q_c] & 0 \\ 0 & 0 & 0 \end{bmatrix}$$

where  $[Q_{fi}]$  and  $[Q_c]$  are the elasticity matrices of the bottom and top face sheet as well as of the core.

The non-zero matrix elements of the  $3 \times 3$  core elasticity matrix  $[Q_c]$  are

$$Q_{c11} = E_{z_c}, \quad Q_{c22} = G_{xz_c}, \quad Q_{c33} = G_{yz_c}$$

where  $E_{z_c}$  is the Young's modulus and  $G_{xz_c}$  as well as  $G_{yz_c}$  are the shear moduli of the core. To simplify matters, the face sheets are assumed to be consisting of one single orthotropic ply leading to the following non-zero matrix elements in the upper triangle of the symmetric  $6 \times 6$  elasticity matrix  $[Q_{fi}]$  of face sheet  $i$ :

$$\begin{aligned} Q_{fi11} &= \frac{E_{xfi}}{1 - \nu_{xyfi}^2 \frac{E_{yfi}}{E_{xfi}}}, & Q_{fi12} &= \frac{\nu_{xyfi} E_{yfi}}{1 - \nu_{xyfi}^2 \frac{E_{yfi}}{E_{xfi}}}, \\ Q_{fi22} &= \frac{E_{yfi}}{1 - \nu_{xyfi}^2 \frac{E_{yfi}}{E_{xfi}}}, & Q_{fi33} &= G_{xyfi}, \\ Q_{fi44} &= \frac{z^2 E_{xfi}}{1 - \nu_{xyfi}^2 \frac{E_{yfi}}{E_{xfi}}}, & Q_{fi45} &= -\frac{z^2 \nu_{xyfi} E_{yfi}}{1 - \nu_{xyfi}^2 \frac{E_{yfi}}{E_{xfi}}}, \\ Q_{fi55} &= \frac{z^2 E_{yfi}}{1 - \nu_{xyfi}^2 \frac{E_{yfi}}{E_{xfi}}}, & Q_{fi66} &= z^2 G_{xyfi} \end{aligned}$$

where  $E_{xfi}$  and  $E_{yfi}$  are the Young's moduli in the  $x$ - and  $y$ -direction,  $G_{xyfi}$  is the shear modulus and  $\nu_{xyfi}$  is the in-plane Poisson's ratio. The coordinates  $z_i$  amount to  $z_1 = z + \frac{h_c}{2}$  and  $z_2 = z - \frac{h_c}{2}$ .

Equation (2) is analytically integrated with respect to the  $x$ -,  $y$ -, and  $z$ -direction leading to the stiffness matrix  $[K]$  of the finite sandwich element:

$$\int_V \delta \vec{\varepsilon}^T [Q] \vec{\varepsilon} dV = \delta \vec{u}^T [K] \vec{u} = \delta \vec{u}^T \vec{F} \quad \text{with} \quad \vec{u}^T = [u_1^T, u_2^T, u_3^T, u_4^T]$$

where  $u_j^T$  with  $j = 1, \dots, 4$  are the displacement vectors of the element nodes with the following order of degrees of freedom:

$$u_j^T = [u_{f1j}, v_{f1j}, w_{f1j}, \Theta_{xf1j}, \Theta_{yf1j}, w_{c_j}, u_{f2j}, v_{f2j}, w_{f2j}, \Theta_{xf2j}, \Theta_{yf2j}]$$

#### 4. STABILITY ANALYSIS

The stability analysis is based on the approach described in [5]. In principal, the stability problem is solved by determining the smallest eigenvalue of the global stiffness matrix which contains the prestresses. In the case of the considered sandwich structure, the membrane stresses of the face sheets are taken into account as prestresses.

The global stiffness matrix which corresponds to a specific load state  $F_1$  can be split up into the stiffness matrix without prestresses  $[K_0]$  and the geometric stiffness matrix  $[K_\sigma]$  leading to:

$$[K(F_1)] = [K_0] - 1 \cdot [K_\sigma]$$

If the global stiffness matrix is linearised, the general eigenvalue problem is formulated for a balanced structure based on the equilibrium condition as

$$[K] \delta \vec{u} = [K(\lambda \cdot F_1)] \delta \vec{u} = ([K_0] - \lambda \cdot [K_\sigma]) \delta \vec{u} = 0$$

The resulting critical eigenvalue can be improved with a modification of the prestresses leading to an improved geometric stiffness matrix.

#### 5. VERIFICATION

The described element is implemented into an FE-program. The implementation is sketched, and numerical examples are shown to illustrate the element capabilities.

##### 5.1 NASTRAN implementation

The determined FE-matrix has been implemented into a DMAP-program for MSC/NASTRAN according to [6]. Based on this approach, the FE-program calculates the element data from the NASTRAN input file, determines the stiffness matrix by calling an external program and finally solves the underlying system of equations.

### 5.2 Numerical example

A static and a stability analysis of a sandwich plate based on the proposed element formulation are illustrated. The geometry and the material properties of the sandwich are shown in Figure 2. The global coordinate system is located in the midplane of the sandwich plate.

The calculated values are compared to results of FE-computations performed by the FE-program MARC. The MARC-models consist of bilinear-thick shell elements and of trilinear solid elements (type 75 and 7 according to [7]) for modelling the face sheets and the core respectively. The core elements are connected to the midplane of the shell elements resulting in a slightly increased core thickness of 39.1 mm. The meshes of the MARC-model and of the idealisation with the proposed sandwich element are the same in the  $x$ - $y$ -plane. To simplify matters, the latter idealisation is referred to as user defined finite element (UDFE-)model. With four solid elements in the through-thickness direction of the core, a sufficient convergence was found for the MARC-models. The reduction in the degrees of freedom in the  $z$ -direction from the MARC-model to the UDFE-idealisation amounts consequently to about 40 %. As symmetric problems are considered, only one quarter of the sandwich plate is discretised.

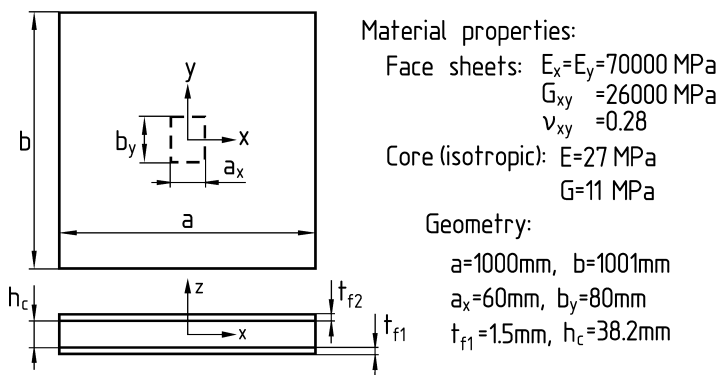


Figure 2. Material properties and geometry of analysed sandwich plate.

In the static case, the plate is subjected to a pressure of  $-2.5$  MPa acting on a centered rectangle on the top face sheet with the dimensions of  $a_x$  in the  $x$ -direction and  $b_y$  in the  $y$ -direction (see Figure 2). The top face sheet is thinner than the bottom face layer. The thickness amounts to  $t_{f2} = 0.3$  mm. The plate is simply supported along all edges. In Figure 3 the  $z$ -deflections of the top face layer and the stresses  $\sigma_x$  at the midplane (marked by  $m$  in the diagrams) and at the outside top (marked by  $t$ ) in the top face sheet are shown for the proposed finite element (indicated by UDFE) and the MARC-computations. The results

of two different MARC-models are illustrated. This comprises one model with an isotropic material law of the core (indicated by iso in the diagrams) and the other with an orthotropic material law where  $E_{x_c}$ ,  $E_{y_c}$  and  $G_{xyc} \approx 0$  (indicated by ortho). The stresses are averaged values per node. The results are valid along the plate centerline in the positive  $x$ -direction starting from  $x = 0$  and  $y = 0$ .

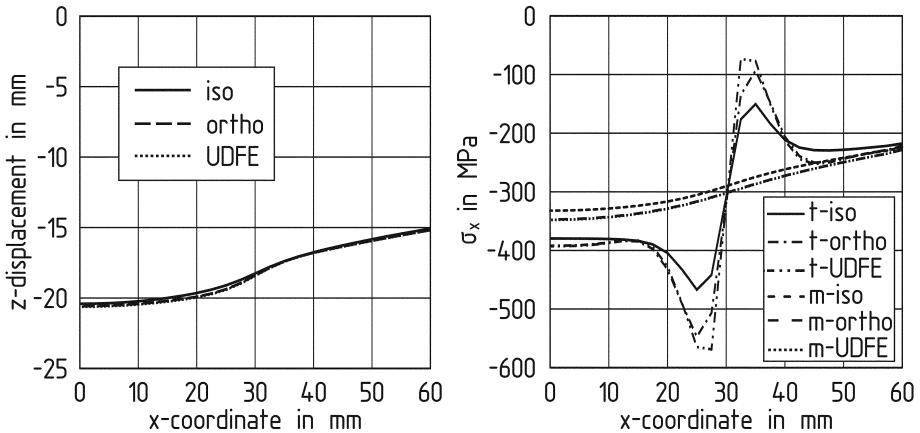


Figure 3. Displacement in global  $z$ -direction and normal stress  $\sigma_x$  of top face sheet.

The results of the  $z$ -displacement as well as of the normal stress agree very well between the UDFE- and the MARC-model with orthotropic core. The largest deviation in the  $z$ -deflection is smaller than 0.3 % between both models. For the results of the normal stresses slightly larger deviations occur in the transfer region of the loaded to the unloaded area at  $x = 30$  mm where strongly localised effects are existent. However, it can be expected that these deviations will be reduced if a finer mesh is used in this area.

The results of the UDFE-model and the second MARC-model considering an isotropic core show an increase in the deviations compared to the MARC-model with the previously described orthotropic core material law. The UDFE-model is not as stiff as the MARC-model, and the maximum deviation of the  $z$ -displacements amounts to about 2 %. The deviations of the absolute values of the UDFE-stresses are highest in the transfer area of the loaded to the unloaded region at the top of the upper face sheet. The deviation of the stresses at the plate midplane is smaller than 5 %. With increasing distance to the plate center the stress trends approach each other.

For the stability problem, the sandwich plate is simply supported in the through-thickness direction along the edges with constant  $y$ . The other edges are free. The sandwich face sheets have the same thickness with  $t_{f1} = t_{f2}$

and are subjected to in-plane compression in the  $y$ -direction. In Figure 4 the calculated critical mode shapes of the UDFE-model are compared to the ones of a MARC-idealisation with isotropic core material law. A global buckling mode shape with one half wave is predicted to occur in each case. The critical stress level in the face sheets of the UDFE-model amounts to 93.28 MPa with a deviation smaller than 0.4 % compared to the global buckling stress of the face layers of 92.99 MPa according to [8, pp. 51–63]. The critical buckling stress in the face sheets of the MARC-model is computed to 93.09 MPa.

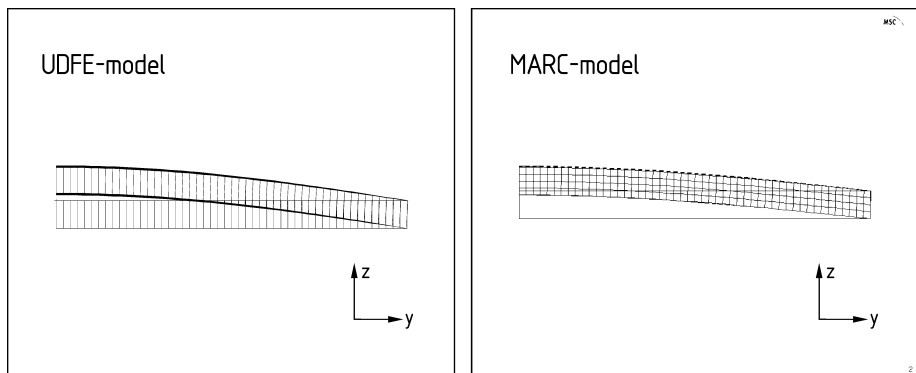


Figure 4. Mode shapes of UDFE- and MARC-model.

## 6. CONCLUSION

A finite element for the static and the stability analysis of sandwich plates is presented. The element formulation is based on a three-layer sandwich model consisting of the face sheets and the core as single subsystems. The face sheets are described by plate elements using the Kirchhoff–Love hypothesis. The displacement functions of the core are derived on the basis of the underlying partial differential equations and by interconnecting the core to the face layers through appropriate compatibility conditions. This approach leads to an element formulation of 44 degrees of freedom which is applicable for static and stability problems of sandwich plates. The stability analysis is performed using the geometric stiffness matrix which is calculated on the basis of the membrane prestresses of the face sheets.

The developed element is implemented into the FE-program NASTRAN. Numerical computations are conducted considering a static as well as a stability problem. The numerical examples are compared to MARC-computations indicating the influence of the introduced simplifications. It is shown that a good accuracy of the results can be achieved and that simultaneously the de-

degrees of freedom are reduced significantly with the proposed sandwich element in comparison to standard FE-idealizations.

## REFERENCES

- [1] H. Bansemir. *Ein Beitrag zur Biegetheorie von Sandwichplatten und Plattenstreifen sowie zur Krafteinleitung in versteifte orthotrope Scheiben*. PhD thesis, Technische Universität München, Germany, 1973.
- [2] Y. Frostig, M. Baruch, O. Vilnay and I. Sheinman. High-order theory for sandwich-beam behavior with transversely flexible core. *Journal of Engineering Mechanics*, 118(5):1026–1043, 1992.
- [3] S. Oskooei and J.S. Hansen. Higher-Order Finite Element for Sandwich Plates. *AIAA Journal*, 38(3):525–533, 2000.
- [4] K.-J. Bathe. *Finite-Elemente-Methoden*. Springer, Berlin, 2nd edition, 2002.
- [5] A. Rittweger. *Statik, Stabilität und Eigenschwingungen anisotroper Rotationsschalen beliebigen Meridians mit der Übertragungsmatrizen-Methode*. PhD thesis, RWTH Aachen University, Germany, 1992.
- [6] MSC.Software Corporation. *MSC.Nastran 2001 – DMAP Programmer's Guide*. 2 MacArthur Place, Santa Ana, CA 92707, USA, 2001.
- [7] MSC.Software Corporation. *MSC.Marc 2001 – Volume B: Element Library, Version 2001*. 2 MacArthur Place, Santa Ana, CA 92707, USA, 2001.
- [8] D. Zenkert (ed.). *Handbook of Sandwich Construction*. Engineering Materials Advisory Services, London, 1997.

# TWO FE FORMULATIONS FOR A RAPID 3D STRESS ANALYSIS OF COMPOSITE SANDWICH STRUCTURES

Anja Wetzel and Luise Kärger

*Institute of Composite Structures and Adaptive Systems, German Aerospace Center (DLR),  
Lilienthalplatz 7, 38108 Braunschweig, Germany*

anja.wetzel@dlr.de, luise.kaerger@dlr.de

**Abstract** A rapid 3D stress analysis of sandwich structures made from composite face sheets and a lightweight core is needed for an efficient simulation of impact damage tolerance and resistance. For that reason, two finite shell element formulations based on layer-wise theories are developed using pure displacement approaches. The number of layers is confined to three, one for each skin laminate and one for the core, accounting for the very different stiffness of skin and core material. In order to obtain reasonable transverse shear stiffness properties and also improved transverse shear and normal stresses the equilibrium approach by Rolfes and Rohwer [1] is extended to a three-layered sandwich structure.

**Keywords:** 3D stress analysis, finite elements, composite, sandwich.

## 1. INTRODUCTION

The design of various aerospace structures such as slightly curved fuselage and wing panels requires rapid analysis tools such as CODAC (Composite Damage Tolerance Analysis Code). The finite element program CODAC [2] is capable of simulating the damage resistance and damage tolerance of stringer-stiffened panels due to low-velocity impact.

Besides monolithic structures also sandwich structures are very attractive for aerospace applications, since they are very weight efficient shell constructions capable to carry high bending loads. Furthermore, the core can be used for thermal and acoustic insulation purposes, and a higher impact resistance is provided. Sandwich structures are characterized by a rather small stiffness of the core as compared to the face sheets.

For analyzing sandwich structures with tools like CODAC, corresponding finite element formulations are needed covering the behavior of sandwich struc-

tures with composite face sheets and a soft core. As contribution to a design tool, they have to be computationally very fast. Moreover, these formulations must provide good results for both in-plane and transverse stresses in order to be able to predict the complex failure modes during degradation.

In the following, two three-layered isoparametric eight-node shell elements of the 'serendipity' family are presented. Two examples will demonstrate the accuracy and applicability of these finite element formulations for static loading. The numerical results are compared to the analytical solutions by Pagano [3, 4].

## 2. FINITE ELEMENT FORMULATION ASSUMING PLANE STRESS

For the first element formulation (S89) by Kärger et al. [5] transverse normal stress effects are neglected, which leads to modified constitutive equations with accordingly reduced stiffness properties by eliminating the transverse normal strains from the constitutive equations through static condensation. Therefore, it is sufficient to describe the out-of-plane displacement as constant through the thickness in the kinematical approach

$$\begin{bmatrix} u_L \\ v_L \\ w_L \end{bmatrix} = \begin{bmatrix} u_L^0 \\ v_L^0 \\ w_L^0 \end{bmatrix} + z_L \begin{bmatrix} \psi_{xL} \\ \psi_{yL} \\ 0 \end{bmatrix} . \quad (1)$$

The in-plane displacements are assumed to be layer-wise linear. The displacements of the layer reference plane  $u_L^0$ ,  $v_L^0$  and  $w_L^0$  (with  $L = 1, 3$  for face sheets,  $L = 2$  for core) can be expressed by three translational degrees of freedom of the sandwich reference plane  $u^0$ ,  $v^0$  and  $w^0$  and the rotational degrees of freedom  $\psi_{xL}$ ,  $\psi_{yL}$  resulting in a total number of nine degrees of freedom per node as shown in Figure 1. This kinematical approach is widely discussed in literature, e.g. [6].

Straightforward application of the material law leads to layer-wise constant transverse shear stresses, which violate the boundary conditions at the sandwich surfaces as well as the shear equilibrium conditions at the layer interfaces. Furthermore, an overestimated transverse shear stiffness follows from these approximated transverse shear stresses. In order to obtain reasonable transverse shear stiffness properties and also improved transverse shear and normal stresses the equilibrium approach by Rolfes and Rohwer [1] is applied. It was designed for laminated composite plates based on the FSDT and is subsequently extended to a three-layered sandwich structure. In the following, the formulations of transverse shear stiffness and transverse stresses are presented. A detailed description can be found in Kärger et al. [5].

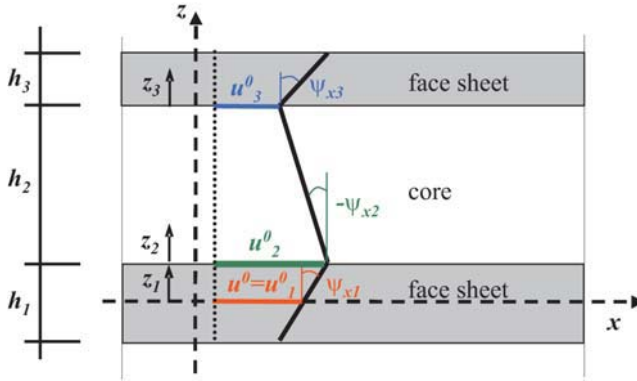


Figure 1. Kinematics of element S89.

### 2.1 Transverse shear stresses

By solving the equilibrium conditions in in-plane directions the transverse shear stresses

$$\boldsymbol{\tau}_z(z) = \begin{bmatrix} \tau_{xz} \\ \tau_{yz} \end{bmatrix} = - \int_{\zeta = -\frac{h_1}{2}}^z \begin{bmatrix} \sigma_{xx,x}^{(k)} + \tau_{xy,y}^{(k)} \\ \sigma_{yy,y}^{(k)} + \tau_{xy,x}^{(k)} \end{bmatrix} d\zeta \quad (2)$$

are obtained in dependence on the derivatives of the in-plane stresses. The derivatives of the in-plane stresses can be replaced by the derivatives of the layer-wise membrane forces and bending moments of the section. Following the assumptions of cylindrical bending modes around the in-plane axes and a constant sum of the layer-wise membrane forces, the transverse shear stresses

$$\begin{aligned} \boldsymbol{\tau}_{zL}(z) &= \begin{bmatrix} f_{L11} & f_{L12} & f_{L13} & f_{L14} & f_{L15} & f_{L16} \\ f_{L21} & f_{L22} & f_{L23} & f_{L24} & f_{L25} & f_{L26} \end{bmatrix} \begin{bmatrix} R_{xz1} \\ R_{yz1} \\ R_{xz2} \\ R_{yz2} \\ R_{xz3} \\ R_{yz3} \end{bmatrix} + \boldsymbol{\tau}_{zL-1}(z_{L0}) \\ &= \mathbf{f}_L(z)\mathbf{R} + \boldsymbol{\tau}_{zL-1}(z_{L0}) \end{aligned} \quad (3)$$

of each single layer  $L$  can be calculated directly from the transverse shear forces  $\mathbf{R}$  of all three layers, where the connecting matrix  $\mathbf{f}_L(z)$  describes the thickness distribution. Thereby, second derivatives of the shape functions are avoided.

## 2.2 Transverse shear stiffness

The complementary transverse shear energy can be expressed by either the transverse shear stresses or the transverse shear forces. Equating these expressions

$$\frac{1}{2} \int_{-\frac{h_1}{2}}^{\frac{h_1}{2}+h_2+h_3} \boldsymbol{\tau}_z^T(z) \mathbf{G}^{-1} \boldsymbol{\tau}_z(z) dz = \frac{1}{2} \mathbf{R}^T \mathbf{H}^{-1} \mathbf{R} \quad (4)$$

leads to the improved transverse shear stiffness for a three-layered sandwich structure

$$\mathbf{H} = \left[ \int_{-\frac{h_1}{2}}^{\frac{h_1}{2}} \tilde{\mathbf{f}}_1^T \mathbf{G}_1^{-1} \tilde{\mathbf{f}}_1 dz + \int_{\frac{h_1}{2}}^{\frac{h_1}{2}+h_2} \tilde{\mathbf{f}}_2^T \mathbf{G}_2^{-1} \tilde{\mathbf{f}}_2 dz + \int_{\frac{h_1}{2}+h_2}^{\frac{h_1}{2}+h_2+h_3} \tilde{\mathbf{f}}_3^T \mathbf{G}_3^{-1} \tilde{\mathbf{f}}_3 dz \right]^{-1} \quad (5)$$

where  $\mathbf{G}_L$  contains the transverse shear moduli and  $\tilde{\mathbf{f}}_L$  is composed of the matrices  $\mathbf{f}_L$  mentioned in Equation (3).

## 2.3 Transverse normal stress

Solving the equilibrium equation in thickness direction for the transverse normal stress

$$\sigma_{zz}(z) = - \int_{\zeta=-\frac{h_1}{2}}^z (\tau_{xz,x}^{(k)} + \tau_{yz,y}^{(k)}) d\zeta + q_{z0} \quad (6)$$

as described in [7] and with consideration of Equation (3), the transverse normal stress is determined by

$$\sigma_{zzL}(z) = - \int_{z_{L0}}^z (\tilde{\mathbf{f}}_{Lx}(z) \mathbf{R}_{,x} + \tilde{\mathbf{f}}_{Ly}(z) \mathbf{R}_{,y}) d\zeta + q_{z0} \quad , \quad (7)$$

where  $\tilde{\mathbf{f}}_{Lx}$  is composed of the first rows  $\mathbf{f}_{Lx} = [f_{L11} \ f_{L12} \ f_{L13} \ f_{L14} \ f_{L15} \ f_{L16}]$  of matrices  $\mathbf{f}_L$ , respectively. Similarly,  $\tilde{\mathbf{f}}_{Ly}$  is built using the second rows of matrices  $\mathbf{f}_L$ .

## 2.4 Finite element analysis

The improved transverse shear stiffness  $\mathbf{H}$ , defined by Equation (5), is used to determine the displacements and strains. The latter are applied to the material law  $\mathbf{R} = \mathbf{H} \boldsymbol{\gamma}_z$  in order to calculate the transverse shear forces, which in turn are necessary to obtain the transverse shear and normal stresses by means

of Equations (3, 7). In addition, the in-plane stresses result from the in-plane strains by applying the condensed constitutive equations. Numerical examples given in section 4 will show that this finite element formulation is a good compromise between accuracy and numerical effort.

### 3. FINITE ELEMENT FORMULATION BASED ON A 3D STRESS STATE

The second element formulation (S815) by Wetzel et al. [8] accounts for the full 3D stress state. Again, the in-plane displacements are described by a layer-wise linear approach. Unlike element S89, however, the material expansion or compression in thickness direction is included in the kinematical approach

$$\begin{bmatrix} u_L \\ v_L \\ w_L \end{bmatrix} = \begin{bmatrix} u_L^0 \\ v_L^0 \\ w_L^0 \end{bmatrix} + z_L \begin{bmatrix} \psi_{xL} \\ \psi_{yL} \\ \psi_{zL} \end{bmatrix} + z_L^2 \begin{bmatrix} 0 \\ 0 \\ \varphi_{zL} \end{bmatrix} \quad (8)$$

This accounts for local transverse normal strain effects due to concentrated impact loading in connection with a soft core material. The kinematical approach is shown in Figure 2 and leads to 15 degrees of freedom per node.

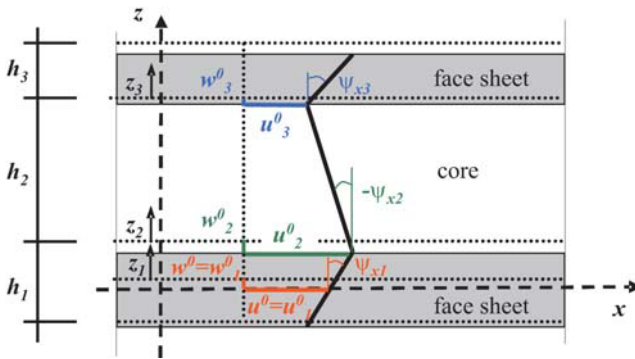


Figure 2. Kinematics of element S815.

All stiffness components and in-plane stresses are determined based on a layer-wise full 3D material law. For the transverse stresses improved values are obtained by utilizing the equilibrium approach similar to the element S89 with a small modification: The transverse shear forces are not calculated by using the improved transverse shear stiffness **H** but the usual transverse shear

material stiffness  $\mathbf{G}$ , e.g.

$$R_{xzL} = \int_{z_{Lbottom}}^{z_{Ltop}} (G_{xzL} \gamma_{xzL}(z_L)) dz_L \quad . \quad (9)$$

## 4. NUMERICAL EXAMPLES

### 4.1 First example

A simply supported plate with a sinusoidally distributed transverse load is analyzed. The loading is applied to the upper surface of the plate as shown in Figure 3. Both face sheets are composed of bi-directional laminates with the

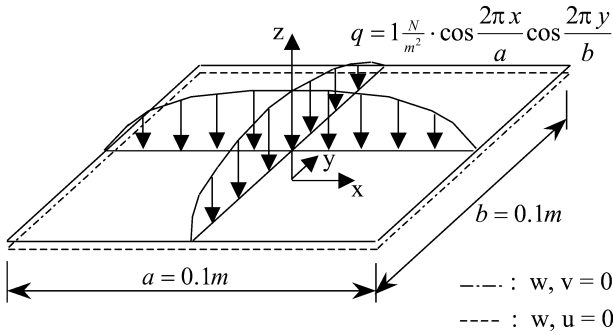


Figure 3. Example 1: simply supported plate.

lay-up  $[0_6/90_6]_s$  made of HTA/6376C prepreg material. The space between the face sheets is filled with a closed-cell rigid foam plastic core. The data of the material properties are listed in Table 1.

Figure 4 shows the results for the in-plane displacement  $u$  of a point at the edge of the plate and the transverse displacement  $w$  at the plate center point, each compared to the analytical solution by Pagano [4]. Both elements reproduce the linear in-plane displacements in the face sheets very accurately but the non-linear in-plane displacements in the core can only be approximated linearly due to the assumed displacement approach.

For element S89 the average values for the transverse displacement are found to be reasonable. Nevertheless, the transverse normal strain can only be obtained using the material law and the assumption  $\sigma_{zz} = 0$ . Element S815 delivers good results for the transverse displacements.

The in-plane stresses, e.g.  $\sigma_{xx}$  shown in Figure 5a, can be simulated accurately by both elements. As demanded, both elements also give good transverse shear and normal stresses demonstrated by Figures 5b–5d. Element S815 re-

Table 1. Material property data.

	$E_x / \frac{N}{m^2}$	$E_y / \frac{N}{m^2}$	$E_z / \frac{N}{m^2}$	$\nu_{yz}$	$\nu_{xz}$	$\nu_{xy}$
face sheets	$140 \cdot 10^9$	$9.5 \cdot 10^9$	$9.5 \cdot 10^9$	0.6380	0.2700	0.2700
foam core	$36 \cdot 10^6$	$36 \cdot 10^6$	$36 \cdot 10^6$	0.3846	0.3846	0.3846
honeycomb	$2.8 \cdot 10^5$	$2.8 \cdot 10^5$	$138 \cdot 10^6$	$4.5 \cdot 10^{-4}$	$4.5 \cdot 10^{-4}$	0.4900
	$G_{yz} / \frac{N}{m^2}$	$G_{xz} / \frac{N}{m^2}$	$G_{xy} / \frac{N}{m^2}$			
face sheets	$2.9 \cdot 10^9$	$5.8 \cdot 10^9$	$5.8 \cdot 10^9$			
foam core	$13 \cdot 10^6$	$13 \cdot 10^6$	$13 \cdot 10^6$			
honeycomb	$30 \cdot 10^6$	$44 \cdot 10^6$	$7 \cdot 10^4$			

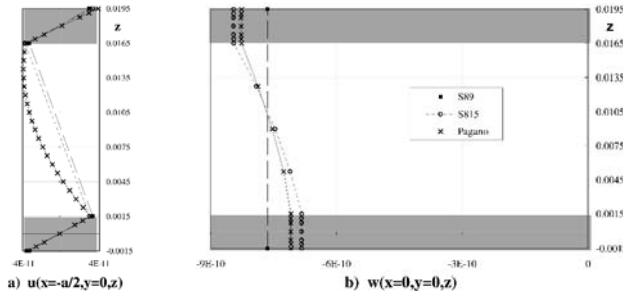


Figure 4. Example 1: displacements.

produces the different maximum values of the transverse shear stresses in the face sheets better than element S89. For element S815 the transverse normal stress can be either calculated by applying Rolfes and Rohwer’s equilibrium approach (S815\_R&R) or the material law (S815\_MLaw). Both methods lead to reasonable results for this example as shown in Figure 5d. However, the stresses calculated by the material law are not continuous through the thickness.

## 4.2 Second example

A sinusoidally distributed static load resembling an impact loading is concentrated at mid-span of the upper surface of a beam as shown in Figure 6. The reference solution by Pagano [3] requires load functions distributed all along the beam length. Therefore, the concentrated sinusoidal load is developed into a Fourier series with 200 terms that models the load accurately.

According to the solution by Pagano the boundary conditions are chosen symmetrical to the middle of the beam: The beam is simply supported at both ends, and the longitudinal displacement is restrained at beam center.

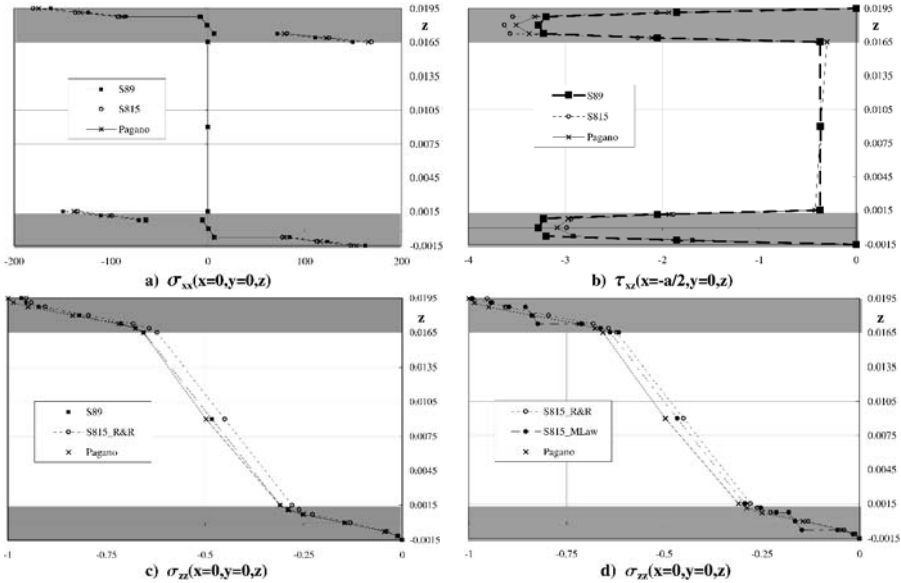


Figure 5. Example 1: stresses.

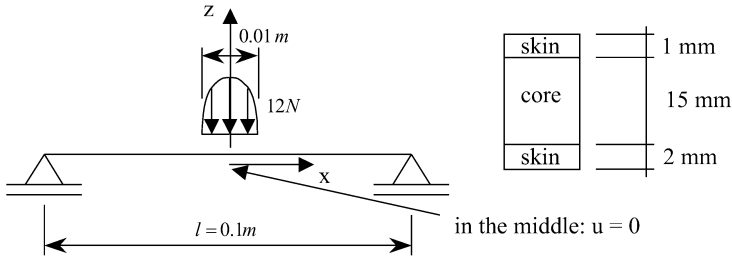


Figure 6. Example 2: simply supported beam.

As a protector layer the upper face sheet is designed thinner than the lower one. The lay-ups for the face sheets are  $[0/90]_s$  and  $[0/90_2/O_2/90]_s$ , respectively. Again, the face sheet laminates are made of the prepreg material HTA/6376C while the Nomex honeycomb core is similar to the core material HRH10-1/8-3.0. The material property data are specified in Figure 1.

A good correlation of the numerical and analytical transverse displacements has been found, as demonstrated in Figure 7. Applying element S89, the through-thickness constant transverse displacements deliver reasonable intermediate values between the displacements at the top and the bottom surface.

For both in-plane and transverse stresses (see Figures 8 and 9) element S815 provides much better results than element S89. Although element S89 gives

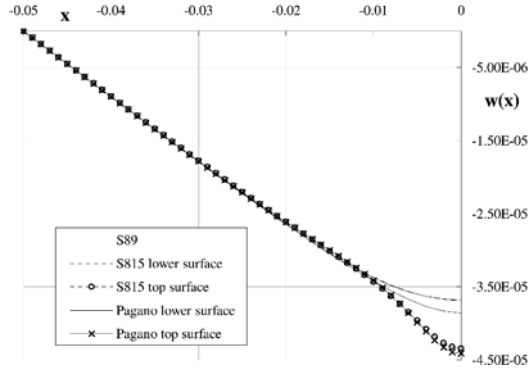


Figure 7. Example 2: transverse displacement.

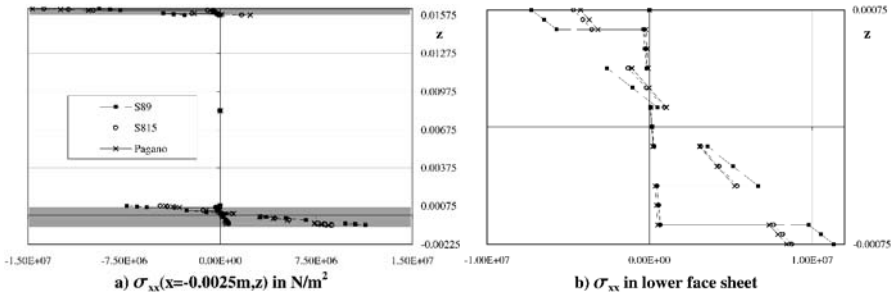


Figure 8. Example 2: in-plane stresses.

usable results for the in-plane stresses, it is not able to deliver accurate values for the transverse shear and normal stresses in case of a concentrated loading. Element S89 does not provide the maximum value of the transverse shear stress in the lower face sheet. The latter was already observed in the first example. As a consequence, the transverse shear stresses of the core are overestimated in the numerical solution using element S89.

### 5. CONCLUSION

Two three-layered shell elements were presented assuming a plane and a full 3D stress state, respectively. The equilibrium approach by Rolfes and Rohwer was extended to a three-layered structure in order to determine the transverse stresses. Both elements were found appropriate for distributed loads. The application of element S815 gives more accurate results compared to the application of element S89, especially for concentrated loads. The advantage of element S89 is its low computational effort, e.g. for analyzing a plate repres-

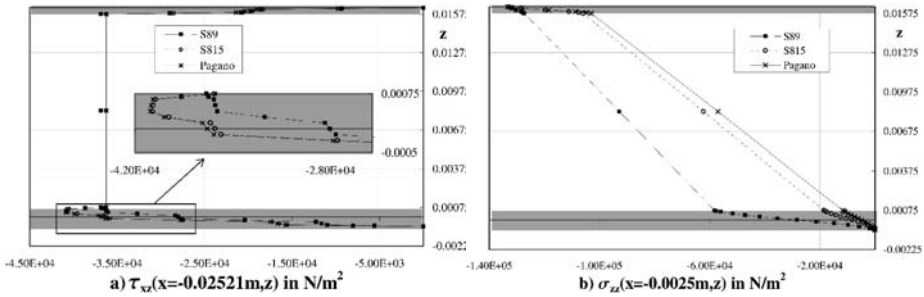


Figure 9. Example 2: transverse stresses.

ented by 400 finite elements the computational time applying S89 is less than one third compared to that of element S815.

## REFERENCES

- [1] R. Rolfes and K. Rohwer. Improved transverse shear stresses in composite finite elements based on first order shear deformation theory. *International Journal for Numerical Methods in Engineering*, 40:51–60, 1997.
- [2] R. Rolfes, J. Baaran, J. Juhasz, A. Kling, Ph. Nolden, and G. Kuhlmann. High performance tools for failure, damage tolerance and stability analysis of composite structures. *WCCM V, Vienna, Austria*, 2002.
- [3] N.J. Pagano. Exact solutions for composite laminates in cylindrical bending. *Journal of Composite Materials*, 3:398–411, 1969.
- [4] N.J. Pagano. Exact solutions for rectangular bidirectional composites and sandwich plates. *Journal of Composite Materials*, 4:20–34, 1970.
- [5] L. Kärger, A. Wetzel, R. Rolfes and K. Rohwer. A three-layered sandwich element with improved transverse shear stiffness and stress based on FSDT. *Submitted for publication to Computers and Structures*, 2004.
- [6] J.N. Reddy. *Mechanics of Laminated Composite Plates and Shells - Theory and Analysis*. CRC Press, Boca Raton, USA, 2004.
- [7] R. Rolfes, K. Rohwer and M. Ballerstaedt. Efficient linear transverse normal stress analysis of layered composite plates. *Computers and Structures*, 68:643–652, 1998.
- [8] A. Wetzel, L. Kärger, R. Rolfes and K. Rohwer. Evaluation of two finite element formulations for a rapid 3D stress analysis of sandwich structures. *Accepted for publication to Computers and Structures*, 2004.

# SANDWICH MATERIALS SELECTION CHARTS

Jochen Pflug and Ignaas Verpoest

*Katholieke Universiteit Leuven, Department of Metallurgy and Materials Engineering (MTM), Kasteelpark Arenberg 44, B-3001 Leuven, Belgium*

**Abstract** This paper presents an approach to facilitate comparison and optimization of sandwich material combinations. Equivalent homogenised sandwich material properties (bending stiffness, density and cost) are presented graphically in materials selection charts to enable an efficient performance per cost evaluation. The effects of core shear deformations and panel production costs can be included in those sandwich materials selection charts.

**Keywords:** materials selection, material efficiency, cost optimization.

## 1. INTRODUCTION

Beside the weight advantages the economical advantages are vital for the potential of sandwich construction in many applications. For cost sensitive applications sandwich material combinations are even more in competition with monolithic construction than in weight critical application.

Sandwich construction with a low cost core material can be not only more lightweight but also more cost effective, especially since the advancement and automation of production processes enable a reduction of production cost for lightweight sandwich panels. However, for low cost applications sandwich construction is frequently not considered because of limited knowledge about their cost saving potential. It is thus important to provide tools to evaluate and present the cost saving potential of sandwich material combinations already in the stage of materials selection.

For a given sandwich material combination an optimization, including shear deformations of the core as well as optimizations towards a maximum bending strength, involving different failure modes, can be performed. Those optimizations have been discussed in detail in [1–3], but in practice the calculation with one single optimal material option is often not sufficient because many different material options need to be considered. Especially for cost optimal sandwich design a cost efficient comparison of all material options and geometrical parameters is essential. To solve this problem genetic algorithms have been

proposed [4]. Inspired by a paper on the combination of materials and shape from Ashby [5] the authors applied in an earlier publication [6] the concept of materials selection charts to sandwich constructions. This technique offers an alternative to numerical methods and provides a transparent method for sandwich materials selection.

### 1.1 Cost saving potential of sandwich construction

Sandwich construction allows using a core from a different, more light-weight and less expensive material. In Table 1 weight saving and material cost saving potential with an expensive core and a low cost core are compared. The potential economical advantage with low cost core materials is as big as the potential weight saving due to low density core materials.

Table 1. Weight saving and material cost saving potential of sandwich construction.

<b>Sandwich effect on bending stiffness weight and cost</b>	monolithic $h_1 = 2 t_1$ 	sandwich $h = 1.2 h_1$ $t = 0.3 t_1$ 	optimised $h = 2.4 h_1$ $t = 0.06 t_1$ 
Relative thickness	1	1.2	2.4
thickness ratio $t/h$	0.5	0.125	0.0125
Relative bending stiffness	1	1	1
Relative weight (core density 20 times lower)	1	0.345	0.177
Relative material cost with an expensive core (equal cost per volume)	1	1.2	2.4
Relative material cost with a low cost core (20 times lower cost per vol.)	1	0.345	0.177

To enable a high cost saving it is however essential that the core material has sufficient mechanical properties. The primary mechanical requirement for the core is to prevent the movement of the skins relative to each other in plane (by sufficient out-of-plane shear properties) and out-of-plane (by sufficient out-of-plane tension/compression properties).

In the following the different elements enabling to include sandwich materials and cost aspects in efficiency evaluations will be discussed, then the sandwich material selection charts will be presented and finally the effect of core shear deformations will be included.

## 2. SANDWICH MATERIAL EFFICIENCY

The material efficiency is usually defined as a mechanical performance per weight, e.g. for buckling and bending stiffness of plates, the material efficiency per weight is  $E^{1/3}/\rho$  (with  $E$  the elastic modulus and  $\rho$  the material density). However, since a maximal economical advantage is often targeted the optimization of stiffness per weight or strength per weight should be part of a performance per cost optimization. In [7] Ashby presented a general procedure for multi-objective optimization based on cost value functions.

### 2.1 Value of weight saving

As shown in Table 1 sandwich construction can enable substantial cost reductions due to the less amount of raw material and/or less expensive material used in the core leading to a direct reduction in material cost. However, additional cost savings, due to the effect of a weight reduction on the operating cost and where applicable on the ecological cost should be considered. To include those cost reductions into the comparison of material efficiency per cost, the benefit of weight savings  $C_{w\text{Value}}$  in €/kg has to be determined. This value is dependent on the application area and may vary for different components. Nevertheless, the value of a weight reduction is often easy to define if weight reduction is a requirement for a component. The value may be established by a life cycle analysis but most realistic is to use what the customer is willing to pay for a weight reduction.

### 2.2 Equivalent sandwich material properties

The sandwich bending modulus, the sandwich density as well as the material costs can be expressed in function of the ratio between the skin thickness  $t$  and the sandwich height  $h$ . A sandwich material combination with the same thickness ratio  $t/h$  has its own set of material properties (bending modulus  $E_H$ , density  $\rho_H$  and material cost  $C_{wH}$ ) and can thus be considered as a sandwich material [6]. A recent publication by Ashby on the design of hybrid materials proposes to use this approach as a general tool for selecting material combinations [8]. For symmetrical sandwich materials the homogenized properties can be calculated using the following equations:

$$E_H = E_s - (E_s - E_c) \left(1 - 2\frac{t}{h}\right)^3, \quad (1)$$

$$\rho_H = \rho_s - (\rho_s - \rho_c) \left(1 - 2\frac{t}{h}\right), \quad (2)$$

$$C_{wH} = \left(C_{ws} \rho_s - (C_{ws} \rho_s - C_{wc} \rho_c) \left(1 - 2\frac{t}{h}\right)\right) / \rho_H. \quad (3)$$

The symbols  $E_c$ ,  $G_c$ ,  $\rho_c$ ,  $C_{wc}$  are used for the E-modulus, shear modulus, material density and material cost of the core, while  $E_s$ ,  $\rho_s$ ,  $C_{ws}$  and  $E_H$ ,  $\rho_H$ ,  $C_{wH}$  are used for the properties of the skins and the sandwich material.

### 2.3 Sandwich production cost

Sandwich construction often leads to somewhat higher production cost compared to monolithic structures. Maximization of performance per cost requires finding the best compromise between mechanical performance and material cost, production cost and weight.

The material efficiency based on cost  $ME_C$  includes not only material cost and the value of weight saving but also the production cost. The total cost per volume  $C_{vSum}$  combines thus the cost paid for the material  $C_{wH}$  and the cost expected due to the weight of a part during in-service and life cycle of the component and the production costs.

$$ME_C = \frac{E_H^{(1/3)}}{C_{vSum}} = \frac{E_H^{(1/3)}}{C_{wH} \rho_H + C_{wValue} \rho_H + \frac{C_{aPanelProd}}{h}}. \quad (4)$$

This allows to define a cost saving factor  $\Phi_{Cost}$ , which is a direct measure of the economical advantage compared to an equal bending stiff monolithic panel made from the skin material with the material efficiency  $ME_{Cs}$ .

$$\Phi_{Cost} = \frac{ME_C}{ME_{Cs}} = \frac{ME_C \left(C_{ws} \rho_s + C_{wValue} \rho_s + \frac{C_{asPanelProd}}{h}\right)}{E_s^{(1/3)}}. \quad (5)$$

The cost required to produce a sandwich panel  $C_{aPanelProd}$  of thickness  $h$  include cost for producing core and skin layers plus cost of bonding the skins onto the core. Those costs usually depend on the panel surface area and are thus given in €/m<sup>2</sup>. They can be compared to the production cost for a monolithic panel from the skin material  $C_{asPanelProd}$ . The inclusion of sandwich panel production costs affects the material efficiency and can result in a significantly different cost optimal thickness ratio.

## 3. MATERIALS SELECTION CHARTS

The material selection and the production process selection usually determine a large part of the cost of a structure. The selection process needs thus to

be included in the stage of screening and comparing different design and material options [9]. Materials selection charts [10] can be used to compare how efficiently different materials fulfill a certain structural function, e.g. bending stiffness. The company Granta Design implemented the concept of material selection in software tools [11].

### 3.1 Sandwich material combinations in selection charts

For sandwich construction the material efficiency per weight in bending  $E^{1/3}/\rho$  is especially important because bending stiffness is the main advantage of the sandwich concept. The performance of different sandwich panels can be compared to each other and to monolithic panels by calculating their material efficiency per weight coefficient for buckling and bending  $E_H^{1/3}/\rho_H$ . The properties of sandwich material combinations are shown in materials selection charts as a function of the non-dimensional ratio between skin thickness and sandwich height  $t/h$  [6].

Figure 1 presents an example of a sandwich materials selection chart displaying the homogenized properties of a sandwich material combination of aluminum skins and a paper honeycomb core.

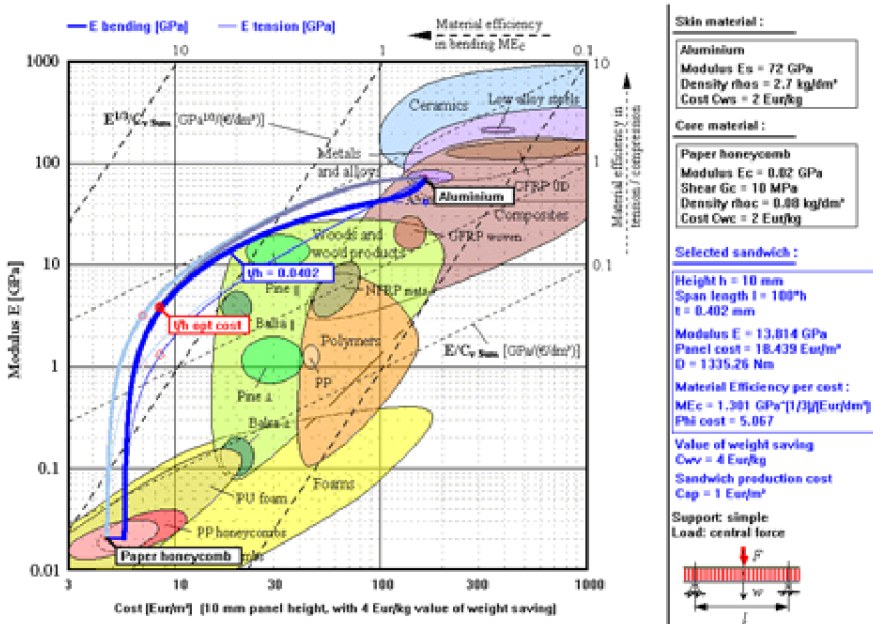


Figure 1. Sandwich materials selection chart.

This graphical presentation enables the direct assessment of weight savings and cost savings in function of geometrical parameters. The effect of select-

ing a different skin or core material on the sandwich properties can be shown graphically in such modulus versus density or modulus versus cost diagrams. The properties of all possible sandwich panels with this material combination (thickness ratios from 0 to 0.5) are shown on this curve. The maximum material efficiency in bending is at high  $E^{1/3}/C_{vSum}$  values in the upper left corner of the diagram.

Sandwich material selection diagrams make the complex effects of sandwich design transparent and allow communicating efficiently the advantages of sandwich material combinations by a graphical presentation of the complex theoretical relations in sandwich construction.

The loading conditions, strength criteria and surface requirements of a specific application often demand a larger than optimal skin thickness. In most cases a rather slow decrease of the material efficiency close to the optimum allows to increase the thickness ratio  $t/h$  slightly without a large penalty. The proposed sandwich selection diagrams allow assessing the effects of non-optimal thickness ratios. Note that the optimal bending efficient sandwich material has always an  $E_H/\rho_H$  ratio, which is equal to the tension/compression efficiency of the skin material  $E_s/\rho_s$ .

### 3.2 Effect of core shear deformations

To include the effect of core shear stiffness in the selection chart the ordinary classical sandwich theory (OST) and non-dimensional ratio between the span length and the sandwich height  $l/h$  can be used.

The shear reduced homogenized bending modulus is calculated to lead to an equivalent total deflection. In classical sandwich theory the shear stiffness uses the shear area, which is not equal to the sandwich material cross section. A homogenized shear modulus  $G_{cH}$  can be obtained if the shear stiffness is divided by the material cross section. The homogenized shear modulus is also expressed by a function of the sandwich thickness ratio  $t/h$ .

$$G_{cH} = G_c \left( 1 + \frac{t^2}{h^2} \frac{1}{(1 - 2t/h)} \right). \quad (6)$$

The partial bending deflection  $w_b$  with the bending deflection constant  $B_b$  and the partial shear deflection  $w_s$  with the shear deflection constant  $B_s$  can both be expressed in function of the non-dimensional ratio between span length  $l$  and the sandwich height  $h$ .

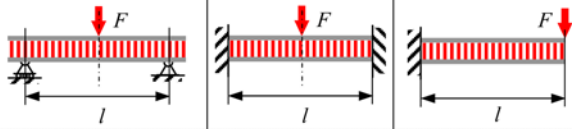
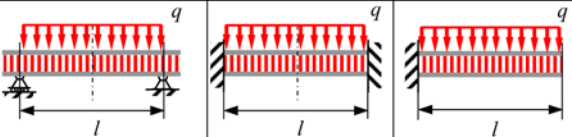
Via Equations (1) and (6) they are furthermore a function of the non-dimensional sandwich thickness ratio  $t/h$ .

$$w_b = \frac{Fl^3}{B_b D} = \frac{l^3}{h^3} \frac{F/b}{B_b} \frac{12}{E_H}, \quad (7)$$

$$w_s = \frac{Fl}{B_s S} = \frac{l}{h} \frac{F/b}{B_s} \frac{1}{G_c H}. \tag{8}$$

The ratio between shear and bending deflection is affected by the span length to sandwich height ratio  $l/h$  and by the loading and support condition via the constants  $B_b$  and  $B_s$ . The constants  $B_b$  and  $B_s$  are shown for some very common load cases in Table 2 [2]. The bending deflection is proportional to  $l^3/h^3$  the shear deflection is proportional to  $l/h$ . Note that this is for uniform monolithic materials not different. Only due to their large shear modulus and since the span length is usually long compared to the panel height their shear deflection can be most often neglected. However, it has to be stressed that the ordinary classical sandwich theory with the simple superposition of the shear deflection to the bending deflection neglects the locally interaction with deformations at load introduction and support points and is only correct if the core is transversely stiff and the skins are thin compared to the sandwich height.

Table 2. Shear and bending deflection constants and load case factor.

Shear and bending deflection constants	Simply supported beam, span length $l$	Clamped beam, span length $l$	Cantilever beam, length $l$
Loading condition: single load $F$ 			
shear constant $B_s$	4	4	1
bending constant $B_b$	48	192	3
Load case factor $F_{LC} = 12B_s/B_b$	1	1/4	4
Loading condition: distrib. load $F = q l$ 			
shear constant $B_s$	8	8	2
bending constant $B_b$	384/5	384	8
Load case factor $F_{LC} = 12B_s/B_b$	5/4	1/4	3

To facilitate the comparison of shear deflections and bending deflections it is nevertheless of interest to express shear stiffness as a bending modulus. The

deflection over the span length will differ but the maximal bending deflection of a monolithic panel from a material with a modulus equal to the shear equivalent bending modulus  $E_{Gc}$  would be equal to the maximal shear deflection. Furthermore, the homogenized bending modulus  $E_H$  and the shear equivalent bending modulus  $E_{Gc}$  can be combined to a shear reduced homogenized bending modulus  $E_{GH}$ . This allows including the shear weakness of core material into the sandwich materials selection charts.

$$E_{Gc} = 12 \frac{B_s}{B_b} \frac{l^2}{h^2} G_{cH}, \quad (9)$$

$$E_{GH} = \frac{1}{\frac{1}{E_{Gc}} + \frac{1}{E_H}}. \quad (10)$$

To further simplify the equation a load case factor  $F_{Lc}$  can be defined which combines  $12B_s/B_b$  and is for the three point bending load case equal to one. It must however be remembered that the shear reduced homogenized bending modulus  $E_{Gc}$  is only valid for the comparison of maximal deflection for a given ratio between span length and sandwich height and a given loading case. Furthermore, it is required to be aware of different behavior and different failure modes of sandwich materials.

For the same span length and the same sandwich panel thickness the effect of the shear modulus on the efficiency is very dependent on the skin material properties. The core shear affects bending performance of sandwich material combinations especially at rather high thickness ratios. With relatively thick skins a high bending stiffness leads to a larger effect of the core shear deformation.

### 3.3 Further developments

The effect of local core compression deformations at loading and support points can be additionally included by elastic foundation (Winkler foundation) approaches. It has been stressed that in modern sandwich construction low cost core materials with rather low out-of-plane compression stiffness may result in transversely flexible sandwich panels, which demand the use of an high-order theory (HST) [12].

The additional inclusion of the core compression modulus  $E_{cz}$  leads to more complex equations but can prevent the selection of a core with insufficient compression stiffness. This is important for low cost polymer foam cores, because they often exhibit, compared to low cost honeycomb cores, especially low out-of-plane compression performance.

For the optimization of bending stiffness performance in the stage of materials selection the OST and a Winkler foundation model are adequate to prevent

the selection of core materials with insufficient shear or compression performance.

The presented approach may also be applied for strength per cost sandwich selection charts. Such strength sandwich materials selection charts need to take different failure modes into account.

#### 4. CONCLUSION

It can be concluded that sandwich selection charts have the potential to enable a more straightforward and more transparent comparison of sandwich materials. They may enable to enhance the understanding of the differences and the cost saving potential of sandwich construction in industry. The sandwich materials selection charts may help to promote sandwich construction especially in low cost application areas where even the simple OST is rarely used today by industry. However, it has to be stressed that especially for strength estimations the special phenomena of sandwich constructions have to be considered.

#### REFERENCES

- [1] Zenkert, D., *The Handbook of Sandwich Construction*, EMAS Chameleon Press, London, 1997.
- [2] Ashby, M.F. and Gibson, L.J., *Cellular Solids – Structure and Properties*, Cambridge University Press, Cambridge, 1997.
- [3] Wiedemann, J., *Leichtbau Konstruktion*, Vol. 2, Springer-Verlag, Berlin, 1997.
- [4] Bassetti, D. et. al., “Genetic algorithm and performance indices applied to optimal design of sandwich structures”, in *Mechanics of Sandwich Structures*, A. Vautrin (ed.), Kluwer Academic Publisher, Dordrecht, pp. 387–395, 1998.
- [5] Ashby, M.F., “Materials and Shape”, *Acta Metall. Mater.*, Vol. 39/6, pp. 1025–1039, 1991.
- [6] Pflug, J., Vangrimde, B. and Verpoest, I., “Material efficiency and cost effectiveness of sandwich materials”, in *Sampe Conference*, Longbeach, USA, pp. 1925–1937, May 2003.
- [7] Ashby, M.F., “Multi-objective optimization in material design and selection”, *Acta Metall. Mater.*, vol. 48/1, pp. 359-369, 2000.
- [8] Ashby, M.F., “Designing hybrid materials”, *Acta Metall. Mater.*, Vol. 51, pp. 5801–5821, August 2003.
- [9] Ashby, M.F., *Materials and Process Selection in Mechanical Design*, Butterworth Heineemann, Oxford, 1999.
- [10] Ashby, M.F., *Materials Selection in Mechanical Design*, Pergamon Press, Oxford, 1992.
- [11] Ashby, M.F. and Cebon, D., *Granta Design*, Cambridge Engineering Selector, CES4 Software for Materials Data Management, Product Overview, 2003.
- [12] Frostig, Y., “Classical and high-order computational models in the analysis of modern sandwich panels”, *Composites: Part B*, Vol. 34, pp. 83–100, 2003.

# OPTIMAL DESIGN OF LAMINATED EXTENDED & HONEYCOMB CORES SANDWICH PANELS UNDER OUT-OF-PLANE LOAD WITH SIMPLY SUPPORTED BOUNDARY CONDITIONS USING GENETIC ALGORITHM

M.J. Jamali<sup>1</sup>, I. Rajabi<sup>2</sup> and M.H. Kadivar<sup>1</sup>

<sup>1</sup>*Department of Mechanical Engineering, Shiraz University, Iran;* <sup>2</sup>*Mechanical Engineering, Malek-e-Ashtar University, Iran*

**Abstract** This paper presents discrete optimization of laminated sandwich panels with simply supported edges, under out-of-plane load that include honeycomb and extended cores. Because of problem complexity and discontinuity of variables, evolutionary algorithm (GA) is preferred for this optimization

**Keywords:** sandwich panel, laminated composite, optimization, genetic algorithm.

## 1. INTRODUCTION

Many recent researches have been published that have been determined critical load for failures of sandwich panels [1, 2] and various methods to optimize sandwich panels under in-plane loads had been considered. Classical solutions are the important methods to predict best selection for weight minimization. But, with laminate applications as sandwich facings and their stacking sequence complexity, evolutionary algorithms (e.g. genetic algorithm) are considered [3, 4].

## 2. OPTIMIZATION PROBLEM

For this optimization problem, out-of plane load causes many constraints comprised deflection limit, strength, local instabilities that in continue are described completely.

### 2.1 Deflection limit constraint

Because of using deflection coefficient ( $K_w$ ), it is necessary to consider large deflection and displacement of middle surface. Also, Shear deformation of plates that have considerable thickness, should assess to predict shear behavior of bending. Also, sandwich plate has symmetry plane of geometry and materials in the middle surface. The assumptions consist following basics: the materials are linear elastic, only nonlinear term is corresponded to lateral deflection,  $w$  and deflection  $w$  could be divided into two terms:  $w = w_b + w_s$  and  $t_f \ll t_c$ ; Thus, the facings carry bending moments as tensile and compressive stresses and the core carries transverse shear stresses. The strains expressions in terms of the displacements derive as follows:

$$\begin{aligned} \varepsilon_x &= \frac{\partial u}{\partial x} + \frac{1}{2} \left( \frac{\partial w}{\partial x} \right)^2 - z \frac{\partial^2 w_b}{\partial x^2}, & \varepsilon_y &= \frac{\partial v}{\partial y} + \frac{1}{2} \left( \frac{\partial w}{\partial y} \right)^2 - z \frac{\partial^2 w_b}{\partial y^2} \\ 2\varepsilon_{xy} &= \frac{\partial u}{\partial y} + \frac{\partial v}{\partial x} + \frac{\partial w}{\partial x} \frac{\partial w}{\partial y} - 2z \frac{\partial^2 w_b}{\partial x \partial y}, & 2\varepsilon_{xz} &= \frac{\partial w_s}{\partial x}, & 2\varepsilon_{yz} &= \frac{\partial w_s}{\partial y}. \end{aligned}$$

If Hook’s law for an orthotropic material is applied and it is assumed that the stress component in the  $z$ -direction vanishes everywhere, the constitutive relation for each layer can be achieved [2]. Combining these equations and integrating over the thickness of sandwich plate, the in-plane forces, the moments and the shearing forces are obtained. In continue an analytical solution is presented for the nonlinear deformation [5]. The total energy,  $U$ , of the plate can be expressed as the sum of internal strain energy and the potential energy due to external loads  $q$ . Also, the following deflection functions satisfy simply supported boundary conditions:

$$w = (\bar{w}_b + \bar{w}_s) \sin \alpha x \sin \beta y, \quad u = \bar{u} \sin 2\alpha x \sin \beta y, \quad v = \bar{v} \sin 2\beta y \sin \alpha x.$$

Inserting the deflection functions into the energy expression, the total strain energy of the plate expressed in the following

$$U_1 = \sum_{i=1}^{33} u_i = U_1(\bar{u}, \bar{v}, \bar{w}_b, \bar{w}_s), \quad U_2 = \frac{4qab}{\pi^2} (\bar{w}_b + \bar{w}_s).$$

Hence, minimization of the potential energy with respect to  $\bar{u}, \bar{v}, \bar{w}_b, \bar{w}_s$  gives adequate equations to find these parameters. The final expression yield:

$$\bar{w}_s = \beta_7 \bar{w}_b, \quad \bar{u} = \beta_8 \bar{w}_b^2, \quad \bar{v} = \beta_9 \bar{w}_b^2 \quad \text{and} \quad \bar{w}_b^3 + a_2 \bar{w}_b + a_3 = 0,$$

where the constants  $\beta_7, \beta_8, \beta_9, a_2$  and  $a_3$  are function of the plate properties, including length and the stiffness matrices [5]. Considering above nonlinear

theory of sandwich plate, deflection limit constraint could be achieved as following:

$$G_w = K_w \frac{h}{w_{\max}} - 1 \geq 0.$$

That  $h$  refers to total thickness of sandwich plate.

## 2.2 Strength constraint

In this study, the Tsai–Wu failure criterion [6] is stipulated

$$\lambda_s^{(k)} = (F_{11}\sigma_1^{(k)}\sigma_1^{(k)} + F_{22}\sigma_2^{(k)}\sigma_2^{(k)} + F_{66}\tau_{12}^{(k)}\tau_{12}^{(k)} + 2F_{11}\sigma_1^{(k)}\sigma_2^{(k)} + F_1\sigma_1^{(k)} + F_2\sigma_2^{(k)})^{-1},$$

where the strength parameters  $F_{11}$ ,  $F_{22}$ ,  $F_{66}$ ,  $F_{12}$ ,  $F_1$  and  $F_2$  are given by:

$$F_{11} = -1/(X_c X_t), F_1 = 1/X_t + 1/X_c, F_{22} = -1/(Y_c T_t),$$

$$F_2 = 1/Y_t + 1/Y_c, F_{66} = 1/S^2, F_{12} = -\frac{1}{2}\sqrt{F_{11}F_{22}}.$$

$X_t$ ,  $X_c$ ,  $Y_t$ ,  $Y_c$  are the tensile and compressive strengths of the composite material in the material directions, and  $S$  is the in-plane shear strength. Therefore, the upper and lower facings failure and core failure constraints are achieved as ( $F.S$  in below equations is factor of safety.)

$$G_{\text{tension}}^{\text{facings}} = \min_{k=1,2,3,\dots,n} \{\lambda_s^{(k)} / F.S - 1\} \geq 0,$$

$$G_{\text{compression}}^{\text{facings}} = \min_{k=1,2,3,\dots,n} \{\lambda_s^{(k)} / F.S - 1\} \geq 0,$$

$$G_s^{\text{core}} = 1/F.S - (\tau_{13}/S_{13}^c + \tau_{23}/S_{23}^c) \geq 0.$$

Finally, total strength constraint is described as:

$$G_s = \min\{G_{\text{tension}}^{\text{facings}}, G_{\text{compression}}^{\text{facings}}, G_s^{\text{core}}\} \geq 0$$

## 2.3 Local instabilities constraint

Face wrinkling may occur across of the extended core and many cells of the honeycomb core. In honeycomb core sandwiches, another type of local instability, which is generally referred to as the face dimpling, may occur. For these local instabilities, in-plane load can be assumed as

$$N_x = \frac{\sum_{k=1}^n \sigma_{11 \max}^{(k)} t^{(k)}}{n}, \quad N_y = \frac{\sum_{k=1}^n \sigma_{22 \max}^{(k)} t^{(k)}}{n},$$

where  $\sigma_{11 \max}^{(k)}$  and  $\sigma_{22 \max}^{(k)}$  refer to maximum normal stresses for each layer of facing which is under compressive bending stress. Also,  $n$  is number of under compression facing layers. Wrinkling constraint can be expressed as [4]

$$G_{fw} = \min\{\overline{N_x^{fw}}/N_x, \overline{N_y^{fw}}/N_y\} - 1 \geq 0,$$

where

$$\overline{N_x^{fw}} = \left[ \left( \frac{1}{N_x (1 + G_{\text{compression}}^{\text{facings}})} \right)^3 + \left( \frac{1}{N_x^{fw}} \right)^3 \right]^{-1/3},$$

$$\overline{N_y^{fw}} = \left[ \left( \frac{1}{N_y (1 + G_{\text{compression}}^{\text{facings}})} \right)^3 + \left( \frac{1}{N_y^{fw}} \right)^3 \right]^{-1/3},$$

$$N_x^{fw} = \left[ \left( D_{11} - \frac{D_{22}^2}{D_{22}} \right) EcGxz \right]^{1/3},$$

$$N_y^{fw} = \left[ \left( D_{22} - \frac{D_{12}^2}{D_{11}} \right) EcGyz \right]^{1/3}$$

and, the face dimpling constraint can be written as [4]

$$G_{fd} = \min\{\overline{N_x^{fd}}/N_x, \overline{N_y^{fd}}/N_y\} - 1 \geq 0,$$

where

$$\overline{N_x^{fd}} = \left[ \left( \frac{1}{N_x (1 + G_{\text{compression}}^{\text{facings}})} \right)^3 + \left( \frac{1}{N_x^{fd}} \right)^3 \right]^{-1/3},$$

$$\overline{N_y^{fd}} = \left[ \left( \frac{1}{N_y (1 + G_{\text{compression}}^{\text{facings}})} \right)^3 + \left( \frac{1}{N_y^{fd}} \right)^3 \right]^{-1/3},$$

$$N_x^{fd} = \frac{9}{t_f^2} \left[ D_{11} - \frac{D_{12}^2}{D_{22}} \right] \left( \frac{t_f}{t_d} \right)^{3/2},$$

$$N_y^{fd} = \frac{9}{t_f^2} \left[ D_{22} - \frac{D_{12}^2}{D_{11}} \right] \left( \frac{t_f}{t_d} \right)^{3/2},$$

where  $t_f$  and  $t_d$  are facing thickness and cell diameter, respectively.

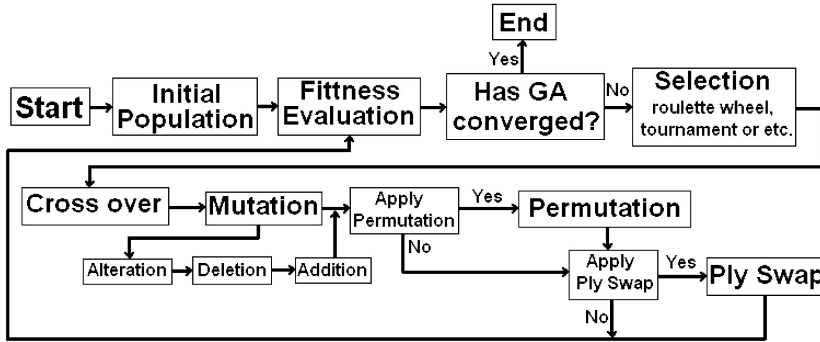


Figure 1. Schematic procedure of GA optimization.

### 2.4 Objective function

The optimization problem can be formulated as finding the stacking sequences and material selection of the facing and the core thickness and core materials in order to minimize the weight  $W$  of the panel. The set of design variables is expressed as a vector  $\vec{x} = (t_c(q), \theta_1, \theta_2(p), \dots, \theta_n(p), p, q)$  where  $n$  is an implicit design variable dictated by the number of layers in the one facing stacking sequence; also,  $p$  and  $q$  represent facing layers and core materials integer variables, respectively. The optimization problem with deflection, strength failure and buckling constraints can be expressed as

$$\min_{\vec{x}=[t_c(q), \theta_1, \theta_2(p), \dots, \theta_n(p), p, q]} \left\{ W(\vec{x}) = \left[ 2 \sum_{k=1}^n t_f^{(k)} \cdot \rho_f^{(k)} + (t_c \cdot \rho_c) \cdot F \right] (a \cdot b) \right\}$$

such that

- $G_w(\vec{x}) \geq 0$  (Deflection limit constraint),
- $G_s(\vec{x}) \geq 0$  (Strength failure constraint),
- $G_{fw}(\vec{x}) \geq 0$  (Face wrinkling constraint),
- $G_{fd}(\vec{x}) \geq 0$  (Face dimpling constraint),
- $G_g(\vec{x}) \geq 0$  (Geometry constraint),

where  $\rho_f$  and  $\rho_c$  are material densities of the facing layers and core, respectively; and  $F$  is effective manufacturing parameter differed for various cores. Also,  $G_g$  is defined regarding assumption of core to facing thickness.

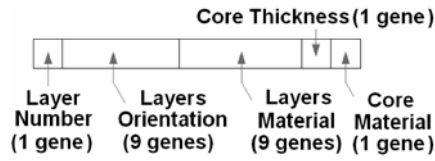


Figure 2. A variable chromosome and its genes.

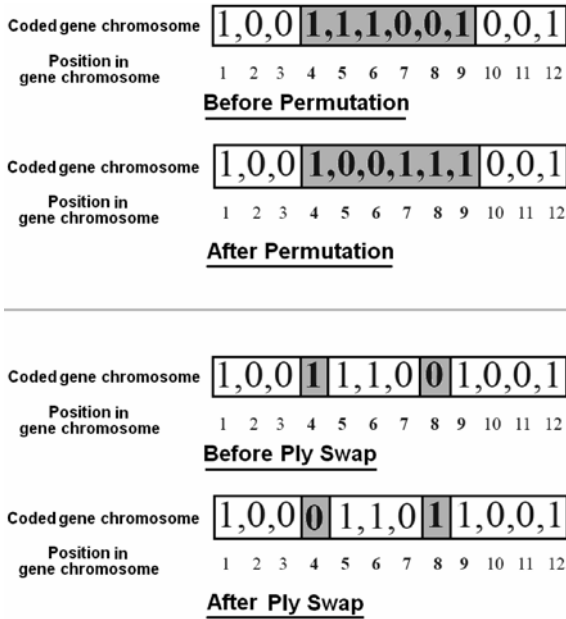


Figure 3. Procedure of permutation and ply swap.

Table 1. Parameters in genetic algorithm.

Population size	25
Number of variables	21
Probability of mutation	0.1
Probability of cross over	0.75
Probability of permutation &/or ply swap	0.75

### 3. GENETIC ALGORITHM METHOD

A genetic algorithm is a powerful technique for search and optimization problems with discrete variables, and is therefore particularly useful for optimization of composite laminates. Figure 1, depicts schematic procedure of GA.

Figure 2, shows variables chromosome of GA optimization and number of its genes for each variable.

Layer number of facings (is limited: 3 to 9 layer for each facings), layers orientation (is comprised these ranges:  $[0, \pm 45, 90]$ ), layers material (is included glass, carbon and Kevlar<sup>®</sup>), core thickness and core material are optimization problem variables. The GA in this paper applies an elite strategy and tournament selection. Table 1, lists the parameters used in GA. In the advanced GA for stacking sequence and material selection of facing layers, new operator as permutation and ply swap are utilized. The procedures of these new operators have been shown in Figure 3.

For fitness function description, the critical constraint is defined as

$$G_{cr} = \min\{G_w, G_s, G_{fw}, G_{fd}, G_g\}$$

and the constrained optimization problem is transformed into an unconstrained maximization problem for the genetic algorithm. This is done by using penalty parameters. The fitness function to be maximized is defined as

$$F_f(\vec{x}) = \begin{cases} -W(\vec{x}) + G_{cr}\delta & G_{cr} \geq 0 \\ -W(\vec{x})(1 - G_{cr})^r & G_{cr} \leq 0 \end{cases} ,$$

where  $\delta$  and  $r$  are bonus and penalty parameters, respectively.

### 4. RESULTS

Material properties of facing layers and cores are listed in Tables 2 and 3, respectively. For three cases that include advanced GA with permutation, ply swap and both them, optimization problem has been run for the uniform pressure  $q$  was 10 kPa and the dimensions of the sandwich panel were  $a = 800$  mm and  $b = 700$  mm. fitness vs. generation GA procedure are plotted in Figure 4, that two runs for each case has been applied to depict each operator what effects has on rapidly converge to the maximum fitness.

The results of optimum design of extended and honeycomb laminated sandwich panel for various uniform pressure distribution are presented in Table 4. These results are determined from advanced GA, using both permutation and ply swap for a special plate dimensions and for other dimensions, can be achieved also. In this table  $G$ ,  $K$  and  $C$  are explanations of glass, Kevlar<sup>®</sup> and carbon fibrous cloth, respectively.

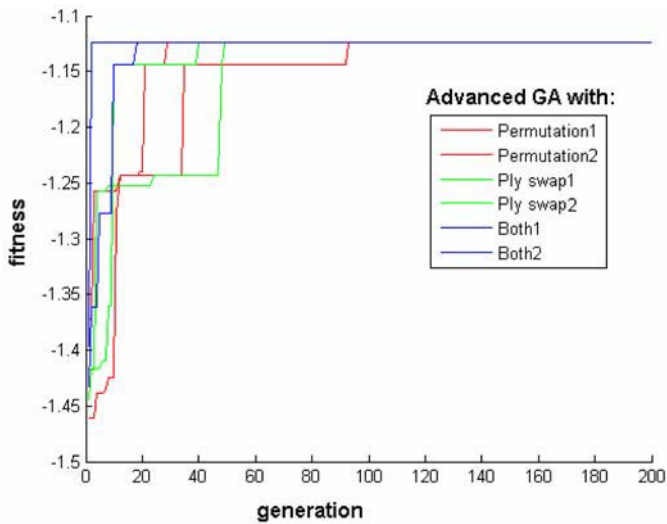


Figure 4. Fitness vs. generation for advanced GA.

Table 2. Material properties of fibrous bidirectional cloth.

Material	Density (kg/m <sup>3</sup> )	E <sub>11</sub> =E <sub>22</sub> (MPa)	G <sub>12</sub> (MPa)	$\nu_{12}$	S <sub>11</sub> =S <sub>22</sub> in tension (MPa)	S <sub>11</sub> =S <sub>22</sub> in comp. (MPa)	S <sub>shear</sub> (MPa)
Glass	0.185	15.1e3	4.5e3	0.1	225	150	80
Carbon	0.180	50e3	10e3	0.25	320	250	100
Kevlar®	0.170	30e3	6e3	0.2	290	100	90

Table 3. Material properties of cores.

EXTENDED CORES						
Material	Balsa	Divinycell® H	Divinycell® HD	Core-Cell®	Rohacel®	
Density (kg/m <sup>3</sup> )	90	95	100	98	110	
E (MPa)	613	95	90	100	125	
G(MPa)	96	30	20	36	45	
S <sub>shear</sub> (MPa)	1.6	1.2	1.5	1.2	2.1	
HONEYCOMB CORES						
Material	Density (kg/m <sup>3</sup> )	Cell diameter (mm)	G <sub>13</sub> (MPa)	G <sub>23</sub> (MPa)	S <sub>13</sub> (MPa)	S <sub>23</sub> (MPa)
HRH-10	53	9.5	37	24.5	1.1	0.9
HRH-78	51	7	33	20	0.85	0.7

Table 4. Results of extended and honeycomb core laminated sandwich panels for various uniform pressure with panel dimensions:  $a = 800$ ,  $b = 700$ .

pressure	Lay. No.	Layer orientation	Layer material	$t_c$ (mm)	Core mat.	$F_f$
10	3	$\pm 45/\pm 45/0-90$	G/K/K	12	HRH-78	-1.1238
20	4	$\pm 45/0-90/0-90/0-90$	G/K/K/K	12	HRH-10	-1.3851
30	5	$0-90/0-90/\pm 45/\pm 45/\pm 45$	G/G/K/K/K	15	HRH-10	-1.6153
40	4	$\pm 45/\pm 45/0-90/0-90$	G/G/K/C	18	Corecel <sup>®</sup>	-1.7711
50	5	$\pm 45/\pm 45/0-90/0-90/0-90$	G/K/K/K/C	18	Div.HD	-2.0193
60	6	$0-90/\pm 45/0-90/0-90/0-90/0-90$	G/K/K/K/K/C	18	Div.H	-2.2220

## 5. CONCLUSION

Advanced GA operators for stacking sequence and layer materials selections are applied to a standard GA, to replace time-consuming calculations and reliability of this optimization problem. In this method, the searching efficiency is highly improved. From the analysis above, the following conclusions can be drawn.

1. Permutation and ply swap are two useful operators that modify GA standard operators. These operators reduce time consuming of search in each population with their applications and ameliorate pressure and diversity in each chromosome that are the basic concepts of GA program.
2. Deletion, alteration and addition are used to improve performance of mutation operator and behavior of GA to achieve the global optimum selection.
3. For fitness function, the effects of bonus and penalty parameter are very sensible and should be consider accurately. In this advanced GA optimization problem, these parameters are function of uniform pressure loaded on sandwich plate.
4. As shown in Table 4, honeycombs are better selection as sandwich panel cores in low pressure and by increasing pressure use of these cores decrease. In spite of them, extended cores such as foams and balsa are preferred in high pressure loaded sandwich panels.

**REFERENCES**

- [1] Zenkert, D., *An introduction to sandwich construction*, Cameleon press, London, United Kingdom, 1995.
- [2] Vinson, J. R., *The behavior of sandwich structures of isotropic and composite materials*, Technomic publication, Lancaster, Pennsylvania, U.S.A., 1999.
- [3] Soremkun, G. A., *Genetic algorithms for composite laminate design and optimization*, Master's thesis, Department of Engineering Science and Mechanics, Virginia Polytechnic Institute and State University, Blacksburg, VA, 1997.
- [4] Gantovnik, V. B., Gurdal, Z. and Watson, L. T., "A genetic algorithm with memory for optimal design of laminated sandwich composite panels", *Composite Structures*, Vol. 58, pp 513–520, 2002.
- [5] Riber, H. J., "Non-linear analytical solutions for laterally loaded sandwich plates", *Composite Structures*, Vol. 39, No. 1–2, pp 63–83, 1997.
- [6] Tsai, S. W., and Wu, E. M., "A general theory of strength for anisotropic materials", *Journal of composite materials*, Vol. 5, pp 58–80, 1971.

# DESIGNING SANDWICH INSERTS AND CORE JUNCTIONS FOR MAXIMUM STRUCTURAL STIFFNESS USING DISCRETE MATERIAL OPTIMIZATION

Jan Stegmann and Erik Lund

*Institute of Mechanical Engineering, Aalborg University, Pontoppidanstraede 101, 9220 Aalborg, Denmark*

js@ime.aau.dk, el@ime.aau.dk

**Abstract** In the present paper the structural optimization approach Discrete Material Optimization (DMO) is introduced and applied to stiffness maximization of locally reinforced sandwich structures. The aim of the optimization is for each element to choose the material from the set of candidate materials that minimizes the objective the most. A design study of a sandwich panel in three-point bending shows that the DMO method is successful in providing valuable clues to efficient design of such structures.

**Keywords:** multiphase material optimization, shell structures, composite laminates.

## 1. INTRODUCTION

The use of laminated composites has been steadily increasing in recent years, particularly in the aerospace, automotive and wind turbine industries, where laminated composites are used for e.g. hulls, stabilizers, car bodies and wings, which are all highly complex structures. Such structures consist of stiff fiber reinforced polymers or soft core materials stacked in a number of layers and bonded together by a resin, and the design problem is to determine the stacking sequence by proper choice of material and fiber orientation of each FRP layer in order to obtain the desired structural performance. This is a very challenging design problem that calls for use of sophisticated structural optimization tools.

To solve such problems efficiently the *Discrete Material Optimization* (DMO) method has been introduced in [1] for multi-layered shell structures in particular but the method has also been developed for single-layered 2D and 3D continua in general. In this work the DMO method is applied to detailed

2D models of sandwich panels with the purpose of finding clues to designing core inserts that will reduce the local strain and stress concentrations and thus increase strength.

The DMO method can be formulated for a number of design criteria but in the present work a global stiffness criteria is used. Thus, the objective of the optimization is to minimize the compliance (maximize the stiffness) of the structure, which is equivalent to minimizing the total strain energy. It has been shown that the design that fulfills this criteria is one of *uniform strain energy* provided that the mass and energy density are constant [2] and furthermore, that no geometrical constraints prevent it. This implies that the optimal stiffness design has a more uniform utilization of the material and thus that local strain and stress concentrations are reduced. However, for sandwich structures the mass and energy density is not constant due to the presence of multiple materials and consequently, the optimal designs obtained for such structures will in general not have uniform strain energy density for the entire domain but an “even distribution” of strain energy density (in some sense) over each material (or sub-domain). Still, the method can provide an improved design with a better utilization of material and a reduced level of local strain and stress concentrations, which is highly relevant for local reinforcement design.

The design optimization method described in this work is a gradient based technique that introduces a new parametrization of the problem. However, before this new parametrization is introduced the analysis tools used and the optimization problems to solve are described.

## 2. THE OPTIMIZATION PROBLEM

The discrete material optimization problem is stated as a minimization of compliance (maximization of stiffness), subject to a constraint on total mass, i.e. the optimization problem is one of finding the stiffest structure given a limited amount of material:

$$\begin{aligned} \text{Objective : } & \min \text{ Compliance} \\ \text{Subject to : } & \text{Static equilibrium} \\ & \text{mass} < \text{allowable mass} \end{aligned} \tag{1}$$

The governing equations are included in (1) as a constraint but in practice the optimization problem is solved using a NAND (Nested ANalysis and Design) approach where the governing equations are solved prior to solving the optimization problem.

Obtaining the structural response given a set of boundary conditions is done using the finite element method. Displacements will presently be assumed small and material behavior linear but the proposed parametrization can easily be used for nonlinear problems as well. The elements used are nine-node plane

elements and the element stiffness matrix,  $\mathbf{K}^e$ , is obtained in the standard way as:

$$\mathbf{K}^e = \int_V (\mathbf{B}^e)^T \mathbf{C}^e \mathbf{B}^e dV \tag{2}$$

where the matrix  $\mathbf{B}^e$  is the strain-displacement matrix and  $\mathbf{C}^e$  is the constitutive matrix of the element (the superscript  $e$  refers to “element”). As usual the global stiffness matrix is obtained as the sum of element stiffnesses over all elements,  $N^e$ , i.e.  $\mathbf{K} = \sum_{m=1}^{N^e} \mathbf{K}_m^e$ . This stiffness matrix is used to solve the linear static equilibrium:

$$\mathbf{K}\mathbf{u} = \mathbf{p} \tag{3}$$

where  $\mathbf{u}$  and  $\mathbf{p}$  are the global vectors of displacements and external forces, respectively. Hence the objective function for the minimization problem can be defined as the compliance,  $C$ , which is the work done by the external forces:

$$C(\mathbf{u}) = \mathbf{u}^T \mathbf{p} = \mathbf{u}^T \mathbf{K}\mathbf{u} = 2U \tag{4}$$

Here  $U$  is the total strain energy. Thus the optimization problem in (1) may be stated in more rigorous mathematical terms as:

$$\begin{aligned} \text{Objective : } & \min_{\mathbf{x}} C(\mathbf{u}) = \mathbf{u}^T \mathbf{p} \\ \text{Subject to : } & m \leq m_c \\ & \mathbf{0} \leq \mathbf{x}_{\min} \leq \mathbf{x} \leq \mathbf{1} \end{aligned} \tag{5}$$

where  $m$  is the mass of the structure,  $m_c$  is the allowable mass and  $\mathbf{x}$  contains the design variables. When doing multi material optimization the mass constraint is important since it effectively determines the amount of light material in the final structure.

Solution of the problem in (5) is done using analytical design sensitivities and the Method of Moving Asymptotes by Svanberg [3]. Consequently, the DMO method requires full access to the finite element source code.

### 3. THE DISCRETE MATERIAL OPTIMIZATION METHOD

The basic idea in the Discrete Material Optimization (DMO) parametrization is essentially an extension of the ideas used in structural topology optimization but in stead of choosing between solid and void we want to choose between any distinct number of materials. This methodology can be stated as: *for all elements in the structure find one distinct material from a set of pre-defined candidate materials such that the objective function is minimized.* This was first introduced as *multiphase topology optimization* by Sigmund and co-workers who used it for designing materials with extreme thermal expansion

and later also for designing materials with extreme bulk modulus [4, 5]. In this context different materials may be any material we can describe using a constitutive matrix e.g. such as Carbon or Glass Fiber Reinforced Plastic (CFRP / GFRP), polymer foam, steel, aluminum or any other material at any orientation (for orthotropic materials). As such, the proposed formulation is very versatile and can be used to optimize the material constitution of structures in general and composite structures in particular.

### 3.1 The methodology

As in topology optimization the parametrization of the DMO formulation is invoked at the finite element level. The element constitutive matrix,  $\mathbf{C}^e$ , is expressed as a weighted sum of pre-selected candidate materials, each characterized by a constitutive matrix,  $\mathbf{C}_i$ . In general, this may be expressed as a sum over the element number of candidate materials,  $n^e$ :

$$\mathbf{C}^e = \sum_{i=1}^{n^e} w_i \mathbf{C}_i = w_1 \mathbf{C}_1 + w_2 \mathbf{C}_2 + \dots + w_{n^e} \mathbf{C}_{n^e}, \quad 0 \leq w_i \leq 1 \quad (6)$$

It follows that the number of candidate materials is also the number of element design variables and if  $N^e$  is the number of elements, the total number of design variables for single layered structures is  $n^e \times N^e$ .

The weights,  $w_i$ , in (6) must have values between 0 and 1 as no matrix can contribute more than the physical material properties and a negative contribution is physically meaningless. In this way the weights on the constitutive matrices become “switches” that turn on and off stiffness contributions such that the objective is minimized and a distinct choice of candidate material is made. The task of the optimization is therefore to eliminate the influence of all but one of these materials by driving all but a single weight factor,  $w_i$ , to zero.

The simplest choice of weight functions would be to extend the classical topology optimization parametrization to multiple design variables,  $x_i$ , as:

$$\begin{aligned} \mathbf{C}^e &= \sum_{i=1}^{n^e} \underbrace{(x_i^e)^p}_{w_i} \mathbf{C}_i \\ &= (x_1^e)^p \mathbf{C}_1 + (x_2^e)^p \mathbf{C}_2 + \dots + (x_{n^e}^e)^p \mathbf{C}_{n^e}, \quad 0 \leq x_i \leq 1 \end{aligned} \quad (7)$$

In this formulation each design variable scales only one constitutive matrix and has no influence on any of the other matrices. To push the design variables towards 0 and 1 the SIMP method has been adopted by introducing the power,  $p$ , as a penalization of intermediate values of  $x_i$  (see e.g. [6] for details). The method in (7) is not very efficient as it fails to push the design to its limit values.

In stead we use the following interpolation, which is a simple extension of (7):

$$C^e = \sum_{i=1}^{n^e} \underbrace{\left[ (x_i^e)^p \prod_{j=1}^{n^e} [1 - (x_{j \neq i}^e)^p] \right]}_{w_i} C_i \tag{8}$$

The difference from (7) is the term  $(1 - x_{j \neq i}^e)$ , which is included so that an increase in  $x_i$  automatically involves a decrease in all other weights. This helps drive the design towards 0/1 and the method has proven quite effective for the problems tested. Writing out (8) more clearly illustrates the difference from (7):

$$C^e = \underbrace{(x_1^e)^p [1 - (x_2^e)^p] [1 - (x_3^e)^p]}_{w_1} C_1 + \underbrace{(x_2^e)^p [1 - (x_1^e)^p] [1 - (x_3^e)^p]}_{w_2} C_2 + \underbrace{(x_3^e)^p [1 - (x_1^e)^p] [1 - (x_2^e)^p]}_{w_3} C_3 \tag{9}$$

The disadvantage of (8) is that the weighting functions in general do not add up to unity, which is highly impractical when computing physical quantities such as structural mass. To circumvent this a scaled version of (8) could be used such that the weight factors are expressed as:

$$w_i = \frac{\bar{w}_i}{\sum_{k=1}^{n^e} \bar{w}_k} \tag{10}$$

where  $\bar{w}_i$  are computed as  $w_i$  in (8). This formulation gives faster convergence to a “near optimum” compliance value but it cannot converge fully since it is less effective in driving the weights to 0/1 since the scaling to unity alters the effect of the penalization (see [7] for details).

### 3.2 Implementation

The method has been implemented in the finite element based system MUST [8], which is aimed at analysis and design of structural problems as well as multidisciplinary problems such as fluid-structure interaction problems. The system is capable of reading input from an external preprocessor such as Ansys. To run the optimization it is only necessary to add the following information to the input file:

- Information about the analysis to perform (linear/nonlinear, stress, buckling etc.)
- Definition of the optimization problem to solve (objective and constraint functions)

- Specifications for the optimization algorithm about number of iterations, convergence criteria, penalization powers etc.
- Definition of design variables. A specified design variable may be linked to a material set or a real constant set in the finite element model, and one design variable specification automatically generates a number of design variables for the problem. The design variables may be generated automatically either for each finite element or for a patch of elements (for example for a group of elements linked to the same material or the same constant set).
- Definition of the candidate materials to use. Each design variable is linked to a list containing information about the number of layers to use, the number of design variables for each layer, the candidate materials to use and their orientation for each layer. Finally, initial values of the design variables can be defined or computed automatically to ensure uniform initial weighting.

Thus, it is a relatively simple task to run an optimization on an existing analysis model provided that the analysis model is well defined in terms of materials.

#### 4. NUMERICAL EXAMPLE – SANDWICH PANEL

The three-point bending problem has been studied extensively with respect to local reinforcement by e.g. [9, 10] and the results seem to be very promising with regard to lowering the local strains and stresses by fairly simple means. In this example we apply compliance minimization to the three point bending problem to investigate if this method will provide useful clues to efficient designs.

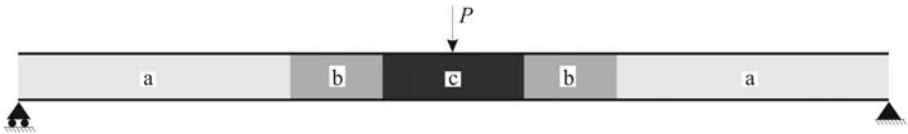


Figure 1. Sandwich panel with applied center load and support conditions. The three regions,  $a$ ,  $b$  and  $c$ , allow for various configurations of the core material.

The panel under consideration has a length of  $L = 800$  mm and a height of  $h = 44.2$  mm. The core accounts for  $h_c = 40$  mm and layers of  $h_f = 2.2$  mm make up the top and bottom face sheets, see Figure 1. The face sheets are orthotropic glass/epoxy with  $E_x = 54$  GPa,  $E_y = 18$  GPa,  $G_{xy} = 9$  GPa and  $\nu_{xy} = 0.25$  and the fibres are oriented along the length of the panel. The core is taken to be isotropic polymeric foam with  $E = 60$  GPa,  $\nu = 0.3$  and  $\rho = 60$  kg/mm<sup>3</sup> – this material will be designated Foam A.

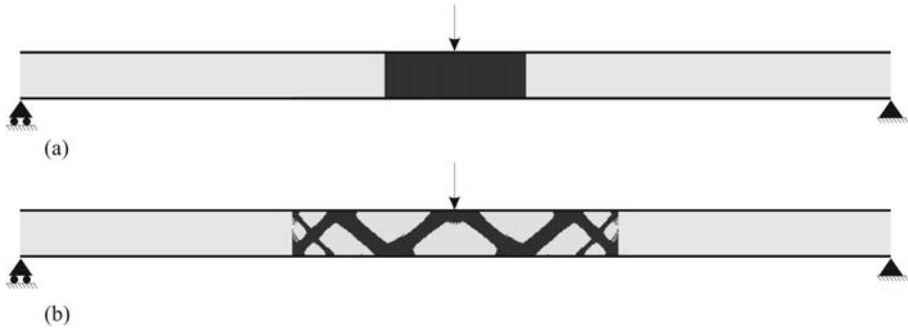


Figure 2. Sandwich panel with reference material distribution (a) and material distribution obtained using DMO. Light grey is Foam A, dark grey is Foam B.

The design study starts from an initial design where region  $c$  in Figure 1 is taken to be a higher density polymeric foam, Foam B, with  $E = 310$  GPa,  $\nu = 0.3$  and  $\rho = 200$  kg/mm<sup>3</sup> while regions  $a$  and  $b$  remain as Foam A. This constitutes the most simple reinforcement imaginable and will serve as a *reference solution* in the following, see Figure 2(a).

Now, the design optimization is set up by allowing the optimizer to choose between Foam A and Foam B in regions  $b$  and  $c$  in Figure 1, but with the restraint that the total mass must not exceed the total mass of the reference solution. The panel is modeled with a finite element mesh of 35 200 9-node 2D elements and the number of elements in the design regions is 12 000, which brings the number of design variables to 24 000 (two design variables pr. element - Foam A or Foam B). The optimization successfully identifies a distinct material in each element, resulting in the material distribution shown in Figure 2(b).

Not surprisingly, the result of the optimization is a truss-like reinforcement pattern, which is a typical result in topology optimization. The deflection of the center point is in the optimized configuration reduced by 6.5% but more interestingly, the strain energy distribution within each material, Foam A and B, is considerably more “smooth” in the optimal design as shown in Figure 3. This is important in relation to reducing local strain concentration, but the optimizer cannot generate uniform strain energy density since two materials will always be present.

However, the obtained design would not be easy to realize so in stead we use the geometric components from Figure 2(b) to construct two alternative designs. The characteristic feature of the optimal design is the slope of the material reinforcement, which can found to approximately 40°. The most simple reinforcement is therefore an inclined, solid region (a wedge) with a slope of 40°, see Figure 4(a). Another possibility would be to let the core follow the truss design in the optimal result as illustrated in Figure 4(b). To keep the re-

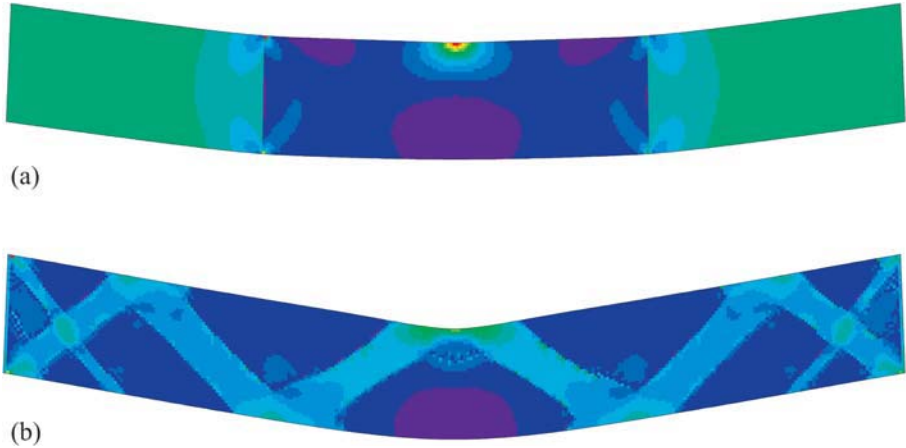


Figure 3. Strain energy density distribution in the design region for (a) initial design and (b) optimized design. Displacement scale is 10 for both plots.



Figure 4. Suggested design based on optimization results. Light grey is Foam A, dark grey is Foam B.

inforcement local, only the first two bends are included – this reduces the total weight of the core by approximately 20% since the amount of both Foam A and B is reduced.

The resulting designs both perform better than the initial design in Figure 2(a) in terms of smooth energy density distribution, but both designs have a slightly larger center point displacement, see summary in Table 1. This is natural for the truss-like design because the amount of material, both Foam A and B, has been significantly reduced. For the wedge design, the increased displacement is a result of the large amount of virtually unstrained material towards the bottom face sheet, see Figure 5. For the truss-like structure the maximum strain energy density occurring in and around the design region has been significantly reduced to about 35% compared to the initial design, see Table 1. Whether the suggested designs will actually perform better than the initial design must be investigated through experimental methods.

## 5. CONCLUSIONS

In the present paper Discrete Material Optimization (DMO) is introduced as a gradient based technique for maximizing structural stiffness (and thus

Table 1. Comparative table of design performance relative to the initial design in Figure 1(a).

	max strain energy density	max displacement
Initial design	1.000	1.000
Optimized design	502*	0.939
Wedge design	1.204	1.014
Truss-like design	0.354	1.019

\* This is an artificial result caused by strain concentrations in the regular finite element mesh.



Figure 5. Strain energy density distribution in the design region for (a) solid 40° wedge design and (b) truss-like design. Displacement scale is 10 for both plots.

strain energy) of locally reinforced sandwich structures by optimizing material choice. The method operates on a fixed domain, i.e. shape and thicknesses are defined *a priori* and remain fixed, and as such we deal entirely with solving a material selection problem. The DMO method is derived from multiphase material optimization in the sense that the element stiffness is computed from a weighted sum of candidate materials. The aim of the optimization is for each element to choose the material from the set of candidate materials that minimizes the objective the most. The candidate materials may be either isotropic or orthotropic with a given fiber angle.

A design study of a sandwich panel in three-point bending shows that the DMO method is successful in finding a minimum compliance design. The result cannot be realized directly, but based on the result, two derived reinforcements are suggested and investigated in detail with regard to strain energy density distribution. The study shows that the strain energy density distribution can be significantly improved, thus reducing the occurrence of local strain

and stress concentration. As such, the design study shows that the DMO optimization can provide valuable clues to efficient design of locally reinforced sandwich structures.

The Discrete Material Optimization method is currently being extended to local criteria and geometrically nonlinear structural behavior. Only single load cases have been studied here, but facilities for multiple load cases have also been implemented using a weighted sum formulation for the compliance, such that a real life load spectrum can be taken into account.

## REFERENCES

- [1] J. Stegmann and E. Lund. Discrete material optimization of general composite shell structures. *International Journal for Numerical Methods in Engineering*, 62(14):2009–2027, 2005.
- [2] P. Pedersen. *Optimal Designs – Structures and materials, Problems and Tools*. Department of Mechanical Engineering, Technical University of Denmark, 2003. [www.fam.mek.dtu.dk/pp.html](http://www.fam.mek.dtu.dk/pp.html).
- [3] K. Svanberg. The method of moving asymptotes – A new method for structural optimization. *Numerical Methods in Engineering*, 24:359–373, 1987.
- [4] O. Sigmund and S. Torquato. Design of materials with extreme thermal expansion using a three-phase topology optimization method. *Journal of the Mechanics and Physics of Solids*, 45:1037–1067, 1997.
- [5] L.V. Gibiansky and O. Sigmund. Multiphase composites with extremal bulk modulus. *Journal of the Mechanics and Physics of Solids*, 48:461–498, 2000.
- [6] M.P. Bendsøe and O. Sigmund. *Topology Optimization – Theory, Methods and Applications*. Springer, second edition, 2003.
- [7] J. Stegmann. *Analysis and Optimization of Laminated Composite Shell Structures*. Ph.D. Thesis, Institute of Mechanical Engineering, Aalborg University, Denmark, 2004. Special report no. 54.
- [8] MUST. Institute of Mechanical Engineering, Aalborg University, Denmark. [www.ime.aau.dk/must](http://www.ime.aau.dk/must), June 2004.
- [9] E. Bozhevolnaya and A. Lyckegaard. Structurally graded core inserts in sandwich panels. *Composite Structures*, 68:23–29, 2005.
- [10] E. Bozhevolnaya and A. Lyckegaard. Local effects at core junctions of sandwich structures under different types of load. *Composite Structures*, 2005, in press.

# **FRACTURE AND DAMAGE TOLERANCE**

# ON RESIDUAL COMPRESSIVE STRENGTH PREDICTION OF COMPOSITE SANDWICH PANELS AFTER LOW-VELOCITY IMPACT DAMAGE

Zonghong Xie<sup>1</sup>, Anthony J. Vizzini<sup>2</sup> and Mao Yang<sup>1</sup>

<sup>1</sup>*College of Astronautics, Northwestern Polytechnical University, Xi'an, 710072, China; Email: xzhae@nwpu.edu.cn*

<sup>2</sup>*Department of Aerospace Engineering, Mississippi State University, Mississippi State, MS 39762, USA. Email: vizzini@ae.msstate.edu*

**Abstract** This paper introduces a Nonlinear Finite Element Analysis on damage propagation behavior of composite panels under in-plane uniaxial quasi-static compression after a low-velocity impact. The major damage modes due to the impact were incorporated into the model. A consequential core crushing mechanism was incorporated into the analysis. The critical far field stress corresponding to the onset of damage propagation near the damage zone was captured successfully with a good correlation with experimental data. These values can be used to predict the residual compressive strength of low-velocity impacted composite sandwich panels.

**Keywords:** sandwich structures, impact, delamination, finite element method.

## 1. INTRODUCTION

Sandwich structures in aerospace applications can offer a very high specific bending stiffness due to their optimal use of components. However, these sandwich panels usually have very low damage resistance and are susceptible to impact damage. Damages from low energy impact are of particular concern in aerospace applications because they can lead to 30% to 40% reduction in compressive strength of composite sandwich panel [1], while easily go undetected in routine visual inspections. Damages at or below the Threshold of Detectability (TOD) must be considered during the

damage tolerant design and in the establishment of inspection methods and intervals of aerospace sandwich panels.

This work focuses on damage tolerance study of composite sandwich panels with Barely Visible Impact Damage (BVID). Typically, the major damage modes of BVID include the permanent indentation on the impacted front facesheet, partially crushed core beneath the impacted location, and the delaminations between the plies of the front facesheet, as shown in Figure 1.

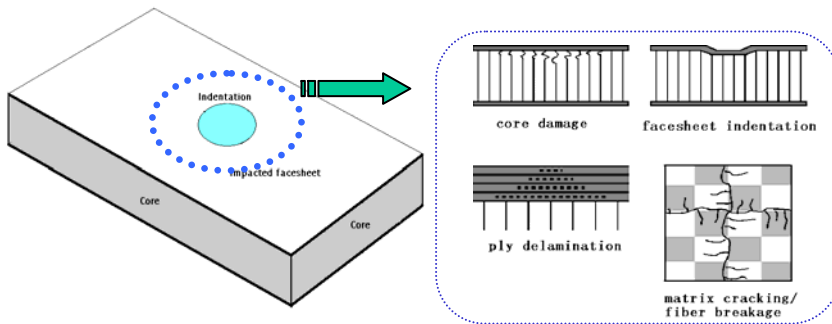


Figure 1. The composite sandwich panel with low-velocity impact damage.

The present of many forms of the damage modes make modeling the damage region very difficult. In the published literature, work on numerical modeling of both the sandwich construction and the damage modes to study the residual strength of an impact damaged composite sandwich panel is quite limited. Kassapoglou simplified the problem by modeling all the effects of impact damage as a single equivalent delamination [1]. This one-parameter analogous model cannot indicate actual damage propagation. Minguet modeled the damage as an initial indentation in the facesheet with a damaged core beneath the impacted site [2]. His model captured the lateral indentation propagation behavior. Tsang modified Minguet's method by only considering the impacted facesheet and modeling the core under it as a two-parameter elastic foundation [3]. Moody developed Minguet and Tsang's method by incorporating a compliance change in material at the impacted location to include the effect of the material damage [4]. None of the forgoing models have considered all the major impact damage modes physically existed.

Individual simplifications such as loss in stiffness, equivalent delamination, or residual indentation may not capture all of the damage mechanisms required for an accurate analysis of the sandwich compression after impact behavior. In this work, all the major impact damage modes, including the residual indentation, the initially crushed core, and the delaminations were incorporated into the finite element model with corresponding geometric parameters measured from the real specimens to study the problem. A consequential core crushing mechanism was included

in the analysis by using element deactivation technique through a solving-control program coded in ANSYS Parametric Design Language (APDL) [5]. Sandwich Compression After Impact (SCAI) tests were conducted. The numerical results were compared with the experimental data for validation purpose.

## **2. SANDWICH COMPRESSION AFTER IMPACT TEST**

Sandwich Compression After Impact (SCAI) Tests were performed as an experimental approach to obtain the residual compressive strength of composite sandwich panels after low-velocity impact [3, 4, 6, 7].

SCAI tests conducted at the Composite Research Laboratory (CORE) at University of Maryland, College Park successfully revealed the damage propagation behavior of low-velocity impacted composite sandwich panels under in-plane uniaxial compression [7]. Sandwich panels, comprised of two thin laminated facesheets and honeycomb core, were manufactured with dimensions of 356mm in length, 82mm in width, and 25.6mm in thickness. The facesheets were made by AS4/3501-6 graphite/epoxy unidirectional pre-impregnated tape with lay-up sequence of  $[0/90]_s$ . The core material was Phenolic (Nomex) honeycomb core with 3mm cells. A BVID was inflicted at the center of the panel using a drop tower with a 25mm diameter stainless steel hemispherical tup at impact energy of about 5.88 Joules. Strain gages were placed along the central lines of the impacted facesheet in both longitudinal and width direction. Each specimen was fixed in two ends in longitudinal direction and compressed on the uniaxial testing machine under stroke (displacement) control until the ultimate catastrophic failure occurred.

The general damage propagation behavior and failure mechanism were observed in the tests: first the indentation in the impacted facesheet becomes bigger and deeper; then part of laminate surrounding the damage region becomes unstable and the indentation begins to propagate in the width direction, i.e. the direction perpendicular to the load; under increasing compressive load, indentation keeps propagating until its edge reaches a critical location roughly between 25mm and 30mm away from the damage center along the width central line; a sudden fracture across the damage region in the impacted facesheet occurs at this moment, causing a complete loss in its load bearing capacity; load then all transfers to the back facesheet, which buckles and breaks immediately; the catastrophic failure of the whole sandwich structure occurs.

From SCAI tests, once the damage propagates to a critical location on the impacted facesheet, subsequent catastrophic failure occurs immediately. This suggests that one effective approach to predict the final catastrophic failure

of impact damaged sandwich structures might be to predict the initiation of the damage propagation at critical locations on the path of indentation propagation.

Data of strain gage readings, stroke, and load were all collected in the tests. By plotting the far field stress against the strain gage reading on the path of damage propagation, one can easily determine the far-field stress applied corresponding to the initiation of damage propagation at strain gage locations. Figure 2 shows a typical data curve from the SCAI test on a specimen numbered UMD-A3-1. The far field stress is defined as the compressive load divided by the sum of the cross section areas of two facesheets. This value serves as a global parameter to represent the load bearing capacity of the whole sandwich structure. The longitudinal strain is the strain gage reading of gage 2 located 25 mm away from the center of the damage zone along the width direction. It provides critical local information of the initiation of damage propagation at strain gage 2.

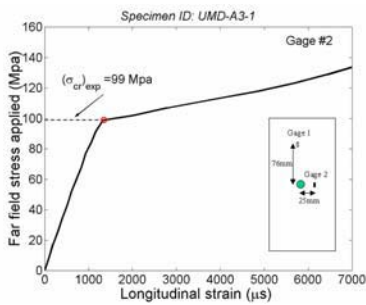


Figure 2. Far field stress vs. longitudinal strain (typical test data).

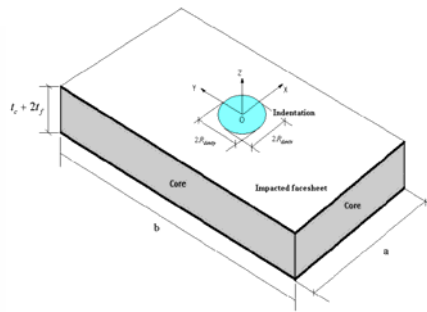


Figure 3. The coordinate system in FEA.

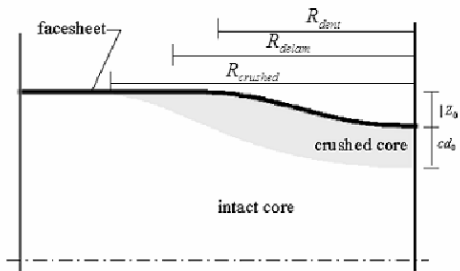
On the test data curve, the point where the curve slope suddenly decreases corresponds to the initiation of damage propagation at this strain gage location. On this point, the honeycomb core under the strain gage 2 suddenly is crushed due to excessive compressive stress. Consequently, the facesheet above loses the support, resulting in a sudden increase of local deformation and local strain. An apparent softening point then occurs.

The far field stress corresponding to this apparent softening point can be used to predict the residual compressive strength of the damaged sandwich panel. For this specific case, the characteristic stress is about 99 MPa with less than 5% variation due to the chosen interval in test data collection.

### 3. FINITE ELEMENT MODEL DESCRIPTION AND SOLUTION

Finite Element Method is used to numerically simulate SCAI test. Several assumptions are made in the modeling: no flaws on specimens except for the specific damage from low-velocity impact; no penetration on the impacted facesheet; no significant in-plane material damage (fiber breakage or resin fracture) in the impacted area (i.e. no significant compliance change in facesheet material in the impact region); the core material is incapable of sustaining any load once it crushes.

As shown in Figure 3, the origin of the coordinate system for the model is chosen at the center of the residual indentation with the  $x$ - $y$  plane lying on the top surface of the impacted facesheet. The  $x$ -axis and  $y$ -axis are along the width and longitudinal directions respectively, while the  $z$ -axis is normal to



the impacted facesheet, pointing towards the outside of the panel.  $a$  and  $b$  are the width and length of composite sandwich panel.  $t_f$  and  $t_c$  are the thickness of the facesheet and core material.  $R_{dentx}$  and  $R_{denty}$  are the radii of the residual indentation in  $x$  and  $y$  axis respectively.

Figure 4. Cross section through damage region [7].

#### 3.1 Damage characterization and modeling

The low-velocity impact damage includes indentation on the impacted facesheet, a corresponding region of crushed core, and delaminations within the facesheet. Figure 4 sketches the cross section of typical impact damage on a sandwich panel.  $R_{dent}$ ,  $R_{delam}$  and  $R_{crushed}$  represent respectively the in-plane radii in either longitudinal or transverse directions (either  $x$  or  $y$  directions) of initial indentation, delamination, and initial core crushing region.  $|Z_0|$  and  $cd_0$  stand for the maximum depth of the indentation and the core crush region (measured from the bottom of the impacted facesheet) respectively.

The in-plane radii  $R_{dent}$  and the maximum depth  $|Z_0|$  of indentation were measured by using a dial gage and the table of a milling machine, where the dial gage was used to measure the out-of-plane location of the facesheet while the milling machine table provided for an accurate measurement of the

in-plane location of dial gage probe. The in-plane radii of delamination and the parameters for core crushing region were measured from sectioned sample specimens. The detail information regarding damage characterization can be found in [7].

The residual indentation is assumed to be in a shape of one-half ellipsoidal surface defined as:

$$\frac{x^2}{(r_x)^2} + \frac{y^2}{(r_y)^2} + \frac{z^2}{(r_z)^2} = 1 \quad (1)$$

where  $r_{x,y,z}$  are corresponding to  $R_{dentx}, R_{denty}, |Z_o|$  respectively.

The part of the core crushed in the impact event is modeled as a gap between the facesheet and untouched core material. The cut-off was defined by Equation (1) also with  $R_{dentx}, R_{denty}$ , and  $cd_0 + |z_0|$  substituting  $r_x, r_y$ , and  $r_z$  respectively.

Delaminations can only be determined through sectioning of sample specimens. According to the study of Kassapoglou [1], the delamination between the innermost ply and its neighbor in the impacted facesheet is the largest one with the most significant influence on structural behavior. To reduce the complexity in modeling, only this delamination is included in the current model. It is defined as a gap between the aforementioned two layers with an elliptical in-plane shape:

$$\frac{x^2}{(r_{delamx})^2} + \frac{y^2}{(r_{delamy})^2} = 1 \quad (2)$$

### 3.2 Nonlinear core crushing behavior

Honeycomb core is quite different from normal continuums in material properties as a cellular solid. Flatwise core crushing test was conducted to investigate the material characteristics of honeycomb core. The test setup is illustrated in the left hand side in Figure 5.

In this test, 25 mm thick Nomex honeycomb core with 3 mm diameter cells were cut into 50 mm by 50 mm blocks. All the core specimens were compressed along the thickness direction with two steel plates put on both bottom and top of specimens to make sure that the load is evenly distributed over the plane. The specimen is compressed under stroke (displacement) control on MTS machine until crushed to about 75% of its original thickness.

A typical stress vs. strain curve from the flatwise honeycomb core crushing test is plotted on the right hand side in Figure 5, in which the stress is the compressive load divided by the in-plane cross section area of core specimen and the strain is the stroke (displacement) divided by the original honeycomb core thickness. This picture shows that there exists an ultimate core crushing strength  $(\sigma_3^{core})_{ultimate}$  corresponding to the crippling of a virgin honeycomb core. After the initiation of the core crushing, the stress suddenly drops to about one-half of this ultimate value. The core keeps being

crushed thereafter under roughly constant compressive stress, resulting in a plateau section in the stress/strain curve. This constant compressive stress is named as plateau strength  $(\sigma_3^{core})_{plateau}$ , which is corresponding to the core crippling strength after the initiation of core crushing.

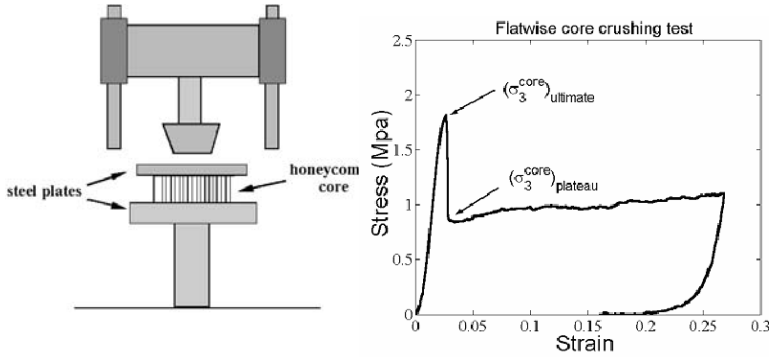


Figure 5. Flatwise core crushing test and resulting stress vs. strain curve.

### 3.3 Model description

The whole sandwich panel, including two laminated facesheets and honeycomb core, was modeled in ANSYS5.7. Major damage modes due to low-velocity impact, including the residual indentation, the partially crushed core and the delamination, were all incorporated into the model with corresponding geometric parameters characterized from the real test specimens. Layered 8-node solid elements were used for the laminated facesheets. Orthotropic 8-node solid elements were used for the honeycomb core. Delamination was incorporated into the model with point-to-surface contact elements defined along its two sides. Due to the symmetries, only one quarter of the sandwich structure was modeled as shown in Figure 6.

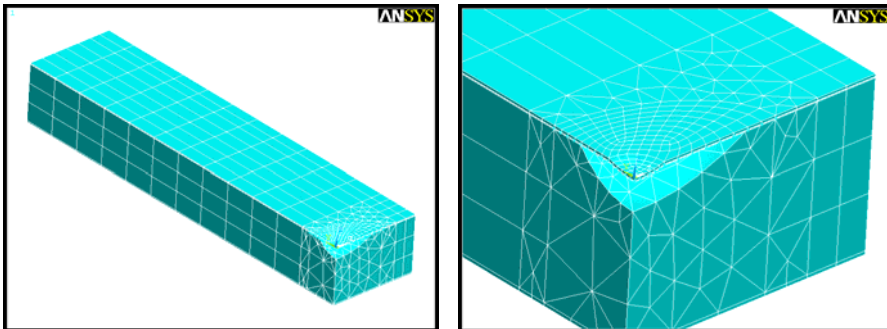


Figure 6. Meshed finite element model with enlarged damage zone.

The sandwich panel was fixed on the two ends in the longitudinal direction while free on two other sides like in SCAI tests. A uniform in-plane displacement in the longitudinal direction under stroke control was applied quasi-statically on one end of the panel.

A program developed in ANSYS Parametric Design Language (APDL) was used to control the solving process as well as incorporate the nonlinear consequential core crushing mechanism into the analysis via an element deactivation technique [5]. Postprocessing was performed. The numerical results were compared with experimental data.

## 4. RESULTS ANALYSIS

### 4.1 Nominal far field stress vs. local strain

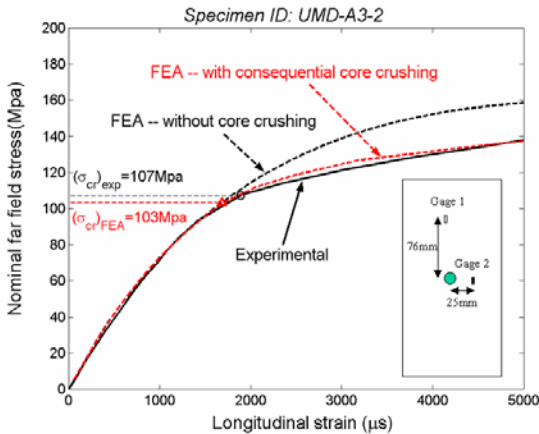


Figure 7. Comparison of FEA results with test data.

The nominal far field stress is defined as the sum of the reaction force in the longitudinal direction at the end of the panel divided by the cross section area of two facesheets. The local strains are the strain component in the loading direction at the strain gage locations. These strain values are point values and do not represent the averaging effect of the strain gages.

Figure 7 shows the curve of nominal far field stress vs. local strain from results of finite element analysis on specimen UMD-A3-2 along with the corresponding experimental data from the SCAI test. A good correlation between the mathematical results and experimental data can be seen. The far field stress corresponding to the initiation of the damage propagation at the strain gage location has been successfully captured in the finite element analysis. For this specific case, according to the finite element results, the estimated nominal far field stress corresponding to the onset of damage propagation at the location 25mm away from the damage center in the width direction is around 103 MPa, which is very close to the value of 107 MPa from experimental data.

According to SCAI tests, once the damage propagates to a critical strain gage location, catastrophic failure of the whole sandwich construction happens right away. Therefore, the nominal far field stress corresponding to the initiation of damage propagation at a carefully chosen critical location on the path of damage growth can be used as a characteristic value to predict the residual compressive strength of damaged composite sandwich panels. As stated above, this characteristic far field stress can be captured accurately via both experimental and numerical approaches.

For the sandwich panels with BVID studied at University of Maryland, if the critical strain gage location is chosen at the point 25mm away from the center of original impact damage on the width central line of the impacted facesheet, the characteristic far field stress is around 110 MPa, while the residual strength of the panel is roughly about 1.3 times of this value according to experimental data.

## 4.2 Indentation propagation

Two profiles are defined along the centerlines on the top of the impacted facesheet. The out-of-plane deflections along these two profiles indicate the pattern of damage propagation in the width and longitudinal directions ( $x$  and  $y$  directions here). Figure 8 shows the pattern of deflections along  $x$  and  $y$  profiles with the elimination of global bending effect. Note that the dash-dot lines indicate the edge of initially crushed core and  $\Delta D$  stands for the far field displacement (stroke) applied.

Figure 8 shows that the indentation becomes deeper and wider when the far field displacement increases. Under increasing load, indentation propagates in the width direction ( $x$ -axis) until the final failure of structure due to progressive core crushing, while is arrested in the longitudinal direction ( $y$ -axis). These indentation propagation behaviors are as same as those observed in the SCAI tests.

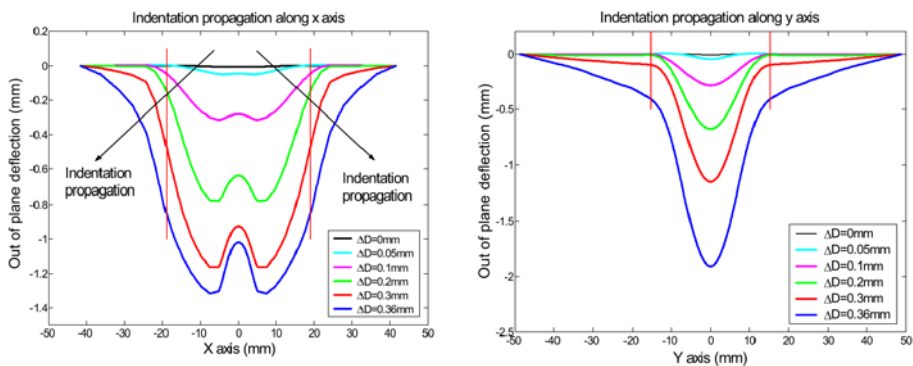


Figure 9. Indentation propagation along width and longitudinal directions.

## 5. CONCLUSIONS

Major low-velocity impact damage modes on a composite sandwich structure, including permanent indentation, delamination, initially crushed core with expanded area, were all incorporated into the nonlinear Finite Element Model. The consequential core crushing mechanism was introduced into the analysis.

Indentation propagation behavior same as that observed in SCAI tests was successfully captured in Finite Element Analysis. The far field stress vs. local strain curve showed a good correlation with the experimental data. Consequential core crushing that triggers the progressive damage propagation has been successfully captured along the path of damage growth. It is shown as an apparently softening point on a far field stress vs. local strain curve from both experimental and numerical data.

SCAI tests repeatedly show that once the damage propagation reaches a critical location on the path of damage growth, catastrophic failure of the whole structure occurs right away. Thus, the far field stress corresponding to the onset of the damage propagation at a specified critical location along the damage propagation path can be used to predict the residual load bearing capacity, i.e. the residual strength, of impact damaged composite sandwich structures.

Both the SCAI tests and Finite Element Analysis show that the damage propagation is a local phenomenon. In general, it has little influence on the behavior of the untouched side of the panel.

## REFERENCES

1. Kassapoglou, C., Jonas, P. J., and Abbott, R., "Compressive Strength of Composite Sandwich Panels after Impact Damage: An Experimental and Analytical Study," *Journal of Composite Technology & Research*, Vol. 10, 1988, pp.65-73.
2. Minguet, Pierre J., "A model for predicting the behavior of impact-damaged minimum gage sandwich panels under compression," AIAA91-1075-CP, 1991.
3. Tsang, P.H.Wilson, June 1994, "Impact resistance and damage tolerance of composite sandwich panels," Ph.D thesis, Massachusetts Institute of Technology.
4. Moody, R.C. and Vizzini, A.J., "Incorporation of a compliance change due to impact in the prediction of damage growth in sandwich panels," Proceedings of the 13th International Conference on Composite Materials, Beijing, China, June 2001.
5. ANSYS Incorporation, "APDL Programmer's Guide," SAS IP Inc., 2000.
6. Cvitkovich, M.K. and Jackson, W.C., "Compressive Failure Mechanisms in Composite Sandwich Structures," *Journal of the American Helicopter Society*, Vol. 44, No. 4, October 1999, pp. 260-268.
7. Moody, R.C., "Damage Tolerance of Impacted Composite Sandwich Panels," Thesis for Master of Science, University of Maryland at College Park, 2002.

# INVESTIGATION OF PARAMETERS DICTATING DAMAGE AND ENERGY ABSORPTION CHARACTERISTICS IN SANDWICH PANELS

G. Zhou<sup>1</sup>, M. Hill<sup>1</sup> and N. Hookham<sup>2</sup>

<sup>1</sup>*Department of Aeronautical and Automotive Engineering, Loughborough University,  
Loughborough, Leicestershire LE11 3TU, UK*

<sup>2</sup>*Hexcel Composites, Duxford, Cambridge CB2 4QD, UK*

**Abstract** Bending behaviour of composite-skinned sandwich panels with both aluminium and nomex honeycombs have been investigated under a quasi-static loading with both HS and FE indenters. Damage mechanisms were identified as core crush, top-skin delamination and skin failure. A combination of skin thickness and indenter nose shape dictates not only the nature of these damage mechanisms but also their energy-absorbing capacity.

**Keywords:** sandwich panels, damage characteristics, composite skins, energy absorption.

## 1. INTRODUCTION

Light weight sandwich panels generally consist of strong, stiff and thin composite skins and weak but thick core. They have now been widely used for load-bearing purposes in the aerospace, land transport, marine and civil construction industries due to their high specific bending stiffness and strength under distributed loads in addition to their good energy-absorbing capacity. For aerospace applications usually involving honeycomb cores, meeting a minimum damage tolerance requirement has the profound effect on the design of honeycomb sandwich panels [1]. This could be especially so, if the damage is induced by a concentrated load [2-7]. The variation of a finite cell size and discontinuous contact surfaces of the honeycomb core could react differently to changes in diameter [2-3, 5-6] and/or the nose

shape [7] of indenter/impactor. As a result, the thickness of composite skins [2-3, 4, 6-7] and the density [3, 7] and thickness [2, 6] of the core need to be tailored in a design analysis to meet a specific performance requirement. A multitude of damage mechanisms could thus occur at different stages of loading, dependent on specific combinations of the parameters. Major damage mechanisms in the composite sandwich panels in bending include core crush, skin-core debond, skin delamination and skin fracture. The understanding of initiation and propagation of these damage mechanisms as well as their energy-absorbing characteristics therefore imposes a tremendous challenge.

The present investigation is intended to study damage mechanisms of composite-skinned sandwich panels in bending with both aluminium and nomex honeycombs and their potential change induced by varying skin thickness, core density and indenter nose shape. The additional focus is on energy-absorbing characteristics of identified damage mechanisms. Both quasi-static and impact loads were applied, only the results associated with a quasi-static loading are discussed here. A fuller discussion of aluminium honeycomb sandwich panels was reported in [7].

## 2. SANDWICH MATERIALS AND PANEL MANUFACTURE

Composite skins were made of unidirectional carbon/epoxy T700/LTM45-EL prepreg with a ply thickness of 0.128 mm. A symmetric lay-up of  $(0/90)_{ns}$  ( $n = 1, 2, 3, \text{ or } 4$ ) was selected due primarily to the strength considerations. Three types of 5052 aluminium honeycomb used are 3.1-3/16-10 ( $50 \text{ kg/m}^3$ ), 4.4-3/16-15 ( $70 \text{ kg/m}^3$ ) and 5.7-3/16-20 ( $90 \text{ kg/m}^3$ ). The honeycomb core depth was 12.7 mm for all the cores. Adhesive VTA260 was selected for interfacial bonding. Two types of nomex honeycomb used are HRH-3/16-4.0 ( $64 \text{ kg/m}^3$ ) and HRH-3/16-6.0 ( $96 \text{ kg/m}^3$ ). Nomex was dried before being bonded at  $65^\circ\text{C}$  for 8 hours.

Laminate skins of  $0.3 \times 0.3 \text{ m}$  were laid up with UD prepreps for four different thickness, each of 4, 8, 12, or 16 plies. They were cured in an autoclave at  $60^\circ\text{C}$  under a pressure of 0.62 MPa (90 psi) for 18 hours. To aid adhesion, the skins were degreased before bonding. Each skin was separately bonded to the core in an oven at  $60^\circ\text{C}$  for 16 hours. The sandwich panel was then cut into four smaller panel specimens each of  $150 \text{ mm} \times 150 \text{ mm}$  using a diamond coated slitting saw. Two strain gauges were bonded on each specimen with one at the bottom centre in parallel with  $0^\circ$  fibres and the other at 20 mm away from the top centre (to avoid being damaged during

loading). Here the 0° direction of carbon fibres in the skins was aligned to the ribbon direction of the honeycomb core.

### 3. EXPERIMENTAL PROCEDURES

To understand damage initiation and propagation in the sandwich panels subjected to bending, both bending and local indentation tests on a rigid base were conducted. For the bending tests, each sandwich panel specimen was clamped between two thick steel plates with a 100-mm annular ring cut-out as shown in Figure 1 and was loaded with either a hemispherical (HS) or flat-ended (FE) steel indenter of 20 mm in diameter. For the local indentation tests, either the sandwich panels or the honeycomb cores were held onto a rigid base and were loaded in the same manner.

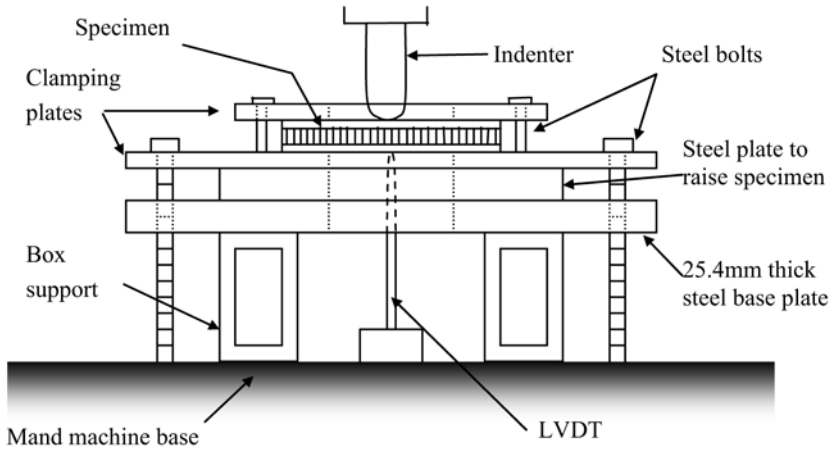


*Figure 1.* Experimental set-up of a panel bending test.

All the tests were carried out at a loading rate of 5 mm/min on a Mand universal testing machine. Applied load, indenter displacement and strain gauge data were recorded through an Orion delta 3530D acquisition system, in addition to the deflection of the bottom surface of the panel using a linear variable differential transformer (LVDT). A number of diagnostic tests were carried out to determine the nature of damage, and the corresponding specimens were sectioned for a microscopic study. The mechanical properties of cross-ply composite skins required for analysis were determined experimentally in tension, compression, in-plane shear, flexure and interlaminar shear (ILS) according to respective ASTM standards.

#### 4. DAMAGE MECHANISMS IN SANDWICH PANELS

The nature of the initiation and propagation of damage mechanisms was ascertained through examination of response curves and microscopic inspection of cross sections cut from the corresponding diagnostic specimens. The bending behaviour of the sandwich panels up to catastrophic failure is represented by four complete load-displacement curves as shown in Figure 2. Either two or three distinctive stages of deformation are identified and are characterised by the critical loads for initial damage and secondary damage and/or ultimate failures. These characteristics are clearly dependent on a combination of skin thickness and indenter nose shape in addition to core density. The critical loads are very repeatable. The common damage features are that the catastrophic failure was always found to correspond to failure of the top skin with the bottom skin remaining undamaged.

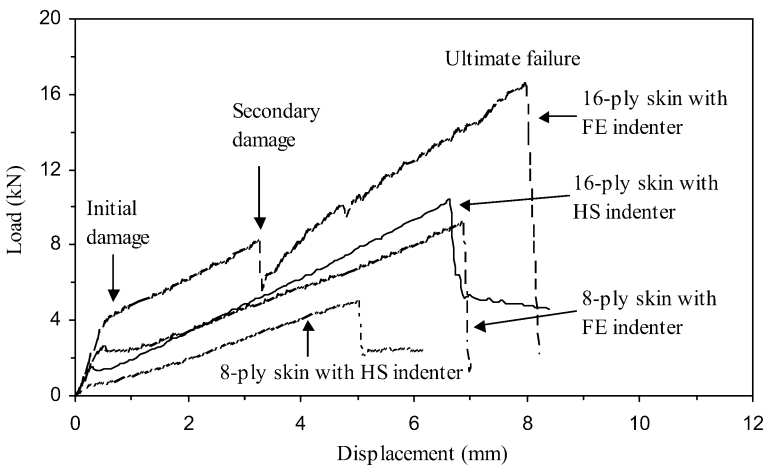
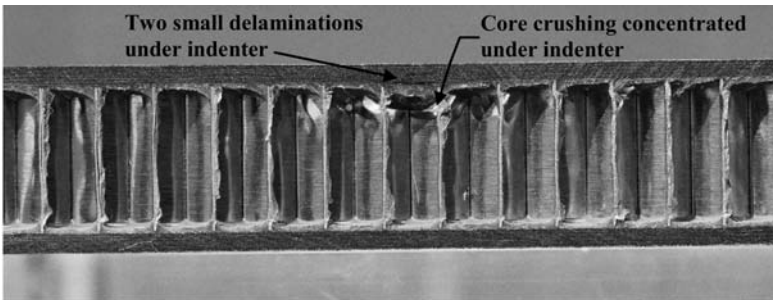


Figure 2. Load-displacement curves of sandwich panels with 70-kg/m<sup>3</sup> aluminium core.

The nature of damage mechanisms at the initial threshold load varies, depending primarily on indenter nose shape and skin thickness [7]. For the HS indenter, it was found to be a combination of core crush and small delaminations in the top skin in the shape of a cone due to high local stress concentration, as shown in Figure 3. When the skin is relatively thin, the flexural rigidity of the sandwich panels is relatively low. As a result, the bending resistance of the top skin was too small to shield the contact stress so that the large amount of this stress was directly transferred to the core underneath in a steady manner (without a load drop). Thus as the skin thickness was increased, the load drop appeared and its magnitude increased. Under the FE indenter, the initial damage mechanism induced was found to

be just core crush with no top-skin delamination. Since an increase in skin thickness increased the blunting effect on the honeycomb underneath, core crush becomes an unstable event so that the previous trend is reversed. That is, the initial load drops are visible only in panels with 4-ply and 8-ply skins and do not appear for 12-ply and 16-ply skins. In addition, there is no local skin-core debond before the ultimate failures, so the load transfer from the top skin to the core was good.



*Figure 3.* A photograph of a failed sandwich panel with 12-ply skins and 70-kg/m<sup>3</sup> core.

Beyond the initial threshold load, a slope reduction of 60% to 80% indicates a rapid densification of core crush. For panels loaded by the HS indenter, such densification was also accompanied by propagation of the top-skin delaminations. For panels loaded by the FE indenter, continued core crush and spreading left the top skin unsupported so that delaminations occurred in the top skin and is indicated by a load drop in Figure 2 as the secondary damage. The thicker skins (e.g. 16 plies) had more profound load drops. A slight slope stiffening can also be observed due to stretching of the top skins. Although the continued core crush and spreading could also contribute to the slope stiffening, the fact that the crushed core depth reached only the middle depth of the sandwich panel suggests that skin damage and stretching provided the major bending resistance. Figure 4 shows a failed sandwich panel with aluminium core loaded by the HS indenter.

#### **4.1 Effect of skin thickness**

Increasing skin thickness (by less than 23% with respect to the overall panel thickness) generally increases not only the flexural rigidity of the sandwich panels but also local bending and indentation resistance. As shown in Figure 5, the initial threshold loads were increased with increasing skin

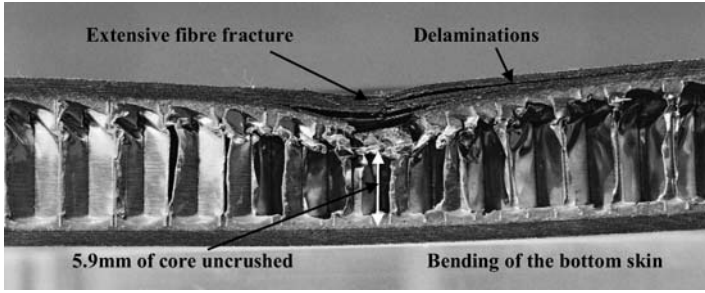


Figure 4. A photograph of a failed sandwich panel with 12-ply skins and 70-kg/m<sup>3</sup> core.

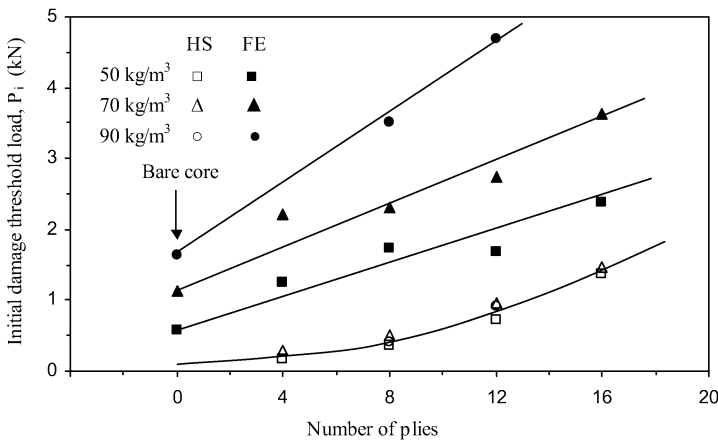


Figure 5. Variation of initial damage threshold loads with the variation of skin thickness.

thickness. While such increase seems non-linear for the HS indenter independent of core density, it is more or less linear for the FE indenter. The thicker the core is, the greater the increase becomes.

In Figure 6, the ultimate failure loads also increased almost linearly. Here, core density did not contribute to such increase, as expected, since the top skin was found earlier to primarily provide the load-bearing capacity. Such enhancement is estimated to be around 0.52 kN per ply for the HS indenter and 0.97 kN per ply for the FE indenter.

### 4.2 Effect of indenter nose shape

Varying the indenter nose shape with the same diameter of 20 mm induced by far the most significant effects on the initial threshold and ultimate failure loads shown in Figures 5 and 6. In particular, the nature of induced damage mechanisms was different. The fundamental difference

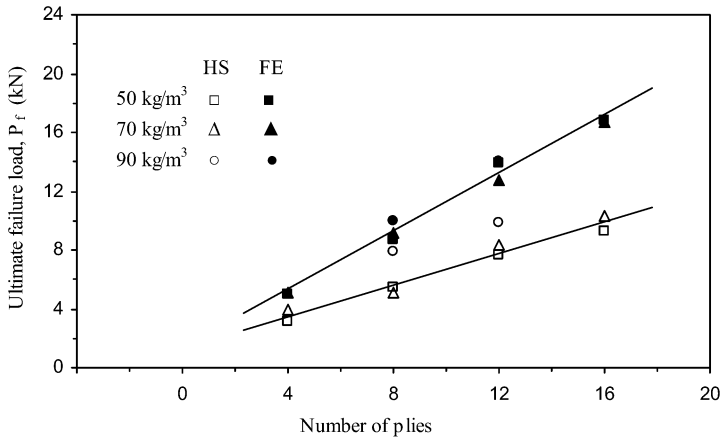


Figure 6. Variation of ultimate failure loads with the variation of skin thickness.

between the two nose shapes lies in contact areas and pressure distributions. The contact area of the HS indenter increased with load due to bending and local indentation. Moreover, the highest contact pressure was at the apex as depicted in [8]. On the contrary, the contact area of the FE indenter remained constant during loading and was equal to the cross-sectional area of the indenter. The highest contact pressure was around the indenter edge [8] so that the load was distributed over a larger skin area, which in turn provided greater resistance. Moreover, the extent of core crush in this case is much greater than that of skin delamination. As a result, greater membrane stretching of the skins could be involved. Because of these differences, a two-stage deformation process was identified for the HS indenter, consisting of the simultaneous occurrence of core crush and the onset of delamination in the top skin and continued core crush and delamination propagation up to the top skin fracture. A three-stage deformation process was established sequentially for the FE indenter with core crush, the onset of delamination in the top skin and continued core crush and shear-out of the top skin. Core crush under this circumstance was more of a ‘flexural’ nature, thereby providing greater resistance. All these results indicate that the HS indenter with much greater stress concentration imposes a greater threat to sandwich panels than the FE indenter. Interestingly, the fact that the slopes in the post-initial-damage regions of the curves do not differ much suggests that continued core crush is insensitive to the variation of indenter nose shape.

### 4.3 Effect of honeycomb density

The relatively low density of the honeycomb cores used in this investigation is intended for the sandwich panels to absorb a substantial

amount of energy before their load-bearing capacity is exceeded. As a result, the limited linear elastic region of the bending behaviour means that the effect of varying core density by a relatively modest amount on the panel flexural rigidity is equally limited. This is indicated in Figure 2, in Figure 5 for the initial threshold loads associated with the HS indenter and in Figure 6 for the ultimate failure loads. Although an exception to these is that the denser cores did increase the initial threshold loads substantially associated with the FE indenter, varying core density did not affect the nature of the identified damage mechanisms. This is in accordance with the early finding that the loading-bearing capacity is dictated by the strength of the top skin.

#### 4.4 Effect of honeycomb material

Nomex honeycomb sandwich panels were made only with either 8-ply or 12-ply skins. Their bending response is compared with that of aluminium honeycomb sandwich panels in Figure 7. The flexural rigidity of the latter in the elastic region is almost twice that of the former. Beyond the initial threshold, the rest of the bending behaviour is very similar in terms of slope and ultimate load. Since the nomex density is less than half of aluminium, nomex honeycomb sandwich panels may have some advantage, especially in consideration of energy absorption.

### 5. ENERGY ABSORPTION CHARACTERISTICS

In the present sandwich panels with relatively weak cores and thin skins, the initial threshold loads are only 10% to 30% of the respective ultimate failure loads. Panel deflections at the initial thresholds constitute between 20% and 30% of respective total displacements for the HS indenter and between 40% and 50% for the FE indenter. The responses after the initial threshold loads were almost linear. This type of the bending behaviour characteristics provide an indication of a good energy-absorbing potential.

The absorbed energy (AE) was calculated as the closed area of each load-displacement curve. The displacement at which loading was reversed beyond the peak (ultimate failure) load was chosen such that the passage of the peak was ensured. To avoid inconsistency, an incident energy (IE) defined by the area under the load-displacement curve with the load linearly following down to the displacement axis from the peak is used instead. Measured AE was found to be within 94% of IE. As shown in Figure 8 for panels with aluminium core, IE increases by 2.43 J per ply for the HS indenter, irrespective of core density. For the FE indenter, IE increases more sharply as more honeycomb cells were crushed as discussed earlier. For thin-skin (4-

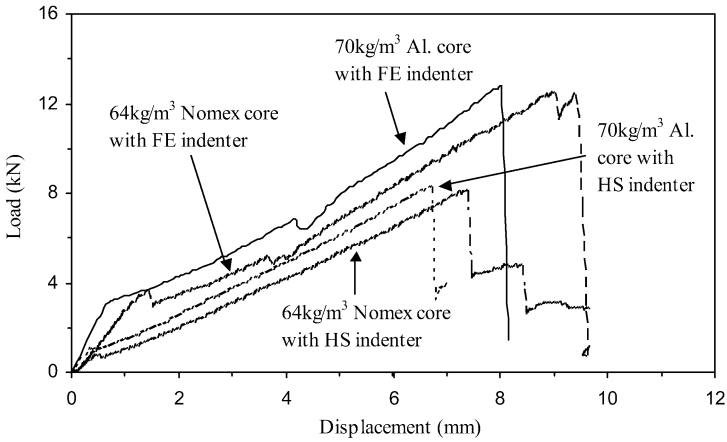


Figure 7. Load-displacement curves of sandwich panels with both nomex and aluminium cores.

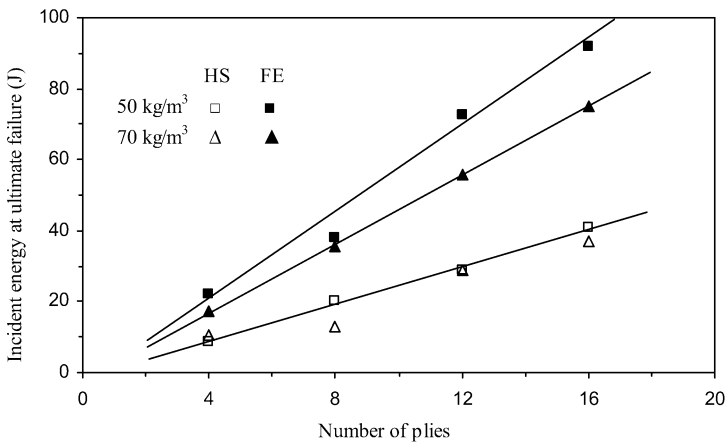


Figure 8. Variation of absorbed energy with skin thickness and indenter nose shape.

ply and 8-ply) panels associated with the FE indenter, their IE increased by 4.26 J per ply. For panels with 12-ply and 16-ply skins, increasing core density seems to have led to a reduction of energy absorption. This strongly suggests that the trends of improving the damage resistance and the energy absorption capacity of the sandwich panels could be opposite so that a balance between the two must be achieved.

In addition, either IE or AE via the aforementioned damage mechanisms is only partial as the complete core crush and failure of the bottom skin can absorb the significant additional amount of energy.

## 6. CONCLUSIONS

Clamped composite-skinned honeycomb sandwich panels in bending have been investigated under quasi-static loading with both HS and FE indenters. The identified damage mechanisms are a simultaneous occurrence of core crush and the onset of delamination in the top skin and continued core crush and delamination propagation up to the ultimate skin failure for the HS indenter. For the FE indenter, they are core crush, top skin delamination and continued core crush and top skin shear-out. Either increasing skin thickness or changing indenter nose shape not only significantly increased both the initial threshold and ultimate failure loads but also dictated the energy-absorption capacity of the panels. Under the FE indenter, the occurrence of top skin delamination required loads much higher than that for core crush. Increasing core density was shown to have affected neither the critical loads nor the energy-absorbing capacity.

## REFERENCES

1. Kassapoglou, C., Jonas, P.J. and Abbott, R., Compressive strength of composite sandwich panels after impact damage: an experimental and analytical study, *J. of Composite Technology and Research*, 10, 65-73, 1988.
2. Williamson, J.E. and Lagace, P.A., Response mechanisms in the impact of graphite/epoxy honeycomb sandwich panels, *Proc. of 8<sup>th</sup> American Society for Composites*, 287-297, 1994.
3. Tsotsis, T.K. and Lee, S.M., Characterisation of localized failure modes in honeycomb sandwich panels using indentation, *Composite Materials: Testing and Design, ASTM STP*, 1274, 139-165, 1996.
4. Herup, E. and Palazotto, A.N., Low-velocity impact damage initiation in graphite/epoxy/nomex honeycomb-sandwich plates, *Composites Science and Technology*, 57, 1581-1598, 1997.
5. Hoo Fatt, M.S. and Park, K.S., Dynamic models for low-velocity impact damage of composite sandwich panels-Part B: damage initiation, *Composite Structures*, 52, 353-364, 2001.
6. Raju, K.S. and Tomblin, J.S., Damage characteristics in sandwich panels subjected to static indentation using spherical indentors, *AIAA-2001-1189*, 103-111, 2001.
7. Zhou, G., Hill, M., Loughlan, J. and Hookham, N., Damage characteristics of composite honeycomb sandwich panels in bending under quasi-static loading, to appear in *J. of Sandwich Structures and Materials*.
8. Zhou, G., Static behaviour and damage of thick composite laminates, *Composite Structures*, 36, 13-22, 1996.

# REAL-TIME DAMAGE DETECTION OF HONEYCOMB SANDWICH STRUCTURES USING SMALL-DIAMETER FIBER BRAGG GRATING SENSORS

Shu Minakuchi, Yoji Okabe and Nobuo Takeda

*Dept. of Advanced Energy, Graduated School of Frontier Sciences, The University of Tokyo, 5-1-5 Kashiwanoha, Kashiwa-shi, Chiba 277-8561, Japan*

**Abstract** The authors developed new techniques to detect inside damages in honeycomb sandwich structures using small-diameter optical fiber sensors. We embedded sensors in the adhesive layer between the core and the facesheet. From a decrease in the transmitted optical power and the change in the form of the reflection spectra from fiber Bragg grating (FBG) sensors, the debonding and the impact damage could be detected sensitively in real-time.

**Keywords:** honeycomb sandwich structures, optical fiber sensors, debonding, impact damage.

## 1. INTRODUCTION

Honeycomb sandwich structures consist of a lightweight thick honeycomb core and two strong skins such as carbon fiber reinforced plastic (CFRP) laminates bonded by thin adhesive films. Since they have high specific stiffness and high thermal insulation property, they are expected to be more applied to aerospace structures. But honeycomb sandwich structures are deteriorated by the complicated damages, such as debonding and impact damage as shown in Figure 1. Excessive load than expected one, repeated loads or water absorption in the core introduce the debonding between the core and the facesheet. Since the weakest region in the structure against the out-of-plane loading depends on the material combinations of the core, the

adhesion and the facesheet, the fracture pattern of debonding varies for each combination. In the Figure 1 (a), the core with the fillet peels off the facesheet. The fillet is defined as the adhesive rich region formed at the root of the core walls. On the other hand, in Figure 1 (b), the fillet is broken and the cohesion failure is induced. After the impact loading such as tool drop or sudden strikes of birds and stones, the core walls beneath the impact region crush and the facesheet is highly deformed. Although these three kinds of damages are very difficult to be visually found from the outside, they cause significant reduction in the in-plane compressive strength. In order to improve the reliability of honeycomb sandwich structures, smart technology to detect inside damages in-real time is needed [1, 2].

In this research, we applied small-diameter fiber Bragg grating (FBG) sensors, whose outside diameter is  $52\mu\text{m}$ , to detect the debonding and the impact damage quantitatively in real-time.

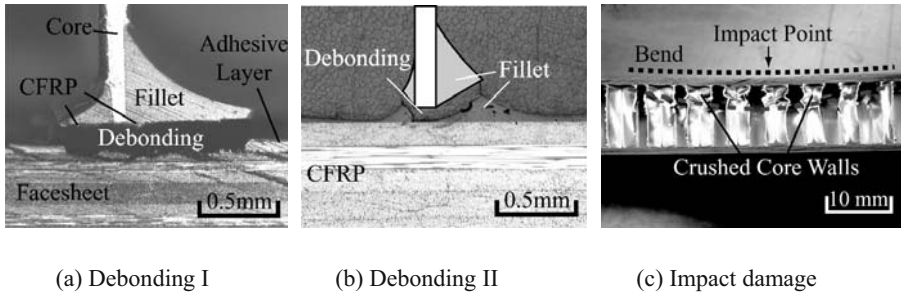


Figure 1. Damages in honeycomb sandwich structures.

## 2. DAMAGE DETECTION TECHNIQUES

Newly developed techniques of the damage detection are shown in Figure 2. The small-diameter FBG sensors are embedded in the adhesive layer (typical thickness:  $125\ \mu\text{m}$ ) between the core and the facesheet. When the debonding I is induced, the intensity of transmitted light decreases by the micro bend or the breakage of the optical fiber. When the debonding II is caused, the reflection spectrum from FBG sensor recovers its original shape by the release of non-uniform thermal residual strain along the sensors induced by fillets. On the other hand, when the impact damage is introduced, the bend of the facesheet induces the tensile and the compressive stresses in the FBG sensor at convex and concave parts, respectively. Consequently, the reflection spectrum is deformed due to the impact damage. With these three techniques, we detect the damages in the honeycomb sandwich structures

quantitatively in real-time. These techniques have the potential to be applied to honeycomb sandwich structures with any material combinations.

The specimens used in this research consist of the CFRP facesheet and the aluminum honeycomb core. This configuration is the most popular one for aerospace structures. Since the fracture pattern depends on the material combination of specimen, we used many kinds of the facesheet and the core. The adhesive to bond the facesheet and the core was REDUX312UL (HEXCEL Co.) for all specimens.

When the small-diameter FBG sensors are embedded in the adhesive layer, there is no space for optical fibers to go through because the core and the facesheet closely contact. Hence small slits were formed on the top of the core walls by a wire discharge cutter. The cross-sectional micrograph of the embedded small-diameter optical fiber is shown in Figure 3. The optical fiber is embedded in the adhesive layer successfully.

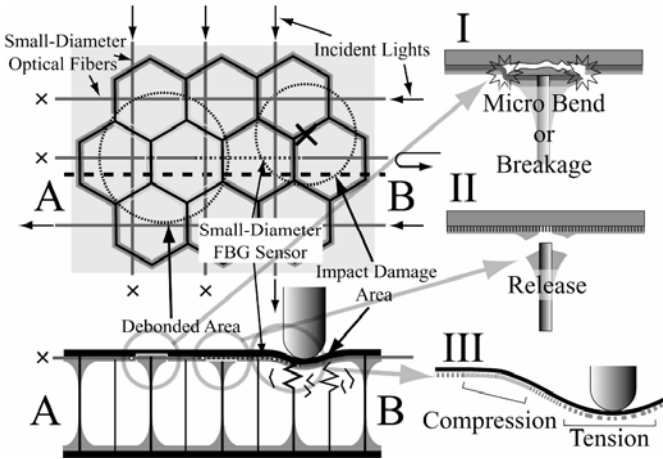


Figure 2. Damage detection techniques.

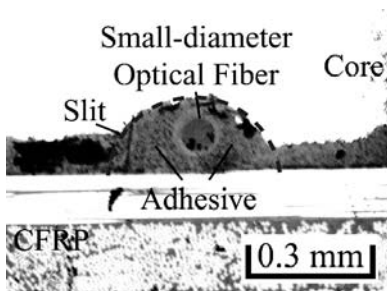


Figure 3. Cross-sectional micrograph of the embedded small-diameter optical fiber.

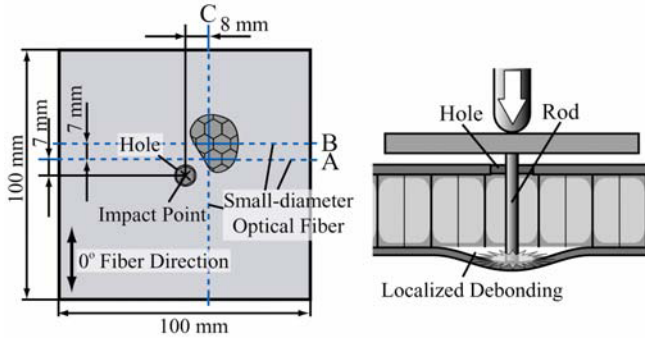
### 3. DEBONDING DETECTION

#### 3.1 Debonding detection using decrease in transmitted optical power

The specimen is shown in Figure 4. The facesheet is CFRP (UM55/#144, TOHO TENAX Co., Ltd., [0/90/45/-45]<sub>s</sub>) and the core is aluminum honeycomb (AL 1/4-5052-001, Showa Aircraft Industry Co., Ltd.). Three optical fibers A, B and C were embedded in the adhesive layer. Since the debonding caused in the actual use is localized and invisible from outside, we modified the specimen to introduce the real debonding. A hole, whose diameter is about 10 mm, was drilled through the upper facesheet and a rod was inserted. We applied impact loading to the lower facesheet through the rod by a drop-weight impactor (Mini-Tower, INSTRON). During the impact loading, the optical fibers were illuminated by a LD light source (AQ4211(155), Ando Electric Co., Ltd.) and the transmitted optical powers were measured with an optical power meter (AQ2732, Ando Electric Co., Ltd.).

The measured transmitted optical powers are shown in Figure 5. The changes in the power were observed in A and C. From this result, A and C seemed to pass through the debonded area. It was expected that A suffered from a strong micro bend at the center of the debonded area and it was finally broken. On the other hand, C suffered from a weak micro bend at the edge of the debonded area so that the transmitted optical power hardly changed. In order to find out the positions where the loss of the transmitted light was caused, the specimen was inspected with an ultrasonic microscopic (UM-3, Olympus) and by illumination of the optical fibers with He-Ne laser. The comparison of these observations is shown in Figure 6. As expected from the changes in the transmitted optical powers, A and C passed through the debonded area, and furthermore the He-Ne laser light leaked in the debonded area.

These results indicate that we can detect the debonding from the decrease in the transmitted optical power and furthermore identify the size and the location of the debonding from the positions of the damaged optical fibers.



(a) Specimen with three embedded optical fibers (b) Debonding test

Figure 4. Schematics of the experiment for debonding detection.

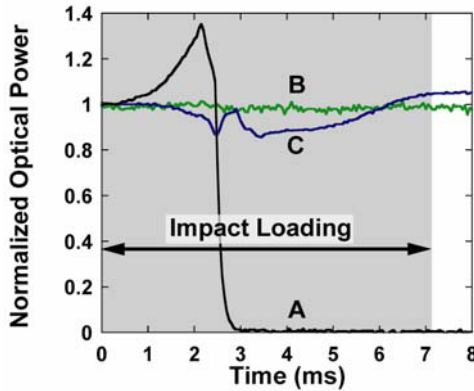
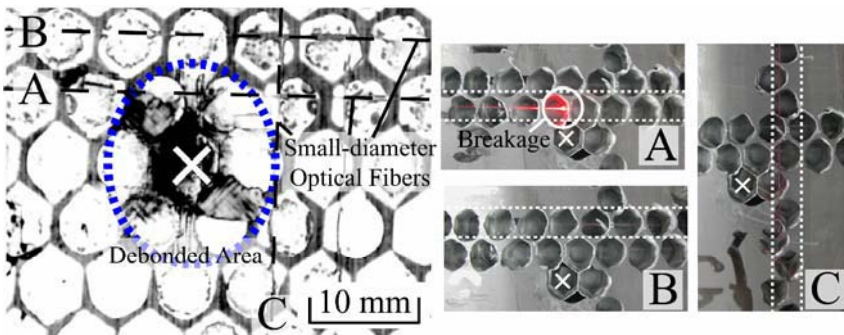


Figure 5. Measured transmitted optical powers of three optical fibers.



(a) Ultrasonic C-scan

(b) Leakage of He-Ne light

Figure 6. Photographs of ultrasonic C-scan and leakage of He-Ne light.

### 3.2 Debonding detection by monitoring of reflection spectrum from FBG sensor

The specimen consists of CFRP facesheets (T700S/2500, Toray Industries, Inc., [0/90/45/-45]<sub>s</sub>) and aluminum honeycomb core (AL 1/4-5052-003, Showa Aircraft Industry Co., Ltd.). As shown in Figure 7, the small-diameter FBG sensor is embedded in the adhesive layer. The gage length is 10 mm, and the center of the sensor was just below the core wall. First, the reflection spectra during the curing process of adhesive films were measured to investigate the effect of the fillet on the spectrum. The optical fiber was illuminated by an amplified spontaneous emission (ASE) light source (AQ4310(155), Ando Electric Co., Ltd.) and the reflection spectrum from the FBG was measured by an optical spectrum analyzer (AQ6317, Ando Electric Co., Ltd.).

The observed spectra are shown in Figure 8. At the room temperature of 25 °C before curing, the spectrum had only one sharp narrow peak. Also at curing temperature of 125 °C, the spectrum kept its shape and the center wavelength shifted to longer wavelength corresponding to the temperature increase. However, at room temperature of 25 °C after the curing process, the form of the spectrum was distorted obviously. Since the fillets are formed at the curing temperature of 125 °C, this may be due to the non-uniform thermal residual strain caused by the fillet. Debonding is detected using this phenomenon. It is expected that the spectrum will recover its original shape if the non-uniform thermal residual strain is released by debonding of the core with the fillets from the facesheet.

The measured reflection spectra during the flatwise tensile loading by a material testing system (AG-I, Shimazu Co.) are shown in Figure 9. The form of the spectrum changed corresponding to the out-of-plane tensile loading. This indicates that the out-of-plane strain can be measured from the change in the spectrum. After debonding, the components away from the maximum peak disappeared and the spectrum almost recovered its original shape as expected.

In order to confirm the experimental results, the theoretical simulation was conducted. As shown in Figure 10, all of the CFRP facesheets, the aluminum honeycomb core, the adhesive layer, the fillets, and the small-diameter FBG sensor were modeled in detail for finite element analysis (FEA) with ABAQUS code. Especially, after debonding, the structure was modeled by removing the core and the fillets. By this analysis, tri-axial normal strain applied to the FBG before and after debonding was calculated. The reflection spectra were simulated using a couple mode theory and a transfer matrix method from the strain distributions along the FBG.

Figure 11 shows the change in the calculated strain distributions caused by the occurrence of debonding. As shown in these graphs, large non-uniformity of the strain appears around the fillet and is relieved by the debonding. Moreover, the reflection spectra calculated using the strain distribution are shown in Figure 12. Since the calculated spectra before and after the debonding reproduced the change in the measured reflection spectra very well, the experiment was confirmed to be appropriate and it was found that the debonding can be detected by monitoring of the spectrum shape.

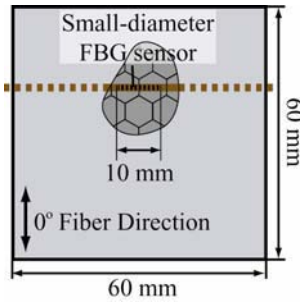


Figure 7. Specimen with embedded FBG sensor.

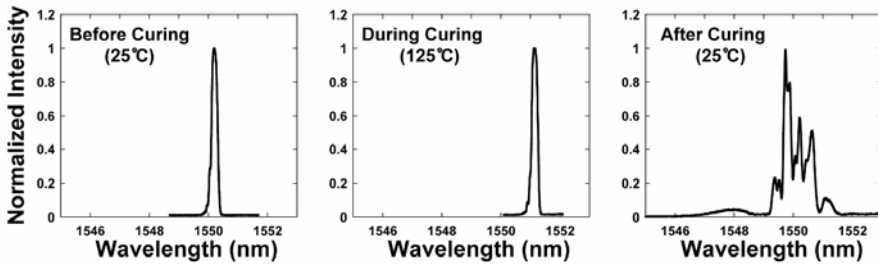


Figure 8. Measured spectra during the curing process of the adhesive films.

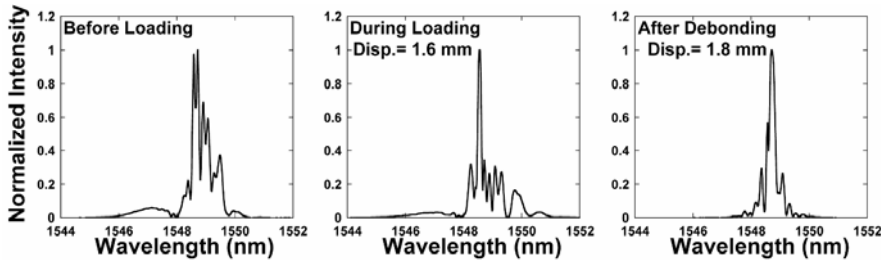


Figure 9. Measured spectra during flatwise tensile loading.

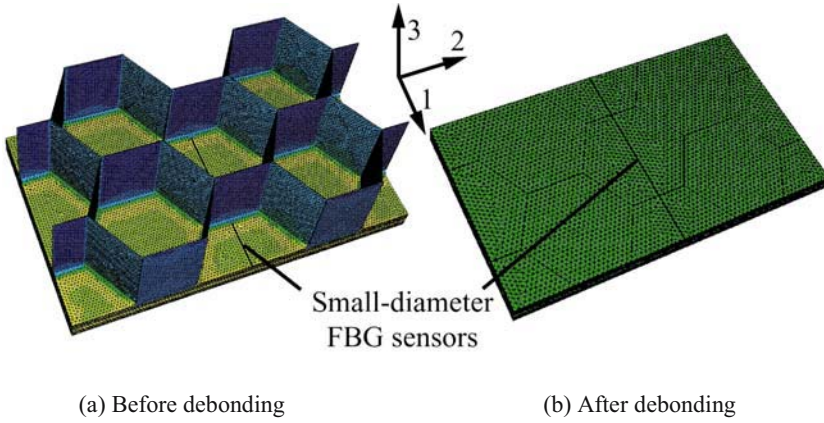


Figure 10. Finite element models.

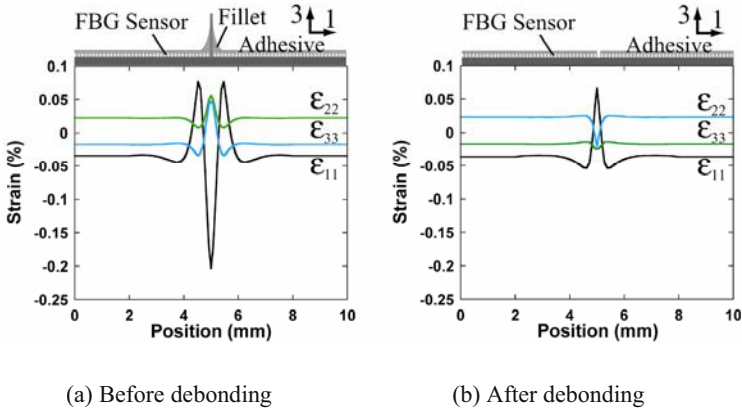


Figure 11. Calculated strain distributions along the FBG.

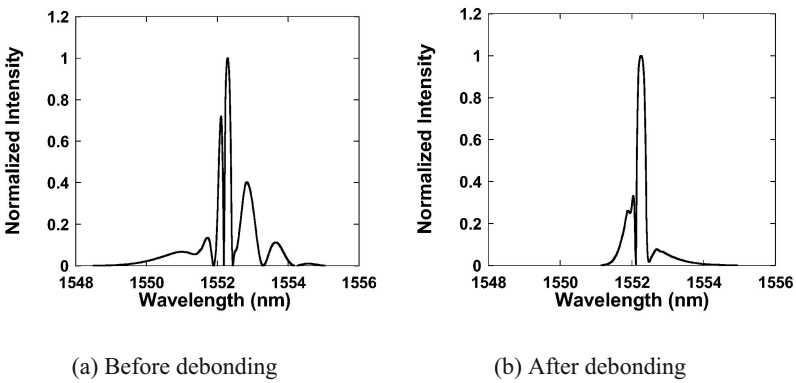


Figure 12. Calculated reflection spectra. These spectra correspond to the measured spectra in Figure 9.

#### 4. IMPACT DAMAGE DETECTION

Since chirped FBGs have grating period that increases monotonously, the Bragg wavelength is different depending on the position and the reflection spectrum becomes broad. Thus the reflection spectrum from the chirped FBG is expressed as a function of the position along the grating. In this research, the chirped FBG sensors were applied to detect the impact damage more quantitatively. The gage length of the sensor was 50 mm. As shown in Figure 13, the longest grating period part of the sensor was positioned near the impact point where the tensile strain was expected to be generated after the impact loading. In Figure 13, the part of the shorter and the longer grating period are expressed by black and white in the gradation, respectively. Two levels of impact energies of 1.0 J and 2.0 J were applied to the center of the specimen with a drop-weight tester. It is expected that the strain distribution along the sensor changes sensitively as the impact damage becomes larger, and the reflection spectrum becomes broader. After each impact loading, the deformation of the facesheet was measured by a CCD laser displacement sensor (LK-030, Keyence).

The measured deformation of the facesheet and the reflection spectra are shown in Figure 14. As the impact energy increased, the dent of the facesheet became deeper and broader. On the other hand, the spectrum before impact loading has periodical distortions. The number of the dips in the spectrum was eight and agreed with that of the fillets located above the sensors. This indicates that the spectrum was disturbed by the distribution of the non-uniform thermal residual strain due to the fillets. Then, the spectrum deformed after the impact loading. As the impact damage became larger, the tensile and the compressive strains along the sensor increased, and the spectrum became broader, consequently. It was confirmed that the impact damage could be detected quantitatively with the chirped FBG sensor.

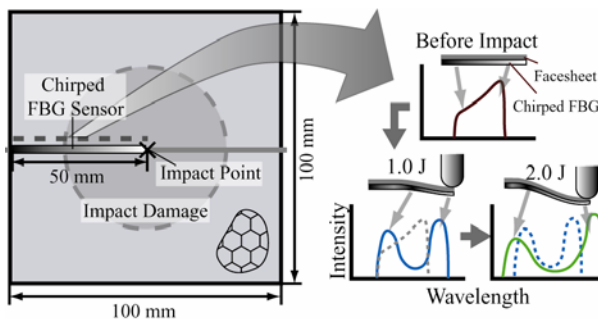
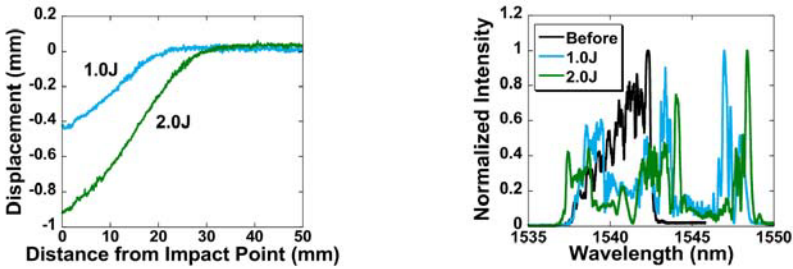


Figure 13. Specimen for impact damage detection.



(a) Deformations of facesheets after impact loading (b) Reflection spectra of chirped FBG

Figure 14. Measured deformations of facesheets and reflection spectra.

## 5. CONCLUSION

In this research, we established three real-time detection techniques of some particular damages in honeycomb sandwich structures using small-diameter FBG sensors: (I) debonding detection from the decrease in the transmitted optical power by the micro bend or the breakage of optical fibers, (II) debonding detection by the FBG sensors using the release of residual strain induced by the fillets and (III) impact damage detection using chirped FBG sensors that detect the change in the strain distribution due to the deformation of the facesheet. The feasibility of these techniques was confirmed through experimental tests, and, especially, the technique (II) was also verified by theoretical simulations.

## ACKNOWLEDGEMENT

This study was supported by Industrial Technology Research Grant Program in '03 from New Energy and Industrial Technology Development Organization (NEDO) of Japan.

## REFERENCES

1. Bocherens, E., Bourasseau, S., Dewynter-Marty, V., Py, S., Dupont, M., Ferdin, P. and Berenger, H., "Damage detection in a radome sandwich material with embedded fiber optic sensors" *Smart materials and structures*, Vol. 9, No. 3, pp. 310-315, 2000.
2. Blaise, E. and Chang, F.-K., "Built-in diagnostics for debonding in sandwich structures under extreme temperatures," *Structural health monitoring – the demands and challenges*, F.-K.Chang ed., CRC Press, pp. 154-163, 2001.

# THE INFLUENCE OF FACE SHEET WRINKLE DEFECTS ON THE PERFORMANCE OF FRP SANDWICH STRUCTURES

Brian Hayman<sup>1</sup>, Christian Berggreen<sup>2</sup> and Robert Pettersson<sup>2</sup>

<sup>1</sup>*Section for Structural Integrity and Laboratories, Det Norske Veritas AS, N-1322 Høvik, Norway;* <sup>2</sup>*Department of Mechanical Engineering, Technical University of Denmark, DK-2800 Kgs. Lyngby, Denmark*

**Abstract** Wrinkle defects may reduce the compressive strength of a face laminate for in-plane loading applied perpendicularly to the line of the wrinkle. To be able to decide whether a repair is needed it is necessary to know the magnitude of the strength reduction for a given wrinkle geometry. In the studies reported here, the influence of wrinkle defects on the in-plane compressive strength of quasi-isotropic CFRP laminates used in PVC foam-cored sandwich panels has been investigated by three approaches: testing of sandwich beam specimens in four-point bending, testing of sandwich panels with in-plane compression, and finite element simulation. Wrinkles involving different numbers of plies have been considered. Two different sandwich lay-ups typical of deck and hull bottom panels in a naval ship have been included.

**Keywords:** FRP sandwich structures, wrinkle defects, compressive strength.

## 1. INTRODUCTION

A wrinkle is a type of production defect that arises in laminated composites. It is caused by a slight excess of reinforcement in one or more of the plies in relation to the surface area available. These plies are unable to lie completely flat and form a small, outward buckle or wrinkle. With the introduction of carbon fibre reinforced plastics (CFRP) on a large scale with resin infusion production processes, it seems that this type of defect has become quite common in composite ship production. A contributory factor is thought to have been the introduction of relatively heavy, non-crimp fabrics that are supplied in rolls, such that the plies at opposite faces of the fabric

have slightly different lengths when unrolled. The wrinkle may involve only the outermost plies of the laminate, but may also start deeper down in the lay-up, in extreme cases involving the entire thickness (Figure 1).

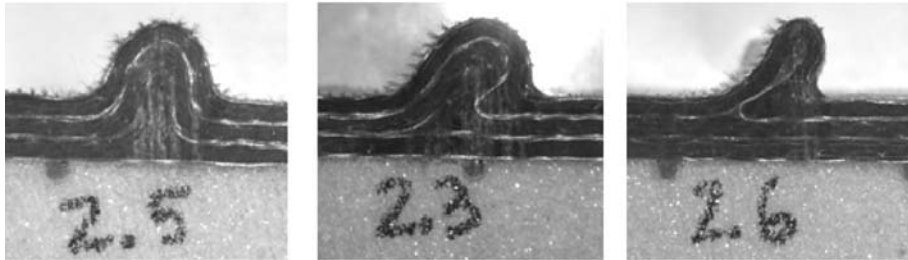


Figure 1. Sections through wrinkle defects of differing depths.

Such wrinkles may reduce the compressive strength of a laminate for in-plane loading applied perpendicularly to the line of the wrinkle. To be able to decide whether a repair is needed, it is necessary to know the magnitude of the strength reduction for a given wrinkle geometry. Attention here is confined to sandwich configurations, in which the core seems to have a stabilising effect, as compared to a single-skin configuration.

In the studies reported here, the influence of wrinkle defects on the in-plane compressive strength of quasi-isotropic CFRP laminates used in PVC foam-cored sandwich panels has been investigated by three approaches:

- testing of sandwich beam specimens in four-point bending
- testing of sandwich panels with in-plane compression
- finite element simulation.

Wrinkles involving different numbers of plies have been considered. Two different sandwich lay-ups typical of deck and hull bottom panels in a naval ship have been included. In the test beams and panels, the wrinkles were induced artificially during production.

## 2. LAY-UPS CONSIDERED

Two different CFRP sandwich lay-ups were considered:

### 2.1 Type 1 lay-up

Each face laminate consists of 4 fabric layers, with 2 unidirectional plies in each fabric, making a total of 8 plies. The fabrics are non-crimp Devold CFRP 450 gsm with LT and DB configurations based on T700 carbon fibres. The lay-up is quasi-isotropic and symmetric, and each laminate has a total

thickness of 1.8 mm. The face laminate lay-up is  $[0/90/45/-45]_s$ . The core is Divinycell H80 PVC foam with a thickness of 60 mm, making a total thickness of the panel of 63.6 mm. This lay-up is representative of decks and superstructures in naval vessels.

## 2.2 Type 2 lay-up

Each face laminate consists of three type 1 laminate lay-ups stacked together,  $\{[0/90/45/-45]_s\}_3$ . Thus each laminate has a total of 24 plies, giving a thickness of 5.4 mm. For the sandwich beam tests, the core was Divinycell H200 PVC foam with a thickness of 60 mm, making a total thickness of the panel of 70.8 mm. For the panel compression tests the core thickness was reduced to 50 mm, giving a total thickness of 60.8 mm. The lay-up is representative of hull structures in naval vessels.

## 3. MATERIAL PROPERTIES

Extensive testing of similar laminates has been performed by the Royal Institute of Technology (KTH) in Stockholm. Table 1 shows the modulus of elasticity,  $E$ , the shear modulus,  $G$ , and Poisson's ratio,  $\nu$ , provided by KTH based on a fibre fraction of 53% by volume. The unidirectional ply properties, estimated by back-calculating from the above laminate properties, are  $E_{11} = 114$  GPa,  $E_{22} = 9$  GPa,  $G_{12} = 3$  GPa,  $\nu_{12} = 0.25$ .

The tests performed at KTH gave strain values between 0.8% and 0.9% for ultimate compressive failure. On this basis, the ultimate compressive strain  $\epsilon_f$  was at first assumed to be the average value, 0.85%. Assuming  $E = 114$  GPa as given above, and linear behaviour up to failure, this implies an ultimate compressive strength of 365.5 MPa.

The core materials are both Divinycell H-grade foam cores from the DIAB group. The elastic properties and ultimate shear strength  $\tau_u$ , shown in Table 1 are taken from the Divinycell H series data sheet.

The matrix used in the laminates is the epoxy based vinylester NORPOL DION 9102-501 from Reichhold. Table 1 shows relevant material properties. The elastic moduli quoted in the manufacturer's data sheet for bending and tension are quite similar and the value shown is the mean value of the two. The ultimate tensile strength is given as 76 MPa. Based on linear behaviour, the elastic component of strain at this stress level is 2.2%. The fracture strain for the vinylester is quoted as 4.5 %, which indicates that the resin's response is quite non-linear. The value shown in Table 1 for the yield strength of the resin in shear,  $\tau_y$ , was provided by KTH.

Table 1. Mechanical properties for the face laminates, resin and core materials.

	E [MPa]	G [MPa]	$\nu$	$\tau_u$ [MPa]	$\tau_y$ [MPa]
Face laminate	43 000	16 000	0.32		
Resin	3350				42
H80 core	85	31		1.0	
H200 core	310	90		3.3	

#### 4. TESTS ON SANDWICH BEAMS IN FOUR-POINT BENDING

Sandwich beams of types 1 and 2, with and without wrinkle defects, were supplied by Kockums AB. The wrinkles were initiated at various levels within one face laminate. The outermost and innermost plies in all cases ran in the longitudinal direction relative to the beam. The beams were tested in four-point bending, as shown in Figure 2, by Skaar and Huth [1]. The region of length  $L_1$  between the load application points is in pure bending, with the upper face laminate in compression. In order to investigate the effect of wrinkle defects on the compressive strength of a face laminate, tests were performed on beams having wrinkles running across the width of the beam near the centre of this region. The failure loads were compared with those measured for beams without wrinkles, and with theoretical values based on the laminate properties given in Section 3. The tests were fully documented with photographs and descriptions of the observed failures.

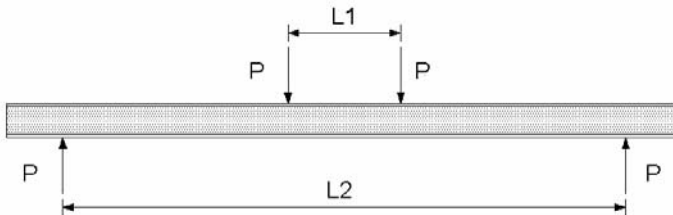


Figure 2. Four-point bend test.

A sandwich beam of this type may fail in various ways:

- Compressive failure of the upper face laminate in the central region
- Tensile failure of the lower face laminate in the central region
- Shear failure of the core between the load point and the support
- Local bending failure of a face laminate at a load point or a support.

As the upper and lower face laminates were equal, and the tensile strength of CFRP laminates is normally higher than the compressive strength, tensile failure of the lower laminate was unlikely. Local bending

failure could be avoided by providing adequate distribution of the local loading by means of pads placed under the load points and over the supports.

To ensure that failure of the beam would not occur by shear failure in the core,  $L_2$  was made as large as possible (1000 mm) with the available test facility and  $L_1$  as small as practicable (200 mm). Additionally, in the Type 1 beams the H80 core in all but the central 80 mm long region (which contained the wrinkles in those specimens having wrinkles) was replaced by H200 core. In the Type 2 beams the corresponding parts of the H200 core were replaced by HCP90 foam with an ultimate shear strength of 6.7 MPa.

All the beams with wrinkle defects failed by compressive failure of the face laminate at or very close to the defect. However, there were some difficulties in determining the strength of the beams without wrinkles. The type 1 beams without wrinkles appeared to fail prematurely by wrinkling (local buckling) of the face laminate above the joint between the H80 and H200 core blocks. In fact the theoretical wrinkling load for these beams, based on the Hoff formula, was found to be lower than the load that would be required to cause compressive fibre failure. The stress concentration associated with the core joint is believed to have lowered the failure load further. There were also some problems with the Type 2 beams without wrinkle defects as these appeared to fail at a load corresponding to a compressive strain of only about 0.5%, compared with the expected 0.8 - 0.9%. This may reflect the presence of other defects in the beams without wrinkle defects; in fact all the beams had a certain waviness in the upper surface of the upper face laminate. This introduces uncertainty when attempts are made to determine the strength reduction caused by the intentionally built-in wrinkle defects.

Following discovery of this anomaly, KTH performed new compression tests on specimens cut from the face laminates of a Type 2 beam. These indicated ultimate compressive strains of about 0.55% for specimens taken from the upper face laminates, while the lower face laminates (which were moulded against a smooth surface, and which were not subject to compression in the beam tests) did achieve compressive strains of about 0.85%. Figure 6 shows the compressive strengths of the panels, normalised with respect to the calculated strength without defects based on 0.55% strain.

## **5. TESTS ON SANDWICH PANELS WITH IN-PLANE COMPRESSION**

In an attempt to avoid the uncertainties of the beam testing, a further series of panels was produced by Kockums AB. These were similar to those used in the beam tests, but were cut into panels 300 mm x 100 mm and

tested in pure compression (Figure 3) by Pettersson [2]. As shear failure was not a problem, the basic core materials (H80 for Type 1, H200 for Type 2) could be used throughout the panels, thus avoiding problems at the transition between core blocks of unequal density. End tabs were fitted to the Type 1 panels to reduce local problems at the load introduction.

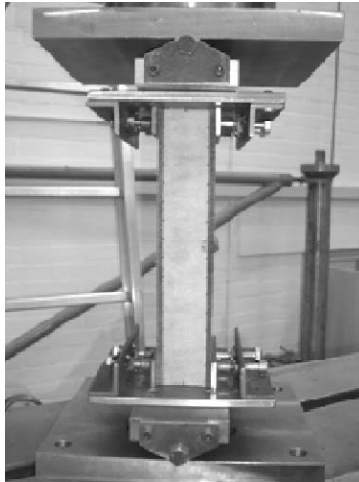


Figure 3. Test set-up for compression testing of sandwich panels.

The Type 1 panels without wrinkle defects again failed by wrinkling (local buckling). The Type 1 panels with wrinkles confined to the two outermost plies also failed at locations some way from the wrinkles, probably due to local fibre waviness. The Type 2 panels without wrinkles failed at strains between 0.61% and 0.67%, with a mean of 0.63%. These are higher than from the beam tests, but still short of the expected 0.8-0.9%. The results are summarised in Figure 6. The results for both Type 1 and Type 2 panels have been normalised with respect to the 0.63% strain case.

## 6. NUMERICAL SIMULATION

Finite element modelling was performed by Pettersson [2] using the commercial software ANSYS. Both the beam tests and the panel compression tests were simulated. Two-dimensional models were used in all cases. Each ply of the face sheet was modelled separately to obtain an accurate material model in the region where the geometry of the wrinkle causes some out-of-plane behaviour in the plies. Local co-ordinate systems parallel to the plies have been used in regions of curvature to ensure accurate results in the material directions.

### 6.1 Geometric modelling

The left-hand diagram in Figure 4 shows how the geometry was modelled for the specific case of a Type 1 lay-up where six of the eight reinforcement plies are involved in the wrinkle. The unshaded region between the wrinkle and the flat plies is assumed to be filled with resin.

To produce realistic geometries for the Type 2 laminates it was necessary to introduce additional resin-only regions between certain layers. Three different types were defined according to how many of the plies were involved in the wrinkle. One type is shown in the right-hand diagram in Figure 4.

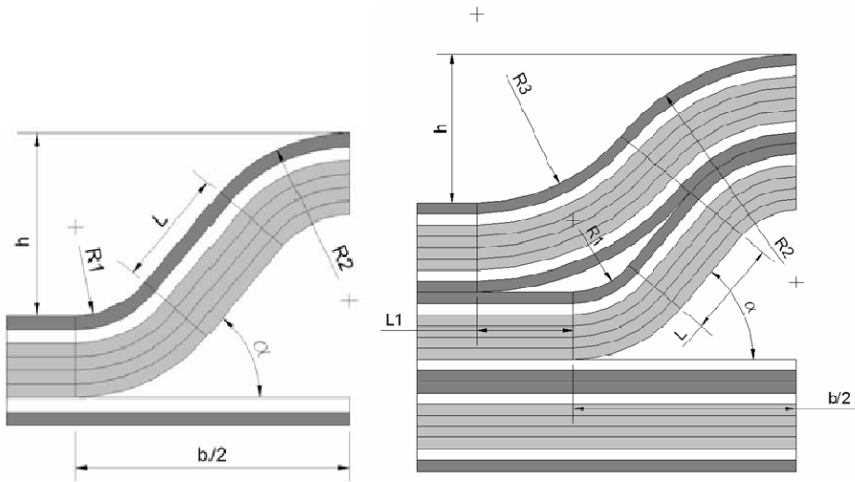


Figure 4. Parametric descriptions of geometry for wrinkle defect in (left) Type 1 laminate and (right) Type 2 laminate with wrinkle starting in middle region of laminate.

### 6.2 Finite element solution

A typical finite element mesh is shown in Figure 5. The ANSYS element type used was the PLANE42 linear isoparametric element, with PLANE82 quadratic elements in some regions where the mesh was locally highly distorted. In most cases a linear analysis was performed. However, some limited studies were performed assuming non-linear properties in the resin-only regions. The principal failure mode considered was compressive fibre failure, characterised by the maximum compressive strain in the fibre direction reaching a critical value. Contours of this strain are shown in Figure 5 for the particular case illustrated. By assuming the same critical value for cases both with and without wrinkles, the ratio between the strength with a wrinkle and that without wrinkles could be found directly.

The critical regions for the compressive fibre strain were found to be at the surface of the laminate in the concave transition region at the edge of the wrinkle and in the plane plies beneath the wrinkle in cases where not all plies are involved in the wrinkle.

It is found that at least three elements should be used through the thickness of the plies to obtain reliable results. Also the transition radius (R1 in Figure 4) should be divided in a sufficient number of element segments, at least eight for normal wrinkle geometries.

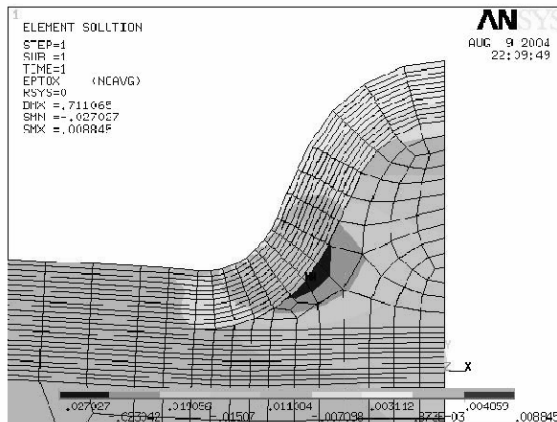


Figure 5. Finite element mesh for face laminate part of beam model with contours of strain in the fibre direction.

Checks were also made of the interlaminar shear stresses, and these were found in many cases to exceed the assumed ultimate value of 42 MPa at loads lower than those for fibre failure, and at loads sometimes much lower than those observed in the tests. As the matrix material has quite a non-linear behaviour, some limited studies were carried out to establish whether such high interlaminar shear stresses were realistic. These studies showed that they were indeed greatly overestimated, but it was not possible within the time available to establish reliably values, and to study the effect of the non-linear behaviour on the fibre strains. Thus the results presented here are all based on the fibre strains established by linear analysis.

### 6.3 Results

The results of the FE analyses are presented, together with those of the tests, in Figure 6. The agreement is seen to be quite good, with the FE results being generally on the conservative side. It is interesting to note that a wrinkle affecting just the outermost layers of the face laminate reduces the

strength by about 30%. For the Type 1 lay-up, the involvement of more plies than that has only a modest effect on the strength, whereas the strength drops off more or less linearly with increasing number of plies involved in the wrinkle for the Type 2 laminate. This is not surprising since the Type 1 laminate has 0° fibres only in the innermost and outermost plies, while in the Type 2 lay-up there are 0° plies distributed at various depths in the laminate. However, it should be noted that this effect is less marked in the test results than in the FE results. It is possible that the geometrical descriptions of the Type 2 wrinkles involving more than just the outermost plies are too unfavourable.

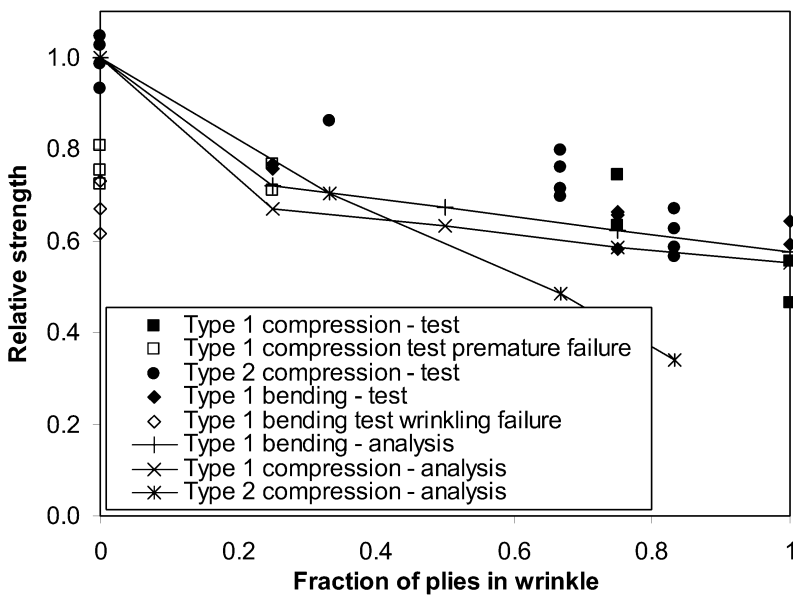


Figure 6. Relative strength of beams and panels with wrinkles from tests and as predicted by FE analysis.

A detailed parametric study showed that the transition between the wrinkle defect and the remaining face sheet tends to be a critical region, likely to initiate failure due to both direct compressive strains and shear stresses out-of-plane. Besides the wrinkle depth, the curvature in this region may be an important parameter to study when evaluating the criticality of a wrinkle defect.

## 7. OVERALL CONCLUSIONS

The effect of wrinkle defects on the compressive strength of the face laminates of sandwich panels has been investigated by means of two experimental test series and FE calculations. A detailed description of a wrinkle defect has been implemented in the FEM code ANSYS.

Although some unresolved questions remain, moderately good agreement has been obtained between the results of using the three approaches, with the FE analysis predictions being generally conservative. It is shown that the compressive strength is reduced with increasing number of plies involved in the wrinkle. When all plies are involved in the wrinkle the tests indicate that the compressive strength is reduced by up to 55%, while the FE analyses suggest that the reduction may be more severe than this in some cases. However, care must be taken when estimating a strength reduction on the basis of tests because other random production defects may influence the strength in the absence of obvious wrinkles.

## ACKNOWLEDGEMENTS

The tests and analyses were performed by MSc students at the Technical University of Denmark [1,2] in collaboration with the SaNDI Project, THALES JP3.23: Inspection and Repair of Sandwich Structures in Naval Ships [3,4]. Kockums AB kindly supplied all the sandwich panels for testing, with core materials provided by DIAB AB.

## REFERENCES

1. Skaar, R. and Huth, V., *Effect of Wrinkle Defects on the Compressive Strength on CFRP Laminates in Sandwich Structures*, MSc Thesis, Department of Mechanical Engineering, Technical University of Denmark, 2003.
2. Pettersson, R., *Effect of Wrinkle Defects on the Compressive Strength of CFRP Laminates in Sandwich Structures*, MSc Thesis, Department of Mechanical Engineering, Technical University of Denmark, 2004.
3. Hayman, B., *Inspection and Repair of Sandwich Structures Based on Damage Tolerance Principles*, 6th International Conference on Sandwich Construction, Fort Lauderdale, Florida, USA, 2003.
4. Hayman, B. and Zenkert, D., *The Influence of Defects and Damage on the Strength of FRP Sandwich Panels for Naval Ships*, PRADS 2004, Travemünde, Germany, 2004.

# RESIDUAL STRENGTH OF DEBONDED SANDWICH PANELS LOADED WITH LATERAL PRESSURE

*Experimental Investigation and Fracture Mechanical Modeling*

Perttu Jolma<sup>1</sup>, Sebastian Segercrantz<sup>1</sup> and Christian Berggreen<sup>2</sup>

<sup>1</sup>VTT Technical Research Centre of Finland, FIN-02044 Espoo, Finland

<sup>2</sup>Department of Mechanical Engineering, Technical University of Denmark, DK-2800 Kgs. Lyngby, Denmark

**Abstract** For the determination of debonded sandwich panel residual strength with lateral loading a parametric finite element model is developed. The parametric model allows an arbitrary positioning of the debond within the panel and consists of both solid and shell elements. A fracture mechanical approach using the crack flank displacements obtained from the FEA solution combined with measured mixed-mode fracture toughness values are used to determine the ultimate failure load. Experiments were conducted to compare against the analysis results. The comparison of numerical and experimentally achieved results showed that the used modeling approach predicts the failure load and failure mode well.

**Keywords:** damage tolerance, debond, interface fracture, lateral pressure loading.

## 1. INTRODUCTION

The use of sandwich structures in marine applications is increasing. The advantageous properties provided by the sandwich concept can be utilized in hulls and superstructures. The integrity of the face-to-core bond is essential in sandwich structures. Flaws where the face-to-core bond is lost are called face-to-core debonds. Problems in the sandwich manufacturing process can result in debond formation. Impacts or improper design of load-introductions may also cause sandwich interface damage similar to the manufacturing-induced debonds.

The presence of debonds may affect the strength of sandwich panels in different ways. The most significant debond-induced failure modes are buckling of face and debond crack propagation. The crack may propagate within the interface, at an angle into the core or even into the face. Most of the previous studies have focused on the buckling type failure mode in sandwich beams, e.g. Hansen [1] or in panels, e.g. Berggreen [2] resulting from in-plane compression of the face. The buckling or opening of a debond causes mode I dominated interface crack tip conditions. The hull panels in marine structures are subjected to lateral pressure loads causing transverse shear stresses in the core. The transverse shear induces sliding mode II dominated crack tip conditions. The failure behavior of mode II dominated debonds in panels with lateral pressure load has previously been studied by Falk [3].

Methodologies for production control and damage inspection of sandwich structures in naval ships were developed in the European project Thales JP3.23 “SaNDI - Inspection and repair of sandwich structures in naval ships”. The present study was conducted in the part of the project where residual strength determination tools were developed.

## **2. SANDWICH PANEL CONFIGURATION**

The sandwich panel configuration and debond dimensions and locations were selected to be representative of typical sandwich panels in marine hulls. The panels were scaled down from full-scale proportions. A lateral pressure load acts on the supported panel area. The panel is simply supported. The panel configuration has an overhang outside the support and load area to simulate the surrounding structure and to reduce edge effects. The panel was designed to fail by core shear when loaded laterally, conforming to dimensioning practices in classification society rules.

The effect of debonds is investigated in three different panel locations. The locations and diameters are: panel center, 200 mm (1), near support edge, 100 mm (2) and near support corner 200 mm (3). All debonds are inside the support, between the pressure side face and the core. Positions 1 (corner) and 2 (edge) were chosen, since core shear stresses are highest near the supports. The position 2 (edge) is near the core shear stress maximum. Core shear stresses are low at the center of the panel. The central debond was chosen for studying whether the in-plane compression in the pressure side face would provoke buckling of the debonded face or if the lateral pressure load would prevent it.

The panel, debond locations, load and boundary conditions are presented in Figure 1. The debonds are located between the pressure side face and the core. The sandwich panel support dimensions are 980 x 625 mm.

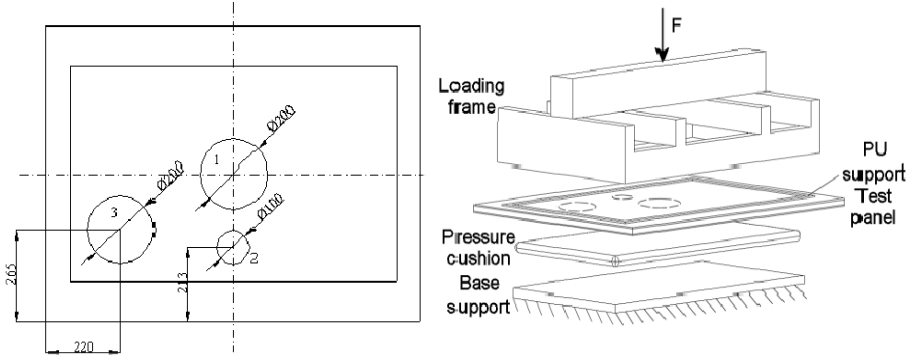


Figure 1. The tested panel, debond locations and test arrangement principle.

One intact and three debond flawed panels were manufactured with hand lay-up. Circular patches of wax paper were used to form the debonds. The debonds bulged outwards in the cured panels, indicating complete separation between the face and the core. The face laminates consist of stitched non-crimp glass fiber fabrics and chopped strand mats laminated with polyester resin. The face laminate thickness is 4.5 mm. The material property data of the face laminate are based on laminate tests. The core material is 30 mm thick cross-linked Divinycell H80 PVC foam. The material properties are listed in Table 1.

Table 1. Material properties.

	$E_x$ [MPa]	$E_y$ [MPa]	$E_z$ [MPa]	$G_{xy}$ [MPa]	$G_{yz}$ [MPa]	$G_{xz}$ [MPa]	$\nu_{xy}$	$\nu_{yz}$	$\nu_{xz}$
Face	12360	12360	8400	4520	2700	2700	0.295	0.320	0.290
Core	81.6			31.0			0.300		

For fracture mechanical calculations the fracture toughness,  $\Gamma$ , is needed. RISØ National Laboratory conducted face tearing tests, Berggreen [2], where the mode-mixity varied between  $0^\circ$  and  $-60^\circ$ , indicating a kinking angle upwards, into the face. However, at  $0^\circ$  mode-mixity the crack kinked into the core, hindering further interface measurements. The average value near  $0^\circ$  mode-mixity is  $310 \text{ J/m}^2$ . With the considered debond locations the mode-mixities at crack front critical positions are positive, indicating crack propagation into the core. Because appropriate fracture toughness values in the positive mode-mixity range were not available, the constant value of  $\Gamma=310 \text{ J/m}^2$  was used in the analyses.

### 3. ANALYSIS APPROACH

In this study the debonds are considered as circular cracks. The fracture mechanical calculations are based on nodal displacements of the crack flanks obtained from finite element analysis. A planar problem, plane strain state and Linear Elastic Fracture Mechanics (LEFM) are assumed.

Generally, crack loading is not purely mode I or mode II but a mix-up of the modes. In a bi-material interface crack the mode-mixity is not only dependent of the stress and strain state of the crack tip vicinity, but also of the material parameters.

The displacement and stress field close to the crack tip is given by the Lekhnitskii-Eshelby-Stroh (LES) formulation, which can be specialized to describe the opening ( $\delta_2$ ) and sliding ( $\delta_1$ ) relative displacements of the bi-material crack flanks, Hutchinson and Suo [4]:

$$\sqrt{\frac{H_{11}}{H_{22}}}\delta_1 + i\delta_2 = \frac{2H_{11}(K_1 + iK_2)r^{1/2+i\varepsilon}}{\sqrt{2\pi}(1 + 2i\varepsilon)\cosh(\pi\varepsilon)}$$

where  $K$  is the complex stress intensity factor given as,  $K=K_1 + iK_2$ . The crack flank relative displacements ( $\delta_1$  and  $\delta_2$ ) and the distance from the crack tip,  $r$ , are clarified in the Figure 2.

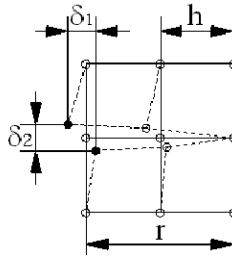


Figure 2. Relative displacements of crack flanks.

The non-dimensional orthotropic constants,  $H_{11}$  and  $H_{22}$  and the oscillatory index,  $\varepsilon$ , and are given in Berggreen and Simonsen [5]. The expression for mode-mixity suggested by Hutchinson and Suo [4] and modified Irwin expression, linking the stress intensity factor with the Griffith-energy are:

$$\psi = \arctan \left[ \frac{\text{Im}(Kh^{i\varepsilon})}{\text{Re}(Kh^{i\varepsilon})} \right], \quad G = \frac{H_{11}|K|^2}{4 \cosh^2(\pi\varepsilon)}$$

where  $h$  is the characteristic length of the crack problem, often chosen as the face thickness. Using the expressions above, explicit formulations for the mode-mixity and the Griffith-energy as functions of the relative crack flank displacements can be derived:

$$\psi = \arctan\left(\sqrt{\frac{H_{22}}{H_{11}} \frac{\delta_1}{\delta_2}}\right) - \varepsilon \ln\left(\frac{r}{h}\right) + \arctan(2\varepsilon),$$

$$G = \frac{\pi(1 + 4\varepsilon^2)}{8H_{11}r} \left( \frac{H_{11}}{H_{22}} \delta_2^2 + \delta_1^2 \right)$$

Crack flank displacements are needed to determine the crack tip conditions using the derived expressions. Nodal displacements obtained from the panel finite element model are used. The panels were modeled using ANSYS 8.0 finite element analysis software. A parametric input file is used to enable calculation of various panel and debond configurations. The model is meshed using four noded shell elements (SHELL181) for the faces and eight noded solid elements (SOLID45) for the core. Solid elements of the type SOLID64 are used to model the debonded face to get more accurate crack flank displacement data. The load is introduced as a pressure load on the face elements. The support out-of-plane displacements are fixed, in-plane displacements and rotational degrees of freedom are left free. A detail of the debond region mesh is presented in Figure 3.

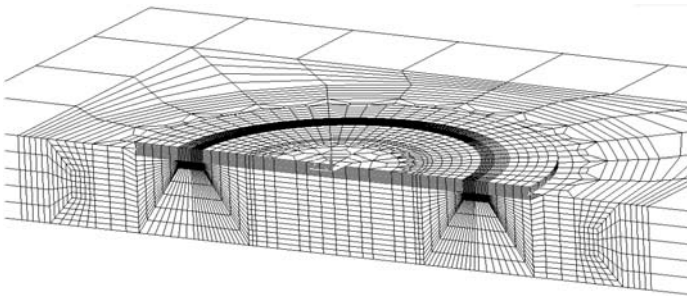


Figure 3. Debond finite element mesh.

To prevent a hinge in the intersection where the face element type shifts, multipoint constraints (MPC) were employed to connect the incompatible degrees of freedom. To prevent the face from overlapping with the core 3D surface contact elements (CONTA174 and TARGE170) are used in the

debond area. The modeled contact is frictionless. More details can be found in Segercrantz [6].

The models were solved using sparse solver and Newton-Raphson iteration. Geometrical non-linearity was included. The acquired solution was used in the fracture mechanical calculation.

The nodal displacement data for the initially coincident node pairs requires coordinate transformations to filter out the global rotation. A straight line is fitted to the displaced nodes of the core side crack flank using the method of least squares. The line is used as reference when calculating the relative displacements of the crack flanks ( $\delta_1$  and  $\delta_2$ ).

The Griffith-energies and mode-mixities are calculated using the relative crack flank displacements  $\delta_1$  and  $\delta_2$ . The calculated fracture parameters apply at the point where the node pair is located. The parameters are evaluated for several node pairs along the crack flanks. A linear extrapolation of the fracture parameters to the crack tip is then performed using the CSDE-method, Berggreen [2, 5]. The calculated Griffith-energies along the crack front are compared against the fracture toughness value to determine the failure load of the panel.

#### 4. EXPERIMENTAL PROCEDURE

The test setup is composed of a rigid steel loading frame, which is loaded with a servo-hydraulic testing machine. The panel is via its boundaries pressed against a water-filled cushion, lying on a base support, to create a uniform pressure load. The boundary conditions are close to simply supported with regard to both moment and in-plane loads and act in the vertical direction with respect to the panel surface. Polyurethane strips were used to introduce the panel support reaction on a wider area than traditional steel rollers and to allow rotation. Water pressure inside the cushion is measured together with the load introduced by the testing machine. Panel midpoint deflection is measured with an inductive displacement gauge.

#### 5. RESULTS

The intact panel analysis was performed with a separate model. The load at which the core shear yield strength is reached in the most critical positions was determined to be 80 kN.

In the panel analysis fracture parameters were calculated in 24 positions around the crack perimeter. The results are presented in polar diagrams, oriented so that the  $0^\circ$  direction is aligned with the short side of the panels,

pointing towards the panel center and the  $90^\circ$  direction is aligned with the long side of the panels, pointing towards the panel center. The distribution of parameters along the crack front of the corner debond panel is presented in Figure 4. The loads corresponding to reaching the condition  $G=I$  at most critical position along the crack front are presented in Table 2.

Table 2. Calculation and experimental results.

	Analysis failure load [kN]	Analysis critical positions	Analysis failure criterion	Experiment failure load [kN]	Experiment failure mode
Intact panel	80	-	Core shear yield stress	258	Core shear rupture around support
Center debond	224	$0^\circ$ and $180^\circ$	Griffith-energy	279	Core shear rupture around support
Edge debond	69	$180^\circ$	Griffith-energy	64	Crack propagation from debond
Corner debond	90	$165^\circ$ and $270^\circ$	Griffith-energy	90	Crack propagation from debond

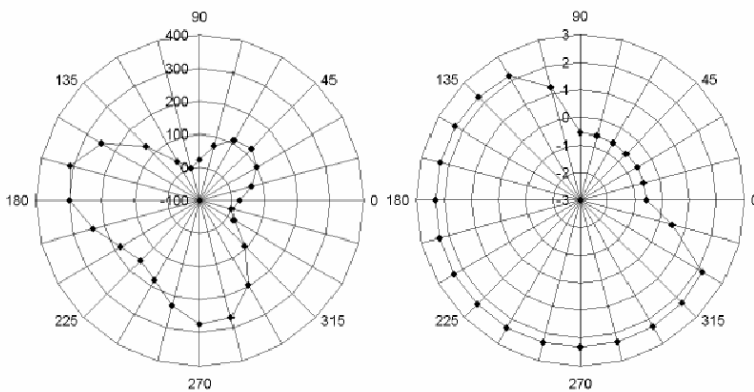


Figure 4. Extrapolated Griffith-energy (left) and mode-mix (right) at a load of 90kN along the corner debond panel crack front.

In the experiments the panels were loaded under displacement control, until a significant and distinctive load drop was observed in the load-deflection relation, indicating damage propagation. This first propagation was considered to correspond with the failure criteria used in the calculations.

The intact panel showed significant plastic yielding of the core, evident in the load-deflection relationship from 80 kN onwards, Figure 5. The panel

failed at a load of 258 kN, through core shear rupture, surrounding the entire load bearing support perimeter.

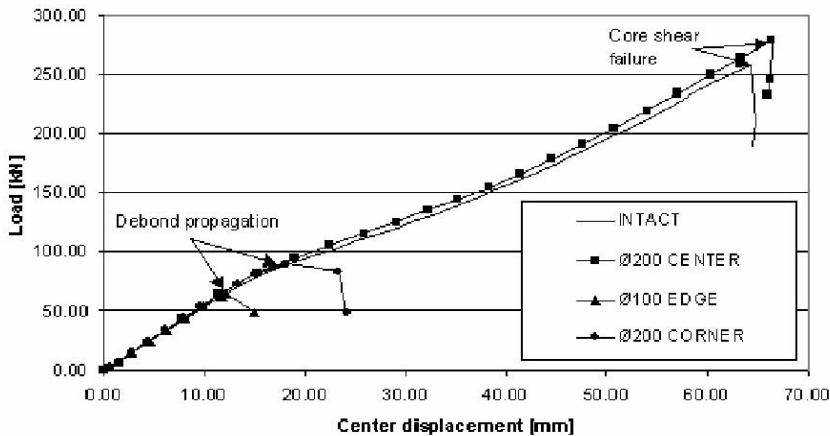


Figure 5. Panel load-deflection relationships in the experiments.

The edge debond panel was loaded until the load-deflection curve kinked at a load of 64 kN, accompanied with a clearly audible crackle. The load was not increased after this point, to preserve the appearance of damage growth. A large area of core shear and interface fracture could be seen through the transparent GFRP faces.

The behavior of the corner debond panel under loading was similar to the edge debond panel. The crack propagated at 90 kN.

The behavior and the failure mode of the central debond panel resembled the intact panel. The central debond panel failed at a load of 279 kN, which is slightly higher than the failure load of the intact panel. The load-deflection relationships of the tested panels are presented in Figure 5. The failure loads determined by analysis and experiments are presented in Table 2.

The destructive inspection (panel sectioning) results show that the model predicted the propagation initiation points well. Because of the debond crack kinking the steepest crack angle observed in the post-mortem inspection indicates the propagation point. Further away from the initiation point the angle approaches normal 45-degree shear crack angle. The measured crack kinking angles were in the order of 80-degrees. The steep crack kink angle in the corner debond panel is clearly seen in Figure 6.



Figure 6. Crack propagation from the corner debond.

## 6. DISCUSSION

A considerable reduction compared to the ultimate rupture load of the intact panel was observed to result from the corner and edge debonds. However, when compared to the panel yield limit, the strength reductions were less prominent. The yield limit of the core should be used as a basis for the comparisons, because this limit is used in practical design to determine the allowable loads. The edge and corner debonded panels failed at relatively low loads compared to the intact and central debond panels. The corner debond panel failed at a slightly higher load than the edge debonded panel.

In the panel experiments where the debond proved to be critical the crack kinked into the core. This indicates a positive mode-mixity. No fracture toughness values for positive mode-mixities were available, therefore a single estimated value was used, which may affect the failure load prediction accuracy. No friction was modeled in the finite element calculations. The friction can have a considerable effect on mode II dominated conditions. The initial opening present in the test panel debonds likely lessened the friction effects. The debond opening and friction are not easily measurable and can not be used as parameters in a model used to make maintenance decisions. Ignoring the friction is a conservative assumption.

In the experiments the central debond did not affect the behavior or failure mode of the panel. This may result from suppression of outwards buckling and mode I opening of the debonded face due to the pressure load. This effect can be thought to be un-conservative. If the lateral pressure load would not be present on the debond area the central debond might buckle and the panel fail at a much lower load. This must be considered in application of the developed model to marine structures.

The analyses of the central debond and intact panel are not valid above core yield loads, since the core material non-linear behavior was not

modeled. It has been found in the previous research that linear elastic material models are satisfactory in the fracture mechanics of PVC core. However, a non-linear material model would be needed to capture the global non-linear behavior of the panel at load levels above the core yield.

## 7. CONCLUSIONS

Residual strength of laterally loaded sandwich panels with debond flaws was investigated by analysis and experiments. The results show good agreement between the developed modeling approach and the conducted tests. The failure loads, modes and the propagation locations agreed well. Considerable ultimate strength reduction of the panels was observed in the cases where a debond was located in the regions of high core shear strength utilization. However, the strength reductions were not as significant when compared to the intact panel yield strength. The developed parametrical finite element model and fracture mechanical approach has considerable potential for further developments.

## ACKNOWLEDGEMENTS

This work was part of the “SaNDI - Inspection and Repair of Sandwich Structures in Naval Ships” (THALES JP3.23) project with participants from Norway, Denmark, Sweden, Finland and the United Kingdom. The support of the Ministries of Defence of the five participating nations is gratefully acknowledged.

## REFERENCES

1. Hansen, U., Compression Behavior of FRP Sandwich Specimens with Interface Debonds, *Journal of Composite Materials*, 32(4):335-360, 1998.
2. Berggreen, C., Damage Tolerance of Debonded Sandwich Structures, PhD Thesis, Department of Mechanical Engineering, Technical University of Denmark, 2004.
3. Falk, L., Foam Core Sandwich Panels with Interface Disbonds, *Composite Structures*, 28:481-900, 1994.
4. Hutchinson, J. W. and Suo, Z., Mixed Mode Cracking in Layered Materials, *Advances in Applied Mechanics*, J.W.Hutchinson and T.Y.Wu (eds.), 29:63-191, 1992.
5. Berggreen, C. and Simonsen, B.C., Residual Strength of In-Plane Loaded Debonded Sandwich Panels – Fracture Mechanical Modelling. In O.T. Thomsen and A. Lyckegaard (eds), *Proceedings of 7th International Conference on Sandwich Structures*, Aalborg, Denmark, August 29–31, 2005 (this volume).
6. Segercrantz, S., Strength of Laterally Loaded Sandwich Panels with a Debond - Experiments and FE Modelling, Master's Thesis, Department of Mechanical Engineering, Helsinki University of Technology, Finland, 2004.

# MEASUREMENT OF INTERFACE FRACTURE TOUGHNESS OF SANDWICH STRUCTURES

Rasmus C. Østergaard and Bent F. Sørensen

*Material Research Department, Risø National Laboratory, Frederiksborgvej 399, 4000 Roskilde, Denmark*

**Abstract** Sandwiches are analyzed by the application of linear elastic fracture mechanics. An expression for the energy release rate is found by analytical evaluation of the J-integral. Also, a method for determining the mode mixity is described and applied. The theory presented is applied to a test method and the fracture toughness of two sandwiches are measured as function of the mode mixity.

**Keywords:** sandwich, LEFM, fracture toughness, mode mixity and J-integral.

## 1. INTRODUCTION

Fracture in brittle solids is often analysed by the application of linear elastic fracture mechanics (LEFM). In this work concepts of LEFM are applied to debonding between skin and core in sandwich materials. In LEFM, when applied to interfaces between dissimilar materials, the energy release rate,  $G$ , and a mode mixity  $\psi$  crack tip. A fracture criterion often applied is based on the energy release rate to be equal to some critical materials value, namely the critical energy release rate of fracture toughness,  $G_c$ . Experimental results show that for fracture in interfaces between some material combinations  $G_c$  depends on the mode mixity [1–3].

In the following, an analysis is carried out where the J-integral is used calculating the energy release rate for a versatile load situation. The sandwich is loaded at the edges by forces  $P_n$  and moments  $M_n$ ,  $n=1..3$ . The

loads are defined as force or moment pr. unit width. The load situation is sketched in Figure 1. A method is also presented whereby the mode mixity can be extracted from a specific finite element (FE) solution of the problem and hereafter can be recalculated for any combination of the moments and forces.

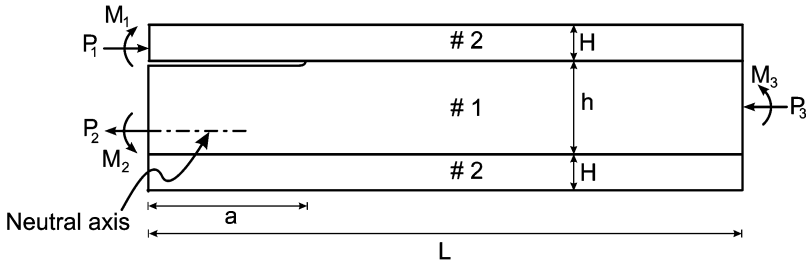


Figure 1. The sandwich is loaded with moments and forces at its ends.

Finally, some experimental results are presented where fracture toughness has been measured as function of the mode mixity. The sandwiches that have been tested have PVC cores with two different densities and GFRP skins.

## 2. MECHANICS OF AN INTERFACE CRACK BETWEEN TWO DISSIMILAR ELASTIC SOLIDS

### 2.1 Material constitutive law

First, let us describe the materials behaviour. Both the core material (#1) and the skin material (#2) are assumed to exhibit linear elastic deformation behaviour when small deformations are considered, which is reasonable for the constituents typically used in sandwich materials. The following constitutive relation describes the elastic deformations in the materials

$$\epsilon_i = \sum_{j=1}^6 s'_{ij} \sigma_j, \quad i = 1..6, \tag{1}$$

$$\begin{aligned} \epsilon_i &= \{ \epsilon_{11} + \epsilon_{22} + \epsilon_{33} + \epsilon_{23} + \epsilon_{13} + \epsilon_{12} \}, \\ \sigma_i &= \{ \sigma_{11} + \sigma_{22} + \sigma_{33} + \sigma_{23} + \sigma_{13} + \sigma_{12} \}. \end{aligned}$$

The tensor  $s'_{ij}$  is given by

$$s'_{ij} = \begin{cases} s_{ij} & \text{for plane stress} \\ s_{ij} - s_{i3}s_{j3}/s_{33} & \text{for plane strain} \end{cases} \quad (2)$$

The relation between the engineering constants and the stiffness tensor  $s_{ij}$  can be found in various composite textbooks, e.g. [4].

### 2.2 The singular stress field

Near the crack tip a singular stress field becomes dominant. This stress field is given by the equation [5]

$$\sqrt{\frac{H_{22}}{H_{11}}} \sigma_{22} + i\sigma_{12} = \frac{1}{\sqrt{2\pi}} Kr^{i\varepsilon-1/2}. \quad (3)$$

Here  $K = K_1 + iK_2$  is the complex stress intensity factor,  $i = \sqrt{-1}$ ,  $r$  is the radial distance along the  $x_1$ -axis and  $\varepsilon$  is the oscillatory index given as

$$\varepsilon = \frac{1}{\sqrt{2\pi}} \ln\left(\frac{1-\beta}{1+\beta}\right),$$

where  $\beta$  is a Dundurs' parameter [5],  $H_{11}$  and  $H_{22}$  are stated in the Appendix.

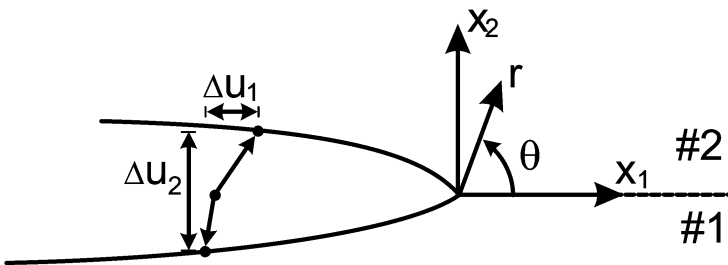


Figure 2. Definition of the crack face displacements.

The crack opening components  $\Delta u_n$  are defined from the displacement  $u_n$  of two material points coinciding in the un-deformed state

$$\Delta u_n = u_n(r, \theta = \pi) - u_n(r, \theta = -\pi), \quad (4)$$

where  $n$  takes the values 1 and 2, that refers to the coordinate direction  $x_n$  in the coordinate system in Figure 2. The crack opening components of the crack sides is related to the complex stress intensity factor,  $K$ , through

$$\sqrt{\frac{H_{11}}{H_{22}}}\Delta u_2 + i\Delta u_1 = \frac{2H_{11}}{\sqrt{2\pi}}(1 + 2i\varepsilon)\cosh(\pi\varepsilon)Kr^{i\varepsilon+1/2} \tag{5}$$

and the energy release rate can be related to the complex stress intensity factor through

$$G = \frac{H_{11}}{4\cosh^2(\pi\varepsilon)}|K|^2. \tag{6}$$

The mode mixity is defined as

$$\psi = \arctan \frac{\text{Im}(Kl^{i\varepsilon})}{\text{Re}(Kl^{i\varepsilon})}, \tag{7}$$

where  $l$  is a arbitrarily chosen length parameter.

### 3. ANALYSIS OF THE SANDWICH

In [6] an analysis was conducted where the stress state around the crack tip was shown to be dependent on only two generalized load parameters

$$P = -P_1 + C_1P_3 + C_2M_3/h \quad \text{and} \quad M = -M_1 + C_3M_3. \tag{8}$$

Here  $C_1$ ,  $C_2$  and  $C_3$  are dimensionless constants, given in the appendix.

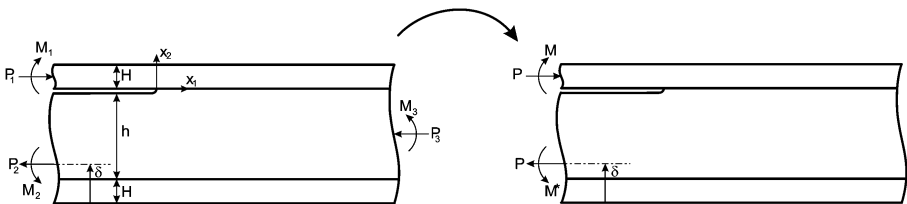


Figure 3. The stress state at the crack tip in the sandwich to the left can be achieved by analyzing the sandwich to the right, loaded with two reduced load parameters,  $P$  and  $M$ .

The energy release rate has been found by evaluating the J-integral [7] along the external boundary of the specimen. Since  $J=G$  when LEFM is applicable,  $G$  can be expressed in terms of the reduced load parameters as

$$G = \frac{\bar{s}'_2}{2} \left( \frac{P^2}{hU} + \frac{M^2}{h^3V} + 2 \frac{PM}{\sqrt{UV}h^2} \sin \gamma \right), \tag{9}$$

where  $U$  and  $V$  and  $\gamma$  are dimensionless constants given in the appendix, and  $\bar{s}'_2 = s'_{11}$  for material #2. By combining (5), (6), (7) and (9) while setting  $l=H$  the mode mixity is upon some manipulation expressed as

$$\tan \psi = \frac{\lambda \sin \omega - \cos(\omega + \gamma)}{\lambda \cos \omega - \sin(\omega + \gamma)}, \quad \lambda = \sqrt{\frac{V}{U}} \frac{Ph}{M} \text{ for } M \neq 0 \tag{10}$$

and  $\psi=\omega$  for  $M=0$ . Here  $\omega$  is a load independent phase angle that must be determined by numerical means.  $\omega$  is only a function of the geometry and the material parameters, so when  $\omega$  is known for one configuration, the mode mixity for any load combination can be calculated by (10). When  $\psi$  and  $G$  are determined the stress state around the crack tip is uniquely characterized. A discussion on how to choose  $l$  is to be found in [8] and [9].

#### 4. EXTRACTION OF THE MODE MIXITY FROM A FINITE ELEMENT MODEL

In this section the numerical method for determining  $\omega$  is treated. A method for extracting the mode mixity from an isotropic finite element solution is presented in [6]. In the present paper a brief recapitulation of the method is given together with a generalization of the basic equations so orthotropic materials can be handled. For a detailed description of the method consult the reference.

Assume that a finite element solution to a problem of the type in Figure 1 is known. The solution must be found with a mesh adequate for analyzing the deformations in the K-dominated zone close to the crack tip [10, 11]. By manipulation of (5), (6) and (7) it is found that the crack face displacements can be related to the energy release rate through

$$G = \lim_{r \rightarrow 0} \left\{ \frac{\frac{\pi}{4}(1/2 + \varepsilon^2)}{rH_{11}} \left( \left( \frac{H_{11}}{H_{22}} \Delta u_2 \right)^2 + \Delta u_1^2 \right) \right\} \quad (11)$$

and to the mode mixity through

$$\psi = \lim_{r \rightarrow 0} \left\{ \arctan \frac{\Delta u_1}{\Delta u_2} + \arctan 2\varepsilon + \varepsilon \ln(r/l) \right\} \quad (12)$$

as mentioned earlier, in the present work  $l$  is set equal to  $H$ .

These equations are only valid at the limit  $r \rightarrow 0$  because only here the singularity dominates the stress field. However, since the FE model is not able to resolve the singular stresses, the crack face openings very close to the crack tip should not be used. Instead, values of  $G$  and  $\psi$  are estimated by linear extrapolation in the interval  $H/10 < r < H/100$  of the right hand sides of (11) and (12) to  $r=0$ .  $\omega$  is now found by solving (10) with the reduced load parameters and the mode mixity inserted.

The accuracy of the model has been checked by comparing the estimated  $G$  found by extrapolating the right hand side of (11) to the exact computation of  $G$  found by (9). The computations used in this paper had a deviation less than 0.5%.

## 5. EXPERIMENTAL APPLICATION

The theory presented in the above sections was applied to a specific test setup whereby the critical energy release rate could be measured for varying mode mixities. The test is based on a DCB specimen loaded by pure moments as illustrated with Figure 1 by setting  $P_1 = P_2 = P_3 = 0$ . A detailed description of the test method is to be found in [12].

Sandwiches with PVC foam (Divinycel H80 and H130) core were tested. The H80 PVC foam has the elastic properties  $E=85\text{MPa}$ ,  $\nu=0.3$  and the density  $\rho=80\text{ kg/m}^3$ . H130 foam  $130\text{ kg/m}^3$  has the elastic properties  $E=175\text{MPa}$ ,  $\nu=0.3$  and the density  $\rho=130\text{ kg/m}^3$  [13].

The skin materials were glass laminates made from a multi-axial fabric and polyester resin. In between the laminate and the core material a chopped strand mat was placed. The laminates were fabricated by hand layup. The thickness of the skin laminates were  $H=6.7\text{mm}$  and the core thickness was  $h=40\text{mm}$ . The materials were tested to determine the necessary elastic parameters:  $E_{11}=14.9\text{GPa}$ ,  $E_{22}=16.5\text{GPa}$ ,  $E_{33}=7.53\text{GPa}$ ,  $\nu_{21}=0.20$ ,  $\nu_{13}=0.199$ ,  $\nu_{23}=0.16$ ,  $G_{12}=2.2\text{GPa}$ .

For the sandwich with H80 core the phase angle  $\omega$  was found to be  $\omega = 60.2^\circ$ . For the sandwich with H130 core the corresponding value was  $\omega = 66.0^\circ$ . Now, when  $\omega$  is known, both the energy release rate  $G$  and the mode mixity  $\psi$  can be determined analytically from the equations (9) and (10), respectively.

During the tests, all specimens were loaded by  $M_I$  (all other = 0) until crack initiation was seen and the crack had propagated 15mm.

After the test, depending on the mode mixity, different failure mechanisms were seen; for mode mixities above approximately  $-35^\circ$  for the sandwich with H130 and  $-40^\circ$  for H80 the crack grew just below the interface, in the core material. With this behaviour the crack tip was sharp and confined with in a few cell diameters. The fracture toughness was almost constant during the crack growth. The growth took place in jumps of approximately 2-3cm, but the same critical energy release rate was obtained at the onset of each jump. Towards a larger negative mode mixity, the crack tended to grow towards the skin material whereby fibre bridging was activated and an elongation of the fracture process zone was observed. The development of the fiber bridging was accompanied by a significant increase of the fracture toughness. In cases with a large negative mode mixity the bridging zone stretched to a length several times the skin thickness. Fibre bridging was accompanied by stable crack propagation.

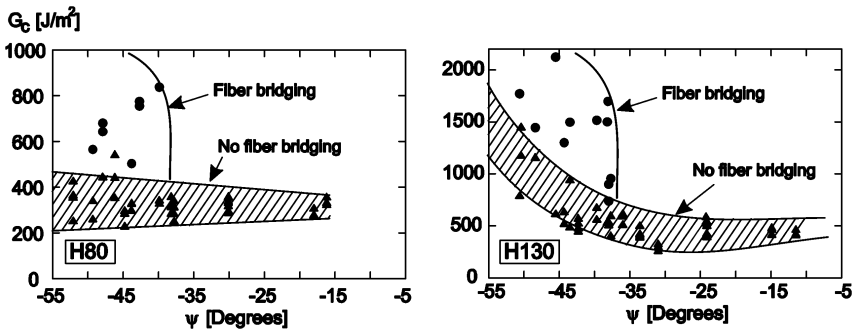


Figure 4. The figure shows fracture toughness as function of mode mixity. Triangular data points represent values where fiber bridging was not present. Circular data points represent maximum toughness values where fiber bridging had evolved in the crack.

In Figure 4 the fracture toughness is depicted as function of mode mixity for the two sandwiches under investigation. To get a slightly more physical understanding of the mode mixity axis; for mode mixities to the right of the figures the crack was dominated by normal opening (“mode I”) and at mode mixities to the left the crack was dominated by tangential separation (“Mode II”). In Figure 4, triangular data points represent crack growth not influenced

by bridging fibres. This situation was encountered in two cases: When the crack was growing below the interface or when fibre bridging had not started to evolve. Regarding the latter case, during the test the crack tip was observed in the beginning to jump approximately 10-20mm before the fibre bridging was activated.

## **6. DISCUSSION**

The first sections comprised a general analysis of an interface crack in a sandwich. The analysis was based in the assumption that the sandwich materials conformed to LEFM which implies that the fracture process zone should be small compared with other relevant geometries [14]. Based on the experimental results reported in the previous section it is clear that for many load combinations the fracture process is strongly non-linear and application of LEFM would be highly inappropriate. For the mode mixities where fibre bridging was not activated the fracture process was confined within one or a few cell diameters. In these cases LEFM is possibly not violated and would be appropriate for describing the fracture.

Since the equation for the energy release rate has been calculated from the J-integral [7] this equation is valid even if the large scale bridging occurs. The mode mixity measure, on the other hand, loses its validity and another measure for describing the “mode” should be introduced. Therefore the data points in Figure 4 representing steady state fracture toughness should not be related to the mode mixity axis since this has lost its validity. In [12] an appropriate method is described where the mode mixity is replaced by a phase angle describing the relation between tangential and normal opening at the crack tip.

## **ACKNOWLEDGEMENTS**

Parts of this work was part of the SaNDI (THALES JP3.23) project with participants from Norway, Denmark, Sweden, Finland and the United Kingdom. The support of the Ministries of Defence of the five participating nations is gratefully acknowledged. BFS was supported by the Danish Energy Authority under the Ministry of Economics and Business Affairs through a EFP2001-fund (journal no. 1363/03-0006).

**APPENDIX**

The following constants are to be used in the equations above

$$A_1 = \frac{1}{\eta}, I_1 = \frac{1}{12\eta^3}, A_2 = \frac{1}{\eta} + \Sigma, \eta = \frac{h}{H};$$

$$I_2 = \frac{1}{3\eta^3} + \frac{\Delta}{\eta} \left( \Delta - \frac{1}{\eta} \right) + \Sigma \left[ \left( \frac{1}{\eta} - \Delta \right)^2 + \left( \frac{1}{\eta} - \Delta \right) + \frac{1}{3} \right],$$

$$\Delta \equiv \frac{\delta}{h} = \frac{1 + 2\Sigma\eta + \Sigma\eta^2}{2\eta(1 + \Sigma\eta)}, A_3 = \frac{2}{\eta} + \Sigma, I_3 = \frac{2}{3\eta^3} + \frac{1}{\eta^2} + \frac{1}{2\eta} + \frac{\Sigma}{12}$$

$$C_1 = \frac{1}{A_3\eta}, C_2 = \frac{1}{2I_3} \left( \frac{1}{\eta} + \frac{1}{\eta^2} \right), C_3 = \frac{1}{12I_3\eta^3}.$$

$$\frac{1}{U} = \frac{1}{A_2} + \frac{1}{A_1} + \frac{\chi^2}{I_2}, \frac{1}{V} = \frac{1}{I_2} + \frac{1}{I_1}, \frac{\sin \gamma}{\sqrt{UV}} = \frac{\chi}{I_2}, \chi = \frac{3}{2\eta} + 1 - \Delta$$

$$H_{11} = \left[ 2n\lambda^{1/4} s'_{11} s'_{22} \right]_{\#1} + \left[ 2n\lambda^{1/4} s'_{11} s'_{22} \right]_{\#2}$$

$$H_{22} = \left[ 2n\lambda^{-1/4} s'_{11} s'_{22} \right]_{\#1} + \left[ 2n\lambda^{-1/4} s'_{11} s'_{22} \right]_{\#2},$$

$$n = \sqrt{(1 + \rho)/2}, \lambda = \frac{s'_{11}}{s'_{22}}, \rho = \frac{2s'_{12} + s'_{66}}{2\sqrt{s'_{11} s'_{22}}}.$$

**REFERENCES**

1. H. Cao and A.G. Evans, An experimental study of the fracture resistance of bimaterial interface, *Mechanics of Materials*, Vol. 7, pp. 295-305, 1989.
2. K.M. Liechti and Y.S. Chai, Biaxial loading experiments for determining interfacial toughness, *J. Appl. Mech.*, Vol. 58, pp. 680-687, 1991.
3. M.D. Thouless, Fracture of a model interface under mixed-mode loading, *Acta. Met.* Title, Vol. 38, pp 1135-1140, 1990.
4. R. M. Jones, *Mechanics of composite materials*, McGraw-Hill, 1975.
5. Z.Suo, Singularities, interfaces and cracks in dissimilar anisotropic media, *Proc. R. Soc. Lond. A*, Vol. 427, pp. 331-358, 1989.

6. R.C. Østergaard and B.F. Sørensen, Interface crack in sandwich specimens, Submitted to International Journal of Fracture, 2005.
7. J.R. Rice, A path-independent integral and the approximate analysis of strain concentration by notches and cracks, Journal of Applied Mechanics, Vol. 35, pp. 376-386, 1968.
8. J.W. Hutchinson and Z. Suo, Mixed mode cracking in layered materials, Advances in applied mechanics, Vol. 29, pp. 63-191, 1992.
9. J.R. Rice, Elastic Fracture Mechanics Concepts for Interfacial Cracks, Journal of Applied Mechanics, Vol. 55, pp. 98-103, 1988.
10. P.P.L. Matos, R.M. McMeeking, P.G. Charalambides and M.D. Drory, A method for Calculating Stress Intensities in Bimaterial Fracture, International Journal of Fracture, Vol. 40, pp.235-254, 1989.
11. J.L. Beuth, Separation of crack extension modes in orthotropic delamination models, International Journal of Fracture, Vol. 77, pp.305-321, 1996.
12. B.F. Sørensen et. al., A general mixed mode fracture mechanics test specimen: The DCB-specimen loaded with uneven bending moments, Risø-R-1394(EN), Risø National Laboratory, Denmark, 2004.
13. D. Zenkert, The handbook of sandwich constructions, Engineering Materials Advisory
14. Services Ltd., UK, 1997.
15. G. Bao and Z. Suo, Remarks on crack-bridging concepts, Appl. Mech. Rev, Vol. 45, pp. 355-361, 2001.

# NUMERICAL STUDY OF FRACTURED SANDWICH COMPOSITES UNDER FLEXURAL LOADING

E.E. Theotokoglou<sup>1</sup>, L.A. Carlsson<sup>2</sup>, C.D. Vrettos<sup>1</sup> and H. Mahfuz<sup>2</sup>

<sup>1</sup>*Faculty of Applied Sciences, Department of Mechanics-Laboratory of Strength Materials, The National Technical University of Athens, Zographou Campus, Theocaris Bld., GR-0157 73 Athens, Greece, Email: [stathis@central.ntua.gr](mailto:stathis@central.ntua.gr)*

<sup>2</sup>*Department of Mechanical Engineering, Florida Atlantic University, Boca Raton, FL 33431, USA, Email: [carlsson@acc.fau.edu](mailto:carlsson@acc.fau.edu)*

**Abstract** Fatigue crack growth of foam core sandwich beams loaded in flexure has been investigated numerically. Extensive fatigue data from foam core sandwich composites under flexural loading were analyzed. A first core-skin debond parallel to the beam axis is considered. A static non-linear elastic two-dimensional finite element analysis of the sandwich beam is performed to evaluate the stress intensity factors at the crack tips.

**Keywords:** sandwich beam, fatigue crack growth, flexural loading, finite element method, stress intensity factors.

## 1. INTRODUCTION

The sandwich structural concept where thin, stiff facings are separated by a low density, compliant core material has arisen much attention for the design of light-weight structures in the building transportation and sporting industries.

In sandwich structures, low density foam core are receiving increasing attention. Mechanical properties of cellular foams have been studied by Gibson and Ashby [1]. Ashby et al. [2] investigated the fracture mechanisms of linear elastic foam. Zenkert and Backlund [3] studied the mode-I crack propagation of PVC cellular foam. Harte and Fleck [4] investigated failure modes in aluminium foam core sandwich panels loaded in cyclic flexure

fatigue. Burchardt [5] numerically and Burman and Zenkert [6] numerically and experimentally have investigated fatigue characteristics of foam. Noury et al. [7] studied fatigue crack growth in rigid PVC cellular foam under combined mode-I and mode-II loading.

The foam in sandwich structures is typically the weakest part and is the first to fail under static or cyclic loading. Interface debond damages between the face and the core can originate either from the manufacturing process or during service. In sandwich structures interfacial defects have been studied by Carlsson et al. [8-10] and Zenkert et al. [11-13].

Data from fatigue crack tests performed in [14] for foam core sandwich composites under flexural loading were analyzed. At first a core-skin debond  $a_1$  parallel to the beam axis is considered (Fig. 1), in accordance with experimental data [14]. When subjected to flexural loading, this debond will propagate slowly along the top interface and eventually kinked into the core as a shear crack. Stress intensity factors are calculated using Finite Element Method, and assuming linear fracture mechanics and plane strain conditions. Results from the finite element analysis combined with the experimental data predict the crack growth behaviour under flexural loading. The simplicity of the proposed procedure and the numerical model developed, make it possible the prediction of the crack propagation for various types of sandwich beams under flexural loading.

## 2. NATURE OF THE PROBLEM

The sandwich considered is depicted in Figure 1 and is composed of PVC-core and face sheets from isotropic glass (Table 1). The dimensions of the test specimen were  $L = 228.6$  mm (support span) and  $b = 63.5$  mm (width). The core thickness was  $t_2 = 12.7$  mm and the face sheet thickness was  $t_1 = 2.28$  mm. The overall thickness was 17.26 mm.

Static tests were first conducted to generate ultimate strength data [14]. Flexural fatigue tests on sandwich beams were performed at room temperature under load control at a stress ratio of 0.1, using a sinusoidal wave form. Fatigue data was generated for a minimum of three specimens at stress levels  $r$  of 90%, 85%, 80%, 75%, 70%, 65% and 60% of the ultimate flexural strength.

Specimens were tested for fatigue at various stress levels under the conditions described earlier [14]. Three distinct damage events take place before the failure of the specimen.

Damage event 1: The crack initiation and propagation was on the compression side just below the top face sheet/core interface. This delamination crack was about 1-1.5mm below the interface. The crack runs

parallel to the beam axis from the point of initiation towards the end support (Figure 1). Damage event 1 occupies about 85% of fatigue life.

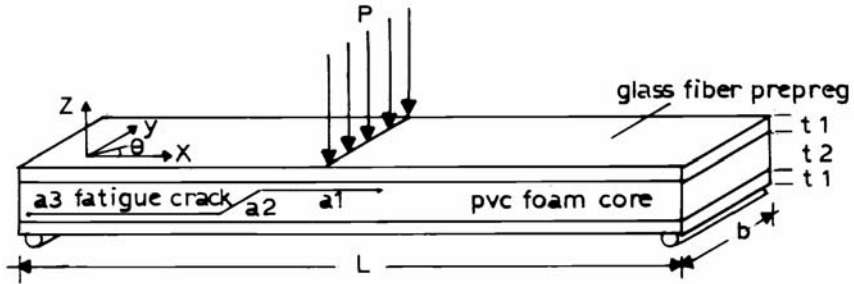


Figure 1. A sandwich beam under flexural loading.

Table 1. Specimen properties.

Material	$E$ ( $N/mm^2$ )	$\nu$
Face sheets (isotropic glass)	16300	0.3
PVC foam core (R75 by DIAB [14])	80	0.4

Damage event 2: The propagated crack in event-1 kinks at a certain distance and shears through the core thickness. The crack reaches the bottom face sheet/core interface at the end of this event.

Damage event 3: Delamination takes place at bottom face/core interface using the separation of the core from the face sheet. This is also a rapid event and occupies the remaining 7-8% of fatigue life.

During fatigue cycling, the crack length was measured by using mechanical and optical means. The total crack growth is depicted as  $a_1$  for event-1,  $a_2$  for event-2 and  $a_3$  for event-3. From the plot of the crack lengths via  $N$  (number of cycles) at different stress levels in [14], it is observed that the length of the crack depends on the stress level. Lower is the stress level, the longer is the crack in damage event-1. Thus, at lower stress levels ( $r = 0.65, 0.70, 0.75$ ) damage event-1 dominates the fatigue life and consequently event-1 crack propagation may be used to develop a failure model for sandwich composites.

### 3. ANALYSIS MODEL

The sandwich beam considered is shown in Figure 1. Considering the lower stress level  $r = 0.70$ , the load  $P$  is taken sinusoidal with the following characteristics

$$P_{\max} = 0.7P_{\text{ultimate}} = 943.46N \quad (1)$$

where  $P_{\text{ultimate}}$  the static failure load of the beam, and

$$s_r = P_{\min} / P_{\max} = 0.1 \quad (2)$$

For the stress level  $r = 0.70$ , the number of cycles ( $N$ ) is related to the crack length  $a_1$  in damage event-1, by the following equation [14]

$$N = 44a_1^2 + 2133a_1 + 28976, \quad (3)$$

which is the best fitting quadrature curve obtained from the graph of experimental data [14].

By differentiating equation (3), the crack propagation rate is obtained and is given by

$$da_1/dN = 1/(88a_1 + 2133) \quad (4)$$

For different crack lengths  $a_1$ , the number of cycles and the crack propagation rate, are given in Table 2.

Table 2. Crack length  $a_1$  against  $N$  and  $da_1/dN$ .

Model	Crack length $a_1$ (mm)	Number of cycles (equation (3))	Crack propagation rate (mm/cycle) (equation (4))
0	0	0	$4.688 \times 10^{-4}$
1	1	31153	$4.502 \times 10^{-4}$
2	5	40741	$3.886 \times 10^{-4}$
3	10	54706	$3.319 \times 10^{-4}$
4	20	89236	$2.569 \times 10^{-4}$
5	30	132566	$2.095 \times 10^{-4}$
6	40	184696	$1.769 \times 10^{-4}$
7	50	245626	$1.531 \times 10^{-4}$
8	60	315356	$1.349 \times 10^{-4}$
9	65	353521	$1.273 \times 10^{-4}$

The cracked sandwich beam is analyzed using the finite element method. Because of high stress gradients around the interface, fairly fine mesh consisting of two dimensional plane strain elements was used. The assumption of plane strain is justified throughout. The dimensions of the sandwich beam considered are shown in Figure 1. The details of the finite element mesh near the crack tip are shown in Figure 2.

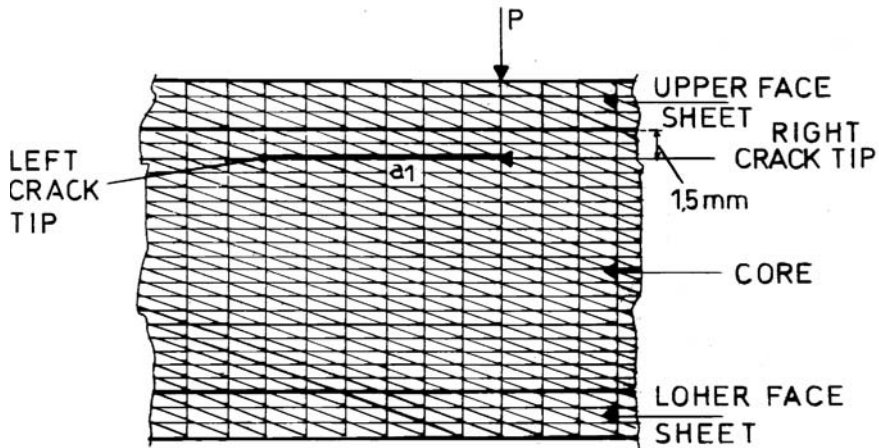


Figure 2. Mesh detail at the crack tip.

The finite element analysis is performed with the use of the general purpose finite element program ANSYS [15]. The 6 node two-dimensional plane strain triangular elements (plane 2) were used in order to model the beam. The frictionless contact area at the crack surfaces is modeled with 2-node linear contact elements (contact 12) [15], in order to prevent one surface from entering into the other. Singular elements (mid-side nodes at  $\frac{1}{4}$ ) were used at the two crack tips. Finally the finite element mesh consists of 6200, 6-node elements (plane 2), 70, 2-node contact elements (contact 12) and 12 singular elements.

In order to analyze the event-1 crack propagation a small crack is considered at 1.5mm below the interface under the central load introduction and parallel to the beam axis. This small crack is considered propagating under the interface. For the different crack lengths the stress intensity factors,

$$\Delta K_{\text{I}} = K_{\text{I}}^{\text{max}} - K_{\text{I}}^{\text{min}}, \quad \Delta K_{\text{II}} = K_{\text{II}}^{\text{max}} - K_{\text{II}}^{\text{min}}, \quad (5)$$

are calculated automatically from Ansys [15] for the left and right crack tip. The results for  $\Delta K_I$  and  $\Delta K_{II}$  are given in Tables 3 and 4.

Table 3. Stress intensity factors at the left crack tip.

Model	Crack length $a_1$ (mm)	Mode I $\Delta K_I$ $(N/m^{3/2})$	Mode II $\Delta K_{II}$ $(N/m^{3/2})$
0	0	0.00000000	0.00000000
1	1	0.00156870	0.0015974
2	5	0.00345681	0.3050712
3	10	0.00224595	0.7604730
4	20	0.00067662	1.5596910
5	30	0.00054041	2.3451120
6	40	0.00061104	3.0890160
7	50	0.00081648	3.8784690
8	60	0.00103446	4.6078830
9	65	0.00113274	4.9427910

Table 4. Stress intensity factors at the right crack tip

Model	Crack length $a_1$ (mm)	Mode I $\Delta K_I$ $(N/m^{3/2})$	Mode II $\Delta K_{II}$ $(N/m^{3/2})$
0	0	0.00000000	0.00000000
1	1	0.00015986	0.0000154
2	5	0.00406413	0.0309015
3	10	0.00415712	0.1916334
4	20	0.00365198	0.6289479
5	30	0.00332987	1.1729340
6	40	0.0302841	1.7084340
7	50	0.00285535	2.3819040
8	60	0.0253355	3.0939930
9	65	0.00234171	3.4193880

In Figures 3 and 4  $\Delta K_{II}$ -values for the different crack lengths  $a_1$  as a function of the crack propagation rate, are also given.

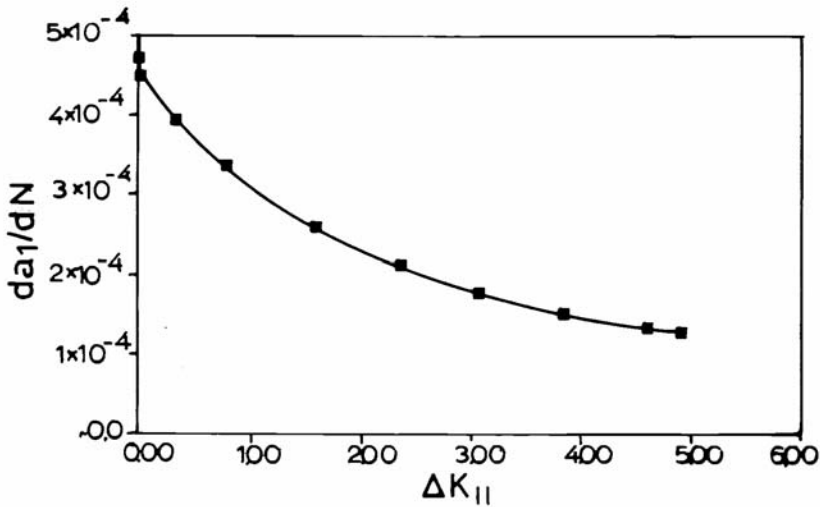


Figure 3.  $\Delta K_{II}$  as a function of  $da_1/dN$  at the left crack tip.

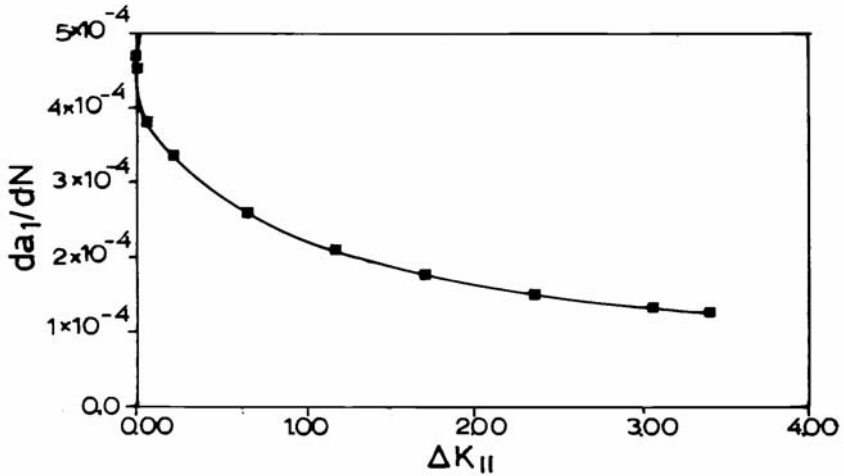


Figure 4.  $\Delta K_{II}$  as a function of  $da_1/dN$  at the right crack tip.

#### 4. CONCLUSIONS

The static behavior of R75 PVC foam sandwich composite loaded in three-point flexure has been examined numerically. The crack propagation

process was simulated numerically with finite element models for the different crack lengths in the core of a sandwich beam very close to the core-skin interface and parallel to the beam axis. The finite element analysis was static and non-linear elastic. The non-linearity concerned contact elements. The stress intensity factors at the vicinity of the crack tip were calculated for the different crack lengths using the linear fracture mechanics approach.

The crack lengths considered in the core were in accordance with the crack initiation and propagation in the core of the sandwich beam just below the top face in the sub-interface, observed in the experiments.

From the numerical investigation it follows that the core is mainly subjected to shear. The crack propagation on the compression side is generally mode II dominated. The crack propagation rate is decreasing as the crack propagates.

The above stress analysis gives only a first indication of the failure mode that takes place in a sandwich beam under flexural loading. More work is required in order to predict the crack kinking into the core.

## REFERENCES

1. Gibson, L.H. and Ashby, M.F., "Cellular solid-structure and properties", 2nd ed. Cambridge: Cambridge University Press; 1997.
2. Ashby, M.F., Gibson, L.J. and Maiti, S.K., "Fracture Toughness of Brittle Cellular Solids", *Scr. Metall.*, Vol. 18, pp. 213-217, 1984.
3. Zenkert, D. and Backlund, J., "PVC sandwich core materials-mode I fracture toughness", *Compos. Sci. Technol.*, 34:225-42, 1989.
4. Harte, A.M. and Fleck, N.A., "The fatigue strength of sandwich beams with alloy foam core", *Internal Journal Fatigue*, 23:499-507, 2001.
5. Burchardt, C., "Bonded sandwich T-joint for maritime applications", Ph.D. Dissertation, special Report No. 32, Institute of Mechanical Engineering, Aalborg University, 1996.
6. Burman, M. and Zenkert, D., "Fatigue crack initiation and propagation in sandwich structures", Doctoral Thesis, Report 98-29, Department of Aeronautics, Royal Institute of Technology, 1998.
7. Noury, P.M.C., Sheno, R.A. and Sinclair, I., "Fatigue crack growth in rigid PVC cellular foam under combined mode-I and mode-II loading", *Proceedings of Fourth International Conference on Sandwich Construction*, Editor Karl-Axel Olsson, EMAS Publishing, Vol. 2, pp. 491-502, 1998.
8. Carlsson, L.A., Sendlein, L.S. and Merry, S. L., "Characterization of Face Sheet/Core Shear Fracture of Composite Sandwich Beams", *Journal of Composite Materials*, Vol. 25, No. 1, pp. 101-116, 1989.
9. Carlsson, L.A., "On the Design of the Cracked Sandwich Beam (CSB) Specimen", *Journal of Reinforced Plastics and Composites*, Vol. 10, pp. 434-444, 1991.
10. Carlsson, L.A., and Prasad, S., "Interfacial Fracture of Sandwich Beams", *Engineering Fracture Mechanics*, Vol. 44, No 4, pp. 581-590, 1993.

11. Zenkert, D., "Damage Tolerance of Foam Core Sandwich Constructions", Ph. D. Thesis, Report 90-8, Department of Aeronautics, Royal Institute of Technology, Stockholm, Sweden, 1990.
12. Zenkert, D., "Damage of Sandwich Beams with Interfacial Debondings", *Composite Structures*, Vol. 17, pp. 331-350, 1991.
13. Zenkert, D. and Falk, L., "Interface Debondings in Foam Core Sandwich Beams and Panels", In *Proceedings 8th International Conference on Composite Materials (ICCM/VIII)*, Vol. 3-H, July 15-19, Honolulu, 1991.
14. Kulkarni, N., Mahfuz, H., Jeelani, S. and Carlsson, L.A., "Fatigue crack growth and life prediction of foam core sandwich composites under flexural loading", *Composite Structures*, Vol. 59, pp. 499-50, 2003.
15. ANSYS Engineering Analysis System User's Manual, Swanson Analysis Systems, Inc., 1992.

# DEPENDENCE OF SANDWICH DAMAGE INITIATION AND CRACK PROPAGATION ON CORE MATERIAL FRACTURE PROPERTIES

Lukas Berger<sup>1</sup>, Markus Morgenthaler<sup>1</sup>, Wesley Cantwell<sup>2</sup>, Kurt Feichtinger<sup>3</sup> and Russell Elkin<sup>3</sup>

<sup>1</sup>*Alcan Airex AG, CH-5643 Sins, Switzerland,* <sup>2</sup>*The University of Liverpool, Liverpool L69 3GH, United Kingdom,* <sup>3</sup>*Alcan Baltek Corp., Northvale, NJ, 07647, USA*

**Abstract** In this investigation, three-point bend tests were performed on pre-cracked and unnotched sandwich structures offering a wide range of fracture toughnesses. It has been shown that an areas-based method is the most appropriate for characterizing the fracture toughness of the sandwich structures. It has also been shown that tough core materials are less sensitive to delaminations between core and skin than their more brittle counterparts.

**Keywords:** fracture mechanics, toughness of core materials, pre-crack, sandwich structures, surface imperfections.

## 1. INTRODUCTION

Shear strength and stiffness are usually considered as being fundamentally important criteria in the selection of a core material for sandwich applications. In this respect, amongst the wide range of continuous cores currently available, Balsa and crosslinked PVC cores offer the best strength to weight ratios. When damage occurs, however, linear core materials are able to undergo significant ductile and plastic deformation before failure and, as a consequence, exhibit a superior impact behavior compared with their more brittle counterparts.

Defining a link between the fracture behavior of sandwich structures and linear elastic fracture mechanics (LEFM) is not an easy task. This is in part due to the fact that ductile materials do not generally obey the laws of linear

elasticity, but also because of the complex cell structure of foam cores, which can influence the radius of the crack front. Such a link is highly desirable in order to predict the fracture behavior of a sandwich structure. Another advantage of this link would be that the requirements of the quality of the surface of the core could be defined.

Some work has been conducted by Zenkert, however, this was limited to relatively brittle cores such as those based on crosslinked PVC and PMI foams [1]. In a previous study, the fracture toughness data of a wide range of cores had been determined using the single edge notch bend geometry [2]. It has been shown that the fracture toughness,  $K_{Ic}$ , depends solely on the density of the foam and not on the damage tolerance of the core material; therefore,  $K_{Ic}$  cannot be used to differentiate between the damage tolerances of different core materials [2]. The critical strain energy release rate,  $G_{Ic}$ , was somewhat better in this respect; however, the best results were obtained when considering the work of fracture of the core materials as a criterion for damage tolerance.

The objective of this study is to analyze the fracture mechanics data of sandwiches with a number of core materials in Mode II and to compare these with the previously-published data obtained from Mode I tests [2]. It is hoped that this way a clearer relationship can be found between damage tolerance as it is experienced in practice in sandwich three or four point bend tests and fracture toughness data as they are measured with methods of fracture mechanics than was found in the previous paper [2].

## 2. EXPERIMENTAL

### 2.1 Sample preparation

The core materials selected for this study are summarized in Table 1; the mechanical properties are taken from the relevant datasheets for the nominal foam density. The fracture mechanics data (determined according to ASTM D5045-91) are taken from previously-published data [2], with the exception of the T90 material, which is an experimental PET foam; here, tests were performed according to the procedure described in an earlier study [2].

Sandwich samples were fabricated with two layers of triaxial 840 g/m<sup>2</sup> glass fiber reinforced epoxy skins. The skins were produced using a resin infusion technique; core and skins were bonded with an epoxy resin (Araldite AW134/HY991). The core thickness  $c$  was 10 mm, the skin thickness  $t$  was approximately 1.2 mm and the width of the samples  $B$  was 28 mm. One set of samples contained a pre-crack made of a folded

aluminum foil (see Figure 1) which was placed between the skin and the core before the two were bonded.

Table 1. Core materials used in this investigation and their properties (datasheet values and fracture mechanics data from [2]).

Material	Base polymer	Nom. Density	Shear strength	Kq	Gq	Work of fracture
		kg/m <sup>3</sup>	MPa	MPa√m	J/m <sup>2</sup>	J/m <sup>2</sup>
Airex C70.75	Crossl. PVC	80	1.2	0.095	179	166
Airex R63.80	Lin. PVC	90	1.0	0.219	768	4453
Airex R82.80	PEI	80	1.1	0.158	477	592
Airex T90.100	PET	100	0.9	0.140	427	672
Baltek SL45	Balsa	89	1.56	0.048	75	115
Rohacell 71WF	PMI	71	1.3	0.132	169	136

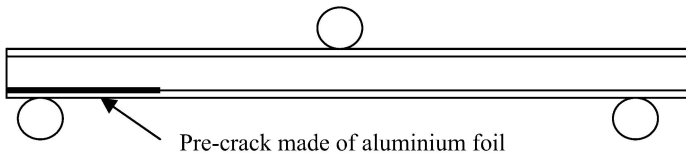


Figure 1. Sandwich samples for three point bend tests on samples containing a pre-crack.

## 2.2 Mechanical testing and data analysis

The three point bend tests were performed according to ASTM C393. The span was set to 120 mm and the diameter of the rollers was 20 mm.

From the three point bend test, the fracture energy  $G$  of the pre-cracked samples was determined in two ways as described in an earlier study [3]: firstly, by using a compliance calibration procedure based on the following equation:

$$G = \frac{P^2}{2B} \frac{dC}{da}$$

The compliance,  $C$ , was measured on samples with pre-crack lengths,  $a$ , of 0, 10, 20 and 30 mm. The slope of the compliance vs. crack length curve was calculated by fitting a second order polynomial to the data points.

Secondly, an areas method was applied where the area under the load vs. displacement curve was divided by the resulting fracture area.

Skin adhesion tests were performed using the Airex standard AM064, which is a peel test similar to the method proposed by Cantwell and Davies [3]. In this test, the skins are peeled off the core of the sample, and the energy under the load-deformation curve is divided by the resulting fracture surface area.

### 3. RESULTS AND DISCUSSION

Typical load deformation curves of uncracked samples are shown in Figure 2. In the case of the R63.80 and R82.80 samples, no shear crack occurred in the core, instead, the samples failed by indentation of the upper skin. All of the remaining samples failed as a result of core shear, involving a shear crack at 45° to the sample axis in the foam cored samples, and a vertical crack parallel to the wood fiber axis in the Balsa-cored samples.

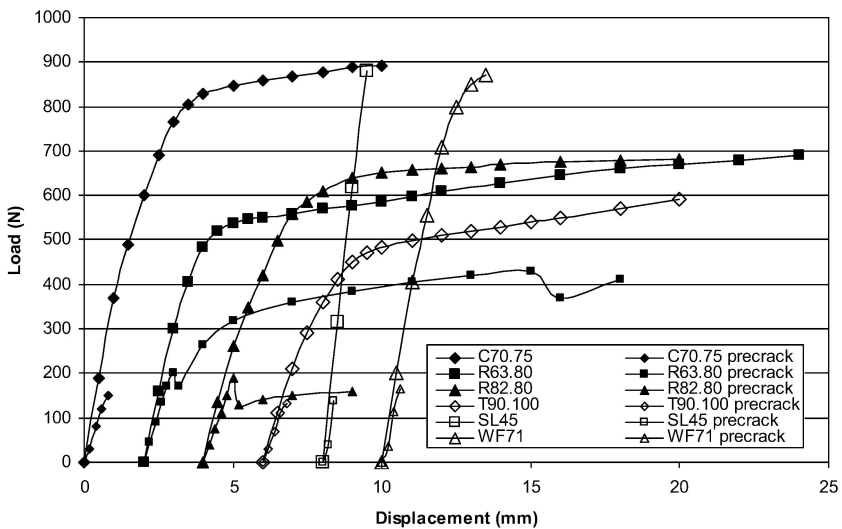


Figure 2. Typical load displacement curves following three point bend tests on uncracked samples (large symbols) and 30mm pre-cracked samples (small symbols). The curves are offset for clarity.

Load-deformation curves from samples containing a pre-crack are also shown in Figure 2. In the R63.80 and R82.80-based samples, the crack propagated in a stable manner, whereas crack propagation was unstable in all of the other specimens. In all cases, the crack propagated at an angle of approximately  $70^\circ$  to the sample axis.

The uncracked samples based on either crosslinked PVC foam (C70.75) or PET foam (T90.100) underwent some plastic deformation before failing, whereas failure in the pre-cracked samples involved little or no plastic deformation; the samples based on the PMI foam (Rohacell 71 WF) and the balsawood (SL 45) failed without any appreciable plastic deformation in both the uncracked and pre-cracked conditions. It is worth noting that in the pre-cracked R63.80 samples, the crack initially propagated into the resin rich area located in front of the pre-crack, before propagating very slowly into the core.

Figure 3 shows the variation of the compliance of a C70.75 sample as a function of crack length. In calculating the fracture energy, the slope of the compliance vs. crack length curve at a crack length of 30 mm was taken, since this was crack length at which the samples subsequently failed. The results of the tests are summarized in Table 2.

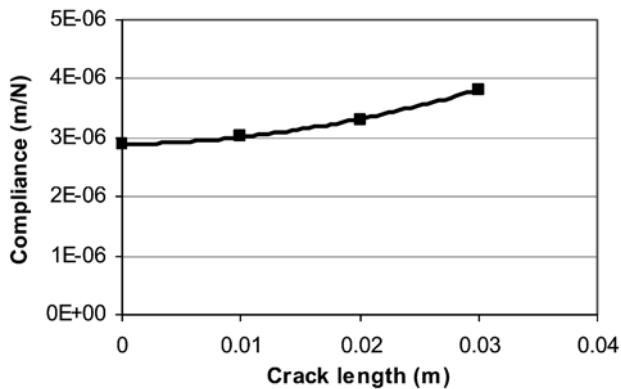


Figure 3. The variation of specimen compliance with crack length for the C70.75 samples.

Table 2. Results of tests performed in this study.

	Density	Failure load without p.c.	Deflection w/o pre-crack	Failure load with pre-crack	Deflection with pre-crack	Fracture energy $G$ (Compl. cal. method)	Fracture energy $G$ (area method)	Peel energy
	kg/m <sup>3</sup>	N	mm	N	mm	J/m <sup>2</sup>	J/m <sup>2</sup>	J/m <sup>2</sup>
C70.75	82.3	890	6.1	140	0.67	26±6	133	305
R63.80	106.6	690	22	200 <sup>1</sup> 430 <sup>2</sup>	1.1 <sup>1</sup> 12 <sup>2</sup>	44±10 <sup>1</sup> 5600±1100 <sup>2</sup>	237 <sup>1</sup> 2420 <sup>2</sup>	2987
R82.80	74.8	680	15	192	1.1	46±6	285	432
T90.100	102.9	590	14	130	0.8	26±5	135	115
SL45	77.8	880	1.5	140	0.45	16±4.5	122	205
71WF	71.9	870	3.7	170	0.64	42±8	117	85

<sup>1</sup> crack propagation into resin rich area in front of crack tip, <sup>2</sup> crack propagation into core

As expected, the failure load is much lower if a pre-crack is present compared to samples without pre-cracks. Similar observations were made when samples containing resin filled grooves or with unfilled grooves were tested in a similar set-up [4]. From Figure 4, it is obvious that the R63 cored samples are least affected by the presence of the pre-crack in terms of maximum deflection. From this graph it can be concluded that R63 is the toughest core material among those investigated here. It can also be concluded that its toughness is least affected by the presence delaminations between core and skin.

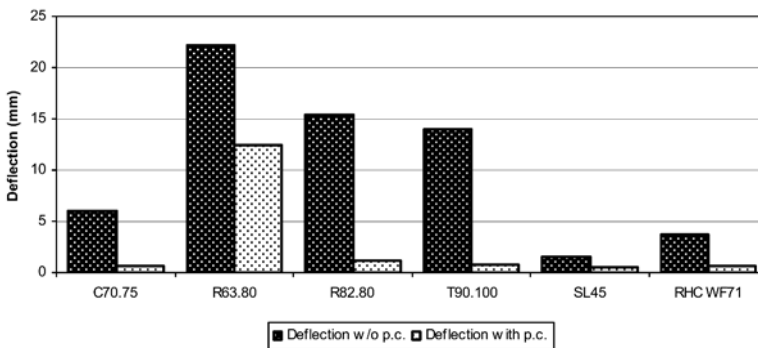


Figure 4. Maximum deflection of uncracked and pre-cracked samples.

If the fracture energies are compared in more detail (see also Figure 5), it is obvious that the fracture toughness as measured using the compliance

calibration method is not suitable for giving useful information about the toughness of the material. In contrast, the areas method gives higher results than the compliance-based method, with the scatter in the results being in the range of 10 to 20 %. These values are relatively close to the work of fracture data listed in Table 1.

The standard deviation in the peel energy data is also in the range of 10 to 20 %. The values are again quite similar to those obtained using the areas method to determine the fracture energy or the work of fracture. It can be speculated that the failure modes are similar (if the adhesion between skin and core is sufficient, the crack propagates entirely in the core material and not between skin and core). The exception is the T90.100 system, where the work of fracture is significantly larger than the fracture toughness or the peel energy. However, in this system, the crack propagation direction in the work of fracture test samples was perpendicular to the extrusion direction, whereas it was parallel to this direction in the peel tests. Therefore, the results can not be directly compared. In the sandwich samples, the extrusion direction was in the sample axis; here, the uncracked material behaved in quite a ductile manner whereas pre-cracked samples failed in a very brittle manner.

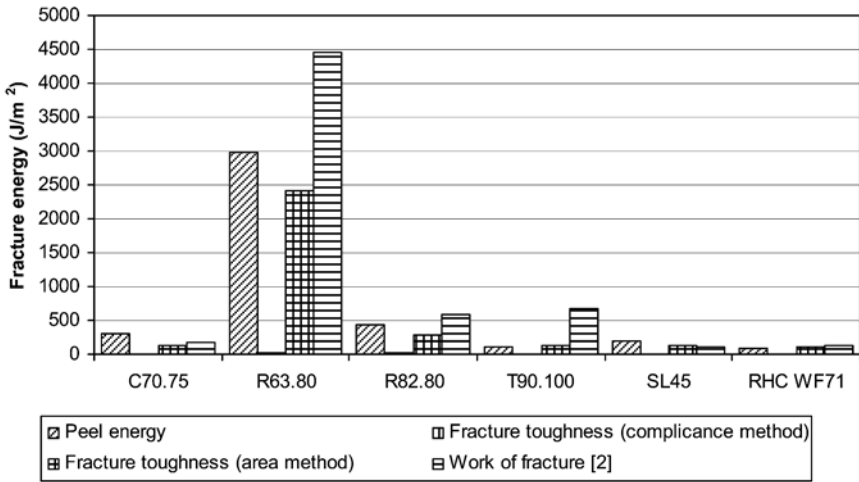


Figure 5. Comparison of peel energy, stress energy release rate (area and compliance method) and work of fracture as reported in Tables 1 and 2.

## 4. CONCLUSIONS

The fracture toughness of various sandwich core materials has been measured using two different methods. It has been shown that a compliance-based method is not suitable to distinguishing between tough and brittle core materials. In contrast, an areas-based method is more satisfactory, the range of results agreeing with work of fracture data measured in tests according to ASTM D5045-91, indicating that the failure modes were similar. There is also a good agreement between the fracture energies and the peel energies of the samples manufactured here, again indicating that the failure modes are similar.

It was also shown that tough core materials like R63 are less sensitive to delaminations between core and skin than their more brittle counterparts.

## REFERENCES

1. Zenkert, D., *The Handbook of Sandwich Construction*, EMAS, 1997.
2. Berger, L., Morgenthaler, M., Kuang, K., Reyes, G., Cantwell, W.J., "Fracture Behaviour, Damage Initiation and Crack Propagation in Sandwich Core Materials", Sixth Int. Conference on Sandwich Structures, 2003.
3. Cantwell, W. J. and Davies, P., "A Study of Skin-Core Adhesion in Glass Fibre Reinforced Sandwich Materials", *Applied Composite Materials*, 3, p 407-420, 1996.
4. Berger, L., Morgenthaler, M., Loiselet, K., Dransfeld, C., "Filling or not Filling the Slits in Contourable Sandwich Cores with Resin? – Effect on the Properties of the Sandwich Construction", *Proceedings of 25th SAMPE Europe conference*, Paris, March 30 to April 1, 2004.

# DEPENDENCE OF INPLANE SANDWICH SHEAR DEFORMATION ON CORE MATERIAL TYPE AND THICKNESS

Markus Morgenthaler, Lukas Berger, Kurt Feichtinger and Russell Elkin  
*Alcan Airex AG, CH-5643 Sins, Switzerland, Alcan Baltek Corp. Northvale, NJ, 07647, USA*

**Abstract** In this study in plane shear tests on sandwich plates were performed using two different experimental set-ups. Failure modes, as well as maximum failure loads were compared with predictions using sandwich calculation equations given by Zenkert and Plantema. It could be shown, that the prediction of failure load and mode was quite consistent with measurements for panels of 10mm thickness or more. Very thin panels could not be predicted correctly.

**Keywords:** inplane shear, sandwich plates, core material, skin wrinkling, shear buckling, shear strength.

## 1. INTRODUCTION

In plane shear loads are often encountered in sandwich structures, such as shear webs in windmill blades or stringers or bulkheads in the hull of a boat. Usually the forces are carried by the fibre reinforced faces, For optimum load transfer, the fibres are oriented in a direction of  $\pm 45^\circ$  with respect to the axis of the beam. The shear strength of the core is of minor importance, but the core must resist the shear buckling of the sandwich. Because of the high compressive loads in the faces, face wrinkling needs to be considered as well.

The objective of this study is to find a suitable experimental setup to test in plane shear properties of sandwich plates. Therefore, two different methods are used to investigate the influence of the core on the in plane shear properties of the sandwich plates. Several parameters are varied: Core

type and density, thickness of core and thickness of the reinforced faces, in order to favour different failure modes like general shear buckling, skin wrinkling and shear failure of the skins. The resulting loads and failure modes are compared to sandwich calculation equations given by Zenkert and Plantema [1, 2].

## **2. EXPERIMENTAL**

To measure the in plane shear properties two different experimental setups have been constructed for a standard tensile testing machine. The first setup (later referred to as «Type 1») is designed based on the principle of the rail shear test of composite materials (ASTM D4255). The size of the sample is increased to allow the analysis of shear buckling and face wrinkling of sandwich structures. The second setup («Type 2») is a square sample with incorporated aluminium bars on every side. Both types use steel frames to induce the applied load through the incorporated aluminium bars into the sample.

### **2.1 Test geometry**

In Figures 1 and 2 the two sample geometries are shown. Figure 1 shows the geometry of the type 1 sample. Aluminium bars are incorporated into the sample in order to transverse the load uniformly onto the sandwich. The two outer bars are attached to the bottom of the frame of the testing machine. The middle bar is mounted to the crosshead. In plane shear is subjected to both sandwich parts.

Figure 2 shows the geometry of the type 2 sample. Also aluminium bars are incorporated into the sandwich at the edges. Two opposite corners of the sandwich are mounted to the testing machine.

In Figure 3 pictures of the two test setups in the testing machine are shown.

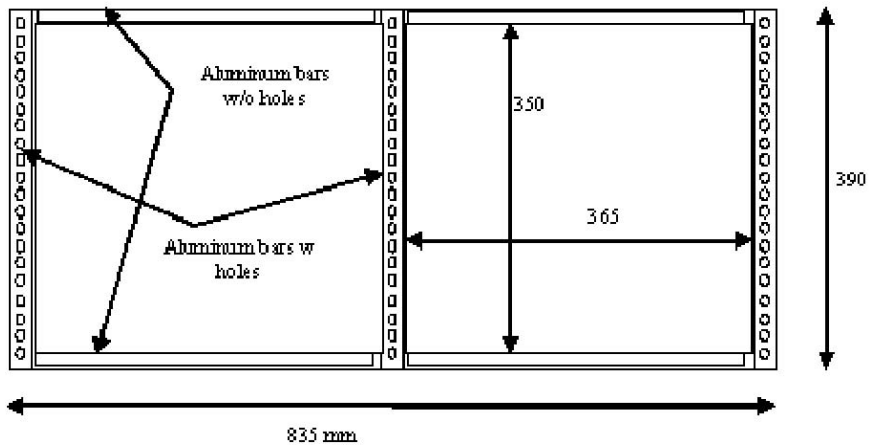


Figure 1. Sample geometry Type 1.

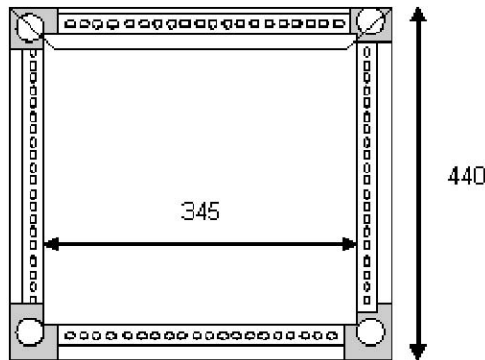


Figure 2. Sample geometry Type 2.

## 2.2 Sample preparation

The list of samples tested in this study is presented in Table 1. The skins were made in vacuum infusion technology using biaxial glass fabrics with a glass weight of 300 g/m<sup>2</sup>. The skins were then bonded to the core material using an Araldite epoxy adhesive (Araldite AW134/HY991) also under a vacuum bag. The area around the edges and along the centre line of the type 1 samples was reinforced with skin layers in order to avoid a failure near the steel rail.



Figure 3. Test setup for type 1 (left side) and type 2 (right side) in a Zwick tensile testing machine.

Three samples were tested in type 1 mode (sample ID: 1,2 and 3). All other samples were tested in type 2 mode. The density of the foam, the thickness of the foam and the skin thickness were parameters, that varied through the test series.

Table 1. Samples used in this investigations.

Sample ID	Type	Core material	Core thickness [mm]	Skin type	Skin thickness [mm] / area weight [g/m <sup>2</sup> ]
1	1	C70.55	5	2 x Biax +/- 45° (A2)	0.74 / 1018
2	1	C70.55	10	2 x Biax +/- 45° (A1)	0.72 / 1000
3	1	SB100	5	2 x Biax +/- 45° (A3)	0.74 / 1017
4	2	C70.55	5	2 x Biax +/- 45° (A8)	0.71 / 997
5	2	C70.55	10	2 x Biax +/- 45° (A10)	0.68 / 1024
6	2	C70.55	5	4 x Biax +/- 45° (A7)	1.29 / 1957
7	2	C70.55	10	4 x Biax +/- 45° (A7)	1.29 / 1957
8	2	C70.55	15	4 x Biax +/- 45° (A7)	1.29 / 1957
9	2	C70.130	5	2 x Biax +/- 45° (A8)	0.71 / 997
10	2	C70.130	10	2 x Biax +/- 45° (A11)	0.68 / 1025

## 2.3 Mechanical testing and analysis

The samples were fixed to a steel frame and mounted on the tensile testing machine. The samples were then stressed with a crosshead speed of 1 mm/min. Force and deflection were recorded, failure load and shear stiffness were calculated and photographs of the failure mode taken.

The possible failure modes of in plane shear stresses are

- a) General shear buckling (sb) of the sandwich plate, as discussed by Plantema [2].
- b) Skin shear (ss or ipss) failure as discussed by Zenkert [1].
- c) Skin wrinkling (sw) for cores with low compressive and shear modulus, as discussed by Zenkert [1].

The equations used to predict the respective failure loads are taken from the indicated references. Using equation (1) the skin wrinkling condition was calculated. Security factors were then calculated for all three failure modes. The stress level was adjusted so one of the security factors would be zero and all other greater than zero. This way the main failure mode could be calculated as well as the expected failure load. In table 2 the predicted security factors are listed.

$$\sigma = a\sqrt[3]{E_f E_c G_c} \quad (1)$$

Table 2. Predicted security factors for the three main failure modes expected for the samples tested in this study.

Sample ID	Security factor skin wrinkling (sw)	Security factor shear buckling (sb)	Security factor in plane shear strength of skins (ipss, ss)
1	<b>1.00</b>	2.3	2.8
2	1.08	<b>1.00</b>	1.21
3	<b>1.00</b>	11.48	1.78
4	2.36	<b>1.00</b>	2.88
5	<b>1.00</b>	1.07	1.21
6	2.75	<b>1.00</b>	3.36
7	1.33	<b>1.00</b>	1.62
8	1.16	<b>1.00</b>	1.22
9	3.28	<b>1.00</b>	2.19
10	1.5	1.33	<b>1.00</b>

### 3. RESULTS

#### 3.1 In plane shear load curves

In Figures 4 and 5 the force–displacement curves of the in plane shear tests are shown. The first three samples were tested in type 1 mode. All other samples are tested in type 2 mode.

Type 1 mode measurements showed an overall deformation of the sample during the test, that resulted in a non consistent shear field in the sample. Although the samples were stiffened in the non clamped edges by incorporating an aluminium bar of the same thickness as the core the sample was bent at the unclamped edges. Comparison to the theoretical values is therefore quite poor.

Type 2 mode measurements did not show this bending, since all edges of the sample are well fixed in the steel frame.

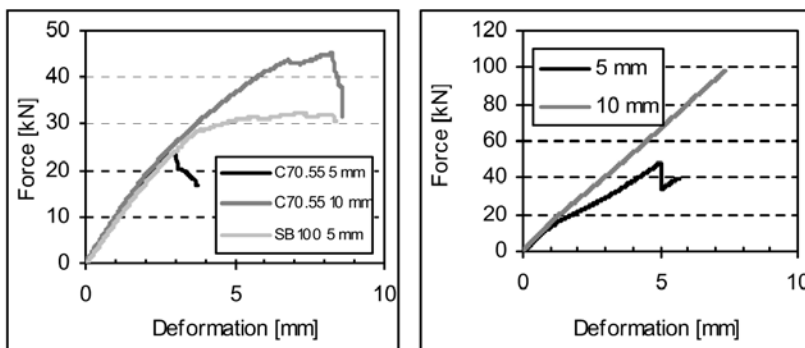


Figure 4. Force–displacement curves. Left side: Samples deformed in the type 1 mode inplane shear (samples 1, 2 and 3). Right side: C70.55 with thin skins deformed in type 2 mode (samples 4 and 5).

#### 3.2 Failure modes

According to the theoretical predictions three different failure modes were expected for the tests. General buckling is expected for thin samples and relatively low compressive modulus of the core material (C70.55). For thicker samples as well as for cores with relatively high compressive modulus (C70.130 or Balsa wood) failure in skin shear (as compression or tensile failure in fibre direction) is expected. For some samples with cores with low compressive and shear moduli skin wrinkling may also occur.

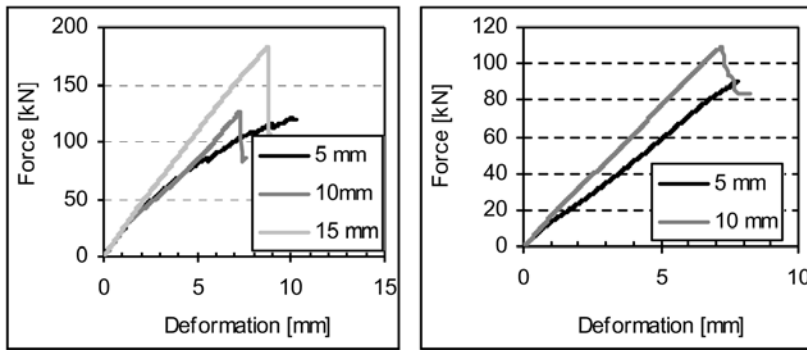


Figure 5. Force–displacement curves. Left side: C70.55 with thick skins deformed in type 2 mode (samples 6, 7 and 8). Right side: C70.130 with thin skins deformed in type 2 mode (samples 9 and 10).

The photographs in Figure 6 show the failure modes observed with type 1 mode. Although the free edges of the sample have been reinforced with an incorporated aluminium bar the sample did show buckling in this area. Sample 2 with 10 mm thick C70.55 did show a rupture of the skin near the fixation of the center rail. It can be concluded that test setup type 1 is not suitable for this investigation. In order to favor the desired failure modes, the samples would need to be reinforced around the load introduction and open edges, which has an influence on the shear buckling and shear strength of the samples as well.



Figure 6. Failure of type 1 mode in plane shear tests. Bending (buckling) of free edges for sample 1 and sample 3.

For type 2 in plane shear testing all failure modes could be observed. In figure 7 sample 4 and 9 show in plane shear strength (ipss) failure of the skin material. Figure 8 shows shear buckling (sb) of samples 5 and 7 both with 10 millimeter C70.55 as core material but different skin thicknesses.

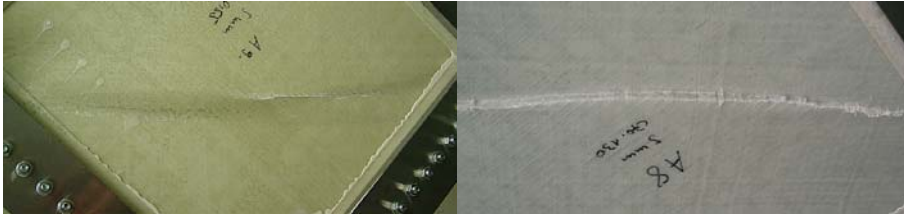


Figure 7. Skin shear (ss) failure of sample with 5mm C70.55 with thin skins (4), and 5mm C70.130 with thin skins (9).



Figure 8. Shear buckling (sb) failure of the sample with 10mm C70.55 and thin skins (5) and 10mm C70.55 with thick skins (7).



Figure 9. Skin wrinkling (sw) failure for sample with 10mm thick C70.130, with thin skins (10) The failure occurred in compression in direction  $45^\circ$  to the sample edges, in fibre direction.

Finally in Figure 9 the skin wrinkling (sw) failure mode is observed for the sample 10.

### 3.3 Comparison to theoretical predictions

From the measured curves the maximal force and the shear stiffness of the panels could be calculated. The data are shown in table 3. Obviously the shear stiffness is mainly depending on the skin properties and not influenced by the thickness of the sandwich. For the samples with 2 biaxial skin layers on each side the shear stiffness was measured to be 14 - 16 kN/mm, for the samples having 4 biaxial layers. the values are between 21 and 23 kN/mm. Since it is not double the value of the thinner skins, it can be speculated that the machine deformation was quite significant. However, the measured shear stiffness of the panels are within reach of the theoretical predictions of 9.9 kN/mm for thin, respectively 19.5 kN/mm for thick skins.

The comparison between predicted and measured failure load and failure mode is different. For some samples (5, 7, 8, 10) the agreement is very good. For these samples also a failure mode predicted with a safety of less than 1.5 was found. In this test series these tests were sandwich plates with core thicknesses of 10mm or more. The other samples (4, 6 and 9) with 5mm core material did show a rather poor agreement in failure load, as well as in failure mode.

Table 3. Comparison of predicted and observed in plane shear stress and failure modes.

Sample ID	Max Force predicted [kN]	Max Force observed [kN]	Shear stiffness [kN/mm]	Failure mode predicted	Failure mode observed
1	56.1	23.8	9.4	sw	n.a
2	129.5	45.3	9.9	sb, sw, ipss	n.a.
3	88.1	32.4	9.2	sb	n.a.
4	37.1	48.3	14.1	sb	ipss, sb
5	89.2	98.6	15.3	sw, sb, ipss	sb
6	63.4	120.5	21.9	sb	sb, ipss
7	131.7	126.9	22.7	sb, sw	sb
8	174.7	182.6	21.0	sb, sw, ipss	ipss, sb
9	49.4	90.3	14.6	sb	ipss
10	108.0	109.4	16.5	ipss, sb, sw	sw

## 4. CONCLUSIONS

In plane shear measurements of sandwich panels were done with two experimental test set-ups. One test setup failed because the sample was able to be bend and therefore disturbing the shear field in the sample. By using a square sample mounted on each side to a steel frame these problems could be overcome.

The measured panel stiffness, failure load and failure mode did show good agreement with theoretical predictions from Zenkert and Plantema. However, thin sandwich structures could not be predicted correctly.

## **REFERENCES**

1. D. Zenkert, *The Handbook of Sandwich Construction*, EMAS, 1997.
2. F.J. Plantema, *Sandwich Construction*, John Wiley & Sons, 1966.

# RESIDUAL STRENGTH OF IN-PLANE LOADED DEBONDED SANDWICH PANELS: EXPERIMENTAL INVESTIGATION

Christian Lundsgaard-Larsen and Christian Berggreen

*Department of Mechanical Engineering, Technical University of Denmark, DK-2800 Kgs. Lyngby, Denmark*

cl@mek.dtu.dk and cbe@mek.dtu.dk

Alexandros Nøkkentved

*Material Research Department, RISØ National Laboratory, DK-4000 Roskilde, Denmark*

**Abstract** Face/core debond damaged sandwich panels exposed to uniform and non-uniform compression loads are studied experimentally. The panel geometry is full-scale rectangular with a centrally located circular prefabricated debond. The results show a considerable strength reduction with increasing debond diameter, with the failure mechanisms varying between buckling driven debond propagation and face compression failure for large and small debonds respectively.

**Keywords:** debond damage, residual strength, composite materials, sandwich panels.

## 1. INTRODUCTION

Imperfections and production flaws are very common in sandwich structures. Experiences from the Royal Danish Navy have shown that one of the most common and critical damages is debonding between face and core [1]. In marine sandwich structures these damages may occur due to slamming, collisions with buoyant objects or impacts during docking or handling operations on the deck.

The aim of this study is to produce experimental results to be compared with the numerical model presented in [2]. Furthermore, the aim is to investigate and develop methods for testing the compressive strength of damaged sandwich panels. To attain this objective, rectangular sandwich panels with prefabricated debond damages are tested in two different test rigs developed for this study.

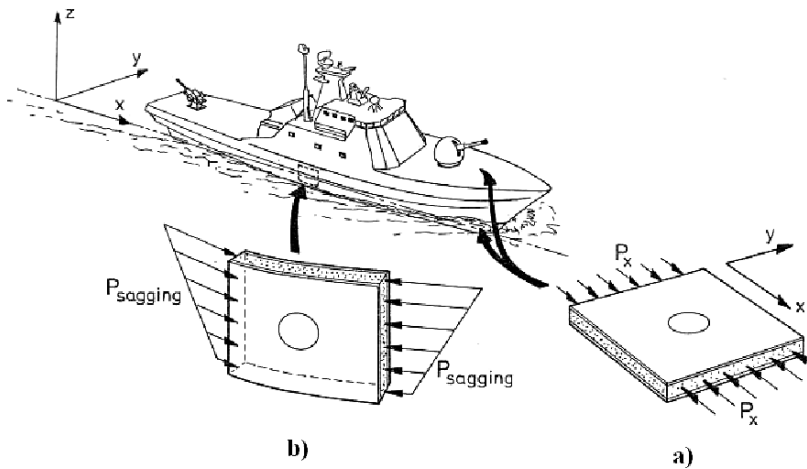


Figure 1. Uniformly loaded panel a) located in bottom or deck of a vessel and a panel loaded non-uniformly b) due to location in the side structure just above the neutral axis in sagging condition.

- A test-rig that introduces a uniform compressive load, similar to the forces acting on the bottom or deck structure of a vessel, see Figure 1a.
- A test-rig that introduces a non-uniform compressive load, similar to the forces acting on the side structure of vessel, see Figure 1b.

## 2. DESCRIPTION OF SPECIMENS

Two different series each of ten specimens are produced. The panels in the first series are  $560 \times 610$  mm and tested by applying in-plane uniform load to the shorter edges. The panels in the second series measures  $580 \times 800$  mm and are loaded non-uniformly. For each series eight of the ten panels are constructed with a Divinycell H80 ( $80 \text{ kg/m}^3$ ) structural cross-linked PVC foam core and two with an H200 ( $200 \text{ kg/m}^3$ ) core. The faces consist of four hand lay-up glass fibre mats. Two  $300 \text{ g/m}^2$  chopped strand mats (CSM300) and two  $850 \text{ g/m}^2$  non-crimp quadro-axial mats (DBLT850), placed symmetrically about the midplane of each face (CSM/0/45/90/ - 45)<sub>s</sub>. The adhesive bond-age is polyester resin and the total thickness of each face is approximately 3.2 mm. For each series seven out of ten specimens are produced with a prefabricated circular debond between core and face layer with three different diameters ( $\text{Ø}100$ ,  $\text{Ø}200$  and  $\text{Ø}300$  mm). The remaining specimens are intact prior to testing. In practice the debonded panel area is manufactured by substituting the adhesive polyester with uncured polyester, covered by a thin paper sheet before applying the face layer. All the panels are reinforced at the pressure edges with

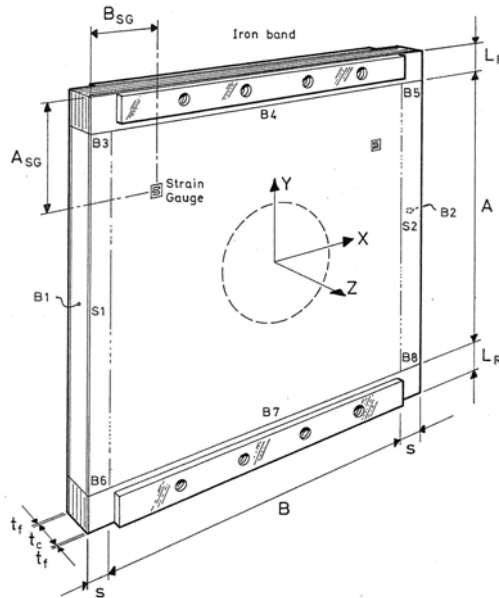


Figure 2. Panel specimen geometry of series 1 with debond location, strain gauge location and plywood reinforcement. Two more strain gauges are attached to the opposite face. In the series 2 case four more strain gauges are attached to the lower half of the panel.

plywood inserts, see Figure 2, and reinforced with two steel bars bolted onto the outside of the panel upon installation in the test rig, to prevent the edge from delaminating during application of the load. In Figure 2 the position of the strain gauges is furthermore indicated. A similar figure and further details for the non-uniform loaded panels can be found in [3].

The face properties are found by material testing at RISØ National Laboratory. Only specimens consisting solely of DBLT850 are used in these material tests. Therefore, the laminate properties of the faces are found by combining the in-plane measured properties of the DBLT850 laminates and table data for the CSM300 mats, Zenkert [4]. The in-plane properties for the quasi-isotropic laminates are  $E_x = E_y = 12820$  MPa,  $G_{xy} = 4600$  MPa and  $\nu_{xy} = 0.295$ .

Mechanical face properties in all directions and table properties for the Diviycell H80 and H200 cores are given in [3].

### 3. DESCRIPTION OF TEST RIGS

The experiments are carried out by means of two different special designed test rigs. To achieve reliable and reproducible results a thorough and extensive product development is carried out according to the principles given by Ulrich and Eppinger [5]. Drawings of the test rigs are given in Figure 3.

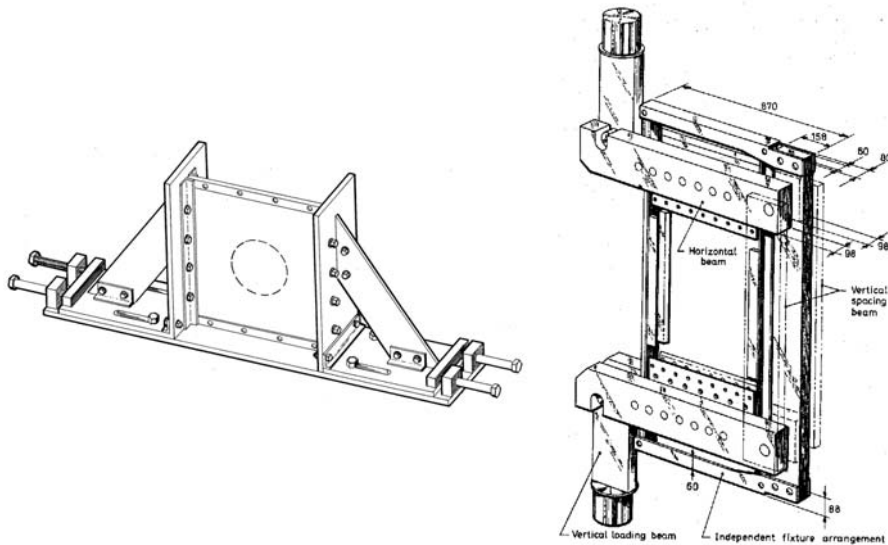


Figure 3. Test rig designed for uniform loading (left) and non-uniform loading (right). The load is applied vertically either directly on the panel (left) or through connection bolts (right).

The test rig in Figure 3 (left) is designed for the uniform loaded tests. The test rig consists of two vertical towers with steel ribs, designed to prevent the vertical panel edges from moving in the out-of-plane direction. Teflon tape is applied on the inside of the steel ribs, thus limiting friction. Load is applied in displacement controlled directly on the ply-wood reinforced top of the panel by a Mohr & Federhaff testing machine.

The test rig designed for the non-uniform load tests, see Figure 3 (right), was initially developed to study crack propagation of 10-20 mm thick steel plates by applying tension forces up to 3 MN. The rig is redesigned to apply a compressive non-uniform load to sandwich panels. The load is applied through the two connection bolts, see Figure 3 (right).

Boundary conditions are investigated in order to make the experiment reproducible, and easier to model. In brief, the boundary conditions are chosen so that a panel edge is either completely clamped or free with respect to a certain degree of freedom. Furthermore, mounting the panel in the test rig must be as simple as possible to reduce laboratory time.

The loaded horizontal edges of the test panel are restricted from translations and rotations in all directions since the edges is reinforced by plywood inserts, see Figure 2, and bolted between two steel bars. The vertical edges are considered free to move in the in-plane directions, though restricted in the out-of-plane direction. Physically this is obtained by covering the areas S1 and

S2 by steel ribs, see Figure 2. Similarly arrangement is made on the opposite side of the panel. More details can be found in [3].

During the experiment the displacement of the loaded edge is slowly increased while monitoring force, strain gauge signals and out-of-plane displacement of the debonded face using two orthogonal extensometers, located at the debond centre and panel centre on the front and backside of the panel respectively. By subtracting the extensometer on the intact side from the extensometer on the debonded side, global buckling of the panel is filtered, and only local debond displacement is measured. The orthogonal extensometers can be seen in Figure 5.

## **4. LOAD INTRODUCTION**

For both the uniform and non-uniform case the force and displacement are measured at the piston of the test machine. In the uniform load case a horizontal steel beam attached to the test machine is supplying the compressive loading. The beam is specially shaped to be able to slide down between the vertical steel ribs. The non-uniform load case is obviously more complicated and is treated below.

### **4.1 Non-uniform loading**

Due to the importance of a well-defined load profile the skewness of the load is investigated by strain gauge measurements.

The strain distribution is measured by eight strain gauges mounted on the faces of each panel as seen in Figure 2. The strain gauges measure only strain in the loading direction (vertically). The skewness of the load is assumed to be linear since the loaded edges of the panel are reinforced with plywood and fixed to the side beams using the steel reinforcements.

The displacement of the loaded edge is determined as the panel height multiplied by the measured strain, on the assumption that the edge remains straight and the measured strain is constant through the panel height. This assumption is verified using a finite element model. Additionally, the vertical displacement of the panel corners is found by extrapolation of the displacements in the strain gauge positions.

From the strain gauge measurements, load profiles for different time steps up to failure of the panel is found and plotted in Figure 4. In general, the load shape is almost triangular in the beginning of the test and develops in some cases into a trapezoid load profile, while in other cases it remains triangular.

The displacement profiles measured by the strain gauges are used as input to the advanced finite element model presented in [2, 6].

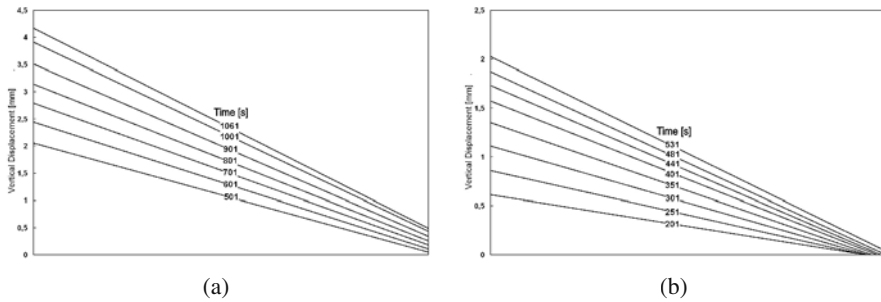


Figure 4. Averaged loading profiles (front and back) from the H80  $\text{\O}100$  (a) and  $\text{\O}200$  mm (b) case.

## 5. RESULTS

In the following, the results from the experimental investigation are presented and discussed.

Two different failure modes are observed during the experiments:

- Gradually developing local buckling of the debonded face area leading to propagation of the debond.
- Compression failure of the face laminates.

Generally, panels with large debond diameters fail due to spread of the debond, see Figure 5a, and intact panels or panels with small debond sizes fail due to face compression failure, see Figure 5b.

In the following, a representative panel case will be considered to illustrate the test procedure. A non-uniformly loaded specimen with a H80 core material and  $\text{\O}200$  mm debond diameter has been chosen. However, similar conclusions and observations exist for the remaining test specimens and are found in [1] and included to some extent in [6] in connection with comparison with theoretical ultimate failure predictions.

For the considered panel case the out-of-plane debond displacement is almost zero up to the local debond buckling load at 113 kN, see Figure 6. Afterwards a steadily growing buckle is observed until a point where the debond propagates fast to the most loaded side with a loud noise. At this point the force decreases approx. 25% and the test is stopped immediately. The panel withstands a relatively large amount of force after failure due to the remaining intact face.

Failure loads are listed for all tested panels in Table 1, along with the buckling load of the debonded face, when identified clearly. The failure mode for initially damaged panels are buckling of the debonded area leading to propagation of the debond, except for one non-uniformly loaded  $\text{\O}100$  panel, which fails due to face fracture. All intact panels fail due to face compression, how-

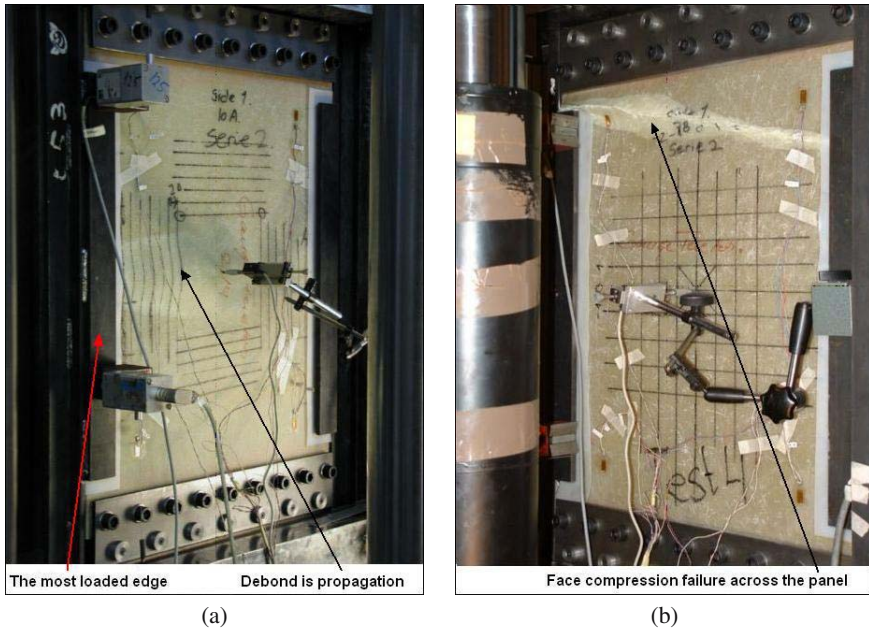


Figure 5. Two different failure modes observed. In a) the debond is propagating towards the most loaded edge, and in b) face compression failure across the panel is observed.

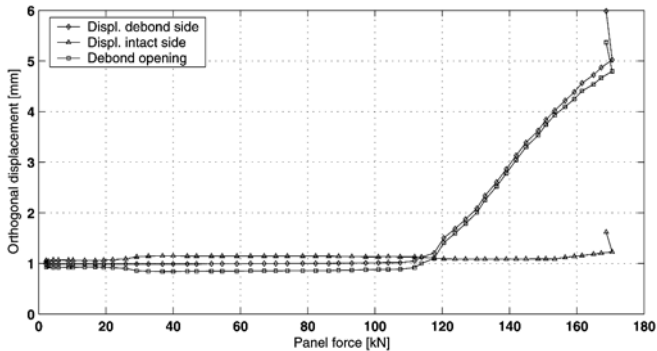


Figure 6. Out-of-plane displacement as a function of panel force for the H80 core and Ø200 mm debond diameter case. Note the 1.0 mm initial debond opening.

ever, for the H80 panels the compression failure is introduced by wrinkling of the face.

For panels with H80 core material the crack propagates just below the interface on the core side following initiation of debond buckling, thus no fibre bridging is observed visually. In contrast, large-scale fibre bridging is observed for the damaged panel with H200 core, where the crack front propagates directly in the interface.

Table 1. Failure load and buckling initiation load (where possible to identify).

Specimen	Core	Damage	Uniform load case		Non-uniform load case	
			Buckling	Failure	Buckling	Failure
A	H80	Ø100 mm	90 kN	222 kN	260 kN	307 kN
B	H80	Ø100 mm	85 kN	218 kN	-	318 kN
A	H80	Ø200 mm	-	162 kN	168 kN	180 kN
B	H80	Ø200 mm	-	139 kN	113 kN	171 kN
A	H80	Ø300 mm	-	140 kN	-	167 kN
B	H80	Ø300 mm	-	127 kN	99 kN	173 kN
A	H80	Intact	-	270 kN	-	248 kN
B	H80	Intact	-	370 kN	-	286 kN
A	H200	Ø200 mm	-	180 kN	-	195 kN
A	H200	Intact	-	414 kN	-	333 kN

The force where out-of-plane displacement of the debond initiates are registered for debond damaged panels, where possible to identify. Some panels are discarded due to either indistinctly determined bifurcation point or due to buckling in parts of the debond area not being subject to measurement by the orthogonal extensometer. The local buckling load levels are indicated in Table 1.

## 5.1 Panel residual strength

One of the main objectives of this study is to determine the influence of debond damages on the residual strength of sandwich structures. In order to establish a residual strength prediction for the considered panel types, intact panel specimens are also tested. Results comparing residual strength as a function of damage size are shown in Figure 7 for the uniform and non-uniform load case.

A strength factor being the ratio between experimentally determined failure loads for intact and damaged panels is used to describe the residual strength. The average strength factor between the A and B-tests of panels with varying debond diameter is seen in Figure 7 for panels of H80 core material. In the uniform load case the residual strength is clearly decreasing with increasing initial debond diameter. For a Ø100 mm debond the strength is reduced to 69% compared to the intact panel in the uniform load case. In contrast to this the debond size of Ø100 mm is not critical to the non-uniform load case, since the strength factor is above one, namely 17% larger than the strength of intact panels. A possible explanation for this could be general hand lay-up production tolerances, and that these imperfections in the panels have a larger influence on the compression strength than the Ø100 mm debond. Another

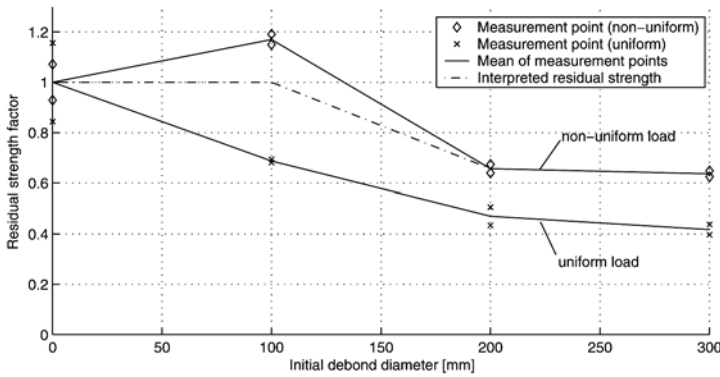


Figure 7. Residual strength factor for panels with H80 core based solely on experimental results. Uniform (left) and non-uniform (right) compression.

possibility is that the small debond damage causes a different distribution of stresses in the panel, which leads to a higher failure strength. The strength factor of panels with debonds of  $\text{Ø}200$  and  $\text{Ø}300$  mm is for the uniform load case 47% and 42% respectively and for the non-uniform load case 66% and 64% respectively. From these results it could be concluded that panels are more sensitive to the prescribed debond damages when loaded uniformly compared to non-uniformly. However, as the determination of the panel intact strength is scattered to some degree for both uniform and non-uniform loading, this conclusion has to be taken with some caution.

The residual strength for panels with H200 core with  $\text{Ø}200$  mm debond is 43% and 59% for the uniform and non-uniform loaded panels respectively. This corresponds with results for panels with H80 core described above.

## 6. CONCLUSION

The compressive strength of debond damaged sandwich panels exposed to uniform and non-uniform compressive load has been investigated. Two test rigs for full-scale testing is designed and constructed for this purpose. Full-scale experiments are performed using two different Divinycell cores: H80 and H200. The panels are manufactured with built-in debond defects which are of circular shape and placed centrally. Three different debond damages are chosen:  $\text{Ø}100$ ,  $\text{Ø}200$  and  $\text{Ø}300$  mm.

A  $\text{Ø}100$  mm debond reduces the compressive strength (maximum force) approximately 31% for uniformly loaded panels, whereas panels loaded non-uniformly show no reduction of the compressive strength. For panels with debond diameters of either  $\text{Ø}200$  or  $\text{Ø}300$  mm the strength is reduced 53-58% and 34-36% for the uniform and non-uniform load case respectively.

Experiments carried out in this study are full-scale, and the manufacturing method for the test panels is similar to the methods used in shipbuilding, thus it is plausible that a debond damage located in a ship's side structure would propagate the same way if exposed to the same critical load cases.

## ACKNOWLEDGEMENTS

This work was part of the "SaNDI – Inspection and Repair of Sandwich Structures in Naval Ships" (THALES JP3.23) project with participants from Norway, Denmark, Sweden, Finland and the United Kingdom. The support of the Ministries of Defence of the five participating nations is gratefully acknowledged. The test panels were produced by DANYARD AALBORG A/S. The support is greatly appreciated.

## REFERENCES

- [1] Berggreen, C., *Damage Tolerance of Debonded Sandwich Structures*, PhD Thesis, Department of Mechanical Engineering, Technical University of Denmark, September 2004.
- [2] Berggreen, C. and Simonsen, B.C., Residual strength of in-plane loaded debonded sandwich panels - fracture mechanical modelling, In O.T. Thomsen, E. Bozhevolnaya, and A. Lyckegaard, editors, *Proc. of 7th International Conference on Sandwich Structures, Aalborg, Denmark, August 29 to 31, 2005* (this volume).
- [3] Nøkkentved, A., Lundsgaard-Larsen, C. and Berggreen, C., Non-uniform compressive strength of debonded sandwich panels – I. Experimental investigation, *Journal of Sandwich Structures and Materials*, in press, 2005.
- [4] Zenkert, D., *The Handbook of Sandwich Construction*, EMAS, UK, 1997.
- [5] Ulrich, K.T. and Eppinger, S.D., *Product design and development*, McGraw-Hill, Boston, second edition, 2000.
- [6] Berggreen, C. and Simonsen, B.C., Non-uniform compressive strength of debonded sandwich panels – II. fracture mechanics investigation, *Journal of Sandwich Structures and Materials*, in press, 2005.

# RESIDUAL STRENGTH OF IN-PLANE LOADED DEBONDED SANDWICH PANELS: FRACTURE MECHANICAL MODELLING

Christian Berggreen

*Department of Mechanical Engineering, Technical University of Denmark,  
DK-2800 Kgs. Lyngby, Denmark*

cbe@mek.dtu.dk

Bo Cerup Simonsen

*Department for Maritime Technical Consultancy, Det Norske Veritas,  
N-1322 Høvik, Norway*

Bo.Cerup.Simonsen@dnv.com

**Abstract** This paper presents a FEM based numerical model for prediction of residual strength of damaged sandwich panels. As demonstrated, the model can predict the maximum load carrying capacity of real-life panels with debond damages, where the failure is governed by face-sheet buckling followed by debond growth. Comparison of the theoretical predictions is carried out against a series of large-scale experiments described in Lundsgaard-Larsen et al. [1].

**Keywords:** debonding, fracture mechanics, buckling, propagation.

## 1. INTRODUCTION

With the increasing ability to optimize the structures to the performance limit of the constituent materials and with the willingness to do so in practice, the reserve margin for structural degradation and damage tolerance becomes significantly smaller.

Damages to the core in a sandwich structure related to an impact event could be core shear fracture near the impact zone and/or crushing of the core under the impact zone, which is investigated thoroughly by Shipsha [2]. The core crushing results in a permanent dent and for some core types accompanied with a cavity, leaving the face and core separated in a zone extending in a radial direction from the impact location. The phenomenon of separation of face and core in an isolated area is designated a *debond*.

Another damage scenario which results in a debond damage is production flaws. If the glue forming the interface between face and core is missing in parts of the panel, because of poor production quality a debond is initially present in the panel. The production debonds are typically more difficult to identify, as they do not necessarily leave any visible damage to the face sheet or permanent dent in the surface.

Several investigations of the debond damage type have been carried out in the past, beginning with Zenkert [3], who investigated the strength of foam core sandwich beams with various debonds and interface propagated shear cracks using the finite element method and experimental testing. Among other publications are: Prasad and Carlsson [4, 5], in which foam core sandwiches with isotropic facings are investigated, and lately Aviles [6], where analytical elastic foundation models able to predict buckling of debonded beams and panels are presented together with an extensive experimental investigation of uniform in-plane compression loaded sandwich panels with various debond damages.

The objective of this paper is primarily to present a general methodology for the prediction of residual strength of debonded fibre reinforced sandwich structures with foam cores. Furthermore, on the basis of a new fracture mechanical mode-mixity method and validation against the experimental results presented in [1], the model presented in this paper will be used to enlighten the criticality of debonds and predict considerable strength reductions in compression loaded sandwich panels exposed to various damages, which have resulted in different sizes of debonds between face and core. More details can be found in [7, 8].

## 2. DEFINITIONS AND ASSUMPTIONS

As mentioned above the debond may be a product of a number of the damages described earlier. Therefore, the main scope of this paper is not to investigate the actual debond producing damage event itself, but rather the consequences of the subsequent debond with regard to the structural integrity.

A number of assumptions have been adopted in order to treat the debond damage in a general way by use of Linear Elastic Fracture Mechanics (LEFM):

- The debonded face and underlying core are assumed to be intact and homogeneous, with the same apparent orthotropic and isotropic material properties respectively as the remaining intact core and face layer.
- The current natural debond geometry is idealised by a circular debond, with the diameter  $D$ , as indicated in Figure 1a.
- The interfaces between the faces and the core will be treated as plane interfaces between two solids, and the debond will be represented by an area where there is no continuous adhesion between the two solids.

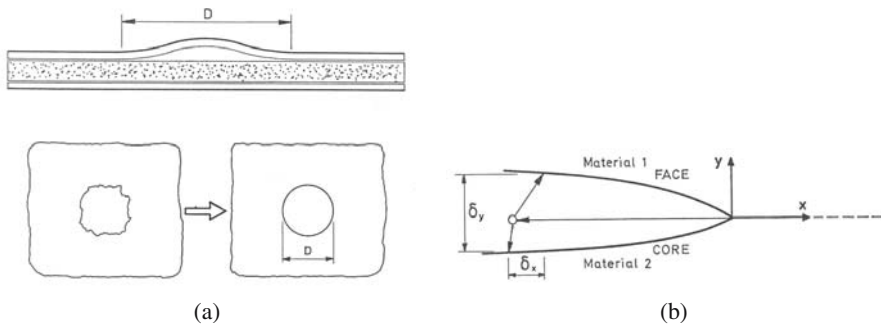


Figure 1. Idealization of a natural debond to circular-shaped debond geometry (a). Sandwich bimaterial crack tip geometry (b).

- The size of the microstructure is assumed to be much smaller compared to any other dimensions and the failure process zone is assumed to be much smaller compared to the  $K$ -dominated zone, normally comparable to  $h/50$ , where  $h$  is the characteristic length of the crack geometry, often chosen as the face thickness.

### 3. FRACTURE MECHANICS IN SANDWICH STRUCTURES

When an interface crack is advancing between two dissimilar materials, it will mostly happen in a mixed mode condition. The main consequence is that not only is the present Griffith-energy level needed for an interface crack in a structural simulation, but also the mode-mixity, in order to compare the present crack tip loading with fracture toughness distributions as function of mode-mixity. Normally, the mode-mixity is not linked directly to the opening and shearing displacements of the crack flanks or the normal and shear stresses in front of the crack tip, as seen in homogeneous fracture mechanics, but a distortion exists, so special mode-mixity methods have to be employed in order to extract the mode-mixity.

Several mode-mixity methods have been presented in the literature. The three most commonly used methods are: The *Virtual Crack Extension* method, the classical and modified *Virtual Crack Closure Technique* (short VCCT) and the *Crack Surface Displacement* method (short CSD).

A detailed description and analysis of the above mentioned methods can be found in [7], with special regard to application in foam core sandwich interfaces by using a finite element code with an automatic crack propagation routine. However, none of the investigated mode-mixity methods from the literature were found to possess qualities adequate for the application in

automated propagation routines in sandwich interfaces. Consequently, a new mode-mixity method, based on extrapolation of crack flank displacement results, is derived and named the *Crack Surface Displacement Extrapolation* method (short CSDE). An overview of this new method is presented below. Further details can be found in [7].

By application of the definition of mode-mixity suggested by Hutchinson and Suo [9] and the modified Irwin expression, the general Lekhnitskii-Eshelby-Stroh displacement field for a bimaterial interface crack can be specialized, so that mode-mixity and Griffith-energy can be expressed in terms of the relative crack flank displacements: (see Figure 1b)

$$\Psi_K = \arctan \left( \sqrt{\frac{H_{22}}{H_{11}}} \frac{\delta_x}{\delta_y} \right) - \varepsilon \ln \left( \frac{|x|}{h} \right) + \arctan(2\varepsilon) \quad (1)$$

$$G = \frac{\pi (1 + 4\varepsilon^2)}{8 H_{11} |x|} \left( \frac{H_{11}}{H_{22}} \delta_y^2 + \delta_x^2 \right) \quad (2)$$

$H_{11}$ ,  $H_{22}$  and the oscillatory index  $\varepsilon$  are given in [8].

If the two relations for the mode-mixity and the Griffith-energy, Equations (1) and (2), are applied these quantities can be found in a finite element solution solely from the relative nodal displacements of the crack flanks. Consequently, both the mode-mixity and the Griffith-energy will be affected by the oscillations, but they will be small away from the near crack tip zone and therefore without practical importance. In Figure 2 the Griffith-energy has been plotted for crack flank node pairs with increasing distance from the crack tip. The same graphs can be plotted for the mode-mixity.

The CSD (Crack Surface Displacement) method uses an externally determined Griffith-energy, for example by means of a J-integral calculation, and the mode-mixity is used, from the node pair where the Griffith-energy, calculated by use of Equation (2), equals the externally determined value. This method does not strictly give a physical meaning and might lead to erroneous results if a node is chosen inside the numerical error zone as indicated in Figure 2 (left).

The CSDE method, which is presented schematically in Figure 2 (right), uses solely the results from the relative crack flank displacements. It is observed in numerous investigations that the transition from the external displacement field to the internal crack dominated field is more or less linear. By use of this information, the linear transition zone is simply linearly extrapolated into the crack tip. This can be done for both the Griffith-energy and the mode-mixity calculated by relative nodal crack flank displacements, but normally it is sufficient to do this numerical extrapolation on the Griffith-energy and then reuse the linear borders on the mode-mixity curve.

The accuracy of the CSDE method is in general dependent on how far the extrapolation zone is extended from the crack tip. If the CSDE method is to

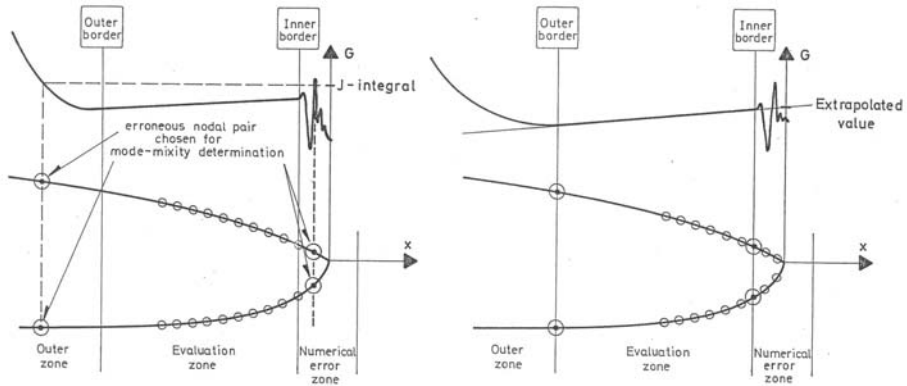


Figure 2. The Griffith-energy plotted for crack flank node pairs with increasing distance from the crack tip. Drawback of the CSD method (left) and the principle of the CSDE method (right).

achieve high linearity in the extrapolation, it is necessary that the high mesh density zone in a finite element calculation is located so close to the crack tip that the structural outer displacement field has only a small influence on the Griffith-energy and the mode-mixity, determined from the relative crack flank displacements. This is generally only possible in 2-D as the high mesh density zone is relatively CPU inexpensive. However, in 3-D the computational cost of the high mesh density is increased considerably.

To avoid a weak linearity in 3-D, a path independent J-integral is therefore used along the crack front to determine the Griffith-energy. The mode-mixity is determined in the same way as in 2-D accepting a certain non-linearity in the extrapolation. It has been chosen to neglect the mode III deformations and use the 2-D version of the expressions for the Griffith-energy and the mode-mixity as a function of the crack flank displacements, Equations (1) and (2), as well as the 2-D version of the path independent J-integral. This limitation can be justified, because the mode III contribution will be limited in most debond cases compared to the opening mode I part of the Griffith-energy. Both the 2-D J-integral and the 2-D expressions for the Griffith-energy and the mode-mixity have been verified for application in 3-D and validated against experimental results in [7].

#### 4. NUMERICAL FAILURE MODEL

A 2-D crack propagation model has earlier been presented in [10] in order to simulate crack propagation in a sandwich beam. Based on considerations presented in [7, 8], the 3-D failure model simulation algorithm may briefly be described in the following manner:

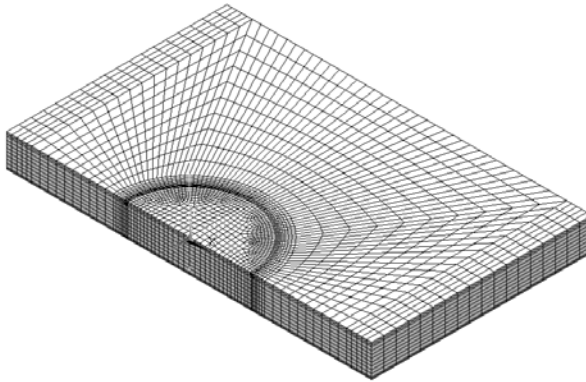


Figure 3. Distribution of linear (grey) and parabolic (white) elements. A 1/2-model of a panel with a  $\text{Ø}200$  mm debond is shown.

- 1 A displacement controlled geometrical non-linear finite element calculation is performed to introduce imperfections into the model, using the *Debond Closure Prevention Device* (DCPD), presented in [7] to account for the initial debond opening encountered in all tested panels in [1].
- 2 The displacement loads are introduced/scaled.
- 3 A displacement controlled geometrical non-linear finite element calculation is performed.
- 4 An arbitrary number of crack front positions are investigated using the 3-D version of the CSDE method.
- 5 If the fracture toughness is not exceeded in any crack front positions, the routine is carried on from step 2, scaling the displacement loads and using an incremental scaling factor (uniform case).
- 6 If the fracture toughness is exceeded in any crack front position, the calculation stops and the panel is regarded as *failed*.

The model consists of a combination of 8-noded linear and 20-noded parabolic elements, see Figure 3. The 8-noded linear elements are applied in a small inner zone with a radius of two elements from the crack tip. These elements are more robust when large distortions are encountered, and the solution in these elements is excluded from the CSDE method as indicated earlier. The rest of the crack tip mesh consists 20-noded parabolic elements, including a number of element rings surrounding the crack tip, where the actual Griffith-energy and mode-mixity determination is carried out.

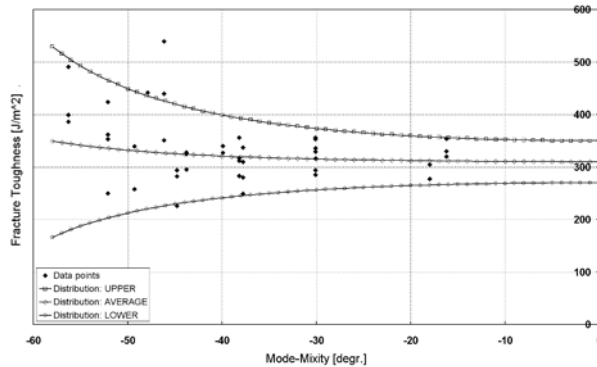


Figure 4. Interfacial fracture toughness for a GFRP/H80 PVC foam core bimaterial.

Fracture toughness distributions as a function of mode-mixity are presented in Figure 4 for the combined CSM and quadro-axial face layup configuration chosen in [1] and Divinycell H80 PVC foam core. Similar fracture toughness measurements for H130 and H200 cores can together with a description of the measurement method and distribution expressions be found in [7].

## 5. COMPARISON WITH EXPERIMENTAL RESULTS

In [1] experimental results for uniform and non-uniform in-plane compression case are presented. In this section the numerical failure model will be compared to the experimental results and residual strength considerations will be carried out for the tested debond range, and hereby generating examples of residual strength charts.

It is common to the two panel test series that the in-plane loading of the panel resulted in outwards buckling of the debonded face in a local buckling mode. This failure behaviour is seen both in experimental and numerical investigations. The outward buckling happens in all cases gradually, and in almost all cases the local buckling ends with a very rapid propagation of the debond front to the edge of the panel. Furthermore, this crack propagation is located just below the glue interface in the core.

In Table 1 the results from the experiments and the theoretical simulation with the 3-D failure model are presented, for each of the debonded H80 and H200 panels with uniform and non-uniformly compression loading respectively. Relatively good correlation are seen for the H80  $\varnothing 200$  and  $\varnothing 300$  mm debonded panels for the uniform compression case, however some disagreement is seen in the buckling mode for the  $\varnothing 100$  and  $\varnothing 300$  mm debonds, as a one wave debond buckling mode is predicted by the model, but a two wave mode is seen in the experiments with the  $\varnothing 300$  mm debonds, most likely due to

Table 1. Measured experimental and theoretically predicted failure loads. (\*) Analytical wrinkling failure load. (†) Theoretical face compression failure load.

Specimen	Core	Damage	Uniform		Non-uniform	
			Experimental	Predicted	Experimental	Predicted
A	H80	Ø100 mm	222 kN	303 kN	307 kN	340 kN
B	H80	Ø100 mm	218 kN	-	318 kN	342 kN
A	H80	Ø200 mm	162 kN	152 kN	180 kN	153 kN
B	H80	Ø200 mm	139 kN	-	171 kN	151 kN
A	H80	Ø300 mm	140 kN	116 kN	167 kN	100 kN
B	H80	Ø300 mm	127 kN	-	173 kN	100 kN
A	H80	Intact	270 kN	594 kN*	248 kN	-
B	H80	Intact	370 kN	-	286 kN	317 kN
A	H200	Ø200 mm	180 kN	221 kN	195 kN	221 kN
A	H200	Intact	414 kN	748 kN†	333 kN	447 kN†

unwanted production introduced adhesion prior to debond buckling. The same behaviour is seen for the H80 Ø300 mm debonded panels with non-uniform compression, however, good agreement is seen for the Ø100 and Ø200 mm debonded panels. More details can be found in [7, 8].

In Figure 5 the average residual strength factor has been plotted for varying debond sizes. For each debond diameter the results from the two identical specimens are averaged. Additionally, for the experimental results the variations from the average value at each debond size are indicated. In the uniform compression case the residual strength is made non-dimensional by the analytically calculated wrinkling strength of the intact panel. In the non-uniform compression case the residual strength factors are made non-dimensional by the failure load obtained from the numerical modelling of the wrinkling introduced compressive failure of the intact panels.

For the uniform compression case it is seen that the residual strength decreases with increasing debond diameter. Numerical and experimental results show considerable strength reductions with average residual strength factors around 20–25% for debond diameters around Ø200–300 mm. For smaller debond diameters, the experimental results show average residual strength factors around 37%, whereas the numerical results yield a non-conservative 51%. Furthermore some discrepancies are seen for smaller debonds which are most likely due to large influence from imperfections on the debond buckling for high face thickness – debond diameter ratios as indicated above. However, it can be concluded that all numerical predictions of the residual strength are in good agreement for large debond diameters.

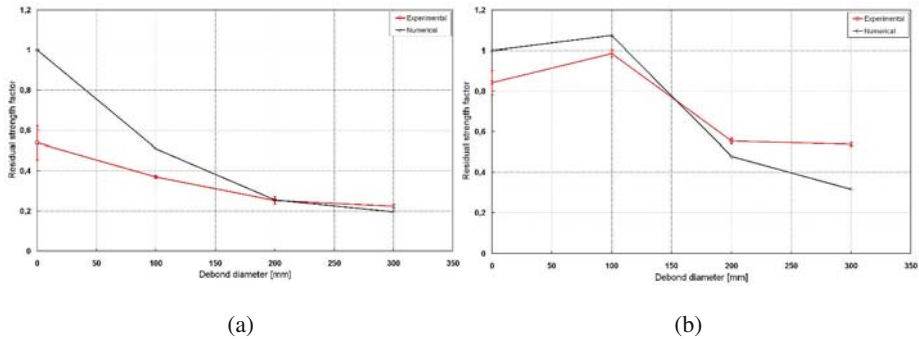


Figure 5. Average residual strength factors from experimental results and numerical calculations. Uniform compression with H80 core (a) and non-uniform compression with H80 core (b).

For the non-uniform compression case it is first of all seen that both experimental and numerical investigations show that small debonds below at least  $\text{Ø}100$  mm are not critical. As in the pure compression case both experimental and numerical results show considerable strength reduction with average residual strength factors around 32-55% for debond diameters larger than  $\text{Ø}200$  mm. For debond diameters from approximately  $\text{Ø}150$  mm and up the numerical model yields increasingly conservative results compared to the experimental values. However, for practical engineering purposes, the results in both uniform and non-uniform compression are acceptable.

## 6. CONCLUSION

With a continuous development towards more weight optimised and thus fragile structures, the ability to assure the necessary structural reliability of real, damaged structures is of ever increasing relevance. This paper is concerned with a failure mode which is believed to be particularly relevant for FRP-sandwich structures: failure caused by propagation of a debond damage. The paper presents the theory behind the new procedure and examples of validation and application. As demonstrated, the method can predict the maximum load carrying capacity of real-life panels with debond damages, where the failure is governed by delamination growth and face sheet buckling. This opens up for a number of important engineering applications, for example risk-based inspection and repair schemes.

## ACKNOWLEDGEMENTS

This work was part of the “SaNDI – Inspection and Repair of Sandwich Structures in Naval Ships” (THALES JP3.23) project with participants from Norway, Denmark, Sweden, Finland and the United Kingdom. The support

of the Ministries of Defence of the five participating nations is gratefully acknowledged. Fracture toughness measurements performed by RISØ National Laboratory are greatly appreciated.

## REFERENCES

- [1] Lundsgaard-Larsen, C. Berggreen, C. and Nøkkentved, A., Residual strength of in-plane loaded debonded sandwich panels – Experimental investigation, in: O.T. Thomsen, E. Bozhevolnaya, and A. Lyckegaard (eds), *Proceedings of 7th International Conference on Sandwich Structures*, Aalborg, Denmark, August 29–31, 2005, this volume.
- [2] Shipsha, A., *Failure of Sandwich Structures with Sub-Interface Damage*, PhD Thesis, Department of Aeronautics, Royal Institute of Technology, Sweden, 2001.
- [3] Zenkert, D., *Damage Tolerance of Foam Core Sandwich Constructions*. PhD Thesis, Department of Aeronautics, Royal Institute of Technology, Sweden, 1990.
- [4] Prasad, S. and Carlsson, L.A., Debonding and crack kinking in foam core sandwich beams – I. analysis of fracture specimens, *Engineering Fracture Mechanics*, 47(6):813–824, 1994.
- [5] Prasad, S. and Carlsson, L.A., Debonding and crack kinking in foam core sandwich beams – II. experimental investigation, *Engineering Fracture Mechanics*, 47(6):825–841, 1994.
- [6] Aviles, F., *Local Buckling Analysis and Debond Propagation in Sandwich Columns and Panels*, PhD Thesis, Department of Mechanical Engineering, Florida Atlantic University, 2005.
- [7] Berggreen, C., *Damage Tolerance of Debonded Sandwich Structures*, PhD Thesis, Department of Mechanical Engineering, Technical University of Denmark, 2004.
- [8] Berggreen, C. and Simonsen, B.C., Non-uniform compressive strength of debonded sandwich panels – II. fracture mechanics investigation, *Journal of Sandwich Structures and Materials*, in press, 2005.
- [9] Hutchinson, J.W. and Suo, Z., Mixed mode cracking in layered materials. *Advances in Applied Mechanics*, J.W. Hutchinson and T.Y. Wu (eds), 29:63–191, 1992.
- [10] Berggreen, C., Simonsen, B.C. and Törnqvist, R., Modelling of debond and crack propagation in sandwich structures using fracture and damage mechanics, in: J.R. Vinson, Y.D.S. Rajapakse and L.A. Carlsson (eds), *Proceedings of 6th International Conference on Sandwich Structures*, Ft. Lauderdale, FL, March 31–April 2, 2003, Boca Raton, FL: CRC Press, pp. 682–693.

# RESISTANCE OF FASTENINGS OF SANDWICH PANELS

Paavo Hassinen

*Helsinki University of Technology, Laboratory of Structural Mechanics,  
P.O. Box 2100, FIN-02015 TKK, Finland*

**Abstract** Fastenings are an essential part of the sandwich constructions. Mechanical fastenings are needed to fix the panels to the frame of a building and fasteners are used to mount additional covering and components to a face of a sandwich panel. The paper studies failure modes on typical fastenings and introduces models to evaluate the resistance and to adjust the test results for design equations.

**Keywords:** sandwich panel, fastening, metal sheet, screw, modelling, adjustment, experiment, design.

## 1. INTRODUCTION

Light-weight sandwich panels have to be fastened to the frame of the building. Typically, mechanical screw fasteners are used, the type of which depends on the material and thickness of the supporting structure. In addition, there are needs to fix additional covering sheets, installations and components to the sandwich panels to be finally supported by the frame through the panels. The fasteners for additional claddings are normally screws and rivets of different sizes. The fastenings and sandwich panels constitute a complete building system, the study of which has to take into account the interactions between the panels, fastenings and the frame.

Fastenings of sandwich panels are loaded by tensile forces caused by the wind suction load but also by the difference of the temperature between the face layers in multi-span panels. Fastenings are loaded by shear forces due to the self-weight and other dead-loads and claddings fixed to the wall panels. Dead-loads and the live-loads on inclined roofs cause also shear force

components to the fastenings. Sandwich panels are often mounted on cold-formed thin-walled profiles, which are supported against the lateral buckling by the panels. The stabilizing effect as well as the utilization of the diaphragm action of the sandwich panels result in shear forces in the fastenings between the panels and the supporting structure.

Components, coverings and installations have often to be fixed to the sandwich panels, and in many cases the screw and rivet fastenings are made into an external or internal face layer, only. The fixings cause tensile and shear forces in the fastenings. A wide selection of screw and rivet fasteners are in use for the fixing to a single face layer.

Hidden fastenings other less-visible fastenings used to fasten the panels to the frame of a building and placed in the longitudinal joints of the panels have been developed to meet new architectural requirements. The static response, mode of failure and the resistance depend on the type of the fastenings. No general classifications has been given to hidden fastenings.

## 2. FAILURE MODES

The fasteners and the points of the fastenings in sandwich panels may fail by a tensile or a shear failure mode or by a combination of these depending on the loading and on the resistance of the panel, the fastener and the supporting structure. Three failure modes can be separated (Figure 1);

- 1) pull-through failure at the point of the fastening in the panel,
- 2) bending, tensile or a shear failure of the shaft or the head of the fastener or
- 3) pull-out failure or shear of the fastener from the supporting structure.

The failure modes of the fastenings fixed to one face layer, are typically pull-out or shear failures in the face. The failure modes correspond the third failure in Figure 1. In rivet fastening also the failure of the shaft of the rivet may determine the resistance. Loads of the fastener fixed to one face layer only, cause stresses in the bond and core layer, also. However, the experimental observations have shown, that the pull-out failure mode is limited to a small area in the face layer only, if the distance from the end of the panel is large enough.

In the studies at Helsinki University of Technology, the first failure mode depending on the geometry and the strength of the face and core layers and on the geometry of the fastener, has been investigated. This failure mode dominates the design of the typical fastenings of sandwich panels used in civil engineering applications. The second and third failure modes results typically in higher resistances, but may, however, become dominant in some

loading cases. Thus, the second and third failure modes shall not be forgotten in the design. Loading arrangements for the testing of the single fastenings are given in the European Recommendations for Sandwich Panels [1].

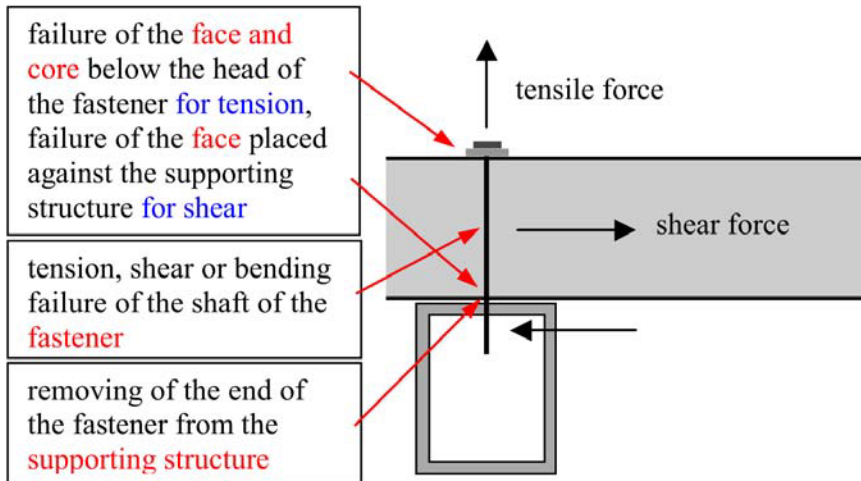


Figure 1. Failure mechanism of the fastening.

### 3. MODELLING OF FAILURE

The resistance and stiffness of the screw fastenings against the pull-over failure through the outer face depends on several parameters describing the geometry of the sandwich panel and the fasteners and the mechanical properties of the face and core layers. Numerical simulations have shown, that the most important parameters are the thickness and the strength of the outer face layer, on which the washer and the head of the fasteners are supported [2]. The models for the tensile resistance (1) and stiffness (2) base on parameter analyses of the results of numerical finite-element simulations. The models result in a first estimate on the resistance and stiffness and they can be used in planning of experimental studies of fastenings. Resistance and stiffness used in the design work in practice, have to be based on adequate test series.

$$F_{Rt, num} = ((1,77d - 0,71c)f_{Fy} + 1818f_{Cy}t_F)t_F \quad (1)$$

$$k_{t,num} = \frac{F}{\delta} = \left( 0.38 \sqrt{\frac{E_C}{E_{C0}} \frac{H_{C0}}{H_C}} + \frac{t_F}{t_{F0}} \sqrt{\frac{f_{Cy}}{f_{Cy0}}} + \sqrt{\frac{f_{Fy}}{f_{Fy0}} \frac{d}{d_0}} - 0.17 \frac{c}{c_0} \right) k_0 \quad (2)$$

In the expressions (1) and (2)  $d$  and  $c$  are the diameter of the washer and the shaft of the screw,  $t_F$  is the steel core thickness of the face,  $H_C$  is the depth of the core,  $f_{Cy}$  and  $f_{Fy}$  are the yield stress of the core and the face and  $E_C$  is the modulus of elasticity of the core. The parameters in the second expression are  $E_{C0} = 10 \text{ N/mm}^2$ ,  $H_{C0} = 100 \text{ mm}$ ,  $t_{F0} = 0.53 \text{ mm}$ ,  $f_{Cy0} = 0.10 \text{ N/mm}^2$ ,  $f_{Fy0} = 320 \text{ N/mm}^2$ ,  $d_0 = 19 \text{ mm}$ ,  $c_0 = 5.5 \text{ mm}$  and  $k_0 = 200 \text{ N/mm}$ .

The European standard [3] gives design equations against the tensile and shear failures of fastenings in pure metal structures. The design equation for tensile resistance of the fastener in a sandwich structure has to include all the three failure modes shown in Figure 1.

$$F_{td} = \sum \gamma_{Fi} \psi_i F_{ti} \leq \min \begin{cases} F_{Rtk,pull-over} / \gamma_{M2} \\ F_{Rtk,fastener} / \gamma_{M2} \\ F_{Rtk,pull-out} / \gamma_{M2} \end{cases} \quad (3)$$

Similar equations can be written for the analysis of the shear resistance of the fastening (Figure 1).

$$F_{vd} = \sum \gamma_{Fi} \psi_i F_{vi} \leq \min \begin{cases} F_{Rvk,pull-over} / \gamma_{M2} \\ F_{Rvk,fastener} / \gamma_{M2} \\ F_{Rvk,pull-out} / \gamma_{M2} \end{cases} \quad (4)$$

In equations (3) and (4)  $\gamma_{Fi}$  and  $\gamma_{M2}$  are load and material safety factors and  $\psi_i$  a combination factor to take into account the unlikely simultaneous existence of the full loads of all actions.  $F_{ti}$  and  $F_{vi}$  are tensile and shear forces of different actions and  $F_{Rtk}$  and  $F_{Rvk}$  characteristic values of the tensile and shear resistance.

Because the typical mode of tensile failure of the screw fastenings used to fix the panels to the frame of a building locates in the outer face close to the head of the screw and the typical mode of the shear failure in the inner face, there are only weak interactions if any between the tensile and shear failures in the first failure mode. Thus, no design equations for the

interaction for the panel fastenings are normally needed. The case is different for the fastenings used to fix additional coverings to a single face of the panel. The tensile and shear loads cause the failure in the point of the fastener in the face. Thus, the interaction studies are needed. European standard for thin-walled steel structures give a design equation for the interaction based on the linear interpolation between the tensile and shear failure [3].

$$\frac{F_{t,Sd}}{F_{Rtk}/\gamma_{M2}} + \frac{F_{v,Sd}}{F_{Rvk}/\gamma_{M2}} \leq 1 \quad (5)$$

In the equation, the resistances  $F_{Rtk}$  and  $F_{Rvk}$  represent the characteristic tensile and shear resistances based on the combined mode of the failure. The design equation for the interaction corresponds the failure mode of a fastener fixed to a single face layer and therefore, may be valid for sandwich panels, also.

#### 4. ADJUSTMENT OF TEST RESULTS

The mechanical and geometrical properties of the test specimens usually differ from the nominal values of the properties used in the design of the product. In sandwich panels, important properties are the thickness of the panel and the face layers and strength and modulae of elasticity of the face and core. Because of the difference, the test results have to be adjusted to correspond the nominal values of the test structure. The adjustment is based on the calculation model describing the resistance of the specimen. The adjustment should not be too large because of the limited capability of the calculatio model to describe the failure mode of the structure. In European Recommendations for Sandwich Panels [1] the expression (6) is given to adjust the test results of fastenings.

$$F_{R,adjusted} = F_{R,observed} \left( \frac{f_{y,nom}}{f_{y,observed}} \right)^{\alpha} \left( \frac{t_{nom}}{t_{observed}} \right) \quad (6)$$

where  $\alpha=0$ , if  $f_{y,observed} \leq f_y$  and  $\alpha=1$ , if  $f_{y,observed} > f_y$  .

The model (1) shows the yield stress  $f_{Fy}$  and the thickness  $t_F$  of the face to be the most important parameters in the evaluation of the resistance of the screw fastening. Thus, the model (1) supports the validity of the adjustment model (6) given in the Recommendations [1].

## 5. SUMMARY

Experimental research produces realistic and relevant results supposing that the loading arrangements correspond the real loading cases existing in practice. Because the resistance and the stiffness of the fastening depend on a number of parameters describing the fastener, the sandwich panel and the supporting structure, the test results are, strictly speaking, applicable only for the combination studied in the tests. Properties of the fasteners and the panels in the tests usually differ from the nominal values of the properties given for the design of the sandwich structures. Therefore, the test values have to be adjusted to correspond the nominal properties of the structure. A model is needed for the adjustment. The contribution shows a model based on numerical simulations to support the validity of the adjustment model given in design Recommendations. Characteristic tensile and shear resistances used in the design should base on experimental data.

Analytical models on the stiffness and resistance create understanding on the importance of different geometrical and physical parameters of the fastening. Analytical models allow interpolation and a slight extrapolation of the test results in the design and product development. The analytical models can also be used in further adjusting of the test results for the design work. Modelling is needed for the fastenings used to fix in one face layer, only.

## REFERENCES

1. European Recommendations for Sandwich Panels. CIB/ECCS Report Publication 257, 2000 and European Recommendations for Sandwich Panels. ECCS Publication 115, 2001.
2. Meriläinen, J. (2001). Computational modelling of the core layer of a sandwich panel applied to evaluation of the resistance of the fastening (in Finnish), M.Sc. Thesis, Helsinki University of Technology, Laboratory of Structural Mechanics.
3. prEN 1993-1-3: 2004. Eurocode 3: Design of Steel Structures. Part 1-3: General rules, Supplementary rules for cold-formed members and sheeting, July 2004.

# EXPERIMENTAL FAILURE MODE DETERMINATION OF GRP/PVC-FOAM SANDWICH T-JOINTS

## *Static and Dynamic Experiments*

Alexander W.J. Gielen and Wim Trouwborst

*TNO Built Environment and Geosciences, P.O. Box 49, 2600 AA Delft, The Netherlands*

sander.gielen@tno.nl, wim.trouwborst@tno.nl

Douglas C. Loup

*Naval Surface Warfare Center, Carderock Division, 9500 MacArthur Blvd, West Bethesda,  
MD 20817-5700, USA*

LoupDC@nswccd.navy.mil

**Abstract** Application of GRP/PVC-Foam sandwich structures on naval ships strongly depends on the mechanical strength and collapse behaviour of the joints of the structure. Quasi-static and dynamic experiments were executed to determine the failure modes and failure progression of T-joints. The results were used to determine the focus of the material tests, and to determine the main properties of failure models that were developed.

**Keywords:** sandwich T-joint, static loading, dynamic loading, failure modes.

## 1. INTRODUCTION

Application of composites on navy ships is increasing for hull and top-side structures. In the recent past single skin composite T-joints were investigated [1] and appropriate failure models for use in finite element analyses were derived [2]. The attention has now shifted towards GRP sandwiches, because of the structural and weight advantages over single skin composites. However, the joints between the sandwiches form the weaker link with respect to the strength and resistance against impulsive loading conditions and they may affect the integrity of large sections in the ship in an unfavourable way [3]. In order to better understand the failure processes in these joints and to furnish an experimental foundation for the development of appropriate failure models

for sandwiches, a large number of destructive tests were executed on T-joints, representative for joints in hull and top-side structures.

We adopted the research methodology as described in [1]. The main elements of this method are given in Figure 1. The current paper only deals with the structural experiments. Another paper in these proceedings [4] deals with the material characterization.

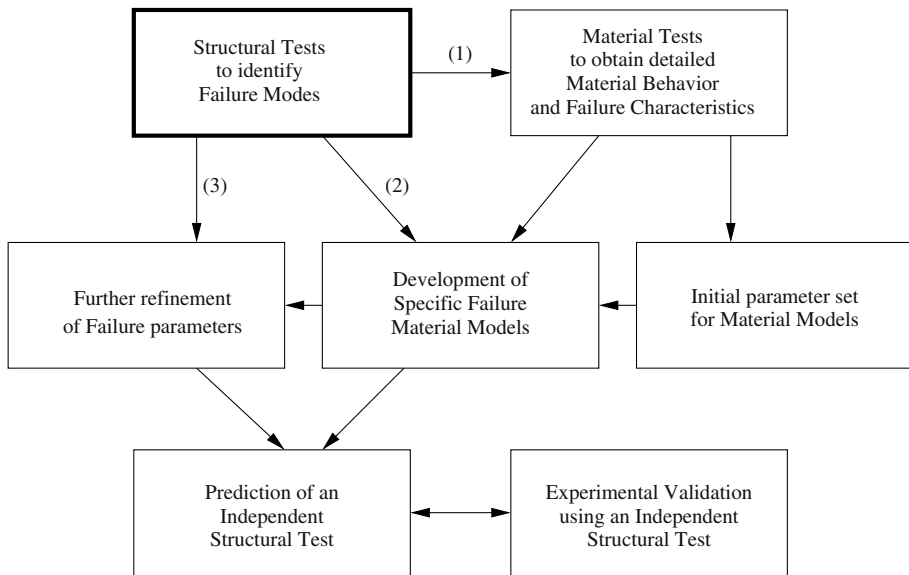


Figure 1. DYCOSS Research methodology for sandwich structures.

The structural experiments aim at clarifying the following questions (see arrows in Figure 1): (1) Which material behaviour needs to be determined in detail? (2) What kind of material models are needed to predict this? (3a) What is the load for failure initiation? (3b) Where does the failure initiate, and how does that compare to traditional prediction methods? (3c) If a crack is formed, at what speed and how does it propagate?

## 2. SETUP OF THE EXPERIMENTS

The T-joints (see Figure 2) consisted of panels of GRP skins with the PVC-foam cores. The skin to core thickness ratio is typically 1:17. The sandwich panels were joined using a PVC foam block and hand laid-up overlaminates using a vacuum bagging resin transfer molding technique. The height of the block is half the panel core thickness. The overlaminate thickness was matched

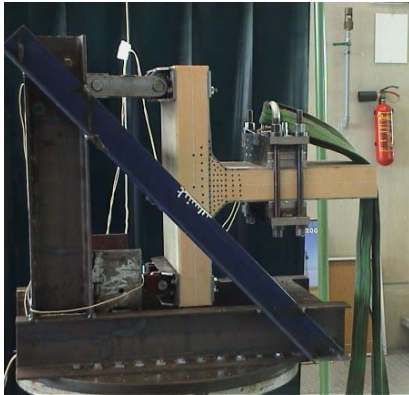


Figure 2. T-joint in shear setup on a shock testing machine.

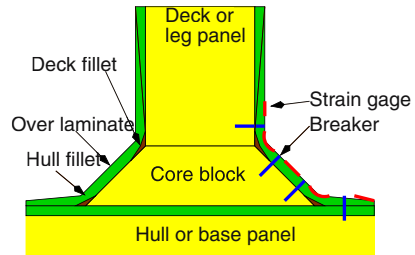


Figure 3. Joining of the panels using a core-block and over-laminates. The location of strain gages and breakers is indicated.

to the thickness of the skins of the panels. The overlaminate was tapered over a length of 1.5 times the panel thickness.

In Figure 3 it is shown how the panels are joint. The core block forms the transition between the panels. The fillets are used to smooth the edges and obtain acceptable radii for the over-laminates.

The instrumentation of the joint consisted of breakers, gages, force and displacement gages or accelerometers and a hi-speed video system. The breakers were specially developed, consisting of a graphite pencil core with a 0.5 mm diameter, conducting silver paint, and insulated copper wire (Figure 4), to track formation of cracks in the core-block. The deformation of the skins in the core-block region was measured using strain gages. These strain gages were glued to the skin at the locations indicated in Figure 3 and Figure 5. For the global load monitoring we used a force cell and displacement sensors in the quasi-static case. In the dynamic case the shock table acceleration and the mass acceleration was measured. A high-speed video system was used to visually record the test. The frame rate was 5000 fps and the resolution was 100x256 pixels.

The joints were subjected to quasi-static loading and dynamic loading. For the quasi-static loading a crane was used and for the impulsive load a shock testing machine was applied. Three configurations were investigated, that we named (1) Bending, (2) Shear, and (3) Pull (see Figure 6). In the static case the joint was pulled at the arrow location. In the dynamic case a mass was located at the arrow and the joint was moved at the constraints. The constraints consist of hinges. One hinge is fixed, the other is mounted on a pendulum,



Figure 4. Graphite pencil core breaker: The breaker consists of a graphite core of 0.5 mm diameter and a length of 20-40 mm. At the ends insulated copper wire is attached using an electric conducting silver paint. As a reference a normal match is included in the picture.



Figure 5. Instrumentation of the joint: On the left side, five strain gages are glued on the skin. The gages 2 and 4 are glued on the hull and deck fillet, respectively. On the right side, four breakers are inserted into the skin and the foam core.

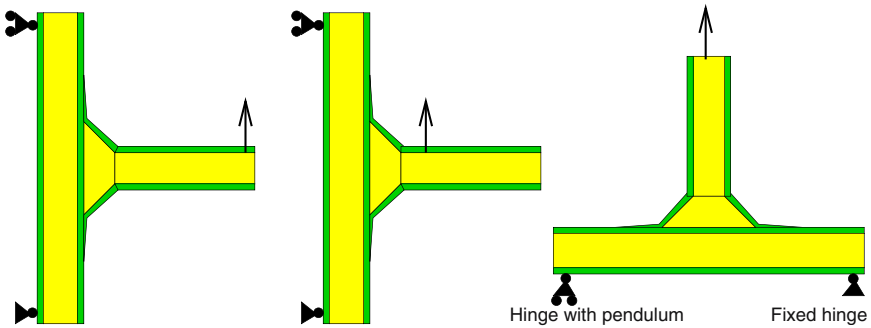


Figure 6. Loading configurations: (left) Bending, (middle) Shear, (right) Pull. In the static case the load is applied at the arrow by pulling with a crane. In the dynamic case a mass is attached at the arrow location and the constraints are moved by the shock testing machine.

such that translation of the hinge in one direction is possible. These hinges allow free bending of the base panel without introducing additional tension or compression loads [1].

### 3. RESULTS

The lateral static and dynamic loading of the sandwich T-joints was executed successfully. High quality data was obtained, as the tests had a high degree of repeatability ( $< 3.2\%$  standard deviation over average in joint load for a repeated test with one joint,  $n = 4$ ) and reproducibility ( $\leq 9.6\%$  standard deviation over average in joint load for the same test with different joints,  $n = 3$ ). The reproducibility of the tests mainly depends on the quality of the joints and is considered very good.

It is not possible to discuss all the results in detail. Therefore a few examples were picked from the results to illustrate the kind of data we gathered to support our main conclusions.

The instrumentation with the newly developed breakers and strain gages, in combination with the hi-speed video worked well and provided valuable information on the occurrence of damage in the sandwich (Figure 7 and Figure 8). The jump in the breakers and strain gages round 9ms can be nicely matched to the high-speed video recordings. Note that the crack reaches B4 just after the crack is initiated. B3 fails early and is due to the large elastic deformations in that area. B2 shows failure due to elastic deformations, then reconnects and fails again when the crack actually arrives overthere. A similar behaviour is seen on B1.

The following failure modes were identified:

- **Foam damage:** Visible foam damage occurred in tension and shear. Given the published compression strength of H100 [5] and the loading of the joint with respect to the load distribution as determined in an analysis study performed within the project, compression failure is very likely to have happened, but this cannot be visually confirmed. The cracking mode was mode I for perpendicular loading and mode II or mixed I-II for parallel loading.
- **Foam-composite interface damage:** Except a single panel, all other panels showed foam-composite failure in the core block area. For bending and shear separation mainly occurred at the overlamine interface in mode I and II, while for pull the base-panel to core-block interface was the most important one in mode I.
- **Foam-fillet interface damage:** In all cases where a crack came near the fillet, the deck fillets stuck to the over-lamine and the hull fillets stuck either to the over-lamine or hull laminate but never to the foam.

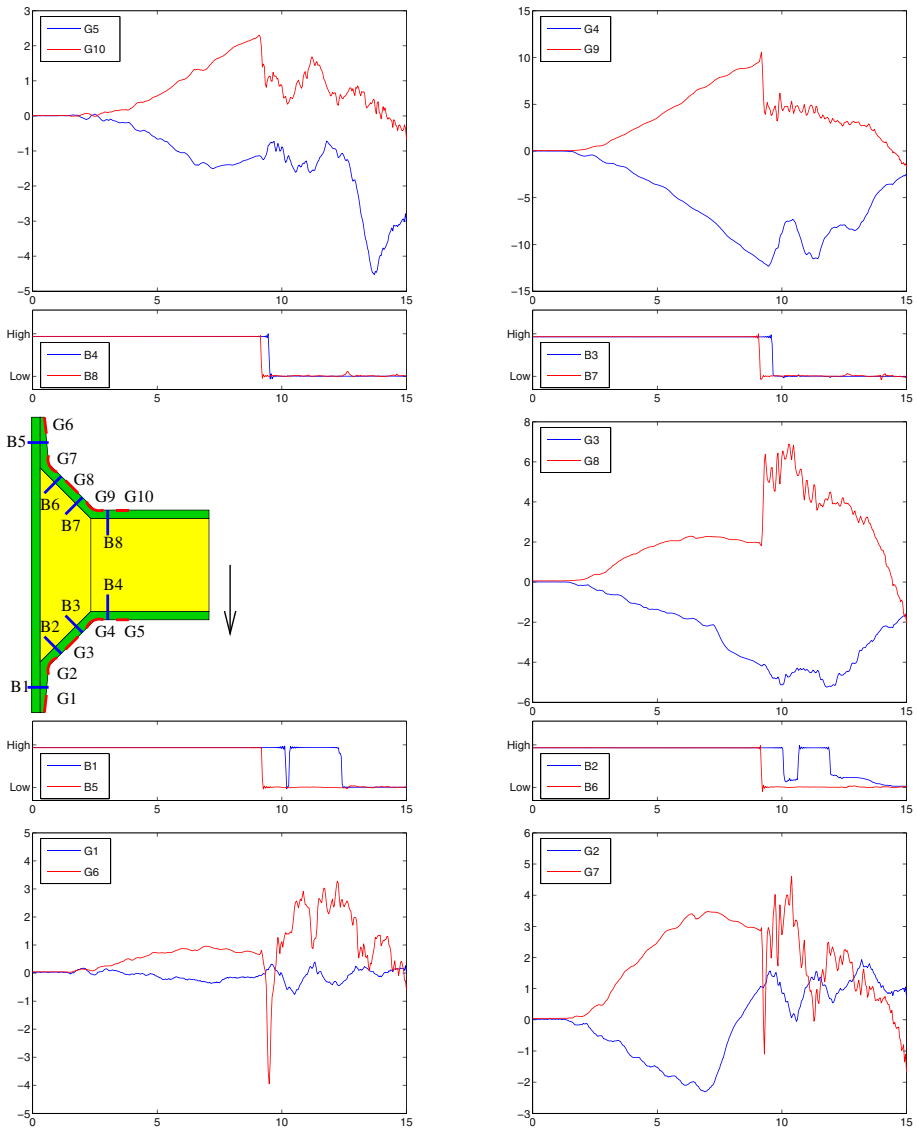


Figure 7. Strain and breaker response v.s. time for the dynamic lateral shear. Gages and breakers at the bottom side are blue, the ones at the top side are red. Strain measures is milli-strains (mm/m). The x-axis is time in milliseconds (ms). The arrow in the location overview is to indicate that the joint failed in the “swing down”.

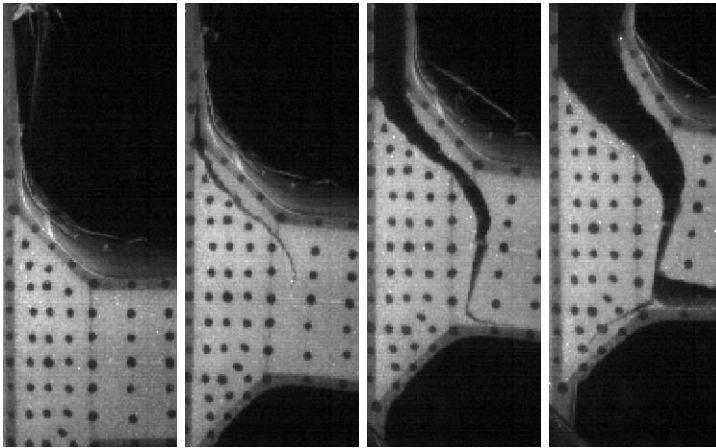


Figure 8. Hi-speed video stills of dynamic shear test at 1.2, 9.2, 13.2, 16.2 ms.

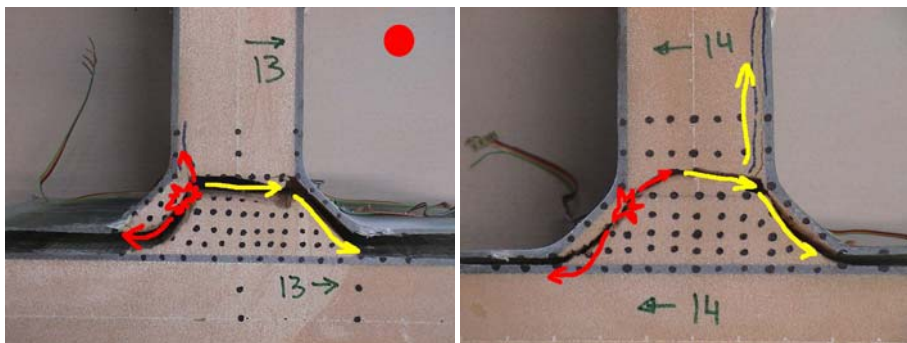


Figure 9. Final crack pattern and crack progression for the static (left) and dynamic (right) case for the shear configuration. The crack is initiated at the “spark” location and firstly progresses along the red arrow, and accordingly along the yellow arrow.

- Composite–composite interface damage: When the deck panel separates from the hull the composite-composite over-laminates separates. Separation occurs mainly in mode I for Bending and Pull loading, and mixed mode I-II for Shear loading.

In the dynamic case the global load at failure was less than in the static case (Bending 74%, Shear 41%, Pull 84%), while the deformation in the damaged area was at a similar level (see Table 1 for the Shear case). This indicates that in the dynamic case the global and local load are not directly linked, and the global load is not an appropriate measure for the joint strength. Furthermore, the crack pattern as well as the crack progression showed similar histories for

Table 1. Strains at break dynamic compared to static values at 49% and 100% load. Note that the order of gages of the dynamic test is swapped to account for the opposite failure direction of the dynamic test.

<i>Tension side</i>					<i>Compression side</i>				
<i>Gage</i>	<i>Static</i>		<i>Dynamic</i>		<i>Gage</i>	<i>Static</i>		<i>Dynamic</i>	
	49%	100%	<i>Break</i>	<i>Gage</i>		49%	100%	<i>Break</i>	<i>Gage</i>
G1	0.29	0.60	0.66	G6	G6	-0.33	-0.19	-0.08	G1
G2	1.64	3.22	2.87	G7	G7	-1.49	-1.54	1.00	G2
G3	0.84	1.89	1.96	G8	G8	-1.32	-5.17	-4.12	G3
G4	3.88	9.28	9.59	G9	G9	-3.39	-8.04	-11.68	G4
G5	0.66	2.02	2.30	G10	G10	-0.74	-1.88	-1.13	G5

the static and the dynamic case (Figure 9). Finally, Table 1 shows the strains on the gages for a static shear test (SS) at 49% loading and break levels and the strains on the gages of dynamic shear test (DS) at break, when the crack starts to form and the first breaker (number 7) fails. All the tension gages (G1-5 of SS, and G6-10 of DS) are larger for DS than the 100% level of SS, except G7/DS – G2/SS. Still, G7/DS has a value closer to the 100% level of G2/SS than the 49% level. On the compression side (G6-10 of SS, and G1-5 of DS) the pattern is less consistent. Still, G4/DS is much larger than G9/SS at 100%, while G3/DS and G5/DS are closer to the SS 100% than 49% levels.

The crack velocity was determined on one of the T-joints that was loaded in pull-off mode (Figure 10). Two cracks formed in the joint. The velocity of the first crack ranged between 24 and 66 m/s, when the major loading direction was tangential to the crack and 50 to 315 m/s when the load was perpendicular to the crack. The second crack had a velocity between 191 and 370 m/s and is mainly perpendicular to the loading direction. This procedure was repeated for other T-joints with similar results. If we compare these values to the sound velocity in the foam  $c = \sqrt{E/\rho} \approx 1100$  m/s [5], it is clear that the crack velocity is well below this value ( $< 12\%$ ) for the crack formation with the load tangential and intermediate (20-40%) for the crack perpendicular to the loading direction.

The high-speed video recordings revealed that the damage was not always initiated at the expected location. For example in the pull configuration the crack was initiated in the leg panel and progressed towards the core block. It appeared that the crack was initiated on the skin-foam interface or just in the foam material (no instrumentation was near that location). It might be due to the large differences in modulus of the skin and foam material or secondary bending effects in the leg panel, introducing significant interface tension. The material model and analyses of the tests, that are currently being performed, will help in better understanding these tests.

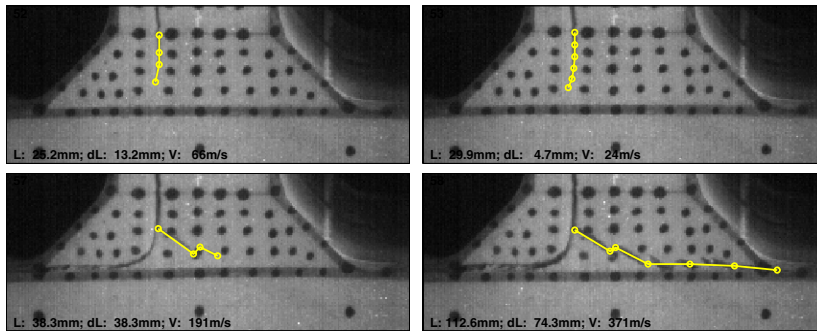


Figure 10. Crack tracking with dynamic pull-off loading. For the first crack the bond-line is taken as reference point, and for the second crack the first crack is taken as reference point. The numbers in the figures refer to the frame number in the hi-speed recording.

Furthermore, in the high-speed videos it was clearly visible that the core block was quite distorted just before failure. Strain estimates extracted from the video images show principle strains of  $-4.5\%$  and  $6\%$  in the shear configuration. These values are well beyond the linear strain limit ( $\epsilon = \sigma/E$ ), which is  $1.3\%$  for compression and  $2.5\%$  for tension [5].

#### 4. DISCUSSION

Static and dynamic tests were executed on sandwich T-joints. Detailed failure behaviour and fracture progression information was captured using specially developed breakers, strain gages, and hi-speed video recordings. Global behaviour was measured using force and displacement gages, or accelerometers in the static and dynamic test, respectively.

Based on the findings in the T-joint tests it was decided that the material behaviour investigation should focus on the detailed behaviour of the foam, in particular the non-linear behaviour and the fracture properties. Furthermore, in the pull configuration the foam-skin interface properties are expected to play an important role.

The differences in failure loads between the static and the dynamic tests may be due to redistribution effects of loads, load propagation effects, as well as strain rate dependency effects. As the rate effects of the skins appeared to be minimal in previous research [1, 2] and the foam makes up the majority of the T-joint volume, the strain rate dependency of the foam will be investigated [4].

Some specific details in the tests could not yet be explained. For this a detailed examination of the foam material behaviour is needed. Furthermore, a numerical analysis of the test will help in better understanding the behaviour.

## ACKNOWLEDGMENTS

The results of this research were obtained in the “Dycoss-2” project, a joint research project executed by TNO and NSWC-CD. The project is sponsored by the Royal Netherlands Navy and the Office of Naval Research, USA.

## REFERENCES

- [1] G. J. Meijer, E. A. Rasmussen, P. P. M. Lemmen, R. L. C. Lemmen, and D. Palmer. Dynamic behavior of composite ship structures (DYCOSS); tests and analyses efforts. In *70th Shock and Vibration Symposium*, Albuquerque NM, USA, 15-19 November 1999.
- [2] P. P. M. Lemmen, G. J. Meijer, and E. A. Rasmussen. Dynamic behavior of composite ship structures (DYCOSS) failure prediction tool. In *70th Shock and Vibration Symposium*, Albuquerque NM, USA, 15-19 November 1999.
- [3] B. Hayman and D. Zenkert. The influence of defects and damage on the strength of FRP sandwich panels for naval ships. In *Proceedings of the 9th PRADS conference*, Lübeck-Travemünde, Germany, 12-17 September 2004.
- [4] D. C. Loup, R. C. Matteson, and A. W. J. Gielen. Material characterization of PVC foam under static and dynamic loading. In *Proceedings of the 7th International Conference on Sandwich Structures.*, Aalborg, Denmark, August 2005.
- [5] Divyncell H grade, data sheet. <http://www.diabgroup.com>, 2002.

# FLEXURAL BEHAVIOUR OF ALUMINIUM FOAM/COMPOSITE STRUCTURES

*An Investigation into the Deformation Mechanism and Strain Distribution under 4 Point Bending in Comparison with Polymer Foam Core Structures*

M. Styles, P. Compston and S. Kalyanasundaram

*Department of Engineering, FEIT, Australian National University, Canberra ACT 0200, Australia*

**Abstract** The deformation mechanism of an aluminium foam core/thermoplastic composite facing sandwich structure was compared with an equivalent polymer foam core sandwich structure under 4pt bend loading. Full field strain analysis showed the metal core deformed extensively mid-beam while the polymer foam had high strain concentrations under the load rollers.

**Key words:** aluminium foam, flexural loading, strain distribution.

## 1. INTRODUCTION

Polymer foam cores are widely used in sandwich structures for a variety of applications but have limited function in high temperature systems. Metal foams have attractive properties for use as sandwich cores, including good stiffness and strength to weight ratios, high impact energy absorption, good sound damping, electromagnetic wave absorption, thermal insulation and non combustibility [1]. Metal foams may therefore be more appropriate where multi-functionality is valuable [2]. The bulk material behaviour of aluminium foam has been investigated and a distinct size effect has been observed [3, 4]. The mechanical properties of the foam were found to increase to a plateau level as the ratio of specimen size to cell size increased [3]. Previous studies have looked at the failure behaviour of metal foam sandwich structures using ductile metal skins [5, 6], producing failure mechanism maps that identify load criteria to generate either face yield,

indentation or core shear as the dominant failure mechanism. Some work has investigated the fracture and impact response of aluminium foam sandwich structures with composite skins showing the combination has high energy absorbing properties [7, 8]. Studies have been conducted on such composite structures under 3 point bend loading, focusing on the failure modes produced by varying core thickness and span length [9]. The structures were found to fail mainly by either core shear or by upper skin compression failure. While prior work has made some initial investigations, further mechanical characterization of these structures is required to fully understand the structural behaviour.

The present study examines the quasistatic mechanical behaviour of aluminium foam sandwich structures with thermoplastic composite skins, focusing on localised deformation mechanisms. The work presented here is a first step towards developing useful constitutive models of aluminium foam sandwich structures with composite skins. Initial investigations have considered the flexural behaviour of a thin sandwich structure under 4 point bending loading, using ALPORAS aluminium foam and Twintex® skins, a commingled glass fibre thermoplastic composite. The high temperature resistivity of metal foams makes it possible to use thermoplastic-based composite skins, which can reduce manufacturing time when compared to thermoset-based composite skins. A polymer foam core sandwich structure with glass/polyester skins was also examined as a reference for the performance of the metal foam. Real time strain analysis was incorporated using a 3D optical measuring technique (ARAMIS, GOM mbH, Germany) to provide an indication of the strain distribution throughout the sandwich cores. This full field strain analysis provides a valuable insight into the localised deformation progression and therefore the overall mechanical behaviour properties of the foams under typical loading.

## **2. EXPERIMENTAL METHOD**

### **2.1 Sample manufacture**

Sandwich panels with dimensions 200 × 200 mm were manufactured for this study. Single ply sheets of plain weave Twintex (glass fibre thermoplastic, from Saint-Gobain Vetrotex, 745gsm) and sheets of hot-melt polypropylene adhesive (Glucol Ltd., UK) were stacked either side of the 10mm thick ALPORAS aluminium foam (a closed cell aluminium foam from Gleich, GmbH, Germany, density 0.23 g/cm<sup>3</sup>). The panel was placed in a picture frame mold, which was heated to 185°C in a platen press and held under 2.5

MPa briefly before being rapidly cooled. A polymer foam core sandwich structure panel was manufactured using 10mm thick Divinycell H100 (a closed cell polymer foam from Diab) and 1 ply plain weave e-glass (630gsm)/ UV curing polyester resin. The resin contained 0.5pph of photoinitiator (Irgacure 819) and each skin was cured through 10 minutes exposure to UV light (sunlight). The skins were manufactured so as to have an equivalent thickness and fibre:resin mass fraction to the twintex skins used in the aluminium foam sandwich. Samples from both panels were cut to a width of 25mm using a diamond tipped saw.

## 2.2 Mechanical test procedure

The sandwich structures were tested in a four-point bend following ASTM Standard C393-63. The appropriate support span dimension  $a_1$  was determined from the relationship  $a_1 = 2fF/S$ , which depends on the facing thickness  $f$  (mm), the allowable facing stress  $F$  (MPa) and the allowable core shear stress  $S$  (MPa). The allowable facing stress for each facing type was determined from testing following ASTM Standard D790M-86. The testing was conducted at 10mm/min using an Instron Universal tester. The support span was 150mm, and the load span 50mm. Load and support rollers had a diameter of 14mm. A load-displacement plot was recorded for each test.

Mechanical properties were calculated using simple beam bending theory adapted to sandwich structures. The maximum core shear stress was obtained with Eq. (1) [10],

$$\tau_{\max} = \frac{P_{\max}}{D} \left( \frac{E_f f d}{2} + \frac{E_c c^2}{4} \right) \quad (1)$$

where  $P_{\max}$  is the maximum load on the sample in N,  $D$  the flexural rigidity in  $\text{Nm}^2$ ,  $f$  the sandwich thickness,  $d$  the distance between the facing centroids,  $c$  the core thickness,  $E_f$  the modulus of the facings in  $\text{N/m}^2$  and  $E_c$  the modulus of the core. The maximum stress in the facings and core were calculated using Eq. (2) and Eq. (3) respectively [10] where  $M$  is the maximum bending moment and  $h$  the sandwich thickness.

$$\sigma_f = \frac{Mz}{D} E_f \quad \text{where } z = \frac{c}{2} + \frac{1}{2} \left( \frac{h}{2} - \frac{c}{2} \right) \quad (2)$$

$$\sigma_c = \frac{Mz}{D} E_c \quad \text{where } z = \frac{c}{2} \quad (3)$$

## 2.3 Strain analysis

Full-field, real-time strain analysis during testing of each sandwich structure was conducted. The system used was ARAMIS, which gives an advanced deformation and strain analysis using 3D image correlation. It is able to provide a full-field stress-strain measurement using a photogrammetric method as the sandwich structure deforms under load [11]. Each sample was sprayed with a contrasting ‘speckle’ pattern, which deformed along with the sample. Two high-resolution, digital CCD cameras recorded the deformation. Figure 1 shows a schematic of the experimental arrangement. The images are evaluated using photogrammetric principles to track small correlation areas in each successive image and produce 3D coordinates of the surface of the sample [12]. This digital image processing provides a full-field contour of the strain distribution throughout the test. Here, the images focused on the area between the top two loading pins of the 4-point bend arrangement. The image sampling time was 500ms.

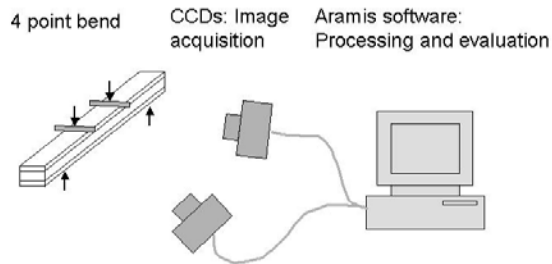


Figure 1. Experiment arrangement.

## 3. RESULTS/DISCUSSION

### 3.1 Failure behaviour of Al foam sandwich structure

Figure 2 shows a typical load-displacement curve for the aluminium foam sandwich structure. There is an initial linear elastic behaviour followed by steady failure and damage progression. The structure was found to fail in compression with initial failure occurring in the top facing with fibre fracture and some skin wrinkling in the area between the loading rollers. Some core failure was visible in the center of the span between the load rollers with the core deforming initially by cracking followed by crushing of the cells. There was no visible debonding between the core and

skins, and no damage to the bottom facing. The damage progression appeared to be steady and consistent and this can be seen in the smooth curve of the load-displacement plot. The load at yield (point (a) in Figure 2) was 0.353 kN with a yield displacement of 4.327 mm. The load curve then drops to a minimum of 0.22 kN before slowly rising to an apparent plateau of just above 0.3 kN. This plateau region has been widely observed in bulk aluminium foam as a result of progressive plastic collapse of the cells [13].

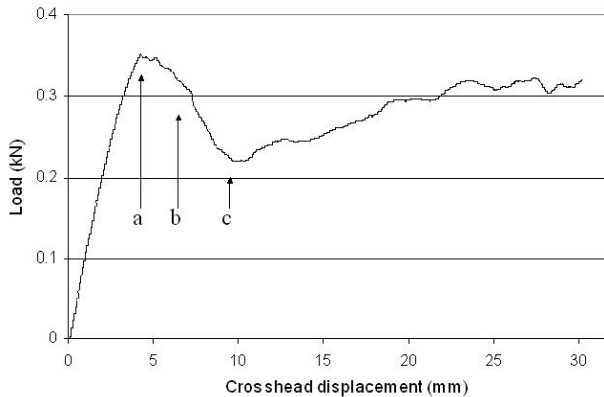


Figure 2. Typical load-displacement curve plot for a 10mm Al foam sandwich structure.

The strain distribution of the aluminium foam sandwich is shown in Figure 3. Figures 3(a), (b) and (c) show three frames corresponding to points (a), (b) and (c) on the load-displacement plot in Figure 2. The strain analysis initially showed dispersed regions of higher strain throughout the sample. This distribution continued during the elastic region of the loading. Figure 3(a) corresponds to the yield point (a) and shows these dispersed regions of higher strain. The areas of slightly higher strain appeared to correspond to the larger cells visible on the surface of the foam. As the test went beyond the yield point, a region of high strain formed in the centre of the sample where cracking and deformation of the core was observed. This concentrated region of strain can be seen in Figure 3(b). The region of high strain continued to develop as the test continued, increasing in area and magnitude. Figure 3(c) shows the strain distribution corresponding to point (c) at the arrest of the load drop. The central high strain region reached maximum values in the order of 200% whereas the remainder of the sample had a maximum strain of 60% with an average of 4%. Figure 3(d) shows the three dimensional surface of the sample at the same displacement as (c). Notably, the surface had a significant deformation as the cells deformed out of the plane.

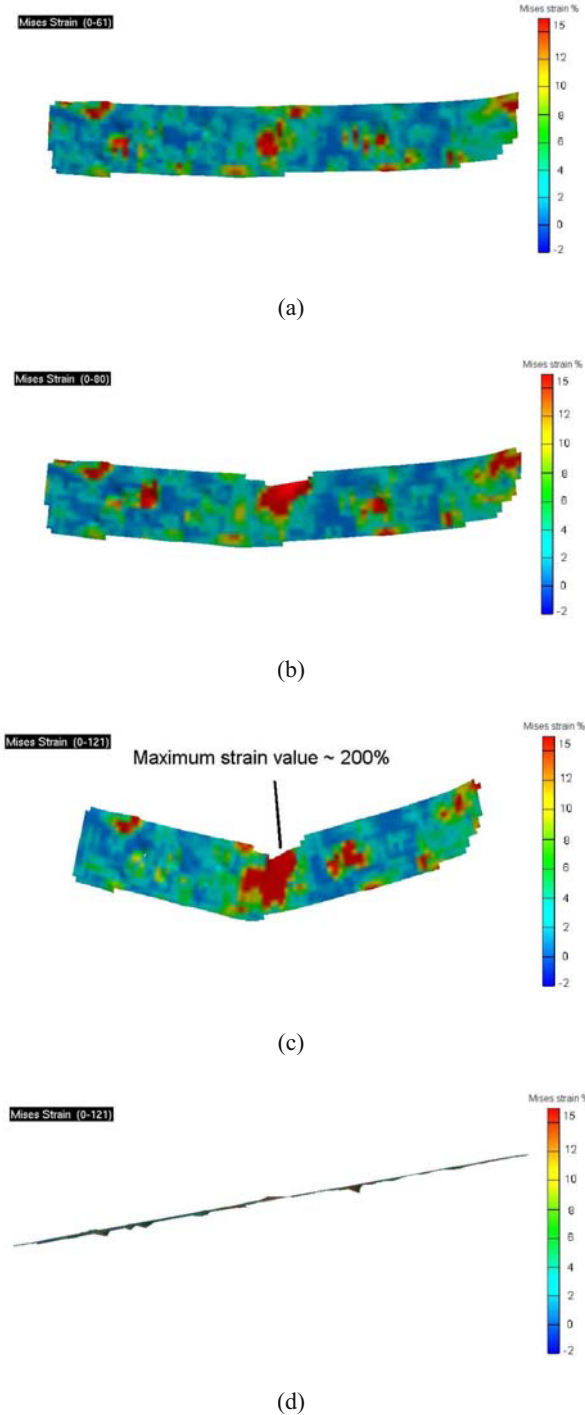


Figure 3. Typical 4pt bend Alporas strain maps at (a) 5mm, (b) 6.5 mm, (c) 10mm crosshead displacement, (d) shows 3D contours at 10mm crosshead displacement.

### 3.2 Failure behaviour of Polymer foam sandwich structure

Figure 4 shows a typical load-displacement curve for the Divinycell sandwich structure. Initial elastic behaviour was followed by a rapid load drop and catastrophic failure once the structure has passed the yield point. This contrasts with the steady drop in load seen in the aluminium foam structure. Similarly, the displacement over which the structure yields and drops to a plateau load is much smaller than in the aluminium foam. The structure was found to fail in compression with initial failure occurring in the top facing with fibre fracture underneath the loading rollers. Some minor core failure occurred toward the end of the test as the top of the core began to deform beneath the load rollers. There was no visible debonding between the core and skins, and no damage to the bottom facing. For the polymer foam structure, the load at yield (see point (a) in Figure 4) was 0.453 kN with a yield displacement of 3.221 mm. The load curve then drops to a minimum of 0.172 kN at 4.48 mm before slowly rising to an apparent plateau of just above 0.21 kN.

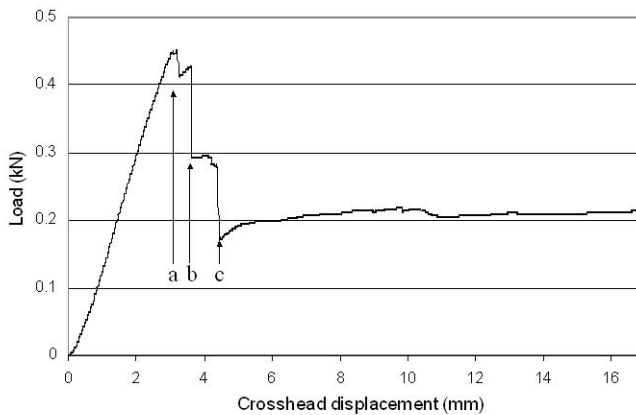
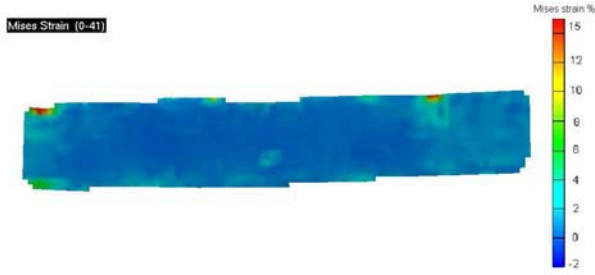
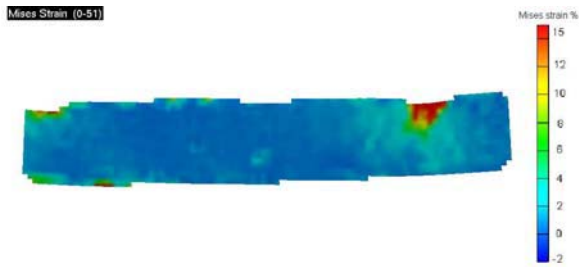


Figure 4. Typical load-displacement curve plot for a Divinycell sandwich structure.

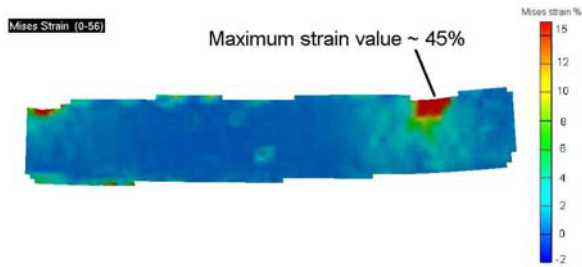
Figure 5 shows three frames corresponding to points (a), (b) and (c) in Figure 4. The strain distribution of the Divinycell sandwich under bending loading was initially very uniform with no regions of high strain. As the load increased towards the yield load, the strain distribution remained fairly consistent with very little variation in value. At the yield load, regions of higher strain began to appear in areas corresponding to beneath the load rollers.



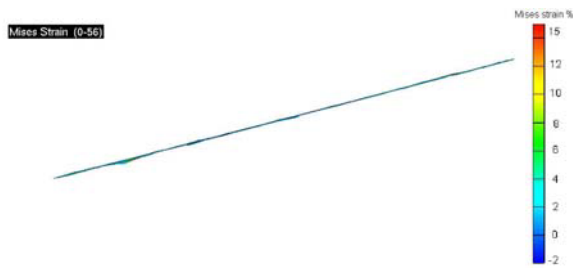
(a)



(b)



(c)



(d)

Figure 5. Typical 4pt bend Divinycell strain maps at (a) 3 mm, (b) 3.5 mm, (c) 4.5 mm crosshead displacement, (d) shows 3D contours at 4.5 mm crosshead displacement.

This corresponds to the failure and deformation observed in the top skin and core under the load rollers. These regions of high strain continued to increase in magnitude and area as the test progressed. The remainder of the structure appears to maintain the initial strain throughout the test. The high strain regions reached values in the order of 45% whereas the remainder of the sample had a maximum strain of 15% with an average of 1%. These values are much smaller than those seen in the aluminium foam structure. Figure 5(d) shows the three dimensional surface of the sample at the same displacement as (c). This shows far less out of plane deformation than is seen in the aluminium foam deformation.

### 3.3 Mechanical properties

The mechanical properties calculated from the 4-point bend results are given in Table 1. Both sandwich structures were made with a similar core thickness and fibre:resin mass fractions in the skins to enable direct comparison. The maximum core stress was much greater for the aluminium foam, following the difference in compressive modulus between the cores; with Alporas having a modulus in the order of 1.10 GPa while the H100 has a modulus of 0.125 GPa (Gleich, Diab product data sheets). Within scatter, the maximum core shear stress and maximum facing stress show no significant difference.

Table 1. Average mechanical properties for each structure (standard deviation in parentheses).

Sandwich Structure	Max Core Stress (MPa)	Max Core Shear Stress (MPa)	Max Facing Stress (MPa)	Energy to yield load (J)	Energy to arrest of load drop (J)
Alporas	13.64 (1.61)	1.90 (0.23)	126.44 (15.03)	1.30 (0.20)	2.92 (0.48)
H100 Divinycell	1.61 (0.22)	1.58 (0.21)	145.55 (19.84)	0.68 (0.15)	0.84 (0.25)

Furthermore, the energy absorption properties of the sandwich structures were considered by integrating the load-displacement curves. The energy absorbed up to the yield load was significantly greater in the aluminium foam. Similarly, the energy absorbed up to point (c) in the load-displacement curves, where the drop in the load halted, was considerably higher in the aluminium foam. The polymer foam appears to absorb minimal energy after its initial yielding while the aluminium foam structure continues to absorb energy as it progressively deforms. This increased energy absorption is consistent with previous studies [7].

## 4. CONCLUSION

The deformation mechanism of an aluminium foam core/thermoplastic composite facing sandwich structure under 4-point bend loading was found to be significantly different to that of an equivalent polymer foam core sandwich structure. A full field strain analysis showed that the metal core had an irregular strain distribution consistent with the irregular core distribution. A very high strain concentration was observed at a central deformation area where fracture occurred. The polymer foam had an even strain distribution with strain concentrations under the loading rollers. The energy absorbed up to yield was greater in the metal foam and continued to be greater as the structures deformed. This energy absorption characteristic of the aluminium foam structure, while displaying equivalent or enhanced mechanical properties compared to a polymer core, suggests such metal foam structures could be advantageous in a variety of structural situations.

## REFERENCES

1. L.J. Gibson, Mechanical behaviour of metallic foams, *Annu. Rev. Mater. Sci.* 2000 **30**: 191-227
2. A-M. Harte, N.A. Fleck, M.F. Ashby, Sandwich panel design using Aluminium Alloy foam, *Advanced Engineering Materials* 2000 **2** (4): 219-222
3. E.W. Andrews, G. Gioux, P. Onck, L.J. Gibson, Size effects in ductile cellular solids. Part II: experimental results, *International Journal of Mechanical Sciences* 2001 **43**: 701-713
4. J.F. Rakow, A.M. Waas, Size effects in metal foam cores for sandwich structures, *American Institute of Aeronautics and Astronautics Journal* 2004 **42** (7): 1331-1337
5. H. Bart-Smith, J.W. Hutchinson, A.G. Evans, Measurement and analysis of the structural performance of cellular metal sandwich construction, *International Journal of Mechanical Sciences* 2001 **43**: 1945-1963
6. C. Chen, A-M. Harte, N.A. Fleck, The plastic collapse of sandwich beams with a metallic foam core, *International Journal of Mechanical Sciences* 2001 **43**: 1483-1506
7. W.J. Cantwell, P. Compston, G. Reyes, The fracture properties of novel aluminium foam sandwich structures, *Journal of Materials Science Letters* 2000 **19**: 2205-2208
8. G. Reyes, W.J. Cantwell, The high velocity impact response of composite and FML-reinforced sandwich structures, *Composites Science and Technology* 2004 **64**: 35-54
9. S. McKown, R.A.W. Mines, Static and Impact behaviour of metal foam cored sandwich beams, *High Performance Structures and Materials, High Performance Structures and Materials II*, 2004, v7: 37-46
10. Sandwich Concept, DIAB Sandwich Handbook, [www.diabgroup.com](http://www.diabgroup.com)
11. J. Tyson, T. Schmidt, Advanced Photogrammetry for Robust Deformation and Strain Measurement, *Proceedings of SEM 2002 Annual Conference*, Milwaukee WI, June 2002
12. J. Tyson, T. Schmidt, Dynamic Strain measurement using advanced 3D Photogrammetry, *Proceedings of IMAC XXI*, Kissimmee, FL, Feb 2003
13. L.J. Gibson, M.F. Ashby, *Cellular Solids: Structure and Properties*, Cambridge University Press, Cambridge, 1997

# REPAIR CLASSIFICATION FOR SANDWICH PANELS WITH HAIL DAMAGE

M. Das and E. Madenci

*Department of Aerospace and Mechanical Engineering, The University of Arizona, Tucson, AZ 85721, USA*

H. Razi

*Stress Methods and Allowables, Boeing Commercial Airplanes, Seattle, WA 98124, USA*

**Abstract** Hail strikes of possibly exceeding an energy level of 50 Joules may cause multiple-site damage to thin gauged composite airplane structures. If not repaired properly, they may trigger an extensive damage to airplane structures and disruptions to airline operations, and therefore posing a major maintenance and repair concern for the airlines. It is important both for the OEM and the airlines to be able to classify the hail strike damage for appropriate repair procedure. Therefore, this study presents a methodology to assist engineers in the classification of the repair type for hail strike damage. The methodology involves an accurate prediction of the stress and strain fields, and residual strength prediction.

**Keywords:** repair, sandwich, indentation, residual strength.

## 1. INTRODUCTION

Thin gauged composite airplane structures may suffer from hail strikes resulting in dents and punctures at multiple sites. Disregarding such damage may cause a significant loss of stiffness leading to an extensive damage to airplane structures and disruptions to airline operations. Therefore, hail strike damage poses a major maintenance and repair concern for the airlines.

Depending on the severity of the hail strikes, the Original Equipment Manufacturer (OEM) classifies the repair as either “major” or “minor”. A minor repair has no appreciable effect on the airline operations. However, a major repair has a significant effect, and may require extensive static, fatigue, and damage tolerance strength justification and/or testing. Such repairs are mostly not covered by the aircraft Structural Repair Manual (SRM).

For a major repair, the repair scheme must be submitted to the OEM for their approval before the start of a repair. However, the minor repairs can be approved by the airline’s design engineers provided that they submit the

justification of the classification to the OEM. Federal Aviation Agency (FAA) or European Aviation Safety Agency (EASA) request from the airlines that approval be obtained for any repair by the Original Equipment Manufacturer (OEM). It is important both for the OEM and the airlines to be able to classify the hail strike damage for appropriate repair procedure in order to minimize the disruption of operations. Therefore, this study presents a methodology to assist engineers in the classification of the repair type for hail strike damage.

Stress analysis of sandwich panels with defects such as dents and punctures is a formidable task because of the presence of dissimilar materials and sharp changes in geometry. In addition, computational difficulties arise because the thickness of the facesheets is highly disproportionate to the in-plane dimensions. Razi et al. (1999) presented an analytical method to determine the stress distribution in sandwich panels with arbitrarily located damage. Each damage was modeled as a soft inclusion. This approach is limited to in-plane loading, and disregards the presence of transverse normal and shear stresses in the skin. Furthermore, the core sustains only shear loading, and thus disregards the presence of transverse displacements.

However, the effect of local bending is significant in the vicinity of the punctures and dents in predicting the stress field, thus predicting residual strength. Furthermore, the location of damage sites in relation to each other and their size influence the stress field significantly. An accurate and robust strength analysis of the damaged sandwich panels is essential to predict the influence of damage because it is necessary for establishing allowable damage limits. As discussed by Razi (2000), the residual strength and allowable damage size are dictated by damage diameter and indentation depth.

Accurate analysis of sandwich panels with common defects can be performed by employing standard three-dimensional finite elements or elements based on the layer-wise (zig-zag) theory. Although these elements accurately model a sandwich panel, they are computationally costly especially in the presence of defects due to the mesh refinement presented by disproportionate length scales in the thickness and planform dimensions. An alternative to these elements is an element by Das et al. (2004ab) based on a single-layer plate theory in which the weighted-average field variables capture the panel deformation and stress field in the thickness direction.

Although many criteria such as point stress, strain energy density and energy release rate exist in the literature for determining failure stresses in composite materials, they entail certain limitations. Their major limitation arises from the fact that fracture process in composites involves fiber-breakage, matrix cracking, fiber-matrix debonding and laminae separation during loading. In other words, a damage zone develops in the regions of stress concentration rather than a "clean" crack. In order to account for the culmination of these failure processes, Damage Zone Model (DZM) in conjunction with a finite element

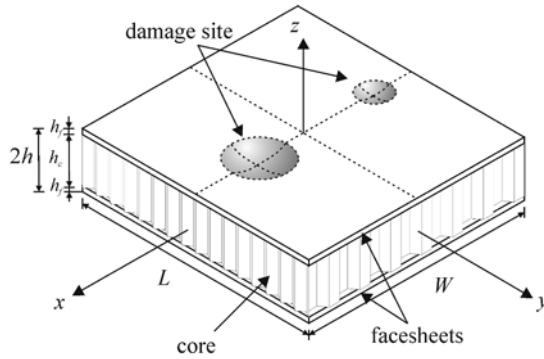


Figure 1. Geometry of a sandwich panel with facesheet damage.

model was introduced by Backlund (1981), and Clarin et al. (1985). This criterion provides failure stress prediction, and its validity for laminates and sandwich panels was substantiated by extensive experimental measurements at Boeing Company by Razi et al. (1998) and Razi (2000).

## 2. PROBLEM STATEMENT

The construction of a sandwich panel with face sheets and a core is illustrated in Figure 1. The mid-plane of the sandwich panel coincides with the  $(x, y)$  plane of the reference coordinate system.

As shown in Figure 1, the panel has a uniform thickness of  $2h$ . The thicknesses of the core and face sheets are denoted by  $h_c$  and  $h_f$ , respectively. The panel has a rectangular planar geometry with length  $L$  and width  $W$ . The face sheets, as well as the core, can be composed of homogeneous, elastic, and orthotropic material layers. Each ply forming the face sheets has elastic moduli  $E_1$ ,  $E_2$ , and  $E_3$ , shear moduli  $G_{12}$ ,  $G_{13}$ , and  $G_{23}$  and Poisson's ratios  $\nu_{12}$ ,  $\nu_{13}$  and  $\nu_{23}$ , where subscripts 1 and 2 are the material coordinates. For an isotropic core material, the Young's modulus and Poisson's ratio are defined as  $E_c$  and  $\nu_c$ , respectively. For an orthotropic core, its moduli,  $E_{xx}$ ,  $E_{yy}$ ,  $E_{zz}$ ,  $G_{xy}$ ,  $G_{yz}$  and  $G_{xz}$ , and Poisson's ratios,  $\nu_{xy}$ ,  $\nu_{yz}$  and  $\nu_{xz}$ , are defined with respect to the reference frame.

As shown in Figure 1, a single and multiple damage sites in the form of a dent, puncture and facesheet cutout may exist in the sandwich panel. Dent damage is defined as a permanent surface depression without facesheet cracking. Puncture is defined as a surface depression with several cracking represented by a reduction in stiffness. Puncture with extensive facesheet cracking has a 100% stiffness reduction, thus resulting in a facesheet cutout. The damaged sandwich panel may experience in-plane and out-of-plane loading; thus

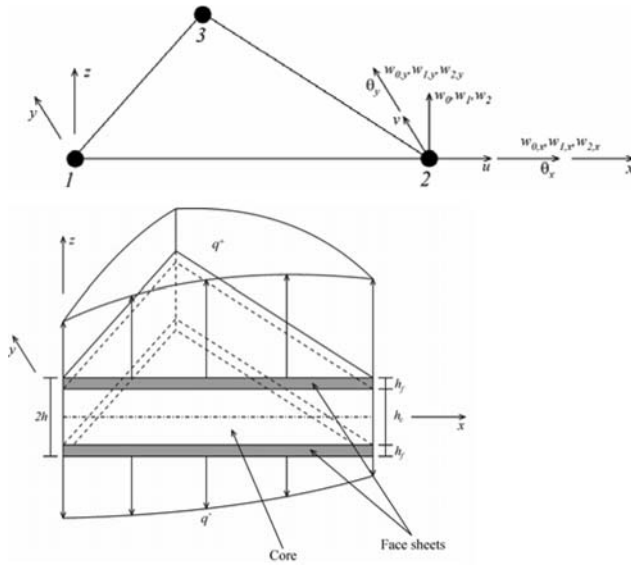


Figure 2. Geometric description of the thick sandwich plate element.

requiring the complete description of the stress and strain fields for accurate residual strength prediction.

The problem posed herein concerns the determination of the complete stress and strain fields and the residual strength prediction of sandwich panels with dents and cutouts under general boundary and loading conditions.

### 3. SOLUTION METHOD

#### 3.1 Complete stress and strain fields

Extreme differences in anisotropic material properties in sandwich panels and the presence of local bending in the vicinity of punctures and dents pose computational difficulties in performing stress analysis under in-plane and out-of-plane loading. The presence of arbitrary multiple damage size and sites further complicates the analysis.

In order to take advantage of the computational efficiency of the single-layer theory, this study utilizes a new triangular finite element for modeling sandwich panels with defects. The capability of this new triangular sandwich finite element developed by Das et al. (2004ab) was demonstrated by two distinct damage configurations in the form of a face sheet cutout and core crushing under either tension or bending, Das et al. (2004c).

The sandwich element is composed of two face sheets with a soft core in between as shown in Figure 2. The face sheets, as well as the core, can be

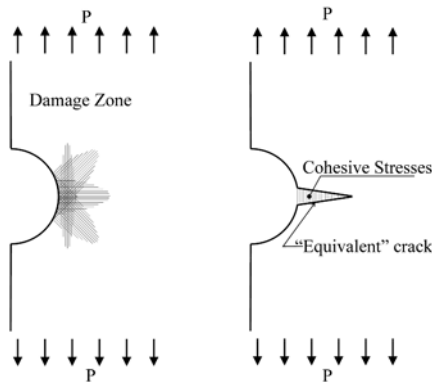


Figure 3. Composite panel (a) with a damage zone, and (b) a cohesive crack.

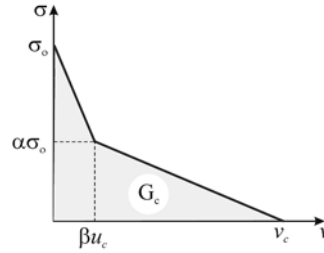


Figure 4. Bi-linear softening behavior in the damage zone.

composed of homogeneous, elastic, and orthotropic material layers. This new element based on the {3, 2}-order plate theory in conjunction with the hybrid energy functional captures the variation of displacement and stress fields in the in-plane as well as the thickness direction.

In the stress analysis of panels with a facesheet cutout or a dent, the elements are required to have a constant thickness of  $2h$ . However, they can have different stacking sequence, number of plies and ply properties. In order to include the presence of a cutout, the elements in the cutout region are assigned a layer of a “dummy” material with a stiffness value of three orders of magnitude less than that of the facesheet. Similarly for a dent, the core thickness varies depending on the location of the element, and the dent above the facesheet is filled with a “dummy” material with a stiffness value two orders of magnitude less than that of the facesheet.

### 3.2 Residual strength prediction

The Damage Zone Model introduced by Backlund (1981), and Clarin et al. (1985) and later extended by Razi et al. (1998) is employed for residual strength prediction of sandwich panels with various types of damage. Prior to failure, a Damage Zone (DZ) develops in the region of stress intensification in the facesheet as illustrated in Figure 3a. As shown in Figure 3b, DZ manifests itself as strain-softening material partially intact and still sustains loading.

DZ is replaced with a through the thickness crack while imposing cohesive stresses,  $\sigma(x)$  on the crack surfaces. Extensive DZ is represented by either reduction or removal of the cohesive stresses. The removal of the cohesive stresses represents a completely impaired damage zone leading to the creation of crack surfaces. A real crack is formed for a crack opening displacement,  $u(x)$  greater than its critical value of  $u_c$ . DZM is based on a bilinear softening

law, shown in Figure 4, and thus, a progressive failure analysis accounts for the formation and growth of the crack.

DZM requires the elastic moduli and undamaged (unnotched) strength,  $\sigma_0$  of the laminate and the bi-linear softening behavior of cohesive stress and crack opening with a break point of  $(\alpha, \beta)$  for failure prediction. As discussed by Razi et al. (1998), the damaged (notch) strength is insensitive to the value of " $\alpha$ ", i.e.,  $\alpha = 0.5$ . The characteristic length,  $L_{ch}$  related to the apparent fracture energy,  $G_c$  is dependent on the material lay-up, damage type and geometry. The characteristic length,  $L_{ch}$  is determined by performing notched strength tests for two different configurations having the same material lay-up, damage type and ratio of damage diameter to specimen width. Computing the notched strength for varying values of  $L_{ch}/W$  and  $\beta$ , and searching for  $\beta$  which gives the same value of  $L_{ch}$  for both the small and large specimen establish the value of  $\beta$ .

The implementation of DZM is achieved by first generating the finite element discretization of the facesheet having a refined mesh in the region of damage zone, and then performing sub structuring in order to minimize the computations required for each load step in the prediction of failure load. The size of the damage zone is in the order of the characteristic length,  $L_{ch}$ . In the present analysis, it is assumed that the damage zone can propagate along the full length of the panel. Also, the discretization along the damage zone, the distance between the two consecutive DZ nodes is specified by  $\Delta a = L_{ch}/10$ . The sub structuring reduces the complete stiffness matrix of the finite element model to a condensed stiffness matrix which relates only the external load and DZ nodal forces to the external displacement and DZ nodal displacements.

The load necessary to trigger the propagation of cohesive crack formation is determined by searching for an external load and displacement as well as DZ nodal forces and nodal displacements such that the stress at the "crack" tip equals the unnotched strength,  $\sigma_0$  while cohesive stresses act on the "crack" surfaces. As shown in Figure 5, failure occurs when crack growth becomes unstable accompanied by a drop in the external load. Although the material behavior is linear, the relationship between the applied load and damage zone length is nonlinear because of the softening in DZ. The resulting maximum load is taken as the ultimate load of the structure. The details of the various steps involved in the DZM are given by Clarin et al. (1985).

The DZM analysis for a panel with a cutout or slit can be readily performed once the notched strength of the sandwich panel is determined through an experiment. In the case of a panel with a dent or punch, replacing the impact zone with a cutout in order to perform the DZM analysis would result in a conservative estimate of the residual strength. Therefore, the stiffness of the material in the damaged region of a dent or puncture is reduced from that of

the undamaged material based on the extent of damage severity. In the case of a facesheet cutout or slit, the reduction in stiffness is 100%.

The reduction in stiffness of the material in the region dent is established by matching the stress concentration from the sandwich panel analysis with the actual dent geometry arising from damage severity with those of the facesheet having a material (inclusion) with degraded properties. The stiffness reduction is established by considering varying stiffness values for the inclusion. Then, the DZM is readily applied to the facesheet with an inclusion whose degree of degradation represents the dent and the puncture.

## 4. NUMERICAL RESULTS

The capability of the current analysis is demonstrated by considering sandwich panels with a facesheet cutout, slit and dent. The facesheet is composed of three plies with a stacking sequence  $[45^\circ/0^\circ/0^\circ]$  and thickness of  $h_f = 0.0498$  in. The thicknesses of the panel is  $2h = 1.0$  in. The width and length of the panel are specified as  $W = 4$  in and  $L = 12$  in. In the presence a facesheet with a dent, the indentation radius and depth are specified as  $r = 0.65$  in and  $Y = 0.042$  in, respectively. The material properties for the face sheets are specified as  $E_{xx} = E_{yy} = 6.92 \times 10^6$  psi and  $E_{zz} = 1.0 \times 10^6$  psi,  $G_{xy} = 1.77 \times 10^6$  psi and  $G_{yz} = G_{xz} = 885 \times 10^3$  psi,  $\nu_{xy} = \nu_{yz} = \nu_{xz} = 0.217$ . The unnotched strength of the laminate is  $\sigma_0 = 3.46 \times 10^4$  psi. For this material, fracture process zone is characterized by a linear softening behavior, i.e.,  $\beta = 0.5$ . The core properties are specified as  $E_{xx} = 51.0$  psi,  $E_{yy} = 26.0$  psi and  $E_{zz} = 20.0 \times 10^3$  psi,  $G_{xz} = 6.5 \times 10^3$  psi,  $G_{yz} = 3.5 \times 10^3$  psi and  $\nu_{xy} = 0.333$  and  $\nu_{yz} = 0.0$ .

### 4.1 Validation against fem with brick elements

Concerning sandwich panels with a facesheet cutout under in-plane and bending loads, the validity of the stress analysis with this new sandwich element is established by comparing against finite element predictions with conventional solid elements using ANSYS, a commercially available finite element program. The facesheet cutout has a radius of  $r = 0.65$  in. The comparison of the normalized stress,  $\sigma_{yy}$  in the direction of the applied tension load, along the center line is shown in Figure 6. The results from the current analysis are in good agreement for both in-plane and bending loads with those of ANSYS.

Concerning the sandwich panels with a dent, the comparison of the normalized stress,  $\sigma_{yy}$  in the direction of the applied load along the center line in each layer of the facesheet with a dent for both in-plane and bending loading are shown in Figures 7 and 8, respectively. The results obtained from the present analysis capture the stress concentration in the vicinity of the dent. The degree

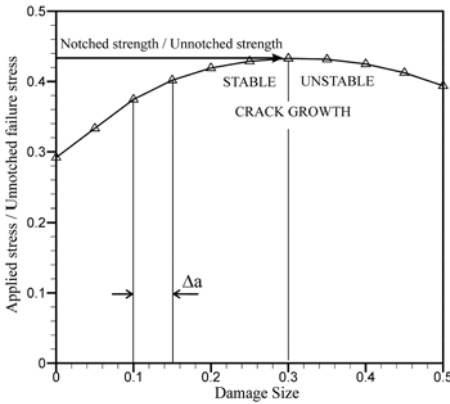


Figure 5. Failure load as the cohesive crack becomes a “real” crack.

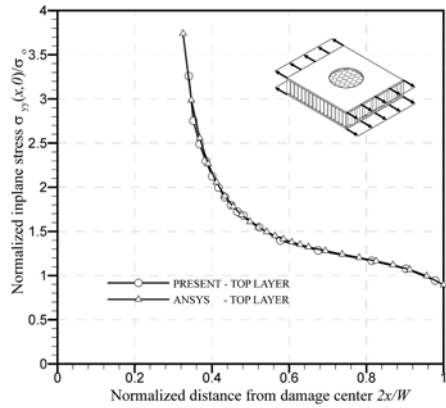


Figure 6. Sandwich panel with a facesheet cutout – in-plane loading.

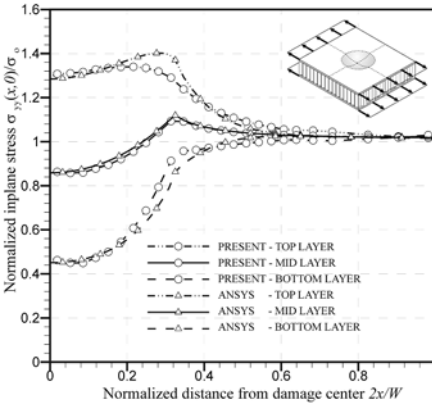


Figure 7. Sandwich panel with a dent in-plane loading.

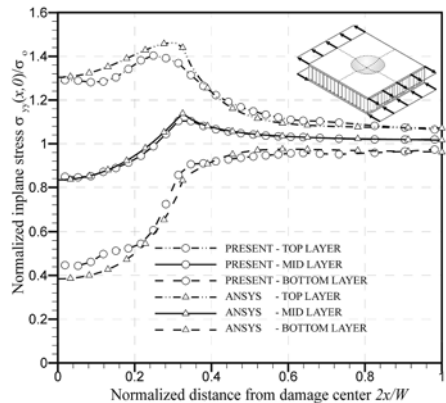


Figure 8. Sandwich panel with a dent out-of-plane bending.

of stress concentration for a panel subjected to bending is slightly higher as compared to the in-plane load.

## 4.2 Residual strength prediction

After establishing the validity of the stress analysis, the DZM analysis of a sandwich panel with a facesheet cutout under tension is performed. Utilizing one experimental data for notched strength permits the determination of the characteristic length,  $L_{ch}$ . The DZM analysis is then performed for the facesheet with a cutout as shown in Figure 9. The residual strengths for varying slit sizes are shown in Figure 10. The notched strength for a small slit width is comparable to that of the panel with a circular cutout, but as the dam-

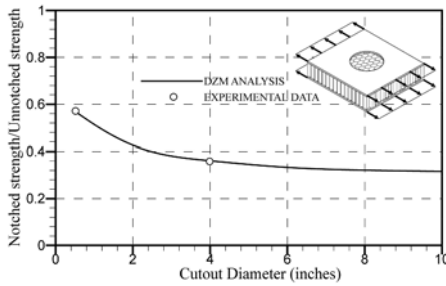


Figure 9. Residual strength of the facesheet with a circular cutout.

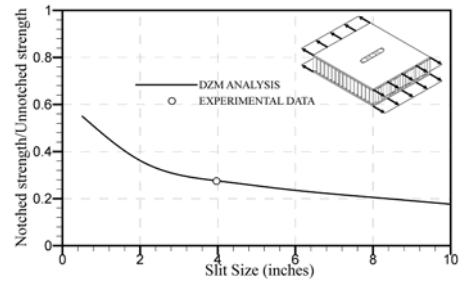


Figure 10. Residual strength of the facesheet with a slit.

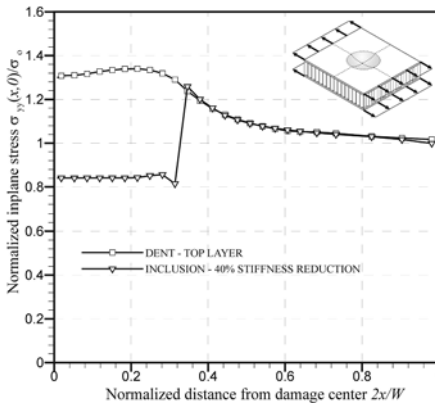


Figure 11. Stiffness reduction for the inclusion representing the dent.

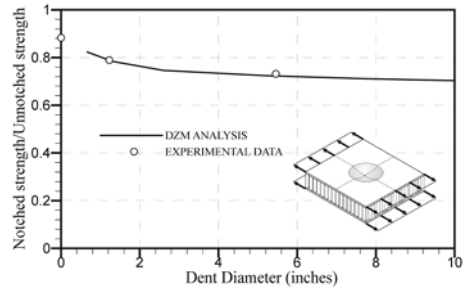


Figure 12. Residual strength of a sandwich panel with a dent.

age size increases the stress concentration for the panel with a slit increases thereby decreasing the notched strength.

As shown in Figure 11, the stiffness of the dented region (inclusion) is established by matching the stress concentration from the sandwich panel analysis with the actual dent geometry and stiffness reduction arising from damage severity with those of the facesheet having an inclusion whose degree of degradation represents the dent. After the stiffness reduction is established, then the DZM is readily applied to the facesheet with an inclusion. For increasing dent size, the residual strength prediction is shown in Figure 12.

## 5. CONCLUSIONS

In order to assist the engineers in the classification of repair type for hail strike damage, a methodology has been developed and validated against limited data. The stress analysis and the residual strength prediction are robust and credible. In order to minimize the disruption of operations, both the OEM and the airlines must be able to classify the hail strike damage for appropriate repair

procedure. With the appropriate experimental data, this approach assists the field engineer at the airlines to calculate allowable strength and damage limit, and develop a design guide for minor repair and major repair. Repair usually involves the replacement of the damaged fiber reinforcement, and core to meet regulatory requirements. Therefore, the repaired cutout and the crushed core have mechanical properties degraded from those of the undamaged materials. This approach is also capable of predicting the strength of the repaired panels.

## REFERENCES

- [1] Backlund, J., 1981, "Fracture Analysis of Notched Composites", *Computers and Structures*, pp. 145–154.
- [2] Clarin, P., Backlund, J., Hollman, K., Aronson, C-G., 1985, *FRACOM 1 – User's Manual, Version 1.0*, Department of Aeronautical Structures and Materials, The Royal Institute of Technology, Stockholm, Sweden, Report No. 85-10.
- [3] Das, M., Barut, A., Madenci, E., and Ambur, D.R., 2004, "Complete Stress Field in Sandwich Panels with a New Triangular Finite Element of Single-Layer Theory", *Computer Methods in Applied Mechanics and Engineering* (in press).
- [4] Das, M., Guven, I. and Madenci, E., 2004, "Three-Dimensional Analysis of Sandwich Panels with Common Defects", 45rd AIAA/ASME/ASCE/AHS/ASC Structures, Structural Dynamics, and Materials Conference, Palm Springs, California, Paper No. 2004-1840.
- [5] Razi, H., Ward, S.H. and Bickford, M.D., 1998, "Strength Prediction of Notched Thin-Skin Honeycomb Sandwich Structures", *Proceedings, Fourth International Conference on Sandwich Construction*, Stockholm, Sweden, EMAS Publishing, West Midlands, UK, pp. 784–807.
- [6] Razi, H., Ward, S.H. and Bickford, M.D., 1998, "Strength Prediction of Notched Thin-Skin Honeycomb Sandwich Structures", *Proceedings, Fourth International Conference on Sandwich Construction*, Stockholm, Sweden, EMAS Publishing, West Midlands, UK, pp. 784–807.
- [7] Razi, H., Sergeev, B., Shkarayev, S. and Madenci, E., 1999, "Analysis of Sandwich Panels with Multiple-Site Damage", *Engineering Fracture Mechanics*, Vol. 64, pp. 255–268.
- [8] Razi, H., 2000, "Residual Strength of Thin-Gage Honeycomb Sandwich Panels with Impact Damage at multiple Sites", *Proceedings, Fifth International Conference on Sandwich Construction*, Zurich, Switzerland, EMAS Publishing, West Midlands, UK, pp. 629–642.

# DAMAGE TOLERANCE ASSESSMENT OF REPAIRED COMPOSITE SANDWICH STRUCTURES

Richard Trask, Bob Cripps and Ajit Shenoj

<sup>1</sup>*Department of Aerospace Engineering, University of Bristol, Queen's Building, University Walk, Bristol BS8 1TR, UK*

<sup>2</sup>*Royal National Lifeboat Institution, West Quay Road, Poole, Dorset BH15 1HZ, UK*

<sup>3</sup>*School of Engineering Sciences, University of Southampton, Highfield, Southampton SO17 1BJ, UK*

**Abstract** Polymer sandwich configuration is now extensively used in many engineering structural applications such as ships, boats, spacecraft and aircraft. The design and manufacturing aspects of such materials are well known and regulations and codes exist to help designers, producers and operators of such artifacts. However, maintenance and repair are issues that have received relatively little attention. The aim of the research is to understand the influence of BVID upon structural repairs made to advanced composite sandwich structures and to determine whether a tapered scarf repair is as damage resistant and damage tolerant as the original structure.

**Keywords:** damage tolerance, repair, BVID.

## 1. INTRODUCTION

The design and manufacture of structural repairs to marine composite sandwich structures is now considered as a standard process. Existing designs are often employed assuming the structural continuity of the bonded interface remains through the operational life of the repair and that the manufacturing process has sufficient control to eliminate all forms of processing defects. However, in reality, the nature of composite materials (separate fibres and liquid resin), and the methods used to produce

composite repairs are prone to manufacturing defects. Furthermore, repairs in marine structures tend to be undertaken near to the waterline, which is precisely the region where a repeated impact event of a similar or greater impact energy may occur. These observations suggest that operational vessel may be operating with damaged or defective repairs.

Whilst on operational duty the hull of an advanced composite marine craft may be damaged, thus requiring a repair to be made to restore the structural efficiency of the sandwich structure. The main cause of operational damage to composite structures is impact damage [1]. Impact damage can be classified as either low or high velocity. Low velocity impact events are often referred to impact events in the range 1 to 10 ms<sup>-1</sup> where the contact period is such that the whole structure has time to respond to the loading [2]. In a high velocity impact event a stress wave is generated which propagates through the material. The time frame in this event is so fast that the structure is unable to respond to the stress wave resulting in very localised damage. Marine craft are often subjected to repeated light docking collisions and collisions with floating debris and other vessels (see Figure 1 for examples of operational damage experienced by marine rescue craft). Aerospace structures suffer impact damage from runway debris and accidental impact damage during routine maintenance periods. These types of impact events can be considered as low velocity events.

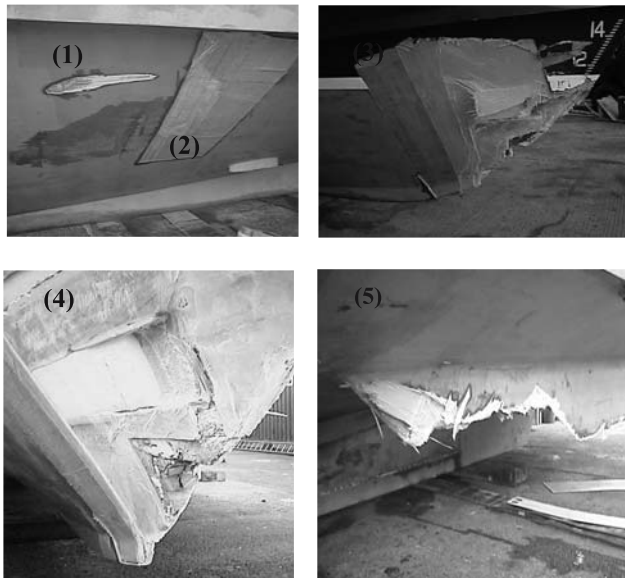


Figure 1. Photographic evidence of operation impact damage to marine composite sandwich structures.

The damage identified in Figure 1 has been characterized as follows:

1. The wearing away of a portion of the laminate by either natural (rain, wind, etc.) or man-made (over-blasting, slight collision). Damage confined to the outer skin surface of the sandwich structure.
2. Localised surface indentation, damage confined to outer laminate skin. Matrix cracking, fibre breakage likely to occur.
3. Moderate impact damage greater than the damage initiation threshold for core crushing (permanent deformation) initiating debonding in face/core interface
4. Extended surface indentation resulting from significant impact damage, often associated with witness marks from the impactor and delamination damage. Penetration of outer skin, matrix cracking, delamination, fibre fracture, damage to core material and debond in face/core interface
5. External forces exceed the fibre tensile strength or the compressive strength of the matrix material resulting in the complete failure of the skin. Failure may have occurred from an impact penetration or overload of structure.

The aim of this paper is to present some aspects of a comprehensive study on the performance of repaired sandwich structures [3] with a view to understand the influence of BVID upon structural repairs made to advanced composite sandwich structures and to determine whether a tapered scarf repair is as damage resistant and damage tolerant as the original structure.

## **2. DAMAGE TOLERANCE PHILOSOPHY FOR DAMAGE SANDWICH STRUCTURES**

In sandwich structures the question of damage resistance and damage tolerance is of critical concern since the inability of designers to predict the critical damage modes often leads to conservative designs with large factors-of-safety.

At present the research into composite damage tolerance is still relatively new. In essence this is due to the extent of information required to generate a damage tolerance philosophy, i.e. the philosophy depends upon a comprehensive knowledge of the composite structure, the operational loads, knowledge of the starting defects and the defects formed during operation, identification of the critical defect types, the advantages and disadvantages of standard non-destructive techniques (NDT), the determination of NDT inspection frequencies and theoretical and experimental methods to predict damage growth rates.

To illustrate the magnitude of the task of generating damage tolerance philosophy for composite sandwich structures lets consider impact damage to the face laminate generating barely visible impact damage (BVID) – see point 2 in Figure 1. This form of BVID damage could result in delamination damage within the laminate skin. The magnitude of the induced damage depends upon a multitude of factors including the outer skin lay-up configuration and thickness, core material and thickness, interface properties between the outer skin and the core, fabrication techniques, impact velocity and energy, indenter shape, boundary conditions, and environmental factors, i.e. temperature and sea state. Damage initiation thresholds as well as the damage size depend on the properties of the core material and the relationship between the properties of the core material to those of the facings. To assess all these material property variations requires a clear understanding of the material-structure-damage interaction characteristics.

Although only delamination damage in the laminate skin has been considered in the example above, in composite sandwich structures a range of defect types could be the critical defect, i.e. delamination within the outer skin, debonding within the skin and core interface, core-crushing arising from impact damage or core shear cracks due to fatigue. In theory, each of these defects could occur within the operational life of the composite sandwich structure, and therefore a damage tolerance philosophy would be required for each of these critical defect types.

Some initial insight into the development of this interaction can be gained from examination of the damage tolerance approaches applied to composite laminates [4-7]. Although research in this area has been ongoing since 1985, the question of whether a structural repair in a composite laminate, or a composite sandwich structure, is as damage resistant and damage tolerant as the original structure still has to be considered.

### **3. REPAIR PHILOSOPHY FOR DAMAGED SANDWICH STRUCTURES**

The repair philosophy for damaged sandwich structures greatly depends upon the particular component and the extent of the damage incurred, e.g. a sandwich panel with one or both skins punctured. Since composite structures are employed in different industries with different design philosophies, current repair concepts include a wide range of approaches from highly refined and structurally efficient but expensive flush patch repairs to externally mechanically attached metal or composite patch [8]. Two of the most common repair approaches for composite structures, the tapered scarf flush repair and an externally bonded patch have been presented in Figure 2.

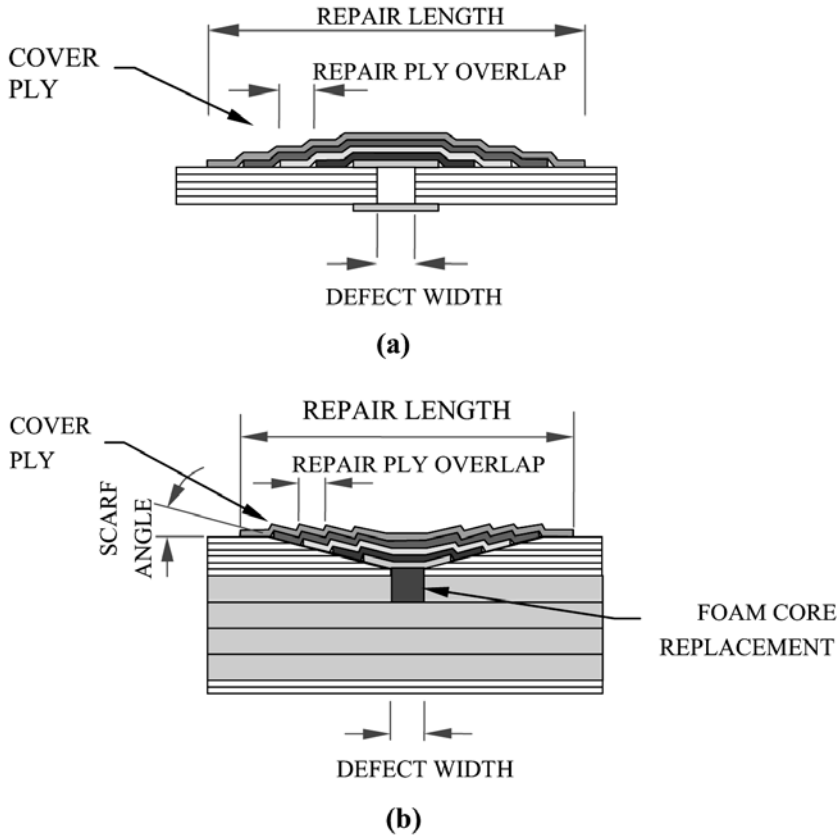


Figure 2. Repair design options (a) external patch [9], (b) tapered scarf repair [10].

In general, any form of structural repair will necessitate the removal and reinstatement of the damaged material. In these repairs it is assumed that all the damage has been removed and none introduced through the action of undertaking the repair. By comparison, temporary repairs are often undertaken with patches bonded directly over the damaged area, i.e. external repair with the damage remaining insitu.

The design of composite repairs is based upon the minimization of shear stresses between the repair and the parent structure through maximization of the bonded area. The design of external patches, and the protective overlaminates/cover ply for the scarf repair, is based upon the minimization of the transverse tensile stresses, achieved through the maximization of the bonded transfer length. Any form of manufacturing defect or operational damage affecting these parameters could result in the repair being overloaded resulting in premature failure during operational service.

#### 4. DAMAGE TOLERANCE ASSESSMENT OF REPAIRED SANDWICH STRUCTURES

To determine the damage tolerance performance of a structural repair to an advanced composite sandwich structure, the impact response of structural repair must be known, i.e. how the damage forms within a repair, whether the damage is critical or what effect it has on the structural integrity. Furthermore, characterization of the impact damage tolerance, the initiation and propagation of critical defects, and the assessment of the residual strength must be undertaken. A damage tolerant flow chart for a tapered scarf repair is given in Figure 3.

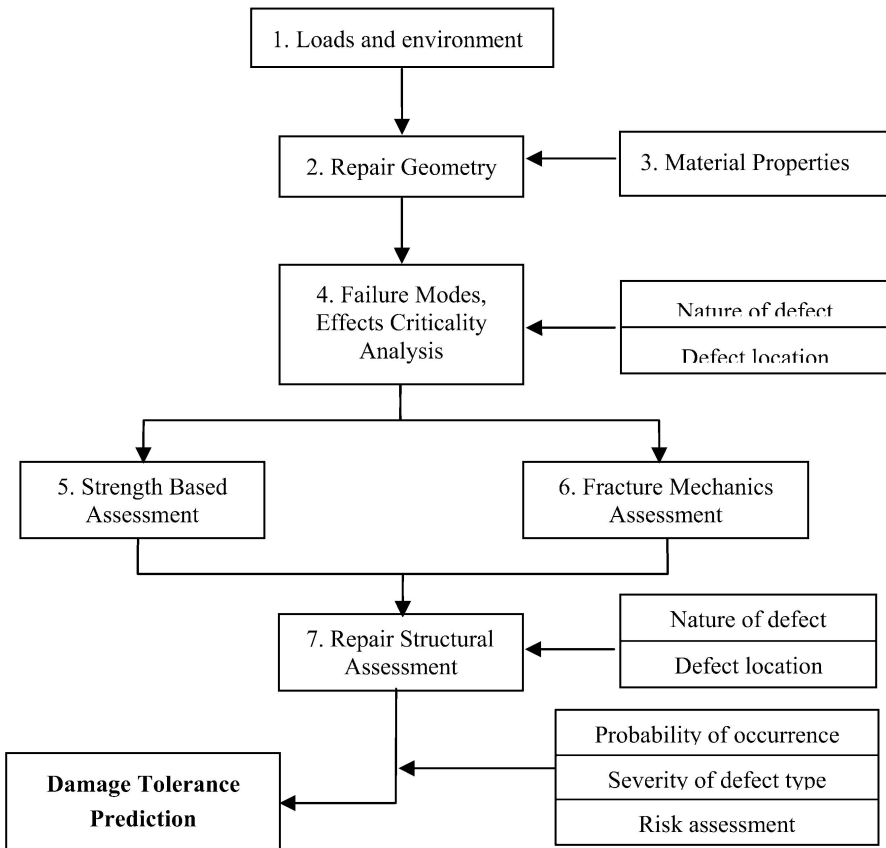


Figure 3. Flow chart design methodology for the damage tolerance assessment of repaired composite sandwich structures.

The methodology outlined within this figure requires a database of background knowledge about the environmental loads, the proposed repair geometry and key material properties before the strength based and fracture mechanics based assessments can be undertaken.

In this paper the failure mode, effects and criticality analysis (identified as box 4 in Figure 3) and the influence the repair geometry (box 3 in Figure 3) on the nature of the defect will be discussed. The remaining information in support of the damage tolerance flowchart will be presented at forthcoming conferences and through technical publications.

A standard 3-degree tapered scarf repair, currently employed by the Royal National Lifeboat Institution (RNLI) in the repair of its composite rescue craft was subjected to different impact energies at two different locations, namely the start of the tapered interface and the end of the overlaminates. Impact tests were undertaken using a simple vertical drop weight frame with the option to vary the impact energy by changing the drop height, the weight of impactor, and the size of impactor was devised and used to conduct the low velocity impact tests. The design was very similar to the rig used in [11]. A range of impact energies were used to determine the onset of damage within the two different repair joint configurations, namely the start of the tapered interface and at the end of the overlaminates. The damage area formation as a function of the impact energy for the pristine laminate (i.e. no repair present), the tapered scarf impact location and the overlaminates impact location has been presented in Figure 4.

The result in Figure 4 illustrates that a composite sandwich beam containing a 3° scarf taper repair is less damage tolerant to a 50mm wide flat-nosed impactor than the original laminate. The results illustrate that the threshold energy to initiate failure along the scarf taper is comparable with the 'pristine' beam in both cases. However, the damage area measurements revealed that the magnitude of the damage between the un-repaired and repaired beams is comparable at the end of the overlaminates impact location, whilst the damage area is almost doubled at the tapered scarf impact location. At the start of the tapered interface, it has been observed that the bonded replacement core has considerable influence upon the way the damage manifests itself within the repair, i.e. the vertical column of adhesive disintegrates under the impact load thereby prompting a rapid increase of damage at the leading edge of the scarf taper repair (see Figure 5a).

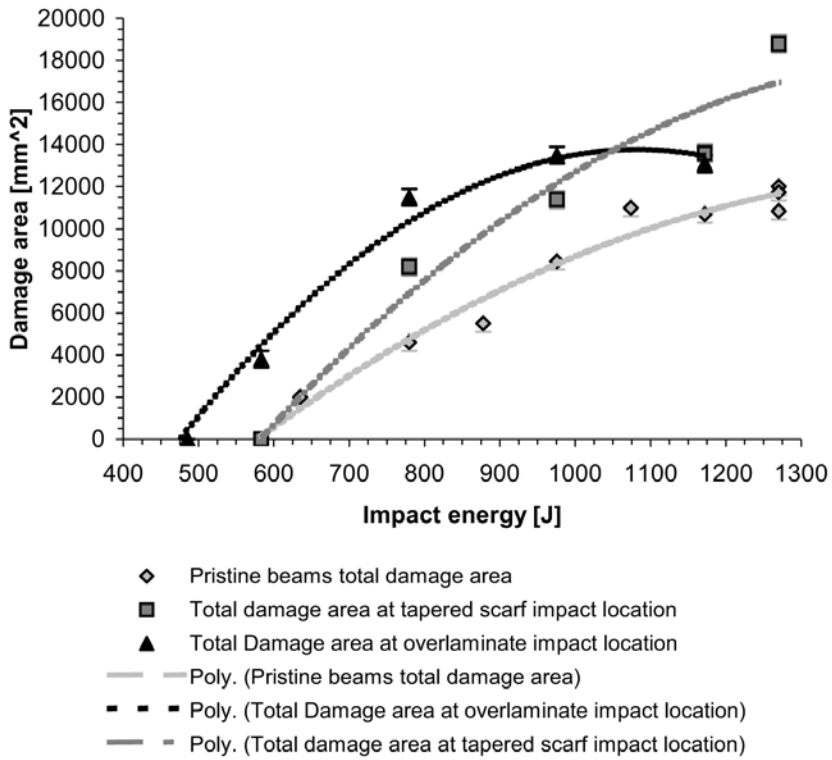


Figure 4. Relationship between average delamination area and impact energy for 3° tapered scarf repair and pristine beams.

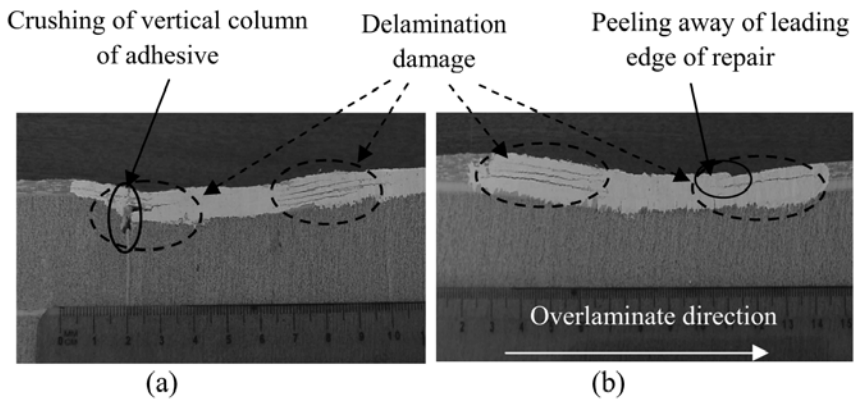


Figure 5. (a) BVID impact on the scarf taper interface of a tapered scarf structural repair, (b) BVID impact on the overlamine of tapered scarf repair structural repair.

At the overlamine impact location, a damage threshold was observed for the leading edge of the repair to start ‘peeling’ away from the original parent laminate (this is shown in Figure 5b). This observation is critically since the design rules for bonded joints proposed by Hart-Smith [10] aims to reduce the tensile transverse stresses in the adhesive and the shear stress concentrations at the ends of the joint to maximise the durability of the repair scheme. However, if an impact energy threshold exists for the initiation of a ‘peel’ crack at the repair edge then the current repair design for the minimisation of peel stresses is inappropriate for repairs in regions of high impact probability.

## **5. CONCLUSIONS**

The purpose of this paper has been to introduce the starting blocks for the formation of a damage tolerance design tool for structural repairs to marine sandwich structures.

The research undertaken within this project has uniquely characterises the damage tolerance performance of a tapered scarf structural repair, in a composite sandwich structure, in relation to barely visible impact damage. In particular, the focus has been to characterise of the damage formation and impact damage tolerance threshold for two critical defects.

This research indicates (1) the damage formation in a composite repair is greater than in a pristine beam for the same corresponding energy level (2) the susceptibility of the internal edge of the tapered repair to damage formation causing a reduction in available repair area to transmit the loads resulting in a potential increase in shear stress at the bonded interface, and (3) an impact event at the end of the overlamine may be sufficient to overcome the tensile transverse stresses of the repair resin and cause failure of the patch/parent laminate interface. The result from this research indicates the need to update the repair design guidelines originally developed in the 1970s for repairs in regions of high impact probability.

## **ACKNOWLEDGMENTS**

The authors wish to kindly acknowledge the financial support of the Royal National Lifeboat Institution throughout the duration of this project.

## REFERENCES

1. Zhou G. 'Prediction of impact damage thresholds of glass fibre reinforced laminates', *Composite Structures*, **31**, pp 185-193, 1995.
2. Pavier M. and Clarke M., 'Experimental Techniques for the investigation of the effects of impact damage on carbon-fibre composites', *Composites Science and Technology*, **55**, pp157-169, 1995.
3. Trask, R.S. 'Damage Tolerance of Repaired Composite sandwich Structures', PhD Thesis, University of Southampton, 2004.
4. Baker, A.A., Jones, R. and Callinan, R.J. 'Damage tolerance of graphite/epoxy composites', *Composite Structures*, **4**, pp15-44, 1985.
5. Zhou G. 'The use of experimentally-determined impact force as a damage measure in impact damage resistance and tolerance of composite structures', *Composite Structures*, **42**, pp375-382, 1998.
6. Tomblin J., Lacy T., Smith B., Hooper S., Vizzini A. and Lee S., 'Review of damage tolerance for composite sandwich airframe structures', DOT/FAA/AR-99/49, 1999.
7. Irving P.E., 'Achievement of damage tolerant designs in metal and composite aircraft structures', IMechE conference on 'In-service structural integrity, NDE and repair', 30<sup>th</sup> May 2002, BAWA, Bristol, UK.
8. Schwan F.J. 'Design of Structure with Composites' in Handbook of Composites 2<sup>nd</sup> Ed, ed. Peters S.T., Chapman & Hall, 1998.
9. Davis M. and Bond D. 'Principles and practices of adhesive bonded structural joints and repairs', *Int. J. Adhesion & Adhesives*, **19**, pp91-105, 1999.
10. Hart-Smith, L.J. 'Adhesive bonded scarf and stepped-lap joints', *NASA CR-112237*, January 1973.
11. Mines R.A.W., Worrall C.M. and Gibson A.G. 'The static and impact behaviour of polymer composite sandwich beams', *Composite*, **25** (2), pp 95-110, 1994.

# **DYNAMICS, VIBRATION AND SOUND**

# DYNAMICAL TRANSIENT RESPONSE OF SHALLOW SANDWICH PANEL SUBJECTED TO PRESSURE FIELD

Sergey Kadyrov and Vitalij Skvortsov

*State Marine University of St. Petersburg, Lotsmanskaya str. #3, St. Petersburg 19008, Russia*

**Abstract** Dynamical transient behavior of a shallow sandwich panel subjected to impulsive pressure load is studied. Governing equations and boundary conditions are derived from the Hamiltonian of this mechanical system. The problem is solved by the use of finite difference (FD) technique, which is illustrated by an example

**Keywords:** sandwich panel, Hamilton principle, transient dynamics, numerical solution.

## 1. INTRODUCTION

There are many publications devoted to construction of theories of sandwich plates (see, for example, [1–3]), but the problem of modeling the transient dynamics of sandwich plates and shells is still actual. Apparently, the variational principle is a natural tool of deriving dynamical equations. In this paper, the system of partial differential equations for generalized forces and relations between generalized forces and five generalized displacements (three components of a displacement vector and field of shear angles in a core) is derived. This system is linear, but some of its coefficients are not constant and they are defined by the curvature tensor of the panel. Direct finite difference (FD) numerical modeling perhaps is the only reliable way to explore time history in details.

## 2. GOVERNING EQUATIONS AND BOUNDARY CONDITIONS OF DYNAMICS OF SHALLOW SANDWICH PANEL

### 2.1 Basic assumptions

The shell is considered as being shallow. Assuming the mid-surface of a sandwich core as a reference, we shall use in-plane Cartesian coordinates

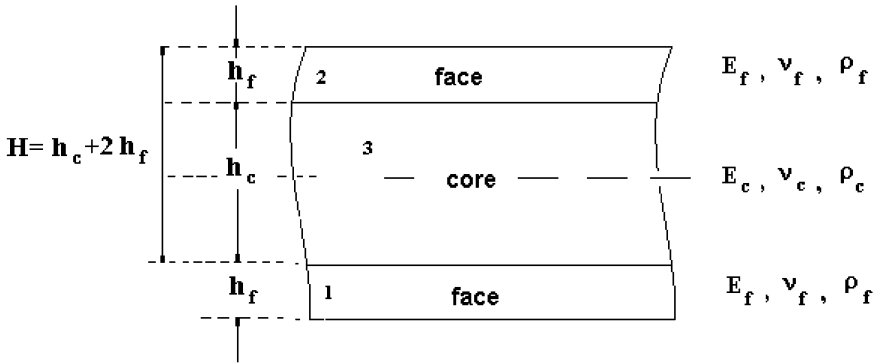


Figure 1. Notations for sandwich panel.

$x_1, x_2$ . The coordinate coincides with the direction of a normal vector. All notations for geometrical and physical parameters of the sandwich core and faces (supposed to be identical) are shown in Figure 1.

Accordingly to so-called third-order shear model [3] a certain distribution of three-dimensional displacements  $u_i^{3D}(x_1, x_2, z)$ ,  $w^{3d}(x_1, x_2, z)$  are adopted, namely

$$\begin{aligned} u_i^{3D}(x_1, x_2, z, t) &= u_i(x_1, x_2, t) + f_a(z)\theta_i(x_1, x_2, t) - f_b(z)w_{,i} \\ w^{3D}(x_1, x_2, z, t) &= w(x_1, x_2, t) \end{aligned} \tag{1}$$

(hereafter derivatives of a function  $f(x_1, x_2, z, t)$  will be demoted as  $f_{,1}, f_{,2}, f_{,z}, \dot{f}$ , respectively). Here

$$\begin{aligned} f_a(z) &= \begin{cases} \pm H/2, h_c/2 < |z| \leq h_c/2 + h_f \\ zH/h_c, |z| \leq h_c/2 \end{cases} \\ f_b(z) &= z - f_a(z) \end{aligned} \tag{2}$$

are the shape functions  $u_i(x_1, x_2, t), i = 1, 2$  are tangential displacements in the mid-surface and  $w(x_1, x_2, t)$  is the normal displacement (the same in all cross-section). To clarify the geometrical meaning of parameters  $\theta_1, \theta_2$ , let's find transversal shear strains inside the core ( $|z| < h_c/2$ ):

$$\varepsilon_{iz}^3 = u_{i,z}^{3D} + w_{,i} = \frac{H}{h_c}(\theta_i + w_{,i}). \tag{3}$$

Thus,  $\theta_i$  is the angle of rotation of the normal due to shear in the core relative to axis  $x_i$ .

The tangential strains are

$$e_{ij} = \frac{1}{2}(u_{i,j}^{3D} + u_{j,i}^{3D}) - k_{ij} w, \tag{4}$$

where  $k_{ij}$  are initial curvatures of the panel. Substituting (4) into (3) we finally get

$$\begin{aligned} \varepsilon &= e_{ij} + f_a \alpha_{ij} - f_b \chi_{ij} - k_{ij} w \\ e_{ij} &= \frac{1}{2}(u_{i,j} + u_{j,i}) - k_{ij} w, \alpha_{ij} = \frac{1}{2}(\theta_{i,j} + \theta_{j,i}), \chi_{ij} = w_{,ij}. \end{aligned}$$

Variational equation equivalent to Hamilton principle applied for an arbitrary part of the panel bounded by lines  $x_1 = 0, x_1 = X_1, x_2 = 0, x_1 = X_2$  in the time interval  $(t_1, t_2)$  has a form

$$\int_{t_1}^{t_2} \int_0^{X_1} \int_0^{X_2} (\delta W - \delta T + \delta A) dx_1 dx_2 dt = 0$$

The terms under the integral and  $\delta$  signs are:

$W$  – the potential energy (the strain energy) of a sandwich panel,

$T$  – the kinetic energy of a sandwich panel,

$\delta A$  – the work exerted by an external surface load,

(hereafter all variables are referred to an unit volume).

If  $\sigma_{ij}^m$  are the tangential components of a stress tensor inside the faces ( $m = 1, 2$ ) and the core ( $m = 3$ ), and  $\sigma_{iz}^3$  are the shear stresses inside the core, then variation of the potential energy at any instant of time is equal

$$\delta W = \int_{1+2+3} \sum_{m=1}^3 \sum_{i,j=1}^2 \sigma_{ij}^m \delta \varepsilon_{ij} dz + \int_2 \sum_{i=1}^2 \sigma_{iz}^3 \delta \varepsilon_{iz}^3 dz. \quad (5)$$

In the framework of the present model (see formulae (3) and (5), the material of the core is considered as incompressible, shear stresses inside the core are distributed uniformly and they are negligible outside the core. Using shape functions, formula (5) may be rewritten as

$$\delta W = \sum_{i,j=1}^2 T_{ij} \delta e_{ij} + \sum_{i,j=1}^2 M_{ij} \delta \chi_{ij} + \sum_{i,j=1}^2 H_{ij} \delta \alpha_{ij} + \sum_{i=1}^2 Q_i \delta (\theta_i + w_{,i}). \quad (6)$$

In formula (8) some internal generalized forces are introduced:

$$T_{ij} = \sum_{m=1}^3 T_{ij}^m = \sum_{m=1}^3 \int_m \sigma_{ij}^m dz \quad \text{longitudinal force,}$$

$$M_{ij} = \sum_{m=1}^3 M_{ij}^m = - \sum_{m=1}^3 \int_m f_b \sigma_{ij}^m dz \quad \text{bending moments,}$$

$$H_{ij} = \sum_{m=1}^3 H_{ij}^m = \sum_{m=1}^3 \int_m f_a \sigma_{ij}^m dz \quad \text{torques,}$$

$$Q_i = \int_m \frac{H}{h_c} \sigma_{iz}^3 dz \quad \text{shear forces due to shear effects into the core.}$$

The kinetic energy of a sandwich panel at any instant of time is equal to

$$T(x_1, x_2, z, t) = \frac{1}{2} \rho^{3D} \left[ (\dot{u}_1^{3D})^2 + (\dot{u}_2^{3D})^2 + (\dot{w})^2 \right], \quad (7)$$

where  $\rho^{3D}(x_1, x_2, z)$  is a density of the sandwich panel material. The work of an external surface load is equal to

$$A(x_1, x_2, t) = p_1 u_1 + p_2 u_2 + q w. \quad (8)$$

## 2.2 Governing equations

Standard algebraic transformations of (5)-(8) yield the system of equations for dynamics of a shallow sandwich panel:

$$\left\{ \begin{array}{l} T_{11,1} + T_{12,2} = \rho \ddot{u}_1 - p_1, \quad T_{12,1} + T_{22,2} = \rho \ddot{u}_2 - p_2 \\ F_{1,1} + F_{2,2} - (T_{11} k_{11} + T_{22} k_{22} + 2T_{12} k_{12}) = \rho \ddot{w} + q \\ H_{11,1} + H_{12,2} - Q_1 + j_{ab} \ddot{w}_{,1} - j_a \ddot{\theta}_1 = 0 \\ H_{12,1} + H_{22,2} - Q_2 + j_{ab} \ddot{w}_{,2} - j_b \ddot{\theta}_2 = 0 \\ F_1 = M_{11,1} + M_{12,1} + Q_1 + j_b \ddot{w}_{,1} - j_{ab} \ddot{\theta}_1 \\ F_2 = M_{12,1} + M_{22,2} + Q_2 + j_b \ddot{w}_{,2} - j_{ab} \ddot{\theta}_2 \end{array} \right. \quad (9)$$

In these formulas some averaged inertial parameters obtained by integrating along axis  $z$  are used

$$\rho = 2\rho_f h_f + \rho_c h_c, \quad j_a = \frac{\rho_f h_f H^2}{2} + \frac{\rho_c h_c H^2}{12},$$

$$j_b = \frac{\rho_f h_f^3}{2} + \frac{\rho_c h_c h_f^2}{12}, \quad j_{ab} = -\frac{\rho_f \rho_c h_c h_f}{12}.$$

Equations (9) have to be complemented by boundary conditions, which may be derived from the same variational equation. For example, displacements  $w, u_1, u_2$  and angle  $w_{,1}$  should be specified at the boundary  $x_2 = const$  if the edge is constrained. Alternatively (if the edge is free), moments  $M_{22}, H_{22}, H_{12}$  and generalized force  $Q_2$  should be known. It is important that the last two equations in (9) are valid not only inside the volume of a plate, but also at all its boundaries.

Now it is necessary to express internal forces and moments in terms of displacements and their derivatives. Using Hook’s law and definitions of internal forces and moments, one can derive

$$\begin{aligned}
 T_{ij} &= B[(u_{i,j} + k_{ii}w) + \nu_b(u_{j,i} + k_{jj}w)], \quad i = 1, 2 \\
 T_{12} &= B \frac{1 - \nu_b}{2}(u_{1,2} + u_{2,1} + 2k_{12}w), \\
 M_{ii} &= -D_b(w_{,ii} + \nu_b w_{,jj}), \quad i = 1, 2, \quad M_{12} = -D_{ab} \frac{1 - \nu_b}{2} w_{,12}, \\
 H_{ii} &= D_a \frac{1 - \nu_a}{2}(\theta_{i,j} + \theta_{j,i}), \quad i = 1, 2, \quad H_{12} = D_a \frac{1 - \nu_a}{2}(\theta_{1,2} + \theta_{2,1}), \\
 Q_i &= S(\theta_i + w_{,i}), \quad i = 1, 2.
 \end{aligned}$$

Averaged stiffness and Poisson ratio in these formulas are derived by integration along axis  $z$ :

$$\begin{aligned}
 B &= 2 \frac{E_f h_f}{1 - \nu_f^2} + \frac{E_c h_c}{1 - \nu_c^2}, \quad B\nu_b = 2 \frac{E_f \nu_f h_f}{1 - \nu_f^2} + \frac{E_c \nu_c h_c}{1 - \nu_c^2}, \quad S = \frac{E_c H^2}{(1 + \nu_c)h_c}, \\
 D_a &= \frac{E_f h_f H^2}{2(1 - \nu_f^2)} + \frac{E_c h_c H^2}{12(1 - \nu_c^2)}, \quad D\nu_a = \frac{E_f \nu_f h_f H^2}{2(1 - \nu_f^2)} + \frac{E_c \nu_c h_c H^2}{12(1 - \nu_c^2)}, \\
 D_b &= \frac{E_f h_f^3}{6(1 - \nu_f^2)} + \frac{E_c h_c h_f^2}{12(1 - \nu_c^2)}, \quad D\nu_b = \frac{E_f \nu_f h_f^3}{6(1 - \nu_f^2)} + \frac{E_c \nu_c h_c h_f^2}{12(1 - \nu_c^2)}.
 \end{aligned}$$

### 3. FINITE DIFFERENCE METHOD

#### 3.1 FD equations and some features of the numerical procedure

FD equations may be deduced by the traditional way replacing all the derivatives by their finite differences analogies. FD grid is characterized by the mesh widths  $h_1, h_2, \tau$ , so  $h_1 = X_1/(N - 1), h_2 = X_2/(M - 1), t = \tau n$ . The analysis of equations (9) shows that a FD system cannot be constructed as an explicit one because functions  $F_1, F_2$  are obviously linked with the derivatives “containing” information about the numerical solution at the next time step. By the use of equations (9), it is possible to exclude  $\theta_1, \theta_2$  and to work out the system

$$\begin{cases}
 F_1 + \frac{j_a j_b - j_{ab}^2}{j_a} C \ddot{w}_{,1} = M_{11,1} + M_{12,1} + Q_1 - \frac{j_{ab}}{j_a}(H_{11,1} + H_{12,2} - Q_1) \\
 F_2 + \frac{j_a j_b - j_{ab}^2}{j_a} \ddot{w}_{,2} = M_{12,1} + M_{22,2} + Q_2 - \frac{j_{ab}}{j_a}(H_{12,1} + H_{22,2} - Q_2) \\
 F_{1,1} + F_{2,2} - \rho \ddot{w} = q - (T_{11}k_{11} + T_{22}k_{22} + 2T_{12}k_{12})
 \end{cases}$$

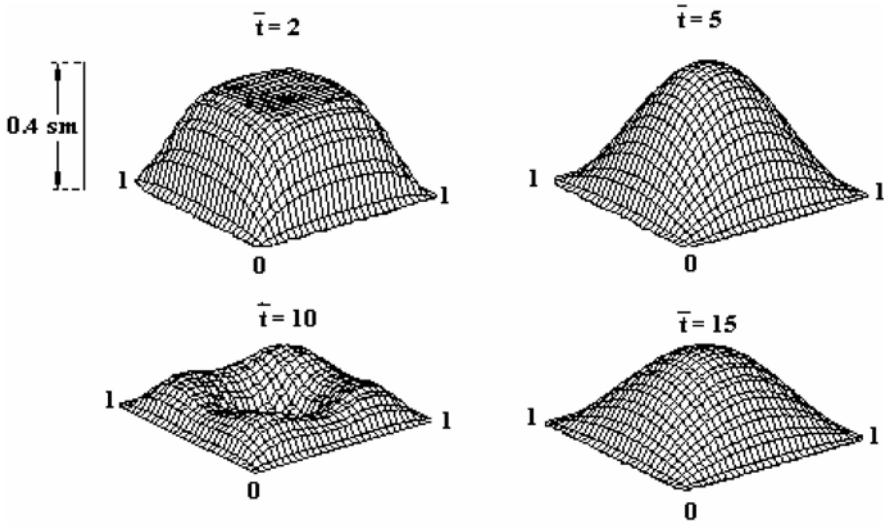


Figure 2. Time history of displacement  $w(x_1, x_2, \bar{t})$ .

Here all variables calculated at the next time step are transferred to the left hand side. FD analogs of these equations is a SLAE of order  $N \cdot M \cdot 3$  with respect to magnitudes of  $F_1, F_2, w$  at the next time step. The inversion of the matrix can be performed only once. Then from FD analogs of stayed equations numerical values of  $u_1, u_2, \theta_1, \theta_2$  at the next time step may be solved explicitly. It should be noted that the numerical realization of proposed scheme is rather inconvenient, so let us consider particular cases when some simplifications are possible. The simplest one is the formulation for a clamped panel when boundary values of the generalized forces may be found directly from equations (9). Then system in consideration may be reduced to two FD equations with respect to  $F_1, F_2$  and explicit FD equation for displacement  $w$ , so the order of SLAE in this case is  $2 \cdot N \cdot M$ . It appears that if Poisson ratio of the materials of a core and of faces may be assumed to be the same, boundary values of the forces  $F_1, F_2$  also may be found at the free edge directly from equation (9). This permits one to reduce the order of governing SLAE to  $2 \cdot N \cdot M$ .

### 3.2 A numerical example

Let us consider the response of the clamped cylindrical panel (a radius of curvature along the axis  $x_1 = X_1/10$ ) of a square in-plane shape ( $X_1 = X_2 = 1\text{m}$ ) to the uniformly distributed pressure of  $P = 1\text{MPa}$ . The parameters of sandwich panel composition are  $E_f = 20\text{ GPa}, E_c = 2\text{ GPa}, \rho_f = 800\text{ kg/m}^3, \rho_c = 100\text{ kg/m}^3, h_f = 5\text{ mm}, h_c = 50\text{ mm}, \nu_f = \nu_c = 0.3$ .

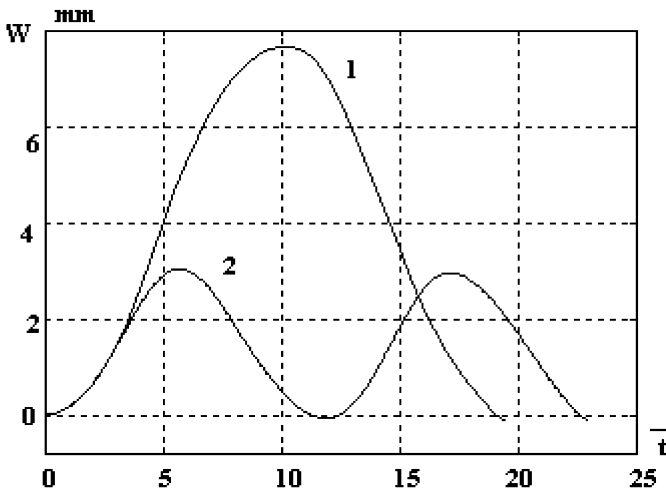


Figure 3. Time history for (1: 1-D theory [4], 2: present theory).

Time history of displacement  $w(x_1, x_2, \bar{t})$  is shown in Figure 2. Here  $\bar{t} = (E_f/\rho)^{0.5}t/X_1$  is a non-dimensional time. To verify the computations it is possible to compare these results with the ones obtained in [5] by the use of a model of the curved sandwich beam. A comparison of the displacement at the central point  $W(\bar{t})$  for the panel and for a curved beam of a unit width is illustrated in Figure 3.

#### 4. CONCLUSIONS

The system of partial differential equations for dynamic behavior of a sandwich panel is derived from the Hamilton principle. This system is linear, but some coefficients are variable in in-plane coordinates and they are defined by the initial curvature tensor of a panel.

A direct FD technique is suggested as a tool to explore transient dynamical response of a structure to the impulse loading. This numerical method gives the possibility to estimate the roles of various parameters (geometrical and physical, the kinds of constraints and so on) in different excitation conditions and different boundary conditions. The suggested method can readily be extended to capture the non-linear effects.

#### REFERENCES

[1] Grigoliuk, E.I. and Chulkov, P.P., *A Theory of Multilayered Plates*, Moscow, Nauka, Russia (in Russian), 1975.

- [2] Zenkert, D., *An Introduction to Sandwich Construction*, Cameleon Press, London, United Kingdom, 1995.
- [3] Skvortsov, V.R., “Symmetrically inhomogeneous through thickness plate as a sandwich plate having a soft core”, in *Transactions of Academy of Sciences of USSR Mechanics of a Rigid Body*, 1993, No. 1, pp. 162–168 (in Russian)
- [4] Kadyrov, S., A 2-d model of the interaction between a pressure wave and a submerged sandwich panel, in *Proceedings of the UITAM Symposium on Diffraction and Scattering in Fluid Mechanics and Elasticity*, Manchester, 2000, pp. 269–283.

# EFFECT OF TRANSVERSE CORE COMPRESSIBILITY ON DYNAMIC BUCKLING OF SANDWICH STRUCTURES

Jörg Hohe

*Fraunhofer Institut für Werkstoffmechanik, Wöhlerstr. 11, 79108 Freiburg, Germany*

joerg.hohe@iwf.fraunhofer.de

Liviu Librescu and Sang Yong Oh

*Virginia Polytechnic Institute and State University, Department of Engineering Science  
and Mechanics, Blacksburg, VA, 24061, USA*

librescu@vt.edu, sangyong@vt.edu

**Abstract** The present study is concerned with the analysis of the transient response of soft-core sandwich structures in the postbuckling range using a higher-order geometrically nonlinear shell model including the transverse core compressibility. The transverse compressibility results in the development of a chaotic vibration with unpredictable wrinkling amplitudes and has significant effects on the eigenfrequency.

**Keywords:** transient loading, overall buckling, face wrinkling, chaotic vibration.

## 1. INTRODUCTION

Standard structural sandwich panels are consisting of three principal layers, two stiff high-density face sheets which are adhesively bonded to a thick core layer which is in general made from a soft low-density material. Due to the thick core layer consisting of a soft material, local face wrinkling instabilities might develop.

It has been shown by Frostig et al. [3, 4] that the development of the face wrinkling instability can have distinct effects on the overall static response of soft core sandwich structures. Especially, interactions of the local wrinkling and the overall buckling modes have to be expected due to the geometrically nonlinear nature of the buckling phenomenon. Other studies on combined local and overall buckling of structural sandwich panels under quasi-static loading

conditions have been provided by Starlinger and Rammerstorfer [10], da Silva and Santos [1], Wadee and Hunt [11] as well as in recent contributions by the present authors [5, 6].

On the other hand, only few contributions are available concerning the dynamic buckling of sandwich structures, such as the work of Dube et al. [2] and Nayak et al. [9] on the transient response of sandwich structures should be mentioned. Maekinen [8] as well as Xue and Hutchinson [12] considered the response of sandwich structures subjected to blast and shock wave loading.

The present study is concerned with the effect of the transverse compressibility on the transient dynamic response of soft core sandwich structures, which has not been included in the previous contributions. The study utilizes a multilayer, v. Kármán type nonlinear sandwich shell theory, which is based on the standard Kirchhoff–Love hypothesis for the face sheets and a higher order expansion for the core displacements [5]. Consistent equations of motion and boundary conditions are derived by means of Hamilton’s principle. The transient dynamic problem is solved using an extended Galerkin procedure in conjunction with a fourth order Runge–Kutta scheme for time integration. The algorithm is applied to the dynamic response of plane and doubly curved sandwich structures under rapidly applied tangential edge loads and transverse pressure loads. In the case of combined face wrinkling and overall buckling, chaotic local vibrations with unpredictable amplitudes may occur.

## 2. HIGHER-ORDER SANDWICH SHELL THEORY

Consider a sandwich structure according to Figure 1. The structure is assumed to be symmetric with respect with respect to the global midsurface which forms the reference surface. The thicknesses of the face sheets and the core are denoted by  $t^f$  and  $t^c$  respectively whereas  $r_\alpha$  with  $\alpha = 1, 2$  are the radii of curvature. Since the face sheets are assumed to be thin, the Kirchhoff–Love hypothesis is adopted. In this case, the three dimensional displacements  $v_i^t$  and  $v_i^b$  can be expressed by

$$v_\alpha^t = u_\alpha^a + u_\alpha^d - \left( x_3 + \frac{1}{2}(t^c + t^f) \right) u_{3,\alpha}^a - \left( x_3 + \frac{1}{2}(t^c + t^f) \right) u_{3,\alpha}^d \quad (1)$$

$$v_3^t = u_3^a + u_3^d \quad (2)$$

$$v_\alpha^b = u_\alpha^a - u_\alpha^d - \left( x_3 - \frac{1}{2}(t^c + t^f) \right) u_{3,\alpha}^a + \left( x_3 - \frac{1}{2}(t^c + t^f) \right) u_{3,\alpha}^d \quad (3)$$

$$v_3^b = u_3^a - u_3^d \quad (4)$$

in terms of the displacement functions

$$u_i^a = \frac{1}{2}(u_i^t + u_i^b) \quad (5)$$

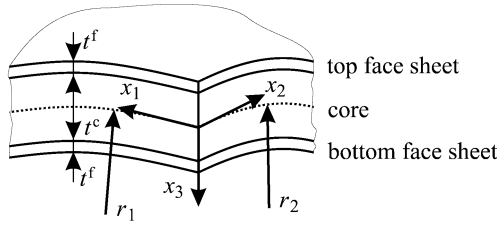


Figure 1. Structural sandwich panel.

$$u_i^d = \frac{1}{2}(u_i^t - u_i^b) \tag{6}$$

defined as the average and the half difference of the face sheet’s individual mid-surface displacements. As usual in tensorial index notation, the abbreviation  $(\dots)_{,i} = \partial(\dots)/\partial x_i$  is adopted. For the core displacement field, a second order power series expansion

$$v_\alpha^c = u_\alpha^a - \frac{t^f}{2}u_{3,\alpha}^d - \frac{2x_3}{t^c}u_\alpha^d + \frac{t^f}{t^c}x_3u_{3,\alpha}^a + \left(\frac{4(x_3)^2}{(t^c)^2} - 1\right)\Omega_\alpha^c \tag{7}$$

$$v_3^c = u_3^a - \frac{2x_3}{t^c}u_3^d \tag{8}$$

is adopted, where the displacement functions  $\Omega_\alpha^c$  describe the warping of the core.

From the power series expansion of the face sheet and core displacements, the deformation of the three individual layers are expressed in terms of the components

$$\gamma_{ij} = \frac{1}{2}(u_{i|j} + u_{j|i} + u_{k|i}u_{k|j}) \tag{9}$$

of the Green–Lagrange strain tensor and adopting the principles of shallow shell theory. In Equation (9), the notation  $(\dots)_{|i}$  indicates the covariant derivative with respect to  $x_i$ , taking the curvature of non-plane structure into account. In the v. Kármán sense, only the nonlinear terms with respect to the transverse ( $x_3$ -) direction are kept whereas all other nonlinear terms are discarded.

Consistent equations of motion and boundary conditions are derived from Hamilton’s principle

$$\int_{t^0}^{t^1} (\delta U - \delta W - \delta T) dt = 0 \tag{10}$$

where  $\delta U$ ,  $\delta W$  and  $\delta T$  are the variations of the strain energy, of the work done by the external loads and of the kinetic energy, respectively, in case of a virtual displacement  $\delta u_i^a$  and  $\delta u_i^d$  of the sandwich structure during the time interval

$[t^0, t^1]$ . Substitution of the strain and displacement components in terms of the displacement functions  $u_i^t$  and  $u_i^b$  and integration by parts wherever feasible yields a single homogeneous equation for the virtual displacements  $\delta u_i^t$  and  $\delta u_i^b$  as well as the virtual rotations  $\delta u_{3,\alpha}^t$  and  $\delta u_{3,\alpha}^b$ . Since the virtual displacements and rotations are arbitrary an independent, the corresponding coefficients must vanish independently. From the area integrals in the resulting expression, the nonlinear equations of motion

$$0 = N_{\alpha\beta,\beta}^a \tag{11}$$

$$0 = N_{\alpha\beta,\beta}^d + N_{\alpha 3}^c/t^c \tag{12}$$

$$0 = M_{\alpha\beta,\alpha\beta}^a + (u_{3,\alpha\beta}^a + \overset{\circ}{u}_{3,\alpha\beta}^a)N_{\alpha\beta}^a + (u_{3,11}^d + \overset{\circ}{u}_{3,11}^d)N_{11}^d + N_{11}^a/r_1 + N_{22}^a/r_2 + ((t^c + t^f)/2 - u_3^d - \overset{\circ}{u}_3^d)N_{\alpha 3,\alpha}^c/t^c - 2(u_{3,\alpha}^d + \overset{\circ}{u}_{3,\alpha}^d)N_{\alpha 3}^c/h^c + \hat{q}_3^a - (m^f + m^c/2)\ddot{u}_3^a \tag{13}$$

$$0 = M_{\alpha\beta,\alpha\beta}^d + (u_{3,\alpha\beta}^a + \overset{\circ}{u}_{3,\alpha\beta}^a)N_{\alpha\beta}^d + (u_{3,\alpha\beta}^d + \overset{\circ}{u}_{3,\alpha\beta}^d)N_{\alpha\beta}^a + N_{11}^d/r_1 + N_{22}^d/r_2 + 2(t^c/2 - u_3^d - \overset{\circ}{u}_3^d)N_{33}^c/t^c + \hat{q}_3^d - (m^f + m^c/6)\ddot{u}_3^d \tag{14}$$

are obtained where  $\overset{\circ}{u}_3^a$  and  $\overset{\circ}{u}_3^d$  are prescribed initial geometric imperfections,  $m^f$  and  $m^c$  are the integrated mass densities of the face sheets and the core respectively whereas  $\hat{q}_3$  denotes the prescribed transverse distributed load. The tangential and bending stress resultants are defined by

$$\{N_{\alpha\beta}^b, M_{\alpha\beta}^b\} = \int_{\frac{1}{2}t^c}^{t^f + \frac{1}{2}t^c} \tau_{\alpha\beta}^t \left\{ 1, x_3 - \frac{1}{2}(t^c + t^f) \right\} dx_3 \tag{15}$$

$$\{N_{i3}^c, M_{i3}^c\} = \int_{-\frac{1}{2}t^c}^{\frac{1}{2}t^c} \tau_{i3}^t \{1, x_3\} dx_3 \tag{16}$$

$$\{N_{\alpha\beta}^t, M_{\alpha\beta}^t\} = \int_{-t^f - \frac{1}{2}t^c}^{-\frac{1}{2}t^c} \tau_{\alpha\beta}^t \left\{ 1, x_3 + \frac{1}{2}(t^c + t^f) \right\} dx_3 \tag{17}$$

where  $\tau_{ij}$  are the components of the second Piola–Kirchhoff stress tensor. Similar to the face sheet displacement functions (5) and (6), average and difference stress resultants  $N_{\alpha\beta}^a$  and  $M_{\alpha\beta}^a$  are introduced for the face sheets. Full details are given in a previous paper by the present authors [5, 6].

### 3. SOLUTION PROCEDURE FOR DYNAMIC PROBLEMS

The sandwich shell theory outlined in the previous section is applied to the dynamic analysis of sandwich plates and shells with rectangular projection

where all three principal layers consist of orthotropic linear elastic materials. The structures are assumed to be simply supported along all four edges. Within the  $x_1$ - $x_2$ -surface, the edges can either be movable or may be restrained with respect to their tangential displacements. Under these conditions, an appropriate assumption for the transverse displacements is given by

$$u_3^a = w_{mn}^a \sin(\lambda_m^a x_1) \sin(\mu_n^a x_2), \quad \lambda_m^a = \frac{m\pi}{l_1}, \quad \mu_n^a = \frac{n\pi}{l_2} \quad (18)$$

$$u_3^d = w_{pq}^d \sin(\lambda_p^d x_1) \sin(\mu_q^d x_2), \quad \lambda_p^d = \frac{p\pi}{l_1}, \quad \mu_q^d = \frac{q\pi}{l_2} \quad (19)$$

where  $l_1$  and  $l_2$  are the tangential dimensions of the panel. The symbols  $m, n, p$  and  $q$  are the number of modal waves with respect to the  $x_1$ - and  $x_2$ -directions for the global instability and the face wrinkling instability respectively. The modal amplitudes  $w_{mn}^a$  and  $w_{pq}^d$  of both instability modes remain to be determined.

For the initial geometric imperfections  $\overset{\circ}{u}_3^a$  and  $\overset{\circ}{u}_3^d$ , a similar assumption with the same wave numbers but constant prescribed modal amplitudes  $\overset{\circ}{w}_{mn}^a$  and  $\overset{\circ}{w}_{pq}^d$  is made. A consistent solution for the corresponding tangential displacements  $u_\alpha^a$  and  $u_\alpha^d$  can be obtained from the first two equations of motion together with the material equations (see [5] for details). The solution for  $u_i^a$  and  $u_i^d$  satisfies the first two equations of motion as well as the essential boundary conditions exactly whereas the non essential boundary conditions are satisfied in an integral average sense.

The remaining unknowns  $w_{mn}^a$  and  $w_{pq}^d$  are determined numerically using an extended Galerkin procedure. Substituting the assumption for the transverse displacements together with the consistent solution for the tangential displacements into Hamilton's principle yields a single homogeneous equation for the virtual modal amplitudes  $\delta w_{mn}^a$  and  $\delta w_{pq}^d$ . Since the virtual displacements are arbitrary and independent, the corresponding coefficients must vanish independently, resulting in a coupled system of two equations for the two remaining unknowns. The system has the structure

$$\ddot{w}_{mn}^a(t) = \sum_{i=0}^3 \sum_{j=0}^3 C_{ij}^a(t) (w_{mn}^a(t))^i (w_{pq}^d(t))^j \quad (20)$$

$$\ddot{w}_{pq}^d(t) = \sum_{i=0}^3 \sum_{j=0}^3 C_{ij}^d(t) (w_{mn}^a(t))^i (w_{pq}^d(t))^j \quad (21)$$

where  $t$  denotes the time. The coefficients  $C_{ij}^a(t)$  and  $C_{ij}^d(t)$  are lengthy expressions depending on the material properties, on the panel geometry as well as on the prescribed load history. The initial value problem is solved numerically

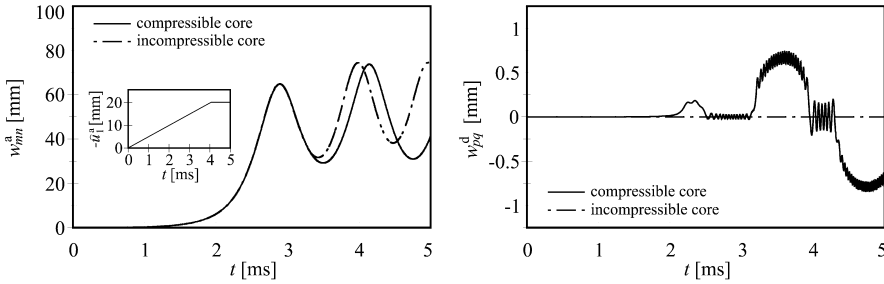


Figure 2. Amplitudes for overall and face wrinkling instability.

using an explicit fourth-order variable step Runge–Kutta scheme. Full details on the solution procedure will be presented in a forthcoming paper [7].

#### 4. RESULTS

As a first example, the sandwich shell model presented in Section 2 together with the solution procedure presented in Section 3 is applied to the transient dynamic analysis of a square sandwich plate with  $l_1 = l_2 = 500$  mm and  $r_1 = r_2 = \infty$  which is simply supported along all four external edges. The thicknesses of the core and the face sheets are  $t^c = 1$  mm and  $t^f = 18$  mm respectively. The face sheets are assumed to consist of isotropic aluminum with  $E^f = 70$  GPa,  $\nu^f = 0.3$  and  $\rho^f = 3700$  kg/m<sup>3</sup> whereas a weak low density material with  $E^c = 0.7$  GPa,  $\nu^c = 0.3$  and  $\rho^c = 37$  kg/m<sup>3</sup> is assumed for the core.

The structure is loaded by a rapidly applied tangential edge deflection of the  $x_2$ -parallel edge which is increased linearly from zero level towards a final value of  $\hat{u}_1 = -20$  mm during a time interval of  $\Delta t = 4$  ms. Throughout the loading history, the opposite edge is kept fixed whereas the remaining edges are freely movable within the tangential directions. Initially, the structure is assumed to be in an equilibrium state with vanishing velocities. In this context, overall and local buckling modes with  $m = n = q = 1$  and  $p = 55$  are assumed, involving the lowest amount of strain energy in the corresponding static buckling problem. In order to regularize the bifurcation behavior, non-vanishing initial geometric imperfections are applied for both, the overall as well as the local mode.

The results for the modal amplitudes  $w_{mn}^a$  and  $w_{pq}^d$  of the overall instability and the local face wrinkling mode respectively are presented in Figure 2. Results for a classical sandwich plate model with a transversely incompressible core are added for comparison. Overall dynamic buckling occurs from  $t \approx 1.5$  ms onwards, when a non-vanishing modal deflection  $w_{mn}^a$  develops, which oscillates around the transverse deflection in the corresponding static load case. A face wrinkling instability with non-vanishing deflection  $w_{pq}^d$  is

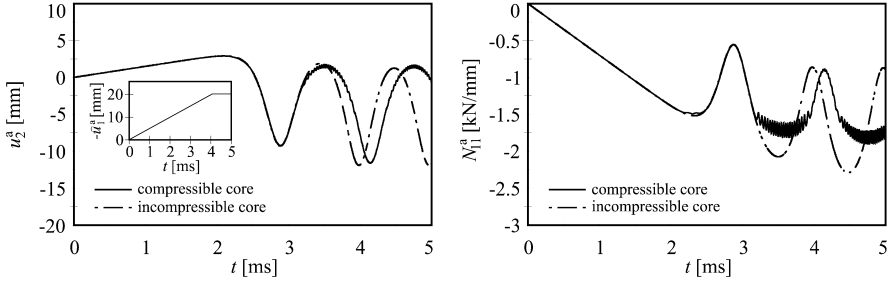


Figure 3. Resulting perpendicular edge deflection and resulting edge load.

first observed at  $t \approx 2$  ms, vanishes at  $t \approx 2.4$  ms with a local vibration remaining and re-develops during the period from  $t \approx 3.1$  ms till  $t \approx 3.9$  ms. From the time of the first development of the face wrinkling mode onwards, increasing differences between the results based on the current higher-order sandwich model with transversely compressible core and the results based on the classical model with transversely incompressible core are observed even in terms of the overall deflection  $w_{mn}^a$ . In this context, both, the amplitude of the overall vibration as well as the generalized eigenfrequency of this nonlinear vibration are affected.

The reason for the distinct effect of the transverse core compressibility on the overall response of the structure can be explained from the resulting edge load  $N_{11}^a$  presented in the second plot of Figure 3. During the first period of the loading history, the structure remains stable with a monotonic increase in the resulting edge load. Once the static buckling load for the overall instability mode ( $N_{11}^a \approx 1$  kN/mm) is reached, an oscillating transverse deformation  $w_{mn}^a$  and thus an oscillating resulting edge load  $N_{11}^a$  develops. During the high-compression periods of this vibration at low transverse deflections  $w_{mn}^a$  (at  $t \approx 3.5$  ms, 4.8 ms,  $\dots$ , see Figure 2), the buckling load for the face wrinkling instability is exceeded, resulting in the temporary development of a local deflection  $w_{pq}^d$ . Since the presence of face wrinkling weakens the structure with respect to its tangential stiffness, the oscillation of the resulting tangential edge load  $N_{11}^a$  is cut off during the high-compression periods. This weakening of the structure results in a decreasing generalized eigenfrequency compared to the classical model based on the assumption of a transversely incompressible core.

As it can be observed in the first plot of Figure 3 featuring the tangential deflection  $u_2^a$  of the edges perpendicular to the loaded edge, the resulting nonlinear vibration is not sinusoidal. Furthermore, the resulting vibration is of chaotic nature, as it can be observed in the second plot of Figure 2. During the low-compression periods, when the buckling load for the face wrinkling instability is not exceeded and therefore no face wrinkling occurs except a re-

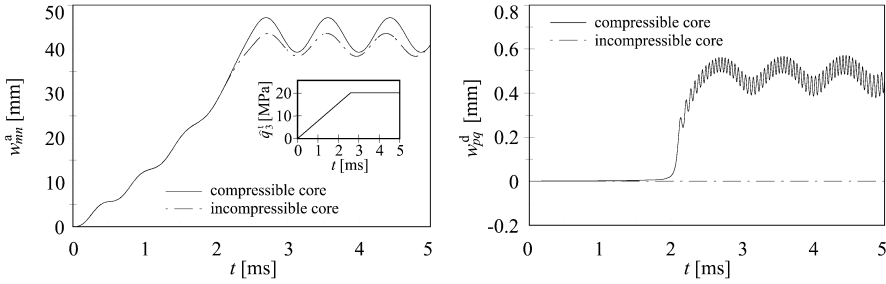


Figure 4. Amplitudes for overall and face wrinkling instability.

maining vibration around  $w_{pq}^d = 0$ . The amplitude of this vibration is different for each individual low-compression period since it depends on the initial conditions at the beginning of this period. In a similar manner, the amplitudes of the local vibration during the high-compression periods will be different in each individual oscillation cycle (although this is not the case for the first two full cycles in Figure 2). Due to the nonlinear nature of the buckling phenomena, the overall and the local vibration do exchange energy resulting in the observed chaotic behavior with unpredictable amplitudes and thus unpredictable local stresses at later stages of the vibration.

As a second example, the problem of a spherical sandwich cap under a rapidly applied transverse pressure load is considered. The structure is identical to the previously considered plate except that non-zero curvatures are assumed and that the core thickness is increased to  $t^c = 23$  mm resulting in an overall panel thickness of 25 mm. The radii of curvature are  $r_1 = r_2 = 500$  mm. The transverse load is increased from zero level to  $\hat{q}_3^t = 20$  MPa during the first 2.5 ms of the load history and is kept constant afterwards. The buckling mode is the same as in the first example except that the number of modal half waves for the face wrinkling instability reduces to  $p = 50$  due to the increased core thickness resulting in decreased wrinkling resistance. The structure is simply supported along all four external edges which are assumed to be immovable with respect to the tangential directions.

The time dependent amplitudes of the overall transverse deflection and the face wrinkling deformation for this problem are presented in Figure 4. Similar as in the analysis of the plane sandwich structure, it is observed that the transverse compressibility of the core has distinct effects even in the overall response of the structure. Again, both the generalized eigenfrequency of the nonlinear vibration induced by the rapid loading process as well as the amplitude of this vibration are affected. In the present case, the weakening of the structure due to the development of a face wrinkling instability mode from  $t \approx 2$  ms onwards results in a decrease of the compressive stiffness of the struc-

ture. The decrease in the stiffness results in an additional acceleration and an increase in the amplitude of the free nonlinear vibration following the loading process at  $t \geq 2.5$  ms. Since the additional acceleration due to the development of the face wrinkling mode is suppressed by the neglect of the transverse core compressibility in the classical model, the classical sandwich shell theories with incompressible core would underestimate the amplitude of the resulting vibration.

## **5. CONCLUSION**

The present study is concerned with the effect of the transverse core compressibility of structural sandwich panels under dynamic loading conditions. The effect is investigated analytically utilizing a higher-order, effective multilayer sandwich model derived previously by the authors. The model is based on the Kirchhoff–Love hypothesis for the face sheets whereas a third-order displacement expansion is employed for the core. Consistent equations of motion are derived by means of Hamilton’s principle. An analytical solution is obtained by means of an extended Galerkin procedure in conjunction with a variable step Runge–Kutta scheme of the fourth order to solve the time-dependent dynamic problem.

The model is applied to a dynamic buckling and postbuckling analysis of sandwich structures subject to rapid loading conditions. In a comparison with results based on a standard, transversely incompressible sandwich model, it is observed that the transverse compressibility has a distinct effect on the dynamic structural response. Since the transverse compressibility of the core enables the development of a face wrinkling instability mode, a model including this effect yields lower resulting in-plane edge loads, if the structure is loaded by prescribed time dependent edge displacements and the buckling load for development of the face wrinkling instability is exceeded. Due to the lower resulting in-plane loads, lower generalized eigenfrequencies are obtained in the analysis of the nonlinear vibration problem. Thus, the classical, transversely incompressible sandwich models might be inadequate to model the dynamic response of sandwich structures in the postbuckling regime.

Due to the nonlinear nature of the buckling phenomenon, the overall vibration of the sandwich structure and the local face wrinkling vibration can exchange energy. Therefore, a dynamic response of the chaotic type results, leading to vibrations with unpredictable amplitudes and thus unpredictable local stresses.

## **ACKNOWLEDGEMENT**

This work has been financially supported by the Office of Naval Research under grant no. N00014-02-1-0594. The financial support and the interest and

encouragement of the grant monitor, Dr. Y.D.S. Rajapakse, are gratefully acknowledged.

## REFERENCES

- [1] L.A.P.S. da Silva and J.M.C. Santos. Localised formulations for thick “sandwich” laminated and composite structures. *Computational Mechanics* 22:211-224, 1998.
- [2] G.P. Dube, P.C. Dumir and A. Mallick. Dynamic buckling of laminated thick shallow spherical cap based on a static analysis. *Mechanics Research Communications* 27:561-566, 2000.
- [3] Y. Frostig. Buckling of sandwich panels with a flexible core—high-order theory. *International Journal of Solids and Structures* 35:183-204, 1998.
- [4] Y. Frostig, M. Baruch, O. Vilnay and I. Sheiman. High-order buckling theory for sandwich-beam behavior with transversely flexible core. *Journal of Engineering Mechanics* 118:1026-1043, 1992.
- [5] J. Hohe and L. Librescu. A nonlinear theory for doubly curved anisotropic sandwich shells with transversely compressible core. *International Journal of Solids and Structures*, 40:1059–1088, 2003.
- [6] J. Hohe and L. Librescu. Core and face sheet anisotropy in deformation and buckling of sandwich panels. *AIAA Journal*, 42:149-158, 2004.
- [7] J. Hohe, L. Librescu and S.Y. Oh. Dynamic buckling of flat and curved sandwich panels with transversely compressible core. *Composite Structures*, in press.
- [8] K. Maekinen. The transverse response of sandwich panels to an underwater shock wave. *Journal of Fluids and Structures* 13:631-646, 1999.
- [9] A.K. Nayak, R.A. Shenoi and S.S.J. Moy. Transient response of composite sandwich plates. *Composite Structures* 64:249-267, 2004.
- [10] A. Starlinger and F.G. Rammerstorfer. A finite element formulation for sandwich shells accounting for local failure phenomena. In: D. Weissman-Berman and K.A. Olsson (eds.). *Sandwich Construction 2*. Proc. 2<sup>nd</sup> Int. Conf. Sandwich Constructions (Gainesville, FL, USA, March 09-12 1992). EMAS Publishing, London 1992, 161-179.
- [11] M.A. Wadee and G.W. Hunt. Interactively induced localized buckling in sandwich structures with core orthotropy. *Journal of Applied Mechanics* 65:523-528, 1998.
- [12] Z. Xue and J.W. Hutchinson. Preliminary assessment of sandwich plates subject to blast loads. *International Journal of the Mechanical Sciences* 45:687-705, 2003.

# DYNAMIC CHARACTERISATION OF MARINE SANDWICH STRUCTURES

Mark Battley<sup>1</sup>, Ivan Stenius<sup>2</sup>, Johan Breder<sup>2</sup> and Susan Edinger<sup>3</sup>

<sup>1</sup>*Industrial Research Ltd., P.O. Box 2225 Auckland, New Zealand*

<sup>2</sup>*Royal Institute of Technology, KTH, Naval Systems, SE-100 44 Stockholm, Sweden*

<sup>3</sup>*High Modulus (NZ) Ltd., P.O. Box 302-191, NHMC, Auckland, New Zealand*

**Abstract** Dynamic experimental and theoretical methods for sandwich panel structures subjected to water slamming are described, including a unique servo-hydraulic controlled slam test system and a pressure based transient finite element technique. The pressure simulation method accurately represents the pressures observed in slamming tests, and the transient dynamic finite element modelling can simulate sandwich panel responses to a slamming load.

**Keywords:** dynamic, marine, slamming, testing, finite element analysis.

## 1. INTRODUCTION

Sandwich structures are widely used within the marine industry, particularly as hull panels. The usual design approach is to treat them as being subjected to a uniformly distributed static pressure whose magnitude is given by empirical formulae. In reality the water pressure acting on most hull structures is neither uniformly distributed nor static. In particular, slamming events typically generate high magnitude pressure pulses of very short duration that move across the panel as the hull enters the water.

Some marine scantling authorities allow the use of so-called “direct calculation” methods, where tools such as finite element analysis (FEA) can be used for design. Using these tools for a dynamic load case such as slamming poses significant challenges for the designer, both in defining realistic load cases, and accurately and efficiently analysing the dynamic response of the panel. This paper addresses these problems by focusing on testing and analysis methods for slam loaded sandwich panels, including:

- Dynamic panel testing with a unique servo-hydraulic controlled system.
- Prediction of slam induced pressure loads.
- Transient FEA methods for predicting panel structural responses.
- Correlating measured and predicted pressures and panel responses.
- Comparisons of dynamic panel responses to static panel behaviour.

## **2. SANDWICH PANEL TESTING METHODS**

Marine sandwich composites are commonly characterised by testing pseudo-statically loaded four point sandwich beams. These tests provide an indication of their stiffness and strength, but do not accurately represent the distributed pressure loadings and high loading rates experienced in service by marine vessels. DNV specifies a high speed version of four point bending beam tests in their High Speed Light Craft Rule [1]. Compared to pseudo-static testing, results of such tests show significant increases in strength and stiffness for some core materials [2].

Previous experimental measurements of slamming events have been performed on actual vessels, by using “drop tests” where a specimen is dropped from a defined height onto the water surface, and also by using scale models in towing tanks. Many drop tests have used rigid models to investigate the resulting pressure distributions, such as those by Chuang [3], who performed experiments on slamming of wedge-shaped bodies, and Wraith [4], who performed drop test on rigid V-shaped, single and double curved specimens. Drop tests using non-rigid panels include those by Hayman et al. [5], Katsaounis and Samuelides [6], and Faltinsen [7].

The main drawback of drop tests is that there is no direct control of the specimen motion once it hits the water, the retardation rate primarily being dependent on the mass of the specimen and fixtures. In reality the velocity profile during a slamming event depends on the overall behavior of the vessel and the position of the panel. A panel near to the keel may have a nearly constant velocity throughout the slamming event, whereas one near the dynamic waterline of the boat will have a velocity that approaches zero at the end of the slamming event. In the case of real vessels, instrumentation is often limited by restricted access to the hull skin, and by the need to destructively modify the panels for some measurements such as pressure and core strains. It is also difficult to reproduce particular conditions in real vessel testing due to the large number of variables present. To address these limitations a Servo-hydraulic Slam Testing System (SSTS) has been developed at Industrial Research Limited.

The SSTS, shown in Figures 1 and 2, uses a custom designed computer controlled high speed servo-hydraulic system to control the motion of a panel during water impact. The system can be programmed to have a constant velocity throughout the slam event, or to follow a changing velocity profile. This enables measured or predicted motions for real vessels to be reproduced in a laboratory where comprehensive instrumentation can be used in a repeatable situation. The SSTS has also been used for both dynamic material characterization [2] and for measurement of dynamic pressure distributions as part of research in fluid/structure dynamic analysis and design methods [8].



*Figure 1.* From left to right: Overview showing the tank and instrumentation system, Specimen and specimen fixture inside the tank, Sketch showing the ram (1), load cell (2), specimen fixture (3), panel (4), side plates (5), back plate (6).



*Figure 2.* Slamming impact in the SSTS.

The cylindrical water tank has a diameter of 3.5 m and a water depth of typically 1.5 m. The specimen fixture slides on vertical rails and is attached to the hydraulic ram through a load cell. Hydraulic accumulators supply oil to the ram, and the velocity is determined by a servo-valve controlled by a closed-loop controller using position and acceleration feedback. Vertical panels on the sides and behind the panel constrain the flow to 2D behaviour. The ram has a stroke of 1.4m, of which approximately 0.4m is traveled in air prior to impact, up to 0.5m during the impact event, and a further 0.5m to stop. The SSTS can achieve velocities of up to 10 m/s.

The specimen fixture is made primarily of carbon fibre/epoxy foam core sandwich composites and can be adjusted to deadrise angles of 0, 10, 20, 30 and 40°. The panel has simply supported edges and a nominal size of 500mm by 1000mm. Other size specimens can be fitted with appropriate support fixtures. Instrumentation includes arrays of pressure transducers (PCB 113 A26), resistance strain gauges (MM EA-13-125SAC-350 or similar), accelerometers (PCB 321 A02), a 100kN load cell (PT LPC 10000), and displacement transducers for the overall motion (Vishay REC-139L) and the local panel response (Schaevitz 1000 HCD). All strains were measured across the short span centerline of the panel, with one gauge at the centre, and one 25mm in from both the keel and chine edges. Static testing of the same type and size of panels was also undertaken using a water filled rubber bladder to apply a uniform pressure. The panel was enclosed in a steel frame with simply supported edges.

### 3. SIMULATION OF SLAMMING PRESSURES AND STRUCTURAL RESPONSES

One of the first major works on dynamic water loads was that by von Karman who studied slamming pressures on seaplane pontoons [9], his work forming the basis for many subsequent developments. As shown in Figure 3, the pulse starts with a short rise time pressure peak that moves from the keel towards the chine, followed by a more constant residual pressure.

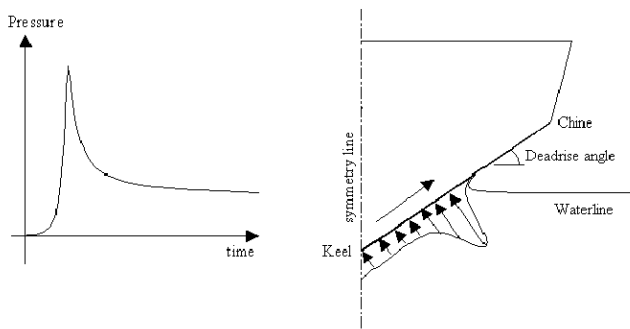


Figure 3. Idealised pressure pulse shape  
(a) As function of time (b) Travelling across the hull.

Pulse magnitude and time domain shape depend primarily on the instantaneous velocity and deadrise angle relative to the water surface. The classical approach of von Karman and Wagner [10] is based on a 2-dimensional wedge. The calculated pressure is the mean pressure of the wetted area of the wedge, and is related to Bernoulli's equation for dynamic pressure in an incompressible fluid. This is multiplied by a constant which is

a function of deadrise angle and an assumption of added mass of water. A modification of von Karman's work was made by Payne, [11], who considered a wedge impacting on water with a spray root. Wagner's approach has been widely utilised as the basis of methods for predicting the maximum pressures, including those by Stavovy and Chuang [12] and Faltinsen and Zhao [13].

In this work the shape of the pressure pulse is based on the formulation developed in previous work by Battley and Stenius [14]. The time domain shape is defined by the peak pressure ( $P_p$ ), residual pressure ( $P_r$ ), rise time ( $t_r$ ), fall time ( $t_f$ ), and rise and fall pressure ratios as shown in Figure 4. The rise pressure ratio ( $r_2$ ) is the pressure relative to the peak pressure at half of the rise time ( $t_r/2$ ), while the fall pressure ratio ( $r_2$ ) is the ratio of the pressure at the fall time ( $t_f$ ) to the residual pressure. Input parameters are the velocity profile during the slamming event and the panel geometry. The instantaneous local velocity and deadrise angle are calculated across the panel, and then a series of time-history curves generated to represent the progression of the pressure pulse across the panel in the correct format for the finite element software input file. The maximum pressure is calculated using Stavovy and Chuang's semi-empirical method [12], while the residual pressure is based on 0.4 times the mean pressure from Payne [11]. The 0.4 factor and empirical formulae for the rise and fall times and pressure ratios have been defined based on pressure data from testing in the SSTs.

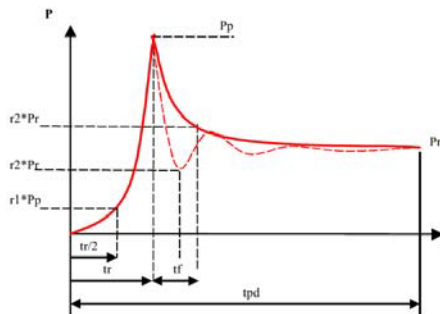


Figure 4. Simulated pressure pulse.

Modal transient finite element analysis was used to model the structural response of a sandwich panel to slamming events using EMRC NISA Version 10.5. The panel was modelled with a rectangular 20x20 mesh of 2<sup>nd</sup> order sandwich shell elements. Pressures were defined as described above, with a pressure-time history curve applied to each row of elements. The analysis process has two stages, firstly an eigenvalue analysis, and then a modal transient analysis applies the loads and calculates the response. This

analysis approach is very quick, total solution time on a desktop PC being less than 60 CPU seconds.

The testing and analysis methods described here have been applied to a range of panels, only one configuration being presented here. For this panel skin laminates are 2.5mm thick resin infused glass/epoxy, with 4 layers of 610g/mm<sup>2</sup> quadraxial plies. The foam core is 130 kg/m<sup>3</sup> HEREX C70.130. Material properties are given in Table 1. The materials were treated as linear elastic. The core is non-linear at large strains; however these analyses were only focussed on the initial linear region of the panel behaviour. A viscous damping ratio of 0.5 was used, and 50kg of added mass applied to approximate the effect of water contact on the natural frequency of the panel.

Table 1. Material properties for the sandwich panel.

Property	Skin plies	Core
E (MPa)	12500	115
G (MPa)	4800	45
$\nu$	0.30	0.30
Density (kg/m <sup>3</sup> )	1760	130
Thickness (mm)	2.6	19.7

## 4. RESULTS

### 4.1 Pressure loads

Slamming tests were undertaken using a rigid panel (50mm balsa core, carbon fibre/epoxy skins) to determine pressures at 10, 20, 30 and 40° deadrise for velocities of 0.5 to 6m/s. Figure 5 shows pressure traces from a typical 5m/s slam at 10° deadrise as an example. The progression of the pressure pulse across the panel can be clearly seen. All transducers lie on the centre of the panel across the short span, p1 being closest to the keel and p5 to the chine. The pressure near to the keel edge is lower than further across the panel showing that it takes an initial immersion before the full pressure is generated, but there is generally good consistency. Figure 6 compares three measured pressure traces at 3 and 5 m/s to those predicted by the pressure model described in Section 3, showing very good correlation. Figure 7 compares the predicted and measured peak and residual pressures for velocities of 1 to 6m/s, also showing excellent correlation. The lower experimental values at 6m/s are believed to be due to force limitations of the hydraulic system meaning that the SSTS was unable to maintain a constant velocity throughout the slam event for this size panel at 10° deadrise.

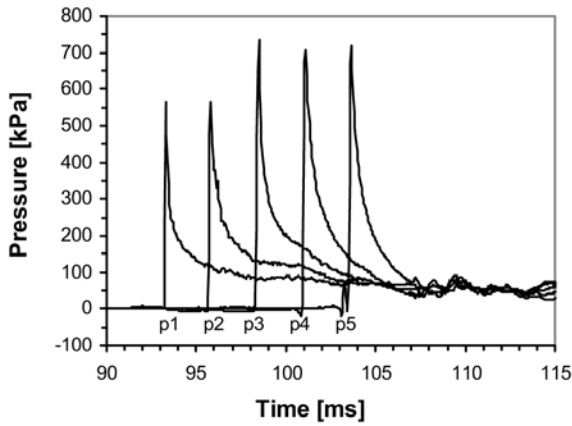


Figure 5. Pressure traces for 5m/s slam of 10 degree rigid panel.

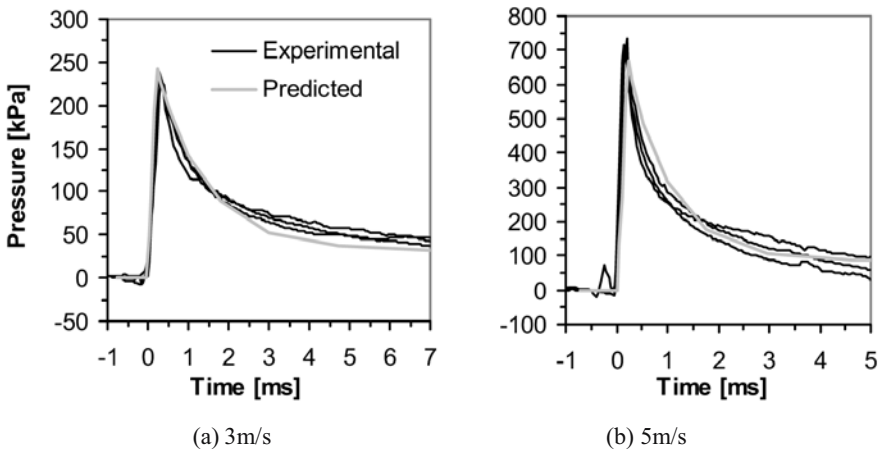


Figure 6. Measured and predicted pressure curves at 3m/s and 5m/s.

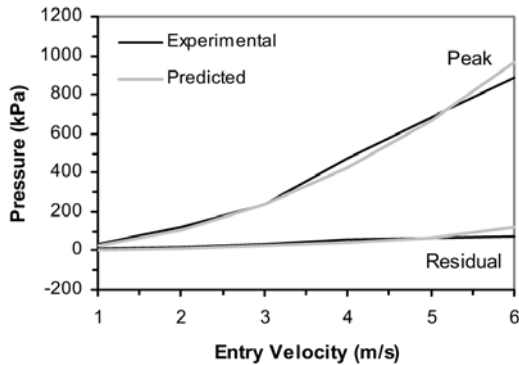


Figure 7. Pressure magnitudes from 1 to 6 m/s.

## 4.2 Panel responses

Figure 8 shows a typical slam test result, with the deflection and strains predicted by transient FEA. The keel and chine edge strains provide an indication of local deformation and hence transverse forces near the support edges. These two strains clearly show the progression of the pressure pulse across the panel; the keel strain increasing at the start of the event and then remaining relatively constant, while the chine strain does not start to increase until approximately half way through the event then rises quickly.

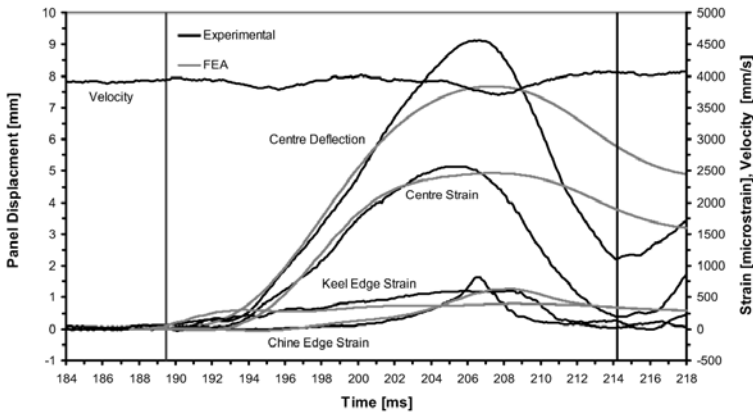


Figure 8. Slam event of  $10^\circ$  panel at 4m/s with transient FEA predictions. The blue vertical line represents the water surface, and the black line full immersion of the panel.

The same trends are apparent in the predicted strains, although the theoretical chine strain is not as peaky as the experimental. The magnitudes of all three predicted strains are reasonably close to the experimental results, although the predicted deflection is lower than measured and the predicted values do not decrease as quickly as the measurements. For this particular case the FEA solution was not sensitive to changes in the natural frequency of the panel due to added mass of water, however for cases when the loading rate was close to the natural frequency this did prove to be important. Figures 9 and 10 compare dynamic test results to static panel tests and dynamic FEA predictions. The dynamic test data was generated by repeating slamming tests with increased impact velocity until panel core shear failure occurred at the chine edge. Figure 9 compares the deflection to the strain at the centre of the panel, showing that the dynamic panel tests produce higher deflections for a certain strain than uniform static loading. The transient FEA predictions correlate well with the dynamic tests. Figure 10 compares the deflection at the centre of the panel to the chine edge strain, the deviation from linearity in the static and dynamic tests showing the onset of yield in

the core. Changes in the chine edge strain proved to be a reliable indicator of core shear failure for both dynamic and static panel tests.

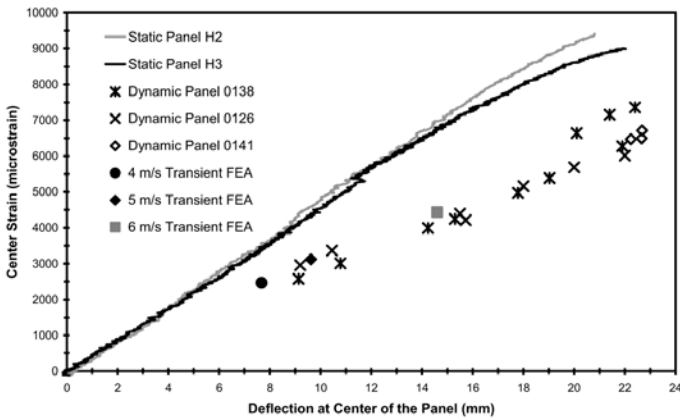


Figure 9. Deflection vs. panel centre strain.

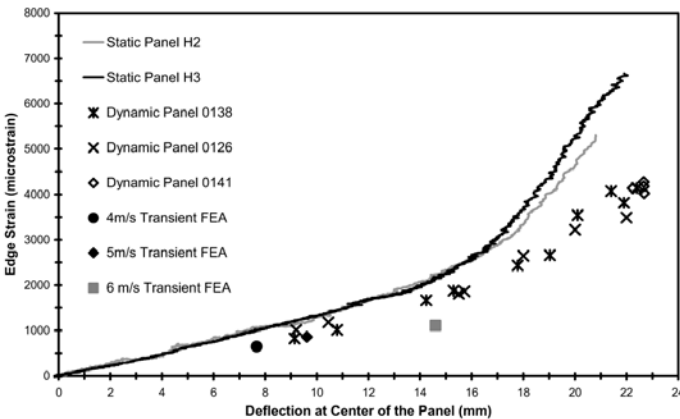


Figure 10. Deflection vs. panel edge strain.

## 5. CONCLUSIONS

A unique servo-hydraulic slam testing system provides the ability to characterise slamming pressures and sandwich panel structural responses in a controlled, well instrumented situation where panels are subjected to realistic dynamic pressure loadings. The pressure prediction method presented predicts magnitudes and time histories that correlate very well with experimental measurements in the SSTs. Modal transient finite element analysis methods are shown to be able to predict the dynamic structural responses of sandwich panels to a reasonable level of accuracy.

The experimental and theoretical results presented demonstrate that slam loaded panels behave fundamentally differently to uniformly statically loaded panels. The dynamic panels have higher deflections relative to bending strains, confirming that the load distribution is not well represented by a uniformly distributed pressure. Under dynamic loading the transverse shear is more significant than bending compared to a uniformly loaded panel. Uniform pressure based design methods result in panels that do not have an optimal balance of shear to bending properties, which may lead to excessive laminate weight or inadequate shear strength or stiffness. Further research is being undertaken to incorporate these results into design methodologies.

## ACKNOWLEDGEMENTS

This work was supported by the New Zealand Foundation for Research, Science and Technology, and a Technology New Zealand Technology for Business Growth project. Mr P Beck and K Thorandt provided invaluable assistance in the development of the SSTs.

## REFERENCES

1. DNV Rules for High Speed, Light Craft and Naval Surface Craft, "Hull Structural Design, Fibre Composite and Sandwich Construction", Det Norske Veritas, Jan 2003 Pt3 Ch 4.
2. Downs-Honey, R., Edinger, S. and Battley, M., "Slam Testing of Sandwich Panels", SAMPE 2005, Long Beach CA, 1-5 May 2005.
3. Chuang, S.-L., "Experiments on Slamming of Wedge-Shaped Bodies", J. of Ship Research, 1967.
4. Wraith, R.G., "Pressure Loads on Ship Hull Plating Caused by Slamming", PhD Thesis, 1998, Dept. of Mechanical and Manufacturing Eng, University of Melbourne, Australia.
5. Hayman, B., Haug, T. and Valsgard, S., "Slamming Drop Tests on a GRP Sandwich Hull Model", 2nd Int. Conf. on Sandwich Construction, Florida, USA, 1992.
6. Katsaounis, G. and Samuelides, M., "Comparison of Structural Behavior of Wet Deck Panels Made of Different Materials Under Slamming Loads", FAST99, Seattle, USA, 1999.
7. Faltinsen, O.M., "Hydroelastic Slamming", J. Marine Science Technology, pp. 49-65, 2000.
8. Stenius, I. and Rosen, A., "Explicit FE Analysis of Hull-Water Impacts", FAST 2005.
9. von Karman, Technical Report TN 321 NACA, 1929.
10. Wagner, Zeitschrift Für Angewandte Mathematik und Mechanik, 12(4), pp. 192-235, 1932.
11. Payne P., "The Vertical Impact of a Wedge on a Fluid", Ocean Eng., 1981, Vol. 8, No. 4.
12. Stavovy, A.B. and Chuang, S.-L., "Analytical Determination of Slamming Pressures for High-Speed Vehicles in Waves", Journal of Ship Research, pp. 190-198, 1976.
13. Zhao, R. and Faltinsen, O., "Water Entry of Two-Dimensional Bodies", J. of Fluid Mechs.
14. Battley, M.A. and Stenius, I., "Dynamically Loaded Marine Composite Structures", 14th International Conference on Composite Materials (ICCM-14), San Diego, 14-18 July 2003.

# LOCAL FREE VIBRATION ANALYSIS OF INITIALLY STRESSED CURVED SANDWICH BEAMS

W. Wang and R.A. Shenoi

*School of Engineering Sciences, University of Southampton, Southampton, SO17 1BJ, UK*

**Abstract** A theoretical approach is provided to investigate the problem of local free vibration of an initially stressed curved sandwich beam. The equation of motion of the skin is derived from energy principles and based upon small displacements away from an initial, loaded equilibrium state. The core material is simplified as an elastic foundation and the skins are considered as composite beams on an elastic foundation. The investigation shows that the vibration frequencies and modes are dependent not only on the flexural rigidity and length of beam and foundation modulus, but also on geometry of curvature and axial compressive/tensile force.

**Keywords:** local free vibration, curved sandwich beam.

## 1. INTRODUCTION

There is a large body of literature dealing with specific aspects of vibration and buckling of sandwich beams or panels, including the global and local cases. However, a bit more detailed review will find that up to now most work in this area pays attention only to flat beam/panel configuration. Comparably few analyses relate to curved sandwich beams [1-3]. Further, there are almost no papers dealing with vibration of initially stressed curved sandwich beams which are used in many practical working conditions [4]. It is already known that geometrical curvature has a significant influence on the mechanical properties such as through-thickness stress and local instability etc. of sandwich beams. Therefore it is imperative to study its

effects on the vibration properties of curved sandwich beams. The purpose of this paper is to investigate the local vibration of skins of a curved sandwich beam subjected to initially loads.

## 2. PROBLEM STATEMENT AND APPROACH

A general curved sandwich beam with core and inner skin and outer skin is considered, the core material is simplified as an elastic foundation and the skins are simplified as composite beams in this paper, as shown in Figure 1. Thus the above problem is reduced to the problem of a stressed curved composite beam on an elastic foundation, as shown in Figure 2.

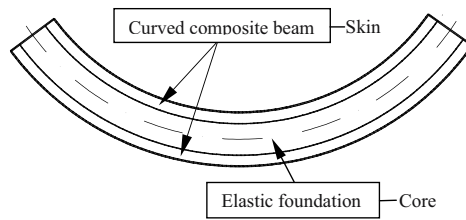


Figure 1. Curved sandwich beam.

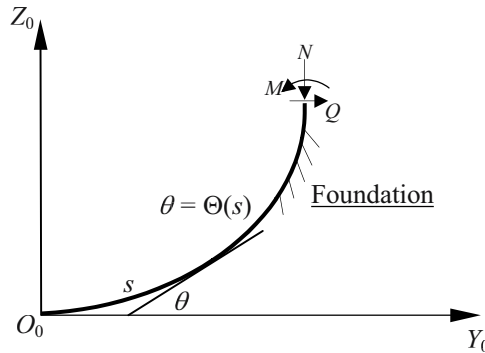


Figure 2. Beam geometry.

The equations of motion of the skin are derived from energy principles and based upon small displacements away from an initial, loaded equilibrium state. The displacement, axial force and bending moment etc. of a curved beam with arbitrary curvature on an elastic foundation are obtained first by curved beam theory. Then, by assuming the small displacement relationships, the energy method is used to determine the natural frequencies of this stressed curved beam on an elastic foundation. One usual case, a half circular sandwich arch beam subjected to a pure bending, is specially analysed in details as an application.

### 3. GENERAL SOLUTION

#### 3.1 Initial loaded equilibrium state of curved composite beam on an elastic foundation

Consider a curved beam with arbitrary curvature resting on an elastic foundation. Assuming the intrinsic equation of its free shape is  $\theta = \Theta(s)$ , where  $s$  is measured along the length of the arc and  $\theta$  is the slope at  $s$ ,  $N$  and  $M$  are axial load and bending moment respectively, as shown in Figure 2.

It should be noted that the composite laminate may possess the tension-bending coupling property. Such material behaviour can be readily dealt with at the expense of introducing additional parameters into the problem [5]. However the general character of the results will not change. Therefore the properties of the curved beam-skin are assumed to be homogeneous, orthotropic, linearly elastic. For the case of this curved beam on an elastic foundation, the governing differential equation for static equilibrium can be obtained [5]:

$$\begin{aligned} & \frac{d^4 w}{ds^4} + \left(\frac{d\theta}{ds}\right)^2 \frac{d^2 w}{ds^2} + 4 \frac{d\theta}{ds} \frac{d^2 \theta}{ds^2} \frac{dw}{ds} + \left[ 2 \frac{d\theta}{ds} \frac{d^3 \theta}{ds^3} + 2 \left(\frac{d^2 \theta}{ds^2}\right)^2 + \frac{k}{D} \right] w \\ & = \frac{1}{D} \left( q + \frac{d\theta}{ds} N \right) + \frac{d^2 \theta}{ds^2} \frac{d^2 v}{ds^2} + 2 \frac{d^3 \theta}{ds^3} \frac{dv}{ds} + \frac{d^4 \theta}{ds^4} v \end{aligned} \quad (1)$$

where  $v$  and  $w$  are the longitudinal and transverse displacement respectively,  $k$  is elastic stiffness of foundation,  $D$  is the flexural rigidity of skin.

### 3.2 General Solution

Assuming the vibration deflection of curved beam lying on an elastic foundation is based on the equilibrium place, then the actual transverse deflection of curved beam is:

$$\bar{w} = w + \delta w \quad (2)$$

It is assumed that  $\delta w$  can be expressed by a Fourier series corresponding to the simply supported boundary condition as follows:

$$\delta w = \left( \sum_{m=1}^{\infty} a_m \sin \frac{m\pi\theta}{\alpha} \right) \exp(j\omega t) \quad (3)$$

Note the relationship [5]:

$$\kappa = v \frac{d\theta}{ds^2} - \frac{dw}{ds^2} - w \left( \frac{d\theta}{ds} \right) \quad (4)$$

$$M = D\kappa$$

The strain energy change of bending of the beam due to the small displacement  $\delta w$  is:

$$\Delta V_1 = \frac{1}{2} \int_0^s \bar{M}\bar{\kappa} ds - \frac{1}{2} \int_0^s M\kappa ds \quad (5)$$

The deformation energy change of the elastic foundation due to the small perturbation  $\delta w$  is:

$$\Delta V_2 = \frac{1}{2} k \int_0^s \bar{w}^2 ds - \frac{1}{2} k \int_0^s w^2 ds \quad (6)$$

The kinetic energy of the beam is:

$$\Delta T = \frac{1}{2} \int_0^s \rho \left( \frac{\partial \bar{w}}{\partial t} \right)^2 ds = \frac{1}{2} \int_0^s \rho \left( \frac{\partial (\delta w)}{\partial t} \right)^2 ds \quad (7)$$

where  $\rho$  is mass density of the curved skin.

Meanwhile, the change of the length of curved beam in circumferential direction is:

$$\delta l = \frac{1}{2} \int_0^s \left( \frac{\partial \bar{w}}{\partial s} \right)^2 ds - \frac{1}{2} \int_0^s \left( \frac{\partial w}{\partial s} \right)^2 ds \quad (8)$$

the relative change of the angle between two end cross sections of curved beam is:

$$\delta\beta = \left. \frac{\partial (\delta w)}{\partial s} \right|_s \Big|_0 \quad (9)$$

Finally from the energy principles [7]:

$$\Delta V_1 + \Delta V_2 + \Delta T = N\delta l + M\delta\beta \tag{10}$$

the governing equation of motion can then be derived.

## 4. APPLICATION TO A CIRCULAR ARCH

### 4.1 Specific solution

As an application of the above approach, the case of a circular sandwich arch beam subjected to a pure bending is analysed here. As for a circular beam there is

$$\frac{d\theta}{ds} = \frac{1}{R} = \text{Constant} \tag{11}$$

and because the sandwich beam is subjected to pure bending, in static equilibrium state, the transverse displacement of the skin as well as axial force and bending moment in the skin is constant along the beam,

$$w = w_0, N = N_0, M = M_0 \tag{12}$$

By substituting these two results into related equations in the above section, all the expressions can be much reduced and simplified. The final equation of vibration can be derived as:

$$\left( \sum_{m=1}^{\infty} a_m^2 \left\{ N_0 \frac{\pi^2}{R\alpha} \left( 1 + \frac{D}{kR^4} \right) m^2 - \frac{D\alpha}{R^3} \left( 1 - \left( \frac{m\pi}{\alpha} \right)^2 \right)^2 - kR\alpha \right\} + \rho R \alpha \omega^2 \right) \exp(2j\omega t) = \left( 2N_0 \frac{D}{kR^4} \frac{\alpha}{\pi} \left( 1 + \frac{D}{kR^4} \right) \sum_{m=1,3,5,\dots}^{\infty} \frac{a_m}{m} \right) \exp(j\omega t) \tag{13}$$

where  $\alpha$  is the arch angle of the beam. This equation can hold true if and only if the coefficient expressions in two sides are both equal to zero:

$$\left\{ \begin{aligned} \sum_{m=1}^{\infty} a_m^2 \left\{ N_0 \frac{\pi^2}{R\alpha} \left( 1 + \frac{D}{kR^4} \right) m^2 - \frac{D\alpha}{R^3} \left( 1 - \left( \frac{m\pi}{\alpha} \right)^2 \right)^2 - kR\alpha \right\} + \rho R \alpha \omega^2 &= 0 \\ 2N_0 \frac{D}{kR^4} \frac{\alpha}{\pi} \left( 1 + \frac{D}{kR^4} \right) \sum_{m=1,3,5,\dots}^{\infty} \frac{a_m}{m} &= 0 \end{aligned} \right. \tag{14}$$

From the first equation, the  $m$ th mode circular frequency can be obtained:

$$\omega_m^2 = \frac{1}{\rho} \left[ \frac{D}{R^4} \left( 1 - \left( \frac{m\pi}{\alpha} \right)^2 \right)^2 + k - \frac{N_0}{R^2} \left( \frac{m\pi}{\alpha} \right)^2 \left( 1 + \frac{D}{kR^4} \right) \right] \tag{15}$$

The second equation leads to the limitation condition:

$$N_0 = 0 \text{ or } \sum_{m=1,3,5,\dots}^{\infty} \frac{a_m}{m} = 0 \tag{16}$$

This limitation condition actually corresponds to an additional specific boundary condition of the problem. That also shows that if a sandwich beam is globally stressed (which means  $N_0 \neq 0$  in skins), and if the deflection curve of local vibration of its skin is odd number simply sine wave, then the amplitudes of every half wave are not equal. For an example, the simplest case of this kind is  $m=3$ , then there is:

$$\delta w = a_1 \left( \sin \frac{\pi\theta}{\alpha} - 3 \sin \frac{3\pi\theta}{\alpha} \right) \exp(j\omega_3 t) \tag{17}$$

the inflection points are at  $\theta = \frac{\alpha}{\pi} \arcsin \frac{\sqrt{6}}{3}$ ,  $\alpha - \frac{\alpha}{\pi} \arcsin \frac{\sqrt{6}}{3}$  respectively.

If let  $R \rightarrow \infty$ , and noting  $R\alpha = l$ , then equation (15) will converge to the straight beam case:

$$\omega_m^{*2} = \frac{D}{\rho} \left( \frac{m\pi}{l} \right)^4 + \frac{k}{\rho} - \frac{N_0}{\rho} \left( \frac{m\pi}{l} \right)^2 \tag{18}$$

It is exactly the result of straight beam on an elastic foundation and with translational restraints at both ends and subjected to a compressive axial force.

If the beam is half circular arch with  $\alpha = \pi$ , then from equation (15),  $\omega$  reaches minimum theoretically when

$$m^2 = 1 + \frac{N_0}{2} \left( \frac{R^2}{D} + \frac{1}{kR^2} \right) \tag{19}$$

then there is

$$\rho \omega_{\min}^2 = k \left( 1 + \frac{D}{kR^4} \right) - \frac{\left[ \frac{2D}{R^2} + N_0 \left( 1 + \frac{D}{kR^4} \right) \right]}{4D} \tag{20}$$

In the following, two specific conditions are further studied.

### 4.2 Flexible skin on a hard core

First consider the condition of relatively small  $D$  or relatively large  $k$ . If  $\frac{kR^4}{D} \gg 1$ , the critical buckling/wrinkling force of the compressed skin is  $N_{cr} = 2\sqrt{Dk}$ , [5,6]. However, it should be noted that this formula is only fit for the case of wrinkling, in which the number of buckling half waves must be large enough [5,6]. Then equation (19) can be simplified as

$$m^2 = 1 + \frac{N_0 R^2}{2D} = 1 + \frac{N_0}{N_{cr}} \sqrt{\frac{kR^4}{D}} \tag{21}$$

Therefore, under the present condition  $m^2$  will be very big provided that axial load  $N_0$  is not very tiny compared with wrinkling critical load  $N_{cr}$ . From equation (20)

$$\begin{aligned} \frac{\rho\omega^2}{k} &= 1 - \left(\frac{N_0}{N_{cr}}\right)^2 \left(\frac{2D}{N_0 R^2} + 1\right)^2 = 1 - \frac{m^2}{m^2 - 1} \left(\frac{N_0}{N_{cr}}\right)^2 \\ &\approx 1 - \left(\frac{N_0}{N_{cr}}\right)^2 \end{aligned} \tag{22}$$

Figure 3 shows the above relation.

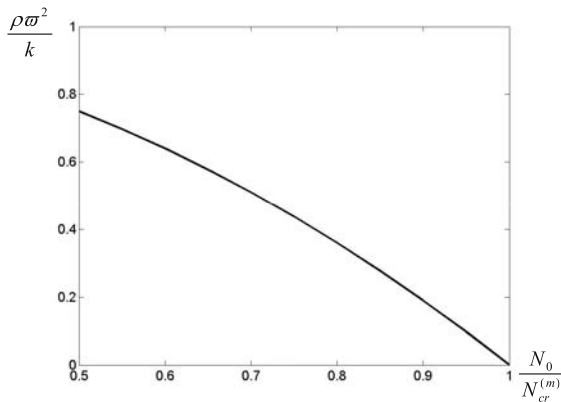


Figure 3. Flexible skin on a hard core case.

### 4.3 Stiff skin on a soft core

If the foundation—core material is soft or the beam—skin is relatively stiff, where  $kR^4/D \ll 1$ , buckling in which the number of the half

wavelength is 2 rather than wrinkling in which the number of half wavelength is very big is more likely to occur in the skin [5,6]. Therefore in this condition, noting the arch angle of the beam is  $\pi$ , the critical buckling force of the compressed skin [5,6] can be simplified as

$$N_{cr}^{(2)} = \frac{9kR^2}{4} \tag{23}$$

substituting it into equation (19):

$$m^2 = 1 + \frac{N_0 R^2}{2D} \left( 1 + \frac{D}{kR^4} \right) \approx 1 + \frac{9}{8} \frac{N_0}{N_{cr}^{(2)}} \tag{24}$$

Because minimum of  $m$  is 2, and noting  $kR^4/D \ll 1$  and  $\alpha = \pi$ , then from equation (15)

$$\frac{\rho R^4 \omega^2}{D} \approx 9 \left( 1 - \frac{N_0}{N_{cr}^{(2)}} \right) \tag{25}$$

Figure 4 shows the above relation.

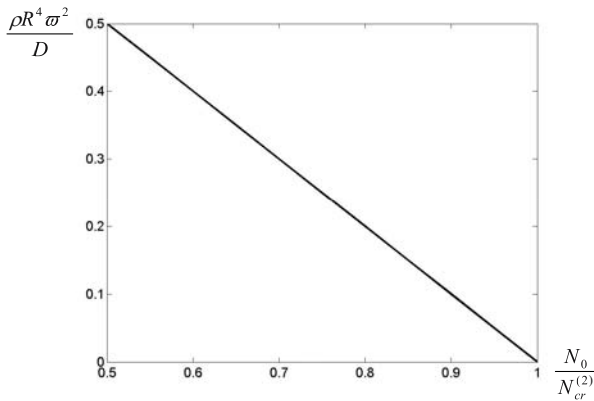


Figure 4. Stiff skin or soft core case.

## 5. CONCLUSIONS

A theoretical approach is developed for the problem of local free vibration of an initially stressed curved sandwich beam. The investigation shows that the vibration frequencies and modes are dependent not only on the flexural rigidity and length of beam and foundation modulus which are as expected, but also significantly on geometry of curvature and axial

compressive/tensile force in the skin. It is found that  $kR^4/D$  is a very important parameter in determining the vibration mode corresponding to the lowest frequency, where  $k, R, D$  are respectively core material modulus, radius of curvature and flexible rigidity of the beam. When  $kR^4/D \gg 1$  which means hard core and comparably flexural skin, the lowest frequency corresponds to the high order mode ( $m \approx \sqrt[4]{kR^4/D}$ ); when  $kR^4/D \ll 1$  which means soft core and comparably stiff skin, the lowest frequency corresponds to the simplest mode  $m = 2$ .

## REFERENCES

1. Bozhevolnaya, E. and Frostig, Y., "Free vibration of curved sandwich beams with a transversely flexible core", *Journal of sandwich structures and materials*, Vol. 3, No. 4, pp 311-342, 2001.
2. Bozhevolnaya, E. and Sun, J.-Q., "Free vibration analysis of curved sandwich beams", *Journal of sandwich structures and materials*, Vol. 6, No. 1, pp 47-73, 2004.
3. Sakiyama, T., Matsuda, H. and Morita, C., "Free vibration analysis of sandwich arches with elastic or viscoelastic core and various kinds of axis-shap and boundary conditions", *Journal of sound and vibration*, Vol. 203, No. 3, pp505-522, 1997.
4. Chen, L.-W. and Shen, G.-S., "Vibration and buckling of initially stressed curved beams", *Journal of sound and vibration*, Vol. 215, No. 3, pp 511-526, 1998.
5. Wang, W., *Analytical Approaches to Predict Flexural Behaviour of Curved Laminates and Sandwich Beams*, PhD. thesis, University of Southampton, UK, 2002.
6. Wang, W. and Sheno, R. A., "Analytical Solutions to Predict Flexural Behaviour of Curved Sandwich Beams", *Journal of sandwich structures and materials*, Vol. 6, No. 3, pp 199-216, 2004.
7. Timoshenko, S. and Gere, J., *Theory of Elastic Stability* (second edition), McGraw-Hill Book Company, New York, 1961.

# VIBRATION ANALYSIS OF COMPOSITE SANDWICH PLATES AND LAYUP OPTIMIZATION

Hideki Sekine,<sup>1</sup> Hiroshi Shirahata,<sup>2</sup> and Mariko Matsuda<sup>3</sup>

<sup>1</sup>*Tohoku University, Sendai, Japan*  
sekine@plum.mech.tohoku.ac.jp

<sup>2</sup>*Tohoku University, Sendai, Japan*  
sirahata@cc.mech.tohoku.ac.jp

<sup>3</sup>*Tohoku University, Sendai, Japan; currently, Kobe Steel, Ltd., Kobe, Japan*  
m-matsuda@rd.kcrl.kobelco.co.jp

**Abstract** This paper is concerned with the vibration analysis of rectangular, symmetric composite sandwich plates and the layup optimization of top and bottom laminated FRP composite faces. The fundamental frequency of the composite sandwich plate is discussed in the subspace of four in-plane lamination parameters of the laminated FRP composite face, and the optimum laminate configuration which maximizes the fundamental frequency is determined.

**Keywords:** composite sandwich plate, laminated FRP composite face, fundamental frequency, layup optimization.

## 1. INTRODUCTION

A composite sandwich plate consists of a comparatively thick, light core and top and bottom thin faces, and has been widely used in various industries. Generally, the core is of honeycomb or polymer material, and the face is of a laminated FRP composite. To achieve performance of strength and stiffness of the composite sandwich plate, the design of laminate configuration of the face is necessary.

Analytical studies of vibration were conducted on the sandwich plate with homogeneous and isotropic faces [1, 2]. Moreover, Khatua and Cheung [3] carried out a vibration analysis of the sandwich plate with orthotropic faces using the finite element method based on a multilayer plate theory, and Ng and Das [4] using the Galerkin method for a skew sandwich plate. Mirza and Li [5] recently proposed an analytical method based on the reciprocity theorem for a vibration problem of sandwich plate.

recently proposed an analytical method based on the reciprocity theorem for a vibration problem of sandwich plate.

Vibration problems of composite sandwich plates were analyzed by applying the classical lamination theory and the Mindlin plate theory to the laminated FRP composite face [6, 7, 8, 9, 10]. A vibration analysis based on a higher-order shear deformation theory was also conducted to obtain a more accurate solution [11, 12].

Few vibrational optimization problems have been studied on the composite sandwich plate. Duffy and Adali [13] examined the layup optimization using the fiber orientation angles of laminated FRP composite face as design variables, but only the angle-ply laminate configuration was studied. Therefore, sufficient design knowledge for configuring the laminated FRP composite face has not been obtained.

In this study, we examine the vibration characteristics of rectangular, symmetric composite sandwich plates and the layup optimization of the top and bottom laminated FRP composite faces. The core is of honeycomb, and its transverse shear deformation is taken into account by applying a higher-order shear deformation theory. The face is sufficiently thin, compared with the core, and the in-plane and out-of-plane displacements of the face are uniform through the thickness. A two-dimensional finite element method is developed for the analysis using an eight-node isoparametric element. First, the fundamental frequency of the composite sandwich plate is discussed in the subspace of four in-plane lamination parameters of the laminated FRP composite face. Next, the optimization problem is formulated by using the in-plane lamination parameters as design variables. The optimum laminate configuration of the laminated FRP composite face, which maximizes the fundamental frequency of the composite sandwich plate, is determined.

## 2. FREE VIBRATION ANALYSIS OF COMPOSITE SANDWICH PLATES

A rectangular, symmetric composite sandwich plate, whose core is of honeycomb, and top and bottom faces are of a laminated FRP composite, is illustrated in Figure 1. The Cartesian coordinate system  $(x, y, z)$ , whose  $x$  and  $y$  axes run on the mid-line of two sides of the rectangular composite sandwich plate, is adopted. The side lengths of the rectangular composite sandwich plate are  $a$  and  $b$  in the  $x$  and  $y$  directions, respectively, and the thickness is  $h$ . The thickness of the core is  $h^c$ , and that of the face is  $h^f$ . The fiber orientation angle of the face is indicated by  $\theta(z)$ . The deformation of the composite sandwich plate is schematically presented in Figure 2.

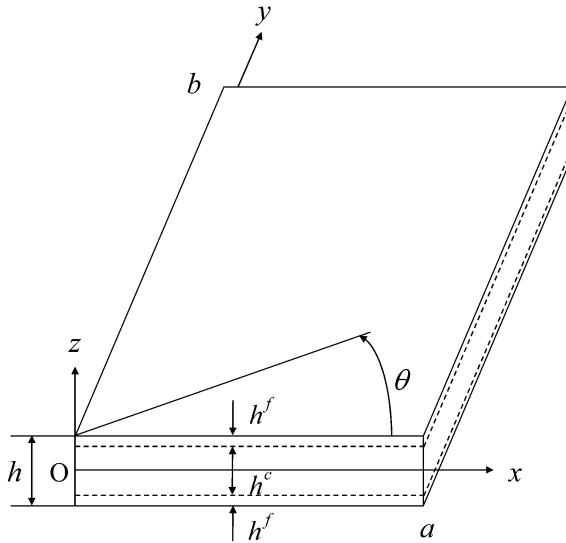


Figure 1. Rectangular, symmetric composite sandwich plate and Cartesian coordinate system.

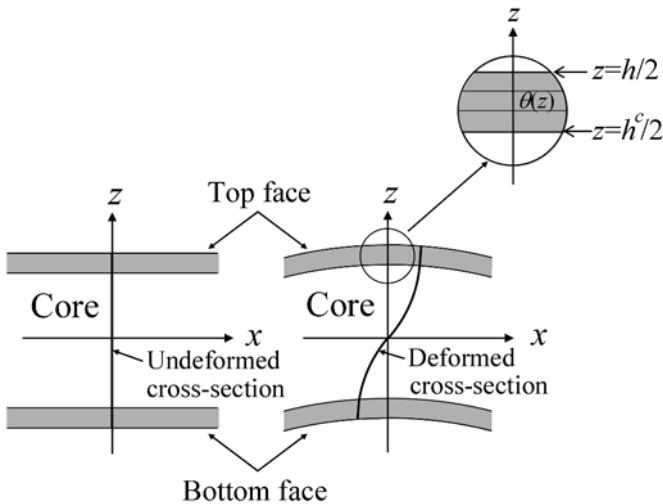


Figure 2. Schematic view of deformation of composite sandwich plate.

## 2.1 Elastic fields of core and face

**2.1.1 Core.** A higher-order shear deformation theory is applied to consider the transverse shear deformation of core. By adopting a cubic function of

$z$  for the displacements in the  $x$  and  $y$  directions  $u^c, v^c$ , and a quadratic function of  $z$  for the displacement in the  $z$  direction  $w^c$ , the displacement field is given in the following equations [14].

$$u^c(x, y, z, t) = a_0(x, y, t) + a_1(x, y, t)z + a_2(x, y, t)z^2 + a_3(x, y, t)z^3 \quad (1)$$

$$v^c(x, y, z, t) = b_0(x, y, t) + b_1(x, y, t)z + b_2(x, y, t)z^2 + b_3(x, y, t)z^3 \quad (2)$$

$$w^c(x, y, z, t) = c_0(x, y, t) + c_1(x, y, t)z + c_2(x, y, t)z^2 \quad (3)$$

where  $a_0, b_0$ , and  $c_0$  are displacements on the mid-plane of core;  $a_1$  and  $b_1$  are rotations of the cross-sections perpendicular to the  $x$  and  $y$  directions; and  $c_1, a_2, b_2, c_2, a_3$ , and  $b_3$  are the higher-order terms.

**2.1.2 Face.** When the face is sufficiently thin, the in-plane and out-of-plane displacements of the face are uniform through the thickness, and the displacements agree with those on the surface of core. Therefore, the displacements of the face are expressed as follows:

$$u_k^f = a_0 + d_{1k}a_1 + d_{2k}a_2 + d_{3k}a_3 \quad (4)$$

$$v_k^f = b_0 + d_{1k}b_1 + d_{2k}b_2 + d_{3k}b_3 \quad (5)$$

$$w_k^f = c_0 + d_{1k}c_1 + d_{2k}c_2 \quad (6)$$

where

$$d_{1k} = -(-1)^k \frac{h^c}{2}, \quad d_{2k} = \left(\frac{h^c}{2}\right)^2, \quad d_{3k} = -(-1)^k \left(\frac{h^c}{2}\right)^3 \quad (7)$$

Here,  $k = 1$  and  $2$  correspond to the top and bottom faces, respectively.

When the in-plane lamination parameters of the laminated FRP composite face  $\xi_i (i = 1, 2, 3, 4)$  are introduced, the feasible region is given by [15]

$$\xi_1^2 + \xi_3^2 \leq 1 \quad (8)$$

$$(\xi_2 - \xi_1^2 + \xi_3^2)^2 + (\xi_4 - 2\xi_1\xi_3)^2 \leq (1 - \xi_1^2 - \xi_3^2)^2 \quad (9)$$

## 2.2 Formulation of the two-dimensional finite element method

An equation of motion for obtaining fundamental frequency and its corresponding vibration mode of the composite sandwich plate is formulated using an eight-node two-dimensional isoparametric element.

The shape function of an eight-node two-dimensional isoparametric element is  $\mathbf{N}$ , then  $\mathbf{q} (= [ a_0 \ b_0 \ c_0 \ a_1 \ b_1 \ c_1 \ a_2 \ b_2 \ c_2 \ a_3 \ b_3 ]^T)$  is expressed using  $\bar{\mathbf{q}}$  which is  $\mathbf{q}$  at the node of the element  $p$ , in the following equation.

$$\mathbf{q} = \mathbf{N}\bar{\mathbf{q}} \quad (10)$$

By use of  $\bar{\mathbf{q}}$ , the strain energy of the element  $p$  is given by

$$\begin{aligned}
 U_p = & \frac{1}{2} \int_{S_p} \bar{\mathbf{q}}^T \mathbf{N}^T \begin{bmatrix} \mathbf{C}^{c(0)} \\ \mathbf{C}^{c(2)} \end{bmatrix}^T \begin{bmatrix} \mathbf{A}^c & \mathbf{D}^c \\ \mathbf{D}^c & \mathbf{F}^c \end{bmatrix} \begin{bmatrix} \mathbf{C}^{c(0)} \\ \mathbf{C}^{c(2)} \end{bmatrix} \mathbf{N} \bar{\mathbf{q}} dS_p \\
 & + \frac{1}{2} \int_{S_p} \bar{\mathbf{q}}^T \mathbf{N}^T \begin{bmatrix} \mathbf{C}^{c(1)} \\ \mathbf{C}^{c(3)} \end{bmatrix}^T \begin{bmatrix} \mathbf{D}^c & \mathbf{F}^c \\ \mathbf{F}^c & \mathbf{H}^c \end{bmatrix} \begin{bmatrix} \mathbf{C}^{c(1)} \\ \mathbf{C}^{c(3)} \end{bmatrix} \mathbf{N} \bar{\mathbf{q}} dS_p \\
 & + \sum_{k=1}^2 \frac{1}{2} \int_{S_p} \bar{\mathbf{q}}^T \mathbf{N}^T \mathbf{C}_k^f \mathbf{A}^f \mathbf{C}_k^f \mathbf{N} \bar{\mathbf{q}} dS_p \tag{11}
 \end{aligned}$$

where  $S_p$  is the area of the element  $p$ ;  $\mathbf{A}^c$  is the in-plane stiffness of core  $\mathbf{C}^c$  is the out-of-plane stiffness of core  $\mathbf{C}$  and  $\mathbf{F}^c$  and  $\mathbf{H}^c$  are the higher-order terms;  $\mathbf{A}^f$  is the in-plane stiffness of face.

Similarly, the kinetic energy of the element  $p$  is presented by

$$T_p = \frac{1}{2} \rho^c \int_{S_p} \dot{\bar{\mathbf{q}}}^T \mathbf{N}^T \mathbf{Z}^c \mathbf{N} \dot{\bar{\mathbf{q}}} dS_p + \sum_{k=1}^2 \frac{1}{2} \rho_k^f \int_{S_p} \dot{\bar{\mathbf{q}}}^T \mathbf{N}^T \mathbf{Z}_k^f \mathbf{N} \dot{\bar{\mathbf{q}}} dS_p \tag{12}$$

where the superimposed dot indicates the differentiation with respect to time, and  $\rho^c$  and  $\rho_k^f$  are the densities of core and face, respectively.

Consequently, the total strain energy and the total kinetic energy are presented by

$$U = \sum_p U_p \tag{13}$$

$$T = \sum_p T_p \tag{14}$$

By substituting Eqs. (13) and (14) into Hamilton’s principle, the equation of motion for free vibration is formulated as follows:

$$\mathbf{M} \ddot{\tilde{\mathbf{q}}} - \mathbf{K} \tilde{\mathbf{q}} = 0 \tag{15}$$

where  $\tilde{\mathbf{q}}$  is listed from  $\bar{\mathbf{q}}$  for individual nodes for the whole structure including all elements, and  $\mathbf{M}$  and  $\mathbf{K}$  are the mass matrix and stiffness matrix, respectively. The solution of free vibration is presented in the following form

$$\tilde{\mathbf{q}} = \boldsymbol{\phi} e^{i\omega t} \tag{16}$$

Then, the equation of motion represented by the  $j$ -th fundamental frequency  $\omega_j$  and the corresponding vibration mode  $\boldsymbol{\phi}_j$  is given by

$$\mathbf{K} \boldsymbol{\phi}_j = \omega_j^2 \mathbf{M} \boldsymbol{\phi}_j \tag{17}$$

### 2.3 Numerical examples and consideration

Consider the rectangular, symmetric composite sandwich plate whose core is of aluminum honeycomb and face is of a laminated CFRP composite. The aluminum honeycomb of the core is made of sheet-like aluminum foil by conducting an undulate folding and bonding alternately the parts together. Material properties of the aluminum honeycomb core and the CFRP composite lamina are displayed in Tables 1 and 2.

For the two-dimensional finite element analysis, the rectangular composite sandwich plate is divided equally into ten elements in the  $x$  and  $y$  directions, respectively.

Henceforth, the results of fundamental frequency are given in the following non-dimensional form

$$\omega_1^* = \omega_1 / \sqrt{\frac{E_L \times 10^{-4}}{\rho_k^f a^2}} \tag{18}$$

When the rectangular composite sandwich plate is simply supported on the four edges, the fundamental frequency of the composite sandwich plate is discussed in the subspace of four in-plane lamination parameters of the laminated CFRP composite face. In Figure 3, the contours of non-dimensional fundamental frequency  $\omega_1^*$  on the plane of in-plane lamination parameter are indicated in the cases of  $(\xi_3, \xi_4) = (0, 0)$ ,  $(\xi_1, \xi_2) = (0.2, 0.5)$  and  $(\xi_1, \xi_2) = (-0.2, -0.5)$  when  $a/b$ ,  $a/h$  and  $h^c/h$  are taken as  $a/b = 1.0, 1.5, 2.0$ ,  $a/h = 50$  and  $h^c/h = 0.9$ . It is found from the figure that  $\omega_1^*$  reaches a maximum at  $(\xi_3, \xi_4) = (0, 0)$  when the values of  $\xi_1$  and  $\xi_2$  are prescribed. This means that the existence of the in-plane extension-shear coupling, i.e.,  $\xi_3, \xi_4 \neq 0$ , produces an effect that makes  $\omega_1^*$  small. On the other hand, it is seen that  $\omega_1^*$  becomes maximum on the boundary of feasible region on the  $\xi_1$ - $\xi_2$  plane in the case of  $(\xi_3, \xi_4) = (0, 0)$ .

Table 1. Material properties of aluminum honeycomb core.

$E_z$ (GPa)	$G_{yz}$ (MPa)	$G_{zx}$ (MPa)	$\rho^c$ (kg/m <sup>3</sup> )
1.09	147.1	323.6	75.0

Table 2. Material properties of CFRP composite lamina.

$E_L$ (GPa)	$E_T$ (GPa)	$\nu_{LT}$	$G_{LT}$ (GPa)	$\rho_k^f$ (kg/m <sup>3</sup> )
153.0	10.9	0.3	5.6	1590.0

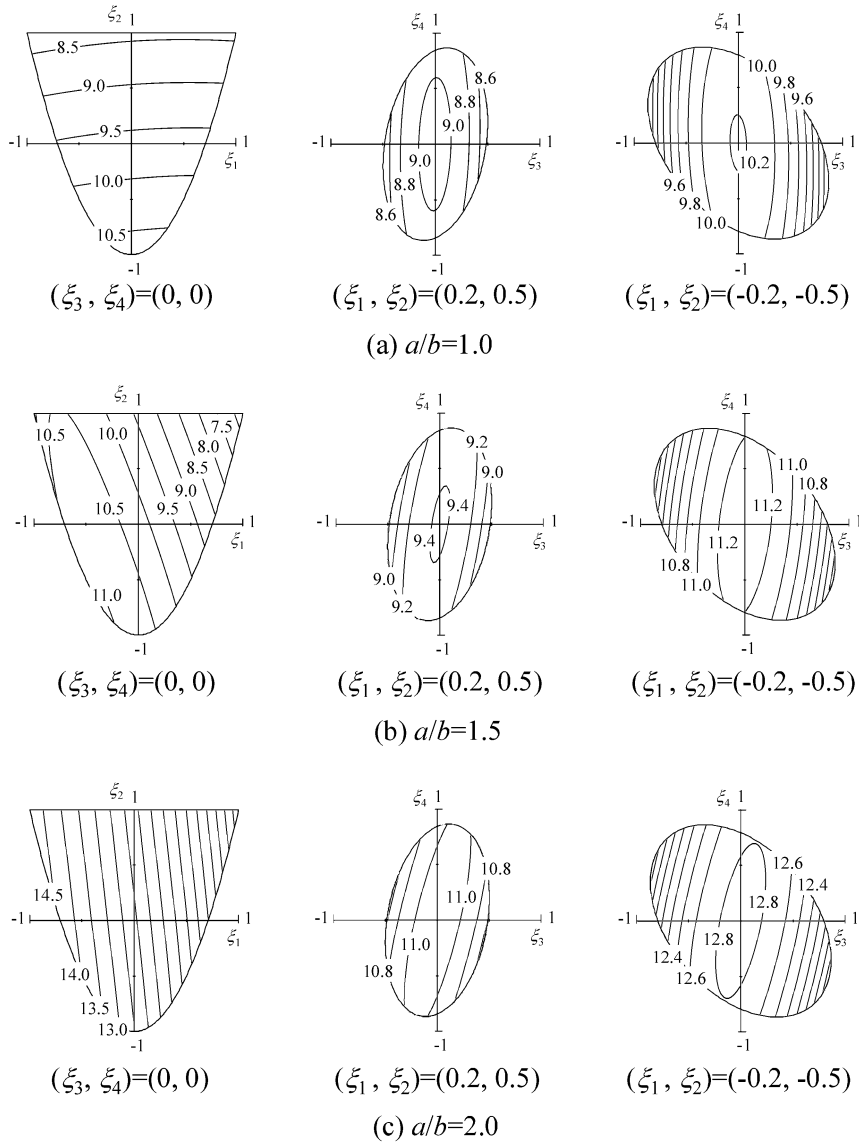


Figure 3. Contours of non-dimensional fundamental frequency  $\omega_1^*$  on the plane of in-plane lamination parameter.

### 3. LAYER OPTIMIZATION OF LAMINATED FRP COMPOSITE FACE

In this section, we examine the layup optimization problem of the laminated FRP composite face by a nonlinear mathematical programming method. The laminate configuration of the face is optimized using the four in-plane lamination parameters of the laminated FRP composite face as design variables.

#### 3.1 Formulation of the layup optimization problem

The layup optimization problem that the fundamental frequency of the composite sandwich plate is maximized, can be formulated as

$$\begin{aligned}
 &\text{maximize} && \omega_1^*(\xi_1, \xi_2, \xi_3, \xi_4) \\
 &\text{subject to} && \xi_1^2 + \xi_3^2 \leq 1 \\
 & && (\xi_2 - \xi_1^2 + \xi_3^2)^2 + (\xi_4 - 2\xi_1\xi_3)^2 \leq (1 - \xi_1^2 - \xi_3^2)^2 \quad (19) \\
 &\text{design variables} && \xi_1, \xi_2, \xi_3, \xi_4
 \end{aligned}$$

Constraints of this layup optimization problem indicate the feasible region of in-plane lamination parameter; this feasible region is expressed by Eqs. (8) and (9). The feasible direction method is used as an optimizer and the golden section method as a one-dimensional search in the ADS program [16].

#### 3.2 Optimization results

Table 3 lists the values of the optimum in-plane lamination parameters and the optimum laminate configuration of the laminated CFRP composite face

Table 3. Optimum lamination parameters and laminate configuration.

Boundary condition	Aspect ratio (a/b)	$\omega_1^*$	Optimum lamination parameters				Optimum laminate configuration
			$\xi_1$	$\xi_2$	$\xi_3$	$\xi_4$	
Simply supported	1.0	10.71	0.013	-1.000	-0.004	0.014	[44.6° <sub>0.50</sub> /-44.6° <sub>0.50</sub> ]
	1.5	11.81	-0.504	-0.493	-0.003	0.000	[60.1° <sub>0.50</sub> /-60.1° <sub>0.50</sub> ]
	2.0	14.84	-1.000	1.000	-0.001	0.000	[90.0° <sub>1.00</sub> ]
Clamped	1.0	16.98	0.443	1.000	0.002	0.000	[0.0° <sub>0.72</sub> /90.0° <sub>0.28</sub> ]
	1.5	22.07	-1.000	1.000	-0.001	0.000	[90.0° <sub>1.00</sub> ]
	2.0	28.95	-1.000	1.000	0.000	0.000	[90.0° <sub>1.00</sub> ]

when  $a/b$ ,  $a/h$  and  $h^c/h$  are taken as  $a/b = 1.0, 1.5, 2.0$ ,  $a/h = 50$  and  $h^c/h = 0.9$ . The rectangular composite sandwich plate is simply supported and clamped on the four edges. It is recognized from the table that the optimum values of the in-plane lamination parameters  $\xi_3$  and  $\xi_4$  are determined as  $\xi_3 = \xi_4 = 0.0$ , disregarding the error of numerical calculation. The optimum laminate configuration is of angle-ply or  $90^\circ$  unidirectional for the simply supported composite sandwich plate, and of  $0^\circ/90^\circ$  cross-ply or  $90^\circ$  unidirectional for the clamped one.

#### 4. CONCLUSIONS

We have examined the vibration characteristics of rectangular, symmetric composite sandwich plates and the layup optimization of the laminated FRP composite face. It has been based on the premise that the face is sufficiently thin, compared with the core. A two-dimensional finite element method has been developed by applying a higher-order shear deformation theory. First, the fundamental frequency of the composite sandwich plate has been discussed in the subspace of four in-plane lamination parameters of the laminated FRP composite face. The result has proved that the in-plane extension-shear coupling produces the decrease of the fundamental frequency. Next, examining the optimum laminate configuration of the laminated FRP composite face, which maximizes the fundamental frequency of the composite sandwich plate, we have found that the maximum fundamental frequency is realized in the case of the nonexistence of in-plane extension-shear coupling. Then, the optimum laminate configuration is of angle-ply or  $90^\circ$  unidirectional for the simply supported composite sandwich plate, and of  $0^\circ/90^\circ$  cross-ply or  $90^\circ$  unidirectional for the clamped one.

#### References

- [1] Y.Y. Yu. Flexural vibrations of elastic sandwich plates. *Journal of Aerospace Sciences*, 27(4): 272-282, 1960.
- [2] C.E.S. Ueng. Natural frequencies of vibration of an all-clamped rectangular sandwich panel. *Transactions of the ASME, Journal of Applied Mechanics*, 33(3): 683-684, 1966.
- [3] T.P. Khatua and Y.K. Cheung. Bending and vibration of multilayer sandwich beams and plates. *International Journal for Numerical Methods in Engineering*, 6(1): 11-24, 1973.
- [4] S.S.F. Ng and B. Das. Free vibration and buckling analysis of clamped skew sandwich plates by the Galerkin method. *Journal of Sound and Vibration*, 107(1): 97-106, 1986.
- [5] S. Mirza and N. Li. Analytical approach to free vibration of sandwich plates. *AIAA Journal*, 33(10): 1988-1990, 1995.
- [6] H.H. Kanematsu, Y. Hirano, and H. Iyama. Bending and vibration of CFRP-faced rectangular sandwich plates. *Composite Structures*, 10(2): 145-163, 1988.
- [7] M. Rais-Rohani and P. Marcellier. Buckling and vibration analysis of composite sandwich plates with elastic rotational edge restraints. *AIAA Journal*, 37(5): 579-587, 1999.

- [8] K. Sekine, O. Ichinomiya, and K. Maruyama. Bending and vibration analysis of composite rectangular sandwich plates (Effect of transverse shear deformation on face layers). *Transactions of the Japan Society of Mechanical Engineers, Series C*, 62(602): 3908-3914, 1996 (in Japanese).
- [9] L.J. Lee and Y.J. Fan. Bending and vibration analysis of composite sandwich plates. *Computers & Structures*, 60(1): 103-112, 1996.
- [10] A. Nabarrete, S.F.M. de Almeida, and J.S. Hansen. Sandwich-plate vibration analysis: Three-layer quasi-three-dimensional finite element model. *AIAA Journal*, 41(8): 1547-1555, 2003.
- [11] T. Kant and Mallikarjuna. A higher-order theory for free vibration of unsymmetrically laminated composite and sandwich plates - Finite element evaluations. *Computers & Structures*, 32(5): 1125-1132, 1989.
- [12] T. Kant and K. Swaminathan. Analytical solutions for free vibration of laminated composite and sandwich plates based on a higher-order refined theory. *Composite Structures*, 53(1): 73-85, 2001.
- [13] K.J. Duffy and S. Adali. Optimal fibre orientation of antisymmetric hybrid laminates for maximum fundamental frequency and frequency separation. *Journal of Sound and Vibration*, 146(2): 181-190, 1991.
- [14] S. Oskoei and J.S. Hansen. Higher-order finite element for sandwich plates. *AIAA Journal*, 38(3): 525-533, 2000.
- [15] H. Fukunaga and H. Sekine. A laminate design for elastic properties of symmetric laminates with extension-shear or bending-twisting coupling. *Journal of Composite Materials*, 28(8): 708-731, 1994.
- [16] G.N. Vanderplaats and H. Sugimoto. A general-purpose optimization program for engineering design. *Computers & Structures*, 24(1): 13-21, 1986.

# FLEXURAL VIBRATIONS OF A THREE-LAYER SANDWICH BEAM

*Using Ordinary Fourth Order Beam Theory in Combination with Frequency Dependent Parameters to Predict the Flexural Dynamics of a Sandwich Beam*

Daniel Backström and Anders Nilsson

*The Marcus Wallenberg Laboratory for Sound and Vibration Research,  
Department of Aeronautical and Vehicle Engineering, Kungl. Tekniska Högskolan  
Teknikringen 8, SE-100 44 Stockholm, Sweden*

baxtrom@kth.se, achn@kth.se

**Abstract** The purpose of this work has been to evaluate the possibility of using modified lower order methods – such as the Bernoulli-Euler or Timoshenko beam theories with frequency dependent parameters – to calculate the response of sandwich beams subject to different end conditions. The models have been verified by measurements on a freely suspended asymmetric sandwich beam with aluminium laminates and a plastic foam core, indicating good agreement.

**Keywords:** sandwich, beam, Bernoulli–Euler, Timoshenko, vibration.

## 1. INTRODUCTION

The need for strong and lightweight materials within the aircraft-, vehicle- and shipbuilding industries is increasing in the present-day society. Sandwich technology, which has been available to the industry since the 1950s, constitutes an important tool in the search for lighter, faster and more economical aircraft, rockets, cars, trains and ships.

The purpose of the work presented here is to provide means for quick but accurate modelling of composite beams using modified 4th order theory, such as the *Bernoulli–Euler* and *Timoshenko* beam theories. By implementing frequency dependent parameters, these low-order methods can achieve reasonably accurate predictions of the flexural dynamics of sandwich beams.

## 2. SIXTH ORDER THEORY

In order to obtain estimates for the frequency dependent parameters used by the low-order methods, the dynamic properties of a sixth order sandwich beam model is investigated. This model was derived for symmetric structures by Nilsson and Nilsson in [1] and generalized by Backström in [2], and takes into account the effects of pure bending of the entire structure, pure shear of the core, pure bending of the laminates due to shear of the core, and rotational inertia of the entire sandwich cross-section. The laminates are assumed to be thin enough to be correctly described by thin-beam theory. Also, they are assumed to move in phase, which is the case well below the “mass-spring-mass” frequency of the beam.

Thus, from [2], the set of governing equations are

$$(D_1 + D_2) \left( \frac{\partial^4 w}{\partial x^4} - \frac{\partial^3 \beta}{\partial x^3} \right) - G_c h_c \left( \frac{\partial^2 w}{\partial x^2} - \frac{\partial \beta}{\partial x} \right) + \mu_{\text{tot}} \frac{\partial^2 w}{\partial t^2} - p = 0, \quad (1)$$

$$- D_{\text{tot}} \frac{\partial^2 \beta}{\partial x^2} + (D_1 + D_2) \left( \frac{\partial^3 w}{\partial x^3} - \frac{\partial^2 \beta}{\partial x^2} \right) - G_c h_c \left( \frac{\partial w}{\partial x} - \beta \right) + I_{\text{tot}} \frac{\partial^2 \beta}{\partial t^2} = 0, \quad (2)$$

where  $w$  is the total lateral deformation,  $\beta$  is the angle of deformation due to pure bending of the structure,  $D_1$  and  $D_2$  are the bending stiffnesses per unit width of the laminates,  $D_{\text{tot}}$  is the total bending stiffness per unit width of the beam,  $I_{\text{tot}}$  is the mass moment of inertia per unit width of the beam,  $G_c$  is the effective shear modulus,  $h_c$  is the thickness of the core and  $\mu_{\text{tot}}$  is the total mass per unit length and width of the beam.

The boundary conditions are given as

$$F = -(D_1 + D_2) \left( \frac{\partial^3 w}{\partial x^3} - \frac{\partial^2 \beta}{\partial x^2} \right) + G_c h_c \left( \frac{\partial w}{\partial x} - \beta \right) \quad \text{or} \quad w = 0, \quad (3)$$

$$M = -D_{\text{tot}} \frac{\partial \beta}{\partial x} + (D_1 + D_2) \left( \frac{\partial^2 w}{\partial x^2} - \frac{\partial \beta}{\partial x} \right) \quad \text{or} \quad \beta = 0, \quad (4)$$

$$\frac{\partial^2 w}{\partial x^2} - \frac{\partial \beta}{\partial x} = 0 \quad \text{or} \quad \frac{\partial w}{\partial x} = 0, \quad (5)$$

where  $F$  is shear force per unit width and  $M$  is bending moment per unit width.

By assuming a time and space dependence  $e^{i(\omega t - kx)}$ , where  $\omega$  is the angular frequency and  $k$  the wavenumber, the *dispersion relation* – a sixth order polynomial equation – is obtained, see (6). This equation has even powers in  $k$  and

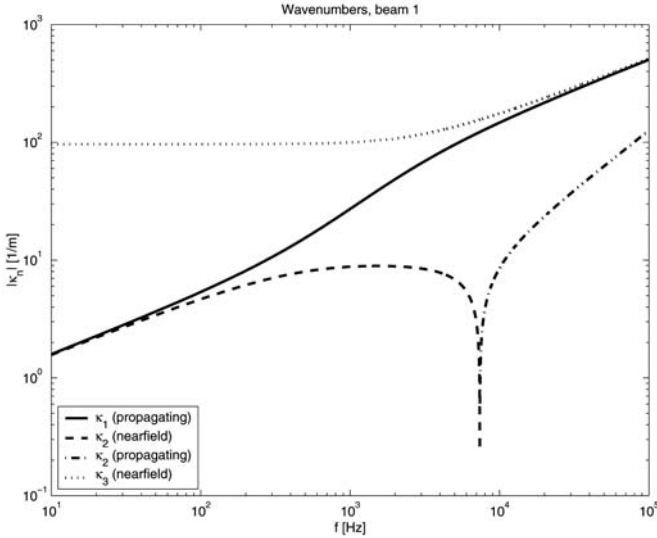


Figure 1. Wavenumbers of a typical sandwich configuration.

can easily be rewritten as a third order equation using a simple substitution.

$$\begin{aligned}
 & (D_1 + D_2)D_{tot}k^6 + (G_c h_c D_{tot} - \omega^2 I_{tot} (D_1 + D_2)) k^4 \\
 & - \omega^2 (\mu_{tot} (D_1 + D_2 + D_{tot}) + G_c h_c I_{tot}) k^2 + \mu_{tot} \omega^2 \\
 & \times (\omega^2 I_{tot} - G_c h_c) = 0.
 \end{aligned} \tag{6}$$

The three independent solutions are plotted for a given sandwich configuration in Figure 1. Below the cut-on frequency for rotational waves, there is one propagating wave corresponding to a real-valued  $k_1$ , and two nearfields corresponding to the imaginary  $k_2$  and  $k_3$ . The magnitudes of the wavenumbers are denoted  $\kappa_j$  and are defined by  $k = \pm\kappa_1, \pm i\kappa_2$  and  $\pm i\kappa_3$ .

### 2.1 Free vibration

The solution to the homogenous problem, i.e. when  $p = 0$  in equation (1), is obtained from inserting the homogenous solution into the given boundary conditions. This yields a matrix nullspace problem, where the eigenfrequencies are obtained from  $\det M = 0$ , where  $M$  is the  $6 \times 6$  system matrix, and the mode shapes can be obtained by assuming a unit first element in the coefficient vector and solving the reduced non-singular system. For simply supported end conditions the eigenfrequency relation is reduced to  $\sin \kappa_1 L = 0$ . Thus, by inserting  $\kappa_1 L = m\pi$  into (6) and solving for  $\omega$ , we obtain an explicit expression

for the eigenfrequencies of the system:

$$\omega_m = \frac{m^2 \pi^2}{L^2} \sqrt{\frac{D_{\text{tot}} \{ (D_1 + D_2) \pi^2 m^2 + G_c h_c L^2 \}}{\mu_{\text{tot}} \{ (D_{\text{tot}} + D_1 + D_2) \pi^2 m^2 + G_c h_c L^2 \}}}. \quad (7)$$

## 2.2 Forced vibration

The inhomogenous problem – when a force or bending moment distribution is exciting the beam – can be solved in terms of *Green's functions*. Consider a beam excited by a point force per unit width  $F_0 e^{i\omega t}$  at  $x = x_0$ , parallel to the  $z$ -axis. The boundary conditions at  $x = 0$  and  $x = L$  together with the coupling conditions at  $x = x_0$  yields a system of 12 equations, sufficient to solve for the unknown coefficient vectors as functions of the exciting force amplitude  $F_0$ . In matrix notation, where  $\mathbf{M}_-$  and  $\mathbf{M}_+$  denote the boundary condition matrices corresponding to  $x = 0$  and  $x = L$ , respectively, we have

$$\underbrace{\begin{pmatrix} \mathbf{M}_- & \mathbf{0} \\ & \mathbf{M}_c \\ \mathbf{0} & \mathbf{M}_+ \end{pmatrix}}_{\mathbf{M}_{\text{tot}}} \underbrace{\begin{pmatrix} \bar{\mathbf{A}}_- \\ \bar{\mathbf{A}}_+ \end{pmatrix}}_{\mathbf{A}_{\text{tot}}} = \bar{\mathbf{F}}, \quad (8)$$

where  $\mathbf{M}_c$  is a  $6 \times 12$  matrix describing the coupling conditions and  $\bar{\mathbf{A}}_{\text{tot}}$  is a vector containing the unknown coefficients.  $\bar{\mathbf{F}}$  contains the force amplitude  $F_0$  as its only non-zero element. The coupling conditions are obtained from (3) to (5), together with geometrical conditions considering continuity in total deformation  $w$ , total slope  $\frac{\partial w}{\partial x}$  and slope due to pure bending,  $\beta$ .

## 3. MODIFIED BERNOULLI-EULER THEORY

The simplest of the beam theories is the classical fourth order *Bernoulli-Euler* theory, which assumes that the lateral deformation of the beam is due to pure bending only, neglecting the effects of shear and rotational inertia. The governing equation is (for example, from [3])

$$D \frac{\partial^4 w}{\partial x^4} + \mu \frac{\partial^2 w}{\partial t^2} = p, \quad (9)$$

where  $D$  is the bending stiffness per unit width,  $\mu$  the mass per unit length and width and  $p$  the applied force per unit length and width of the beam. Inserting the ansatz  $w = w_0 e^{i(\omega t - k_{\text{BE}} x)}$ , where  $k_{\text{BE}}$  is the Bernoulli-Euler wavenumber, into (9) gives the dispersion relation as

$$k_{\text{BE}}^4 - \frac{\mu \omega^2}{D} = 0. \quad (10)$$

Table 1. Approximate values of  $\alpha_m L$  for some simple boundary conditions.

$m$	1	2	3	$\geq 4$
Simply supported	$\pi$	$2\pi$	$3\pi$	$m\pi$
Free-free or clamped-clamped	4.730	7.853	11.996	$\frac{2m+1}{2}\pi$
Clamped-simply supported	3.927	7.069	10.210	$\frac{4m+1}{4}\pi$
Clamped-free	1.875	4.694	7.855	$\frac{2m-1}{2}\pi$

Now, by solving (10) for the bending stiffness and replacing  $k_{BE}$  with  $k_1$ , obtained from (6), we obtain a simple estimate for the frequency dependent bending stiffness of a homogenized sandwich beam:

$$D_{app}(\omega) \approx \frac{\mu\omega^2}{k_1^4}. \tag{11}$$

The problem with this approach is the discarding of the two other wave numbers, implying that the effects of nearfields are not described as accurately as they could be. The apparent bending stiffness – as applicable to Bernoulli–Euler theory – should depend on boundary conditions in order to achieve an accurate description of the problem. For example, using (11) one will obtain the same eigenfrequencies for both clamped and free end conditions. This is true for Bernoulli–Euler beams, but not for sandwich composites. Also, the low-frequency asymptote of the bending stiffness will in general be overestimated (from thick beam statics, see for example [4]).

Another approach is to obtain a discrete estimate of the apparent bending stiffness from measured or calculated eigenfrequencies of the beam configuration. Thus,

$$D_{app}(\omega_m) = \frac{\mu\omega_m^2}{\alpha_m^4}, \tag{12}$$

where  $\alpha_m L$  is tabulated in Table 1.

A continuous bending stiffness curve can then be obtained by means of interpolation. The obvious disadvantage of this approach is the need for estimated eigenfrequencies of the system.

In Figure 2, the two different estimates are displayed for three common boundary conditions, for a typical sandwich beam configuration. The low-frequency asymptote of the bending stiffness also depends on the type of boundary condition and, in the case of forced response, on the force distribution. Note the typical reversed s-shape of the curves: the low-frequency asymptote of the bending stiffness is the high static bending stiffness of the sandwich beam. In the high-frequency region, where the core becomes transparent, the bending stiffness goes towards the sum of the bending stiffnesses of the laminates.

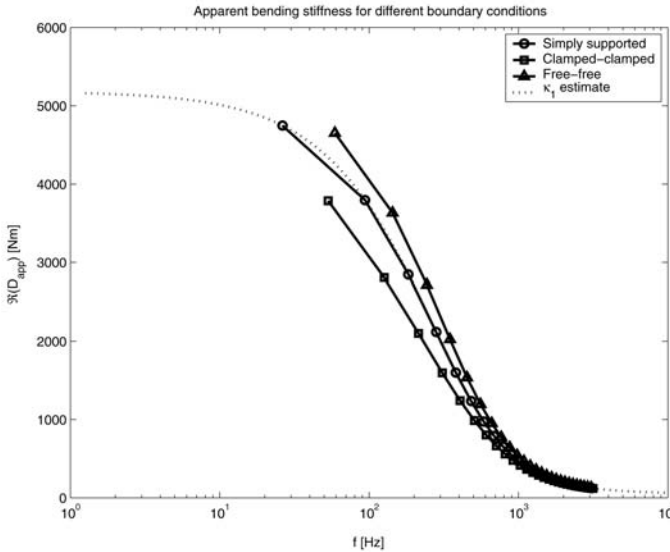


Figure 2. Different estimates of the apparent bending stiffness of a typical sandwich beam.

### 4. MODIFIED TIMOSHENKO THEORY

An alternative to the simple Bernoulli–Euler theory is the fourth order Timoshenko beam theory, where the effects of shear and rotational inertia of a homogenous beam are taken into account. The governing equation can be obtained from (6) by setting  $D_1 = D_2 = 0$ . Thus, the Timoshenko dispersion relation is (assuming the rotational inertia is negligible)

$$k_T^4 - \frac{\mu\omega^2}{Gh}k_T^2 - \frac{\mu\omega^2}{D} = 0, \tag{13}$$

where  $k_T$  is the Timoshenko wavenumber,  $G$  is the effective shear modulus of the beam and  $h$  the beam thickness. Thus, Timoshenko theory has two independent wavenumbers as compared to Bernoulli–Euler theory which has only one. Now, in order to modify this beam theory so that it approximates sandwich behaviour, we consider a fourth order polynomial equation with roots equal to the main propagating wavenumber  $\pm\kappa_1$  and the first nearfield wavenumber  $\pm\kappa_2$  (neglecting the second nearfield  $\kappa_3$  should be a valid simplification since it is highly localized to edges):

$$(k - \kappa_1)(k + \kappa_1)(k - i\kappa_2)(k + i\kappa_2) = k^4 + (\kappa_2^2 - \kappa_1^2)k^2 - \kappa_1^2\kappa_2^2. \tag{14}$$

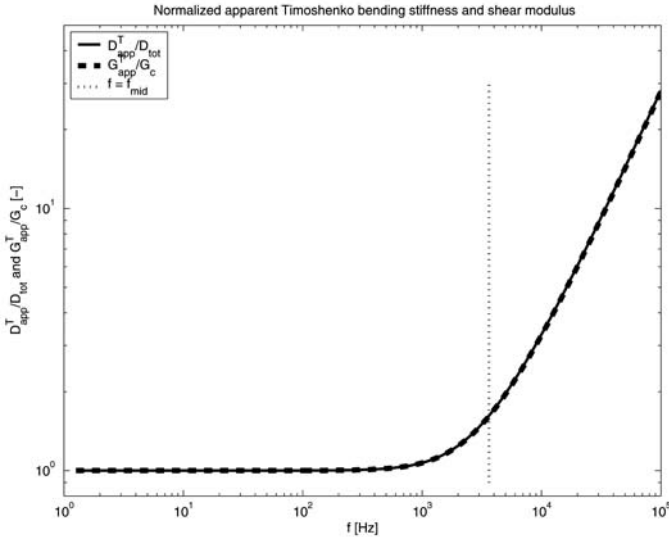


Figure 3. Apparent Timoshenko bending stiffness and shear modulus.

Now, by identifying the polynomial coefficients in (13), we obtain

$$\begin{aligned}
 D_{app}^T(\omega) &= \frac{\mu_{tot}\omega^2}{\kappa_1^2\kappa_2^2}, \\
 G_{app}^T(\omega) &= \frac{\mu_{tot}\omega^2}{h_c(\kappa_1^2 - \kappa_2^2)},
 \end{aligned}
 \tag{15}$$

where  $D_{app}^T$  and  $G_{app}^T$  are the apparent bending stiffness and shear modulus (also,  $\mu$  has been replaced by  $\mu_{tot}$  and  $h$  by  $h_c$ ). It can be shown that these entities have the following properties:

$$\begin{aligned}
 D_{app}^T(\omega) &\approx \begin{cases} D_{tot}, & \omega \ll \omega_{mid} \\ D_{tot} \frac{\sqrt{\mu_{tot}(D_1+D_2)}}{G_ch_c} \omega, & \omega \gg \omega_{mid} \end{cases} \\
 \omega_{mid} &= \frac{G_ch_c}{\sqrt{\mu_{tot}(D_1 + D_2)}}, \\
 G_{app}^T(\omega) &\approx \frac{G_c}{D_{tot}} D_{app}^T(\omega), \quad \omega \ll \omega_{mid} \text{ or } \omega \gg \omega_{mid}.
 \end{aligned}
 \tag{16}$$

where  $\omega_{mid}$  is a limit frequency below which ordinary Timoshenko theory provides a good approximation of the dynamics of the sandwich beam. In Figure 3 the normalized apparent Timoshenko bending stiffness and shear modulus are displayed for a typical sandwich beam.

The advantage of using modified Timoshenko theory instead of Bernoulli-Euler theory lies in the fact that the frequency dependent parameters utilized

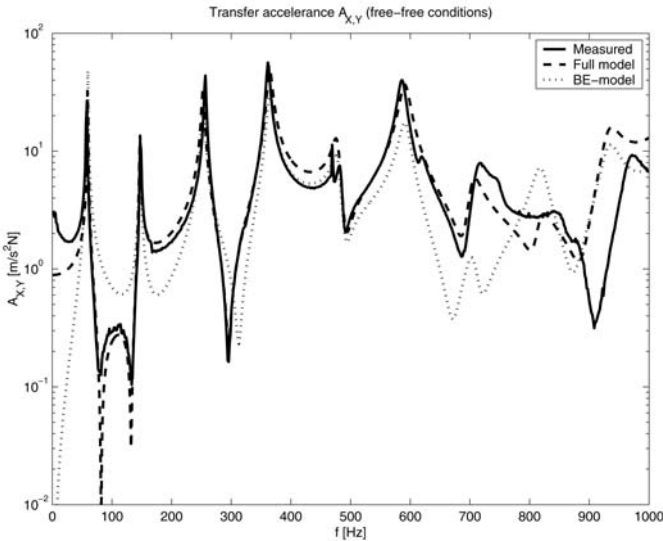


Figure 4. Predicted and measured transfer acceleration of a free-free sandwich beam.

by the Timoshenko model are independent of boundary conditions. The disadvantage is the increased complexity of the model.

## 5. VALIDATION

The modified Bernoulli–Euler theory has been validated against the sixth order theory and measurements, by comparing predicted and measured transfer acceleration functions (see Figure 4). For the modified Timoshenko theory, predicted eigenfrequencies for different boundary conditions have been compared to those obtained from the sixth order theory (see Figure 5). As can be seen from these figures, excellent results can be obtained using these modified methods.

## 6. CONCLUSIONS

The presented modified beam models provide a simplified approach to predicting the flexural dynamics of sandwich beams subject to different end conditions. The modified Bernoulli–Euler model is simple to implement, but the need for boundary condition-dependent estimates of the bending stiffness limits its applicability. The modified Timoshenko theory is by its nature a more complex model, but it does not suffer from the mentioned weakness of the Bernoulli–Euler theory.

One important potential application for these modified theories is FE modelling of complex structures comprising sandwich beam or plate elements. How-

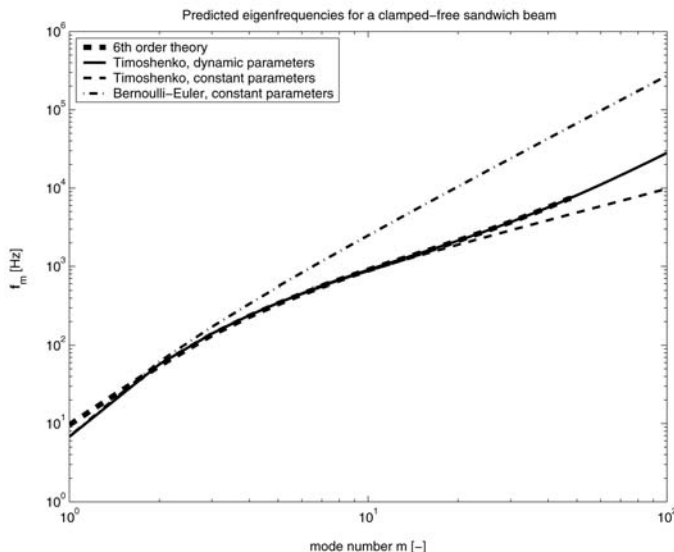


Figure 5. Predicted eigenfrequencies of a cantilever sandwich beam.

ever, the mentioned need for a boundary condition-dependent bending stiffness estimate in order to obtain the best possible results limits the usage of the modified Bernoulli–Euler theory. Also, transmission of energy across joints is not correctly described by either method in the high-frequency range.

Another application could be the calculation of the sound transmission loss of sandwich composite panels, using existing formulae together with frequency-dependent parameters.

## REFERENCES

- [1] E. Nilsson and A. C. Nilsson. Prediction and measurement of some dynamic properties of sandwich structures with honeycomb and foam cores. *Journal of Sound and Vibration*, 251(3):409–430, 2002.
- [2] D. Backström. *Modelling the Flexural Dynamics of Sandwich Beams using Bernoulli-Euler or Timoshenko Theory with Frequency Dependent Parameters*. Kungl. Tekniska Högskolan (KTH), Stockholm, 2004.
- [3] S. S. Rao. *Mechanical Vibrations*. Addison Wesley, 1990.
- [4] D. Zenkert. *An Introduction to Sandwich Construction*. Chameleon Press, London, 1995.

# AN EFFECTIVE 2D LINEAR ELASTICITY VIBRATIONAL MODEL FOR LAYERED AND SANDWICH CLAMPED-CLAMPED UNIDIRECTIONAL STRIPS

Stanislaw Karczmarzyk

*Institute of Machine Design Fundamentals, Warsaw University of Technology,  
02-524 Warsaw, Narbutta 84, Poland*

**Abstract** An effective new model for vibration analysis of the layered, and in particular sandwich, one-span, clamped-clamped (C-C) strips and beams is presented in the paper. The model is derived directly from the local linear elasticity model (solution) for the corresponding simply supported (S-S) structures after replacing the Fourier sinus series eigenfunctions with the Bernoulli-Euler eigenfunctions. The approach is verified by comparisons of numerical results obtained with the data available in the literature. Number of layers is unlimited but the model was elaborated for the structures composed of five layers.

**Keywords:** five-layer sandwich strip, vibration, linear elasticity, local semi-inverse approach, effective 2D model for the C-C structure.

## 1. INTRODUCTION

The paper is proposed after taking into consideration the following suggestions appearing in or resulting from the literature. First, in the past some effective edge solutions for the sandwich structures have been suggested. The solutions enable us to obtain easy fixing of the edges and a possibility of carrying the bending moment on one hand however they imply necessity of including in mathematical models of the structures some refined edge boundary conditions [1,2] on the other hand. Consequently, the latter fact implies higher costs of the static and vibration analysis of the structures.

Second, if we look for instance for an effective, low cost and enough accurate model of flexural free vibration of layered (in particular sandwich) 2D unidirectional clamped-clamped (C-C) structures we will find some difficulties to find the solution which would be proper for our purposes. In most papers we may easily find models which are easy to use and effective for the simply supported structures. The same remark refers to numerical results. It is rather difficult to find out in the literature numerical results (e.g. eigenfrequencies) for the unidirectional clamped-clamped sandwich and not very slender structures.

Third, the reader may find some suggestions in the literature that stiffness of the core of a sandwich structure should be a continuous function of the space variable in the thickness direction. Obviously, the core should be most stiff on its outer surfaces and most soft in the middle surface. Such demand is rather unrealistic because of the technology difficulties and the costs however it can be satisfied to some extent by replacing the homogeneous core by a three-layer core composed of two outer layers and a middle layer. The outer layers of the core must be (made) of a stiffer material than the middle layer. Let us notice finally that a sandwich structure with the three-layer core is composed of five layers. Moreover, the middle layer (the essential core) can be better protected against the impact loads than its counterpart in the classical sandwich three-layer structure.

As far as the author knows, the analytical local models for the vibration analysis of the five-layer sandwich structures have not been elaborated directly within the theory of linear elasticity so far. The present paper is proposed (also) to fill the gap. It is noted however that dynamics of laminated structures have been studied, e.g. in [3], within the procedure based on the three-dimensional theory of elasticity associated with so-called layerwise framework.

It is proposed here a new effective 2D linear elasticity vibration model for layered and in particular sandwich one-span clamped-clamped (C-C) unidirectional structures. Both the free and forced vibration have been taken into consideration. The model was elaborated after taking into account some conclusions resulting from the numerical analysis presented in paper [2]. To obtain the new effective model (computational procedure) a new hypothesis was assumed. The same functions of space variables as those appearing in papers [1, 2] are used. An effective numerical approach for the five-layer structures was proposed and the hypothesis introduced was verified for a few cases of vibrating layered structures. The verification was made by comparing the numerical results obtained according to the new model (procedure) with the corresponding results predicted by other models existing in the literature.

All through-the-thickness boundary and compatibility conditions for the displacements and stresses as well as the cross-sectional warping in each layer have been satisfied in the model proposed. The edge boundary conditions are similar to those published in papers [1, 2]. However, the edge conditions have been considered in a specific way - discussed in further text.

Accuracy of the model was tested by means of the results available in the literature - given in papers [4–6]. This presentation is a brief version of the paper [7] actually prepared to send to an editor.

## 2. AN OUTLINE OF THE LOCAL STATEMENT TO VIBRATION PROBLEM OF THE S-S STRIP

The equations of motion for the  $j$ -th layer, the Hooke law and the interface compatibility conditions of the local statement of the problem are expressed, in the well known form, by (1), (2) and (3), respectively:

$$\partial(\sigma_{kl})_j / \partial x_l = \rho_j \partial^2 u_{lj} / \partial t^2, \quad k, l = 1, 2, \quad (1)$$

$$(\sigma_{kl})_j = 2\mu_j (\varepsilon_{kl})_j + \lambda_j (\varepsilon_{nn})_j \delta_{kl}, \quad \delta_{kk} = 1, \quad k \neq l \Rightarrow \delta_{kl} = 0, \quad (2)$$

$$(\hat{\sigma}_{kl})_j = (\hat{\sigma}_{kl})_{j+1}, \quad (\hat{u}_l)_j = (\hat{u}_l)_{j+1}. \quad (3)$$

Symbols,  $\sigma_{kl}$ ,  $\varepsilon_{kl}$ ,  $u_l$  and in (1), (2) denote the stresses, displacements and strains, respectively. The analysis is limited to the isotropic layers. The compatibility conditions are satisfied between two adjoining layers denoted by the subscripts  $j$  and  $j+1$ . The boundary conditions on the outer surfaces of the structure composed of  $p$  layers are as follows,

$$(\hat{\sigma}_{kn})_1 = q_{k1}(x_1), \quad (\hat{\sigma}_{kn})_p = q_{kp}(x_1), \quad k = 1, 2, \quad l = 1, \quad n = 2. \quad (4)$$

Obviously, when the free vibration is considered the right-hand side functions appearing in (4) are equivalent to zero while for the forced vibration the functions must be defined. In the case of the forced flexural vibration only the right-hand side functions for the normal loading must be defined since those referring to the shear stresses are equivalent to zero.

The edge boundary conditions, within the local approach, for the simply supported (S-S) structure can be expressed as follows,

$$u_{n_j}(\hat{x}_l) = 0, \quad (\sigma_{ll}(\hat{x}_l))_j = 0, \quad l = 1, \quad n = 2. \quad (5)$$

The edge conditions (5) are not the exact linear elasticity boundary conditions. They are artificial, thus rather impossible for exact observation in the realistic structures, since both the deflections  $u_{2j}$  and the normal stresses  $(\sigma_{11})_j$  for each ( $j$ -th) layer are equivalent to zero at the edges irrespective of the value of the variable  $x_2$  (in the thickness direction).

The local linear elasticity vibration problem, for the layered simply supported (S-S) strip or beam, expressed by (1)-(5), was solved by many authors by means of the following kinematic assumptions,

$$\begin{aligned} u_{x_j} &= -\sum_m g_{jm}(z) \partial W_m / \partial x T_m(t), \quad W_m(x) = \sin(m\pi x / L), \\ u_{z_j} &= \sum_m f_{jm}(z) W_m(x) T_m(t), \quad m = 1, 2, 3, \dots \end{aligned} \quad (6a,b)$$

The relationships between the coordinates appearing in (1)-(5) and those used in (6) are as follows,  $x_1 \equiv x$ ,  $x_2 \equiv z$ . It is noted that the Fourier series functions of variable  $x$ ,  $\sin(\alpha_m x)$  while  $\alpha_m = m\pi/L$ , satisfy the edge boundary conditions (5). The corresponding functions of variable  $z$  are unknown however they are obtainable from the equations of motion (1) after taking into consideration the Hooke law. Symbol  $T_m(t)$  denotes the exponential time function while  $L$  is length of the structure. Application of the assumptions (6) to solve the equations of motion (1), and consequently the vibration problem, or the static bending problem when  $T_m(t)=1$ , of one-dimensional and two-dimensional structures, has been called in the literature as the semi-inverse approach (method). It is sometimes called as the "exact" linear elasticity approach.

Let us notice finally that the final (numerical) forms of the free vibration problem and the forced vibration problem within the semi-inverse approach can be expressed as follows, respectively,

$$\det(\underline{A}_m) = 0, \quad \underline{A}_m C_m = q_m, \quad m = 1, 2, 3, \dots \quad (7a,b)$$

The matrices in (7a,b) for the S-S structures result entirely from through-the-thickness conditions (3), (4). The symbols  $C_m$  and  $q_m$  denote the unknown vector and the loading vector, respectively. Obviously, the vector  $q_m$  is obtained after expansion of the loading into the Fourier sinus series.

### 3. A NEW EXTENSION OF THE SEMI-INVERSE APPROACH FOR THE C-C BEAM AND STRIP

The present author combined the semi-inverse approach and the superposition technique in order to obtain a few local linear elasticity solutions to vibration and static problems of one-span, layered, one-dimensional and two-dimensional, structural members with fixed ("clamped") edges [1, 2, 8, 9]. Moreover, the combined approach was also successfully applied to solve the forced vibration problem of a multi-span layered unidirectional structure [10].

In all the above solutions the present author has not applied the Fourier series. Unlike the displacements (6a), the displacement fields and the solutions given in [8, 9, 10] have been obtained without the a-priori expansions of the functions of the space variables into series. On the other hand, the solution given in [1] has been obtained with application of the a-priori expansions of the displacements and stresses into the series (but) composed of the Bernoulli-Euler eigenfunctions.

The approach presented in paper [1] enables us to include in the problem statement some refined edge boundary conditions which very well correspond to the realistic edge fixing ("clamping") of the sandwich structures by means of edge stiffeners such as e.g., the C-profiles. Unfortunately, dimensions of the stiffness matrix of the final (numerical) form of the problem solved in [1] depend on the number of components of the Bernoulli-Euler series and the fact is not convenient for many reasons.

In this paper a new effective application of the semi-inverse approach to solve some vibration problems of unidirectional layered (including sandwich) clamped-clamped (C-C) structures is proposed. After taking into consideration some basic conclusions resulting from the analysis given in paper [2] a new hypothesis is proposed and verified numerically.

It is shown here that by replacing the Fourier series eigenfunctions (6b) with the Bernoulli-Euler eigenfunctions one obtains directly from the solutions (7a,b) for the simply supported (S-S) structures some enough accurate solutions for the corresponding C-C structures.

The Bernoulli-Euler symmetric eigenfunctions can be expressed as follows [1, 2],

$$\phi_m(x_1) = \frac{\cos(\alpha_m x_1)}{\cos(\alpha_m L/2)} - \frac{\cosh(\alpha_m x_1)}{\cosh(\alpha_m L/2)}, \quad m = 1, 2, 3, \dots, \quad (8a)$$

$$\alpha_1 L/2 \cong 2.36504, \quad \alpha_m L/2 \cong (4m-1)\pi/4, \quad m = 2, 3, 4, \dots \quad (8b)$$

The Bernoulli-Euler unsymmetric eigenfunctions are as follows [1, 2],

$$\psi_n(x_1) = \frac{\sin(\gamma_n x_1)}{\sin(\gamma_n L/2)} - \frac{\sinh(\gamma_n x_1)}{\sinh(\gamma_n L/2)}, \quad n = 1, 2, 3, \dots, \tag{9a,b}$$

$$\gamma_1 L/2 \cong 3.927, \quad \gamma_n L/2 \cong (4n + 1)\pi/4, \quad n = 2, 3, 4, \dots .$$

The relationship between the space variable  $x$  appearing in the Fourier functions (6b) and the variable  $x_1$  in expressions (8a), (9a) is given below,

$$x = x_1 + L/2. \tag{10}$$

The hypothesis proposed here can now be expressed as follows. By replacing the functions  $W_m(x)$  for  $m=1,3,5, \dots$  with the functions  $\phi_m(x_1)$  for  $m=1,2,3, \dots$  we transform the symmetric vibration problems (7a,b) for the S-S structure to the corresponding problems of symmetric vibration of the C-C structure. Analogously, after replacing the functions  $W_m(x)$  for  $m=2,4,6, \dots$  with the functions  $\psi_n(x_1)$  for  $n=1,2,3, \dots$  we transform the unsymmetric vibration problems (7a,b) for the S-S structure to the corresponding problems of unsymmetric vibration of the C-C structure.

As a consequence of the above statements we should express (for the C-C structure) the displacements as follows,

$$\begin{aligned} u_{x_j} &= -\sum_m g_{jm}(z) \partial \phi_m / \partial x_1 T_m(t), \\ u_{z_j} &= \sum_m f_{jm}(z) \phi_m(x) T_m(t), \quad m = 1, 2, 3, \dots \\ u_{x_j} &= -\sum_m g_{jn}(z) \partial \psi_n / \partial x_1 T_n(t), \\ u_{z_j} &= \sum_m f_{jn}(z) \psi_n(x) T_n(t), \quad n = 1, 2, 3, \dots . \end{aligned} \tag{11a,b}$$

It is noted however that the displacements (11a,b) do not satisfy the equations of motion (1) for any value of the variable  $z$ . (It is reminded that the axis  $z$  is perpendicular to the interfaces between adjoining layers.). Apart from that, the final (numerical) forms (7a,b) of the vibration problems of the C-C structures have been obtained without the formal satisfying the edge boundary conditions. The edge conditions are only included in the Bernoulli-Euler eigenfunctions applied in the model (procedure). This means that the

numerical results predicted by the procedure proposed here may not be enough accurate for some structures.

#### 4. ASSESSMENT OF THE NUMERICAL RESULTS

Eigenfrequencies predicted by the procedure proposed in this paper were compared with numerical data existing in the literature for the classical three-layer slender sandwich C-C beam [4, 5] and for a three-layer steel-aluminium-steel sandwich C-C beam [6]. In Tables 1, 3 the parameters of the beams are given. The comparisons for the C-C beams are presented in Tables 2 and 4, respectively.

Table 1. Parameters of the classical sandwich three-layer beam.

Layer	h [mm]	E [Pa]	$\nu$	$\rho$ [kg/m <sup>3</sup> ]
Face 1	0.40624	$0.6890 \cdot 10^{11}$	0.33	2687.3
Core	6.34750	$0.1833 \cdot 10^9$	0.33	119.69
Face 2	0.40624	$0.6890 \cdot 10^{11}$	0.33	2687.3

Table 2. Eigenfrequencies of the three-layer classical sandwich C-C beam, L=1218.72 mm.

Mode no.	1(s)	2(a)	3(s)	4(a)	5(s)	6(a)
$\omega_K$ [rad/s]	220.50	597.91	1144.04	1834.65	2645.10	3551.41
$\omega_R$ [rad/s]	229.88	617.81	1173.84	1872.01	2685.55	3596.01
$\omega_{sak}$ [rad/s]	210.88	567.77	1081.15	1727.31	2484.50	3332.22
$\Delta_{RK}$ [%]	4.08	3.22	2.54	1.99	1.51	1.24
$\Delta_{Ksak}$ [%]	4.56	5.31	5.82	6.21	6.46	6.58

Table 3. Parameters of the sandwich steel-aluminium-steel beam.

Layer	h [mm]	E [Pa]	$\nu$	$\rho$ [kg/m <sup>3</sup> ]
Face 1	0.5	$0.2067 \cdot 10^{12}$	0.33	8061
Core	19.0	$0.6890 \cdot 10^{11}$	0.33	2687
Face 2	0.5	$0.2067 \cdot 10^{12}$	0.33	8061

Table 4. Eigenfrequencies of the steel-aluminium-steel sandwich thickset C-C beam.

Mode no.	1(s) L=231	2(a) L=231	3(s) L=231	4(a) L=115.5	5(s) L=115.5	6(a) L=115.5
$\omega_K$ [rad/s]	12826.37	33602.97	61654.75	47198.31	112486.5	189090.0
$\omega_S$ [rad/s]	12646.85	33685.46	60881.99	45019.18	108514.3	183536.0
$\Delta_{KS}$ [%]	1.42	-0.25	1.27	4.84	3.66	3.03

It can be seen in Table 2 that eigenfrequencies  $\omega_R$  of the classical sandwich beam with a soft core resulting from the Raville et al. solution [4] are higher than the present author results  $\omega_K$  - predicted by the procedure proposed. The percentage differences  $\Delta_{RK}$  between  $\omega_R$  and  $\omega_K$  are higher for

the lower vibration modes. On the other hand, the eigenfrequencies  $\omega_K$  are higher than the eigenfrequencies  $\omega_{sak}$  given in the paper by Sakiyama et al. [5]. It means that the procedure proposed in the paper predicts rather accurate results for the slender classical sandwich (three-layer) structures.

In Table 4 one can observe a good agreement (small percentage differences  $\Delta_{KS}$ ) between the present author numerical results  $\omega_K$  and the results denoted by  $\omega_S$  given by Silverman [6] for a thickset sandwich steel-aluminium-steel beam. The agreement is better for the more slender structure 231 mm long than for the second one 115.5 mm long.

The good agreement between  $\omega_K$  and  $\omega_S$  revealed in Table 4 means that the procedure (model) proposed in this paper enables us to obtain accurate eigenfrequencies for the C-C classical unidirectional laminated structures when stiffnesses of the adjoining layers are comparable.

Unfortunately, the present author did not find in the literature numerical results for not slender classical three-layer sandwich strips or beams as well as for the five-layer sandwich structures. Therefore, the computations were made only for two five-layer sandwich strips. Parameters of the first five-layer strip are given in Table 5 while its fundamental eigenfrequencies for different values of length L and for the C-C edges are listed in Table 6.

Table 5. Parameters of the 1<sup>st</sup> five-layer sandwich strip.

Layer	h [mm]	E [Pa]	$\nu$	$\rho$ [kg/m <sup>3</sup> ]
Layer 1 - face 1	1	$0.6890 \cdot 10^{11}$	0.276	2680
Layer 2	0.75	$0.3900 \cdot 10^{10}$	0.08	1175
Layer 3 - core	61.5	$0.3059 \cdot 10^9$	0.85	32.8
Layer 4	0.75	$0.3900 \cdot 10^{10}$	0.08	1175
Layer5 - face 2	1	$0.6890 \cdot 10^{11}$	0.276	2680

Table 6. Fundamenal eigenfrequencies of the 1<sup>st</sup> five-layer sandwich C-C strip.

L [mm]	1000	1200	1400	1600	1800	2000
$\omega_{1cc}$ [rad/s]	2416.77	1792.22	1376.65	1087.52	879.00	724.22

It is noted that  $\nu=0.85$  in Table 5 refers to the core (made) of the honeycomb structure. Due to this value of the Poisson ratio the honeycomb middle layer (core) can be treated as an isotropic material.

In Table 7 the geometrical parameters of the second five-layer sandwich strip are given. The physical (strength) parameters in this case are the same as in the Table 5. Again the first mode eigenfrequencies both for the C-C structure and for its S-S counterpart were calculated and listed in Table 8.

Table 7. Geometrical parameters of the 2<sup>nd</sup> five-layer sandwich strip [mm].

Layer1 - face1	Layer 2	Layer 3 - core	Layer 4	Layer 5 - face 2
1	1.5	60	1.5	1

Table 8. First mode eigenfrequencies of the symmetric vibration of the 2<sup>nd</sup> five-layer sandwich C-C strip and first mode eigenfrequencies of the same S-S strip [rad/s].

L [mm]	1000	1200	1400	1600	1800	2000
$\omega_{1cc}$	2238.05	1660.22	1275.60	1007.82	814.99	671.35
$\omega_{1ss}$	1122.9	809.1	609.1	473.7	379.0	313.4

It is noticed that eigenfrequencies of the second five-layer sandwich strip are lower than of the first one. One can also observe in Table 8 that the eigenfrequencies of the C-C strip are approximately two times higher than eigenfrequencies of the S-S strip.

In Table 9 the maximum deflections of the second five-layer C-C strip of length 1.2 m are listed. The maximum value of the uniformly distributed loading of the structure equals to  $0.2 \cdot 10^4$  Pa. The results were computed, according to the procedure proposed in the paper, for fifteen members of the Bernoulli-Euler series (8a).

Table 9. The maximum flexural displacements of the 2<sup>nd</sup> five-layer sandwich C-C strip 1.2 m long under uniformly distributed harmonic load in the vicinity of the first eigenfrequency.

$\omega$ rad/s	1600	1620	1640	1650	1670	1680	1700	1800
$u_z$ [m]	$.12 \cdot 10^{-2}$	$.18 \cdot 10^{-2}$	$.36 \cdot 10^{-2}$	$.71 \cdot 10^{-2}$	$.74 \cdot 10^{-2}$	$.33 \cdot 10^{-2}$	$.18 \cdot 10^{-2}$	$.05 \cdot 10^{-2}$

It is finally noted that the eigenfrequency given in Table 8 was confirmed by the results listed in Table 9. Within the frequency range (1600, 1650) rad/s the deflections increase in domain of frequency while in the range (1670, 1800) rad/s the deflections decrease in domain of frequency.

## 5. CONCLUDING REMARKS

A new procedure (model) for vibration analysis of multi-layer (including five-layer sandwich) C-C strip and beam was proposed and assessed for some data available in the literature. Only isotropic layers have been taken into consideration. The model predicts accurate results for the classical three-layer sandwich slender C-C beams and for the three-layer steel-aluminium-steel not slender C-C beams. The model can also be applied for the vibration analysis of the laminated C-C structures when the stiffnesses of the adjoining layers are comparable.

## ACKNOWLEDGMENT

The author wishes to thank to Chairman of the 7<sup>th</sup> International Conference on Sandwich Structures Professor Dr. O.T. Thomsen and to the

Aalborg University as well as to the Organising Committee for exempting him from the conference registration fee.

## REFERENCES

1. Karczmarzyk, S., "New 2D Approach and Solution to the Static Transverse Bending Problem for a Sandwich Strip with Realistic Clampings of the Edges", *Journal of Sandwich Structures and Materials*, Vol. 6, No. 1, pp 7-45, 2004.
2. Karczmarzyk, S., Meyer-Piening, H.-R. and Caviezel, M., "Numerical and Experimental Analysis of the Influence of Edge Conditions on the Deflection of a Clamped-Clamped Asymmetric Sandwich Strip", *Journal of Sandwich Structures and Materials*, Vol. 5, No. 4, pp 119-145, 2003.
3. Liew, K.M., Zhang, J.Z., Ng, T.Y., Reddy, J.N., "Dynamic Characteristics of Elastic Bonding in Composite Laminates: A Free Vibration Study", *ASME Journal of Applied Mechanics*, Vol. 70, November, pp 860-870, 2003.
4. Raville, M.E., Ueng, E.-S. and Lei, M.-M., "Natural Frequencies of Vibration of Fixed-Fixed Sandwich Beams", *ASME Journal of Applied Mechanics*, Vol. 28, September, pp 367-371, 1961.
5. Sakiyama, T., Matsuda, H. and Morita, C., "Free vibration analysis of continuous sandwich beams with elastic or viscoelastic cores by applying the discrete Green function", *Journal of Sound and Vibration*, Vol. 198, No. 4, pp 439-454, 1996.
6. Silverman, I. K., "Natural frequencies of sandwich beams including shear and rotary effects", *Journal of Sound and Vibration*, Vol. 183, No. 3, pp 547-561, 1995.
7. Karczmarzyk, S., "An effective vibration analysis of viscoelastic realistic sandwich unidirectional structures with including thermal effects", is prepared to send to an editor.
8. Karczmarzyk, S., "An exact elastodynamic solution to vibration problems of a composite structure in the plane stress state", *Journal of Sound and Vibration*, Vol. 196, No. 1, pp 85-96, 1996.
9. Karczmarzyk, S. "New elastodynamic solutions to forced vibration problems of layered rectangular viscoelastic plates", in *Mechanics of Sandwich Structures* (A. Vautrin, Ed.), Kluwer Academic Publishers, Dordrecht/Boston/London, pp. 223-230, 1998.
10. Karczmarzyk, S., "Two-dimensional solutions to forced vibration problems of multi-span, layered, viscoelastic beams and strips", in *Sandwich Construction 4*, (K.A. Olsson, Ed), EMAS Publishing, Cradley Heath, West Midlands, UK, Vol. 2, pp 769-780, 1998.

# MINIMIZATION OF ACOUSTIC RADIATION FROM COMPOSITE SANDWICH STRUCTURES

H. Denli and J.Q. Sun

*Department of Mechanical Engineering, University of Delaware, Newark, DE 19716, USA*

sun@me.udel.edu

**Abstract** This paper presents a study of structural-acoustic optimizations of sandwich structures for minimal sound radiation. A sublaminar modeling approach of sandwich structures with a proper balance of accuracy and computational efficiency is adopted in this work. Finite elements are used to compute the vibration response and acoustic radiation of the structure. The material and geometric properties of an anisotropic sandwich are treated as design parameters. The objective of optimization is to minimize the acoustic power radiated by the structure. A piecewise objective function is studied that includes nonlinear constraints of the optimization problem in a nature way by taking advantages of the pattern search algorithm. Numerical examples are presented to show the effectiveness of the structural-acoustic optimization in terms of the reduction of the radiated sound power.

**Keywords:** sandwich optimization, minimum sound transmission, anisotropic materials.

## 1. INTRODUCTION

Composite sandwich structures are widely used in the aerospace industry. These structures can be tailored to optimally achieve certain objectives. Our objective is to minimize the acoustic power radiated by the structure. This is accomplished by optimizing the structure with respect to a set of material or geometrical parameters. Optimizing material and geometric properties has become practically feasible due to the advances in composite manufacturing technologies and in numerical methods.

Minimization of structural sound radiation with respect to the geometry of beams and plates has been studied in detail by Koopmann, Belegundu and Tinnsten [1–3]. Thamburaj and Sun have studied optimization problems of sound transmission loss with respect to geometric and anisotropic material parameters of sandwich beams [4,5]. Cunfare and Naghshined have developed an inverse approach to design structures that radiate sound inefficiently [6–8].

The inverse approach proposes to first develop surface velocity profiles with minimum acoustic radiation known as "weak radiators" [9], and then optimize the structure with respect to a set of structural design parameters to meet the desired velocity profiles.

Structural modeling of laminated structures is a key step in optimization studies. The model needs to be computationally efficient, and sufficiently accurate to describe the inter-laminate dynamics of the sandwich structure. Many structural models have been proposed in the literature and can be found in the review articles [10, 11]. A class of models in which we are interested have been reviewed by Reddy and Noor et al. [12, 13]. These models originally developed for thick laminated structures consist of a combination of fully and partially layerwise models and variable kinetic theories.

In this work, an optimization of sandwich structures for minimal sound radiation is studied. A method of sequentially coupled structural-acoustic system is presented. First, we develop a layerwise theory with sublaminated approach to model the sandwich structure, and derive the equations of motion of the structure under harmonic excitations by using finite elements. Next, we obtain the acoustic power radiated by the structure by using the Rayleigh integral leading to a quadratic form in terms of the normal velocities on the radiating surface of the sandwich. Finally, we study the optimization problem for minimizing the acoustic power with respect to a set of design parameters subject to the constraints. The optimization problem is solved by using a direct search optimization technique [14]. Numerical results are presented to demonstrate the theoretical development.

## **2. STRUCTURAL ANALYSIS**

The analysis of sandwich structures with anisotropic material discontinuity between laminates requires the determination of three-dimensional (3-D) stress field [15]. However, direct 3-D modeling of the sandwich is computationally inefficient. Layerwise models have been proposed to improve the computational efficiency. Even though the layerwise theory is computationally more efficient than direct 3-D theories, the number of degrees of freedom in the layerwise theory still depends on the number of actual physical layers. A compromising solution for computational efficiency and accuracy is to use sublaminated approach with layerwise modeling [16]. Each sublaminated contains a number of physical layers which are modelled by this sublaminated using the equivalent single layer theory.

Consider a sandwich beam as an example. The sandwich beam is split into several sublaminates which are constructed out of a group of physical layers. We assume that the displacement fields of each sublaminated are expanded in

power series of the thickness coordinate of the sublaminates

$$u^k(x, z^k) = \sum_{m=1}^M (z^k)^m u_m^k(x), \quad w^k(x, z^k) = \sum_{n=1}^N (z^k)^n w_n^k(x), \quad (1)$$

where  $k$  is an index of the sublaminates,  $z^k$  is the local thickness coordinate, and  $u_m^k(x)$  and  $w_n^k(x)$  are the lateral and transverse displacement shape functions.

Based on these kinematic assumptions, we develop a finite element model of the sandwich beam. The elemental displacement field of the  $k^{th}$  sublaminates can be expressed as a function of nodal displacements.

$$\mathbf{w}_e^k = \left\{ \begin{matrix} u_e^k \\ w_e^k \end{matrix} \right\} = \mathbf{Z}_M \mathbf{B}_M \mathbf{u}_e^k, \quad (2)$$

where  $\mathbf{Z}_M$  matrix is the only function of transverse coordinate  $z^k$  and  $\mathbf{B}_M$  matrix is the only function of in-plane coordinates, and  $\mathbf{w}_e^k$  is the local displacement vector. The infinitesimal strain-displacement relationship is

$$\left\{ \begin{matrix} (\epsilon_x)_e^k \\ (\epsilon_z)_e^k \\ (\gamma_{xz})_e^k \end{matrix} \right\} = \begin{bmatrix} \frac{\partial}{\partial x} & 0 \\ 0 & \frac{\partial}{\partial z} \\ \frac{\partial}{\partial z} & \frac{\partial}{\partial x} \end{bmatrix} \mathbf{w}_e^k, \quad \text{or } \gamma_e^k = \mathbf{Z}_K \mathbf{B}_K \mathbf{u}_e^k, \quad (3)$$

where again  $\mathbf{Z}_K$ , and  $\mathbf{B}_K$  are the matrices depending on only transverse and lateral coordinates respectively.

In the  $l^{th}$  physical layer of the  $k^{th}$  sublaminates of the beam, the stresses can be computed from the constitutive relation as  $\tau_e^l = \mathbf{Q}^l \gamma_e^k$  where  $\mathbf{Q}^l$  is the  $3 \times 3$  elastic modulus matrix. Thus, the element stiffness and mass matrices of the  $k^{th}$  sublaminates can be expressed as

$$\mathbf{K}_e^k = b \int_{-1}^1 (\mathbf{B}_K)^T \left( \int_{h_{i-1}}^{h_i} \mathbf{Z}_K^T \mathbf{Q}^l \mathbf{Z}_K dz \right)^k \mathbf{B}_K \frac{L_e}{2} dr, \quad (4)$$

$$\mathbf{M}_e^k = b \int_{-1}^1 (\mathbf{B}_M)^T \left( \int_{h_{i-1}}^{h_i} \mathbf{Z}_M^T \mathbf{R}^l \mathbf{Z}_M dz \right)^k \mathbf{B}_M \frac{L_e}{2} dr,$$

where  $b$  is the width of the beam,  $L_e$  is the element length and  $\mathbf{R}^l$  is the mass density matrix of the  $l^{th}$  physical layer.

The assembly of local element matrices and nodal displacements along transverse and lateral directions gives the global mass and stiffness matrices and global nodal displacement vector denoted by  $\mathbf{K}$ ,  $\mathbf{M}$  and  $\mathbf{u}$  respectively.

Assume that the sandwich beam is subject to a harmonic excitation such that the nodal force vector takes the form  $\mathbf{f} e^{j\omega t}$ . Further, we assume that the

structural damping loss of the beam is characterized by a nodal damping matrix  $\mathbf{C}$ , and the solution of the system is in the form  $\mathbf{u}e^{j\omega t}$ . By going through the steps, we arrive at the equations of motion for  $\mathbf{u}$  in the frequency domain as

$$[\mathbf{K} + j\omega\mathbf{C} - \omega^2\mathbf{M}]\mathbf{u} = \mathbf{f}. \tag{5}$$

The boundary conditions of the sandwich beam can be imposed on  $\mathbf{u}$  in the solution process. In the analysis below, we shall assume a Rayleigh damping such that  $\mathbf{C} = \alpha\mathbf{K} + \beta\mathbf{M}$  where  $\alpha$  and  $\beta$  are prespecified constants.

### 3. ACOUSTIC ANALYSIS

Assume that the sandwich beam is infinitely baffled. In this study, we neglect the reverse fluid loading on the bottom surface of the beam. Consider a plane acoustic wave of frequency  $\omega$  that excites the top of the beam. The resultant acoustic pressure distribution on the beam is given by

$$p_i(x, \omega) = Ae^{jk \cos(\theta)x} e^{j\omega t} \equiv p_i(x)e^{j\omega t}, \tag{6}$$

where  $k$  is the wave number of the sound wave,  $\theta$  is the incident angle and  $A$  is the pre-described amplitude of the acoustic pressure. On the bottom surface of the beam, the transmitted acoustic pressure  $p_t(\mathbf{r}_{S'})e^{j\omega t}$  at an observation point  $\mathbf{r}_{S'}$  due to the surface normal velocity  $v(\mathbf{r}_S)$  can be written as

$$p_t(\mathbf{r}_{S'}) = \frac{i\omega\rho_a}{2\pi} \int_S v(\mathbf{r}_S) \frac{e^{-ikR}}{R} dS. \tag{7}$$

where  $\rho_a$  is the air density,  $\mathbf{r}_S$  is the position vector of the surface element  $dS$  with the normal velocity  $v(\mathbf{r}_S)$ ,  $S$  is the vibrating surface of the beam, and  $R = |\mathbf{r}_S - \mathbf{r}_{S'}|$ . In the two dimensional space, we shall denote  $\mathbf{r}_S = (x)$  and  $\mathbf{r}_{S'} = (s)$ . Equation (7) is known as the Rayleigh integral.

Consider a receiver point  $\mathbf{r}_{S'}$  on the radiating surface of the beam. The acoustic power  $W$  radiated from the baffled beam is given by a quadratic expression of the normal velocities as

$$W = \frac{1}{2} \mathbf{v}^T \mathbf{B} \mathbf{v}^*. \tag{8}$$

where  $\mathbf{v}$  is the normal velocities of the radiating surface elements. Let  $\mathbf{x}^T = [x_1, x_2, \dots, x_N]$  be a vector of  $N$  design variables containing geometric and material parameters of the sandwich beam. Clearly, the radiated acoustic power is a function of  $\mathbf{x}$  besides other factors. Hence, we denote  $W = W(\mathbf{x})$ .

#### 4. OPTIMIZATION

To design a structure so that it radiates minimum acoustic power, we pose a constrained nonlinear optimization problem as

$$\text{minimize } f(\mathbf{x}) = W(\mathbf{x}), \mathbf{x} \in R^N \quad (9)$$

$$\text{subject to } \mathbf{x}_{lb} \leq \mathbf{x} \leq \mathbf{x}_{ub}, \quad (10)$$

$$g_i(\mathbf{x}) = 0, i = 1, \dots, q, \quad (11)$$

$$c_i(\mathbf{x}) \leq 0, i = q + 1, \dots, p \quad (12)$$

where  $f(\mathbf{x})$  is the objective function to be minimized with respect to the design variables  $\mathbf{x}$ .  $\mathbf{x}_{lb}$  and  $\mathbf{x}_{ub}$  denote the lower and upper bounds of the design variables.  $g_i(\mathbf{x})$  and  $c_i(\mathbf{x})$  are equality and inequality constraints of the design parameters.

An example of design variables is  $\mathbf{x}^T = [t^1, \rho^1, Q_{jk}^1; \dots t^l, \rho^l, Q_{jk}^l; \dots]$  where the superscripts refer to a physical layer of the laminate,  $t^l$  is the thickness,  $\rho^l$  is the mass density and  $Q_{jk}^l$  is the  $(jk)^{th}$  component of the stiffness matrix of the physical layer. The maximum allowable thickness  $t_0$  of the beam, the overall mass  $m_0$  and the smallest allowable fundamental frequency  $\omega_0$  of the structure may be employed as the constraints for the optimization problem

$$\sum_{l=1}^P t^l \leq t_0, \quad bL \sum_{l=1}^P t^l \rho^l \leq m_0, \quad \omega_1(\mathbf{x}) \geq \omega_0, \quad (13)$$

where  $P$  stands for the total number of physical layers, and  $\omega_1(\mathbf{x})$  denotes the fundamental frequency of the structure. The mass matrix  $\mathbf{M}$  is always positive definite and the stiffness matrix  $\mathbf{K}$  is semi-positive definite. These two conditions can also be used as constraints.

We apply a pattern search technique to solve the optimization problem subject to linear and nonlinear constraints. This search technique is a subset of direct search methods [17, 18]. The pattern search algorithm looks for the optimum by making two sequential moves. One is called the exploratory move and the other the pattern move. The first move explores the local behavior of the objective function to form the pattern, and the second establishes a global step size in the identified pattern direction. In the present application, we have nonlinear constraints given by Equation (13). To take the advantage of the fact that the pattern search algorithm does not compute derivatives of the objective function, we can impose these nonlinear constraints by including them as part of the objective function. An example of the extended objective function is given by

$$f(\mathbf{x}) = \begin{cases} \gamma, & \text{if } bL \sum_{l=1}^P t^l \rho^l \leq m_0, \\ \gamma, & \text{if } \omega_1(\mathbf{x}) \geq \omega_0, \\ W(\mathbf{x}), & \text{otherwise,} \end{cases} \quad (14)$$

where  $\gamma > 0$  is a sufficiently large number to penalize the violation of the nonlinear constraints.

Inclusion of the nonlinear constraints into the objective function allows us to increase the computational efficiency because the nonlinear constraints, particularly the fundamental frequency constraint, are already computed during the process of obtaining the radiated acoustic power  $W(\mathbf{x})$ . As a result, imposing these nonlinear constraints does not add additional computational burden with the current approach. The rigorous proof of the convergence and stability of the pattern search algorithm with such a nonlinear piece-wise objective function is elusive at this time. However, the numerical results presented later provide the strong anecdote validation of this approach.

## 5. NUMERICAL RESULTS

Extensive numerical simulations have been conducted to study the optimization problem of the sandwich beam for minimum acoustic radiation. A simply supported sandwich beam of a  $2m$  long and  $0.025m$  wide is considered in the numerical studies. The geometrical and material properties of the baseline beam define the initial condition of the optimization problem. The top and bottom skins of the baseline beam are assumed to be identical and made of graphite epoxy. The stiffness components and the mass density for the skins are  $Q_{11}^s = 1.67 \times 10^{10}$  Pa,  $Q_{12}^s = 5.00 \times 10^9$  Pa,  $Q_{22}^s = 1.08 \times 10^{10}$  Pa,  $Q_{22}^s = 1.08 \times 10^{10}$  Pa,  $Q_{33}^s = 6.40 \times 10^9$  Pa and  $\rho^s = 1760$  kg/m<sup>3</sup>. The core material is Klegecell foam. The stiffness components and the mass density of the core are  $Q_{11}^c = 1.30 \times 10^8$  Pa,  $Q_{12}^c = 5.20 \times 10^7$  Pa,  $Q_{22}^c = 0.80 \times 10^8$  Pa,  $Q_{33}^c = 5.00 \times 10^7$  Pa and  $\rho^c = 130$  kg/m<sup>3</sup>. The Rayleigh damping coefficients  $\alpha$  and  $\beta$  are chosen to be 0.001 for all layers just to avoid the resonant responses. The thicknesses of the lower skin, core and upper skin of the initial beam are  $2mm$ ,  $50mm$  and  $2mm$  respectively. The top surface of the beam is excited by a plane wave acoustic pressure with a  $30^\circ$  incident angle at 200 Hz and the magnitude of the resultant acoustic wave is  $1 \times 10^3$  Pa.

The stiffness components  $Q_{11}$ ,  $Q_{12}$ ,  $Q_{22}$  and  $Q_{33}$  of all three layers are considered as the design parameters to minimize the objective function in Equation (9). The lower and upper bounds of the design parameters are fixed by 0.25 and 4.0 times of the initial values. The minimum fundamental frequency is bounded by the fundamental frequency of the baseline beam. Also, the semi-positive definiteness of the stiffness matrices is imposed. Note that this beam is uniform along the length.

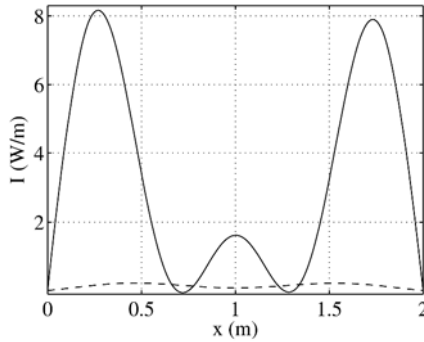


Figure 1. Acoustic intensity distribution along the beam. Solid line refers to the baseline beam. Dashed line refers to the optimized uniform beam.

The acoustic intensities of the baseline and optimized beams are plotted in Figure 1. The acoustic power computed from the areas under the intensity curves are 6.72 Watt and 0.28 Watt respectively. Since the driving frequency is close to the third mode of the baseline beam, the intensity distribution of the baseline beam is mostly shaped by the velocity profile of the third mode. However, for the optimized beam, the intensity profile is a combination of the first and third modes. An acoustic power level (APL) index is defined to determine the improvement by the optimized beam relative to the initial beam.

$$APL = 10 \times \log_{10} \left( \frac{W}{W_{ref}} \right), \tag{15}$$

where  $W$  is the acoustic power radiated from the beam and  $W_{ref}$  is a reference power level which is the radiating surface area times  $10^{-12}$  Watt/m<sup>2</sup> for the air. In addition, an acoustic transmission loss (ATL) is introduced to evaluate the acoustic power transmitted through the beam,

$$ATL = 10 \times \log_{10} \left( \frac{\frac{1}{2} \operatorname{Re} \int_0^L p_{net} v_t^* b dx}{W} \right), \tag{16}$$

where  $v_t$  is the normal velocity of the top surface where the excitation is applied. APL and ATL as a function frequency are shown in Figure 2.

We have extended this study to non-uniform sandwich beams. The beam is divided into 6 segments. In each segment, the design variables of the layers are uniform. The baseline uniform beam is optimized under the same constraints. The results are compared with the optimized uniform beam. Figure 3 shows the intensity distributions for both optimized beams. The acoustic power of the non-uniform beam is reduced to 0.097 Watt, which is about 1/3 of the optimized uniform beam. APL and ATL of the two optimized beam are compared in

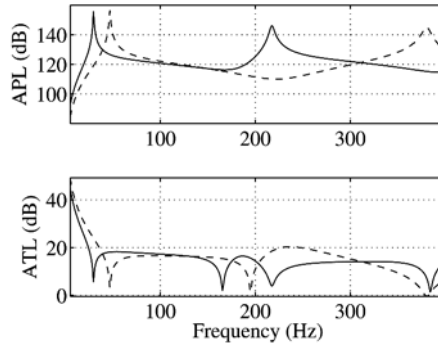


Figure 2. APL and ATL of the beam as a function of frequency. Solid line refers to the baseline beam. Dashed line refers to the optimized uniform beam.

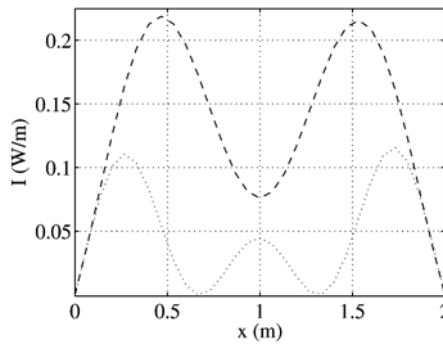


Figure 3. Acoustic intensity distribution along the beam. Dashed line refers to the optimized uniform beam. Dotted line refers to the optimized non-uniform beam.

the frequency domain in Figure 4. The acoustic transmission loss is improved more than the acoustic power level by means of non-uniformity in the design parameters along the beam.

## 6. CONCLUDING REMARKS

We have presented a structural-acoustic optimization study of sandwich structures with anisotropic material properties. The objective of optimization is to minimize the radiated acoustic power from the structure excited by a plane acoustic wave. Various constraints of the optimization problem are considered. The components of the elastic modulus matrix are considered as the design variables. The acoustic radiation of the optimized sandwich beam is compared

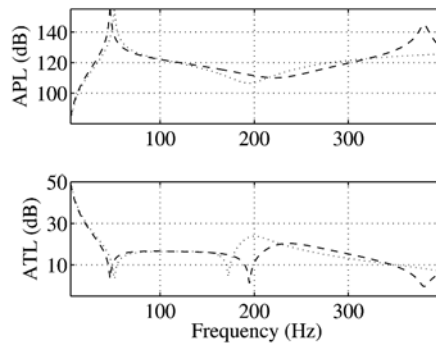


Figure 4. APL and ATL as a function of frequency. Dashed line refers to the optimized uniform beam. Dotted line refers to the optimized non-uniform beam.

with that of the baseline beam. Significant reduction of the sound radiation can be achieved with the optimized sandwich beam. Furthermore, we have found that the non-uniform sandwich beam with more independent design variables for optimization can have much higher reduction in sound radiation than the uniform beam with less independent design variables.

## ACKNOWLEDGEMENTS

This research is supported by a grant (CMS-0219217) from the National Science Foundation.

## REFERENCES

- [1] A. D. Belegundu, R. R. Salagame, and G. H. Koopmann. General optimization strategy for sound power minimization. *Structural Optimization*, 8(2-3):113–119, 1994.
- [2] G. H. Koopmann and J. B. Fahline. *Designing Quiet Structures*. Academic Press, Inc., San Diego, California, 1997.
- [3] M. Tinnsten. Optimization of acoustic response - a numerical and experimental comparison. *Structural and Multidisciplinary Optimization*, 19(2):122–129, 2000.
- [4] P. Thamburaj and J. Q. Sun. Optimization of anisotropic sandwich beams for higher sound transmission loss. *Journal of Sound and Vibration*, 254(1):23–36, 2002.
- [5] P. Thamburaj. *Structural-acoustic Studies of Sandwich Structures for Global Transport Aircraft*. Ph.d., University of Delaware, 2001.
- [6] K. A. Cunefare. The minimum multimodal radiation efficiency of baffled finite beams. *The Journal of the Acoustical Society of America*, 90(5):2521–2529, 1991.
- [7] K. Naghshineh, G. H. Koopmann, and A. D. Belegundu. Material tailoring of structures to achieve a minimum radiation condition. *Journal of the Acoustical Society of America*, 92(2):841–855, 1992.

- [8] K. A. Cunefare. Optimization techniques in structural acoustic design. *The Journal of the Acoustical Society of America*, 95(5):2834, 1994.
- [9] H. Denli, S. Frangakis, and J. Q. Sun. Normalizations in acoustic optimization with rayleigh integral. *Journal of Sound and Vibration*, In Press.
- [10] O. Elbeyli, P. Thamburaj, and J. Q. Sun. Structural-acoustic studies of sandwich structures: A review. *Shock and Vibration Digest*, 33(5):372–384, 2001.
- [11] T. Wang, V. S. Sokolinsky, S. Rajaram, and S. R. Nutt. Assessment of sandwich models for the prediction of sound transmission loss in unidirectional sandwich panels. *Applied Acoustics*, 66(3):245–262, 2005.
- [12] A. K. Noor, W. S. Burton, and C. W. Bert. Computational models for sandwich panels and shells. *Applied Mechanics Reviews*, 49(3):155–199, 1996.
- [13] J. N. Reddy. *Mechanics of Laminated Composite Plates: Theory and Analysis*. CRC Press, Inc., Boca Raton, Florida, 1997.
- [14] R. M. Lewis, V. Torczon, and M. W. Trosset. Direct search methods: Then and now. *Journal of Computational and Applied Mathematics*, 124(1-2):191–207, 2000.
- [15] T. Kant and K. Swaminathan. Estimation of transverse/interlaminar stresses in laminated composites - a selective review and survey of current developments. *Composite Structures*, 49(1):65–75, 2000.
- [16] J. N. Reddy. An evaluation of equivalent-single-layer and layerwise theories of composite laminates. *Composite Structures*, 25(1-4):21–35, 1993.
- [17] V. Torczon. On the convergence of pattern search algorithms. *SIAM Journal on Optimization*, 7(1):1–25, 1997.
- [18] R. M. Lewis and V. Torczon. Pattern search algorithms for bound constrained minimization. *SIAM Journal on Optimization*, 9(4):1082–1099, 1999.

# ON WAVE PROPAGATION IN SANDWICH PLATES UNDER HEAVY FLUID LOADING

Sergey Sorokin<sup>1</sup> and Nigel Peake<sup>2</sup>

<sup>1</sup>*Institute of Mechanical Engineering, Aalborg University, Pontoppidanstraede 101, DK-9220 Aalborg, Denmark*

<sup>2</sup>*Department of Applied Mathematics and Theoretical Physics, Wilberforce Road, Centre for Mathematical Sciences, Cambridge CB3 0WA, United Kingdom*

**Abstract** This talk addresses wave propagation in an unbounded fluid-loaded elastic sandwich plate of symmetric composition. Several aspects are highlighted, including the interaction between shear and flexural waves and the coupling between the “in-phase” and “anti-phase” waves (with respect to transverse deflections of skins).

**Keywords:** wave propagation, fluid-loaded sandwich plate.

## 1. INTRODUCTION

Sandwich plates and shells are widely used in many technical applications, e.g., naval architecture, aerospace or chemical industry, etc. because this composition of a thin-walled structure conveniently combines the properties of high strength and low weight. In practice, it is often the case that a sandwich plate of symmetric composition is subjected to some symmetry-breaking loading. Most typically, the symmetry is broken by an uneven static pre-stress of skin plies or – which is particularly relevant for naval and aerospace engineering – by a difference in properties of the surrounding media. In these cases, the exact theory may be used straightforwardly, but it is relatively difficult to solve the transcendental dispersion equation and to identify the modes. It also presents serious difficulties to join the elementary theories, which are valid in refined symmetric case [1–3] to capture the symmetry-breaking effects, because they are derived independently based on some assumptions, which are not consistent with each other. The meaningful alternative to overcome these difficulties is offered by use of a perturbation theory, which is perfectly applicable because the above mentioned symmetry-breaking effects are weak. This paper addresses exactly the issues of asymptotic analysis of interaction of weakly

coupled elastic and acoustic waves. Due to limitations on the volume of a conference paper, only the mathematical model is presented and discussed here. The numeral data obtained by the use of this model and the physical interpretation of results can be found in the references [1–5]. They are presented in the conference lecture.

## 2. A MODEL OF A SANDWICH PLATE WITH HEAVY FLUID LOADING

Consider an infinitely long sandwich plate consisting of two thin and relatively stiff plies (skins) and a soft core ply between them. It is loaded on both sides by acoustic media, in general, of different properties. Mechanical properties of skin and core plies of sandwich plates used, for example, in naval or aerospace structures are very different. Specifically, elastic and geometry parameters of skin plies considered individually are normally those of conventional thin plates, so that their dynamics are adequately described by a standard Kirchhoff theory. However, due to the interaction between skin and core plies, it is not sufficient to take into account only their flexural wave motions, and the longitudinal components of displacements also should be included to analysis of the wave propagation. The corresponding governing equations are

$$\begin{aligned}
 D_1 w_1^{(4)} + \sigma_1 h_1 w_1'' + \rho_1 h_1 \ddot{w}_1 &= q_{w1} + m'_1 - p_+ \left( x, t, \frac{h}{2} + h_1 \right), \\
 E_1 h_1 u'' - \rho_1 h_1 \ddot{u}_1 &= -q_{u1}, \\
 D_3 w_3^{(4)} + \sigma_3 h_3 w_3'' + \rho_3 h_3 \ddot{w}_3 &= q_{w3} + m'_3 + p_- \left( x, t, -\frac{h}{2} - h_3 \right), \\
 E_3 h_3 u'' - \rho_3 h_3 \ddot{u}_3 &= -q_{u3}.
 \end{aligned} \tag{1}$$

Here  $u_k(x, t)$  and  $w_k(x, t)$ ,  $k = 1, 3$  are the longitudinal and the flexural displacements of the mid-surfaces of skin plies. Respectively,  $q_{wk}(x, t)$  and  $q_{uk}(x, t)$ ,  $k = 1, 3$  are the distributed longitudinal and transverse forces acting on skin plies. The distributed moments  $m_k(x, t)$ ,  $k = 1, 3$  are also taken into account.  $D_k$ ,  $k = 1, 3$ , is the conventional formulation of cylindrical stiffness, primes and dots denote derivatives on spatial and temporal co-ordinates  $x$  and  $t$ , respectively. The elastic properties of the material of each ply are specified by densities  $\rho_k$ ,  $k = 1, 3$ , Young moduli  $E_k$ ,  $k = 1, 3$ , and Poisson coefficients  $\nu_1 = \nu_3 = \nu$ . The right hand sides of Equation (1) are composed of stresses acting at the interfaces between skin and core plies. In general, they may also contain external driving forces and moments, but as far as propagation of free waves is concerned an external loading is omitted. An acoustic pressure in (1) is defined as  $P_{\pm}(x, t, z) = -\rho_{fl} \dot{\phi}_{\pm}(x, t, z)$ , and velocity potentials in an

acoustic medium satisfy the wave equation

$$\Delta\varphi_{\pm} - \frac{1}{c_{fl}^2}\ddot{\varphi}_{\pm} = 0. \quad (2)$$

The continuity conditions at the fluid-structure interfaces are formulated as

$$\begin{aligned} z = -\frac{h}{2} - h_3 : \dot{w}_3(x, t) &= \frac{\partial\varphi_-(x, t, z)}{\partial n_-} = \frac{\partial\varphi_-(x, t, z)}{\partial z}, \\ z = \frac{h}{2} + h_1 : \dot{w}_1(x, t) &= -\frac{\partial\varphi_+(x, t, z)}{\partial n_+} = \frac{\partial\varphi_+(x, t, z)}{\partial z}. \end{aligned} \quad (3)$$

As has been discussed in the Introduction, the core ply of a sandwich plate is much thicker and it is composed of material which is much softer than the skin plies. Thus, an elementary theory of plates is not applicable and the dynamics of a core ply should be described by the standard theory of elasto-dynamics. In the plane problem formulation, Lamé equations are

$$\frac{\partial^2\phi}{\partial x^2} + \frac{\partial^2\phi}{\partial z^2} - \frac{1}{c_1^2}\frac{\partial^2\phi}{\partial t^2} = 0, \quad \frac{\partial^2\psi}{\partial x^2} + \frac{\partial^2\psi}{\partial z^2} - \frac{1}{c_2^2}\frac{\partial^2\psi}{\partial t^2} = 0. \quad (4)$$

Here

$$c_1^2 = \frac{E(1-\nu)}{\rho(1+\nu)(1-2\nu)}$$

and

$$c_2^2 = \frac{E}{2(1+\nu)\rho}$$

are velocities of acoustic and shear waves in the material, respectively. The material density of the core ply, its Young's module and Poisson coefficient are denoted as  $\rho$ ,  $E$  and  $\nu$ , respectively. Potentials  $\phi$  and  $\psi$  are introduced to formulate displacements as

$$u_2 = \frac{\partial\phi}{\partial x} - \frac{\partial\psi}{\partial z}, \quad w_2 = \frac{\partial\psi}{\partial x} + \frac{\partial\phi}{\partial z}. \quad (5)$$

Then stresses are defined as

$$\begin{aligned} \sigma_x &= \lambda\Delta\phi + 2\mu\left(\frac{\partial^2\phi}{\partial x^2} - \frac{\partial^2\psi}{\partial x\partial z}\right), \quad \sigma_z = \lambda\Delta\phi + 2\mu\left(\frac{\partial^2\phi}{\partial z^2} + \frac{\partial^2\psi}{\partial x\partial z}\right), \\ \tau_{xz} &= \mu\left(2\frac{\partial^2\phi}{\partial x\partial z} + \frac{\partial^2\psi}{\partial x^2} - \frac{\partial^2\psi}{\partial z^2}\right). \end{aligned} \quad (6)$$

In these equations,  $\lambda$  and  $\mu$  are Lamé elastic moduli, defined as

$$\lambda = \frac{\nu E}{(1+\nu)(1-2\nu)}, \quad \mu = \frac{E}{2(1+\nu)}.$$

The system of differential equations (4) should be solved with the following compatibility conditions at the interfaces:

$$z = \frac{h}{2} : w_2(x, z, t) = w_1(x, t), u_2(x, z, t) = u_1(x, t) + \frac{h_1}{2} \frac{\partial w_1(x, t)}{\partial x},$$

$$z = -\frac{h}{2} : w_2(x, z, t) = w_3(x, t), u_2(x, z, t) = u_3(x, t) - \frac{h_1}{2} \frac{\partial w_3(x, t)}{\partial x}.$$

Since the functions  $u_k(x, t)$ ,  $w_k(x, t)$ ,  $k = 1, 3$  are defined for the mid-surfaces of skin plies, the continuity conditions at the interfaces for the longitudinal displacements are formulated with the components

$$\pm \frac{h_k}{2} \frac{\partial w_k(x, t)}{\partial x}, \quad k = 1, 3$$

(i.e., the angles of rotation due to the flexural motion) taken into account. It is consistent with the governing Equations (1) for the skin plies, where distributed moments are also included. This formulation is valid as long as the elementary Kirchhoff theory is applicable to describe wave motion in the skins.

The interfacial distributed forces and moments are formulated as

$$q_{w3}(x, t) = \sigma_z \left( x, -\frac{h}{2}, t \right), \quad q_{u3}(x, t) = -\tau_{xz} \left( x, -\frac{h}{2}, t \right),$$

$$m_3(x, t) = \frac{h_3}{2} \tau_{xz} \left( x, -\frac{h}{2}, t \right), \quad q_{w1}(x, t) = -\sigma_z \left( x, \frac{h}{2}, t \right),$$

$$q_{u1}(x, t) = \tau_{xz} \left( x, \frac{h}{2}, t \right), \quad m_1(x, t) = \frac{h_1}{2} \tau_{xz} \left( x, \frac{h}{2}, t \right). \quad (7)$$

Hereafter the scaling is introduced as:  $x = \bar{x}h$ ,  $z = \bar{z}h$ ,  $u_j = \bar{u}_jh$ ,  $w_j = \bar{w}_jh$ ,  $j = 1, 2, 3$ .

Propagation of a harmonic coupled acoustic and elastic wave in an infinitely long plate with heavy fluid loading is considered, so that

$$\bar{u}_j = U_j \exp(k\bar{x} - i\omega t), \quad \bar{w}_j = W_j \exp(k\bar{x} - i\omega t), \quad j = 1, 2, 3,$$

$$\phi = \Phi(\bar{z}) \exp(k\bar{x} - i\omega t), \quad \psi = \Psi(\bar{z}) \exp(k\bar{x} - i\omega t). \quad (8)$$

Hereafter bars over non-dimensional variables are omitted,  $\omega$  is a positive excitation frequency and  $k$  is, *a priori*, a complex wave number. Equations (8) are substituted into (5), (7) and the problem in elasto-dynamics for the core ply is formulated as

$$\frac{d^2\Phi}{dz^2} + \left[ k^2 + \left( \frac{\omega h}{c_1} \right)^2 \right] \Phi = 0, \quad \frac{d^2\Psi}{dz^2} + \left[ k^2 + \left( \frac{\omega h}{c_2} \right)^2 \right] \Psi = 0,$$

$$\begin{aligned}
 z = \frac{1}{2} : \frac{d\Phi}{dz} + k\Psi &= h^2 W_1, & k\Phi - \frac{d\Psi}{dz} &= h^2 U_1 + \frac{hh_1}{2} k W_1, \\
 z = -\frac{1}{2} : \frac{d\Phi}{dz} + k\Psi &= h^2 W_3, & k\Phi - \frac{d\Psi}{dz} &= h^2 U_3 - \frac{hh_1}{2} k W_3.
 \end{aligned} \quad (9)$$

Velocity potentials in the acoustic media are sought in the form

$$\varphi_{\pm}(x, t, z) = \varphi_{\pm}^{(0)}(z) \exp(kx - i\omega t), \quad (10)$$

so the wave Equation (2) is reduced to a one-dimensional Helmholtz equation

$$\frac{d^2 \varphi_{\pm}^{(0)}}{dz^2} + \left[ k^2 + \left( \frac{\omega h}{c_{fl}} \right)^2 \right] \varphi_{\pm}^{(0)} = 0. \quad (11)$$

The solution of this equation is sought as

$$\varphi_{+}^{(0)}(z) = A_{1+} \exp(i\gamma_{f11} z) + A_{1-} \exp(-i\gamma_{f11} z), \quad \gamma_{f11} \equiv \sqrt{k^2 + \left( \frac{\omega h}{c_{k11}} \right)^2}.$$

$$\varphi_{-}^{(0)}(z) = A_{3+} \exp(i\gamma_{f13} z) + A_{3-} \exp(-i\gamma_{f13} z), \quad \gamma_{f13} \equiv \sqrt{k^2 + \left( \frac{\omega h}{c_{f13}} \right)^2}.$$

The parameters  $A$  should be selected to satisfy compatibility conditions (4) at fluid-structure interfaces and the radiation condition, which is formulated at infinity for the upper and the lower half-spaces occupied by the acoustic medium. Elementary algebra gives the following expressions for velocity potentials

$$\begin{aligned}
 \varphi_{+}^{(0)}(z) &= \frac{\omega h^2}{\gamma_{f11}} W_1 \exp(i\gamma_{f11} z), & z > \frac{1}{2}, \\
 \varphi_{-}^{(0)}(z) &= \frac{\omega h^2}{\gamma_{f13}} W_3 \exp(-i\gamma_{f13} z), & z < -\frac{1}{2},
 \end{aligned}$$

then the amplitudes of the contact acoustic pressure at the surfaces of skin plies are formulated via the amplitudes of displacements as

$$\begin{aligned}
 p_{+} &= -\frac{i\rho_{f11}\omega^2 h^2}{\sqrt{k^2 + \left( \frac{\omega h}{c_{f11}} \right)^2}} W_1, & z = \frac{1}{2}, \\
 p_{-} &= \frac{i\rho_{f13}\omega^2 h^2}{\sqrt{k^2 + \left( \frac{\omega h}{c_{f13}} \right)^2}} W_3, & z = -\frac{1}{2}.
 \end{aligned} \quad (12)$$

Finally, Equations (1) are reduced to

$$\begin{aligned} \left[ \frac{E_1 h_1^3}{12(1-\nu^2)h^3} k^4 + \sigma_1 \frac{h_1}{h} k^2 - \rho_1 h h_1 \omega^2 - \frac{i\rho_{f11} h^2}{\gamma_{f11}} \right] W_1 &= \hat{q}_{w1} - k\hat{m}_1, \\ \left[ \frac{E_3 h_3}{12(1-\nu^2)h^3} k^4 + \sigma_3 \frac{h_1}{h} k^2 - \rho_3 h h_1 \omega^2 - \frac{i\rho_{f13} h^2}{\gamma_{f13}} \right] W_3 &= -\hat{q}_{w3} + k\hat{m}_3, \\ \left[ \frac{E_1 h_1}{h} k^2 + \rho_1 h h_1 \omega^2 \right] U_1 &= -\hat{q}_{u1}, \\ \left[ \frac{E_3 h_3}{h} k^2 + \rho_3 h h_3 \omega^2 \right] U_{-} &= \hat{q}_{u3}. \end{aligned} \quad (13)$$

The right-hand sides in Equations (13) are defined by formulae (7). These equations are valid for an arbitrarily composed sandwich plate with heavy fluid loading at its both sides.

### 3. COUPLING OF IN-PLANE ANF ANTI-PLANE MODES

In the earlier paper [1], the symmetric composition of a sandwich plate ( $h_1 = h_3$ ,  $E_1 = E_3$ ,  $\rho_1 = \rho_3$ ) has been considered and two uncoupled classes of linear wave motions (in-phase and anti-phase ones) have been identified and analysed separately. However, it is realistic to assume that even in the case of symmetric original composition of a sandwich plate one of skin plies may experience somewhat larger stress than its counterpart and that fluid loading is different (e.g., water and air) on opposite sides of the plate. In such a case, the uncoupled in-phase and anti-phase wave motions should interact due to these symmetry breaking effects.

It is convenient to introduce the in-phase and the anti-phase components of displacements of skin plies as

$$W_+ = \frac{W_1 + W_3}{2}, \quad U_- = \frac{U_1 - U_3}{2}, \quad W_- = \frac{W_1 - W_3}{2}, \quad U_+ = \frac{U_1 + U_3}{2}. \quad (14)$$

The stresses (6) are substituted into formulae (7) and these interfacial forces and moments are substituted into Equations (13) to yield the system of homogeneous linear equations with respect to  $W_+$ ,  $W_-$ ,  $U_+$ ,  $U_-$ . It is appropriate to write these equations as follows

$$\begin{aligned} z_{11}W_+ + z_{12}U_- + z_c W_- &= 0, & z_{21}W_+ + z_{22}U_- &= 0, \\ z_c W_+ + z_{33}W_- + z_{34}U_+ &= 0, & z_{43}W_- + z_{44}U_+ &= 0. \end{aligned} \quad (15)$$

The coefficients  $z_{ij}$ ,  $i = 1, 2$  and  $i, j = 3, 4$  are very cumbersome and therefore they are not presented here in an explicit form. When the determinant of

the system (15) is set to zero, a dispersion equation is obtained. This equation is valid for determining wave numbers as a function of excitation frequency for arbitrary parameters of sandwich plate composition and fluid loading. Its numerical solution is obtained by use of the algorithm suggested in [1].

A plate of symmetric composition is considered and the coupling between in-phase and anti-phase components is produced either by different pre-stress of identical skin plies or by a difference in properties of the acoustic media on opposite sides of the plate. Then it is possible to determine wave numbers by use of perturbation theory. It is convenient to present the dispersion equation in the form

$$(z_{11}z_{22} - z_{12}z_{21})(z_{33}z_{44} - z_{34}z_{43}) - z_c^2 z_{22} z_{44} = 0. \quad (16)$$

The parameter  $z_c$  quantifies the coupling between in-phase and anti-phase modes. The wave numbers of these modes are determined by the equations

$$F_1(k, \omega) \equiv z_{11}z_{22} - z_{12}z_{21} = 0, \quad F_2(k, \omega) \equiv z_{33}z_{44} - z_{34}z_{43} = 0. \quad (17)$$

These equations are solved in [1]. The coupling coefficient is

$$z_c = \frac{\sigma_1 - \sigma_3}{E_1} \frac{h_1}{h} k^2 - \frac{i\rho_{f11}\omega^2 h^2}{E_1\gamma_{f11}} + \frac{i\omega_{f13}\omega^2 h^2}{E_1\gamma_{f13}}. \quad (18)$$

The symmetry breaking effects may be analysed in the framework of a perturbation theory, if the parameter  $z_c$  may be regarded as small. In naval engineering, it is typical to deal with plates and shells which are loaded on one side by water and on the other side by air, or a fluid with different properties (e.g., an oil). Then the symmetry may be broken both by an uneven static pre-stress and by an uneven fluid loading. As is well-known, the fluid loading parameter of density ratio is of order  $10^{-1}$ , whereas the static pre-stress parameter is approximately two orders of magnitude weaker. Then the effect of fluid loading surely dominates the effect of static pre-stress so that the perturbation parameter may be reduced as

$$z_c = -\frac{i\omega_{f11}\omega^2 h^2}{E_1\gamma_{f11}} + \frac{i\omega_{f13}\omega^2 h^2}{E_1\gamma_{f13}}. \quad (19)$$

In the case of loading by water at one side of a plate (say, underneath a plate, i.e.,  $\rho_{f13} = 10^3 \text{kg/m}^3$ ) and by an air at another side it is realistic to put  $\rho_{f11} = 0$ .

#### 4. RESULTS AND DISCUSSION

The model formulated in the previous Sections is applied to study the wave propagation effects in a sandwich plate under heavy fluid loading. The results of this analysis and conclusions reported in [1–5] are presented at the Conference. They are not reproduced here to fit the paper into the allocated space.

## 5. CONCLUSIONS

The system of equations which describes propagation of acoustic and elastic harmonic waves in a sandwich plate of arbitrary composition with heavy fluid loading on both sides is derived. This system is specialised for the practically meaningful case of symmetric composition of such a plate and a classic perturbation theory is applied to study the symmetry-breaking coupling effects in wave propagation introduced by uneven pre-stress or by uneven fluid loading. A very good agreement between the results of asymptotic analysis in the cases of regular and singular perturbations and the results of direct solution is observed.

## REFERENCES

- [1] Sorokin, S.V., "Analysis of Wave Propagation in Sandwich Plates with and without Heavy Fluid Loading", *Journal of Sound and Vibration*, Vol. 36, pp. 1039–1062, 2004.
- [2] Sorokin, S.V. and Peake, N., "Vibrations of Sandwich Plates with Concentrated Masses and Spring-Like Inclusions", *Journal of Sound and Vibration*, Vol. 237, pp. 203–222, 2002.
- [3] Sorokin, S.V., "A Note on the Effect of Compressibility on the Propagation of Free Waves in Sandwich Plates with Heavy Fluid Loading", *Journal of Sound and Vibration*, Vol. 270, pp. 433–440, 2004.
- [4] Sorokin, S.V. and Peake, N., "On Symmetry-Breaking Effects in Propagation of Waves in Sandwich Plates with and without Heavy Fluid Loading", *Journal of Sound and Vibration*, submitted, 2005.
- [5] Sorokin, S.V., "Analysis of Propagation of a Wave of Anti-Plane Deformation in a Sandwich Plate", *Journal of Sound and Vibration*, submitted, 2005.

# WAVE PROPAGATION IN A SANDWICH PLATE LOADED BY A VISCOUS COMPRESSIBLE FLUID

A.V. Chubinskiy<sup>1</sup> and S.V. Sorokin<sup>2</sup>

<sup>1</sup>*State Marine Technical University of St. Petersburg, Lotsmanskaya str. #3, St. Petersburg 190008, Russia*

<sup>2</sup>*Institute of Mechanical Engineering, Aalborg University, Pontoppidanstraede 101, DK-9220 Aalborg, Denmark*

**Abstract** This paper addresses wave propagation in an unbounded elastic sandwich plate loaded by a layer of viscous compressible fluid. The dispersion equation is derived and the location of dispersion curves as a function of the depth parameter is analyzed. The viscosity-induced attenuation of waves in this wave guide is compared with the wave attenuation in a rigid duct filled with a viscous fluid and in a similar wave guide, where a sandwich plate is replaced by a conventional Kirchhoff plate.

**Keywords:** wave propagation, fluid-loaded sandwich plate, effects of viscosity.

## 1. INTRODUCTION

The time harmonic linear wave propagation in elastic structures with heavy fluid loading is traditionally considered within the framework of a theory of a compressible inviscid fluid (a classical model of the acoustic medium). This model is perfectly valid for analysis of vibrations of elastic structures submerged into an unbounded volume of a fluid (e.g., a ship hull in water) or vibrations of thin-walled fluid-conveying structures (e.g., a water-filled tube). However, in some situations, which are rather common for various industrial applications, propagation of an acoustic wave in a narrow gap between, say, two elastic plates or shells should be considered and the attenuation effect produced by viscosity of a fluid cannot be ignored. The regime of fluid's motion in this case is laminar (no mean flow is considered) and Navier–Stokes equations may be linearised. Then it is possible to apply a theory suggested in [1] to describe wave motion in a fluid. It is typical that an elastic structure has a sandwich-type material composition. The wave propagation in a sandwich plate loaded by a layer of an acoustic medium has been analysed, for example, in [2]. To the best of the authors' knowledge, the similar problem for an elastic

sandwich plate loaded by a layer of compressible viscous fluid has not yet been considered in the literature. The paper addresses exactly this case.

## 2. THE DISPERSION EQUATION FOR A FLUID-LOADED SANDWICH PLATE

A theory of sandwich plates is taken in the form suggested in [3, 4]. Equations of motion of a fluid-laded plate are formulated as

$$D_1 w^{IV} - \Gamma(\theta' + w'') + M\ddot{w} - I_1 \ddot{w}'' = p + N\tau'_{zx},$$

$$-D_2 \theta'' + \Gamma(\theta + w') + I_2 \ddot{\theta} = -N\tau_{zx}.$$

The elastic parameters in these equations are ( $E = E_{\text{skin}}$ ,  $h = h_{\text{skin}}$ ):

$$D_1 = \frac{Eh^3}{12(1 - \nu_p^2)} \left(2 + \frac{\gamma}{\varepsilon^3}\right) = Eh^3 \bar{D}_1,$$

$$D_2 = \frac{Eh^3}{2(1 - \nu_p^2)} \left(1 + \frac{1}{\varepsilon}\right)^2 = Eh^3 \bar{D}_2,$$

$$\Gamma = \frac{Eh}{2(1 + \nu_p)} \left(1 + \frac{1}{\varepsilon}\right)^2 \gamma_g \varepsilon = Eh \bar{\Gamma}, \quad M = \rho_{pl} h \left(2 + \frac{\delta}{\varepsilon}\right) = \rho_{pl} h \bar{M},$$

$$I_1 = \frac{\rho_{pl} h^3}{12} \left(2 + \frac{\delta}{\varepsilon^3}\right) = \rho_{pl} h^3 \bar{I}_1, \quad I_2 = \frac{\rho_{pl} h^3}{12} \left(1 + \frac{1}{\varepsilon}\right)^2 = \rho_{pl} h^3 \bar{I}_2,$$

$$N = \frac{h}{2} \left(2 + \frac{1}{\varepsilon}\right) = \frac{h}{2} \bar{N},$$

$$\varepsilon = \frac{h_{\text{skin}}}{h_{\text{core}}}, \quad \delta = \frac{\rho_{\text{core}}}{\rho_{\text{skin}}}, \quad \gamma = \frac{E_{\text{core}}}{E_{\text{skin}}}, \quad \gamma_g = \frac{G_{\text{core}}}{G_{\text{skin}}}.$$

For definiteness, a sandwich structure composed of isotropic individual layers is considered, so that  $\gamma = \gamma_g$ . The Poisson's ratio is assumed to be the same for all plies.

Dynamics of a viscous fluid is governed by equations for scalar and vector velocity potentials, as suggested in [1]:

$$\left[ \left(1 + \frac{4\nu}{3c_{fl}^2} \frac{\partial}{\partial t}\right) \Delta - \frac{1}{c_{fl}^2} \frac{\partial^2}{\partial t^2} \right] \varphi = 0, \quad \left( \nu \Delta - \frac{\partial}{\partial t} \right) \vec{\psi} = 0.$$

Continuity conditions at fluid-structure interface,  $z = H$  ( $H$  is a half of the depth of the layer of a viscous fluid), are

$$\frac{\partial \varphi}{\partial x} + \frac{\partial \psi}{\partial z} = \frac{h}{2} \left(2 + \frac{1}{\varepsilon}\right) \left( \frac{\partial^2 w}{\partial t \partial x} + \frac{\partial \theta}{\partial t} \right), \quad \frac{\partial \varphi}{\partial z} - \frac{\partial \psi}{\partial x} = \frac{\partial w}{\partial t}.$$

The second set of conditions at  $z = -H$  is

$$\frac{\partial \varphi}{\partial x} + \frac{\partial \psi}{\partial z} = 0, \quad \frac{\partial \varphi}{\partial z} - \frac{\partial \psi}{\partial x} = 0.$$

The acoustic pressure and the shear stresses are formulated as

$$p = \rho_{fl} \left( \frac{4\mu}{3\rho_{fl}} \Delta - \frac{\partial}{\partial t} \right) \varphi, \quad \tau_{zx} = 2\rho_{fl} \nu \left( 2 \frac{\partial^2 \varphi}{\partial x \partial z} + \frac{\partial^2 \psi}{\partial z \partial z} - \frac{\partial^2 \psi}{\partial x \partial x} \right).$$

The solution of the problem in wave propagation is sought in the form

$$\varphi = A(z) \exp(kx - i\omega t), \quad \psi = B(z) \exp(kx - i\omega t),$$

$$w = D \exp(kx - i\omega t), \quad \theta = F \exp(kx - i\omega t).$$

Standard algebraic transformations give the dispersion equation in a non-dimensional form

$$T_1 + \frac{iP\Omega\mu\Delta^2}{12\chi S} T_2 + \frac{P^2\Omega^2\mu^2\bar{N}^2}{24\chi^2 S^2} T_3 = 0, \quad (1)$$

$$\begin{aligned} T_1 = & \frac{\Delta^4}{\chi^6} K^6 \bar{D}_1 \bar{D}_2 - \frac{\Delta^4}{\chi^4} K^6 \bar{\Gamma} (\bar{D}_1 + \bar{D}_2) + \frac{\Delta^2}{\chi^6} K^4 \Omega^2 (\bar{D}_2 \bar{I}_1 + \bar{D}_1 \bar{I}_2) - \\ & - \frac{\Delta^2}{\chi^4} K^2 \Omega^2 (\bar{I}_1 \bar{\Gamma} + \bar{I}_2 \bar{\Gamma} + \bar{D}_2 \bar{M}) + \frac{1}{\chi^6} K^2 \Omega^4 \bar{I}_1 \bar{I}_2 + \frac{\Delta^2}{\chi^2} \Omega^2 \bar{M} \bar{\Gamma} - \\ & - \frac{1}{\chi^4} \Omega^4 \bar{I}_2 \bar{M}, \end{aligned}$$

$$\begin{aligned} T_2 = & \left( -4\alpha^2 + 4K^2 + 3i \frac{\Omega}{\mu} \right) \left[ -S_{12} \beta \bar{\Gamma} + \frac{1}{\chi^2} \left( S_{12} \beta - \frac{K^2 \bar{N} S_{11}}{\chi} \right) \right. \\ & \left. \left( \bar{D}_2 K^2 + \bar{I}_2 \frac{\Delta^2}{\Omega^2} \right) \right] + \frac{12 \bar{N} \alpha K^2}{\chi} \left[ \frac{S_{32} \beta}{\chi} \left( \bar{D}_2 K^2 + \bar{I}_2 \frac{\Omega^2}{\Delta^2} \right) + \right. \\ & \left. + \bar{N} S_{32} \left( \frac{1}{\chi^2} (\bar{D}_1 + \bar{D}_1) K^4 + \left( \frac{1}{\chi^2} \bar{I}_1 K^4 + \frac{1}{\chi^2} \bar{I}_2 K^4 - \bar{M} \right) \frac{\Omega^2}{\Delta^2} \right) \right] + \\ & + \frac{6 \bar{N} (-\beta^2 - K^2)}{\chi^2} \left[ K^2 \frac{S_{22} \beta}{\chi} \left( \bar{D}_2 K^2 + \bar{I}_2 \frac{\Omega^2}{\Delta^2} \right) + \right. \\ & \left. + \bar{N} S_{21} \alpha \left( \frac{1}{\chi^2} (\bar{D}_1 + \bar{D}_1) K^4 + \left( \frac{1}{\chi^2} \bar{I}_1 K^4 + \frac{1}{\chi^2} \bar{I}_2 K^4 - \bar{M} \right) \frac{\Omega^2}{\Delta^2} \right) \right], \end{aligned}$$

$$T_3 = \left( -4\alpha^2 + 4K^2 + 3i \frac{\Omega}{\mu} \right) [-2\alpha\beta K^2 (S_{12}S_{31} + S_{11}S_{32}) + (-\beta^2 - K^2)(-K^2 S_{11}S_{22} - \alpha\beta S_{12}S_{21})],$$

$$S = (\alpha\beta \cos \alpha \sin \beta - K^2 \sin \alpha \cos \beta)(\alpha\beta \sin \alpha \cos \beta - K^2 \cos \alpha \sin \beta),$$

$$S_{11} = -\alpha\beta(\cos 2\alpha \cos 2\beta - 1) - K^2 \sin 2\alpha \sin 2\beta,$$

$$S_{12} = -\alpha\beta \cos 2\alpha \sin 2\beta + K^2 \sin 2\alpha \cos 2\beta,$$

$$S_{21} = -\alpha\beta \sin 2\alpha \cos 2\beta + K^2 \cos 2\alpha \sin 2\beta,$$

$$S_{22} = -\alpha\beta(\cos 2\alpha \cos 2\beta - 1) - K^2 \sin 2\alpha \sin 2\beta,$$

$$S_{31} = -\alpha\beta \sin 2\alpha \cos 2\beta + K^2 \cos 2\alpha \sin 2\beta,$$

$$S_{32} = \alpha\beta \sin 2\alpha \sin 2\beta + K^2(\cos 2\alpha \cos 2\beta - 1),$$

$$\alpha = \sqrt{K^2 + \Omega^2}, \quad \beta = \sqrt{K^2 + i \frac{\Omega}{\mu}},$$

$$\chi = \frac{H}{h}, \quad P = \frac{\rho_{fl}}{\rho_{pl}}, \quad \Delta = \frac{c_{pl}}{c_{fl}}, \quad K = kH, \quad \Omega = \frac{\omega H}{c_{fl}}, \quad \mu = \frac{\nu}{c_{fl}H}.$$

Apparently, the dispersion equation (1) has infinitely many roots, which may be founded numerically.

### 3. DISPERSION CURVES

Explore the location of dispersion curves  $K_m(\Omega)$ . For definiteness, the following parameters of a sandwich plate composition are specified:  $\varepsilon = 10$ ,  $\gamma = 0.0001$ ,  $\delta = 0.1$ ,  $\nu = 0.3$ . This plate is loaded by water, so that  $P = 0.128$ ,  $\Delta = 3.258$ . The depth parameter is selected as  $\chi = 10$  and the viscosity parameter is  $\mu = 10^{-6}$ .

Dispersion curves  $K_m(\Omega)$  are plotted in the frequency range  $0.02 \leq \Omega \leq 1.18$ . In Figure 1a, real parts of roots of the dispersion equation are shown, whereas in Figure 1b a dependence of imaginary parts of these roots is displayed. Curve 1 in Figures 1a and 1b displays a dependence of real and imaginary parts of a wave number of the “structure-dominated” mode. This mode of dominantly flexural type “almost propagates” (meaning that its decay is controlled solely by the viscous effect in a fluid) at any  $\Omega$ . Curve 3 in Figures 1a and 1b shows a dependence of real and imaginary parts of a wave number of the “fluid-dominated” mode. This mode is evanescent at small  $\Omega$ , but at  $\Omega \approx 0.46$  it transforms into a propagating (in the above mentioned sense) one. This is the first “cut-on” frequency parameter for the given depth parameter  $\chi = 10$ . Curve 2 in Figures 1a and 1b presents a dependence of real and imaginary parts of a wave number of the second “structure-dominated” mode.

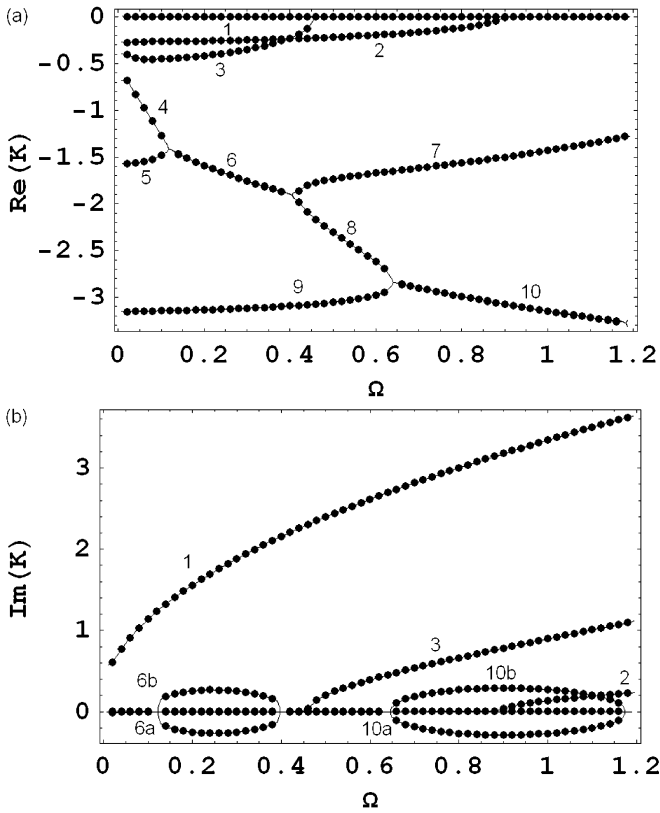


Figure 1. Dispersion curves versus frequency parameter  $\Omega$  at  $\chi = 10$ : (a) real parts of complex roots; (b) imaginary parts of complex roots.

This mode is also evanescent at small  $\Omega$ , and at  $\Omega \approx 0.9$  (the second “cut-on” frequency) it transforms to the “almost propagating” type. In Figure 1a branch 4 decays and merges growing branch 5 into branch 6 at  $\Omega \approx 0.12$ . Wave numbers corresponding to branches 4 and 5 have very small imaginary parts. Curve 6 presents two complex conjugate wave numbers, with imaginary parts 6a and 6b shown in Figure 1b. This curve splits into growing branch 7 and decaying branch 8. Branch 7 reaches zero at some frequency  $\Omega > 1.18$ . It means that corresponding mode transforms from the evanescent to the “almost propagating” type. This is the third “cut-on” frequency. Branch 8 merges branch 9 into branch 10 at  $\Omega \approx 0.66$ . Curve 10 presents two complex conjugate wave numbers, their imaginary parts are shown by curves 10a and 10b in Figure 1b.

Apparently, an arbitrary large number of “cut-on” frequencies may be founded numerically from Equation (1) by setting  $K = 0$ . The influence of a depth parameter on “cut-on” frequencies is illustrated in Figure 2, where “cut-on”

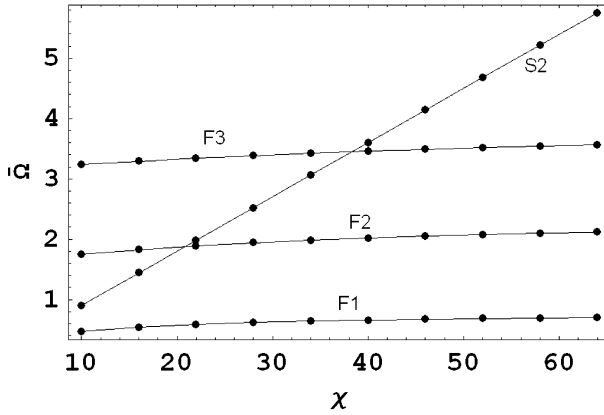


Figure 2. “Cut-on” frequency  $\bar{\Omega}$  versus depth parameter  $\chi$ .

frequencies for the second “structure-dominated” mode and the three lowest “fluid-dominated” modes are plotted versus the depth parameter  $\chi$ . Curve S2 corresponds to “structure-dominated” mode, curves F1, F2, F3 correspond to the first, the second and the third fluid-dominated modes, respectively. Curve S2 intersects curves F2 and F3 at  $\chi \approx 21$  and  $\chi \approx 38$ . This fact can be observed in Figure 1a, by exploring intersecting branches 2 and 3. Here the second “structure-dominated” mode has larger “cut-on” frequency than the first “fluid-dominated” one at  $\chi = 10$ .

All “viscous cut-on” frequencies have small positive imaginary and the same real parts (up to the sixth digit) in comparison with the “acoustic” ones. The “acoustic cut-on” values can be easily found from

$$\Omega = \sqrt{\frac{\Gamma}{I_2}} \Delta \chi.$$

Other “cut-on” frequencies can be found from

$$-\frac{M\Omega^2}{\chi} + P\sqrt{\Omega^2} \cot(2\sqrt{\Omega^2}) = 0.$$

#### 4. VISCOSITY-INDUCED WAVE ATTENUATION

Three models are considered: the model of a rigid duct filled in by a viscous compressible fluid, the model of a layer of a viscous fluid bounded by a Kirhhoff plate at one side and by a rigid wall at another one and the model of a layer of a viscous fluid bounded at one side by a sandwich plate and by a rigid wall at another one (in two latter cases, the width of a layer of fluid is the same as the width of a duct). Due to viscosity of a fluid, all waves are

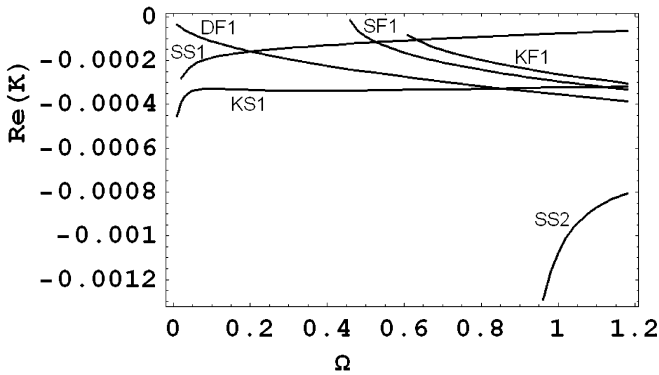


Figure 3.  $\text{Re}(K)$  versus frequency parameter  $\Omega$  for propagating modes.

of evanescent or “almost propagating” type. The space- and time-dependence is selected as  $\exp(kx - i\omega t)$ , and  $\text{Re}(K)$  should be regarded as a logarithmic decrement of a wave. Apparently, in the case where an ideal acoustic medium is considered, the condition  $\text{Re}(K) = 0$  defines “truly” propagating modes. In the case of a sandwich plate loaded by a viscous fluid, the attenuation of “almost propagating” modes is defined by  $\text{Re}(K) < 0$ .

In Figure 3, real parts of roots of dispersion equation are shown versus excitation frequency  $\Omega$  for “almost propagating” waves. The designation of curves is introduced in the following way. First letters: “S” denotes “Sandwich”, “K” denotes “Kirchhoff”, “D” denotes “Duct”. Second letters: “S” denotes “Structure”, “F” denotes “Fluid”. The numbers are introduced to count fluid-dominated and structure-dominated modes. For example, curve “SS1” presents the first structure-dominated mode in a sandwich plate loaded by viscous fluid, and “DF1” refers to the first fluid mode in a rigid duct filled by viscous fluid. Apparently, large magnitudes of the module of suggest that the mode is heavily damped by the viscosity effects in a fluid. Thus, it is easy to determine, which mode is attenuated greater at the given frequency.

As is seen from Figure 3, the structure-dominated mode “KS1” is damped heavier than the structure-dominated mode “SS1” at the same frequency. The first fluid-dominated modes from the viewpoint of their suppression due to fluid’s viscosity may be ranked in the following sequence: KF1, SF1, DF1. However, it is necessary to keep in mind, that these modes have different “cut-on” frequencies.

To conclude a brief presentation of the obtained results, explore the attenuation of an incident acoustic wave which travels through a layer of compressible viscous fluid of thickness  $H$  bounded at one side by a rigid wall and by a sandwich plate at another side over the distance  $L$ .

Table 1. Decay coefficient of different modes.

	$\Omega = 0.10$	$\Omega = 0.50$	$\Omega = 1.00$	$\Omega = 1.18$
SS1	17.0%	11.2%	7.4%	6.3%
SF1	–	8.6%	25.6%	28.3%
SS2	–	–	65.9%	55.3%

A ratio of the amplitude of a transmitted wave to the amplitude of an incident one is written as

$$\tilde{A} = \frac{A_{\text{out}}}{A_{\text{in}}} = \exp\left(\text{Re}\left(\frac{L}{H}K\right)\right).$$

Then the quantity  $(1 - \tilde{A})100\%$  (a “decay coefficient”) characterizes the energy losses due to fluid’s viscosity. Its magnitudes for different modes at several excitation frequencies are presented in Table 1 for the same parameters of a sandwich plate composition and for the same depth parameter. Empty spaces in some cells of Table 1 indicate that a given mode does not propagate at a given frequency even if viscosity is neglected.

## 5. CONCLUSIONS

The model of viscous compressible fluid is used to analyze propagation of waves in narrow gaps between rigid walls and elastic plates of sandwich composition. The location of dispersion curves and effects of wave attenuation are studied.

## REFERENCES

- [1] Guz, A.N., “Mechanics of the Brittle Fracture of Materials with Initial Stresses”, Naukova Dumka, Kiev, 1983 (in Russian).
- [2] Sorokin, S.V., “Analysis of Vibrations and Energy Flows in Sandwich Plates Bearing Concentrated Masses and Spring-Like Inclusions in Heavy Fluid Loading Conditions”, *Journal of Sound and Vibration*, 253(2), pp. 485–505, 2002.
- [3] Sorokin, S.V., “Analysis of Wave Propagation in Sandwich Plates with and without Heavy Fluid Loading”, *Journal of Sound and Vibration*, 271(3), pp. 1039–1062, 2004.
- [4] Skvortsov, V.R., “Symmetrically Inhomogeneous through Thickness Plate as a Sandwich Plate Having a Soft Core”, *Transactions of the Academy of Sciences of Russia, Mechanics of a Rigid Body 1*, pp. 162–168, 1993 (in Russian).

**IMPACT**

# IMPACT DAMAGE ON LIGHTWEIGHT SANDWICH PANELS

Daowu Zhou and W.J. Stronge

*Department of Engineering, University of Cambridge, Cambridge CB2 1PZ, UK*

**Abstract** Collision experiments and finite element analysis were carried out to investigate damage on sandwich panels struck by spherical missiles at small velocities. Analytical models based on either quasi-static or dynamic behaviour of structures were developed to calculate impact force during low speed impact on circular sandwich panels. The results of the analytical and numerical models and the experimental measurement were compared. The dependence of damage on both structural parameters and impact variables was investigated.

**Keywords:** impact damage, circular sandwich panels, quasi-static, modal superposition.

## 1. INTRODUCTION

Ultra-light sandwich panels are increasingly desirable and interesting for vehicle construction because of their high bending stiffness and lightweight. However, one drawback of sandwich panels is its susceptibility to localized surface damage from low speed impact of small missiles; e.g. hailstones or dropped tools.

In general, surface damage to lightweight sandwich panels involves two type of deformation: (1) plastic local deformation in a local contact region immediately adjacent to the impact site and (2) elastic deflection of the surrounding panel. Localized indentation of sandwich panels has been investigated extensively [1]. In addition to local indentation, there is global elastic deformation of the surrounding plate. In the range of low speed impact, the sandwich plate deflection can be approximated as a quasi-static process which employs a lumped parameter force-deflection model [1]. However, the simplified analytical model is only applicable if the ratio of colliding mass to plate is relatively large because a range of high modes and

frequencies of the plate are also excited if the mass ratio is small [2, 3]. In this case, a modal superposition method which incorporates more modes of plate vibration will be required to accurately model the impact force and displacement.

This paper addressed the impact response and damage of thin, lightweight circular sandwich panels with simply supported boundaries. A localized indentation law was first presented and incorporated into an elastic Reissner-Mindlin plate analysis that was based on the quasi-static behavior of the panel (appropriate for a large mass ratio of colliding missiles to plate). A modal superposition analysis was also carried out to analyse the dynamic panel response when the mass ratio is small. Numerical simulation was performed for comparison with the analytical models as well as calculating the residual indentation. Experimental measurements were used to validate the theoretical and numerical models.

## 2. ANALYTICAL MODELS

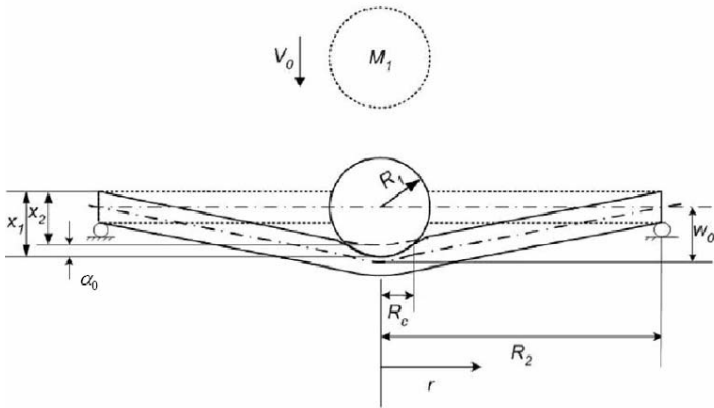


Figure 1. Spherical ball striking center of a circular, simply supported, sandwich panel.

Figure 1 shows a cross-section of the plate and colliding sphere. We consider a rigid sphere with radius  $R_1$  and mass  $M_1$  that is striking the center of a circular sandwich panel at velocity  $V_0$  at normal obliquity. The panel has radius  $R_2$  and is composed of two facesheets and a core with thicknesses  $h_f$  and  $h_c$ , respectively. The transverse shear modulus of the core is represented by  $G_c$  and Young's modulus of the facesheet material is  $E_f$ . The central relative deflection (indentation) of the contact region at the center of the upper facesheet is denoted by  $\alpha_0$  while the global transverse

deflection at the center of the panel is represented by  $w_0$  measured at the mid-surface.

## 2.1 Contact law for local indentation

This localized load-displacement relation of the sandwich panel under a fully rigid support is investigated in Ref. [4], using the principle of minimum potential energy to calculate the panel deformation. The load-indentation relationship can be expressed as

$$P = \frac{16\pi}{3} \sqrt{D_f q \alpha_0 \left(1 + 0.488 \frac{\alpha_0^2}{h_f^2}\right)} \quad (1)$$

where  $P$  is the impact force,  $D_f = E_f h_f^3 / [12(1 - \nu^2)]$  is the bending stiffness of the facesheet and  $q$  is the crushing strength of the core. The first term on the right side of Equation (1) is related to bending of the facesheet and the second term is due to local membrane stretching.

## 2.2 Quasi-static solution for global panel deflection

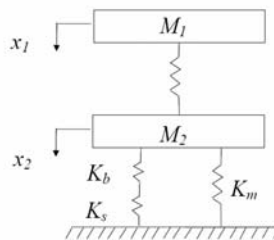


Figure 2. Spring-mass model for impact analysis.

The lumped parameter model of dynamic panel response is an appropriate first approximation for the history of impact force and deflection of the panel. As shown in Figure 2, the missile has mass  $M_1$  and displacement  $x_1$ . The sandwich panel has an effective mass  $M_2$ , an effective bending stiffness  $K_b$ , an effective shear stiffness  $K_s$  and an effective membrane stretching stiffness  $K_m$ . The effective mass of the panel  $M_2$  will be obtained by equating the kinetic energy in the continuous plate to the kinetic energy of the lumped mass. With the contact indentation law in Equation (1) and the effective panel mass, the equations of motion of the two degree of freedom vibration systems are given by

$$\begin{cases} M_1 \ddot{x}_1 + P = 0 \\ M_2 \ddot{x}_2 + K_{bs} x_2 + K_m x_2^3 - P = 0 \end{cases} \quad (4)$$

If the impact energy is large, the sandwich panel will have a large global deflection and the local indentation  $x_1 - x_2 = 0$  becomes negligible. The model can be simplified as the single degree of freedom system,

$$(M_1 + M_2) \ddot{x}_1 + K_{bs} x_1 + K_m x_1^3 = 0 \quad (5)$$

### 2.3 Modal superposition analysis

When the mass ratio between the colliding missile and the plate is small, the sandwich panel can be treated as a continuum with infinite degrees of freedom rather than a discrete approximation in order to obtain impact force and deflection. In this case, the modal analysis needs to be carried out because high vibration modes of the panel may be superimposed on the fundamental vibration of the impactor-panel system. The present analysis employed first order shear theory (Mindlin plate approximation) to approximate the governing equation of a sandwich panel [5]. The effects of the inertia and the membrane stretching in facesheets are ignored. By employing the Green function to solve the governing equation of the sandwich plate, the central deflection of the plate is given by

$$w_0(t) = \frac{1}{\rho_s} \sum_{k=1}^{\infty} \frac{[\Phi_k(0)]^2}{\omega_k \int_0^{R_2} 2\pi r \Phi_k(r) \Phi_k(r) dr} \int_0^t \sin[\omega_k(t-\tau)] P(\tau) d\tau \quad (6)$$

where  $\rho_s$  is the mass of the sandwich panel per unit area and  $\omega_k$  and  $\Phi_k$  are respectively the natural frequencies and axisymmetric mode shapes of the plate [6]. The local indentation  $\alpha(t) = x_1(t) - w_0(t)$  can be written as

$$\alpha_0(t) = V_0 t - \frac{1}{M_1} \int_0^t (t-\tau) F(\tau) d\tau - w_0(t) \quad (7)$$

For a first order approximation, however, the nonlinear force-indentation relation can be further approximated by a linear relation. The impact force and central deflection of the plate can then be numerically determined.

### 3. VALIDATION OF ANALYTICAL MODELS

#### 3.1 Material and impact experiment

An example of thin and lightweight sandwich panels can be seen in Figure 3. This sandwich structure, called HSSA (Hybrid Stainless Steel Assembly), consists of stainless steel sheets (316L) that sandwich a core composed of stainless fibres aligned roughly normal to the faceplates. The total thickness of this panel is only 1.2 mm. Basic mechanical properties of the constituents of this material are given in Table 1 [7]. A static through-thickness compression test of the core [8] is also shown in Figure 3.

Table 1. Mechanical properties of sandwich panel.

	Facesheet	Fibrous Core*	Single Fibre
Thickness (mm)	0.2	0.8	0.025 (Diameter)
Density (Kg /m <sup>3</sup> )	7800	624	7800
Poisson Ratio	0.3	0	0.3
Young's modulus (MPa)	210E3	100	210E3
Yield Stress (MPa)	306	1.9 – 2.3	1,100

\*Through – thickness direction

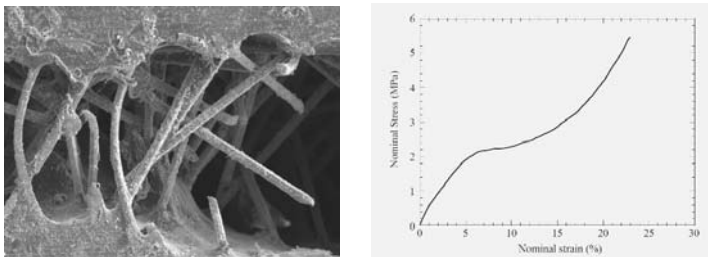


Figure 3. SEM and experimental through-thickness compression of lightweight sandwich panel with HSSA fibrous core.

#### 3.2 Experiment

A drop test was carried out to determine the surface damage to an HSSA panel resulting from normal impact of a steel sphere. The experiment consisted of a sphere striking the center of a simply supported, circular, HSSA sandwich panel at speed in the range from 1 m/s to 5 m/s. Details of the sphere and panel sizes are shown in Table 2. The profile of the residual

indentation was measured by a profile meter, which obtains the residual indentation depth to an accuracy of 1 mm.

Dynamics of panel response to impact were measured by strain gauges on a sandwich panel with a radius of 115 mm. Six strain gauges in three pairs (proximal and distal surfaces), were placed at different locations on the facesheets as shown in Figure 4. Signals from strain gauges were amplified by six signal conditioning amplifiers and stored in a data logger.

Table 2. Parameters in the impact experiment.

Impactor (Steel Ball)		Panel (HSSA)		
Mass (g)	Radius (mm)	Mass (g)	Effective Mass $M_2$ (g)	Radius (mm)
11.9	7.14	14.7	0.72	36.0
		24.1	1.34	46.0
35.8	11.90	69.2	5.98	78.0

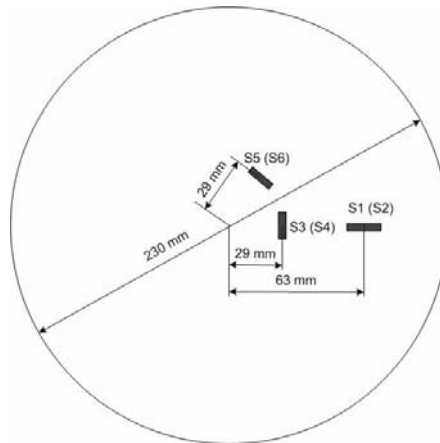


Figure 4. Locations of strain gauges on sandwich panel (S1, S3 and S5 are on top facesheet).

### 3.3 Finite element modelling

The present simulation, using ABAQUS 6.3, focuses on simply supported circular sandwich panels, corresponding to the sizes tested in the experiment. The colliding body was assumed to be rigid with the same mass and surface curvature as specified in the experimental study. The element mesh of the FEM model is shown in Figure 5. All parts of the sandwich panel were meshed with 4-node axisymmetric CAX4R elements. There were roughly 20 contact elements on the impact surface. Convergence studies indicated that this mesh was fine enough to accurately simulate the core. The facesheet was assumed to behave as an elastic-plastic material with strain hardening behaviour and the core was simulated by a crushable foam

material model. Isotropic hardening of the core was considered by using the uniaxial compression test. The associated flow law was used for simplicity.

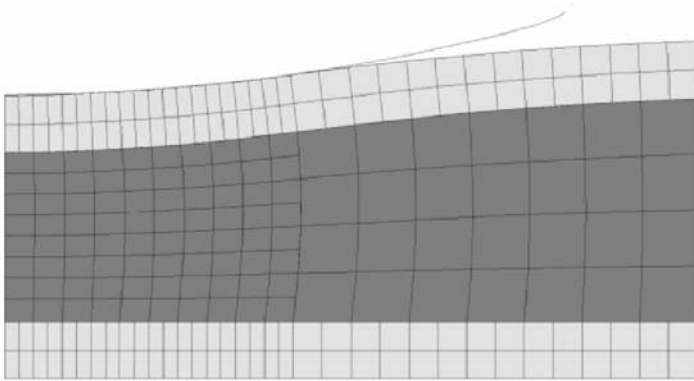


Figure 5. Deformed mesh of HSSA sandwich panel for impact analysis.

## 4. RESULTS AND DISCUSSION

### 4.1 Comparison of FEM model and experiment

Figure 6 illustrates the dynamic strain response histories at specific gauge locations (S1, S2 and S3 as shown in Figure 4). Comparisons between the finite element solutions and experimental results are given. It is noted that the radial strains at S1 and S2 have approximately the same magnitude but opposite sign. These two points are far from the impacted point and hence the dynamic response is mostly a result of bending. The compressive circumferential strain in Figure 6(c) is a consequence of radial stretching of the panel. Effects of wave propagation are not obvious.

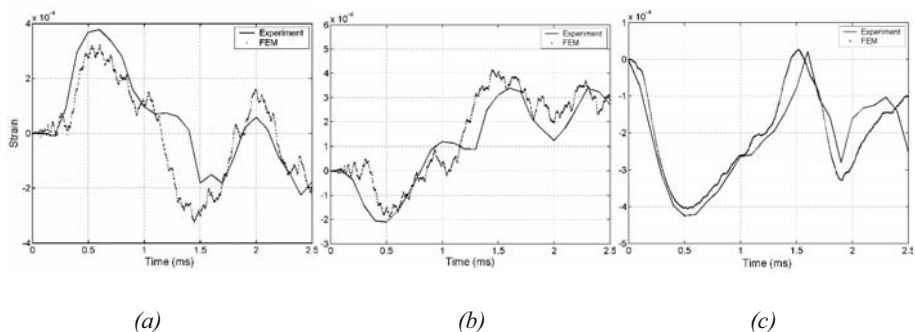


Figure 6. Dynamic radial strain history at point S1, S2, S3 on HSSA sandwich panel.

### 4.2 Effect of mass ratio on validity of analytical models

Figure 7 shows a comparison of different calculations, 2 DOF spring-mass model, 1 DOF, modal superposition and FEM, in predicting the history of the impact force. The mass ratios between the colliding missile and the effect mass of the panel are  $m=25.7$ , 15.9 and 1.92, respectively. Detailed specifications of the sandwich panels are (a) panel radius 46 mm, sphere 35.8 g, striking velocity 2.43 m/s (b) panel radius 36 mm, sphere 11.9 g, striking velocity 1.98 m/s (c) panel radius 78 mm, sphere 11.9 g, striking velocity 2.43 m/s. It is seen that both spring-mass models give similar prediction of the maximum forces in Figure 7(a). This similarity indicates that the local deformation (indentation) is negligible in comparison with the overall deflection in the case of a large mass ratio impact phenomenon. The result from modal superposition solution is less than the other predictions; this is due to neglect of membrane stretching in facesheets.

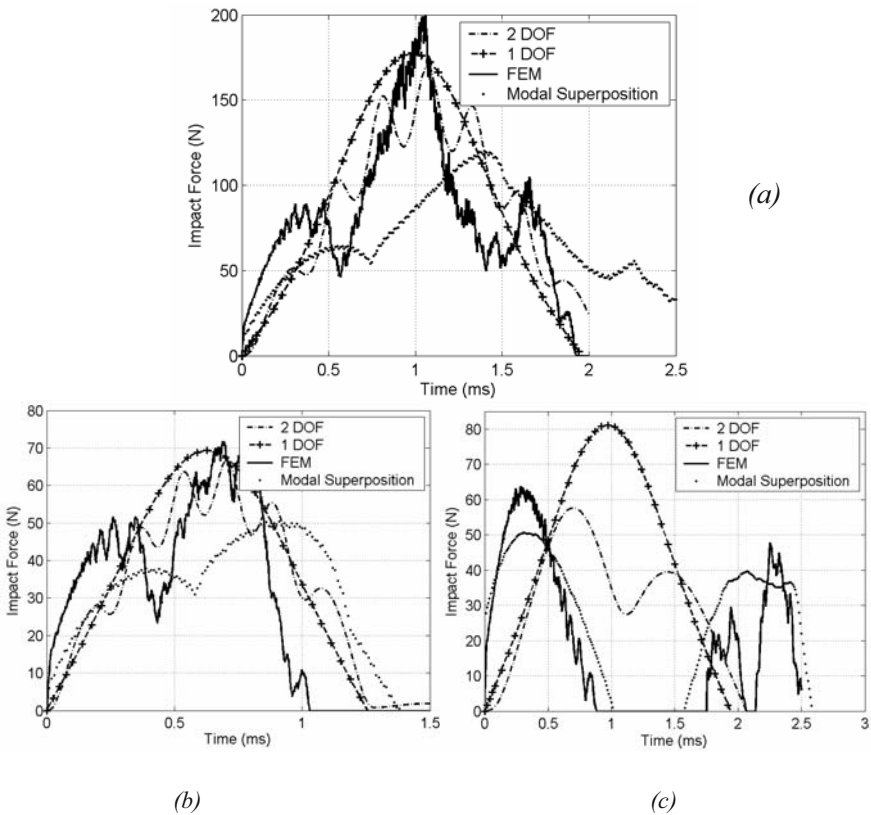


Figure 7. Calculated time-history of impact force for a sandwich panel struck by a sphere for mass ratios (a)  $m=25.7$ , (b)  $m=15.9$ , (c)  $m=1.92$ .

In the case of an intermediate range of mass ratio in Figure 7(b), both spring-mass models and modal solution are appropriate in analysing the dynamic response of sandwich panels. Different from only one main pulse shape in Figure 7(a), there are two main peaks in the FEM simulation for this mass ratio. In the modal superposition calculation, 40 modes were included and the time step chosen was  $5 \mu s$ , giving approximated 300 steps for the entire pulse. It can be seen that the difference of maximum impact forces between spring-mass models and finite element solution is less than 7%. However, either the 1 DOF or 2 DOF model cannot capture the pulse shape of the impact force. In contrast, modal superposition method shows a better agreement with the FEM result except for the discrepancy between the two peak forces; this difference is again partly due to neglect of membrane stretching of the facesheets.

If the mass ratio is small, only the modal superposition approach will provide an accurate estimate of the dynamic response of the sandwich panel. As shown in Figure 7(c), the spring-mass model completely fails in predicting the pulse shape of the impact force and the maximum impact force. However, the modal superposition analysis that considers 40 modes generates a good agreement with the FEM simulation.

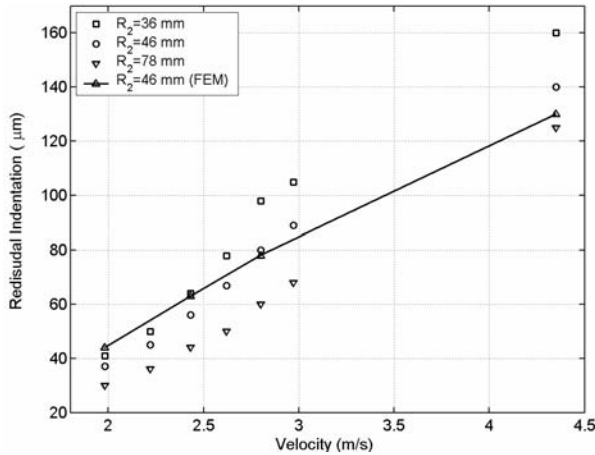


Figure 8. Measured and calculated residual indentation depth of sandwich panel HSSA centrally impacted by a ball of mass 11.9 g.

### 4.3 Residual indentation

Figure 8 gives the average experimental residual indentations of sandwich panels as a function of the impact energy. It can be seen that the residual indentation decreases with increasing panel size under the same

impact energy. A comparison of measured localized indentation depth with the simulated results for a sandwich panel with a radius of 46 mm hit by a steel ball of mass 11.9 g is also given.

## 5. CONCLUSIONS

On the basis of the contact relation, analytical models based on quasi-static and dynamic behaviours of the sandwich panel were developed in order to calculate impact force under low velocity impact on circular sandwich panels. Validity of these models strongly depends on mass ratio between the mass of the colliding missile and the effective mass of the sandwich plate. When the mass ratio is large (e.g.  $m > 16$ ), the local indentation stiffness can be ignored and spring-mass model (either 1 DOF or 2 DOF) can be used to estimate the impact response of the panel. When the mass ratio is in the intermediate range ( $8 < m < 16$ ), either the spring-mass model or modal superposition may be used to estimate the dynamic response of the panel. If the mass ratio is small ( $0 < m < 8$ ), only modal superposition can accurately predict the dynamic response of the sandwich panel.

Impact damage of sandwich panels can be numerically simulated based on a suitable choice of material model for the sandwich core. Residual indentation of the sandwich panel depends on the impact force, which is determined by the size of the panel, projectile mass and striking energy.

## REFERENCES

1. Abrate, S., Localized impact on sandwich structures with laminated facings. *Applied Mechanics Review*, 50(2), 69-82, 1997.
2. Swanson, S.R., Limits of quasi-static solutions in impact of composite structures. *Composites Engineering*, 2(4), 261-267, 1992.
3. Olsson, R., Mass criterion for wave controlled impact response of composite plates. *Composite Part A: Applied Science and Manufacturing*, 31(8), 879-887, 2000.
4. Zhou, D., and Stronge, W.J., Dynamic indentation of lightweight sandwich panels. 11th European Conference on Composite Materials (ECCM-11), Rhodes, Greece, 2004.
5. Zenkert, D., *An introduction to sandwich construction*, Chameleon Press, London, 1995.
6. Zhou, D. and Stronge, W.J., Modal frequencies of circular sandwich panels. *Journal of Sound and Vibration*, submitted for publication, 2005.
7. Zhou, D. and Stronge, W.J., Mechanical properties of fibrous core sandwich panels. *International Journal of Mechanical Sciences*, 2005, to appear.
8. Markaki, A.E. and Clyne, T.W., Mechanical and electrical properties of stainless steel sandwich sheet with fibrous metal cores, designed for automotive applications. *Metal and Ceramic Composites: Automotive Applications*, B. Cantor, ed., Oxford-Kobe Materials Seminar, 2004.

# BALLISTIC RESISTANCE OF 2D & 3D WOVEN SANDWICH COMPOSITES

Arun Shukla<sup>1</sup>, Joseph Grogan<sup>1</sup>, Srinivasan A. Tekalur<sup>1</sup>, Alex Bogdanovich<sup>2</sup>, and Robert A. Coffelt<sup>2</sup>

<sup>1</sup>*Dynamic Photomechanics Laboratory, MEAM, University of Rhode Island, Kingston, RI, USA*

<sup>2</sup>*3 Tex Corporation, Cary, NC 27511, USA*

**Abstract** In the present study, ballistic resistance of sandwich composite structures for vehicle armor panel applications was investigated. The core material of the sandwich structure was a layer of Alumina ceramic and a layer of composite backing, sandwiched between 2D plain weave composite skins. The ballistic performance of sandwich materials with 3D backing was compared to the baseline 2D plain weave backed composites. An IMACON 200 high-speed camera was used to obtain high-speed photographs of the ballistic events of penetration and damage. These images were analyzed to study real time damage mechanism of the strike face surface of several targets and subsequently to obtain average resistive force of target points during impact. Velocities of projectile (armor piercing bullets) were recorded in all the experiments and were found to be in the range of 915 - 975 m/s. Post mortem analyses, which included sectioning of panel, were performed. Results showed that armor panels with 3D woven backing had a higher ballistic efficiency than the 2D baseline panels, strike face damage mechanics were predominantly axi-symmetric about the impact point and panels with 3D backing had controlled delamination and fewer complete penetrations.

**Keywords:** sandwich composite structures, armor panels, 3D weave, ballistic resistance.

## 1. INTRODUCTION

Sandwich composite structures have been used in structures where weight saving is crucial. They are well known for their advantages of high modulus/weight and strength/weight ratios, and high energy absorption

through a variety of local failure modes. Energy absorption has been observed through various failure modes such as fiber breakage, matrix cracking, adhesive bond separation, and at a global scale as a delamination. Several sandwich structures are presently in service on marine vessels, aerospace industry and recently in automobiles and defense industries. These structural sandwich composites are composed of the core, facesheets, and the facesheet/core interphase regions. Over the years, many researchers have studied sandwich structures with special emphasis on the face sheets. Recent studies have directed attention towards the properties of core materials. In the present study, a sandwich composite structure utilized for protecting armored vehicles, was characterized for ballistic resistance. The significance of composite armors arise from the fact that conventional metallic armors are relatively heavy in construction. On the other hand, reinforced composites have been used for armor construction. But their susceptibility to impact damage have limited their widespread applications.

Woven composites have been utilized in various engineering and structural applications. Woven composites by nature are an ideal candidate for use in high performance ballistic and military applications, such as vehicle and personal body armor [1-3]. Woven fiber epoxy composites combine the beneficial properties of both polymer resins (ability to absorb and mitigate kinetic energy) and high performance fibers (high to ultrahigh elastic modulus). Most importantly, they are capable of providing equivalent ballistic protection at a significantly reduced areal weight as compared with traditional metal-based armor. One of the objectives of this study is to assess the effectiveness of 2D and 3D woven composites in ceramic composite armor systems.

## **2. EXPERIMENTAL PROCEDURE**

### **2.1 Materials**

All woven composites used in this study comprised of S-2 glass fibers. S-2, or Structural, glass fiber is a high strength high modulus fiber commonly used in high performance structures, and many performance critical applications (e.g ballistics). Silica,  $\text{SiO}_2$  forms the basis for S-2 glass fiber (approximately 65%), with additional traces of Alumina,  $\text{Al}_2\text{O}_3$ , (25%) and MgO (10.0 %). Two different weaving techniques were utilized to prepare the backing material, namely, 2D Plain weave and 3 D weave.

2D Plain weaves were made by the interlacing of two or more orthogonal sets of yarns (commonly referred to as the warp and weft fibers) on a loom.

The majority of weaves are orthogonal, with warp and weft fibers woven perpendicular to each other. Three-dimensional orthogonal woven composites, hereafter referred to as 3D composites are different from traditional 2D laminates in that they are able to sustain loads in three linearly independent directions. Fiber performs constructed in a three dimensional fashion not only contain warp and weft fibers in plane of the lamina, but also a certain fraction in the through thickness, or z-direction. While such a characteristic has the greatest potential for improving mechanical performance, low-cost 3D reinforcements have not been available on an industrial scale. A schematic of a typical lamina constructed through a 3Weave<sup>TM</sup> weaving process is illustrated in Figure 1. The essence of the 3Weave process is two or more of the filling yarns are simultaneously inserted from one or both sides, thus building an increment of 3D fabric length with every revolution of the weaving machine. In the 3Weave performing process, a third set of yarns, called Z-yarns, then integrates all sets of yarns into a single woven fabric lamina.

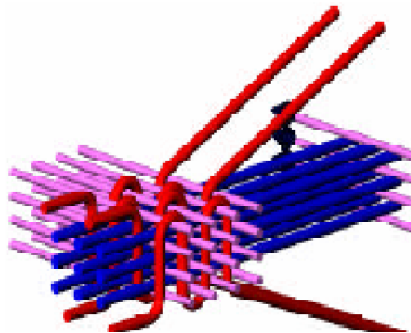


Figure 1. Schematic of a three dimensional 3Weave process.

Several advantages of 3D preforms become obvious. 3D fabric preform laminas may be constructed to any given thickness, whereas a 2D plain weave lamina thickness is limited by the out-of-plane waviness of the fabric. One ply of a 3D fabric preform could conceivably replace dozens or even hundreds of 2D plain weave lamina, which can reduced manufacturing times and costs considerably. In addition, fiber kinking of the warp and weft fibers is greatly reduced, thus maintaining the inherent strength and stiffness of the fibers. The Z-yarns also provide a substantial resistance mechanism to delamination under bending and shearing loads.

The amount of z-direction reinforcement is crucial to the performance of a 3D weave. The Z-yarns tends to create voids in the spatially separated layers of the warp and fill layers, reducing the volume that could otherwise be occupied by fill and warp yarns. Available experimental data and

theoretical estimates [4] conclude that the in-plane volume fraction drops considerably when increasing Z-fiber volume content above 4-5%. However, it has been shown [4] that at least 2-3% Z-fiber content is necessary to suppress delamination and significantly increase fracture resistance and damage tolerance of the resulting 3D composite. Thus, preforms with approximately 2-4% of Z-fiber volume content result in an optimum mechanical performance.

The 2D plain weave composites were constructed with a 24oz/yd<sup>2</sup> fabric (hereafter labeled as 24oz 2D) while the 3D composites were constructed with 90, 93, 98, and 190oz/yd<sup>2</sup> fabric (hereafter labeled as 90oz 93oz 98oz 190oz/3D). Relative in plane fiber volume fractions within individual warp and fill layers ranged from approximately 45-50%. Z-direction fiber volume fractions ranged from 2.0 - 4.0%, with the lowest seen in the 190oz 3D lamina. Average lamina thickness was largely controlled by total number of layers within individual 3D lamina constructions, and ranged from 0.10 - 0.22 inches. Unit cell sizes for all 3D composite lamina were approximate to the 0.4" x 0.4" 24oz 2D unit cell.

## **2.2 Ballistic testing**

### **2.2.1 Armor panel construction**

Figure 2 illustrates the basic construction and composition of the vehicle armor panels used in this study. There are two main ballistic components of a ceramic composite armor system: the ceramic strike face and the structural composite backing. The strike and back face cover layers hold fractured ceramic tiles in place for additional support against subsequent projectile impact.

Ceramic strike face materials are commonly used for the containment of blast fragments and bullet penetrators. The most common ceramic materials used are alumina (Al<sub>2</sub>O<sub>3</sub>), Boron Carbide (B<sub>4</sub>C), Silicon Carbide (SiC) and titanium diboride (TiB<sub>2</sub>); Alumina (85% pure) is most widely used due to its lower cost. The vehicle armor panels tested in this study were composed of alumina ceramic strike facings.

Fiber-based composites are commonly used as armor backings because of their low weight and excellent energy absorption characteristics. S-2 Fiberglass, Kevlar, and Spectra are commonly used in conjunction with high strength epoxy resins to create effective composite backings. The majority of the vehicle armor panels used in this study were comprised of S-2 fiberglass woven composite laminate backing with either a 2D or 3D construction, as defined previously.

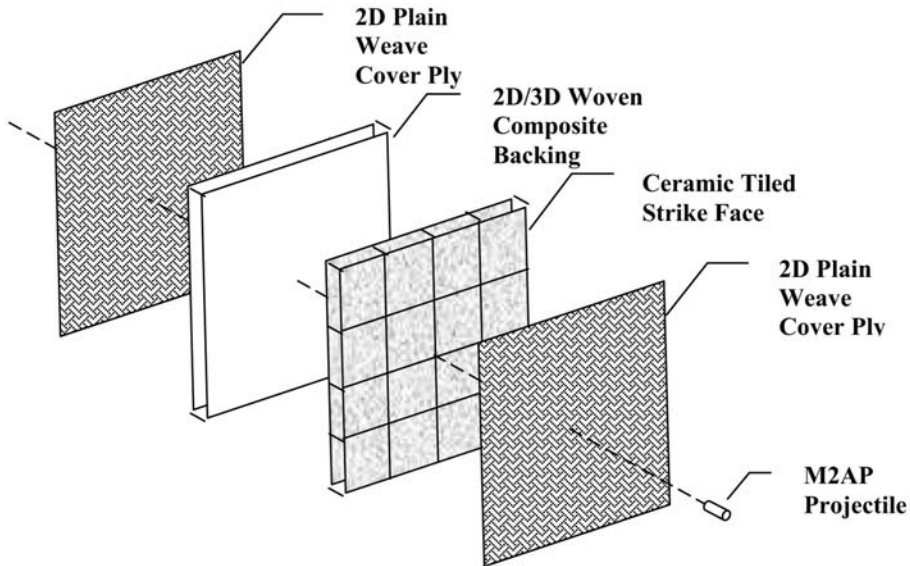


Figure 2. Schematic of typical vehicle armor panel construction.

Because of their laminated structure, composite backing are more susceptible to damage, most often in the form of delamination. Traditional composite backing have included some extent of through-thickness stitching to increase damage tolerance. One important aspect of this study was to assess the effect of the 3D 3Weave on the damage tolerance of the composite backing.

### 2.2.2 Ballistic test panels

A total of 13 vehicle armor panels were tested in the ballistics laboratory at URI. All vehicle armor panels had constructions similar to Figure 2, consisting solely of a tiled ceramic strike face and a woven composite backing. The strike face of each vehicle armor panel consisted of a 4 x 4 array of square strike face ceramic tiles, each approximately 4" x 4" x 0.35" thick. The tiles were glued together using high strength Derakane 8084 Resin, creating a 16" x 16" square facing. Tile quad points intersections were reinforced with 304 Stainless quad shims approximately 1.5" x 1.5" x 0.06" in size to improve ballistic efficiency. Each of the sixteen panels also consisted of a 2D/3D woven composite backing, approximately 0.75" thick. Number of laminas used in the composite backing varied to obtain an approximately equal backing thickness in all armor panels, allowing for a

fair ballistic comparison. All panels were faced with Coors Tek CAP 4 Alumina Ceramic tiles. All types of 2D (24oz) and 3D (90oz 93oz 98oz 190oz) were represented. The front and back faces were faced with a 16" x 16" layer of 24oz 2D fabric. An additional layer of 24oz S-2 fabric was added to the strike face and folded over to the back of the target by approximately 2", and all four corners were miter cut on a 45 degree angle. All panels were fabricated using a Vacuum Assisted Resin Transfer Molding method in a closed mold having approximately 16.3"x 16.3" in-plane dimensions. Armor panel areal densities varied from 11.8-12.4 psf.

### 2.2.3 Experimental setup

The URI ballistics laboratory consists of a 24 ft<sup>3</sup> steel target chamber with a 4 ft<sup>3</sup> steel tunnel attached for safety reasons, and a steel target mounting fixture (Figure 3) The muzzle of the rifle was inserted into a hole at end of the tunnel, and the entire rifle was kept level through use of an adjustable steel support. The composite vehicle armor panels were mounted with c-clamps onto a 17" x 17" target fixture constructed of 1" box channel steel with radius edges to mitigate shearing at the inside support edges. The target was c-clamped to the fixture on all four corners. This target fixture has a 14" window, allowing for a 1" support of the perimeter of the test panels, which provided a stable and realistic target mounting. The entire steel target fixture is attached to a set of channels that allow for vertical and horizontal adjustments perpendicular to the line of projectile impact.



Figure 3. Schematic of ballistic gun range and velocity screens.

### 2.2.4 Firing procedure

A schematic of the target firing template sequence is shown in Figure 4.

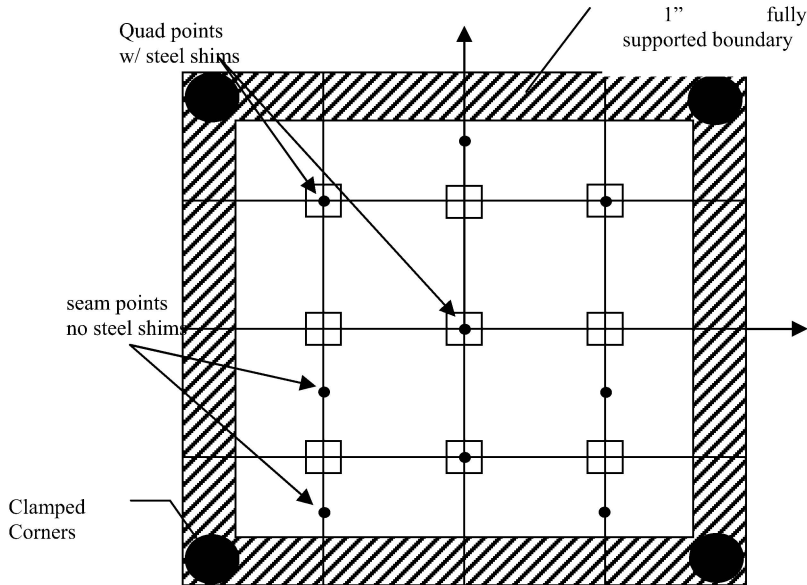


Figure 4. Strike face view of mounted vehicle armor panel with labeled target points (fired 1 through 9, inclusive).

Nine target points, consisting of various quad and seam tile points, were labeled, as shown in the figure. Quad points were defined as the four-way intersection of strike face tiles, while seam points were defined as the two-way intersections. Both quad and seam tile points were deemed the weakest structural and ballistic points on each panel, as the inherent strength of these points relies solely on tile intersection boundaries. Distance between target points was at least 2.5", in order to minimize effects of completed test shots on subsequent test shots. Nine M2AP projectiles were fired at target points 1-9, inclusive, perpendicular to the strike face of each vehicle armor panel. Propellant charges were adjusted to control projectile velocity, in order to establish a V50 for each panel. Smokeless gun powder was the propellant charge used in this study.

### **3. RESULTS & DISCUSSIONS**

#### **3.1 Ballistic results**

##### **3.1.1 V50 and CP/PP analysis for AL<sub>2</sub>O<sub>3</sub> ceramic faced panels**

Overall, V50 ranged from 3181-3255 ft/sec (2.3% variation). Number of complete penetrations was generally lower in 3D composite backed panels than 2D panels. Areal densities ranged from 11.7 –12.4 (5.9% variation). Because of such low variations in areal density and V50 values, all panels were very similar as far as these particular ballistic parameters. Because of the complexities of the system (shot location, general panel degradation), the V50 value are approximate, and somewhat difficult to established within nine shots of each panel. Thus, a general conclusion is that panels with 3D woven composite backings have a higher ballistic efficiency based on the lower amount of complete penetrations.

##### **3.1.2 Cover layer delamination/damage areas versus projectile velocity**

Projectile velocities ranged from 3000-3300 ft/sec for all panels. There is no significant repeated trend observed for each case, but several qualitative results are worth mentioning:

- (1) A general decrease in delamination/damage areas with increasing in projectile velocity can be observed in some of the panels. Panels impacted with lower velocity projectile have less kinetic energy to absorb, which would effectively decrease delamination/damage areas (delamination is one form of energy absorption).
- (2) In general, delamination and damage areas were lower with complete penetrations than partial penetrations. This is also indicative of energy absorption characteristics. For a complete penetration, projectiles do not distribute all of their kinetic energy into the panel, which would result in a lower delamination area.
- (3) Delamination Area shows a greater variation to projectile velocity than damage area.

#### **3.2 Post mortem analysis**

The post mortem analysis of each vehicle armor panel consisted the following:

- (1) Assessment and comparison of visible strike face cover layer damage caused by projectile impact for each shot.
- (2) Assessment and comparison of damage caused to the ceramic facing and main woven composite backing for all vehicle armor panels.
- (3) Damage characterization in 2D & 3D composite backings.

### 3.2.1 Ceramic facing and woven composite backing damage

Water jet sectioning was conducted each vehicle armor panel each type of 2D/3D composite backing to quantify the extent of damage to the main composite backing caused by projectile impact. Peak performance panel (least number of CP) were chosen for sectioning.

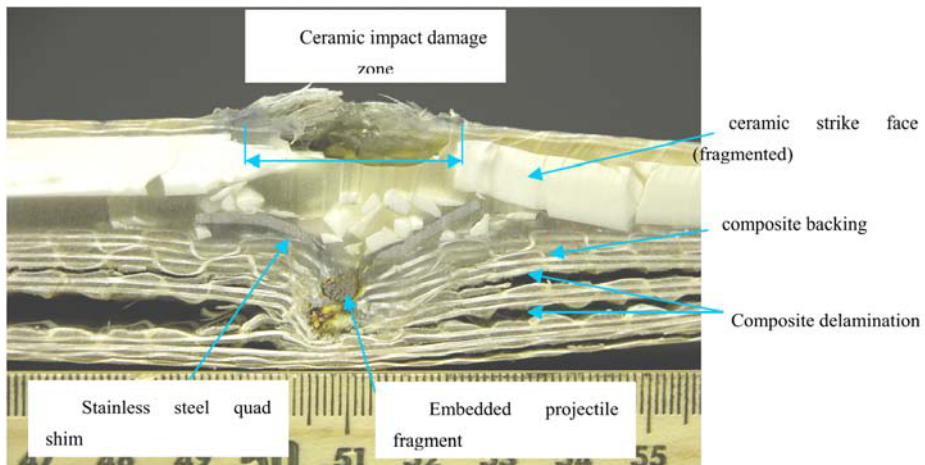


Figure 5. Sectioned view of individual round in vehicle armor panel with 3D woven backing.

Figure 5 shows a typical sectioned view of an individual shot point. The Ceramic facing typically sustained a severe damage impact zone, characterized by a noticeable gap. Through thickness fragmentation also occurred, fracturing the ceramic into several pieces of varying size. Interlaminary delamination was the primary damage mode viewed in all composite backings. The length and location of delamination was noted for all panels.

## 4. CONCLUSIONS

Vehicle Armor Panels with 2D and 3D woven composite backings were tested in the URI ballistics laboratory. Each panel was fired in a predetermined shot pattern. Post mortem analysis showed that armor panels with 3D woven backing had a higher ballistic efficiency than the 2D baseline panels, with controlled delamination and fewer complete penetrations. Delamination was more localized in the cases of the 24oz 2D composite vehicle armor panel. However, due to higher complete penetrations, it is believed that the projectile was able to penetrate the backing through direct tearing of the in-plane crimped fibers, without energy absorption through delamination.

The majority of the delamination within the 3D composite vehicle armor panels transversed the full length of the panel. Because of the uncrimped nature of the warp and weft fibers, the individual lamina effectively act as a woven net to stop penetration, and allow kinetic energy to be absorbed mainly through intralaminar delamination. The severity (opening) of the delamination in the 3D composite armor panels decreased with increasing preform areal density, with the most controlled delamination seen in the vehicle armor panels with 98oz/3D and 190oz/3D composite backings. This could be due to the thickness lamina preforms, which would effectively increase the section moment of inertia, and decreasing resulting bending and through thickness shearing stresses.

## ACKNOWLEDGEMENTS

The support of Army Research Office through grant No. C-DAAD 19-02-C-0044 and Office of Naval Research under grant No. N000140410268 is gratefully acknowledged by the authors.

## REFERENCES

1. Bless, S.J. and Hartman, D.R., "Ballistic Penetration of S-2 Glass Laminates," Proc. 21st Int. SAMPE Technical Conference, September 1989, p. 825.
2. Bogdanovich, A., Coffelt, R.A. et al., "Innovative Materials for Lightweight Armor," Contract No. DAAD17-01-C-0086, U.S. Army Report, September 2003.
3. Viechnicki, D.J., Anctil, A.A., Papetti, D.J. and Prifti, J.J., "Lightweight Armor – A Status Report," MTL-TR-89-8, January 1989; DTIC Doc AD-D150 327.
4. Bogdanovich, A., Coffelt, R.A., et al., "3-D Orthogonal Woven Composites in Armor Systems," C-DAAD 19-02-C-0044, U.S. Army STTR Phase II Report, June 2002–June 2004.
5. Czarnecki, G.J., "Estimation of the V50 Using Semi-Empirical (1-point) Procedures," Composites Part B Engineering, Vol. 29B (1997), pp. 321-329.

# IMPACT AND INDENTATION BEHAVIOR OF SANDWICH PANELS

## *Modeling and Experimental Testing*

Carl-Johan Lindholm

*Technical Service, DIAB, Laholm, Sweden*

**Abstract** The behavior of sandwich panels subjected to local loads and low-velocity impact is studied with analytical and numerical methods as well as quasi-static testing and low-speed impact testing. The results indicate that the core thickness has no influence on the initial part of the indentation behavior for a panel if the core thickness is larger than a certain critical core thickness. Both the analytical model and the numerical calculations agreed well with both the quasi-static testing and the low-velocity impact test.

**Keywords:** foams, indentation, impact, modeling.

## 1. INTRODUCTION

The present paper reports on progress in research on localized loads and impact on sandwich panels. The objective with the project is to find and validate methods to design sandwich structures subjected to localized loads and impact. Several studies of the indentation on sandwich panels have been performed in the past. For example Abrate [1], who in his work summarized recent, modeling techniques for localized impact on composite structures and Olsson [2], who presented an “Engineering Method for Prediction of Impact Response and Damage in Sandwich Panels”.

In order to give a short introduction to the problems associated with an indentation on a sandwich panel a typical test set up is shown in Figure 1 with the corresponding load-displacement curve in Figure 2. The local indentation underneath a hemispherical indenter may be divided into three segments. In segment 1 both the core and the face sheets are undamaged. Segment one ends at the point denoted  $F_{cr}$ , which is the load where core

crushing is initiated. Segment 2 is dominated by a decreased overall stiffness due to the softening of the core material. In segment 3, the region of crushed core material underneath the indenter is growing at the same time as the membrane effects increases in the face.

In the present paper the first stages (1 and 2) of the indentation behavior are investigated. The study is performed with analytical and numerical methods as well as experimental methods, both quasi-static testing and low-velocity impact testing. In [3] the influence of the core material properties were investigated, one objective with this paper is to determine the influence of the core thickness. The intention is furthermore to investigate if static models also can be used for low-velocity impacts.



Figure 1. Experimental set-up for indentation testing.

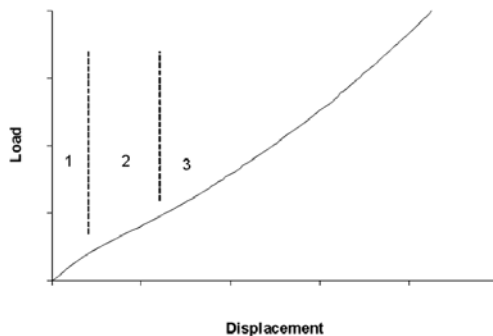


Figure 2. Typical response of a sandwich panel subjected to a hemispherical indenter.

## 2. EXPERIMENTAL ANALYSIS

### 2.1 Materials and test specimens

The sandwich panels considered in this study consisted of GRP facings and Divinycell H100 PVC foam core [4]. The face sheets consisted of Gamma Tensor Q840-G glass fiber fabric which corresponds to a lay up of  $[0^{\circ}_{240}/45^{\circ}_{200}/90^{\circ}_{200}/-45^{\circ}_{200}]_{2s}$ . All panels were manufactured with vacuum infusion with Reichhold PD1341 polyester as resin. The face sheets on the panels were approximately 1.4 mm thick. The fiber volume fraction of the face sheets was measured to 0.42-0.47. According to the rules of mixture and lamination theory [5] the equivalent Young Modulus would be 15 MPa if  $E_{\text{fiber}}=70$  GPa and  $E_{\text{matrix}}=3.1$  GPa [6]. Panels were manufactured with core thicknesses of 10, 40 and 60 mm, the density for respective panel were 103, 103 and 104 kg/m<sup>3</sup>.

### 2.2 Quasi-static testing

The quasi-static indentation tests were performed with an Instron universal testing machine, the test set up is shown in Figure 1. The test panels rested on a rigid metal foundation. The velocity of the crosshead was set to 2 mm/min and a 5 kN loadcell was used. The indentation was recorded by the crosshead movement. The recording rate was 10 Hz giving 300 data points per millimeter. The indenter was hemispherical with a radius of 12.5 mm.

### 2.3 Low-velocity impact

The impact tests were performed with a drop test rig. During the drop tests the acceleration was measured with an accelerometer attached on the hemispherical indenter. The displacement was measured with an optical measurement device. Hence both the velocity and the maximum force could be calculated after the test. The accelerometer was calibrated at a frequency of 79.7 Hz and the calibrating values were 9.85-9.95 m/s<sup>2</sup>, hence the deviation is 0.01 m/s<sup>2</sup>. The sampling frequency was 100 kHz. The impact testing was performed with the same hemispherical indenter as in the quasi-static testing, which had a total mass of 2.6 kg.

The drop height was calculated to give a maximal indentation of the core of 2 mm. By calculating the energy from the quasi-static tests e.g. the area under the load-displacement curve, the drop height was calculated from the relation of potential energy,  $W=m \cdot g \cdot h$ , where  $W$ =energy,  $m$ =impactor mass,  $g$ =acceleration of gravity, (9.82 m/s<sup>2</sup>). In this case  $W=1600$  Nmm and  $m=2.6$

kg, hence  $h=60$  mm. The impact velocity,  $v$ , was then estimated from the relation of kinetic energy,  $W=m\cdot v^2/2$ . In this case  $v=1.1$  m/s. After the test the velocity was also calculated using the data from the optical device. The measured velocity agreed well with the predicted, hence the friction in the test rig could be neglected in the evaluation of the results.

### 3. ANALYTICAL CALCULATION

The indentation model used in this study was originally proposed by Olsson [2]. The model includes core crushing, large face sheet deflections and delaminations. Since the focus of this study was to investigate indentations at low loads prior to and including core crushing the delamination part was excluded in all calculations. The mechanical properties used for the foam core was taken from [4], Young's modulus,  $E_c=125$  MPa and compressive strength,  $\sigma_c=1.7$  MPa. More details on how the model has been used can be found in [3].

### 4. FINITE ELEMENT ANALYSIS

The FE analysis was performed with the FE package ABAQUS. An axisymmetric model was made that included the nonlinear material behavior of the foam core and the geometrical nonlinear behavior due to membrane stresses in the face sheet and also the contact phenomena under the indenter. The two-dimensional mesh is shown in Figure 3. The top face of 1.4 mm was modeled with two elements through the thickness and the core of 20 mm was modeled with 11 elements through the thickness. The mesh was selected after a convergence analysis with 1 to 4 elements in the face sheet and a refinement of the elements in the core to half the size of the one used in this mesh. Four-node elements (CAX4) were used. The bottom face was neglected, instead all nodes at the bottom of the core were constrained in all degrees of freedom in order to simulate a rigid support. The indenter was modeled as a rigid hemisphere.

The response of the core material was modeled using \*CRUSHABLE FOAM and \*CRUSHABLE FOAM HARDENING in ABAQUS. The material properties of the foam core were taken from a uniaxial test carried out at KTH according to ASTM D1621. In the test the extensometer was mounted on the steel plates which compressed the specimen. The linear part of the foam core's material behavior is modeled with Young's modulus,  $E_c=87.5$  MPa, initial yield stress in uniaxial compression,  $\sigma_c^0=1.4$  MPa and Poisson's ratio=0.32. Hydrostatic compressive test performed with a test

similar to ASTM D3102 indicated that the initial yield stress in hydrostatic compression  $p_c^0 = \sigma_c^0$ . For the \*CRUSHABLE FOAM option in ABAQUS also the initial yield strength in hydrostatic tension,  $p_t$ , is needed. However for this case the core should not be stressed in hydrostatic tension and hence the value of  $p_t$  should not influence on the result. Nevertheless,  $p_t$  was set to  $1.9p_c^0$ . In order to verify the material model a calculation simulating a compression test was performed with one element, the result is shown in Figure 4 and reflects very well the results from the actual compression test, except the second plateau which occurs because the input curve ends at 5 MPa.

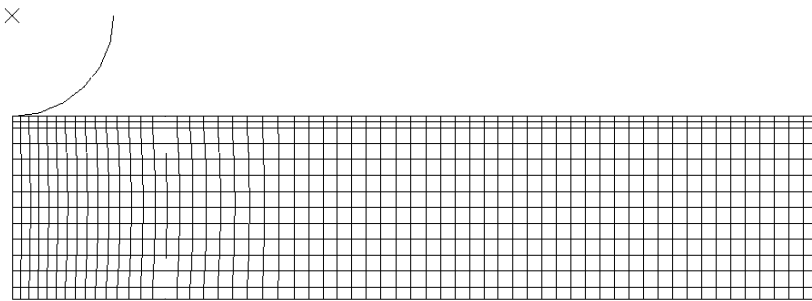


Figure 3. Finite element mesh.

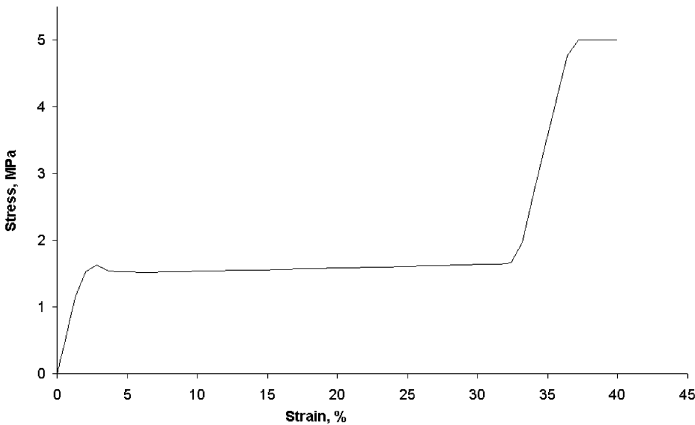


Figure 4. Uniaxial compression - ABAQUS 1 element.

## 5. RESULTS AND DISCUSSION

### 5.1 Quasi-static testing and theoretical result

From the indentation test with different core thickness an indentation curve from each sample is presented, see Figure 5. The most representative curve from each sample has been selected. As can be seen the behavior of the three different panels are much similar. Hence, the results indicate that once a certain "critical" core thickness is reached a further increase of core thickness will not influence on the initial indentation behavior. The result also implies that for this particular sandwich configuration the "critical" thickness is less than 10 mm. Olsson's [2] model designates this critical thickness as,  $h_{c\_max}$ , which depend on the material properties of the core and the bending stiffness of the face. For the tested sandwich configuration  $h_{c\_max}=9$  mm.

The load-indentation response predicted by Olsson's model and the FE model are shown in Figure 6 together with experimental results. Both models agreed well with the experimental results.

The load at which core crushing is initiated,  $P_{cr}$ , was measured during the test by observing the load where the linear load-displacement behavior ended. The details on how the end of the linear part is defined can be found in [3]. In order to predict,  $P_{cr}$ , with the FEA a model with refined mesh was used, where the element size was in the magnitude of the cell size of the core material. The value of  $P_{cr}$  was recorded when the compression stress in the element right under the face exceeded the core materials compression strength. The calculated values on  $P_{cr}$ , are shown in table 1 together with the experimental value. Since both the analytical and FE analysis predicted a  $P_{cr}$  almost half the value of the experimental determined this may indicate that the experimental method overestimate the load, which may be accurate since the experimental method only use the response on the load-displacement curve as measurement. Hence, no further conclusion can be made on how well the theoretical predictions fit with the reality considering,  $P_{cr}$ . However, it should be noticed that it is also hard to evaluate the stress at the border of two materials with a FE model. If  $P_{cr}$  instead is taken when two elements below the face sheet is stressed above the compression strength of the core  $P_{cr}=295$  N.

Table 1. The load at which core crushing is initiated.

	Experiment	Olsson	FEA
$P_{cr}$ , [N]	270	127	160

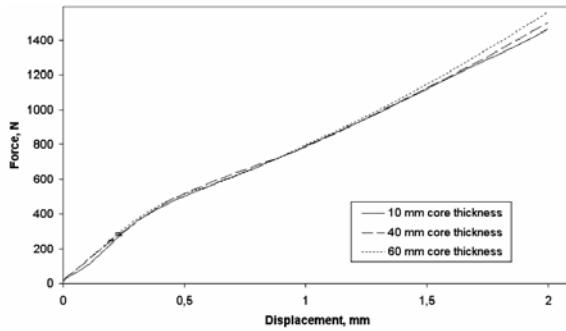


Figure 5. Results from the indentation test with different core thickness; a representative curve from each sample has been selected, the load  $P_{cr}$  is marked for each curve.

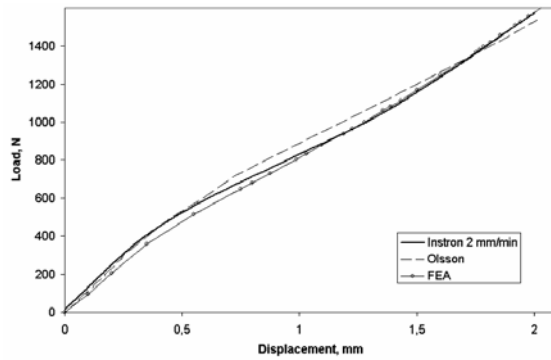


Figure 6. Indentation response from quasi-static testing, analytical prediction and FE analysis.

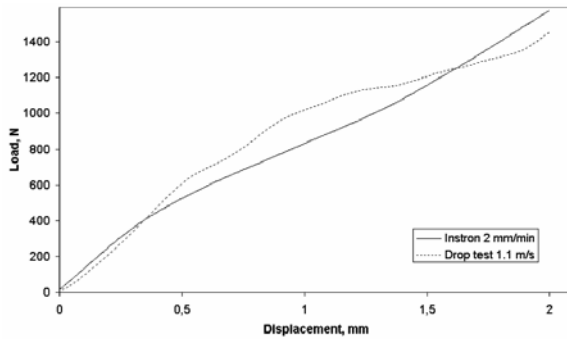


Figure 7. Indentation response from quasi-static testing and drop weight testing.

## 5.2 Low-velocity impact testing

The load-displacement response from the drop rig test is presented in Figure 7 together with the result from the quasi-static testing. The load-displacement curve from the drop test shows fairly good conformity with the quasi-static test. Even if the result from the accelerometer has been filtered, there is still an oscillation on the curve which probably depends on the background frequency. Due to the oscillation no estimation could be made on where the elastic part of the impact ends. The maximum displacement measured at the drop test with the optical device corresponds well to the predicted 2 mm.

## 6. CONCLUSION

Based on the static indentation test results on specimens with varying core thickness, it can be concluded that the core thickness has no influence on the initial part of the indentation behavior once a certain core thickness has been exceeded. Hence also the load at which core crushing is initiated is independent of the core thickness for this case, which is in accordance with the analytical model proposed in [2].

Both the analytical and the numerical model agreed well with the quasi-static testing considering the indentation response. Further the results indicate that the static models could be used to predict the response on low-velocity impact.

## REFERENCES

1. Abrate S., *Impact on Composite Structures*, Cambridge University Press, 1998.
2. Olsson R., "Engineering Method for Prediction of Impact Response and Damage in sandwich Panels", *Journal of Sandwich Structures and Materials*, Vol. 4 – January 2002.
3. Lindholm C.-J and Abrahamsson P., "Modeling and testing of the indentation behavior of sandwich panels subject to localized load", 6th International Conference on Sandwich Structures, Florida, 2003.
4. DIAB AB, Laholm, Sweden, Divinycell H-grade Technical Manual, 1999.
5. Zenkert D., *An Introduction To Sandwich Construction*, Engineering Materials Advisory Services Ltd. 1995.
6. Åström B.T., *Manufacturing of Polymer Composites*, Chapman & Hall, 1997.

# A COMPARISON OF LOW ENERGY IMPACT BEHAVIOUR IN ALUMINIUM FOAM AND POLYMER FOAM SANDWICH STRUCTURES

P. Compston, M. Styles and S. Kalyanasundaram

*Department of Engineering, FEIT, Australian National University, Canberra ACT 0200, Australia*

**Abstract** Energy absorption of polymer and aluminum foam sandwich structures with glass-fibre composite skins was similar for 5-25J impacts. The polymer foam structure exhibited localized fibre fracture and core crushing as impact energy increased. The aluminum foam structure exhibited extensive plastic deformation, radiating from the impact point, at all impact energies.

**Keywords:** aluminium foam, low energy impact, out-of-plane deformation.

## 1. INTRODUCTION

Stiff and lightweight polymer foam cores are commonly used in sandwich structures for a variety of applications, but these cores are brittle which can adversely affect impact behaviour [1]. Mines et al. [2] studied low velocity impact behaviour of polymer foam sandwich structures and developed phenomenological models for perforation. The authors concluded that sandwich structure impact performance, characterized by perforation resistance, would be improved through increased energy absorption to initial and final composite skin failure and, critically, core crushing failure. However, Kindervater [3] has concluded that there is little scope of improving the energy absorbing capabilities of these commonly used core materials. Therefore, novel core materials will be required in order to make significant improvements in the impact performance of sandwich structures.

Metal foams have a number of attractive properties which highlight their potential for use as cores in sandwich structures; good stiffness and strength

to weight ratios, good sound damping, electromagnetic wave absorption, thermal insulation and non combustibility [4]. Another characteristic of interest is impact performance. It has been shown that the main failure mode is progressive crushing of the cell structures in the foam [4], which has potential to absorb significant amounts of impact energy. Relatively recent work with aluminium foam has highlighted good impact performance in sandwich structures with composite skins, with significant impact energy absorbed through buckling and crushing in the foam core [5, 6]. In addition, McKown and Mines [7] investigated low velocity impact of aluminium foam with composite skins and identified the major failure modes as upper skin failure and progressive crushing of the core followed by core shear failure.

The disadvantages of commonly used polymer foam structures and the possible advantages of aluminum foam structures under impact have been identified. However, there is no work on a direct comparison of impact performance and failure modes. The current study investigates the low energy impact behaviour of aluminium foam and polymer foam based sandwich structures under identical impact conditions. Polymer and aluminum foam sandwich structures with composite skins will be subjected to impacts in the range of 5-25J. Characterisation will focus on energy absorption and sample deformation.

## **2. EXPERIMENTAL METHOD**

### **2.1 Materials and manufacture**

An aluminium foam sandwich panel, 200 x 200 mm, was made by placing a single ply of 745-gsm plain weave glass-fibre/polypropylene prepreg (Twintex, Vetrotex Inc.) either side of a sheet of 5.2 mm thick closed cell aluminium foam (ALPORAS Gleich, GmbH, Germany). The glass content of the Twintex was 60% by weight, giving a fibreglass weight of 447-gsm. The density of the aluminum foam was 0.23 g/cm<sup>3</sup>. For bonding, two layers of 50 µm thick polypropylene adhesive (Glucol, Glucol Ltd. UK) were placed at each bi-material interface. The mould was heated to 185°C in a platen press then stamped and held at a pressure of 2.5 MPa while cooled rapidly using a water cooling system. The average sample thickness was 5.9 mm and density 0.550 g/cm<sup>3</sup>.

A sandwich structure with polymer foam core was manufactured with 1-ply of 450-gsm plain weave fibreglass (Colan) either side of a 5.2 mm thick closed cell PVC-based foam (Klegecell, Diab). The composite skins were made by wet lay-up using a vinylester resin matrix (Derakane 411-350, Dow

Chemical). The weight of the fibreglass was chosen to match closely the fibre weight in the Twintex, hence giving similar fibre content for each sandwich structure. The polymer foam panel was cured at room temperature for 24 hours and then post-cured at 71°C for 18 hours, as per the resin manufactures instructions, to achieve maximum resin properties. The average sample thickness was 6.2 mm and density 0.549 g/cm<sup>3</sup>.

## **2.2 Impact testing and characterisation**

Impact testing was conducted using an in-house built double pendulum impact tester. Samples of dimensions 80 x 80 mm were placed in a sample holder and impacted with a hemispherical impactor 10 mm in diameter. Samples were impacted with incident energies ranging from 5 to 25 J, in 5 J increments. The mass of the impactor and sample holder was nominally 5 kg, therefore the incident energies were achieved by varying the drop height. The impact velocity range was 1.4–3.1 m/s. Shaft encoders recorded the rebound position of the pendulum arms after impact. The absorbed energy was taken as the difference between the incident potential energy and the energy corresponding to the rebound peaks. The failure and deformation behaviour were elucidated using optical microscopy and by scanning impacted samples with a FaroArm (model PO8) 3-D measuring system. The scanned data was analysed using Polyworks/Inspector™ software and a deformation profile was produced.

## **3. RESULTS/DISCUSSION**

### **3.1 Impact behaviour**

A typical plot of the change in potential energy during the impact test is shown in Figure 1 for aluminium foam samples impacted at 5 and 25 J. A plot of absorbed energy versus incident potential energy for each sandwich structure is shown in Figure 2. There is a reasonably linear relationship between incident and absorbed energy, and the value for absorbed energy is similar for each sandwich structure. It is noted that the results for the 20J impacts do not fit the linear relationship perfectly, but this is attributed to experimental scatter.

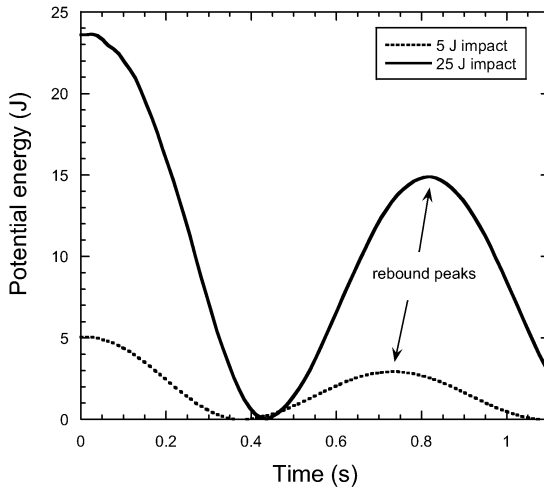


Figure 1. Potential energy versus time for aluminum foam sandwich impacted at 5 and 25 J.

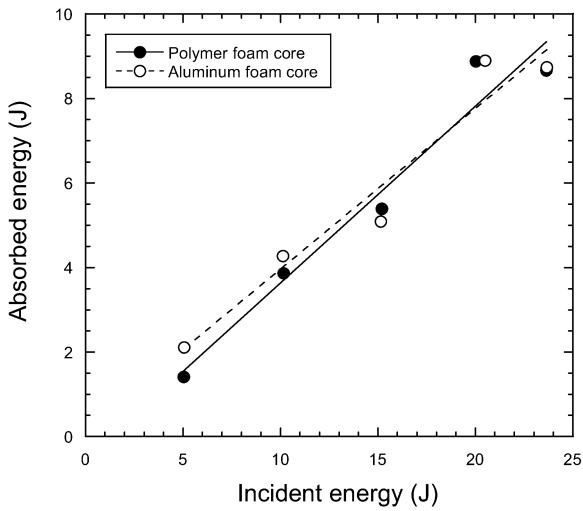


Figure 2. Absorbed energy versus incident impact energy.

Although the energy absorption is similar, there were significant differences in failure behaviour between the structures. Micrographs of cross-sections of polymer foam core samples impacted at 5 and 25 J are shown in Figure 3. Matrix cracking and core indentation are the main failure modes at 5J. At 25 J, there is penetration of the sample, with skin fracture and extensive core crushing through to the back-face. In contrast, the aluminum foam core samples impacted in Figure 4 both show core crushing as the main failure mode, with the amount of crushing greater for the 25J impact. This is consistent with observations in previous work [6,7]. The aluminum foam core samples also show greater permanent deformation than their polymer core counterparts.

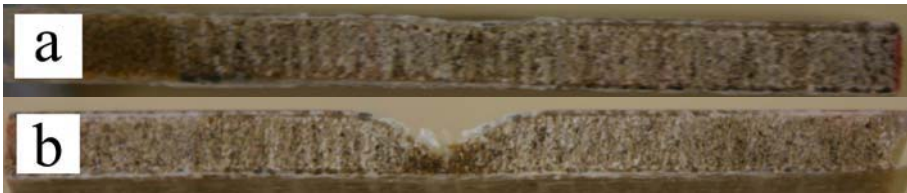
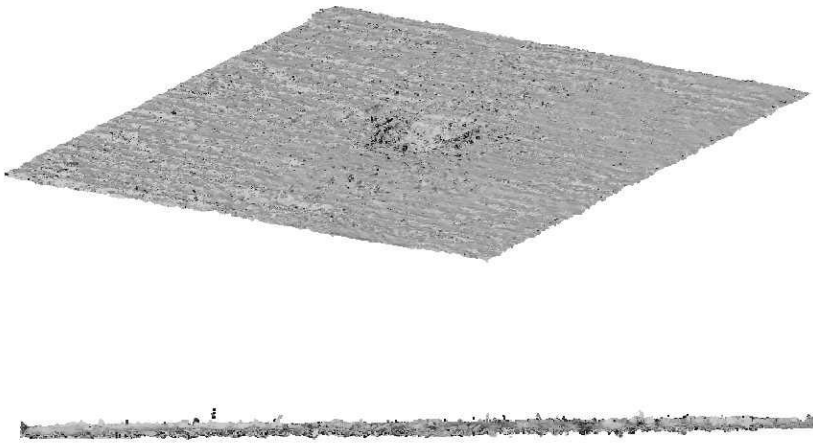


Figure 3. Cross-sections of polymer foam core samples impacted at: (a) 5 and (b) 25 J.

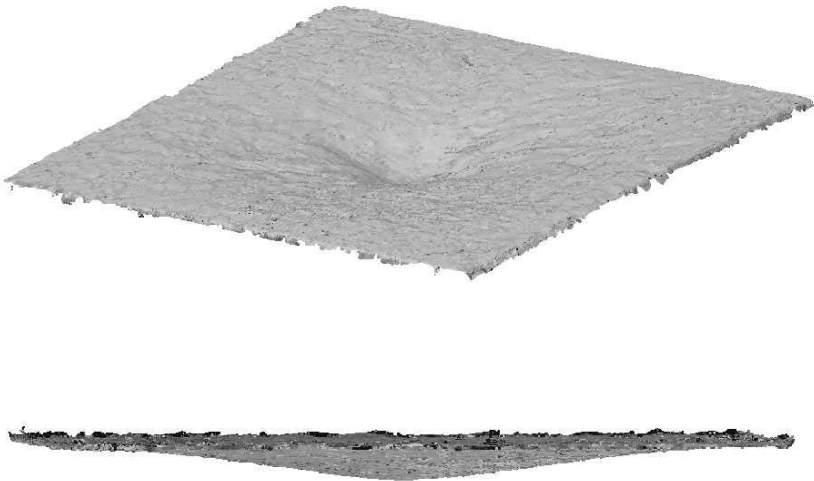


Figure 4. Cross-sections of aluminum foam core samples impacted at: (a) 5 and (b) 25 J.

The difference in the out-of-plane deformation between the two structures is captured in more detail with the FaroArm laser scanner. Examples of the scanning output are given for the polymer and aluminum foam sandwich samples impacted at 25J as they shown major differences in failure. The 3-D profile of the polymer foam core sample in Figure 5 shows the front face indentation depth and the 2-D side profile indicates little back-face deformation. In contrast, the 3-D and 2-D profiles for the aluminium foam core sample in Figure 6 show extensive out-of-plane deformation on the front and back faces.



*Figure 5.* 3-D front-face and 2-D profiles of polymer foam sandwich impacted at 25J.



*Figure 6.* 3-D front-face and 2-D profiles of aluminium foam sandwich impacted at 25J.

All samples were scanned and the maximum front face indentation and back-face displacement were measured. The results are plotted against impact energy for polymer and aluminium foam core samples in Figures 7 and 8 respectively. There is clear divergence between maximum displacement for indentation on the front face and out-of-plane deformation on the back face of the polymer foam sandwich, with increasing impact energy. This indicates that thickness reduction is therefore significant for the polymer foam core structures with increasing impact energy, as indicated by the micrographs in Figure 3. The aluminium foam core samples show different behaviour. The values for front face indentation and back face displacement appear to increase linearly with increasing impact energy, with the difference between the two values remaining relatively constant. This indicates only a slight reduction in thickness, due to the core crushing observed in Figure 4, and that the extent of core crushing in the aluminium foam samples is similar for all samples over the impact energy range investigated.

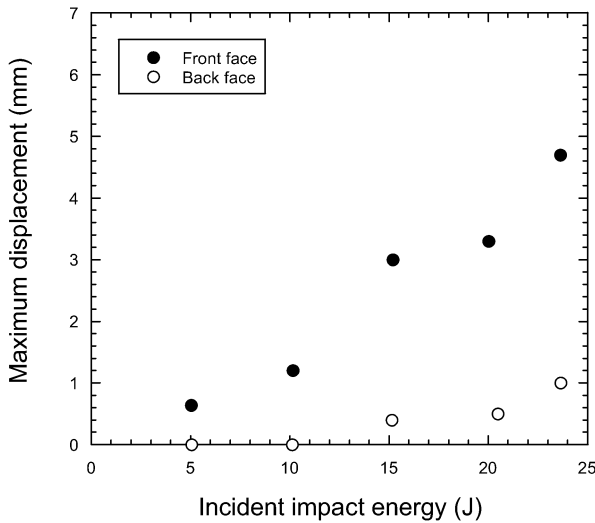


Figure 7. Maximum front face and back face displacement for polymer foam sandwich.

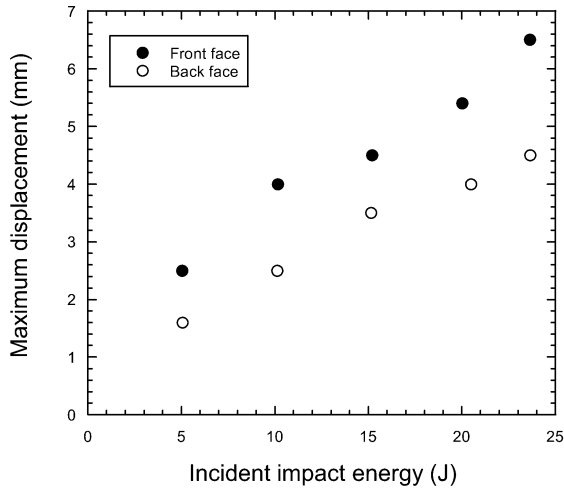


Figure 8. Maximum front and back face displacement for the aluminium foam sandwich.

Scanning also produced 2-D displacement maps from the back faces of the impacted samples. Figure 9 shows the maps from the 5 J impact on the aluminium and polymer foam core samples. There is no significant displacement on the polymer foam yet there is extensive displacement, radiating from the impact point, on the aluminium foam structure. The displacement maps from the samples impacted at 25 J, Figure 10, show that there is now some back-face displacement of the polymer foam core sample. The aluminium foam sample shows the same radiating displacement pattern, along with an increase in the magnitude of displacement compared to the sample impacted at 5 J. The increased ductile deformation of the aluminium foam sample is clear compared to the elastic behaviour of the polymer foam samples. This has advantages for inspection of sandwich structures. The extensive out-of-plane deformation is likely to improve detection of impact damage and alleviate the problem of barely visible impact damage in composite and sandwich structures that behave elastically. The aluminium foam structures are relatively intact, compared to the more catastrophic failure of the polymer foam structures. This suggests post-impact mechanical performance may be improved with an aluminium foam core. The sample geometry for the current impact set-up does not facilitate post-impact testing with standard test methods such as ASTM. Further work will investigate appropriate testing of these samples to assess residual properties.

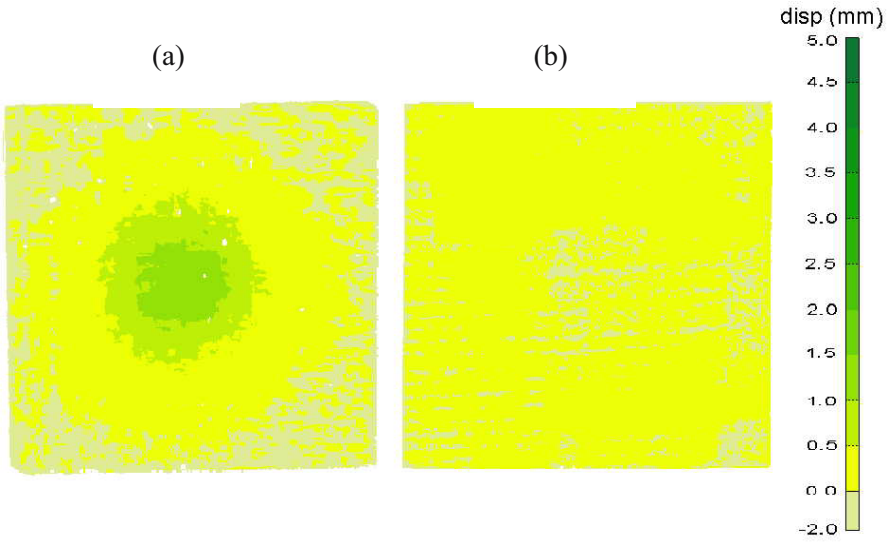


Figure 9. Back-face displacement map for samples impacted at 5J: (a) aluminium foam core and (b) polymer foam core sandwich structures.

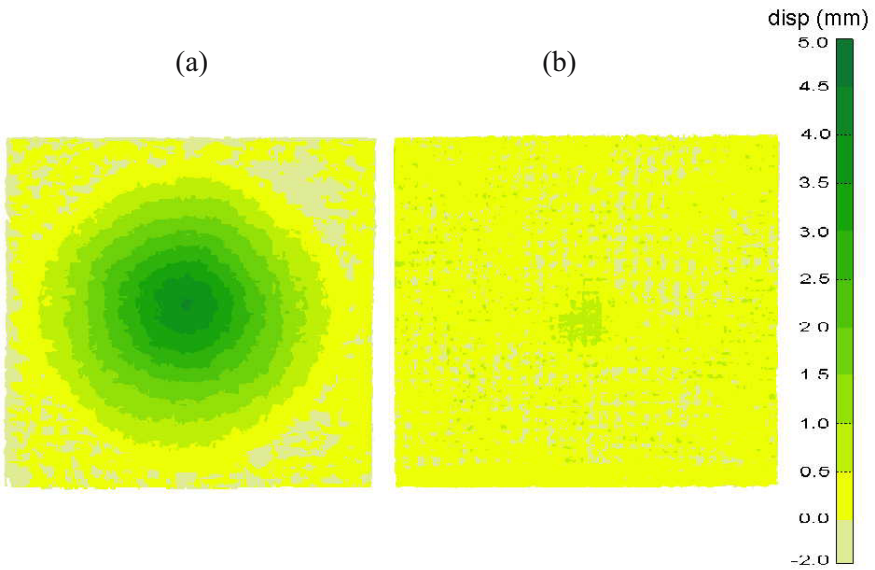


Figure 10. Back-face displacement map for samples impacted at 25J: (a) aluminium foam core and (b) polymer foam core sandwich structures.

#### 4. CONCLUSION

Polymer foam core and aluminium foam core sandwich structures were impacted at energies ranging from 5–25 J. Energy absorption for each structure was similar but significant differences in failure mode were observed. Damage in the polymer foam was localised and characterized by matrix cracking and core indentation at low energy, and composite skin fracture and core crushing at high energy. In contrast the aluminium foam core samples experienced some foam cell crushing at all impact energies and minor composite skin buckling damage at the higher energies. 3-D laser scanning clearly showed extensive out-of-plane, plastic deformation radiating from the impact point. This deformation is likely to be the main energy absorbing mechanism in the aluminium foam core structure. The polymer foam core samples showed very little out-of-plane deformation, even at the higher impact energies. The lack of catastrophic localized failure such as that exhibited by the polymer foam core structure, suggests that the aluminium foam core structure will exhibit improved damage tolerance. A method for assessing post-impact mechanical properties of the sample geometry used in this study will be the subject of future work.

#### REFERENCES

1. M.A. Hazizan, W.J. Cantwell. The low velocity impact response of foam based sandwich structures. *Composites Part B* 2002 **33**: 193-204.
2. R.A.W. Mines, C.M. Worrall, A.G. Gibson. Low velocity perforation behaviour of polymer composite sandwich panels. *Int. J. Impact Engng* 1998 **21**: 855-879.
3. C.M. Kindervater, H. Georgi. Composite strength and energy absorption as an aspect of structural crash resistance. In: *Structural Crashworthiness and Failure* (eds. N. Jones, T. Wierzbicki) pp. 189-235, Elsevier, Oxford (1993).
4. L.J. Gibson, Mechanical behaviour of metallic foams, *Annual Reviews Material Science* 2000 **30**: 191-227
5. W.J. Cantwell, P. Compston, G. Reyes, The fracture properties of novel aluminium foam sandwich structures, *Journal of Materials Science Letters* 2000 **19**: 2205-2208
6. G. Reyes Villanueva, W.J. Cantwell. Low velocity impact response of novel fiber-reinforced aluminium foam structures. *Journal of Materials Science Letters* 2003 **22**: 417-422.
7. S. McKown, R.A.W. Mines, Static and Impact behaviour of metal foam cored sandwich beams, *High Performance Structures and Materials, High Performance Structures and Materials II*, 2004, v7: 37-46.

# NUMERICAL MODELING OF SANDWICH PANEL RESPONSE TO BALLISTIC LOADING

## *Energy Balance for Varying Impactor Geometries*

Jørgen Kepler and Michael Rygaard Hansen

*Institute of Mechanical Engineering, Aalborg University, 9220 Aalborg East, Denmark*

**Abstract** A sandwich panel is described by an axisymmetric lumped mass/spring model. The panel compliance is simplified, considering only core shear deformation. Transverse penetrating impact is modeled; impactor diameter is significantly smaller than panel size. Experimental data for the total loss in impactor kinetic energy and momentum and estimated damage energy are given. For a selection of impactor tip shapes, the numerical model is used to evaluate different force-histories between the impactor and the panel during penetration

**Keywords:** localized impact, energy balance, elastic panel response, damage.

## 1. INTRODUCTION

A typical sandwich panel, designed primarily for a good ratio between bending stiffness and weight, tends to be sensitive to localized loads in general. Localized impact loads are one case often encountered in transportation vehicles, where the low mass of sandwich panels is particularly desirable, and it is often the actual limiting load.

This paper treats the case of a sandwich panel, 500 mm  $\times$  500 mm, with thin orthotropic GFRP face-sheets ( $t_f \approx 3$  mm) and thick PVC foam core (core thickness  $2H = 40$  mm), simply supported along the edges, being penetrated transversely by a hard cylindrical impactor (mass 1 kg, diameter 50 mm) at velocities between 70 and 95 m/s. The impactor diameter is thus comparable with the panel thickness, while much smaller than the panel length dimensions. The absorption of energy in the sandwich panel is of particular interest, being divided into panel damage energy, panel elastic energy and panel kinetic energy.

Three impactor tip shapes were considered: Hemispheric (radius 25 mm), a 45 degree cone and an 18.4 degree (sharp) cone, shown in Figure 1.

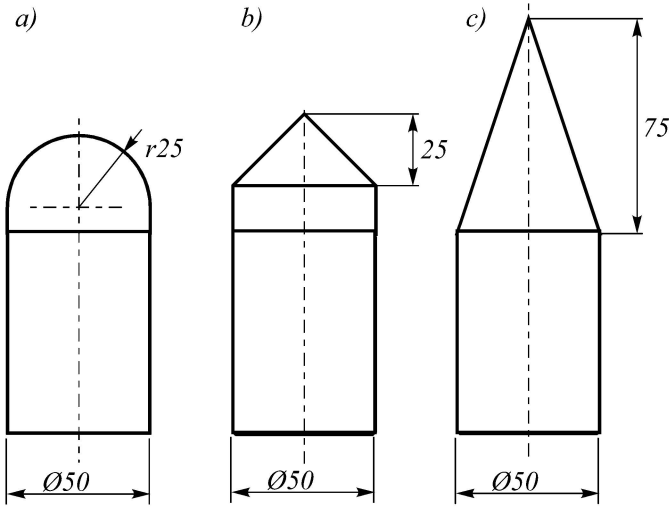


Figure 1. Impactor shapes. (a) hemispherical tip; (b) 45° cone tip; (c) 18.4° cone tip.

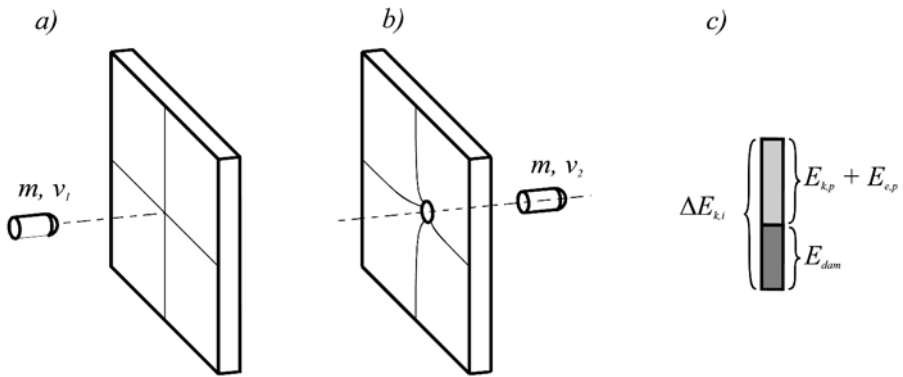


Figure 2. Penetrating impact on sandwich panel. (a) Before impact, impactor velocity  $v_1$ , impactor mass  $m$ ; (b) After impact, impactor velocity  $v_2$ , impactor mass  $m$ ; (c) Energy balance, where the loss of impactor energy  $\Delta E_{k,i}$  is balanced by damage energy  $E_{dam}$ , panel elastic energy  $E_{e,p}$  and panel kinetic energy  $E_{k,p}$ .

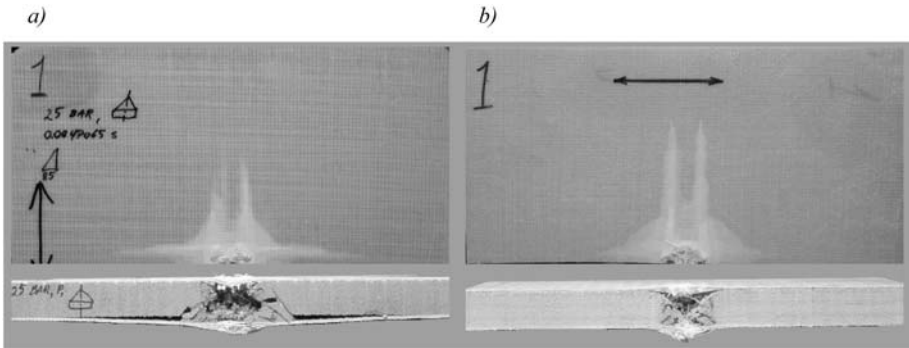


Figure 3. Face view (top) and cut-through (bottom) of simply supported (a) and backed (b) sandwich panels.

Figure 2 outlines the situation and energy balance.

In this paper, a numerical method for modeling the panel response is presented, and applied to a number of experiments with measured total energy absorption and estimated and verified panel damage energies, i.e. with known values for  $\Delta E_{k,i}$  and  $E_{\text{dam}}$ . The full description of experiments and damage energy estimates may be found in [1] and [2]. An analytical approach to the same situation is described in [3].

## 2. DAMAGE ENERGY ESTIMATES

Three damage energies were identified as important:

- Local fibre stretching until fracture. By measuring the mode II cracks formed by fibre pullout, the elastic energy in the fibre bundles was estimated using the failure strain and modulus of elasticity of the fibres.
- Core material compression. The chosen PVC foam core material was modeled with a constant crushing strength until densification. The crushing type was determined by the impactor tip shape.
- Friction between core material and impactor. Again, depending on the impactor tip shape, the friction between impactor and densified foam was estimated.

Delaminations, core fracture and debonding were also estimated, but these invariably produced insignificant energy contributions due to the poor fracture toughnesses of core and matrix materials.

For verification of the damage energy estimates, additional experiments were performed. In these, a panel would be supported on the back face sheet with only a small hole in the backing support to allow for impactor exit. Fig-

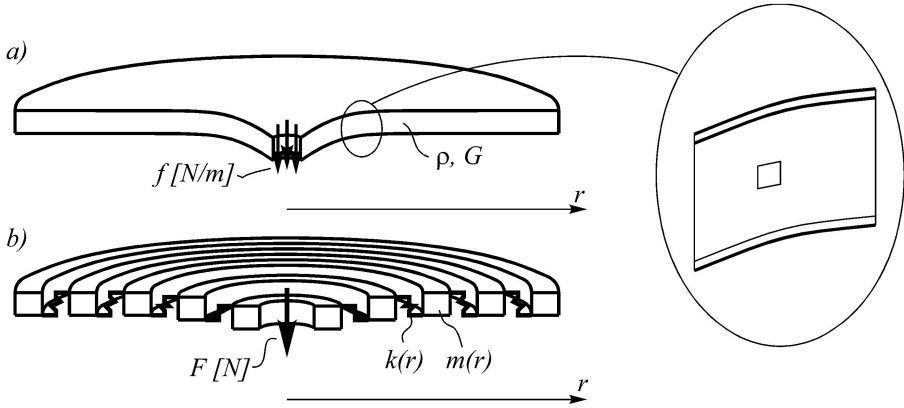


Figure 4. Shear-deformable sandwich panel (a) and discretized model (b).

ure 3 shows typical examples of (otherwise similar) simply supported and backed test specimens.

In Figure 3, the damage patterns are seen to be qualitatively and quantitatively similar (except for debonding and core cracking in the simply supported specimen). The total energy absorption in the backed specimens agree (within 20%) with the estimated damage energy absorption in the simply supported specimens, thus confirming the approximate validity of the damage energy model.

### 3. NUMERICAL MODEL

The sandwich panel is represented by a number of concentric rings, connected by shear springs, as a serial lumped-mass model. Only the shear stiffness of the core is considered, since the impact duration is short (1–2 ms) and the panel extension is limited to 1000 mm. The structural waves will travel at a velocity of

$$v_{\text{shear}} = (G/\rho_{\text{avg}})^{1/2} \cong 300 \text{ m/s,}$$

where  $G$  is Core shear modulus  $\cong 30 \text{ MPa}$ ,  $\rho_{\text{avg}}$  average density of sandwich panel  $\cong 335 \text{ kg/m}^3$  (see [4]), whereby the waves will not reflect back to the impact point during the duration of the impact. Thus, the plate extension will not significantly affect the energy absorption. Figure 4 shows the discretization.

The mass of the individual elements are found by considering a ring element bounded by inner and outer radii

$$m_i = \rho_{\text{avg}}(2H + 2t_f)\pi(r_{i+1}^2 - r_i^2), \quad 1 \leq i \leq N$$

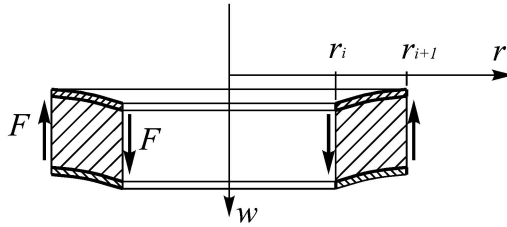


Figure 5. Shear-deformable ring element.

and the spring constant by subjecting the same element to shear deformation, as outlined in Figure 5, whereupon the spring constant becomes

$$k_i = \frac{4\pi HG}{\ln\left(\frac{r_{i+1}}{r_i}\right)}, \quad 1 \leq i \leq N - 1.$$

The inner radius corresponds to the impactor radius (25 mm). Thus, a small mass discrepancy will occur, but this can be added to the innermost ring element mass.

The number of segments were set to  $N = 1000$  (with equal radial increments), in order to obtain convergence of the results.

#### 4. CALCULATION PROCEDURE

In short, the panel response is generated as follows:

1. A contact force history  $F(t)$  is postulated, representing an impulse equal to the lost impactor momentum. The impact duration  $T$  is set according to the impactor penetration length and the average measured impactor velocity.
2. The panel response is generated by applying said force to the inner ring element through a sufficient number of time steps. For each time step, the elastic and kinetic energy of the panel are easily evaluated, and constant total momentum is used as a control criterion.

The quality criterion for any (arbitrarily selected) force history  $F(t)$  is as follows: When  $t = T$ , the panel energies are evaluated. These should correspond to the value as predicted from the total energy balance (as outlined in Figure 1).

#### 5. EXPERIMENTAL DATA

In Table 1 data derived from the experimental work is listed for six different tests.

Table 1. Experimentally derived data for six tests.

Test #	Tip type	$v_1$ [m/s]	$v_2$ [m/s]	$\Delta E_{k,i}$ [J]	$E_{\text{dam}}$ [J]	$T$ [ $\mu\text{s}$ ]
1	Hemisph.	72	39	1820	810	829
2	Hemisph.	95	68	2170	940	564
3	Cone 45°	70	39	1700	740	844
4	Cone 45°	94	74	1660	870	548
5	Cone 18.4°	72	51	1300	600	748
6	Cone 18.4°	94	77	1420	680	538

Relative force [ ]

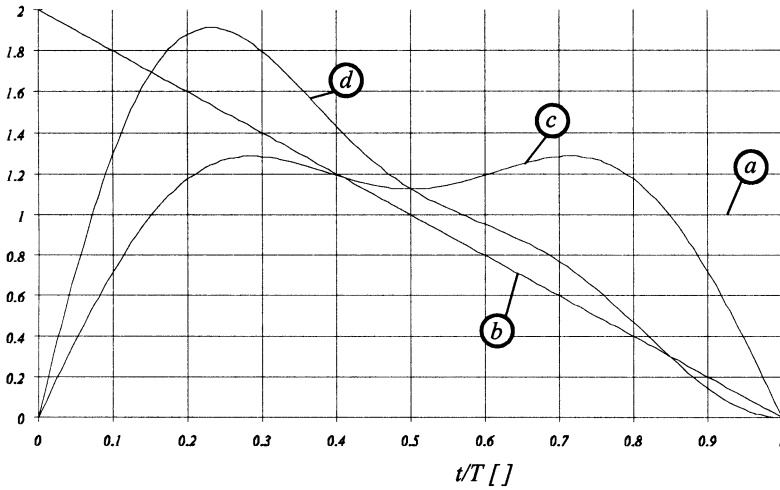


Figure 6. Force histories. (a) Constant force; (b) Triangular; (c) 2 term sine series; (d) Combination of (b) and (c).

## 6. FORCE HISTORIES

Four force-histories were suggested, as shown normalized in Figure 6.

The force histories (c) and (d) were chosen to simulate force peaks when penetration of the face sheets occur, and the declining histories (b) and (d) were chosen to simulate a larger force in the initial phase while the inner panel segments are being accelerated.

Table 2. Experimentally and numerically determined kinetic energy loss.

Test #	Measured $\Delta E_{k,i}$ [J]	Constant $\Delta E_{k,i}^*$ [J]	Triangular $\Delta E_{k,i}^*$ [J]	Two term sine $\Delta E_{k,i}^*$ [J]	Combined $\Delta E_{k,i}^*$ [J]
1	1820	1394	1761	1520	1834
2	2170	1660	2074	1826	2191
3	1700	1240	1556	1347	1618
4	1660	1284	1520	1380	1588
5	1300	879	1051	941	1089
6	1420	987	1162	1058	1213

## 7. RESULTS

The elastic and kinetic energy of the panel are computed at any instant of time as:

$$E_{e,p} = \sum_{i=1}^{N-1} \frac{1}{2} \cdot k_i \cdot (w_{i+1} - w_i)^2 \quad E_{k,p} = \sum_{i=1}^N \frac{1}{2} \cdot m_i \cdot \dot{w}_i^2.$$

These values are added to the estimated damage energy yielding a value,  $\Delta E_{k,i}^*$  that may be compared to the experimentally determined loss in impactor kinetic energy:

$$\Delta E_{k,i}^* = E_{k,p} + E_{e,p} + E_{dam}.$$

The simulated results are listed in Table 2 for each of the six tests previously listed in Table 1.

From the results in Table 2 it is clear, that the triangle and combined model seems to reflect the actual behaviour quite well for the hemisphere and the 45° cone with the combined marginally better. Hence, the impact seems to be delivered predominantly early on during penetration. This is even more pronounced for the 18.4° cone where major part of the momentum loss seems to happen in an even more limited amount of time.

## 8. CONCLUSIONS

The proposed numerical modeling, and in particular the shear deformation assumption, is clearly feasible for simulation of sandwich panel response when subjected to transverse localized impact loads. It will be infeasible if the load is appreciably distributed, if the impactor strikes at an inclined angle or if the panel is curved. In those cases, the force transfer and wave propagation will no longer be dominated by the core shear stiffness.

There is, in general, a good correlation between computed/estimated and experimental results. The triangular and combined force histories show a clear

tendency towards a force history shape that declines during impact; this is in good agreement with the expected behavior.

The model still relies on experimental data for estimating the damage energies. Friction and core compression are easily estimated from the impactor geometry (see [1]), but the size of the mode II delaminations formed by stretching of fibre bundles, ultimately indicating the fibre stretching energy until fracture, still remain to be determined analytically. This is currently being investigated.

## **REFERENCES**

- [1] Kepler, J., Impact Penetration of Sandwich Panels at Different Velocities – an Experimental Study: Part I: Parameters and Results, *Journal of Sandwich Structures and Materials*, Vol. 6 No. 4, 2004.
- [2] Kepler, J., Impact Penetration of Sandwich Panels at Different Velocities – an Experimental Study: Part II: Interpretation of Results and Modeling, *Journal of Sandwich Structures and Materials*, Vol. 6 No. 5, 2004.
- [3] Skvortsov, V., Kepler, J. and Bozhevolnaya, E., Energy Partition for Ballistic Penetration of Sandwich Plates, *International Journal of Impact Engineering*, Vol. 28, 2003.
- [4] Sayir, M. B., Biegewellen in Sandwich-Strukturen, *Schweizerische Ingenieur und Architekt*, No. 7, 1983.

# LOW VELOCITY IMPACT INVESTIGATIONS OF SANDWICH PANELS WITH DIFFERENT CORES

Wilfried Göttner and Hans-G. Reimerdes

*Institut für Leichtbau, RWTH Aachen University, Wüllnerstraße 7, D-52062 Aachen, Germany*  
goettner@ilb.rwth-aachen.de, hg\_reim@ilb.rwth-aachen.de

**Abstract** The behaviour of sandwich panels with different core structures after low velocity impact damage was investigated. The material properties are measured and the damage extensions are detected by ultra sonic testing. To assess the strength of the damaged sandwich structures, the panels are investigated in 4-point-bending tests until failure.

**Keywords:** sandwich panel, slotted honeycomb core, X-core, K-core, barely visible impact damage, 4-point-bending test.

## 1. INTRODUCTION

Sandwich structures are being increasingly used in various aerospace applications. Impact damage is often of concern in the performance of sandwich designs. Even if in case of CFRP-facesheets the impact damage is barely visible (BVID) the compression and bending strength are reduced significantly after impact. There is considerable interest in developing innovative sandwich composites that offer multi-functionality in addition to satisfying load bearing capability after impact [1–3]. Reinforcing the foam with pins is one such concept with a potential to improve the transverse stiffness and strength over traditional sandwich composites [4].

In this paper results of low velocity impact tests on sandwich panels are presented. All investigated panels have the same quasi-isotropic CFRP-face sheets. Goal of this work is to investigate the impact behaviour of panels having different cores. Besides nomex honeycomb core, slotted nomex honeycomb core, and slotted aramid honeycomb core, foam cores with embedded CFRP pins (K-core and X-core) are investigated. The pins are connected to the face sheets to reinforce the panel's mechanical properties.

The tests are performed using a drop tower with an impact body, which has a ball-shaped head of one inch in diameter. Variable impact energies are used

to generate different damage mechanisms in the panels. During the tests the reaction force, the displacement and the impact velocity are measured. After impact the achieved degree of damage in the upper face sheet and in the core is measured by means of ultrasonic scanning. Selected specimens with impact damage are cut out of the panels and analysed under a scanning-electron microscope.

Specimens with and without impact damage are loaded in 4-point-bending tests in order to measure the reduction of strength due to the impact damage. Together with the results of the impact tests, the material properties and the failure modes, conclusions of the failure mechanisms are drawn.

## 2. SPECIMEN

Five different types of flat sandwich panels are investigated. All of them have got the same CFRP-facesheets, while their cores are different, allowing to investigate the influence of the core on the impact behaviour.

### 2.1 Investigated cores

Three different honeycomb cores and two advanced cores out of foam with embedded CFRP-pins are investigated.

Baseline is a classical NOMEX honeycomb (HC) core with 4.8 mm cell width and a density of  $48 \text{ kg/m}^3$ . The other two honeycomb cores are slotted allowing venting of the cells in order to avoid moisture absorption. The slotted part of the core is fixed to the outer surface which is exposed to impacts. The cell width for these cores is also 4.8 mm. Two different core materials are used, NOMEX (HC-S) with a density of  $57 \text{ kg/m}^3$ , and aramid fibres (HC-S-A) with a density of  $47 \text{ kg/m}^3$ .



Figure 1. X-core and K-core structure.

Two additional panels have cores made out of Rohacell foam with embedded CFRP-pins oriented in a three dimensional truss network [5]. In case of the X-core the tips of the rods penetrate both face sheets to provide a superior skin to core bonding (see Figure 1, [5]). There are 24 rods distributed over a surface area of  $9 \times 9 \text{ mm}^2$ , while the rods have an inclination of  $60^\circ$  to  $70^\circ$  to the face sheet. The rods have a diameter of 0.25 mm. The density of the X-core is  $88 \text{ kg/m}^2$ .

The second type of foam core with embedded pins is the K-core (Figure 1). Unlike the X-core the tips of the rods are pressed flat to the foam surface to provide flexibility in laminating the face sheets using out-of-autoclave proces-



Figure 2. Investigated sandwich panels after impact, honeycomb (HC), honeycomb-slot (HC-S), honeycomb-slot-aramid (HC-S-A), K-core and X-core.

Table 1. Data of investigated cores.

Type of core	HC	HC-S	HC-S-A	X-core	K-core
height (mm)	15.0	15.0	15.0	12.3	10.7
cell width (mm)	4.8	4.8	4.8	n.a.	n.a.
density (kg/m <sup>3</sup> )	47	57	47	88	82
compr. strength (N/mm <sup>2</sup> )	2.5	2.7	1.6	7.2	6.8

sing. The pins have a diameter of 0.5 mm and there are 6 of them distributed over an area of  $9 \times 9 \text{ mm}^2$  with the same inclination to the face sheets like the X-core structure. The K-core has a density of  $82 \text{ kg/m}^3$ .

In Figure 2 the different investigated cores are presented.

In order to be able to interpret the results of the impact tests with the different cores, their compression strength was measured in a simple quasi-static compression test. Here the foam cores with embedded CFRP-pins showed more than twice the compression strength of the honeycomb cores. All relevant data of the cores is collected in Table 1

## 2.2 Face sheets

All panels have got the same face sheets made out of 8 pre-impregnated plies of UD carbon fibre (Tenax HTA 800) with an overall thickness of 1 mm. The stacking sequence of  $[-45^\circ, 0^\circ, 45^\circ, 90^\circ]_s$  gives quasi-isotropic properties. The tensile strength and the Young’s modulus of the face sheets was determined by tensile tests. The tests showed a significant reduction of the properties of the X-core and K-core facesheets. This is due to changes in the fibre-orientation resulting from the interaction with the CFRP-pins. The measured data are presented in Table 2.

Table 2. Data of face sheets.

Type of core	honeycomb	X-core	K-core
Young's modulus (N/mm <sup>2</sup> )	52000	50000	49500
tensile strength (N/mm <sup>2</sup> )	625	562	515

### 3. EXPERIMENTAL SETUP AND TEST EXECUTION

To achieve smooth bearing conditions and to avoid oscillations of higher frequencies during the impact tests the specimens are fixed to a frame made out of laminated wood. In order to prevent spring-back, nylon plates are pushing with a down force of 50 N at the corners of the test items. The bearing clearance is changed to simulate different impact situations. First, the test specimens are supported with a bearing clearance of  $350 \times 350 \text{ mm}^2$ . In the second step the panels are impacted with a bearing clearance of  $150 \times 150 \text{ mm}^2$ . In the third type of tests the whole rear face of the sandwich panel is supported by a laminated wood, allowing no deformation of the rear surface. To identify the impact energy leading to barely visible impact damage (BVID) drop heights of 0.1 m, 0.2 m, 0.3 m, 0.4m, 0.5m, 1.0 m, 1.5 m and 2.0 m are first tried out.

The impactor has got a ball-shaped head with a diameter of one inch and a mass of 700 g. In the centre of the impactor head an acceleration sensor is integrated to measure the reaction force. The analog recording of the measuring data is accomplished with a sampling rate of 10 kHz. A laser measuring system mounted at the side of the drop tower, measures the displacement versus time and triggers the data recording. After impact an automatic mechanism captures the mass to prevent multiple impact.

To determine the strength after impact, 4-point-bending tests are carried based on DIN EN 6061 [6]. For this purpose sandwich panels with and without impact are cut into items of  $400 \times 75 \text{ mm}^2$ .

## 4. RESULTS

To investigate the behaviour of the sandwich panels with BVID, impact tests with two different impact energies are performed. These are 3.1 and 5.8 Joule, which correspond to drop heights of 0.5 m and 1.0 m, respectively.

### 4.1 Impact tests

During and after impact the reaction force, the indentation depth, and the delaminations are measured.

**Reaction forces.** For the impact energy of 3.1 Joule the reaction forces are given for the different panels in Figure 3 dependent on the bearing conditions.

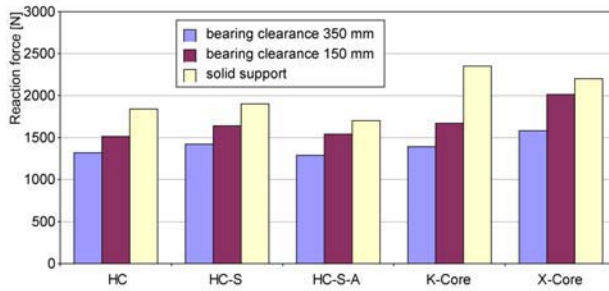


Figure 3. Reaction force dependent on the bearing conditions (impact energy: 3.1 Joule).

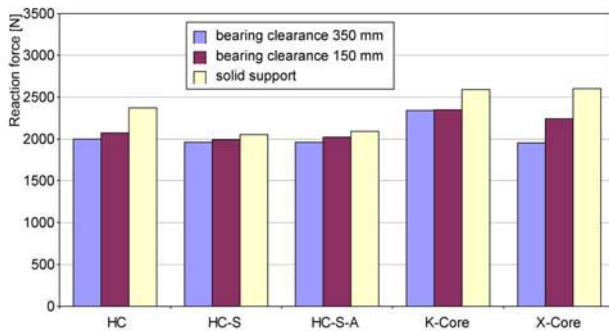


Figure 4. Reaction force dependent on the bearing conditions (impact energy: 5.8 Joule).

It is shown that the reaction force increases with decreasing the bearing clearance from 350 mm to 150 mm due to the increased stiffness of the system. Are the panels supported over the total back surface, a further increase of the reaction forces is measured.

Figure 3 reveals, that different cores show different reaction forces. The results indicate, that the reaction forces correlate to the compression strength of the different cores. Impacts with this low energy lead to first delaminations in the face sheets and to small core damages. Fiber failures appear in low quantities and take no influence on the impact behaviour. Thus the structures act nearly in an elastic manner.

In case of impacts with 5.8 Joule, significant fiber cracks are observed in the face sheets. In these cases the reaction forces get mainly determined by the tensile strength of the face sheets. Figure 4 shows an average impact force of 2170 N for the different sandwich panels.

**Indentation depths.** Residual dent depths are measured after impact. For an impact energy of 3.1 Joule Figure 5 shows the indentation depths of the sandwich panels dependent on the different bearing conditions. Like the reaction forces,

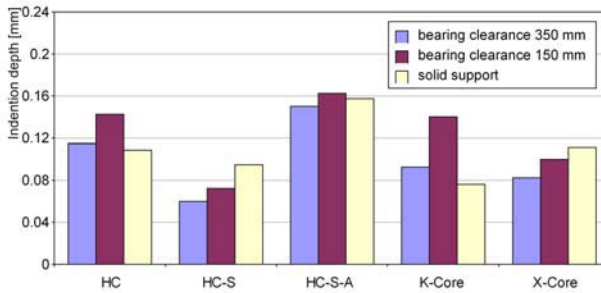


Figure 5. Indentation depths dependent on the bearing conditions (impact energy: 3.1 Joule).

the dents of the panels exhibit, that the indentation depths depend mainly on the compression strength of the cores.

Cores with a low compression strength give only little support to the top layer, thus the face sheet gets more burdened and a deeper dent occurs. Sandwich panels with high compression strength like X-, K-core and the slotted NOMEX honeycomb (HC-S) with high core density result in a little dent in the top layer. This is observed at impact energies which simply lead to delamination failure without significant fiber cracks in the face sheets. Do the impacts at higher energies result in significant fiber cracks, reverse behaviour is indicated. As a result of fiber disorientation in the face sheets, the top layers of the X- and K-cores are more fragile, which leads to extensive dents. The panels with slotted cores show significant dents at these impact loads as well. In this case the lowest indentation depths are observed by the standard honeycomb structure. This behaviour can be seen in Figure 2 which shows the panels after impacts of 13.7 Joule.

**Delaminations.** The damage extensions caused by the impacts are determined by ultrasonic C-scans, B-scans and by images from a scanning electron microscope. Analyses of the scans reveal, that damages of the sandwich structures already occur at impact energies lower than 0.7 Joule. First fiber cracks are observed by scanning with an electron microscope the specimens which are impacted with 2.5 Joule. Impact energies less than 2 Joule lead mainly to delaminations in the face sheets and to core damages. Alike the results of the reaction forces, the damage extension correlate to the compression strength of the different cores. Thus the smallest damages are observed at the HC-S-A panel and the largest at the K-core and the X-core structures (Figure 6).

A non-optimal bonding of the face sheets (in case of the K-core) due to the manufacturing process and fibre disorientation in the face sheets result in superproportional delamination in case of the sandwich structures with foam core and embedded CFRP-pins. Impact energies larger than 3 Joule lead to signifi-

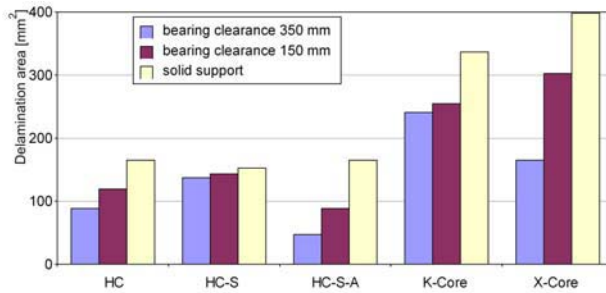


Figure 6. Delamination area dependent on the bearing conditions (impact energy: 3.1 Joule).

cant fiber cracks in the face sheets. With increasing impact energy and stiffness of bearing conditions, the damage extensions of the different sandwich structures become more even. Our tests did not confirm, that embedded CFRP-pins offer a better control of delamination growth, as reported in [1].

#### 4.2 4-point-bending tests

The 4-point-bending tests are carried out according to DIN EN 6061. The panels are cut into specimens of  $400 \times 75 \text{ mm}^2$  and loaded in an universal testing machine. The load versus displacement is measured until collapse of the structure. The specimens which are damaged by impact energies of 3.1 and 5.8 Joule are compared to those without impact damage.

**Residual strength.** Although the investigated sandwich panels have different bending stiffnesses (due to different core heights), the collapse loads of the different panels are approximately on the same level. Nevertheless, the failure modes are different. Sandwich panels with a stiff core achieve a higher collapse load than those with a soft core. By comparison it has to be taken into account, that the K- and X-core panels have a smaller height than the others, which leads to a smaller bending stiffness. If the results of the X-core specimens are projected to the height the honeycomb panels have, an increase of their collapse load of about 20 % is calculated. Figure 7 shows that BVID which is achieved by an impact energy of 5.8 Joule leads to a significant reduction of the collapse load between 50 % and 60 %. Decreasing the impact energy to 3.1 Joule leads to indentation depths, which are 80 % smaller than at 5.8 Joule. Nevertheless, a reduction of the bending strength of about 40 % is observed. The investigations show that the sandwich panels are extremely sensitive against impact damages.

**Failure modes.** Three different failure modes are observed during 4-point-bending tests after impact. The failure behaviour is primarily determined by the core properties, mainly the out of plane stiffness.

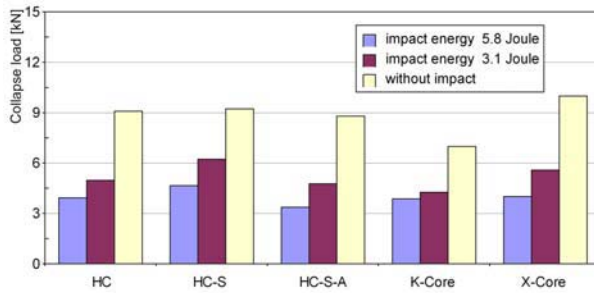


Figure 7. Bending strength after impact for the different sandwich panels.

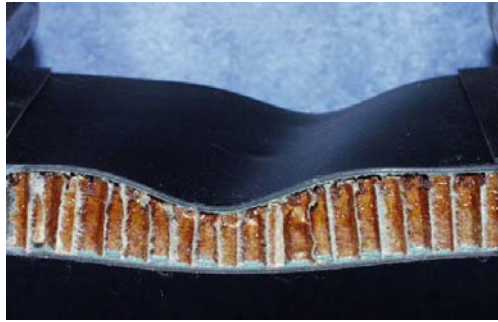


Figure 8. Failure mode of an impacted honeycomb sandwich panel with low compression strength of the core.

The first failure mode observed is wrinkling of the upper face sheet. It occurs independent of the impact energy at HC and HC-S-A panels with the lowest out of plane stiffness. Locally predamaged core cells give reduced support to the face sheet during bending load and it buckles deeply into the core (Figure 8).

The second failure mode occurs with sandwich panels having a core with high compression strength like K- and X-core. In this case the cores are strong enough to support the face sheet without out of plane deflection. Instead, the upper face sheet fails over the full width of the panel as shown in Figure 9. This failure mode occurs whether the specimen has got an impact damage or not.

The slotted honeycomb panels (HC-S) which have the highest compression strength of all investigated honeycomb cores show the third failure mode. During the 4-point-bending test the core fails close to the upper face sheet in tension allowing outward buckling of the face sheet (Figure 10).

This failure mode results from the decreased tension strength of the core due to slotting and is observed whether the specimen is impacted or not.



Figure 9. Failure mode of an impacted X-core panel with high compression strength of the core.



Figure 10. Failure mode of an impacted slotted-honeycomb panel with a high density core.

## 5. CONCLUSION

The impact behaviour of sandwich panels out of CFRP-face sheets and five different cores has been investigated. Two levels of low impact energy (3.1 and 5.8 Joule) leading to barely visible impact damages have been applied to the specimens. The achieved damage dimensions have been quantified by means of ultrasonic B- and C-scans and by use of a scanning electron microscope. After impact 4-point-bending-tests have been performed in order to find the effect on the bending strength at the different panels.

The investigated cores can be divided into two groups, the honeycomb cores and the foam cores with embedded CFRP-pins. The later show higher compression strength and higher out of plane stiffness than the others. Two of the honeycomb cores are slotted in order to allow venting between the cells. A realistic comparison of the different core design is hardly possible, as they do have different densities, and as the height of the panels is also not equal.

The following findings were attained:

- In case of 3.1 Joule impact energy delamination in the face sheet as well as core failure are observed. The higher energy of 5.8 Joule leads in addition to fibre failure.
- The delamination area increases with the stiffness of the panel's support.
- The 3.1 Joule impacts already result in a 40 % reduction of the residual bending strength. This reduction is increased to 50 % - 60 % at 5.8 Joule impact energy.
- The failure mode in 4-point-bending is in case of the honeycomb cores wrinkling of the compressed face sheet. Cores with low compression strength fail in compression while those with low tensile strength (e. g. due to slotting) fail in tension.
- In case of the X-core panel with perfect connection of face sheet and core and with high compression strength of the core, fracture of the face sheet was observed.
- The panels with foam core and embedded CFRP-pins show before and after impact higher bending strength than the others.

## REFERENCES

- [1] Magee C. Dardzinski P. Freitas, G. and T. Fusco. Fiber insertion process for improved damage tolerance in aircraft laminates. *Journal of Advanced Materials*, pp. 36–43, 1994.
- [2] E. J. Herup and A. N. Palazatto. Low velocity impact damage initiation in graphite/epoxy nomex honeycomb sandwich plates. *AIAA Paper 96-1519 (A96-26976)*, 37th AIAA/ASCE/ASME/AHS SDM Conference, pp. 1765–1773, 1996.
- [3] E. J. Herup. *Low Velocity Impact on Composite Sandwich Plates*. PhD thesis, Air Force Institute of Technology, Dayton, Ohio, 1996.
- [4] U. K. Vaidya. Low velocity impact response of laminated sandwich composites with hollow and foam-filled z-pin reinforced core. *Journal of Composite Technology*, 21(2):84–97, April 1999.
- [5] Inc. AZTEX. <http://www.zfiber.com/x-cor.php>, last visited: 11.03.2005.
- [6] Normenstelle Luftfahrt (NL) im DIN Deutsches Institut für Normung, 50672 Köln Kamkestraße 8. *Fibre reinforced plastics, Test method, Determination of sandwich flexural strength 4-point-bending*, ics 49.040.10 edition, April 1996.

# MECHANICAL BEHAVIOR OF RUBBER-FILLED MULTIFUNCTIONAL HONEYCOMB SANDWICH COMPOSITE

Huang Hao, Chee-Ryong Joe and Dong-Uk Kim

*Department of Mechanical Design and Manufacturing, Changwon National University, Korea*

**Abstract** A rubber-filled multifunctional honeycomb sandwich composite was developed in this paper. This structure was composed of facesheets, honeycomb core and vulcanized liquid silicon rubber (LSR) in the honeycomb cells. The rubber fillings were designed to support honeycomb cell walls, act as viscoelastic dampers and dissipate impact energy functionally. In order to investigate the impact and damping performance of this new developed composite, low-velocity impact and vibration tests were conducted to the fabricated specimens in two groups, with and without rubber filled. Each group had three kinds of specimens with various stacked carbon/epoxy laminate facesheets,  $[0/90]_{4s}$ ,  $[0/45/-45/90]_{2s}$ ,  $[45/-45]_{4s}$ . Damage areas of each impacted specimen were inspected by ultrasonic C-scan. For vibration tests, displacement response and damping ratio were checked and compared. The experimental results provided a good agreement with our material design concept.

**Key words:** honeycomb sandwich composite, liquid silicon rubber, impact behavior, damping.

## 1. INTRODUCTION

Sandwich composite material has been widely used in the aircraft and aerospace industries because of its high strength to weight and stiffness to weight ratios. Typically sandwich composite is formed by bonding thin, strong facesheets to a thick, lightweight core. Each component of this composite is relatively weak and flexible but when working together they

provide an extremely stiff, strong and lightweight structure. Recently with the increasing concern of damping and impact performance, the new concept of multifunctional sandwich composite has been inducted. This composite is applied not only for the structural purposes but also for many other attributes, such as energy absorption, shielding, sound insulation and etc.

As we know, the core cells of the honeycomb structure provide readily free space for the dampers to be inserted into. Wang and Yang [1] carried out an experimental investigation on the damping behavior of laminated honeycomb cantilever beams with fine solder balls enclosed in the cells as dampers. Vaidya et al. [2, 3] considered sandwich constructions with reinforced cores by way of three-dimensional Z-pins embedded into form, honeycomb cells filled with foam, and hollow/space accessible Z-pin.

However these material designs only some special aspect of reinforcement. In this paper, a rubber-filled sandwich composite structure is presented. It is formed with a honeycomb core and viscoelastic fillings. The honeycomb core enhances the stiffness of entire composite structure. The viscoelastic fillings inserted in the honeycomb cells can absorb and dissipate energy to reach the effects of improved damping and impact performance. For verification, the low velocity impact tests and vibration tests are performed on fabricated specimen in two groups, with and without rubber filled. The damage areas of impacted honeycomb sandwich panel are visually inspected by acoustic C-scan.

## 2. DESCRIPTION OF MATERIAL CONCEPT

Typical honeycomb core sandwich composite is constructed by facesheets, honeycomb core, and adhesive films. Figure 1(a) is the section view of a common hexagon honeycomb core. The core proposed in this paper model is illustrated in Figure 1(b). The cells of the honeycomb core are filled with viscoelastic material, such as rubber. This concept optimizes the relationship between the honeycomb core and rubber and utilizes the benefits of both, that is, stiffness from honeycomb core and damping effect from rubber. They form a natural spring-damper system. Further, the cell walls of the honeycomb core are backed up by the rubber so that the total surface allows external forces to dissipate over a much larger area than that offered by the honeycomb core alone. This construction leads to a great resistance to shock-wave propagation along the surface, which means less impact damage and better damping effect.

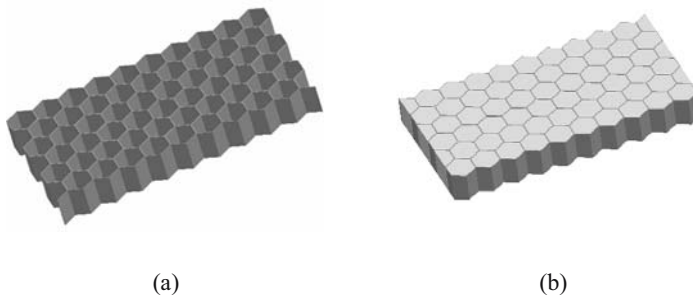


Figure 1. Concept of Rubber-filled multifunctional sandwich composite.  
(a) Traditional honeycomb core (b) Rubber-filled honeycomb core.

A similar concept can be found in the paper of Woo-Young Jung and Amjad J. Aref [4]. They also proposed a combined honeycomb and solid viscoelastic material system for structure damping applications. In their study, the viscoelastic material was laid between the facesheets along with the honeycomb core. Functionally the viscoelastic material was independent to the honeycomb core in the whole structure only if the interface material was stiff enough to resist deformation at the interface. While in this study, the rubber is inserted into the honeycomb cells and works together with the cell walls. Thus, it is difficult to have the sliding at the interface in cell unit and expected to provide a stable and continuous material system.

### 3. EXPERIMENTS

#### 3.1 Specimen preparation

Two group of sandwich composite specimen were fabricated under laboratory conditions. One is the common honeycomb sandwich composite structure and the other is rubber-filled one. The face-skin laminate panel has the thickness 1 mm with lay-up carbon/epoxy prepreg, USN125 from SK Chemicals. Three types of facesheets were prepared with different stacking sequence:  $[0/90]_{4s}$ ,  $[0/45/-45/90]_{2s}$ ,  $[45/-45]_{4s}$ , which were fabricated using an autoclave. The laminates were cut to dimensions 150 mm  $\times$  100 mm by a cutter. The honeycomb core (Nomex-5/32-2.4 supplied by Hexcel Composites) was cut with the ribbon direction in the longitudinal direction of the facesheet panel.

For the first group the pre-cured facesheets subsequently bonded to the Nomex honeycomb core by the FM 73 adhesive film. After fixed by G-clamp the specimens were cured in the chamber. Curing cycle was adopted

as follows: 1 hour from the ambient temperature to 121°C; 2 hours at 121°C; and 1 hour from 121°C to the ambient temperature. As to the second group, one piece of facesheets was first bonded to honeycomb core. Cavities were naturally formed between the facesheet and honeycomb-core cell walls and liquid silicon rubber (LSR) was injected into the cavities. The LSR chosen in this study was ShinEtsu Silicon one component RTV. This kind of silicon rubber was originally sealed in liquid state. After cured it became solid silicon rubber. Obviously liquid rubber was the only choice to achieve our proposed material model. After injection the other piece of facesheet with adhesive film was covered to the honeycomb core. The specimens were also cured in the chamber after fixed by G-clamp. Curing cycle could be referred to that of the first group. At the end the cycle specimens were carefully brought out of the oven and then placed in room environment for three days to ensure silicon rubber fully vulcanized.

## **3.2 Experimental settings**

### **3.2.1 Low velocity impact test**

The honeycomb sandwich specimens were subjected to low velocity impact by a drop-weight impact machine, as shown in Figure 2(a). It was comprised of an impact tip which was steel and had a hemispherical indenter of 15.75 mm diameter. The weight was dropped through a nominally frictionless guide tube to hit the center of the specimens. Specimens were supported by a 76.2 mm by 127 mm cut-out frame. Light gate was applied to check impact velocity and rebound velocity. A load cell was mounted on falling mass. The force measured between the mass and the specimen was recorded by digital data acquisition system, Lecroy Oscilloscope.

The initial potential energy was set to 25J for each specimen, which was reached by adjust the height of drop-weight releasing. The tests details were referred to SACMA SRM 2R-84 [5]. After impact test, the damaged specimens were inspected by C-scan method: ULTRAPAC II, Ultrasonics by Physical Acoustics. The frequency of probe used was 5MHz.

### **3.2.2 Vibration test**

The vibration tests were conducted on prepared specimens on a horizontal table. The specimens were fixed in cantilever state as shown in Figure 2(b). The width of clamped area is 20 mm. The gap sensor was set under the sandwich composite panel with 4 mm gap. B&K Type 8202 impact hammer was used to hit the cantilevered sandwich panels. The hammer in this study

was the type with plastic tip. The force range of was 300 to 1000 N and approximate frequency range was 0 to 2000 Hz.

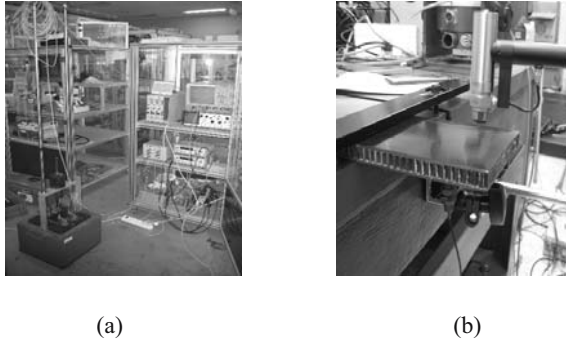


Figure 2. (a) Low velocity impact test device (b) Vibration test device.

## 4. RESULTS AND DISCUSSION

### 4.1 Low-velocity impact test

After drop-weight test, the damaged specimens were observed by visual inspection of the specimens faces, shown in Figure 3.



Figure 3. Visual appearance of impacted face.

Each impacted faces of the sandwich panels (the one on which the indenter hit) showed a concave indentation varied with different stacking sequence. The cracks around the concave developed at the  $0^\circ$  and  $90^\circ$  in the facesheet of  $[0/90]_{4s}$  sandwich specimen, while at  $45^\circ$  and  $-45^\circ$  in the facesheet of  $[45/-45]_{4s}$  ones. The damaged area appeared in a circular location for  $[0/45/-45/90]_{2s}$  specimens for its quasi-isotropic laminated facesheets. Among the three types, the damage of the  $[0/45/-45/90]_{2s}$  facesheet was the severest.

Figure 4 represented force-time and energy-time histories of low-velocity drop weight impact for  $[0/90]_{4s}$  facesheets with and without rubber filled respectively. The energy-time curve was drawn in dash lines. The energy value at the plateau of the energy curve coincided with the absorbed energy when the indenter and the specimen contacted. The absorbed energy in the Figure 4(b) was obviously higher because of the viscoelastic fillings.

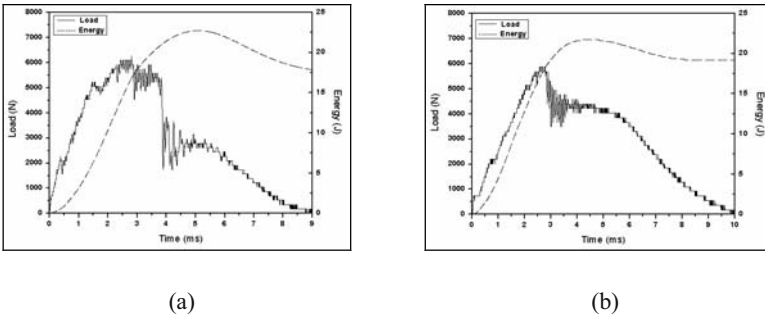


Figure 4. Load & Energy curve of low velocity impact test ( $[0/90]_{4s}$  facesheets).  
 (a) No rubber filled (b) Rubber filled.

The similar phenomenon could be explained to the sandwich panels with  $[0/45/-45/90]_{2s}$  facesheets in Figure 5 and  $[45/-45]_{4s}$  facesheets in Figure 6. Further, for each case the load of rubber-filled specimen was less than that of no-rubber-filled one. The peak of force-time response of the specimens without rubber filled had a much broader fluctuating area, while the impact load decreased rapidly for the rubber-filled specimen. It was thought that the rubber in the cells of the honeycomb core buffered the impact velocity of indenter to some extent, so that the impact load decreased correspondingly.

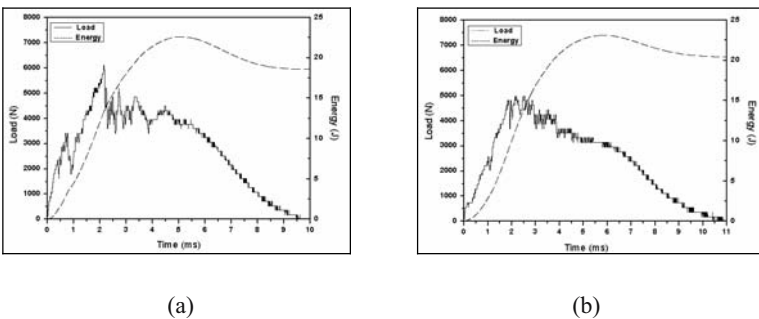


Figure 5. Load & Energy curve of low velocity impact test ( $[0/45/-45/90]_{2s}$  facesheets).  
 (a) No rubber filled (b) Rubber filled.

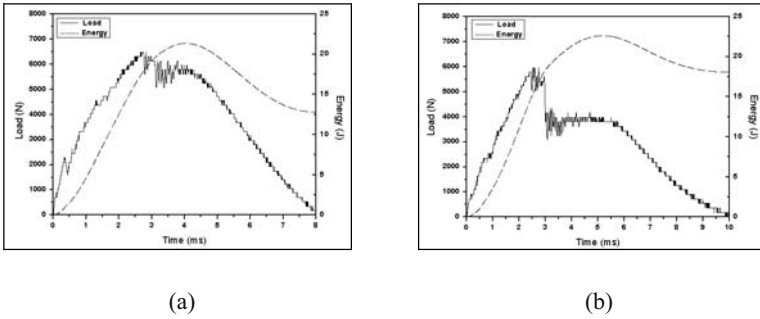


Figure 6. Load & energy curve of low velocity impact test ( $[45/-45]_{4s}$  facesheets).  
 (a) No rubber filled (b) Rubber filled.

Figure 7~9 provided the C-scan photographs of top and bottom plate for the entire specimens. As seen, the top facesheets of  $[0/90]_{4s}$ , and  $[45/-45]_{4s}$  sandwich panels without rubber filled had large damaged area distinguished as the continuous red area, while that with rubber filled did not have obvious concentrated damaged portions. In the case of  $[0/45/-45/90]_{2s}$  facesheets, it was found that the bottom plate of the sandwich panel without rubber filled had the track of damage.

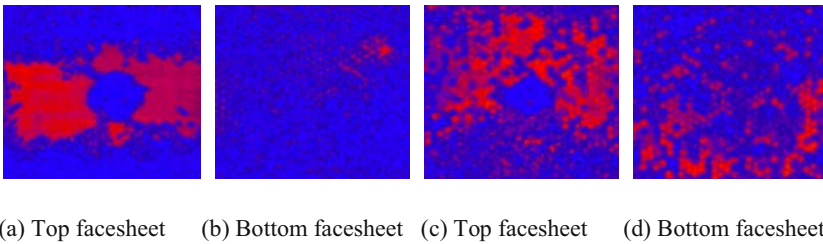


Figure 7. C-scan of damaged sandwich composite panels ( $[0/90]_{4s}$  facesheets).  
 (a), (b) No rubber filled (c), (d) Rubber filled.

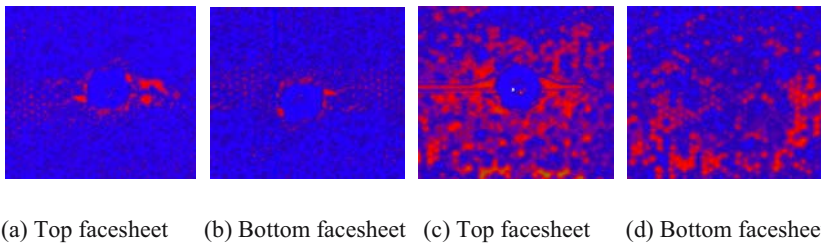
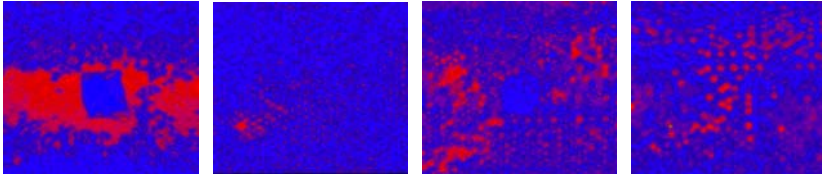


Figure 8. C-scan of damaged sandwich composite panels ( $[0/45/-45/90]_{2s}$  facesheets).  
 (a), (b) No rubber filled (c), (d) Rubber filled.



(a) Top facesheet (b) Bottom facesheet (c) Top facesheet (d) Bottom facesheet

Figure 9. C-scan of damaged sandwich composite panels ( $[45/-45]_{4s}$  facesheets).  
(a), (b) No rubber filled (c), (d) Rubber filled.

## 4.2 Vibration test

Figures 10~12 provided the time response decay curve measure by gap sensor for each specimen. From the graphs one could find that the specimen with rubber filled had much short response time. The response time of common sandwich panels is about 600ms, while that of rubber filled sandwich panel only need 300ms.

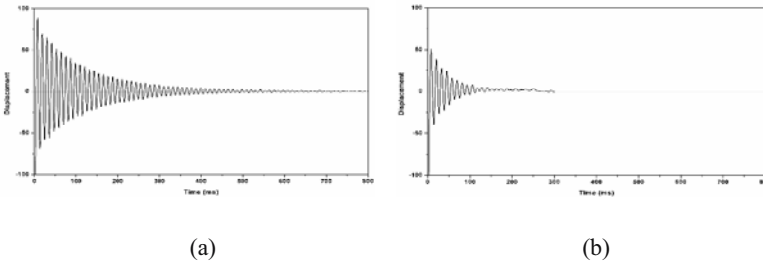


Figure 10. Displacement response of sandwich panels with  $[0/90]_{4s}$  facesheets.  
(a) No rubber filled (b) Rubber filled.

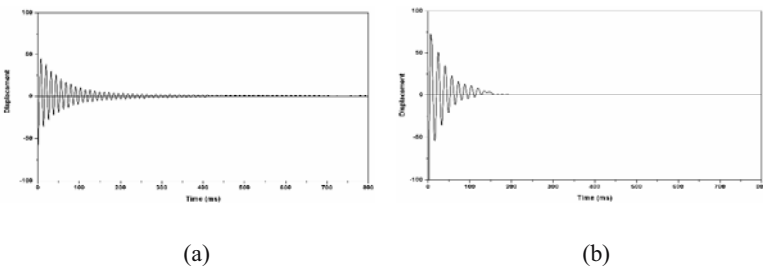


Figure 11. Displacement response of sandwich panels with  $[0/45/-45/90]_{2s}$  facesheets.  
(a) No rubber filled (b) Rubber filled.

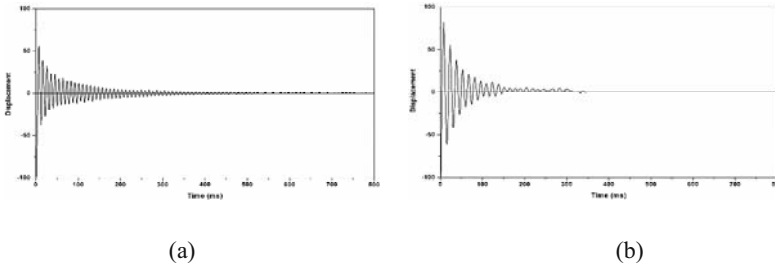


Figure 12. Displacement response of sandwich panels with  $[45/-45]_{4s}$  facesheets. (a) No rubber filled (b) Rubber filled.

Figure 13 gave the comparison graph of the damping ratios calculated by the decay curves. The sandwich specimens with rubber filled have much higher damping ratios than the traditional ones. It shows that the rubber play a great role of energy dissipation and structure damping for this new developed composite material.

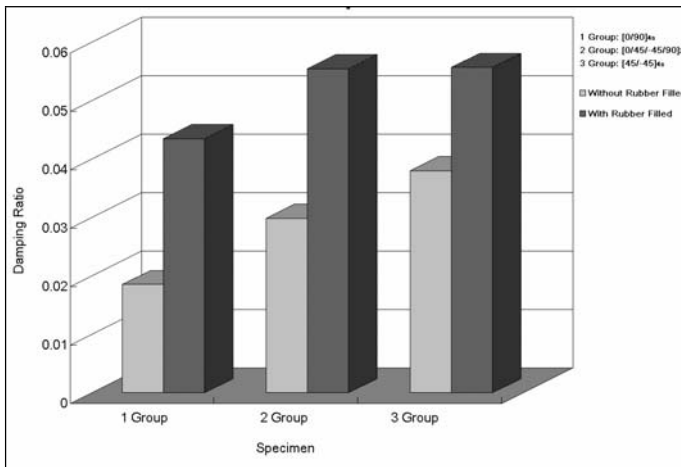


Figure 13. Chart of damping ratios.

## 5. CONCLUSION

The experimental study of new developed rubber-filled multi-functional sandwich composite was presented for the concern of dynamic and impact performance. From the test results the following conclusions could be drawn:

- The sandwich panel with rubber filled had much short response time. The decay time of common sandwich panels is about 600ms, while that of rubber filled sandwich panel only need about 300ms.
- The damping ratios of the sandwich panels with rubber filled were 2.35, 1.46, 1.86 times larger than that of common sandwich panels.
- From the low-velocity-impact test result one could find that the absorbed energy of the sandwich composite panels with rubber filled was obviously higher than that without fillings.
- From the C-scan photographs, it could be seen that sandwich panels without rubber filled had large damaged area, while that with rubber filled did not have obvious concentrated damaged portions.
- The impact damage areas of the rubber-filled honeycomb composite panel were much smaller than that of traditional panels at 20%, 17.7%, 33% for  $[0/90]_{4s}$ ,  $[0/45/-45/90]_{2s}$ ,  $[45/-45]_{4s}$  respectively.

## REFERENCES

1. B. Wang and M. Yang, "Damping of honeycomb sandwich beams", *Journal of Materials processing Technology*, Vol. 105, pp. 67-72, 2000.
2. U.K. Vaidya, S. Nelson, B. Sinn and B.Mathew, "Processing and high strain rate impact response of multi-functional sandwich composites", *Composite Structure*, Vol. 52, pp. 429-440, 2001.
3. U.K. Vaidya, M.V. Hosur, D. Earl and S. Jeelani, "Impact response of integrated hollow core sandwich composite panels", *Composites: Part A*, Vol. 31, pp. 761-772, 2000.
4. Woo-Young Jung and Amjad J. Aref, "A combined honeycomb and solid viscoelastic material for structural damping application", *Mechanics of Materials*, Vol. 35, pp. 831-844, 2003.
5. SACMA, "SACMA Recommended Test Method for Compression after Impact Properties of Oriented Fiber-Resin Composites", SRM 2R-84.

# STITCHING EFFECT ON STATIC AND DYNAMIC BEHAVIOUR OF SANDWICH STRUCTURES

B. Lascoup<sup>1</sup>, Z. Aboura<sup>2</sup>, K. Khellil<sup>1</sup> and M. Benzeggagh<sup>1</sup>

<sup>1</sup>*Université de Technologie de Compiègne, Laboratoire de Mécanique Roberval UMR CNRS 6066 Dept GM - Polymères et Composites, BP 20529, 60206 Compiègne Cedex, France*  
<sup>2</sup>*L3M. IUT de Tremblay en France Paris 8-Rue de la Râperie 93290 Tremblay-en-France, France Institute of Mechanical Engineering, Aalborg University, 9220 Aalborg East, Aalborg*

**Abstract** Beyond the improvement of the structure stiffness, the stitches reinforce adhesion between the core and the skin and allows the structure to tolerate impacts of low energies. Even if we consider the increase of the mass of the panels which moderates the mechanical performances (specific properties), the interest of such reinforcements is considerable. The materials then created presents a real structural potential.

**Keywords:** stitches, mechanical behaviour, impact, post-impact behaviour acoustic emission.

## 1. INTRODUCTION

Sandwich structures are a good example of the potential offered by composite materials. Their major advantage is its high flexural stiffness per weight ratio. The lightweight foam core serves to place the stiffer face sheet material further away from the neutral axis where its resistance to flexural loads is amplified. Nevertheless, the weakness of this association is the interface that is susceptible to delaminate and in general has limited strength since there are no reinforcements bridging the foam and the skins. In the case of the monolithic composite materials, the introduction of reinforcement through the thickness has shown its own interest [1–3]. To date, the stitching of sandwich structures has received minimal attention.

In this study, the stitches are used as a strong complement to bond the two skins and the core. The purpose of this reinforcement is not only to ensure a good link between the sandwich components but also to increase the mechanical properties of this material.

## 2. MATERIAL PRESENTATION

The studied sandwich results from a traditional sandwich composed of a 35 kg/m<sup>3</sup> polyurethane foam core and two thin skins in woven glass fiber. Stitches are added binding these three components transversely. These stitches, made up of a glass yarn, are not vertical, they form a 45° angle with horizontal. The “pattern” thus created, is a cross (Figure 1) and the stitching step is 25mm. Due to the stitching process, the spacing between the rows is 25 mm.

“X” axis is defined as the direction of the rows of the stitches and “Y” axis as the perpendicular direction. “Z” axis represents the thickness.

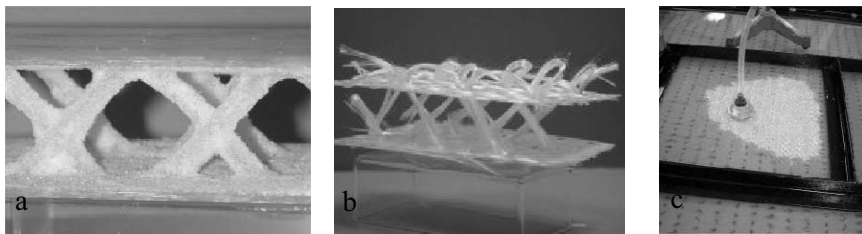


Figure 1. Stitched sandwich: (a) without foam, (b) without foam and resin, (c) injection.

The total thickness of the panels, after injection of polyester resin (RTM process of the laboratory) is 22 mm: 20 mm core thickness and each skin has a 1 mm thickness. During the injection process, the stitches act like channels and allow the out-flow of the resin towards the lower face.

The glass fiber ratio of the skins is 23% for the unstitched sandwich and 25% for the stitched one: the dimension of the air-gap chosen for the thickness of the skins (1mm for 2 plies) involves an accumulation of resin during the impregnation explaining the quite lower fiber ratio. Concerning the stitches, this ratio is 15%; this value is controlled by the ratio between the diameter of the yarn of glass (2400 tex) and the diameter of the needle. After its passage, the needle leaves a print in the shape of a hollow roll and the resin fills in the space between the two diameters during the injection.

After injection, a significant mass improvement is observed due to stitches implementation. Indeed this mass increase from 5.45 kg/m<sup>2</sup> for an unstitched sandwich to 6.38 kg/m<sup>2</sup> for a stitched one.

### 3. QUASI-STATIC BEHAVIOUR

To determine the improvement involved by adding stitches, typical mechanical tests are performed: 4 points bending test, core shear test and flatwise compression test. A particular attention is given to the failure mode due to the presence of the stitches.

The tests are carried out on a INSTRON 1186 universal tensile testing machine in accordance with the EN 14125 ISO, ASTM C365-03 and ASTM 273 standards. Figure 2 presents mechanical result obtained from these tests.

	Compression		Shearing		Bending	
	Ez	Max. Stress	Gxz	Max. Stress	Ef	Max. Stress
Unstitched	14.6 ±0.8	0.28 ±0.01	3.1 ±0.1	0.20 ±0.03	1532 ±78	7.6 ±0.2
Stitched sandwich	95.5 ±2.1	2.27 ±0.14	19.4 ±2.9	1.26 ±0.19	4667 ±188	30.4 ±3.9

Figure 2. Mechanical improvement involved by stitching.

Compared to an unstitched sandwich, the benefit of the stitch introduction is considerable. Rigidity and ultimate stress are quite higher. But, while being rigidified, the material becomes more brittle and the rupture gets more fragile.

#### Failure mode of stitched sandwiches

➤ *Bending test.*

The supports press locally on the stitches deforming the higher skin between two consecutive points of stitch anchoring. Foam breaks with a 45° angle failure. Delaminating begins at the interface core/skin but is stopped transversely by the stitches and do not cross the entire sandwich. At the ultimate stress, stitches pierce the lower skin (Figure 3a) and the complete ruin of material occurs when the upper skin breaks.

➤ *Flatwise compression test.*

The determination of the mode of failure is difficult due to the presence of the foam which masks the chronology of the degradation of the stitches. However, the failure takes place at the base of each stitch at the point of anchoring, which is a weak zone where the yarns are curved. Buckling seems to be the principal phenomenon responsible for these mode of failure. After the relaxation of the compressive stresses, foam takes its original thickness due to its own elasticity. From outside, it is difficult to know whether the material is deteriorated or not.

➤ *Core shear test.*

Failure is carried out in the foam core with a angle of  $45^\circ$ . This failure is then followed by an interfacial decoherence of the skin compared to the unstitched specimens. This phenomenon is delayed because of the bond between the skins and the core. It appears simultaneously with the failure of the yarns of stitch. However, in this case, foam does not play a significant role and the stitches behaviour controls the aptitude of material to resist during the shearing testing. The point of anchoring of the stitches conditions the failure. As for the flatwise test, the points of anchoring are the weakness where the stitches are subjected to a combined tension / shearing state of stress. Differences appears between the two orientations of the cross pattern. One stitch row is in tension while the other is in compression. The tension stress involves the first failure, others stitches turn around their point of anchoring as shown by Figure 3b.

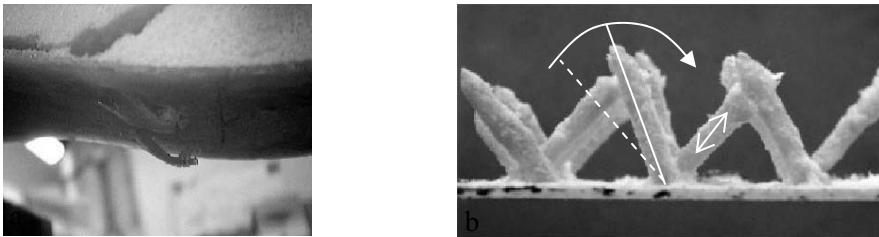


Figure 3. Failure modes: (a) stitch piercing trough the skin in a bending test  
(b) rupture of stitches in core shear test.

Previous studies [4] have shown the influence of structural parameters such as step and angle of stitching on the mechanical behaviour. These parameters can be adapted to better respond to a particular request: for example, vertical stitches involve higher  $E_z$  modulus than angled stitches.

## 4. LOW VELOCITY IMPACT AND POST-IMPACT BEHAVIOUR

Drop-weight impact testing is performed to investigate the effects of stitching on damage resistance of sandwich panels.

The dimensions (310mm x 150mm) of the specimen are chosen to allow compression after impact.

### 4.1 Impact



*Figure 4.* Impactor device.

Impact testing is performed using an instrumented drop weight impact system as shown in Figure 4.

The impact tester consists of a 35 kN capacity load cell and a 20 000g accelerometer mounted onto a crossbeam. The crossbeam was attached to two vertical guide columns with linear bearings. The indenter head is threaded into the load cell. The crossbeam is raised to the height that produced the desired input energy for impact testing. The weight of the indenter head, load cell, and crossbeam is 13kg.

The impact force produced during the impact event is recorded as a function of time using a PC-based data acquisition system.

The specimens are centred and clamped on both ends onto the base plate of the impactor which contains a 100 mm diameter hole centered directly beneath the impact head as shown in figure 5a. Figure 5b shows a panel clamped to the impactor base plate. This device centered on the impactor locates the damages and avoids the generation of damage other than those due to the impactor such as the effects of bending.

Impacting is performed using a 50mm diameter hemispherical impactor and impact energies were 60J and 130J defined by the drop height.

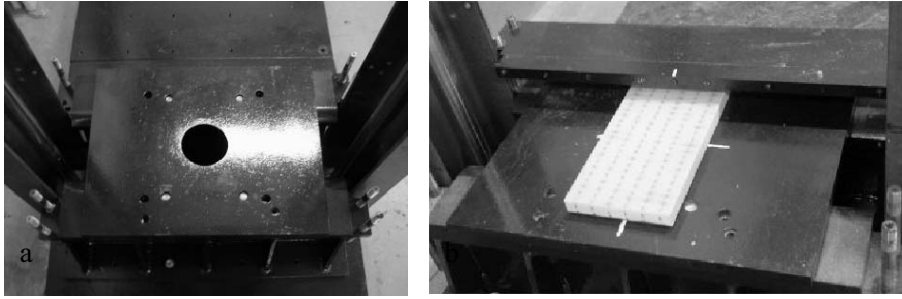


Figure 5. Impactor device: (a) 100mm hole in the base plate, (b) clamped sample.

Impact force is recorded as a function of time during each impact event. Figure 6 compares the typical evolution of the impact load for both materials.

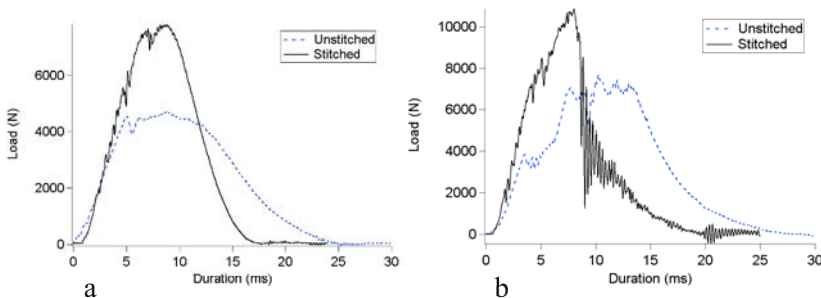


Figure 6. Load versus duration during impact test: (a) 60J, (b) 130J.

At low energy (Figure 6a), the unstitched sandwich undergoes degradations (delaminating foam/core) characterized by constant stage of load whereas the stitched sandwich presents a classical Gaussian load impact curve. The stitched structure thus does not undergo much damage on this energy level.

When energy becomes higher (Figure 6b), degradations of the unstitched sandwich are accentuated. For the stitched one, a brutal fall is observed, synonymous of a local stitches degradations.

Energy absorption is almost the same for both materials, but in the case of unstitched sandwich, energy is used to delaminate whereas in the case of stitched sandwich, energy is here used to degrade stitches.

Moreover, the structural deformation during the impact was determined by the use of strain gages. Thus, two gages were stuck on the two faces of the sandwich near the point of impact.

The comparison of the evolutions gives an idea of the capacity of the structure to transmit the deformation of the impacted skin to the other. Figure 7 shows the typical deformation during a 130J impact for the unstitched sandwich and the stitched one.

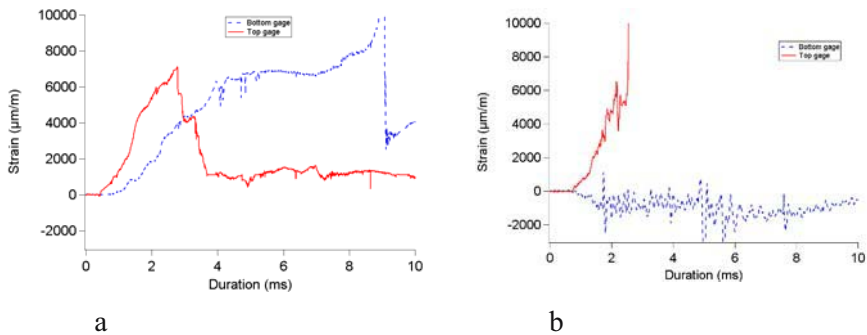


Figure 7. Comparison of top skin and bottom skin strain during impact test: (a) unstitched sandwich, (b) stitched sandwich.

For each material, the upper skin (which receives the impact) is submitted to a similar strain rate. But, the lower skin becomes deformed much more in the case of an unstitched one.

Indeed, concerning the unstitched sandwich, after a time lag corresponding to foam's compaction, the lower skin is highly deformed.

On the contrary, regarding to the stitched sandwich, the deformation of the lower skin is very weak due to the fact that most of the energy is absorbed by stitches.

These different modes of deformation indicates that impact energy is used by the degradation of the stitches in the case of a stitched sandwich whereas it is transmitted from upper skin to the lower one in the case of unstitched sandwich.

## 4.2 Compression After Impact (CAI)

The objective of the edgewise compression testing is to determine whether stitching improve the in-plane load carrying capacity of sandwich structures and to quantify the improvements in ultimate failure. As a mean of

testing residual strength, compression is also chosen because it is among the most critical loading conditions for composites materials.

Edgewise compression testing is carried out according to ASTM C364.

End loading fixtures, as shown in Figure 8a, are machined to clamp and hold the top and bottom edges of the specimens. These fixtures are designed to prevent localized damage at the ends of the face sheets. Anti-buckling devices maintains the two unloaded edge as shown in Figure 8b.

Edgewise compression specimens are cut to a length of 310 mm. This length allows for a 15 mm unsupported gage length when the specimens are clamped in the test fixture. Specimens are 150 mm wide.

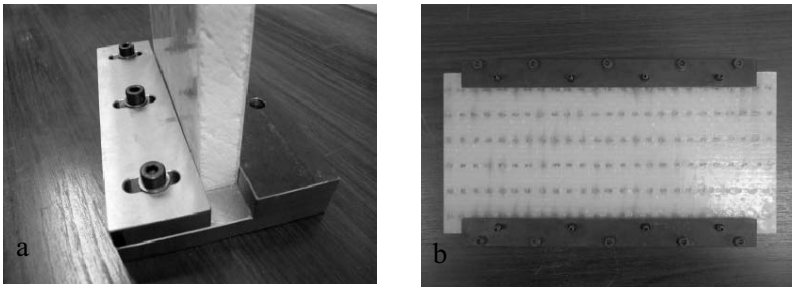


Figure 8. CAI device: (a) end loading fixture, (b) anti-buckling device of the unloaded edge.

The specimen is loaded at a constant crosshead speed of 1 mm/min until significant load drop was observed in the load-displacement curve, which was attributed to the final failure or buckling.

The principal parameters raised during the test are rigidity and the maximum loading. Figure 9 gives the representation of these parameters according to the energy of impact.

The performances of material depend on its capacity to be opposed to buckling. Consequently, the presence of the stitches ensures that this maintains. Measured rigidity and maximum load are appreciably improved by the presence of stitches and influence of impact is limited.

The maximum load is much more sensitive to the degradations generated by the impact. Indeed, at low energy, unstitched sandwich is not very sensitive because the degradations raised after the shock are limited (delamination only) whereas for the stitched ones, the losses are relatively significant.

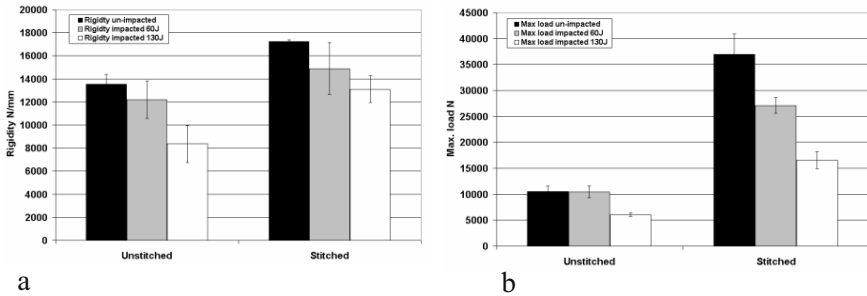


Figure 9. CAI result comparing non impacted and impacted structures: (a) rigidity, (b) max load.

The acoustic emission technology is used to apprehend the type of degradations during the CAI tests and their evolution. Figure 10 shows the evolution of the number of events classified by amplitude in dB during the time of the test.

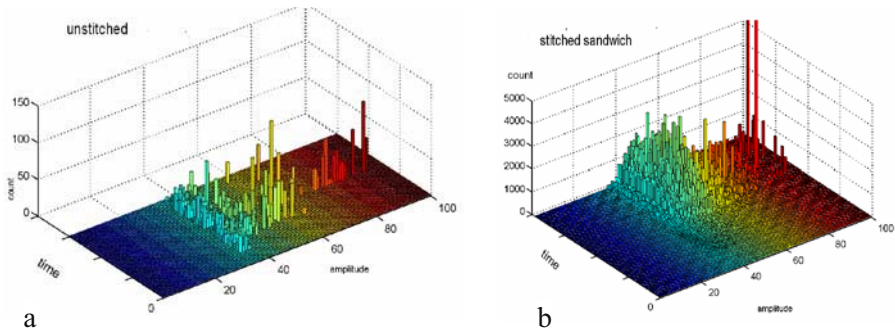


Figure 10. Acoustic emission signature of non impacted specimen during Compression After Impact testing: (a) unstitched, (b) stitched.

Concerning the not impacted unstitched sandwich, Figure 10a shows very few events located in a zone ranging between 35dB and 65dB, relating to ruptures within the resin and of the interface fibre/resin [5]. The events concerning the fibre ruptures ranging between 75dB and 100dB are limited enough. The failure of such a unstitched structure is carried out primarily by buckling.

As regards the stitched sandwich, figure 10b shows a completely different behaviour. Beyond those centred around 50 db (matrix

degradation), the failure produce much more events at high amplitude synonymous of stitch failure.

## 5. CONCLUSION

Comparatively to the unstitched sandwich panels, the introduction of stitches increases significantly the stiffness and ultimate stress under bending, core shear and flatwise compression. The gain brought by the presence of the stitches exceeds sometime a factor 10.

With regard to the impact resistance, the presence of the stitches improves the maximum load whereas the energy absorbed remains unchanged. Moreover, the interest of this stitch is clearly highlighted on the compression after impact tests.

## ACKNOWLEDGEMENTS

The authors wish to thank M. Joseph Maquet from STRUCTISO (France) for his partnership throughout this project.

## REFERENCES

1. Z. Aboura, M.L. Benzeggagh, F. Billaut and B. Dambrine, "Mode I interlaminar failure of stitched textile composites materials: Proposition of predictive reinforcement model", *ICCM 10 Vancouver* (August 1995).
2. Z. Aboura, Y. Lamaa and M.L. Benzeggagh, "On the effect of the nature of three-dimensional preforms on the mechanical properties of CFRP", *Composite Testing and Model Identification*, Châlons-en-Champagne, 28-30 January 2003.
3. A.P. Mouritz, M.K. Bannister, P.J. Falzon and K.H. Leong, "Review of applications for advanced three-dimensional fibre textile composites", *Composites: Part A* 30 (1999) 1445-1461.
4. B. Lascoup, Z. Aboura and M. Benzeggagh, "Effect of the structural parameters on mechanical behaviour of stitched sandwiches", *Proceeding of ECCM-11*, Rhodes, Greece (2004).
5. S. Barre and M. Benzeggagh, "On the use of acoustic emission to investigate damage mechanisms in glass-fibre-reinforced polypropylene", *Composites Science and Technology*, Vol. 52 (1994), 369-376.

# **PROCESSING AND FABRICATION**

# CONTINUOUS MANUFACTURING AND PERFORMANCE OF 3D REINFORCED SANDWICH STRUCTURES

G. Le Roy<sup>1</sup>, C. Binetruy<sup>2</sup> and P. Krawczak<sup>2</sup>

<sup>1</sup>*NAPCO Technologies, 14 rue de Beauce, 75003 Paris, France,*

*E-mail: le-roy-napco@wanadoo.fr*

<sup>2</sup>*Ecole des Mines de Douai, Polymers and Composites Technology Department, 941 Rue Charles Bourseul, 59508 Douai, France*

**Abstract** The patented Napco<sup>®</sup> technology presented in this paper is designed to create in a continuous way 3D tailored sandwich structures while maintaining the production efficiency. The through-thickness reinforcement is obtained from regular fabrics. This process allows the production of complex preforms that can be post formed and impregnated with liquid resin using a closed molding production method or thermoformed in the case of thermoplastic composites.

**Keywords:** sandwich, manufacturing, 3D structure.

## 1. INTRODUCTION

The high strength, high specific weight and durability of sandwich composites make these materials highly attractive for aerospace marine and ground transportation applications. In this latter case, sandwich components have been successfully introduced to several applications such as roof panels in train and in bus structures, front cabins of high-speed locomotives, interior panels etc. Minimizing the weight of a structure is becoming a common key design objective as it allows many options such as higher speed, longer range, larger pay loads, less engine power and better operating economy. The sandwich material must be light whilst remaining economically viable. Moreover high shear strength and modulus are also major considerations and the core should have good load bearing capability, sufficient compressive

strength to withstand local indentation loads. Finally good thermal stability as well as good fatigue resistance is usually required.

Consequently, in order to increase the load carrying capacity of the sandwich construction without penalizing its lightness, it is desirable to maximize the through-thickness stiffness and strength of the core. One strategy of achieving this is to add through-thickness reinforcement to the core, with the ends of the reinforcement material embedded in composite face sheets. The best option is to have a continuous 3D reinforcement to increase the delamination strength and toughness between face sheets and core. In recent years several investigators have considered a number of innovative designs to improve the strength of foam cores such as 3D weaving [1], 3D Z-pins embedded in foam [2], stitch bonding [3] and hollow integrated core sandwich [4]. Usually those solutions lead to the decrease of the production rate and the increase of the part cost.

The patented Napco<sup>®</sup> technology presented in this paper is designed to create in a continuous way 3D tailored sandwich structures while maintaining the production efficiency [5]. The main features of this technology are presented in this paper.

## 2. NAPCO TECHNOLOGY

The Napco<sup>®</sup> technology is a manufacturing process of 3D fibrous structures and 3D sandwich composites in which the face fabrics and core are integrated together in one construction. A machinery called “3D Web Linker” has been specially designed and produced by the company Laroche S.A in partnership with the inventor (Figure 1). The sandwich construction is based on the needle punching. The through-thickness reinforcement is obtained from regular fabrics such as chopped strand mats, continuous fiber mats and fabrics made of pre-oriented fiber yarns. A multi-needle arrangement set at desired through-thickness pattern and density, penetrate the assembly of glass fabric layers and the foam core on both sides. During this process, the needles take glass yarns from faces and carry them through the rigid foam. As the needles are withdrawn, fibers remain inside the core (Figure 2). Then the sandwich panel assembly is advanced by a desired spacing to produce the next set of bounds.

This process allows manufacturing of single sandwich from 3 mm up to 60 mm in thickness, or multiple sandwich using an additional fiberglass mats inserted between foam cores. The maximum fiber density is currently of 18 fiber bonds / cm<sup>2</sup> with regular needles. Optimized needles are being developed to increase the amount of fibers carried through the sandwich thickness. The maximum production speed depends on the fiber bounds

density, a value of 3 up to 10 m/min is achievable with an industrial machinery. The width of sandwich components ranges from 1m up to 4m with commercially available machines.



Figure 1. “3D WEB LINKER®” machine installed in horizontal feed in position for insertion of rigid cores and panels.

This process allows the production of complex preforms that can be post-formed (radius of curvature of 0.5 m or less) and impregnated with liquid resin using a closed molding production method or thermoformed in the case of thermoplastic composites. Another processing route is being investigated that would allow one to infuse on-line the 3D reinforced sandwich structure including injection of grinded materials.

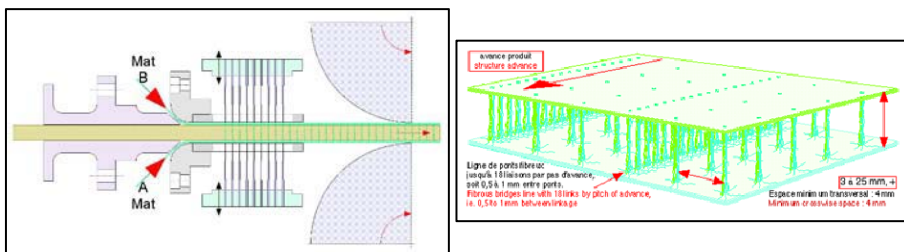


Figure 2. Schematic illustration of the Napco technology and the 3D sandwich construction.

### 3. APPLICATIONS

The applications of the Napco<sup>®</sup> technology cover a wide range from traditional textile to advanced polymer composites. Some of them are detailed hereafter. A few auxiliary actions are implemented in the Napco<sup>®</sup> technology to enable a wide range of capabilities. Table 1 reports actions currently available.

Table 1. Auxiliary actions of the Napco<sup>®</sup> technology.

Auxiliary actions	Working position	
	Horizontal	Vertical
Guiding of solid inserts	X	
Distribution of grinded materials		X
Injection of viscous material	X	X
Spraying	X	
Blowing	X	

#### 3.1 Manufacturing of 3D textile preforms

The Napco<sup>®</sup> technology offers the potential of creating integrally textile sandwich structures. Compared to other process designed to produce distance fabrics, this technology is a highly automated process that leads to significant cost benefits. Figure 3 shows a variety of 3D textile preforms manufactured by means of this technology.



Figure 3. Example of textile preforms produced with the Napco<sup>®</sup> technology.

### 3.2 Manufacturing of 3D sandwich preforms

Once the 3D sandwich preform is produced, it can be impregnated by a liquid resin means of any composite molding technique. Closed mold methods (Liquid Composite Molding) are found to be appropriate. For those technologies, it has been noticed that the transverse fibrous bounds are properly impregnated. In addition, they help to balance resin flow on both sides of the sandwich.

Another processing route is being investigated that would allow one to infuse on-line the 3D reinforced sandwich structure. This one-step consolidation process is expected to lead to further cost benefits.

The manufacture of double-curved sandwich parts is still carried by hand lay up, except for thermoplastic composite. The Napco® technology offers potential improvements in manufacturability as it facilitates the post-forming of initially flat sandwich preforms into simple or double-curved shapes. To achieve this, a dedicated strategy for needle placement is necessary to break the foam core and create disconnected blocks of foam separated by the pile yarns. It is not necessary to use grooved foams to achieve this operation.

A few examples of flat and curved 3D reinforced sandwiches are presented in Figure 4.

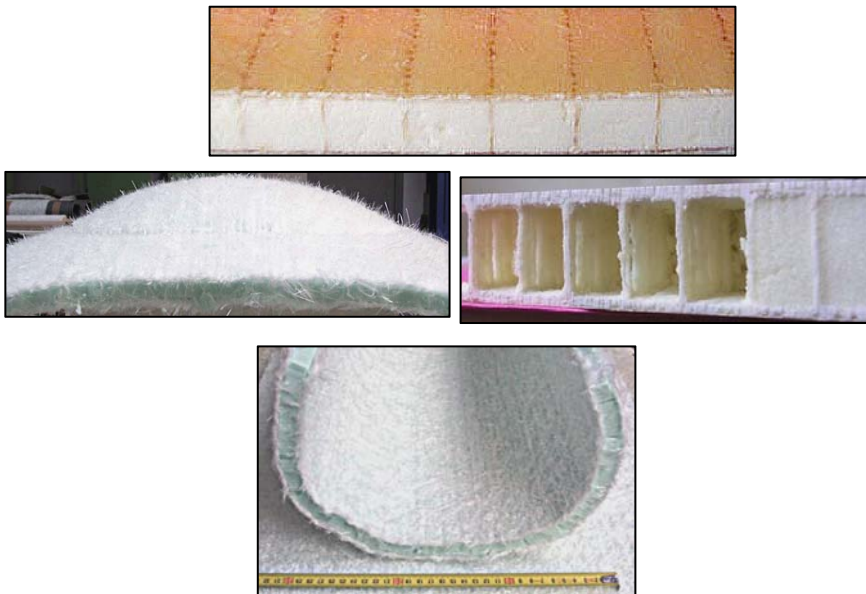


Figure 4. Illustration and example of sandwich preforms and panels produced with the Napco® technology.

Figure 5 shows an example of complex automotive part made of sandwich preforms manufactured with the Napco® technology.



Figure 5. Example of a resin transfer molded automotive part with a sandwich preform produced with the Napco® technology.

### 3.3 Recycling of materials

Another interesting feature of this technology is the ability to recycle scraped materials used in the form of crushed or grinded elements. Figure 6 shows the “3D Web Linker” machine installed in vertical feed position to allow grinded materials to be inserted simultaneously inside the sandwich preform.



Figure 6. Example of sandwich panels made of recycled materials and produced with the Napco® technology.

Examples of application are presented in Figure 7. The line of fiber bounds creates channels for storage of powders, pellets, particles, hollow spheres, etc. They are inserted while creating the hollow cells or channels with the Napco<sup>®</sup> machinery working in vertical position.



Figure 7. Example of sandwich panels made of recycled materials and produced with the Napco<sup>®</sup> technology.

### 3.4 Hollow integrated core sandwich

This construction has several advantages as the upper and lower skins are integrated with the hollow core, thus preventing the weak interface between the core and skin seen in traditional sandwich construction and the interstitial space provide multi-functionality in terms of storage, routing of electronic wires, fire retardancy, space for embedding miniature components etc (figure 8). Solid inserts as metal, wood or plastic profiles can be embedded in cavities.

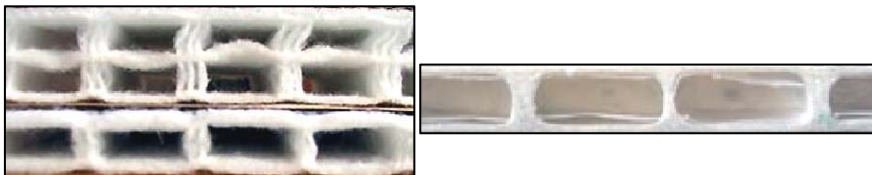
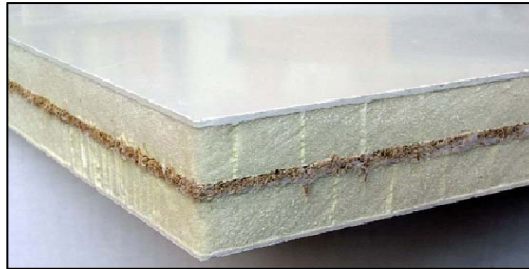


Figure 8. Example of hollow perform produced with the Napco<sup>®</sup> technology.

### 3.5 Manufacturing of multiple sandwich

This process allows manufacturing of multiple sandwich up to 60 mm in thickness using an additional fiberglass mat inserted between foam cores. An example of such a panel is presented in Figure 9.



*Figure 9.* Example of a double sandwich produced with the Napco® technology. It is made with two foam cores, one vegetal non-woven fabric in the center and fiberglass mats in composite skins.

## 4. MECHANICAL PROPERTIES

Flexural tests were carried out according to ASTM C 393 standard. Tested specimens were cut out from flat panels constituted of two composite skins made from polyester resin reinforced by one layer of fiberglass mat ( $350 \text{ g/m}^2$ , Saertex), a  $40 \text{ kg/m}^3$  PUR foam core and various fiber bounds densities and steps. The total thickness is 23 mm; 20 mm core thickness and skin thickness of 1.5 mm. Figure 10 shows the fiber bound density in the length (highest) and width direction (lowest). Figure 11 presents a typical 3-point bending test in the direction of the lowest fiber bound density. For sake of comparison, a non-reinforced sandwich made with the same materials has a bending strength of 10 MPa. Figure 12 presents the core shear strength measured with the ASTM C 393 standard. Although ASTM C 273 should have been preferred, testing results showed that the core shear strength can be increased by a factor two as the fiber bound density is about twice as high.

The vertical pile yarns look like a multiple series of miniature I-beam columns, distributing loads and providing better mechanical properties compared with the non-reinforced sandwich. The strength of the reinforced sandwich is improved by increasing the fiber bound density. Current works are addressing the effect of the fiber bound size on mechanical properties. The fiber bound size depends on the needles used to drive fibers through the core.



Figure 10. Fiber bound steps and density.

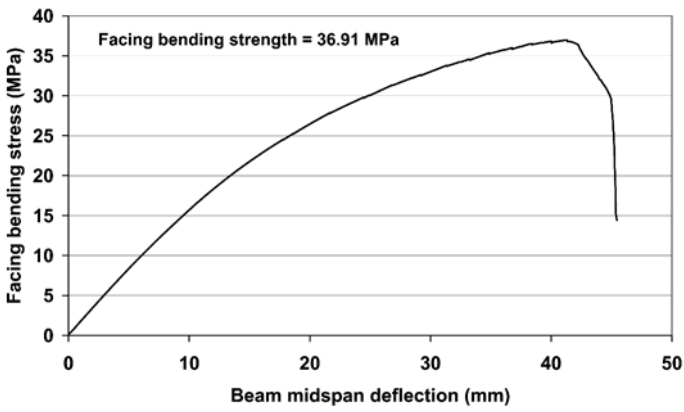


Figure 11. 3-point bending test (fiber bounds steps and density: 16 x 6.3, 496).

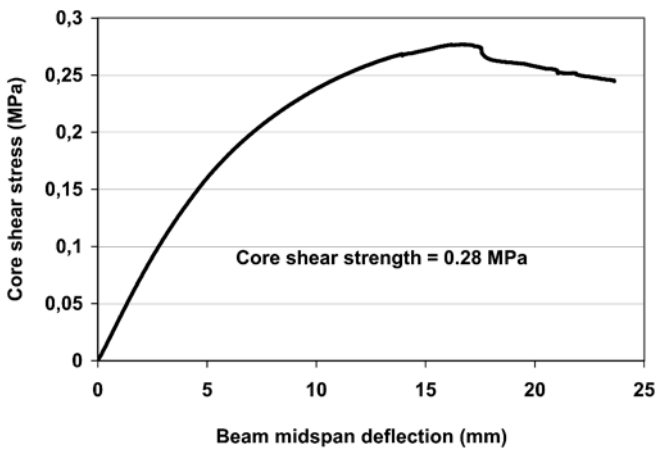


Figure 12. Core shear test (fiber bounds steps and density: 16 x 6.3, 496).

## 5. CONCLUSION

The patented Napco® technology presented in this paper is designed to create in a continuous way 3D tailored sandwich structures while maintaining the production efficiency. It is a reliable, industrial, reproducible and cost effective process for manufacturing of sandwich structures. Single or multiple sandwiches with thickness varying from 3mm up to 60mm can be produced. A flat sandwich preform can be post-formed in a doubly curved shape using a dedicated strategy for needle placement to break the foam core and create disconnected blocks of foam separated by the pile yarns. Dry sandwich preforms produced with this technology can be easily infused using any Liquid Composite Molding process.

The mechanical performance can be tailored to actual needs by adjusting the number and pattern of through-the-thickness fiber bounds. Additional functions can be integrated to the sandwich panel thanks to the insertion of extra components in spaces created by this technology.

## REFERENCES

1. M. K. Bannister, R. Braemar and P. J. Crothers, "The mechanical performance of 3D woven sandwich composites" *Composite Structures*, Vol. 47, No. 1-4, pp. 687-690, 1999.
2. U. K. Vaidya, S. Nelson, B. Sinn and B. Mathew, "Processing and high strain rate impact response of multi-functional sandwich composites", *Composite Structures*, Vol. 52, No. 3-4, pp. 429-440, 2001.
3. P. Potluri, E. Kusak and T. Y. Reddy, "Novel stitch-bonded sandwich composite structures", *Composite Structures*, Vol. 59, No.2, pp. 251-259, 2003.
4. M. V. Hosur, M. Abdullah and S. Jeelani, "Manufacturing and low-velocity impact characterization of hollow integrated core sandwich composites with hybrid face sheets Novel stitch-bonded sandwich composite structures", *Composite Structures*, Vol. 65, No.1, pp. 117-127, 2004.
5. European patent No. EP 0 594 700 B1.

# A NOVEL EXTRUSION-WELDED SANDWICH STRUCTURE FOR THERMOPLASTIC COMPOSITE STORAGE TANKS

E. Lagardere<sup>1</sup>, M.-F. Lacrampe<sup>1</sup>, O. Skawinski<sup>1</sup>, P. Krawczak<sup>1</sup>, C. Ducret<sup>2</sup> and M. Gilletti<sup>3</sup>

<sup>1</sup>*Ecole des Mines de Douai, Polymer and Composites Technology Department, 941, Rue Charles Bourseul, BP 838, 59500 Douai Cedex, France*

<sup>2</sup>*Saint-Gobain Vetrotex International, 767 Quai des Allobroges, BP 929, Chambéry, France*

<sup>3</sup>*Allibert Buckhorn, Route de la Garenne, BP 24, 27600 Gaillon, France*

**Abstract** A new concept of thermoplastic sandwich structures is presented. It relies on a fibre-reinforced core based on glass/thermoplastic commingled yarn and neat thermoplastic skins. Such a structure has been developed so as to manufacture a new range of storage tanks. The use of composites in the tank core structure results in a significant reduction of the total wall thickness, at identical industrial performances with the neat thermoplastic solution.

**Keywords:** sandwich structure, glass/thermoplastic composites, reinforced core, creep.

## 1. BACKGROUND TO THE STORAGE TANK MANUFACTURING

Large capacity (high volume) plastic-based storage tanks are usually manufactured from fibre-reinforced thermosetting resins (for instance unsaturated polyester). This family of materials and their manufacturing processes (filament winding, centrifugation, hand or spray lay-up) have shown their ability to meet clients requirements regarding mechanical properties and cost-effectiveness. However, due to environmental guidelines, severe issues recently appeared regarding the recycling of manufactured industrial products or the release of volatile organic components such as styrene.

Other materials have also been used and related processing technologies have been developed such as extrusion-welding (winding of extruded tapes on a mandrel, Figure 1) in order to produce neat thermoplastic tanks. This solution has advantages such as its corrosion and chemical resistance and its high purity, which make it appropriate for direct contact with a wide range of products (water, powders, grains, fertilizers). However, one drawback of the

neat thermoplastic solution is its low thermomechanical resistance (especially creep at high temperature in case of PE or limited impact resistance at low temperature in case of PP for example). These solutions are therefore often limited to lower capacity storage tanks.

As a consequence, it appeared interesting to develop a solution that associates the advantages of both the fibre-reinforced thermosets tanks and the neat thermoplastic tanks. That leads to a concept of thermoplastic composite storage tanks with neat thermoplastic liners. Different ways may be considered to introduce fibres in the neat thermoplastic during the manufacturing process. One solution is the impregnation of fibres by a nozzle or an impregnated wheel [1]. Another possibility is the impregnation of fibres pulled in a bath of molten polymer [2]. Yet, the impregnation time can be very long. Thus, the above mentioned solutions are usually not able to meet both cost-effectiveness requirements and good quality impregnation of fibres by the thermoplastic matrix. The use of semi-products such as thermoplastic hybrid yarns (obtained either by thermoplastic powder impregnation of reinforcement fibres or by commingling unidirectional thermoplastic and reinforcement fibres together in a yarn) [3, 4] may be considered to overcome this problem. Adapted processing technologies for these advanced thermoplastic composites have to be developed as well, as pultrusion, continuous laminating or in-line moulding through a double-belt press, batch moulding (bladder moulding, diaphragm forming, etc.), automated tape laying or regular filament winding [5] do not meet either the shape or the cost-effectiveness requirements of storage tanks manufacturing.

Allibert Buckhorn has chosen to use commingled yarns and has developed a new range of tanks based on an original thermoplastic PP sandwich structure and the adaptation of the extrusion-welding process. The following section presents the materials and the processing technology used to produce these tanks. In order to validate the choice of the sandwich components and so as to be able to properly design the manufactured tanks which are intended to sustain hydrostatic pressures, the impact toughness and the long term creep behaviour are assessed as well.

## **2. EXPERIMENTALS**

### **2.1 Manufacturing process of the sandwich structure**

The method chosen by Allibert Buckhorn to manufacture these innovative structures is still based on the extrusion-welding process. The inner skin layer in contact with the tank contents is made of neat thermoplastic. The reinforced layer based on glass/polypropylene commingled yarn constitutes the core of the sandwich and is covered by another outer layer of neat thermoplastic (Figure 2). The processing conditions (temperatures, consolidation pressures, etc.)



Figure 1. Extrusion-welding process of storage tanks [photo Allibert Buckhorn].

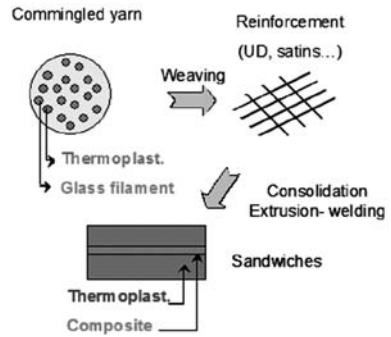


Figure 2. Thermoplastic sandwich structure with a composite core and non-reinforced skins.

Table 1. Tensile properties of the UD glass/PP core material at room temperature.

Mechanical properties	Nominal values	Test method
Tensile modulus along the fibre direction	29440 MPa	ISO 527
Tensile strength along the fibre direction	761 MPa	
Transverse tensile modulus	3540 MPa	
Transverse tensile strength	15.7 MPa	

Table 2. Tensile properties of the PP skin layer at room temperature.

Mechanical properties	Nominal values	Test method
Tensile modulus	~1300 MPa	ISO 527
Tensile stress at yield	~30 MPa	

have been optimised so as to guarantee excellent adhesion between the different layers.

## 2.2 Materials and testing methods

The skin material used to manufacture the storage tanks is a polypropylene homopolymer. The reinforced core material is a unidirectional glass/PP roving with 60wtRPP60 from Saint-Gobain Vetrotex International), but bi-directional glass/PP woven fabrics (twill, satin, etc.) may be used as well. The main properties at room temperature of these materials are reported in Tables 1 and 2.

Both instrumented Charpy and falling-weight impact tests were carried out at low temperature ( $-20^{\circ}\text{C}$ ) on neat PP and sandwich “PP-glass/PP-PP” samples. The Charpy impact tests were conducted according to ISO 179-2. A pendulum

hammer (ZWICK) impacted the specimens with a 7.5 J impact energy. The top of the striker is instrumented with a load transducer so that “force vs. displacement” curves can be obtained. The drop tests were performed according to ISO 6603-2, using an instrumented impact testing system which consists of a drop tower equipped with an impactor, a high speed acquisition system, and a load transducer mounted in the impactor. The weight (30 kg) and the height (0.56 m) were kept constants for all tests (corresponding to an impact energy of 164.8 J). The specimens were clamped within two steel frames having a rectangle opening  $100 \times 75$  mm in sides, and striking them at centre by a hemispherical impactor 30 mm in diameter.

Tensile creep tests were carried out according to ISO 899-1 on standard uni-directional glass/PP composite test samples at room and higher temperature (90°C). Tests along the fibre direction were conducted on four direct loading creep machines (ZWICK DSM 6100-F), whereas transverse tensile creep tests were performed on six lever arm creep test systems developed in house. The specimens were instrumented with 350-ohm strain gauges and thermal compensation was accomplished using a half-bridge circuit thanks to a compensating unloaded strain gauge. Creep life curves have been determined.

Moreover, a creep test on a full-scale reinforced tank has started more than one year ago and is still in progress.

### **3. RESULTS AND DISCUSSION**

#### **3.1 Impact toughness assessment**

Force vs. displacement curves have been recorded during both Charpy and falling-weight impact tests (Figure 3). On this basis, it is possible to calculate the crack initiation (or first damage) impact energy, which corresponds to the energy absorption capacity of the material before damage initiation. It is defined as the energy when the force reaches its maximum (Figure 3) according to ISO 179-2 and ISO 6603-2 standards.

Table 3 shows the results for both Charpy and falling-weight impact tests conducted at  $-20^{\circ}\text{C}$  on neat PP and sandwich “PP/glass-PP/PP” plates. The plate samples (about 4 mm thick) were specially manufactured for this purpose by thermo-compression with processing conditions (temperatures, times, etc.) similar to those used during manufacturing of the fibre-reinforced thermoplastic storage tanks.

Even if it is worth mentioning that the falling-weight impact test better reflects than Charpy tests “real life” impacts that can occur on storage tanks, it clearly appears that the addition of a fibre-reinforced core significantly improves the initial-damage impact resistance, compared to the neat thermoplastic solution. The limited impact resistance of PP at low temperatures can thus be corrected this way.

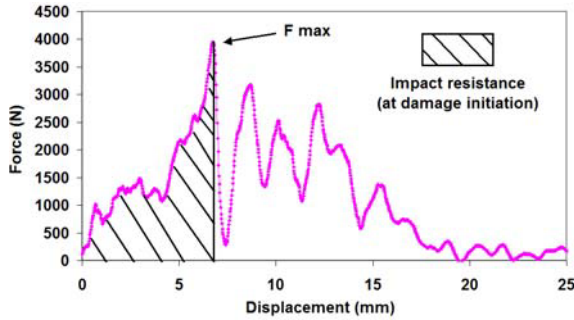


Figure 3. Typical force vs. displacement curves obtained from both instrumented Charpy and Falling-weight impact tests and calculation of the impact resistance.

Table 3. Low-temperature ( $-20^{\circ}\text{C}$ ) impact resistance.

Material	Charpy impact resistance ( $\text{kJ/m}^2$ )	Falling-weight impact resistance (J)
PP / glass-PP,(4/1) satin fabric / PP*	9.8	16.7
Neat PP	0.5	7.1

\*Warp direction of the satin fabric in the longitudinal direction of the test sample.

## 3.2 Creep behaviour assessment

As the performance of the neat PP skin layers was already known and in order to build a database allowing a proper design of the new storage tanks, long-term mechanical tests were performed on the unidirectional glass/PP composite core material only. Then, the behaviour of the sandwich structure under constant load may be calculated and deduced from these data using the classical laminate theory.

**3.2.1 Tensile creep of the sandwich core material.** Tensile creep test have been carried out on standard test coupons cut out of unidirectional glass/PP plates. The 2 or 3 mm thick plates samples were specially manufactured by filament winding on a flat mandrel, and then consolidated by compression and high temperature. Tensile creep life curves have been determined at room temperature and at  $90^{\circ}\text{C}$ , in both fibre direction and transverse direction (perpendicular to fibre direction).

Regarding the tensile tests parallel to the fibre direction, a creep life curve was obtained at room temperature on 13000h while tests at  $90^{\circ}\text{C}$  are still in progress. Yet, a comparison between the first obtained points at  $90^{\circ}\text{C}$  and the creep life curve at room temperature is presented in Figure 4.

In order to illustrate this statement, a comparison has been drawn with the tensile creep life curves of “neat” E and R glass [6] (rigorously E or R glass

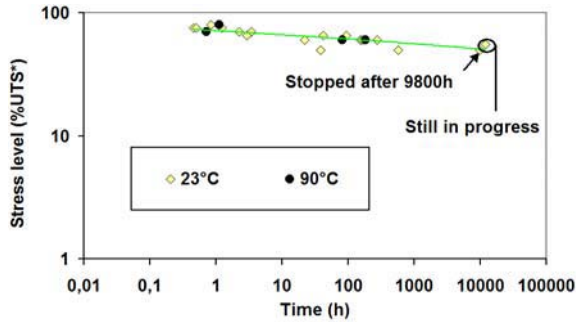


Figure 4. Creep life curves of the unidirectional glass/PP composite for tensile tests along the fibre direction at room temperature and 90°C (\*Ultimate Tensile Stress).

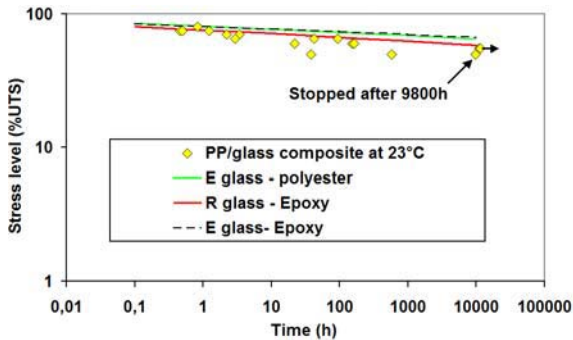


Figure 5. Comparison between tensile creep life curves of the unidirectional glass/PP composite tested along the fibre direction and "neat" E and R glass at room temperature.

filaments impregnated with a very low fraction of thermosetting resin). Glass and unidirectional glass/PP composite have a very similar behaviour, showing a very limited influence of the thermoplastic matrix in that direction (Figure 5). It shows that the temperature does not significantly affect the composite behaviour in creep. This was expected as the load is applied in the fibre direction. In that case the mechanical behaviour is governed by the fibres, and glass is known to be not very creep sensitive.

Concerning the tensile creep tests perpendicular to the fibre direction, the obtained creep curves at room temperature and 90°C are plotted in Figure 6. They illustrate that the temperature influences the behaviour of the composite due to the fact that the fibres do not have a significant role in that direction, where the mechanical behaviour is governed by the PP matrix.

Besides, a comparison has also been drawn in Figure 6 between the creep life curves of "neat" PP-homopolymer [7] and the ones of the unidirectional glass/PP composite. It shows that when the unidirectional glass/PP compos-

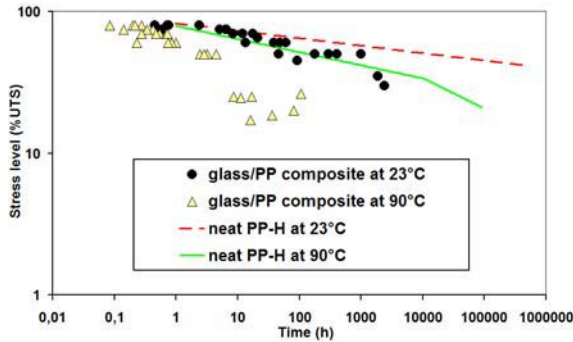


Figure 6. Creep life curves of the unidirectional glass/PP composite tested along the transverse direction and compared to creep life curves of a neat PP (homopolymer).

ite is tested in the transverse direction, fibres tend to modify the ability of the neat PP matrix to deform. Acting as damage initiation sites (for example at fibre/matrix interface defects), the presence of fibres may decrease the matrix deformability under the applied stress. Considering the behaviour of the neat PP at room temperature, it is possible to assume that the creep curve of the composite at the same temperature will not show any brittle-ductile transition. This transition depends mainly on the yield point of the PP. However, the susceptibility to the brittle fracture mode is strongly influenced by molecular weight, molecular weight distribution and the degree and type of branching in the molecule [8]. As a matter of fact, this phenomenon should not appear in the same range of time for the glass/PP composite because of the fibres presence and an extrapolation of the experimental creep life curve over 1–1.5 decade is possible.

**3.2.2 Full-scale creep test on a prototype tank.** A creep test was also started more than one year ago (14000 h) and is still in progress on a full-scale sandwich PP-glass/PP-PP tank (1.6 m in diameter, with a total height of 4 m and a reinforced height of 2 m) that is filled with water heated up to 80°C (Figure 7). The reinforcement used in the core is unidirectional (in the hoop direction of the tank) and its thickness is 0.5 mm.

This prototype tank has been instrumented with sixteen 350-ohm bi-directional strain gauges. The hoop strains measured with strain gauges at different locations show no significant increase thus far in the reinforced area (Figure 8). This full-scale test has also proved that the temperature (up to 100°C) has no effect on sandwich hoop strain. The tank contents were heated up to 95°C and no difference in hoop strain was observed between 80°C and 95°C for the reinforced area, although the non-reinforced area is highly influenced by temperature (room and contents).

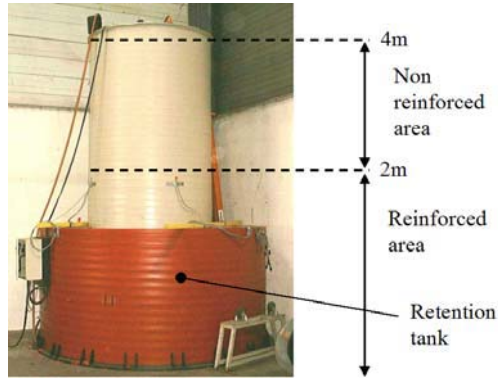


Figure 7. Full-scale creep test on a prototype sandwich composite tank.

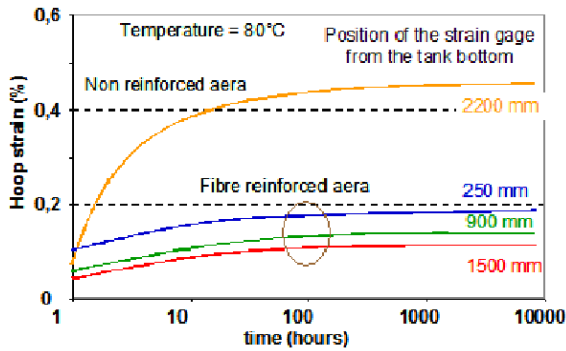


Figure 8. Creep curves at 80°C according to strain gauge location in both fibre-reinforced and non-reinforced areas of the storage tank.

## 4. CONCLUSIONS

A new concept of thermoplastics sandwich structure for extrusion-welded storage tanks has been developed, which consists of a fibre-reinforced core (glass/polypropylene) and of neat polypropylene skins. Compared to regular neat polypropylene tanks, this sandwich structure provides improved impact resistance at low temperature, reduced creep under pressure and temperature, and minimized overall wall thickness. The use of composites in the tank structure also reduced material consumption by as much as 60%, compared to the neat thermoplastic solution at identical industrial performances and use conditions (temperature, pressure).

Combined with the advantages provided by the thermoplastics used, these properties open the way to new opportunities for Allibert Buckhorn: high-temperature storage tanks for chemical fluids, greater storage capacity for

drinking water or solid particles such as grains or fertilizers, or high purity products (for medical applications for instance).

## **ACKNOWLEDGEMENT**

The authors would like to thank the French Economy, Finance and Industry Ministry (MINEFI, contract No. 024906044) for its financial support on this project.

## **REFERENCES**

- [1] Lutz, A. and Harmia, T., 1998, "Impregnation techniques for fibre bundles or tows", in *Polypropylene: An A-Z Reference*, J. Karger-Kocsis (ed.), pp. 301–306.
- [2] Bijterbosch, H. and Gaymans, R.J., 1993, "Impregnation of glass rovings with a polyamide melt. Part 1: Impregnation bath", *Composites Manufacturing*, 4:85–92.
- [3] Gibson, A.G. and Manson, J.A., 1992, "Impregnation technology for thermoplastic matrix composites", *Composites Manufacturing*, 3:223–233.
- [4] Anonymous, 2005, "Advanced thermoplastic composites (ATC)", *JEC Composites*, 14:47–51.
- [5] Buck, M., 2005, "Advanced thermoplastics composites processing", *JEC Composites*, 14:54–56.
- [6] Saint Gobain Vetrotex International Data Sheets.
- [7] NF EN 1778: Characteristic values for welded thermoplastics constructions – Determination of allowable stresses and moduli for design of thermoplastic equipment.
- [8] Brown, N., 1988, "Creep, stress, relaxation and yield", in *Engineered Materials Handbook Vol. 2: Engineering Plastics*, ASM International, pp. 728–733.

# THE OPPORTUNITIES OF FLEXIBLE FOAM PROCESSING FOR RIGID FOAM SANDWICH CORES

## *Blending Two Foam Classes into One*

Henri Mispreuve and Leendert den Haan

*FoamPartner Group, Fritz Nauer AG, Oberwolfhauserstr. 9, CH-8633 Wolfhausen, Switzerland*

**Abstract:** In order to benefit from the processing advantages of soft foam, as well as the high mechanical properties of rigid foam, a new type of polyurethane foam StructUre™ has been developed. It can, after fast and easy processing in its flexible state, be further cross-linked to a rigid state by means of high energy electrons. This results in a high-level mechanical property profile, making the originally soft foam suitable for application as rigid sandwich core material.

Key words: E-Beam cross-linking, core material, foam, cost-effective processing.

## 1. INTRODUCTION

The suitability of materials for use as sandwich cores was often focussed on their technical capabilities and mechanical properties [1, 2]. On the other hand, the ability of core materials to be processed and shaped at reasonable cost was identified as an important factor for the commercial success and wide-spread use of sandwich structures [3, 4].

Rigid foam, among other core materials like balsa wood and honeycombs, has become widely accepted for demanding sandwich structures. Compared with soft foam however, the processing of all of these core materials is substantially more complex and time-consuming. But soft foam has so far never been an option for use in structural sandwich applications because of its moderate mechanical properties. A recently developed, brand-new product now puts this situation in a completely new perspective.

## **2. 3D SANDWICH DESIGN – PRACTICAL LIMITATIONS OF TODAY’S CORE MATERIALS**

Today’s high performance sandwich core materials have proven to be very effective as far as their mechanical properties are concerned. Nomex- and Aluminium-Honeycombs, as well as rigid PEI-, PMI-, PUR- and PVC-based foam are among today’s most frequently used core systems for demanding sandwich structures. Lightweight balsawood presents yet another alternative to the mentioned core materials.

Besides their mechanical properties, the ability of core materials to be processed into three-dimensional shape plays an important role in the steadily increasing use of high-tech sandwich applications. Structural engineers strive for modern, aerodynamic design in conjunction with the need for weight reduction, resulting in optimised, non-angular styling. Obviously, the industry has come up with methods to transform and adapt the shape of available core materials to designers’ wishes.

In situ foaming could be considered the simplest method to achieve complex shapes. However, this process is not without its difficulties. Usually, the cell structure and density distribution within such foamed parts is difficult to control. Expensive tooling and production machinery is further required. Quality control is complex. For these reasons, sandwich core materials used today are typically manufactured in blocks, often batch-wise produced. Required components are cut or CNC-milled to size from these blocks.

The extensive use of honeycomb cores in the aircraft industry, which requires many curved parts, is a good example showing, that the industry has found ways to bring basically two-dimensional, semi-finished core materials into the third dimension. This despite the fact, that because of saddle-bending effects, it is not at all easy to form and stabilise honeycombs into curved shapes. Also sheets of rigid foam can be preformed to some extent, usually by thermoforming. However, increasing the temperature with a uniform heat gradient is difficult to achieve, as their typically closed cell structure essentially results in their behaviour as thermal insulator.

In order to adapt Balsawood and, to some extent, brittle rigid foam to curved structures like for instance boat hulls, they are cut to small blocks, kept together by a thin tissue, which is glued to one side. The clear disadvantage of this system is the discontinuation of the actual core material. The gaps in between the small block need to be bridged with a filler paste.

It is fair to say, that even though sandwich structures can be found more and more, they have hardly come into use for very large volume productions, such as in the automotive industry. One of the reasons is a direct result of the previously discussed difficulties to three-dimensionally shape present core

materials. If this can be achieved at all, it is complex and furthermore too time consuming to fit into required, short cycle times.

On the other hand, flexible foam is extensively used in the automotive industry. It can be efficiently processed, for instance by contour-cutting, a process for which a cutting pattern of a continuous, rotating band knife is CNC-programmed. Another process often used is profiling. This process makes use of simple streamlined, wooden tools, which are pressed into the flexible foam. A straight cut through the locally compressed foam results in a profiled foam surface after pressure release. The profile achieved is actually the negative of the positive tool, or alternatively the positive, if a negative tool profile has been used. Further, die-cutting (or stamping) is common practice.

All these processes make use of fast operating machinery. Cutting times per piece are typically in the order of seconds, or well under one minute if the part is extremely complex. The mechanical properties of flexible foam allow a broad field of application, such as cushioning, acoustical insulation, filtration, sealing, etc. Thus flexible foam meets the shaping and cycle time requirements for large-volume automotive production. But could it further be made to meet the specifications for demanding sandwich core materials?

### **3. STRUCTURE<sup>TM</sup> – A NEW CLASS OF PUR-FOAM**

In order to benefit from the processing advantages of flexible foam, as well as from the high mechanical properties of rigid foam, StructUre<sup>TM</sup> was developed. This new type of polyurethane foam (PUR) is the result of a technological breakthrough. As is typical for PUR-foam, it results from the reaction of polyol with isocyanate and water. This reaction results in CO<sub>2</sub>, which functions as an environmentally friendly blowing gas. The molecular design of StructUre<sup>TM</sup> furthermore incorporates built-in groups, containing inactive, molecular double-bonds. These double-bonds can be broken-up to build radicals, which can search for and find partners within the molecular structure it is part of. This results in strong, additional cross-links and a three-dimensional, stiff network (Figure 1).

The concept of StructUre<sup>TM</sup> is based upon a continuous, i.e. endless production of soft, flexible foam, which, after processing and shaping, can be transformed into rigid foam by means of high energy electrons (E-beam). On impact, excited molecules initiate and sustain cross-linking, which results in an otherwise unobtainable level of mechanical properties.

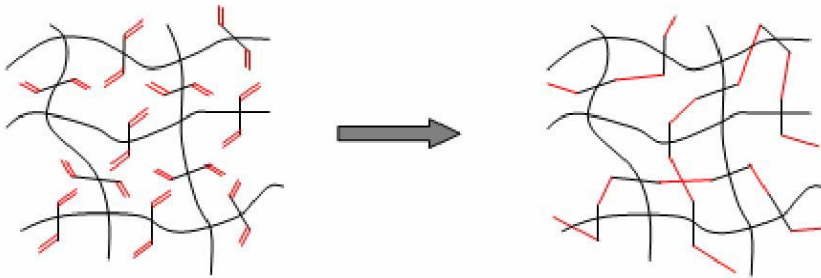


Figure 1. Molecular structure – from soft to rigid.

#### 4. E-BEAM CROSS-LINKING: TOMORROW'S TECHNOLOGY, AVAILABLE TODAY

E-beam cross-linking has been identified as the innovative means to modify plastic materials [5, 6]. Free electrons are generated by sending a high voltage current through an electrical wire (similar to the working principle of a light bulb). Powerful magnetic fields accelerate the emitted electrons to a high level of kinetic energy. These linear moving electrons are then scanned into a beam, which covers a defined surface (similar to a television screen). Goods can now be transported through the resulting beam and be modified. This process neither generates, nor stores radio-activity!

E-beam accelerators can be found in service centres all over the world. A typical lay-out of such a facility is shown in Figure 2. These centres are frequently used to sterilise medical goods. But they can also be used to modify properties such as heat resistance and toughness of plastics, like for instance polyethylene.

E-beam cross-linking offers many processing advantages. It takes place at ambient temperature, which results in the absence of thermal stresses within the material. The process itself can be accurately adjusted and controlled, with the energy dose being the only variable. Above all, it is extremely fast and efficient with a processing time in the order of seconds. Therefore, a continuous operating system can be set up. The high throughput enables and fits perfectly to large series production.

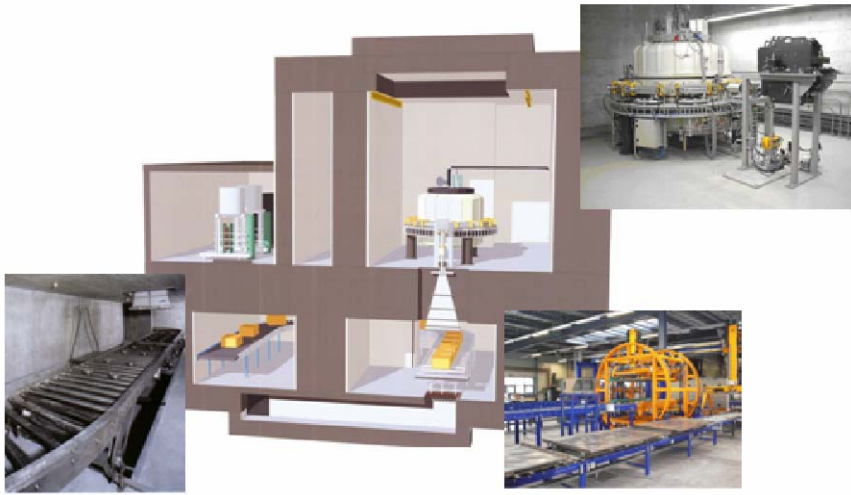


Figure 2. Typical lay-out of an e-beam service centre (Copyright Studer Hard/IBA sa).

One method of processing is to pack StructUre™, still in its soft state, in a defined position or pre-manufactured shape into ready for shipment, cardboard boxes and then to pass these boxes through the e-beam (Figure 3).

Another option is to place soft StructUre™ between reusable, electron transparent moulds and to pass these through the e-beam (Figure 4).

Mould-halves can be made from StructUre™ as well, pre-treated to a rigid state. Investigation has shown that StructUre™-E720 for instance, with a density of  $57 \text{ kg/m}^3$ , can be treated to a depth of approximately 350 mm with an effective dose variation of only  $\pm 5\%$  (Figure 5). As most sandwich structures use cores with thicknesses between 5 mm and 40 mm, this leaves foam thickness up to approximately 300 mm for the top half of the mould. The bottom mould-half does not need to be electron transparent and can for instance be made of wood.

Whilst using one of the methods described before, local densification of StructUre™ is another option (Figure 6). This can for instance be necessary in positions, where fixation elements will result in an increased concentration of bearing loads.

Certain, defined areas within the product can further be cross-linked with a different degree of rigidity. This can be achieved by shielding-off part of the electron beam with dense material in thin sheets (Figure 7). This option can for instance be used to make a product locally more damage tolerant.

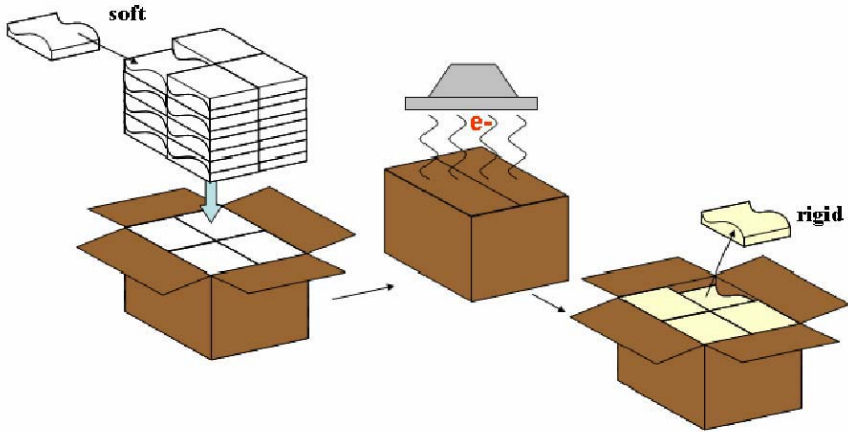


Figure 3. E-beam cross-linking of StructUre™ in closed carton boxes.

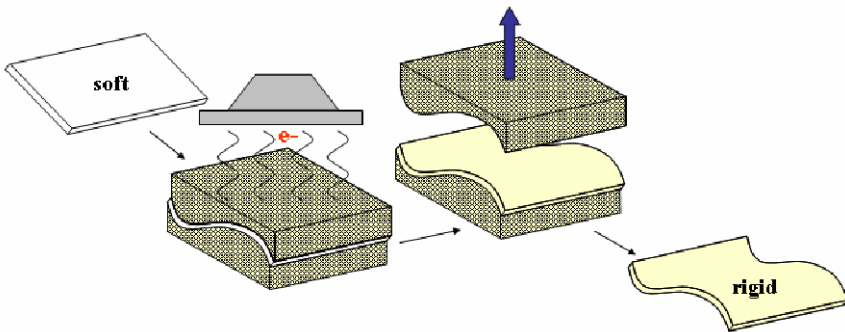


Figure 4. E-beam cross-linking of StructUre™ between mould-halves.

## 5. FINE-TUNING OF MECHANICAL PROPERTIES

Product modifications can be achieved in two alternative ways. First, depending on the electron energy intensity and the resulting degree of cross-linking, a wide range of foams, from flexible, through semi-rigid to rigid, can be produced from any starting, soft product. This means, that on the basis of a required, final product specification, first a check should be made, whether it can be achieved by choosing the optimum energy dose for available StructUre™ grades. Figure 8 for instance shows, that if a tensile strength  $> 300$  kPa and an elongation at break  $> 45\%$  is specified, StructUre™-E720 should best be radiated with 25 kGy, being the optimum dose in the exact centre of the allowable tolerance range.

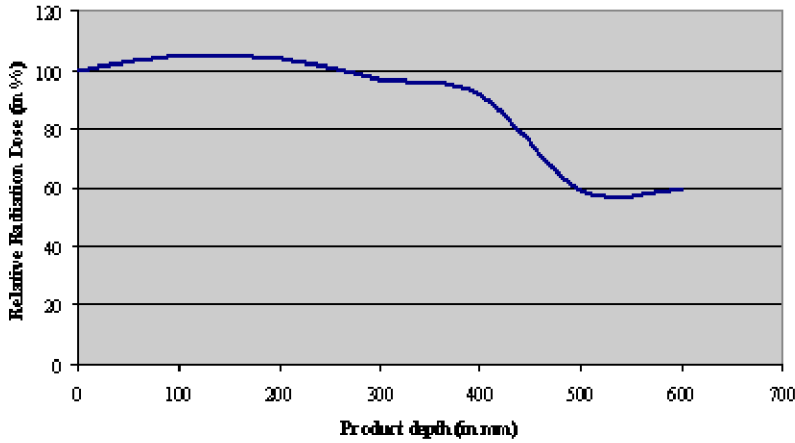


Figure 5. Effective electron dosage at material depth (StructUre™-E720, 100% = 32 kGy).

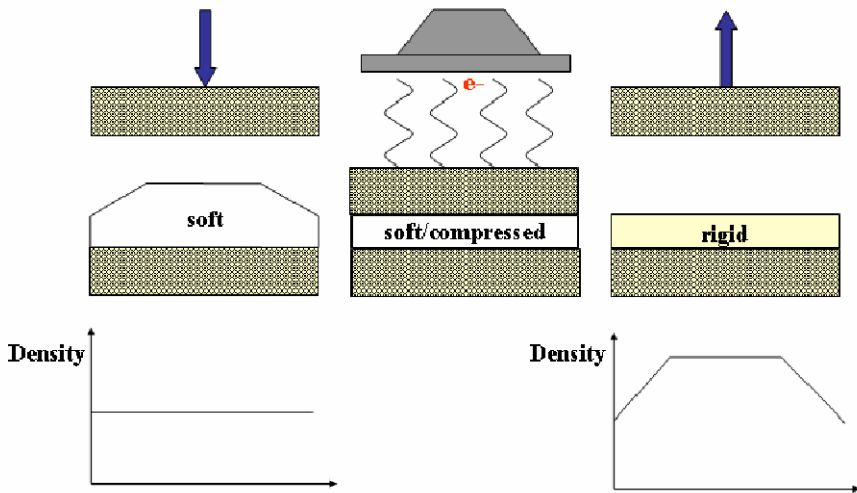


Figure 6. Local variation of final density of StructUre™.

Second, if no match with available StructUre™ grades can be found, the development of new product formulations is optional (Figure 9). The chemistry of polyurethanes is extremely versatile, allowing for an almost unlimited amount of grades, optimised for specific performance, such as high compressive strength, chemical resistance, UV-stabilization, etc.

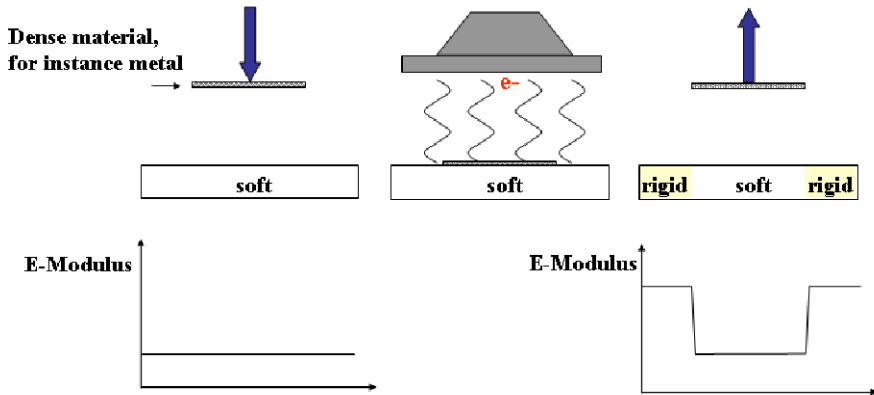


Figure 7. Local variation in final rigidity.

Open-cell, space-frame like cell structures can further be achieved by optional reticulation of StructUre™ prior to cross-linking. For this process, a soft foam block is placed into a pressure chamber, which is next filled with an explosive gas mixture (Figure 10). A controlled explosion tears away the thin cell walls, leaving the more solid pillars free of damage. The result is a 100% open cell, soft foam, which next can be cross-linked to a rigid state.

This brings advantages for certain applications, which were out of range for the present (closed cell) rigid foams. For instance dimensionally stable, load-bearing filtration components can be manufactured this way.

## 6. THE SHAPE OF THINGS TO COME

StructUre™ offers engineers the potential to combine increased freedom of 3D-design with savings in weight and cost. The basic soft foam can be slab stock manufactured on a large scale with available, continuous operating production equipment, be further efficiently processed using fast cutting machinery and be electron radiated in available, also continuous operating service centres with free capacity. For the first time, basic materials and manufacturing processes can fulfil requirements for the mass production of sandwich cores. This may allow sandwich structures to be used for high volume productions, such as for the automotive industry. New sandwich solutions, incorporating acoustic insulation, damage tolerance and air ventilation are now feasible. Modular design can be pushed forward, as lightweight sandwich structures could ideally function as the dimensionally stable, styling, load-bearing basis of such modules.

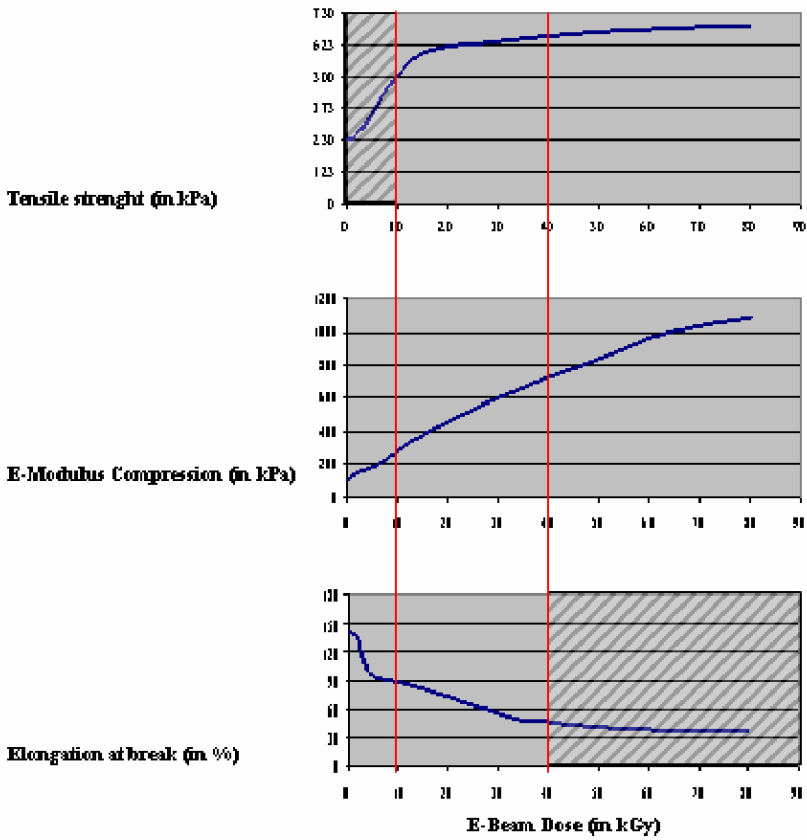


Figure 8. Example of choosing an optimum energy dose for StructUre™-E720 (Note: more rigid grades are under investigation at the time of publication).

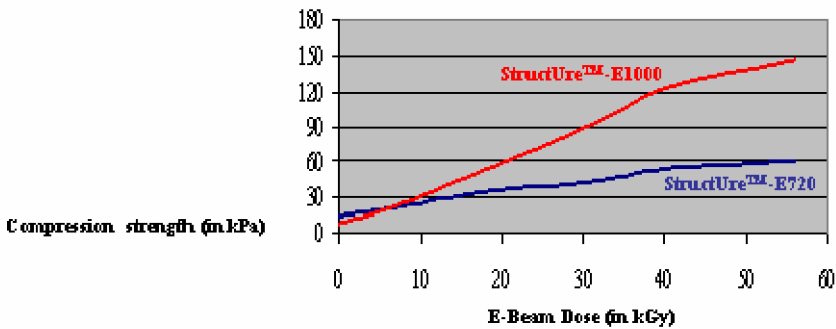


Figure 9. Compression strength of 2 alternative StructUre™ grades.



*Figure 10.* Soft foam reticulation chamber.

## REFERENCES

1. Danielsson, M. and Olsson, K.-A., "High resilience rigid foam core material for high dynamic stress/strain energy absorption applications", Proceedings of the Third International Conference on Sandwich Construction, Southampton, 1995.
2. Bitzer, T.N., "Recent honeycomb core developments", Proceedings of the Third International Conference on Sandwich Construction, Southampton, 1995.
3. den Haan, L., "Can high performance and cost-savings be combined for foam core sandwich structures?", JEC-Conference, Paris, 1995.
4. den Haan, L. and Reif, G., "Challenges of teaming-up sandwich technology and business success in rail transportation", Proceedings of the Fourth International Conference on Sandwich Construction, Stockholm, 1998.
5. n.n., "Electron-beam curing of polymeric composites as an enabling technology for advanced manufacturing", The International Composites Expo, Cincinnati, 1999.
6. Norris, R.E., Janke, C.J., Eberle, C. and Wrenn, G.E., "Electron beam curing of composites", Future Car Congress, 2000.

# FORMABILITY OF LIGHTWEIGHT, VIBRATION DAMPING AND MEDIUM PERFUSED SANDWICH SHEETS

*Analysis through Practical Experiments and FEM-Simulations*

Reiner Kopp<sup>1</sup>, Marc Nutzmann<sup>2</sup> and Johan van Santen<sup>1\*</sup>

<sup>1</sup>*Institute of Metal Forming (IBF), RWTH Aachen University, Intzestrasse 10, D-52056 Aachen, Germany;* <sup>2</sup>*Muhr und Bender KG, Hachenburgerstrasse 31, D-57586 Weitefeld, Germany*

**Abstract** The unique optimization potential of sandwich sheets with respect to a defined criterion, e.g. weight reduction, originates from the combination of different materials into one sheet. Due to this material combination, the sheet behaves differently from conventional sheet materials during forming and in addition unique failure modes like delamination might occur. Within the framework of two, separate research projects these unique features of sandwich sheets were analyzed through practical experiments and FEM-analyses.

**Keywords:** sandwich sheet, deep drawing, bending, delamination.

## 1. INTRODUCTION

The responsibility of the automotive industry to reduce exhaust gases, mainly CO<sub>2</sub>, is a major drive for many new developments. Besides innovations in the engine technology with the aim of a more efficient mileage, the reduction of weight is today another important research topic. Next to high strength materials and tailored blanks, sandwich sheets are capable of achieving this objective. These types of sandwich sheets are characterized by a low ratio of skin to core thickness, enabling a high bending stiffness at low weight. Sandwich sheets can however be used successfully for noise insulation and vibration damping as well. In that case the ratio of skin to core thickness is higher, as a thin core layer or adhesive of 50 to 100 µm is already sufficient to convert the vibrations into frictional

heat, while they are transmitted through the different layers of the sandwich. Within the framework of this situation the major goal of the research project APOLISS “Application of Lightweight Sandwich Sheets” was to broaden the currently still restricted usage of sandwich sheets for automobile components through the examination of their formability, joinability and to evaluate their applicability for mass production, Figure 1 [1].

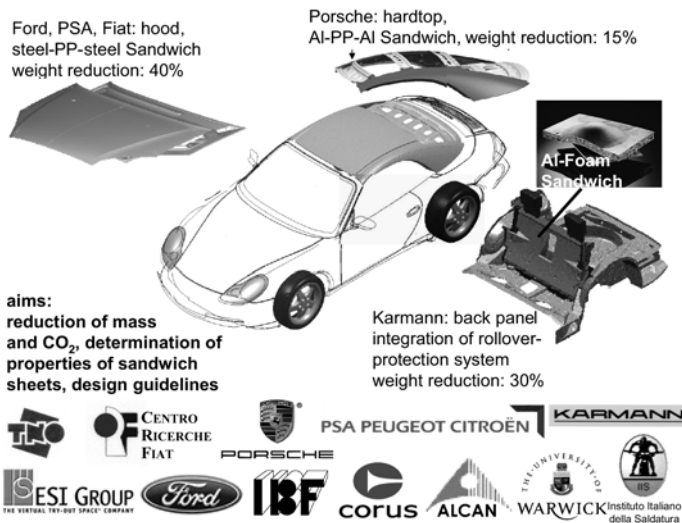


Figure 1. Research within the European project APOLISS.

Although most developed sandwich sheets can be classified into either the lightweight construction or the vibration damping group, there are some exceptions. A clarifying example for that is the utilization of a sandwich sheet called ‘grid sheet’ as a heat shield for steam turbine casings. Grid sheet consists of two face sheets and a core of expanded metal, woven wire mesh, perforated plate, or sheet metal with slot dimples that are joined by either resistance welding or adhesive bonding [2]. The welded variant disposes of cavities that can be perfused with a cooling medium, facilitating the increase of the steam inlet temperature [3]. Hereby the power plant efficiency can be increased to protect the natural fuel resources and to reduce the emissions of environmentally harmful gases. The production and testing of this heat shield is investigated within the Collaborative Research Center SFB 561 “Thermally highly loaded, porous and cooled multi-layer systems for combined cycle power plants”, Figure 2.

The IBF was, respectively is responsible for the evaluation of the formability of the sandwich sheets concerned. Within the project APOLISS the formability and failure modes of various industrially available lightweight and vibration damping sandwich sheets were evaluated by

executing deep drawing experiments and other forming processes. Since the welded grid sheets are required to have a cylindrical slightly conical shape, the behavior in bending processes, among other forming processes, was investigated. To increase the insight in the forming behavior and especially delamination of sandwich sheets not only experiments, but also FE-simulations were executed.

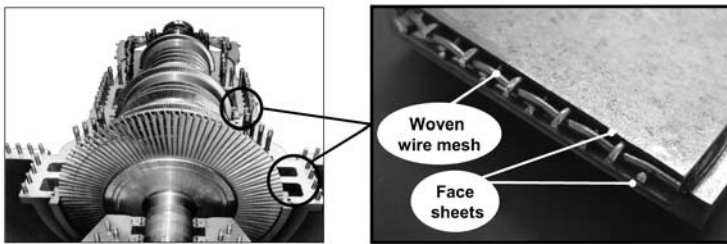


Figure 2. Research within the Collaborative Research Center SFB 561.

## 2. DEEP DRAWING OF LIGHTWEIGHT AND VIBRATION DAMPING SANDWICH SHEETS

Since deep drawing is an important forming operation in the sheet metal forming industry, it is essential that new materials show good deep drawing properties. Although the cupping test is a principle test, showing hardly any resemblance to more complex parts found in the automotive industry, it has turned out to be a good test to characterize the failure modes and deep drawing properties of sandwich sheets. Defects that can be recognized using this test are: tendency to wrinkling, squeezing of the core, and delamination. The latter is a defect, unique to sandwich materials, which can not be observed for normal sheet and which is next to that difficult to detect. FE-simulations were used to investigate this defect and the obtained results were validated by checking deep drawn parts on delamination defects.

### 2.1 Delamination in cupping tests

An exceeding of the maximal shear stress of the joint or the bonding between the individual layers is the cause for the separation of the layers. Delamination can occur during the production of the sandwich sheet or during down-stream processing. In forming processes delamination is observed in areas with local wrinkling, Figure 3. To avoid delamination it is important to identify the exact cause. Eligible ways to analyze parts are the contact-free, non-destructive testing methods computer tomography and the lock-in thermography [4]. Both methods have the ability to detect smallest

debondings or delaminations. With the lock-in thermography it is possible to identify, through optical waves inside the part induced by flash lights, the smallest temperature differences in a few milliseconds. These temperature gradients might be evidence for delamination.

Tests with parts made of sandwich sheets showed that delamination often occurs in areas of small or sharp-edged radii. By cutting the part in exactly the identified area, visible evidence was obtained to verify, if delamination had really occurred. For some lightweight sandwich sheets delamination could not be observed, as the face sheets fail before the bonding between the layers was able to fail.

## 2.2 FE-simulation of deep drawing

To increase the insight in the phenomenons taking place during the forming of sandwich sheets, FE-simulations were executed. Several approaches can be used to model the forming of sandwich sheets:

- One-Part-Model with different material layers, in which the nodes between the layers are shared.
- Two-Layers-Substitution-Model with two layers, which are for example combined with springs for interaction between the layers and which act as spacers as well.
- Three-Layers-Model where each layer has its own nodes.

In the first model each layer is provided with its specific material data and a permanent cohesion is suggested, making the simulation of delamination impossible. The second model is a substitution model where the core is not modeled. On the one hand this saves computing time, especially for large parts, on the other hand the core or intermediate layer cannot be provided with material data. The latter model consisted of three independent layers with the possibility to provide each layer with its own material data, which is a prerequisite for the simulation of delamination.

An interaction between the layers can be modeled through a contact definition. The software LS-Dyna disposes of a feature to simulate a loss of contact, i.e. delamination, through an exceeding of a user defined shear stress. The simulation of shear stress, which is predominantly absorbed by the soft plastic core, was modeled through the use of twelve volume elements divided over the overall thickness of the sandwich sheet, resulting in accurate results. Figure 3 shows the results of a FE-simulation, in which a delamination can be clearly recognized.

To increase the insight in the causes of delamination, the equation for estimating the deep drawing force in cupping tests according to Siebel [5] was analyzed.

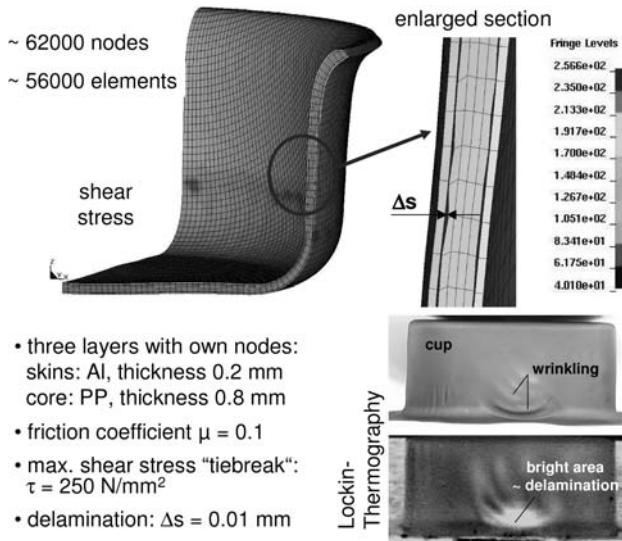


Figure 3. Simulation and validation of delamination in a cup test.

$$F_{\max} = \pi \cdot d_1 \cdot s_0 \cdot \left[ e^{\mu_3 \frac{\pi}{2}} \cdot \left( 1.1 \cdot k_{fml} \cdot \ln \frac{d_{\max}}{d_1} + \frac{2 \cdot \mu \cdot F_N}{\pi \cdot d_{\max} \cdot s_0} \right) + k_{fml} \cdot \frac{s_0}{2 \cdot R_z} \right]$$

$d_1$  represents the punch diameter;  $s_0$  the initial sheet thickness;  $\mu$  corresponds to the friction coefficient;  $d_{\max}$  to the maximum drawable diameter;  $F_N$  to the blank holder force and  $k_{fm}$  and  $R_z$  stand for the average flow stress between inner and outer radius, and die radius respectively. This equation is normally only used for conventional sheet materials, but can be used successfully for deep drawing of sandwich sheets as well. For that, each layer is to be considered separately and the sum of all individual forces corresponds to the necessary deep drawing force. This approach has shown good resemblance to experimental results for various sandwich materials.

Due to different tribological conditions for each layer, varying forming stresses occur within the sandwich sheet (see Siebel equation). The resulting shear stress in the sandwich sheet, should be withstood by the core of the sandwich. If the maximum shear stress is exceeded, delamination will be observed. The discrepancy between the test conditions in shear tensile testing (to determine the maximum shear stress) and during the cupping tests are the most important reason that the prediction of delamination is not (yet) possible with the Siebel equation. FEM-analyses might be a helpful tool to expand the validity of the Siebel equation and up to that moment the equation can be used successfully to estimate the deep drawing force.

### 3. DIE BENDING OF WELDED GRID SHEET

In the preliminary specifications for the heat shield a curvature radius of 400 mm was laid down. Since the grid sheets can only be produced in a flat manner, the heat shield elements have to be bent afterwards. To obtain an optimal permeability, an interlayer of woven wire mesh showed the best performance. Although there are other forming processes capable of producing the required shape, die bending was selected to explore the forming behavior of welded grid sheets. To increase the insight in the forming behavior of welded grid sheet next to experiments FE-simulations were executed.

#### 3.1 Die bending experiments

In die bending two fundamentally different variants can be recognized: free bending and coining. During free bending, the work piece is bent without pressing the punch to the bottom of the die. Instead, the work piece is pressed completely into the die by the punch during coining. The latter method was preferred, since it is more precise and therefore radius fluctuations are less likely to occur. However, it remains difficult to predict the amount of spring back in advance. For that reason a flexible die bending tool was constructed, which facilitated the infinitely variable positioning of both die and punch, Figure 4. This in turn allowed the compensation of the spring back and the adjustment of the geometry of the bent segment. To get a rough estimation of the required basic tool radii the equation below, introduced by Gardiner, in which the strains above the yield strength are estimated to be constant, was used.

$$\frac{R}{R'} = 4 \cdot \left( \frac{R \cdot R_{p0,2}}{E \cdot t} \right)^3 - 3 \cdot \left( \frac{R \cdot R_{p0,2}}{E \cdot t} \right) + 1$$

$R$ , represents the tool radius;  $R'$  the sheet radius after spring back;  $t$ , corresponds to the sandwich sheet overall thickness and  $R_{p0,2}$  and  $E$  stand for the 0.2% yield strength, and Young's modulus respectively.

Based on this equation a die having a radius of 200 mm and a punch with a radius 196 mm were manufactured. Additional process parameters that can be varied to improve the dimensional accuracy or formability are: forming temperature, and coining force.

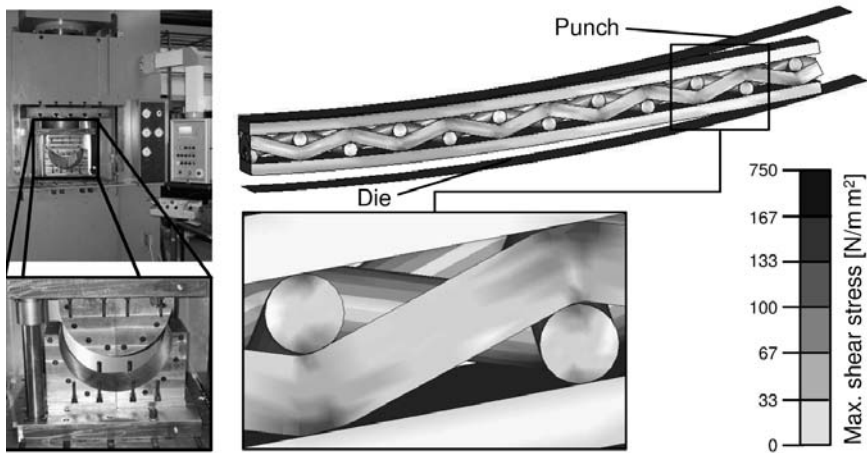


Figure 4. Die bending equipment and corresponding FE-simulation results.

Insight in the spring back behavior of grid sheet was obtained through the execution of various experiments. The effect of different tool geometries on the radius of the grid sheet was discussed in [6]. The conventional tool configuration, i.e. closed die and closed punch, turned out to deliver the best results. For that reason subsequent experiments were executed using this tool configuration. Since a permanent contact between face sheet and core is essential to obtain a predictable spring back behavior, the grid sheets underwent a heat treatment previously to forming. During preliminary experiments it was namely observed that some of the welding points failed during forming, i.e. delamination. Experiments revealed that this can be avoided, if a suitable heat treatment is used. The effect of this heat treatment on the spring back behavior was discussed in [7].

Since a radii ratio  $R/R'$  of 0.83, obtained in the experiments, corresponded relatively well to the estimated ratio of 0.82 or 0.86 respectively (Gardiner equation), it can be concluded that this equation is suitable for getting a first impression of the spring back behavior of welded grid sheet. The first estimated ratio was calculated using a Young's modulus of  $210,000 \text{ N/mm}^2$ , determined in tensile testing, the latter with a Young's modulus of  $170,000 \text{ N/mm}^2$ , determined using RFDA (Resonance Frequency and Damping Analysis). Since the estimation of the radius according to Gardiner is quite accurate, a die radius of ca. 300 mm should deliver the desired radius of 400 mm.

### 3.2 FE-simulation of die bending

Since experiments had already demonstrated that welded grid sheet is quite resilient, which affects the final geometry of the bent segment to a large extent, FE-simulations were executed to increase the insight into the specific forming fundamentals of welded grid sheet. Due to the resilience of welded grid sheet an important challenge was to reproduce the elastic spring back of the bent segments after stress removal in the FE-simulation. As grid sheet is next to that a relatively complex sandwich sheet with its specific composition: anisotropic interlayer, joining technique, etc., the FE-simulation was made quite complex.

To enable an extensive analysis of both the anisotropic core and the welding points, a 3-dimensional model was constructed with the software Programmer's Environment for Pre-Postprocessing (PEP) [8]. The FE-model was built up out of unity cells that were adapted to the original dimensions of the grid sheet. After the construction of the FE-model, the actual die bending process was simulated in LS-Dyna. Die bending experiments had already demonstrated that the welding points sometimes fail at arbitrary locations. Therefore, one of the requirements for the simulation of the die bending process was to model the welding points in a correct way. Ideally, a critical shear stress is defined, which releases the connection between the nodes concerned. Most LS-Dyna contact cards are however only applicable for shell elements, but one contact definition was identified that allowed the definition of maximum plastic strain. If this defined maximum is exceeded, the contacts between the nodes corresponding to a welding point are released. Unfortunately, it is not possible to experimentally determine a maximum plastic strain for the welding points to fail. Alternatively, the die bending process itself was simulated to explore eligible realistic values for the maximum plastic strain. The number of failed welding points was used as a comparison criterion.

After the forming simulation is completed and the grid sheet is completely pressed into the die, the spring back of the bent segment has to be simulated. The spring back calculation of the grid sheet was accomplished using an implicit solver, which is predominately preferred in literature [9]. LS-Dyna provides a tool, designated "dynain" in LS-Dyna nomenclature, which uses the output file called "dynain" of the explicit forming simulation. Figure 4 shows the concentration of stresses at the welding points, which corresponds to reality. Results of the simulations are discussed in more detail in [7].

#### **4. CONCLUSIONS AND FUTURE PROSPECTS**

Automobile sheet materials have to possess excellent forming properties; in most cases good deep drawing properties. Although commercially available sandwich sheet materials show promising results, there still are guidelines that have to be kept into mind during forming to avoid defects. Simulation offers the possibility to model forming processes with sandwich sheets and their typical failure modes, e.g. wrinkling, sliding or delamination of the layers, and delamination. Experimentally, the existence of delamination in sandwich sheets could be localized through contact-free and non-destructive measurement systems and verified through subsequent cutting of the deep drawn part. In the APOLISS project the lack of form stability of the plastic core at temperatures over 180 °C in the paint coating process and the low buckling resistance at small peen impact have been identified to be the most critical points that must be solved. The development of better, primarily temperature resistant plastics and the application of high strength steels as sandwich skins and multifunctional compounds will increase the application potential of sandwich sheets in the future.

Although the spring back of welded grid sheet can be accounted for in the design of die bending tools with the help of the equation developed by Gardiner, it remains difficult to produce grid sheet segments with very high accuracy. Next to that the developed adjustable tools were unable to compensate the spring back without introducing a deviation of the circular shape. For that matter the forming of grid sheet with another flexible bending process, 3- or 4-roll bending is planned to be evaluated in the future. This type of forming process is even capable of producing conical parts in a flexible way, which correspond better to the final shape of a steam turbine.

First FEM-simulations revealed that it is possible to simulate the forming of complex sandwich structures like grid sheet in great detail. However, at this moment the gathered simulation experience is insufficient to use FEM-simulation as a stand-alone tool. A validation with practical experiments continues to be necessary. To evaluate the best suitable failing criterion and corresponding failing value, the simulation of shear tensile tests are planned. Unfortunately, shear tensile tests that were executed at the ISF resulted in a deflection of the face sheets, which affected the failing of the grid sheet to a large extent. Therefore, it is planned to construct a testing fixture that introduces a 'pure' shear stress load in the interlayer and the welding points connecting face sheet and core. Subsequently, the simulation of the die bending process should be repeated and the results compared with previous simulation results. Furthermore, the gained experiences should be extended to the simulation of other forming processes, e.g. 3- or 4 roll bending.

## ACKNOWLEDGEMENTS

The authors would like to thank the European Community (EC) for the financial support of the project “APOLISS” (Application of Lightweight Sandwich Sheets) and the associated project partners for their cooperation. Furthermore, the authors gratefully acknowledge the financial support of the German Research Foundation (DFG) within the Collaborative Research Center (SFB 561) “Thermally highly loaded, porous and cooled multi-layer systems for combined cycle power plants”. Finally, the authors would like to express their gratitude towards Mr. P. Hohmeier, a former researcher at the IBF, for his research work on the bending of welded grid sheet.

## REFERENCES

1. Kopp, R., Abratis, C., Nutzmann, M. “Lightweight Sandwich Sheets for Automobile Applications”, WGP Annals, Vol. XI/2, 2004.
2. Dilthey, U. and Kopp, R., “Verfahren zur Herstellung von Metallverbundplatten”, German patent, DE 3935120, 1991.
3. Bohn, D., “New Materials and cooling systems for high temperature, highly loaded components in advanced combined cycle power plants”, Proceedings Conference on Materials for Advanced Power Engineering, Liège, pp. 107-120, 2002.
4. Nutzmann, M., Kopp, R., “Umformung von Mehrschichtverbunden für Leichtbauteile im Fahrzeugbau”, Proceedings 19. ASK Conference, Aachen, pp. 123-132, 2004.
5. Lange, K., Umformtechnik, Band 3: Blechbearbeitung, Springer-Verlag, Berlin, Germany, 1990.
6. Dilthey, U. et al., “Development of Porous Steel Structures for Steam Turbines”. Advanced Engineering Materials, Vol. 3, No. 3, pp. 111-119, 2001.
7. Kopp, R., Franzke, M., Hohmeier, P., van Santen, J., “Bending of Sandwich Structures with Usable Cavities for Active Cooling Applications in Steam Turbines”, WGP Annals, Vol. XII/1, 2005.
8. Franzke, M., PEP-Programmer’s Environment for Pre-Postprocessing, User manual 3.30, Institute of Metal Forming (IBF), Aachen, 2001.
9. Roll, K., Rohleder, M., “Simulation der Rückfederung in der Blechumformung”, Proceedings Industriekolloquium, Claustahl-Zellerfeld, 2000.

# FABRICATION AND MECHANICAL PROPERTIES OF FUNCTIONALLY GRADED MICRO POROUS METALS BY MIM-BASE POWDER SPACE HOLDER METHOD

Kazuaki Nishiyabu<sup>1</sup>, Satoru Matsuzaki<sup>2</sup> and Shigeo Tanaka<sup>2</sup>

<sup>1</sup>*Osaka Prefectural College of Technology, 26-12 Saiwai, Neyagawa 572-8572, Osaka, Japan*

<sup>2</sup>*Taisei-Kogyo Co., Ltd., 26-1 Ikeda-kita, Neyagawa 572-0073, Osaka, Japan*

**Abstract** This study describes the manufacturing method based on metal powder injection moulding for micro porous metal components with high functionally graded sandwich structure. The effectiveness of sandwich structure produced by co-sintering and co-injection moulding processes to compensate the deficiencies on the mechanical property of porous structures, was investigated.

**Keywords:** micro porous metal, metal injection moulding, powder space holder method, co-sintering, co-injection moulding, functionally graded sandwich structure.

## 1. INTRODUCTION

Sandwich structures are an interesting concept for producing stiff light-weight panels. The panels are basically consisted of two skins adhesively bonded onto a core material such as classical sandwich construction using honeycomb cores made of aluminium, paper or polymeric composites, and form cores made of polymer or aluminium. The typical problem is the delamination of the skins from the core because of the interface existing between them in classical sandwich construction using the above-cited cores. It is, therefore, desirable to produce one component sandwich structures without any bonding between two skins and core. So far, a large size of composites sandwich structured panel has been mainly studied and used for tations, architectures and packaging and

so on. However an enhanced use of sandwich structures for comparatively small components will be essential for high functionality of the products.

Metal foam and cellular metals, on the other hand, have been widely studied [1-4]. However, these do not deal with micro-sized porous structure and complicated shaped metal components, which are strongly desired in higher performance applications for filter, catalyst electrode, heat shield and medical implant and so on. Furthermore the combination of highly dense and porous metals is promising for the materials with a high specific modulus and high functionality. However the control of pore size and its distribution is not easy in practice and much more so the production of porous graded metals with complicated shapes.

The aim of this study is to develop the net-shape manufacturing method for micro-sized porous metal components with high functionally graded sandwich structures. In this paper, the three manufacturing methods such as 1) hot-press forming, 2) sequential injection moulding, and 3) co-injection moulding for 1) multilayered porous structure, 2) multi core-in-sheath porous structure and 3) steamed bread-like porous structure, respectively, were demonstrated using stainless steel and titanium.

## **2. NET-SHAPE MANUFACTURING METHOD FOR MICRO POROUS METAL COMPONENTS**

The concept of the production method for micro porous metals we developed based on metal injection moulding (MIM) process is illustrated in Figure 1. The production method for porous materials, namely space holder method was applied to MIM process. This novel method was named as powder space holder (PSH) method or PSH-MIM method by authors.

### **2.1 Metal powder injection moulding (MIM) process**

MIM is a manufacturing method combining the traditional powder metallurgy process and plastic injection moulding. It has over the past decade established itself as a comparative manufacturing process for small precision components. It is capable of producing in small volumes complex shapes from almost all types of materials including metals, ceramics, inter-metallic compounds, and composites [5, 6]. Recently MIM has been studied not only for hard metals, but also for materials such as titanium, copper and aluminium [7, 8]. As shown in Figure 1(a), in a conventional MIM process, the feedstock materials are composed of metal powder and binders, and a high densification after debinding and sintering is very important for high quality MIM products.

## 2.2 Powder space holder (PSH) method

In highly porous structured MIM products shown in Figure 1(b), many spaces require retention after sintering. In addition to metal powder and binders, coarse spherical materials made of thermoplastics were used as lost material for formation of fine porous structures in MIM components. Fraction and combination in size of space holding particle and metal powder in addition to sintering conditions determine the porous structure. Many applications welcome the advantages that this proposed method is a net-shaped production for micro porous metal components with 3 dimensional complicated shapes and high functionality graded structures and can be applied to most kinds of metal powder, such as stainless steels, aluminium, copper, titanium, nickel and their alloy as the representative materials.

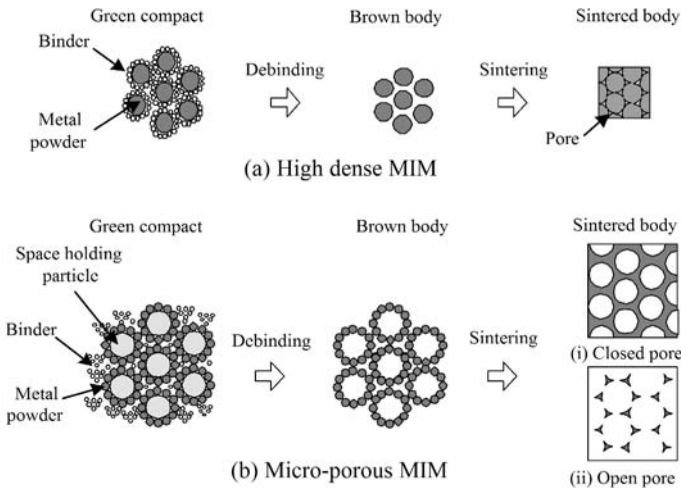


Figure 1. MIM and Powder space holder method for producing micro porous metals.

## 3. EXPERIMENTS

### 3.1 Materials and porous compounds

The experimental materials used for MIM feedstock and porous compounds are listed in Table 1. The metal powders used are austenitic stainless steel, 316L and pure titanium produced by water-atomization method. The binder used is from the polyacetal family. As the materials for

pore formation, polymethylmethacrylate (PMMA) which consists of spherical particles of  $10\mu\text{m}$  and  $180\mu\text{m}$  in mean diameter were used. These materials were co-mixed and pelletized with kneader and extruder. Fraction of PMMA particles was varied from 0 to 80vol.% as experimental parameter, but metal powder loading was held constancy of 50vol.% in MIM feedstock.

Table 1. Experimental materials and fraction of compound.

	Compositions	Mean diameter	Volume fraction	
			MIM feedstock	Porous compound
Metal powder	Stainless steel, 316L	$9\mu\text{m}$	50vol.%	20-100vol.%
	Pure titanium	$24\mu\text{m}$		
Binder	Wax, Polyacetal family	-----	50vol.%	
Space holding particle	Polymethylmethacrylate (PMMA)	$10\mu\text{m}$ $180\mu\text{m}$	-----	0-80vol.%

### 3.2 Consolidation methods for sandwich structures

To form the green compacts with sandwich structures, hot press forming [9], sequential injection moulding and co-injection moulding [10] were presented in this paper. Co-sintering is capable of producing the multilayered metals with porous graded structures.

#### 3.2.1 Hot press forming method

As shown in Figure 2, the circular shape of the green compacts ( $80\text{mm}$  in diameter,  $1\text{mm}$  in thickness) was prepared by hot press moulding for the simplicity. The specimens were produced individually using dense MIM feedstock or porous compounds with various fractions of space holding particles, and re-hot pressed the laminates stacked in desired sequence. The hot press moulding was conducted under constant conditions that die temperature and gage pressure was  $200^\circ\text{C}$  and  $2.5\text{MPa}$ , respectively.

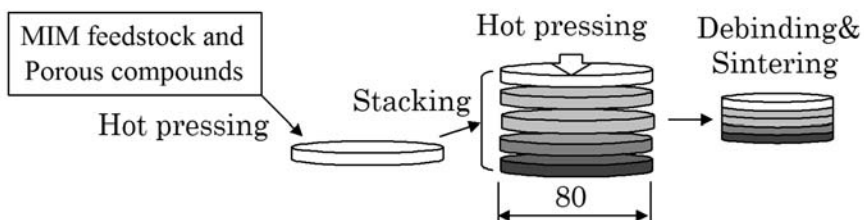


Figure 2. Hot press forming method.

### 3.2.2 Sequential injection moulding method

Sequential injection moulding method used for producing the multilayer porous structured parts are illustrated in Figure 3. In the 1<sup>st</sup> step, inner material was moulded into the die, in the 2<sup>nd</sup> and 3<sup>rd</sup> steps, middle and outer materials were over-moulded after inserted the over-moulded parts in turn. Three layers structural green compacts were obtained using dense MIM feedstock and porous compounds with various fractions of PMMA particles.

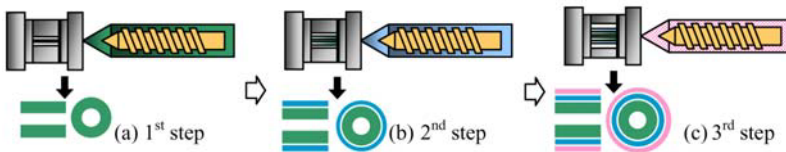


Figure 3. Sequential injection moulding method.

### 3.2.3 Co-injection moulding method

Co-injection moulding method is characterized by possessing sandwich structure in porous MIM components as shown in Figure 4. Co-injection moulding of flat specimens applied to the hot runner system with a double gate which could be injected sequentially two kinds of materials.

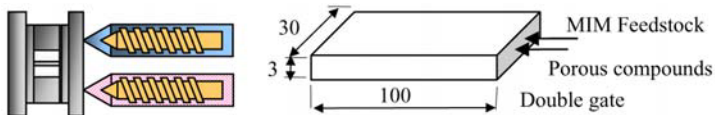


Figure 4. Co-injection moulding method.

## 3.3 Debinding-sintering conditions and evaluation

Debinding and sintering were sequentially processed at 600°C for 2hr in N<sub>2</sub> and at 1050-1200°C for 2hr in Ar gas atmospheres in the vacuum furnace. The relative density i.e. reciprocal of porosity of sintered specimens was measured with micrometer calliper and analytical balance. Pore size was measured with Porometer (PMI, CPF-1100-AXLSP). Surface structure was observed by SEM and 3 points bending test of the sintered specimens were conducted in recording the images under loading with a digital microscope.

## 4. RESULTS AND DISCUSSIONS

### 4.1 Multilayer porous structure by hot press forming

Figure 5 shows SEM images of the porous graded metals produced by co-sintering the laminated green compacts, which were stacked with various volumetric fractions of PMMA particles in several sequences; type (a) 60,30,0,30,60vol.% and type (b) 0,30,60,30,0vol.% with inverse symmetry. It is clarified from these SEM images that the macroscopically graded porous structures reveal and no defects appear in the interfacial region between each layer.

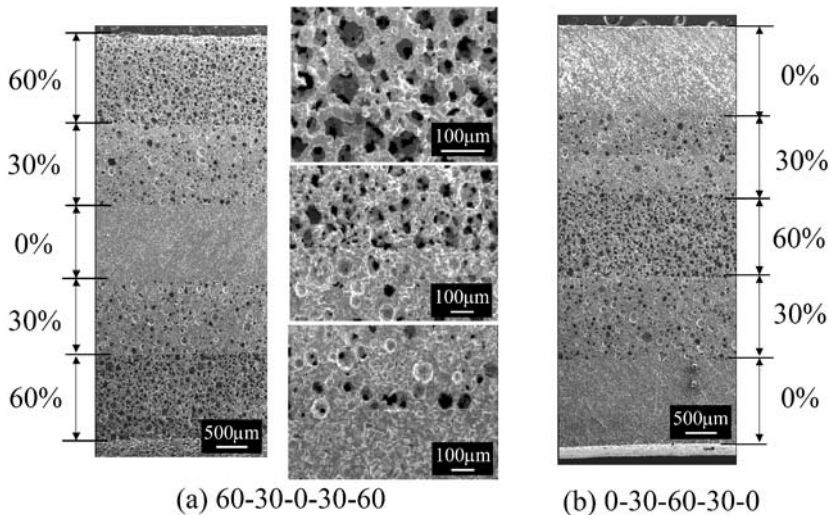


Figure 5. Structure of porous graded metals produced by co-sintering hot-pressed parts.

Figure 6 shows the bending stress - strain curves and bending modulus of homogeneous porous specimens and porous graded ones. The ultimate stresses of homogeneous porous specimens with 30 and 60vol.% PMMA particle are very low, and the bending modulus decrease drastically with increasing in fraction of PMMA particle. The behaviour can be also confirmed from fracture aspects shown in Figure 7. Obvious crack propagation was appeared in the lower tensile side. On the other hand, either porous graded specimens shown a large deformation behaviour as with dense 0vol.% PMMA specimen. Definite differences in bending modulus were appeared between type (a) 60-30-0-30-60 and type (b) 0-30-60-30-0 specimens. The bending modulus is higher for type (b) specimens and is lower for type (a) specimens than approximated values. This is because the

multi-cracks occurred in the lower skin layer with open porous structure, which was subjected to tensile load, in type (a) specimens.

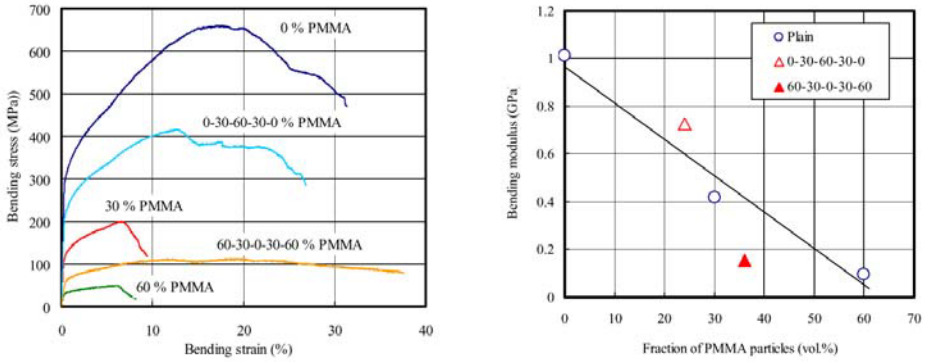


Figure 6. Bending properties of specimens with various fractions of PMMA particles

Homogeneous structure		Porous graded structure	
(i) 0	(ii) 60	(a) 60-30-0-30-60	(b) 0-30-60-30-0
23.1 %ε	11.6 %ε	23.1 %ε	23.1 %ε

Figure 7. Fracture aspects of porous specimens under bending load.

## 4.2 Multi core-in-sheath porous structure by sequential injection moulding method

Figure 8 shows the structure of multi core-in-sheath porous metals produced by insert injection moulding. Open pore appeared in the outer cylindrical layer, and closed pores are visible in the middle layer. No defects are recognized in the interfacial region between each layer. Figure 9 shows the axial compressive stress – strain curves of homogeneous and multi core-in-sheath porous specimens. In case of homogeneous porous specimens, the specimens with 65vol.% PMMA particle deformed largely at low compressive stresses, and the yielding stress decreases drastically with increasing in fraction of PMMA particle. However multi core-in-sheath porous metals sustains at comparatively high compressive stress.

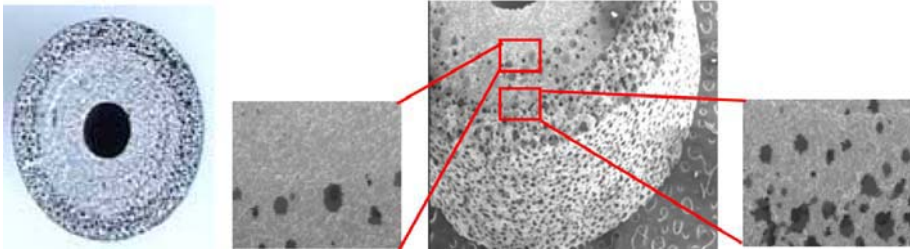


Figure 8. Structure of multi core-in-sheath porous metals.

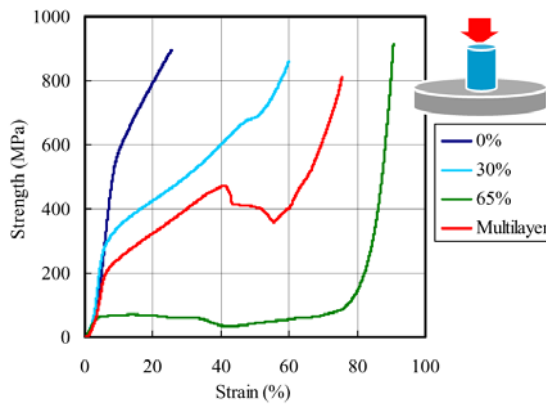


Figure 9. Compressive stress – strain curves of homogeneous and multilayered porous metals.

### 4.3 Steamed bread-like porous structure by co-injection moulding method

Figures 10(a) and (b) exhibit cross-section of the sandwich structure in longitudinal and lateral directions. The core material in dark colour is recognized in the centre of the specimens, and the skin material in light colour formed about 200-300 micrometer in thickness. When the fraction of PMMA particle is 30vol.%, the core material forms closed pores, while when the fraction of PMMA particle is 60vol.%, it forms open pores. From these photographs observed by SEM, it is clearly showed that the boundary region between core (porous) and skin (dense) materials of sintered specimens is free from any defects.

Figure 11 shows the results of bending test of the plain porous and sandwich porous specimens with various fractions of PMMA particles. The sintered specimens with sandwich porous structure showed higher bending strength than that with plain porous structure.

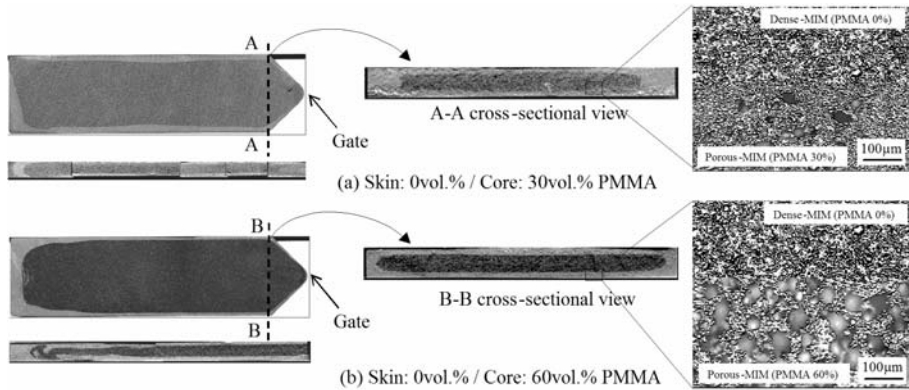


Figure 10. Cross-sectional views of sandwich structure in longitudinal and lateral directions.

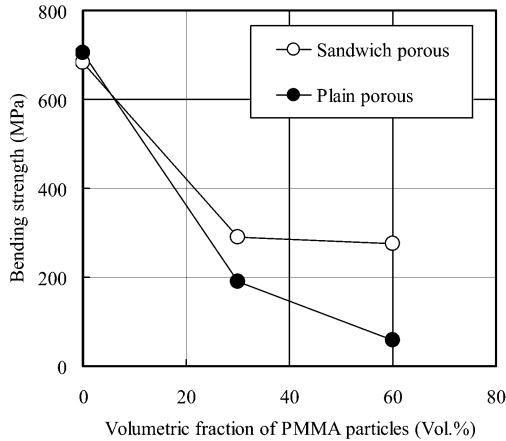


Figure 11. Bending strength plotted by function of PMMA particle.

## 5. CONCLUSION

The manufacturing methodology of micro porous metal components by applying a powder space holder method to metal injection moulding process was presented in this paper. From the experimental results, it was concluded that the micro sized metal porous materials could be fabricated with optimizing the fraction of spherical materials for spaces and the conditions of sintering process, and the porosity could be easily controllable and the micro sized pores were formed homogeneously. Furthermore to advance the manufacturing method proposed, the green compacts with graded content of

space holding particles were stacked by hot press moulding and co-sintering process was utilized to form micro porous graded structure. By comparing the mechanical properties of the materials with homogeneous porous specimens and porous graded structure, it was confirmed that desired functionally graded porous structures can be produced easily and porous graded structures were effective to enhancing the mechanical properties of porous metals. This method would be applicable to injection or extrusion mouldings; then net-shaped production of metal components with complex three-dimensional shapes could be achieved.

## REFERENCES

1. Gibson L.J. and Ashby M.F., *Cellular Solids-Structure & Properties*, Pergamon Press, 1988.
2. DFG Priority Programme 1075, *Metal Foam and Cellular Metals*, 1999.
3. Ashby M.F., Evans A., Fleck N.A., Gibson L.J., Hutchinson J.W. and Wadley H.N.G., *Metal Forms: A Design Guide*, Elsevier Science, 2000.
4. Haydn N.G. Wadley, *Cellular Metals Manufacturing*, *Advanced Engineering Materials*, 4, No.10, 2002.
5. German R.M., *Powder Metallurgy Science*, 2<sup>nd</sup> edition, Metal Powder Industries Federation (MPIF), 1984.
6. German R.M. and Bose A., *Injection Moulding of Metals and Ceramics*, Metal Powder Industries Federation (MPIF), 1997.
7. Tan L.K., "Characterization of Injection Moulded Aluminium (aluMIM<sup>TM</sup>)", *International Powder Injection Moulding Conference 2003 (PIM2003)* 2003.
8. Nishiyabu K., Matsuzaki S., Ishida M., Tanaka S. and Nagai H., "Development of Porous Aluminium by Metal Injection Moulding", *Proceedings of the 9th International Conference of Aluminium Alloy (ICAA-9)*, pp. 376-382, 2004.
9. Nishiyabu K., Matsuzaki S., Okubo K., Ishida M. and Tanaka S., "Porous Graded Materials by Stacked Metal Powder Hot-Press Moulding", *Materials Science Forum Vols.492-493*, pp. 765-770, 2005.
10. Matsuzaki S., Okubo K., Ishida M., Tanaka S. and Nishiyabu K., "Development of Porous Materials in Metal Injection Moulding", *International Conference on Powder Injection Moulding 2004 (PIM2004)*, 2004.

# SANDWICH INJECTION MOULDING AND PHYSICAL PROPERTIES OF CUP-STACKED CARBON NANOTUBE / POLYPROPYLENE AND POLYPROPYLENE

Kenji Okubo<sup>1</sup>, Shigeo Tanaka<sup>1</sup>, Naoyuki Oya<sup>2</sup>, Kazuaki Nishiyabu<sup>2</sup>, Takashi Yanagisawa<sup>3</sup> and Masanori Tomita<sup>3</sup>

<sup>1</sup>*Taisei-Kogyo Co., Ltd., 26-1 Ikeda-kita, Neyagawa 572-0073, Osaka, Japan*

<sup>2</sup>*Osaka Prefectural College of Technology, 26-12 Saiwai, Neyagawa 572-8572, Osaka, Japan*

<sup>3</sup>*GSI Creos Co., 2-3-1 Kudan-minami, Chiyoda-Ku, Tokyo 101-0052, Japan*

**Abstract** This study describes the manufacturing method and physical properties of sandwich structure tubes using cup-stacked carbon nanotube/polypropylene and polypropylene. The effectiveness of sandwich structure produced by sequential injection moulding to enhance the axial and transverse compressive properties of thermoplastics was investigated. It was shown that compressive properties of the sandwich tubes of positioning rich nanotube materials to the outer layer.

**Keywords:** carbon nanotube, polypropylene, sequential injection moulding, sandwich structure, compressive property.

## 1. INTRODUCTION

A carbon nanotube (CNT) has been gathering growing attentions as it is known to possess interesting and excellent physical properties based on its unique structure incorporating a honeycomb graphite lattice rolled into a cylinder. The size of a CNT is as small as nanometer size in the diameter and micrometer size in the length, which indicates that a CNT has a fibrous structure. Since the C=C bond in graphite is the strongest bond in nature, a CNT should have ultimate strength along the longitudinal axis whereas it should have flexible characteristics in the perpendicular axis. Further, a CNT

has excellent thermal properties such as restricted thermal expansion and electrical properties such as a unique electrical conductivity that depends on the variety of possible helical geometries known as chirality [1]. These theoretical findings in characteristics of a CNT have stimulated global interests to perform a variety of experimental developments of purified and continuous CNTs with desired helical geometries [2, 3].

The efforts have provided fair possibilities in the future to realize actual industrial applications of CNTs including innovatively small semiconductor devices and outstandingly strong structural materials. For the structural use, it will be a good step starting with compound mixtures consisted of CNTs and various matrices such as polymers. Particularly, in the case of blending CNTs and thermoplastic polymers, conventional industrial moulding techniques such as injection moulding can be applied for mass productions. Since a CNT has extremely small size compared with conventional carbon fibres, it is capable of making small structural components at micrometer size with improved physical properties and without considerable size-precision losses. Furthermore, it is presumed that flow behaviour of thermoplastic resin should not change so significantly when blended with CNTs, whereas it may be considerably affected by blending with conventional carbon fibres.

However, there are several technical and economic problems in the use of CNTs as reinforcements. Because CNTs have chemically inert graphite sidewalls, the adhesion between CNTs and matrices should be generally poor. Moreover, it is generally accepted that uniform dispersions of CNTs in matrices are challenging problems. In order to produce reliable structural components, it is important to modify the CNT sidewall structure and examine the blending and moulding procedures. Furthermore, CNTs are still expensive materials to be used for mass productions. Therefore, it is also important to find an effective macro-structure for CNT/polymer compounds to have improved physical properties with reduced amount of CNTs. One of such structures may be found in a sandwich structure, which has combinations of layers with various amounts of CNTs. By designing the layer stacking sequence carefully, it may be possible to produce large structural parts from CNT/polymer compounds with reduced costs. In this study, sandwich structure specimens were prepared from structurally modified CNTs and thermoplastic polypropylene by means of a sandwich injection moulding process, and their mechanical performances were experimentally investigated in order to obtain effective sandwich structures.

## 2. EXPERIMENTS

### 2.1 Materials used

It is thought that surface and sidewall structure of CNTs are crucial for physical performances of CNT compounds [4-6]. In this study, CNTs with ‘cup-stacked’ sidewall structure depicted in Figure 1 were used as reinforcements. The cup-stacked CNT (CSCNT) was grown from a metallic catalyst supplying hydrocarbon gas by means of a CVD technique. The CSCNT has graphite cups consecutively stacked forming hollows inside and relatively rough sidewalls, which should be effective to enhance interfacial adhesion compared with the ideal single-wall CNT. It should also have a fair amount of flexibility to form a curvature by allowing some amount of slipping between each graphite cup. This property is significantly important when the CSCNTs are filled in structural components with complicated shapes. Typical physical properties expected in the CSCNT were listed in Table 1.

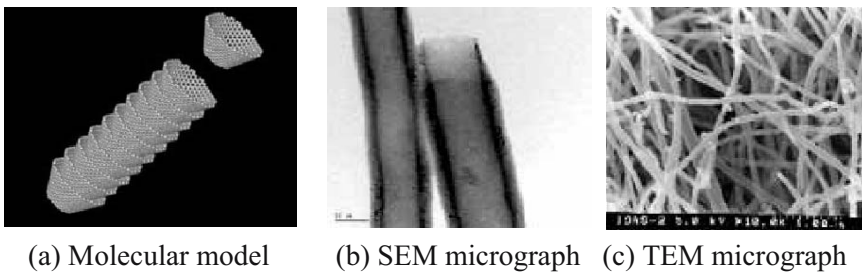


Figure 1. Structure of cup-stacked CNT.

Table 1. Physical properties of cup-stacked CNT.

Physical properties	Value
Fibre diameter	80 nm
Strain to failure	0.5 %
Tensile strength	7.0 GPa
Density	2.1 g/cm <sup>3</sup>
Electric resistance	55 $\mu\Omega$ cm

The CSCNTs and polypropylene (Novatec MA3, Japan Polychem Inc.) were pulverized and mixed in the melt state, and subsequently extruded and pelletized as CSCNT/PP compounds. The compound pellets with different CSCNT quantities (0wt%, 5wt% and 10wt%) were obtained. Table 2 shows thermal and mechanical properties of CSCNT/PP compounds obtained in the

previous study [7]. These results indicated that physical properties of the compounds were higher than polypropylene matrix, and improved with increasing the CSCNT quantities. In this study, several configurations of sandwich structures were prepared from these compounds as described later.

Table 2. Thermal and mechanical properties of CSCNT/PP compounds.

CSCNT quantity (wt%)	Coefficient of thermal expansion ( $1 \times 10^{-4}/K$ )	Elastic modulus (MPa)
0	2.34	1360
5	1.97	1495
10	1.71	1542

## 2.2 Preparation of sandwich tube specimens

A sandwich injection moulding technique was used to prepare thick tube specimens with CSCNT/PP compounds as depicted in Figure 2. The specimen consisted of three layers (inner, middle and outer) for which different quantities of CSCNT blended. These sandwich specimens were tested in compression tests as described later. Stacking sequences of each layer used in this study were listed in Table 3. The first configuration (0/5/10) had PP layer as the inner layer, and proportionally increased the CSCNT quantity to the outer layer. The second configuration (10/5/0) had proportionally decreased CSCNT quantities from the inner to the outer layers. The third and fourth configurations (10/0/10 and 5/0/5) had PP in the middle layer sandwiched between CSCNT/PP compounds. It is expected that the four configurations should exhibit different mechanical behaviour when tested in axial and transverse compression, since there should be considerable difference in strain in each layer.

Figure 3 illustrates the sequential injection moulding method used for producing the thick sandwich tube specimens. PP or CSCNT/PP compound was injected into the first cavity to mould the inner layer, and subsequently the middle and the outer layers were over-moulded after inserted the over-moulded parts in turn. The moulding conditions used in this study were listed in Table 4. One of the advantages of using CSCNT as reinforcements was that resin flow behaviour was not significantly affected as long as small amount of CSCNT was used. Figure 4 shows viscosity data preliminary determined for each CSCNT quantity at 473K. It was indicated that viscosities of CSCNT/PP were not higher than that of PP, which means that the same moulding condition can be used for each layers of the sandwich specimens. After moulding the sandwich specimens, product dimensions were inspected but no significant size variation was confirmed. This suggests that CSCNT had no influences regarding the resin flow procedure and size precisions of the final products.

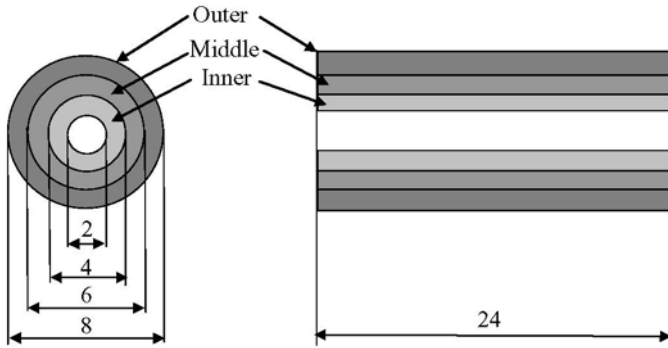


Figure 2. Scheme of thick tube specimen with sandwich structure.

Table 3. CSCNT quantities used for each layer in sandwich tube specimens.

Specimen ID	Inner •wt%•	Middle •wt%•	Outer •wt%•
0/5/10	0	5	10
10/5/ 0	10	5	0
5/0/5	5	0	5
10/0/10	10	0	10

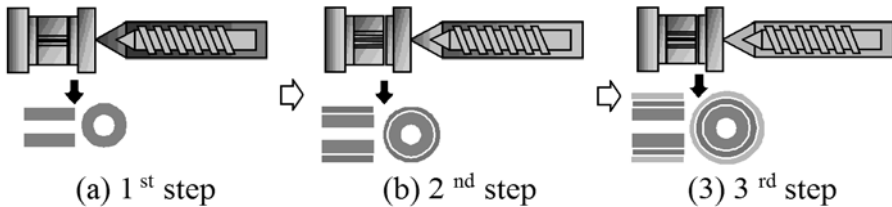


Figure 3. Sequential injection moulding method.

Table 4. Moulding conditions for sandwich tube specimens.

Moulding conditions	Values
Injection rate	50 mm/sec
Injection pressure	40 MPa
Holding pressure	40 MPa
Material temperature	473 K

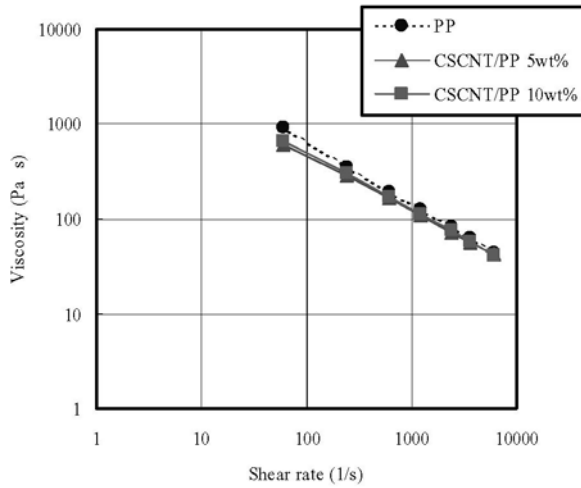


Figure 4. Resin viscosities determined at 473K.

### 2.3 Compression tests

Axial and transverse compression tests for sandwich tube specimens were carried out by means of a universal testing machine (AG-10TD, Shimadzu Co., Ltd. cross-head speed: 1mm/min) at room temperature as shown in Figure 5. Signals of load and displacement data were digitally collected via A/D converter (NR-2000, Keyence Co., Ltd.) with the sampling frequency of 5Hz.

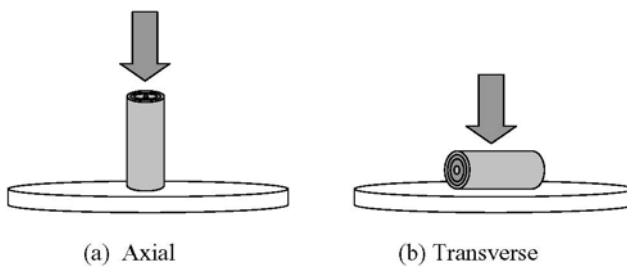


Figure 5. Overview of compression tests.

### 3. RESULTS AND DISCUSSIONS

#### 3.1 Axial compressive property

Stress vs. displacement curves obtained from the axial compression tests were shown in Figure 6. Due to the difference of stacking sequences and quantities of CSCNT, differences were confirmed in the slope of each curve and the yield stress. Figure 7 compares the yield stress obtained from each stacking sequence. It is evident that the specimen 0/5/10 indicated the highest value because this configuration had the stiff layer at the outside position where the radial strain due to the Poisson's effect should be significant. It is presumed that the outer stiff layer restricted the radial deformation and consequently improved the axial compressive properties of the whole sample. The specimen 10/5/0 actually indicated the lowest compressive property because the inner stiff layer did not effectively contribute to the suppression of radial strain.

It is also interesting to note that the specimen 0/5/10 showed even higher compressive property than that of the specimen 10/0/10, despite the total quantity of CSCNT was 5wt% smaller. On the other hand, the specimen 10/5/0 indicated lower property than the specimen 5/0/5 although the former had 5wt% rich CSCNT. These results suggest that axial compressive properties of sandwich tube can be improved with reduced amounts of CSCNT by proportionally positioning CSCNT rich materials to the outer layer.

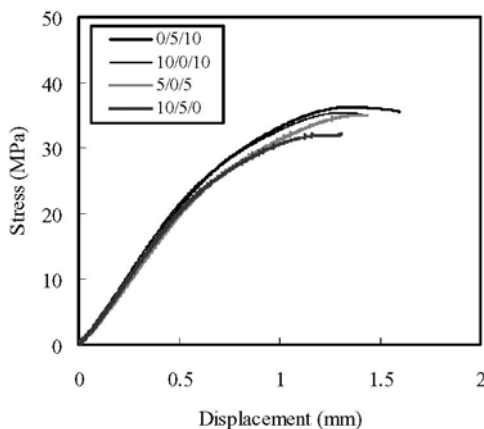


Figure 6. Stress vs. displacement curves obtained from axial compression tests.

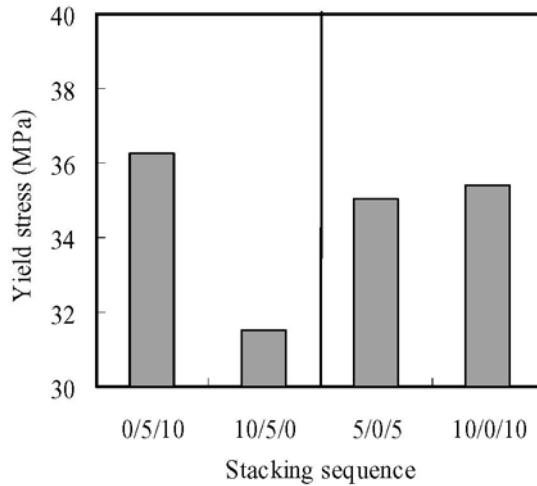


Figure 7. Yield stresses of sandwich tube specimens in axial compression.

### 3.2 Transverse compressive property

Stress vs. displacement curves obtained from the transverse compression tests were shown in Figure 8. Each specimen showed brittle failure that appeared in the decrease of compressive stress as indicated by the dotted circle. The initial failure occurred at relatively smaller deformation in the cases of the specimens 5/0/5 and 10/0/10, whereas the specimens 0/5/10 and 10/5/0 indicated relatively larger deformation before the initial failure. These results probably mean that inter-layer debonding tended to occur in the cases of the specimens with the middle PP layer inserted, since there should be significant discontinuous stress distributions between PP and CSCNT/PP layers.

Fracture aspects and their magnified views obtained by scanning electron microscopy were presented in Figure 9. Fractures were classified into brittle cracks in the rich CSCNT layers subjected to tension and inter-layer debonding between PP and CSCNT/PP layers. It is noted that only the specimen 0/5/10 indicated a brittle crack in the outer layer that contained 10wt% CSCNT, whereas all other specimens exhibited a crack in the inner layer because the inner layer was subjected to the most significant strain. It is deduced that the initiation of a tensile crack may be delayed by positioning a rich CSCNT layer outside in the case of the sandwich structure used.

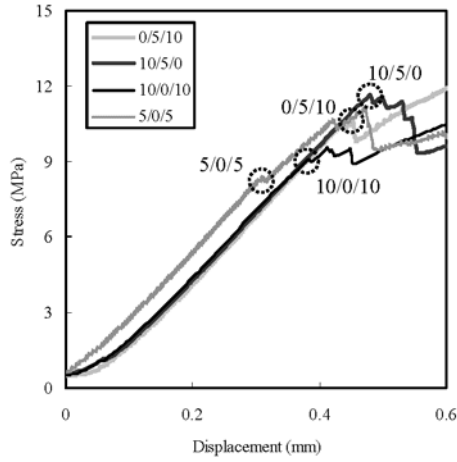


Figure 8. Stress vs. strain curves obtained from transverse compression tests.

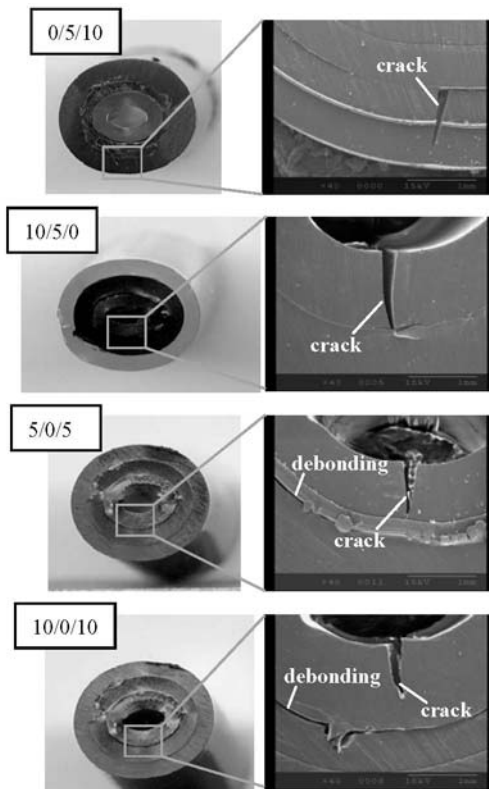


Figure 9. Fracture aspects of transversely compressed sandwich tube specimens.

## 4. CONCLUSIONS

Thick tube specimens were produced from CSCNT/PP compounds by means of a sequential injection moulding technique, and their mechanical properties were experimentally investigated by axial and transverse compression tests. It was shown that injection moulding could be applied for CSCNT/PP with the same moulding conditions as the normal PP matrix, because CSCNT had no considerable influence on resin flow behaviour as long as small amounts of CSCNT used.

Axial compressive properties of the sandwich tube specimens varied depending on the stacking sequences. It was shown that yield stress of the sandwich tube improved by proportionally positioning CSCNT rich materials to the outer layer, because the stiff outer layer effectively contributed to the suppression of radial strain.

It was also effective to proportionally position CSCNT rich materials to the outer layer in transverse compression, because it was capable of preventing inter-layer debonding between PP and CSCNT/PP layers and the initiation of brittle crack in the inner layer that was subjected to the most significant strain. It was revealed that thick sandwich structural parts can be produced with CSCNT/PP compounds, and their physical properties and material costs can be optimised by carefully designing the stacking sequences in the sandwich structure.

## REFERENCES

1. Saito, R., Dresselhaus, G. and Dresselhaus, M.S., "Physical properties of carbon nanotubes", London: Imperial College Press, 1998.
2. Ren, Z.F. et al., "Synthesis of large arrays of well-aligned carbon nanotubes on glass", *Science*, 282 (1998), 1105.
3. Zhu, H.W., Xu, C.L., Wu, D.H., Wei, B.Q., Vajtai, R. and Ajayan, P.M., "Direct synthesis of long single-walled carbon nanotube strands", *Science*, 296 (2002), 884.
4. Schadler, L.S., Giannaris, S.C. and Ajayan, P.M., "Load transfer in carbon nanotube epoxy composites", *Applied Physics Letters*, 73/26 (1998), 3842.
5. Xu, X., Thwe, M., Shearwood, C. and Liao, K., "Mechanical properties and interfacial characteristics of carbon-nanotube-reinforced epoxy thin films", *Applied Physics Letters*, 81/15 (2002), 2833.
6. Barber, A.H., Cohen, S.R. and Wagner, H.D., "Measurement of carbon nanotube-polymer interfacial strength", *Applied Physics Letters*, 82/23 (2003), 4140.
7. Oya, N., Nishiyabu, K., Yanagisawa, T., Higaki, S. and Tanaka, S., "Physical Properties of Carbon Nanotube/Polypropylene Compounds", *Proceeding of the 11th European Conference on Composite Materials (ECCM-11)*, May 31-June 3, Rhodes, Greece, 2004 (CD-ROM).

# NEW ROHACELL® DEVELOPMENT FOR RESIN INFUSION PROCESSES

Jonas Scherble and Thorsten Jahn

*Röhm GmbH&Co KG, Kirschenallee, D-64293 Darmstadt, Germany*

**Abstract** Two new types of ROHACELL® foam specially designed for resin infusion processes are now commercially available. In comparison to the heat resistant ROHACELL® type the new foams have smaller cell sizes leading to significantly lower surface resin uptakes of the sandwich core in resin infusion processes. The mechanical properties of the new foams are excellent and even better than those of the common heat resistant type.

**Key words:** resin transfer molding, foam core, PMI-foam, peel strength.

## 1. INTRODUCTION

Resin transfer molding (RTM) offers the opportunity for significant cost savings in the fabrication of composite structures. However, the implementation of different core materials and the manufacturing of sandwich constructions have been restricted by some process problems such as creep due to high pressure and high temperature in the curing process, resin consumption of the core, etc. Due to their open material structure honeycomb core materials can only be used after complicated modifications.

Customers who are using the RTM process demand a core material to combine the already known strong mechanical properties of ROHACELL® with a low resin absorption of the core material itself. Due to processing even 100% closed-cell foam cores have open cells on their surfaces, which are penetrated by resin under RTM conditions yielding an undesirable increase in the total weight of the sandwich part.

In this paper, two new types of ROHACELL<sup>®</sup> are introduced which were specially designed for RTM processes.

## **2. RESIN-TRANSFER-MOLDING**

Currently, there is a wide range of different RTM processes, e.g. Vacuum Assisted RTM (VA-RTM), Differential Pressure RTM (DP-RTM), Structural Reaction Injection Molding (SRIM), Single Line Injection (SLI), Vacuum Assisted Resin Infusion (VARI), Quickstep<sup>®</sup>, SCRIMP<sup>®</sup>, etc. All these processes have in common that a pressure gradient is used to impregnate a composite preform by low viscous resin. Depending on the respective process, pressure may be applied on the resin reservoir, the composite preform may be evacuated prior to injection, the viscosity of the resin may be lowered by rising its temperature, etc. The preform may be kept in shape by a matched die mold or in a vacuum bag.

In RTM, low-viscous resins are preferred for different reasons:

- the resin shall thoroughly flow through the mold
- for high-viscous resins high injection pressures are needed, increasing the cost of tools and demanding resistant core materials
- complete impregnation of fibers

As a matter of course the resin will not only fill the gaps between fibers, but also all the voids in the sandwich preform. For this reason honeycomb core materials with their open material structure can only be used in RTM after complicated modifications. Foams, on the other hand, should have a high fraction of closed cells as possible, making ROHACELL<sup>®</sup> with its 100% closed-cell structure the foam of choice for RTM.

Due to machining all foam cores have open cells on their surfaces, which are penetrated by resin under RTM conditions yielding an undesirable increase in the total weight of the sandwich part (Figure 1).

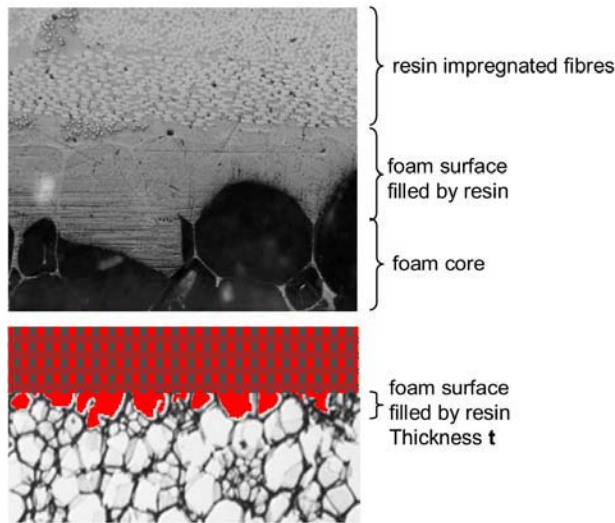


Figure 1. Cross section of sandwich.

In the following chapters, a method to estimate the surface resin uptake by means of an oil uptake is introduced and suggestions for lowering the surface resin uptake are discussed. The development of two new types of ROHACELL<sup>®</sup> designed for RTM is described. Finally, the strength of the skin to core bonding is discussed.

### 3. SURFACE RESIN UPTAKE

The surface resin uptake of a core material, i.e. the amount of resin which is absorbed by the core surface during sandwich processing, may have a strong impact on the total weight of a sandwich construction. Considering a sandwich with thin fiber reinforced surfaces and a 20 mm 50 kg/m<sup>3</sup> core the weight calculates as follows:

Table 1. Estimation of contributions to sandwich weight.

	g/m <sup>2</sup>	%
sandwich surface (fibers and resin)	2*500	36
resin absorbed by core surface	2*400	<b>28</b>
Core 20 mm, 50 kg/m <sup>3</sup>	1000	36
Totals	2800	100

### 3.1 Estimation of surface resin uptake

The surface resin uptake of a foam core is caused by opened cells on its surface. The extent, to which these cells are filled by resin, depends on many parameters like viscosity of resin, pressure difference applied during processing, capability of resin to wet the core material (surface energy), resin additives and the way the core was machined, e.g. by sanding or machining. Therefore, it is not possible to give a general value for the surface resin uptake of a certain material. For any sandwich, the exact value has to be determined under the respective processing conditions.

In order to compare core materials, the surface porosities can be determined by measuring the surface oil absorption capability by putting a sample of known volume into a cavity, evacuating and filling the cavity with vegetable oil. Vegetable oil is used because its viscosity is comparable to that of RTM-resins under processing conditions. Balancing allows for the determination of the oil amount absorbed to the sample surface. The following figure gives an overview of the oil volumes absorbed by some foam core materials:

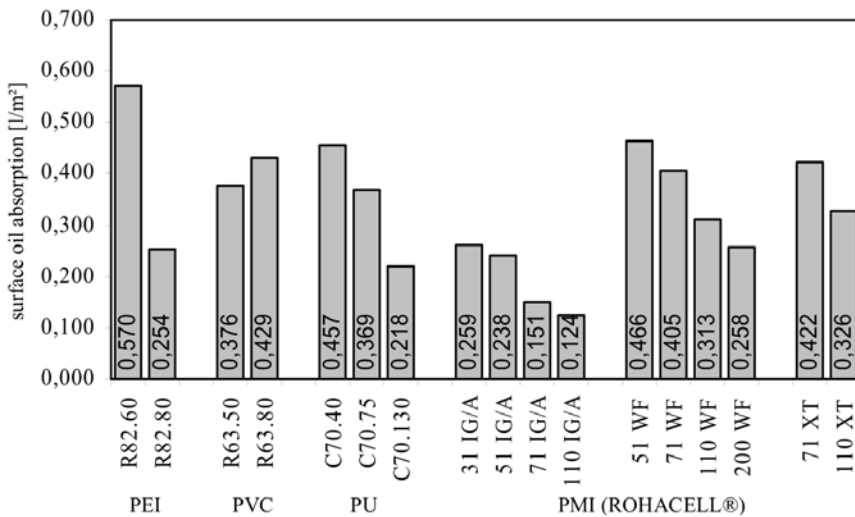


Figure 2. Oil absorption on surface of selected foams.

The oil absorptions of all materials are in the range of some 100 ml/m<sup>2</sup>. The surface oil absorption depends on the density and on the type of material. The influence of the density arises from the fact that the mean cell diameters increase with decreasing foam density due to the increasing degree

of foaming. The larger cells result in larger voids on the foam surface after machining.

### 3.2 Lowering the surface resin uptake

From the discussion above it appears that the reason for the surface resin uptake of the foam cores are the open cells on the core surface. This raises the question how the resin uptake may be lowered in order to save weight. One might think of several possibilities, which are discussed below:

1. Increase Resin viscosity by changing processing conditions, additives, etc.: inappropriate to RTM, because complete filling of the mold and complete impregnation of the fiber preform is required.
2. Closing the surface e.g. by spackling or by films will lower the amount of resin absorbed, but means a weight gain itself and includes additional processing steps.
3. Thermal flattening of surface: It is possible to close the open cells on the surface by thermal treatment under slight pressure. The foam surface will look like the following:

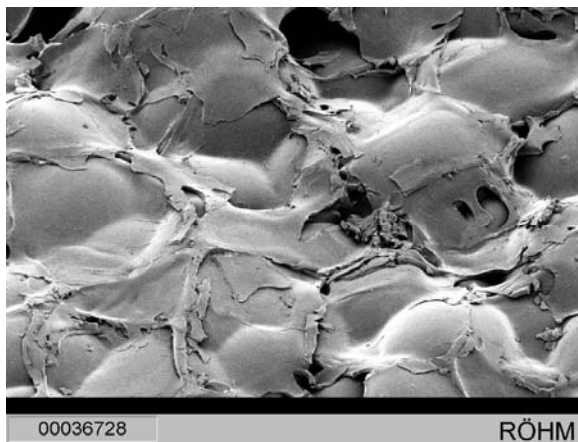


Figure 3. Foam surface after thermal flattening.

Although it is possible to close most of the voids in the surface in this way, the thermal treatment means additional processing steps with the need for specially designed molds. The molds restrict the method to simple shapes and there is some weight gain of the core since it must be reduced from some oversize to its final shape.

4. Reduce the cell diameter of the foam. In Figure 1, the thickness of the layer of cells filled by the resin is designated as  $t$ . It can be assumed that

surface resin uptake  $\sim t \sim$  cell diameter

So the reduction of the cell diameters should lower the surface resin uptake while the processing of the sandwich does not need to be changed. In the following chapter, two new ROHACELL<sup>®</sup> types with lower cell diameters will be introduced which are specially designed for RTM.

#### 4. FOAM CORES FOR RTM

In the construction of a sandwich with an excellent strength to weight ratio many parameters need to be optimized. For example, a high fiber volume content of the surface is needed as well as voids and porosity must be avoided. To achieve this, many RTM-processes use pressures of up to 0.7 MPa at elevated temperatures to assure a good flow of the resin. High performance resins, e.g. Hexcel's RTM-6 need to be cured at temperatures in the range of 180°C. Besides other properties, the foam core material must be sufficiently resistant to compressive creep.

ROHACELL<sup>®</sup> WF-HT does not show significant creep at conditions of up to 0.5 MPa and 180°C at a density of 75 kg/m<sup>3</sup>. The material exhibits moderate oil absorption of 0.40 l/m<sup>2</sup>, which might not be acceptable in certain weight critical applications. For this reason we developed a method to tailor the mean cell diameter of ROHACELL<sup>®</sup> in order to lower the surface oil absorption while keeping up the excellent thermo mechanical properties of ROHACELL<sup>®</sup> WF:

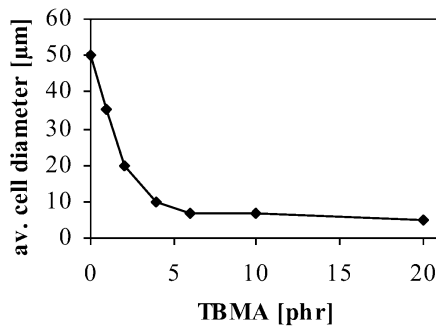


Figure 4. Tailoring the mean cell diameter of ROHACELL<sup>®</sup>.

Two new types of ROHACELL<sup>®</sup> have been made available:

- RIST = Resin Infusion Structural. This foam has a medium cell size with reduced resin uptake while keeping up a good bonding to the surface.
- RIMA = Resin Infusion Manufacturing Aid. This foam offers a negligible surface resin uptake whereas a weaker bonding between the core and the surface as revealed by the climbing drum peel test has to be taken into account.

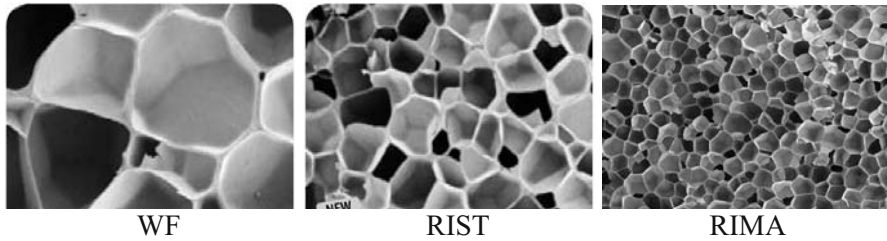


Figure 5. SEM micrographs of different ROHACELL<sup>®</sup> foams.

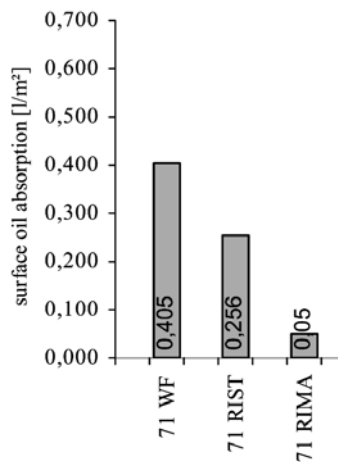


Figure 6. Surface oil absorption of ROHACELL<sup>®</sup> types.

Figures 5 and 6 show that the finer cell structure of ROHACELL<sup>®</sup> RIST and RIMA indeed results in a dramatic lowering of the surface oil absorption. Due to its fine cell structure, the mechanical properties of ROHACELL<sup>®</sup> RIMA are even better than those of WF (Table 2).

Table 2. Mechanical properties of selected ROHACELL<sup>®</sup> foams.

ROHACELL <sup>®</sup>		51 WF	51 RIMA	71 WF	71 RIST	71 RIMA	110 WF	110 RIMA
density	[kg/m <sup>3</sup> ]	52	42	75	75	65	110	93
compressive strength	[MPa]	0,8	0,79	1,7	1,75	1,67	3,6	
tensile strength	[MPa]	1,6	1,65	2,2		2,58	3,7	3,97
Young's modulus	[MPa]	75	59	105		90	180	139
strain @ break	[%]	3	9,8	3		10,5	3	8,4
heat dist. temp.	[°C]	205	220	200		225	200	

## 5. SURFACE BONDING

It has already been mentioned that the low surface resin uptake of the fine-celled foams results in a lower surface bonding in terms of the climbing drum peel test (ASTM D1781). In this test, the sandwich skin is clamped to a rotating drum exerting a moment of torque on the skin to core bonding. The torque necessary to rotate the drum is called the peel force. The following table gives peel forces for sandwiches based on different ROHACELL<sup>®</sup> types:

Table 3. Peel forces of sandwiches based on different ROHACELL<sup>®</sup> cores.

ROHACELL <sup>®</sup>		71 WF	71 RIST*	71 RIMA
density	[kg/m <sup>3</sup> ]	70	76	72
peel strength	[Nmm/mm]	35,7	28,8	3,5
failure		foam	foam	foam
surface resin uptake	[g/m <sup>2</sup> ]	550	280	<50

\*foam showed some creep compression

As expected, the surface resin uptake went down with smaller cell sizes. However, in the same manner the peel strength reached very small values for the RIMA-foam. Remarkably, for all sandwiches tested, it was the foam material itself which failed in the test, i.e. there was always a thin foam layer remaining on the peeled off skins. So there was no failure of the bonding between the foam and the resin, but it was the foam which broke in a layer close to the skin. The reason for this behavior is found, when one takes a closer look on the climbing drum peel test. In the test, the peel forces concentrate in a very small area resulting in high mechanical stresses on the foam in the surrounding of the peel front. The following picture illustrates this.

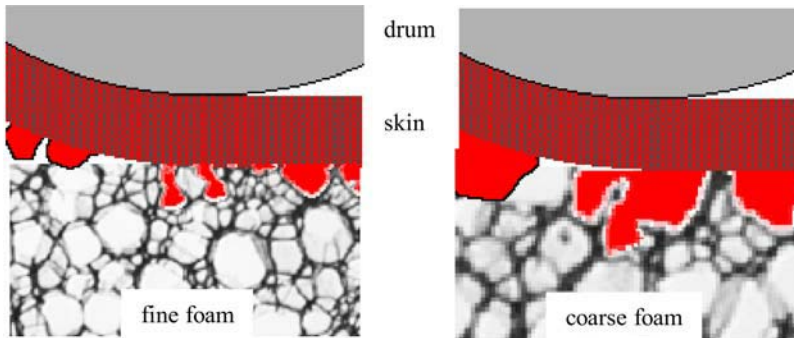


Figure 7. Peeling of a fine and a coarse foam in comparison.

When the peel forces concentrate in an area close to the peel front, the resin filled voids will disperse these forces to a larger area. For a fine celled foam the voids are small dispersing forces only to a small area. The resulting stress will easily exceed the strength of the foam and the skin is peeled off. In contrast the larger resin filled voids of a coarse celled foam disperse forces to a larger area lowering the stresses.

In the climbing drum peel test the concentration of the peel forces in the peel front is very extreme. The other extreme is the complete dispersion of the peel forces over the whole sandwich surface, as it is done in the flat wise tensile test. Here, the sandwich surfaces are adhesively bonded to loading blocks. It is interesting to see that the sandwich fails by a crack in the core under these conditions, with tensile strengths which are typical for the foam core.

Since both tests do not resemble conditions found in the normal application of sandwiches, it should be discussed if there are more appropriate tests to determine the strength of a sandwich as well as of a damaged sandwich. One suggestion is a 4-point bending test of a sandwich beam, where some of the skin is artificially detached.

# DEVELOPMENT AND VALIDATION OF A CONTINUOUS PRODUCTION CONCEPT FOR THERMOPLASTIC HONEYCOMB

J. Philipp Bratfisch<sup>1</sup>, Dirk Vandepitte<sup>1</sup>, Jochen Pflug<sup>2</sup> and Ignaas Verpoest<sup>2</sup>

<sup>1</sup>*Department of Mechanical Engineering, Division Production Engineering, Machine Design and Automation (PMA);* <sup>2</sup>*Department of Metallurgy and Materials Engineering (MTM), Katholieke Universiteit Leuven, Kasteelpark Arenberg 41, B-3001 Leuven, Belgium*

**Abstract** The continuous production of thermoplastic honeycomb cores is a recent development at K.U.Leuven. The production equipment has been improved to deliver high quality material. This equipment is used for the determination of optimum process parameters. This paper describes the production equipment, its development and the experiments that have been done.

**Keywords:** honeycomb, thermoforming, fusion bonding, robust experimental design.

## 1. INTRODUCTION

Since more than four years, the folded honeycomb material “ThermHex” is developed at the K.U. Leuven. ThermHex is a thermoplastic sandwich core material that is produced from a single and endless sheet. The sheet material, thermoplastic film, is processed in 3 successive steps to honeycomb core, as shown in Figure 1. The “ThermHex” concept has been patented [1]; its production process is subject to research at the laboratory for lightweight structures. There, the production steps were defined and tested, with the goal to develop a continuous production process, feasible for production at industrial scale. In 2004, the full implementation in functional machinery has been achieved. The operational production units are since then available for experimentation. In the first part of this article, the design of solutions for each production step is described, mentioning alternative design possibilities. In the second part, the realized units are, after their

implementation, experimentally validated. The constraints of production are mentioned for the third and final production step.

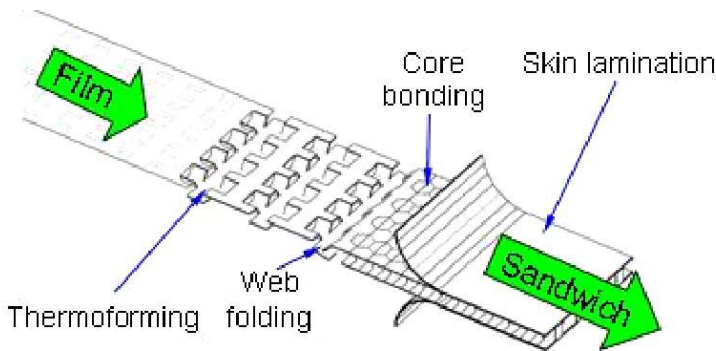


Figure 1. ThermHex production concept.

The objective of this development is the design of the “ThermHex” production process. Both machine design and the way of operation are analyzed, to finally predict the constraints of the industrial production, with an envisaged speed of up to 10 m/min.

The production at continuous speed helps to reduce production costs. Consequently, this honeycomb sandwich material becomes economically feasible in markets where high production costs up to now prevent the broad use of similar materials [2].

## 2. CONCEPT REALISATION

For the three production steps, the machine concepts and designs are defined. The facilities are developed and realized in the laboratory for lightweight structures. The scale of the lab units is kept limited to a width of 400 mm. The core is produced from a single thermoplastic sheet by three successive in-line operations, which are shown in Figure 1:

1. Thermoforming thermoplastic film to a web with regular pattern;
  2. Folding the half-hexagonal web into a honeycomb;
  3. Relaxation and bonding of the honeycomb core;
- Lamination of skins is an additional step to produce a sandwich.

### 2.1 Thermoforming

Thermoforming is the first production step. Input material is plain thermoplastic film. From the different concepts for thermoforming only those which can reach line speeds of 40 m/min or more are considered. The

input material is chosen for 15 to 20 % talc filled PP films with a thickness of about 0,2 mm. The ThermHex thermoforming pattern is repetitive, with a pitch of 28,8 mm for the chosen geometry. Rotary tools provide highest speed of operation. The maximal line speed of modern platen thermoforming machines comes however close to the envisaged speed. The necessity of indexing between the succeeding strokes makes them unattractive for ThermHex, given the high demands concerning accuracy for the further processing [3].

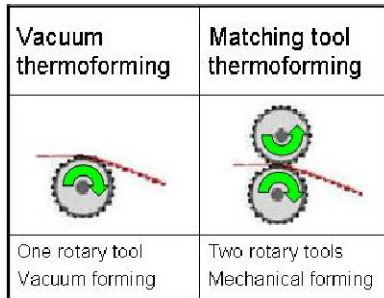


*Figure 2.* Rotary thermoforming concepts.

Figure 2 shows the two simplest alternatives of the tool arrangement: Either vacuum thermoforming, with one rotary tool plus vacuum as forming medium or deep drawing with matching tools as forming medium.



*Figure 3.* Laboratory vacuum thermoforming unit.

For the lab thermoforming unit vacuum thermoforming is selected. This design can be realized at lower costs, because only one tool roller is needed. This process is limited to airtight sheets, as are the PP-talc-film mentioned before.

The concept is realized as lab unit in 400 mm forming width, shown in Figure 3. The shown unit is object of a parametrical study, performed to assess the influence of the processing parameters.

## 2.2 Web folding

This step is the most original of the ThermHex concept. It is found that the thermoformed web folds best when compressed in length direction. After preliminary tests and studies, the matrix in Figure 4 is drawn, from which two concepts were realized in small scale. All mentioned concepts rely on the known method of web compression, during which the web folds up by itself, withheld by a stationary channel from moving out of the plane [4]. The web compression is maintained until bonding, the following production step.

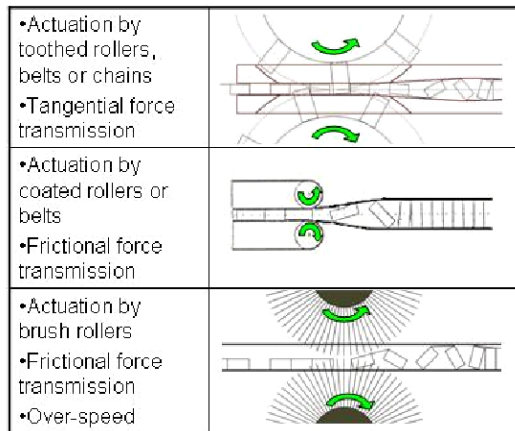
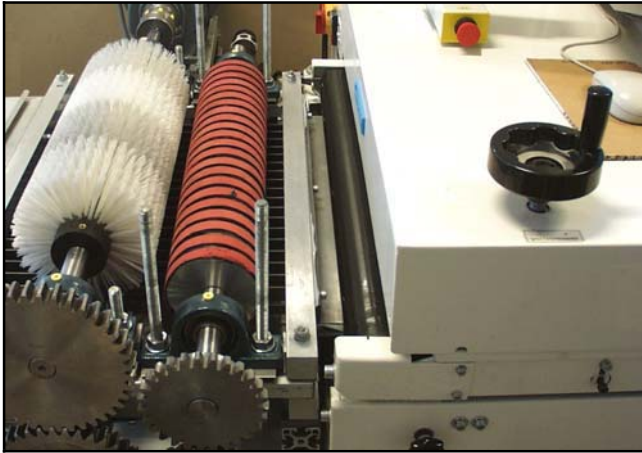


Figure 4. Web folding concepts.

Finally, the third concept with web actuation by brush rollers is realized, turning at over-speed. The unit was built, tested and optimized. Figure 5 shows the recent version, together with the double belt used for core bonding.

The web folding process depends on those process parameters that have influence on the compression inside the channel. The double belt unit, used in the following production step, is by its speed determining the constraints of the folding process. For the web folding, all settings for the brush rollers and the compression rollers depend on the speed setting of the double belt.



*Figure 5.* Web folding and core bonding unit at PMA lab.

### 2.3 Core bonding

For the bonding of the folded web, a double belt press is directly connected to the web folding unit. Besides the double belt, no design alternatives exist in this case. Figure 6 shows a sketch of the type of double belt unit acquired for the test laboratory.

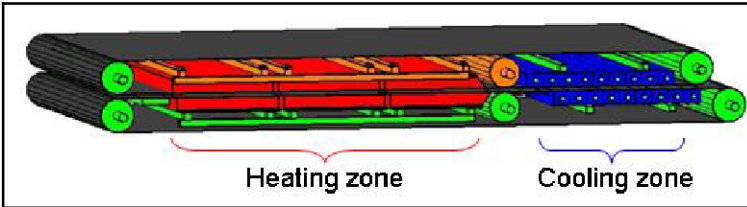


*Figure 6.* Double belt drawing.

The folded and compressed web enters the unit from the left side; it gets a heat treatment and is cooled directly thereafter, with a thickness calibration between heating and cooling. Inside the heating zone, the outer layers of the web, the skin elements, are melted. After the welding, cooling is necessary to restrict the heat input in the core and to get flat surfaces. The type of bonding is referred to as fusion bonding [5].

Double belt laminators are industrial standard equipment [6]; the front end of the one at the laboratory is shown in Figure 5, together with the web folding unit.

The processing variables in this step influence the quality of the core for a great part. The study on the core bonding processing in the laboratory is documented in the following chapter.

### 3. EXPERIMENTAL STUDY

#### 3.1 Experiments design

In this chapter, the experimental study is described, which is based on the method of robust experiment design [7]. Objective of the study is mainly the determination of the influence of each processing parameter on the process. For each production step, an experimental plan is set up:

Firstly, measurable and exhaustive quality parameters are defined that describe the quality of the product with sufficient accuracy.

Secondly, all process parameters are categorized; those parameters that are variable and should be optimized are distinguished from those that are either fixed or not to optimize. With the first category, an orthogonal matrix is formed; those of the latter are kept constant.

Table 1 shows the different types of parameters that have to be distinguished. Two examples of each are shown for the core bonding experiment.

Table 1. Parameter table with examples for Core Bonding.

Process parameters			Quality parameters (effect)
Set parameters (signals)	Varied parameters (study)	Other parameters (noise)	
▪ Cooling water flux	▪ Heating elements temperature	▪ effective Calibration pressure	▪ Core thickness
▪ Heating zone length	▪ Belt speed	▪ effective cooling zone temperature	▪ Core strength

After execution of the experiments, the measured parameters are taken to assess each processing parameters influence on the chosen quality parameters. The dependencies and the optimal settings can be determined.

This DOE approach is common for similar studies [8, 9]. The objective of the experiments lies on the finding of the parameter effects; knowledge that can be used in the later industrial practice.

### 3.2 Core bonding experiments

The described approach is used for all three production steps; this article, however, treats exclusively the study of the core bonding process, after which the ThermHex core production is finished.

#### 3.2.1 Parameter selection and testing

The quality parameters representing the final sandwich core quality are chosen with regard to the purpose of the sandwich core resulting from the process and with regard to the best possible assessment of the fusion bonding process. The latter is important to directly measure the effect of each processing parameter. Four parameters are chosen for:

- Geometrical parameters: Thickness (variations), Flatness
- Mechanical parameters: Bond strength, Transversal stiffness

*Table 2. Orthogonal test array for Core Bonding.*

Run	Levels				Parameter settings			
	A	B	C	D	Temperature [°C]	Belt Speed [m/min]	Calibration [mm]	Belt Distance [mm]
1	1	1	1	1	U: 170 / L: 180	2,5	0	7,4
2	1	2	2	2	U: 170 / L: 180	4	0,5	7,7
3	1	3	3	3	U: 170 / L: 180	5,5	1	8
4	2	1	2	3	U: 185 / L: 195	2,5	0,5	8
5	2	2	3	1	U: 185 / L: 195	4	1	7,4
6	2	3	1	2	U: 185 / L: 195	5,5	0	7,7
7	3	1	3	2	U: 200 / L: 210	2,5	1	7,7
8	3	2	1	3	U: 200 / L: 215	4	0	8
9	3	3	2	1	U: 200 / L: 210	5,5	0,5	7,4

In the experiment, processing parameters are varied in order to estimate the effect of each of them on the quality parameters. Table 2 represents the test plan, with the shape of an orthogonal array:

Four parameters (**A** = heater Temperature, **B** = Belt speed, **C** = opening of the Calibration rollers, **D** = opening or vertical distance of upper and lower belt) are varied at 3 levels (**1** = low, **2** = middle, **3** = high). 9 experimental runs are performed with the given parameter combinations. The L<sub>9</sub> array plan is standardized for this experiment [7]. In the table, the

temperature settings inside the upper and lower belt are different, in order to reach identical belt surface temperatures.

It is not considered that the chosen processing parameters interact with each other. This is, because the quality parameters are chosen accordingly. For example, the mechanical parameters transversal strength depends for the greatest part on the quality of the weld line between cell walls and skin elements, which is a matter of heat input. Therewith, belt speed and heating temperature do not interact, as each one has linear influence on the heat input. The same is for the belt and calibration opening.

After performance of the 9 runs, the geometrical and mechanical quality parameters are measured. Each measurement is taken at least 5 times from randomly chosen locations over length and width of the sample. The geometrical parameters are measured using distance gauges (micrometers). For the mechanical parameters an Instron 1193 test machine is used; the force is recorded over displacement.

### 3.2.2 Parameter effects

The effects of each processing parameter on each quality parameter are determined assuming the “minimal-the-better” formulas for thickness variation and for waviness; for the transversal stiffness and strength, the “maximal-the-better” case is applied.

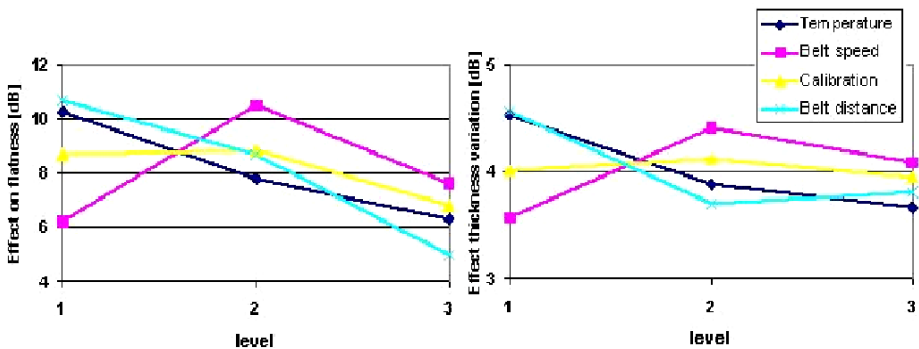


Figure 7. Geometrical effects, core bonding experiment.

Figures 7 and 8 show the process parameter effects over the according level (taken from Table 2). The effects are given in dB as a common unit.

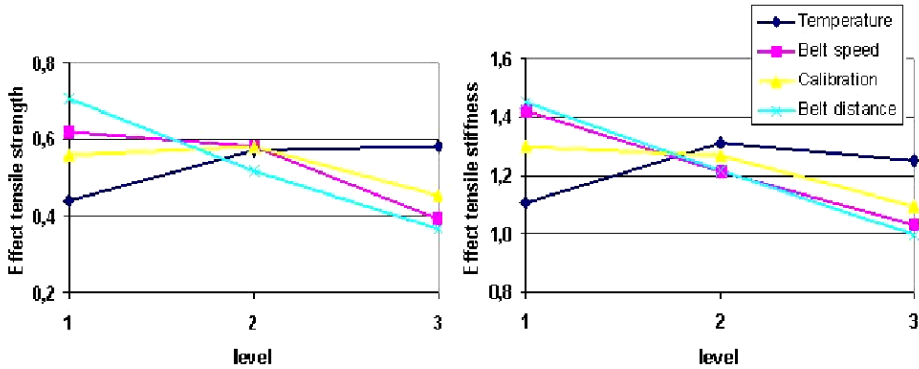


Figure 8. Mechanical effects, core bonding experiment.

### 3.2.3 Discussion

The major result of the experiments is the effect of the processing parameters on the core quality.

- **Temperature:** The heating element temperatures effect on geometrical and mechanical quality is contrary as the effect of heat on both is different: while increasing heat facilitates core deformation, it improves the formation of good bond lines.
- **Belt speed:** Belt speed has a linear influence on the transferred heat. Lower belt speed results in less heat input. As the cooling elements temperature remains constant, lower belt speed means less cooling. Especially samples processed at lower speed and at higher temperature show thermal induced deformations, which mainly determine the geometrical properties.
- **Calibration:** The effect of the calibration roller position on the measured parameters is the least significant of all processing parameters. This parameter does not need optimization.
- **Belt distance:** This parameter has the greatest effect on the measured quality variables. It can be clearly seen that a closer opening of the belts is advantageous for the process. This parameter has influence as well on the heat transfer as directly on the core thickness.

This list of parameter effects can be taken for the definition of production parameters on any other production unit for ThermHex. For the used unit, the optimal parameter combinations can be detected from Figures 7 and 8:

Temperature: Level 1; Belt speed: Level 2; Calibration: Level 1 or 2; Belt distance: Level 1.

## 4. CONCLUSION

ThermHex is considered to become a competitive core material, for example in the automotive sector, because of its continuous and fast production process.

In this work, the definition and design of production machinery was presented, based on the ThermHex concept. The first in continuous mode functional laboratory scale units serve for experimental studies, of which one was presented and discussed.

Having proven the feasibility of the set-up and having determined optimal processing parameters, the experimental results can be taken to define an industrial production process. Further research is in progress, focusing on sandwich materials with ThermHex core of the described quality being laminated with different skins. The core production presented in this article is envisaged to be implemented in a sandwich production line comprising, next to the here described machinery, lamination equipment.

## REFERENCES

1. Pflug, J. and Verpoest, I. "Thermoplastic folded honeycomb and method for the production thereof", International Patent Application, WO 0032382, 2000.
2. Asselin, C. "Lightweight structures concern all sectors", Composites International, Vol. 48, pp. 58-68, 2001.
3. Throne, J. and Beine, J. "Thermoformen", Hanser, ISBN 3-446-21020-2, 1999.
4. Bänisch, U. and Richter, V. "Verfahren und Vorrichtung zur Herstellung von gefalteten Flächenbahnen", German Patent Application, DE 19603076, 1997.
5. Ageorges, C. and Ye, L., "Fusion Bonding of Polymer Composites", Springer, ISBN 1852334290, 2002.
6. Meyer, "Machine Systems worldwide for the automotive industry", MEYER Maschinenfabrik GmbH Presentation Map, Germany (no date).
7. Phadke, M.S., "Quality Engineering using robust design", Gesellschaft für Managementtechniken und Technologietraining, 1989, ISBN 3-90615156-16-8.
8. Harper, P.R., "Thermoplastic die attach for hermetic packaging", International Journal of Microelectronics and Electronic Packaging, Vol. 17/4, 1994.
9. Gryspeert, C. and Haesendonck, S., "Kwaliteitscontrole van gewikkelde composiet-constructies met Taguchi-analyse", Master Thesis 95EP01, K.U.Leuven / PMA, 1995.

# SANDWICH PANEL WITH A PERIODICAL AND GRADED CORE

*Manufactured Using Rapid Prototyping*

Jens Nygaard<sup>1</sup>, Anders Lyckegaard<sup>1</sup> and Jesper Christiansen<sup>2</sup>

<sup>a</sup>*Institute of Mechanical Engineering, Aalborg University, Pontoppidanstræde 105, DK-9220 Aalborg, Denmark*

<sup>b</sup>*Institute of Production, Aalborg University, Fibigerstræde 16, DK-9220 Aalborg, Denmark*

**Abstract** This paper presents a technique for the production of graded sandwich cores. A significant failure mode of sandwich panels is the indentation of the foam core in regions at which local forces are introduced into the sandwich panel. The aim of this work is to synthesise a microstructure that can diminish this failure mode. By applying a rapid prototyping technique a periodic, open beam structure has been synthesised. Additionally the structure has been graded in the longitudinal direction by alternating over the beam diameter. The obtained structure was joined with aluminium face sheets to form a sandwich beam. The panel was subjected to a three point bending test and the results were compared to a finite element model.

**Keywords:** sandwich panels, periodic structure, graded material, rapid prototyping.

## 1. INTRODUCTION

Sandwich structures are typically a three layered structure comprised of two thin, stiff and strong face sheets separated by a thick, compliant and lightweight core material. This construction has gained widespread acceptance as an excellent way to obtain extremely lightweight components and structures with very high bending stiffness, high strength and high buckling resistance, see e.g. Zenkert [1]. Sandwich structures are often used in light weight applications such as aircraft, marine applications and wind turbine blades.

Introducing concentrated loads into the sandwich structure should be done with much care, because sandwich structures are generally prone to core indentation and local bending of the face sheets due to the low transverse stiffness of the core materials and the low bending stiffness of the face sheets. The preferred design solution is to introduce stiff core inserts made from wood, metal or dense polymeric foam under the concentrated load, see Figure 1.

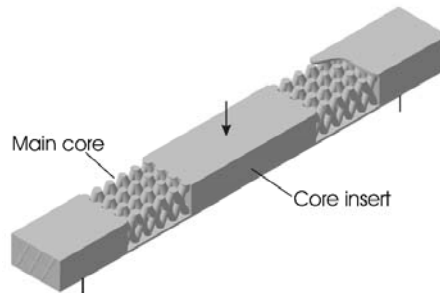


Figure 1. Sandwich panels are often fitted with core inserts to support concentrated loads.

This design introduces new difficulties near the junction between the core insert and the main core, where stress concentrations in the core and local bending of the face sheets will occur due to the different elastic properties of the two core materials. This was analysed theoretically by Skvortsov and Thomsen [2].

To remedy this weakness a structurally graded core material is suggested. Structurally graded core materials have been suggested by other researchers, but in the form of through the thickness variation of stiffness, see e.g. Apetre and Sankar [3]. Here we suggest a core, which is graded length-wise such that the highest stiffness is located under the concentrated load, and the core gradually reduces stiffness towards region with free boundaries, see Figure 2. The desired properties for the core material include an increased transverse stiffness in order for the sandwich to sustain concentrated loads. The increased stiffness shall insure that local bending of face sheets is avoided and the transfer of transverse load to the main core is successful.

It will be demonstrated that rapid prototyping may be used for the manufacturing of this kind of graded, periodic structure, which can be tailor made for any special application. In the present case the core material is strengthened where concentrated loads are introduced when the sandwich panel is tested in three point bending.



Figure 2. Structurally graded sandwich core material used to support concentrated loads.

Additional advantages of periodic structures compared to stochastic structures, like PVC foam cores, is their inferior structural performance as mentioned by Haydn et al. [4], and the possibility of including multifunctionality into the structure as presented by Evans [5]. The application of periodic cores for sandwich panels was suggested by Chiras et al. [6] and Bitzer [7].

Since 1980s quite a few techniques of rapid prototyping, also known as solid freeform fabrication or layered manufacturing, have been invented and some commercially developed. By building three dimensional parts in a layer-by-layer additive manner, these techniques allow freeform fabrication of parts of complex geometry directly from their CAD models, without having to use special fixtures as in the material removal processes.

Generally, a specimen is build up in layers, generated successively. Each layer is made by depositing a polymer which chemical composition is dependent on the selected technology. The deposit within each layer can be generated by a nozzle that moves in the plane of that layer like a two dimensional printer. The advantage is that individual layers can be designed by CAD and hence it is possible to design a three dimensional microstructure which is able to meet specific stiffness properties. In this case the microstructure is constituted by a spatial distribution of cylinders of varying diameter. This features the relation between local relative density of the structure and local stiffness.

## 2. EXPERIMENTAL PROCEDURE

A periodic structure is obtained by repeating a unit consisting of eight beams constructed as shown in Figure 3. The fully developed structure consists of 4 x 31 beam elements. In total 12 mm high, 31 mm wide, and with an intermediate distance between the beams of 6.9 mm. Two 0.5 mm thick face sheets are then glued to this structure.

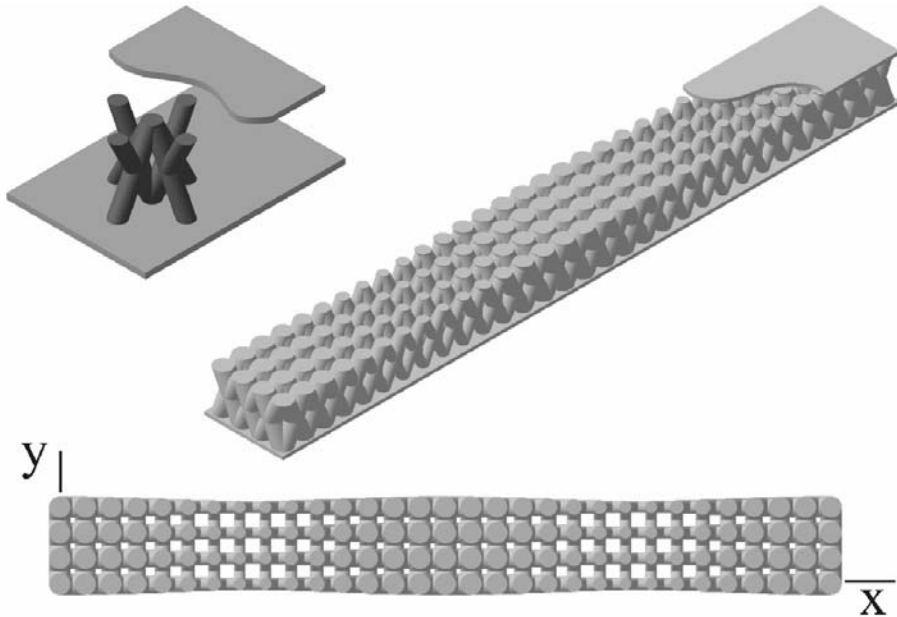


Figure 3. The layout of the periodic and graded beam structure.

All beams are angled at  $60^\circ$  to the face sheet in order to avoid the usage of an additional supporting structure during manufacturing. The supporting structure is typically an alternative polymer that has to be chemically removed after rapid prototyping. It is introduced in order to reduced the creep that occurs during manufacturing when the deposited polymer is still well above its glass transition temperature and able to flow.

The symmetry lines of the individual beams are aligned making it a periodic structure, see figure 3. The graded structure is obtained by varying the diameter of the beams by follow the trigonometric distribution:

$$D(x) = 3.8 + 1.2 \cos\left(\frac{\pi x}{45}\right)$$

This gives a minimum diameter of 2.6 mm and a maximum of 5 mm. This geometry was syntesised using CAD and the obtained geometrical model was applied as input for both the rapid prototyping and a finite element modelling.

A Stratasys Prodigy Plus machine was applied for the manufacturing using an ABS polymer as the precursor. The modulus of elasticity for the ABS is 1.627 GPa and the Poisons ratio is 0.4 [8]. Standard grade aluminium was applied as face sheet and glued to the ABS core using a two component

epoxy adhesive. The obtained sandwich panel was loaded in a three point bending test. From this test the applied force and deflection was measured using a 2000N load transducer and a dial gauge position. At intermediate steps of loading a 4 mega pixel camera was monitoring the setup.

### 3. RESULTS

The obtained results from the three point bending test feature a study of the deformation by using image processing. Hence the overall deflection of the panel, the difference in deflection between the upper and lower face sheets, and the movement of selected local beam surfaces is analysed. The image analysis is based on high resolution images of the setup as shown in Figure 4. It is performed using MatLab utilised with the DipImage Toolbox [9].

All images are grey scaled and with a resolution of  $101\mu\text{m}$  per pixel. For each image its second derivative of the gray scale is calculated and the obtained image is thresholded. This enhances all edges in the image. Noise is then removed by segmentation and by excluding all features smaller than 50 pixels. In this step specific edges which is to be analysed is extracted from the image. The precision of the location of an edge is improved below pixel resolution by using the product of the second derivative image and the segmented image as input for a polynomial curve fitting. From the obtained polynomial curve the points of local maxima is extracted. These points corresponds to the location of the maximum gradient in the grey scale image and hence the location of the edge.

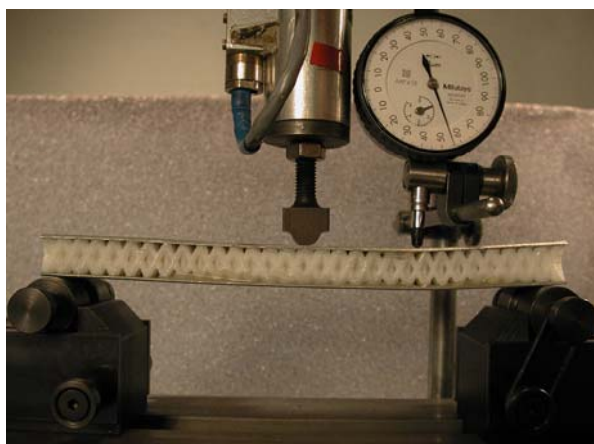


Figure 4. Image of the specimen just prior to failure.

Using this optical approach the deflection of the lower face sheet have been calculated. The result are shown in Figure 5 and compared to a finite element model of the structure. The FE model is based on Timoshenko beams for the graded, periodic structure and shell elements for the face sheets which includes both bending and membrane capabilities. Boundary conditions equivalent to the three point bending test was applied to the FE model. The same magnitude of overall deflection was obtained when the FE model was subjected to a load of 503N. The experimentally measured force was 680N indicating that the FEM is estimating a lower stiffness. The difference in loading are accounted for by the fact that the model of the core material consists of beam elements not taking into to account the overlap that exists at the ends where multiple beams are meeting and share volume, and variation of the Young's modulus of the ABS.

As seen from Figure 4 the dial gauge position is mounted in the right side of the setup. The maximum deflection at  $x = 145$  mm measured using the gauge was 1.265 mm. Using image processing the maximum deflection was calculated to 1.25 mm at this point.

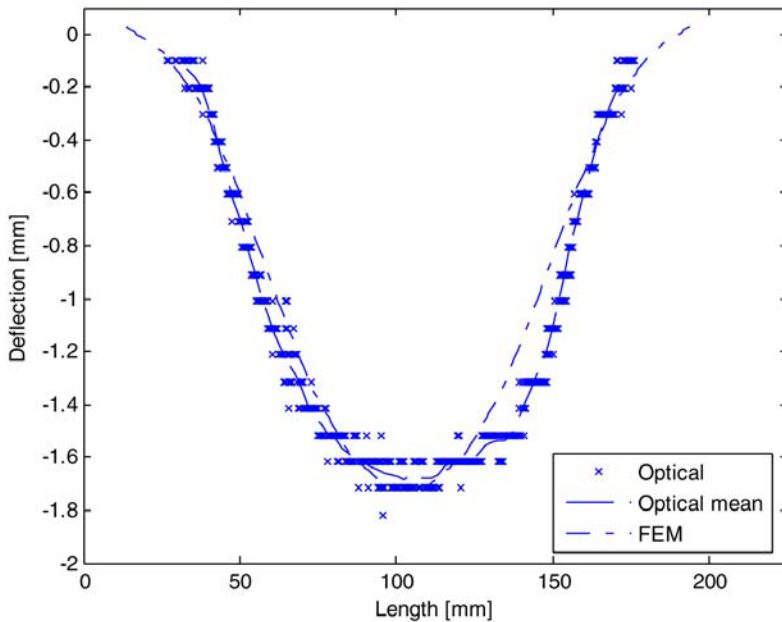


Figure 5. Deflection of the lower face sheet.

The difference in lateral deflection between the upper and lower face sheet have been studied. The FEM result is shown in Figure 6 using full lines and the crosses correspond to the results obtained using the optical approach.

The opening in the ends shown as peaks at  $x = 10$  and  $x = 170$  and the changes in the low density regions at  $x = [20:70]$  and  $x = [110:160]$ , are to some extent seen in the experimental results. The experimental results show no negative difference at  $x = 140$ , but do show two peak at  $x = 120$  and  $x = 160$ .

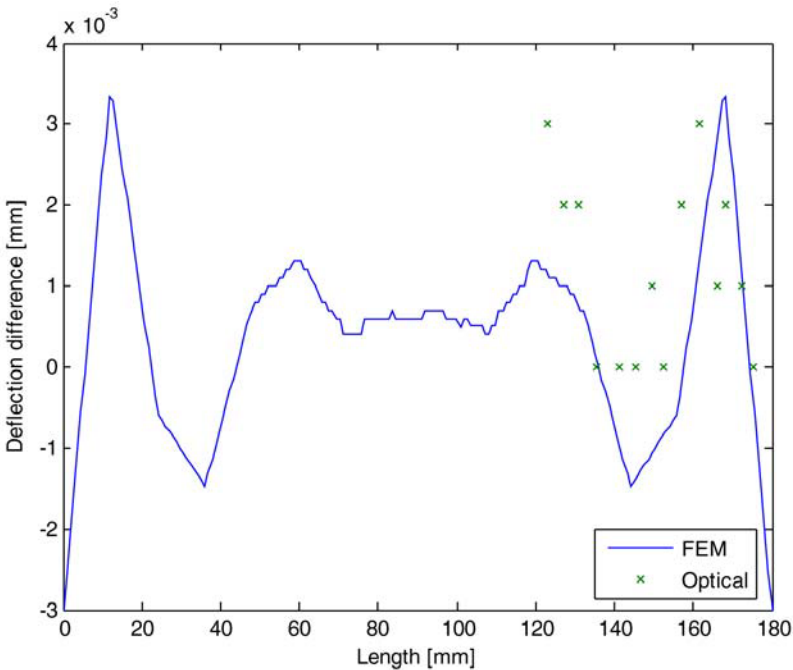


Figure 6. Difference between the lateral deflection of the upper and lower face sheet.

The local deformation of individual beams has been studied in two instances. The rotation of the beams located at  $x = 47$ ,  $x = 52.9$ , and  $x = 76.8$  were identified. Only in the last case a rotation was observed as shown in Figure 7.

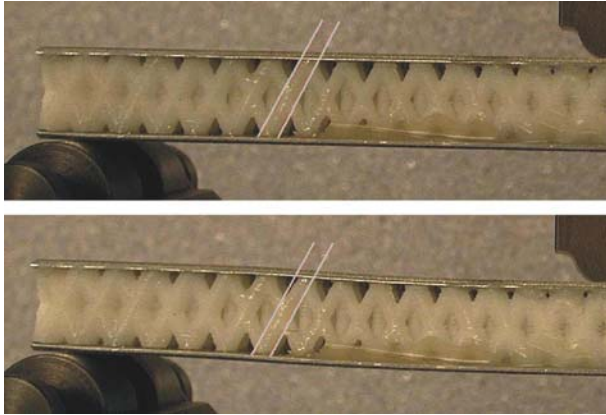


Figure 7. Displacement of the surface of a local beam element in the low density region.

The upper left surface of this beam was selected for edge detection using image processing and the coordinates of the pixels that constitutes the triangle located at the left side of the beam was extracted from an image taken from the unloaded situation and an image taken just prior to failure. These coordinates are plotted in Figure 8 and show the rotation and translation of the triangle. Two lines are fitted to the points describing the surface of the beam and the angle between them is calculated to  $5^\circ$ . The FEA found an angular rotation of the end node of  $3.5^\circ$ .

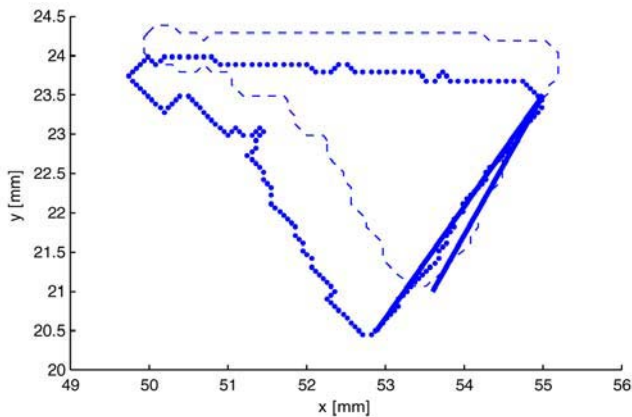


Figure 8. Edge detection of the triangular region located at the upper left to the beam identified in Figure 7 (thin lines correspond to the undeformed geometry and thick lines correspond to the deformed geometry).

The tested specimen failed by delamination of the upper face sheet in the right side, see Figure 4. In close vicinity to the location of the delamination

failure a beam surface was selected for image processing. This surface is marked in Figure 9.

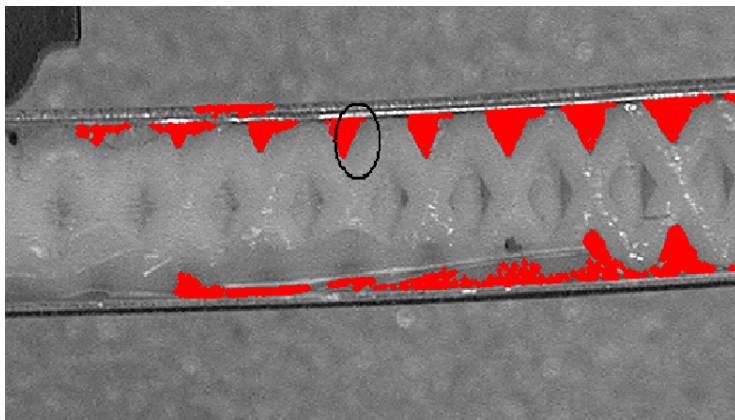


Figure 9. Displacement of the surface of a beam element located in the low density region close to the point of the delamination failure.

Again the pixels constituting the edge describing the beam surface was extracted from images acquired in the unloaded and loaded situation and plotted in Figure 10. The plotted data have been rotate  $60^\circ$  around the z-axis in order to improve the visualisation of the surface movement. The maximum lateral movement of the surface is approximately 0.5 mm. The FEA documents that this beam is in a state of compression at 32N when the overall structure is loaded as shown in figure 5.

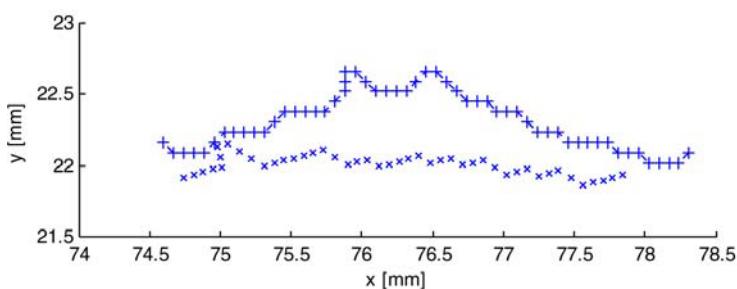


Figure 10. Movement of the beam surface indicated in Figure 9.

Rotation of individual beams is controlled by the angular rotation of the face sheets. This introduces a moment over the local beam which also experiences a state of compression due to the difference in deflection between the upper and lower sheets.

## 4. CONCLUSION

A sandwich core was manufactured using rapid prototyping. It is synthesised of cylindrical beams. It is a periodic structure and it features a graded stiffness due to a variation of the beam diameter.

The obtained specimen was subjected to a three point bending test in which it failed by delamination. Using image processing on images of the unloaded and loaded specimen, the overall deflection was calculated and compared to a finite element analysis.

Local effects in the face sheets and beam elements were also studied. This included the difference in lateral deflection between the upper and lower face sheet. The FEA indicated a dependence on the graded structure and this trend was also experimentally identified using image processing.

Local deformation of the surface of individual beam elements was documented using image processing and compared to FEA results and showed rotation and compression of individual beam elements.

## REFERENCES

1. Zenkert, D., 1997, Handbook of Sandwich Structures, Cameleon Press.
2. Skvortsov, V.S. And Thomsen, O.T., 2003, Analytical estimates for the stresses in face sheets of sandwich panels at junctions between different core materials. In Proceedings of the 6th International Conference on Sandwich Structures (ICSS-6), Fort Lauderdale, FL, USA, pp. 551-559.
3. Apetre, N.A. and Sankar, B.B., 2003, Composite sandwich plates with functionally graded cores. In Proceedings of the 6th International Conference on Sandwich Structures (ICSS-6), Fort Lauderdale, FL, USA, pp. 227-239.
4. Wadleya, H.N.G., Fleck, N.A. and Evans, A.G., 2003, Fabrication and structural performance of periodic cellular metal sandwich structures, Composites Science and Technology 63, 2331–2343.
5. Evans, A.G., 2001, MRS Bull. 26 (10).
6. Chiras, S. et al., 2002, Int. J. Solid Struct. 39, 4093-4105.
7. Bitzer, T. Honeycomb Technology, Chapman and Hall 1997.
8. ABS FDM Materials Properties, Stratasys, 2005.
9. Hendriks, C.L.L. et al., 2002, DIPIImage User Manual, Pattern Recognition Group, Faculty of Applied Physics, Delft University of Technology.

# INVESTIGATION OF THE CURE PROCESS FOR THICK COMPOSITE SANDWICH PANELS

Daniel K. Jensen

*Institute of Mechanical Engineering, Aalborg University,  
Pontoppidanstraede 101, DK-9220 Aalborg East, Denmark  
dkj@ime.aau.dk*

**Abstract** A numerical and experimental investigation of the temperature distribution during the cure process of a composite sandwich panel manufactured from thick thermoset carbon/epoxy prepreg skin layers and a thermally stable closed cell foam core is presented. The temperature distribution at solidification is subsequently determined from the numerical analysis. The results from the numerical and experimental analyses are compared and good agreement is found.

**Keywords:** cure simulation, thick prepreg skin layers, closed cell foam core.

## 1. INTRODUCTION

As the research and development of composite sandwich structures has increased significantly in recent years, these structures have gained a significant role in a wide range of applications. Manufacturing of advanced composites primarily involves the use of either polymeric thermosetting or thermoplastic materials, which demand a high processing temperature for the curing (hardening) phase. For thermoset materials the high processing temperature is usually achieved by curing the composite in an oven. The development of advanced high-strength thermoset prepreg systems, together with thermally stable closed-cell foam core materials, has opened the possibility of manufacturing large composite sandwich structures in a one-step cure process a so-called co-cure process, using simple vacuum bag processing. Although this type of processing is relatively simple and costeffective, there are some drawbacks. The performance of a composite structure depends on several factors, of which an important one is the influence from manufacture induced parameters. This includes the thermally induced residual stresses caused by the mismatch in the coefficients of thermal expansion parallel and perpendicular to the fiber directions. Despite this, the influence from the manufacturing is

traditionally either completely left out in the design and optimization phase, or the applied theories are based on various simplifications. In principle, the thermally induced residual stress  $\sigma^{th}$  is computed from

$$\sigma^{th} = E(\varepsilon^{tot} - \varepsilon^{th}) \quad (1)$$

where  $E$  is the modulus of elasticity,  $\varepsilon^{tot}$  the total strain, and the thermally induced strain is given by  $\varepsilon^{th} = \alpha \Delta T$ , where  $\alpha$  is the coefficient of thermal expansion and  $\Delta T$  is the temperature difference between the solidification temperature of the resin and the "service temperature" of the final structure. In classical laminated plate theory the oven temperature is taken as the solidification temperature and is considered constant throughout the structure. However, a thermoset resin cures exothermically, i.e. it generates heat during curing. At the same time most composites have relatively poor heat conducting properties. The assumption of constant temperature is thus only valid for very thin structures. As the range of applications of thermally processed composite structures expands, there has been a significant increase in the overall size of sandwich structures and thus also in the thickness of the skin layers. A more accurate and realistic prediction of the thermally induced residual stresses is thus necessary. This aspect is especially important for the co-curing of foam core sandwich structures, as the thermal conductivity of the foam core is very low and thus acts as an insulating layer. This can give rise to a significant temperature gradient through the structure during curing. Ultimately, the temperature distribution at solidification can be very different from the applied oven temperature, which must be taken into account.

As the use of fiber reinforced composite structures is increasing significantly, the area of cure simulation of thermoset resin systems has obtained increased attention in various research communities. The works by Li et al. [1], Park et al [2], and Liu and Hillier [3] have demonstrated that the effects of the exothermic cure reaction exert large influence on the temperature distribution during the thermal processing. Bogetti et al. [4], [5] and Lahtinen [6] have worked on determining the structural impact from the cure process. Most research has until now mainly focused on the modeling of monolithic laminates. The present paper will center on determining the temperature distribution at curing when manufacturing thick-skin sandwich panels with thermoset carbon/epoxy prepreg skin layers and a thermally stable closed-cell foam core, using vacuum bag processing. The paper will also illustrate that for some structures, with a uniform cross-section, a 1D approach for analyzing the thermal impact can be adopted with good results, as the thermal loading is mainly governed by the through-the-thickness thermal properties of the structure.

The exothermic cure process of the thermoset resin will be simulated with a transient finite element model. The thermochemical modeling of the exothermic cure reaction will be based on a purely phenomenological model us-

ing a so-called Arrhenius type equation. To verify the thermochemical simulation model of the manufacturing process, a composite sandwich panel will be manufactured and the temperature during curing will be measured at key positions within the setup. The results of the simulation and experiment will subsequently be compared.

## 2. CURE REACTION THEORY

The curing of a thermoset resin is a thermochemical reaction, where the molecules of the resin are triggered to cross-link and form a dense immobile structure by imposing an elevated temperature. The cure reaction is in itself highly complex, and to circumvent this, several purely phenomenological models have been developed over the years.

### 2.1 Cure reaction model

The present paper follows the procedure of modeling the cure reaction by a so-called Arrhenius type equation. According to this, the internal energy release  $Q$  of the resin material can be written as, see [7, 8]

$$Q = \rho H_R \dot{\psi} \quad (2)$$

where  $\rho$  is the resin density,  $H_R$  the total heat of reaction of the resin material, and  $\dot{\psi}$  the cure rate or time derivative of the resin. The cure rate of the resin is determined by the Arrhenius type equation. The actual form of the Arrhenius equation depends on the reaction pattern displayed by the specific resin. During the curing phase most resin types convert from one molecular structure directly to the final immobile structure, displaying a homogeneous reaction pattern. Some resin types, however, convert to one or more intermediate molecular states, with subsequent changing of reaction patterns depending on the degree of cure. This has to be taken into account when determining the Arrhenius equation. The Arrhenius equation selected to fit the cure reaction pattern of the prepreg material used in the present paper is

$$\dot{\psi} = A e^{(-E/(RT))} \psi^m (1 - \psi)^n \quad (3)$$

where  $A$  is an amplitude constant,  $E$  the apparent activation energy of the resin,  $R$  the universal gas constant, and  $m$  and  $n$  are exponential constants. The degree of cure  $\psi$  ranges from 0 to 1 for a non-cured and a fully-cured material, respectively.

### 2.2 Material characterization

The standard procedure for determining the cure reaction properties of a resin is to apply so-called differential scanning calorimeter analysis or DSC.

In a DSC analysis the energy release of a small sample of resin is measured at different isotherms and by dynamic temperature measurements. The DSC results are then fitted to the Arrhenius equation with the temperature and the degree of cure being the only variables. A prepreg material consists of a distinct resin and fiber phase where only the resin phase contributes to the exothermic energy release. For a prepreg material it is, however, not possible to separate the two phases for the DSC analysis. The resulting material characterization is given as volume averaged properties of the entire prepreg material. For the following numerical modeling and experimental verification the material system T700/SE84LV carbon/epoxy prepreg from SP-systems was used. Details regarding the DSC method can be obtained from Um et al. [9]. The DSC analysis for the material used for the present study was performed on a Mettler Toledo 822<sup>e</sup> DSC instrument. The corresponding Arrhenius parameters are shown in Table 1.

Table 1. Arrhenius parameters for T700/SE84LV carbon/epoxy prepreg.

Parameter	Unit	Value
$\rho$	[Kg/m <sup>3</sup> ]	1555.0
$H_R$	[J/Kg]	104300
$A$	[s <sup>-1</sup> ]	2795830.5
$E$	[J/mol]	67001.3
$R$	[J/(molK)]	8.3145
$m$	[—]	0.51
$n$	[—]	1.11

For more information about the correlation between the fitted values and those obtained from the DSC analysis the reader is referred to Jensen [10]. The point of cure at which the resin material solidifies can be determined by means of a glass transition temperature or  $T_g$  analysis. The transitional degree of cure at which the present resin material converts from gel-like to solid state is estimated to be  $\psi_s \approx 0.81 \sim 0.89$ . The  $T_g$  measurement was performed on the same instrument as that used for the DSC analysis.

### 3. EXPERIMENTAL SETUP

To obtain as realistic results as possible the experiment should ideally be carried out on a size-scale corresponding to an actual structure. However, this is usually not possible so the following assumption is made. The width and length dimensions of a thick-skin composite sandwich structure are typically considerably larger than the thickness. Moreover, a typical manufacturing setup will cause little thermal impact at the sides of the structure due to the edge dam

system normally employed. It is thus assumed that the major thermal impact is governed by the through-the-thickness properties of the structure, and hence a quasi 1D analysis approach is adopted. The experimental test piece is a 200 mm  $\times$  200 mm cut-out of the composite panel investigated. To minimize the thermal flux on the sides of the test piece, a dam system consisting of a foam core and a coarse nylon mesh is placed at each side of the setup. When under vacuum, heat will only be transferred through the nylon mesh. As the nylon mesh surface area touching the experimental setup is very small, the heat flux at the sides is reduced to a minimum. In order to verify the validity of the 1D assumption, the through-the-thickness temperature is measured at a section close to the edge of the setup, and subsequently compared with that measured at the center of the setup. The temperature measurement is carried out via embedded Type-K thermocouples. A schematic illustration of a one-half section of the experimental setup, including measuring points, is shown in Figure 1.

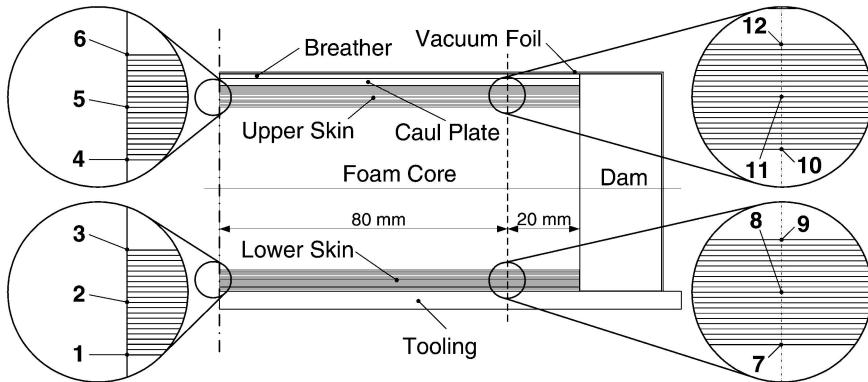


Figure 1. One-Half of the cross-section of the experimental setup showing the measuring positions of the thermocouples, as well as the various materials constituting the experimental setup.

The setup uses a steel tooling, an aluminum caul plate, a polyester breather cloth and nylon vacuum foil. Each skin layer consists of 20 layers of prepreg in a  $[0^\circ, 90^\circ]_{10s}$  layup configuration. This amounts to a skin thickness of 5.8mm. The foam core material used is 71 WF PMI closed-cell foam from Rohacell. The foam core has a thickness of 44.5mm. The oven cycle for the present experiment is set to go from an initial temperature of 20°C to 110°C in 500s and then to keep that temperature for the duration of the experiment.

#### 4. NUMERICAL MODEL

The analysis procedure presented in the following can be extended to model all types of prepreg systems. However, in order to correspond to the prepreg

system used for the experimental study, the present model is based on a so-called "low-bleed" approach, which implies virtually no resin flow. Internal mass transport is hereby neglected, which simplifies the analysis to solving only a transient heat transfer field problem. The governing equation for a transient finite element based problem with convective boundary conditions (oven heating) and internal energy release (exothermic cure reaction) is given by the following equation, see [11]

$$[C]\{\dot{T}\} + ([K_\kappa] + [K_h])\{T\} = (\{F_h\} + \{F_Q\}) \tag{4}$$

where  $[C]$  is the heat capacity matrix,  $[K_\kappa]$  the conduction matrix,  $[K_h]$  the convection matrix,  $\{\dot{T}\}$  a vector containing the time derivatives of the temperature,  $\{F_h\}$  the load contribution from the convective boundary conditions, and  $\{F_Q\}$  is the load contribution from the internal energy release. The components of (4) are given by

$$\begin{aligned} [K_\kappa] &= \sum_{\Omega^e}^{n_e} \int_{\Omega^e} [B]^T [\kappa] [B] dV^e & \{F_h\} &= \sum_{\Gamma^e}^{n_{abe}} \int_{\Gamma^e} [N]^T h T_f dS^e \\ [K_h] &= \sum_{\Gamma^e}^{n_{abe}} \int_{\Gamma^e} [N]^T h [N] dS^e & \{F_Q\} &= \sum_{\Omega^e}^{n_{ae}} \int_{\Omega^e} [N]^T Q dV^e \\ [C] &= \sum_{\Omega^e}^{n_e} \int_{\Omega^e} [N]^T \rho c_p [N] dV^e & & \begin{aligned} a: & \text{affected} \\ b: & \text{boundary} \\ e: & \text{elements} \end{aligned} \end{aligned} \tag{5}$$

Here,  $\kappa$  is the thermal conductivity,  $h$  the convection coefficient,  $\rho$  the material density,  $c_p$  the specific heat of the material,  $T_f$  the temperature of the surrounding fluid (oven temperature), and  $Q$  is the internal energy release obtained from Equation (2). The symbol  $\Gamma^e$  denotes the boundary of the affected finite elements, and  $\Omega^e$  denotes the domain of the finite elements. For the time integration an explicit Runge-Kutta time integration scheme was employed. The basic explicit form for solving for the time-step  $k + 1$  with the time-step size  $\Delta t$  is

$$\begin{Bmatrix} \{T\} \\ \{\psi\} \end{Bmatrix}_{k+1} = \begin{Bmatrix} \{T\} \\ \{\psi\} \end{Bmatrix}_k + \begin{Bmatrix} \{\dot{T}\} \\ \{\dot{\psi}\} \end{Bmatrix}_k \Delta t \tag{6}$$

where the time derivative of the temperature  $\{\dot{T}\}_k$  at time step  $k$  is determined from a simple rewriting of Equation (4), and the time derivative of the degree of cure  $\{\dot{\psi}\}_k$  is given by Equation (3). To improve the accuracy and prevent instability in the time integration an adaptive time-step control following the procedure of Cash and Karp [12] was applied. The numerical model is further simplified by using a "diagonalized" or lumped mass matrix. For the present analysis a HRZ-mass lumping scheme is employed, see Cook et al. [13]. To initiate the analysis procedure it is necessary to state the initial values. The

initial temperature is taken as the temperature measured at the beginning of the experiment. The initial degree of cure is set to  $\psi_0 = 1 \times 10^{-8}$ , i.e. corresponding to a very small numerical value. The 1D finite element model is based on a thin strip representing the cross-section of the manufacturing setup. The strip is meshed with 4-node quadrilateral elements, with one element in the width direction. The only boundary conditions applied are the convective boundary conditions applied to the upper and lower edge elements.

## 5. RESULTS AND COMPARISON

The temperatures measured at the center and edge of the experimental setup are compared in Figures 2 and 3. The temperatures are very similar at these measuring points which confirms that the assumed 1D approach is applicable for this type of analysis.

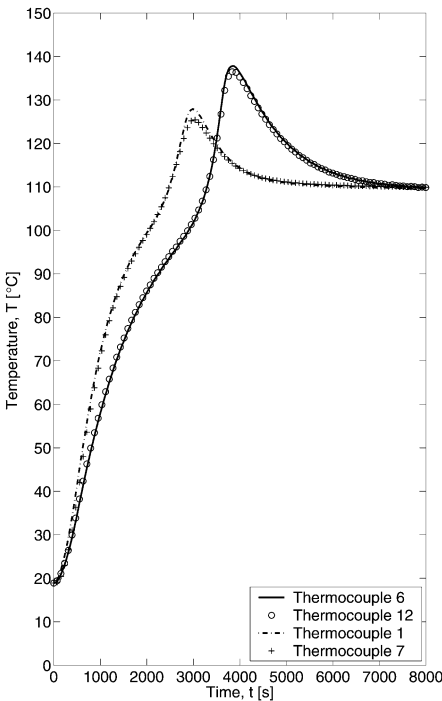


Figure 2. Comparison of the temperatures measured at the outer thermocouples at the center and edge of the experimental setup.

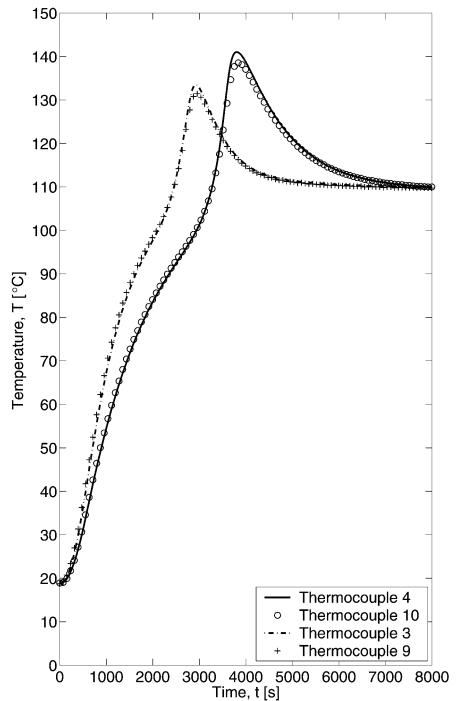


Figure 3. Comparison of the temperatures measured at the inner thermocouples at the center and edge of the experimental setup.

The experimental results shown above clearly illustrate the effect of the exothermic cure reaction. Initially the temperature distribution is dominated by the thermal loading of the convective boundary conditions. At a certain point, however, the cure reaction begins, causing a steeper temperature increase until a point where no reaction enthalpy is left in the resin. Following this point the thermal loading is again dominated by the convection in the oven. Subsequently the temperature distribution within the experimental setup becomes equal to that of the surrounding hot air. The temperature distribution obtained from the experimental investigation is compared with that obtained from a numerical 1D through-the-thickness transient finite element analysis as shown in Figures 4 to 6. The temperature distribution at a transitional degree of cure of  $\psi_s = 0.85$  is shown in Figure 7.

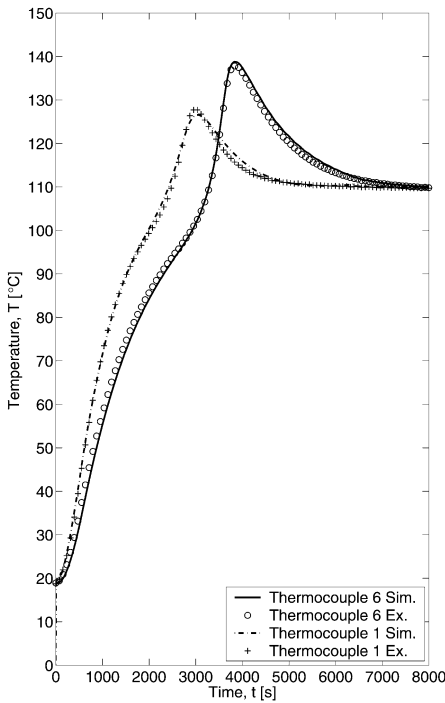


Figure 4. Comparison of the simulated and experimentally measured temperature at the outer thermocouples, No. 6 and 1.

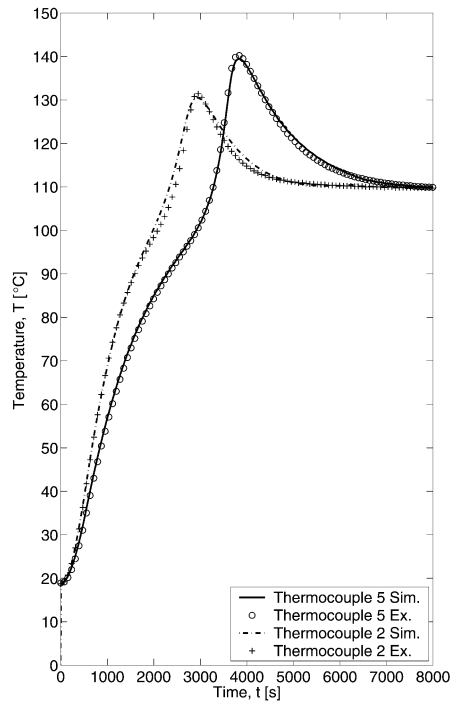


Figure 5. Comparison of the simulated and experimentally measured temperature at the middle thermocouples, No. 5 and 2.

The comparison between the numerical results and those obtained experimentally illustrates that the exothermic cure reaction can have a significant influence on the temperature distribution during the curing of thermoset resin systems. The comparison also illustrates that, for structures with uniform

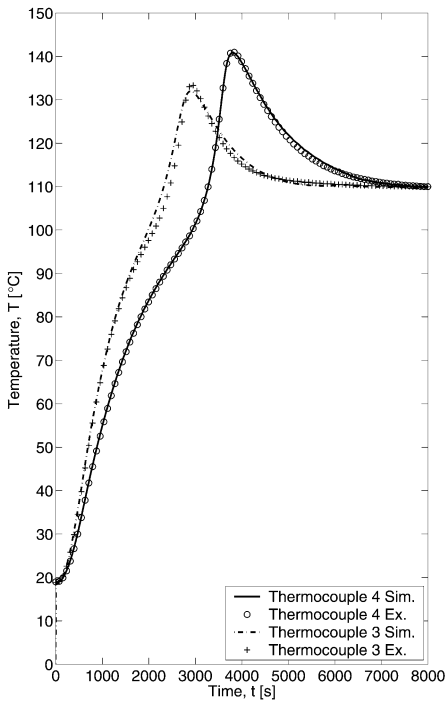


Figure 6. Comparison of the simulated and experimentally measured temperature at the inner thermocouples, No. 4 and 3.

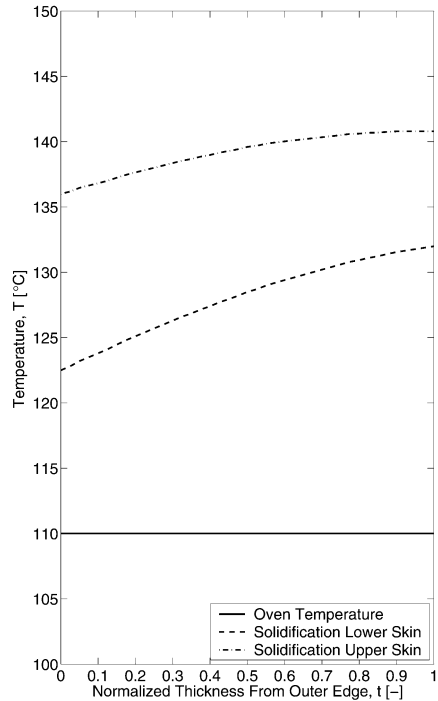


Figure 7. Temperature distribution at a transitional degree of cure of  $\psi_s = 0.85$ .

cross-section, the temperature distribution during the manufacturing process can be estimated by a 1D through-the-thickness analysis. The through-the-thickness temperature at solidification are larger than the oven temperature and the temperature is also different in the two skin layers. Thus to compute a more realistic distribution of the thermally induced residual stresses from Equation (1), the solidification temperature obtained from the cure simulation must be used instead of the oven temperature for this type of structure. Another important result from the analysis is the time-lag which occurs between the curing of the lower and upper skin. This time-lag is caused by the difference in thermal conductivity of the the main tooling at the lower skin and the auxiliary manufacturing materials at the upper skin. Again illustrating the significance of including influence from the manufacturing.

## 6. CONCLUSION

This paper has presented a method for determining the temperature distribution during a one-step cure process of a composite sandwich panel with thick skin layers from a "low-bleed" thermoset prepreg system and a thermally stable closed-cell foam core. Although the approach results in a very simplified numerical model, the results obtained illustrate that for the specific layup considered, the temperature distribution can be determined by a 1D through-the-thickness transient heat transfer problem. The results show that the exothermic cure process of a thermoset resin can have a significant effect on the temperature distribution during the cure process. The resulting temperature profile at the transitional degree of cure is very much different from that obtained by the "classical" approach of taking the oven temperature as the solidification temperature. It is thus important to include a more realistic modeling of the thermally induced residual stresses in a structural analysis.

## REFERENCES

- [1] M. Tucker III and C.L. Li. Modeling and simulation of two-dimensional consolidation for thermoset matrix composites. *Composites, Part A*, 33:877–892, 2002.
- [2] H.C. Park and L.W. Sung. Cure simulation of thick composite structures using the finite element method. *Journal of Composite Materials – Lancaster*, 35(3):188–201, 2001.
- [3] X.L. Liu and W. Hillier. Heat transfer and cure analysis for the pultrusion of a fiberglass-vinylester i beam. *Composite Structures*, 47:581–588, 1999.
- [4] T.A. Bogetti and Jr. Gillespie, J.W. Process-induced stress and deformation in thick-section thermoset composite laminates. *Journal of Composite Materials*, 26(5):626–60, 1992.
- [5] T.A. Bogetti, J.W. Gillespie and R.L. McCullough. Influence of processing on the development of residual stresses in thick section thermoset composites. *International Journal of Materials and amp; Product Technology*, 9(1):170–182, 1994.
- [6] H. Lahtinen. Calculation of residual stresses of cross-ply laminates. *Journal of Composite Materials*, 37(11):945–967, 2003.
- [7] M. Li, Q. Zhu, P.H. Geubelle and C.L. Tucker III. Optimal curing for thermoset matrix composites: Thermochemical considerations. *Polymer Composites*, 22 No. 1:118–131, 2001.
- [8] M. Li and C.L. Tucker III. Optimal curing for thermoset matrix composites: Thermochemical and consolidation considerations. *Polymer Composites*, August 30:N/A, 2001.
- [9] I.M. Daniel, M.K. Um and B.S. Hwang. A study of cure kinetics by the use of dynamic differential scanning calorimetry. *Composites Science and Technology*, 62:29–40, 2002.
- [10] D.K. Jensen. Simulation of the exothermic cure process for "low-bleed" thermoset prepreg systems. *Proceedings of 17th Nordic Seminar on Computational Mechanics (NSCM 17) Stockholm*, 1(1):187 pp., 2004.
- [11] J.N. Reddy and D.K. Gartling. *The Finite Element Method in Heat Transfer and Fluid Dynamics*. CRC, 1st edition, 1994. ISBN: 0-8493-9410-4.
- [12] J.R. Cash and A.H. Karp. *AcM transactions on mathematical software*. *ACM*, 16:201–222, 1990.
- [13] D.S. Malkus R.D. Cook and M.E. Plesha. *Concepts and Applications of Finite Element Analysis*. Wiley, 3rd edition, 1989. ISBN: 0-471-84788-7.

# **NDE AND ENVIRONMENTAL DEGRADATION**

# AUTOMATED ULTRASONIC INSPECTION OF LARGE-SCALE SANDWICH STRUCTURES

Thomas Mathiasen Wulf

*Plastics and Composites, FORCE Technology, DK-9220 Aalborg East, Denmark*

**Abstract** This paper represents the results obtained from the successful ultrasonic developing work performed within the EUCLID RTP3.21 [1] and the JP 3.23 THALES [2] projects. New automated ultrasonic method for large-scale inspection of sandwich structures applied in the marine industry has been developed. On basis of several laboratory and field tests it can be concluded that the method shows great potential in revealing typical manufacturing and in-service defects.

**Keywords:** NDT, sandwich structures, composite, inspection, ultrasound, field test.

## 1. INTRODUCTION

Within the marine industry high-performance materials such as sandwich composites are attractive materials for lightweight constructions. Their increasing applications for especially load-carrying purposes require an extended knowledge of possible hidden flaws incurred after fabrication or in service.

Typical and often critical defect types that may effect the strength and durability of sandwich structures are:

- Fiber fracture
- Matrix cracking
- De-lamination and dry areas in the skin laminates
- De-bonding between skin and core
- Core defects like shear cracks and core crushing

Almost all these defects are invisible from the outside and therefore the need for reliable and effective non-destructive testing (NDT) methods exists.

As the results of the latest development within the field of NDT on composite materials, new automated ultrasonic methods for large-scale inspection of sandwich structures have been developed and showing great potential in revealing these typical defects. These methods have been developed within the European projects called “EUCLID RTP 3.21” [1] and “JP 3.23 THALES Project” [2].

This paper represents the results obtained from the successful ultrasonic developing work performed within these projects.

One of the aims was to investigate the detection capabilities of typical manufacturing and in-service defects by commercial available ultrasonic methods, however, at project on-set no techniques were capable of penetrating the heavily sound damping structure of sandwich panels applied in the marine industry.

Another important aim was to develop portable equipment for effective on-side inspection of e.g. the hull structure of a ship.

## **2. APPLIED ULTRASONIC TECHNIQUES**

Through-transmission techniques with separate receiver and transmitter transducers on opposite sides of the composite component, is often used for their testing. The great advances of this technique is that the sound has to travel only once in the thickness direction and the inspection evaluation is simply done by comparing amplitude levels of received signals. However, through-transmission techniques are in general not practicable for in-field inspections, where access is often limited to one side of the structure.

A more applicable ultrasonic technique for in-field inspections is the Pulse-Echo technique with a single transducer transmitting ultrasonic waves into the component. The same transducer receives the echo, before the next pulse is sent. This method evaluates the signals based on time spent from pulse initiation to the reflected signal is back in the crystal, and on the amplitude level of the reflected signal.

A composite sandwich panel consists of relatively high-density skin laminate materials as GRP and CFRP, and a relatively low-density core material as PVC foam and Balsa core materials. It is often complicated and rather impossible to get any useful information about internal defects in composite sandwich structures by means of traditional ultrasonic parameter choice applied on e.g. steel structures. Mainly because of the inhomogeneous composite materials, large density difference between the applied skin and

core materials, and also because of the extremely high sound damping within especially the low-density core material.

Resolution, sensitivity and propagation of the waves into the material are very frequency dependent, due to the relatively high attenuation in composite components. For the inspection of the skin laminate it is important to use a wavelength (transducer frequency) where the glass or carbon fibers are as close to being ignored as possible in order to detect real defects. The best frequency choice for skin laminates varies from 15-35 MHz on thin (0,5-1 mm) well-consolidated carbon skins to 0,5-2 MHz on thick hand lay-up GRP laminates.

New promising results from laboratory Pulse-Echo inspections (inspections only from one side) of heavy sandwich panels shows that it is now possible to make clear detection of skin-core de-bonding, core cracks and impact damage by means of special high damped broadband transducers in the frequency range from 0,1-2 MHz.

### **3. RESULTS FROM LAB. PULSE-ECHO INSPEC.**

The experimental work performed within the two mentioned projects has been carried out by means of portable automated scanning equipment from the new P-scan System 4 generation developed by FORCE Technology. In order to be able to gain information on defects in sandwich structures it is necessary to apply special sensor characteristics, special manipulator devices and dedicated post processing software for presentation and evaluation of results. In order to achieve the required sensitivity in the applied contact ultrasonic technique in Pulse-Echo mode, it has been necessary to optimize pulse and scanning parameters such as probe frequency, pulse characteristics, frequency filtering on receiver amplifier, and coupling conditions.

Several numbers of sandwich components used for marine applications with different material combinations, qualities and thickness have been inspected within the two mentioned projects. Both virgin samples, samples with inserted artificial defects, and samples with damage from mechanical and blast tests have been inspected. The material used for the skin laminate is either GRP or CFRP in the thickness range from 2-9 mm. The core material is either PVC foam or Balsa wood in the density range from 80-200 kg/m<sup>3</sup> and in the thickness range from 40-200 mm.

In the following sections some of the results achieved from the parameter setting optimization are visualized by presentation of automated scanning results obtained with portable P-scan equipment.

### 3.1 Detection of GRP skin/Balsa core de-bonding

Within EUCLID RTP3.21 it was decided to perform blast tests on large GRP/Balsa sandwich structures in order to test and simulate the survivability of such structures. Before and after the blast test, several ultrasonic inspections were performed in order to reveal possible defects. The responds from the blast in ambient air resulted in some damages in the structure like skin-core de-bonding as illustrated in Figure 1.

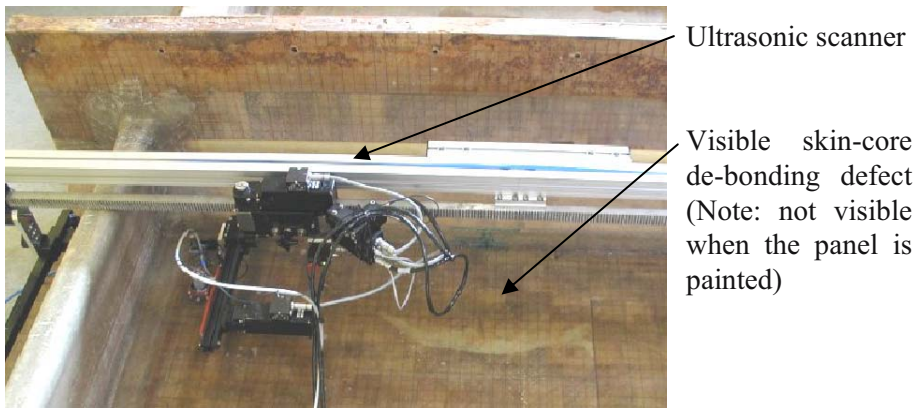


Figure 1. Automated ultrasonic inspection of skin-core de-bonding defect in sandwich structure exposed for blast in ambient air.

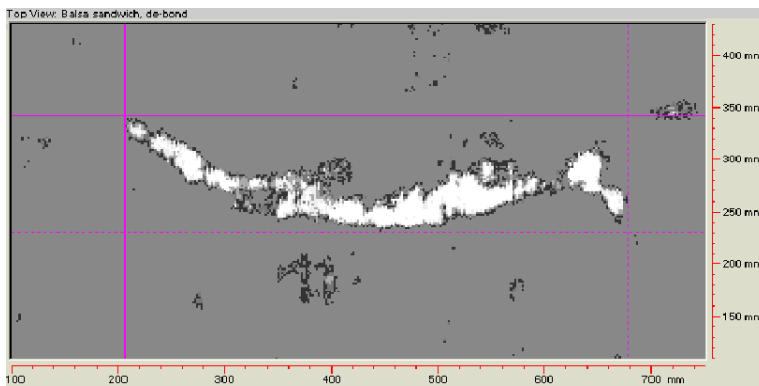


Figure 2. C-scan presentation of scanned area with skin-core de-bonding defect.

The skin-core de-bonding defects are clearly detected by means of automated ultrasonic scanning in Pulse-Echo mode. The defect is detected by evaluation of the amplitude level of received skin-core interface echoes.

The amplitude differences between well bonded areas and de-bonded areas are approx. 6dB (gain factor 2).

### 3.2 Detection of core shear crack in GRP/PVC foam

Within the saNDI project several defect types have been simulated in different sandwich test samples. One of the defect types of interest is shear cracks in the core material as indicated in Figure 3.

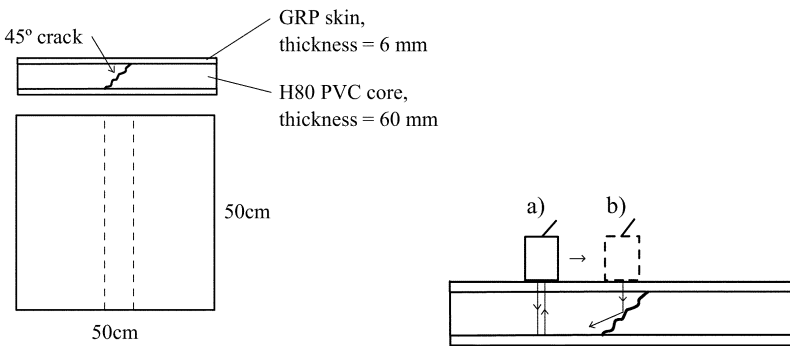


Figure 3. Left: GRP/PVC foam sandwich panel with shear crack. Right: a) Ultrasonic transducer transmitting waves into the panel. b) When the transducer is placed upon the shear crack defect the transmitted waves are scattered in other directions and the back-wall echo disappears.

The shear crack defect is detected by means of the method indicated in Figure 3. A scanning result is presented in Figure 4.

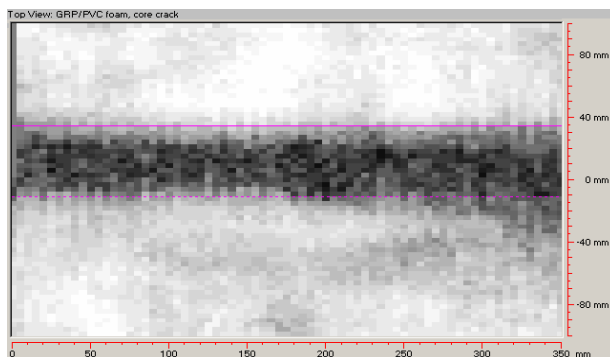


Figure 4. C-scan presentation of a panel with a shear crack in the core.

The shear crack defect is clear by detected by means of large amplitude drop (>10 dB) on rear side skin-core interface echoes (dark area).

### 3.3 Detection of impact damage in CFRP/PVC foam

Another relevant defect type in sandwich structures is the so-called impact damage, which is characterized by delaminations and cracks in the skin laminate. Depending of the impact energy, the core is often crushed just underneath the damaged skin area in considerable larger areas compared to the damage skin area. Within the saNDI project there has been manufactured CFRP-PVC foam sandwich panels with impact damage simulated by means of falling weight tests. One of the test panels has the following specifications:

CFRP skin thickness:	2 mm
H80 PVC foam thickness:	40 mm
Impactor:	75 mm hemispherical
Impact energy level:	75 J and 100 J

The panel has two impact damages, one with impact energy level of 75 J and another with 100 J. The 75 J impact damage is almost invisible on the skin surface, while the 100 J impact damage appears with skin surface indentation in a relatively small area of 30x50 mm.

The panel has been inspected by means of automated ultrasonic scanning equipment in Pulse-Echo mode from the damage size with two different methods. The results are presented in Figure 5 and 6 in C-scan mode. The C-scan presented in Figure 5 is the scanning result from only skin inspection, where no information about possible core damages is obtained. In Figure 6 the result from full panel inspection is presented.

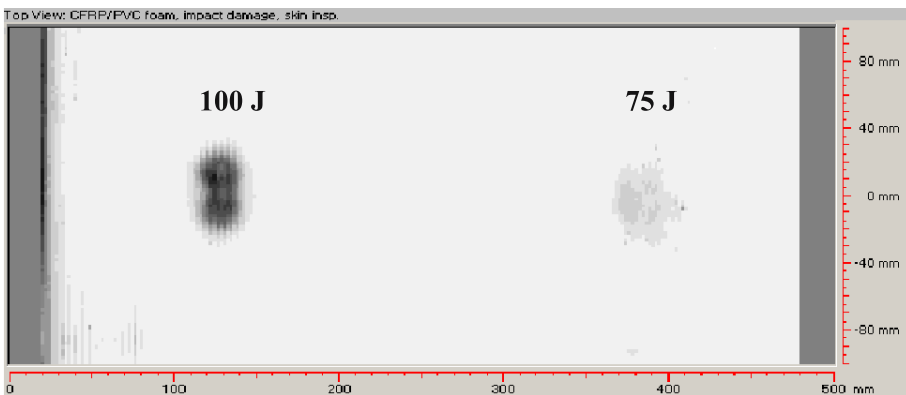


Figure 5. C-scan of panel with impact damages. Damaged area in the skin.

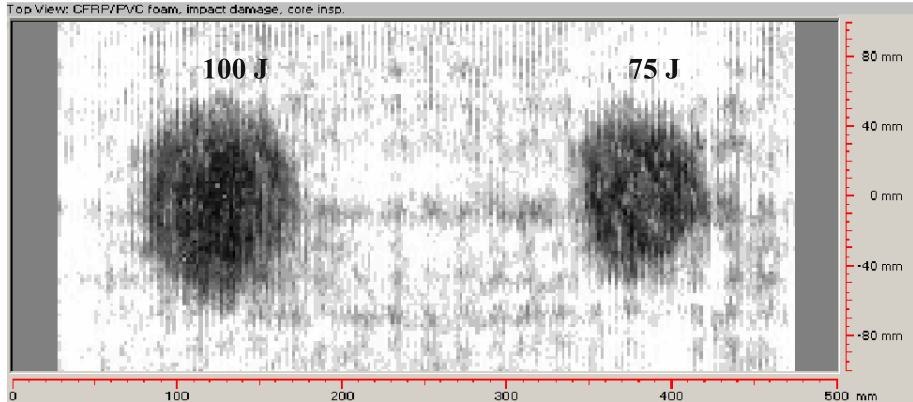


Figure 6. C-scan of panel with impact damages. Damaged area located in the core.

As seen on Figure 6 the extent of the core damage is clearly detected by large amplitude drops on rear side skin-core interface echoes. The defect size is now much larger (about  $100 \times 100 \text{ mm}^2$ ), compared to the indications seen on Figure 5, which indicate large core crushing damage.

#### 4. SCANNER EQUIPMENT FOR FIELD INSP.

Within the EUCLID RTP3.21 project some of the efforts have been put into further development of a portable automated ultrasonic track scanner (based on the existing ATS-1 scanner system from FORCE Technology) for large-scale inspection of composite structures. Because the scanner runs on its own track, the scanner is suitable for inspection of large composite structures, non-ferritic structures or structures with complex geometries. The scanner is built up by modules of 2-3m sections, and can, if needed, be enlarged to cover a scanning length of 6m. The scanner unit is controlled by the new P-scan generation called **P-scan System 4**, developed by FORCE Technology.

This scanner has proved to be very flexible in different inspection set-ups from the inspection of straight and slightly curved panels to the inspection of geometrical complicated joints. In the following figure the applicability and flexibility of this scanner are illustrated.

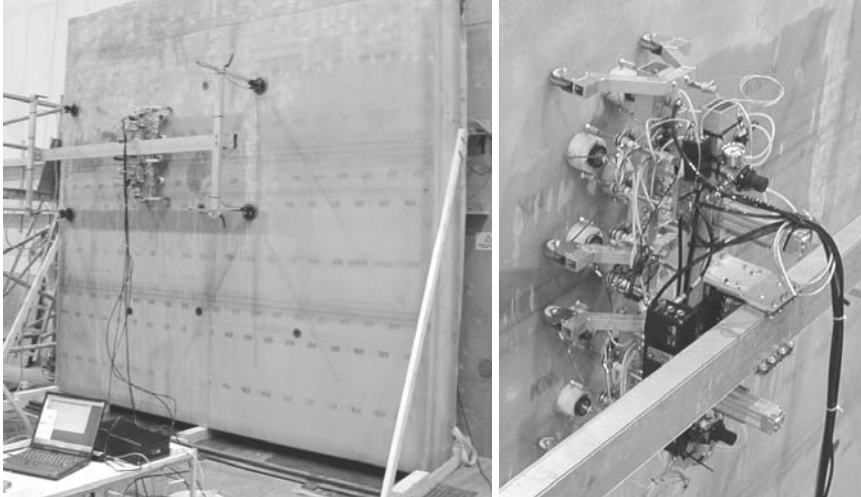


Figure 7. Top: Portable scanner unit applied on naval ship hulls. Bottom: Scanning of a stiffener in a large composite sandwich structure.

The speed/cost parameter is often one of the crucial parameters that determine what kind of NDT method that is the most effective. Therefore some of the work in the saNDI project is focused on developing faster inspection and scanning techniques. The critical defect size in large sandwich structures is of course here an important parameter and varies from relatively small areas near highly stressed structural parts to larger areas in low-stressed areas. However, compared to e.g. the aerospace industry, where small defects in the mm-size level are not acceptable, the critical defect size in the marine industry is probably closer to the m-size level.

A way of scanning a surface rapidly is by applying several transducers scanning the surface in lines (B-scan inspections) instead of the more time consuming area scanning technique (C-scan inspection) with only one or two transducers. This scanning concept has been implemented in the development of a new 8 channel portable Multi Probe Scanner (MPS).

A prototype version of this MPS with 8 transducers placed in a fixed array, with mutual distance of 100 mm, has now been developed. The new scanner is illustrated in Figure 8.



*Figure 8.* New portable 8 channel Multi Probe Scanner.

The scanner only moves the transducers in one direction; hence only 8 B-scans are recorded and therefore this technique is dedicated to spot check inspection. On basis of different field inspections the scanner has proven to be fast in different scanning set-ups.

## **5. CONCLUSION**

This paper represents the results obtained from the successful ultrasonic developing work performed within the EUCLID RTP3.21 [1] and the JP 3.23 THALES [2] projects.

New ultrasonic method for large-scale inspection of sandwich structures applied in the marine industry has been developed. By applying special high damped broadband transducers in the frequency range from 0,1-2 MHz, it has now been possible to detect typical defect types like skin-core debonding, core cracks and crushed core from impact damage. The method works in Pulse-Echo mode, which only requires access to one side of the structure.

An existing portable track scanner (ATS-1) for detailed inspection of large composite structures has been improved. The scanner has been enlarged and is now covering an effective scanning area of 6 x 0,5 m<sup>2</sup>. This

scanner has been tested on-side naval ships and proven to be versatile and flexible in different inspection set-ups, from the inspection of straight and slightly curved panels to the inspection of geometrical complicated joints.

In order to reduce the scanning time and thereby reducing the inspection costs a new 8 channel Multi Probe Scanner (MPS) has been developed and tested on-side naval ships. This scanner is designed for fast spot-check inspection of large composite structures with an effective scanning time of 2,4 m<sup>2</sup>/min.

## **ACKNOWLEDGMENTS**

The author acknowledges the EUCLID financial support for the development work and approval of this publication given by the Ministries of Defence of Denmark, Norway, United Kingdom, The Netherlands, France and Italy. Danyard Aalborg is acknowledged for manufacturing the test specimens.

This work was part of the SaNDI (THALES JP3.23) project with participants from Norway, Denmark, Sweden, Finland and the United Kingdom. The support of the Ministries of Defence of the five participating nations is gratefully acknowledged. All the partners including the shipyards within the international industrial consortium [2] are acknowledged for the design and manufacturing of test specimens.

## **REFERENCES**

1. [http://research.dnv.com/euclid\\_rtp3.21](http://research.dnv.com/euclid_rtp3.21)
2. <http://research.dnv.com/SaNDI/>

# EVALUATION OF SANDWICH MATERIALS USING ULTRASONIC AIR-COUPLED SCANNING TECHNIQUE

Kaj K. Borum

*Materials Research Department, Risø National Laboratory, P.O. Box 49, 4000 Roskilde, Denmark*

**Abstract** The ultrasonic Air-coupled scanning technique was used to evaluate the quality of sandwich panels. Scans of panels with defects such as debond between skin laminate and foam core, core crack and defects arising from mechanical tests are presented. The air-coupled technique is an easy technique to use since it can be performed directly in atmospheric air.

**Keywords:** ultrasonic scanning, air-coupled technique, non-destructive testing, defects, core crack, debond.

## 1. INTRODUCTION

The ultrasonic air-coupled technique has been developed heavily in the recent years. Better transducers that can overcome the high ultrasonic damping from the interface air/sandwich material have been developed.

An air-coupled through-transmission technique using separate sender and receiver transducer was evaluated for the ability to characterise the quality of sandwich materials. The main advantage of this technique compared with immersion technique is that the measurements can be performed in atmospheric air.

In order to have reference specimens with well-defined defects a series of test specimens with artificial defects were produced. The artificial defects were core cracks and debond between skin laminate and foam core. The scanning technique was used to characterize both the artificial defects and the damage that arose from mechanical tests on sandwich panels. The scans were also used to evaluate the quality of repair of the panels.

## 2. ULTRASONIC AIR-COUPLED TECHNIQUE

The ultrasonic air-coupled system is called Airtech 2400 and is manufactured by Ingenieurburo Dr. Wolfgang Hillger in Germany (see Figure 1). More information on the system can be found in [1]. The main advantage of the air-coupled technique compared to conventional ultrasonic equipment is that it avoids the disadvantages of immersion in water or the use of coupling gel and the time-consuming cleaning after the inspection.

Sandwich composites are inhomogeneous and anisotropic materials with extremely high sound attenuation. Often it is not possible to use pulse-echo technique because insufficient sound is reflected from the material. Through-transmission immersion technique with separate receiver and transmitter transducers on opposite sides of the component can be used to overcome some of the damping problem. However, the air-coupled technique eliminates the need of using a coupling media and is therefore a convenient system compared to immersion techniques (see [2] for a description of the immersion technique).

The difference in signal amplitude between transmitter and receiver transducer is app.  $-138$  dB due to the high difference in the acoustic impedance between the piezoelectric material and air and also between sandwich material and air. To overcome the high damping of the ultrasound at the interface air/sandwich material a special high power transducer with integrated preamplifier was used. It includes a composite system with impedance matching to air.

Two pairs of transducers were used: 50 kHz and 120 kHz. The lower frequency gives a lower attenuation and consequently a better penetration is obtained but a lower frequency also gives a lower axial resolution. Therefore, a trade-off between penetration and axial resolution must be made. For panels with foam core thickness above 60mm the 50 kHz transducers were used.

The scanning speed is lower for air-coupled technique compared to immersion technique. The pulse repetition frequency is dependant on the travel time from the sender transducer to the receiver transducer and due to the much lower ultrasonic speed in air (340 m/s) compared to water (1500 m/s) the pulse repetition frequency is much lower for the air-coupled technique.

The through-transmission technique requires access to both sides of the specimen and it has therefore limited use for in-field inspection which normally only allows for one-side access.

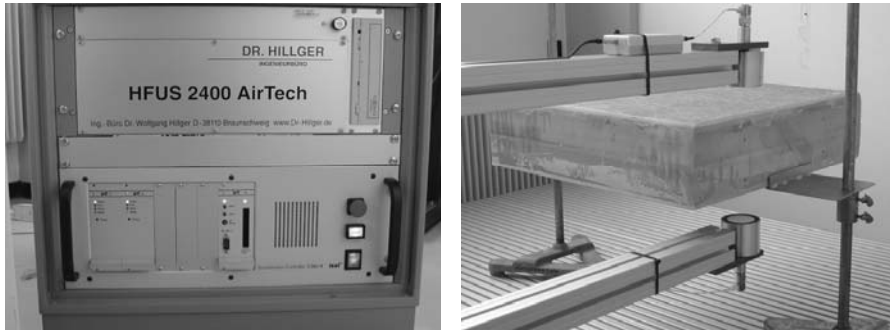


Figure 1. Ultrasonic air-coupled equipment. Left: Picture of the ultrasonic system unit and motor controller. Right: The transducer fork fixture mounted with 50 MHz transducers is shown. Panels up to 1m x 1.5m can be scanned.

### 3. SCANNING RESULTS

In the following a number of scanning examples are presented. The scale on all the plots are in dB and a high transmitted signal gives a dark tone (to the right on the greyscale).

#### 3.1 Scanning of panels with artificial defects

A series of panels with artificial defects: debond between skin laminate and foam core and core cracks were scanned. The material was glass-fiber skin laminate (6-9mm) and foam core (H80 – H200, 60 – 120mm core thickness). The resolution in the scans was 2mm between the measuring points in both directions. A pair of 50 kHz transducers was used.

The debond was made by applying a thin layer of uncured polyester on the core and cover it with a thin paper sheet before applying the skin layer. The core cracks were made by cutting cracks perpendicular to the surface in half depth of the core thickness. The opening at the surface were about 1mm. The core cracks were covered with a paper sheet (app. 15mm broad) before applying the skin layer.

In Figure 2 a scan of a panel with an artificial debond is shown. There is a high contrast of 20 dB between an intact and the debond area. The panel was scanned again after mechanical compression test and the debond was found to have increased to cover to whole width of the panel.

The scan of the panel with artificial core cracks is shown in Figure 3. The cracks are seen clearly and the contrast between an intact area and the crack is 17 dB.

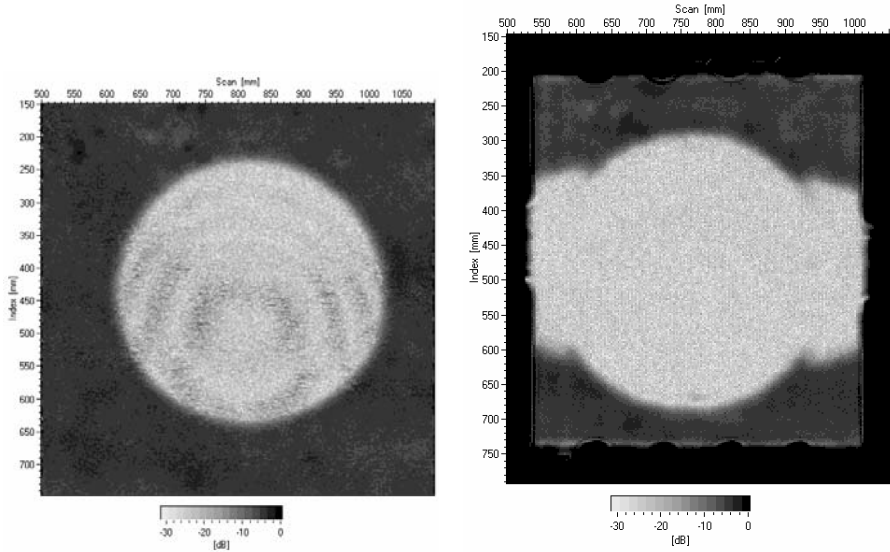


Figure 2. Scan of a panel with an artificial debond between skin laminate and foam core. Left: Scan of the panel with the initial debond defect. The panel measure 1m x 1m but only the inner 0.6m x 0.6m was scanned. Right: Scan after mechanical compression test. The panel was decreased in size in order to fit into the testing machine. The debond area has grown from the initial debond area to cover the whole width of the specimen.

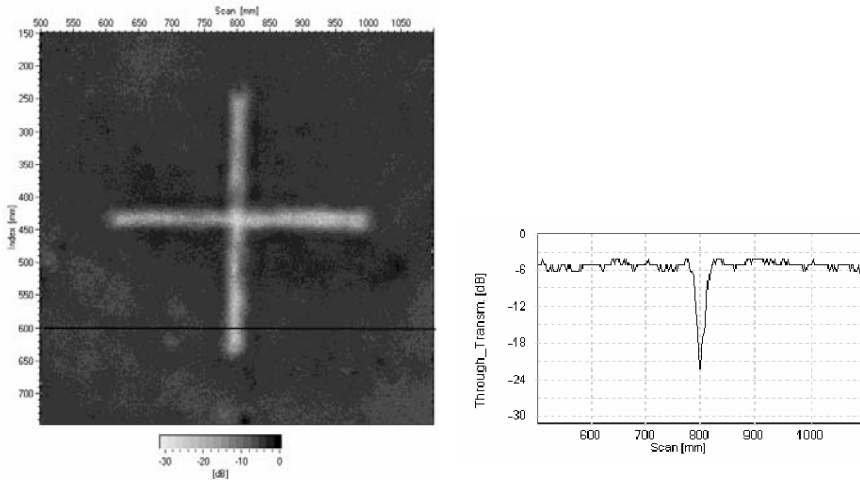


Figure 3. Left: Scan of a panel with an artificial core crack between skin laminate and foam core. The panel measures 1m x 1m but only the inner 0.6m x 0.6m was scanned. Right: Echo profile at the position indicated in the scan plot to the left. At the crack there was a drop of 17 dB in the received signal.

### 3.2 Scanning of panels after compression test

A series of panels were tested by mechanical compression tests. The specifications were: H80 foam core, core thickness 25mm, glass-fibre skin laminate thickness 3mm and dimension 560mm x 610mm. Some of the panels were made with an artificial debond in the middle of the panel. The panels were scanned after mechanical compression test and again after repair of the panels by resin injection. A pair of transducers of 50 kHz was used. The repair was not fully successful since for most panels only parts of the debonded areas were repaired properly. An example is shown in Figure 4. After repair the panel was tested again by compression test and the panel was scanned once again. The result is shown in Figure 6. The debond had propagated to a larger area than after the first compression test showed in Figure 4.

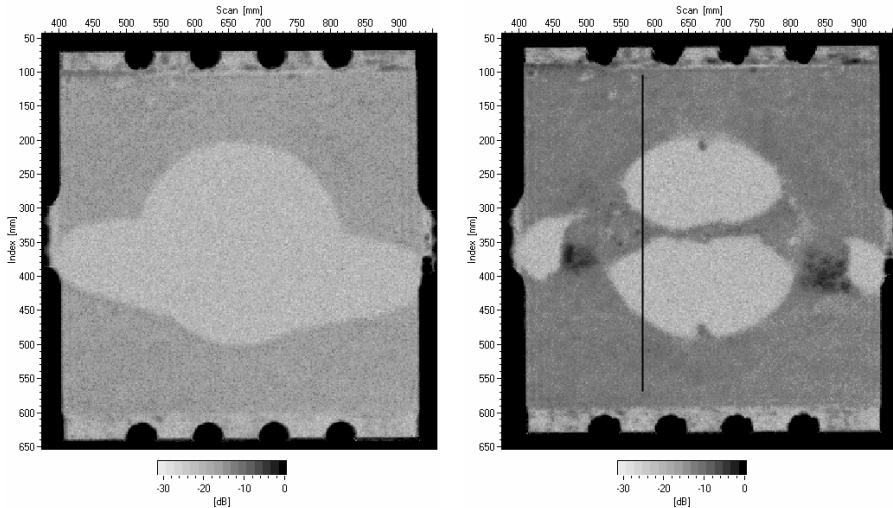


Figure 4. A panel with a Ø300 debond. Left: Scan after first compression test. Right: scan after repair by resin infusion. Only parts of the debonded areas are fully repaired.

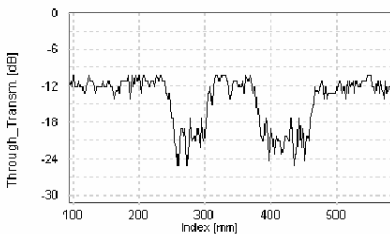


Figure 5. Echo profile in the line showed in Figure 4 right. In the repaired areas there are drops of app. 13 dB in transmitted signal indication that the repair is not successful in these areas.

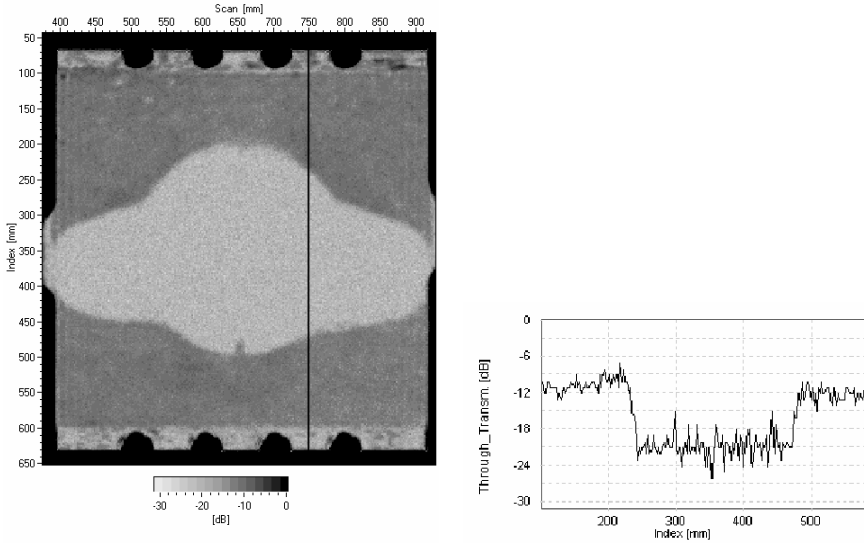


Figure 6. Left: Scan of a panel with a debond after mechanical compression test. The debond has propagated to a larger area than after the first compression test showed in Figure 4. Right: Echo profile at the position of the vertical line in the left scan plot. There is a decrease of app. 12 dB in the debonded area.

### 3.3 Scanning of panels after lateral pressure test

A series of panels were tested by lateral pressure test. For these test a series of specimens with varying debond size and positions were manufactured. An example of a scanning after the lateral test was performed is shown in Figure 7. The specifications for this panel was: H200 foam core, core thickness 30mm, glass-fibre skin laminate thickness 3mm and dimension 850mm x 1120mm. During manufacture an artificial debond ( $\text{Ø}200$ ) was made in lower right corner. From the initial debond two debonds propagate in vertical and horizontal directions. The debond was very clearly detected by the air-coupled scanning technique and the debonds could also be seen directly by visual inspection – see photograph of the panel in Figure 7.

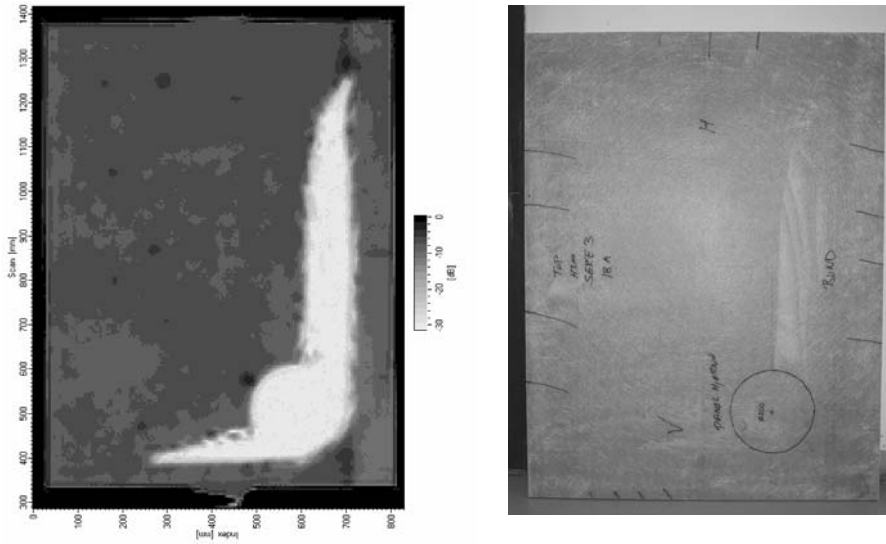


Figure 7. Panel with debond. Left: SSan after lateral pressure test. Right: Photograph of the tested panel.

### 3.4 In-situ scanning during mechanical test

The air-coupled scanning system was used in-situ to detect crack propagation. This work was done as part of a task that should predict damage tolerance in sandwich materials. More details can be found in [3]. The test setup is shown in Figure 8. The idea was to measure the position of the crack front at different stages during the loading of the panels. The specification for panel 18A was: H200 foam core, core thickness 50mm, glass-fibre skin laminate thickness 4.5mm and dimension 70mm x 500mm. In this case it was possible to use 120 kHz transducers that gives a better resolution than the 50 kHz transducers.

In order to introduce a vertical load to the lower skin laminate two steel plates were placed on each side of the skin laminate. A part of the core was removed and an initial starter crack was made with a razor blade extending 5mm away from the plate on each side. A constant displacement force was applied to the lower skin layer which resulted in crack propagation in the interface layer between skin laminate and foam core. In figure 9 a scan plot is shown. A black line indicates the crack front. The crack front is generally not a straight line due to local inhomogeneities in the materials. There is a drop of app. 17 dB from the intact area to the debonded area. It was difficult to see the crack front visually and therefore this technique was a good tool for finding the extension of the cracks.



*Figure 8.* Photograph of the in-situ ultrasonic measurement during mechanical testing. The air-coupled transducers are seen to the right. The lower skin laminates is pulled downward, which causes cracks to propagate between skin laminate and core.

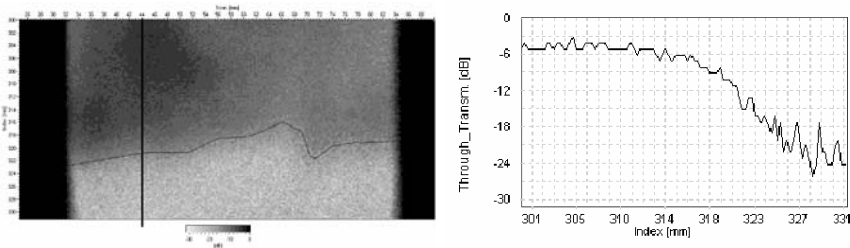


*Figure 9.* In-situ measurement of crack propagation. Left: Scan plot of the crack propagation. The crack front is marked with a black horizontal line. In the area under the black line the attenuation is higher due to debond between skin laminate and foam core. Right: A line profile taken at the position of the vertical line in the scan plot. There is a decrease of 17 dB in the debonded area.

#### 4. SUMMARY AND CONCLUSIONS

The main aim of this work was to characterise the quality of sandwich panels using the air-coupled through-transmission technique. The technique has the advantage that measurements can take place in atmospheric air. Access to both sides is necessary, which limits the in-field use. As a production and laboratory technique it is a good alternative to traditional immersion scanning technique.

Panels with artificial initial defects were scanned before and after repair and again after mechanical testing. The ultrasonic scanning could easily detect the artificial defects as well as the debonds arising from the mechanical testing. The air-coupled technique is an efficient method to measure the debonded area, normally difficult to observe by a visual inspection. The technique can be used to evaluate the quality of repair by resin infusion. In case of insufficient repair the ultrasonic damping remains high. The contrast between debonded and sound material is in most cases in the range 12-25 dB, which is a high contrast.

The air-coupled technique can also be used in-situ during mechanical tests to follow crack propagation between skin laminate and foam core.

Although the scanning is relative slow (app. 1 hour for 1 m<sup>2</sup>) the technique is automated and therefore requires little manpower.

## **ACKNOWLEDGEMENTS**

This work was part of the SaNDI (THALES JP3.23) project with participants from Norway, Denmark, Sweden, Finland and the United Kingdom. The support of the Ministries of Defence of the five participating nations is gratefully acknowledged.

## **REFERENCES**

1. Hillger, W. (2000), Ultrasonic Testing of Composites -- From laboratory Research to In-field Inspections (2000). In Proceedings (cd-rom) from 15th World Conference on Non-Destructive Testing, Rome, 15-21 October 2000,
2. Gundtoft H.E and Borum, K.K. (1996), Evaluation of Advanced Fibre Composites And Sandwich Structures by Ultrasonic Examination. In Krishnadas Nair, C.G. (ed.) Proceedings of the 14th World Conference on Non-Destructive Testing, New Delhi, 8-13 December 1996, Ashgate Publishing Company.
3. Borum, K.K. and Berggreen, C. (2004), Examination of Sandwich Materials Using Air-Coupled Ultrasonics. In: Proceedings (CD-ROM). 16th World Conference on Nondestructive Testing, Montreal (CA), 30 August-3 September 2004 (Canadian Institute for NDE, Hamilton, 2004) 10 p.

# STRUCTURAL NDE OF CFRP COMPOSITE MATERIALS USING FIBER BRAGG GRATING SENSORS

Jinsong Leng, Yanju Liu, Xingli Xu and Shanyi Du

*Centre for Composite Materials and Structures, Harbin Institute of Technology, No. 2 YiKuang Street, P.O. Box 3011, Harbin 150080, P.R. China*

lengjs@hit.edu.cn

**Abstract** In this paper, the Fiber Bragg Grating (FBG) sensors are real time employed to simultaneously monitoring the cure process of CFRP composite laminates with and without damage. Furthermore, the NDE of smart composite laminates embedded FBG sensors are performed by using the 3-point bending test.

**Keywords:** NDE, fibre optic sensor, Fiber Bragg Grating (FBG), smart composite.

## 1. INTRODUCTION

In recent years, advanced composite structures are used extensively in many industrial areas such as aerospace, aircraft, automobile, pipeline, civil engineering. The quality and reliability is the key of the advanced composite structure that is often used under harsh environment. To improve the performance of advanced composite structures, the processing monitoring is definitely demanded to obtain the properly cure rate and cure cycle.

A number of cure monitoring techniques have been used in the past including dielectric analysis, nuclear magnetic resonance, Raman spectroscopy [1–3]. Also, a sort of non-destructive evaluation (NDE) techniques have been developed in the past including ultrasonic scanning, acoustic emission (AE), shearography, stimulated infrared thermography (SIT), vibration testing, sonics, radar, conductivity, etc. [4]. The challenge is to develop new techniques which can perform the on-line structural health assessment started from manufacture of composite structures to the real service of these structures in field. That implies we need combine the cure monitoring methods and NDE technology together. However, the classical techniques of cure monitoring and NDE methods are difficult to combined and not well suited for on-line structural monitoring, because of the difficulties in making *in situ* implementation.

Recently smart materials and structures provide the possibility of structural health monitoring on-line and in situ. Smart materials and structures, not only have traditional structural materials' functions, but also have actuating, sensing and microprocessing capability. Fiber optic sensors (FOSs) are very important sensors used in smart materials and structures because of their many advantages. One of the main advantages is that these sensors are very light in weight and small enough that they can be embedded in composite materials in a nonobtrusive manner that does not degrade structural integrity. Fiber optic sensors in smart structures are an enabling technology that will allow engineer to add nervous system to their designs, enabling damage assessment and many other capabilities to structures that would be very difficult to achieve by other means [5–8].

A sort of fiber optic sensors have been developed to monitor the cure process of the composite materials such as fluorescence optrode sensors, fiber optic interferometric sensor based ultrasonic wave, infrared transmitting fiber optic sensor, fiber optic sensor based on reflective index, fiber optic cure sensor based on the microbend effect, evanescent wave spectroscopy [9–11].

In this paper, the experimental results of cure monitoring of smart composite laminates with and without damages by using the Fiber Bragg Grating (FBG) sensors are presented. By the way, the NDE of smart composite laminates embedded FBG sensors are performed by using the 3-point bending measurement.

## 2. PRINCIPLE OF FIBER BRAGG GRATING (FBG) SENSORS

The uniform FBG includes a segment of optical fiber in which a periodic modulation of the core refractive index was made. Usually, in-fiber FBG can be fabricated on the photosensitive (Ge-doped or hydrogen soaked) singlemode optical fiber by using the UV laser source in 240–248 nm. Basically, the principle of the fiber Bragg grating (FBG) sensor is based on the measurement of the changes in reflective signal, which is the center wavelength of back-reflected light from a Bragg grating, depends on the effective refractive index of the core and the periodicity of the grating. According the Bragg condition, the Bragg wavelength can be expressed as [11]:

$$\lambda_B = 2n_{eff}\Lambda \quad (1)$$

Here  $\lambda_B$  is the Bragg grating wavelength,  $\Lambda$  is the grating periodic spacing,  $n_{eff}$  is the effective reflective index of the fiber core. So the Bragg wavelength will shift with changes in either  $n_{eff}$  or  $\Lambda$ . When a external mechanical or thermal deformation are subjected onto the grating area, the effective reflective index will changed as well as the periodic spacing. The Bragg wavelength shift caused by the change of strain ( $\Delta\varepsilon$ ) and change of temperature ( $\Delta T$ ) can be

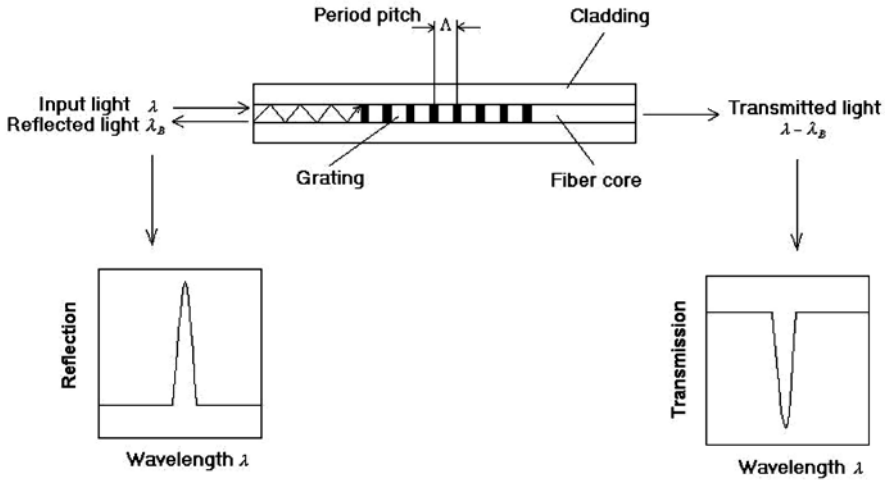


Figure 1. Schematic illustration of Fiber Bragg grating (FBG) sensor.

expressed in the form

$$\Delta\lambda_B = \alpha\Delta\varepsilon + \beta\Delta T \quad (2)$$

where

$$\alpha = \lambda_B(1 - p_e) \quad (3)$$

$$\beta = \lambda_B(\alpha_\Lambda + \alpha_n) \quad (4)$$

where  $p_e$  is an effective strain-optic constant.  $\alpha_\Lambda$  is the thermal expansion coefficient (approximately  $0.55 \times 10^{-6}$  for silica).  $\alpha_n$  is the thermo-optic coefficient, approximately equal to  $8.6 \times 10^{-6}$  for the Germanium doped silica-core fiber.  $\alpha$  and  $\beta$  are the relevant wavelength-strain sensitive factor and wavelength-temperature sensitive factor, respectively.

### 3. EXPERIMENTS AND RESULTS

In order to detect and evaluate the damages of composite materials during the cure process, two composite specimens with and without delamination were cured in heat-press machine simultaneously. The dimension of CFRP laminates ( $0_4/90_4/90_4/0_4$ ) is 240 mm  $\times$  240 mm  $\times$  2 mm. One of CFRP specimens has a circular delamination with 30 mm in diameter that was made by using a PTFE film disc. One FBG sensor was embedded between first and second layers of CFRP prepregs in the  $0^0$  direction. The delamination was located between 8th and 9th layers. A K-type thermocouple sensor was embedded in the CFRP composite laminate as a reference temperature sensor to monitor the temperature during cure.

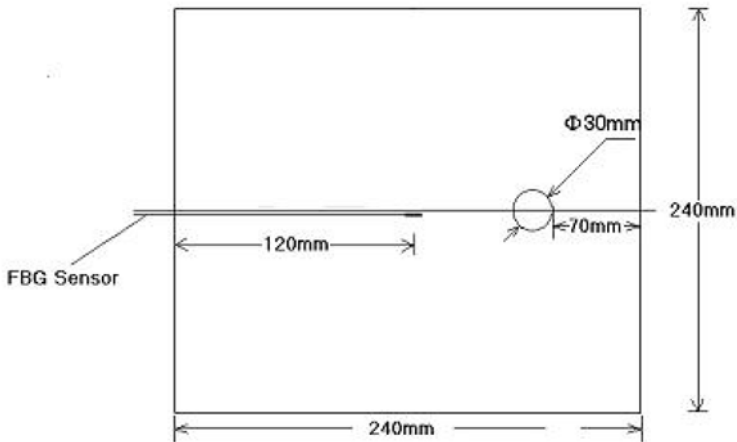


Figure 2. Schematic diagram of CFRP composite specimen ( $0_4/90_4/90_4/0_4$ ) with one delamination.

The length of each fiber optic sensor element was about 10 mm. Figure 2 shows the schematic diagram of CFRP composite specimen ( $0_4/90_4/90_4/0_4$ ) with the indicating location of fiber optic sensors as well as the delamination. In order to avoid any edge effect, the FBG sensor was placed at the middle of the panel. In this experiment, the sample to sample variation in CFRP is very small like 0.1 mm, so this will not affect the cure monitoring results. As the size of the CFRP sample is large enough, and the sensor was located in the middle of the composite coupon, so there was not any edge effect.

Figure 3 shows the cure temperature curve of the CFRP laminates by using the thermocouple. In fact, the cure process of composite materials includes three main phases. First stage is ramp-up phase. During this phase, the temperature of the heat-press machine is increased to  $120^\circ\text{C}$ . The epoxy matrix becomes viscous in this stage. This duration demands one hour. The second stage is real cure phase. During this stage, the thermoset polymer matrix had been cross-linked and resin begins to cure. The cure phase takes approximately one hour. The cooling-down phase of composite is the third stage, which is cooled the composite specimen to room temperature. The time of cool-down stage is nearly 3.5 hours in our laboratory.

The cure monitoring curves of CFRP composite laminates with and without damages by using FBG sensors are shown in Figure 4. The both cure curves have similar track with cure temperature curve shown in Figure 4. The major reason is that the influence of the varied temperature on FBG sensor is more significant rather than effect of shrinkage strain on FBG sensor. From this graph, the three major cure phases can be seen. It is also observed that there are differences between the cure curves of composite with and without damages,

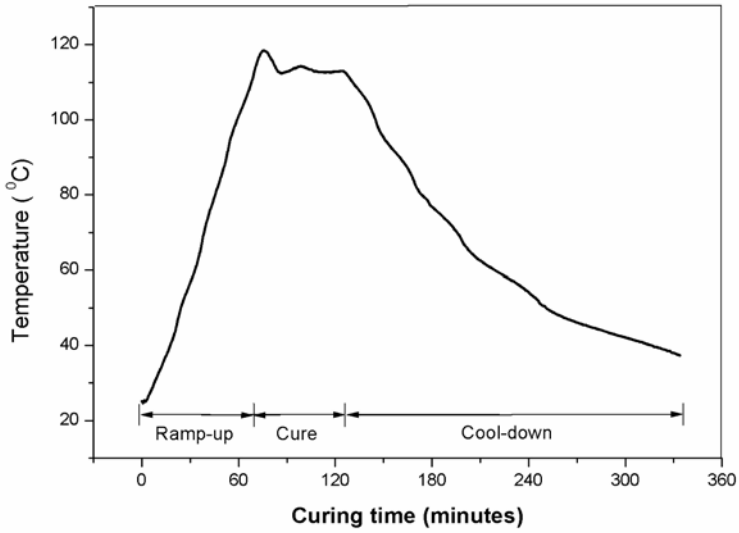


Figure 3. Cure temperature curve of the CFRP laminate by using the thermocouple.

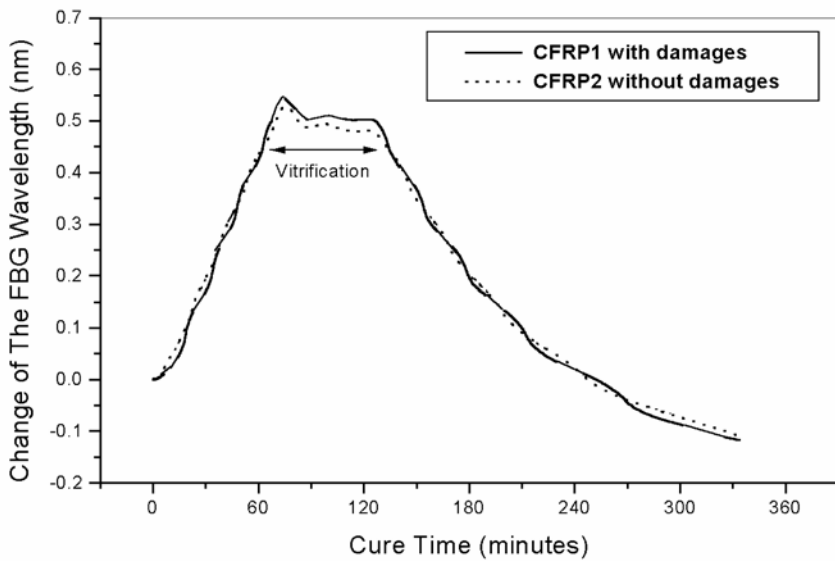


Figure 4. Cure monitoring curves of CFRP composite laminates (0<sub>4</sub>/90<sub>4</sub>/90<sub>4</sub>/0<sub>4</sub>) with and without damages by using the FBG sensors.

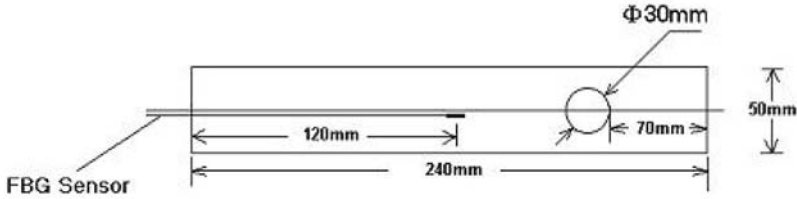


Figure 5. Diagram illustration of chopped CFRP composite specimen with delamination for 3-point bending test.

especially in the vitrification phase and final cure strain. However, there are not very clearly to show the significant difference between the two curves. Possible reason is that locations of the FBG sensors are not very close to the location of the delamination in the composite panel. So the FBG sensors are not very sensitive to the damage. However, the final cure strain still was proved that the cure strain of composite specimen with damage is higher than that of composite specimen without damage. At the meantime, the vitrification phase still could be used as a criterion of defective detection. Thus, the damage of composite could be detected under cure process on-line.

In this paper, the FBG sensor was also examined to evaluate structural integrity. In fact, the 3-point bending measurement of CFRP laminates with and without damages is performed to compare the difference of flexural strain. The specimens are chopped from above mentioned CFRP composite coupon ( $0_4/90_4/90_4/0_4$ ) as shown in Figure 2. The dimension of chopped CFRP composite specimen is 240 mm  $\times$  50 mm  $\times$  2 mm. The diagram illustration of chopped CFRP composite specimen with delamination was shown in Figure 5. The experiments were done in an INSTRON mechanical testing machine.

Figure 6 shows the 3-point bending test of the same CFRP specimens by using embedded FBG sensors. It is can clearly see that the flexural strains with and without delamination are much different under same bending loading.

The flexural strain of damaged CFRP composite specimens is more than that of undamaged CFRP specimens. By the way, the bending modulus of CFRP specimens with delamination is less than that of CFRP specimens without delamination. Because the delaminations in CFRP composite laminate causes significant stiffness degression of CFRP laminates.

#### 4. CONCLUSIONS

In this paper, the experiments of real-time cure monitoring of smart composite laminates with and without damages by using the FBG sensors are performed. Furthermore, the 3-point bending test of composite laminates with and without damages was carried out by using the FBG sensors. Compare the

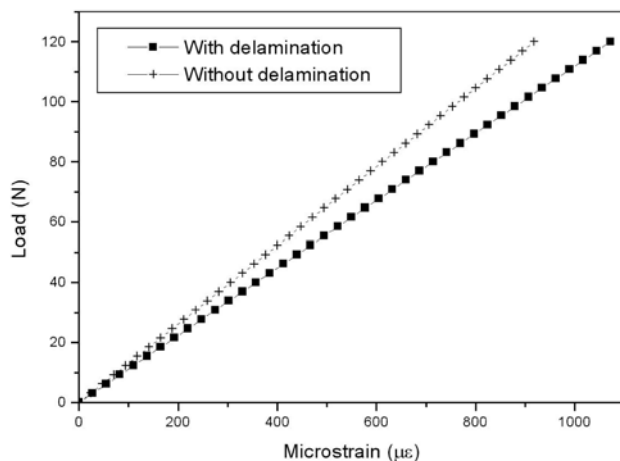


Figure 6. Comparison of experimental results of 3-point bending test of CFRP composite laminates with and without delamination by using embedded FBG sensors.

cure compressive strain of composite laminates with and without damages, we can obviously see that the cure strain of composite without damages is less than cure strain of composite with a circular delamination in the  $0^0$  direction. The embedded FBG sensor also can be used to inspect the delamination of composite laminates under 3-point bending test.

## REFERENCES

- [1] F.I. Mopsik, S.S. Chang and D.L. Hunston, Dielectric measurements for cure monitoring, *Material Evaluation*, 47 (1989) 448.
- [2] J.M. Barton, G.J. Buist, I. Hamerton, B.J. Howlin, J.R. Jones and S. Liu, High temperature  $^1\text{H}$  NMR studies of epoxy cure: a neglected technique, *Polymer Bull.*, 33 (1994) 215–219.
- [3] C.J. Debakker, G.A. George, N.A. St. John and F.M. Fredeicks, The kinetics of the cure of an advanced epoxy-resin by Fourier transform Raman and near-infrared spectroscopy, *Spectrochimica Acta Part A – Molecular Spectroscopy*, 49 (1993) 739–752.
- [4] D.M. McCann and M.C. Forde, Review of NDT methods in the assessment of concrete and masonry structures, *NDT&E International*, 34 (2001) 71–84.
- [5] R.M. Measures, Fiber optic strain sensing, in: *Fiber Optic Smart Structures*, E. Udd (ed.), John Wiley & Sons, New York 1995.
- [6] K.T.V. Grattan and B.T. Meggitt, *Optical Fiber Sensor Technology: Devices and Technology*, Chapman & Hall, 1998.
- [7] S.Y. Du, J.S. Leng and D.F. Wang, *Smart Material Systems and Structures*, Science Press, Beijing, 2001.
- [8] J.S. Leng and A. Asundi, Active vibration control system of smart structures based on FOS and ER actuator, *Smart Materials and Structures*, 8 (1999) 252–256.

- [9] V.M. Murukeshan, P.Y. Chan, L.S. Ong and L.K. Seah, Cure monitoring of smart composites using Fiber Bragg Grating based embedded sensors, *Sensors and Actuators* 79 (2000) 153–161.
- [10] A.L. Kalamkarov, S.B. Fitzgerald and D.O. MacDonald, The use of Fabry Perot fiber optic sensors to monitor residual strains during pultrusion of FRP composites, *Composites: Part B*, 30 (1999) 167–175.
- [11] A. Othonos and K. Kalli, *Fiber Bragg Gratings, Fundamental and Applications in Telecommunications and Sensing*, Artech House Inc., (1999) 95–99.

# STUDY OF THE HYGRO-MECHANICAL BEHAVIOR OF CORRUGATED CARDBOARD

Samir Allaoui<sup>1</sup>, Zoheir Aboura<sup>2</sup> and Malk Benzeggagh<sup>1</sup>

<sup>1</sup>*Laboratoire Roberval de Mécanique, U.T.C Centre de Recherche Royallieu, B.P. 20529, F-60205 Compiègne Cedex, France*

<sup>2</sup>*L3M, IUT de Tremblay en France Paris 8, Rue de la Râperie, F-93290 Tremblays-en-France, France*

**Abstract** Corrugated cardboard is very sensitive to atmospheric conditions. The aim of this work is to study the effects of these parameters, especially the relative humidity (RH), on the mechanical behavior of corrugated cardboard sandwich structure. Tensile and three-point bending tests were used under various rates of relative humidity. An analytical model based on the classical laminate plate theory is used to predict the elastic behavior of the corrugated cardboard under different atmosphere conditions. The model is then extended to predict the inelastic behavior of the corrugated cardboard from the behavior of its components.

**Keywords:** corrugated cardboard, hygro-mechanical behavior, modeling.

## 1. INTRODUCTION

Corrugated cardboard pertaining to papers family is one of the most used packing currently. Its employment does not cease increasing each year and covering the various types of packing, such containers and pallets, and extending to other fields such as the dwellings. This success is due to the various virtues of this material: good protection of the product, low cost and can be recycled as well as biodegradable. Biodegradable product are more and more demanding as being a major concern again the protection of the environment and hence respect a durable development.

For a better optimization and diversification of the use of corrugated cardboard, knowledge of its mechanical characteristics and failure, as well as the apprehension of its behavior, is necessary.

The corrugated cardboard is an orthotropic sandwich with the surface plies (facing) providing bending stiffness, separated by a lightweight bending core (fluting) that provides shear stiffness. Two main directions characterize this material. The first noted MD (machine direction) corresponds to the direction

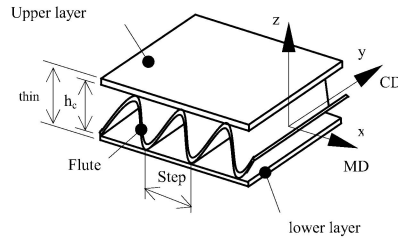


Figure 1. Cardboard panel geometry.

Table 1. Mechanical and geometrical characteristics of the constituent of the corrugated cardboard.

	$H$ (mm)	$E_{MD}$ (Mpa)	$E_{CD}$ (Mpa)	$\nu_{xy}$	$\nu_{yx}$
Upper layer	0.235	4514.53	1895.83	0.282	0.215
Flute	0.19	4458.6	1944.5	0.277	0.115
Lower layer	0.235	4703.75	1854.3	0.353	0.088

of manufacturing of the material. The second noted CD (cross direction) corresponds to the transverse direction and coincides with the  $y$  axis (Figure 1).

Aboura et al. have developed an approach regarding corrugated cardboard as monolithic material and have adapted simple's mechanical tests to characterize this material [1, 2]. The tests were carried out under a controlled atmosphere (23°C and 50% RH) according to the recommendations of French standard NF Q 03–010. They developed an analytical model to predict elastic and inelastic behavior of the material [1, 3]. This model is based on the classical laminate plate theory and was inspired by different studies [4–6].

This work purposes to study the effect of the atmosphere conditions, in particular the effect of moisture, on the mechanical behavior of the corrugated cardboard.

First, a study the moisture equilibrium corresponding to the water content in each layer and the sandwich is done. Once the moisture equilibrium achieved, the corrugated cardboard was tested in tensile and three-point bending tests at controlled atmosphere. The relative humidity levels used vary from dry conditions (35% RH) to severe conditions (90% RH). The difficulty at these conditions consists in handling the least possible the specimens. Methodology of measurement developed in a previous study [7] is used. Finally the analytical model developed by Aboura et al. was used to predict the elastic properties of the material at different atmospheres.

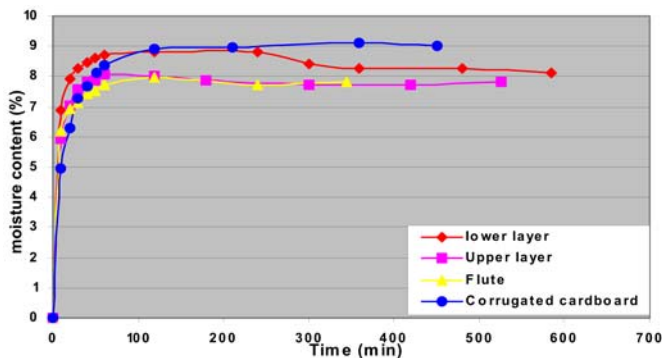


Figure 2. Moisture content at equilibrium for corrugated cardboard and its constituents.

## 2. MOISTURE EQUILIBRIUM OF THE MATERIAL

Two layers and one flute compose the corrugated cardboard used in this study. All the constituents are composed with 100% cellulose recycled fibers. Table 1 shows the constituents geometrical and mechanical characteristics. The thickness of the sandwich is 4.1 mm.

Mechanical tests will be made under various controlled atmospheres. Specimens must be preliminary conditioned to reach a state of moisture equilibrium in these conditions. Standard French norm NFQ 03–010 recommends 24 hours conditioning for any kind of paperboards.

Square specimens of 5 cm of the corrugated cardboard and its components were made. They were conditioned in a climatic chamber under conventional conditions (23°C and 50% RH) during 24 hours. Once the equilibrium is reached, the specimens were weighed and these measurements were used as references. It assumed that the equilibrium at 50% RH corresponds to a moisture content of 6% (dry basis) in each specimen [8]. Then, a rate of 95% RH is imposed followed by a regular weighing of specimens to evaluate the moisture content. The balance used has a precision of 0.01 mg.

After 100 minutes the moisture equilibrium was achieved. This state corresponds to moisture content of 8% at 9% for corrugated cardboard and its components (Figure 2). If the dry basis is considered, the moisture content will be 15%.

## 3. MECHANICAL TESTS UNDER VARIOUS RH

Tensile and three-points bending tests were carried out on specimens of corrugated cardboard on a tensile testing machine, which is equipped with a climatic chamber. The temperature is fixed at 23°C and the atmospheric conditions vary between 35% to 90% RH.

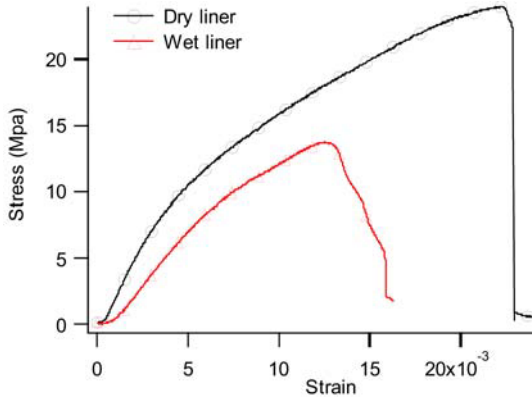


Figure 3. Tensile test of dry layer and wet one at 90% RH (CD).

Before the tests, specimens were conditioned in a climatic chamber under each value of RH, during 24 hours to reach a state of moisture equilibrium. A thermo-hygrometer (precision of  $\pm 3\%$  RH) was used to control the rate of humidity.

### 3.1 Tests conditions

The difficulty of the tests consists in handling the least possible the specimens. For that, the methodology of measurement which are developed in previous study [7] is used.

A particular attention is done at high level of moisture. Indeed, a phenomenon of condensation occurs which produce a water drop and then risk to wet the paperboard. This effect is shown on Figure 3. The Young's modulus and the maximum stress and strain are strongly affected by this phenomenon. It is then important at high RH to check before each test that the specimen is not wet.

Another phenomenon is observed during the conditioning of the specimens. By increasing RH, a deformation of the cardboard is observed inducing a curvature. This phenomenon has been modeled for the case of paperboard by Gendron [8]. This phenomenon is more pronounced in the CD.

These shapes did not affect the tensile tests. For the three-points bending tests, specimens were tested in two configurations. The load is applied on the convex part of the specimen in the first configuration and on the concave part for the second one. It was found that the elastic behavior is the same one for the two cases. On the other hand the stress and deflexion of collapse are more significant for the specimens tested on the concave part (Figure 4) and this under all the atmospheres. For the follow bending tests, we will alternate

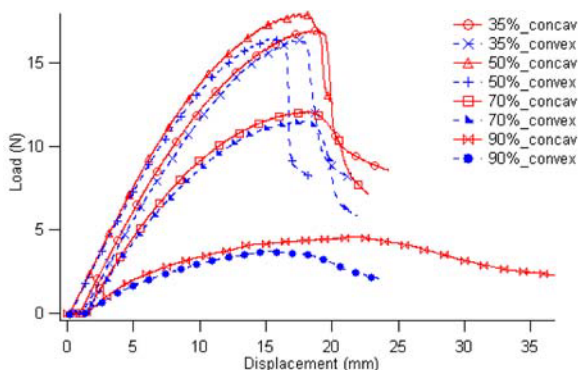


Figure 4. Bending test on convex and concave configuration under different rates of RH (corrugated cardboard in CD).

Table 2. Results of tensile and bending tests under different rates of RH.

		Relative Humidity %			
		35	50	70	90
		<b>Machine Direction</b>			
Bending results	Rigidity (Mpa)	1283.71	1334.57	1166.62	729.09
	Standard deviation (Mpa)	53.62	95.1	33.88	15.66
	Er (%)	-3.81	0	-12.58	-45.37
	<b>Cross Direction</b>				
	Rigidity (Mpa)	804.9	813.06	682.45	373
	Standard deviation (Mpa)	14.08	29.42	22.76	35.92
Er (%)	-1.003	0	-16.06	-54.12	
		<b>Machine Direction</b>			
Tensile Results	Young modulus (Mpa)	648.88	644.45	621.25	430.83
	Standard deviation (Mpa)	25.21	28.15	18.3	9.72
	Er (%)	0.69	0	-3.6	-33.15
	<b>Cross Direction</b>				
	Young modulus (Mpa)	488.66	433.1	422.5	275
	Standard deviation (Mpa)	21.33	21.1	11.09	24.19
Er (%)	12.83	0	-2.45	-36.5	

between the two configurations, and an average of mechanical results will be done.

### 3.2 Results and discussion

Table 2 shows the results obtained during tensile and bending tests. The conventional conditions (23°C and 50% RH) are used as references. Parameter *Er*, which is a relative deviation from references conditions, is calculated as

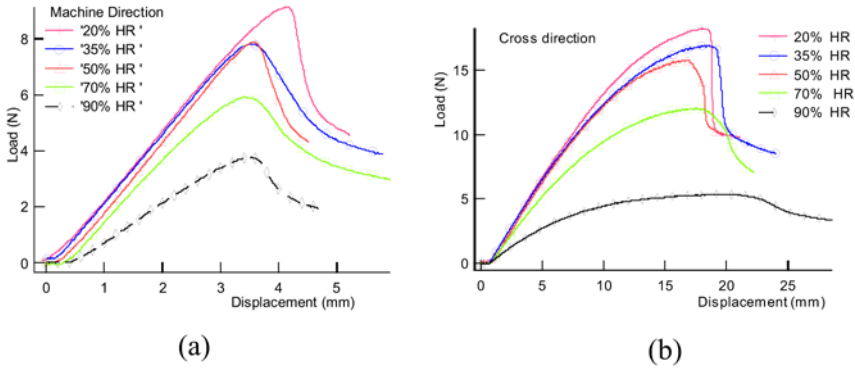


Figure 5. Three-point bending curves under different rates of RH.

follow:

$$Er = \frac{\text{Elastic properties at RH} - \text{Elastic properties at 50\% RH}}{\text{Elastic properties at 50\% RH}} \times 100 .$$

In dry conditions (35% RH), the elastic characteristics do not change and remain in the field of dispersion ( $Er < 4\%$ ), except for the corrugated cardboard in the CD tensile test where  $Er = 12, 83\%$ .

The increase of moisture makes fall the elastic characteristics. This fall is more significant on the bending tests. Indeed, by increasing the moisture content at 70% RH, the Young modulus do not change in the two directions of material. Contrary to tensile tests, the bending stiffness falls under these conditions. The maximum value of fall is 16% in the CD. In the very wet conditions (90% RH), the elastic characteristics break down. The falls of these parameters vary from 33,15% for the Young’s modulus in the MD to a maximum of 54% for the bending stiffness in the CD.

The elastic limit and the failure stress change according to the rate of moisture in the cross and machine direction (Figures 5 and 6).

The effect of moisture is more significant in the cross dirsection than in the machine direction. This can be explained by the fact that the behavior of material in the cross direction depends on the hydrogen lies between the cellulose fibers which change when the paperboard was subjected to a change in humidity content.

#### 4. ANALYTICAL MODELING

An analytical model of the elastic behavior of corrugated cardboard was developed [1, 2]. It takes into account mechanical properties and geometrical parameters (core thickness, fluting step, skin thickness) of the components. This model, based on the classical laminate plate theory, was extended to pre-

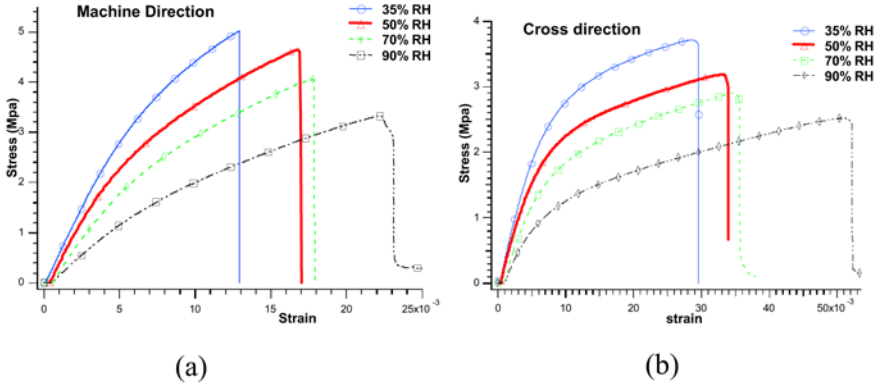


Figure 6. Tensile curves under different rates of RH.

Table 3. Mechanical characteristics of the liners and flute under different rates of RH.

		Relative Humidity (%)		
		50	70	90
Upper layer	$E_{MD}$ (Mpa)	4322	4037	2894
	$E_{CD}$ (Mpa)	2048	1902	1477
Flute	$E_{MD}$ (Mpa)	5107	4805	3319
	$E_{CD}$ (Mpa)	1962	1830	1161
lower layer	$E_{MD}$ (Mpa)	4433	4493	3099
	$E_{CD}$ (Mpa)	2033	1828	1000

Table 4. Model results under different rates of RH.

		Relative Humidity (%)		
		50	70	90
$E_{MD}$ model	(Mpa)	<b>712</b>	<b>686.07</b>	<b>475.01</b>
Model / exp.	(%)	10.48	10.43	10.25
$E_{CD}$ model	(Mpa)	<b>391.47</b>	<b>384.55</b>	<b>253.98</b>
Model / exp.	(%)	-9.61	-8.98	-7.65
$G_{xy}$ model	(Mpa)	<b>200.85</b>	<b>195.76</b>	<b>131.37</b>

dict the inelastic behavior of the material [3]. This study purpose to test the validity of this approach under different atmospheres conditions.

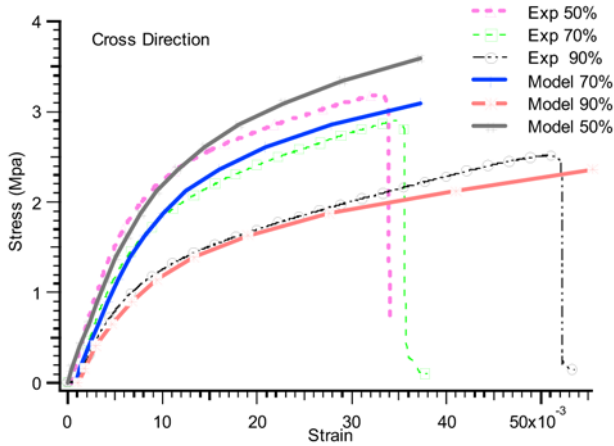


Figure 7. Modeling of the mechanical behavior of the corrugated cardboard under different rates of RH.

## 4.1 Elastic properties

The model need as input the elastic properties of the skins an flute obtained by tensile tests under different rates of 50%, 70% and 90% of RH (Table 3). The predicted properties at each rate of RH are compared to the experimental results (Table 4).

At 50% HR, the model estimates the Young modulus with an error of 10% compared to the experiment. This error is caused by the fact that the model does not take account of the effect of the manufacture process. During this process the skins lose some of their rigidity.

The model results at each rate of RH compared to the experimental ones gives practically the same error. This error is about 10% in the MD. In the CD we note a light fall of the error in estimation of the elastic characteristics. However this fall remains in the field of dispersion (2%). From that we deduce that the interface between the skins and flute does not affect the behavior of corrugated cardboard. We note that the model predict correctly the elastic properties.

## 4.2 Inelastic behavior

To predict the inelastic behavior of the corrugated cardboard, the model requires the knowledge of the behavior laws of the components of corrugated cardboard [3]. Considering the assumption of iso-strain, in a first approach, the model will be fed by the experimental results of tests carried out on the skins and flute under different atmospheric conditions. The inelastic predict behavior of the model in the MD is shown on the Figure 7.

On the whole of the rates of humidity, a good correlation between the results of the model and experimental ones is noted. At 50% RH, and 70% RH the inelastic predicted behavior over estimate the experiment one contrary at 90% HR. This is probably due to the effect of the interfaces which are not taking into account on the model.

The prospect for this study is to develop a macro-micro law of the behavior of cellulose fibers. This law will make it possible to predict the behavior of the skins and thereafter that of the corrugated cardboard.

## 5. CONCLUSION

The paperboard is a very sensitive material to the environmental conditions, especially moisture, but also with any handling. The corrugated cardboard showed sensitivity to the relative humidity of the environment tests. A particular attention must be made during these tests in order to not perturb the results.

Concerning elastic properties, they change significantly beyond 70% RH. This effect is more perceptible on bending characteristics than the tensile ones. Thus bending stiffness falls by 54% when the RH reaches 90%.

For the behavior beyond elastic phase, it has been shown that the failure characteristics, stress and strain failure, are even more sensitive to the effect of moisture.

The effect of the moisture in the cross direction is more significant than in the machine direction because of privileged orientation of the cellulose fibers.

An analytical model developed in previous study was applied to predict the behavior of the corrugated cardboard under atmospheric conditions. It has been found that this approach can predict correctly the elastic an inelastic behavior.

## REFERENCES

- [1] Aboura Z., Talbi N., Allaoui S. and Benzeggagh M.L. "Elastic behavior of corrugated cardboard: Experiments and Modeling" *Composite Structures*, 2004, 63, 53–62.
- [2] Aboura Z., Allaoui S. and Benzeggagh M.L. "Etude et modélisation du comportement élastique d'une structure sandwich de type carton ondulé", *JNC 13, Strasbourg* 2003, 1027–1036.
- [3] Allaoui S., Aboura Z. & Benzeggagh M.L. "Elastic and inelastic modeling of corrugated cardboard", *ICCM 15, Durban South Africa*, 2005.
- [4] Ishikawa T, Chou TW. "Stiffness and strength behavior of woven fabric composites". *Journal of Material Science*. 1982, 17, 3211–3220.
- [5] Aboura, Z., Chouchaoui, C.S. and Benzeggagh, M.L., "Analytical model of woven composite laminate. Superposition effect of two plies" *ECCM 6, 1993, Bordeaux*.
- [6] Scida D., Aboura Z., Benzeggagh M.L. and Bocherens, E., "Prediction of elastic behavior of hybrid and non-hybrid woven composite" *Composites science and technology*. 1997, 57, 1727–1740.

- [7] Allaoui S., Aboura Z. & Benzeggagh M.L. “Effets des conditions environnementales sur le comportement mécanique de structures sandwich de type carton ondulé”, JNC14, Compiègne 2005, 1165–1174.
- [8] Gendron G., Dano M.L. and Cloutier A. “A numerical study of the hygro-mechanical deformation of two cardboard layups” *Composite Sc. and techn.*, 2004, 64, 619–627.

**NEW MATERIALS AND  
MATERIALS CHARACTERISATION**

# NEW CONCEPTS FOR SANDWICH STRUCTURES

Joachim L. Grenestedt

*Department of Mechanical Engineering, Lehigh University, Bethlehem, PA 18015, USA*

**Abstract** This paper summarizes a number of presumably new concepts within the general area of sandwich structures. The concepts have been analyzed numerically and/or analytically, manufactured, and tested. The concepts include strip or grid skin sandwich for light weight structures; graded or laminated sandwich cores; "artificial" balsa cores with higher strength and stiffness than conventional end grain balsa; and steel truss / sandwich skin hybrid ship hulls.

**Keywords:** grid skin, laminated core, balsa, hybrid structures.

## 1. INTRODUCTION

An important aspect of most engineering structures is light weight in combination with high strength and stiffness. Sandwich construction, with fiber reinforced polymer skins and foam or honeycomb cores, is excellent for such applications. However, there are many ways to further improve strength and/or stiffness, or reduce weight, using sandwich construction. A few different concepts that were recently studied are outlined below.

## 2. STRIP AND GRID SKIN SANDWICH

For sandwich panels with very thin skins, the weight of the adhesive connecting the skin to the core reaches relatively high proportions. For example, a sandwich panel with a 200 g/m<sup>2</sup> carbon fiber skins typically uses adhesive films weighing approximately 150 g/m<sup>2</sup> for bonding each skin to the core. The weight of the adhesive may be significantly reduced by using a

strip or grid skin, as shown in Figure 1, rather than a full skin. This reduces the surface area of the adhesive, and thus the total weight of the adhesive. Another advantage of strip or grid skin sandwiches is that they are expected to wrinkle at higher stresses than full skin sandwich. So-called zebra skin sandwich panels, with skins consisting of equally spaced strips, were recently investigated by Bekisli and Grenestedt [1].

Wrinkling, which is buckling of the sandwich skins at short wave lengths, is a critical failure mode for light composite skin sandwich panels loaded in compression or bending. Several analytical, numerical and experimental efforts have been made to determine the wrinkling loads of sandwich structures. Gough, Elam, and de Bruyne [2] possibly performed the earliest theoretical work on this problem. They derived an expression which, apart from a multiplicative factor, conceivable is still the most used formula. Hoff and Mautner [3] used a different kinematic assumption, and studied symmetric and anti-symmetric wrinkling of sandwich. A review of wrinkling in sandwich is provided by Ley, Lin and Mbanefo [4].

Shield [5] and Grenestedt and Olsson [6] presented two-dimensional (2D) elastic theories for the buckling of face layers bonded to an elastic semi-infinite substrate in plain strain. In both studies, 1D beam approximations for the skins were also derived and compared with the 2D results. In the study by Bekisli and Grenestedt [1], the wrinkling loads of composite sandwiches with full skins and zebra skins were determined using both 2D and 3D FE simulations, as well as approximate analytical analysis. The wrinkling mode of a strip attached to a thick foam core is shown in Figure 2. This model had periodic boundary conditions, thus simulating a sandwich with evenly spaced strips.

The strength benefit of a zebra skin sandwich can be seen in Figure 3, which shows wrinkling strain (in the loading direction) versus  $b/w$ , where  $b$  is the width of the skin strip, and  $w$  is the width of the unit cell (which equals the spacing of the skin strips). The wrinkling strain is given for various ratios of skin to core stiffnesses,  $E_s/E_c$ , and for  $h/w=0.01$  and  $h/w=0.1$ , where  $h$  is the thickness of the skin. A simple example using some data from Figure 3 may highlight some of the potential weight savings. If  $E_s/E_c=2000$  (i.e., the skins are 2000 times stiffer than the core), then a full skin sandwich has the wrinkling strain  $\varepsilon_c=0.38\%$  according to the FE results of Figure 3. A zebra skin with  $b/w=0.2$  has the wrinkling strain  $\varepsilon_c=0.49\%$ . Thus, if the skin thickness of the full skin sandwich is  $h$ , then a zebra skin sandwich with the skin thickness  $0.38h/(0.49 \times 0.2)=3.9h$  will have the same load carrying capability in compression. The mass of the zebra skin will be 78% of that of the full skin. The weight of the sandwich is further reduced due the reduced amount of adhesive required to attach the zebra skin to the sandwich core. For smaller  $b/w$  as well as for larger  $h/w$ , the effect is even more pronounced. Preliminary experiments have been performed, using waterjet

cut aluminum zebra skins, CNC hotwire cut polystyrene foams, and thermoplastic film adhesives. The specimens were adhesively bonded in an alignment fixture, which was also used for the mechanical testing. This was done in order to reduce uneven load introduction as well as geometric imperfections.

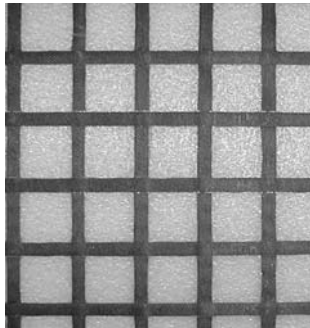


*Figure 1.* Carbon fiber grid skin on polystyrene foam core.

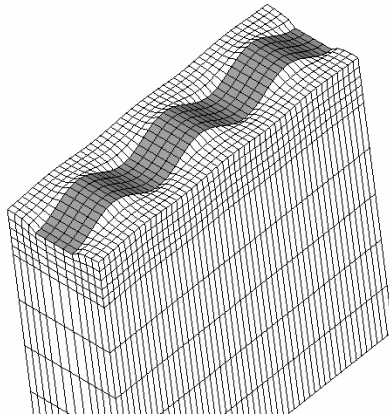


*Figure 2.* Wrinkling mode of a stiff skin strip on a compliant foam core.

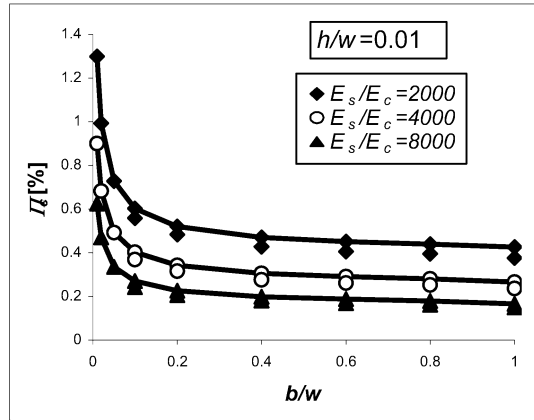


Figure 3. Wrinkling strains for zebra skin sandwich versus  $b/w$  for  $h/w=0.01$ . Connected markers represent analytical estimates and unconnected markers represent FE results.

### 3. GRADED OR LAMINATED CORE SANDWICH

Foam cores are usually homogeneous through the thickness, but there are a number of potential advantages of using a graded core. If the core were graded such that it was stronger and stiffer beneath the skins, then higher skin peeling strength, higher impact strength, and higher wrinkling strength would be expected. Further, high ductility foam cores often have less heat and styrene resistance. This may be improved by grading the foam core from a high ductility material in the center to more heat and styrene resistant foams on the surfaces. Graded foams of these types have been manufactured and tested by Danielsson and Grenestedt [7]. The results were very encouraging.

Many of the advantages of graded foam cores can be achieved using laminated foam cores. The main disadvantages are added weight due to the adhesive bonding, discontinuous stiffness within the core, and increased manufacturing cost.

Wrinkling strength of laminated core sandwich panels have been investigated by Grenestedt and Olsson [6] and Grenestedt and Danielsson [8]. Analyses were performed using 1D and 2D elastic buckling, 2D elastic-plastic buckling, and Finite Element analyses. Specimens as depicted in Figure 4 were carefully prepared and tested. In Figure 5, some of the wrinkling test results are summarized. Details are provided in [8].

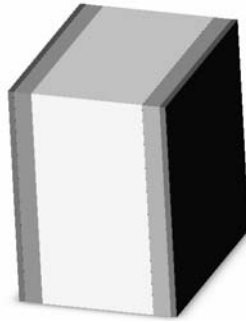


Figure 4. Sandwich specimen with two aluminum skins (thickness  $h_1$ ), two high density foam core laminae (thickness  $h_2$ ), and a thick low density core center.

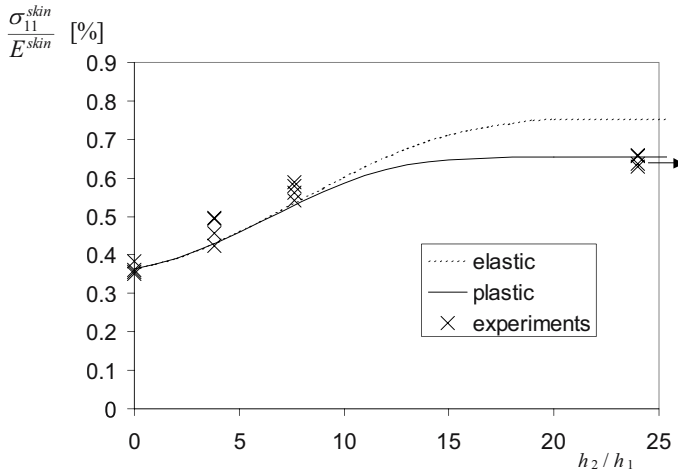


Figure 5. Comparison between experimental and theoretical wrinkling stress for a sandwich with a layered core. Elastic analysis (dotted line), elastic-plastic analysis (full line), and experiments (X).

#### 4. HIGH STRENGTH AND HIGH STIFFNESS BALSAM CORES

End grain balsa is a common core material in sandwich structures. The main properties of interest of a sandwich core, in particular for marine applications, are shear stiffness and shear strength. Balsa is highly anisotropic but the end grain arrangement does not utilize the anisotropy for the benefit of shear properties. A new kind of balsa core, shown in Figure 6, was developed, numerically analyzed, manufactured and tested by Grenestedt and Bekisli [9, 10]. This new core, which consists of an assembly

of irregularly shaped balsa blocks, allows the grains in various blocks to be oriented for example at  $45^\circ$  to the normal of the plane of the core. The resulting effective out-of-plane shear stiffness is isotropic. Numerical analyses predict a superior shear stiffness, which was also confirmed by experiments.

The balsa blocks of the first test specimens were CNC milled, which was quite time consuming. For the later versions, a special manufacturing technique was developed. This technique employed a fixture which fed balsa blocks through a twisted wire saw blade while simultaneously rotating it, Figure 7. This allowed balsa blocks to be rapidly fabricated. Test specimens were made by assembling the blocks and vacuum infusing a low viscosity epoxy adhesive. Shear specimens with the size 600 mm x 100 mm x 50 mm were manufactured. The specimens had 2.4 times higher stiffness and 25% higher strength than conventional end grain balsa specimens of the same dimensions, cut from the same block of balsa and tested in the same loading fixture and loading frame.



*Figure 6.* Specially shaped balsa blocks that are space filling (the shape is a generalized Voronoi structure) and have all grains oriented  $45^\circ$  from the normal, but in four different in-plane directions. CAD model (left), one balsa block (middle), and a specimen containing many balsa blocks being shear tested (right).

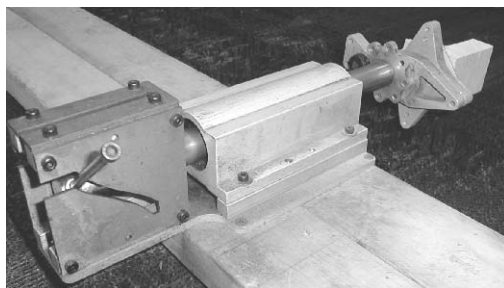


*Figure 7.* Equipment developed to translate and rotate a balsa block through a twisted wire saw blade.

## 5. COMPOSITE / STEEL HYBRID SHIP HULLS

Composites are gaining popularity in larger ship structures, such as hulls and superstructures. There is considerable interest in combining composites with steel in a so-called hybrid ship, with the goal to obtain a structure with superior characteristics. Composite sandwich panels have benefits such as low weight, high strength, good thermal and sound insulation, flatness for signature requirements, corrosion resistance, etc. Steel has other benefits, including high stiffness, high ductility, isotropy, ease of manufacturing and ease of outfitting. A hybrid ship structure could combine many of these attributes.

A number of issues related to hybrid ship hulls have been dealt with in recent years. The design of the various types of joints between the different materials is a major challenge. The joints may be between a composite topside structure and a steel deck, between smaller composite plates attached to a steel “rib cage”, between a composite bow and/or stern and a steel center section, etc. Studies focusing on such issue include those of Grenestedt and colleagues [11-18].

One of many concepts for a hybrid ship hull is to use a (stainless) steel truss, closed out with large composite sandwich panels. The concept, suggested by Barsoum [19], has a number of benefits, including easy outfitting before the composite panels are attached, heavy items can be mounted to the steel truss, controlled blow-out panels to release internal blast pressure are simple to incorporate, and high stiffness / low cost steel control global stiffness. Recent testing also show that the steel provide superior toughness and residual strength when compared to an all-composite hull. This concept was recently studied by Grenestedt and Cao [18], Figures 8-9. A 142 m model of a destroyer was developed, analyzed, and structurally optimized. A numerical study indicated that the hull concept may have some considerable benefits and a second study was initiated to manufacture and test a scaled down section of the hull. A six meter model was CAD modeled, FE analyzed and structurally optimized. The stainless steel truss was cut by waterjet and laser, and assembled using TIG and MIG welding. Sixty composite sandwich plates were manufactured by vacuum infusion and adhesively bonded to the steel truss. Before bonding the plates to the steel truss, 110 specimens with various bonded joint configurations were manufactured and tested. A joint configuration which resulted in no adhesive failure was selected for the hull specimen. A six point loading setup was designed such that the maximum (scaled) bending moment according to ABS was achieved in one section of the hull girder, simultaneously as the maximum shear according to ABS was achieved in a different section. No one part of the hull experienced the maximum bending moment and shear.

Rather, the areas of maximum moment and maximum shear were separated. The hull was instrumented with 192 strain gages and 33 LVDT. The specimen was loaded in both simulated sagging and hogging conditions. Testing was done by multiple loadings and unloadings, starting at 10% of expected yield load and incrementally increasing the load. The hull was loaded to 40% above ABS load under sagging conditions, and slightly above design load under hogging. After these tests, sandwich panels were removed to simulate battle damage. Even with nine panels removed, from all the highest loaded sections, the hull could still carry the full design load. At this point, the hull was loaded to failure, which occurred at approximately 30% above design load.

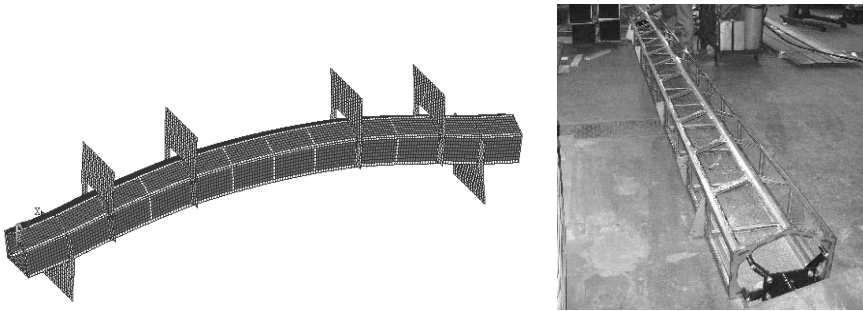


*Figure 8.* Finite Element model of the 6 meter specimen (left) and the stainless steel truss the specimen before the composite panels were attached (right).

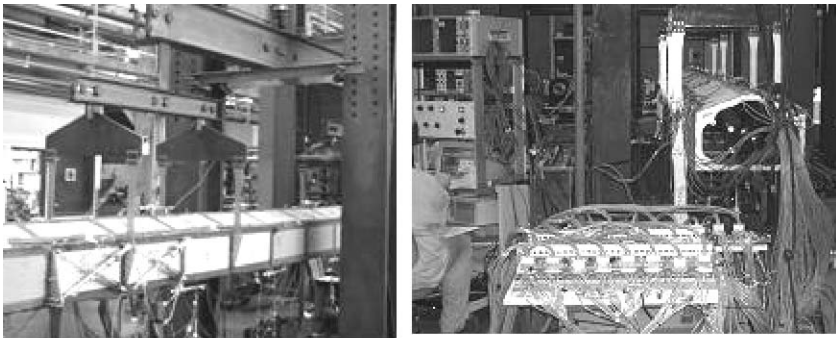


*Figure 9.* Six meter specimen during testing.

## ACKNOWLEDGEMENTS

This material is based upon work supported in part by the National Science Foundation under Grant No. 0092406, in part by the Office of Naval Research under Grant No. N00014-03-1-0597, and in part by the Department of Mechanical Engineering and Mechanics, Lehigh University. Special acknowledgement goes to my students, former and present, and to Bill Maroun.

## REFERENCES

1. Bekisli, B., Grenestedt, J.L., "Wrinkling of Zebra Skin Sandwich Panels", *Journal of Composites, Technology, & Research*, Vol. 25, No. 4, 2003, pp. 196-201.
2. Gough, G.S., Elam, C.F., de Bruyne, N.A., "The Stabilization of a Thin Sheet by a Continuous Supporting Medium", *Journal of Royal Aero. Soc.*, 1940, Vol. 44, pp. 12-43.
3. Hoff, N.J., Mautner, S.E., "The Buckling of Sandwich-Type Panels", *Journal of Aero. Sciences*, 1945, Vol. 12, pp. 285-297.
4. Ley, R.P., Lin, W., Mbanefo, U., "Facesheet Wrinkling in Sandwich Structures", NASA, 1999, CR-1999-208994.
5. Shield, T.W., Kim, K.S., Shield, R.T., "The Buckling of an Elastic Layer Bonded to an Elastic Substrate in Plane Strain", *Journal of Applied Mechanics*, June 1994, Vol. 61, pp. 231-235. Corrections: *J. Appl. Mech.*, December 1994, Vol. 61, pp. 796.
6. Grenestedt, J.L., Olsson, K.-A., "Wrinkling of Sandwich with Layered Core or Non-Symmetric Skins", *Proc. Third International Conference on Sandwich Construction*, Southampton, UK, 12-15 September 1995.
7. Danielsson, M., Grenestedt, J.L., "Gradient Foam Core Materials for Sandwich Structures, Preparation and Characterisation", *Composites Part A*, Vol. 29, Iss. 8, 1998, pp. 981-988.
8. Grenestedt, J.L., Danielsson, M., "Elastic-Plastic Wrinkling of Sandwich Panels with Layered Cores", accepted, to appear in *Journal of Applied Mechanics*, 2004.
9. Grenestedt, J.L., Bekisli, B., "Analyses and Preliminary Tests of a Balsa Sandwich Core with Improved Shear Properties", *International Journal of Mechanical Sciences*, Vol. 45, 2003, pp. 1327-1346.
10. Bekisli, B., Grenestedt, J.L., "Experimental Evaluation of a Balsa Sandwich Core with Improved Shear Properties", *Composites Science and Technology*, Volume 64, Issue 5, April 2004, pp. 667-674.
11. Melograna, J.D., Grenestedt, J.L., "Adhesion of Stainless Steel to Fiber Reinforced Vinyl Ester Composite", *Journal of Composites Technology and Research*, Vol. 24, No. 4, 2002, pp. 254-260.
12. Melograna, J.D., Grenestedt, J.L., "Improving Joints between Composites and Steel Using Perforations", *Composites: Part A*, Vol. 33, 2002, pp. 1253-1261.
13. Melograna, J.D., Grenestedt, J.L., Maroun, W.J., "Adhesive Tongue-and-Groove Joints Between Thin Carbon Fiber Laminates and Steel", *Composites Part A*, Vol. 34, Iss. 2, 2003, pp. 119-124.
14. Melograna, J.D., Grenestedt, J.L., "Revisiting a Wavy Bonded Single Lap Joint", *AIAA Journal*, Vol. 42, No. 2, 2004, pp. 395-402.

15. Grenestedt, J.L., "Steel to Composite Joints in Hybrid Ships", Proc. International Conference of Sandwich Construction, Fort Lauderdale, March 31-April 2, 2003.
16. Cao, J., Grenestedt, J.L., "Test of a Redesigned Glass-Fiber Reinforced Vinyl Ester to Steel Joint for Use between a Naval GRP Superstructure and a Steel Hull", *Composite Structures*, 60, 2003, pp. 439-445.
17. Cao, J., Grenestedt, J.L., "Design and Testing of Joints for Composite Sandwich / Steel Hybrid Ship Hulls", *Composites Part A: Applied Science and Manufacturing*, Vol. 35, No. 9, September 2004, pp. 1091-1105.
18. Grenestedt, J.L., Cao, J., "Ship Hull Consisting of Vierendeel Type Steel Truss and Composite Panels", Proc. Tenth International Conference on Marine Application of Composite Materials (MACM), Melbourne, FL, USA, 2004.
19. Barsoum R., "The Best of Both Worlds: Hybrid Ship Hulls Use Composites & Steel", *AMPTIAC Quarterly* 2003; 7(3): 55-61.

# MAGNESIUM INTEGRAL FOAM – A NEW METALLIC SANDWICH STRUCTURE

Markus Hirschmann, Carolin Körner and Robert F. Singer  
*Institute of Science and Technology of Metals, University Erlangen-Nuremberg,  
Martensstraße 5, 91058 Erlangen, Germany*

**Abstract** Structural foams or integral foams are monolithic components with a solid skin and a cellular core. We developed a new method to produce metallic integral foam with conventional casting machines. The advantages of the material are a low density, a high energy absorption capacity, a high weight specific bending stiffness and a remarkable damping capacity.

**Keywords:** magnesium foam, injection molding, integral foam, structural foam.

## 1. INTRODUCTION

Integral foam parts are monolithic components with a solid skin and a cellular core and a gradual transition from skin to core [1]. The skin gives the part its form and strength, while the cellular core gives the possibility to optimize the weight specific bending stiffness, the energy absorption capacity and the damping capacity.

Magnesium Integral Foam

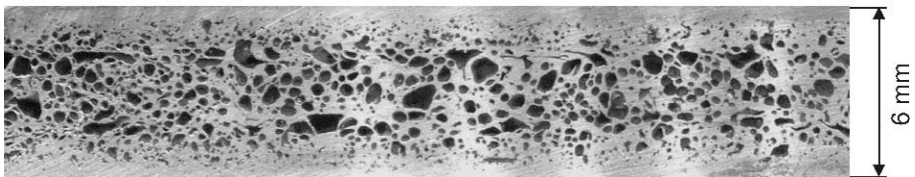


*Figure 1.* Cross section of a magnesium integral foam with solid skin and cellular core [3-5].

In the field of polymers, integral foam is a well known and established material, which is usually been injection molded [2]. For the first time we produced metallic integral foam in a similar way (see figure 1) [3-6]. The focus of this paper is on magnesium integral foam.

## 2. PROCESS

The magnesium integral foam parts are produced with a magnesium injection molding machine (see figure 2). Magnesium granules are metered into the screw of the injection molding machine. Within the screw the magnesium is heated up into the liquid state and transported to the nozzle.

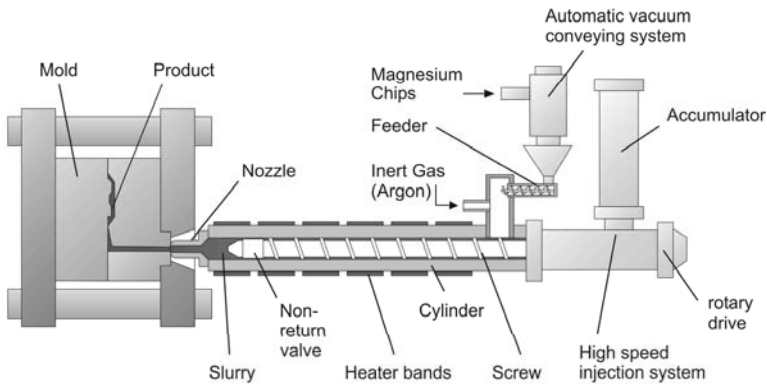


Figure 2. Magnesium injection molding machine [7].

During the next step, the melt is injected into a steel mold (see figure 3). This mold has an integrated mixing chamber in front of the die cavity, where a chemical blowing agent ( $MgH_2$ ) is added to the melt. The high kinetic energy of the melt in combination with the special geometry of the mixing chamber causes a turbulent mixture. This mixture is pressed into the die cavity. The high thermal energy of the melt leads to a decomposition of the blowing agent. Hydrogen gas is released in the center of the casting. Simultaneously the melt starts to solidify to a solid skin at the die walls. Whereas the hydrogen bubbles form a cellular core in the center of the part.

Another way to produce metallic integral foam is to use a high pressure die casting machine. The procedure is almost the same. The difference is that the melt is poured into a filling chamber, where a piston presses the melt into the mold. The advantage of using a die casting machine is that also aluminum or zinc can be processed.

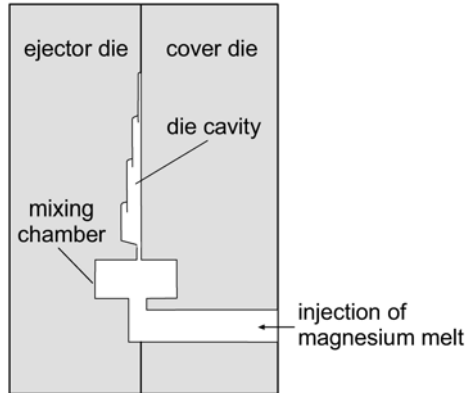


Figure 3. Schematic drawing of the mold with mixing chamber and die cavity [6].

### 3. EXPERIMENT

Samples with a footprint of  $110 \times 120 \text{ mm}^2$  and layers with a thickness of 2 mm, 6 mm, 10 mm and 14 mm were produced (see figure 4). A sample was scanned by X-ray computed tomography at the Development Center for X-ray Technology of the Fraunhofer Institute Fürth. Furthermore, the micro computed tomography system  $\mu$ -CT40 from Scanco Medical was used to measure the density profile and the pore size (voxel size  $10 \mu\text{m}$ , sample geometry  $6 \times 6 \times 6 \text{ mm}^3$  or  $10 \times 10 \times 10 \text{ mm}^3$ ).

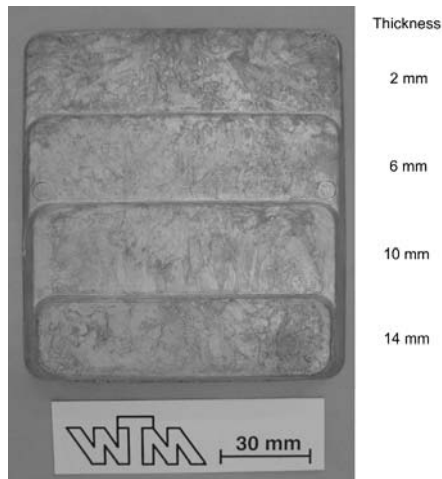


Figure 4. Magnesium integral foam sample with solid skin.

The Young's modulus was measured by impulse excitation technique according to ASTM E 1876 (sample geometry  $6 \times 6 \times 70 \text{ mm}^3$ ). Compression tests (sample geometry  $6 \times 6 \times 6 \text{ mm}^3$ , compression force perpendicular to dense skin, strain rate  $0,001 \text{ s}^{-1}$ ) and three-point bending tests (sample geometry  $55 \times 6 \times 8 \text{ mm}^3$ , support width 40 mm) were carried out to receive an impression of the mechanical behavior. Furthermore, the internal friction  $Q^{-1}$  was determined from damped oscillation measured by impulse excitation technique (sample geometry  $6 \times 6 \times 70 \text{ mm}^3$ ).

## 4. RESULTS AND DISCUSSION

### 4.1 Integral foam part quality

The magnesium integral foam parts have a solid skin (see figure 4) like compact magnesium samples. The density of the investigated integral foam samples is approximately 25 % lower than the density of compact magnesium samples with the same dimensions.

The magnesium integral foam sample shown in figure 4 was scanned by computed tomography. Two dimensional cross sections are depicted in figure 5. The sample has an integral foam structure in the 14 mm, the 10 mm and the 6 mm layer, whereas the 2 mm layer is compact (figure 5, side view). The top view shows a porous core in the 14 mm and 10 mm layer and the compact skin of the 6 mm layer (figure 5, top view).

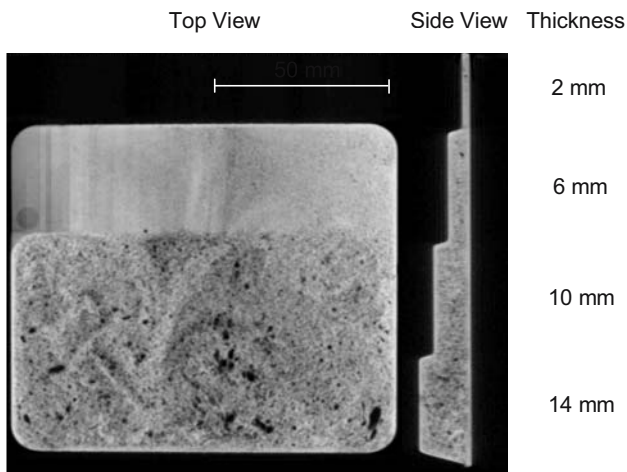


Figure 5. Two dimensional cross sections of a magnesium integral foam sample (computed tomography, Development Center for X-ray Technology, Fürth) [6].

## 4.2 Structure properties

### 4.2.1 Density profile

Magnesium integral foam parts have a density profile similar to polymer integral foam parts (see figure 6). They show a solid skin with an extension of about 0.5 -1.0 mm and a cellular core. A gradual transition between solid skin and foam core is typical. Generally the density profiles are symmetrical. A lower mean density results in a lower foam core density. At the moment, the minimum practicable core density is about 0.9 g/cm<sup>3</sup>.

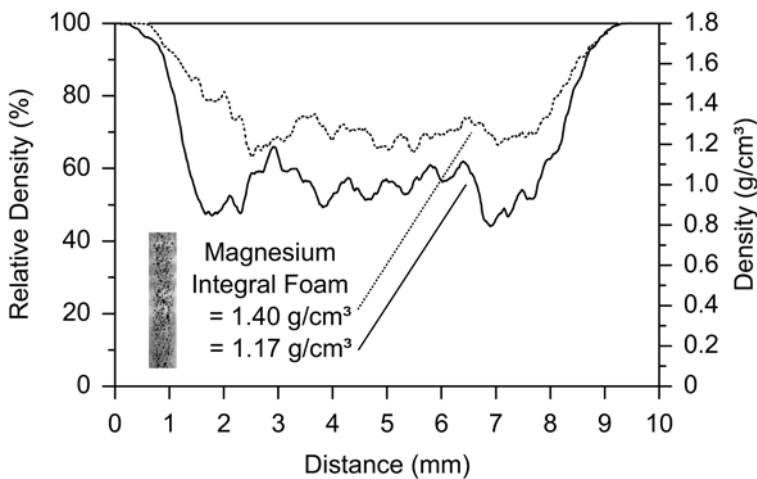


Figure 6. Density profile of two magnesium integral foam parts with different density.

### 4.2.2 Pore structure

The micro computed tomography measurements show a strong coherence between pore size and density profile (see figure 7). No pores exist at the solid skin. In the transition area between solid skin and foam core the pore size increases with decreasing density. The pore size increases from about 25  $\mu\text{m}$  to 200  $\mu\text{m}$  in the transition area. The largest pores with more than 200  $\mu\text{m}$  diameter exist in the centre of the sample. A decrease of the foam core density leads to larger pores in the core. The mean pore size of the investigated samples varies from 50  $\mu\text{m}$  to 500  $\mu\text{m}$ .

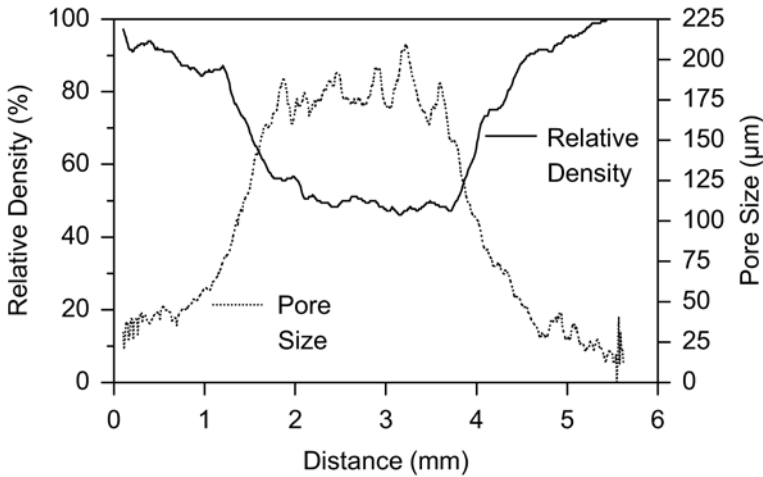


Figure 7. Coherence between density profile and pore size of magnesium integral foam [6].

The pore structure is homogenous in the centre of the integral foam (see figure 8). The pores (dark areas) are formed by the released hydrogen during the foaming process. The magnesium alloy builds a network of pronounced cell walls between the pores (brighter areas).

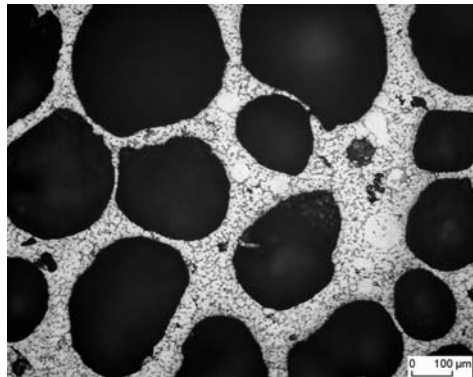


Figure 8. Cross section of the foamed core with homogenous pore structure [4, 6].

### 4.3 Mechanical properties

Integral foam is an interesting material for structural applications because of its promising mechanical properties. In the following sections the Young's modulus, the energy absorption, the weight specific bending stiffness and the damping capacity are presented.

### 4.3.1 Young's modulus

The Young's modulus of compact magnesium at room temperature is about 45 GPa. Magnesium integral foam parts show lower Young's moduli than compact magnesium. The modulus decreases with decreasing density (see figure 9). Nevertheless, the Young's modulus of magnesium integral foam with a density of about 1.0 g/cm<sup>3</sup> is about 20 GPa. This is really huge compared to the Young's modulus of polymer integral foam, which is maximum a few GPa [8].

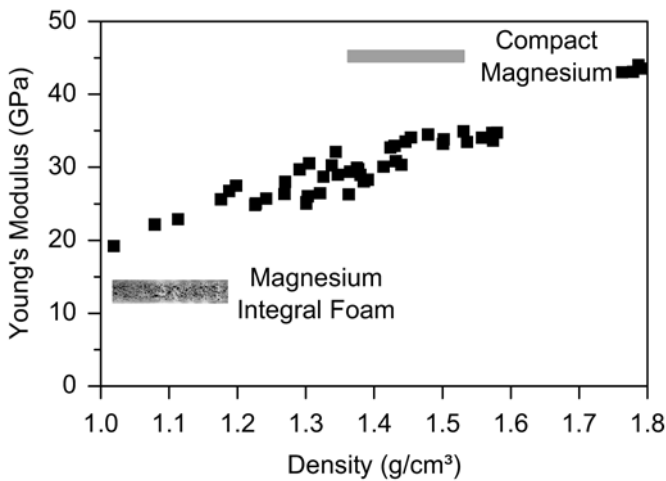


Figure 9. Young's Modulus of magnesium integral foam.

### 4.3.2 Energy absorption

The compression behavior of compact magnesium and magnesium integral foam is depicted in figure 10. The stress-strain curve of compact magnesium is characterized by an elastic region followed by a plastic region. The stress-strain curve of integral foam is completely different. Very little energy is absorbed in the short elastic region. An extended plateau in the stress-strain curve allows large energy absorption at near constant load. Hence, integral foam absorbs much more energy than compact material for a given maximum load. The plateau arises from cell collapse by buckling, yielding and crushing [8].

Magnesium integral foam shows the typical foam like stress-strain curve, if the density is lower than 1.2 g/cm<sup>3</sup>. With decreasing density the plateau is shifted to lower levels [5].

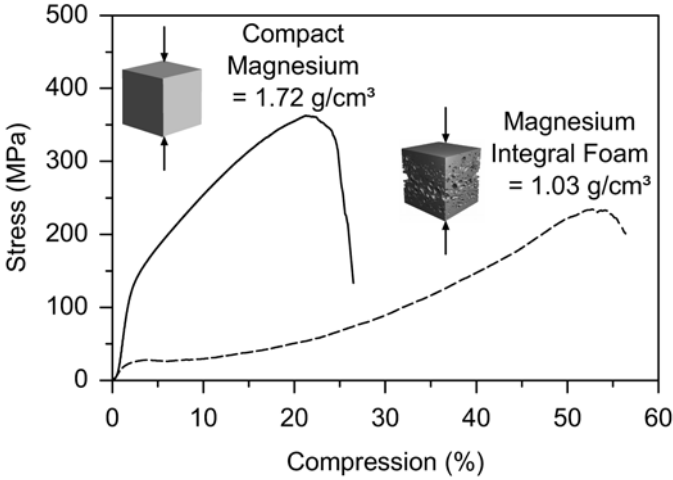


Figure 10. Compression behavior of compact magnesium and magnesium integral foam.

### 4.3.3 Weight specific bending stiffness

Three-point bending tests were carried out to get an impression of the bending behavior of magnesium integral foam compared to compact magnesium. All samples had same weight. With decreasing density the weight specific bending stiffness increases (see figure 11). The weight specific bending stiffness can be increased up to 60 % for integral foam parts with a thickness of 6 mm [3-6].

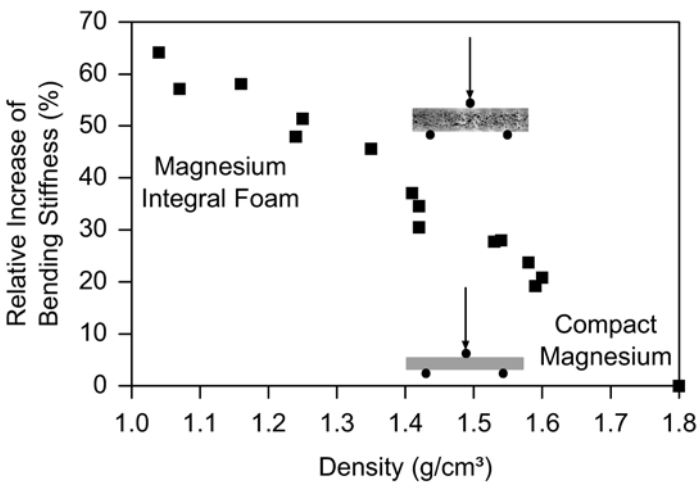


Figure 11. Relative increase of the bending stiffness of magnesium integral foam [3-6].

#### 4.3.4 Damping capacity

High damping materials are needed to attenuate efficiently vibration. Metals, especially light metals, are low damping materials. The damping capacity for magnesium integral foam and compact magnesium is depicted in figure 12. The internal friction  $Q^{-1}$  for compact magnesium alloy was measured to 0.0001. Thus the damping capacity is quite bad. In contrast integral foam has noticeable higher internal friction. The internal friction increases with lower density. So magnesium integral foam could be an interesting material to damp vibrations.

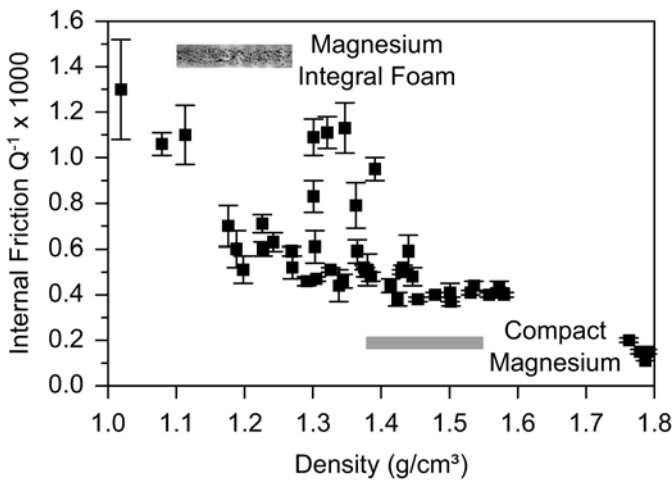


Figure 12. Damping behavior of magnesium integral foam.

## 5. SUMMARY

Magnesium integral foam parts are monolithic sandwich parts with a solid skin, a foamed core and a gradual transition between skin and core. Integral foam can be produced with an injection molding machine or alternatively with a high-pressure die-casting machine.

Magnesium integral foam provides great potential to improve mechanical properties of lightweight structures. The Young's modulus is higher than that of comparable polymer integral foam. The high energy absorption capacity in combination with the high weight specific bending stiffness and the improved damping capacity make the new metallic material interesting for structural applications.

## ACKNOWLEDGEMENTS

A financial grant from the German Research Foundation DFG (SFB396) is gratefully acknowledged. The authors also wish to express their thanks to Andreas Lohmüller and Martin Scharrer from Neue Materialien Fürth GmbH, Fürth, Germany for technical assistance during integral foam production.

## REFERENCES

1. Semerdjiev, S., Introduction to Structural Foam, Cummings Printing Company, Manchester, USA, 1982.
2. Eckhardt, H., "Thermoplastic structural foam - a well known and a new process", Proceedings of the 5th International Conference on Blowing Agents and Foaming Processes 2003, Rapra Technology, Shrewsbury, England, pp. 65-76, 2003.
3. Körner, C., Hirschmann, M., Lamm, M. and Singer, R.F., "Magnesium integral foams", Cellular Metals: Manufacture, Properties, Applications, MIT-Publishing, Berlin, Germany, pp. 209-214, 2003.
4. Körner, C., Hirschmann, M., Bräutigam, V. and Singer, R.F., "Endogenous particle stabilization during magnesium integral foam production", Advanced Engineering Materials, Vol. 6, No. 6, pp. 385-390, 2004.
5. Hirschmann, M., Körner, C., Lamm, M. and Singer, R.F., "Magnesium integral foams – production and properties", Magnesium - Proceedings of the 6th International Conference on Magnesium Alloys and their Applications, Wiley-VCH, Weinheim, Germany, pp. 354-359, 2004.
6. Hirschmann, M., Körner, C. and Singer, R.F., "Injection moulding of magnesium integral foams", Cellular Metals and Polymers, Trans Tech Publications, Utikon-Zurich, Switzerland, 2005.
7. Lohmüller, A., Scharrer, M., Jenning, R., Hilbinger, M., Hartmann, M. and Singer, R.F., "Injection molding of magnesium alloys", Proceedings of the 6th International Conference on Magnesium Alloys and their Applications, Wiley-VCH, Weinheim, Germany, pp. 738-743, 2004.
8. Gibson, L.J. and Ashby, M.F., Cellular Solids: Structure & Properties, Second Edition, Cambridge University Press, Cambridge, UK, 1997.

# NEW IMPROVED FOAM CORE MATERIALS FOR ADVANCED PROCESSING

Stefan Reuterlöv

DIAB AB Box 201, S-312 22 Laholm, Sweden

stefan@se.diabgroup.com

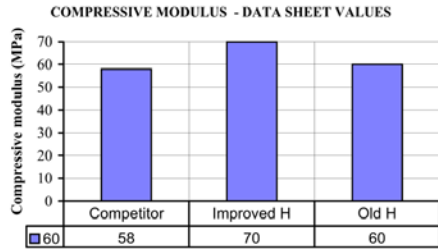
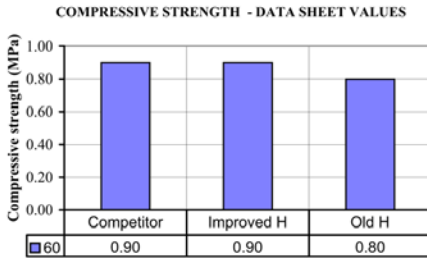
**Abstract** Closed moulding processes put new requirements on the core materials for sandwich structures. Two new foam core material grades have been developed to meet these requirements. The first will replace the existing standard grades but with improved strength, ductility and thermal properties while maintaining the excellent stiffness of today's product. This grade is oriented towards closed manufacturing processes with processing at lower temperatures like infusion, RTM and VARTM and post cure up to 90°C. The second grade will provide full compatibility with low and medium temperature pre-preg and RFI systems for processing up to 160°C.

In addition, for the DIAB core infusion process with a grooved core material, the making up has been improved for weight sensitive applications by using an optimized finer groove pattern in the core surface to minimize resin uptake while still providing an even distribution and wet-out of the fibers.

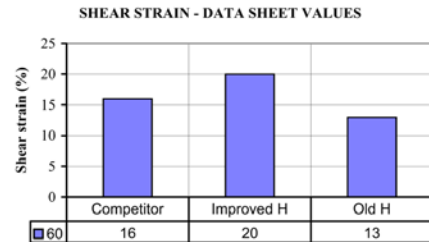
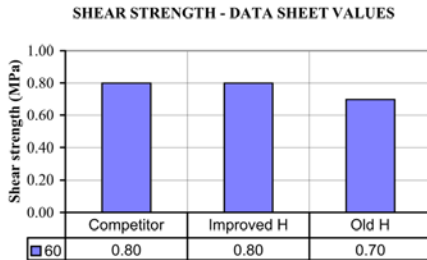
**Keywords:** foam core material, resin transfer molding, manufacturing.

## 1. BACKGROUND

For the last 35–40 years foam core materials has been the natural choice when building sandwich structures for the marine, wind energy and transport industry. Good mechanical properties and easy process ability in combination with acceptable thermal stability has been a winning concept. More advanced processing methods than open moulding has however put new requirements on the core materials. Closed moulding processes like infusion, RFI and pre-pregs all require vacuum consolidation, often at elevated temperature or with high exotherm peaks due to a larger amount of laminate being consolidated at the same time. This has put new requirements on the materials. The temperature stability and strength properties at elevated temperature are more important today than what they used to be. Also optimisation of the products has resulted in higher demands on further weight savings.



Figures 1&2. Compressive strength and modulus according to ASTM D 1621.



Figures 3&4. Shear strength and strain according to ASTM C 273.

## 2. NEW FOAM CORE MATERIALS

Two new foam core material grades have been developed to meet these modern requirements.

The new materials are characterised by higher strength, especially at elevated temperature, while maintaining the excellent stiffness of the original grades. Also the ductility has been much improved while cell size is much finer.

The second grade will also provide full compatibility with low and medium temperature pre-preg and RFI systems for processing up to 160°C.

### 2.1 Standard grade

The first new core material grade (Divinycell H) will replace the existing standard grades but with improved strength, ductility and thermal properties while maintaining the excellent stiffness of today’s product. This grade is oriented towards closed manufacturing processes with cure at lower temperatures, like infusion, RTM and VARTM, and post cure up to 90°C.

Strength properties have on average been improved with approx 10% while the modulus are maintained at least on the same level as before. For the compressive properties the strength has been improved by 12% while the stiffness is improved by 15%, see Figures 1 and 2.

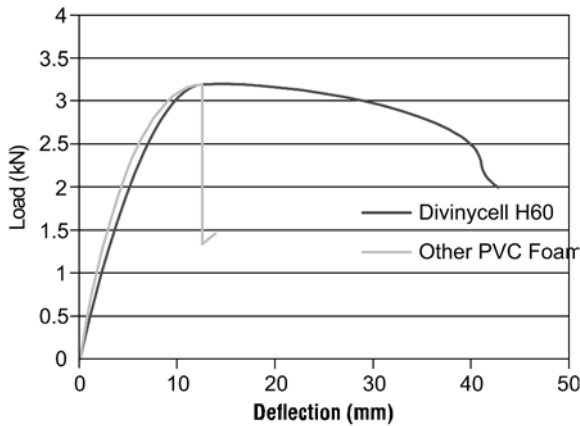


Figure 5. 4-point bending test according to ASTM C 393.

The shear properties are the most important for a core material in a sandwich construction. The shear strength is what normally decides the overall strength for the construction as the core is engineered to be the weak link. The shear stiffness will rule the shear deflection and any buckling failure modes. The shear strength has increased for the new material by 14%, see Figure 3, while the stiffness is kept constant. However the shear elongation at break, or ductility, has also been significantly improved by up to 50%, see Figure 4.

This can be a quite important parameter for panels loaded in fatigue or subjected to slamming or impact loads. When a more brittle core material such as honeycomb might well shatter or delaminate from an impact a more ductile core can absorb the energy when deflecting without permanent damage to the structure. The difference in failure mode due to the higher ductility is readily apparent in Figure 5 where 4-point bending tests has been performed. While the former generation of core material have a brittle failure mode the more ductile new material can yield and still carry significant load.

Closed production methods like infusion can easily produce sandwich structures with up to or even exceeding  $10 \text{ kg/m}^2$  of reinforcement per side. And even though the fibre fraction will be much higher than for hand lay-up that laminate will still contain enough resin to get higher exothermic temperatures. Temperatures in the range from  $80\text{--}100^\circ\text{C}$  is not uncommon and if combined with a pressure load could lead to the collapse of a core material with a lower thermal stability. Other methods that put a higher thermal stress on the core material when infusing is to heat up the resin to lower the viscosity or to cure under elevated temperature. The new grade has significantly better mechanical properties in this temperature range meaning that it can withstand higher temperature or the same temperature for a longer time, see Figure 6.

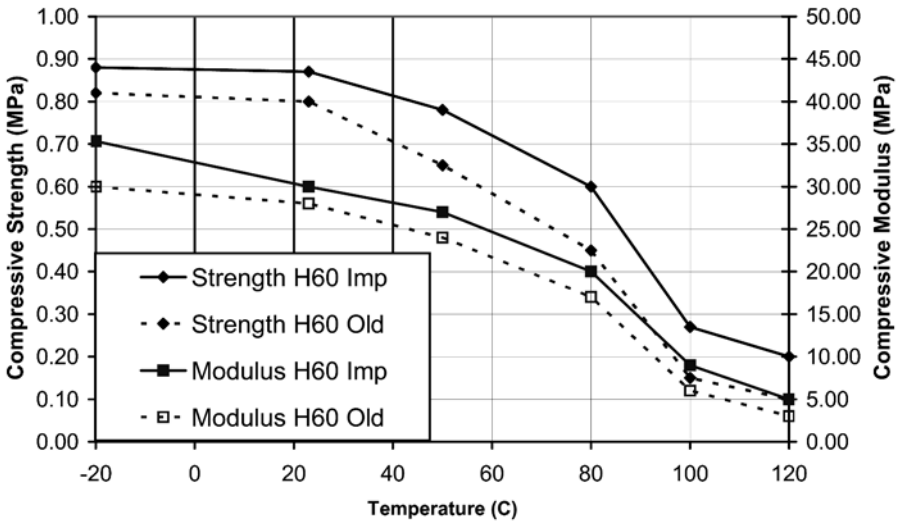
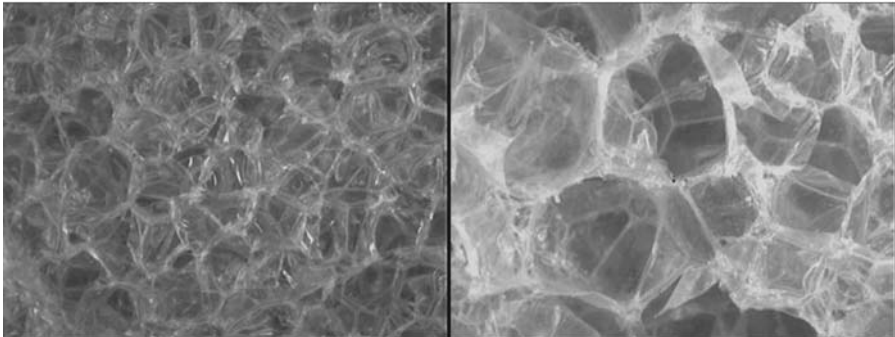


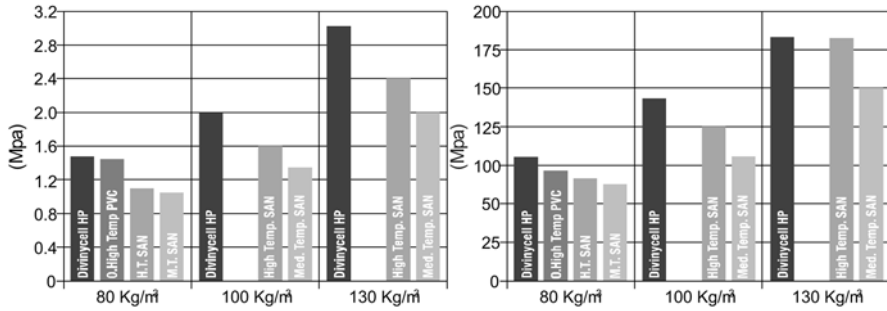
Figure 6. Compressive strength and modulus versus temperature.



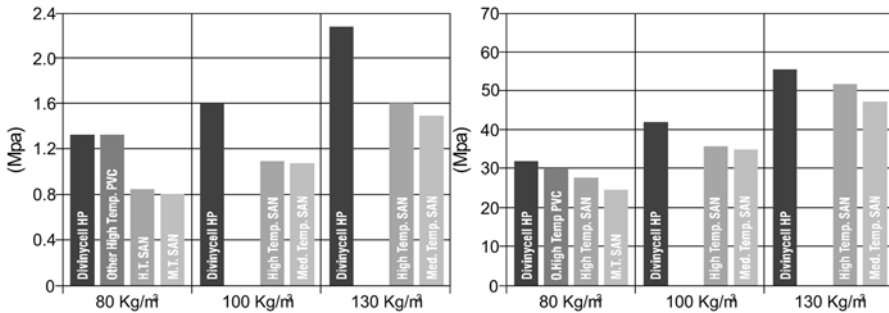
Pictures 1&2. Difference in cell size between the improved and the old foam core.

Due to the better temperature stability the recommended maximum processing temperature can be increased from 80°C to 90°C for the new grade.

Another major improvement with the new material is the much finer cell size. As can be seen in Pictures 1 and 2 the cell size has decreased from around 0.6 mm to close to 0.3 mm for a 60 kg/m<sup>2</sup> density material. The reduction in the cell diameter means that a smaller amount of resin is need for the priming of the core in order to achieve the best possible peel strength. For the old material the recommendation was to use 360 g/m<sup>2</sup> of priming resin while today 175 g/m<sup>2</sup> is required, again for a 60 kg/m<sup>2</sup> density material. This will of course result in savings in the resin consumption and thus on weight as well.



Figures 7&8. Compressive strength and modulus according to ASTM D 1621.



Figures 9&10. Shear strength and modulus according to ASTM C 273.

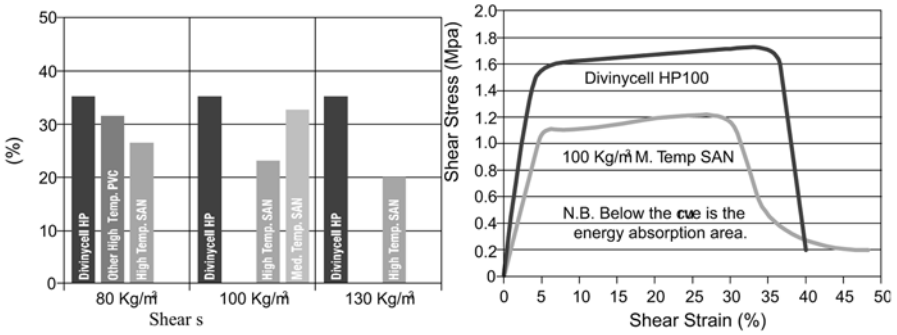
## 2.2 High temperature grade

The high-temperature grade (Divinycell HP) will provide full compatibility with low and medium temperature pre-preg and RFI systems for processing up to 160°C.

Strength properties have as for the standard grade on average been improved with approx 10% while the modulus are maintained at least on the same level as before. For the compressive properties the strength is significantly higher than other similar foam cores while the modulus is at least on the same level or better, see Figures 7 and 8.

The shear properties are the most important for a core material in a sandwich construction. The shear strength is what normally decides the overall strength for the construction as the core is engineered to be the weak link. The shear stiffness will rule the shear deflection and any buckling failure modes. The shear strength has increased and is up to 45% higher than for a SAN-based foam core, see Figure 9. For the stiffness the difference is smaller but still the modulus is somewhat higher at all temperatures, see Figure 10.

The shear elongation at break, or ductility, has also been significantly improved by > 50% compared with the previous generation of high temperat-



Figures 11&12. Shear strain according to ASTM C 273.

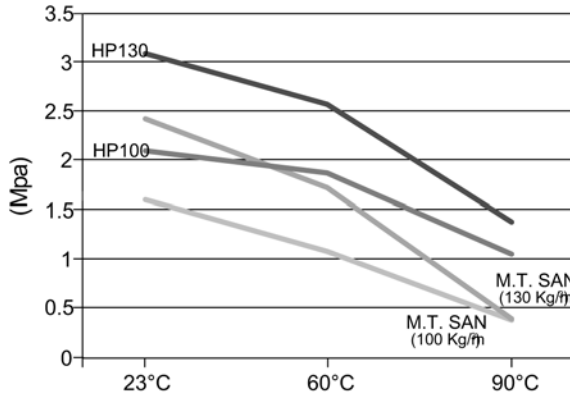
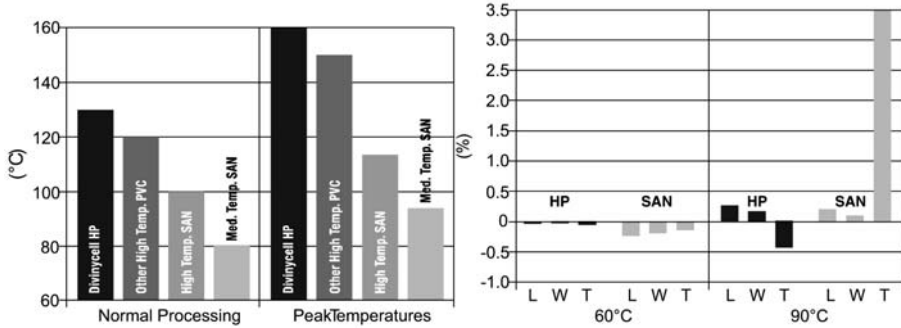


Figure 13. Compressive strength and modulus versus temperature.

ure PVC-based grades, see Figure 11. Today they match or even exceed the elongation at break of SAN-based core materials that is perceived of marketed as ductile or “linear”, see Figures 11 and 12. As the new grade still retains the significantly higher strength and modulus of the “cross-linked” core while having the higher ductility of the “linear” core the energy absorption is close to double that of a SAN-based core, see Figure 12.

The new grade is primarily intended to be used with low (70–90°C) and medium (120–140°C) temperature pre-preg systems although it can be used in other application where its good high temperature properties are needed. The significantly better mechanical properties in this temperature range means that it can withstand higher temperature/vacuum or the same temperature/vacuum for a longer time, see Figure 13.

The recommended normal processing temperature for the new grade is 130°C but due to the increased thermal stability and mechanical properties this can be increased up to 160°C (depending on time/pressure) without significant dimensional changes, see Figures 14 and 15.



Figures 14&15. Recommended processing temperature and dimensional stability.

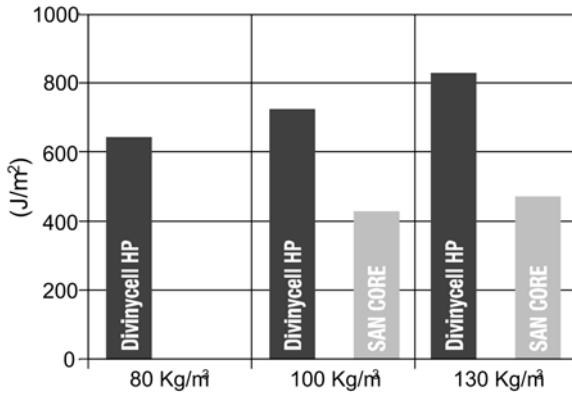


Figure 16. Peel strength of pre-preg (SA80/SE84) tested on DCB specimen.

Another major improvement with the new material is the much finer cell size. The reduction in the cell diameter means that a smaller amount of resin is need for the priming of the core in order to achieve the best possible peel strength. Previous generations of PVC-based core materials were not compatible with certain types of low temperature pre-preg systems. This showed in very low peel strength and sometimes this could lead to blistering. However the new core material has been specifically formulated to work with these materials and combined with the increased ductility the peel strength is excellent, see Figure 16.

### 3. DIAB CORE INFUSION METHOD

The Infusion process utilising DIAB grooved core materials is an innovative, faster and cheaper closed manufacturing method for producing sandwich constructions with fibre composite skins.

The grooved core will significantly improve the flow speed of the resin compared with other methods for distribution of the resin. And as an integral part of the sandwich construction, the grooves in the core, is used for the resin distribution there is no need for consumables like peel-ply, release film and distribution media. This results in big savings as these consumables do not have to be purchased and stored nor laid up, taken away and disposed of.

The fibre fraction for the grooved core infusion method is often comparable with what would be achieved using much more expensive and elaborate pre-preg processing. The parts are also manufactured with a more uniform quality compared with open moulding methods that is dependant on the individual skill of the worker. But may-be the biggest advantage lays in the much improved working conditions on the shop floor. As the wet resin does not have to be handled by hand the facilities can easily be kept tidy. Also as the workers do not come in direct contact with the resin and the emissions are much reduced the need for protective clothing and breathing masks is eliminated.

Quiet long flow lengths can be used as the flow speed for a grooved core in comparison with the other method is several times higher.

Flow lengths between inlet lines are often 3 m or more when using grooved core materials. This can be compared with surface infusion where a flow length of 0.6 m is usual and for flow maths even shorter. Thus only one-fifth the number of inlet hoses has to be laid up, taken away and disposed of. This will lower the complexity of the method; minimize the potential leakages that always can happen at the penetrations of the bags and of course save money both in purchasing the consumables but also in man-hours.

The grooves can be used on both sides of the core or combined with holes to distribute the resin to the opposite side. The grooves can be oriented in only one direction or combined in different directions to form a grid pattern. Normally grooves in only one direction parallel to the intended flow of the resin in combination with holes are enough. However if there are numerous cut outs or similar a grid pattern might be necessary. The advantage with using holes instead of grooves on both sides is that the surface finish is improved. With standard PE resins a slight print through can sometimes be seen on a dark gel coated surface if a grooved core is used. If however holes are used to distribute the resin to the gel coated surface this is prevented.

### **3.1 Low weight method**

The standard core grooving will fulfil the need for most production boat builders, wind energy producers and industrial application. The weight added from the resin uptake in the grooves and perforation is however not desirable when it come to racing sail and power boats and other extreme performance

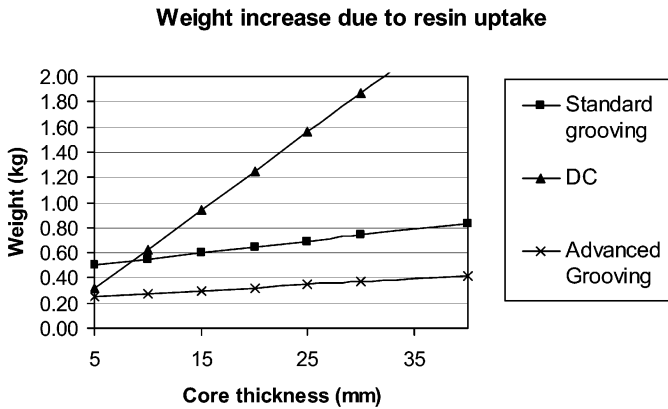


Figure 17. Resin uptake in grooves and perforations.

applications. Normally this added weight is around 600 g/m<sup>2</sup> for a typical core thickness of 15 mm, see Figure 17.

To minimise this slight weight penalty while still retaining the benefits of an even distribution and wet-out of the fibres without consumable the advanced marine grooving has been developed. Basically the groove width has been decreased by 50% while half the number of perforations has been taken away. This decreases the weight increase due to resin in the grooves and perforations to half or 300 g/m<sup>2</sup> for the core thickness of 15 mm, see Figure 17. The drawback of this grooving is of course the significantly slower flow compared with the standard grooving but otherwise all other benefits is kept.

#### 4. CONCLUSION

The increased mechanical properties of the new foam core materials, especially the higher strength at elevated temperature, will mean that they can continue to be used also with modern closed moulding processing and materials.

As such they continue to be the most versatile core materials available, suitable for all different kinds of processing from open hand lay-up to medium temperature pre-pregs.

The increased ductility, up to 50% higher, bridge the gap to more ductile cores and as the strength and stiffness is maintained they provide a unique blend of properties for high performance applications such as racing cars, yachts and aerospace structures.

The combination of the reduction in cell size and the finer infusion grooving will also result in savings in the resin consumption and thus on weight as well making the DIAB core infusion system even more competitive.

**REFERENCES**

- [1] Divinycell, Technical Manual, H-grade, DIAB, Laholm, Sweden.
- [2] Divinycell, Technical Data Sheet, H-grade, DIAB, Laholm, Sweden, 03-2005.
- [3] Divinycell, Technical Data Sheet, HP-grade, DIAB, Laholm, Sweden, 03-2005.
- [4] Zenkert, D., The Handbook of Sandwich Construction, EMAS Publishing, UK, 1997.

# CHARACTERISATION OF NOVEL K-COR SANDWICH STRUCTURES

Pascal Casari<sup>1</sup>, Denis Cartié<sup>2</sup> and Peter Davies<sup>3</sup>

<sup>1</sup>*GeM, Institut de Recherche en Génie Civil et Mécanique, UMR CNRS 6183, BP 92208, 44322 Nantes Cedex 3, France*

<sup>2</sup>*Advanced Materials Department, School of Industrial and Manufacturing Science, Cranfield University, Cranfield MK43 0AL, UK*

<sup>3</sup>*Materials and Structures Group, Ifremer Brest Centre, 29280 Plouzané, France*

**Abstract** Sandwich beams reinforced with K-Cor<sup>TM</sup> are characterized in terms of stiffness, strength and fracture by means of static tests, and compared to traditional sandwich materials. Stiffness is evaluated with a series of three flexure tests applied to each sample. Strength tests show different failure mechanisms for the two architectures. Mode I fracture properties are measured and a significant increase in the core toughness of reinforced samples is revealed.

**Keywords:** K-Cor<sup>TM</sup>, pin reinforced foam cores, fracture, damage tolerance.

## 1. INTRODUCTION

Polymer foam core sandwich construction is becoming more popular for cost and weight efficiency reasons. However, the lack of mechanical properties can sometimes be a problem. The present paper considers a solution where the polymer foam is locally reinforced by rigid carbon fibre rods. This ‘pin’ reinforcement technology has been developed recently<sup>1</sup> and is known under the commercial name of X-Cor<sup>TM</sup> and K-Cor<sup>TM</sup>.

X-Cor<sup>TM</sup> and K-Cor<sup>TM</sup> sandwich panels are structures composed of skins separated with a polymeric foam in which cured carbon fibre rods have been

<sup>1</sup> Aztex Inc, 303 Bear Hill Road, Whaltham, MA, 02154-1196, USA.

inserted in a pre-determined truss configuration. During the manufacturing process, the pins extend beyond each foam surface. For the X-Cor™ panels, uncured face sheets are pressed on each side of the core. During cure, the pins enter the face sheets. The K-Cor™ construction varies by the fact that the length of pins which extends outside the polymeric foam core is pressed flat on the surface of the foam by a hot-press process. The skins (of any material) are then adhesively bonded onto the surface of the core. For both type of cores, the truss transfers some of the through-thickness and shear loads, and enhances the properties of the core [1-3].

Due to the fact that there is no need for an adhesive film in the X-cor™ configuration, the aerospace industry developed this configuration to replace Nomex® honeycomb cores in weight saving exercises. The truss was designed to reproduce the general mechanical properties of the cores already in use. For a specific application, (Sikorsky Comanche access doors) a weight saving of 10 to 15% was achieved by using X-cor™ as opposed to Nomex honeycomb [4]. The transition between solid laminates and X-cor™ truss has been studied by O'Brien et al. [5]. They showed that the failure modes are very specific to the loading conditions applied locally on the truss. Because of the different mechanical links between the pins and the skins in K-cor™, there is no knowledge of the failure modes in the solid laminate to sandwich transition area.

## 2. MANUFACTURING

The sandwich panels were constructed with woven carbon fibre face sheets and Rohacell® polymethacrylamide foam core. Some of the foam cores were reinforced by pultruded carbon fibre / epoxy rods, creating a 2 dimensional truss. The details are as follows.

Two 290mm x 210mm x 12mm blocks of Rohacell® 51IG (density 51kg/m<sup>3</sup>) were chamfered along two edges, creating the ramps. One foam block was reinforced by 0.5mm diameter pultruded T650 carbon fibre / epoxy rods. The rods were inserted using a 6-Axis Kawasaki robot arm (see Figure 1). The pins were inserted in two directions at nominal angles of  $\pm 22^\circ$ , creating a truss in the direction 1-3 of the samples (see Figure 2.). The pin truss extended beyond each surface of the laminate for a free length of approximately 3mm. The pins were folded back, flush with the foam surface using a hot press process. The beams have been specifically designed to study the stress transfer in the transition area between sandwich and solid laminates. The skins are relatively thick in order to study a design of sandwich structure commonly used in the marine industry.

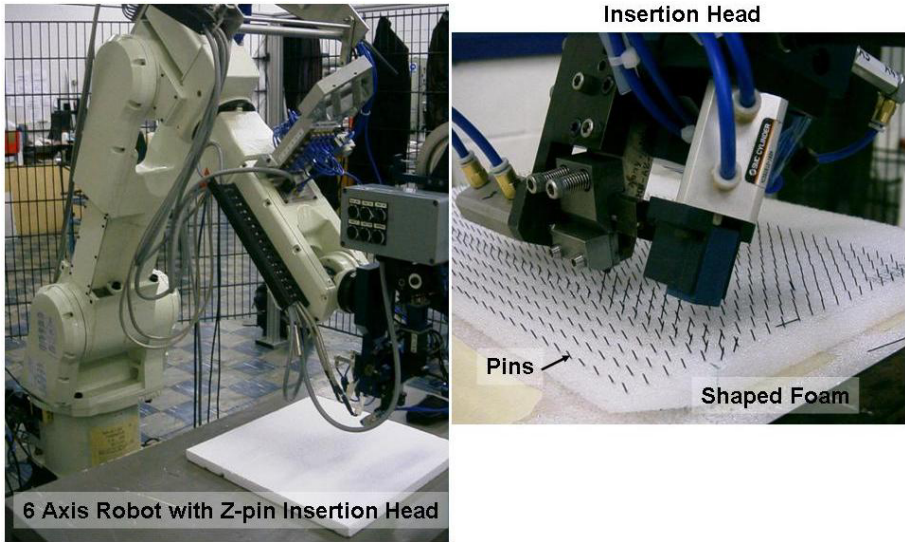


Figure 1. 6-Axis Robot in use at Cranfield University and Close Up on the Insertion head.

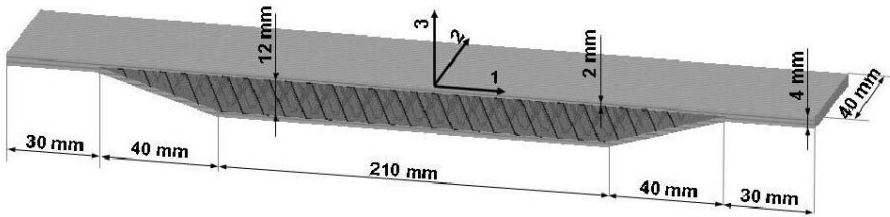


Figure 2. Specimen Geometry.

The face sheets were constructed using 8 plies of 977-6 resin / IM7 woven carbon fibre pre-preg. An AF163-2 adhesive film was used between the foam core and the surface plies. The 8 plies of the top face sheet were laid up and debulked every ply under vacuum to assure good shape conformity with the core. The panels were cured in an autoclave at 135°C at a pressure of 0.2 MPa (2 bars) for 3 hours.

40 mm wide samples were cut using a diamond coated circular saw. The nominal geometry of the samples is given in Figure 2.

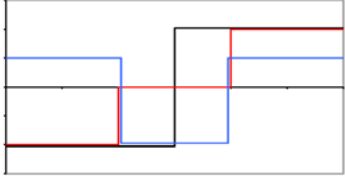
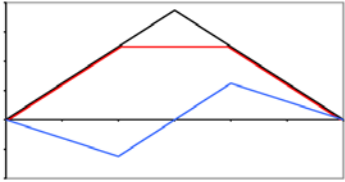
### 3. STIFFNESS

For evaluating the effect of pins on the stiffness, a set of three flexure tests is applied to each sample. This ensures that the beams are loaded with

various bending moments and shear forces and allows a more accurate characterization of shear stiffnesses. The three tests are shown in (Table 1) :

- Three point bending. The bending moment is maximum in the center whereas the shear force alternates from a constant positive value on one side of the loading point to an opposite one on the other side.
- Four point bending test. The aim of this test is to ensure a central part with no shear force and a constant bending moment
- Four point bending test with an asymmetric arrangement. This produces a bending moment diagram with a zero value in the centre, and a shear force which is maximum at this point.

Table 1. Tests and corresponding internal loads on the sandwich samples.

Bending test	Shear force diagrams
<p>3 points</p> 	
<p>4 points symmetrical</p> 	<p>Bending moment diagrams</p> 
<p>4 points antisymmetrical</p> 	

Each test has been conducted on 3 samples from classical and reinforced sandwich beams. The samples have been loaded between 0.5 and 1.5 kN in order to produce a deflection around 1 mm. Table 2 directly reports the bending stiffness results. Obviously, the stiffness of samples reinforced with K-Cor™ is much higher than the classical sandwich value.

Table 2. Bending stiffness (kN/mm).

Material	Sample	3 points	4 pts symmetrical	4 pts antisymmetrical
No pins	1	0.28	0.52	0.58
	2	0.27	0.4	0.43
	3	0.25	0.57	0.40
With pins	1	0.80	1.39	2.12
	2	0.82	1.20	1.77
	3	0.80	1.05	1.97

## 4. FRACTURE

### 4.1 Damage development in flexure

Beam specimens with and without pins were loaded to failure in three point flexure. Two test configurations were used, with the loading on alternate facings of the beams. The same fixture as above was employed. The loading rate was 5mm/min.

#### 4.1.1 Configuration 1

This is the more severe configuration as the joint between the sandwich and the beam end is subjected to both shear and tensile loads.

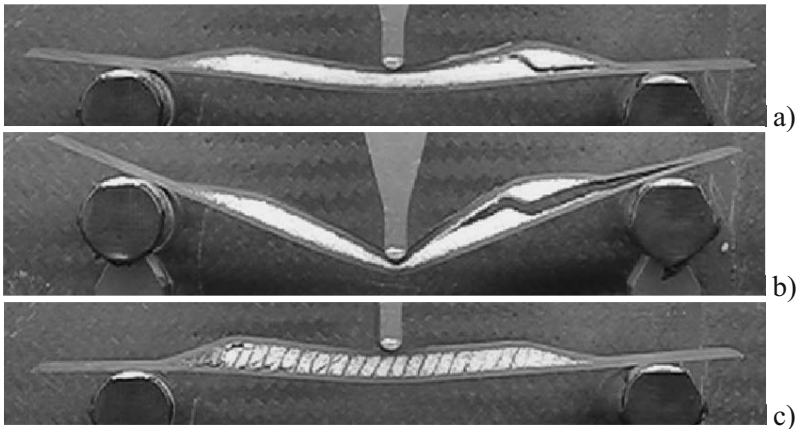


Figure 3. Failure mechanisms of sandwich beams in bending in configuration 1.

For the sandwich without pins the first damage appears at the end of the foam, Figure 3a, as a shear crack. Further loading results in compression failure below the upper load point, and continuing the test leads to core crushing and a final tensile failure in the lower facing, Figure 3b.

The inclusion of pins delays the appearance of first damage. Some cracks still appear in the core foam but the pins maintain the overall integrity of the sandwich up to compressive failure below the upper loading point, Figure Figure 3c. They also delay the crushing of the core so that final tensile failure in the lower facing appears later. The displacement-load curve shows these different steps after an initial linear part.

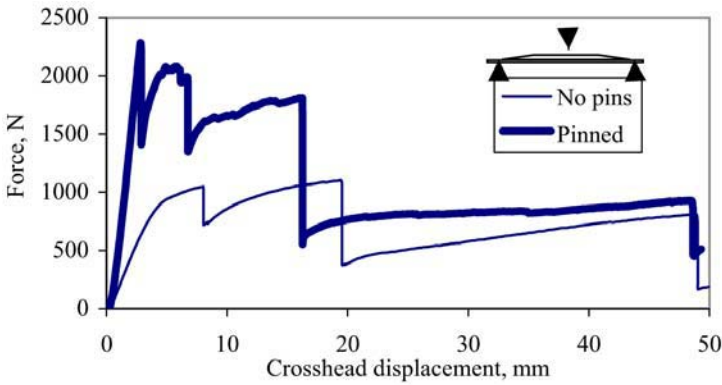


Figure 4. Load-displacement, configuration 1.

#### 4.1.2 Configuration 2

Turning the specimen and loading from the other side results in compression rather than tension at the foam ends. Figure 5 shows examples of load-displacement plots. The loads are slightly higher for both materials.

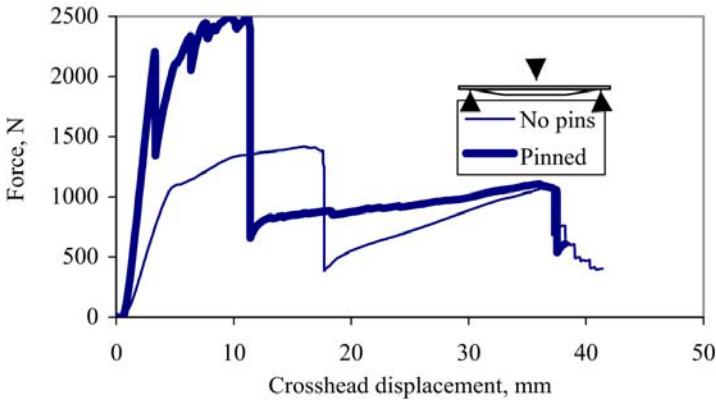


Figure 5. Load-displacement, configuration 2.

For the classical beam (Figure 6a) the failure mechanisms are mostly crushing of the core and indentation of the skin which lead to a yield point on the load-displacement curve following the elastic region. The beam reinforced with K-cor™ (Figure 6b) shows a part cracked in shear on the right side. This series of cracks corresponds to the first peak on the load-displacement curve.

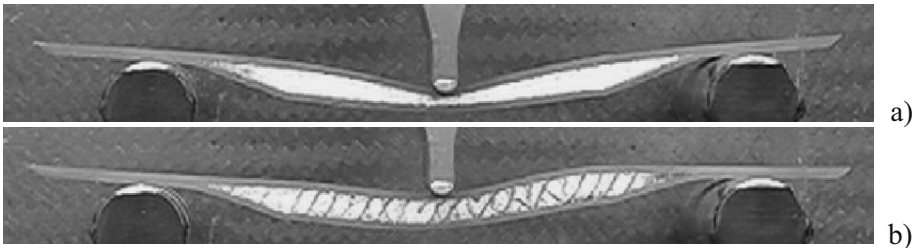


Figure 6. Failure mechanisms of sandwich beams in bending in configuration 2.

## 4.2 Crack propagation in the core

The inclusion of pins clearly has a beneficial effect on the flexural response of these sandwich structures. An additional benefit to be expected is improved damage tolerance. Extensive work on delamination of pinned laminates has clearly shown that pins play a major role in slowing crack propagation or even stopping it completely [6]. It is therefore of interest to examine the role of through-core pinning on crack behaviour in sandwich materials.

Some preliminary crack propagation tests have been performed using a Double Cantilever Beam (DCB) specimen, Figure 7. The starter crack was introduced at core mid-thickness with a saw, then sharpened by a razor blade. Notches in both specimens were the same length, 40 mm from the load point. Load was introduced by bonding aluminium blocks to the facings. Loading is initially mode I. In the foam without pins the crack propagated at mid-thickness in a symmetrical manner as shown in Figure 7. In the K-Cor™ specimen the starter crack did not propagate, a damage zone developed near the lower core/facing interface and propagated there as shown in Figure 7.

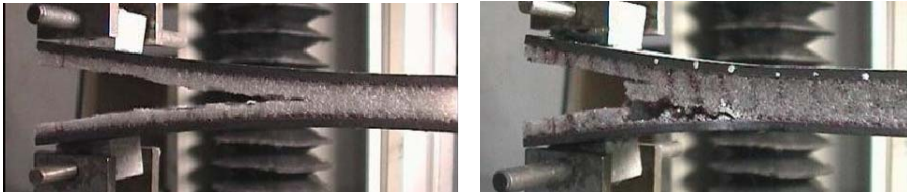


Figure 7. Two types of DCB specimen - sandwich and K-cor™.

Figure 8 shows examples of load-displacement plots. It is apparent that considerably higher energy is necessary to propagate a crack in the pinned foam. The approximate fracture energies ( $G_c$ ) are 460 J/m<sup>2</sup> for the foam and 1690 J/m<sup>2</sup> for the K-Cor™, at least three times higher.

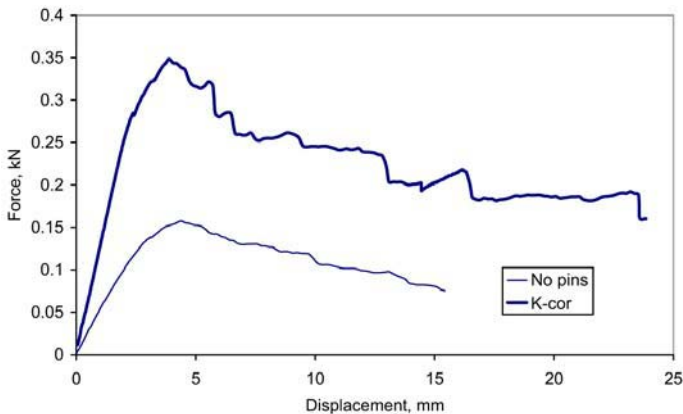


Figure 8. Load-displacement plots, DCB tests, corresponding to 55 mm crack propagation in both materials.

The through thickness pinning provides an effective barrier to crack propagation as shown in Figure 9. These pins must be pulled out or broken before the crack can advance.



*Figure 9.* K-Cor™ DCB specimen, details of crack initiation region.

It should be emphasized that these are preliminary results for one K-Cor™ configuration. An advantage of these materials is that the pinning parameters can be tailored for a particular application; optimization of pin material, density, angle and sandwich manufacturing conditions may result in further significant improvements in damage tolerance.

## **5. CONCLUSION**

This paper presents results from a preliminary study of the mechanical behaviour of a pin reinforced foam core sandwich material. Stiffness, fracture strength and damage tolerance have been examined, and it is apparent that for a similar weight all these properties can be significantly improved.

**REFERENCES**

1. Cartié D.D.R. and Fleck, N.A. "The effect of pin reinforcement upon the through-thickness compressive strength of foam cored sandwich panels". *Composites Science and Technology*, Vol. 63, pp. 2401-2409, 2003.
2. Marasco A.I., Cartié D.D.R., Partridge I.K. and Rezai A., "Mechanical properties balance in novel Z-pinned sandwich panels: Out of plane properties", *Composites Part A*, 2005, in press.
3. Partridge, I.K., Cartié, D.D.R. and Bonnington, T., *Manufacture and performance of Z-pinned composites*, Ch. 3 in *Advanced Polymeric Materials: Structure-Property Relationships*, Advani S., Shonaike G. (eds), CRC Press, April 2003, ISBN 1-58716-047-1.
4. Cartensen T. C, Kunkel E, Magee C. "X-cor advanced sandwich core material". In: 33rd International SAMPE Technical Conference, Seattle, WA, November 2001.
5. O'Brien T. K, Paris I. L., "Exploratory investigation of failure mechanisms in transition regions between solid laminates and X-cor® truss sandwich". *Composite Structures*, Vol 57, pp. 189-204, 2002.
6. Partridge I. K and Cartié D. D. R, "Delamination resistant laminates by Z-Fiber® pinning. Part I Manufacture and fracture performance", *Composites Part A: Applied Science and Manufacturing*, Vol. 35, pp. 55-64, 2005.

# FINITE ELEMENT ANALYSIS ON OUT-OF-PLANE COMPRESSION PROPERTIES OF THERMOPLASTIC HONEYCOMB

Xinyu Fan<sup>1</sup>, Ignaas Verpoest<sup>1</sup> and Dirk Vandepitte<sup>2</sup>

<sup>1</sup>*Katholieke Universiteit Leuven, Department of Metallurgy and Materials Engineering (MTM), Kasteelpark Arenberg 44, B-3001 Leuven, Belgium;* <sup>2</sup>*Department of Mechanical Engineering, Division Production Engineering, Machine Design and Automation (PMA), Celestijnenlaan 300B, B-3001 Leuven, Belgium*

**Abstract** In this paper, the out-of-plane compressive properties of thermoplastic hexagonal honeycombs are investigated by finite element analysis (FEA). Both linear (eigenvalue problem) and nonlinear buckling analyses are performed correspondingly on honeycomb perfect models and a hexagonal imperfect unit-cell model to determine actual honeycomb compressive properties. The numerical FEA results show much better agreement with the experimental results than other conventional theories.

**Keywords:** thermoplastic honeycomb, out-of-plane compression, buckling, FEA.

## 1. INTRODUCTION

Honeycombs are widely used as core materials in sandwich structures. The out-of-plane compressive properties, stiffness and strength, of honeycomb cores are critical for many structural applications and the honeycomb's impact performance. This study utilizes the finite element tools to evaluate actual honeycomb out-of-plane compression behaviour with imperfect geometry and to determine the final properties. The investigated honeycomb material, named ThermHex®, in this article are produced in a continuous process from thermoplastic flat sheet at K.U. Leuven. More information about the process can be found in reference [1].

Since the thin sheet materials, like honeycomb cell walls, can only be compressed in the thickness direction by reason of stability, the actual honeycomb out-of-plane compression behaviour is intrinsically relevant to the honeycomb cell wall's buckling behaviour, not the material compressive properties. The honeycomb compressive modulus and strength should be described as the average steady buckling stiffness and the ultimate collapsing stress (critical stress) of the cell walls.

FE buckling analysis gives two approaches, linear (eigenvalue problem) buckling analysis and non-linear large deformation analysis. The linear buckling analysis theoretically predicts critical load of system instability with ideal geometry of an elastic structure and an ideal load model, whereas the non-linear analysis generally predicts more reliable results for real and imperfect systems. Linear buckling analysis is applied on unit cell and honeycomb models with different scales to obtain the intrinsic correlation between them, then only a unit cell model is adapted and applied to non-linear buckling analysis representing the real honeycomb model. That is because nonlinear FEA is very time consuming

## 2. THEORY REVIEW

Honeycomb out-of-plane (along  $Z$  axis in Figure 1a) compressive properties have been intensively investigated based on metal honeycombs with perfect geometry. In this paper, results from those theories are compared to FEA results.

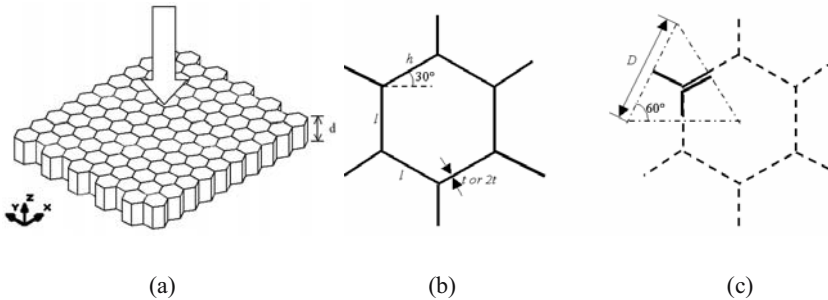


Figure 1. Dimensions of honeycomb. (a) The out-of-plane compressive load is along  $Z$  direction. Honeycomb depth is  $d$ . (b) Geometry of honeycomb unit cell. (c) ThermHex honeycomb angle element. Doubled thickness cell wall has two identical unbonded cell walls.

The conventional hexagonal honeycomb ( $l = h$ ,  $\theta = 30^\circ$ ) dimensions are shown in Figure 1b. The thickness of the cell walls is not everywhere identical  $t$ , 1/3 vertical cell walls have doubled thickness  $2t$  for most expanded honeycomb and the ThermHex honeycomb herein. However, as

shown in Figure 1c, within ThermHex honeycomb, the doubled thickness cell walls in fact consist of two identical unbonded cell walls that are bonded only at the top and bottom edges [2]. Hence the bending stiffness of such  $2t$  cell walls has only twice the bending stiffness of the cell walls with thickness  $t$ .

### 2.1 Out-of-plane compressive modulus

According to conventional viewpoints, without cell wall buckling, the honeycomb out-of-plane Young’s modulus  $E^*$  under compression simply reflects the solid cell wall material’s modulus,  $E_s$ , which is then rescaled by the area of the load-bearing section [3] [4] to estimate  $E^*$  as following:

$$E^* = \frac{2}{(1 + \sin \theta) \cos \theta} \frac{t}{l} E_s = 1.54 \frac{t}{l} E_s = \frac{\rho^*}{\rho_s} E_s \tag{1}$$

Eq.(1) describes the modulus for the ordinary honeycombs with 1/3 doubled thickness cell walls.  $\rho^*$  is the overall density of honeycomb material, and  $\rho_s$  is the density of the solid cell wall material.  $\rho^*/\rho_s$  is the relative density, a dimensionless parameter.

### 2.2 Out-of-plane compressive ultimate strength

*Elastic buckling critical stress:* The honeycomb compression ultimate strength can be deduced from elastic buckling theory of a single plate with proper boundary conditions (BC), which represent the rim clamping situations for each single cell wall. Based on the theory from Timoshenko’s work [5], Zhang and Ashby derived the elastic buckling critical stress for the honeycomb with 1/3 doubled (bonded) cell walls [4], see below Eq.(2). The critical stress  $\sigma_e^*$  is the upper limit value for the axial stress that the plate can support. An interpretation as a value of strength is thus appropriate.

$$\sigma_e^* = \frac{5K}{(1 - \nu_s^2)(1 + \sin \theta) \cos \theta} E_s \left( \frac{t}{l} \right)^3 = 7.19 E_s \left( \frac{\rho^*}{\rho_s} \right)^3 \tag{2}$$

where  $K=5.73$  is used for the case of all four clamped edges of cell walls. Whereas  $K=3.29$  is used for the simply supported edge conditions which prevents only in-plane displacement. Ashby argued that in reality the constraints on the cell wall edges are stronger than the simply supported

ones, but weaker than the fully clamped. Therefore an intermediate value,  $K=4$ , was suggested resulting in Eq.(3):

$$\sigma_e^* \approx 6E_s \left( \frac{\rho^*}{\rho_s} \right)^3 \quad (3)$$

According to the study from Wang [6], it is considered that the initial buckling of a main wall, which has  $2t$  thickness, is constrained by adjacent wall's twisting stiffness. Hence the calculated critical stress is:

$$\sigma_e^* = \frac{23.02}{(1-\nu_s^2)(1+\sin\theta)\cos\theta} E_s \left( \frac{t}{l} \right)^3 = 5.34E_s \left( \frac{\rho^*}{\rho_s} \right)^3 \quad (4)$$

*Crushing strength:* The crushing strength is usually less than honeycomb elastic buckling critical stress. It describes the stress level which keeps honeycomb crushing in a quasi-steady way. Therefore the applied load must overcome first the elastic buckling threshold then drop down dramatically to the crushing level. In Wierzbicki's work [7], the collapse of an angle element from honeycomb was analyzed giving the collapse strength in the following equation, where  $\sigma_y$  is the cell wall material yielding strength.

$$\sigma_p^* = 6.6\sigma_y \left( \frac{t}{l} \right)^{\frac{5}{3}} = 3.21\sigma_y \left( \frac{\rho^*}{\rho_s} \right)^{\frac{5}{3}} \quad (5)$$

All the theories mentioned above actually have another independent parameter, the depth of honeycomb  $d$ , see Figure 1a. A decrease of  $d$  definitely increases the stability of the honeycomb. If  $d > 3l$ , the influence from  $d$  can be neglected [4]. Unfortunately our honeycombs can not satisfy such condition, and they have unbonded double thickness cell walls. Hence a new method must be obtained to estimate the correct compressive properties for our ThermHex honeycombs.

### 2.3 FEA on buckling

FE buckling analysis can be done via two approaches, one is linear buckling analysis (eigenvalue problem), and the other one is nonlinear analysis. The linear buckling analysis is to determine the structure bifurcation point where the primary and secondary loading paths intersect by using a linearized model of elastic stability. The nonlinear buckling analysis

may take into account different types of nonlinearities, including large deformation and material nonlinearities. The computing time of nonlinear analysis can be enormously longer than that of linear analysis.

### **3. MATERIAL**

The honeycomb is made from one type of Polypropylene (PP) with 4% Talc filler inside. The Young's modulus of such Talc-PP sheet is 1.7 GPa and the tensile yield stress is 21 MPa, which are determined by a standard tensile test at room temperature according to ASTM D882. The sheet density is measured to be  $0.9 \times 10^3 \text{ kg/m}^3$ . The honeycomb samples, which have 7.2 mm the depth, 3.7 mm the line segment length of hexagonal cell. Two types of honeycomb are investigated here, one with 0.16 mm cell wall thickness  $t$ , the other one with 0.23 mm. 1/3 cell walls are doubled (with  $2t$  thickness), but not bonded. The honeycombs are tested under flat-wise compressive load (FCT) according to standard ASTM C365. The sample size is 50 mm by 50mm. The results are analyzed and compared to the FEA results.

### **4. FEA RESULTS AND DISCUSSION**

The honeycomb buckling FEA is conducted according to the scheme shown in Figure 2. The computational requirements on linear buckling analysis are much lower than a nonlinear analysis. The conditions in which both analysis types are applied are likewise different. In this paper the linear analysis is performed on perfect honeycomb only for parameter studies, including boundary effects, scale effects and cell wall thickness effects. Full nonlinear analysis is performed only for a modified unit cell model with geometric imperfections. Since the modified unit cell model inherits the characteristics from the infinite honeycomb, it is capable to express the same behaviour as the honeycomb under compression.

The analysis is implemented with FEA software ANSYS®. The honeycomb cell walls are represented by four-node three-dimensional shell elements, SHELL63, using their bending and membrane capabilities. The aforementioned material properties are applied. Single cell wall is meshed with 10 by 20 elements. The uniform thickness cell walls, 0.16 mm or 0.23 mm, are built in the geometric models. The value of RMI (ratio of bending moment of inertia) is set as 2 to simulate the unbonded double thickness cell walls. The other geometry of models is set identical as the real honeycomb geometry mentioned above.

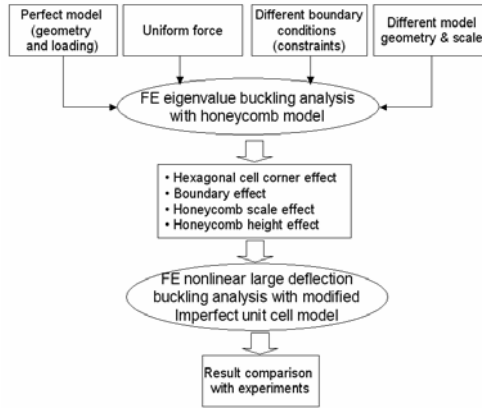


Figure 2. The methodology of FEA on honeycomb out-of-plane compressive behaviours.

### 4.1 Linear buckling analysis

The perfect honeycomb models with 1, 2, 3, 4, 5, 6, 7, 19, 112 cells are analysed. Some of them are shown in Figure 3. Five types of BC on top and bottom of the honeycomb models are investigated, which are indicated in Figure 4. On the top and bottom sides of the honeycomb models, in-plane displacement (UXY) or/and rotation (ROTXYZ) constraints can be applied.

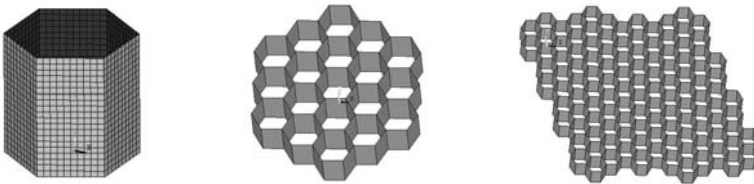
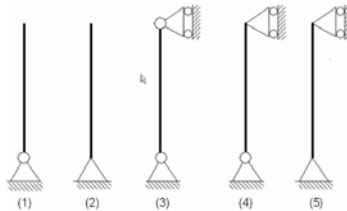


Figure 3. Examples of honeycomb geometric models with 1, 19, 112 cells for linear analysis.

The direct results of linear buckling analysis are the system load factors corresponding different eigenvalues acquired by the software. The nominal honeycomb critical stress is derived from the minimum eigenvalue load factor (to ensure the same buckling mode for different models) recalculated upon the contributing area over which the load is applied. Figure 5 shows the contributing area for one cell wall. The results of critical stresses for different model scales and BC are show in Figure 6. It is obvious to see that when the BC tends to be stricter, the critical strength is getting higher. Both two types of honeycombs with BC case 3 to 5 also show about 20% drop of the honeycomb critical stress when the scale of honeycomb increases from 1

cell to 112 cells. That is because the number of the  $2t$  cell walls per cell becomes less when the scale of honeycomb model increases. The detailed values are shown in Table 1. Such information is very useful for building unit cell model in nonlinear analysis. For the BC case 1 and 2, since one side is totally free, the scale of honeycomb is not dominant anymore, therefore the critical stress doesn't drop when the honeycomb scale increases. The BC case 3 in Figure 4 actually represents the honeycomb constraints under FCT situation, while the BC case 5 represents the situation of compression with bonded stiff skin layers like in sandwich panel. In later nonlinear analysis, only BC case 3 and 5 are considered.



*Figure 4.* The schematic view of five applied BC on honeycomb models. (1) Top: free edge; Bottom:  $UXYZ=0$ . (2) Top: free edge; Bottom:  $UXYZ=0$ ,  $ROTXYZ=0$ . (3) Top:  $UXY=0$ ; Bottom:  $UXYZ=0$ . (4) Top:  $UXY=0$ ,  $ROTXYZ=0$ ; Bottom:  $UXYZ=0$ . (5) Top:  $UXY=0$ ,  $ROTXYZ=0$ ; Bottom:  $UXYZ=0$ ,  $ROTXYZ=0$ .

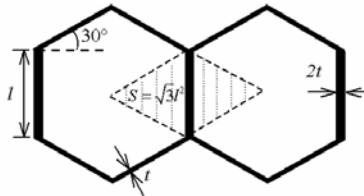


*Figure 5.* The contributing area (shaded), which is used for the calculation of the honeycomb critical stress for one cell wall.

*Table 1.* The quantity of the decrease of critical strength as the number of cells increases from 1 to 112.

	BC case 3	BC case 4	BC case 5
0.16 mm honeycomb	-21%	-21%	-25%
0.23 mm honeycomb	-18%	-22%	-24%

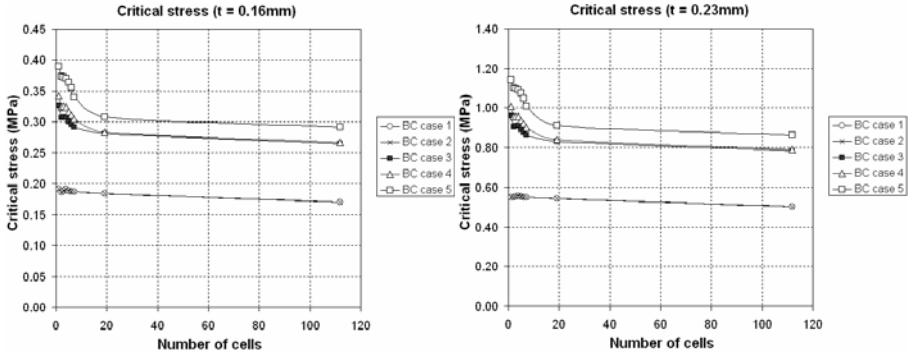


Figure 6. Critical linear buckling strengths of the honeycombs with 0.16 mm and 0.23 mm cell wall thickness.

## 4.2 Nonlinear buckling analysis

From the results of linear analysis, it is obvious that the critical stress of unit cell model is actually higher than the infinite honeycomb model under usual BC. Thus the unit cell model must be modified and adapted to conduct a nonlinear analysis. First the unit cell model should be ‘weakened’ to obtain the same intrinsic mechanical resistance against compressive load as the infinite honeycomb has. Because the honeycomb critical buckling stress is linearly proportional to the bending stiffness of the cell walls with the conditions that honeycomb cell geometry and BC keep constant [3-6], unit cell model can simply ‘weakened’ by decreasing about 20% the cell wall’s bending moment of inertia corresponding to the specific honeycomb type and BC (see Table 1). Thus the unit cell model has the same linear buckling stress as infinite honeycomb model does. However the ‘weakened’ unit cell model is still not prepared yet for nonlinear analysis until the imperfection is introduced in the model. The imperfections can very diversely exist in the honeycomb. Among them, the tilting of cell walls is one of important imperfections. Also tilting cell walls are easy to be realized in the geometry model. Therefore only this type of imperfection is modelled and analysed. Herein a very small cell wall’s tilting angle of 0.02 radian from vertical position is used. At the moment only the results from BC case 3 are compared to the experimental results. Results of BC case 5 are believed to be higher than those of BC case 3, however due to lack of experimental results, they are not compared. In attempt to check the influence from the tilting angle on the result, several tilting angle is applied to the model and the results are also compared with each other. Figure 7 and Figure 8 show the nonlinear analysis results (modulus and ultimate strength) for the

honeycomb with 0.16 mm and 0.23 mm cell wall thickness under BC case 3 compared to the experimental value and other theories. Table 2 gives the results of tilting angle analysis.

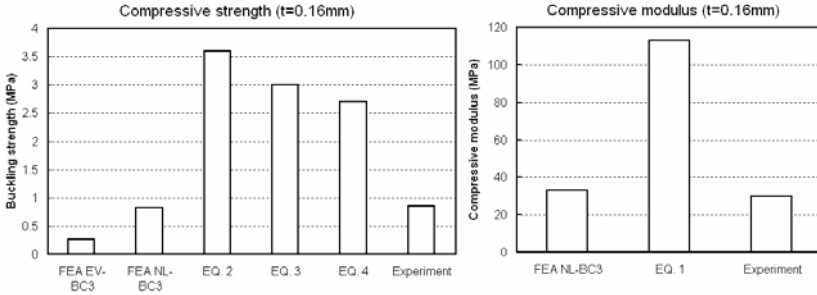


Figure 7. Results comparison for the honeycomb with 0.16 mm cell wall thickness.

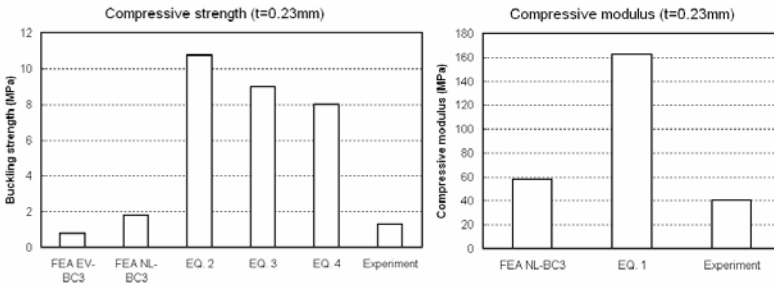


Figure 8. Results comparison for the honeycomb with 0.23 mm cell wall thickness.

Table 2. Results of nonlinear analysis with different cell wall tilting angle.

Cell wall tilting angle (rad)	Modulus (MPa)	Strength (MPa)
0.0035	35.8	0.83
0.0104	35.7	0.83
0.0208	34.3	0.82
0.0347	33.5	0.81
0.0486	33.4	0.80
0.0625	33.7	0.79

From Figure 7 and 8, it can be seen that the results of nonlinear analysis, strength and modulus, have much better agreement with experimental results than the results from the conventional theories, which are not very suitable to estimate our honeycomb’s properties. The results in Table 2 indicate that the modelled geometry imperfection, the tilting of cell walls, does not dramatically influence the final properties when it varies within a very small range. The effect of such imperfection is not to decrease the honeycomb’s

mechanical performance, but to trigger the nonlinear behaviour occurring under compressive load.

## 5. CONCLUSION

This study presents a new approach to analyse the honeycomb's out-of-plane compressive properties. Combined with linear FE buckling analysis on honeycombs with different scales, the unit cell model can be adapted for FE nonlinear analysis representing the infinite honeycomb's behaviour. One type of geometry imperfection, the tilting of cell walls, is introduced into the model to trigger nonlinear behaviour. The results show very good agreement to the experimental data. The conventional elastic buckling theories are not suitable to predict our ThermHex honeycomb properties.

## REFERENCES

1. Pflug, J. and I. Verpoest, *Thermoplastic folded honeycomb and method for the production thereof*. 2000, International Patent Publication: K.U. Leuven Research & Development, Belgium.
2. Pflug, J., I. Verpoest, and D. Vandepitte. Thermoplastic folded honeycomb cores - cost efficient production of all thermoplastic sandwich panels. In *ICCM 13*. 2001. Beijing China: Paper 1531.
3. Gibson, L.J. and M.F. Ashby, *Cellular Solids: Structure and Properties*. 2nd edn. Cambridge Solid State Science Series. 1999: Cambridge University Press, Cambridge.
4. Zhang, J. and M.F. Ashby, The out-of-plane properties of honeycombs. *International Journal of Mechanical Sciences*, 1992. **34**(6):475-489.
5. Timoshenko, S.P. and J. Gere, *Theory of Elastic Stability*. 2nd edn. 1961: McGraw-Hill.
6. Wang, Y., Elastic collapse of honeycombs under out-of-plane pressure. *International Journal of Mechanical Sciences*, 1991. **33**(8):637-644.
7. Wierzbicki, T., Crushing analysis of metal honeycombs. *International Journal of Impact Engineering*, 1983. **1**(2):157-174.

# DEFORMATION OF FOAM CORES IN UNIAXIAL COMPRESSION-TENSION CYCLE

Vitaly Koissin

*Department of Metallurgy and Materials Engineering, Katholieke Universiteit Leuven, Kasteelpark Arenberg 44, B-3001 Leuven, Belgium*

vitaly@kth.se

Andrey Shipsha

*Department of Aeronautical and Vehicle Engineering, Royal Institute of Technology, Teknikringen 8, S-10044 Stockholm, Sweden*

andrey@kth.se

**Abstract** This paper deals with experimental and analytical analysis of the mechanical behaviour of crushed foam cores. Three rigid cellular core materials are tested in uniaxial compression-tension-compression. An analytical model is proposed describing the stress-strain curve in tension and secondary compression. A special emphasis is laid on the relaxation behaviour of a crushed foam core in tension.

**Keywords:** sandwich structure, local loading, crushed foam core, residual dent.

## 1. INTRODUCTION

Due to low bending stiffness of thin faces and low strength of a lightweight core, a local damage in foam cored sandwich structures is one of the concerns. Usually, localised loads result in a prominent deflection of the face and, as a consequence, crushing of the foam core. While the face deflection may remain elastic, the core crushing results in its irreversible deformation. During unloading, the face straightens pulling the crushed core; typically the face does not retain its original position leaving a residual dent. A such local damage may significantly alter the residual local stiffness and strength of a structure. Therefore, the properties of the crushed core have to be accounted for in analysis of repeated loading or the residual dent formation in sandwich structures.

In this study, the behaviour of several polymeric foam cores is characterised under uniaxial compression, up to densification, followed by tension, relaxation control and subsequent compression. The experimental results are compared with the semi-empirical analytical solution showing a good agreement.

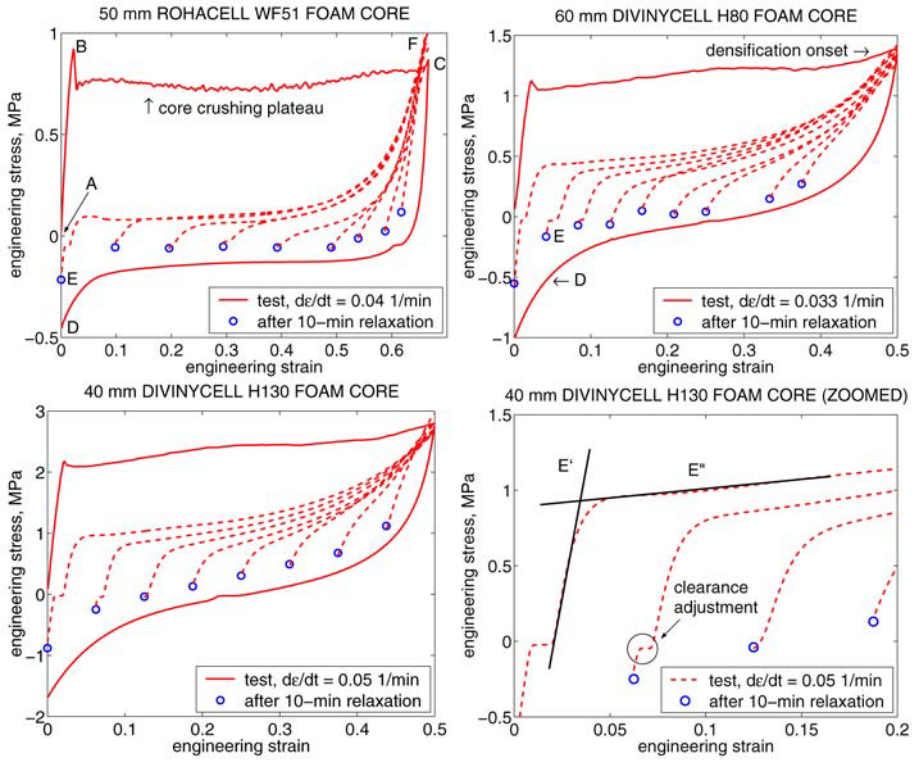


Figure 1. Uniaxial compression/tension stress-strain curves for tested foam.

## 2. MATERIALS AND TEST PROCEDURE

Three foam materials typically used as a core in sandwich structures were considered; one polymethacrylimide foam Rohacell WF51, and two polyvinylchloride foams Divinycell H80 and H130. All foams have a closed-cell structure and nominal densities of 51, 80 and 130 kg/m<sup>3</sup>, respectively.

Cylindrical specimens with a diameter of 50 mm were cut from the foam material blocks in the out-plane direction. The thickness (height) of the specimens was equal to the thickness of the supplied foam blocks that was 50 mm for WF51, 60 mm for H80, and 40 mm for H130. The specimens were bonded between two aluminum cylinders which fit the fixtures in a testing machine.

Quasi-static uniaxial loading was performed in the displacement control at 2 mm/min in several steps as shown in Figure 1. First, the compression was performed until the foam was fully crushed, following the path *A-C* (the region *A-B* represents the elastic response). After that, the crushed foam was unloaded and eventually loaded in tension along the path *C-D*. The specimens were subject to stress relaxation during 10 minutes at a constant strain  $\varepsilon_D \equiv \varepsilon_E$  while the stresses changed along the path *D-E*. Finally, the specimens were

subject to secondary compression (path  $E-F$ ). The stress relaxation and the following compression were carried out for a number of different strains  $\varepsilon_E$  shown by circle markers in Figure 1. Two specimens were used in each set of  $\varepsilon_E$ .

### 3. TEST RESULTS: VIRGIN FOAM CRUSHING

The elastic compressive response of rigid structural foams is in the order of 2% strain as seen from path  $A-B$  in Figure 1 and, in general, follows the classical theory of elasticity, Ref. [1]. However, the plastic behaviour of foams is fundamentally different from that of solid materials. Unlike the plastically incompressible solids, the foam materials exhibit plastic compressibility (crushing) due to bending and buckling of cell walls leading to a collapse of cells. As the consequence of this phenomenon, the compressive response of the tested foams had a long crushing plateau, see path  $B-C$  in Figure 1, and thus was close to the elastic-ideally plastic material model. Visual observations have revealed that all three virgin foams exhibited the progressive crushing mechanism, see e.g. Ref. [2], i.e. that the crushing is initiated and localised in the most “weak” cell layer rather than in the whole volume of the specimen. When the cells in this layer start to compact, i.e. the local compressive strain reaches the densification strain (68% for WF51, 50% for H80 and H130 foams), the stresses quickly increase, and this triggers the crushing of next layer. It should be noted that the path  $B-C$  (excepting its final point) does not represent the real local strain state since averages it over a whole specimen height.

The progressive crushing is also characterised by a distinct boundary between crushed (densification strain state) and un-crushed (elastic strain state) material. In the presented tests, the crushing of H80 and H130 foams was always initiated nearby the midship of the specimens and then spread towards the lower and upper parts. This observation is in agreement with the known fact [3] that there is a slight density (and mechanical properties) variation through the foam block thickness with lower density and strength in the middle. The crushing onset in these foam cores was rather smooth, and the yield drop, point  $B$ , was feebly marked as seen in Figure 1. On the contrary, the WF51 specimens showed a distinct yield drop, especially when the crushing started in the midship being often accompanied by a popping sound. About 1/4 of the total number of the WF51 specimens showed a such crushing onset. In the other WF51 specimens, the crushing started close to one of the edges. Then, the cells compaction either spread gradually toward the other edge producing almost straight stress plateau or, after some time, turned to the midship decreasing the stress plateau as seen in Figure 1 (left top). These 3/4 of the WF51 specimens showed relatively small stress drop at the crushing onset.

The WF51 foam specimens did not show a noticeable change in the diameter during uniaxial compression while H80 and H130 specimens become of a barrel shape increasing its midship diameter by about 6%. Thus, a slight increase in stress along the plateau  $A-B$  in Figure 1 (right top and left bottom) should substantially be attributed to the use of engineering stress.

#### 4. TEST RESULTS: RELAXATION EFFECT OF THE CRUSHED FOAM

The crushed foams exhibited a significant stress relaxation effect after unloading and eventual tension as can be seen in Figure 1. The stress relaxation was measured at the given constant strain  $\varepsilon_D \equiv \varepsilon_E$  during 10 minutes whereas the instantaneous stresses corresponding to the point  $D$  changed to some equilibrium stresses (the point  $E$ ), see Figure 1. Of course, the “equilibrium” state in this case is related only to 10 minutes interval, since further stress relaxation of a comparable magnitude can develop in a logarithmic-like time scale.

It is interesting to observe that the path  $D-E$  sometimes comes from the negative stress domain to the positive one, see Figure 1. Thus, the final stress,  $\sigma_D$ , may be higher in absolute value than the initial stress,  $\sigma_E$ . Analogously, if the relaxation regime started from the positive stress domain, the stress eventually increases. Thus, the term “stress relaxation” should be considered here in a relative sense, since anti-relaxation is observed sometimes in reality.

The most significant stress relaxation was found within first 50 seconds of the relaxation test as shown in Figure 2. It can be seen that the relaxation rate is different for all tested foams whereas the shape of the graphs and the “threshold time” (point  $T$ ) are similar in all cases. The relaxation rate is strongly dependent on the tension of the crushed foam; the highest relaxation rate is observed for specimens extended to their original height ( $\varepsilon_D=0$ ). There is also some evidence that the relaxation rate may depend on the foam density but this conclusion should be supported with a more extensive experimental data set.

Figure 2 (right bottom) illustrates the relative stress relaxation, i.e. change of stress along path  $D-E$ ,  $\sigma_E - \sigma_D$ , sampled from the response curves, Figure 1, and normalized in absolute value against the magnitude of this change at zero strain ( $\varepsilon_D=0$ ). As can be seen, all tested foams show a very similar behaviour and have a distinctive “threshold strain” (approximately 0.11), at which the relaxation magnitude becomes weakly dependent on the strain  $\varepsilon_D$ . This “threshold strain” coincides with the strain, at which the final part of path  $C-D$  shows extensive hardening, Figure 1. It should be pointed out that about 1/3 of the total number of specimens with crushed WF51 foam failed in tension prior to the relaxation regime. This can be explained by a brittle nature of this foam grade.

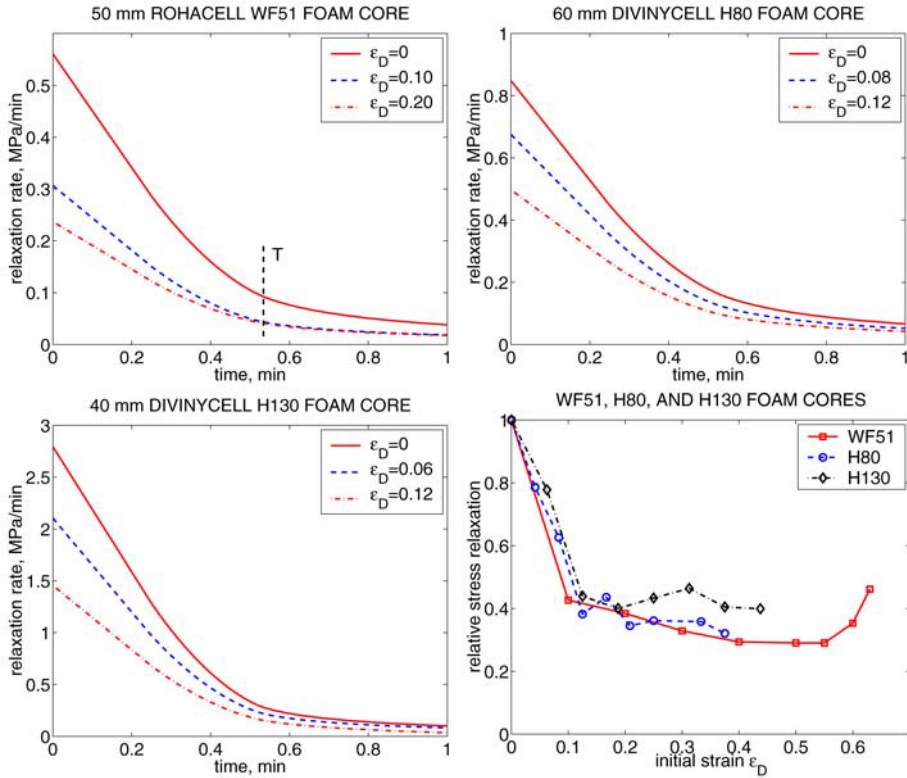


Figure 2. Stress relaxation rate vs. time for crushed WF51, H80, and H130 foams loaded in tension and relative stress relaxation for all three foams (right bottom).

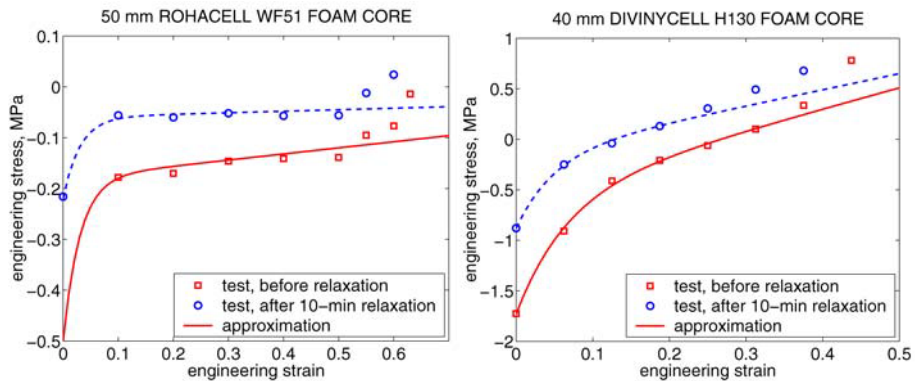


Figure 3. An analytical approximation of the stress-strain curves for the crushed WF51 (left) and H130 (right) foams in uniaxial tension.

The revealed relaxation phenomenon is very important for analytical or finite-element analysis of the residual dent formation in locally loaded sandwich structures. In this case, of course, crushed foam core does not undergo the pure stress relaxation. This is since a reduction in the core reaction immediately reduces the residual dent in the face sheet, that, in turn, strains the core and thus increases its reaction, and so on. A such self-balancing phenomenon is difficult to be modelled exactly but, as believed by the authors, the final reaction of the crushed core can be obtained using the simple test procedure described above. This is supported by a successful use of the presented test results for analytical modelling the residual dent formation in Ref. [4].

## 5. TEST RESULTS: SECONDARY COMPRESSION OF CRUSHED FOAM

The path  $E-F$  of the stress-strain curve, Figure 1, characterizes the crushed foam reaction during secondary compression. There are two distinct linear regions in the beginning of the path  $E-F$  which can roughly be approximated with two moduli,  $E'$  and  $E''$ , as shown in Figure 1 (right bottom). The tests data reveals that these moduli are dependent on the magnitude of strain at the onset of secondary compression,  $\varepsilon_E$ , i.e. on the position of point  $E$ . This is shown in Table 1 where the moduli are given for three different magnitudes of the strain  $\varepsilon_E$ . As can be seen from this table and Figure 1, the first part of the path  $E-F$  generally resembles the compressive response of the virgin foams but has much lower secant modulus and “yield” plateau. A such material response is typical for relatively low values of the strain  $\varepsilon_E$ , while for higher values of  $\varepsilon_E$  (more than 40% of strain for WF51 foam or 20% for H80 and H130) the “elastic” region of secondary compression becomes shorter and less obvious, and the “yield” plateau is not observed, see Figure 1.

The final part of the path  $E-F$  indicates a highly non-linear material response of the crushed foams resembling a stress increase after the onset of densification during primary compression but at lower “densification” strain. For the crushed WF51 foam, some hardening (about 6%) is observed, if compared to the compression of the virgin foam (the point  $F$  is over the point  $C$  corresponding to the primary compression). On the contrary, some softening (about -4%) is observed for the crushed H80 and H130 foams. This difference in the hysteresis loops can be due to some specific properties of the tested foams. It interesting to note that there is no distinct dependence of hardening on the magnitude of the strain  $\varepsilon_E$  for WF51 foam, while softening in H80 and H130 foams decreases with increasing of  $\varepsilon_E$  (from -5% to -2%).

The compressive response of the crushed foams (the path  $E-F$ ) is important for analysis of the repeated local loading of a sandwich structure with locally crushed core. The first part of the path  $E-F$  can particularly be crucial for

Table 1. Stiffness of the crushed foam under repeated compression from different initial strains.

foam	Young's modulus*	initial strain $\varepsilon_E$			modulus $E'$ , MPa			modulus $E''$ , MPa		
		1	2	3	1	2	3	1	2	3
<b>WF51</b>	85	0	0.10	0.20	22.4	8.2	7.8	0	0	0.1
<b>H80</b>	77	0	0.08	0.12	34.6	24.2	18.0	0.5	1.0	1.4
<b>H130</b>	135	0	0.06	0.12	73.1	63.2	46.0	1.5	1.8	2.8

\* Young's modulus of the virgin foam material (mean value), path *A-B* in Figure 1

modelling of a local buckling of the face sheet over the locally crushed core with reduced stiffness. In the previous studies, e.g. Ref. [4], it was shown that the sandwich panels containing a moderate damage in the core had minor inward growth of the residual dent of the face up to the moment of buckling; thus, the supporting core reaction followed the relatively large modulus  $E'$ . In the sandwich specimens having a large damage zone, a considerable residual dent growth was provoked. This caused a noticeable reduction from  $E'$  to  $E''$  in the core support, and, as a result, drastic drop in the local buckling stress.

## 6. APPROXIMATION OF CRUSHED FOAM REACTION

An analytical form of the foam reaction can be obtained using polynomial approximation of the experimental response curves, Figure 1. The path *C-D* of these curves (as well as imaginary path *C-E*) can also be approximated as

$$\sigma_t(\varepsilon) = \sigma_1 + \sigma_2\varepsilon + (\sigma_3 - \sigma_1) \exp(-\kappa\varepsilon). \tag{1}$$

The parameter  $\sigma_3$  represents here the tensile stresses in the crushed foam at the point *D* or *E* and is obtained experimentally. The parameters  $\sigma_1$ ,  $\sigma_2$ , and  $\kappa$  define, respectively, the plateau stress, slope and curvature of the stress-strain curve. These parameters should be selected manually to fit the experimental data and, for considered foams, can be taken according to Table 2. The function (1) well approximates the tensile path of the stress-strain curves as presented in Figure 3. The exceptions are several experimental points on the right but they are uninteresting in the view of the residual dent formation in sandwich structures, since these points are situated in the positive stress domain.

The first part of the compression-after-tension path *E-F* is approximated as

$$\sigma_c(\varepsilon, \varepsilon_E) = \sigma_1(\varepsilon_E) + \sigma_2(\varepsilon_E)\varepsilon + (\sigma_3(\varepsilon_E) - \sigma_1(\varepsilon_E)) \exp(-\kappa(\varepsilon_E)\varepsilon), \tag{2}$$

that is similar to Eq. (1) but with variable coefficients

$$\sigma_1 = \sigma_{11} + \sigma_{12}\varepsilon_E, \quad \sigma_2 = \sigma_{21} + \sigma_{22}\varepsilon_E, \quad \sigma_3 \equiv \sigma_t(\varepsilon_E), \quad \kappa = \kappa_1 + \kappa_2\varepsilon_E + \kappa_3\varepsilon_E^2,$$

Table 2. A possible combination of the parameters in Eq. (1). In the numerator – instant value at the onset of the stress relaxation control; denominator – after 10 min.

foam	$\sigma_y^*$ , MPa	$\sigma_1$ , MPa	$\sigma_2$ , MPa	$\sigma_3$ , MPa	$\kappa$
<b>WF51</b>	0.95	-0.18 / -0.06	0.12 / 0.03	-0.50 / -0.22	33 / 33
<b>H80</b>	1.15	-0.24 / -0.08	0.75 / 0.62	-0.96 / -0.55	22 / 30
<b>H130</b>	2.20	-0.54 / -0.15	2.10 / 1.60	-1.73 / -0.88	15 / 20

\* Yield stress of the virgin foam material (mean value), point *B* in Figure 1

Table 3. A possible combination of the parameters in Eq. (2). Data is given for the repeated compression after 10 min stress relaxation.

foam	$\sigma_{11}$ , MPa	$\sigma_{12}$ , MPa	$\sigma_{21}$ , MPa	$\sigma_{22}$ , MPa	$\kappa_1$	$\kappa_2$	$\kappa_3$
<b>WF51</b>	0.08	-0.12	0.05	1.25	105	-325	250
<b>H80</b>	0.40	-1.15	0.61	3.00	95	-320	200
<b>H130</b>	0.88	-1.44	1.40	8.80	104	-2600	290

which are dependent on the starting deformation  $\varepsilon_E$ , i.e. on the position of the point *E* in Figure 1. The coefficients  $\sigma_{ij}$  and  $\kappa_i$  are selected manually to fit the test data and, for the considered foam materials, can be chosen according to Table 3. The graphs presenting the approximation (2) are given in Figure 5.

## 7. STRAIN ANALYSIS FOR CRUSHED FOAM

For practical applications, the strain  $\varepsilon$  in Eqs. (1) and (2) should be expressed in the term of overall displacement of the face/core interface. Considering the foam core crushing in the uniaxial compression, as schematically illustrated in Figure 4 (a–c), the following relation can be established:

$$h_c = w_0 + (h_c - t_e)(1 - \varepsilon_d) + t_e(1 - \varepsilon_y), \quad (3)$$

where  $\varepsilon_y, \varepsilon_d$  are the yield and densification strains of a foam core, that gives

$$t_e = (h_c \varepsilon_d - w_0) / (\varepsilon_d - \varepsilon_y). \quad (4)$$

On the other hand, considering the uniaxial tension of a pre-compressed foam core, Figure 4 (d),

$$h_c = w_0^r + t_r + t_e(1 + \varepsilon_t), \quad \varepsilon_y \leq |\varepsilon_t| \leq \varepsilon_t^{ult}, \quad (5)$$

where  $\varepsilon_t^{ult} \ll 1$  is the ultimate strain of a virgin foam in the uniaxial tension. Further, the following proportion can be drawn:

$$(w_0 - t_e \varepsilon_y) / \varepsilon_d = (w_0^r + t_e \varepsilon_t) / \varepsilon, \quad (6)$$

which, substituting Eq. (4), results in the exact solution

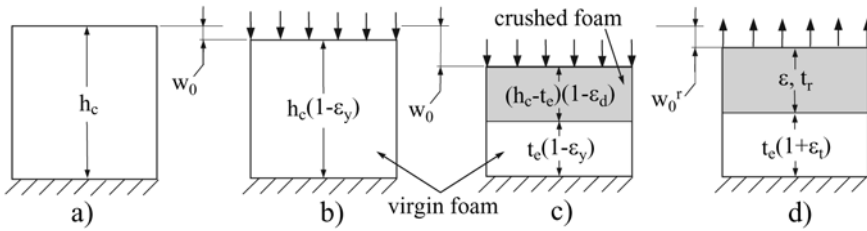


Figure 4. Geometry used to find strains in the crushed and undamaged parts of the foam in uniaxial compression/tension.

$$\varepsilon = \frac{w_0^r(\varepsilon_d - \varepsilon_y) + (h_c\varepsilon_d - w_0)\varepsilon_t}{w_0 - h_c\varepsilon_y}, \tag{7}$$

where the tensile strain in the virgin foam,  $\varepsilon_t$ , can be calculated through the Young’s modulus,  $E_c$ , of a virgin foam and Eq. (1) as

$$\varepsilon_t \equiv \varepsilon_t(\varepsilon) = -\sigma_t(\varepsilon)/E_c. \tag{8}$$

However, it is possible to avoid Eq. (8), since the out-plane stiffness of the crushed foam is much smaller than of the virgin foam. Hence, the strain  $\varepsilon_t$  are negligibly small,  $|\varepsilon_t| \ll \varepsilon_y, \varepsilon_t^{ult}$ , and, accounting also for that  $\varepsilon_y \ll \varepsilon_d$ ,

$$\varepsilon \approx \frac{w_0^r\varepsilon_d}{w_0 - h_c\varepsilon_y}, \tag{9}$$

that may also be utilized when considering the repetitive compression of a crushed foam, path *E-F* in Figure 1.

Figure 5 illustrates the use of Eqs. (1), (2), and (9) for analytical modelling the tension-compression response of crushed foams. The test method was the same as described in Section 2 with the only difference that the specimens were densificated partially; namely, 1/2 of the foam thickness remained undamaged. Figure 5 depicts that the analytical and experimental results are in very good agreement. Thus, the stress-strain diagram of a partially crushed foam specimen can be drawn through the one for a fully crushed specimen. This allows to evaluate the behaviour of the crushed core in locally damaged sandwich structures through the response curve of a fully crushed foam specimen.

## 8. CONCLUSIONS

A semi-empirical form of the foam reaction under uniaxial compression-tension cycle is obtained using approximation of the experimental data. The strains in the densificated and elastic parts of the foam are analytically expressed in the term of overall displacement sampled from the testing machine. The analytically modelled and experimental stress-strain curves are in a very

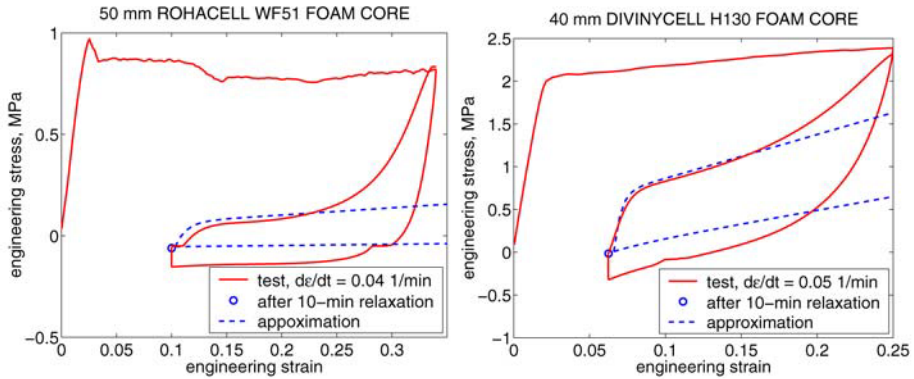


Figure 5. Analytical approximation of the stress-strain curves for the crushed WF51 (left) and H130 (right) foams in uniaxial loading.

good agreement, as for fully crushed specimens, as well as for partially crushed ones. The results of this study may contribute to the development of damage tolerance or residual strength analysis for sandwich structures having local damage in the form of crushed foam core and a residual dent in the face.

The proposed methodology presumes uniaxial stress state of a foam material and its complete integrity. However, a number of specimens with crushed WF51 foam failed in tension; a criterion for failure prediction on such specimens was undetermined. Also, the test results may depend on the strain rate, presence of multi-axial strain state, relaxation time, etc. Therefore, these aspects should be further studied and validated by a complimentary testing.

## ACKNOWLEDGEMENTS

The authors are thankful to Prof. Vitaly Skvortsov (State Marine Technical University, St.-Petersburg, Russia) for his valuable help in the presented analytical study. Some test specimens were kindly supplied by Dr. Per Wennhage (Royal Institute of Technology, Stockholm, Sweden).

## REFERENCES

- [1] G.L. Grenestedt. Effective elastic behavior of some models for 'perfect' cellular solids. *International Journal of Solids and Structures*, 36:1471–1501, 1999.
- [2] Q.M. Li et al. The crush behaviour of Rohacell-51WF structural foam. *International Journal of Solids and Structures*, 37:6321–6341, 2000.
- [3] V. Koissin and A. Shipsha. Mechanical properties of pre-compressed and undamaged Divinycell H-grade foam core. *Report C2001-5*, Dept. of Aeronautics, Royal Institute of Technology, Stockholm, 2001.
- [4] V. Koissin. The local strength of foam cored sandwich structures. *PhD thesis*, Dept. of Strength of Materials, State Marine Technical University, St.-Petersburg, Russia, 2004. (In Russian)

# LOADING RATE EFFECTS ON FOAM CORES FOR MARINE SANDWICH STRUCTURES

Eric Lolive<sup>1</sup>, Pascal Casari<sup>2</sup> and Peter Davies<sup>3</sup>

<sup>1</sup>*IUT Brest, LIME, Laboratoire d'Ingénierie Mécanique et Electrique, 29231 Brest, France*

<sup>2</sup>*GeM, Institut de Recherche en Génie Civil et Mécanique 44322 Nantes, France*

<sup>3</sup>*Materials and Structures group, Ifremer Brest Centre, 29280 Plouzané, France*

**Abstract** This paper presents first results from a project which aims to generate foam core properties under loading rates representative of those encountered during wave impact of racing yachts. First, special instrumentation enabled shear strain rates to be measured in-situ. Then a symmetrical shear test was designed to allow shear stress-strain behaviour to be determined at rates corresponding to those measured at sea. Image analysis was used to validate the test set-up. First results for high density foams indicate that quasi-static data may suffice for design.

**Keywords:** Foam core, PVC, high rate, shear, instrumentation.

## 1. INTRODUCTION

Foam cores are widely used in the sandwich structures used for boat construction. These materials provide weight gains are often preferred to honeycomb cores in areas likely to encounter wave impacts. The selection of foam type and density is generally based on quasi-static design data but the loading rates can be very high in these regions. It is therefore of considerable interest to develop tests which enable properties to be determined at rates corresponding to service loading conditions. Several previous studies have addressed this subject and some data are available [1-4] but the development of new foam grades makes it difficult to compare these data.

The aim of the work described in this paper is threefold. First, measurements on a racing yacht using special shear strain plugs enabled strain rates to be measured. Then a test was designed to enable shear tests to be performed at these rates. Finally data was generated and the test procedure was validated using image analysis.

## 2. SHEAR STRAIN MEASUREMENTS IN-SITU

Special instrumentation was designed and built in order to evaluate the strain rate levels encountered in a sandwich hull loaded under slamming conditions, Figure 1. A similar system has been used on pressure-loaded panels previously [5].

Strain gages are intrusive, and to assess this point, a calibration of strain levels has been performed in the laboratory using standard shear tests on the foam. A ratio of 2.37 was found between the mean strain level and that measured with the shear strain plug.

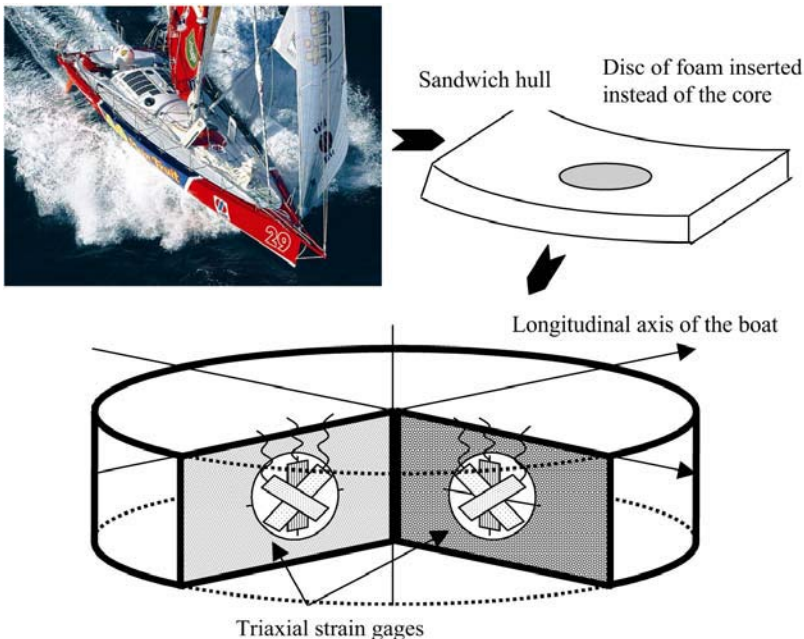


Figure 1. Instrumentation plugs used to measure core strains in-situ.

This ratio was used subsequently, when identical plugs were mounted on the racing yacht shown in Figure 1. Figure 2 shows an example of the data recorded.

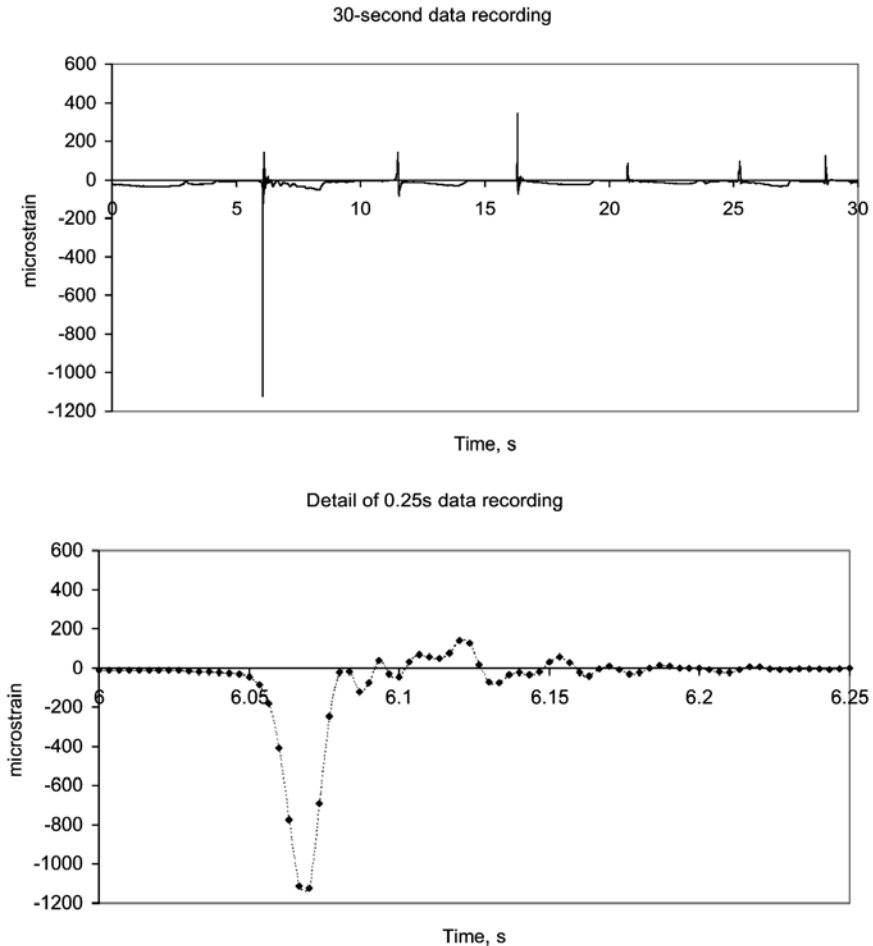


Figure 2. Example of longitudinal shear strain measurements recorded at sea. Upper: 30 second recording, Lower: detail of 0.25 second recording.

Based on recordings such as these, core shear strain rates in the range 10-15%/second were measured. This does not mean that higher rates do not occur but it gives a first indication of the loading rate required for tests to compare different materials. This rate is not excessively high and can be easily achieved with standard hydraulic test machines provided a uniform

strain field can be generated. In this initial part of the project emphasis was placed on shear tests.

### 3. SHEAR TEST

The shear properties of foams are usually determined by standard tests such as ASTM C273, NF T 54-605, Figure 3. The main disadvantage of these tests for high rate loading is the rotating links.

In order to minimize inertia effects during high rate loading a rigid symmetrical fixture was designed, Figure 4.

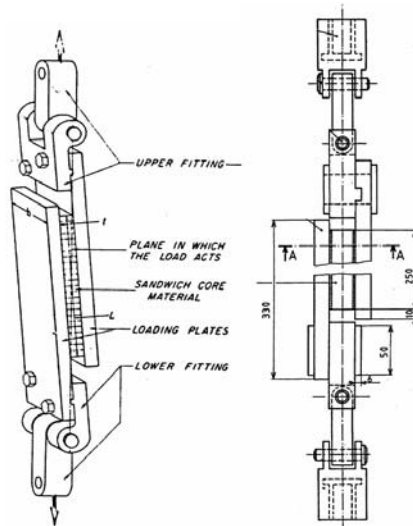


Figure 3. Standard shear test fixtures.

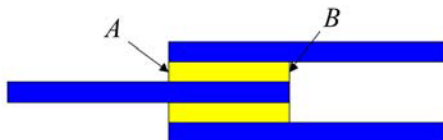
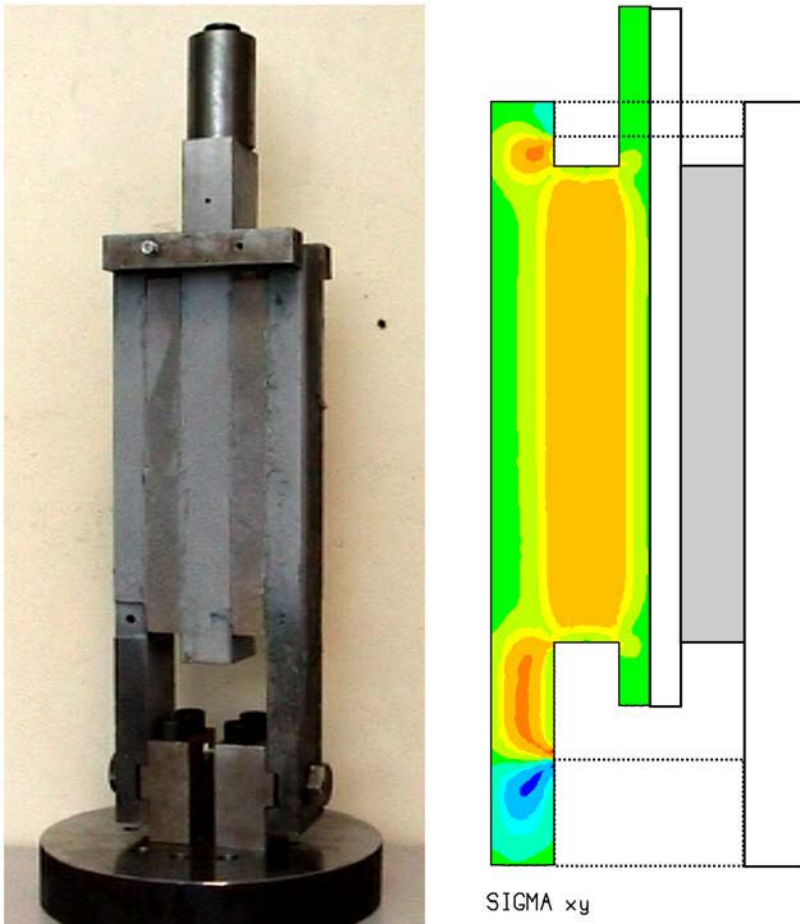


Figure 4. Double rail shear specimen.

This configuration is easy to test but results in high stress gradients at points A and B. In order to limit these stress gradients, which increase as the specimen thickness increases, the fixture was modelled using SAMCEF<sup>®</sup> software. After a series of iterations the final test fixture is shown in Figure 5. The central support is made from aluminium alloy in order to reduce inertia, the outer supports are steel and are linked in order to make the structure rigid and avoid transverse movements. The specimen thickness is that of the panels used, width is 50mm and length is between 150 and 250 mm.



*Figure 5. Test fixture and shear stress distribution.*

FE modelling of this fixture shows a reasonably uniform shear stress field, Figure 5. If we consider the variation in stresses  $\sigma_{xx}$  and  $\sigma_{yy}$  along the specimen length they vary at the specimen ends, as for the standard test

specimens, which leads to failure initiation there. This results in an under-estimation of the non-linear behaviour, but has no influence on the elastic response.

#### 4. TEST PROCEDURE & MATERIALS

The fixture is mounted on a tensile test machine. The outer supports are fixed to the machine base. The central rail is displaced at a constant rate. An inductive transducer measures the relative movement of the inner and outer rails and a load cell measures the force.

The foams tested were PVC foams supplied by Airex as 20mm thick panels. Results from tests on Herex C 70 200 foam will be presented here. The supplier's data values, used in the FE analyses, are shown in Table 1.

Table 1. Foam properties (supplier data).

Property	Herex C 70 200
Compressive modulus (MPa)	260
Tensile modulus (MPa)	180
Shear modulus (MPa)	75
Density (kg/m <sup>3</sup> )	200

First validation tests were performed at a loading rate of 1mm/min. The foam was bonded to the rails using a *Redux 420* epoxy adhesive. These tests indicated a shear modulus of 85 MPa.

In order to remain within the load limits of the test machine (100 kN) the length of the specimen was reduced from 250 to 150mm. This results in a shorter uniform stress region and may invalidate the test, so an FE analysis was performed in order to establish the uniformity of local stresses in the region used for global modulus measurements, Figure 6. For the 150mm length specimen, the error in the shear modulus is estimated at 5%. It was therefore decided to use full strain field measurements, giving local strain measurements, to determine the shear response. Black paint spots sprayed onto a white background layer were used, with image analysis software. An example of the results from preliminary tests is shown in Figure 7. This showed clearly that with one of the early fixtures there was a tendency for the lower part of the fixture to close up during the test. The lower fixing

bolts were under-dimensioned, a subsequent fixture modification eliminated this effect.

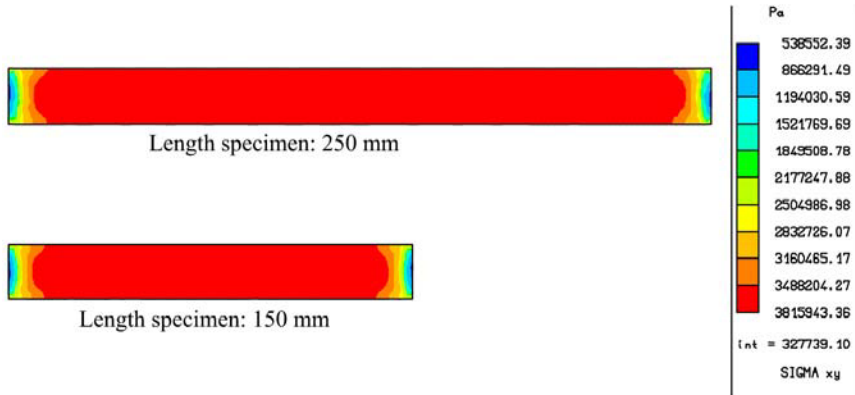


Figure 6. Shear stress distributions, two specimen lengths.

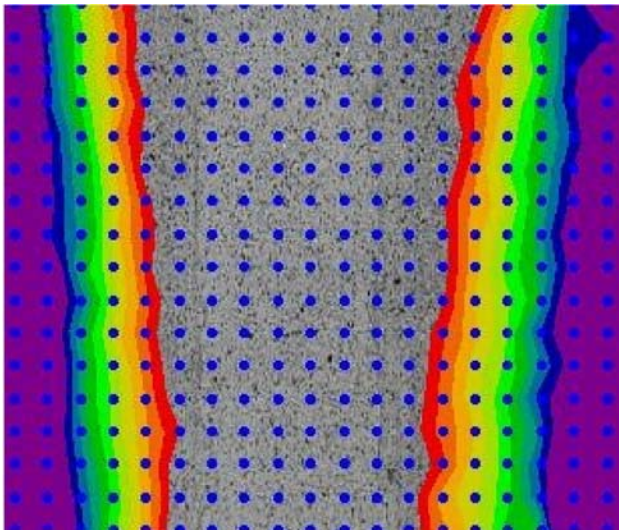


Figure 7. Example of image of test with early fixture.

Following those initial static validation tests the influence of loading rate was examined. Some first results are shown below.

## 5. RESULTS

Tests were performed at three loading rates which are faster than the rates measured at sea. Figure 8 shows the global behaviour laws for the three rates. It is interesting to note that for this rigid  $200 \text{ kg/m}^3$  density material, no significant influence of loading rate is observed, at least up to 5% strain. This is in contrast to previous results reported for lighter foams. The shear moduli values measured are all in the range 85-90 MPa, compared to the value of 85 MPa measured in the test at 1 mm/minute.

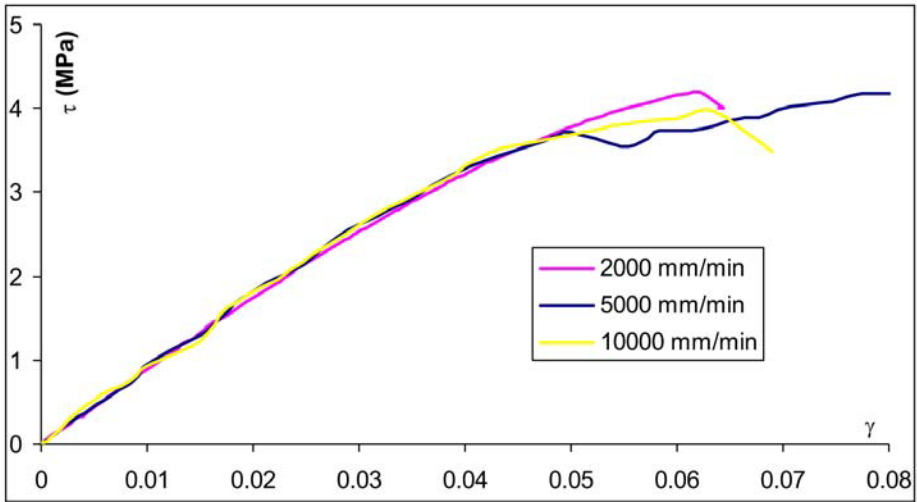


Figure 8. Shear stress-shear strain curves for three loading rates.

## 6. CONCLUSIONS

The aim of this project is to establish the appropriate foam properties to be used in the design of racing yachts and other vessels which are subjected to wave impact loads. Measurements at sea have identified the loading rates for one type of craft under certain sea conditions. A test fixture has been developed and validated using FE analysis and full strain field measurements in order to achieve these (and higher) loading rates. First tests results indicate that quasi-static data may suffice for high density rigid foams. Further work is underway to study lighter foams, other core materials and higher loading rates.

## **ACKNOWLEDGEMENT**

The authors thank Rolland Jourdain, skipper of the 60' IMOCA racing boat SILL for allowing the instrumentation and monitoring of the sandwich hull of the boat.

## **REFERENCES**

1. Feichtinger, K.A., Test methods and performance of structural core materials-IIA Strain rate dependence of shear properties, 5th INERN Conf., October 1990.
2. Buene, L, Echtermeyer, A.T., Hayman, B., Sund, O.E. and Engh, B., Shear properties of GRP sandwich beams subjected to slamming loads, Proc. 2<sup>nd</sup> Sandwich Construction Conf., 1992.
3. Davies, P., Baizeau, R., Wahab, A., Pecault, S., Collombet, F. and Lataillade, J.L., Determination of material properties for structural sandwich calculations, from creep to impact loading, in *Mechanics of Sandwich Structures*, Vautrin (ed.), Kluwer, 1998, 327-336.
4. Van Gellhorn, E. and Reif, G., Think dynamic: dynamic test data for the design of dynamically loaded structures, Proc. 2<sup>nd</sup> Sandwich Construction Conf., 1992.
5. Chakravarty, U., Mahfuz, H., Saha, M. and Jeelani, S., Strain rate effects on sandwich core materials: an experimental and analytical investigation, *Acta Materiala* 31, 2003, 1469-1479.
6. Hayman, B., Wiese, M., Davies, P., Choqueuse, D., Hoyning, B. and Mitusch, P., Foam cored sandwich panels under static pressure loading, Proc. 4<sup>th</sup> Sandwich Construction Conf., 1998.

# CHARACTERIZATION OF THE THERMAL EXPANSION BEHAVIOUR OF A PVC FOAM CORE: NON-LINEARITIES AND GRADIENTS ACROSS THE WIDTH

Pascal Casari, Carlos Ferreira and Frédéric Jacquemin

*GeM, Institut de Recherche en Génie Civil et Mécanique, UMR CNRS 6183,  
BP 92208, 44322 Nantes Cedex 3, France*

**Abstract** A speckle full field interferometric technique is used for characterizing the Coefficient of Thermal Expansion of a PVC foam core through the thickness. A significant gradient is highlighted and is correlated to a gradient in density. A simulation shows the effect of taking such gradient into account on stress level in the core of a sandwich submitted to a temperature variation.

**Keywords:** foam core, density, thermal expansion, speckle.

## 1. INTRODUCTION

Core materials for sandwich constructions appear to have a relatively high coefficient of thermal expansion compared to the one of skin materials. This behaviour plays a significant role in the evolution of the shape of curved shells during cooling down after process or simply under temperature changes [1]. Unfortunately, no accurate results have been found in literature on the identification of the thermal expansion behaviour of foam cores and insufficient information for accurate modelling come from manufacturing companies. Moreover, core materials present gradients in their density, stiffness and fracture behaviour [2]. The effect of stiffness gradients on stress level in the core has been assessed by several authors mostly in a numerical way in what is called “Functionally Graded Cores” [3, 4]. This leads to a questioning about a possible gradient in thermal expansion behaviour

through the thickness of a sandwich structure made of such foam. The goal of this work is to give an experimental answer by means of an approach using a full field displacement measurement method known as speckle interferometry. Thermal properties of a cross-linked PVC foam with a density of  $200 \text{ kg/m}^3$  have been characterized in the range from  $20^\circ\text{C}$  to  $40^\circ\text{C}$ . At the same time, measurements of density gradients have been conducted. At first the density profile through the thickness is characterized. Then, the coefficient of thermal expansion (CTE) is measured and its profile is compared to the density one. The last point consists in evaluating the impact of taking into account the measured profile of CTE through the thickness in the stress state in the core material under thermal loadings of a sandwich structure.

## **2. EXPERIMENTS**

### **2.1 Foam description**

The material used in this investigation is AIREX C70.200 PVC cross-linked cellular foam from Alcan Baltek Corp with a thickness of 50 mm. An observation of the edge of the panel shows a strange colour variation which suggests that the foam may not have a constant density through the thickness. A more accurate observation with a Secondary Electron Microscope (SEM) exhibits a variation of cellular structure with a cell size decreasing from the panel surfaces to the centre (Figure 1). The near side areas are composed of smaller closed cells embedded in thicker edges.

### **2.2 Density gradient determination**

The foam density profile is obtained by matter removal (Figure 2). Some coarse parallelepipedic foam samples are cut from a raw foam panel and the shape of the remaining piece is corrected by means of a polishing operation. Then, the samples are weighed before and after the removal of thin layers of approximately 2 mm by a mechanical polishing. A special care is made to keep the surfaces plane and parallel. The density is then estimated by measuring the weight and the dimensions of the body with high precision callipers.

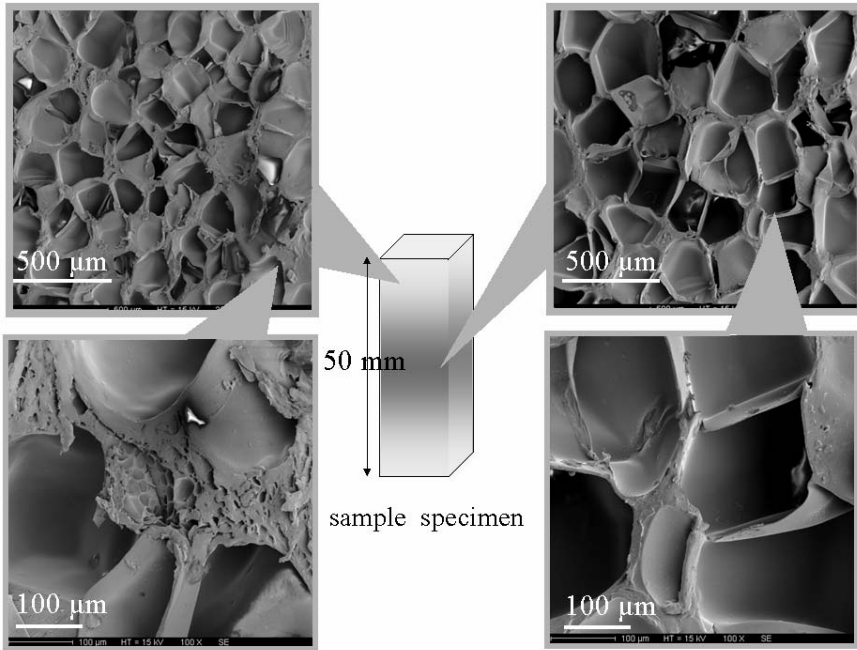


Figure 1. Foam cell structure near the edge and in the middle of the core panel.

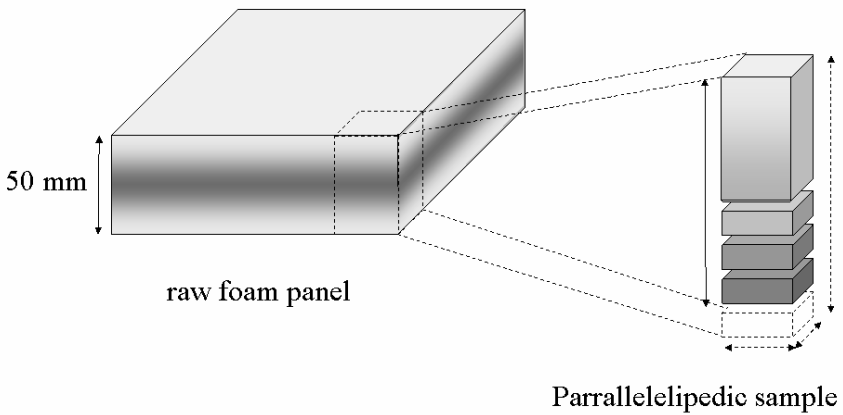


Figure 2. Slices to evaluate the foam density profile. Sample dimensions and weight are measured before and after thin layer removal.

In order to reduce statistical errors due to local measurements, and to characterize the whole thickness, 8 samples have been prepared and tested. The experimental density profile obtained is shown in Figure 3.

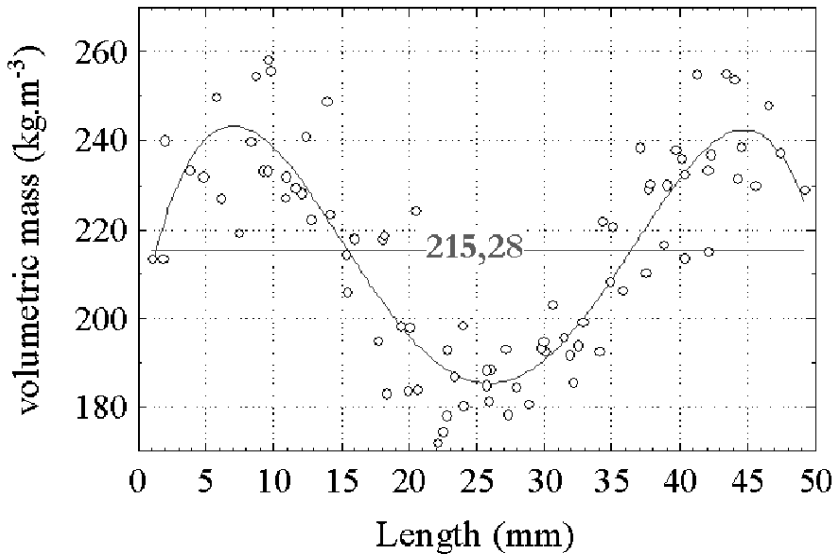


Figure 3. Experimental density profile through the foam panel thickness.

The density profile shows a non-uniform but symmetrical density of the foam through the thickness (Figure 3). A variation of 25% of the density is then observed as maximum in the depths between 5 and 10 mm and the minimum in the centre. The average value is about  $215 \text{ kg/m}^3$  which is higher than the nominal density value given by the manufacturer ( $200 \text{ kg/m}^3$ ).

### 2.3 Gradient of the coefficient of thermal expansion

The optical setup used for the measurement of displacement field due to thermal strains is based on a double laser lighting interferometer to measure in-plane displacements fields of the sample in a thermal chamber. Figure 4 shows the experimental device. A 25 mW He-Ne laser ( $\lambda = 632.8 \text{ nm}$ ) provides a coherent light source while a closed loop controlled piezoelectric transducer (PZT) is used as phase shifter. The intensity distributions of combined light beams are recorded by a monochromatic CCD camera ( $512 \times 512$  pixel sensor). The images are then digitized by means of a Fringe Analysis software.

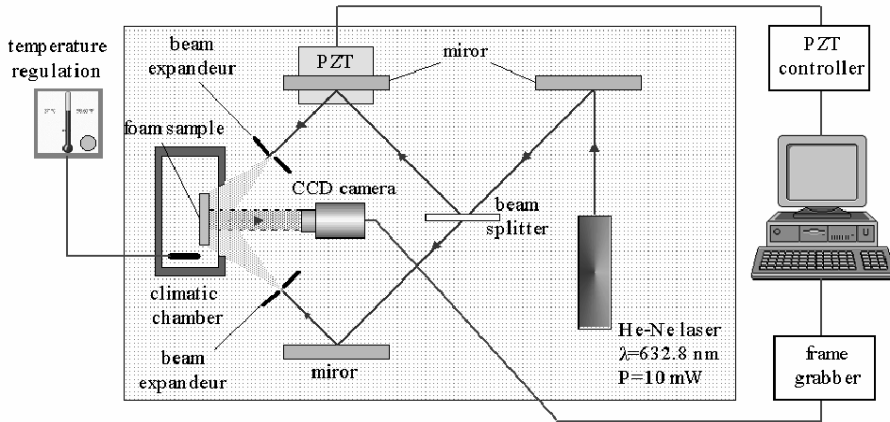


Figure 4. Optical set-up for in-plane displacements measurements of the PVC foam under thermal loading.

The angle between the illuminated beams and the direction of observation is about  $45^\circ$  in order to have a good sensitivity, a large and homogenous illuminated area (5 mm to 50 mm) and to limit geometrical aberrations. For a double illumination interferometer, correlation fringes of inplane  $u$ -displacements will form wherever:

$$u = \frac{n\lambda}{2\sin\theta} \tag{1}$$

where  $\lambda$  is the laser wavelength and  $\theta$  is the illumination angle;  $n$  denotes the fringe order. The characterization procedure (Figure 5) consists in recording phase patterns of the specimen for several temperature levels. The phase distributions (step 1) are easily obtained from the acquisition of at least three captures of interference patterns in which a known phase shifting is imposed by the translation of the mirror moved by a PZT device. After subtracting the phase of the images (step 2), and unwrapping (step 3), displacements are calculated using Equation (1). In order to reduce the influence of noise, the thermal expansion profile is obtained by fitting first the corresponding signal by a high order polynomial function (step 4) which is then differentiated along the  $u$  axis (step 1). The translation from the number of pixels to millimetres is done by a calibration on a graded paper.

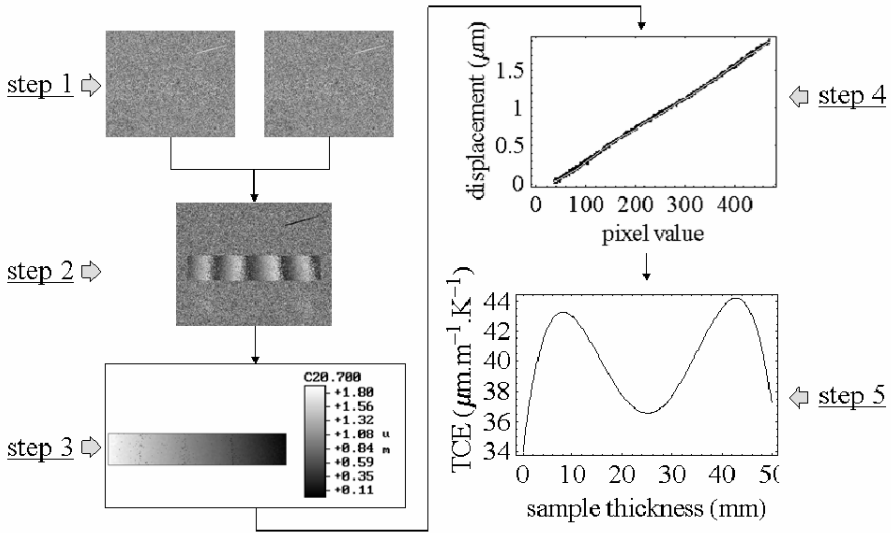


Figure 5. Analysis of the thermal expansion coefficient profile from speckle patterns.

The measurement of the Coefficient of Thermal Expansion (CTE) through the thickness is then done with the technique explained above.

Because of the insufficient camera resolution ( $512 \times 512$ ), the analysis of the full thickness specimen (50 mm) induces a low accuracy (pixel size about  $120 \mu\text{m}$ ). To improve the quality of data, an analysis is made on 3 portions of about 20 mm corresponding to different thickness areas. By this way the pixel size is reduced to about  $40 \mu\text{m}$ . To ensure a good recovery between the areas, the several samples are not cut out from the same parallelepipedal specimen. Minimisation of uncertainties is realised by averaging values obtained for several tests done in a range of temperatures between  $20^\circ\text{C}$  and  $40^\circ\text{C}$ . Figure 6 shows the evolution of the CTE through the thickness. On this plot, each experimental point is the average of 20 results. As it can be seen on this figure, the thermal expansion coefficient is not constant through the panel thickness. A quasi symmetrical profile is observed with two maxima around a distance of 5 mm to the faces.

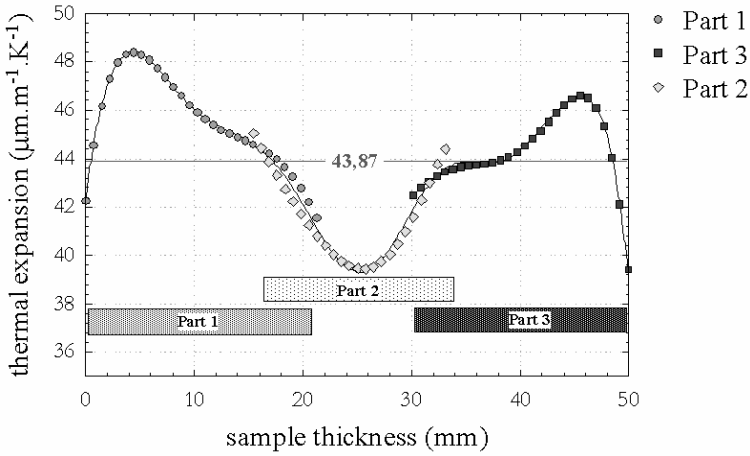


Figure 6. Experimental CTE profile of the PVC foam by speckle interferometry.

In comparison to the density profile (Figure 7), the CTE variation seems to be less important and a change in slope is observed around the depths 17 and 33 mm.

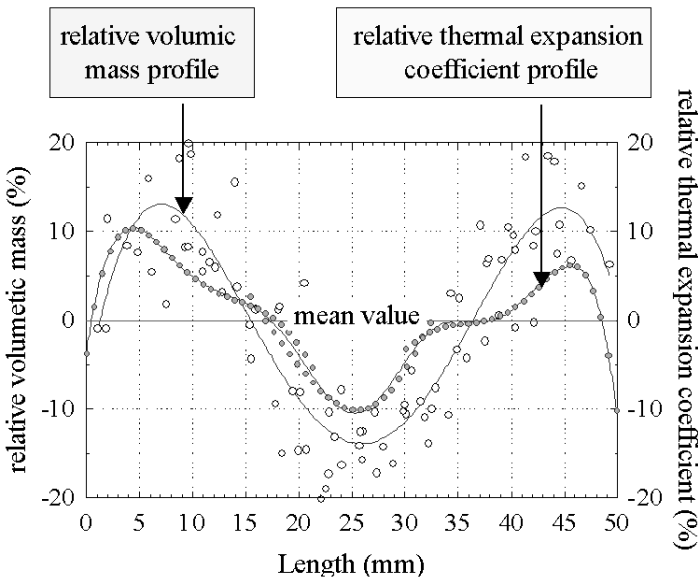


Figure 7. Comparison between CTE and density profiles.

### 3. SIMULATION INCLUDING A CTE GRADIENT

In this part, an infinite sandwich panel is considered with the 50 mm thick foam core under a thermal load. The skins of the sandwich plate are composed of  $[0/45/-45/90]_{2S}$  T700/epoxy stacking sequence with a thickness of 2 mm. The goal is to compare the effect of non-uniform thermal properties through the thickness. Stresses in the sandwich plate are calculated by using the Classical Lamination Plate Theory (CLPT) (see [4] for instance). In a global Cartesian reference frame  $(x,y,z)$ , strains are given by the following equations:

$$\vec{\varepsilon} = \begin{pmatrix} \varepsilon_{xx}(z) \\ \varepsilon_{yy}(z) \\ \gamma_{xy}(z) \end{pmatrix} = \begin{pmatrix} \varepsilon_{xx}^0 - zW_{,xx} \\ \varepsilon_{yy}^0 - zW_{,yy} \\ \gamma_{xy}^0 - 2zW_{,xy} \end{pmatrix} = \begin{pmatrix} \varepsilon_{xx}^0 + k_{xx}z \\ \varepsilon_{yy}^0 + k_{yy}z \\ \gamma_{xy}^0 + k_{xy}z \end{pmatrix} \quad (2)$$

where  $w$  is the out-of-plane displacement,  $k_{xx}$  and  $k_{yy}$  are the curvatures along the  $x$  and  $y$  directions respectively and  $k_{xy}$  is the twist curvature. The hypothesis of plane stress translates into the following stress-strain relationship where  $\underline{Q}$  is the matrix associated to the stiffness tensor:

$$\vec{\sigma} = \begin{pmatrix} \sigma_{xx}(z) \\ \sigma_{yy}(z) \\ \sigma_{xy}(z) \end{pmatrix} = \underline{Q}(\vec{\varepsilon} - \vec{\varepsilon}_T) \quad \text{with} \quad \underline{Q} = \begin{bmatrix} Q_{xxxx} & Q_{xxyy} & Q_{xxxy} \\ Q_{xxyy} & Q_{yyyy} & Q_{yyxx} \\ Q_{xxxy} & Q_{yyxx} & Q_{xyxy} \end{bmatrix} \quad \text{and} \quad \vec{\varepsilon}_T(z) = \begin{pmatrix} \alpha_x(z) \\ \alpha_y(z) \\ \alpha_{xy}(z) \end{pmatrix} \Delta T \quad (3)$$

$\vec{\varepsilon}_T(z)$  are the thermal free strains, in which  $\alpha_x$ ,  $\alpha_y$  and  $\alpha_{xy}$  are the coefficients of thermal expansion of a ply,  $\Delta T$  is the uniform temperature differential from a reference state, the stress-free state. In a local reference frame  $(1,2,3)$  for the ply, the stiffness tensor  $\underline{Q}$  reads:

$$\underline{Q} = \begin{bmatrix} Q_{1111} & Q_{1122} & 0 \\ Q_{1122} & Q_{2222} & 0 \\ 0 & 0 & Q_{1212} \end{bmatrix} = \begin{bmatrix} \frac{E_1}{1-\nu_{12}\nu_{21}} & \frac{\nu_{12}E_2}{1-\nu_{12}\nu_{21}} & 0 \\ \frac{\nu_{12}E_2}{1-\nu_{12}\nu_{21}} & \frac{E_2}{1-\nu_{12}\nu_{21}} & 0 \\ 0 & 0 & G_{12} \end{bmatrix} \quad \text{where} \quad \nu_{21} = \nu_{12} \frac{E_2}{E_1} \quad (4)$$

When  $\alpha(z)$  is given by experimental characterization of the foam core, the thermal free strains and the total strains in Equation (3) do not satisfy compatibility equations. To overcome this difficulty, the identified coefficients of thermal expansion are approximated through a series of fixed horizontal increments. The resultant loads due to the stress fields (3) are given by:

$$\begin{aligned} \vec{N} &= \int_0^e \vec{\sigma}(z) dz = \underline{A} \vec{\varepsilon}_0 + \underline{B} \vec{k} - \vec{N}_T \\ \vec{M} &= \int_0^e \vec{\sigma}(z) z dz = \underline{B} \vec{\varepsilon}_0 + \underline{D} \vec{k} - \vec{M}_T \end{aligned} \quad \text{where} \quad \underline{A} = \int_0^e \underline{Q} dz, \quad \underline{B} = \int_0^e \underline{Q} z dz, \quad \underline{D} = \int_0^e \underline{Q} z^2 dz \quad (5)$$

$$\text{and: } \vec{N}_T = \int_0^e \underline{Q} \vec{\epsilon}_T dz ; \quad \vec{M}_T = \int_0^e \underline{Q} \vec{\epsilon}_T z dz \quad (6)$$

Mid-plane strains and curvatures may be found by inverting relations (5), stresses are then given by (3). The use of increments to approximate the non-uniform coefficients of thermal expansion presents some shortcomings. As the number of sub-ply is finite, the stress field is approximate: the accuracy increases as the number of increments increases, but the maximum number of increments itself is limited by some physical considerations. In the present work a macroscopic approach is proposed and, physically, a sub-ply must be able to represent the homogenised behaviour of the material. This imposes a limitation on its minimum dimensions.

Figure 8 presents the stresses in the foam core of the sandwich plate due to temperature increase of 20°C. Uniform Young moduli and coefficient of thermal expansion induce constant values for the stresses through the thickness of the plate. The introduction of non-uniform Young moduli and a coefficient of thermal expansion involve a great variation of the stress distribution. Near the external core surfaces, the higher compressive stresses appear for a temperature differential of 20°C.

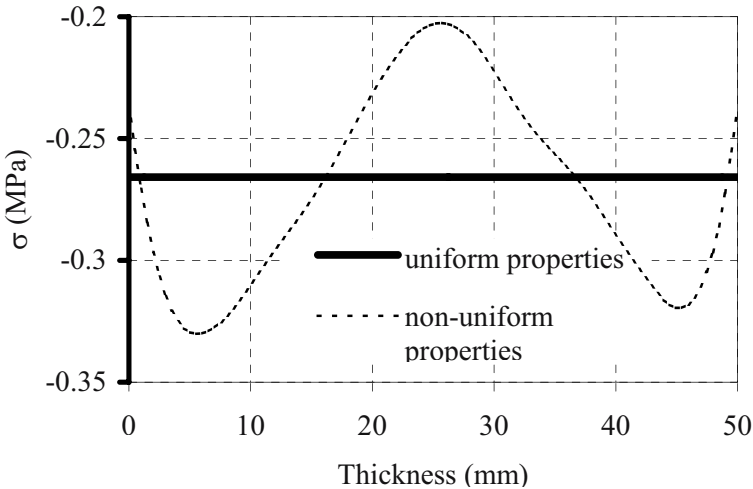


Figure 8. Stresses through the thickness of the foam core for  $\Delta T = 20^\circ\text{C}$ .

On the contrary, stresses induced by a temperature differential of 20°C have no effect on the stress state of the skins of the composite material whether the foam core properties are considered as uniform or not.

#### **4. CONCLUSION AND PROSPECTS**

The experiments conducted on the density profile and especially on the coefficient of thermal expansion give original results which can be used in simulation of thermomechanical behavior of sandwich structures. The measurements realised can be improved but have been fully satisfactory by providing accurate results. Moreover, the simulation shown on a carbon-epoxy sandwich made of the PVC foam highlight the discrepancy between the classical linear approach and the one based on the present work.

The next work should be the characterization of the linearity of the coefficient of thermal expansion versus temperature, and also the characterization of elastic stiffness through the thickness end versus temperature in order to give a complete set of data for thermomechanical modelling. Complementarily to what precedes, a non-linear behaviour law could be proposed in order to allow a proper structural design when significant temperature changes are at stake.

#### **REFERENCES**

1. Casari, P., Devic, C. and Gornet, L., "Characterization of residual stresses in a composite curved sandwich panel", in EUROMECH 453 Internal Stresses in Polymer Composite Processing and Service Life, Saint-Etienne, France, 1-3 Dcember 2003.
2. Davies, P., Casari, P. and Carlsson, L.A., "Mechanical testing of foam cores for sandwich structures", in Proc. ICSS 6 – International Conference on Sandwich Structures, Fort Lauderdale, FL, 31 March–2 April 2003, CRC Press.
3. Apetre, N.A. and Sankar, B.V. "Composite sandwich plates with functionally graded cores", Proc. ICSS 6 – International Conference on Sandwich Structures, Fort Lauderdale, FL, 31 March–2 April 2003, CRC Press.
4. Kilic, B., Das, M., Madenci, E. and Ambur, D.R., "Three dimensional analysis of functionally gradient core sandwich panels with a circular hole", Proc. ICSS 6 – International Conference on Sandwich Structures, Fort Lauderdale, FL, 31 March–2 April 2003, CRC Press.
5. Herakovitch, C., "Mechanics of Fibrous Composites", John Wiley and Sons Publisher, 1997.

# DETERMINATION OF IN-PLANE AND OUT-OF-PLANE ELASTIC CONSTANTS FOR MEDIUM-THICKNESS SANDWICH COMPOSITE SKINS

Helmuth Toftegaard and Stergios Goutianos

*Materials Research Department, Risø National Laboratory, P.O. Box 49, 4000 Roskilde, Denmark*

**Abstract** A full set of elastic constants was determined/estimated for two sandwich composite skin laminates. Out-of-plane compression and shear specimens were cut from skin laminates bonded together to avoid making thick laminates. The approach gives relatively low scatter for the elastic constants and little influence from the bonds as judged from finite element analysis.

**Keywords:** skin laminate, out-of-plane elastic constants, bonded specimen, finite element analysis

## 1. INTRODUCTION

Finite element modeling of thick laminates in applications such as flywheels, add-on armor and wind turbine blades requires a full set of elastic constants describing an orthotropic material. For sandwich laminate skins it may also be relevant to know not only the in-plane (IP) properties but also the out-of-plane (OOP) properties depending on the relative skin thickness and the type of loading.

A full or partial set of elastic constants can be obtained in different ways such as ultrasound [1], plate vibration [2] or mechanical tests [3]. Some of the mechanical OOP test methods [4] require relatively thick material (20-40 mm) – often thicker than the skin laminate to be tested. In some cases manufacturing of thick laminates for testing can be avoided by bonding the skin laminates together to form a thick laminate [5]. IP elastic constants ( $E_{11}$ ,  $E_{22}$ ,  $\nu_{12}$  and  $G_{12}$ ) may be determined from tensile tests on straight-sided specimens and from shear of V-notched (Iosipescu) specimens [6]. Also

OOP shear properties ( $G_{13}$  and  $G_{23}$ ) may be obtained from Iosipescu specimens. The remaining OOP constants ( $E_{33}$ ,  $\nu_{31}$  and  $\nu_{32}$ ) can be determined from compression tests on a prism shaped specimen [7].

The aim of the present study is to demonstrate how a full set of elastic constants can be determined using bonded specimens for the OOP compression and OOP shear tests and to assess the influence of the adhesive bonds on the measured elastic constants. Experimental data are presented for two different skin laminates together with findings from finite element (FE) simulations of the OOP tests.

## 2. EXPERIMENTAL

The test methods outlined above (tension of straight-sided specimens, shear of Iosipescu specimens and compression of prism specimens) were used to determine the elastic constants of two different 10 mm thick E-glass/polyester laminates. The OOP compression and shear specimens were made of laminate sections bonded together with an epoxy adhesive.

### 2.1 Laminates

Two different types of E-glass/polyester laminates were investigated. The first lay-up was mainly plain weave with 9 layers of plain woven rowing of area weight  $600 \text{ g/m}^2$  (PWR600) stitched together with a chopped strand mat of area weight  $300 \text{ g/m}^2$  (CSM300) plus a single chopped strand mat of area weight  $450 \text{ g/m}^2$  (CSM450) on top – i.e. [(CSM300/PWR600)<sub>9</sub> / CSM450]. The second lay-up was multidirectional with 8 layers of  $[0^\circ/45^\circ/90^\circ/-45^\circ]$  and an area weight of  $1177 \text{ g/m}^2$  for each layer – i.e.  $[0^\circ/45^\circ/90^\circ/-45^\circ]$ <sub>8</sub>.

The coordinate systems adapted follow the material axes: For the plain weave laminate direction 1 and 2 are in the warp and weft directions of the weave, respectively. Direction 1 and 2 for the multidirectional laminate are in the directions of the  $0^\circ$  and  $90^\circ$  fibers, respectively. For both laminates direction 3 is in the thickness direction.

### 2.2 In-plane tension

Tensile tests were performed on straight-sided tensile specimens (length  $\times$  width  $\times$  thickness =  $300 \text{ mm} \times 25 \text{ mm} \times 10 \text{ mm}$ ) with  $0^\circ/90^\circ$  strain gauge couples (HBM 6/120XY11) on both major faces. The loading was performed on a mechanical testing machine (Instron 1115) with a 50 kN load cell at a constant cross-head speed of 1 mm/min. No end tabs were used and the

gripping length was 40 mm at each end, leaving a gauge length of approximately 220 mm. Specimens oriented in the 1 and the 2 directions of the laminates were used to measure Young's moduli,  $E_{11}$  and  $E_{22}$ , as well as the major and the minor Poisson's ratio,  $\nu_{12}$  and  $\nu_{21}$ , respectively.

### 2.3 Out-of-plane compression

For each of the two materials a 10 mm thick laminate was milled and ground to produce parallel upper and lower surfaces. The laminate was cut into 4 pieces that were bonded together on top of each other with thin layers of epoxy adhesive (3M DP460 Off-White) to obtain a 37 mm thick laminate. From the thick laminate 5 specimens with dimensions 20 mm  $\times$  20 mm  $\times$  37 mm (width  $\times$  depth  $\times$  height) were cut with sides parallel to the 1 or 2 direction of the thick laminate (Figure 1(a)). The loading was performed between parallel steel platens on a servo hydraulic testing machine (Instron 1342) with a 100 kN load cell at a constant cross-head speed of 0.2 mm/min. Strain gauge couples  $0^\circ/90^\circ$  (HBM 3/120XY11) on each of the four specimen faces were used to measure the OOP Young's modulus,  $E_{33}$ , and the Poisson's ratios,  $\nu_{31}$  and  $\nu_{32}$ .

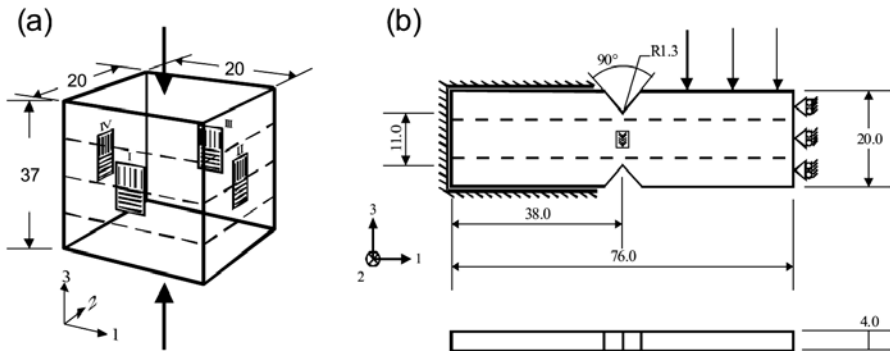


Figure 1. OOP compression specimen with  $0^\circ/90^\circ$  strain gauges on the four vertical faces (a), and OOP shear Iosipescu specimen with  $\pm 45^\circ$  strain gauges on front and backside (b). The dimensions are given in mm.

### 2.4 In-plane shear

A 10 mm thick laminate was milled and ground to produce a laminate with parallel upper and lower surfaces and a thickness around 4 mm. From the 4 mm laminate 5 V-notched beam specimens of Iosipescu type (dimensions as for OOP shear in Figure 1(b)) were cut with the longest sides parallel to the 1 direction. The loading was performed with a special rig

(modified Wyoming II) on a servo hydraulic testing machine (Instron 8032) with a 5 kN load cell at a constant cross-head speed of 0.5 mm/min. Strain gauge couples  $\pm 45^\circ$  (HBM 1.5/120XY21) on both major faces were used to measure the shear modulus  $G_{12}$ .

## **2.5 Out-of-plane shear**

A 10 mm laminate was milled and ground to produce parallel upper and lower surfaces. The part was cut into 3 pieces that were bonded together on top of each other with thin layers of epoxy adhesive (3M DP460 Off-White) to obtain a 30 mm thick laminate. From the thick laminate 5 Iosipescu specimens were cut with the longest sides in the 1 direction (Figure 1(b)). Strain gauge couples  $\pm 45^\circ$  (HBM 1.5/120XY21) on both major faces were used to measure the shear modulus  $G_{13}$ . The other OOP shear modulus,  $G_{23}$ , can be determined in a similar way. Due to budget limitations, however, this was not done.

## **3. EXPERIMENTAL RESULTS**

The data treatment of the experimental measurements was based on a data analysis procedure involving the following average and extrapolation scheme:

1. Engineering stress was used for tension, compression and shear.
2. Each strain signal was offset to ensure zero strain at zero load.
3. Average strains were used for stress-strain and strain-strain curves.
4. Differentiated stress-strain curves lead to tangent modulus-strain curves.
5. Differentiated strain-strain curves lead to tangent ratio-strain curves.
6. Young's moduli and shear moduli were obtained by extrapolation to zero strain of the undisturbed part of the tangent modulus-strain curves.
7. Poisson's ratios were obtained by extrapolation to zero strain of the undisturbed part of the tangent ratio-strain curves.

By averaging the strains the influence from misalignment and friction for the OOP prism specimen are reduced. For the Iosipescu specimens averaging over the two major faces reduces the influence from twisting. The extrapolation to zero strain of the undisturbed part of the tangent modulus-strain curves and the tangent ratio-strain curves makes it possible to avoid the influence from initial disturbances as well as the influence from damage at higher strains. The scheme has been validated for the OOP compression

test using FE analysis [8, 9] to account for influence from aspect ratio, misalignment and friction.

Curves of OOP compression stress-strain and of OOP shear stress-strain are shown for plain weave in Figure 2. Examples of extrapolation are shown for plain weave  $G_{13}$  and  $\nu_{31}$  in Figure 3.

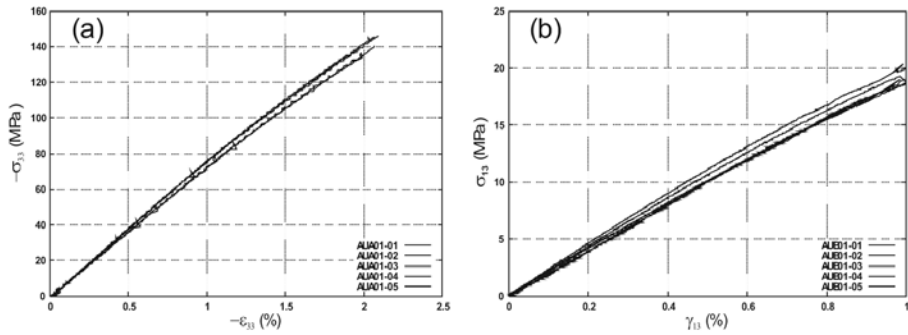


Figure 2. Plain weave glass/polyester OOP compression stress-strain curves (a) and OOP shear stress-strain curves (b).

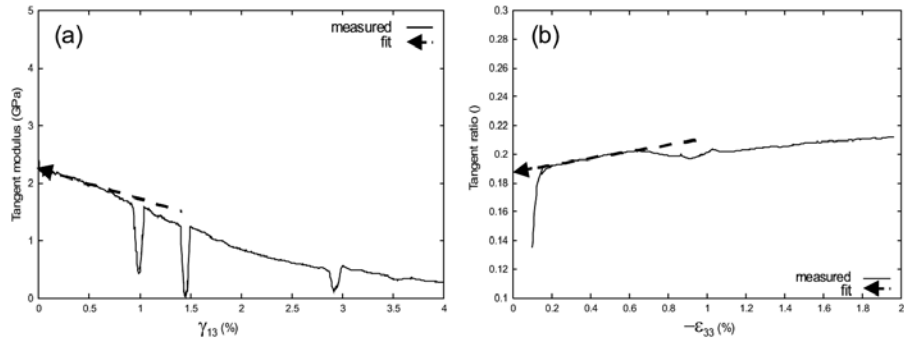


Figure 3. Extrapolation of shear modulus from shear tangent modulus-strain curve (a) and extrapolation of Poisson's ratio from tangent ratio-strain curve (b).

The elastic constants obtained from the experiments are shown in Table 1. The symmetry conditions ( $E_{ii}/\nu_{ij} = E_{jj}/\nu_{ji}$ ) for the laminate compliance matrix are used together with the assumption that  $G_{23} = G_{13}$  to obtain a complete set of elastic constants for the each of the two laminates (Table 1).

The stress-strain curves for OOP compression and OOP shear (Figure 2) show little scatter and the variation coefficient for the OOP elastic constants is in the same range (2-5%) as for the IP constants. This indicates that measurements of elastic constants are undisturbed by the adhesive bonds.

Table 1. Elastic constants (average  $\pm$  one standard deviation) based on experimental tests, symmetry conditions and the assumption that  $G_{23} = G_{13}$ .

Source	Load direction	Elastic constant	Plain weave	Multidirectional
Tension tests	In-plane	$E_{11}$ (GPa)	$14.9 \pm 0.1$	$16.4 \pm 0.3$
	In-plane	$E_{22}$ (GPa)	$16.5 \pm 0.6$	$16.1 \pm 0.2$
	In-plane	$\nu_{12}$ ( )	$0.185 \pm 0.005$	$0.306 \pm 0.005$
	In-plane	$\nu_{21}$ ( )	$0.203 \pm 0.010$	$0.302 \pm 0.010$
Compression tests	Out-of-plane	$E_{33}$ (GPa)	$7.5 \pm 0.2$	$8.5 \pm 0.2$
	Out-of-plane	$\nu_{31}$ ( )	$0.20 \pm 0.01$	$0.17 \pm 0.01$
	Out-of-plane	$\nu_{32}$ ( )	$0.16 \pm 0.02$	$0.15 \pm 0.01$
Shear tests	In-plane	$G_{12}$ (GPa)	$4.1 \pm 0.5$	$6.1 \pm 0.3$
Shear tests	Out-of-plane	$G_{13}$ (GPa)	$2.2 \pm 0.1$	$2.8 \pm 0.1$
Symmetry	Out-of-plane	$\nu_{13}$ ( )	$0.40 \pm 0.06$	$0.33 \pm 0.07$
Symmetry	Out-of-plane	$\nu_{23}$ ( )	$0.35 \pm 0.12$	$0.28 \pm 0.07$
Assumption	Out-of-plane	$G_{23}$ (GPa)	2.2	2.8

#### 4. FINITE ELEMENT ASSESSMENT

The commercial FE code ABAQUS Version 6.5 was used to make 3D models for both the OOP compression and OOP shear tests. In each case the strains at the position of the strain gauges and the load response were obtained from simulations performed in displacement control for specimens with and without bonds. The elastic constants given in Table 1 were used as materials data for the laminates, and the epoxy literature data [10], given in Table 2, were used for the adhesive bonds. The elastic properties of the epoxy are quite close to those of the laminate polyester also given in Table 2. The thickness of the adhesive bonds was estimated to 0.1 mm from polished cross-sections (Figure 4).

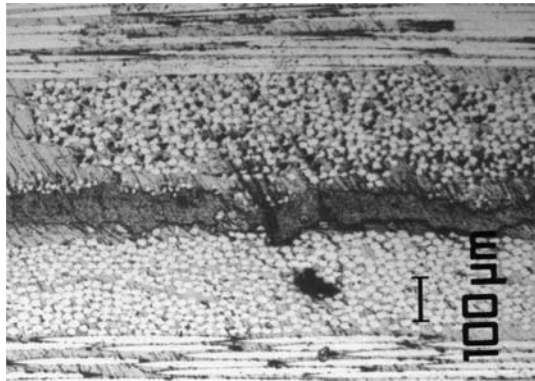


Figure 4. Photomicrograph of a polished section of a multidirectional prism specimen showing the adhesive bond (at the m in 100  $\mu\text{m}$ ) to have a thickness of about 0.1 mm.

Table 2. Elastic constants for epoxy adhesive (3M Scotch-Weld Epoxy Adhesive DP460 Off-White) and laminate polyester ((Reichhold Norpol 200-800).

Material	Young's modulus (GPa)	Poisson's ratio ( )
Epoxy	2.7	0.40
Polyester	3.1	0.40

### 4.1 OOP compression

The FE mesh for the prism specimen is shown in Figure 5 together with details of the strain gauge position relative to the adhesive bond at the centre of the specimen. Reduced integration, 20 node brick elements were used in combination with tie constraints to join the dissimilar meshes of the composite laminates and the thin adhesive layers.

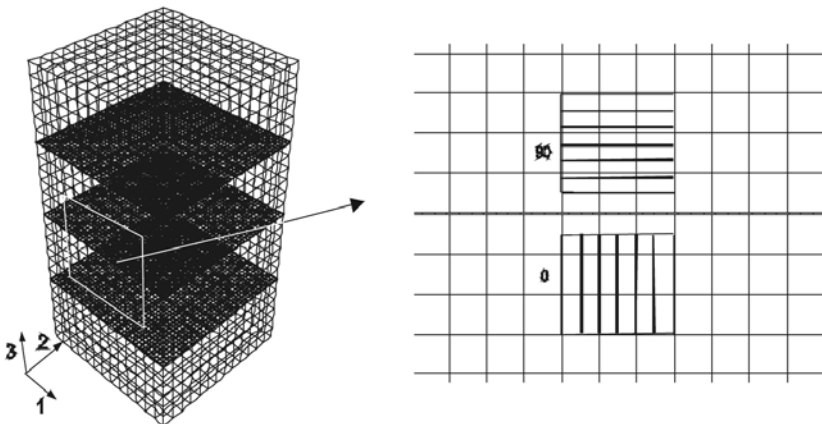


Figure 5. FE mesh of the prism specimen together with strain gauge positions relative to the adhesive bond at the centre of the specimen.

Figure 6(a) shows the simulated compression stress-strain curves for specimens with and without bonds (plain weave). Three different thicknesses (0.1, 0.3 and 0.5 mm) were used for the bonds. The deviation from the ideal case (specimen without bonds) is smaller in the case of 0.1 mm bond thickness. The same trend can be seen in Figure 6(b) where the error in  $\nu_{31}$  is examined for the same bonds thicknesses. The error introduced by the bonds is higher for  $\nu_{31}$  than for  $E_{33}$ . However, in all cases, especially for a bond thickness of 0.1 mm, the error introduced by the bonds in the measured properties is only a few percent as seen in Figure 6.

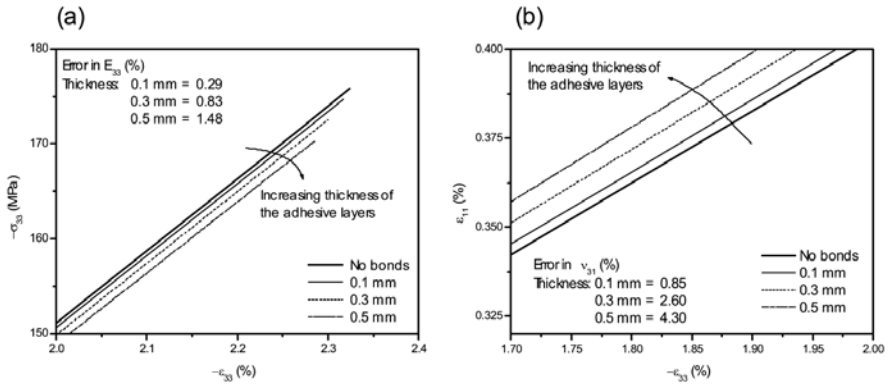


Figure 6. Plain weave glass/polyester simulated OOP compression stress-strain curve (a), and plot of  $\epsilon_{11}$  versus  $-\epsilon_{33}$  for determination of Poisson’s ratio ( $\nu_{31}$ ).

### 4.2 OOP shear

In Figure 7 the FE mesh is shown for the Iosipescu specimen, whereas the boundary conditions are given in Figure 1(b). The position of the strain gauge relative to the adhesive bond at the centre of the specimen is also shown. Reduced integration, 20 node brick elements were used. Similar to the previous case tie constraints were also used.

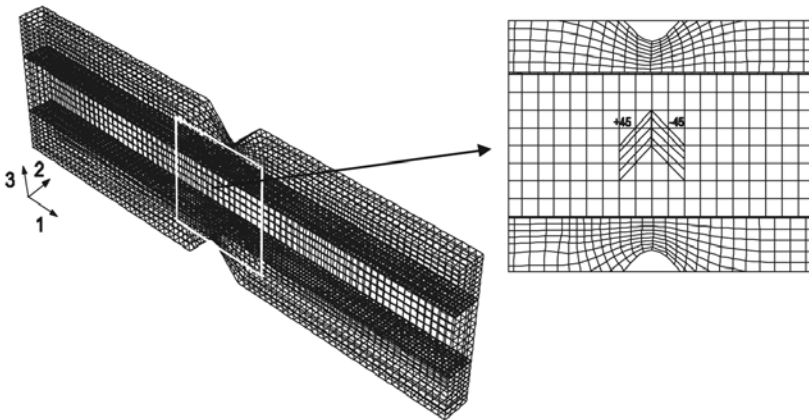


Figure 7. FE mesh of the OOP Iosipescu specimen and strain gauge position relative to the adhesive bonds at the centre of the specimen.

As in the case of the OOP compression tests, the effect of the adhesive bonds on the shear properties,  $G_{13}$ , is very small as can be seen in Figure 8(a)

for multidirectional specimens. The specimen with a bond thickness of 0.1 mm is closer to the specimen without bonds. Finally, in Figure 8(b) the experimental data of a plain weave specimen loaded in shear are compared to model predictions with an adhesive bond thickness equal to 0.1 mm.

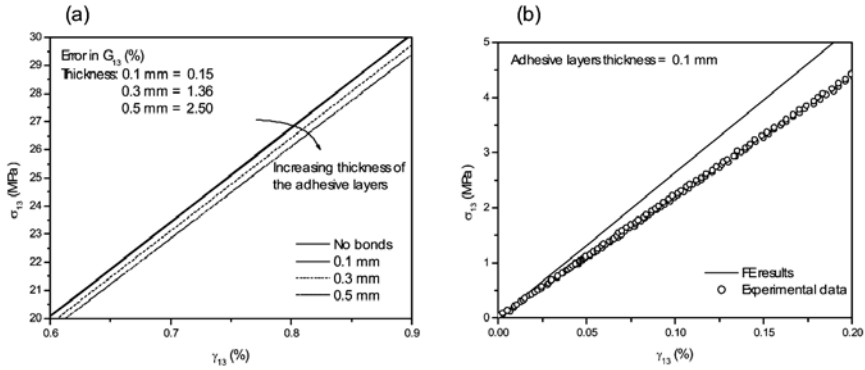


Figure 8. Multidirectional glass/polyester simulated OOP shear stress-strain curves (a), and plain weave glass/polyester simulated and experimental OOP shear stress-strain curves (b).

## 5. SUMMARY AND CONCLUSIONS

The elastic constants of two different skin laminates have been tested in in-plane tension, out-of-plane compression, in-plane shear and out-of-plane shear in order to determine a full set of elastic constants for each laminate.

To avoid making thick laminates the out-of-plane specimens were made by bonding 3 or 4 layers of 10 mm skin laminates together to form a laminate that the specimens could be made from.

The following conclusions were reached:

- The low scatter in the experimentally determined elastic constants for out-of-plane compression and out-of-plane shear indicates that measurements of elastic constants are undisturbed by the adhesive layers.
- The FE simulations of the out-of-plane tests show that the effect of the adhesive layers on the elastic constants is negligible. The error, as expected, increases with increasing adhesive layers thickness. However, even by increasing the adhesive bond thickness by a factor of 5 the errors are still small indicating that the method is reliable.

## ACKNOWLEDGEMENTS

This work was part of the SaNDI (THALES JP3.23) project with participants from Norway, Denmark, Sweden, Finland and the United Kingdom. The support of the Ministries of Defence of the five participating nations is gratefully acknowledged.

The authors wish to thank the staff of the Materials Research Department at Risø National Laboratory: Claus Mikkelsen and Christian Madsen for cutting of specimens, Torben Strauss, Erik Hansen and Frank Adrian for mechanical testing and Erik Vogeley for taking photographs.

## REFERENCES

1. Arnfred, S.A. and Toftegaard, H. "Ultrasonic measurement of elastic constants in fiber-reinforced polymer composites under influence of absorbed moisture", *Ultrasonics*, Vol. 38, pp. 242-246, 2000.
2. Frederiksen, P.S., "Numerical studies for the identification of elastic constants including transverse shear moduli of thick orthotropic plates", *European Journal of Mechanics, A/Solids*, Vol. 16, No. 1, pp. 117-140, 1997.
3. Knight, M., "Three-dimensional elastic moduli of graphite/epoxy composites", *Journal of Composite Materials*, Vol. 16, pp. 153-159, 1982.
4. Broughton, W.R. and Sims, G.D., "An overview of through-thickness test methods for polymer matrix composites", NPL Report DMM(A)148, National Physical Laboratory, Teddington, United Kingdom, 1994.
5. Broughton, W.R., Lodeiro, M. and Sims, G.D., "Experimental validation of shear test methods for through-thickness properties", *Proceedings of the ECCM-7 Conference*, London, Vol. 2, pp. 125-130, 1996.
6. ASTM D 5379 "Standard test method for shear properties of composite materials by the V-notched beam method", 1998.
7. ASTM D695-02a, Standard test method for compressive properties of rigid plastics, 2000.
8. Toftegaard, H., "Simulated stiffness determination from simple compression tests on a thick laminate", *Composites: Part A*, Vol. 30, pp. 849-858, 1999.
9. Toftegaard, H., "Elastic constants from simple compression tests evaluated by numerical simulation", *Proceedings of the 4th European Conference on Composites, ECCM CTS-4, Testing and Standardisation*, Lisbon, Portugal, pp. 310-319, 1998.
10. Kim, J.K. and Lee, D.G., "Characteristics of plasma surface treated composite adhesive joints at high environmental temperature", *Composite Structures*, Vol. 57, pp. 37-46, 2002.

# STOCHASTIC HOMOGENIZATION OF POLYMERIC FOAMS

Jörg Hohe

*Fraunhofer Institut für Werkstoffmechanik, Wöhlerstr. 11, 79108 Freiburg, Germany*

joerg.hohe@iw.fraunhofer.de

**Abstract** The present study is concerned with a probabilistic homogenization analysis of polymeric cellular media to be used as core materials for sandwich structures. The approach is based on a randomized representative volume element in conjunction with a Monte Carlo simulation. The results for stiffness and strength are evaluated by stochastic methods.

**Keywords:** foam mechanics, disordered microstructures, homogenization, stochastic methods, large deformation.

## 1. INTRODUCTION

Solid polymeric foams are common core materials in modern sandwich construction. Their main advantages are their low specific weight due to their high void volume fraction, their low cost and the fact that foam core sandwich structures can be manufactured in a wide range of geometries.

For reasons of numerical efficiency, the analysis of cellular solids during the industrial design process is preferably performed in terms of macroscopic effective properties rather than by a direct model of the given microstructure. The determination of the effective properties can be performed either by experiments or by numerical homogenization analyses. Since the pioneering work of Gent and Thomas [5] appeared in 1963, numerous studies on the theoretical determination of effective mechanical properties of foams have been published. Overviews are given e.g. by Gibson and Ashby [6] or Hohe and Becker [8] and others.

Although solid foams are amorphous media with a highly disordered microstructure (see e.g. experimental studies by Blazy et al. [1] and Ramamurty and Paul [11] showing distinct disorder effects), most of the analytical studies available in literature are based on idealized regular periodic foam models. Only few studies have been performed concerning irregular, random microstructures. Based on a Voronoi tessellation of a large scale representative

volume element, e.g. Silva et al. [12] and van der Burg et al. [13] have analyzed the effect. More recent contributions have been published, among others, by Fazekas et al. [3] and Zhu et al. [15].

On the other hand, it has been pointed out by Fortes and Ashby [4] that a single analysis of a large-scale representative volume element with a random microstructure might be inaccurate since, artificial anisotropies are retained. Instead, a direct probabilistic approach based on a probability function for cell wall orientations is proposed. Other probabilistic approaches have been provided by Cuitiño and Zheng [2], Hall [7] as well as by Warren and Kraynik [14].

The present study is concerned with an alternative probabilistic approach where a previously developed homogenization procedure for periodic media under finite deformation [9] is generalized to cellular solids with a random microstructure. The basic idea of this approach is to determine the exact spatial positions of the cell wall intersections of a cellular solid randomly within prescribed areas. The analysis is performed in multiple numerical experiments which are evaluated by means of stochastic methods.

## 2. HOMOGENIZATION PROCEDURE FOR PERIODIC MODEL FOAMS

The probabilistic homogenization procedure presented in Section 3 generalizes a homogenization procedure for polymeric model foams with a periodic microstructure presented previously (Hohe and Becker [9]). The approach is based on the analysis of a representative volume element for the given microstructure according to Figure 1. For comparison, a virtual volume element of the same shape and size consisting of the homogenized “effective” medium is considered. The properties of the homogeneous volume element have to be chosen such that the macroscopic mechanical behavior of both volume elements is equivalent.

The macroscopic mechanical equivalence of both volume elements is defined by the condition that the average strain energy densities  $\bar{w}$  and  $\bar{w}^*$  in both volume elements have to be equal

$$\bar{w} = \frac{1}{V^{\text{RVE}}} \int_{\Omega^{\text{RVE}}} w \, dV = \frac{1}{V^{\text{RVE}}} \int_{\Omega^{\text{RVE}^*}} w^* \, dV = \bar{w}^* \quad (1)$$

provided that both volume elements experience a deformation which is equivalent on the macroscopic level of structural hierarchy. The deformation of both volume elements is defined to be macroscopically equivalent, if the volume averages

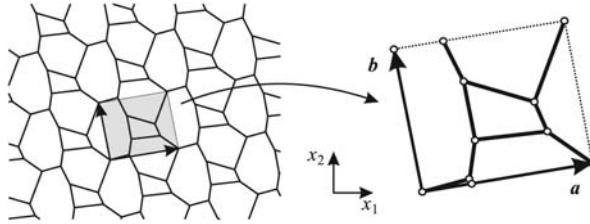


Figure 1. Deterministic two-dimensional cellular microstructure (periodic).

$$\bar{F}_{ij} = \frac{1}{V_{RVE}} \int_{\Omega^{RVE}} F_{ij} \, dV = \frac{1}{V_{RVE}} \int_{\Omega^{RVE*}} F_{ij}^* \, dV = \bar{F}_{ij}^* \quad (2)$$

of the components  $F_{ij} = \partial u_i / \partial x_j + \delta_{ij}$  of the deformation gradient are equal.

The components of the deformation gradient are related to the components  $\bar{\gamma}_{ij}$  of the macroscopic Green–Lagrange strain tensor by

$$\bar{\gamma}_{ij} = \frac{1}{2} (\bar{F}_{ki} \bar{F}_{kj} - \delta_{ij}) \quad (3)$$

where  $\delta_{ij}$  are the components of the unit tensor. The components  $\bar{\tau}_{ij}$  of the effective second Piola–Kirchhoff stress tensor can be determined from the average strain energy density as the partial derivatives

$$\bar{\tau}_{ij} = \frac{\partial \bar{w}}{\partial \bar{\gamma}_{ij}} \approx \frac{\Delta \bar{w}}{\Delta \bar{\gamma}_{ij}} \quad (4)$$

if a hyperelastic material behavior is postulated.

A homogenization scheme based on Equations (1) to (4) basically requires the following four steps:

- identification of an appropriate representative volume element,
- deformation of a numerical (e.g. finite element) model of the representative volume element according to the prescribed effective strain state  $\bar{\gamma}_{ij}$  considering Equation (3),
- computation of the strain energy density for the prescribed strain state and the corresponding partial derivatives,
- determination of the effective second Piola–Kirchhoff stress components  $\bar{\tau}_{ij}$  using Equation (4).

Details on the implementation of this procedure can be found in the original contributions by Hohe and Becker [9, 10].

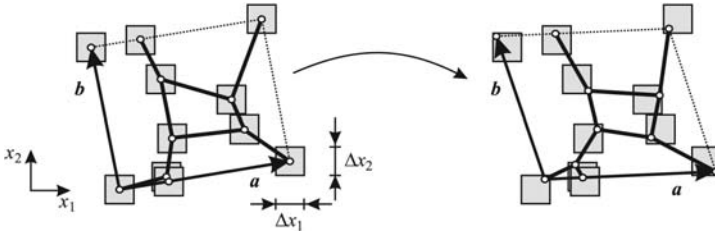


Figure 2. Randomized two-dimensional cellular microstructure.

### 3. PROBABILISTIC APPROACH

The concept for homogenization of perfectly periodic microstructures outlined in Section 2 is now enhanced to cover the effect of microstructural irregularity. For this purpose, the microstructure is randomized prior to the homogenization analysis. The randomization is performed by determining the exact spatial positions  $x_i^{int(j)}$  of cell wall intersections  $j$ , ( $j = 1, \dots, n$ ) randomly within prescribed areas around the positions  $x_i^{int,reg(j)}$  of the corresponding perfectly regular microstructure using a random number generator (see Figure 2). In this context, the spatial dimensions  $\Delta x_i$  form additional material parameters describing the degree of microstructural disorder. In most cases, the choice of equal spatial dimensions  $\Delta x_i$  of the cubes for random determination of the cell wall intersections will be appropriate. The single remaining parameter  $\Delta x$  can easily be determined from micrographic analyses of the respective solid foam.

The random determination of the microstructural geometry and the subsequent homogenization analysis are repeated in a number of numerical experiments. The results are evaluated by means of stochastic methods. Therefore, the effective stress  $\bar{\tau}_{ij}$  for a given macroscopic strain state  $\bar{\gamma}_{ij}$  is given in terms of the mean value

$$\bar{\tau}_{ij}^a = \frac{1}{n} \sum_{k=1}^n \bar{\tau}_{ij}^{(k)} \tag{5}$$

where  $\bar{\tau}_{ij}^{(k)}$  is the effective stress obtained in  $n$  individual numerical experiments. The scatter in the effective stress-strain relation can be assessed in terms of the standard deviation

$$\bar{\tau}_{ij}^s = \left( \frac{1}{n-1} \sum_{k=1}^n \left( \bar{\tau}_{ij}^a - \bar{\tau}_{ij}^{(k)} \right)^2 \right)^{\frac{1}{2}} \tag{6}$$

or the probability density distribution of the effective stresses.

For determination of the probability density distributions, the stress results  $\bar{\tau}_{ij}^{(k)}$  from the individual numerical experiments are arranged in increasing or-

der. In this case, the accumulated probability  $P(\bar{\sigma}_{ij})$  for the occurrence of a stress level of at least  $\bar{\sigma}_{ij}$  is

$$P(\bar{\sigma}_{ij}) = \frac{k^* - \frac{1}{2}}{n} \quad (7)$$

where  $k^*$  is the number of the numerical experiment with  $\bar{\sigma}_{ij}^{(k^*)} = \bar{\sigma}_{ij}$  after the re-arrangement of the stress results into increasing order whereas  $n$  is the total number of numerical experiments performed. From the accumulated probability  $P(\bar{\sigma}_{ij})$ , the probability density distribution is determined by

$$p(\bar{\sigma}_{ij}) = \frac{\partial P(\bar{\sigma}_{ij})}{\partial \bar{\sigma}_{ij}} \quad \left( = \frac{\Delta P(\bar{\sigma}_{ij})}{\Delta \bar{\sigma}_{ij}} \right) \quad (8)$$

where the partial derivative has to be computed numerically.

Advantage of the present probabilistic approach compared to the standard approaches based on the single analysis of a large-scale representative volume element is that not only the mean values of the effective stresses are obtained but additional information about the corresponding scatter bands is derived. The scatter can either be assessed in terms of the standard deviation or directly by determination of the probability density distribution. Therefore, the scheme provides an efficient and easy-to-use procedure for the numerical homogenization of random microstructures.

#### 4. EXAMPLE: TWO-DIMENSIONAL MODEL FOAM

As an example, the effective behavior of a two-dimensional model foam is considered. As a periodic reference microstructure, a regular two-dimensional hexagonal honeycomb is employed. The cell wall material is described by an Ogden type constitutive equation

$$w = \sum_{k=1}^n \frac{\mu_{(k)}}{\alpha_{(k)}} \left( (\lambda_1^{\text{dev}})^{\alpha_{(k)}} + (\lambda_2^{\text{dev}})^{\alpha_{(k)}} + (\lambda_3^{\text{dev}})^{\alpha_{(k)}} - 3 \right) + \sum_{k=1}^n \kappa_{(k)} (J - 1)^{2k} \quad (9)$$

with

$$\lambda_k^{\text{dev}} = J^{-\frac{1}{3}} \lambda_k$$

where  $\lambda_k$  and  $J$  are the principal values of the deformation gradient and the corresponding Jacobian respectively. The material parameters are assumed as  $n = 2$  with  $\alpha_1 = 1.5$ ,  $\mu_1 = 1.4$  GPa and  $\kappa_1 = 0.8$  GPa as well as  $\alpha_2 = 3$ ,  $\mu_2 = 1$  GPa and  $\kappa_2 = 0$  which might be assumed as being within the typical range for polymeric materials.

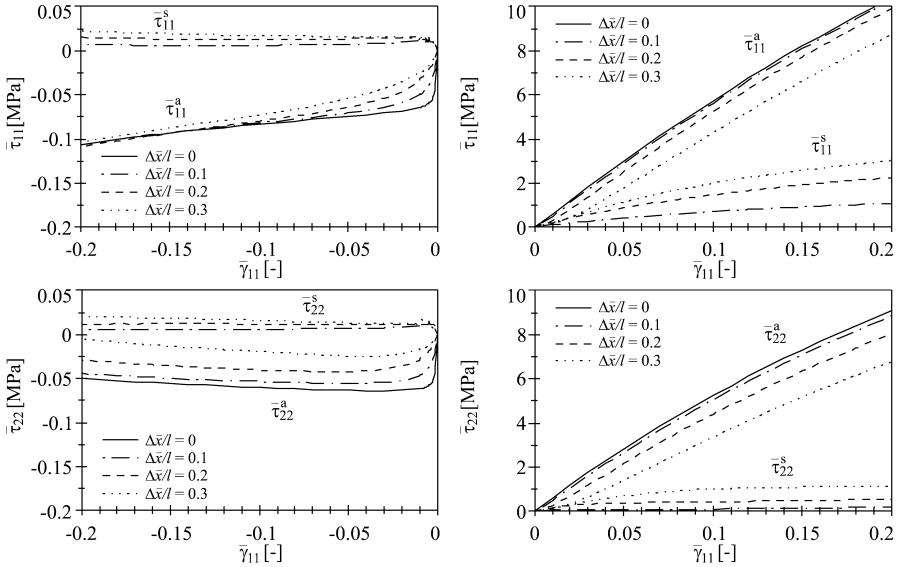


Figure 3. Macroscopic stress-strain relations for uniaxial compression and tension.

Although for simplicity all subsequent examples are related to two-dimensional microstructures, it should be noticed that the approach presented in Sections 2 and 3 can be applied to three-dimensional microstructures in the same manner.

### 5. EFFECTIVE STRESS-STRAIN RELATIONS

As a first example, the macroscopic stress-strain relations of the two-dimensional model foam characterized in Section 4 are analyzed. As an example, the load cases of a uniaxial tensile and compressive deformation are considered. In this context, the normal Green–Lagrange effective strain component  $\bar{\gamma}_{11}$  is varied from zero level up to a level of 20% tensile or compressive strain respectively. The remaining in-plane components  $\bar{\gamma}_{22}$  and  $\bar{\gamma}_{12}$  of the macroscopic Green–Lagrange strain tensor are assumed to vanish throughout the deformation history.

In Figure 3, the results are presented considering the effective normal stress component  $\bar{\tau}_{11}$  acting within the direction of the applied macroscopic deformation as well as the net stress component  $\bar{\tau}_{22}$  perpendicular to this direction. Three different levels  $\Delta x/l$  of microstructural disorder are analyzed, where  $l$  is the (uniform) strut length for the reference model foam with regular hexagonal microstructure. Results for this case are indicated by a solid line in the respective plot.

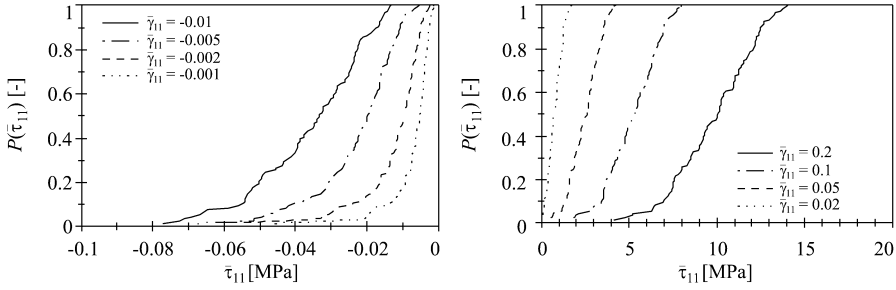


Figure 4. Distribution of the accumulated stress probability for different effective load levels.

It is observed that in the tensile range both, the nominal effective stress  $\bar{\tau}_{11}$  as well as the net stress  $\bar{\tau}_{22}$  decrease with increasing microstructural disorder. Thus, the increasing microstructural disorder leads to a weaker material response on the effective level of structural hierarchy, whereas the perfectly regular hexagonal foam model overestimates the effective stresses and thus the effective stiffness of the material. This effect is caused by a transition in the microscopic mode of deformation. For the perfectly regular microstructure, the deformation under a uniaxial effective strain state is governed by cell wall stretching in the longitudinal direction of the individual struts. For increasingly disordered microstructures, localized bending of the struts in the vicinity of the cell wall intersections becomes more important, leading to a weaker macroscopic material response.

In the compressive range, strong effects of the microstructural disorder are observed especially at low levels  $-\bar{\gamma}_{11}$  of the applied effective strain. In this range, the perfectly regular microstructure exhibits a branching instability in the effective material response caused by buckling of the cell walls. No such instability in the rigorous Eulerian sense occurs for disordered microstructures, resulting in a distinct weakening of the effective material in this range for increasing microstructural disorder.

The accumulated probability  $P(\bar{\tau}_{11})$  for the occurrence of an effective stress level of at least  $\bar{\tau}_{11}$  is presented in Figure 4 at four different compressive and tensile deformation levels  $\bar{\gamma}_{11}$ . A constant degree  $\Delta x/l = 0.2$  of the microstructural disorder is considered. In the tensile range, an increasing level of the applied effective deformation leads to a monotonic increase of both, the average effective stress  $\bar{\tau}_{11}^a$  and the scatter band width characterized by a decreasing slope of the accumulated probability  $P$ . In the compressive range, an additional transition of the curve shape of the accumulated stress probability is observed. At low effective stress levels, a bimodal behavior develops, where the range of a low gradient belongs to microstructures in the pre-buckled state whereas a the zone of a larger gradient of the accumulated probability at

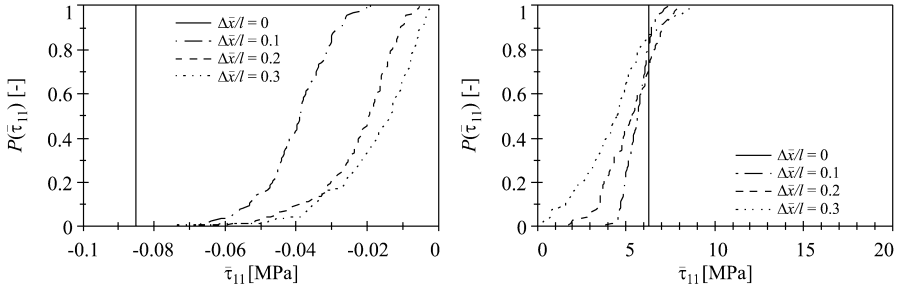


Figure 5. Distribution of the accumulated stress probability for different disorder degrees.

lower effective stress levels indicates a microstructural deformation mode in the postbuckling range.

The effect of the degree  $\Delta x/l$  of microstructural disorder on the stress probability at fixed levels  $\bar{\gamma}_{11} = -0.005$  and  $\bar{\gamma}_{11} = 0.1$  is analyzed in Figure 5. Again, it is observed that an increasing degree of microstructural disorder does not only cause an increasing scatter of the results but also has distinct effects on the average stresses, resulting in a general weakening of the corresponding effective material.

### 6. EFFECTIVE STRENGTH

In a final investigation, the effective strength of ordered and disordered cellular solids is analyzed. In accordance with the weakest link concept, failure of the entire microstructure is assumed if the first strut in the representative volume element fails. Failure of the struts is assessed by a simple maximum stress criterion assuming a maximum permitted v. Mises stress of  $\sigma_e = 125$  MPa. From the effective stress-strain curves, the failure strain  $\bar{\gamma}_{ij}^f$  on the effective level is computed as the effective strain, where the local failure criterion is first satisfied anywhere in the representative volume element.

The results for uniaxial compressive and tensile deformation within the  $x_1$ - and  $x_2$ -directions are presented in Figure 6. It is observed that an increasing degree  $\Delta x/l$  of microstructural disorder leads to a distinct decrease of the effective failure load in the tensile range by about 30%. In the compressive range, the consideration of the microstructural disorder results in the vanishing of the strength anisotropy of the perfectly regular microstructure with different effective failure stresses  $\bar{\gamma}_{11}^f$  and  $\bar{\gamma}_{22}^f$  within the  $x_1$ - and  $x_2$ -directions.

### 7. CONCLUSION

The present study provides a simple analytical scheme for the homogenization analysis of solid foams accounting especially for the microstructural disorder. The scheme is based on a Monte Carlo simulation of randomized

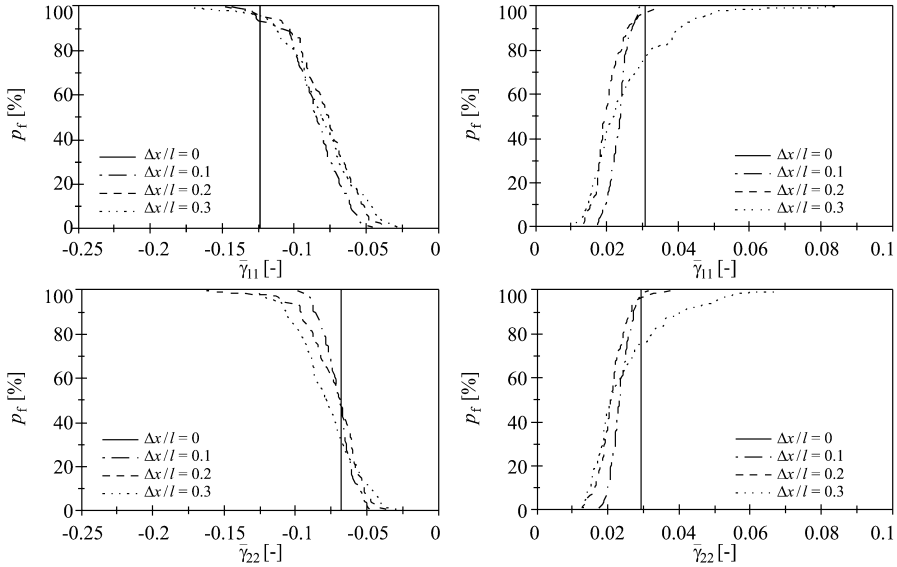


Figure 6. Accumulated failure probability under tensile and compressive deformation.

small-scale representative volume elements in conjunction with a strain energy based approach for the homogenization analysis.

Advantage of the approach is that it fully accounts for the microstructural irregularity. Due to its formulation in terms of numerical experiments in conjunction with a stochastic assessment, both, the average properties of the effective material as well as the scatter can be assessed, which is impossible in the previous approaches based on a single analysis of a large-scale representative volume element consisting of a huge number of base cells.

In a number of numerical examples considering both the effective stress-strain response of random cellular solids as well as their effective strength, it is observed that the microstructural disorder does not only affect the scatter to be expected in the respective effective material properties but also can have distinct effects on the respective average values. In general, an increasing degree of microstructural disorder results in a general weakening of the effective material behavior in terms of both, the effective stiffness and the effective strength. Both of these quantities are overestimated by a classical approach based on a perfectly regular, periodic model for the cellular microstructure.

## REFERENCES

[1] J.S. Blazy, A. Marie-Louise, S. Forest, Y. Chastel, A. Pineau, A. Awade, C. Grolleron and F. Moussy, F. Deformation and fracture of aluminium foams under proportional and multi-axial loading: statistical analysis and size effect. *International Journal of the Mechanical Sciences* 46:217-244, 2004.

- [2] A.M. Cuitino and S. Zheng. Taylor averaging on heterogeneous foams. *Journal of Composite Materials* 37:701-713, 2003.
- [3] A. Fazekas, R. Dendievel, L. Salvo and Y. Bréchet. Effect of microstructural topology upon the stiffness and strength of 2D cellular structures. *International Journal of the Mechanical Sciences* 44:2047-2066, 2002.
- [4] M.A. Fortes and M.F. Ashby. The effect of non-uniformity on the in-plane modulus of honeycombs. *Acta Materialia* 47:3469-3473, 1999.
- [5] A.N. Gent and A.G. Thomas. Mechanics of foamed elastic materials. *Rubber Chemistry and Technology* 36:597-610, 1963.
- [6] L.J. Gibson, and M.F. Ashby. *Cellular Solids – Structure and Properties*. Cambridge University Press, London 1997.
- [7] R. Hall. Effective moduli of cellular materials. *Journal of Reinforced Plastics and Composites* 12:186-197, 1993.
- [8] J. Hohe and W. Becker. Effective stress-strain relations for two-dimensional cellular sandwich cores: Homogenization, material models and properties. *Applied Mechanics Reviews* 55:61-87, 2002.
- [9] J. Hohe and W. Becker. Effective mechanical behavior of hyperelastic honeycombs and two-dimensional model foams at finite strain. *International Journal of the Mechanical Sciences* 45:891-913, 2003.
- [10] J. Hohe and W. Becker. A probabilistic approach to the numerical homogenization of irregular solid foams at finite strain. *International Journal of Solids and Structures* 42:3549-3569, 2005.
- [11] U. Ramamurty and A. Paul. Variability in mechanical properties of a metal foam. *Acta Materialia* 52:869-876, 2004.
- [12] M.J. Silva, W.C. Hayes and L.J. Gibson. The effects of non-periodic microstructure on the elastic properties of two-dimensional cellular solids. *International Journal of the Mechanical Sciences* 37:1161-1177, 1995.
- [13] M.W.D. van der Burg, V. Shulmeister, E. van der Giessen and R. Marissen. On the linear elastic properties of regular and random open-cell foam models. *Journal of Cellular Plastics* 33:31-54, 1997.
- [14] W.E. Warren and A.M. Kraynik. Linear elastic behavior of a low-density Kelvin foam with open cells. *Journal of Applied Mechanics* 64:787-794, 1997.
- [15] H.X. Zhu, J.R. Hobdell and A.H. Windle. Effects of cell irregularity on the elastic properties of 2D Voronoi honeycombs. *Journal of the Mechanics and Physics of Solids* 49:857-870, 2001.

# STOCHASTIC FINITE ELEMENT MODELS OF FOAM MATERIALS

Stefan Hallström and Steven Ribeiro-Ayeh

*Department of Aeronautical and Vehicle Engineering, Royal Institute of Technology (KTH), SE-100 44 Stockholm, Sweden*

**Abstract** Driven by the desire to understand the influence of various mechanical properties and geometric features of foam materials, on the stiffness, failure mechanisms and fatigue life of sandwich materials, 3D finite element models of amorphous cellular structures have recently been developed and analyzed. Different algorithms were used to generate seed points of Voronoi tessellations, such as randomly distorted regular lattice distributions and totally random distributions. Periodic boundary conditions were used on representative volume elements containing hundreds of cells. Some comparison with experimental data from real foam materials was made and the agreement was found to be good. In the presented paper discrepancies between the used models and real foams are discussed and it is concluded that the adopted approach has substantial potential although there are some obvious routes for further improvement.

**Keywords:** finite element, foam, cellular, stochastic, Voronoi, periodic.

## 1. INTRODUCTION

Cellular materials are characterized by an inhomogeneous microstructure where a bulk material constitutes a network of grains, struts, membranes or some combination thereof. The structure could be regular and repetitive but is more often amorphous. The cell walls consist of organic, polymer, ceramic or metallic material and the open space in the material is usually filled with some fluid. The properties of the cellular material are governed by the properties of the bulk material and the entrapped fluid, and the

geometry of the microstructure. A virtually infinite palette of foams could be obtained enabling cellular materials to provide a variety of attributes such as buoyancy, thermal insulation or heat exchange, means for catalytic conversion or shock absorption, and high specific structural stiffness and strength when utilized as sandwich core materials.

The structural performance of foam core sandwich structures is strongly dependent on the mechanics of the solid foam material it contains. In engineering analysis of stiffness and strength, modeling the foam as a continuum is generally sufficient to provide reasonably accurate results. However, in order to fully understand the mechanics of foams, e.g. large deformation behavior, fracture propagation and fatigue mechanisms, one has to consider the cellular structure of these materials.

When subject to mechanical loading, the foam could globally demonstrate the behavior of a dense homogenous material, being both isotropic and satisfy continuum conditions. However, the deformation at micro-level could be very complex and involve combinations of tension, bending, twist and shear of cell walls even for the simplest load cases, and the local strain levels could vary considerably from one location to another in the heterogeneous microstructure.

In order to provide better models of manmade foam materials it is important to understand how these materials are manufactured. Typically, either small gas bubbles or some blowing agent is mixed into a liquid aggregate and at a subsequent stage emission and/or expansion of gas is initiated. Pores in the material is nucleated and driven to grow by their internal pressure to a stage when all of the solid material has been redistributed into cell walls of the foamed material. Due to principles of minimization of surface energy the cell edges generally become thicker than the faces. So called Plateau regions [1] are formed around the edges constituting intersections of cell walls. If the blowing process is kept moderate or interrupted early it produces a closed cell foam structure but if the foaming is driven further, the cell walls could bust leaving only the Plateau struts between the cells and thus resulting in an open cell structure. In sandwich applications closed-cell foams are of primary interest but the adopted approach for analysis is applicable for open-cell foams as well.

The simplest foam models consist of 2-dimensional lattices usually consisting of some regular (e.g. hexagonal) structure. These could be used to bring about some useful insight on the mechanics of foams, such as qualitative scaling laws, etc. [2]. However, in order to model the mechanics of foams accurately one has to take 3-dimensional effects into account and also the fact that foam materials generally exhibit an amorphous microstructure. Real foams in addition contain cells with various distributions of size and topology. Even the thickness of cell walls typically

varies - within a foam material, within cells, and even within single cell walls. The mechanical behavior of the solid (bulk) material could also be non-linear, anisotropic and/or visco-elastic. The complexity of foam materials is obviously immense and modeling of these materials is by no means straightforward.

In previous work by the authors [3–5] finite element models of stochastic cellular structures have been developed, which mimic the mechanical behavior of real foam materials. In the following the adopted approach, some results and their validity are presented and discussed.

## 2. APPROACH

The intent is to generate finite element models in a manner that is similar to the way foam materials are produced in reality, and make these models large enough to provide reliable input for generation of homogenized engineering properties. In order to do this reliably the models have to contain a high enough number of cells and be spatially periodic. This is achieved by generating distributions of cell nuclei in space numerically, and simulating cell growth around the nuclei through generation of Voronoi tessellations [6]. The nuclei are distributed in ways that enable spatially periodic boundary conditions when the morphology coming out from the division of space is finally meshed and analyzed using finite element (FE) software. In the FE discretizations sufficiently dense meshes have to be used to assure numerical convergence in the final analysis.

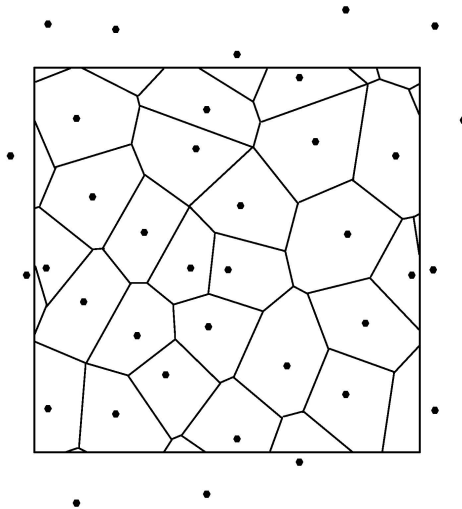


Figure 1. A 2-dimensional illustration of a spatially periodic Voronoi tessellation.

## 2.1 Generation of spatially periodic representative volume elements

First a cubic control volume, or representative volume element (RVE), is defined. Secondly, a distribution of virtual cell nuclei is placed in the RVE. Thirdly, a Voronoi tessellation is formulated by letting all points being closer to one specific nucleus than to any other define a cell. In order to achieve a periodically repetitive unit volume the RVE is considered to be surrounded by 26 identical volumes, each containing identical nuclei distributions. A 2-dimensional spatially periodic Voronoi tessellation is illustrated in Figure 1.

The cell nuclei are defined as the centre points of solid spheres that are packed in space using various numerical algorithms. The sphere locations are either defined by randomly distorted regular packings, such as body centered cubic (BCC) or face centered cubic (FCC) lattices, or using a random sequential adsorption (RSA) algorithm [7]. Perfectly ordered packings of spheres would generate monodisperse Voronoi tessellations containing solely rhombic dodecahedra in the case of FCC and tetrakaidecahedra (Kelvin cells) [8] in the case of BCC. Distortion of the FCC and BCC lattices alters the topologies in the resulting morphologies but since the distortion is kept moderate the resulting cell volume distributions are relatively uniform, i.e. the polydispersity is limited. Distributions generated with RSA had similar volumetric polydispersity as found in the distorted regular lattices [5].

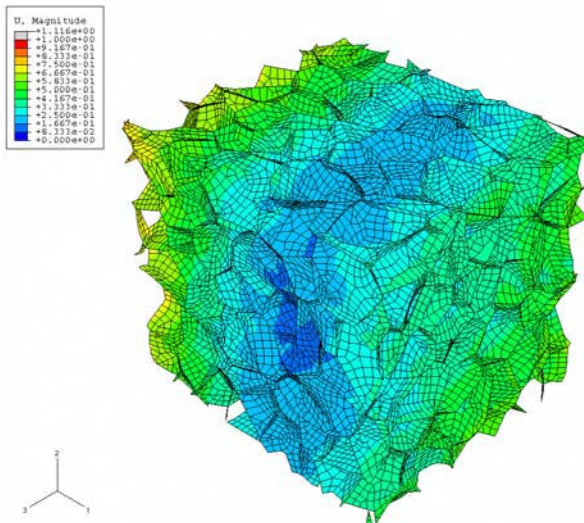


Figure 2. A 300 cell FE model subject to uni-axial tension.

## 2.2 Finite element discretization

Once the cell structure is defined it is possible to measure the distributions of cell volume, cell wall area, cell edge length, et cetera. Some geometric bookkeeping is also necessary for the conversion of the numerical cell models into finite element models. The FE models have to contain a sufficient number of cells to provide an overall isotropic response of the foam model and to ascertain statistically sound results.

The geometrical models are converted into FE models where the faces of the cells are modeled with membrane or shell elements. Beam elements are introduced along the edges of the cells, allowing for modeling of lumped material in the Plateau regions of real foams, coming from matter being drawn to these areas when the foam is still liquid, by a combination of osmotic pressure and surface repelling forces in the cell walls [1, 9]. The extreme situation where all of the material is localized at the edges corresponds to an open cell structure, represented by beam elements only in the models. If, on the other hand, all faces contain only some portion of material the cell structure is closed. The adopted FE approach allows for a reasonably sensible representation of different distributions of solid in foam materials.

The FE models were used to extract Young's modulus, shear modulus, bulk modulus and Poisson's ratio as function of relative density and distribution of solid between the cell edges and faces, and the robustness of the results was tested by varying the number of cells and the mesh density. An example of a 300 cell closed foam model, subject to uni-axial tension, is presented in Figure 2.

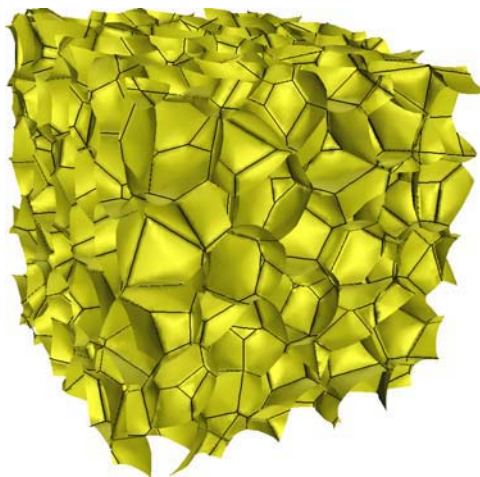


Figure 3. A representative volume element containing 200 cells with curved walls.

### **3. RESULTS**

The work so far has indicated that 300 cells or more give results with reasonable accuracy and consistency [3]. The results were further not found to be overly sensible for variations of mesh density. The influence of cell wall curvature was investigated [4], see Figure 3, and it was found that the stiffness dropped substantially when the wall curvature was increased. The models were made in a way that conserved the relative density of the foam by reducing the wall thickness when the wall curvature was increased and it was specifically shown that the stiffness reduction was related to the curvature and not only to the associated reduction of face thickness. When models generated from distorted regular lattices were compared with models generated from RSA the latter generally provided more consistent results [5].

### **4. DISCUSSION**

The results from the FE models were in good agreement with experimental data of stiffness and Poisson's ratio. However, the agreement does not unambiguously imply that the models were correct since there are properties of the real foam that were never examined and tried to model accurately. For instance there are generally uncertainties about the mechanical properties of the bulk material in real foams and such properties are typically very difficult to determine. The cell size distribution of the real foam was not measured and the shape of the cell faces and Plateau borders were not examined.

In the following section some validity aspects of the adopted approach are discussed. The morphology of real foam materials is governed by a multitude of mechanisms such as e.g. flow of materials, heat transports, chemistry and gravity, et cetera, and the details of the resulting micro structure in a given foam material are inherently far from obvious.

When modeling foam materials with finite elements a number of idealizations have to be made, some of which could be argued to be more severe than others.

#### **4.1 Distribution of solid**

As means for characterization of cellular materials, relations such as relative density and distribution of solid are frequently used. The relative density is simply the ratio between the density of the cellular material  $\rho^*$  and the density of the solid material  $\rho_s$  from which it is formulated. The

distribution of solid is defined as the volume fracture of material in the cell edges, given by

$$\frac{V_e}{V_e + V_f} \quad (1)$$

where  $V_e$  and  $V_f$  are the volumes of solid material in the cell edges and faces, respectively. For honeycombs and closed-cell foams the edges inherently constitute intersections between faces and since the distinction between the two could be quite dubious in real materials the concept of distribution of solid is generally not completely lucid. Even for idealized materials unambiguous separation into edges and faces is impossible. The measure is sensible when idealized theory for stiffened shells applies, i.e. when the thickness of the edges are considerably smaller than their length. In practice neither the volumes nor the mechanical interaction of edges and faces could be dissected. From equilibrium considerations such as aspects of surface energy and osmotic pressure during the formation of liquid foams one can show that the cell edge thickness could never be less than the cell face thickness [1]. Without going into details one can conclude that a consequence is that there is a lower bound for the distribution of solid, which is depending on the relative density of the foam. It is thus not entirely appropriate to express the relation of different properties with respect to solely the relative density or the distribution of solid.

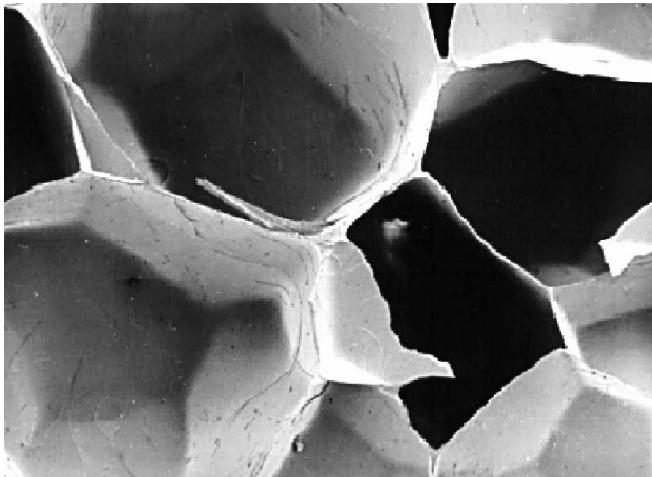


Figure 4. SEM image of Rohacell 51WF.

## **4.2 Minimization of surface energy**

Voronoi tessellations generate polyhedra which inherently satisfy Euler's topological laws for large aggregates of cells [2]. The resulting microstructures satisfy connectivity principles for soap froth, i.e. three faces meet at each edge and four edges meet at each vertex. Plateau's laws for minimisation of surface energy in dry soap froth [1] are however not satisfied. Kraynik [9] reports that the Plateau borders for cells with relatively little material in the faces become relatively thick even for relative densities as low as 0.01, indicating that a beam model for the Plateau regions is not appropriate. However, the result is based on liquid foams satisfying conditions of minimum surface area. Many of the structural foams used as sandwich core materials do not seem to be frozen versions of energetically relaxed soap froths. The Plateau regions for these foams are often less pronounced indicating that other effects than surface tension, such as viscosity or gradual solidification during foaming, are active in the manufacturing processes, see Figure 4.

Even though the foam models not necessarily have to satisfy conditions of minimal surface energy there is reason to believe that very small cell faces and very short cell edges would disappear in most foaming processes since they are highly unstable from a surface energy point of view. So far no attempts have been made to relax the generated Voronoi tessellations but including such efforts in the numerical scheme would likely be beneficial.

## **4.3 Face curvature versus face bending stiffness**

The introduction of curvature [4] was made systematically in the sense that all cell faces were given similar curvature. However, the curvature was constant in individual cell walls and there was no relation between the curvature of neighboring walls. In reality curvature of one cell wall would affect the curvature in adjacent cell walls due to the mechanical coupling over common cell edges. In real foams cell wall curvature would in addition come as a result of minimization of surface energy while in the FE models the total surface area increased when the curvature was introduced. In the models the edges of single cell walls constituted planar polygons with straight edges, even when the faces were curved. In real foams the cell edges could be curved and, in addition, the cell faces polygons could be warped rather than planar.

## 5. CONCLUSIONS

Although substantial efforts have been made to generate realistic stochastic models of closed foam materials the resulting FE models are, despite their complexity, relatively coarse in terms of geometric representation of real foam materials. Some of the mechanical behavior of real foam materials seems to be mimicked well and reasonable results have been derived. Some relaxation of the numerical models, by means of minimizing surface energy, would likely generate even better topological agreement between the models and real foams. Since there are principal differences between the used models and the real foams of interest, further evidence is needed in order to convincingly authenticate the validity of the models. One necessary ingredient in such validation would be to systematically characterize the real foams of interest, in terms of geometric features such as e.g. topology, cell size distributions and cell wall curvature.

## REFERENCES

1. Weaire, D. and Hutzler, S., *The Physics of Foams*, Oxford University Press, Oxford, United Kingdom, 1999.
2. Gibson, L.J. and Ashby, M.F., *Cellular Solids: Structure and Properties*, 2nd edition, Cambridge University Press, Cambridge, United Kingdom, 1997.
3. Ribeiro, S. and Hallström, S., "Stochastic finite element models for the characterisation of effective mechanical properties of cellular solids", submitted for publication (2005).
4. Ribeiro, S. and Hallström, S. "The influence of cell wall curvature on the stiffness of cellular solids", submitted for publication (2005).
5. Ribeiro, S. "The effect of topological disorder on the mechanical properties of cellular solids", submitted for publication (2005).
6. Voronoi, G.F., "Nouvelles applications des parametres continus a la theorie des formes quadratiques, II: Recherches sur les paralleloedres primitives", *Journal für die Reine und Angewandte Mathematik*, Vol. 134, pp. 198-297, 1908.
7. Torquato, S., *Random Heterogeneous Materials: Micro Structure and Macroscopic Properties*, Springer Verlag, New York, 2001.
8. Thomson, W., "On the division of space with minimum partitional area", *Philosophical Magazine*, Vol. 24, No. 151, p. 503, 1887.
9. Kraynik, A., "Foam Structure: from soap froth to solid foams", *Materials Research Society Bulletin*, April 2003, pp. 275-278, 2003.

# **APPLICATIONS AND DESIGN SOLUTIONS**

# APPLICATION OF LOAD CARRYING SANDWICH ELEMENTS IN LARGE WIND TURBINE BLADES

Jacob Fisker Jensen, Jacob Pagh Schultz and Christian Berggreen  
*Department of Mechanical Engineering, Technical University of Denmark,  
DK-2800 Kgs. Lyngby, Denmark*  
cbe@mek.dtu.dk

Kim Branner  
*Wind Energy Department, Risø National Laboratory, DK-4000 Roskilde, Denmark*  
kim.branner@risoe.dk

**Abstract** The present work investigates the possibilities and drawbacks when applying sandwich as opposed to single skin composites in the flanges of the load carrying spar in a future 180 m wind turbine rotor. FEA is applied to investigate two basic designs with single skin and sandwich flanges respectively. For a single skin design, buckling is critical compared to other design criterions. By introducing sandwich, a significant weight reduction and increased buckling capacity is obtained. Tower clearance now becomes critical. Proper choice of core material and thickness is important to prevent face wrinkling and large tip deflection. Geometric non-linear analysis showed sensitivity to imperfections.

**Keywords:** buckling, sandwich, non-linear FEA, sensitivity analysis, wind turbine blades.

## 1. INTRODUCTION

Ever since the modern wind energy industry was established in the late 1970s, the size of the wind turbines has been increasing steadily. The largest wind turbines today have an effect of approximately 4 MW and a rotor diameter of 110–125 m. These turbines are probably at the limit of the size to be erected on-shore. However, off-shore turbines are expected to still increase in size and turbines with an effect of 10 MW and a rotor diameter of 180 meters can be expected within the next decade. In Figure 1 a wind turbine of such dimensions is sketched along with a Great Belt bridge pylon measuring 254 meters above sea level. The main motivation for increasing the size of wind turbines is that the cost of energy production decreases with larger turbines.

Many modern wind turbine blades are constructed with a load carrying main spar that supports the outer shell, as shown in Figure 2, taken from Sørensen et al. [1].

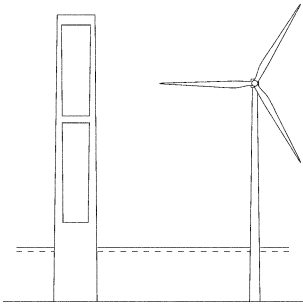


Figure 1. Future offshore wind turbine compared to a Great Belt bridge pylon.

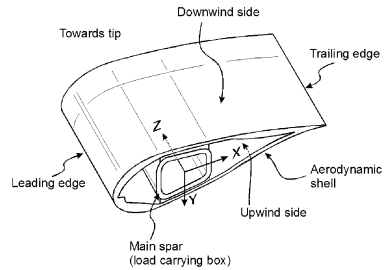


Figure 2. Turbine blade with main load carrying box spar.

The main spar usually extends from the root of the blade to a position close to the tip and the load carrying flange of the spar is usually a single skin construction. Large turbine blades will have very large unstiffened panels, which will be sensitive to failure in buckling. It is therefore obvious that the sandwich principle will be used more widely in the future in order to prevent buckling of the structure. The purpose of this paper is to compare a traditional single skin blade design with one where sandwich panels are used as load carrying elements. The different design requirements for the two designs are furthermore discussed in the present paper.

## 2. BLADE DESIGN

**General.** The purpose of the main spar is to give the blade sufficient strength and stiffness both globally and locally. Globally the blade should be sufficient stiff in order not to collide with the tower during operational and extreme loading. Locally the box girder together with the stiffness of the outer shell ensures that the shape of the aerodynamic profile is maintained as stable as possible. The pressure load on the blade results in edgewise and flapwise bending as well as torsional loading of the blade. The box girder primarily carries the two latter types of loading while the edgewise bending primarily is carried by strengthening of the leading and trailing edges of the aerodynamic profile. Only flapwise bending is considered in the following analysis as the aerodynamic shell is neglected. The blade geometry used in the present study is found through extrapolation from blade data for existing blades. The data can be found in Jensen and Schultz [2]. The spar geometry is extracted from the profiles in Figure 3.

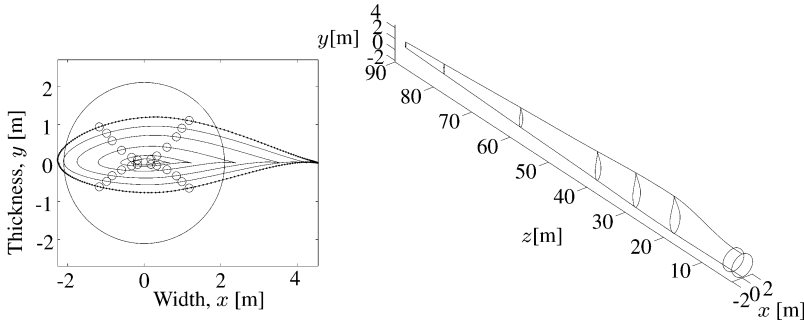


Figure 3. a) Points between circles constitute the spar flanges, b) 3D view of the blade.

A combination of unidirectional (UD) and biaxial (Biax) laminates is used for the skins. The UD material data, corresponding to a glass-epoxy, is taken from Reddy [3]. The core material is varied between three densities of Divinycell H Grade cores. The applied material data can be found in Jensen and Schultz [2].

**Single skin design.** A design consisting of single skin in the flanges and sandwich in the webs is established through an iterative optimization process.

UD layers, each with a thickness of 3.6 mm and 2.5 mm biax layers constitute the flanges and corners. In the webs 2.5 mm biax layers embeds three layers of core, each 5.0 mm in thickness. In Figure 4 the design layouts for the flanges and webs are depicted, each layer being a package of material.

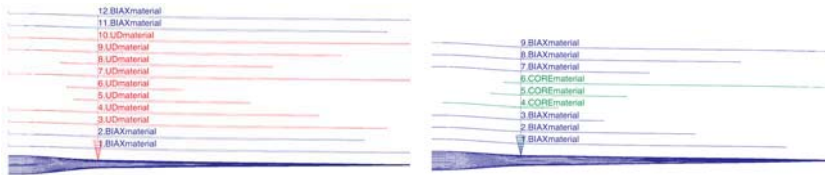


Figure 4. a) Side view of layup for flanges. b) Top view of layup for webs.

**Sandwich design.** A design consisting of sandwich flanges and unchanged webs is established, initially optimizing the extend and thickness of the flange core, followed by reductions in face material thickness. First, an analysis is performed using an approach where core layers are added to the existing single skin design, without reducing face thickness. With this approach the total mass of the spar is only slightly increased. Secondly, face thickness is reduced until

a design criterion is violated. A thorough description of the designs can be found in [2].

### 3. DESIGN CRITERIONS

The single skin and sandwich designs are analyzed by linear calculations, ensuring that no design criterion is violated. A non-linear comparative study of critical criterions is performed to investigate post buckling behavior. This study includes sensitivity analysis to imperfections. The spars are designed with respect to the criterions listed below.

- The buckling load factor,  $\lambda_{cr} = \frac{p_{cr}}{p}$ , must be larger than 1.
- The deflection of the blade tip is restricted by tower clearance to 15.5 m.
- The desired operational tip speed of large wind turbines is about 78 m/s corresponding to 8.2 rpm for a 180 m rotor. The blade eigenfrequencies should not collide with the tower passing frequencies 1P and 3P. 4P can be critical as well but is neglected in this study. Thus, the first flapwise eigenfrequency should be above 0.41 Hz with some margin. As the aerodynamic shell is neglected, only the first flapwise eigenfrequency can be calculated accurately by the spar alone, as the aerodynamic shell offers little flapwise stiffness.
- The Tsai-Wu and Maximum Stress criterions from Reddy [3] are applied. These criterions are violated if the failure index  $\mathcal{F} > 1$ .
- The critical face wrinkling stress is calculated according to the Hoff formula,  $\sigma_{cr} = 0.5\sqrt[3]{E_f E_c G_c}$ . Interaction in two directions is applied as  $\mathcal{W} \equiv (\sigma_1/\sigma_{1cr}) + (\sigma_2/\sigma_{2cr})^3$ , with  $\sigma_1 > \sigma_2$ , see [4]. Face wrinkling occurs when  $\mathcal{W} > 1$ .

### 4. FINITE ELEMENT MODEL OF SPAR

The spar model is created using MSC.Patran as pre- and post processor. The solver MSC.Marc is used for both linear and non-linear analysis.

In Figures 5a–b parts of the mesh at the root and a mid section is shown. Meshing is done with MSC.Marc element type 22, an 8-node quadratic thick shell element including transverse shear effects. The number of elements is approx. 20.000 amounting to about 360.000 degrees of freedom.

**Loading and boundary conditions.** The loading is based on the simple load paradigm, giving the total load on a turbine, taken as 100 N/m<sup>2</sup> times the area swept by the blades. The load distribution corresponds to the typical loading in a 50-year extreme gust wind during stand still. The corresponding shear

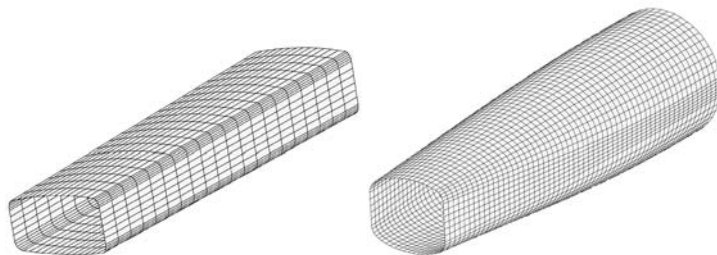


Figure 5. a) Mesh at a mid section. b) Mesh at the root.

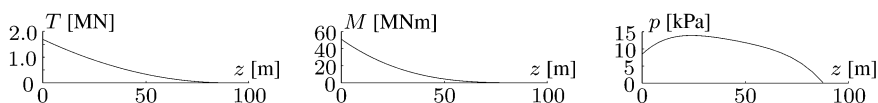


Figure 6. Shear force, moment and pressure distribution.

force, moment and pressure distributions are shown in Figure 6. A flapwise root moment of approximately 51 MNm is obtained. The boundary conditions are simplified to restraining all translational and rotational degrees of freedom at the root edges at  $z = 2.2$  m.

## 5. RESULTS

### 5.1 Single skin design

**Linear calculations.** Comparison of results from Table 1 with the design criterions shows that buckling is critical and that the design is heavily over dimensioned with regards to the other criterions.

Table 1. Results for single skin design.

$w_{tip}$ [m]	$\lambda_{cr} = \frac{p_{cr}}{p}$	$f_1$ [Hz]	$\mathcal{F}$	Mass $10^3$ [kg]
11.0	1.04	0.537	0.44	27.82

**Non-linear analysis.** The tip deflection calculated by transient dynamic analysis is 11.9 m, which is 8 % more than the linear deflection, indicating some importance of including geometric non-linearities, as bending stiffness is reduced at the critical section. In Figure 7 the deformed shape of a part of the spar is shown, the scale being in meters. The figure reveals that buckling

has occurred when the total load,  $\lambda = 1$ , is applied, i.e. at a lower load than predicted by linear buckling analysis,  $\lambda_{cr} = 1.04$ .

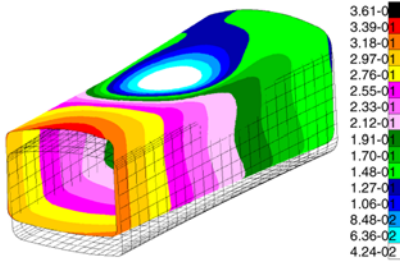


Figure 7. Deformation at  $\lambda = 1$ ,  $\frac{\epsilon}{t} = 0.0$ .

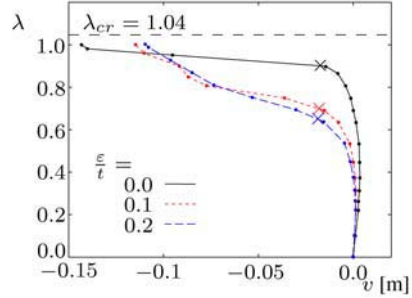


Figure 8. Load-displacement relations.

In Figure 8 load displacement curves for a node in the center of the buckle is shown.  $v$  denotes the magnitude of the snap relative to the displacement of a corner node. The induced imperfections,  $\frac{\epsilon}{t}$ , is a scaling of the linear buckling mode shape, corresponding to a maximum amplitude of 0%, 10% and 20% of the flange thickness  $t$ . For the perfect spar 91% of the load,  $p$ , is applied prior to bifurcation. The imperfections bring down the bifurcation point to 70% and 65% respectively.

Independent of imperfection, the Tsai-Wu failure index is well below 1 in the pre-buckling phase. At bifurcation, stresses are redistributed and in-plane transverse tension in the corner UD brings the failure index above 1, marked by crosses in Figure 8. The outcome is a progressive failure scenario, leading to gross failure, collapsing the spar immediately after bifurcation. This agrees with experience from full scale testing of blades to failure, showing that no post-buckling capacity is present in the tested wind turbine blades, see [5]. The global deflections are not influenced by any of the imperfections, as the tip deflection in all cases was found to 11.9 m, making buckling the most critical criteria.

## 5.2 Sandwich design

**Equal mass approach.** In Table 2 the effect of modifying the single skin design by adding core can be seen.  $t_c$  is the core thickness in the critical section,  $\mathcal{W}$  is the wrinkling index and  $\Delta\text{Mass}$  is the increase in total mass compared to the single skin design.

Separating the flange by a core increases the local stiffness and the study showed that the stiffness of the core plays a minor role for the buckling strength. It appears that  $\lambda_{cr}$  is governed mainly by the thickness of the added core. The

Table 2. Results from sandwich design based on equal masses.

Core	$t_c$ [mm]	$w_{tip}$ [m]	$\lambda_{cr} = \frac{\rho_{cr}}{p}$	$f_1$ [Hz]	$\mathcal{F}$	$\mathcal{W}$	Mass $10^3$ [kg]	$\Delta$ Mass [%]
H 45	20	11.2	1.71	0.522	0.19	1.07	27.88	0.2
H 45	30	11.5	2.10	0.514	0.18	1.08	27.92	0.4
H 45	40	12.0	2.26	0.505	0.18	1.10	27.95	0.5
H 100	20	11.2	1.72	0.521	0.24	0.56	27.97	0.5
H 100	30	11.4	2.10	0.512	0.18	0.57	28.05	0.8
H 100	40	11.9	2.27	0.503	0.17	0.58	28.12	1.1
H 200	20	11.1	1.72	0.518	0.24	0.27	28.12	1.1
H 200	30	11.4	2.10	0.509	0.20	0.31	28.27	1.6
H 200	40	11.9	2.27	0.499	0.17	0.32	28.42	2.1

values for  $\lambda_{cr}$  correspond to increases in buckling strength by 64%, 102% and 117% for core thicknesses of 20 mm, 30 mm and 40 mm respectively.

When sandwich construction is applied, half the fibres are moved towards the neutral axis resulting in decreased global bending stiffness. This effect can be seen clearly on the global deflection of the tip. However, the stiffness of core material is not important, whereas the thickness is governing. The deflections are still well below the allowed 15.5 m, but the table reveals a tendency that the increase in deflections grow almost quadratically with the thickness of the core. This indicates that the maximum deflection criterion will be dimensioning for large core thicknesses.

Introduction of sandwich flanges has resulted in a general decrease of stress level in the spar of about 30%, due to the increased flexibility. As a result of lower stresses the failure indices,  $\mathcal{F}$ , are only half of that from the single skin design. The wrinkling criterion is violated for the H 45 core, where the maximum value of  $\mathcal{W}$  is located in the upper flange at the maximum lengthwise stress component  $\sigma_x$ . A large margin of safety is present for the H 200 core, indicating the importance of the core properties. Finally it is noticed that only moderate increases in mass, of 0.2–2.1%, is introduced by the core.

**Mass optimized design.** The optimized design is based on the design using the H 200 core with a thickness of 30 mm: This design is chosen for two reasons. First, because designs with H 45 and H 100 are likely to wrinkle, especially as face thickness is reduced. Also, for a core thickness of 40 mm or more the tip deflection will reach the design limit before a noticeable reduction of mass can be achieved.

The thickness of biax and UD in the flanges is modified. A certain biax to UD thickness ratio that accommodates especially the buckling and deflection criteria is needed, as these are most critical. Removing too much UD would

Table 3. Results from optimized sandwich design using a 30 mm H 200 core.

$w_{tip}$ [m]	$\lambda_{cr} = \frac{p_{cr}}{p}$	$f_1$ [Hz]	$\mathcal{F}$	$\mathcal{W}$	Mass $10^3$ [kg]	$\Delta$ Mass [%]
15.5	1.36	0.532	0.65	0.41	21.63	-22.3

cause large deflections, whereas the buckling strength is governed mostly by the amount of biax. Thus, an optimal design is achieved when no single criterion dominates, but when more criteria are brought close to their respective limits.

In Table 3 the performance of the mass optimized design is listed. The tip deflection is brought to the design limit of 15.5 m and a buckling reserve of 0.36 is present for this design. The failure index is increased considerably compared to the single skin design and a minor increase in wrinkling index, compared to the equal mass design, is present. The mass has been reduced by 22.3% explaining the increase in  $f_1$ .

It appears, compared to the single skin design, that all design criteria are brought more to the limit, with tip deflection being most critical. Several optimization steps, replacing biax by UD, has been performed. It showed that some reduction in deflection can be achieved at the expense of decreased in-plane transverse stiffness in upper corners, resulting in a failure index larger than 1. The buckling factor is relatively constant, whereas the failure index is very sensitive to the ratio of biax and UD. Also, as will be shown subsequently, the failure index is more sensitive to imperfections than buckling, explaining why  $\lambda_{cr}$  and  $\mathcal{F}$  are not brought more to the limits in the linear design.

**Non-linear analysis.** The objective of the non-linear study is to investigate buckling and stress sensitivity to imperfections, knowing that the tip deflection is not sensitive to these imperfections.

In Figure 9 the linear buckling mode shape corresponding to  $\lambda_{cr} = 1.36$  is shown. This mode shape is applied as imperfection, with maximum amplitudes of 10% and 20% of the flange thickness respectively. In Figure 10 load-displacement relations for the perfect and two imperfect spars are given.

As for the single skin design, deflections for the sandwich design are not influenced by imperfections as the maximum tip deflection, for all imperfections are 7% higher than the corresponding linear, amounting to 16.6 m. In Figure 10 load-displacement relations for the perfect and two imperfect spars are given. Again the load-displacement relations describes the difference in displacement of a mid flange node and a corner node in the most critical section. The  $\frac{\varepsilon}{l} = 0.0$  relation reveals that the perfect spar does not bifurcate as the mid node is displaced more in the positive  $v$ -direction than the corner node at  $\lambda = 1$ . The load-displacement relations for the imperfect spars indicate

that bifurcation does not occur. This is due to the imperfections, leading the flange into the eigen mode shape, taking away the sudden change in geometry that characterizes bifurcation. Still, both imperfect spars exceed  $\mathcal{F} = 1$ , at  $\lambda = 0.96$  and  $\lambda = 0.88$ , as indicated by crosses. The perfect spar does not violate the Tsai-Wu criterion explaining the absence of a cross.

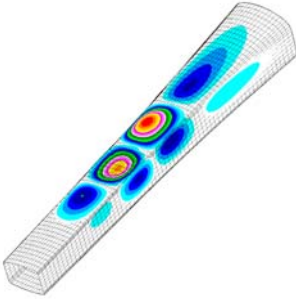


Figure 9. Linear buckling mode induced as imperfection in non-linear analysis.

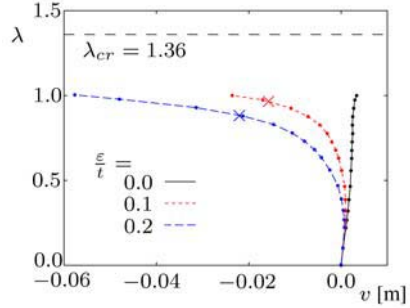


Figure 10. Load-displacement relations for mass optimized spars.

In Figure 11 the failure indices at  $\lambda = 1$  are shown in the most critical sections on deformed plotS. Independent of the imperfections only the corners are critical. Moreover, the Figure shows that core failure at no time becomes critical. The failure indices are all lower than for the perfect single skin spar at  $\lambda = 1$ , indicating that the increase in stresses for the sandwich design is less sensitive to imperfections.

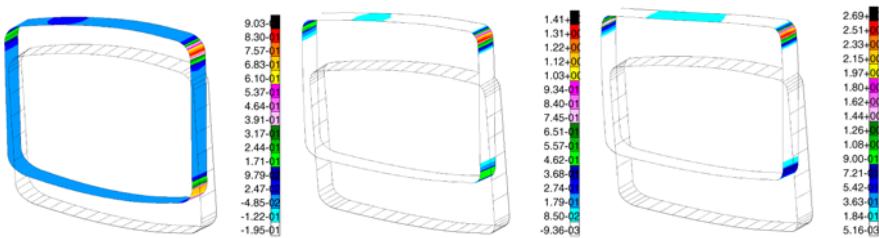


Figure 11. Failure indices  $\mathcal{F}$  at  $\lambda = 1$  for  $\frac{\epsilon}{t} = 0.0$ ,  $\frac{\epsilon}{t} = 0.1$  and  $\frac{\epsilon}{t} = 0.2$ .

The lengthwise compressive stress,  $\sigma_x$ , in the upper flange is higher than by linear analysis, bringing the wrinkling index up to  $\mathcal{W} = 0.45$  for the perfect spar. The imperfections cause redistribution of  $\sigma_x$  across the flanges towards the corners. Hereby, the wrinkling index for the imperfect spars are  $\mathcal{W} = 0.55$  and  $\mathcal{W} = 0.67$ , situated in the flanges near the upper right corner.

Table 4. Main linear results: single skin(ss), equal mass(em) and mass optimized(mo) designs.

Design	Core, $t_c$ [cm]	$w_{tip}$ [m]	$\lambda_{cr} = \frac{P_{cr}}{P}$	$f_1$ [Hz]	$\mathcal{F}$	$\mathcal{W}$	Mass $10^3$ [kg]	$\Delta$ Mass [%]
ss	–	11.0	1.04	0.537	0.44	–	27.82	–
em	H200, 3	11.4	2.10	0.509	0.20	0.31	28.27	+1.6
mo	H200, 3	15.5	1.36	0.532	0.65	0.41	21.63	–22.3

## 6. CONCLUSIONS

The present paper has outlined some important structural differences between essentially different designs. The main results, comparing three designs, are summarized in Table 4. It is clearly shown that by introducing sandwich in the load carrying flange, a significant weight reduction and increased buckling capacity is obtained. Tower clearance now becomes critical, which is also the case for most present wind turbine blades.

The single skin can probably be further optimized by increasing the buckling capacity. For the sandwich design, further weight reductions can most likely be obtained by bringing  $\lambda_{cr}$  more to its limit, while maintaining the present tower clearance. This would require replacement of biax with UD, which increases  $\mathcal{F}$ , especially in the corners. In practice a design applying more biax in the corners would remedy this tendency. However, regardless of corner detail, buckling induces stress redistributions that will ultimately lead to stress failure. Since buckling is sensitive to imperfections, and deflections are not, the most feasible design would include extra buckling capacity, rather than safety on deflections. In particular, due to larger buckling capacity, the sandwich design accommodates these demands better than the single skin design.

## REFERENCES

- [1] Sørensen, B.F., Jørgensen, E., Debel, C.P., Jensen, F.M., Jensen, H.M., Jacobsen, T.K. and Halling, K.M., Improved design of large wind turbine blade of fibre composites based on studies of scale effects (phase 1) – Summary report, *Risø-R-1390(EN)*, Risø National Laboratory, Roskilde, Denmark 2004.
- [2] Jensen, J.F. and Schultz, J.P., Application of load carrying sandwich elements in wind turbine blades, Master's Thesis, Technical University of Denmark, Department of Mechanical Engineering, April 2005.
- [3] Reddy, J.N., *Mechanics of Laminated Composite Plates and Shells*, CRC Press, USA, 2nd edition, 2004.
- [4] Plantema, F.J., *Sandwich Construction*, John Wiley & Sons, New York, 1st edition, 1966.
- [5] Jørgensen, E.R., Borum, K.K., McGugan, M., Thomsen, C.L., Jensen, F.M., Debel, C.P. and Sørensen, B.F., Full scale testing of wind turbine blade to failure - flapwise loading, *Risø-R-1392(EN)*, Risø National Laboratory, Roskilde, Denmark 2004.

# THERMOPLASTIC COMPOSITE SANDWICH STRUCTURE FOR SPORTIVE APPLICATIONS

M.M. Sommer<sup>1</sup>, M. Päßler<sup>1</sup>, R. Schledjewski<sup>1</sup> and M. Stack<sup>2</sup>

<sup>1</sup>*Institut für Verbundwerkstoffe GmbH, 67663 Kaiserslautern, Germany*

<sup>2</sup>*Killarney Plastics Ltd., Killarney, Co. Kerry, Ireland*

**Abstract** Hurling is one of the fastest team games and related to a long term tradition in rules and practice. Former attempts to manufacture composite hurleys by the process of liquid composite molding (RTM) or injection molding failed. With the compression molding process the mechanical properties required, the traditional game performance, and target costs were matched.

**Keywords:** composite, LFRT, GMT, EPP-foam.

## 1. INTRODUCTION

Mainly in Ireland, hurling is a very traditional kind of sports, which is played by nearly the whole population regardless of age. This game is comparable to European field hockey, played on a field of the size for a soccer game.

The main load and stress on the stick (hurley) is a result of hitting the leather ball or the contact with another hurley during the game. The load is comparable to a baseball bat. One main reason for producing a sandwich composite hurley is the limited availability of the traditional material ash, because only the bottom of the tree trunk is suitable for manufacturing the traditional version. The wood grain mirrors the fiber orientation, which is necessary to stand the stress. Many hurleys crack due to the inhomogeneity and durability of the natural product ash wood. Therefore, a steel band is often applied at the bottom of the hurley (boss segment) to avoid the splicing of the wood, which may, however, cause injuries to other players (Figure 1).

In the past, attempts to manufacture composite hurleys by liquid composite molding (RTM) or injection molding processes failed. These technologies could not provide the properties required regarding weight, flexibility, maximum impact load, the traditional game handling and performance, surface appearance, and market price. None of these techniques was able to copy the nature of ash wood in this application.



Figure 1. Traditional ash hurley with steel band.

The solution to this problem is the use of a special sandwich lay-up to reach comparable weight and density. Many different material combinations were investigated and tested.

## 2. MATERIAL SELECTION

The selection of material has an impact on the process parameter adjustment. The project's initial point started with a pre-selection of polyurethane foam core and GMT. This combination has shown an insufficient cavity filling, a very pure surface quality and finally an insufficient mechanical characteristic. The compression molding process allows a very high volume output per cavity, if the component preparation (GMT blank temperature, polyurethanes degree of cross-linking) was appropriate to avoid e.g., buckling of the foam caused by post curing. The interdependence of thermal expansion or additional curing caused by the GMT the process temperature of 230°C is to be considered.

The pre-trials at project beginning and the specimen showed the following defects:

- insufficient mold filling,
- delamination of the composite,
- trapped air inside between the different layers,
- indifferent surface quality,
- difficult handling of the blanks and cores,
- insufficient physical (impact) properties and
- varying press molding and peripheral equipment parameters.

Therefore, material selection represents the most important step to match the development goals:

- acceptable mold filling,
- specific surface structure,
- dimensional stability,
- (long-term) durability according to the purposes,
- meet target weight of 450 g–480 g.

## **2.1 Reinforced polymer materials**

Several reinforcing polymer matrices were used for tryouts even with SMC. Due to the inappropriate properties of thermoset material Killarney Plastics Ltd. selected GMT. Within the project the aim was to investigate a variety of different reinforcing polymer matrices like glass mat reinforced thermoplastic sheets, paper made GMT, natural fiber reinforced thermoplastic sheets, and thermo-formable sheets.

The market for fiber reinforced sheets is decreasing since the introduction long fiber reinforced thermoplastic granules and its version of the direct processing of rovings plus PP-compounds, in short LFT-D, which was introduced by Diefferbacher GmbH in 1997. LFT-D offers nearly the same physical properties as GMT, but it is difficult with this process to produce a comparable sheet out of a flat film extrusion die. This technology of direct compounding bypasses the additional semi-finished product step by direct mixing of the thermoplastics and the glass fiber rovings. A glass fiber content of normally 20% to 40% by weight is feasible and directly fed into the forming press where it is pressed to the final part [1].

Throughout Europe there are only three remaining suppliers of GMT or NMT (glass fiber mat reinforced thermoplastic or natural fiber mat reinforced thermoplastic), in the Netherlands, in Austria, and in Switzerland. In accordance with Killarney Plastics Ltd. the following types of GMT have been selected for the tests (Table 1). The total product range of each supplier is much larger and one has to keep in mind that the whole testing procedure has to be carried out to test the applicability.

Some results of these material trials are that the thermo formable material is difficult to handle in the warm-up condition. The surface is very sticky, which made this product unsuitable for the composite hurley. The 2-mm-thick GMT manufactured similar to paper fabrication extends during the heating process step. This extension during the heating needs to be taken in consideration, while preparing the pre-cuts to match surface, cavity filling, and weight demands. Essentially, there is no processing difference between thermo formable and glass mat (needled) or glass fiber (paper made) semi finished sheets. The GMT (paper made) blanks provide the best surface quality after compression molding and they have the best melt flow. All materials have in common, that they have a fiber content of 20% or 30% by weight.

Natural fiber mat reinforced thermoplastics (flax mat reinforced thermoplastic sheets, content of flax-fiber 40% by weight, thermo formable material) was not able to copy ash wood surface appearance, products of supplier Q with black and natural colored PP-matrix were tested. The black natural fiber version offered the best melt flow to fill the cavity. Generally all test result showed, that the lower the viscosity of GMT the better the surface quality and

Table 1. Reinforced thermoplastic sheets tested.

Supplier	Kind of Material
A	a) GMT, paper made, 30% glass by weight b) Thermo formable, 30% glass by weight
I	a) GMT, paper made, 30% glass by weight; 1.8 mm b) GMT, paper made, 20% glass by weight; 1.8 mm c) GMT, needled mat, 30% glass by weight; 3.7 mm d) GMT, needled mat, 20% glass by weight; 3.7 mm
Q	a) NMT black, 3.0 mm flax, sisal fibers b) NMT natural color, 3.0 mm (flax, sisal fibers) c) GMT, needled mat, 30% glass by weight; 2 mm

cavity filling, but concerning stiffness and durability glass fiber mat reinforced material has to be processed.

## 2.2 Core materials

Ash wood has a density varying around 0.51–0.83 kg/dm<sup>3</sup>. To copy the natural product ash for this application, it was necessary to build up a sandwich structure with a suitable foam material. The requirements on the foam core are:

- good adhesion between the polymer (PP) and the core material,
- high compressive strength to achieve a sufficient internal mold pressure during the press molding process,
- the foam must be suitable for thermoforming,
- ageing or embrittlement must be regarded,
- recyclability (most significant for automotive applications).

In addition to these requirements, furthermore, the process temperatures (mold 25°C–110°C, polymer up to 220°C) should not fatigue the foam core. For the serial production, there is a cost target, which is not to be exceeded and which has an impact on the selection of the foam core, too. The core material should give the possibility to be produced in-house or to be available widely spread on the market. Possible solutions derived out of the requirements may be the utilization of polyurethane (PUR), polymethacrylimide (PMI), or expanding polypropylene (EPP).

Due to the rules of a competitive market the costs have to be regarded for each component, especially the foam core. According to Figure 2 different core materials were investigated.

To fill the cavity completely and to build the lower hurley segment (boss) perfectly (Figure 9), it is necessary to utilize a core with high compressive strength. The higher the compressive strength the better the in-mold pressure.



Figure 2. Cores for the composites hurleys (left: EPP cores, right: PUR, PMI, balsa).

Properties	Unit	PMI 51 WF	PMI RG 110	PUR RG 50	PUR RG 100	PUR (Killarney)	EPP
Density	kg/m <sup>3</sup>	52	110	47–52	95–103	95	60–110
Compressive strength	MPa	0.8	3.6	0.38–0.42	0.95–1.10	1 estimated	0.4–1.4

Figure 3. List of different core materials.



Figure 4. Typical failures (cracking at tools pinching edge, collapse of foam core, breakage of NMT).

### 3. PROCESS PARAMETERS OPTIMIZATION

Many tryouts have been proceeded to develop a technical and economical solution. Out of the range of materials presented in combination with the processing equipment at IVW GmbH more than 130 hurley prototypes have been produced to investigate multiple tasks. The main subject of interest was the handling and feeling during the game. The process parameters optimization was as important as the material selection.

A major problem, that occurred, was the durability of the first sandwich structures (Figure 4).

The very stiff PMI-foam had a bad adhesion to the outer PP-GMT-shell with extremely brittle behavior. The shell material with natural fiber reinforcement, did not provide the strength needed. Blanks with glass fiber reinforcement were selected for the shell material. The special handling was tested by experienced players and their results have been related to the flexural test results. These tests showed, that with an additional unidirectional reinforce-

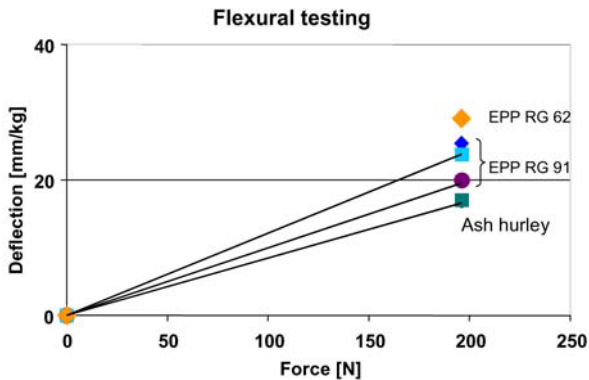


Figure 5. Comparison of traditional hurley with EPP-hurley in flexural testing.

ment a comparable deflection can be achieved like with the traditional hurley. Furthermore, these results showed, that the utilization of expandable polypropylene foam is most recommendable (Figure 5), especially having one matrix, which supports the bonding of the outer shell to the foam core.

To reach the target weight, the EPP's density was compared to the hurley's weight. This sandwich stays at the same level of  $\sim 480$  g and is independent of the foam's density.

Especially using PMI and EPP, the foam squeezes out the GMT by its own surplus weight, due to the different density. This behavior can be explained with the buoyancy law and the property, that the compressive strength is linear to its density. This linearity can only be broken with a special GMT, which has a lower melt viscosity, or with a new mold design, that avoids a squeeze out of material so that the final material weight is loaded in the cavity right from the beginning (Figure 6).

A parallel controlled servo-hydraulic press with additional four hydraulic cylinders ensures a continuous increase towards the maximum force selected and more important a parallelism of both mold halves, that avoids canting in case of utilization a positive mold.

For these reasons the IVW GmbH uses a parallel controlled servo-hydraulic press (manufacturer: Maschinenfabrik J. Dieffenbach GmbH & Co., Figure 7).

The GMT blanks were heated in a hot air oven (manufacturer: Reinhardt, type DT/V). Compared to a convection oven, the hot air is circulated by a powerful fan and transports the heat into the swelling glass mat of the GMT. The swelling occurs only for the special type of GMT, which consists of needed glass mat reinforcements. The paper made GMT keeps nearly its thickness during the heating process.

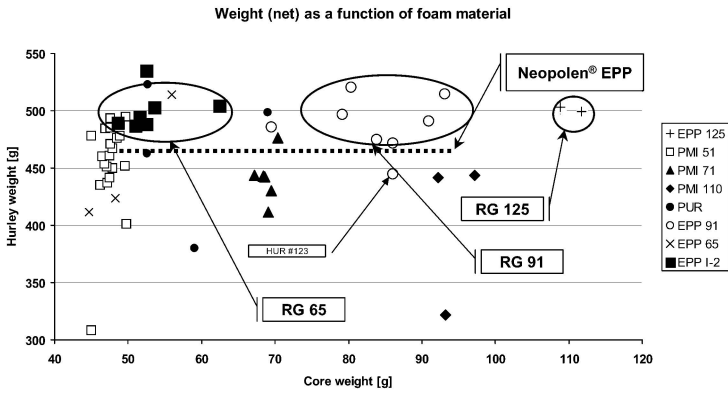


Figure 6. Comparison of traditional hurley with EPP-hurley in flexural testing.



Figure 7. Dieffenbacher press (type PHP/GMT 800/650) parallel controlled at IVW GmbH with maximum force of 8,000 kN.



Figure 8. Hot air oven (type DT/V, manufacturer: E. Reinhardt GmbH).



Figure 9. Typical cavity filling defects and solutions.

Usual heating conditions of the GMT are at 220°C for 7 minutes to assure that the heat reaches the center of the GMT.

To shorten the time, it is possible, to go up to 240°C with the risk to overheat the surface. It is more efficient to stay at the lower temperature of 220°C and to load the oven according to the cycle time to avoid polymers degradation.

#### 4. ECONOMICAL EVALUATION

The most important point apart from the technical realization was the matching of the cost target with a potential of further decrease. The potential can be realized according to tryout under serial conditions. These samples are in field approval by the G.A.A.

#### 5. SUMMARY

For the first time it is now possible to have a full composite hurley at same dimensions, weight, and mechanical or handling properties as the traditional hurley. One sandwich assembly out of multiple combinations was researched to be competitive and comparable to the traditional hurley handling performance. A sandwich structure made of expanded PP-foam (E-PP) at a certain volumetric weight, unidirectional reinforcement, and glass mat reinforced thermoplastics, is an adequate substitute of the wooden hurley with the same performance but a better durability and recyclability. Furthermore, design ele-

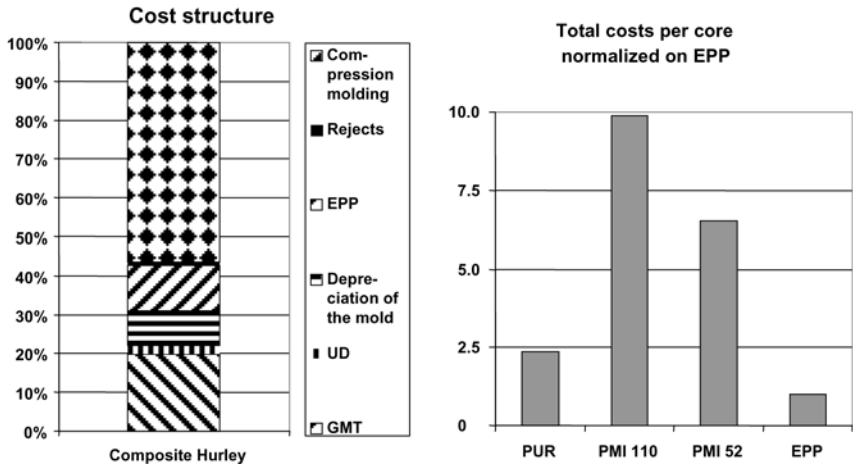


Figure 10. Total cost composition and costs per core in comparison to EPP.



Figure 11. Composites hurleys with different surface appearances.

ments, like a fleece for a wooden appearance, a grained surface, or painting can now be included more easily (Figure 11).

The annual demand of more than 100,000 hurleys and the short supply of ash, therefore, makes this composite application highly advantageous. The composite hurley manufactured by compression molding provides a competitive market price at a constant quality. Finally, utilizing the combination of E-PP and PP-GMT, recycling of this product with only one resin component is easy at the end of life. Also, due to the shortage of ash wood, the composite solution is a contribution to environmental protection. This combination is resulting from development stages of selecting the appropriate materials, process parameters, and testing. It achieved the requirements in mechanical properties, handling, and costs.

For these reasons this development was decorated with the AvK-TV-Innovation Award for environmental protection [2].

## ACKNOWLEDGEMENT

The project partners like to thank the companies Azdel Inc., BASF AG, Isosport Ges. m. b. H., Röhm GmbH & Co. KG, and Quadrant Composites AG for supplying gratuitous material.

## REFERENCES

- [1] Brüssel, R. and Kühfűsz, R., Ein Jahr Serienproduktion von Menzolit-Fibron Lang-Faserverstärktem-Thermoplast mit dem Direktverfahren. "1. Intern. AVK-TV Tagung", AVK-TV, Frankfurt (ed.), Baden-Baden, September 1998, A2-1-9.
- [2] Sommer, M.M., Paessler, M. and Schledjewski, R., The composite hurley – Copying nature. *JEC Composites*, Vol. 10, June–July (2004), p. 19.

# STUDY OF SNOWBOARD SANDWICH STRUCTURES

C. Borsellino<sup>1</sup>, L. Calabrese<sup>1</sup>, R. Passari<sup>1</sup> and A. Valenza<sup>2</sup>

<sup>1</sup>*Department of Industrial Chemistry and Material Engineering, University of Messina, Italy*

<sup>2</sup>*Department of Chemical Engineering, Process and Materials, University of Palermo, Italy*

**Abstract** The aim of the present research is to extend the knowledge of mechanical properties both on single components and on complete structure employed for snowboard. Flexural and torsion tests are performed to acquire important comparison parameters between snowboard sandwich structures that differ for the core material employed (wood, PVC foam core). A simplified FEM model is proposed to simulate the flexural tests of the sandwich structure showing good predictive capability.

**Keywords:** snowboard, sandwich structure, mechanical properties.

## 1. INTRODUCTION

The increasing efforts aimed to find out structures characterised by reduced weight and better mechanical performances, in this last years, have led to the development and the employment of sandwich structures in recreation field or land and sea transportation [1].

The main problem in designing and verifying such structures is their intrinsic anisotropy and non-homogeneity that does not allow their correct modelling. Nowadays the available data on mechanical properties of complex structures, necessary to allow a correct and reliable design, are not sufficient [2].

In the snow sports, the number of snowboarders is increasing rapidly, various industries are developing in the snowboards' manufacturing field. It is important to improve the quality of the composite snowboards to increase the performance of the rider or to reduce the accidents risks. In this field few works are reported in the literature.

Usually the attention is focused to study the vibration properties of the sandwich structure exploring the factors that quiet and damp the snowboard on the snow [3] or to estimate the natural frequency of the snowboard by using a numerical approach proposed for a free vibration [4].

But the manufacturers have introduced a variety of different snowboard designs characterised by different materials and different shapes. The selection and combination of materials and shape in the snowboard design and building, at this moment, relies on a trial and error procedure.

To design a snowboard or to improve its quality, the mechanical properties of the sandwich and its constituents are some of the most important properties to be discussed [5]. In particular properties, such as the bending and torsional stiffness, flex, twist, natural frequencies and damping must be measured by laboratory tests [6].

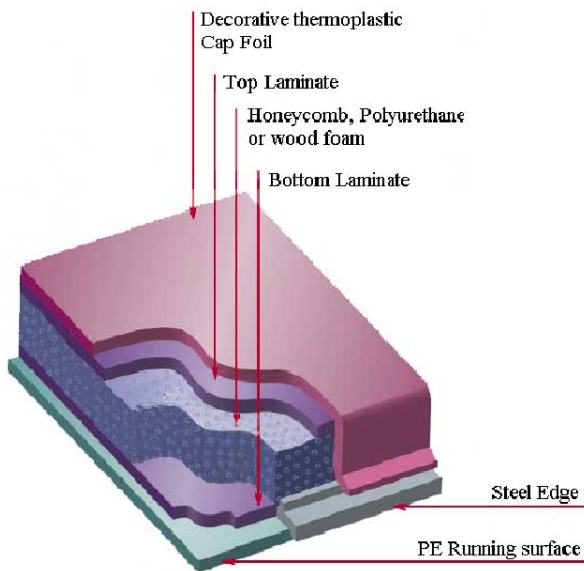


Figure 1. Example of a snowboard sandwich structure.

The purpose of the present work is to extend the knowledge of mechanical properties both on single components and on complete structure employed for snowboard, focusing on the effects induced by different kind of polymeric running surfaces and cores in the sandwich structure performances. At first, wear, wettability and adhesion test are performed on different polyethylene running surfaces. Then three point flexural test are performed to acquire important comparison parameters between snowboard sandwich structures that differs for the core material employed (wood, PVC foam core).

The mechanical properties of each component are used as input data in order to implement the FEM analysis by the commercial ANSYS code [7]. A simplified model is proposed to simulate the flexural tests of the sandwich structure. In addition numerical results obtained for the above mentioned tests on complex sandwich structures are compared with experimental ones showing good predictive capability of the model.

## **2. EXPERIMENTAL PART**

### **2.1 Materials**

In this work three different running surface are studied, an LDPE films manufactured in our laboratory by a hot press, a traditional un-treated HDPE film and a mechanical treated one supplied by Hidro®.

At the same time three different cores for snowboard sandwich are tested:

- silver fir (thickness 9 mm) with a mean density of 343.9 Kg/m<sup>3</sup>
- ash-tree (thickness 9 mm) with a mean density of 703.24 Kg/m<sup>3</sup>
- a PVC foam panel (thickness 8 mm) with a mean density of 61,4 kg/m<sup>3</sup>

The top and the bottom laminate are realised using a triaxial 0°/+45°/-45° glass fabric, by Resintex® (density 740 g/m<sup>2</sup> and thickness 0,67 mm), with a commercial low viscosity epoxy resin, SR 8100 with a the SD 8822 catalyst, by Sicomin®. As decorative thermoplastic cap topsheet with a thickness of 0.3 mm ABS is used.

### **2.2 Mechanical testing**

The samples, used to investigate the mechanical properties of the snowboard sandwich structure, are manufactured by vacuum bagging technique.

#### **2.2.1 Running surface**

To characterise the running surface two specific tests are performed:

- Wear tests are performed on a ‘pin on disc’ test machine. A polymeric sample was placed on the rotating plate with a stationary stainless-steel pin placed in contact on its surface. The wear tests are performed moving cyclically the metallic pin, subject to a fixed load, on the polymeric disc. The metallic probe point has a diameter of about 200 mm. The rotating-plate speed was 0.074 m/s and the maximum contact pin pressure of

about 25.5 MPa. The pin-on-disk test is used as wear machine in order to evaluate the weight loss of the worn material.

- **Wetting test:** Contact angle measurements were carried out according to the sessile drop technique and performed by the contact angle micrometer. In order to measure the wetting angles, pure distilled water at 20°C temperature is employed to deposit a 1 µl drop on the polymer surface. The water drop is deposited accurately with a micro-syringe on the sample surfaces. The contact angle is measured by a CCD camera through the optical image (×10 magnification) captured by suitable PC images software. For each sample, the average value is calculated for 10 drops measurements. A surface profiler Tencor-P10 determined the roughness values of the foil polymer surface, before and after the mechanical/manual abrasion treatment.
- **Adhesion test:** The adhesion properties of the running surface are evaluated by single lap shear test according to ASTM D 5860 standard. The two parts of the joint are UHMWPE foil and a triaxial glass fibres composite laminate. The shear stress was calculated by:  $\tau = T/A$ , where T is the maximum applied load and A is the joint adhesive surface.

### 2.2.2 Core

Two different mechanical tests are conducted to characterise three type of materials used as core in the snowboard sandwich-structure:

- **Flexural test:** The three point bending test is realized to determine the properties of flat sandwich panel subjected to flatwise flexure. In this case the sample dimensions are 9x40x220 mm, with span length of 160 mm. Since the wood core is orthotropic, the specimen is tested in longitudinal and transversal direction. Mechanical testing is realised by employing a Universal Testing Machine model LR 10K by Lloyd Instruments. The crosshead speed is of 2.25 mm/min. Eight tests are made for each sample condition.
- **Torsion test:** The specimen dimension of the sample for torsion test is, according to ASTM D194 Standard, 9x40x400 mm. The samples are twisted by a manual torsion-test device, and the relationships between the torsion moment and the shear strain are obtained.

### 2.2.3 Sandwich

- **Flexural test:** As for the core testing, three bending test are performed for the sandwich samples, with dimension about 12x30x200 mm with a span length of 160 mm. The crosshead speed is of 1.5 mm/min. The tests are

performed in longitudinal and transversal directions of the fibres with respect to the load application point.

- Torsion test: The procedure used to characterise the sandwich samples under torsion load, is the same of the one used for the core. Particularly the dimensions of the samples are 9x40x400 mm.

### 3. RESULTS AND DISCUSSION

#### 3.1 Running surface

Figure 2 shows that the UHMWPE samples have a similar wear behaviour.

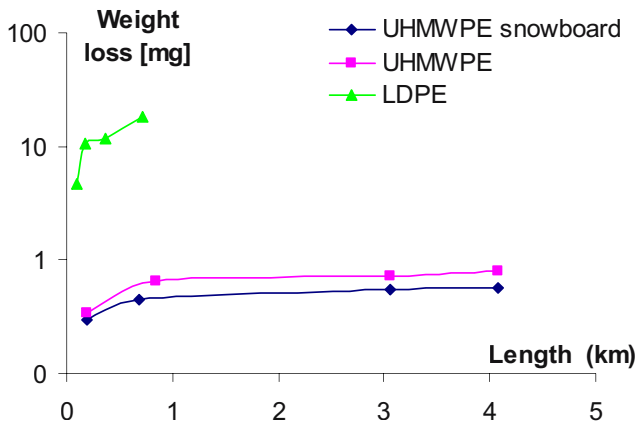


Figure 2. Weight loss vs length in the wear tests.

Initially both samples evidence a gradual increase of the weight loss, then a stabilization region is reached, where the weight loss is less evident. This region takes place at a length of about 0.7 Km. Very poor wear properties are shown from the LDPE sample. The next table summarises the result about wettability and adhesion test.

Table 1. Adhesion and wetting properties at varying superficial roughness of the running surface.

Roughness ( $\mu\text{m}$ )	Shear stress	Wetting angle ( $\theta$ )
1,27	0,184	86,4
2,28	0,217	80,5
4,03	0,589	65,9
7,42	0,676	62,8
25,75	0,826	54,8

The wettability and the adhesion increase with increasing the superficial roughness of the sample. The UHMWPE mechanically pre-treated have the roughness of 4.58  $\mu\text{m}$ .

### 3.2 Core

Table 2 summarises the mechanical properties of the three different cores. The values of G are obtained by three point flexural test at different span lengths while the t is determined by torsion tests.

Table 2. Mechanical properties of cores.

	E [MPa]	$\sigma_{\text{max}}$ [MPa]	G [MPa]	$\tau_{\text{max}}$ [MPa]
Ash-tree (longitudinal)	12142	122.8	879	31.6
Silver fir (longitudinal)	8535	45.49	431	9.8
Ash-tree (transversal)	1149	25.39	160	
Silver fir (transversal)	256	2.49	33.5	
PVC	55	1.39	11.8	

The Ash-tree shows the best performance, because it has a high stiffness combined with a relevant failure stress both under flexural and torsion loading conditions.

### 3.3 Sandwich

The mean values recorded during the mechanical tests are reported in Table 3.

Table 3. Three point flexural properties of sandwiches and cores

	Longitudinal flexural test		Transversal flexural test	
	Pmax [N]	$\delta_{\text{max}}$ [mm]	Pmax [N]	$\delta_{\text{max}}$ [mm]
Sandwich Ash-tree	2342.5	9.2	1095.2	8.9
Ash-tree	1494.7	8.1	146.3	5.8
Sandwich Silver fir	1593	4.2	595.6	7.6
Silver fir	812.6	5.3	49.7	11.2
Sandwich PVC	319.3	4.4	297.2	4.8
PVC	26.5	24.3	26.5	24.3

The experimental results evidence the fundamental role of the sandwich core in the mechanical performance of the structural sandwich that will be produced and tested.

The experiments confirmed how the flexural resistance of the sandwich is strongly increased by the presence of the fabrics, but they also show that the fractures are influenced by the kind of core employed; usually fractures are concentrated at the interface fibre/wood, except for the PVC-core sandwich, where no fractures have been evidenced.

The mechanical tests have allowed the comprehension of the importance of a good adhesion at the sandwich interfaces (able to delay a possible delamination) because the most part of the fractures begin inside the core and propagate itself toward the interface.

The indentation is high for the Silver fir and PVC-core sandwiches and decreases at increasing the compressive yield stress of the core in the direction parallel to the load application. So the study of the compressive resistance should have an important role for the production of the wood-core for the snowboard manufacturers to avoid the problem of the indentation.

The flexural response of the sandwich with a wood-core is very different depending on the direction of the wood fibres with respect to the longitudinal axis of the snowboard or if the core is in lath-wood.

The orthotropic nature of the wood is determinant in such behaviour differences; the core in this case takes part directly to the mechanical characteristics of the whole structure.

In this kind of sandwiches, the presence of a small number of skins (in our case only one tri-axial fabric) emphasizes the mechanical characteristics of the wood employed as core. From this point of view the study of the mechanical characteristics of the core is fundamental in the design of a snowboard table while the choice of the fabrics can be based only on the necessity of increasing the mechanical performances (mainly flexural ones) of the wood core.

By analysing the experimental data of flexural tests of the PVC-core sandwiches we observe that the difference between the maximum loads recorded in longitudinal and tangential direction are negligible and anyway the maximum loads born by the whole structure are much lower than the wood-core sandwiches.

Such kind of structure is characterised by the presence of a core with very poor mechanical performances that is a mere support for the external skins employed to increase the stiffness of the structure by separating them from the neutral axis; in this way the structure will be very light and stiff.

For this type of sandwich the role of the core is almost negligible so the design is oriented to the choice of the fabrics able to supply to the sandwich structure the right stiffness and mechanical resistance able to provide the adequate safety during the use of the snowboard table.

In Figure 3 the torsion behaviour of the tested sandwich structures is shown.

By comparing the three curves we can observe that the resistance of the ash tree-core sandwich is much higher than the others. Even if the slopes of the Silver fir and the ash tree-core are similar (the shear modules for the two sandwiches are respectively 1743 MPa and 1196 Mpa) the shear modulus of the Silver fir-core sandwich is about 40% lower than the ash tree-core one.

On the other hands the PVC-core sandwiches exhibit a very low maximum moment and very high shear stains (the shear modulus is 169 MPa).

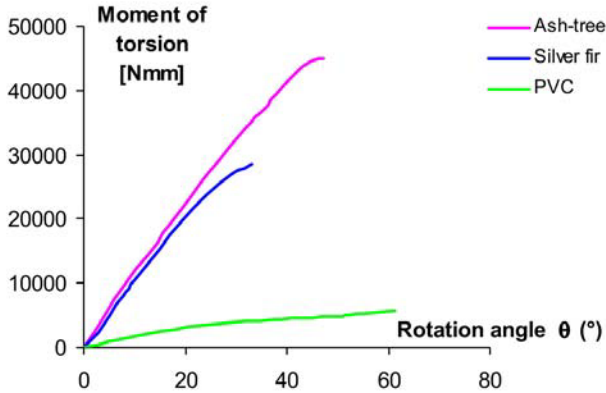


Figure 3. Torsion test of sandwich structures.

#### 4. FINITE ELEMENT MODEL

A numerical simulation of the three point flexural test is conducted for each sandwich structure using the ANSYS 7 finite element software. A 2-D model with 8-node element (Plain 82) is realised. The mechanical and physical properties of the sandwich constituents are obtained via experimental tests or analytical studies [8].

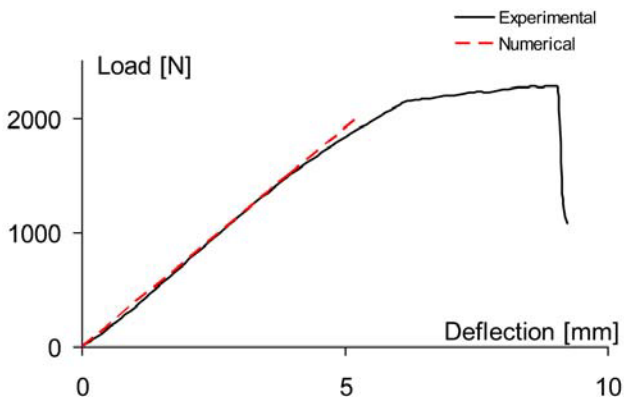


Figure 4. Numerical and experimental load/displacement curve

The post-elastic analysis is intentionally neglected, the aim is to obtain a simple and versatile numerical simulation, conditions always required in an effective design methodology and, particularly, to characterise the composite structure in the elastic regime, where it works.

The comparison of load/displacement curve in elastic field between numerical and experimental data shows good overlapping, so it is possible to draw out that the numerical model is able to reproduce the initial stiffness of the sandwich (Figure 4). This result is similar for the other materials.

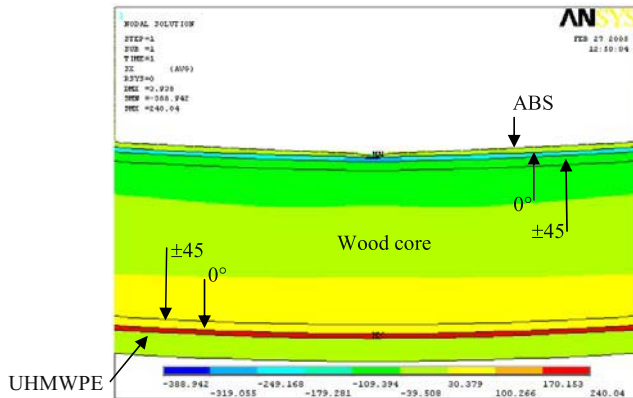


Figure 5. Stresses map the along the wood’s fibres direction for a ash tree sandwich sample.

In Figure 5 the map of the stresses along the wood’s fibres direction for a longitudinal flexural test of the ash tree sandwich sample is reported

The stresses distribution inside the core is un-symmetric; in fact the compressive and tensile areas are subjected respectively to a maximum stress of about 110 MPa and 100MPa. Such small difference is due to the eccentricity between the neutral axis and the symmetry axis.

Similar considerations can be done for the lamina at  $0^\circ$ , for these last we observe that the tensed fibres and the compressed ones are subjected respectively to a maximum stress of 240 MPa and 250 MPa. On the load application area we can observe an intense stresses concentration. In particular the maximum value is about 390 MPa. This fact confirms the slight indentation experimentally observed on such kind of samples.

## 5. CONCLUSION

Several experimental tests have been realised on the snowboard constituents with the aim to get a precise mechanical characterisation in function of their use inside the sandwich structure.

- On the running surfaces, wear and adhesion tests show that UHMWPE, mechanically treated on the side that will be in contact with the fabric to increase the mechanical bonding, has the best mechanical performances.
- On the cores, torsion and three-point flexural tests, have been performed. The Ash-tree shows the best performance, because it has a high stiffness combined with a relevant failure stress both under flexural and torsion loading conditions.

The sandwich structure, produced by vacuum bagging technique, has been subjected to the same kind of tests as the core's samples.

- The flexural response of the sandwich with a wood-core evidences that the core takes part directly to the mechanical characteristics of the whole structure. The study of the mechanical characteristics of the core is fundamental in the design of a snowboard table while the choice of the fabrics can be based only on the necessity of increasing the mechanical performances (mainly flexural ones) of the wood core.
- For this type of sandwich the role of the core is almost negligible so the design is oriented to the choice of the fabrics able to supply to the sandwich structure the right stiffness and mechanical resistance. From the manufacturer's point of view the production of PVC-core sandwich is still very interesting because of the low-cost and easier production being still able to provide the adequate safety during the use of the snowboard table

The experimental results are clarified by the FEM analysis that evidenced the role of each constituent to the stiffness of the whole structure.

## REFERENCES

1. Atkinson, R., Innovative uses for sandwich constructions, *Reinforced Plastics*, 41(2):30–33, 1997.
2. Bannister, M.K., Braemar, R., Crothers, I.P., The mechanical performance of 3D woven sandwich composites, *Composite Structures*, 47:687–690, 1999.
3. Glenne, B., DeRocco, A. and Foss, G., Ski and snowboard vibration, *Sound and Vibration*, 33(1): 30–33, 1999.
4. Sakata, T., Kawai, S. and Kawada, F., Free vibrations of a snowboard, *International Journal of Mechanical Sciences*, 38(6):579–588, 1996.
5. Sakata, T. and Kawai, S., Dynamic bending analysis of snowboards, *Trans. Jap. Soc. Mech. Engrs.*, 61:1469, 1995.
6. Brennan, S.M., Modelling the mechanical characteristics and on-snow performance of snowboards, Ph.D. Thesis, Stanford University, 2003.
7. Manet, V., The use of Ansys to calculate the behaviour of sandwich structures, *Composites Science and Technology*, 58:1899–1905, 1998.
8. Mallick, P.K., *Fiber-Reinforced Composites*, Marcel Dekker Inc., 1993.

# DEVELOPMENT AND EVALUATION OF AN RTM BICYCLE FRAME

Nikos G. Pantelelis

*National Technical University of Athens, P.O. Box 64078, 15710 Athens, Greece*

*E-mail: pande@mail.ntua.gr*

**Abstract** In this paper the complete development and testing of an innovative composite bicycle frame is presented. The frame comprises epoxy resin, glass and carbon fabrics, foam core and metallic inserts produced by the resin transfer moulding technique in a closed mould. The new frame is lighter, stiffer and cheaper from the corresponding aluminium tube frame.

**Keywords:** RTM, frame, polyurethane foam core, bicycle.

## 1. INTRODUCTION

Carbon fibre bicycle frames are sold for sometime but have not gained wide acceptance due to their high cost and competition from advanced metallic alloys. Composite frames are based either on a tube or on a shell structure. The former option has a more conventional design where the metal in a classic tubular frame is replaced by carbon-fibre epoxy-matrix composites whereas the latter option has more potential for innovative and challenging designs. Many attempts for manufacturing such composite frames have been presented by various companies<sup>1</sup> but reporting on these attempts or relevant literature is very poor. On the other hand, there were no attempts towards the cost reduction of these composite frames as in the majority of these frames, high-skilled labour-intensive hand-lay-up techniques with expensive “aerospace technology” are used. Apart from the very high costs associated with this production process another disadvantage is that some of the frames were produced in halves and were bonded together with certain structural weaknesses. However, all body frames are prone to the buckling of the side walls due to their limited thickness and for this

reason most of the manufacturers either abandoned this type of frames or used high cost honeycomb sandwich structures<sup>2</sup>.

Resin Transfer Moulding (RTM) is a relative low cost process for the production of polymer composite complex parts<sup>3-5</sup> for the medium-size production. Perhaps the most important issue in the design of the process is the proper design of the mould in order to achieve part dimensional accuracy, correct fibre impregnation by the resin, optimal curing, low costs and relatively fast production cycles. For optimal results it is important that part and process designs are done simultaneously<sup>6</sup>.

At the present paper the development of a low-cost composite bicycle frame for RTM production is presented. The optimized design has been based on the combined development of both the composite frame and the production process taking full advantage of the sandwich structure. In the production phase, the foam core is used to help the resin infusion and consequently to improve the structural behaviour of the frame. Finally, results from a prototype and some structural tests of the composite frame are reported.

## 2. PROCESS AND STRUCTURAL DESIGN

The main advantage of the body frame is that its volume is significantly higher than an equivalent tubular frame hence the stress distribution can be continuous over the structure but the material distribution might not be optimal. However, using the resin transfer moulding local interventions and patches at the rigid foam core are possible. In order to take advantage of the RTM process the main idea is to use core materials at the inner cavity of the frame keeping the resin and the fibres only at the outer surface of the frame (Figure 1). In this way the body frame can be produced much easier than using a bladder to ensure the proper position and the required contact pressure of the fabrics against the cavity walls but also the structural integrity of the frame increases considerably as the core remains after the process whereas the bladder is removed. Inevitable, the foam core increases the total weight of the frame especially when resin absorption is significant.

Several core materials, such as honeycombs or lightweight foam cores can be used for this purpose but the final choice is a matter of compromises between performance, cost and manufacturability. For the present case, a low cost two-parts polyurethane foam has been chosen. The two parts are mixed manually on-site and cured in the closed cavity resulting in a ready-for-use rigid closed-cell foam core with density of  $80 \text{ kg/m}^3$ , approx.. During the resin injection due to the injection pressure some cells recede and some resin penetrates the core. This, on one hand, improves the structural

behaviour and the fabric impregnation but, on the other hand, increases the weight of the frame considerably. The use of dry fabrics instead of pre-impregnated ones reduces the material and labour costs by at least 50% whereas avoiding the use of the bladder the manufacturing costs and complexity are further decreased.



*Figure 1.* A frame cross section reveals the new sandwich structure of the frame.

For the stress and deformation calculations of the composite frame the most appropriate way is to use the finite element method. For the body frame much more accurate results with adequate details can be achieved by using shell elements in the outer surface of the frame instead of considering the structure as a sandwich panel with the thickness of the total body frame. Furthermore, the foam core can be modelled using solid elements for the total volume of the frame. However, it is still difficult to describe the exact orientations of the fibres all over the frame and to take into account the exact placement of the reinforcements especially in the critical regions such as the assembly points where the maximum stresses are expected. Additionally, we should keep in mind that the shell elements give erroneous results when the thickness of the part becomes comparable to its size. So in regions such as the pedals area which are reinforced locally to withstand the considerable localized loads, solid elements should be used if accuracy is essential. The simulation of the dynamic loads can be done by applying the equivalent dynamic loadings in the static model. Otherwise the damping of the materials should be also considered to further improve the accuracy of the simulation.

### 3. SIMULATION OF THE MOULD FILLING

The selection of the finite element method for the frame design has the advantage that the same finite element model (geometry and mesh) can be used straightforward from the stress analysis of the part to the process simulation as well as for the tooling design and manufacturing. The computer simulation of the resin flow through the fabrics can be achieved with the numerical solution of the Darcy's law (flow through porous media). Even though considerable simplifications are introduced such as saturated flow, steady state flow, incompressibility and no through-thickness flow, the accuracy of the simulations is acceptable comparing to reality. For the simulation of the filling and curing phases a commercial code, RTM-worx<sup>7</sup> has been used. However, the tricky point for an accurate simulation of the filling phase is the appropriate calculation of the fibre preform permeability tensor. The problem is even harder as the permeability tensor components vary through out the cavity either because the fibres' orientation changes as the fabrics drape but also because of the local thickness variations between the closed cavity and the core when the mould is tightly closed resulting in either over-compaction of the fabrics in some regions and/ or less compaction in other areas such as the sharp corners causing minor or major racetracking. In either case, problems will emerge in the production floor requiring skilful and experienced technicians. Therefore, in order to achieve a realistic simulation of the resin flow through the preform the simplest way is to match the simulated results to the real test cases and from there on to start the flow optimisation procedure having all the aforementioned restrictions in mind.

### 4. RESULTS

The development of the new composite body frame was based on an existing mountain bike with an aluminium tubular frame so all the assembly points were maintained to the new design. The basic geometry and the structure of the frame were studied using the I-deas CAD/ CAE software. The structural behaviour of the frame was designed using the finite element method with appropriate modelling of the loads, the geometrical constraints and the materials. The body frame structure was modelled using shell elements for the composite skin while the inclusion of the solid elements for the foam material for the inner core increases considerably the modelling accuracy of the frame. For the modelling of the composite skin material a typical epoxy-matrix with a single biaxial fibreglass lay-up and local patches

of biaxial carbon-fibre lay-up were modelled as a 2D orthotropic material with the equivalent properties for the 2 main axes.

The loading cases that were analysed are:

- A combination of 1200 N at the seat basis and 40 Nm torque at the pedals to simulate the reaction forces from the rider's normal pedalling (Figure 3),
- 80 Nm torque at the pedals to simulate the rider's pedalling when standing on the pedals.
- 3000 N at the front part to simulate the landing from a jump with the front wheel.
- 3000 N at the back to simulate the landing from a jump with the back wheel.

The structural requirements of the new frame were a maximum total deformation of 3 mm and a 3-fold reduction of the maximum value of the von-Mises stresses in all loading cases.

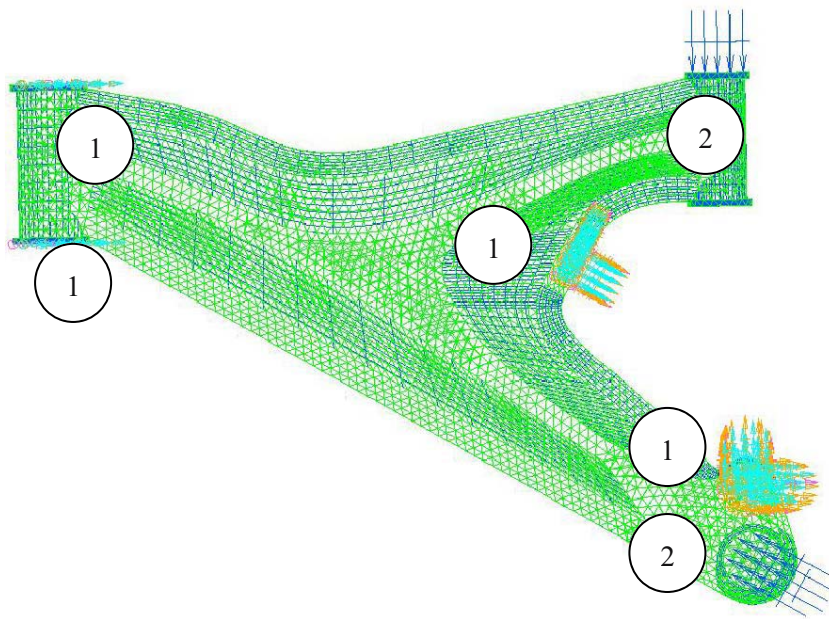


Figure 2. The finite element of the frame using shell elements together with the applied loads (2) and the corresponding geometrical constraints (1).

The geometrical constraints of the model refer to the way the frame is associated with the rest of the components (seat-post, handle bar, front and back suspensions etc.). Simulation results proved that the stress distribution

was kept at low levels ( $< 20$  MPa) except from the regions around the assembly spots where high stresses (200 MPa) were concentrated especially at the pedals area as can be seen in Figure 3. Due to existence of the foam core the buckling of the thin sidewalls is limited maintaining the stiffness of the frame as can be also seen in Figure 3. In any case the structural characteristics of the frame in the design phase need not to be completely defined as these can be tailored and finalized during the tests at the production phase by the rearrangement of the multiaxial fabrics.

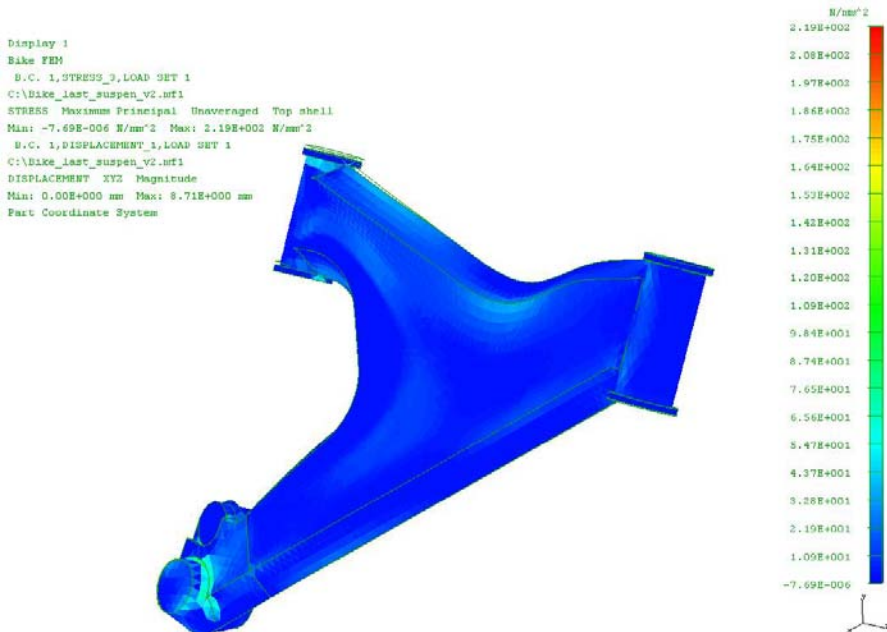


Figure 3. Stress (von-Mises) concentrations at the areas of the applied loadings.

The mould was designed and constructed directly from the corresponding CAD model by generating a Z-code in a CNC lathe using 40 mm thick plaques from hard aluminium alloy.

The target in RTM production is to maintain the quality of the part without generating dry-spots or resin reach areas. In the case of the frame, things are worse as there are two large sidewalls of the frame that are filled simultaneously, in other words there are two parallel pressure fields emerging during resin injection. The two parallel flows of the skins should be synchronised otherwise a transverse differential force will emerge pushing the core towards the other side wall, creating a preferential flow path. To design the process the RTM-worx<sup>7</sup> filling simulation software was used to produce parametric studies for the mould filling process. Because of the

assumptions of the Darcy law, a useful study is the “what-if” scenarios using the simulation software in order to design a robust filling scenario. At the present case, only the most conservative filling strategy was considered: one central inlet gate and three outlet gates at the three outer edges of the closed cavity. As can be seen in Figure 4, at the end of the filling phase the pressure is 0.5 MPa at the inlet gate falling gradually to zero at the outlet gates. Because of the sandwich structure the single inlet gate was changed to two, one at each tool face, in order to ensure two parallel flow fronts at each skin of the sandwich. Locating the inlet gates at the centre of the frame the two independent flow fronts should reach the three outlet ports almost simultaneously at least if the permeability remains constant. However, this is a theoretical prediction which is hardly proven in reality. Deviations such as the non-uniformity in the preform placement or variations in the foam core density and consequently of the local foam stiffness alters the theoretically defined permeability tensor or the local fiber fraction resulting in different flow patterns. Due to this complex filling situation the Vibration Assisted RTM (VIARTM)<sup>8</sup> has proven very helpful for the resin flow homogenisation, quality robustness and void-free composite skin.

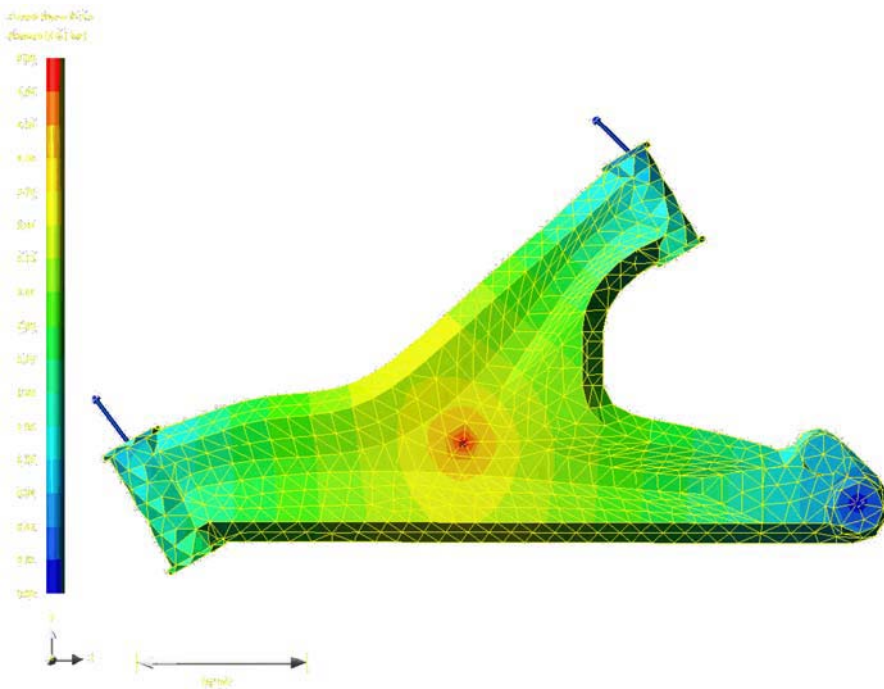


Figure 4. Simulation of the mould filling with resin (pressure distribution).

The first prototype frame (Figure 5) was made of polyurethane foam (305 gr), biaxial stitched glass fabric (190 gr), biaxial stitched carbon fabric (145 gr), Epoxy resin (500 gr) and aluminium inserts (240 gr) resulting in a total weight of 1380 gr, around 100 gr lower than the corresponding aluminium frame.



*Figure 5.* A prototype produced.

In the laboratory testing facilities constructed specifically for this frame, it was revealed that the planar stiffness of the composite frame was 150% higher than the corresponding aluminium frame (Figure 6), in contrast to its perpendicular stiffness which was lower by 150% from the aluminium frame. From the first laboratory tests of this frame it was obvious that the assembly areas were the most problematic areas of the frame. This was not only due to the fact that at these areas either the loadings or the geometrical constraints were applied but also because of the complicated manner that the loads were transferred from the inserts to the sandwich structure of the frame. One important issue that was also studied during these tests was the fatigue of the frame especially at the interface between the skin and the core. The frame's endurance was tested using a cam mechanism applying various frequencies and magnitudes at different locations of the frame. Overall the frame succeeded more than 0.5 million cycles without any indication of

failure while it is still in use in rough terrains without any visible or operational problem.

With respect to the performance of the frame in real conditions it seems that no major differences from the aluminium counterpart exist. Even the lower stiffness in the perpendicular direction is not obvious when using the frame. However, more field tests have been scheduled to evaluate the new frame in more extreme conditions.

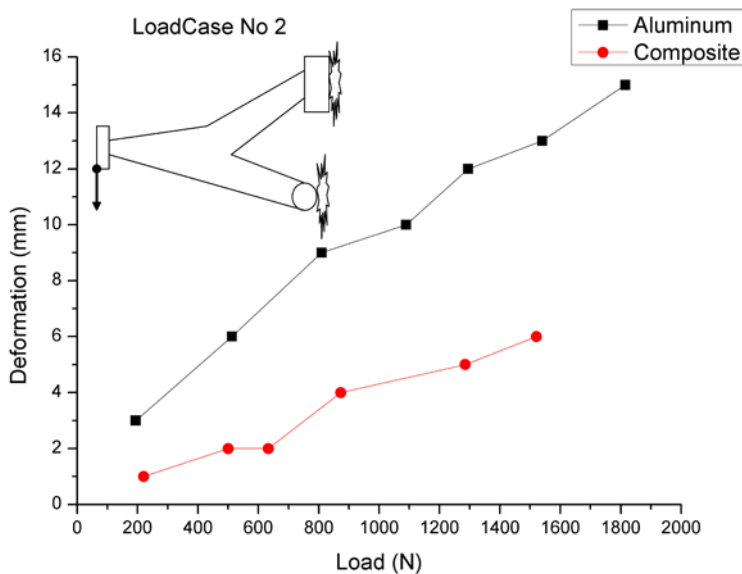


Figure 6. Deformations vs. loads for the aluminium and the composite frame.

## 5. CONCLUSIONS

The development of a low-cost composite bicycle frame has been presented. The concept has been proven: use low cost materials such as standard epoxy resin, glass and carbon fabrics, aluminium inserts and on-site mouldable foam core for the production of a lightweight composite frame with Resin Transfer Moulding. Creating the CAD model of the frame and the finite element shell mesh, numerical simulations provided the field for virtual tests in the structural behaviour and the manufacturing of the new concept. The new frame compares well to the substituted aluminium frame in weight, performance and costs. During the first tests of the frame the low

cost production has been proven but the frames were sensitive to the preform placement in the assembly regions. The solution of some minor problems is underway as well as the seeking of interested partners to bring the new frame concept to the market.

## ACKNOWLEDGEMENTS

The present work was supported by Technika Plastica SA, N.Maniatopoulos SA and the General Secretariat for Research and Technology under the project DSBEPRO 112. Mr Dionyssis Asvestas' contribution in the construction of the testing bed, Mr Yannis Krompas' help in the execution of the simulations and Mr Thomas Vrouvakis' help in the execution of various tests are gratefully acknowledged.

## REFERENCES

1. C. Calfee and D. Kelly, Technical White Paper, 1997.
2. J. Colegrove, Honeycomb reinforced composite fiber bicycle frame, US Pat. No. 6109638, 2000.
3. C.D. Rudd, A.C. Long, K.N. Kendall and C.G.E. Mangin, Liquid Composite Moulding Technologies, Woodhead Publishing, Cambridge, 1997.
4. K. Potter, Resin Transfer Moulding, Chapman and Hall, London, 1997.
5. M.J. Owen, V. Middleton and I.A. Jones, Integrated design and manufacture using fibre-reinforced polymeric composites, Woodhead Publishing, Cambridge, 2000.
6. N.G. Pantelelis and A. Kanarachos, Computer simulations for the optimization of resin flow and tool design towards low-cost RTM, in: Proceedings of the 22<sup>nd</sup> International Conference of SAMPE Europe, CNIT Conference Centre, Paris, 2001.
7. Polyworx, Ammerstol, <http://www.polyworx.com>
8. N.G. Pantelelis, Evaluation of the Vibration Assisted RTM technique in the production of real parts, in: Proceedings of the 7th Flow Processes in Composite Materials, S. Advani (ed.), 2004, pp. 151-156.

# DEVELOPMENT OF NEW REINFORCED LOAD INTRODUCTIONS FOR SANDWICH STRUCTURES

M. Alexander Roth

*DEGUSSA, Röhm GmbH & Co. KG*

**Abstract** This article deals with the design, manufacturing and testing of new innovative load introductions into sandwich structures consisting of fibre reinforced plastics. Vitrally new to these load introductions is the principle of local through-the-thickness reinforcements by threads, resulting in an excellent connection of both face sheets and core and, if necessary, also the load introduction element itself. The threads are introduced into textile face sheets and the core by stitching process. After stitching, the textile face sheets and the threads are impregnated with the polymer matrix using a liquid composite moulding process. The resulting mechanical out-of-plane properties of the so-called IDAK load introductions outperform current state-of-the-art load introductions.

**Keywords:** load introduction, stitching, IDAK.

## 1. INTRODUCTION

Sandwich structures are commonly used in aerospace, marine and other transport applications due to high strength and stiffness to weight ratio. Sandwich panels consist of an upper and a lower face sheet as well as a thick and lightweight core material in between, which are bonded together. The stiff and strong face sheets are used to carry the in-plane stresses while the core is used to carry the shear stresses produced by transverse loads. A sandwich structure is especially suitable for bending and in-plane compression loads. There are common disadvantages to introducing local loads or moments into the sandwich panel as a result of the thin face sheets and the weak core material. Therefore it's necessary to use special load introductions following certain design guidelines with regard to mechanical, material and manufacturing requirements [1]. The face sheets as well as the core material

might break due to the complex three dimensional stress conditions in the area of the load introductions. There are five different kinds of load introductions for sandwich structures (Figure 1) [1]. The left column shows sketches of each kind of load introduction while the right column shows typical failure modes. These conventional load introduction types have at least one of the following disadvantages [1–3]:

- Non-uniform stresses of the different sandwich components
- Local stability problems of the face sheets
- Core failure due to high stress concentration
- Cohesive or adhesive failure of the bonding of load introduction element
- Debonding between face sheet and core material
- High weight

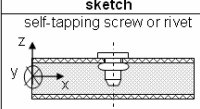
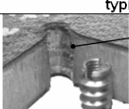
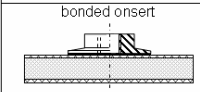
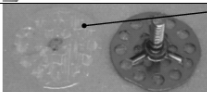
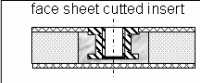
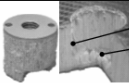
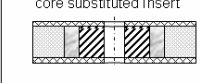
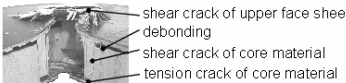
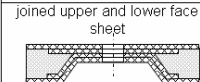
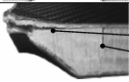
sketch	typical failure mode
 <p>self-tapping screw or rivet</p>	 <p>shear crack of core material</p>
 <p>bonded insert</p>	 <p>cohesive and adhesive failure of the bonding</p>
 <p>face sheet cutted insert</p>	 <p>shear crack of core material tension crack of core material</p>
 <p>core substituted insert</p>	 <p>shear crack of upper face sheet debonding shear crack of core material tension crack of core material</p>
 <p>joined upper and lower face sheet</p>	 <p>debonding shear crack of core material</p>

Figure 1. Different load introduction concepts including typical failure mode.

Thus the current conventional load introduction concepts aren't optimal. This is why, new kinds of through-the-thickness reinforced load introductions are developed, so-called IDAK-concepts [4]. Threads are used as reinforcements, which are inserted into the non-impregnated sandwich components with the aid of a conventional sewing machine. The modified double locked stitch with the loop in the lower face sheet is used as stitching type. The needle inserts the upper thread into the sandwich structure and creates a hole in the used polymer foam. During the stitching process the upper thread makes a loop with the bobbin thread on the lower side of the sandwich panel [5]. As a result of the stitching, the sandwich components and, optionally, the used load introduction element, are fixed. After the sewing process the sandwich structure is impregnated with resin using a liquid composite moulding (LCM) process. After the curing process the impregnated threads

present uni-directional fibre reinforced plastic bars in the core material, which increase the mechanical properties of the core material, the whole sandwich structure and, especially, of the load introduction [4]. Round sandwich test panels with a diameter of 250 mm including a central load introduction are used for the experimental study. The face sheets are made out of bi-axial ( $0^\circ/90^\circ$ ) non-scrimb glass-fibre fabrics with a dry thickness of 0.7 mm [6]. As core material a full-closed polymer foam with a density of  $60 \text{ kg/m}^3$  and a thickness of 8 mm is used [6]. The matrix is made out of epoxy resin. As thread materials polyester-fibre (PES), aramid-fibre (AF) and glass-fibre (GF) yarn with nearly the same cross-section area are used (Table 1).

Table 1. Properties of the used thread materials.

thread material (abbreviation)	polyester (PES)	aramid (AF)	S-glas (GF)
trade name	Amann Saba C 50	Amann Kevlar 50	Slide 150
yarn count [tex = g/km]	68.7	62.1	141.2
density [ $\text{kg/m}^3$ ]	1370	1450	2490
cross-section area [ $\text{mm}^2$ ]	0.050	0.043	0.057
tensile strength [N]	$32.1 \pm 0.6$	$77.1 \pm 5.5$	$114.4 \pm 6.2$

## 2. DEVELOPMENT OF REINFORCED LOAD INTRODUCTIONS

As a result of the different failure modes the mechanical properties of conventional load introductions can be increased with the help of the IDAK-principle. Core cracks and debonding between face sheets, core or load introduction elements can be avoided due to the high stiffness and strength of the impregnated threads. The following load introduction concepts are especially suited for increasing the pull-out strength by using the IDAK-principle:

- bonded onsert (onsert)
- core substituted insert (insert)
- joined upper and lower face sheet (JFS)

Self-tapping screws, rivets and face sheet cutted inserts have a lower potential to increase the mechanical properties by using through-the-thickness reinforcements. Therefore they aren't considered in this study.

### 2.1 Bonded onsert

As bonded onsert a metal element type M1/B38-M6x20 from the company Bighead Bonding Fasteners Ltd., Great Britain [7] is used. The element is made out of steel and consists of a lower thin plate with a diameter of 38 mm, a thickness of 2 mm, 6 inner and 12 outer holes as well as a concentric cylinder with a length of 20 mm and an outer thread (M6). Different de-

sign concepts of stitched inserts in comparison to an unstitched one have been developed (Figure 2). Furthermore different thread materials and density of reinforcement have been analysed. The density of the reinforcement is the amount of inserted threads in z-direction. During the fixation of the insert by stitching, it is necessary to stitch the same position several times to increase the density of reinforcement. All the analysed unstitched and stitched insert-variants are shown in Figure 2. The fixation of the insert and the sandwich structure with threads are symbolized by slight grey loops. The stitching of the sandwich components itself is represented by dark grey lines. O-0 represents the conventional unstitched variant. O-1 is stitched through the thickness of the whole sandwich structure by using the outer holes of the insert plate. AF yarn is used as thread material. On the other hand O-2 is stitched through the thickness of the upper face sheet. Variant O-3 is similar to O-1, except one difference. The sandwich structure itself is sewed with PES yarn before fixation the insert with AF yarn. This PES reinforcement consists of twelve concentric circles from a diameter of 4 mm to 48 mm with a stitch length of 2 mm in radial  $s_r$  and in circumferential direction  $s_\phi$ .

insert-variants	scetch (cross-section)	picture (top view)	thread material	density and geometry of sewing
O-0			---	0
O-1			PES AF GF	216 72, 144, 216, 384 216
O-2			AF	384
O-3			AF + PES	384 D = 0 - 48 mm $s_r = 2$ mm $s_\phi = 2$ mm

Figure 2. Onsert-variants.

## 2.2 Core substituted insert

In this study one unstitched (I-0) and one stitched core substituted insert concept (I-1) are developed (Figure 3). The used insert is made out of aluminium with an outer diameter of 20 mm and with an inner thread M8. Furthermore the insert is sand-blasted and degreased. The stitched reinforcement of variant I-1 consists of seven concentric circles from a diameter of 24 mm till 48 mm with a stitch length of 2 mm in radial  $s_r$  as well as in circumferential direction  $s_\phi$ . AF yarn is used as thread material.

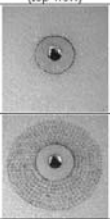
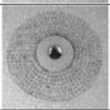
insert-variants	scetch (cross-section)	picture (top view)	thread material	density and geometry of sewing
I-0			---	0
I-1			AF	D = 24 - 48 mm s <sub>r</sub> = 2 mm s <sub>φ</sub> = 2 mm

Figure 3. Insert-variants.

### 2.3 Joined upper and lower face sheet (JFS)

One unstitched (JFS-0) and two stitched JFS-variants (JFS-1 and JFS-2) have been developed (Figure 4). JFS-1 is stitched from a diameter of 2 mm to 48 mm. On the other hand JFS-2 isn't stitched in the monolithic area. The reinforcements are only inserted from the diameter 20 mm till 48 mm. Both stitched variants have a stitch length of 2 mm in radial s<sub>r</sub> as well as in circumferential direction s<sub>φ</sub>. AF yarn is used as thread material.

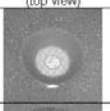
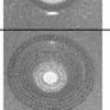
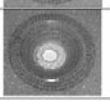
JFS-variants	scetch (cross-section)	picture (top view)	thread material	density and geometry of sewing
JFS-0			---	---
JFS-1			AF	D = 0 - 48 mm s <sub>r</sub> = 2 mm s <sub>φ</sub> = 2 mm
JFS-2			AF	D = 20 - 48 mm s <sub>r</sub> = 2 mm s <sub>φ</sub> = 2 mm

Figure 4. Joined upper and lower face sheet variants.

## 3. MANUFACTURING

A double locked stitch sewing machine (Pfaff: Typ 3574-2/02 [8]) with a specially designed frame work to support the face sheets and the core material, including a clamp to position and fix the onsert, is used. Figure 5 shows the sewing process of the onsert-variant O-3. The onserts are exactly positioned onto the sandwich components with the aid of the sewing process. The quality of the modified double locked stitch is very high for each thread material. The vacuum assistant resin infusion (VARI) process with a female mould and an upper vacuum-bag is used to infiltrate the unstitched and the stitched sandwich plates including the central load introductions with resin.

The VARI-process of the stitched sandwich plates is up to 40 % faster than the unstitched variants.

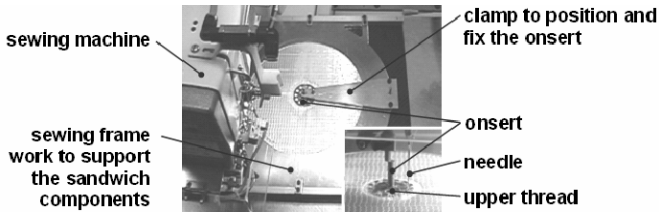


Figure 5. Sewing process of onsert-variant O-3.

## 4. TESTING

The test facility for quasi-static pull-out testing is shown in Figure 6. The different test specimens with central load introduction are clamped horizontally on the edge from diameter 210 mm till 250 mm. The force is transmitted with a hydraulic cylinder, which is positioned perpendicular to the sandwich plate. The test velocity is 2 mm/min for each variant. Force-displacement-diagrams have been recorded for each test specimen.

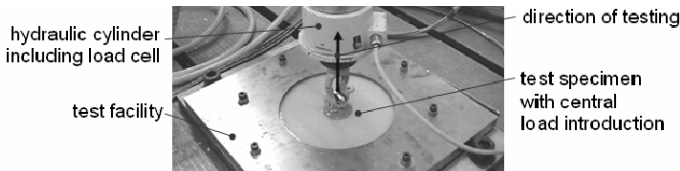


Figure 6. Test facility of quasi-static pull-out testing in z-direction.

### 4.1 Bonded onsert

Figure 7 shows the pull-out force and energy of the different design concepts of the stitched onserts in comparison to the unstitched one. The pull-out energy is the energy necessary to destroy the load introduction. The pull-out force is increased by up to 260 % and the energy is increased by up to 1615 % by using the IDAK-principle. Variant O-0 fails as a result of debonding between the onsert and the upper face sheet. The failure mode of O-1 and O-3 is characterized by cracking of the upper threads in the vertex of the loops. On the other hand variant O-2 fails as a result of shear and tension crack in the core material.

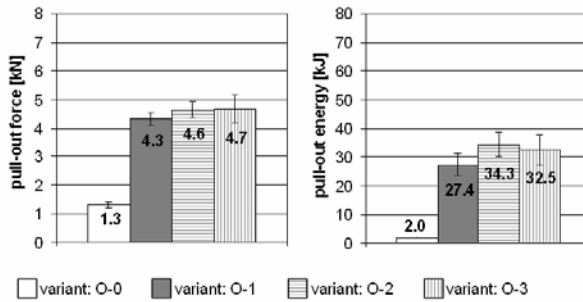


Figure 7. Pull-out force and energy of O-0 to O-3 with AF and density of reinforcement of 384.

Figure 8 shows the pull-out force of the onsert-variant O-1 depending on the density of reinforcement. There is no linear behaviour relating to the pull-out force and density of reinforcement.

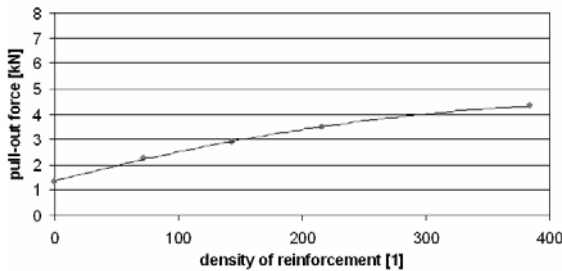


Figure 8. Pull-out force of variant O-1 with AF depending on the density of reinforcement.

The reason for this result is the degradation of the still inserted threads by renewed stitching of the same position, which could be confirmed by microscopic analysis (Figure 9). Furthermore an analytical approach including a degradation model is developed to determine the pull-out force depending on the density of reinforcement.

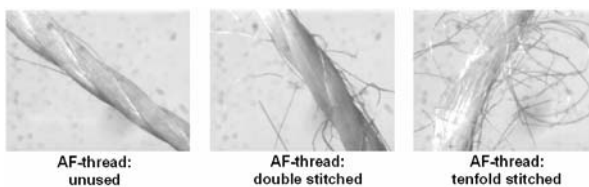


Figure 9. Degradation of still inserted threads by renewed stitching of the same position

Based on onsert-variant O-1, different thread materials with equal density of reinforcement were analysed (Figure 10). The GF stitched onsert-variant has the highest pull-out force and energy of all the analysed thread materials.

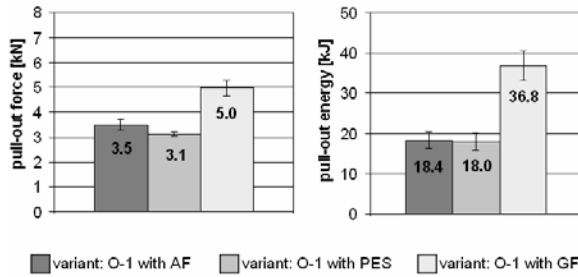


Figure 10. Pull-out force and energy of O-1 with different thread materials and density of reinforcement of 216.

## 4.2 Core substituted insert

Figure 11 shows the pull-out force and energy of the unstitched (I-0) and the stitched insert-variant (I-1). The pull-out force is increased by up to 125 % and the energy by up to 390 % when using the IDAK-principle.

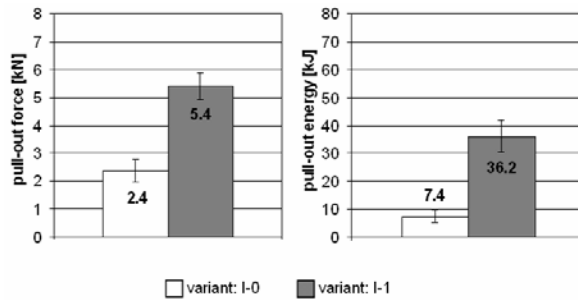


Figure 11. Pull-out force and energy of unstitched (I-0) and stitched insert-variant (I-1).

I-0 failed as a result of the stress concentration in the core material. The core begins to crack at the edge in the area of insert, core and lower face sheet. This crack has an angle of 45° and moves on to the upper face sheet. The debonding between the upper face sheet and the core material (Figure 12, left figure) destroys the sandwich-effect and decreases the stiffness. The failure occurs abruptly at ultimate load. The stitched insert-variant also failed as a result of the stress concentration in the core material but at a higher load level (Figure 12, right figure). The crack can't move on in 45° direction as a result of the stitching. In this case a debonding between upper face sheet and core is avoided. The stitched variant failed at ultimate load owing to shear crack of the upper face sheet. The stitched insert-variant has a very good fail-safe behaviour due to the different failure modes. The higher pull-out force of the stitched in comparison to the unstitched insert is caused by the increased stiffness in the area of the load introduction, through

which the strains and stresses are decreased. This can be confirmed with the help of finite element analysis.

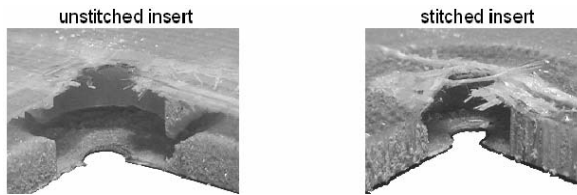


Figure 12. Failure mode of unstitched (I-0) and stitched insert-variant (I-1).

### 4.3 Joined upper and lower face sheet (JFS)

Figure 13 shows the pull-out force and energy of the unstitched (JFS-0) and the two stitched JFS-variants. The pull-out force is increased by up to 38 % and the energy by up to 76 % when using the IDAK-principle. All variants are characterized by shear crack in the face sheets in the monolithic area. JFS-2 has slightly higher pull-out force and pull-out energy in comparison to JFS-1, because the in-plane properties of fibre reinforced plastics are decreased by stitching as is well-known [9].

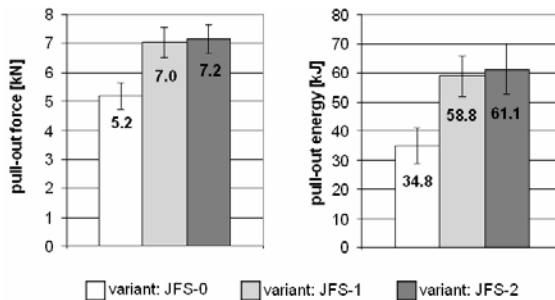


Figure 13. Pull-out force and energy of JFS-0, JFS-1 and JFS-2.

## 5. SUMMARY

New through-the-thickness reinforced load introductions for sandwich structures have been developed to increase the mechanical properties perpendicular to the sandwich plate. The development comprises the design of different stitched load introduction (called IDAK) as well as their manufacturing process. Conventional threads are used as reinforcements, which are inserted into the non-impregnated sandwich components with the aid of a standard sewing machine. Both face sheets, the core and optionally the load introduction element are fixed with threads. After the sewing process the

whole sandwich structure is impregnated with resin using vacuum assistant resin infusion process. The impregnated threads within the core present uni-directional fibre reinforced plastic bars, which increase the mechanical properties of the core material, the whole sandwich structure as well as of the load introduction. Quasi-static pull-out tests perpendicular to the sandwich plate verified the following increased mechanical properties of IDAK load introductions in comparison to conventional unstitched ones:

- Increased stiffness perpendicular to the sandwich plate up to 23 %
- Increased strength perpendicular to the sandwich plate up to 260 %
- Increased transversal shear strength of the core material up to 95 %
- Increased peel-strength between face sheet and core material
- Fail-safe behaviour due to the increased peel-strength and the so-called crack-stop-function of threads
- Increased pull-out energy up to 1615 %

The mechanical properties of stitched load introductions depend on the used design concept, thread material and the used density of reinforcement.

Furthermore the handling of the sandwich components and positioning of the load introduction element during the VARI-process are improved and the infiltration times are decreased up to 40 % as a result of the sewing process.

## REFERENCES

1. Roth, M. A., Himmel, N.: Konstruktion, Auslegung und Prüfung von Krafteinleitungen in Faser-Kunststoff-Verbund-Sandwichstrukturen. Proceedings, "5. Internationale AVK-TV Tagung", AVK-TV e. V., Baden-Baden: 2002, pp. C 2-1-C 2-11.
2. Zenkert, D. (Ed.): The Handbook of Sandwich Construction. London, United Kingdom: Engineering Materials Advisory Services Ltd., 1997.
3. Thomsen, O. T.: Sandwich plates with "through-the-thickness" and "fully potted" inserts: evaluation of differences in structural performance. Composite Structures, Vol. 40, No. 2, pp. 159-174, Elsevier Science, 1998.
4. Roth, M. A.: Krafteinleitungsstelle in Kernverbunden mit in Dickenrichtung des Kernverbundes durchsetzenden Armierungselementen. Gebrauchsmuster DE 203 14 187.3.
5. Stanley, L. E., Adams, D. O.: Development and Evaluation of Stitched Sandwich Panels. NASA, 2001.
6. Gaugler & Lutz oHG: Produktkatalog. Aalen: Wahl-Druck GmbH
7. Bighead Bonding Fasteners Ltd.: The Bighead Book of Brainwaves. 3. Auflage: Portswood Colour Press Ltd., 2000.
8. G. M. Pfaff AG: Pfaff 3574-2/02 Betriebsanleitung. Troisdorf: HAAS-Publikationen GmbH, 1996.
9. Roth, Y. C., Himmel, N.: Stitched Non-Crimp Fabric Laminates: From Manufacturing to In-Plane Properties, ICCM-14, San Diego, California, 2003.

# SANDWICH STRUCTURES WITH COMPOSITE INSERTS: EXPERIMENTAL STUDIES

G. Nageswara Rao<sup>1</sup>, Ullas Agrawal<sup>1</sup> and N.K. Naik<sup>2</sup>

<sup>1</sup>*Pratt and Whitney Center of Excellence, Infotech Enterprises Limited, Plot No. 11, Software Units Layout, Infocity, Madhapur, Hyderabad 500 081, India*

<sup>2</sup>*Aerospace Engineering Department, Indian Institute of Technology Bombay, Powai, Mumbai 400 076, India; E-mail : nknaik@aero.iitb.ac.in*

**Abstract** Studies are presented on the performance of insert assemblies of the sandwich structures with localized through-the-thickness compressive loading. Through-the-thickness and partially inserted fully potted inserts are studied. Insert material considered are: aluminum and 3D woven composite. Experimental results are compared with analytical predictions. It is observed that the specific strength of 3D woven composite inserts is more than that of aluminum inserts.

**Keywords:** sandwich structure, insert, 3D woven composite, localized through-the-thickness loading.

## 1. INTRODUCTION

Honeycomb sandwich structures are widely used in high performance applications. Such structures are characterized by high specific strength and high specific stiffness for flexural loads. But honeycomb sandwich structures are not strong enough to withstand the localized external loads. In case, when localized external loads are acting on sandwich structures, inserts are used. Inserts are potted on mechanically installed in sandwich structures. Inserts can be through-the-thickness or partially inserted onto the sandwich structures.

The insert is part of a detachable fixation device. This entire fixation device is referred to as an insert assembly. It consists of: insert, potting material, upper face-plate, lower face-plate, honeycomb core and the attachment. The external load is transferred to the honeycomb sandwich

structure through the attachment. Higher stress state is generated within the insert assembly because of the localized loading. Inserts provide the capability to attach subassemblies to sandwich structures. They transmit loads to and from the structure.

Generally, metals are used as insert materials. An analytical method is presented by Thomsen [1, 2] to evaluate the stress state within the insert assembly with metal (isotropic) inserts. One of the reasons for higher stresses with metal inserts compared with composite inserts is the significant difference in material mechanical properties on either side of the interfaces between the attachment and insert and also insert and potting material.

The performance of the insert assembly can be enhanced by using 3D woven composites as inserts. An analytical method is developed for the evaluation of insert assemblies with composite inserts under localized through-the-thickness loading. The method is based on the method presented in [1, 2]. It is observed that with composite inserts, the specific strength of the insert is significantly increased. The objective of the present study is evaluation of insert assemblies with through-the-thickness compressive loading experimentally. Through-the-thickness and partially inserted fully potted inserts are studied (Figure 1). Performance of aluminum inserts is compared with those of 3D woven composite inserts. The specific objectives of the study are: deformation behavior, failure behavior and failure modes. Experimental results are compared with the analytical predictions.

## 2. EXPERIMENTAL STUDIES

The experiments were planned for the investigation of the behavior of sandwich structures with inserts under localized through-the-thickness compressive loading. The specific objectives of the study are:

- Deformation behavior
- Failure behavior
- Failure modes

For a typical configuration of the sandwich structure, diameters and thicknesses of the insert assembly are: diameter of attachment,  $D_a = 5$  mm; diameter of insert,  $D_i = 10$  mm; diameter of potting material,  $D_p = 40$  mm; diameter of the support,  $D_h = 120$  mm; thickness of foam core,  $c = 10$  mm and thickness of upper and lower face-plates,  $t = 2$  mm. For partially inserted fully potted inserts, length of the insert was varied from 60 % to 80 % of the core thickness.

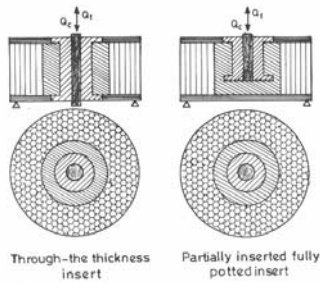


Figure 1. Different types of inserts for honeycomb sandwich structures.

## 2.1 Fabrication of insert assembly

The insert assembly for experimental study consists of six components. They are: insert, potting material, foam core, upper face-plate, lower face-plate and the attachment. Upper face-plate and lower face-plate are made of woven fabric T-300 carbon and epoxy resin using matched-die molding technique. The core is made of polyurethane foam. The attachment is made of mild steel. The insert is made of aluminum and 3D woven composite. The material used for the composite inserts is E-glass/epoxy. The potting material is epoxy resin. The composite face-plates are made in such a way that they provide in-plane quasi-isotropic behavior. The aluminum inserts are machined to the required dimensions. The composite inserts are made using a special split mould.

An aluminum mould is made for the assembly of the above-mentioned six components. The aluminum mould consists of: lower cover plate with reference holes, outer ring and upper cover plate with reference holes.

Assembly of insert assembly for through-the-thickness inserts is carried out as follows:

- Holes of the required size are made in the composite upper face-plate and lower face-plate for the precise positioning of the flanges of the insert.
- Mould release agent is applied through-out the mould surface.
- The bottom plate of the mould and the outer ring are located and assembled with the help of reference holes.
- The bottom face-plate is located on the bottom plate of the mould. Proper location is ascertained with the help of reference holes.
- The attachment-insert assembly is located with respect to the lower face-plate with the help of reference holes.
- The foam core is prepared with a central hole for inserting the insert and pouring the potting material.
- Resin is applied on either side of the foam core.

- Foam core is located around the insert taking the outer ring of the mould as reference.
- The upper face-plate is located.
- The upper plate of the mould is located. The precise location is ascertained with the help of reference holes.
- Resin is injected.
- The insert assembly is left for curing for 24 hours.

The insert assembly is removed from the mould for further finishing. Now, the insert assembly is ready for testing. A similar procedure was used for the fabrication of partially inserted fully potted insert assemblies.

## **2.2 Test apparatus**

The test specimens are tested on Hounsfield Test Equipment – 450 KS, 50 KN UTM. The compressive load was applied through the attachment at a loading rate of 0.25 mm/min during the test. During testing, the compressive load and the displacements of the specimen at three different locations were noted: displacement of the rigid attachment, displacement of the upper face-plate at a distance of 30 mm from the center, displacement of the lower face-plate at a distance of 30 mm from the center.

## **2.3 Test procedure**

- The test specimen was placed on a support ring and then located on Hounsfield Test Equipment – 450 KS, 50 KN UTM.
- Compressive load was applied through the attachment onto the insert assembly.
- The load and displacements of the attachment, lower face-plate and upper face-plate were noted. The loading rate was 0.25 mm/min.
- The loading was continued until the final failure of the insert assembly took place.
- Load-displacement plot was recorded during testing.

## **3. ANALYTICAL METHOD**

An analytical method is developed for the analysis of insert assemblies of the sandwich structures under localized through-the-thickness tensile / compressive loading by considering the in-plane stiffness of the insert, potting material and core. The insert assembly consists of: insert, potting material, core, upper face-plate, lower face-plate and the attachment.

For the mathematical formulation, insert and potting material are assumed as an integral part of the core. The core is relatively thick and compressible whereas the face-plates are relatively thin. Hence, the core is analyzed using higher-order sandwich plate theory whereas the face-plates are analyzed using classical plate theory. The in-plane stiffness of the core (honeycomb or foam) is very small compared with the in-plane stiffness of the insert and potting material. The in-plane stiffness of the insert and potting material are considerable in magnitude. In this formulation, the in-plane stiffness of the insert, potting material and core are considered. The in-plane stiffness of the core is not considered in earlier studies [1, 2].

The analytical method comprises of the following steps:

- The behavior of the sandwich structure with an insert assembly is represented using a set of 30 governing differential equations based on equilibrium equations obtained from the stress, stress resultants, constitutive relations for strains and continuity conditions at the material interfaces. In these equilibrium and constitutive relations, the in-plane stresses in the core are considered.
- The stress relations for the core material are developed from the core equilibrium equations, stress-strain relations of core and continuity conditions. The equilibrium equations for the face-plates are derived by considering an element from the face-plate. The order of the governing equation for the top face-plate is four. But this equation contains the stress components from the core. To get final governing differential equation, the stress components of core material are written in the form of face-plate variables using continuity conditions. After substituting core variables with face-plate variables, the order of the governing equation becomes sixteen. Also, the governing equation of the other face-plate is introduced into the governing equation of the top face-plate through the continuity conditions and core equations to get final governing equation of the sandwich structure. The order of the final governing partial differential equation is 32 and there are 32 unknowns. The 32 unknown variables are fundamental variables to the problem. The coupled boundary conditions are defined to solve the problem in terms of fundamental variables.
- The core governing equations are functions of  $r$ ,  $\theta$  and  $z$ . To get the first order governing partial differential equations to solve the problem,  $z$  is represented in the form of Fourier series.
- After representing  $z$  in Fourier series in core governing differential equations, the 32<sup>nd</sup> order partial differential equation is rewritten into 32 first order coupled partial differential equations in terms of 32 fundamental variables, their derivatives with respect to  $\theta$  and radius  $r$  using the governing equations defined for the core and face-plates.

- Using Fourier expansions, the dependency on derivatives of  $\theta$  in the 32 first order coupled partial differential equations is eliminated.
- Then, the 32 first order coupled partial differential equations become 32 first order coupled exact differential equations.
- To solve the 32 first order coupled exact differential equations, it is necessary to specify 32 boundary conditions. The 16 boundary conditions are specified at the interface of attachment and insert and the other 16 boundary conditions are specified at simply supported outer edge of the inset assembly.
- The 32 first order coupled exact differential equations and boundary conditions constitute a two point boundary value problem.
- The two point boundary value problem is converted into a series of initial value problems by dividing the sandwich structure into a number of segments along radial direction. The series of initial value problems are solved numerically using multi-segment method of direct integration for 32 fundamental variables at each segment using continuity conditions between two adjacent segments.
- Using this procedure, the stress state and the displacement details are determined throughout the insert assembly for the given loading conditions.
- The damage initiation within the insert assembly is determined using a quadratic failure criterion and the corresponding failure initiation load is noted.
- Based on the density of the insert assembly and the load at which failure initiates, specific strength of the insert assembly is determined.
- The input data required for the analysis of insert assembly of the sandwich structure under localized through-the-thickness tensile / compressive loading are: geometry of insert assembly, elastic and strength properties of different components of the insert assembly and the loading conditions.
- Outputs obtained are: transverse, radial and circumferential displacements, through-the-thickness normal and shear stress components in the core, in-plane normal and shear stress components, induced normal stress resultants, induced shear stress resultants and induced bending moment resultants in the face-plates.

#### 4. RESULTS

During the experiments, load and displacement data was noted. Failure initiation and different stages of failure was noted based on sudden discontinuity in load-displacement plots. The results are presented in Table 1.

Load at failure initiation is higher for the case of 3D woven composite inserts compared with that for aluminum inserts. Further, load at failure initiation is higher for the case of through-the-thickness inserts compared with that for partially inserted fully potted inserts. For the case of partially inserted fully potted inserts, the results are nearly identical for the range of insert height considered.

Using the analytical method peak transverse displacement, peak through-the-thickness normal stress and peak transverse shear stress as functions of compressive load for different insert materials are obtained (Table 2). For this study, the same geometrical configurations and material properties as used for the experimental studies are used.

Using quadratic interaction failure criterion, failure function values are determined for different insert materials [3, 4]. Failure initiation is predicted based on failure function values.

Maximum compressive load at failure initiation is higher for the case of 3D woven composite compared with aluminum as an insert material (Tables 1 and 2). The specific strength of the insert is higher for the case of 3D woven composite compared with the case of aluminum insert. Here, specific strength is defined as the ratio of the load at which the failure initiation takes place and the weight of the insert. Specific strength is a dimensionless quantity. Further, the specific strength of the insert is higher for the case of through-the-thickness inserts compared with the case of partially inserted fully potted inserts. Weight of 3D woven composite inserts is less than that of aluminum inserts (Tables 1 and 2). It is generally observed that the experimental specific strength values are marginally lower than the analytically predicted values.

#### **4.1 Failure modes of test specimens**

Generally, higher through-the-thickness normal stress concentrations are observed at the interfaces of attachment and insert, insert and potting material and also potting material and honeycomb core. Higher transverse shear stress concentrations are observed at the interface of attachment and insert. Combined effect of through-the-thickness normal stress and transverse shear stress leads to failure initiation in the insert / potting material / honeycomb core region. It is generally observed that the failure initiates at the interface between the attachment and the insert. The attachment starts sliding downward during compressive loading.

Other possible modes of failure initiation are: delamination between the upper face-plate and the core, delamination between the core and the lower face-plate, possible in-plane failure within the face-plates and core.

*Table 1.* Specific strength of through-the-thickness and fully potted inserts: experimental studies.  
 Volume of through-the-thickness insert,  $V = 1.126 \times 10^{-6} \text{ m}^3$   
 Volume of fully potted insert,  $h = 8 \text{ mm}$ ,  $V = 0.891 \times 10^{-6} \text{ m}^3$   
 Volume of fully potted insert,  $h = 6 \text{ mm}$ ,  $V = 0.773 \times 10^{-6} \text{ m}^3$   
 Density of aluminum =  $2800 \text{ Kg / m}^3$   
 Density of composite =  $1700 \text{ Kg / m}^3$

Insert	At failure initiation		Mass of insert, m (Kg) $\times 10^{-3}$	Specific strength of insert $\times 10^6$	% increase in specific strength of insert	% decrease in mass of insert
	Compressive load, $Q_c$ (KN)	Displacement, w (mm)				
Aluminum	6.8	5.2	3.20	0.217	Reference	Reference
3D woven composite	9.8	6.2	1.91	0.523	141	40.3
Aluminum, h = 6 mm	4.6	3.2	2.16	0.217	0	32.5
Aluminum, h = 8 mm	4.7	3.3	2.49	0.192	-11.5	22.2
3D woven composite, h = 6 mm	4.7	4.1	1.31	0.366	68.7	59.1
3D woven composite, h = 8 mm	4.8	4.2	1.51	0.324	49.3	52.8

*Table 2.* Specific strength of through-the-thickness and fully potted inserts: analytical studies for experimental configurations.

Volume of through-the-thickness insert,  $V = 1.126 \times 10^{-6} \text{ m}^3$   
 Volume of fully potted insert,  $h = 8 \text{ mm}$ ,  $V = 0.891 \times 10^{-6} \text{ m}^3$   
 Volume of fully potted insert,  $h = 6 \text{ mm}$ ,  $V = 0.773 \times 10^{-6} \text{ m}^3$   
 Density of aluminum =  $2800 \text{ Kg} / \text{m}^3$   
 Density of composite =  $1700 \text{ Kg} / \text{m}^3$

Insert	At failure initiation		Mass of insert, $m \text{ (Kg)} \times 10^{-3}$	Specific strength of insert $\times 10^6$	% increase in specific strength of insert	% decrease in mass of insert
	Compressive load, $Q_c \text{ (KN)}$	Displacement, $w \text{ (mm)}$				
Aluminum	7.070	4.24	3.20	0.225	Reference	Reference
3D woven composite	11.170	6.70	1.91	0.596	164.7	40.3
Aluminum $h = 6 \text{ mm}$	5.250	3.67	2.16	0.248	10.2	32.5
Aluminum $h = 8 \text{ mm}$	5.350	3.75	2.49	0.219	-2.7	22.2
3D woven composite $h = 6 \text{ mm}$	5.110	3.82	1.31	0.398	76.6	59.1
3D woven composite $h = 8 \text{ mm}$	5.460	4.09	1.51	0.369	63.7	52.8

## 5. CONCLUSIONS

Experimental investigations are carried out on the behavior of insert assembly of the sandwich structures under through-the-thickness compressive loading. The insert materials used are: aluminum and 3D woven composite. The displacement behavior and the failure initiation load are presented using the analytical method for the same cases of inserts as used for the experimental studies. It is observed that,

- There is a good match between the experimental results and the analytical predictions in terms of transverse displacement and failure load.
- Specific strength of 3D woven composite inserts is higher than that of aluminum inserts.
- Specific strength of through-the-thickness inserts is higher than that of partially inserted fully potted inserts.
- Significant weight saving is possible by using 3D woven composite inserts instead of aluminum inserts.

## ACKNOWLEDGEMENTS

This work was supported by ISRO - IIT (Bombay) Space Technology Cell. Patent pending, Patent Application Number: 496\MUM\2004.

## REFERENCES

1. Thomsen, O.T. and Rits, W., "Analysis and design of sandwich plates with inserts – a higher order sandwich plate theory approach", *Composites Part B: Engineering*, Vol. 29B, No. 6, pp. 795-807, 1998.
2. Thomsen, O.T., "Sandwich plates with 'through-the-thickness' and 'fully potted' inserts: evaluation of differences in structural performance", *Composite Structures*, Vol. 40, No. 2, pp. 159-174, 1998.
3. Sih, G.C. and Skudra, A.M., *Failure mechanics of composites*, North-Holland, Amsterdam, Chapter 2, pp. 71-125, 1985.
4. Brewer, J.C. and Lagace, P.A., "Quadratic stress criterion for initiation of delamination", *Journal of Composite Materials*, Vol. 22, pp. 1141-1155, 1988.

# DEVELOPMENT AND EVALUATION OF FRP SANDWICH BEAMS CONTAINING GLASS FIBERS INTO PHENOLIC FOAM CORE

Goichi Ben<sup>1</sup>, Akiko Shoji<sup>1</sup> and Mituru Souma<sup>2</sup>

<sup>1</sup>College of Industrial Technology, Nihon University; <sup>2</sup>Graduate Student of Nihon University

**Abstract** Phenolic resin has excellent properties of fire resistance, low smoke during burning, and it also has a good balance between its cost and mechanical properties compared with other types of resin used in FRPs. If phenolic resin can be employed as a matrix of FRP, such FRP can have a higher fire safety factor which will be a desirable property in the structures of vessels and railway carriages. However, for the case of the resole type of phenolic resin, water due to condensation reaction remains in the matrix, and this water evaporates resulting in the formation of voids during curing process. In order to develop a new type of phenolic composite that be able to overcome this weakness, we used a foam type of phenolic resin and glass fibers as the matrix and as the reinforcement, respectively. We then developed a new pultrusion technique for the new composite, namely the phenolic foam composite (PFC) and examined its mechanical properties and thermal conductivity. In this paper, we reported a new technology to mold not only a phenolic foam composite but also a sandwich beam in which the PFC as a core and a thin phenolic GFRP or CFRP as facelayers were used. We also examined thermal and bending properties of this sandwich beam.

**Keywords:** phenolic foam core, GFRP, CFRP, pultrusion, bending rigidity, flammability.

## 1. INTRODUCTION

Phenolic resin has excellent properties of fire resistance, low smoke during burning, and it also has a good balance between its cost and mechanical properties compared with other types of resin used in FRPs. If

phenolic resin can be employed as the matrix of FRP, such FRP can have a higher fire safety rate and this is a desirable property for the structures of vessels and railway carriages. Since the viscosity of the resole type of phenolic resin is higher than that of other types of resin, the diluted resole type of phenolic resin with water is used as the matrix. Moreover water is also produced due to the condensation reaction of phenolic resin during the curing process. The matrix using this phenolic resin becomes inhomogeneous due to the voids by evaporated water after the curing process. In order to develop a new type of phenolic composite that can overcome its weakness, we fabricated a beam type of phenolic foam composite using phenolic foam as the matrix and glass fibers as the reinforcement and evaluated its mechanical and thermal properties. This new type of phenolic foam composite had the advantages of light weight and high insulation and could be sawed and/or attached to natural wood with nails because the glass fibers were surrounded by the phenolic foam in the beam. This phenolic foam composite is designated as a PFC in this paper.

The result of flammability test of the PFC indicated that prevention of exhaust gas from the surface of the PFC was important in order to improve its fire resistant property<sup>1-3</sup>. For this reason, we devised a method to cover the upper and the lower surfaces of the PFC with a thin phenolic GFRP or CFRP. This thin FRP consisted of glass or carbon fibers with a higher volume fraction and conventional phenolic resin. The glass or carbon fibers were impregnated with phenolic resin and were placed on the upper and lower surfaces of the PFC beam and they were pultruded together with the PFC. This method could mold the PFC covered with the thin FRP sequentially and unified them without any adhesive process. As a result, uncertain adhesive strength between the PFC and the covering thin FRP could be avoided. This composite looks like a sandwich beam and is denoted as a SWPFC here. The proposed method in this paper can mold an arbitrary length of sandwich beam without adhesive process and its core being reinforced by glass fibers is stronger than a conventional foam core.

## **2. MOLDING METHOD**

### **2.1 Outline of molding method of PFC**

In order to mold the PFC, a pultrusion technique, which can manufacture the FRP having a uniform cross section with an arbitrary length, is very useful because the volume and arrangement of fibers in the cross section of FRP can be almost kept constant. We developed a new system of pultrusion

facilities. In the conventional pultrusion method, the roving glass fibers pulled from a roving rack are impregnated with resin in resin bath before introducing to an iron die, or are impregnated with the injected resin in the interior of die. When the resin of a foam type was used as the matrix with a foaming agent and curing agent, we could not use both ways stated above because phenolic resin including the foaming agent in the resin bath started foaming in a few minutes after mixed with curing agent. In order to solve this problem and to mold the PFC, we developed the feeding machine and the impregnation jig and also selected a special glass roving called a bulky roving. We revised a new system of pultrusion facilities for the PFC as shown in Figure 1. In addition, the foaming start of mixed phenolic resin with curing agent must be controlled in the die successively. We decided the conditions to control the time before foaming and the time during foaming and these times effected on a pulling velocity in the experiments. Furthermore the enough expansion ratio before and after foaming to mold phenolic foam composites was obtain to control the environmental temperature.

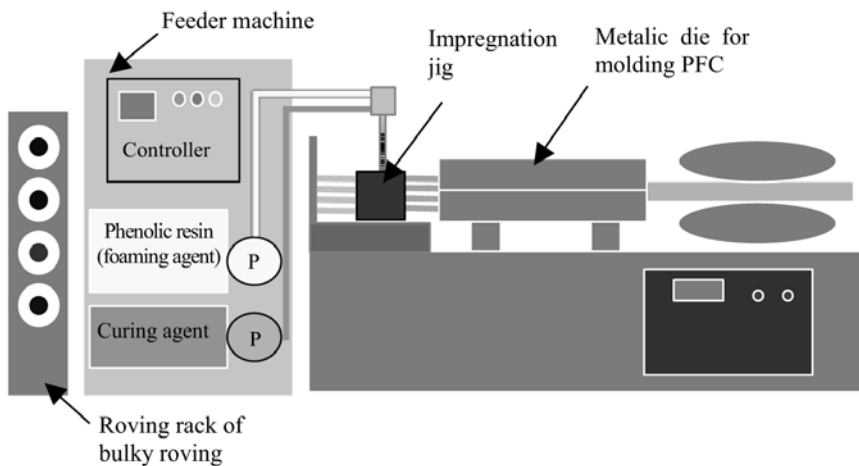


Figure 1. Pultrusion facilities for molding PFC.

## 2.2 Experiment of molding SWPFC

The SWPFC was also molded the same way as the PFC by the pultrusion technique. Based on the molding method of the PFC, we devised a new system of pultrusion facilities of the SWPFC as shown in Figure 2. A resin bath, roving guides and a metallic die shown in Figure 2 inside the bold squares were added to the PFC facilities in order to cover the upper and the lower surfaces of PFC beam with the thin phenolic FRP layer. These added facilities were placed on the same line of molding the PFC. Although the cross section of the molding die for the PFC was 52mm×32mm, the fabricated section of the PFC was about 51.4mm×31.4mm. Since the thickness of the covering thin phenolic FRP was set to 0.5mm as the design value, the section size of the metallic die for covering the PFC was set as 52.4mm×32mm.

There were some differences in the molding conditions between the PFC and the covering thin phenolic FRP layer. We used glass yarn or carbon fibers as the reinforcement of the covering FRP layers against the bulky glass roving for the PFC. Next, the phenolic resin foam used as the matrix of the PFC was cured by acid reaction, while the covering FRP layers were molded by a heat curing. In Table 1, the molding conditions for the PFC and the covering FRP layers are shown. Although the molding method of covering the FRP layers was the same as the conventional pultrusion, it was important that each of glass roving or carbon fibers was arranged accurately and was introduced into the metallic die to mold the covering FRP layers with the uniform thin thickness. As a result, we were able to mold the PFC and sequentially the SWPFC beam by the same line.

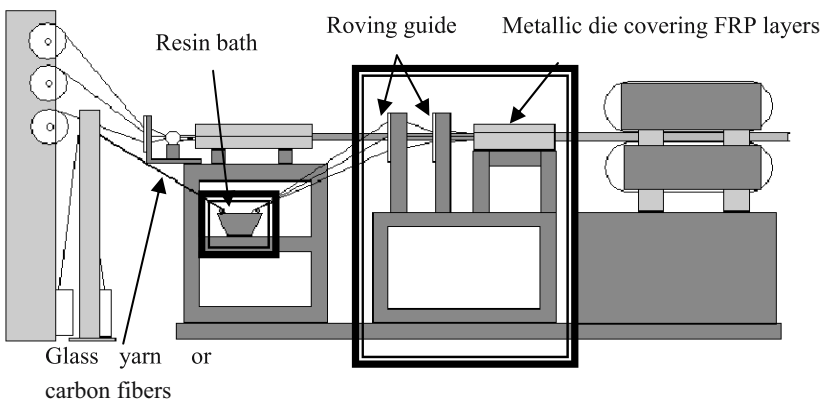


Figure 2. Pultrusion facilities for molding SWPFC.

Table 1. Conditions of molding.

	PFC	GFRP	CFRP
Molding method	Pultrusion (Impregnation jig)	Pultrusion (Resin bath)	Pultrusion (Resin bath)
Reinforcement	Glass fiber (Bulky roving)	Glass fiber (Yarn)	Carbon fiber (Roving)
Matrix	Phenolic resin (with foaming agent)	Phenolic resin	Phenolic resin
Curing method	Acid cure	Heat cure	Heat cure
Die temperature	75°C (max)	180°C (max)	180°C (max)
Content of reinforcement	6vol%	56vol%	53vol%

Since the pultrusion facilities for molding PFC were placed in the front part of the system as shown in Figure 2, the path of glass yarns for covering the surface had to be set properly. For the regular intervals of glass yarns on the upper and the lower surfaces of PFC, the path of glass yarns were fixed by the two yarn guides. In addition, an arrangement and the size of holes in the guides were important to place the yarns for molding the covering FRP with the uniform thickness so that no cracks are formed. The holes with diameter of 2.5mm could squeeze out of phenolic resin properly for keeping uniform volume fraction.

In order to determine the arrangement of holes, we prepared two types of guides of (a) and (b) as shown in Figure 3. The holes of Type (a) were arranged in one line and the angles of roving glasses being introduced to the die were same. On the other hand, the holes of Type (b) were arranged in two lines and the angles from two lines were different and the intervals of holes were smaller than Type (a). Table 2 lists the specification of these roving guides and Figure 4 shows the surface of photographs of the trial products of SWPFC with covering GFRP layer by using Type (a) or (b), respectively. The glass fibers were concentrated on the edges in Type (a) and the covering FRP layer was not fabricated uniformly. On the other hand, the uniform covering FRP layer was obtained in the case of Type (b).

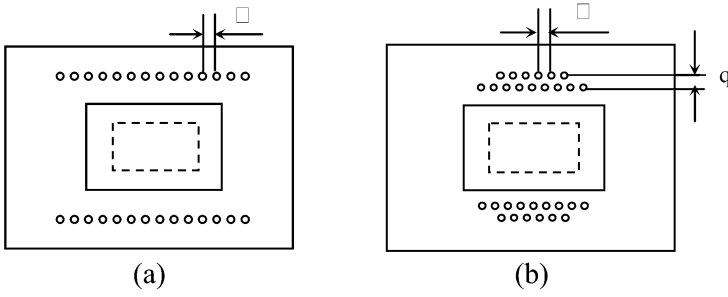


Figure 3. Roving guides.

Table 2. Specifications of roving guides.

	First guide			Second guide		
	Interval p[mm]	Gap g [mm]	Hole diameter [mm]	Interval p [mm]	Gap g [mm]	Hole Diameter [mm]
Type - a	8	–	2.5	6	–	2.5
Type - b	6	10	2.5	4	10	2.5

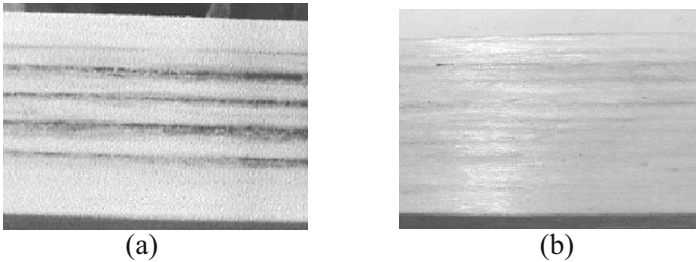


Figure 4. Surface layers in Type (a) and (b) .

### 3. EVALUATION OF SWPFC

#### 3.1 Observation

A trial product of the SWPFC by using Type (b) guide is shown in Figure 5. The thin GFRP or CFRP layer was molded in uniform thickness. The glass yarns or carbon fibers placed uni-directionally and the appearance of surfaces of SWPFC was very smooth. The results of measurement for the section size and the thickness of FRP layer are listed in Table 3. These values remained within the original design values and the FRP layer could be molded with high quality because its standard deviation was small.

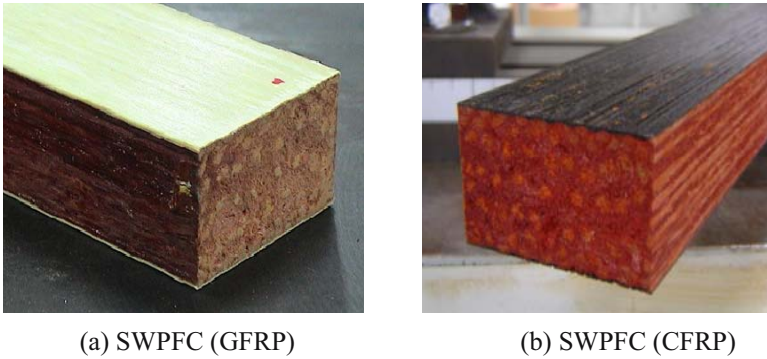


Figure 5. Appearances of SWPFC.

Table 3. Measurement size of SWPFC.

	Height	Width	Thickness of FRP layer
Average [mm]	32.4	51.6	0.514
Standard deviation	0.06	0.06	0.084

### 3.2 Measurement of thermal conductivity

In order to evaluate the thermal insulation performance of SWPFC, we measured the thermal conductivity of the SWPFC. The experimental result is listed in Table 4. Generally speaking, the smaller value of thermal conductivity means the higher thermal insulation. The thermal conductivity of SWPFC with the CFRP layer was a little larger than that of SWPFC with the GFRP layer because the thermal conductivity of carbon fibers was larger than that of glass fibers. The thermal conductivities of SWPFC were almost the same as that of PFC and these values indicated that the thermal insulation performance of SWPFC was sufficiently higher.

Table 4. Thermal conductivity.

	Thermal conductivity [W/mk]
PFC	0.0610
SWPFC (GFRP)	0.0601
SWPFC (CFRP)	0.0673

### 3.3 Flammability test

In order to verify the prevention of exhaust gas by using the GFRP and the CFRP layers for a fire, a flammability test was carried out. The outline of this test was to irradiate a heat of  $50\text{kW/m}^2$  on the surface of specimen by a radiation electricity heater and simultaneously to operate an electricity spark. The exhaust gas from the test specimen was collected and its mass, heat release value and heat released rate were measured. The flammability test was executed in 20 minutes for three kinds of specimen including the PFC specimen. The heat release rate means the change of heat value in a unit time. If the heat release rate for some material increase, such material is in danger of a big fire.

The result of the flammability test is shown in Table 5. The result of SWPFC with the GFRP layer was superior to that of SWPFC with the CFRP layer because of being smaller of the thermal conductivity of glass fiber than that of carbon fiber. In the case of comparison with the PFC, the fire-resisting property of SWPFC was improved, in particular the total heat release of SWPFC was  $2/3$  of PFC and it showed that the flammability of SWPFC was improved 1.5 times of that of PFC. The heat release late and the lost mass of SWPFC was also smaller than those of PFC. Then these results showed that the thin covering FRP layer with high volume fraction of fibers was effective for the improvement of flammability.

Table 5. Results of flammability test.

		PFC	SWPFC (GFRP)	SWPFC (CFRP)
Total heat release	[MJ/m <sup>2</sup> ]	23.06	15.31	16.48
Heat release rate (max.)	[kW/m <sup>2</sup> ]	112.06	86.72	93.68
Lost mass	[g]	12.73	9.14	9.49
Time until ignition	[sec]	60.8	96.6	70.7
Crack penetration		none	none	none

### 3.4 Bending test

The three-point bending test was carried out in order to evaluate the bending properties of SWPFC covered with the GFRP or the CFRP layers and their results are listed in Table 6. The bending rigidities of SWPFC with the GFRP and with the CFRP were about 1.8 times and 3 times as large as that of PFC, respectively. The bending strengths of both SWPFC were 4 times as large as that of PFC. We also evaluated the bending rigidity by a sandwich beam theory. The comparison between the experimental value and that obtained by the sandwich beam theory for the bending rigidity is shown in Figure 6 and they showed a good agreement.

Table 6. Results of bending test.

	Density [g/cm <sup>3</sup> ]	Modulus of Elasticity [GPa]	Bending strength [MPa]
PFC	0.40	4.95	14.8
SWPFC (GFRP)	0.44	8.83	63.5
SWPFC (CFRP)	0.42	14.58	65.7

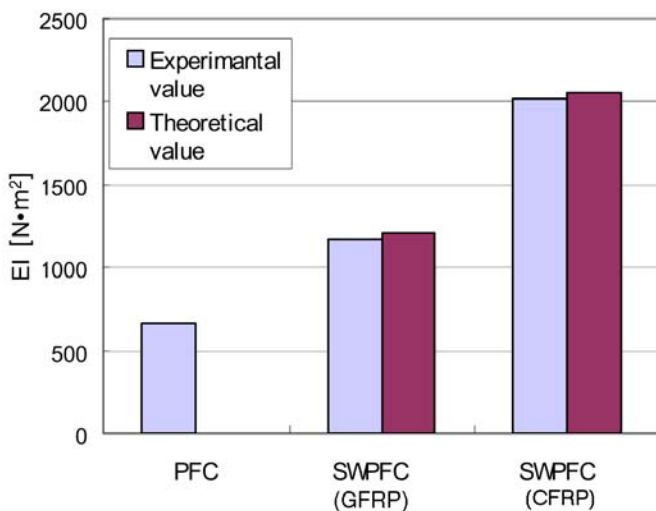


Figure 6. Comparisons of experimental value with theoretical one for bending rigidity.

## 4. CONCLUSIONS

A pultrusion technique to mold a new type of sandwich beam having the foam core reinforced with glass fibers and the surface layers of the FRP (SWPFC) were demonstrated. In this method, the SWPFC was sequentially pultruded by the same line of molding the PFC used as the core. The thin surfaces of SWPFC were smooth and both surfaces of GFRP and CFRP layer were molded higher quality. The thermal conductivities of SWPFC with the GFRP and with the CFRP layer were almost the same as that of PFC and their thermal insulation were sufficiently high. The fire resistance of SWPFC was improved because that the layer of GFRP or CFRP having the higher fiber content preventing the gas from the surface of PFC. The bending rigidities of SWPFC with the GFRP and with the CFRP were about 1.8 times and 3 times as large as that of PFC, respectively. The bending strengths of both of SWPFC were 4 times as large as that of PFC.

## REFERENCES

1. G. Ben and A. Shoji, "Development of Pultrusion Techniques of Phenolic Foam Composite" (in Japanese), *The Journal of the Society of Materials Science Japan*, Vol.52, No. 11, pp. 1379–1384 (2003).
2. G. Ben and A. Shoji, "Development of Pultrusion Thechniques of Phenolic Foam Composites", Report of the Research institute of Industrial Technology, Nihon University, No. 69, pp. 1–10 (2003).
3. G. Ben, A. Shoji and Y. Aoki, "Development of Pultrusion Techniques of Phenolic Foam Composite", *Proceedings of the 10th U.S.-JAPAN Conference on Composite Materials*, pp. 412–419 (2002).

# EXPERIMENTAL AND NUMERICAL ANALYSIS OF HOLLOW AND FOAM-FILLED A-STRINGER/A-FORMER UNDER AXIAL COMPRESSION LOAD AND BENDING MOMENT

René Krämer and M. Alexander Roth  
*DEGUSSA, Röhm GmbH & Co. KG*

**Abstract** The topic of this investigation deals with experimental and numerical analysis of different configurations of hollow and of PMI foam-filled A-stringers/A-formers under axial compression load and bending moment. In this connection the Finite-Element-Analysis (FEA) program ANSYS® is used for the numerical approach. The result of this analysis is that PMI foam-filled A-profiles show significant higher buckling loads in comparison to hollow ones. These improvements depend on the loading conditions, e.g. bending moment and axial compression, as well as the geometry of the A-profile.

**Keywords:** A-stringer, A-former, foam-filled, hollow, axial compression, bending moment.

## 1. INTRODUCTION

This study deals with hollow and PMI foam-filled (ROHACELL®, Röhm GmbH & Co. KG) A-stringers/A-formers with face sheets out of carbon fibre reinforced plastics (CFRP) under axial compression load and bending moment.

Sandwich structures are generally made up of one upper and lower thin and stiff face sheet, which are supported by a thick low density core material [1]. These three components are bonded with two adhesive layers. Sandwich structures have a high bending stiffness and strength to weight ratio in comparison to monolithic structures. This sandwich principle is primarily used for light weight transport applications (e.g. aircrafts, trains,

trucks, cars, boats) and is well known as a natural design concept, e.g. bones and botanical stems [2].

The use of stringer profiles has proven to be the most suitable method for stiffening thin CFRP-shells, typically used as engine air inlet duct panels or engine cowling panels. The most effective stiffening can be achieved by using A- or hat-profiles, e.g. A-stringer or A-former [3]. Structural ROHACELL<sup>®</sup> sandwich foam cores are successfully used in a number of such kinds of aircraft applications. One of the most prominent applications is the air inlet duct panels for the centre engine of the Boeing MD 11 aircraft (Figure 1).

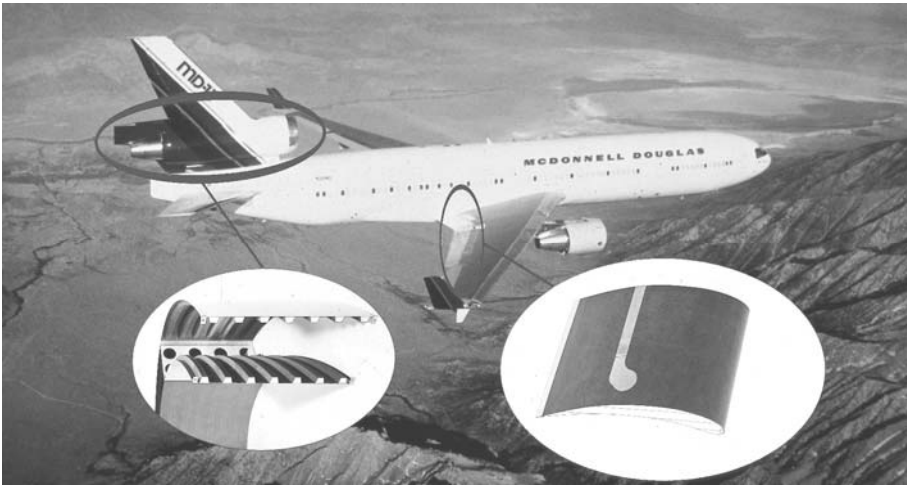


Figure 1. Boeing MD11.

The precisely CNC-machined and thermoformed-to-shape foam profiles contribute to significant cost savings during lay-up. High-performance PMI foam cores offer excellent resistance to creep compression during the cure, resulting in a thorough laminate consolidation without surface dimpling effects. In contrast to honeycomb cores, the isotropic cellular structure of PMI foams provides dimensional stability also against lateral pressure during the autoclave cure, eliminating the necessity of core profile stabilizers, typically used for honeycomb cures. Also the foam core evenly transfers the autoclave pressure to the surface layers of the shell underneath, resulting in a good consolidation without any marks or other surface imperfections. One of the latest applications for foam-filled stringer profiles is the rear pressure bulkhead of the Airbus A340 and A340-600. To date, 1700 CNC-machined and net-shape-thermoformed ROHACELL<sup>®</sup> 71WF-HT stiffeners for the A340 have been delivered ready-to-use to the Airbus plant in Stade, near Hamburg. The net-shaped foam serves as a mandrel during lay-up and cure.

Its high resistance to creep compression and excellent dimensional stability during the cure make it possible to apply the cost effective one step co-curing process at a temperature of 180°C (356°F) and a pressure of 0.35 MPa (50 Psi) for 2 hrs. The PMI foam ensures perfect prepreg consolidation on all surfaces of the stringer profile. Thus it is the perfect substitution of inflatable bladder tools known for high reoccurring costs and a lot of problematic handling issues. More than 170 bulkheads have been successfully manufactured without a single rejection. This underlines the reliability of the process and processing of the ROHACELL® A-stringers. Based on the success of the new A340 bulkhead configuration, incorporating the ROHACELL® foam-filled stringers, the technology concept was adopted for the rear pressure bulkhead of the A380 as well. In this case the foam stringer profiles are up to 2.5 m long with a significantly more complex geometry. The ease of machining and net-shape thermoforming of ROHACELL® was the key for the successful implementation of the foam-filled A-stringer design. To date, 200 ready-to-use foam stringer profiles have already been delivered to Airbus. More than 10 of the large bulkheads have been cured successfully, with zero rejections.

The following case history discusses the potential of a bi-functional usage of PMI foam cores for realizing cost and weight optimized A-stringer profiles. It will be discussed that the foam core can serve as a mandrel during lay-up and cure and as a structural member of the stringer component [3], [4]. Significant weight reductions are being realized by using sandwich constructions in present and future aircraft, and by allowing operation in the postbuckling regime [4]. Foam-filled A-stringers or A-formers (see Figure 2, right) can improve the strength and the fatigue life of the stiffener and the skin/stiffener interface in comparison to hollow A-stringers or A-formers (see Figure 2, left) [3], [4].

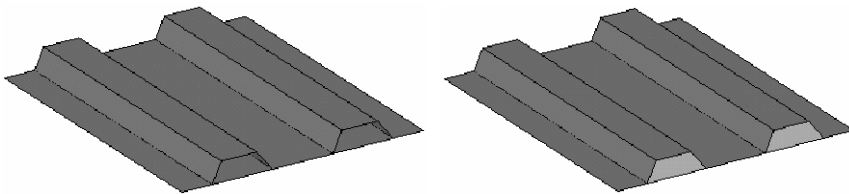


Figure 2. Comparison of hollow (left) and PMI foam-filled A-stringers (right).

Due to its high compressive strength, the foam generates a profile stabilizing effect, which can allow for weight reduction by reducing the number of prepreg plies in the sandwich component. The stability problem of thin-walled composite structures under bending and axial compression loads is very well known. Buckling always occurs in the compression loaded

areas before reaching the actual compression strength of the component. A well proven design approach is to increase the buckling resistance of a shell structure by means of stiffening profiles bonded to the shell. Hollow profiles, however, tend to buckle in the side walls and in the flanges, resulting in premature failure. In contrast to the hollow profile a ROHACELL® foam-filled profile is stabilized by the structural performance of the core, and will maintain its geometry and its strength properties until the yield load. The in-plane compression load of foam-filled A-stringer, where initial buckling effects occur first, can be increased by up to 100 % in comparison to a hollow one (Figure 3) [4]. Furthermore the breakage of foam-filled A-stringer is increased up to 42 % in comparison to a hollow one [4]. This means greater exploitation of the strength properties of the CFRP-skins. The main structural loadings for the core are tensile and compression perpendicular to the sidewalls of the profile.

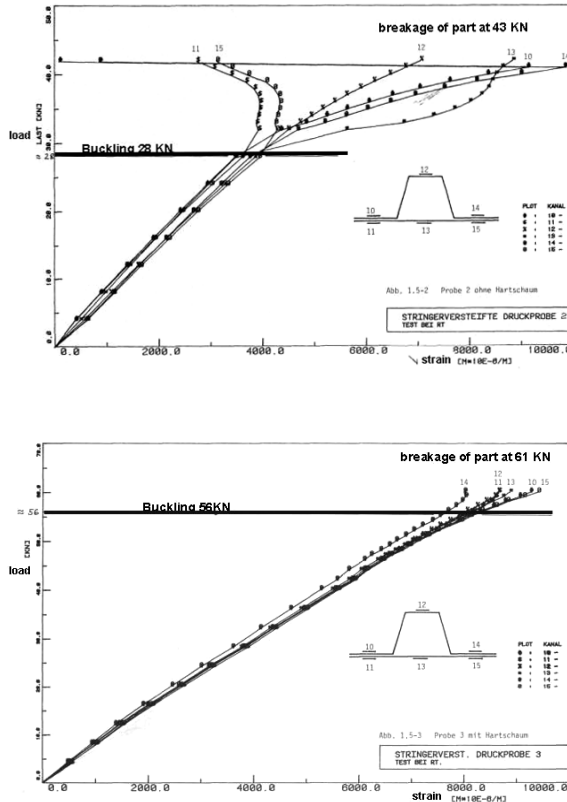


Figure 3. Load/strain-diagram of hollow (top) and PMI foam-filled A-stringers (bottom) under static axial compression load [4].

## 2. CONFIGURATION OF A-FORMER

In this chapter the geometry, lay-up and the used material of the numerical analysed thin CFRP-shell stabilized by A-former are discussed. Furthermore the manufacturing process and the both load cases, i.e. four-point-bending and axial compression, are presented.

### 2.1 Geometry, lay-up and material

The geometry and a picture of a thin CFRP-shell stabilized by PMI foam-filled A-former are shown in Figure 4. The A-former consists of an outer belt, web and an inner belt. A hollow monolithic as well as a PMI foam-filled A-former stabilized shell are analysed in this investigation. The hollow and the PMI foam-filled A-former stabilized shell are manufactured with the aid of a co-curing autoclave process. After the curing process, the foam has to be removed to realize the hollow variant.

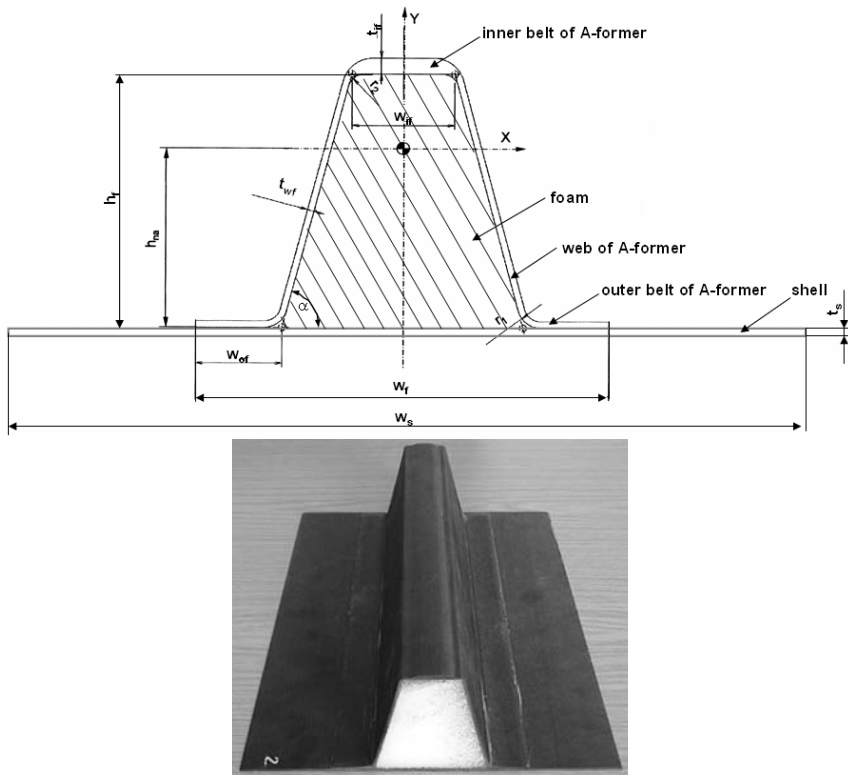


Figure 4. Sketch and picture of the thin CFRP-shell stabilized by PMI foam-filled A-former.

The deviations of the thin CFRP-shell stabilized by A-former are shown in Table 1.

Table 1. Geometry of the thin CFRP-shell stabilized by A-former.

Description	
width of shell $w_s$ [mm]	240
width of A-former $w_f$ [mm]	120
width of the outer belt of A-former $w_{of}$ [mm]	25
width of the inner belt of A-former $w_{if}$ [mm]	35
thickness of shell $t_s$ [mm]	2.422
thickness of the outer belt of A-former $t_{of}$ [mm]	1.9
thickness of the web of A-former $t_{wf}$ [mm]	1.9
thickness of the inner belt of A-former $t_{if}$ [mm]	4.65
height of A-former $h_f$ [mm]	80
angle of A-former $\alpha$ [°]	77.7

The lay-up of the thin shell as well as the outer and inner belt and the web of the A-former are shown in Table 2. Tapes (T) and fabrics (F) made of carbon fibre reinforced plastics with an epoxy resin matrix as prepreg are used for the face sheets. As core material ROHACELL® 71 WF-HT is used [5].

Table 2. Lay-up of shell as well as outer and inner belt and web of A-former.

	material (Fabric, Tape)	angle [°]	thickness [mm]
shell	( $\pm F/(T)_{16}/\pm F$ )	( $\pm 45/(0)_2/(90)_2/(0)_3/+45/-45/(0)_3/(90)_2/(0)_2/\pm 45$ )	2.422
outer belt of A-former	( $\pm F$ ) <sub>9</sub>	( $\pm 45$ ) <sub>9</sub>	1.9
web of A-former	( $\pm F$ ) <sub>9</sub>	( $\pm 45$ ) <sub>9</sub>	1.9
inner belt of A-former	(( $(\pm F/(T)_3$ ) <sub>2</sub> )/ $\pm F/(T/T/\pm F/T)_3$ /T/ $\pm F/((T)_3/\pm F)_2$ )	(( $(\pm 45/(0)_3$ ) <sub>2</sub> )/ $\pm 45/(0/0/\pm 45/0)_3/0/\pm 45/((0)_3/\pm 45)_2$ )	4.65

## 2.2 Load cases

Typical load cases of thin shells stabilized by A-formers are axial compression load as well as pure bending moment. In this case a four-point-bending test (see Figure 5, left) and a axial compression test (see Figure 5, right) are chosen to determine the stability behaviour of PMI foam-filled A-former in comparison to monolithic one. The specimens of the A-former stabilized shell are reinforced in the area of the load transmissions and the bearings to avoid local instability due to the high stress concentration. As a result of these reinforcements, stability problems can be achieved in the middle of the specimens during the four-point-bending test, i.e. in the area of pure bending moment and free transverse force, as well as in the middle of the specimens during the axial compression test.

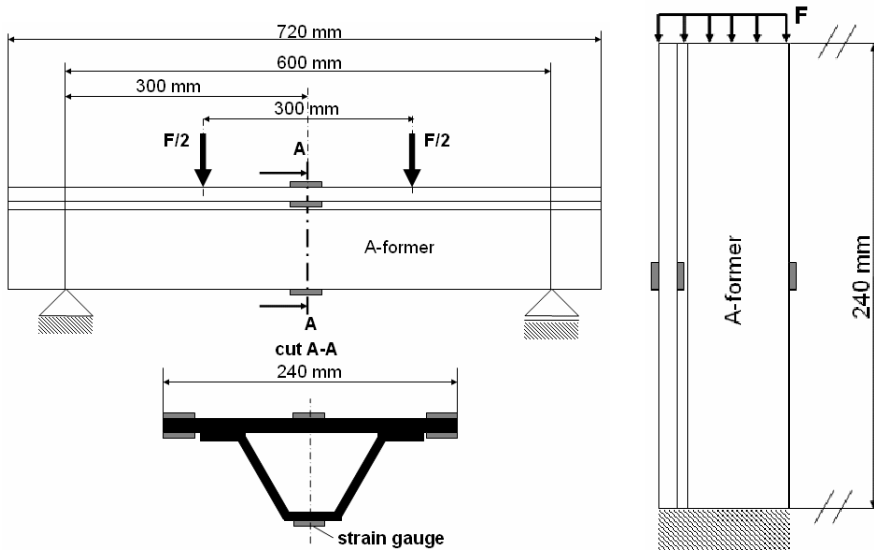


Figure 5. Sketch of the four-point-bending test (left) and axial compression test (right).

### 3. NUMERICAL ANALYSIS

In the following chapter the PMI foam-filled and the monolithic A-former stabilized shell are analysed under pure bending moment and axial compression load with the aid of the numerical FEA program ANSYS® [6]. The CFRP-face sheets are modeled with suitable layered shell elements, which are defined by eight nodes, average layer thickness, layer material direction angle and the orthotropic material properties. The core material of the PMI foam-filled A-former are modeled with 20-nodes solid elements.

The force/strain-diagram of the thin shell stabilized by monolithic A-former in the critical area of the web under bending moment are shown in Figure 6. Furthermore the deformed structure at special load steps are presented to demonstrate the buckling of the web. The buckling load is 28.9 kN. By using a PMI foam, the webs of the A-former are stabilized and reinforced. Therefore the buckling load in the web is increased up to 49 kN, i.e. 69.6 % (see Table 3).

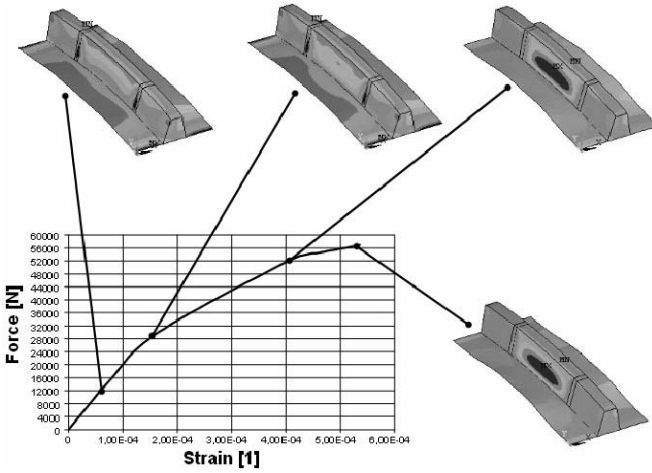


Figure 6. Force/strain-diagram of monolithic A-former stabilized shell in the critical area of the web.

In Figure 7 the force/strain-diagram of the thin shell stabilized by monolithic A-former in the critical area of the shell under bending moment including the deformed structure at special load steps are shown. The buckling load of the thin shell is 31.7 kN. In comparison to the monolithic one the buckling load can be increased up to 34.9 kN by using a PMI foam-filled A-former (see Table 3), In this case, an improvement of approximately 10.1 % can be realized. Therefore, the core material has a higher influence on the buckling load of the web than on the buckling load of the shell.

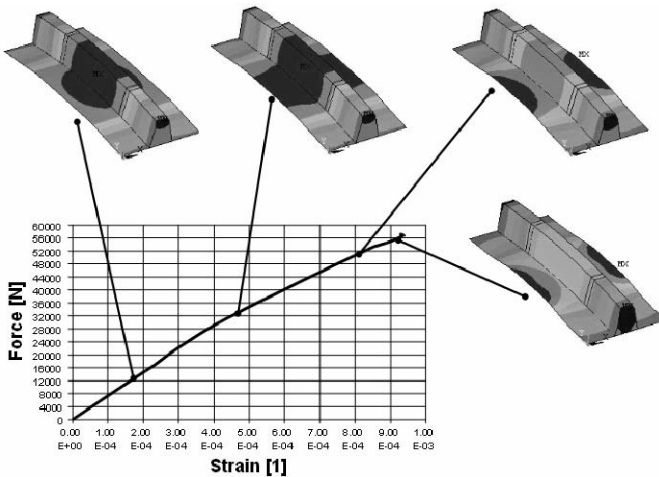


Figure 7. Force/strain-diagram of monolithic A-former stabilized shell in the critical area of the thin shell.

Table 3. Buckling loads of monolithic and of PMI foam-filled A-former stabilized shell under bending moment.

	buckling load of monolithic A-former [kN]	buckling load of PMI foam-filled A-former [kN]	Improvement [%]
web	28.9	49.0	69.6
shell	31.7	34.9	10.1

In Figure 8 the force/strain-diagram of the thin shell stabilized by monolithic (dark grey curve) and stabilized by PMI foam-filled A-form<sup>er</sup> (light grey curve) under axial compression load is shown. The buckling load of the shell can be increased from 47.3 kN to 54.8 kN by using PMI foam-filled A-former (see Table 4).

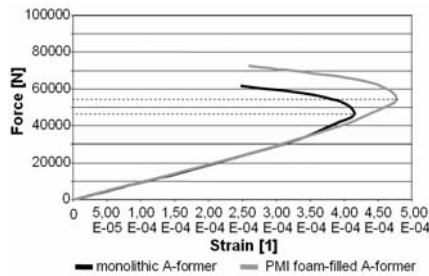


Figure 8. Force/strain-diagram of monolithic and of PMI foam-filled A-former stabilized shell under axial compression load

Table 4. Buckling loads of monolithic and of PMI foam-filled A-former stabilized shell under axial compression load

	buckling load of monolithic A-former [kN]	buckling load of PMI-foam-filled A-former [kN]	Improvement [%]
shell	47.3	54.8	15.9

Furthermore, the thickness of the inner and outer belt and the web of the A-former are reduced to achieve the same structural behaviour of the monolithic A-former. As a result of this investigation, it is shown that the thickness can be decreased up to 17 % by using a PMI foam as structural member, through which one to two CFRP-fabric layers can be saved in comparison to a monolithic A-former. Therefore the whole weight and cost of a thin shell stabilized by PMI foam-filled A-former can be reduced.

Furthermore, different geometrical variants of monolithic and PMI foam-filled A-formers are analysed. The improvement of buckling load by using a PMI foam depend on the thickness of the used face sheet of the A-former, i.e. the thinner the face sheet the higher the increase of buckling load.

## 4. SUMMARY

Using PMI foam cores (ROHACELL<sup>®</sup>) as a mandrel to realize A-stringer/A-former profiles, offers significant cost saving during lay-up and cure of the component. Prepreg can be easily draped over the foam mandrel. The isotropic cellular structure and excellent resistance to compression creep during autoclave cycle make it possible to use the one step co-curing process. It can also be concluded that a PMI foam-filled A-former can contribute to increasing the stability and buckling resistance of a thin-walled CFRP-structure significantly. If ROHACELL<sup>®</sup> is also used as a structural member, the wall-thickness of the covering CFRP face sheets can be reduced by approximately one to two plies, offering a “weight-neutral” solution compared to a monolithic A-former. Thus the bi-functional usage of the PMI foam, serving as a mandrel and as a structural member of the sandwich design, would exploit the full inherent cost and weight saving potential of the ROHACELL<sup>®</sup> foam-filled stiffener design.

## 5. FURTHER WORKS

The numerical results of the analysed geometry of the thin shell stabilized by monolithic and by PMI foam-filled A-former have to be validated with experimental examination. Therefore, a four-point-bending as well as the axial compression test facility will be used.

## REFERENCES

1. Zenkert, D., *The Handbook of Sandwich Construction*. London, United Kingdom: Engineering Materials Advisory Services Ltd., 1997.
2. Nachtigall, W., *Bau-Bionik Natur – Analogien – Technik*. Berlin, Heidelberg, New York: Springer-Verlag, 2003.
3. Ames, H., Rother, M., *Untersuchung über eine kostengünstige CFK-Bauweise für längs- und radialversteifte Schalen*. Endbericht, Dornier GmbH, 1983.
4. Alsup, P.J., *A comparison of composite hat stiffeners using Teflon and remain-in-place foam mandrels subjected to static and fatigue loads*. Air Force Wright Aeronautical Laboratories, 1985.
5. DEGUSSA, Röhm GmbH & Co. KG, Data CD “ROHACELL<sup>®</sup> - The Core for Sandwich Solutions”, July 2004.
6. Swanson Analysis Systems, Inc., *ANSYS Release 8.0 Documentation*. Houston Texas: 2004.

## AUTHOR INDEX

- Aboura, Z., 681, 823  
Agrawal, U., 997  
Allaoui, S., 823  
Aviles, F., 121  
Backström, D., 567  
Bahei-El-Din, Y.A., 107  
Banos, M., 153  
Battley, M., 537  
Becker, W., 301  
Belouettar, S., 211  
Ben, G., 1007  
Benzeggagh, M., 681, 823  
Berger, L., 433, 441  
Berggreen, C., 393, 403, 451, 461, 947  
Bhargava, A., 131  
Bintruy, C., 693  
Bogdanovich, A., 625  
Borsellino, C., 967  
Borum, K.K., 805  
Bozhevolnaya, E., 67, 77, 161  
Branner, K., 947  
Bratfisch, J.P., 763  
Breder, J., 537  
Burman, M., 171  
Calabrese, L., 967  
Cantwell, W., 433  
Carlsson, L.A., 121, 423  
Cartié, D., 865  
Casari, P., 865, 895, 905  
Cecchini, A., 143  
Chen, H., 131  
Christensen, R.M., 117  
Christiansen, J., 773  
Chubinskiy, A.V., 605  
Coffelt, R.A., 625  
Compston, P., 487, 643  
Cripps, B., 507  
Das, M., 497  
Davies, P., 865, 895  
Daya, E., 211  
de Almeida, S.F.M., 221  
de Freitas, M., 271  
Demiray, S., 301  
den Haan, L., 713  
Denli, H., 587  
Du, S., 815  
Ducret, C., 703  
Dvorak, G.J., 107  
Edinger, S., 537  
Elkin, R., 433, 441  
Fan, X., 875  
Feichtinger, K., 433, 441  
Ferreira, A.J.M., 231  
Ferreira, C., 905  
Frostig, Y., 47, 251  
Gielen, A.W.J., 87, 477  
Giletti, M., 703  
Göttner, W., 661  
Goutianos, S., 915  
Grenestedt, J.L., 835  
Grogan, J., 625  
Hallström, S., 935  
Hamed, E., 261  
Hansen, J.S., 221  
Hansen, M.R., 653  
Hao, H., 671  
Hassinen, P., 471  
Hayman, B., 27, 393  
Herrmann, A.S., 13  
Hill, M., 373  
Hirschmann, M., 845  
Hohe, J., 97, 301, 527, 925  
Hookham, N., 373  
Hu, H., 211  
Ionita, A., 193  
Jacquemin, F., 905  
Jahn, T., 753  
Jamali, M.J., 341  
Jeelani, S., 183  
Jensen, D.K., 783  
Jensen, J.F., 947  
Joe, C.-R., 671  
Jolma, P., 403  
Jorge, R.M.N., 231  
Just, F., 153  
Just-Agosto, F., 144  
Kadivar, M.H., 341  
Kadyrov, S., 519

- Kalyanasundaram, S., 487, 643  
 Karczmarzyk, S., 577  
 Kardomateas, G.A., 57  
 Kärger, L., 321  
 Kennedy, G., 221  
 Kepler, J., 653  
 Khellil, K., 681  
 Khitrov, V.V., 291  
 Kim, D.-U., 671  
 Koissin, V., 885  
 Kopp, R., 723  
 Körner, C., 845  
 Krämer, R., 1017  
 Krawczak, P., 693, 703  
 Lacrampe, M.-F., 703  
 Lagardere, E., 703  
 Lascoup, B., 681  
 Le Roy, G., 693  
 Leite, M., 271  
 Leng, J., 815  
 Li, X., 193  
 Librescu, L., 97, 527  
 Lindholm, C.-J., 635  
 Linke, M., 311  
 Liu, Y., 815  
 Lolive, E., 895  
 Loup, D.C., 87, 121, 477  
 Lund, E., 351  
 Lundsgaard-Larsen, C., 451  
 Lyckegaard, A., 67, 77, 161, 773  
 Madenci, E., 497  
 Mahfuz, H., 183, 423  
 Matsuda, M., 557  
 Matsuzaki, S., 733  
 Matteson, R.C., 87, 121  
 Meyer-Piening, H.-R., 201  
 Minakuchi, S., 383  
 Mispreve, H., 713  
 Morgenthaler, M., 433, 441  
 Nageswara Rao, G., 997  
 Naik, N.K., 997  
 Nilsson, A., 567  
 Nishiyabu, K., 733, 743  
 Nøkkentved, A., 451  
 Nutzmann, M., 723  
 Nygaard, J., 773  
 Oh, S.Y., 97, 527  
 Okabe, Y., 383  
 Okubu, K., 743  
 Østergaard, R.C., 413  
 Oya, N., 743  
 Pantelidis, N.G., 977  
 Passari, R., 967  
 Päßler, M., 957  
 Peake, N., 597  
 Pettersson, R., 393  
 Pflug, J., 331, 763  
 Polyakov, V.A., 291  
 Potier-Ferry, M., 211  
 Quispitupa, A., 153  
 Rabinovitch, O., 251, 261  
 Rajabi, I., 341  
 Rangari, V.K., 183  
 Razi, H., 497  
 Reimerdes, H.-G., 241, 311, 661  
 Reuterlöf, S., 855  
 Ribeiro-Ayeh, S., 935  
 Roque, C.M.C., 231  
 Roth, M.A., 987, 1017  
 Scherble, J., 753  
 Schledjewski, R., 957  
 Schultz, J.P., 947  
 Schwarts-Givli, H., 251  
 Segercrantz, S., 403  
 Sekine, H., 557  
 Serrano, D., 143  
 Shafiq, B., 143, 153  
 Sheno, R.A., 507, 547  
 Shipsha, A., 171, 885  
 Shirahata, H., 557  
 Shivakumar, K., 131  
 Shlitsa, R.P., 291  
 Shoji, A., 1007  
 Shukla, A., 625  
 Silva, A., 271  
 Simonsen, B.C., 461  
 Singer, R.F., 845  
 Skawinski, O., 703  
 Skvortsov, V., 281, 519  
 Sommer, M.M., 957  
 Sørensen, B.F., 413  
 Sorokin, S.V., 597, 605  
 Souma, M., 1007  
 Stack, M., 957  
 Stegmann, J., 351  
 Stenius, I., 537  
 Stronge, W.J., 615  
 Styles, M., 487, 643  
 Sun, J.Q., 587  
 Takeda, N., 383  
 Tanaka, S., 733, 743  
 Tekalur, S.A., 625  
 Theotokoglou, E.E., 423  
 Thomsen, O.T., 67, 77, 161, 281  
 Toftegaard, H., 915  
 Tomita, M., 743  
 Trask, R., 507  
 Trouwborst, W., 477  
 Uddin, M.F., 183  
 Valenza, A., 967  
 Vandepitte, D., 763, 875  
 van Santen, J., 723  
 Verpoest, I., 331, 763, 875  
 Vinson, J.R., 3

Vizzini, A.J., 363  
Vrettos, C.D., 423  
Wang, W., 547  
Weitsman, Y.J., 193  
Wetzel, A., 321  
Wohlers, W., 311  
Wulf, T.M., 795  
Xie, Z., 363  
Xu, X., 815  
Yanagisawa, T., 743

Yang, M., 363  
Zahlen, P.C., 13  
Zainuddin, S., 183  
Zenkert, D., 171  
Zhigun, V.I., 291  
Zhong, C., 241  
Zhou, D., 615  
Zhou, G., 373  
Zuardy, I., 13

# SUBJECT INDEX

- 3 point bending, 271
- 3D stress analysis, 321
- 3D structure, 693
- 3D weave, 625
- 3D woven composite, 997
- 4-point-bending test, 661
- adjustment, 471
- A-former, 1017
- air-coupled technique, 805
- aluminium foam, 487, 643
- anisotropic materials, 587
- armor panels, 625
- ASTM C273, 271
- A-stringer, 1017
- axial compression, 1017
- ballistic resistance, 625
- balsa, 835
- barely visible impact damage, 661
- beam, 567
  - theory, 221
- bending, 723
  - moment, 1017
  - rigidity, 1007
- Bernoulli–Euler, 567
- bicycle, 977
- blast, 107
- bonded specimen, 915
- buckling, 57, 461, 875, 947
- BVID, 507
- carbon nanotube, 743
- cellular, 935
  - materials, 171
- CFRP, 1007
- chaotic vibration, 527
- circular sandwich panels, 615
- closed cell foam core, 783
- co-injection moulding, 733
- column, 57
- composite, 321, 795, 957
  - adapted architecture, 13
  - laminated, 341
  - laminates, 351
  - materials, 131, 451
  - plates, 231
  - sandwich plate, 557
  - skins, 373
- compressible core, 261
- compressive
  - property, 743
  - strength, 393
- contact effects, 251
- continuous stiffening, 13
- core
  - compressibility, 301
  - crack, 805
  - effects, 97
  - inserts, 67
  - junctions, 77, 161
  - laminated, 835
  - material, 441, 713
- corrugated cardboard, 823
- co-sintering, 733
- cost,
  - effective processing, 713
  - optimization, 331
- cost/weight effectiveness, 13
- crack
  - extension, 121
  - propagation, 171
- creep, 703
- crushed foam core, 885
- cure simulation, 783
- curved sandwich beam, 547
- damage, 27, 653
  - assessment, 27
  - characteristics, 373
  - detection, 143
  - tolerance, 27, 403, 507, 865
- damping, 211, 671
- DCB, 121
- debond, 403, 805
  - damage, 451
- debonding, 383, 461
- deep drawing, 723
- defects, 27, 805
- delamination, 251, 363, 723
- density, 905
- design, 77, 161, 471

- disordered microstructures, 925
- double cantilever sandwich beam, 131
- dynamic, 537
  - loading, 477
  - response, 97
- E-beam cross-linking, 713
- effective 2D model for the C-C structure, 577
- effects
  - local, 77, 161
  - of sea water, 193
  - of viscosity, 605
- elastic panel response, 653
- elasticity, 57
- energy
  - absorption, 373
  - balance, 653
- EPP-foam, 957
- experiment, 471
- face sheet ply-angle, 97
- failure
  - criterion, 117
  - modes, 477
- fastening, 471
- fatigue, 153, 171, 183
  - crack growth, 423
- FEA, 875
- Fiber Bragg Grating (FBG), 815
- fibre optic sensor, 815
- field test, 795
- finite element, 211, 301, 311, 935, 321
  - analysis, 537, 915
  - dynamic, 107
  - method, 363, 423
- five-layer sandwich strip, 577
- flammability, 1007
- flexible core, 251
- flexural loading, 423, 487
- fluid-loaded sandwich plate, 597, 605
- foam, 193, 713, 935, 635
  - core, 753, 895, 905
  - core material, 855
  - foam-filled, 1017
  - mechanics, 925
- fracture, 117, 865
  - mechanics, 433, 461
  - toughness, 131, 413
- frame, 977
- FRP composite face
  - laminated, 557
- FRP sandwich structures, 27, 393
- functionally graded sandwich structure, 733
- fundamental frequency, 557
- fusion bonding, 763
- genetic algorithm, 341
- geometric constraint, 131
- GFRP, 1007
- glass/thermoplastic composites, 703
- GMT, 957
- graded core material, 67
- graded material, 773
- grid skin, 835
- Hamilton principle, 519
- high-order, 251
- high rate, 895
- high strain rate response, 87
- hollow, 1017
- homogenization, 221, 925
- honeycomb, 763
  - sandwich composite, 671
  - sandwich structures, 383
- hybrid structures, 835
- hygro-mechanical behavior, 823
- IDAK, 987
- impact, 363, 635, 681
  - behavior, 671
  - damage, 383, 615
  - low energy, 643
- indentation, 497, 635
- infinite strip, 291
- injection molding, 845
- inplane shear, 441
- insert, 997
- inspection, 795
- instrumentation, 895
- integral foam, 845
- interface fracture, 403
- J-integral, 413
- K-Cor<sup>TM</sup>, 865
- K-core, 661
- large deformation, 301, 925
- lateral pressure loading, 403
- layup optimization, 557
- LEFM, 413
- LFRT, 957
- limit point, 47
- linear elasticity, 577
- liquid silicone rubber, 671
- load introduction, 987
- local
  - bending effects, 67
  - free vibration, 547
  - loading, 885
  - semi-inverse approach, 577
- localized
  - effects, 47, 261
  - impact, 653
  - through-the-thickness loading, 997
- magnesium foam, 845
- manufacturing, 693, 855
- marine, 537
- material
  - efficiency, 331
  - selection, 331
- mechanical

- behaviour, 681
- properties, 967
- metal
  - injection moulding, 733
  - sheet, 471
- micro porous metal, 733
- minimum sound transmission, 587
- modal superposition, 615
- mode mixity, 413
- modelling, 471, 635, 823
- multi-axial loading, 281
- multiphase material optimization, 351
- nanoparticles, 183
- NDE, 815
- NDT, 795
- non-destructive testing, 805
- nonlinear, 47, 251
  - FEA, 947
  - response, 87
- numerical solution, 519
- optical fiber sensors, 383
- optimization, 341
- orthotropy, 281
- out-of-plane
  - compression, 875
  - deformation, 643
  - elastic constants, 915
- overall buckling, 527
- parametric study, 67
- peel strength, 753
- periodic, 935
  - structure, 773
- phenolic foam core, 1007
- pin reinforced foam cores, 865
- plate
  - buckling, 201
  - deflections, 201
- PMI-foam, 753
- point forces, 291
- polymeric foams core, 271
- polypropylene, 743
- polyurethane foam, 183
  - core, 977
- post-impact behaviour acoustic emission, 681
- powder space holder method, 733
- pre-crack, 433
- propagation, 461
- pultrusion, 1007
- PVC, 895
  - foam, 87
- quasi-static, 615
- radial basis functions, 231
- rapid prototyping, 773
- reinforced core, 703
- repair, 497, 507
- residual
  - dent, 885
  - strength, 451, 497
- resin transfer molding, 753, 855
- rigid bodies, 261
- robust experimental design, 763
- RTM, 977
- sandwich, 57, 121, 183, 271, 321, 413, 497, 567, 693, 947
  - beam, 131, 211, 221, 423
  - composites, 153
  - composite structures, 625
  - future, 3
  - history, 3
  - layups, 193
  - optimization, 587
  - panel, 97, 291, 341, 373, 451, 471, 519, 661, 773
  - plate, 107, 201, 311, 441
  - primary structure, 13
  - sheet, 723
  - shell, 241
  - structure, 3, 143, 261, 363, 433, 703, 743, 795, 885, 967, 997
  - T-joint, 477
  - uses, 3
- scaling, 171
- screw, 471
- sensitivity analysis, 947
- sequential injection moulding, 743
- shallow sandwich shell, 281
- shear, 183, 895
  - buckling, 441
  - strength, 441
- shell structures, 351
- skin laminate, 915
- slamming, 537
- slotted honeycomb core, 661
- smart composite, 815
- snowboard, 967
- speckle, 905
- stability, 241
- static loading, 477
- static/stability analysis, 311
- stitches, 681
- stitching, 987
- stochastic, 935
  - methods, 925
- strain distribution, 487
- stress
  - concentrations, 77, 161
  - intensity factors, 423
- structural foam, 845
- surface imperfections, 433
- symmetric laminates, 231
- testing, 537
- thermal expansion, 905
- thermoforming, 763
- thermographics, 143

- thermoplastic honeycomb, 875
- thick prepreg skin layers, 783
- three-layer theory, 241
- Timoshenko, 567
- toughness of core materials, 433
- transient
  - dynamics, 519
  - loading, 527
- transverse normal stress, 291
- trigonometric layerwise deformation theory, 231
- ultrasonic scanning, 805
- ultrasound, 795
- underwater/in-air explosion, 97
- vibration, 143, 567, 577
- viscoelastic layer, 211
- Voronoi, 935
- wave propagation, 597, 605
- wind turbine blades, 947
- wrinkle defects, 393
- wrinkling, 201, 281
  - face, 301, 527
  - skin, 441
- X-core, 661
- yield, 117
- Z reinforced sandwich, 271
- zig-zag models, 211